Eur. Phys. J. C (2014) 74:3026
DOI 10.1140/epjc/s10052-014-3026-9

THE EUROPEAN PHYSICAL JOURNAL C

Review

The Physics of the B Factories

Received: 29 July 2014 / Accepted: 29 July 2014 / Published online: 19 November 2014

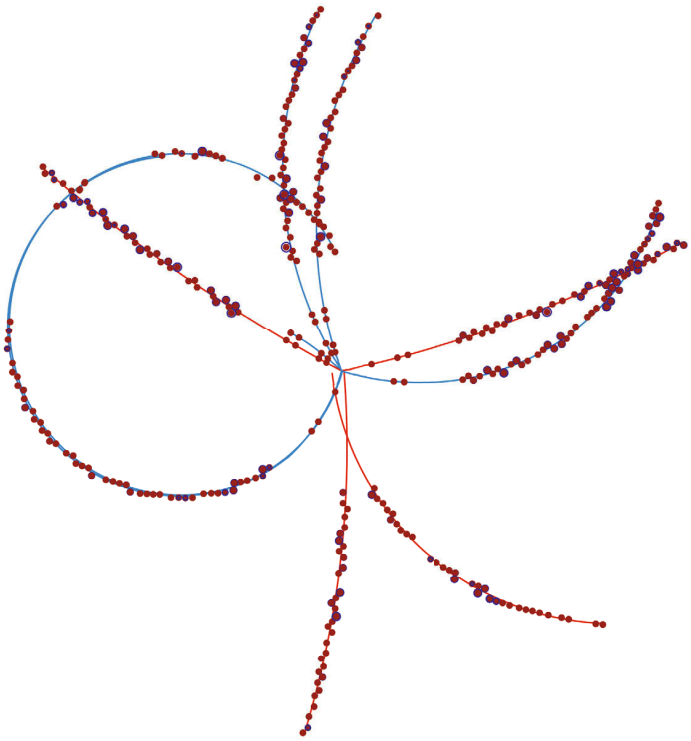

Foreword

"The Physics of the B Factories" describes a decade long effort of physicists in the quest for the precise determination of asymmetry — broken symmetry — between particles and anti-particles. We now recognize that the matter we see around us is the residue — one part in a billion — of the matter and antimatter that existed in the early universe, most of which annihilated into the cosmic background radiation that bathes us. But the question remains: how did the baryonic matter-antimatter asymmetry arise? This book describes the work done by some 1000 physicists and engineers from around the globe on two experimental facilities built to test our understanding of this phenomenon, one at the SLAC National Accelerator Laboratory in California, USA, and a second at the KEK Laboratory, Tsukuba, Japan, and what we have learned from them in broadening our understanding of nature.

Why is our universe dominated by the matter of which we are made rather than equal parts of matter and antimatter? This question has puzzled physicists for decades. However, this was not the question we addressed when we wrote the paper on CP violation in 1972. Our question was whether we can explain the CP violation observed in the K meson decay within the framework of the renormalizable gauge theory. At that time, Sakharov's seminal paper was already published, but it did not attract our attention. If we were aware of the paper, we would have been misled into seeking a model satisfying Sakharov's conditions and our paper might not have appeared.

In our paper, we discussed that we need new particles in order to accommodate CP violation into the renormalizable electroweak theory, and proposed the six-quark scheme as one of the possible ways introducing new particles. We thought that the six-quark scheme is very interesting, but it was just a possibility. The situation changed when the tau-lepton was found and it was followed by the discovery of the Upsilon particle. The existence of the third generation became reality. However, it was still uncertain whether the mixing of the six quarks is a real origin of the observed CP violation. Theoretical calculation of CP asymmetries in the neutral K meson system contains uncertainty from strong interaction effects. What settled this problem were the B Factories built at SLAC and KEK.

These B Factories are extraordinary in many ways. In order to fulfill the requirements of special experiments, the beam energies of the colliding electron and positron are asymmetric, and the luminosity is unprecedentedly high. It is also remarkable that severe competition between the two laboratories boosted their performance. One of us (M. Kobayashi) has been watching the development at KEK very closely as the director of the Institute of Particle and Nuclear Studies of KEK for a period of time. As witnesses, we appreciate the amazing achievement of those who participated in these projects at both laboratories.

The B Factories have contributed a great deal to our understanding of particle physics, as documented in this book. In particular, thanks to the high luminosity far exceeding the design value, experimental groups measured mixing angles precisely and verified that the dominant source of CP violation observed in the laboratory experiments is flavor mixing among the three generations of quarks. Obviously we owe our Nobel Prize to this result.

Now we are awaiting the operation of the next-generation Super B Factories. In spite of its great success, the Standard Model is not an ultimate theory. For example, it is not thought to be possible for the matter dominance of the universe to be explained by the Standard Model. This means that there will still be unknown particles and unknown interactions. We have a lot of theoretical speculations but experimental means are rather limited. There are great expectations for the Super B Factories to reveal a clue to the world beyond the Standard Model.

Makoto Kobayashi
Honorary Professor Emeritus
KEK

Toshihide Maskawa
Director General
Kobayashi-Maskawa Institute for the Origin of Particles and the Universe
Nagoya University

Preface

The inspiration for this book came from François le Diberder. During his term as spokesperson for *BABAR* he laid down a vision for the two B Factory detector collaborations, *BABAR* and Belle, to work together on a book that would describe the methodologies used and physics results obtained by those experiments. A key ideal emphasized from the outset was that this book should be written from a pedagogical perspective; it should be of interest to the student and expert alike. This vision was presented during a *BABAR* collaboration meeting on the island of Elba in May 2008 and a follow up Belle collaboration meeting at KEK, with visiting colleagues from the *BABAR* collaboration, and was embraced by the community. A number of workshops involving people from the theoretical community as well as the two collaborations were held on four continents over the following years. The resulting book, "The Physics of the B Factories", is a testament to the way that this concept captured the zeitgeist on both sides of the Pacific Ocean.

This book is divided into three parts, the first of which provides a brief description of the B Factories, including a short (though not exhaustive) historical perspective, as well as descriptions of the detectors, ancillary data acquisition systems and data (re)processing systems that were built by the two detector collaborations in the late 1990's. The second part of the book discusses tools and methods that are frequently used when analyzing the data collected. These range from details of low level reconstruction algorithms and abstract summaries of statistical methods to high level prescriptions used when evaluating systematic uncertainties on measurements of observables. The third part of the book is devoted to physics results. This includes sufficient theoretical discussion in order for the reader to understand the context of the work being described. We are indebted to our colleagues from the theoretical community who have helped us achieve our goal of explaining the physics of the B Factories in a broader context.

It should be noted that both B Factory experiments are still actively publishing results and as a result the work presented here is a snapshot of the output of the B Factories up to some point in time. Where appropriate, measurements from other experiments have been mentioned, however the focus of this book is on the output of the B Factories. As a result, any brief description of important work by others should be interpreted as a suggestion for further reading on a given topic.

Just as there are two B Factories, many of the observables studied or used in this book have a dual notation in the literature. While preparing this book we have placed the emphasis on the physics rather than trivialities such as convention. The most notable instance of this issue found here is that of the nomenclature used for the angles of the Unitarity Triangle. In order to retain a pedagogical approach we chose a method for selecting between the two notations that is symbolic of their equivalence from the perspective of physics. This choice was decided on the outcome of a coin flip.

It has been a privilege for us to work with our colleagues from the experimental and theoretical communities while compiling this book. The journey of preparing this tome has been as rewarding as being a part of the individual collaborations. This book has come into existence because of the efforts of the many people who have devoted their time and effort writing contributions found herein, and it belongs to the community who helped create it.

Adrian Bevan
Queen Mary University of London

Boštjan Golob
University of Ljubljana
Jožef Stefan Institute

Thomas Mannel
University of Siegen

Soeren Prell
Iowa State University

Bruce Yabsley
University of Sydney

How to cite this work:

The journal version of this book should be used as the correct citation, and the full citation reference is
"Ed. A.J. Bevan, B. Golob, Th. Mannel, S. Prell, and B.D. Yabsley,
Eur. Phys. J. C**74** (2014) 3026, SLAC-PUB-15968, KEK Preprint 2014-3."

Please note that this is the official version of *The Physics of the B Factories.* An auxiliary version of this book will be made available online, both on `arXiv` and the INSPIRE database, under the same entry as the official version of the book. The official version of the book uses the notation ϕ_1, ϕ_2, ϕ_3 for the angles of the Unitarity Triangle, and the auxiliary version uses the notation β, α, γ.

A note on conventions:

This book follows common practice in particle physics by using a relaxed system of natural units. The reduced Planck constant $\hbar$ is set to unity, and electromagnetic expressions include the fine structure constant α rather than dimensionful constants. Nevertheless, the units of energy (GeV, MeV, etc.) are distinguished from those of momentum (GeV/c, MeV/c) and mass (GeV/c^2, MeV/c^2); when length and time are explicitly mentioned, and especially in detector-related discussions, meters and seconds are used rather than the reciprocal of energy.

The treatment of charge conjugation depends on the context. Many analyses are motivated by possible differences between the behaviour of B^0 and $\overline{B}^0$: in such cases, samples of the two states are distinguished. When describing the method, however, if the text specifies reconstruction of $B^0 \to \pi^+ D^-$ with $D^- \to K^+\pi^-\pi^-$, it is usually implied that the equivalent procedure is followed for the charge conjugate mode $\overline{B}^0 \to \pi^- D^+$ with $D^+ \to K^-\pi^+\pi^+$. From time to time, explicit statements are made to resolve potential ambiguities.

Citations follow the author-year format, used in a flexible way. The most common form is surrounded by parentheses (Kobayashi and Maskawa, 1973). However, about 20% of cases incorporate the names of the authors into the grammar of the sentence, as when referring to the classic paper of Kobayashi and Maskawa (1973). Variant forms are used within the text of a parenthesis; all should be clear from the context.

The only unusual feature is the use of three bibliographies: one for *BABAR* papers (page 806), one for Belle papers (page 822), and one for other references (page 835). To avoid tedium, the "et al." is omitted for B Factory papers, citing only the first author of full *BABAR* Collaboration authorlists (Aubert, 2001e), and either the first member (Choi, 2011) or the whole of the first-authorship group (Mizuk, Danilov, 2006) for full Belle Collaboration authorlists. Long authorlists for "other" references are treated normally. The great majority of *BABAR* papers have either Aubert, del Amo Sanchez, or Lees as first author; most early Belle papers have Abe, but from 2002 onwards show great variety. Results are described as being from *BABAR* or Belle if the responsible experiment is not already apparent from the context. Occasionally, a *BABAR* paper and a Belle paper will be cited together, for example in a quoted average or in the body of a table. It should always be clear which bibliography is meant.

In such a long work, there is inevitably some variation in style and usage. As editors, we have endeavoured to keep this to a minimum.

A. J. Bevan*[1], B. Golob*[2,3], Th. Mannel*[4], S. Prell*[5], B. D. Yabsley*[6],

K. Abe[§7], H. Aihara[§8], F. Anulli[§9,10], N. Arnaud[§11], T. Aushev[§12], M. Beneke[§13,14], J. Beringer[§15], F. Bianchi[§16,17], I. I. Bigi[§18], M. Bona[§16,17], N. Brambilla[§13], J. Brodzicka[§19], P. Chang[§20], M. J. Charles[§21], C. H. Cheng[§22], H.-Y. Cheng[§23], R. Chistov[§12], P. Colangelo[§24], J. P. Coleman[§25], A. Drutskoy[§12,26], V. P. Druzhinin[§27,28], S. Eidelman[§27,28], G. Eigen[§29], A. M. Eisner[§30], R. Faccini[§10,31], K. T. Flood[§22], P. Gambino[§16,17], A. Gaz[§32], W. Gradl[§33], H. Hayashii[§34], T. Higuchi[§35], W. D. Hulsbergen[§36], T. Hurth[§33], T. Iijima[§37,38], R. Itoh[§7], P. D. Jackson[§10,31], R. Kass[§39], Yu. G. Kolomensky[§15], E. Kou[§11], P. Križan[§2,3], A. Kronfeld[§40], S. Kumano[§41,42], Y. J. Kwon[§43], T. E. Latham[§44], D. W. G. S. Leith[§45], V. Lüth[§45], F. Martinez-Vidal[§46], B. T. Meadows[§47], R. Mussa[§16,17], M. Nakao[§7], S. Nishida[§7], J. Ocariz[§48], S. L. Olsen[§49], P. Pakhlov[§12,50], G. Pakhlova[§12], A. Palano[§24,51], A. Pich[§52], S. Playfer[§53], A. Poluektov[§27,28], F. C. Porter[§22], S. H. Robertson[§54], J. M. Roney[§55], A. Roodman[§45], Y. Sakai[§7], C. Schwanda[§56], A. J. Schwartz[§47], R. Seidl[§57], S. J. Sekula[§58], M. Steinhauser[§59], K. Sumisawa[§7], E. S. Swanson[§60], F. Tackmann[§61], K. Trabelsi[§7], S. Uehara[§7], S. Uno[§7], R. van de Water[§40], G. Vasseur[§62], W. Verkerke[§63], R. Waldi[§64], M. Z. Wang[§20], F. F. Wilson[§65], J. Zupan[§3,47], A. Zupanc[§3],

I. Adachi[¶7], J. Albert[¶55], Sw. Banerjee[¶55], M. Bellis[¶66], E. Ben-Haim[¶48], P. Biassoni[¶67,68], R. N. Cahn[¶15], C. Cartaro[¶45], J. Chauveau[¶48], C. Chen[¶5], C. C. Chiang[¶20], R. Cowan[¶69], J. Dalseno[¶70], M. Davier[¶11], C. Davies[¶71], J. C. Dingfelder[¶45,72], B. Echenard[¶22], D. Epifanov[¶8], B. G. Fulsom[¶45], A. M. Gabareen[¶45], J. W. Gary[¶73], R. Godang[¶74], M. T. Graham[¶45], A. Hafner[¶33], B. Hamilton[¶36], T. Hartmann[¶64], K. Hayasaka[¶37,38], C. Hearty[¶75], Y. Iwasaki[¶7], A. Khodjamirian[¶4], A. Kusaka[¶8], A. Kuzmin[¶27,28], G. D. Lafferty[¶76], A. Lazzaro[¶67,68], J. Li[¶49], D. Lindemann[¶45], O. Long[¶73], A. Lusiani[¶77,78], G. Marchiori[¶48], M. Martinelli[¶24,51], K. Miyabayashi[¶34], R. Mizuk[¶12,50], G. B. Mohanty[¶79], D. R. Muller[¶45], H. Nakazawa[¶80], P. Ongmongkolkul[¶22], S. Pacetti[¶81,82], F. Palombo[¶67,68], T. K. Pedlar[¶83], L. E. Piilonen[¶84], A. Pilloni[¶10,31], V. Poireau[¶85], K. Prothmann[¶70,86], T. Pulliam[¶45], M. Rama[¶9], B. N. Ratcliff[¶45], P. Roudeau[¶11], S. Schrenk[¶47], T. Schroeder[¶87], K. R. Schubert[¶88], C. P. Shen[¶89], B. Shwartz[¶27,28], A. Soffer[¶90], E. P. Solodov[¶27,28], A. Somov[¶47], M. Starič[¶3], S. Stracka[¶67,68], A. V. Telnov[¶91], K. Yu. Todyshev[¶27,28], T. Tsuboyama[¶7], T. Uglov[¶12,26], A. Vinokurova[¶27,28], J. J. Walsh[¶77,92], Y. Watanabe[¶93], E. Won[¶94], G. Wormser[¶11], D. H. Wright[¶45], S. Ye[¶95], C. C. Zhang[¶96],

S. Abachi[97], A. Abashian[†84], K. Abe[98], K. Abe[75], N. Abe[99], R. Abe[100], T. Abe[7], T. Abe[32], G. S. Abrams[15], I. Adam[45], K. Adamczyk[19], A. Adametz[101], T. Adye[65], A. Agarwal[55], H. Ahmed[55], M. Ahmed[102], S. Ahmed[102], B. S. Ahn[94], H. S. Ahn[49], I. J. R. Aitchison[45], K. Akai[7], S. Akar[48], M. Akatsu[38], M. Akemoto[7], R. Akhmetshin[27], R. Akre[†45], M. S. Alam[102], J. N. Albert[11], R. Aleksan[62], J. P. Alexander[7], G. Alimonti[103], M. T. Allen[45], J. Allison[76], T. Allmendinger[39], J. R. G. Alsmiller[104], D. Altenburg[105], K. E. Alwyn[76], Q. An[106], J. Anderson[36], R. Andreassen[47], D. Andreotti[107], M. Andreotti[107,108], J. C. Andress[109], C. Angelini[77,92], D. Anipko[27], A. Anjomshoaa[53], P. L. Anthony[45], E. A. Antillon[32], E. Antonioli[110], K. Aoki[7], J. F. Arguin[111], K. Arinstein[27,28], K. Arisaka[97], K. Asai[34], M. Asai[112], Y. Asano[113], D. J. Asgeirsson[75], D. M. Asner[114], T. Aso[115], M. L. Aspinwall[116], D. Aston[45], H. Atmacan[73], B. Aubert[85], V. Aulchenko[27,28], R. Ayad[117], T. Azemoon[45], T. Aziz[79], V. Azzolini[46], D. E. Azzopardi[1], M. A. Baak[118], J. J. Back[44], S. Bagnasco[119,120], S. Bahinipati[121], D. S. Bailey[76], S. Bailey[122], P. Bailly[48], N. van Bakel[45], A. M. Bakich[6], A. Bala[123], V. Balagura[12], R. Baldini-Ferroli[9], Y. Ban[124], E. Banas[19], H. R. Band[125], S. Banerjee[79], E. Baracchini[10,31], R. Barate[85], E. Barberio[126], M. Barbero[103], D. J. Bard[45], T. Barillari[32], N. R. Barlow[76], R. J. Barlow[76], M. Barrett[103,127], W. Bartel[61], J. Bartelt[45], R. Bartoldus[45], G. Batignani[77,92], M. Battaglia[15], J. M. Bauer[128], A. Bay[129], M. Beaulieu[111], P. Bechtle[45], T. W. Beck[30], J. Becker[32], J. Becla[45], I. Bedny[27,28], S. Behari[7], P. K. Behera[21,130], E. Behn[36], L. Behr[131], C. Beigbeder[11], D. Beiline[27], R. Bell[†45], F. Bellini[10,31], G. Bellodi[1], K. Belous[132], M. Benayoun[48], G. Benelli[39], J. F. Benitez[45], M. Benkebil[11], N. Berger[45], J. Bernabeu[46], D. Bernard[131], R. Bernet[53], F. U. Bernlochner[55], J. W. Berryhill[63], K. Bertsche[45], P. Besson[†62], D. S. Best[133], S. Bettarini[77,92], D. Bettoni[107], V. Bhardwaj[34], W. Bhimji[116], B. Bhuyan[134], B. Bhuyan[135], M. E. Biagini[9], M. Biasini[81,82], K. van Bibber[136], J. Biesiada[91], I. Bingham[25], R. M. Bionta[136], M. Bischofberger[34], U. Bitenc[3], I. Bizjak[3], F. Blanc[32], G. Blaylock[137], V. E. Blinov[27,28,138], E. Bloom[45], P. C. Bloom[32], N. L. Blount[139], J. Blouw[117], M. Bly[65], S. Blyth[140], C. T. Boeheim[45], M. Bomben[48], A. Bondar[27,28], M. Bondioli[133], G.R. Bonneaud[48], G. Bonvicini[141], M. Booke[†128], J. Booth[133], C. Borean[142,143], A. W. Borgland[15], E. Borsato[144,145], F. Bosi[77], L. Bosisio[142,143], A. A. Botov[27], J. Bougher[146], K. Bouldin[45], P. Bourgeois[62], D. Boutigny[85], D. A. Bowerman[116], A. M. Boyarski[45], R. F. Boyce[45], J. T. Boyd[109], A. Bozek[19], C. Bozzi[107], M. Bračko[3,147], G. Brandenburg[†122], T. Brandt[88], B. Brau[39], J. Brau[139], A. B. Breon[15], D. Breton[11], C. Brew[65], H. Briand[48], P. G. Bright-Thomas[148], V. Brigljević[136], D. I. Britton[54], F. Brochard[131], B. Broomer[32], J. Brose[88], T. E. Browder[103], C. L. Brown[149], C. M. Brown[55], D. N. Brown[15], D. N. Brown[146], M. Browne[45], M. Bruinsma[133], S. Brunet[111], F. Bucci[77,92], C. Buchanan[97], O. L. Buchmueller[45], C. Bünger[64], W. Bugg[150], A. D. Bukin[†27,28], R. Bula[102], H. Bulten[118], P. R. Burchat[66], W. Burgess[45], J. P. Burke[25], J. Button-Shafer[15], A. R. Buzykaev[27], A. Buzzo[119], Y. Cai[45], R. Calabrese[107,108], A. Calcaterra[9], G. Calderini[48], B. Camanzi[127], E. Campagna[77,92], C. Campagnari[63], R. Capra[119,120], V. Carassiti[107], M. Carpinelli[77,92], M. Carroll[25], G. Casarosa[77,92], B. C. K. Casey[103], N. M. Cason[18], G. Castelli[144], N. Cavallo[151], G. Cavoto[10], A. Cecchi[107],

R. Cenci[77,92], G. Cerizza[67,68], A. Cervelli[77,92], A. Ceseracciu[45], X. Chai[21], K. S. Chaisanguanthum[122], M. C. Chang[152], Y. H. Chang[80], Y. W. Chang[20], D. S. Chao[22], M. Chao[133], Y. Chao[20], E. Charles[15], C. A. Chavez[25], R. Cheaib[54], V. Chekelian[70], A. Chen[80], A. Chen[117], E. Chen[22], G. P. Chen[96], H. F. Chen[106], J. -H. Chen[20], J. C. Chen[96], K. F. Chen[20], P. Chen[20], S. Chen[32], W. T. Chen[80], X. Chen[125], X. R. Chen[153], Y. Q. Chen[20], B. Cheng[125], B. G. Cheon[154], N. Chevalier[109], Y. M. Chia[76], S. Chidzik[91], K. Chilikin[12], M. V. Chistiakova[15], R. Cizeron[11], I. S. Cho[43], K. Cho[155], V. Chobanova[70], H. H. F. Choi[55], K. S. Choi[43], S. K. Choi[156], Y. Choi[157], Y. K. Choi[157], S. Christ[64], P. H. Chu[20], S. Chun[97], A. Chuvikov[91], G. Cibinetto[107], D. Cinabro[141], A. R. Clark[15], P. J. Clark[53], C. K. Clarke[1], R. Claus[45], B. Claxton[65], Z. C. Clifton[32], J. Cochran[5], J. Cohen-Tanugi[131], H. Cohn[150], T. Colberg[88], S. Cole[6], F. Colecchia[144,145], C. Condurache[65], R. Contri[119,120], P. Convert[62], M. R. Convery[45], P. Cooke[25], N. Copty[153], C. M. Cormack[1], F. Dal Corso[144], L. A. Corwin[39], F. Cossutti[142], D. Cote[111], A. Cotta Ramusino[107], W. N. Cottingham[109], F. Couderc[85], D. P. Coupal[45], R. Covarelli[81,82], G. Cowan[149], W. W. Craddock[45], G. Crane[45], H. B. Crawley[5], L. Cremaldi[128], A. Crescente[144], M. Cristinziani[45], J. Crnkovic[158], G. Crosetti[119,120], T. Cuhadar-Donszelmann[75], A. Cunha[63], S. Curry[133], A. D'Orazio[10,31], S. Dû[11], G. Dahlinger[88], B. Dahmes[63], C. Dallapiccola[137], N. Danielson[91], M. Danilov[12,26], A. Das[79], M. Dash[84], S. Dasu[125], M. Datta[125], F. Daudo[16], P. D. Dauncey[116], P. David[48], C. L. Davis[146], C. T. Day[15], F. De Mori[16,17], G. De Domenico[62], N. De Groot[65], C. De la Vaissière[48], Ch. de la Vaissière[48], A. de Lesquen[62], G. De Nardo[151,159], R. de Sangro[9], A. De Silva[160], S. DeBarger[45], F. J. Decker[45], P. del Amo Sanchez[85], L. Del Buono[48], V. Del Gamba[77,92], D. del Re[10,31], G. Della Ricca[142,143], A. G. Denig[33,161], D. Derkach[11], I. M. Derrington[32], H. DeStaebler†[45], J. Destree[32], S. Devmal[47], B. Dey[73], B. Di Girolamo[16], E. Di Marco[10,31], M. Dickopp[88], M. O. Dima[32], S. Dittrich[64], S. Dittongo[142,143], P. Dixon[1], L. Dneprovsky†[27], F. Dohou[131], Y. Doi[7], Z. Doležal[162], D. A. Doll[22], M. Donald[45], L. Dong[5], L. Y. Dong[96], J. Dorfan[45], A. Dorigo[144], M. P. Dorsten[22], R. Dowd[126], J. Dowdell[65], Z. Drásal[162], J. Dragic[7], B. W. Drummond[95], R. S. Dubitzky[101], G. P. Dubois-Felsmann[45], M. S. Dubrovin[47], Y. C. Duh[152], Y. T. Duh[20], D. Dujmic[69], W. Dungel[56], W. Dunwoodie[45], D. Dutta[134], A. Dvoretskii[22], N. Dyce[109], M. Ebert[45], E. A. Eckhart[117], S. Ecklund[45], R. Eckmann[163], P. Eckstein[88], C. L. Edgar[76], A. J. Edwards[164], U. Egede[116], A. M. Eichenbaum[125], P. Elmer[91], S. Emery[62], Y. Enari[38], R. Enomoto[7], E. Erdos[32], R. Erickson[45], J. A. Ernst[102], R. J. Erwin[22], M. Escalier[62], V. Eschenburg[128], I. Eschrich[133], S. Esen[47], L. Esteve[62], F. Evangelisti[107], C. W. Everton[126], V. Eyges[5], C. Fabby[47], F. Fabozzi[151], S. Fahey[32], M. Falbo[165], S. Fan[45], F. Fang[103], F. Fang[22], C. Fanin[144], A. Farbin[36], H. Farhat[141], J. E. Fast[114], M. Feindt[161], A. Fella[110], E. Feltresi[144,145], T. Ferber[61], R. E. Fernholz[91], S. Ferrag[131], F. Ferrarotto[10], F. Ferroni[10,31], R. C. Field[45], A. Filippi[16,17], G. Finocchiaro[9], E. Fioravanti[107], J. Firmino da Costa[11], P.-A. Fischer[5], A. S. Fisher[45], P. H. Fisher[69], C. J. Flacco[30], R. L. Flack[116], H. U. Flaecher[149], J. Flanagan[7], J. M. Flanigan[63], K. E. Ford[148], W. T. Ford[32], I. J. Forster[25], A. C. Forti[76], F. Forti[77,92], D. Fortin[55], B. Foster[109], S. D. Foulkes[73], G. Fouque[131], J. Fox[45], P. Franchini[107], M. Franco Sevilla[63], B. Franek[65], E. D. Frank[166], K. B. Fransham[55], S. Fratina[3], K. Fratini[10], A. Frey[167], R. Frey[139], M. Friedl[56], M. Fritsch[33], J. R. Fry[25], H. Fujii[7], M. Fujikawa[34], Y. Fujita[7], Y. Fujiyama[99], C. Fukunaga[168], M. Fukushima[7], J. Fullwood[76], Y. Funahashi[7], Y. Funakoshi[7], F. Furano[144], M. Furman[15], K. Furukawa[7], H. Futterschneider[88], E. Gabathuler[25], T. A. Gabriel[104], N. Gabyshev[27,28], F. Gaede[32], N. Gagliardi[144,145], A. Gaidot[62], J.-M. Gaillard[85], J. R. Gaillard[116], S. Galagedera[65], F. Galeazzi[144,145], F. Gallo[16,17], D. Gamba[16,17], R. Gamet[25], K. K. Gan[39], P. Gandini[67,68], S. Ganguly[141], S. F. Ganzhur[62], Y. Y. Gao[169], I. Gaponenko[45], A. Garmash[27,28], J. Garra Tico[170], I. Garzia[107], M. Gaspero[10,31], F. Gastaldi[131], C. Gatto[151], V. Gaur[79], N. I. Geddes[65], T. L. Geld[47], J.-F. Genat[48], K. A. George[1], M. George[25], S. George[149], Z. Georgette[62], T. J. Gershon[7,44], M. S. Gill[15], R. Gillard[141], J. D. Gilman[32], F. Giordano[158], M. A. Giorgi[77,92], P.-F. Giraud[62], L. Gladney[166], T. Glanzman[45], R. Glattauer[56], A. Go[80], K. Goetzen[87], Y. M. Goh[154], G. Gokhroo[79], P. Goldenzweig[47], V. B. Golubev[27,28], G. P. Gopal[65], A. Gordon[126], A. Gorišek[3], V. I. Goriletsky[171], R. Gorodeisky[90], L. Gosset[62], K. Gotow[84], S. J. Gowdy[45], P. Graffin[62], S. Grancagnolo[142,143], E. Grauges[170], G. Graziani[62], M. G. Green[149], M. G. Greene[172], G. J. Grenier[21], P. Grenier[45], K. Griessinger[33], A. A. Grillo[30], B.V. Grinyov[171], A. V. Gritsan[169], G. Grosdidier[11], M. Grosse Perdekamp[57,158], P. Grosso[16], M. Grothe[30], Y. Groysman[15], O. Grünberg[64], E. Guido[119,120], H. Guler[103], N. J. W. Gunawardane[116], Q. H. Guo[166], R. S. Guo[173], Z. J. Guo[169], N. Guttman[90], H. Ha[94], H. C. Ha[94], T. Haas[45], J. Haba[7], J. Hachtel[32], H. K. Hadavand[174], T. Hadig[45], C. Hagner[84], M. Haire[175], F. Haitani[98], T. Haji[8], G. Haller[45], V. Halyo[45], K. Hamano[55], H. Hamasaki[7], G. Hamel de Monchenault[62], J. Hamilton[45], R. Hamilton[21], O. Hamon[48], B. Y. Han[94], Y. L. Han[96], H. Hanada[176], K. Hanagaki[91], F. Handa[176], J. E. Hanson[22], A. Hanushevsky[45], K. Hara[7], T. Hara[7], Y. Harada[100], P. F. Harrison[44], T. J. Harrison[148], B. Harrop[91], A. J. Hart[148], P. A. Hart[76], B. L. Hartfiel[97], J. L. Harton[117], T. Haruyama[7], A. Hasan[45], Y. Hasegawa[177], C. Hast[45], N. C. Hastings[8], K. Hasuko[57], A. Hauke[105], C. M. Hawkes[148], K. Hayashi[7], M. Hazumi[7], C. Hee[45], E. M. Heenan[126], D. Heffernan[178], T. Held[87], R. Henderson[160], S. W. Henderson[69], S. S. Hertzbach[137], S. Hervé[62], M. Heß[64], C. A. Heusch[30], A. Hicheur[85], Y. Higashi[7], Y. Higasino[38], I. Higuchi[176], S. Hikita[179], E. J. Hill[174], T. Himel[45], L. Hinz[129], T. Hirai[99], H. Hirano[179], J. F. Hirschauer[32], D. G. Hitlin[22], N. Hitomi[7], M. C. Hodgkinson[76], A. Höcker[11], C. T. Hoi[20], T. Hojo[178], T. Hokuue[38], J. J. Hollar[125], T. M. Hong[63], K. Honscheid[39], B. Hooberman[15], D. A. Hopkins[149], Y. Horii[37,38], Y. Hoshi[98], K. Hoshina[179], S. Hou[20,80], W. S. Hou[20], T. Hryn'ova[45], Y. B. Hsiung[20], C. L. Hsu[20], S. C. Hsu[20], H. Hu[125], T. Hu[117], H. C. Huang[20], T. J. Huang[20], Y. C. Huang[173], Z. Huard[47], M. E. Huffer[45], D. Hufnagel[39],

T. Hung[45], D. E. Hutchcroft[25], H. J. Hyun[180], S. Ichizawa[99], T. Igaki[38], A. Igarashi[113], S. Igarashi[7], Y. Igarashi[7], O. Igonkina[139], K. Ikado[38], H. Ikeda[7], H. Ikeda[7], K. Ikeda[34], J. Ilic[44], K. Inami[38], W. R. Innes[45], Y. Inoue[181], A. Ishikawa[7], A. Ishikawa[176], H. Ishino[99], K. Itagaki[176], S. Itami[38], K. Itoh[8], V. N. Ivanchenko[27], R. Iverson[45], M. Iwabuchi[43], G. Iwai[100], M. Iwai[7], S. Iwaida[113], M. Iwamoto[182], H. Iwasaki[7], M. Iwasaki[8], M. Iwasaki[139], T. Iwashita[34], J. M. Izen[95], D. J. Jackson[178], F. Jackson[76], G. Jackson[76], P. S. Jackson[149], R. G. Jacobsen[15], C. Jacoby[129], I. Jaegle[103], V. Jain[102], P. Jalocha[19], H. K. Jang[49], H. Jasper[105], A. Jawahery[36], S. Jayatilleke[47], C. M. Jen[20], F. Jensen[15], C. P. Jessop[18], X. B. Ji[96], M. J. J. John[48], D. R. Johnson[32], J. R. Johnson[125], S. Jolly[127], M. Jones[103], K. K. Joo[7], N. Joshi[79], N. J. Joshi[79], D. Judd[175], T. Julius[126], R. W. Kadel[15], J. A. Kadyk[15], H. Kagan[39], R. Kagan[12], D. H. Kah[180], S. Kaiser[88], H. Kaji[38], S. Kajiwara[178], H. Kakuno[168], T. Kameshima[113], J. Kaminski[45], T. Kamitani[7], J. Kaneko[99], J. H. Kang[43], J. S. Kang[94], T. Kani[38], P. Kapusta[19], T.M. Karbach[105], M. Karolak[62], Y. Karyotakis[85], K. Kasami[7], G. Katano[7], S. U. Kataoka[34], N. Katayama[7], E. Kato[176], Y. Kato[38], H. Kawai[182], H. Kawai[8], M. Kawai[7], N. Kawamura[183], T. Kawasaki[100], J. Kay[65], M. Kay[25], M. P. Kelly[76], M. H. Kelsey[45], N. Kent[103], L. T. Kerth[15], A. Khan[127], H. R. Khan[99], D. Kharakh[45], A. Kibayashi[7], H. Kichimi[7], C. Kiesling[70], M. Kikuchi[7], E. Kikutani[7], B. H. Kim[49], C. H. Kim[49], D. W. Kim[157], H. Kim[45], H. J. Kim[180], H. J. Kim[43], H. O. Kim[180], H. W. Kim[94], J. B. Kim[94], J. H. Kim[155], K. T. Kim[94], M. J. Kim[180], P. Kim[45], S. K. Kim[49], S. M. Kim[157], T. H. Kim[43], Y. I. Kim[180], Y. J. Kim[155], G. J. King[55], K. Kinoshita[47], A. Kirk[148], D. Kirkby[133], I. Kitayama[95], M. Klemetti[54], V. Klose[184], J. Klucar[3], N. S. Knecht[75], K. J. Knoepfel[18], D. J. Knowles[148], B. R. Ko[94], N. Kobayashi[99], S. Kobayashi[185], T. Kobayashi[7], M. J. Kobel[88], S. Koblitz[70], H. Koch[87], M. L. Kocian[45], P. Kodyš[162], K. Koeneke[69], R. Kofler[137], S. Koike[7], S. Koishi[99], H. Koiso[7], J. A. Kolb[139], S. D. Kolya[76], Y. Kondo[7], H. Konishi[179], P. Koppenburg[7], V. B. Koptchev[137], T. M. B. Kordich[172], A. A. Korol[27,28], K. Korotushenko[91], S. Korpar[3,147], R. T. Kouzes[114], D. Kovalskyi[63], R. Kowalewski[55], Y. Kozakai[38], W. Kozanecki[62], J. F. Kral[15], A. Krasnykh[45], R. Krause[88], E. A. Kravchenko[27,28], J. Krebs[45], A. Kreisel[32], M. Kreps[161], M. Krishnamurthy[150], R. Kroeger[128], W. Kroeger[45], P. Krokovny[27,28], B. Kronenbitter[161], J. Kroseberg[30], T. Kubo[7], T. Kuhr[161], G. Kukartsev[15], R. Kulasiri[47], A. Kulikov[45], R. Kumar[186], S. Kumar[123], T. Kumita[168], T. Kuniya[185], M. Kunze[87], C. C. Kuo[80], T. -L. Kuo[20], H. Kurashiro[99], E. Kurihara[182], N. Kurita[45], Y. Kuroki[178], A. Kurup[149], P. E. Kutter[125], N. Kuznetsova[63], P. Kvasnička[162], P. Kyberd[127], S. H. Kyeong[43], H. M. Lacker[184], C. K. Lae[169], E. Lamanna[10,31], J. Lamsa[5], L. Lanceri[142,143], L. Landi[107,108], M. I. Lang[69], D. J. Lange[136], J. S. Lange[187], U. Langenegger[101], M. Langer[62], A. J. Lankford[133], F. Lanni[67,68], S. Laplace[11], E. Latour[131], Y. P. Lau[91], D. R. Lavin[53], J. Layter[73], H. Lebbolo[48], C. LeClerc[15], T. Leddig[64], G. Leder[56], F. Le Diberder[11], C. L. Lee[122], J. Lee[49], J. S. Lee[157], M. C. Lee[20], M. H. Lee[7], M. J. Lee[49], M. J. Lee[15], S.-J. Lee[21], S. E. Lee[49], S. H. Lee[49], Y. J. Lee[20], J. P. Lees[85], M. Legendre[62], M. Leitgab[158], R. Leitner[162], E. Leonardi[10], C. Leonidopoulos[91], V. Lepeltier[†11], Ph. Leruste[48], T. Lesiak[19,188], M. E. Levi[15], S. L. Levy[63], B. Lewandowski[†87], M. J. Lewczuk[55], P. Lewis[45], H. Li[125], H. B. Li[96], S. Li[45], X. Li[49], X. Li[137], Y. Li[84], Y. Li[146], L. Li Gioi[10,31], J. Libby[45,189], J. Lidbury[65], V. Lillard[36], C. L. Lim[43], A. Limosani[126], C. S. Lin[137], J. Y. Lin[152], S. W. Lin[20], Y. S. Lin[20], B. Lindquist[45], C. Lindsay[55], L. Lista[151], C. Liu[106], F. Liu[73], H. Liu[153], H. M. Liu[96], J. Liu[102], R. Liu[125], T. Liu[91], Y. Liu[47], Z. Q. Liu[96], D. Liventsev[7,12], M. Lo Vetere[119,120], C. B. Locke[55], W. S. Lockman[30], F. Di Lodovico[1], V. Lombardo[67,68], G. W. London[62], D. Lopes Pegna[91], L. Lopez[24,51], N. Lopez-March[46], J. Lory[48], J. M. LoSecco[18], X. C. Lou[95], R. Louvot[129], A. Lu[63], C. Lu[91], M. Lu[139], R. S. Lu[20], T. Lueck[55], S. Luitz[45], P. Lukin[27,28], P. Lund[150], E. Luppi[107,108], A. M. Lutz[11], O. Lutz[161], G. Lynch[15], H. L. Lynch[45], A. J. Lyon[76], V. R. Lyubinsky[171], D. B. MacFarlane[45], C. Mackay[109], J. MacNaughton[7], M. M. Macri[119], S. Madani[65], W. F. Mader[88], S. A. Majewski[66], G. Majumder[79], Y. Makida[7], B. Malaescu[11], R. Malaguti[107], J. Malclès[48], U. Mallik[21], E. Maly[88], H. Mamada[179], A. Manabe[7], G. Mancinelli[47], M. Mandelkern[133], F. Mandl[56], P. F. Manfredi[190], D. J. J. Mangeol[54], E. Manoni[81], Z. P. Mao[96], M. Margoni[144,145], C. E. Marker[149], G. Markey[65], J. Marks[101], D. Marlow[91], V. Marques[62], H. Marsiske[45], S. Martellotti[9], E. C. Martin[133], J. P. Martin[111], L. Martin[48], A. J. Martinez[30], M. Marzolla[144], A. Mass[109], M. Masuzawa[7], A. Mathieu[131], P. Matricon[131], T. Matsubara[8], T. Matsuda[191], T. Matsuda[7], H. Matsumoto[100], S. Matsumoto[192], T. Matsumoto[168], H. Matsuo[†193], T. S. Mattison[75], D. Matvienko[27,28], A. Matyja[19], B. Mayer[62], M. A. Mazur[63], M. A. Mazzoni[10], M. McCulloch[45], J. McDonald[45], J. D. McFall[109], P. McGrath[149], A. K. McKemey[127], J. A. McKenna[75], S. E. Mclachlin[†54], S. McMahon[25], T. R. McMahon[149], S. McOnie[6], T. Medvedeva[12], R. Melen[45], B. Mellado[125], W. Menges[1], S. Menke[45], A. M. Merchant[15], J. Merkel[105], R. Messner[†45], S. Metcalfe[45], S. Metzler[22], N. T. Meyer[21], T. I. Meyer[66], W. T. Meyer[5], A. K. Michael[32], G. Michelon[144,145], S. Michizono[7], P. Micout[62], V. Miftakov[91], A. Mihalyi[125], Y. Mikami[176], D. A. Milanes[46], M. Milek[54], T. Mimashi[7], J. S. Minamora[22], C. Mindas[91], S. Minutoli[119], L. M. Mir[15], K. Mishra[47], W. Mitaroff[56], H. Miyake[178], T. S. Miyashita[66], H. Miyata[100], Y. Miyazaki[38], L. C. Moffitt[126], G. B. Mohanty[44], A. Mohapatra[130], A. K. Mohapatra[125], D. Mohapatra[114], A. Moll[70], G. R. Moloney[126], J. P. Mols[62], R. K. Mommsen[133], M. R. Monge[119,120], D. Monorchio[151,159], T. B. Moore[137], G. F. Moorhead[126], P. Mora de Freitas[131], M. Morandin[144], N. Morgan[84], S. E. Morgan[148], M. Morganti[77,92], S. Morganti[10], S. Mori[113], T. Mori[38], M. Morii[122], J. P. Morris[39], F. Morsani[77], G. W. Morton[116], L. J. Moss[45], J. P. Mouly[62], R. Mount[45], J. Mueller[60], R. Müller-Pfefferkorn[88], M. Mugge[136], F. Muheim[53], A. Muir[25], E. Mullin[73], M. Munerato[107,108], A. Murakami[185], T. Murakami[7], N. Muramatsu[194], P. Musico[119], I. Nagai[38], T. Nagamine[176], Y. Nagasaka[112], Y. Nagashima[178], S. Nagayama[7], M. Nagel[32], M. T. Naisbit[76], T. Nakadaira[8],

Y. Nakahama[8], M. Nakajima[176], T. Nakajima[176], I. Nakamura[7], T. Nakamura[99], T. T. Nakamura[7], E. Nakano[181], H. Nakayama[7], J. W. Nam[157], S. Narita[176], I. Narsky[22], J .A. Nash[116], Z. Natkaniec[19], U. Nauenberg[32], M. Nayak[189], H. Neal[45], E. Nedelkovska[70], M. Negrini[107], K. Neichi[98], D. Nelson[45], S. Nelson[45], N. Neri[67], G. Nesom[30], S. Neubauer[161], D. Newman-Coburn[†1], C. Ng[8], X. Nguyen[111], H. Nicholson[195], C. Niebuhr[61], J. Y. Nief[11], M. Niiyama[193], M. B. Nikolich[116], N. K. Nisar[79], K. Nishimura[103], Y. Nishio[38], O. Nitoh[179], R. Nogowski[88], S. Noguchi[34], T. Nomura[193], M. Nordby[45], Y. Nosochkov[45], A. Novokhatski[45], S. Nozaki[176], T. Nozaki[7], I. M. Nugent[55], C. P. O'Grady[45], S. W. O'Neale[†148], F. G. O'Neill[45], B. Oberhof[77,92], P. J. Oddone[15], I. Ofte[45], A. Ogawa[57], K. Ogawa[7], S. Ogawa[196], Y. Ogawa[7], R. Ohkubo[7], K. Ohmi[7], Y. Ohnishi[7], F. Ohno[99], T. Ohshima[38], Y. Ohshima[99], N. Ohuchi[7], K. Oide[7], N. Oishi[38], T. Okabe[38], N. Okazaki[179], T. Okazaki[34], S. Okuno[93], E. O. Olaiya[65], A. Olivas[32], P. Olley[65], J. Olsen[91], S. Ono[99], G. Onorato[151,159], A. P. Onuchin[27,28,138], Y. Onuki[8], T. Ooba[182], T. J. Orimoto[15], T. Oshima[38], I. L. Osipenkov[15], W. Ostrowicz[19], C. Oswald[72], S. Otto[88], J. Oyang[22], A. Oyanguren[46], H. Ozaki[7], V. E. Ozcan[45], H. P. Paar[174], C. Padoan[107,108], K. Paick[175], H. Palka[†19], B. Pan[102], Y. Pan[125], W. Panduro Vazquez[116], J. Panetta[166], A. I. Panova[171], R. S. Panvini[†197], E. Panzenböck[34,167], E. Paoloni[77,92], P. Paolucci[151], M. Pappagallo[24,51], S. Paramesvaran[149], C. S. Park[49], C. W. Park[157], H. Park[180], H. Park[32], H. K. Park[180], K. S. Park[157], W. Park[153], R. J. Parry[25], N. Parslow[6], S. Passaggio[119], F. C. Pastore[119,120], P. M. Patel[†54], C. Patrignani[119,120], P. Patteri[9], T. Pavel[45], J. Pavlovich[146], D. J. Payne[25], L. S. Peak[6], D. R. Peimer[90], M. Pelizaeus[87], R. Pellegrini[67,68], M. Pelliccioni[16,17], C. C. Peng[20], J. C. Peng[20], K. C. Peng[20], T. Peng[106], Y. Penichot[62], S. Pennazzi[81,82], M. R. Pennington[44], R. C. Penny[148], A. Penzkofer[32], A. Perazzo[45], A. Perez[77], M. Perl[45], M. Pernicka[†56], J.-P. Perroud[129], I. M. Peruzzi[9,82], R. Pestotnik[3], K. Peters[87], M. Peters[103], B. A. Petersen[66], T. C. Petersen[11], E. Petigura[15], S. Petrak[45], A. Petrella[107], M. Petrič[3], A. Petzold[105], M. G. Pia[119], T. Piatenko[22], D. Piccolo[151,159], M. Piccolo[9], L. Piemontese[107], M. Piemontese[45], M. Pierini[125], S. Pierson[45], M. Pioppi[81,82], G. Piredda[10], M. Pivk[48], S. Plaszczynski[11], F. Polci[10,11,31], A. Pompili[24,51], P. Poropat[†142,143], M. Posocco[144], C. T. Potter[139], R. J. L. Potter[1], V. Prasad[135], E. Prebys[91], E. Prencipe[33], J. Prendki[48], R. Prepost[125], M. Prest[142], M. Prim[161], M. Pripstein[15], X. Prudent[85], S. Pruvot[11], E. M. T. Puccio[66], M. V. Purohit[153], N. D. Qi[96], H. Quinn[45], J. Raaf[47], R. Rabberman[91], F. Raffaelli[77], G. Ragghianti[150], S. Rahatlou[174], A. M. Rahimi[39], R. Rahmat[139], A. Y. Rakitin[22], A. Randle-Conde[58], P. Rankin[32], I. Rashevskaya[142], S. Ratkovsky[45], G. Raven[118], V. Re[190], M. Reep[128], J. J. Regensburger[39], J. Reidy[128], R. Reif[45], B. Reisert[70], C. Renard[131], F. Renga[10,31], S. Ricciardi[65], J. D. Richman[63], J. L. Ritchie[163], M. Ritter[70], C. Rivetta[45], G. Rizzo[77,92], C. Roat[66], P. Robbe[85], D. A. Roberts[36], A. I. Robertson[53], E. Robutti[119], S. Rodier[11], D. M. Rodriguez[32], J. L. Rodriguez[103], R. Rodriguez[45], N. A. Roe[15], M. Röhrken[161], W. Roethel[65], J. Rolquin[62], L. Romanov[27], A. Romosan[15], M. T. Ronan[†15], G. Rong[96], F. J. Ronga[7], L. Roos[48], N. Root[27], M. Rosen[103], E. I. Rosenberg[5], A. Rossi[81], A. Rostomyan[61], M. Rotondo[144], E. Roussot[131], J. Roy[32], M. Rozanska[19], Y. Rozen[63], Y. Rozen[198], A. E. Rubin[5], W. O. Ruddick[32], A. M. Ruland[163], K. Rybicki[19], A. Ryd[22], S. Ryu[49], J. Ryuko[178], S. Sabik[111], R. Sacco[1], M. A. Saeed[102], F. Safai Tehrani[10], H. Sagawa[7], H. Sahoo[103], S. Sahu[20], M. Saigo[176], T. Saito[176], S. Saitoh[199], K. Sakai[7], H. Sakamoto[193], H. Sakaue[181], M. Saleem[127], A. A. Salnikov[45], E. Salvati[137], F. Salvatore[149], A. Samuel[22], D. A. Sanders[128], P. Sanders[116], S. Sandilya[79], F. Sandrelli[77,92], W. Sands[91], W. R. Sands[91], M. Sanpei[98], D. Santel[47], L. Santelj[3], V. Santoro[107], A. Santroni[119,120], T. Sanuki[176], T. R. Sarangi[199], S. Saremi[137], A. Sarti[107,108], T. Sasaki[7], N. Sasao[193], M. Satapathy[130], Nobuhiko Sato[7], Noriaki Sato[38], Y. Sato[176], N. Satoyama[177], A. Satpathy[47,163], V. Savinov[60], N. Savvas[76], O. H. Saxton[45], K. Sayeed[47], S. F. Schaffner[91], T. Schalk[30], S. Schenk[101], J. R. Schieck[36], T. Schietinger[45,129], C. J. Schilling[163], R. H. Schindler[45], S. Schmid[56], R. E. Schmitz[30], H. Schmuecker[87], O. Schneider[129], G. Schnell[200,201], P. Schönmeier[176], K. C. Schofield[25], G. Schott[161], H. Schröder[†64], M. Schram[54], J. Schubert[88], J. Schümann[7], J. Schultz[133], B. A. Schumm[30], M. H. Schune[11], U. Schwanke[174], H. Schwarz[45], J. Schwiening[45], R. Schwierz[88], R. F. Schwitters[163], C. Sciacca[151,159], G. Sciolla[69], I. J. Scott[125], J. Seeman[45], A. Seiden[30], R. Seitz[111], T. Seki[168], A.I. Sekiya[34], S. Semenov[12], D. Semmler[187], S. Sen[32], K. Senyo[202], O. Seon[38], V. V. Serbo[45], S. I. Serednyakov[27,28], B. Serfass[62], M. Serra[10], J. Serrano[11], Y. Settai[192], R. Seuster[103], M. E. Sevior[126], K. V. Shakhova[171], L. Shang[96], M. Shapkin[132], V. Sharma[174], V. Shebalin[27,28], V. G. Shelkov[15], B. C. Shen[†73], D. Z. Shen[203], Y. T. Shen[20], D. J. Sherwood[127], T. Shibata[100], T. A. Shibata[99], H. Shibuya[196], T. Shidara[7], K. Shimada[100], M. Shimoyama[34], S. Shinomiya[178], J. G. Shiu[20], H. W. Shorthouse[1], L. I. Shpilinskaya[171], A. Sibidanov[6], E. Sicard[111], A. Sidorov[27], V. Sidorov[†27], V. Siegle[57], M. Sigamani[1], M. C. Simani[136], M. Simard[111], G. Simi[144], F. Simon[70,86], F. Simonetto[144,145], N. B. Sinev[139], H. Singh[153], J. B. Singh[123], R. Sinha[204], S. Sitt[48], Yu. I. Skovpen[27,28], R. J. Sloane[25], P. Smerkol[3], A. J. S. Smith[91], D. Smith[148], D. Smith[116], D. Smith[45], D. S. Smith[39], J. G. Smith[32], A. Smol[16], H. L. Snoek[118], A. Snyder[45], R. Y. So[75], R. J. Sobie[55], E. Soderstrom[45], A. Soha[45], Y. S. Sohn[43], M. D. Sokoloff[47], A. Sokolov[132], P. Solagna[144], E. Solovieva[12], N. Soni[123,148], P. Sonnek[128], V. Sordini[11,10,31], B. Spaan[105], S. M. Spanier[150], E. Spencer[30], V. Speziali[190], M. Spitznagel[69], P. Spradlin[30], H. Staengle[137], R. Stamen[7], M. Stanek[45], S. Stanič[205], J. Stark[48], M. Steder[61], H. Steininger[56], M. Steinke[87], J. Stelzer[45], E. Stevanato[144], A. Stocchi[11], R. Stock[206], H. Stoeck[6], D. P. Stoker[133], R. Stroili[144,145], D. Strom[139], P. Strother[1], J. Strube[139], B. Stugu[29], J. Stypula[19], D. Su[45], R. Suda[168], R. Sugahara[7], A. Sugi[38], T. Sugimura[7], A. Sugiyama[185], S. Suitoh[38], M. K. Sullivan[45], M. Sumihama[207], T. Sumiyoshi[168], D. J. Summers[128], L. Sun[29], L. Sun[47], S. Sun[45], J. E. Sundermann[88], H. F. Sung[20], Y. Susaki[38], P. Sutcliffe[25], A. Suzuki[15], J. Suzuki[7],

J. I. Suzuki[7], K. Suzuki[38,45], S. Suzuki[185], S. Y. Suzuki[7], J. E. Swain[53], S. K. Swain[45,103], S. T'Jampens[131], M. Tabata[182], K. Tackmann[15], H. Tajima[8], O. Tajima[7], K. Takahashi[99], S. Takahashi[100], T. Takahashi[181], F. Takasaki[7], T. Takayama[176], M. Takita[178], K. Tamai[7], U. Tamponi[16,17], N. Tamura[100], N. Tan[208], P. Tan[125], K. Tanabe[8], T. Tanabe[15], H. A. Tanaka[45], J. Tanaka[8], M. Tanaka[7], S. Tanaka[7], Y. Tanaka[209], K. Tanida[49], N. Taniguchi[7], P. Taras[111], N. Tasneem[55], G. Tatishvili[114], T. Tatomi[7], M. Tawada[7], F. Taylor[69], G. N. Taylor[126], G. P. Taylor[116], V. I. Telnov[27,28], L. Teodorescu[127], R. Ter-Antonyan[39], Y. Teramoto[181], D. Teytelman[45], G. Thérin[48], Ch. Thiebaux[131], D. Thiessen[75], E. W. Thomas[32], J. M. Thompson[45], F. Thorne[56], X. C. Tian[124], M. Tibbetts[116], I. Tikhomirov[12], J. S. Tinslay[45], G. Tiozzo[144], V. Tisserand[85], V. Tocut[11], W. H. Toki[117], E. W. Tomassini[32], M. Tomoto[7], T. Tomura[8], E. Torassa[144], E. Torrence[139], S. Tosi[119,120], C. Touramanis[25], J. C. Toussaint[62], S. N. Tovey[126], P. P. Trapani[16], E. Treadwell[210], G. Triggiani[77,92], S. Trincaz-Duvoid[11], W. Trischuk[91], D. Troost[15], A. Trunov[45], K. L. Tsai[20], Y. T. Tsai[20], Y. Tsujita[113], K. Tsukada[7], T. Tsukamoto[7], J. M. Tuggle[36], A. Tumanov[91], Y. W. Tung[20], L. Turnbull[175], J. Turner[45], M. Turri[30], K. Uchida[103], M. Uchida[99], Y. Uchida[199], M. Ueki[176], K. Ueno[7], K. Ueno[20], N. Ujiie[7], K. A. Ulmer[32], Y. Unno[154], P. Urquijo[126], Y. Ushiroda[7], Y. Usov[27,28], M. Usseglio[62], Y. Usuki[38], U. Uwer[101], J. Va'vra[45], S. E. Vahsen[103], G. Vaitsas[149], A. Valassi[11], E. Vallazza[142], A. Vallereau[48], P. Vanhoefer[70], W. C. van Hoek[32], C. Van Hulse[200], D. van Winkle[45], G. Varner[103], E. W. Varnes[91], K. E. Varvell[6], G. Vasileiadis[131], Y. S. Velikzhanin[20], M. Verderi[131], S. Versillé[48], K. Vervink[129], B. Viaud[111], P. B. Vidal[1], S. Villa[129], P. Villanueva-Perez[46], E. L. Vinograd[171], L. Vitale[142,143], G. M. Vitug[73], C. Voß[64], C. Voci[144,145], C. Voena[10], A. Volk[88], J. H. von Wimmersperg-Toeller[125], V. Vorobyev[27,28], A. Vossen[211], G. Vuagnin[142,143], C. O. Vuosalo[125], K. Wacker[105], A. P. Wagner[45], D. L. Wagner[32], G. Wagner[64], M. N. Wagner[187], S. R. Wagner[32], D. E. Wagoner[175], D. Walker[109], W. Walkowiak[30], D. Wallom[109], C. C. Wang[20], C. H. Wang[140], J. Wang[124], J. G. Wang[84], K. Wang[73], L. Wang[30], L. L. Wang[11], P. Wang[96], P. Wang[96], T. J. Wang[96], W. F. Wang[45], X. L. Wang[84], Y. F. Wang[106], F. R. Wappler[102], M. Watanabe[100], A. T. Watson[148], J. E. Watson[53], N. K. Watson[148], M. Watt[65], J. H. Weatherall[76], M. Weaver[45], T. Weber[45], R. Wedd[126], J. T. Wei[20], A. W. Weidemann[153], A. J. R. Weinstein[45], W. A. Wenzel[15], C. A. West[63], C. G. West[32], T. J. West[76], E. White[47], R. M. White[153], J. Wicht[7], L. Widhalm[†56], J. Wiechczynski[19], U. Wienands[45], L. Wilden[88], M. Wilder[30], D. C. Williams[30], G. Williams[95], J. C. Williams[76], K. M. Williams[84], M. I. Williams[1], S. Y. Willocq[137], J. R. Wilson[153], M. G. Wilson[30], R. J. Wilson[117], F. Winklmeier[117], L. O. Winstrom[30], M. A. Winter[149], W. J. Wisniewski[45], M. Wittgen[45], J. Wittlin[137], W. Wittmer[45], R. Wixted[91], A. Woch[111], B. J. Wogsland[150], E. Won[122], Q. K. Wong[39], B. C. Wray[163], A. C. Wren[149], D. M. Wright[136], C. H. Wu[20], J. Wu[122], S. L. Wu[125], H. W. Wulsin[45], S. M. Xella[65], Q. L. Xie[96], Y. Xie[53], Y. Xie[9], Z. Z. Xu[106], Ch. Yèche[62], Y. Yamada[7], M. Yamaga[176], A. Yamaguchi[176], H. Yamaguchi[7], T. Yamaki[212], H. Yamamoto[176], N. Yamamoto[7], R. K. Yamamoto[†69], S. Yamamoto[168], T. Yamanaka[178], H. Yamaoka[7], J. Yamaoka[103], Y. Yamaoka[7], Y. Yamashita[213], M. Yamauchi[7], D. S. Yan[203], Y. Yan[45], H. Yanai[100], S. Yanaka[99], H. Yang[49], R. Yang[91], S. Yang[22], A. K. Yarritu[45], S. Yashchenko[61], J. Yashima[7], Z. Yasin[73], Y. Yasu[7], S. W. Ye[106], P. Yeh[20], J. I. Yi[76], K. Yi[45], M. Yi[69], Z. W. Yin[203], J. Ying[124], G. Yocky[45], K. Yokoyama[7], M. Yokoyama[8], T. Yokoyama[179], K. Yoshida[38], M. Yoshida[7], Y. Yoshimura[7], C. C. Young[45], C. X. Yu[96], Z. Yu[125], C. Z. Yuan[96], Y. Yuan[96], F. X. Yumiceva[153], Y. Yusa[100], A. N. Yushkov[27], H. Yuta[183], V. Zacek[111], S. B. Zain[102], A. Zallo[9], S. Zambito[16,17], D. Zander[161], S. L. Zang[96], D. Zanin[16], B. G. Zaslavsky[171], Q. L. Zeng[117], A. Zghiche[85], B. Zhang[48], J. Zhang[7], J. Zhang[32], L. Zhang[73], L. M. Zhang[106], S. Q. Zhang[96], Z. P. Zhang[106], H. W. Zhao[96], H. W. Zhao[128], M. Zhao[69], Z. G. Zhao[106], Y. Zheng[69], Y. H. Zheng[103], Z. P. Zheng[96], V. Zhilich[27,28], P. Zhou[141], R. Y. Zhu[22], Y. S. Zhu[96], Z. M. Zhu[124], V. Zhulanov[27,28], T. Ziegler[91], V. Ziegler[45], G. Zioulas[133], M. Zisman[15], M. Zito[62], D. Zürcher[129], N. Zwahlen[129], O. Zyukova[27,28], T. Živko[3], and D. Žontar[3]

[*] General Editor
[§] Section Editor
[¶] Additional Section Writer
[†] Deceased

[1] Queen Mary, University of London, London, E1 4NS, United Kingdom
[2] Faculty of Mathematics and Physics, University of Ljubljana, 1000 Ljubljana, Slovenia
[3] J. Stefan Institute, 1000 Ljubljana, Slovenia
[4] Theoretische Physik 1, Naturwissenschaftlich-Technische Fakultät, Universität Siegen, Walter-Flex-Straße 3, D-57068 Siegen, Germany
[5] Iowa State University, Ames, Iowa 50011-3160, USA
[6] School of Physics, University of Sydney, NSW 2006, Australia
[7] High Energy Accelerator Research Organization (KEK), Tsukuba 305-0801, Japan
[8] Department of Physics, University of Tokyo, Tokyo 113-0033, Japan
[9] INFN Laboratori Nazionali di Frascati, I-00044 Frascati, Italy
[10] INFN Sezione di Roma, I-00185 Roma, Italy
[11] Laboratoire de l'Accélérateur Linéaire, IN2P3/CNRS et Université Paris-Sud 11, Centre Scientifique d'Orsay, F-91898 Orsay Cedex, France

[12] Institute for Theoretical and Experimental Physics, Moscow 117218, Russia
[13] Physik Department, James-Franck-Straße 1, Technische Universität München, D-85748 Garching, Germany
[14] Institut für Theoretische Teilchenphysik und Kosmologie, RWTH Aachen, D-52056 Aachen, Germany
[15] Lawrence Berkeley National Laboratory and University of California, Berkeley, California 94720, USA
[16] INFN Sezione di Torino, I-10125 Torino, Italy
[17] Dipartimento di Fisica, Università di Torino, I-10125 Torino, Italy
[18] University of Notre Dame, Notre Dame, Indiana 46556, USA
[19] H. Niewodniczanski Institute of Nuclear Physics, Krakow 31-342, Poland
[20] Department of Physics, National Taiwan University, Taipei 10617, Taiwan
[21] University of Iowa, Iowa City, Iowa 52242, USA
[22] California Institute of Technology, Pasadena, California 91125, USA
[23] Institute of Physics, Academia Sinica, Taipei, Taiwan 115, Republic of China
[24] INFN, Sezione de Bari, via Orabona 4, I-70126 Bari, Italy
[25] University of Liverpool, Liverpool L69 7ZE, United Kingdom
[26] Moscow Institute of Physics and Technology, Moscow Region 141700, Russia
[27] Budker Institute of Nuclear Physics SB RAS, Novosibirsk 630090, Russia
[28] Novosibirsk State University, Novosibirsk 630090, Russia
[29] University of Bergen, Institute of Physics, N-5007 Bergen, Norway
[30] University of California at Santa Cruz, Institute for Particle Physics, Santa Cruz, California 95064, USA
[31] Dipartimento di Fisica, Università di Roma La Sapienza, I-00185 Roma, Italy
[32] University of Colorado, Boulder, Colorado 80309, USA
[33] Johannes Gutenberg-Universität Mainz, Institut für Kernphysik, D-55099 Mainz, Germany
[34] Nara Women's University, Nara 630-8506, Japan
[35] Kavli Institute for the Physics and Mathematics of the Universe (WPI), University of Tokyo, Kashiwa 277-8583, Japan
[36] University of Maryland, College Park, Maryland 20742, USA
[37] Kobayashi-Maskawa Institute, Nagoya University, Nagoya 464-8602, Japan
[38] Graduate School of Science, Nagoya University, Nagoya 464-8602, Japan
[39] Ohio State University, Columbus, Ohio 43210, USA
[40] Fermi National Accelerator Laboratory, Batavia, IL 60510, USA
[41] KEK Theory Center, Institute of Particle and Nuclear Studies, KEK 1-1, OHO, Tsukuba, Ibaraki, 305-0801, Japan
[42] Particle and Nuclear Physics Division, J-PARC Center 201-1, Shirakata, Tokai, Ibaraki, 309-11-6, Japan
[43] Yonsei University, Seoul 120-749, South Korea
[44] Department of Physics, University of Warwick, Coventry CV4 7AL, United Kingdom
[45] SLAC National Accelerator Laboratory, Stanford University, Menlo Park, California 94025, USA
[46] IFIC, Universitat de Valencia-CSIC, E-46071 Valencia, Spain
[47] University of Cincinnati, Cincinnati, Ohio 45221, USA
[48] Laboratoire de Physique Nucléaire et de Hautes Energies, IN2P3/CNRS, Université Pierre et Marie Curie-Paris6, Université Denis Diderot-Paris7, F-75252 Paris, France
[49] Seoul National University, Seoul 151-742, South Korea
[50] Moscow Physical Engineering Institute, Moscow 115409, Russia
[51] Dipartmento di Fisica, Università di Bari, I-70126 Bari, Italy
[52] Departament de Física Teòrica, IFIC, Universitat de València – CSIC Apt. Correus 22085, E-46071 València, Spain
[53] University of Edinburgh, Edinburgh EH9 3JZ, United Kingdom
[54] McGill University, Montréal, Québec, Canada H3A 2T8
[55] University of Victoria, Victoria, British Columbia, Canada V8W 3P6
[56] Institute of High Energy Physics, 1050 Vienna, Austria
[57] RIKEN BNL Research Center, Brookhaven, NY 11973, USA
[58] Southern Methodist University, Dallas, Texas 75275, USA
[59] Institut für Theoretische Teilchenphysik, Karlsruher Institut für Technologie, D-76131 Karlsruhe, Germany
[60] University of Pittsburgh, Pittsburgh, PA 15260, USA
[61] Deutsches Elektronen-Synchrotron, 22607 Hamburg, Germany
[62] CEA, Irfu, SPP, Centre de Saclay, F-91191 Gif-sur-Yvette, France
[63] University of California at Santa Barbara, Santa Barbara, California 93106, USA
[64] Universität Rostock, D-18051 Rostock, Germany
[65] Rutherford Appleton Laboratory, Chilton, Didcot, Oxon, OX11 0QX, United Kingdom
[66] Stanford University, Stanford, California 94305-4060, USA
[67] INFN Sezione di Milano, I-20133 Milano, Italy
[68] Dipartimento di Fisica, Università di Milano, I-20133 Milano, Italy
[69] Massachusetts Institute of Technology, Laboratory for Nuclear Science, Cambridge, Massachusetts 02139, USA
[70] Max-Planck-Institut für Physik, 80805 München, Germany
[71] SUPA, School of Physics and Astronomy, University of Glasgow, Glasgow, G12 8QQ, UK

[72] University of Bonn, 53115 Bonn, Germany
[73] University of California at Riverside, Riverside, California 92521, USA
[74] University of South Alabama, Mobile, Alabama 36688, USA
[75] University of British Columbia, Vancouver, British Columbia, Canada V6T 1Z1
[76] University of Manchester, Manchester M13 9PL, United Kingdom
[77] INFN Sezione di Pisa, I-56127 Pisa, Italy
[78] Scuola Normale Superiore di Pisa, I-56127 Pisa, Italy
[79] Tata Institute of Fundamental Research, Mumbai 400005, India
[80] National Central University, Chung-li 32054, Taiwan
[81] INFN Sezione di Perugia I-06123 Perugia, Italy
[82] Dipartimento di Fisica, Università di Perugia, I-06123 Perugia, Italy
[83] Luther College, Decorah, IA 52101, USA
[84] Virginia Polytechnic Institute and State University, Blacksburg, VA 24061, USA
[85] Laboratoire d'Annecy-le-Vieux de Physique des Particules (LAPP), Université de Savoie, CNRS/IN2P3, F-74941 Annecy-le-Vieux, France
[86] Excellence Cluster Universe, Technische Universität München, 85748 Garching, Germany
[87] Ruhr Universität Bochum, Institut für Experimentalphysik 1, D-44780 Bochum, Germany
[88] Technische Universität Dresden, Institut für Kern- und Teilchenphysik, D-01062 Dresden, Germany
[89] Beihang University, Beijing 100191
[90] Tel Aviv University, Tel Aviv, 69978, Israel
[91] Princeton University, Princeton, New Jersey 08544, USA
[92] Dipartimento di Fisica, Università di Pisa, I-56127 Pisa, Italy
[93] Kanagawa University, Yokohama 221-8686, Japan
[94] Korea University, Seoul 136-713, South Korea
[95] University of Texas at Dallas, Richardson, Texas 75083, USA
[96] Institute of High Energy Physics, Beijing 100039, China
[97] University of California at Los Angeles, Los Angeles, California 90024, USA
[98] Tohoku Gakuin University, Tagajo 985-8537, Japan
[99] Tokyo Institute of Technology, Tokyo 152-8550, Japan
[100] Niigata University, Niigata 950-2181, Japan
[101] Universität Heidelberg, Physikalisches Institut, D-69120 Heidelberg, Germany
[102] State University of New York, Albany, New York 12222, USA
[103] University of Hawaii, Honolulu, HI 96822, USA
[104] Oak Ridge National Laboratory, Oak Ridge, Tennessee 37831, USA
[105] Technische Universität Dortmund, Fakultät Physik, D-44221 Dortmund, Germany
[106] University of Science and Technology of China, Hefei 230026, PR China
[107] INFN Sezione di Ferrara, I-44100 Ferrara, Italy
[108] Dipartimento di Fisica e Scienze della Terra, Università di Ferrara, I-44100 Ferrara, Italy
[109] University of Bristol, Bristol BS8 1TL, United Kingdom
[110] INFN CNAF I-40127 Bologna, Italy
[111] Université de Montréal, Physique des Particules, Montréal, Québec, Canada H3C 3J7
[112] Hiroshima Institute of Technology, Hiroshima 731-5193, Japan
[113] University of Tsukuba, Tsukuba 305-0801, Japan
[114] Pacific Northwest National Laboratory, Richland, WA 99352, USA
[115] Toyama National College of Maritime Technology, Toyama 933-0293, Japan
[116] Imperial College London, London, SW7 2AZ, United Kingdom
[117] Colorado State University, Fort Collins, Colorado 80523, USA
[118] NIKHEF, National Institute for Nuclear Physics and High Energy Physics, NL-1009 DB Amsterdam, The Netherlands
[119] INFN Sezione di Genova, I-16146 Genova, Italy
[120] Dipartimento di Fisica, Università di Genova, I-16146 Genova, Italy
[121] Indian Institute of Technology Bhubaneswar, SatyaNagar, 751007, India
[122] Harvard University, Cambridge, Massachusetts 02138, USA
[123] Panjab University, Chandigarh 160014, India
[124] Peking University, Beijing 100871, PR China
[125] University of Wisconsin, Madison, Wisconsin 53706, USA
[126] School of Physics, University of Melbourne, Victoria 3010, Australia
[127] Brunel University, Uxbridge, Middlesex UB8 3PH, United Kingdom
[128] University of Mississippi, University, Mississippi 38677, USA
[129] École Polytechnique Fédérale de Lausanne (EPFL), 1015 Lausanne, Switzerland
[130] Utkal University, Bhubaneswar, India
[131] Laboratoire Leprince-Ringuet, CNRS/IN2P3, Ecole Polytechnique, F-91128 Palaiseau, France
[132] Institute for High Energy Physics, Protvino 142281, Russia

[133] University of California at Irvine, Irvine, California 92697, USA
[134] Indian Institute of Technology Guwahati, Assam 781039, India
[135] Indian Institute of Technology Guwahati, Guwahati, Assam, 781 039, India
[136] Lawrence Livermore National Laboratory, Livermore, California 94550, USA
[137] University of Massachusetts, Amherst, Massachusetts 01003, USA
[138] Novosibirsk State Technical University, Novosibirsk 630092, Russia
[139] University of Oregon, Eugene, Oregon 97403, USA
[140] National United University, Miao Li 36003, Taiwan
[141] Wayne State University, Detroit, MI 48202, USA
[142] INFN Sezione di Trieste, I-34127 Trieste, Italy
[143] Dipartimento di Fisica, Università di Trieste, I-34127 Trieste, Italy
[144] INFN Sezione di Padova, I-35131 Padova, Italy
[145] Dipartimento di Fisica, Università di Padova, I-35131 Padova, Italy
[146] University of Louisville, Louisville, Kentucky 40292, USA
[147] University of Maribor, 2000 Maribor, Slovenia
[148] University of Birmingham, Birmingham, B15 2TT, United Kingdom
[149] University of London, Royal Holloway and Bedford New College, Egham, Surrey TW20 0EX, United Kingdom
[150] University of Tennessee, Knoxville, Tennessee 37996, USA
[151] INFN Sezione di Napoli, I-80126 Napoli, Italy
[152] Department of Physics, Fu Jen Catholic University, Taipei 24205, Taiwan
[153] University of South Carolina, Columbia, South Carolina 29208, USA
[154] Hanyang University, Seoul 133-791, South Korea
[155] Korea Institute of Science and Technology Information, Daejeon 305-806, South Korea
[156] Gyeongsang National University, Chinju 660-701, South Korea
[157] Sungkyunkwan University, Suwon 440-746, South Korea
[158] University of Illinois at Urbana-Champaign, Urbana, IL 61801, USA
[159] Dipartimento di Scienze Fisiche, Università di Napoli Federico II, I-80126 Napoli, Italy
[160] TRIUMF, Vancouver, BC, Canada V6T 2A3
[161] Universität Karlsruhe, Institut für Experimentelle Kernphysik, D-76021 Karlsruhe, Germany
[162] Faculty of Mathematics and Physics, Charles University, 121 16 Prague, The Czech Republic
[163] University of Texas at Austin, Austin, Texas 78712, USA
[164] Harvey Mudd College, Claremont, California 91711, USA
[165] Elon University, Elon University, North Carolina 27244-2010, USA
[166] University of Pennsylvania, Philadelphia, Pennsylvania 19104, USA
[167] II. Physikalisches Institut, Georg-August-Universität Göttingen, 37073 Göttingen, Germany
[168] Tokyo Metropolitan University, Tokyo 192-0397, Japan
[169] Johns Hopkins University, Baltimore, Maryland 21218, USA
[170] Universitat de Barcelona, Facultat de Fisica, Departament ECM, E-08028 Barcelona, Spain
[171] Institute for Single Crystals, National Academy of Sciences of Ukraine, Kharkov 61001, Ukraine
[172] Yale University, New Haven, Connecticut 06511, USA
[173] National Kaohsiung Normal University, Kaohsiung 80201, Taiwan
[174] University of California at San Diego, La Jolla, California 92093, USA
[175] Prairie View A&M University, Prairie View, Texas 77446, USA
[176] Tohoku University, Sendai 980-8578, Japan
[177] Shinshu University, Nagano 390-8621, Japan
[178] Osaka University, Osaka 565-0871, Japan
[179] Tokyo University of Agriculture and Technology, Tokyo 184-8588, Japan
[180] Kyungpook National University, Daegu 702-701, South Korea
[181] Osaka City University, Osaka 558-8585, Japan
[182] Chiba University, Chiba 263-8522, Japan
[183] Aomori University, Aomori 030-0943, Japan
[184] Humboldt-Universität zu Berlin, Institut für Physik, D-12489 Berlin, Germany
[185] Saga University, Saga 840-8502, Japan
[186] Punjab Agricultural University, Ludhiana 141004, India
[187] Justus-Liebig-Universität Gießen, 35392 Gießen, Germany
[188] T. Kościuszko Cracow University of Technology, Krakow 31-342, Poland
[189] Indian Institute of Technology Madras, Chennai 600036, India
[190] Università di Pavia, Dipartimento di Elettronica and INFN, I-27100 Pavia, Italy
[191] University of Miyazaki, Miyazaki 889-2192, Japan
[192] Chuo University, Tokyo 192-0393, Japan
[193] Kyoto University, Kyoto 606-8502, Japan
[194] Research Center for Electron Photon Science, Tohoku University, Sendai 980-8578, Japan

[195] Mount Holyoke College, South Hadley, Massachusetts 01075, USA
[196] Toho University, Funabashi 274-8510, Japan
[197] Vanderbilt University, Nashville, Tennessee 37235, USA
[198] Technion, Haifa, Israel
[199] The Graduate University for Advanced Studies, Hayama 240-0193, Japan
[200] University of the Basque Country UPV/EHU, 48080 Bilbao, Spain
[201] Ikerbasque, 48011 Bilbao, Spain
[202] Yamagata University, Yamagata 990-8560, Japan
[203] Chinese Academy of Science, Beijing 100864, PR China
[204] Institute of Mathematical Sciences, Chennai 600113, India
[205] University of Nova Gorica, 5000 Nova Gorica, Slovenia
[206] University of Frankfurt, 60318 Frankfurt am Main, Germany
[207] Gifu University, Gifu 501-1193, Japan
[208] Tokyo University of Science, Chiba 278-8510, Japan
[209] Nagasaki Institute of Applied Science, Nagasaki 851-0123, Japan
[210] Florida A&M University, Tallahassee, Florida 32307, USA
[211] Indiana University, Bloomington, IN 47408, USA
[212] Sugiyama Jogakuen University, Aichi 470-0131, Japan

Contents

Part A
The facilities

Chapter 1
The B Factories

Editors:
David Leith (BABAR)
Kazuo Abe, Stephen L. Olsen (Belle)

Additional section writers:
Peter Križan, Leo Piilonen, Blair Ratcliff, Guy Wormser

1.1 Introduction

In their classic paper, Kobayashi and Maskawa (1973, "KM") pointed out that *CP* violation could be naturally incorporated into the Standard Model (SM) as an irreducible complex phase in the weak interaction quark-flavor-mixing matrix if the number of quark flavors was six. This was remarkable because at that time only the three quarks of the original Gell-Mann (1964) and Zweig (1964a) quark model — *i.e.*, the u-, d- and s-quarks — were experimentally established. The situation changed dramatically in late 1974 with the discovery of the c-quark at Brookhaven (Aubert et al., 1974) and SLAC (Augustin et al., 1974) and the 1977 discovery of the b-quark at Fermilab (Herb et al., 1977). By 1980, the KM idea, by then embodied in the Cabibbo-Kobayashi-Maskawa (CKM) quark flavor mixing matrix (Cabibbo, 1963; Kobayashi and Maskawa, 1973), was accepted as an integral component of the Standard Model, even though its *raison d'etre*, the *CP*-violating complex phase, had not been measured (Kelly et al., 1980).

1.1.1 Testing the KM idea

In the early 1980's, when the experimental state-of-the-art in B meson physics was defined by the CLEO experiment, where the measurements were based on data samples of a few tens of events (Bebek et al., 1981; Chadwick et al., 1981), Bigi, Carter, and Sanda published papers exploring the possibilities of using B meson decays to test the validity of the KM six-quark mechanism for *CP* violation (Bigi and Sanda, 1981, 1984; Carter and Sanda, 1980, 1981). They concluded that for a relatively small range of the CKM-matrix parameter-space that was allowed at that time — a range that corresponds to a substantial probability for $B^0 - \overline{B}^0$ mixing and a long B meson lifetime — large *CP* violation might be observable in neutral B meson decays to *CP* eigenstates, such as $B^0 \to J/\psi K^0_S$. However, in the early 1980's, no decays of this type had been seen; we now know that their branching fractions are $\sim 0.1\%$ or less. A reasonable conclusion that could be derived from these papers at that time was that definitive tests of the KM idea were hopelessly impractical.

1.1.2 Three miracles

Subsequently, three remarkable developments occurred that completely turned the tables. These included the first emergence of evidence of a long B meson lifetime from experiments at SLAC (Fernandez et al., 1983; Lockyer et al., 1983), and the unexpected discovery by the ARGUS experiment at DESY in 1987 of a substantial rate for $B^0 - \overline{B}^0$ mixing (Albrecht et al., 1987b). These measurements indicated that the CKM-matrix parameters are, in fact, in the range that is accessible to tests of the KM idea. This was helped along by many well-attended international workshops[1] developing each of the different technical approaches and refining the requirements and specifications for each. It became clear that *CP* violation, at the level manifest in the Standard Model, could be experimentally observable somewhere other than in neutral kaons: namely, in the $B^0 - \overline{B}^0$ system. Moreover large *CP* violation was expected, rather than the one-in-a-thousand effect seen in K decay. In addition, Bigi and Sanda (1981) had shown that a measurement of *CP* violation in neutral B meson decays to *CP* eigenstates could be clearly interpreted without theoretical uncertainties. However, an experiment to observe *CP* violation in B decays would require about a thousand-fold larger data samples of B mesons than had been gathered heretofore.

The two fortuitous circumstances mentioned above were accompanied by a third "miracle": extraordinary improvements in the performance of e^+e^- storage rings, with order-of-magnitude luminosity improvements occurring approximately every seven years. In 1980, the original CESR collider typically produced ~ 30 $B\overline{B}$ meson pairs per day; thirty years later, the two B Factories, KEKB and PEP-II, routinely produced more than one million $B\overline{B}$ meson pairs per day, a nearly five orders-of-magnitude improvement! The B Factories built on the success of CESR at Cornell and DORIS-II at DESY to achieve these production rates. These developments were accompanied by less miraculous, but still impressive, advances in the capabilities of large solid-angle detectors, especially in the ability of data acquisition systems to handle the huge event rates associated with the available luminosities, precision tracking and vertexing devices, and the software and storage technologies required to deal with these large data samples.

[1] The main workshops include: Heidelberg (Schubert and Waldi, 1986), Stanford (Bloom, Friedsam, and Fridman, 1988; Hitlin, 1990), Courmayeur (De Sanctis, Greco, Piccolo, and Tazzari, 1988), Zuoz (Locher, 1988), Los Angeles (Cline and Fridman, 1988; Cline and Stork, 1987), Blois (Cline and Fridman, 1991), Syracuse (Goldberg and Stone, 1989), Tsukuba (Kikutani and Matsuda, 1993; Ozaki and Sato, 1991; Yoshimura, 1989), Vancouver (MacFarlane and Ng, 1991), and Hamburg (Aleksan and Ali, 1993).

The remainder of this chapter discusses the historical route taken to develop the ideas necessary to build a B Factory (Section 1.2), followed by an overview of the two storage rings that were built to provide a source of $B^0\overline{B}^0$ meson pairs to explore the B Factory scientific program (Section 1.3). A review of general issues concerning the detector requirements for a B Factory is presented in Section 1.4; a more detailed discussion of the two detectors realized can be found in Chapter 2. We conclude with a brief look at the early physics discoveries of the B Factories (Section 1.5).

1.2 The path to the B Factories

1.2.1 Requirements for a B Factory

The time-dependent method for testing the KM idea is based on the fact that there are decays with interfering amplitudes (see Fig. 1.2.1) where the interference term contains $V_{cd}^*V_{cb}V_{td}V_{tb}^*$. The phase of this quartet of CKM matrix elements is $\phi_1 = \beta$. Note that the *BABAR* experiment uses β to denote this angle, whereas the Belle experiment reports results in terms of ϕ_1; further notational differences are discussed in Chapter 16. In the following we will use the ϕ_1 notation for this phase. The "golden observable" for its determination is the *CP* asymmetry between $B^0 \to J/\psi K_S^0$ and $\overline{B}^0 \to J/\psi K_S^0$. At the B Factories, neutral B mesons are created in pairs at a center-of-mass energy corresponding to the $\Upsilon(4S)$. As a result the wave function of the $B^0\overline{B}^0$ pairs is in a P-wave entangled state, until one of the mesons decays. A further complication arises as neutral B mesons mix with a characteristic frequency Δm_d, so one computes the asymmetry as a function of the proper time difference between the decays of two mesons in an event, and uses knowledge of $B^0\overline{B}^0$ mixing to infer the flavor of one of the B mesons (decaying into a *CP* eigenstate) relative to that of the other B decaying into a flavor specific final state. This initial state preparation at the $\Upsilon(4S)$ enables one to determine the flavor of the b quark for the flavor specific final states with a high efficiency.

The amplitude for the direct decay $B^0 \to J/\psi K_S^0$, shown in the upper right panel of Fig 1.2.1, is proportional to the V_{cb} CKM matrix element. The decay can also proceed via the two-step process $B^0 \to \overline{B}^0 \to J/\psi K_S^0$, shown in the bottom-right panel of the figure. The phase difference between these two amplitudes is $2\phi_1$.

The technique for performing the interference measurement is illustrated in Fig. 1.2.2. A $B^0\overline{B}^0$ pair produced via $\Upsilon(4S) \to B^0\overline{B}^0$ decay is entangled in a coherent quantum state until one of the mesons decays. Most B^0 meson decays produce flavor-specific final states, *i.e.*, the final-state particles can be used to determine whether the decaying meson was a B^0 or a $\overline{B}^0$. For example, a K^+ meson in the final state signals a high likelihood for the $B \to \overline{D} \to K^+$ decay chain and, thus, a higher probability that the parent meson was a B^0 rather than a $\overline{B}^0$. Such a decay is called a "flavor-tag" decay. At the time this B meson decays (t_1 in the figure), the accompanying B meson's flavor is specified as being the opposite.

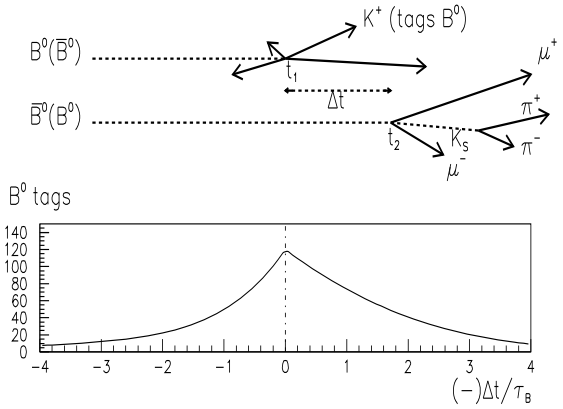

Figure 1.2.2. An illustration of the B Factory flagship measurement of $\sin 2\phi_1 = \sin 2\beta$.

This accompanying meson then propagates in time and the quark flavor content can oscillate from an unmixed state into a mixed one, until it decays (at time t_2). If it decays into a *CP* eigenstate such as $J/\psi K_S^0$, the unmixed and mixed flavor components interfere, producing different decay rates for B^0-tagged and $\overline{B}^0$-tagged mesons. A similar pattern occurs for those cases where the *CP* eigenstate decay occurs before the flavor tag decay (*i.e.* $t_2 \le t_1$) except that in this case the common phase from the mixing diagram has opposite sign. Thus, for B^0-tagged events, the interference is destructive for negative values of $\Delta t = t_2 - t_1$ and constructive for positive Δt values, as indicated in the graph in the lower part of the figure, where the Δt dependence for B^0-tagged events is shown in units of τ_B, the B^0 lifetime (≈ 1.5 ps). The time-integrated asymmetry is zero; asymmetries only show up in the decay-time-dependence of the flavor-tagged distributions. The interference in $\overline{B}^0$-tagged events has the opposite pattern, *i.e.*, constructive interference for negative Δt and destructive interference for positive Δt. Detailed discussions of flavor tagging and time-dependent *CP* asymmetry measurement techniques used by the B Factories can be found in Chapters 8 and 10, respectively.

These considerations set the base-line requirements for an experiment to measure the *CP*-violating phases using the time-dependent *CP* asymmetry technique at the $\Upsilon(4S)$:

High luminosity: The branching fraction for the $B^0 \to J/\psi K_S^0$ decay, the most prominent mode that is useful for these measurements, is $\sim 0.04\%$ and that for $J/\psi \to \ell^+\ell^-$ (where $\ell = e, \mu$) is $\sim 12\%$. Thus, tens of millions of $B^0\overline{B}^0$ pairs are needed. For an e^+e^- collider operating at the $\Upsilon(4S)$, this requires integrated luminosities of ~ 30 fb^{-1} or more.

Boosted $B^0\overline{B}^0$ pairs: The B^0 and $\overline{B}^0$ mesons must have decay lengths in the laboratory that are sufficiently

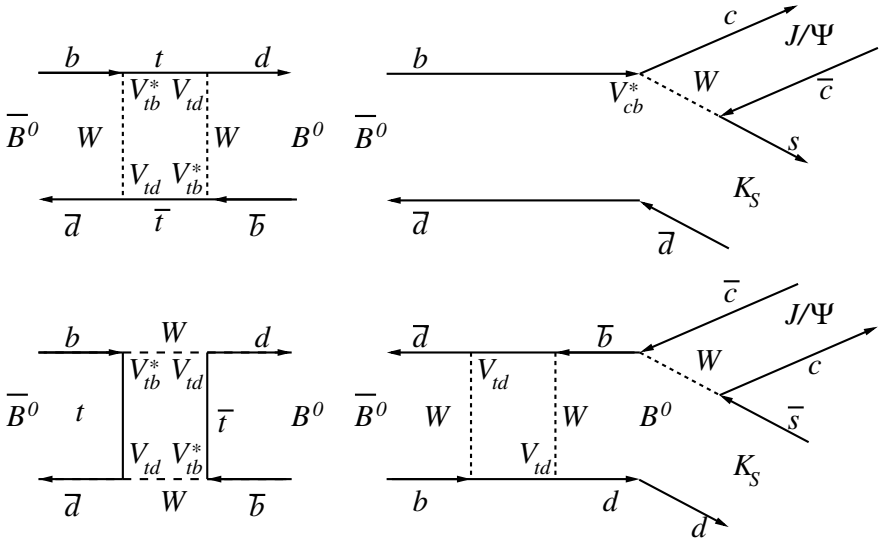

Figure 1.2.1. (left) The dominant quark-line diagrams for $B^0 - \overline{B}^0$ mixing. (right) The interfering diagrams used for the ϕ_1 measurement. As the direct $\overline{B}^0$ decay produces $\overline{K}^0$, and the B^0 decay produces K^0, the relative phase between $\overline{B}^0 \to B^0 \to J/\psi K_S^0$ and $\overline{B}^0 \to J/\psi K_S^0$ contains an additional term due to $K^0 - \overline{K}^0$ mixing (not shown).

long so that the time sequence of their decays can be measured. Also it should be noted that $\Upsilon(4S)$ mesons produced in symmetric colliders are almost at rest in the laboratory frame, and as a consequence one can only measure functions of $t_1 + t_2$, for which any *CP* asymmetry vanishes. Both of these reasons impose the requirement of an asymmetric energy e^+e^- collision in the laboratory frame of reference (see Section 1.2.3).

High-resolution and large-coverage detector with excellent particle identification: The measured amplitude of the *CP*-violating asymmetry is directly proportional to the detector's ability to reconstruct and flavor-tag the accompanying B meson.

1.2.2 Early proposals

At the time, the most successful studies of B mesons were being performed at the CESR and DORIS II e^+e^- colliders operating at the center-of-mass (CM) energy corresponding to the $\Upsilon(4S)$ resonance, which, because it decays into $B\overline{B}$ (and nothing else) nearly 100% of the time, is a copious source of B mesons in a clean, low-background environment. Also, luminosities of $\sim 10^{32}$ cm^{-2} s^{-1}, while a significant advance over previous machines, are two orders-of-magnitude too low to provide samples of B meson decays that are adequate for the *CP* violation measurements.

During the late 1980's a very large number of concepts (twenty-two in all) emerged on the international scene to test *CP* violation in B mesons. Both Hitlin (2005) and Schubert (2007) have presented detailed reviews of these proposals, and how they synergistically evolved to the two B Factories that were eventually built.

1.2.3 Asymmetric colliders

In the late 1980s, as the TRISTAN program at KEK (High Energy Accelerator Research Organization, Tsukuba, Japan) and the SLC program at SLAC (SLAC National Accelerator Laboratory, Stanford, USA) were winding down, workshops and task forces were formed at both labs to investigate possible facilities to attack the *CP* violation problem. In 1987, at a specialized workshop at UCLA that was focused on possibilities for using linear e^+e^- colliders for B physics, Pier Oddone proposed a novel concept of an asymmetric-energy, circular e^+e^- collider. This would operate at the $\Upsilon(4S)$ and produce B mesons with a lab-frame boost sufficient to enable decay-time-dependent measurements (Oddone, 1987), as discussed in Section 1.2.1. The experimental and analysis details on how one might effectively detect *CP* violation in such asymmetric decays are described in Aleksan, Bartelt, Burchat, and Seiden (1989).

Within the US, the 1990 HEPAP Panel on "The HEP Research Program for the 1990's" (Sciulli et al., 1990), recommended that the US should study the science opportunities and technical requirements of a B Factory as a possible component of the future US accelerator program, and vigorously support the necessary R&D funding. Two years later, the next HEPAP Panel (Witherell et al., 1992) recommended that a B Factory be constructed in the US under all budget scenarios under consideration. In the fall of 1992 the Office of Management and Budget (OMB) and the White House were assembling the budget proposal for fiscal year 1994, and included possible initial funding for a B Factory. Both California and New York congressional delegates were working towards the interests of their constituencies. In April 1993 the OMB asked the DOE and NSF to convene a joint review of the two projects, both having already done careful reviews of their respec-

tive proposals — SLAC by DOE and Cornell by NSF. This review (Kowalski et al., 1993) was charged to look at both projects separately and non-competitively, and assess their suitability for the task ahead and the risks that each project posed with respect to achieving the goals, the schedule, and the cost. That fall, Congress recommended incremental growth for HEP funding, including $36 million to start the construction of a B Factory, with the choice of site awaiting the decision from this review. In October 1993 on the basis of this review Secretary of Energy Hazel O'Leary made the decision to go ahead with the construction of the SLAC facility (O'Leary, 1993), and that same month President Clinton announced the construction of a B Factory at SLAC, as a Presidential Initiative, with a four year financial profile (Clinton, 1993). A management team was immediately formed to design and build the PEP-II collider under the leadership of Jonathan Dorfan (SLAC), together with Tom Eliof (LBL) and Robert Yamamoto (LLNL). Complementing this team, an Interim International Advisory Committee was formed by the lab management to advise on the formation of the *BABAR* collaboration's first committees. The detector evolution from this point onward is discussed in more detail in Section 1.4. In the shadow of the cancellation of the Superconductiong Super Collider (SSC) project in Texas in October, 1993, the HEPAP Panel on "The Vision for the Future of HEP" (Drell et al., 1994) was quickly assembled and charged; it met through the short period December 1993 and March 1994. They presented HEPAP, DOE, and Congress with a strong vision of how to pull the US HEP program back from the brink caused by the SSC cancellation decision, and set a path to a healthy, competitive international research program. This plan strongly recommended continuing forward with both the main Injector project at FNAL and the B Factory at SLAC. The three-lab (SLAC, LBL, LLNL) B Factory team worked well together, smoothly solving the problems that arise in all high-tech construction projects, and bringing the project in "on-time" and "on-budget". The high energy ring was completed and beam stored by mid 1997, and the low energy ring was completed, with beam stored, a year later. First collisions were observed that same month, and first collisions with the *BABAR* detector in place were observed in May 1999. Design luminosity was achieved in the fall of 2000.

In Japan, the first official presentation for a B Factory construction took place at the TRISTAN Program Advisory Committee (TPAC) in March 1991. The committee members heard the progress report on the feasibility studies for the machine design and detector configuration that were accumulated from the past several year's work. The committee was convinced that constructing a B Factory at KEK was sufficiently feasible and the project should nicely fit in as a third stage of the TRISTAN project. The committee recommended that KEK should proceed with its construction and, due to the highly competitive situation worldwide, aim for the earliest possible completion of the project. With this official TPAC recommendation, and expression of support from the international community in the form of letters from prominent figures and presence at well-attended meetings, the KEK management began to talk to the funding agency of the Japanese Government and to rearrange the laboratory resources toward the new project.

Of the original leading B Factory proposals mentioned in Section 1.2.2 above, only these two B Factory projects, both based on the Oddone concept of asymmetric energy electron-positron storage rings, PEP-II (PEP-II, 1993) and KEKB (Abe et al., 1993), were to survive. *BABAR* at PEP-II was approved in 1993, and Belle at KEKB was approved the following year, in 1994.

1.2.4 A different approach

Meanwhile a different approach, aimed at using B mesons produced in hadron collisions, was pursued by HERA-B (Hartouni et al., 1995; Padilla, 2000). Here, the plan was to place thin metal targets inside the halo of the proton beam in the HERA electron-proton collider and run parasitically with other HERA experiments. A drawback was that the cross section for producing B mesons in proton-nuclear collisions at the available CM energy is a tiny fraction ($\sim 10^{-6}$) of the total hadronic cross section. Although serious difficulties were anticipated with this approach, the project was approved in 1995 with an expected data-taking start in 1998, one year ahead of the expected start-up of PEP-II and KEKB. Ultimately, however, the huge non-B meson background turned out to be too difficult to contend with and this approach proved not to be competitive with the asymmetric e^+e^- collider approach.

In 1994, the year that the SLAC and KEK B Factories were approved, three sets of proponents for a dedicated B physics experiment at the LHC were encouraged to "join together to prepare a letter of intent for a new collider mode b experiment to be submitted to the LHCC" (Kirsebom et al., 1995). The three projects were called COBEX, GAJET, and LHB, and the merger resulted in the LHCb experiment. The experimental design for LHCb is similar to that of HERA-B, in that it is a single-arm spectrometer. Unlike HERA-B, which relied on a target to create B mesons, LHCb relies on production of B mesons from pp collisions at the LHC. A dedicated spectrometer in the forward region is chosen to take advantage of the large cross section in the forward-backward direction. The LHCb experiment started taking data in 2008, when the LHC started collisions. Another proposed experiment to study CP violation in a hadronic environment was put forward, with the aim of using the Tevatron at Fermilab. This was called the BTeV experiment and it was to have been a two-arm spectrometer, each arm being similar in design to LHCb (Santoro et al., 1999). Only the HERA-B and LHCb experiments were constructed and took data.

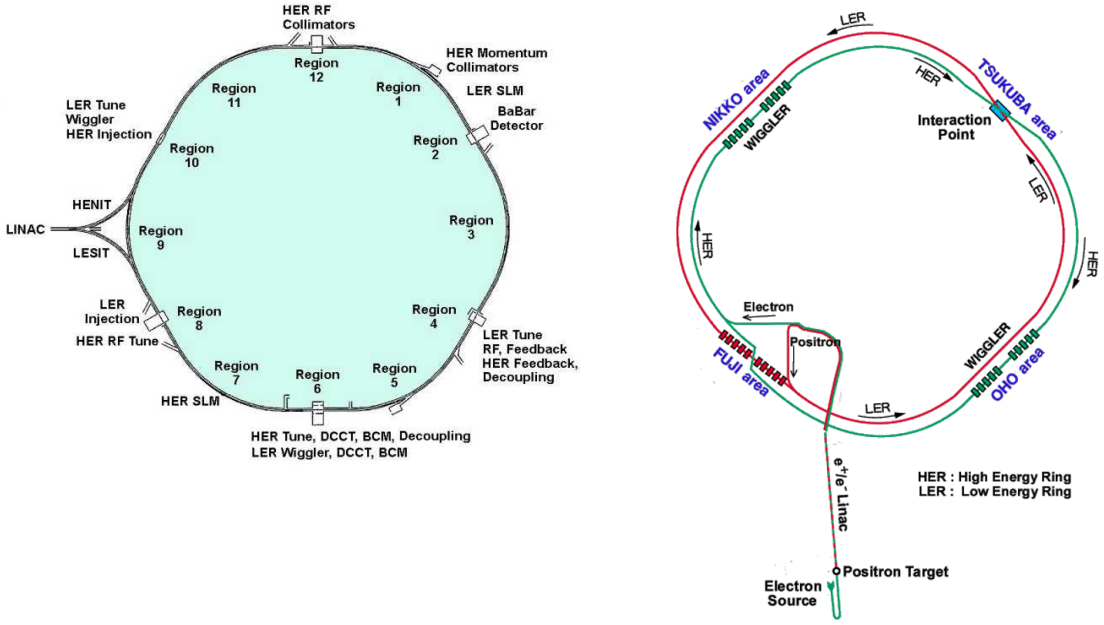

Figure 1.3.1. Schematic view of the PEP-II (left) and KEKB (right) rings. At PEP-II, the two beams are stacked one on top of the other; the *BABAR* experiment is located in an experimental hall at the single interaction region, within region 2 of the PEP-II complex. At KEKB, the two beams are side-by-side, and intersect in the Tsukuba area experimental hall where the Belle detector was placed.

1.3 PEP-II and KEKB

PEP-II was located in the tunnel that had housed the 32 GeV center-of-mass energy PEP e^+e^- storage ring,[2] while the KEKB ring was in the 64 GeV center-of-mass energy e^+e^- TRISTAN storage accelerator tunnel. Figure 1.3.1 shows a schematic overview of the PEP-II and KEKB rings.

Both projects included conversions to meet the B Factory requirements, namely an instantaneous luminosity in excess of 10^{33} cm^{-2} s^{-1} and a boost factor (of the CM frame relative to the laboratory) sufficient for observing the time evolution of B decays. To achieve these requirements, however, some considerable challenges had to be addressed.

Asymmetric energies mean a dedicated ring for each beam. In order to reach a high integrated luminosity one requires an intense positron source and on-energy injection for both rings. For KEKB, this meant that the injection linear accelerator (Linac) energy had to be raised from 2.5 GeV to 8 GeV in order to provide for on-energy injection of 8 GeV electrons and sufficient production of 3.5 GeV positrons. PEP-II had the advantage of the existing powerful SLAC Linac, which could provide the required electron and positron beams with minimal modifications. Both facilities used high-energy electron beams and low-energy positron beams in order to avoid beam-instability problems due to ion trapping, which are most serious at lower energies. Both facilities had only one interaction region (IR) for the detector in order to optimize the luminosity. The luminosity of an e^+e^- storage ring is given by

$$\mathcal{L} = \frac{N_b n_{e^-} n_{e^+} f}{A_{\text{eff}}} \tag{1.3.1}$$

where the numbers of electrons and positrons in each bunch are given by n_{e^-} and n_{e^+}, N_b is the number of bunches, f is the circulation frequency, and A_{eff} is the effective cross-sectional overlapping transverse area of the beams at the interaction point (IP). While the five parameters are independent at lower beam currents, at high beam currents A_{eff} becomes strongly beam-current dependent. As the product $N_b n_{e^-} n_{e^+}$ is increased, A_{eff} increases, thereby limiting the luminosity.

Particles inside a beam bunch are deflected when they pass through the collective electromagnetic fields of the oncoming beam bunch at the IP; as a result, the oncoming bunch collectively acts as a focusing lens. However, these beam-beam effects are highly non-linear and produce spreads in the operating point in the betatron-oscillation tune plane, causing considerable complications in the machine operation. These beam-beam interactions, which become larger as the bunch charges are increased, also limit the luminosity by enlarging A_{eff}.

Attempts to raise the luminosity by raising N_b, the number of bunches in each ring, face a different prob-

[2] A maximum center-of-mass energy of 29 GeV was achieved during the lifetime of PEP.

lem. When a beam bunch circulates with small separation intervals from other bunches, it feels some effects of the other bunches caused by residual oscillating electromagnetic fields produced in the beam chambers and other ring components by the preceding bunches. These effects can drive coupled-bunch instabilities throughout the entire ring that grow as the beam currents increase. Coupled-bunch instabilities in the electron ring are also caused by the presence of residual-gas ions and, for the positron ring, clouds of photoelectrons generated by synchrotron X-rays hitting the beam chamber walls and by photoelectrons reaccelerated by the beam striking the walls to make secondary yields.

In addition to driving coupled-bunch instabilities, the presence of ions and electron clouds enlarges the beam sizes, sometimes leading to beam losses throughout the ring. In fact, this effect turned out to be the most serious problem for both projects, especially "blow-up" of the positron beam caused by the photoelectron clouds.

Large beam currents also imposed serious challenges for the hardware components along the rings. A high-quality vacuum had to be kept in the beam chambers to ensure reasonably long beam lifetimes in an environment where the chamber walls were constantly bombarded by huge fluxes of synchrotron X-rays. Heat energy accumulated in the ring components had to be removed efficiently. Tireless efforts were made throughout the entire period of operation to keep improving the performance of critical hardware components and for finding optimum operating conditions, which were often far from those carefully developed during the design stage. Movable masks used to scrape away unwanted beam-halo particles turned out to be a particularly difficult challenge.

A background simulation effort started in *BABAR* immediately to focus on the ingredients that should be integrated in the PEP-II machine design, namely collimators and synchrotron radiation masks.

The conclusions of these early simulations were clear:

- The background would be severe.
- The uncertainties in the simulation were very large due to many reasons (incomplete knowledge of the physical sources, incomplete description of the machine, crude assumptions on the machine vacuum, etc.).
- An experimental approach to try to control all these approaches was mandatory. This led to the creation of a commissioning detector which started in 1996 (see Section 1.4.3.1).
- The detector design, which was proceeding, had to adopt a safety factor of 10 relative to all background predictions. This "administrative" rule turned out to be extremely difficult to meet initially, and led to changes in the technical implementation of several detector components, but turned out to be very wise and had many pay-offs in the long term.

Many collimators were proposed, with fixed or movable jaws, for inclusion at key locations. It turned out that it was difficult and very costly to implement them all, so only a select few were installed. At Belle, several versions of movable masks were used, each version being a gradual improvement on the previous one.

In a two-ring machine with small bunch spacings, a beam-separation scheme is needed to divert the beams as they leave the IP in order to avoid parasitic interactions. PEP-II used a head-on collision scheme with near-IP bending magnets to steer the e^+ and e^- beam bunches away from each other as soon as possible after the collision. KEKB, on the other hand, used a scheme in which the two beams collide with a small (± 11 mrad) crossing angle. While this scheme had the considerable merit of allowing for shorter bunch spacing and more available space for the detector components near the IP, it was not without risk. A previous attempt to use a small but finite-angle crossing scheme in the DORIS ring at DESY (Piwinski, 1977) had problems that were attributed to beam instabilities from unwanted couplings between betatron and synchrotron motions caused by the crossing angle, and it was generally believed that this effect would get worse at larger crossing angles. However, a theoretical study (Hirata, 1995) concluded that a large horizontal crossing angle in KEKB would, in fact, not be very harmful; based on this, a finite crossing angle was incorporated at an early stage of the design process. Ultimately, crossing-angle-induced transverse-longitudinal couplings were canceled by the use of the world's first operational set of superconducting crab cavities that realign the directions of the beam bunches so they pass through each other head-on (Hosoyama et al., 2008). These were installed in January 2007; with the cavities, and with chromatically corrected IP beta functions, KEKB eventually reached a peak luminosity of $2.1 \times 10^{34}\ \mathrm{cm}^{-2}\,\mathrm{s}^{-1}$, more than twice the original design goal.

As a result of due care and attention in the design of the machines, the excellent performance of the KEKB and PEP-II colliders was comfortably sufficient to allow *BABAR* and Belle to verify the Kobayashi-Maskawa theory of *CP* violation, and, in addition, provide opportunities for a number of other measurements and discoveries, many of which were well beyond the scope of the original physics goals listed in the 1994 Belle Letter of Intent (Cheng et al., 1994) and the *BABAR* Physics Book (Harrison and Quinn, 1998). The machine parameters for the two B Factories during the final stages of their operation are given in Table 1.3.1.

1.4 Detectors for the B Factories

The B Factories have a common set of design requirements which are driven by the physics goals laid down in Section 1.2. The resulting detector designs for *BABAR* and Belle are, broadly speaking, quite similar, with similar operational performance. Any differences resulted from conditions expected from the PEP-II and KEKB accelerator complexes and the technical competences and available resources of the groups who built the various sub-systems. The main requirements are as follows

Light material (*i.e.* high X_0) for the inner detector: The beam pipe, for the length corresponding to the

Table 1.3.1. Machine parameters of PEP-II and KEKB during the last stage of their operation.

Parameters			PEP-II	KEKB
Beam energy		(GeV)	9.0 (e^-), 3.1 (e^+)	8.0 (e^-), 3.5 (e^+)
Beam current		(A)	1.8 (e^-), 2.7 (e^+)	1.2 (e^-), 1.6 (e^+)
Beam size at IP	x	(μm)	140	80
	y	(μm)	3	1
	z	(mm)	8.5	5
Luminosity		($\mathrm{cm}^{-2}\,\mathrm{s}^{-1}$)	1.2×10^{34}	2.1×10^{34}
Number of beam bunches			1732	1584
Bunch spacing		(m)	1.25	1.84
Beam crossing angle		(mrad)	0 (head-on)	± 11 (crab-crossing)

solid angle subtended by the active region of the B Factory detectors, was made of beryllium with a cooled channel between inner and outer walls. Beryllium was chosen to minimize the amount of material in terms of radiation length, to reduce multiple scattering and energy loss of particles crossing the beam pipe.

Vertexing capability: The key to measuring *CP* violating asymmetries is the precise determination of the decay vertex of each B meson in an event. The only viable technology to use at the time the B Factories were being constructed was a silicon-strip-based vertex detector.

Particle identification: In order to classify particles in the final states of interest, over a broad range of momentum, it is not possible to rely on a single particle identification technology. Both experiments constructed drift chambers with sufficiently good specific energy loss (dE/dx) measurement capability to perform charged particle identification for low momentum tracks. This was supplemented at Belle by a Time-Of-Flight system, and an aerogel-based Cherenkov detector for characterizing high momentum particles. At *BABAR*, high momentum track identification was achieved via the Detector of Internally Reflected Cherenkov light (DIRC), which was proposed by Blair Ratcliff (Ratcliff, 1993; Schwiening et al., 2001).

Electromagnetic calorimetry: Many final states of interest, including $B^0 \to J/\psi K^0_S$ where $J/\psi \to e^+e^-$, require that one is able to measure the energy of both electrons and neutral particles. The technology adopted by the B Factories was inspired by the CLEO electromagnetic calorimeter (Kubota et al., 1992): both experiments used CsI(Tl) crystal calorimeters.

K^0_L and muon identification: The expected *CP* asymmetries in $B^0 \to J/\psi K^0_S$ and $B^0 \to J/\psi K^0_L$ are equal in magnitude and opposite in sign: it was realized that to verify any observation of *CP* violation in B decays, it would be important to measure both of these modes. Given the lifetime difference between K^0_S and K^0_L mesons, the K^0_S mesons would be expected to decay in the beam pipe or silicon detector, whereas most K^0_L mesons would pass through the inner part of the detector without decaying. Detection requirements for K^0_L mesons were similar to those required for efficient muon identification, which was important in order to detect the $J/\psi \to \mu^+\mu^-$ contributions for *CP* asymmetry measurements. As a result, the outer parts of the two B Factory detectors were instrumented with layers of active detector sandwiched between absorber material. Belle adopted float-glass based Resistive Plate Chambers (RPCs) operating in limited-streamer mode. *BABAR* initially adopted a Bakelite-based RPC solution for its K^0_L and muon identification. However, soon after operation started it was clear that this needed to be replaced, and a system of Limited Streamer Tubes (LST's) was successfully installed to replace the RPCs for the remainder of *BABAR*'s operational lifetime (see Sections 1.4.3.6 and 2.2.5).

Data handling capability: The design goals of the B Factories were ambitious. If these were to be met, then a significant amount of data would have to be transferred from the detector system front-end, classified by a trigger system, and stored for subsequent processing. As the B Factory design luminosity was surpassed, the data flow and offline computing systems had to be adapted in order to keep up with the output of the machine, and allow members of the Collaborations to produce the physics results that appear in this book.

A more detailed discussion on the B Factory detectors and readout can be found in Chapter 2, and an overview of data taking and Monte Carlo production required for physics analysis can be found in Chapter 3.

1.4.1 The BABAR detector collaboration

The SLAC management decided that with the approval of the B Factory as a new element of the national HEP accelerator program, it should explore how CERN had managed the growing of the large, international collaborations which had designed, built and operated the large detectors at that laboratory. CERN Research Directors Pierre Dariullat and Lorenzo Foa were very generous in providing access to the lab archives, and engaged in full discussions on the CERN procedures and processes, identifying both the strengths and weaknesses. These visits

were very helpful in guiding the initial planning at SLAC. Several other visits to Europe allowed gathering a "temporary international advisory committee" (see below) to listen to their collective wisdom, and advice on moving forward with the formation of national core groups for the detector communities within Italy, France, Germany, UK and the US.

The CERN discussions emphasized the central importance of gathering representatives of all the international agencies involved, to oversee their investments in the scientific collaboration. It was the first time that SLAC, or indeed any DOE Office of High Energy Physics (OHEP) lab, organized an external group of representatives of funding agencies from around the world to regularly review one of its experiments, and the first time that major construction and operational funding from non-DOE sources came to a SLAC experiment. All of this was done through the International Finance Committee (IFC), which will be described later. This committee was a major player in the story of the construction of the *BABAR* experiment, but also in continuing operational support, and indeed was a central figure in solving the serious computing problem in 2001 that was caused by the accelerator team outperforming the PEP-II design luminosity (Section 1.4.3.5).

The international community working on the detector design for the SLAC-hosted asymmetric B Factory held its inaugural gathering at the end of 1993, as the culmination of a two year period of many workshops and detector meetings preparing for a B Factory, hopefully to be built at SLAC. Over the next year there were seven more collaboration meetings preparing the Letter of Intent and the Technical Design Report, and working through the final choices of technology and performance specifications for each detector sub-system. SLAC management recruited a short-lived, yet very important, Interim International Advisory Committee in 1993, to advise the lab on formation of the *BABAR* collaboration's first committees and identify and recruit those top level scientists. The target committee was an Interim International Steering Committee formed in early 1994 with a very important charge. It was to advise the laboratory on creating a detector R&D program (which was funded originally by SLAC, but later substantially supplemented by DOE/OHEP); to select an initial Executive Board of the collaboration; to write the original governance document and socialize it within the collaboration; and to choose the first Collaboration Council. This they did in short order and, having completed their job, the group just as quickly dissolved, with the thanks of the laboratory management.

The first Collaboration Council, in May 1994, quickly gave formal blessing to the collaboration's Governance document, and chose a Nominating Committee to search for the first spokesperson of the detector collaboration, following the search process defined in the newly passed governance rules. The Council ratified the Executive Board selection, and voted on the name for the collaboration, establishing the little French Elephant *BABAR* on "his" way to having an impressive citation count.[3] It was a productive first Council meeting, and a great kick-off for the *BABAR* collaboration. Just seven weeks later, at the July 1994 Collaboration Meeting, the Council formally ratified the nomination of David Hitlin as the first *BABAR* Spokesperson. Indeed, he had been filling the role of interim spokesman of this proto-*BABAR* community since the late 1980's, and had coordinated and led the first five formal meetings of the collaboration.

The detector collaboration had a single spokesperson through the entire construction and commissioning periods, and through the first years of data taking. From that point forward a new spokesperson was chosen from the collaboration every two years.[4] This group of seven individuals were able stewards of the scientific life of the *BABAR* collaboration. Their distinct visions on how to guide the experiment forward, their use of the associated strong management teams and their scientific judgment was no small part of the scientific success of *BABAR*. Within the *BABAR* collaboration the spokesperson is the chief officer of the collaboration, responsible for all scientific, technical, organizational, and financial affairs of the collaboration, and represents the collaboration to the SLAC laboratory, to the DOE/OHEP, and to the international funding agencies, represented by the IFC. The spokesperson is assisted in this heavy responsibility by a Senior Management Team for day-to-day decisions, and by an Executive Board which the spokesperson chairs. The Senior Management Team is chosen by the Spokesperson and ratified by the Executive Board and the Council.[5] The Executive Board is representative of the regional composition of the collaboration, and consists of members distinguished by their scientific judgment, their technical expertise, and their commitment to the experiment, and is chosen by the Council through an election process. The technical life of the collaboration was managed by the Technical Coordinator, who chaired the Technical Board. This was normally a twenty member group comprised of the detector system managers, the lead engineering staff, the computing leadership, and representatives from the accelerator collider team. For an important period of the life of *BABAR*, starting in 1999 for about two years, this group was expanded to include

[3] The name *BABAR* is derived from B and B-bar. The *BABAR* elephant and the many distinctive likenesses of that character, are used with permission of Laurent de Brunhoff, negotiated by David Hitlin. All copyrights were reserved to the owner, which changed to Nelvans after the late 1990's.

[4] *BABAR* Detector Spokespersons: David Hitlin (1993–2000), A. J. Stewart (Stew) Smith (2000–2002), Marcello Giorgi (2002–2004), David MacFarlane (2004–2006), Hassan Jawahery (2006–2008), François Le Diberder (2008–2010), J. Michael Roney (2010–).

[5] As part of the transition from detector construction to operation and data taking and physics analysis, a Senior Management team was formed in 2000, which included the Spokesperson, the Technical Coordinator, a senior technical advisor and lab contact if not covered by the Technical Coordinator, the Physics Analysis Coordinator, the Computing Coordinator and deputy, the past Spokesperson, and the Spokesperson-elect.

a much broader membership and called the Augmented Technical Board, which included all of the old Technical Board but also all of the leaders from electronics, online and off-line monitoring, computing, physics planning, and analysis machinery — a cadre of about 50 staff. For these two years this body worked hard and was a very important part of the *BABAR* story; they can take a lot of the credit for bringing the detector operations and the physics production activity into a true "factory mode," alongside the operations of the PEP-II accelerator complex. The collaboration has been well served by the five strong scientists who served as the *BABAR* Technical Coordinator[6] providing sound technical judgment and strong commitment to top level detector performance and to high efficiency uptime.

The collaboration is represented by a Council[7] with an elected chair and deputy, and made up of representatives from each institution participating in the detector collaboration. The Council is the principal governing body of the collaboration. The Council selects the Spokesperson Nominating Committee, ratifies the Spokesperson nomination, and the selection of the Executive Board. The Council appoints the operating committees of the collaboration — Membership, Speakers Bureau, and Publications Board. The Council has the unusual power to request a full review from the Spokesperson of any decision or action for which it deems such accountability was necessary, and could remove the Executive Board, or even the Spokesperson, under very strict conditions, if this unlikely situation should occur. This served as a balance to the strong and independent authority given to the *BABAR* Spokesperson under the collaboration's governance (see above).

The experiment began in 1993 and by 1995 had 483 members from 77 institutions, drawn from 10 countries — Canada, China, France, Germany, Italy, Norway, Russia, Taiwan, the UK, and the US. By 2005, the collaboration had grown to 625 members, from 80 institutions and 12 countries — with Israel, India, Netherlands and Spain having joined in the meantime, and China and Taiwan leaving. By January 2013 the active membership was still 325, of whom 51 were postdoctoral researchers and 56 graduate students. The experiment has produced 505 PhD theses, a number which is still growing, and is a remarkable testament to the intellectual life of the experiment and the breadth of its academic reach. The collaboration has produced more than one paper each week during a six year period (2004 through 2009) in the world's leading peer-reviewed journals, and a total by fall 2012 of 507 papers. We can celebrate that not only have both the *BABAR* and Belle experiments been "factories" of physics, producing new results over a broad spectrum of topics, but they have been veritable factories in producing candidates for new academic appointments for universities around the world from the pool of graduate students and post doctoral researchers who received their training on the *BABAR* and Belle experiments. They have outstanding training with both technical and operational experience with large detectors and running accelerators, and computing and data production on a factory scale, and hands-on development of creative data analyses in a small group environment.

In order for collaborators to be considered as authors on *BABAR*, they first must perform a substantial service to the experiment, either through the construction or operation of hardware, or by taking on some technical or administrative role required to maintain the quality of physics output from the experiment. Having qualified for authorship, a *BABAR* collaborator automatically signs papers. The authors appear in the author-list in alphabetical order by institute. As a result there is, in general, no direct correlation between the lead authors of a given analysis and the initial authors of a given *BABAR* paper. On occasion, where non-*BABAR* collaborators (mainly students) have made significant contributions to an analysis, requests have been made for those people to be added to the author list on the paper describing that analysis in detail. Such requests, while never a foregone conclusion, were generally granted.

1.4.2 Formation of the Belle collaboration

The Belle collaboration was officially formed at a one-day meeting held at Osaka University on October 7, 1993, where it was formally decided that the results of the previously held workshops (Abe et al., 1993) were encouraging enough to merit proceeding towards the development of a Letter of Intent during the next year (Cheng et al., 1994). This was followed by a series of meetings at which details of the detector design and issues of collaboration governance were discussed.

The collaboration organization was discussed at a second meeting at KEK on November 19–20, 1993. Here, it was decided that there would be three co-spokespersons, one representing each of the major constituencies of the collaboration: the KEK group, non-KEK Japanese groups, and groups from outside of Japan. All three spokespersons were elected by the full collaboration. In the beginning they served for a three year term that could be renewed. This rule was later changed to a two year term and limiting renewals to a single term. In addition, it was decided to have an Institutional Board (IB) comprised of the spokespersons and one representative from each of the collaborating institutions,[8] to deal with organizational and personnel issues, and an Executive Board (EB) consisting

[6] *BABAR* Technical Coordinators: Vera Lüth (1994–1997), Jonathan Dorfan (1997–1999), A. J. Stewart (Stew) Smith (1999–2000), Yannis Karyotakis (2000–2003), Bill Wisniewski (2003–2011).

[7] The *BABAR* Collaboration Council was formed under action of the Steering Committee (chaired by Pier Oddone), in May 1994 with the first chair being Livio Piemontese (1994), followed by Bob Wilson (1996), Erwin Gabathuler (1998), Patricia Rankin (2000), Klaus Schubert (2002), Frank Porter (2004), Gerard Bonneaud (2006), David Leith (2008), George Lafferty (2010), Brian Meadows (2012), and Fabrizio Bianchi (2014).

[8] Belle Institutional Board chairs: Yasushi Watanabe (1994–2000), Seishi Noguchi (1994–2000), Leo Piilonen (2000–2012), Christoph Schwanda (2012–).

of about ten members selected by the spokespersons to advise them on technical and scientific issues.[9] Important matters are discussed in the IB or EB and then proposed to a general meeting of the collaboration. The general organizational principle has been that, insofar as possible, decisions are made at general group meetings, either by consensus or by a vote of those present. Urgent decisions are made by the spokespersons in consultation with the EB. This organization proved to be reasonably successful; when the experiment switched from the construction to the operating phase in 1999, a task force was formed to re-examine the organizational structure, but eventually only minor changes in the basic structure were adopted.

The name "Belle" (proposed by A. Abashian, Virginia Tech) was adopted by a group vote at the third group meeting held in January 1994 at Nara Women's University.[10] The Belle logo (proposed by T. Matsumoto, Tohoku) was selected by a vote at the sixth group meeting at Tohoku University in February 1995.

The experiment began in late 1993 with 136 members from 39 institutions from 7 countries — Japan, China, India, Korea, Russia, Taiwan and the US. The first spokespersons[11] were F. Takasaki, S. Suzuki, and S. Olsen. By 2008, the Collaboration had grown to 275 members, from 60 institutions and 15 countries — with Australia, Austria, Czech Republic, Germany, Italy, Poland, Slovenia, and Switzerland having joined in the meantime. Up to fall 2012, the Collaboration published 370 papers in scientific journals.

Two unique features of the Belle publication policy, developed after considerable discussion and finalized at a meeting at KEK in November 2001, are worth noting:

Authorship confirmation: In Belle, there is no default author list and authorship on a Belle paper is not automatic. An important rule is that after a paper draft has received approval from its internal referees and the relevant physics conveners, it is posted for general review by all eligible authors.[12] During the review period, a collaborator is required to confirm his/her authorship by submitting the statement: "I have read this paper and agree with its conclusions. Please include me as an author." Only then is he/she included in the author list.

Author-list name order: In principle, the order of the names in the author list is alphabetic. However, the persons responsible for preparing a paper can propose to the spokespersons that a single person or a small group of people be listed as first authors. In general, the spokespersons have approved such requests, the exceptions being for important papers central to the main goals of the Belle program (*e.g.*, precision measurements of $\sin 2\phi_1$) or cases where the proponents cannot agree on the specific name order. In these cases, the author list is strictly alphabetic.

When this policy was adopted, it was with the explicit proviso that it could be re-examined and modified at any time. However, it has proven to be quite popular among Belle collaboration members and has never been modified. Almost all Belle papers since 2002 have had a first-author group, with up to seven collaborators appearing out of alphabetical order at the start of the list; the number of confirming authors has been, on average, about half of the total number of eligible authors.

1.4.3 Building the BABAR detector

The *BABAR* collaboration faced a set of design challenges as they prepared their Letter of Intent (LOI) during the period spring 1993 through summer 1994. These included a long list of issues demanding detailed analysis to arrive at conclusions — inheriting an Experimental Hall which was smaller, and had too low a beam height, for an optimal "start-from-scratch" design; determining how to meet the stringent specifications for the silicon vertex detector and drift chamber tracker to manage both the spatial resolution to measure the separated B decay vertices and at the same time handle measuring with adequate precision the broad momentum spectrum of the produced tracks; meeting the strong specifications for the charged particle identification along with good photon detection for both position and energy measurement, and for reliable muon and K^0_L detection. The actual LOI document was produced over a few months, was completed in June 1994, and quickly approved by the SLAC Experimental Program Advisory Committee (EPAC) in July, only one month later.

As with all high tech projects, the detector design, construction, and commissioning came along with its problems. Fitting the collaboration's ambitions to the available budget was a stringent constraint at the outset. A great deal of hard work went into defining the technical details for the final sub-systems in the short nine month period between the submission of the *BABAR* Letter of Intent and the submission of the Technical Design Report, in February 1995. The TDR had essentially the final vertex detector geometry and technical description, a new Drift

[9] Belle Executive Board chairs: Kazuo Abe (1994–2000), Dan Marlow (2000–2002), Alex Bondar (2002–2010), Simon Eidelman (2010–2012), Tom Browder (2012–2013), and Toru Iijima (2013–).

[10] The name Belle is a pun on beauty, the quark of primary interest for the B Factories, which led to a natural choice for the name of the commissioning detector discussed later in this chapter: BEAST. The name can also be decomposed as B-el-le implying electrons (el) and their opposite — positrons (le) — colliding to produce B mesons.

[11] Belle Detector Spokespersons: Fumihiko Takasaki (1994–2003), Shiro Suzuki (1994–2000), Steve Olsen (1994–2006), Hiroaki Aihara (2000–2006), Masanori Yamauchi (2003–2009), Tom Browder (2006–2012), Toru Iijima (2006–2012), Yoshihide Sakai (2009–), Leo Piilonen (2012–), Hisaki Hayashii (2012 –).

[12] Eligible authors are those members of the collaboration that actively contributed to Belle for at least six months in form of construction, maintenance or operation of the detector, software development, contributing to ongoing analyses, etc. They are also required to take a certain number of experimental shifts.

Chamber design with flat aluminum end plates instead of a cleverly shaped carbon fiber construction, the choice of the internally reflected Cherenkov detector, DIRC, and its quartz bar radiators for the particle identification system, and finalizing the choice of the muon detector technology as Resistive Plate Chambers, RPC's. Later on there were other surprises that emerged and had to be dealt with promptly; the flux return iron for the magnet had production schedule problems from the Japanese supplier as did the superconducting magnet coil from Italy, but the IFC came through with an added incentive clause to the magnet steel contract, and the lab management's connections to the US Air Force helped bring the delayed superconducting coil to SLAC on time, via "air mail" on a C5A, as part of a crew training flight. Learning how to grow the cesium iodide crystals and managing the salt delivery schedule for the large electromagnetic calorimeter, and how to successfully polish the quartz bars for the DIRC particle identification system to the exacting dimensional optical specifications, were time-consuming problems that emerged during construction, looked as though they might cause serious schedule problems, required creativity and focused commitment, but were finally solved in time for detector turn-on.

1.4.3.1 The PEP-II commissioning run

Immediately after PEP-II approval in June 1993, it was realized that, because of the existence of the PEP tunnel and the significant reuse of PEP machine components, that PEP-II machine would be ready one or two years before the *BABAR* detector would be. This was considered as a good opportunity to be able to tune the machine without the complications of detector protection and to provide a fast start for *BABAR*. The machine had to reach a luminosity 100 times higher than previously achieved and was doing so with much higher currents. The potential threat posed by backgrounds induced by such currents was considerable. A few years previously at SLAC, muons from the SLC tunnel had been compromising the Mark-II/SLC detector performance, and therefore there was a high degree of consciousness of these issues among members of the PEP-II machine group.

In 1996 there was a call proposing the instrumentation, at minimal costs, of the PEP-II IR in the absence of *BABAR* during two running campaigns: a short one, in 1997, where only the HER ring would be available, and another one in 1998 with both rings. The goal of this instrumentation was manifold:

- understand and quantify the various background sources in both rings,
- provide to the machine reliable background sensors, so background could be reduced while tuning the machine,
- test prototypes of final *BABAR* elements to understand their sensitivity to background,
- test the radiation protection and abort mechanism system.

It was of course not possible to cover all these issues with a very small number of detectors since some of the requirements were potentially conflicting with each other. *BABAR* therefore adopted a "wideband" approach where a variety of detectors were assembled for the commissioning detector. PIN-diodes, silicon strip detector modules, similar to the final *BABAR* ones, a newly built mini-TPC, and reused straw tubes were used to understand the background resulting in charged particles, whereas a newly built movable ring of thallium-doped CsI (or CsI(Tl)) crystals, similar to the *BABAR* ones, were used to monitor neutral background. DIRC and IFR prototypes complemented this equipment.

This set-up and the 1997 and 1998 campaigns turned out to be successful. The large backgrounds observed were mostly due to the not-yet-scrubbed state of the rings; their various sources were understood, and their variation with current properly measured. After the required tuning, simulations were able to reproduce the observed background to within 50%. The correct strategy for a fast start to the *BABAR* experiment in 1999 was established, together with a flexible and reliable abort system.

1.4.3.2 The *BABAR* background remediation effort and detector commissioning

Since *BABAR*'s high potential vulnerability to PEP-II background had been demonstrated both from simulations and from the 1997–1998 background measurement campaign described above, in 1998 a background remediation effort was set up to precisely quantify the adverse effects engendered by high background on the *BABAR* detector and physics analysis. Four areas were identified:

1. long term degradation due to integrated dose,
2. immediate damage due to a radiation burst,
3. high occupancy in the detectors leading to ghosts or to inefficiency,
4. large dead-time in electronics read out leading to dead time and/or inefficiency.

This remediation group took many important decisions to protect *BABAR* in both the short and long term, based on background extrapolations taking account of future running conditions: a very comprehensive set of dosimeters were installed throughout the detector, and an abort strategy was put in place to avoid item (2). The weakest points in the data acquisition (DAQ) chain were identified as bottlenecks two years before they needed upgrading. As a result the DIRC and drift chamber electronics were partially upgraded in good time and without limiting data taking. Good running conditions were defined in order that *BABAR* did not accumulate data that would prove not to be useful.

A strict policy to use up allowed radiation exposure as a function of the integrated luminosity was defined. A 10% occupancy limit in the drift chamber and the vertex detector were thus defined so as to guarantee good physics output, and were correlated to real time background sensors incorporated in the machine diagnostics system to prevent running in worse conditions.

Another crucial aspect of this task force was to prepare a set of 25 machine-detector interface experts that provided 24-7 support in the PEP-II control room, during the first four years of *BABAR* data taking. These background shifts proved invaluable to further the understanding and control of the background issues and to disseminate background related issues to the PEP-II operations crew.

The first short run took place in May 1999, to be followed by a short shut-down to install the full DIRC system, and then operations began again in late October. Physics running began in late 1999 and continued through 2008, when the experiment was turned off with the PEP-II collider having achieved design luminosity (3×10^{33} cm^{-2}s^{-1}) within one year of operation. During its final year the PEP-II collider ran regularly at a daily integrated luminosity of over seven times the design value, with record high circulating currents of both electrons and positrons, and accumulating 557 fb^{-1} of data in the *BABAR* detector. Background issues were always present during the lifetime of *BABAR*, but these were successfully managed to prevent them from seriously damaging the experiment. Once routine operation of PEP-II and *BABAR* had been achieved, the background remediation effort underwent a transition to the Machine-Detector-Interface (MDI) working group that was responsible for maintaining a watchful eye on the background conditions expected within the detector, and over time learned (with the help of accelerator physicists from PEP-II) to use data from both the machine and the detector to measure beam parameters such as emittances, the betatron oscillation amplitude at the IP, and estimates of the beam sizes for bunches of electrons and positrons (Kozanecki et al., 2009). This background remediation and MDI effort was key to *BABAR*'s high luminosity running and was the result of the hard work of many people from all parts of the PEP-II and *BABAR* teams.

1.4.3.3 Other beam-related backgrounds encountered

In addition to the expected background effects dominated by beam-gas terms, some unexpected sources came along the way:

- A luminosity term was readily observed in addition to single beam backgrounds and to backgrounds induced by beam-beam effects. This luminosity term was traced to the presence of off-momentum electrons or positrons after radiative Bhabha scattering. The unfortunate presence of a dipole magnetic field at the IP made *BABAR* very sensitive to these luminosity terms that became relatively more and more important as the machine was getting scrubbed and its peak luminosity increased.
- Electron cloud effects were analyzed in early studies in 1993-1994: they cause bunch-to-bunch instabilities believed to be damped by the proposed feedback systems. In 1999 electron cloud effects were experimentally observed by huge pressure increases in the LER above thresholds and by intra-bunch size enlargement unaffected by bunch-by-bunch feedbacks. The machine was immediately equipped wherever possible with cable coils around the beam pipe providing a 50 Gauss protecting field that pushed the current thresholds far away. Nevertheless, the electron cloud effect was responsible for a significant increase of the positron beam size with current that would finally limit the maximum achievable luminosity.
- Neutron induced background, where neutrons are produced by few-MeV gamma photonuclear reactions, were found to be quite significant in some sub-detectors and even dominant in the case of the IFR.

1.4.3.4 *BABAR* reviews and oversight committees

The detector design and construction were formally overseen by two committees that were standard to the normal SLAC way of doing things — a DOE Lehman Review process for agency oversight of construction readiness and budget soundness, and the usual laboratory Experimental Program Advisory Committee, which had stewardship over the SLAC experimental program. There were two other new, and very important, very helpful, international committees as partners in the detector building story — a Technical Review Committee (the Gilchriese Committee), and the International Finance Committee, the IFC. The Technical Review Committee worked closely with the Detector collaboration, met twice per year through the construction period, and provided advice to both the Spokesperson and the laboratory. The committee worked in sub-committees on specific aspects of the detector construction, or as requested by either the Spokesperson or the Research Director. In practice, the collaboration used this committee in its preparation for the formal technical reviews by DOE — the Lehman Reviews. The IFC met twice per year to review progress of the construction, discuss with the lab management and the Spokesperson progress and concerns, and to set homework for lab and collaboration. Members of the group were very used to working together from many years doing just this same exercise at CERN, trusted each other and the agencies they represented, and took a strong, stewarding responsibility for their new charge — the fledgling North American-hosted *BABAR* experiment. They met by phone in between regular face-to-face sessions when serious, time-urgent problems came up, and were very effective in finding solutions to the unexpected problems when they arose. The IFC were able to ensure that *BABAR* could draw together a critical mass of manpower and institutional support from each of the regions working on the experiment, to ensure success on the central areas of the experiment construction. They, as a group, appreciated that SLAC and the US would carry the largest share of the expenses for building and operating the experiment, but participated in solving all of the many problems that arose as "our joint problem". Largely because of their long history on other experiments at CERN, and the mutual trust they had built up, they were a very important component in guiding and enabling an extraordinary experiment. Both

committees continued their important stewardship roles beyond the end of the construction.

The Technical Review Committee was called back when the lab and the experiment ran into computing problems because the machine performance surpassed the design luminosity, causing a computing load that could not be handled by the laboratory alone, without severe financial hardship. They were also called to help as the detector proposed hardware upgrades to several sub-systems. They performed spectacularly, once again.

The IFC, by the constitution, continued the twice-a-year oversight of the detector collaboration through the operational phase of the *BABAR* experiment. Again, this was a familiar role, as they worked in a similar way at CERN.

The IFC determined the Common Fund component of the construction budget and the operating budget, and negotiated with the lab and the Spokesperson on both of these important, but thorny issues. The financial needs of the collaboration were presented by the Spokesperson after discussion with the laboratory management, while the decision making on what financial support would actually be provided was the IFC's job. They also defined how each region would meet their share of these costs. Typically this was by a negotiated mix of head-count and system responsibility determining the cost sharing in the construction phase, and essentially it was by participating head-count for the operational phase. During construction this Common Fund was around \$4 M per year, totaling \$15.4 M over the construction period, and about \$2.7 M per year during the operations period, until the computing crisis (see the following two sections).

The DOE Lehmann Committee formally base-lined the detector budget in late 1995. Each member of the Technical Review Committee had an individual system assignment, and through the full construction and commissioning schedule these connections were maintained and provided timely advice to the construction team and up-to-date information to the review panel as a whole, and to the lab management. The IFC was a very helpful resource for both the laboratory and for the experiment. They brought a different kind of management layer into the lab — a technically savvy group, and a small enough group to have strong working relationships between each other, in command of substantial financial resources, and very committed to the success of the *BABAR* project. The Technical Review Committee was rather stable in its membership throughout the period of construction, with only a few people stepping down and requiring replacement. However the IFC was rather different, in that the heads of each of the international partner agency offices rotated quite frequently.

1.4.3.5 Computing

From the beginning SLAC had proposed that the lab would provide the computing hardware resources, both processing and data storage, for the *BABAR* experiment. The collaboration, on their part, was to provide the required trained manpower needed to create the software tools and handle the data analysis. Early on, the IFC agreed to support a model for computing where computer professionals were hired to work alongside computer-savvy collaboration physicists. This was a very important early investment that strategically enabled the rest of the *BABAR* computing story and bolstered the scientific output of the experiment. The cost of this manpower was borne by the Common Fund.

Computing became a serious problem around the year 2000 as the PEP-II collider luminosity climbed past the design luminosity and eventually grew to three times that. The cost of upgrading the *BABAR* computing center to handle the increased data analysis and data processing was more than the lab budget could handle. In addition, the existing *BABAR* computing model did not scale to the large number of machines that would be required to keep up with the data taking. The IFC was sympathetic, but requested that the Technical Review Committee examine the problem, and carefully review the technical details of the collaboration's proposal along with the proposed cost model. The new costs were much too large for the non-US countries to support directly with cash. This turned out to be a blessing in disguise because the European IFC members proposed an alternative in which the computing load would be distributed among several "Tier A" computing centers in Europe, in addition to SLAC. Europe had built up a large computing capacity in anticipation of the coming LHC experiments, most of which was lying fallow as the LHC turn-on was delayed. The proposed *BABAR* computing model successfully passed the technical review by the Technical Review Committee, and at a special meeting in Paris in January 2001 the IFC formally agreed that the costs of computing for the *BABAR* experiment, beyond those to support the original PEP-II design luminosity, should be shared by the whole collaboration. In retrospect this spark of creativity not only saved the *BABAR* experiment, but helped set the stage for international grid computing in HEP.

As part of the examination of the computing crisis, the collaboration rethought the needed changes to the existing computing model, and a small, passionate, very focused group worked to implement an entirely new computing model. The largest change was moving from the *Objectivity* data base system to a `Root`-based system, which was done in 2003-2004, but beyond that there were continued optimizations over the following years. The implementation of the new arrangement for handling computing at the distributed agency computing centers was put in place in 2003, with the international Tier A site system set up with SLAC, CCIN2P3 Lyon (France), INFN Padova and CNAF (Italy), GridKa (Germany), RAL (UK) and latterly U. of Victoria (Canada) making up the nodes. The core computing (CPU and disk) came two thirds from SLAC and one third from the other sites. Two years later, this sharing was fifty-fifty through the intense analysis period. This high volume, distributed computing environment was the first successful example of large scale production distributed computing (also known as Grid Com-

puting) in HEP in an actual data-taking experiment. The *BABAR* collaboration set up a Computing Steering Committee, which twice a year examined the foreseen needs for processor power and storage, and reported to the IFC. This ranks among the great achievements of the collaboration and of the funding agencies within the IFC. It built on the large international investment in Grid computing, and on very good international networking. The new computing model, including the change to the `Root` data analysis framework, was in operation by mid 2003 (well ahead of schedule), and allowed the experiment to keep processing the data, even at the higher luminosities.

1.4.3.6 Sub-system upgrades

BABAR, the lab, and the Technical Review Committee engaged in a review of each of the detector sub-systems in the 2003, with the outcome that all of the systems were expected to manage the increases in luminosity promised by the accelerator team, with just nominal improvements (even the expected increased backgrounds), with one exception — the muon system's IFR chambers. The IFR sub-system had become a serious problem around 2001, with dropping efficiency as the accumulated radiation dose increased. New muon chambers had to be designed and built, and then the installation of the new technology successfully implemented without an undue hit to data taking. This was another multi-lab and multi-nation effort to execute this detector upgrade rapidly while still taking data. The collaboration made a heroic effort and made very good progress in production of replacement detectors — this time LST's, which were essentially completed by the end of 2004. Installation in the detector was not completed until 2006, due to a chain of unfortunate accidents unrelated to *BABAR*. The new chambers worked very well, and for the remaining running *BABAR* had high efficiency muon tagging.

1.4.4 Building the Belle detector

As with *BABAR*, the construction phase of the Belle detector had to resolve a number of technical challenges in order to provide a design that would work sufficiently well to deliver the physics goals of the B Factory. As is typical with particle physics experiments, some of the sub-systems under consideration for Belle had proposed variants that had to be studied in detail (Section 1.4.4.1). Along the way the Belle detector team were also presented with several unexpected problems that required timely resolution (Section 1.4.4.2). The commissioning period and the first years of full Belle operation are discussed in Sections 1.4.4.3 and 1.4.4.4 respectively.

1.4.4.1 Design choices and related issues

Beam pipe: The beryllium beam pipe section is made of two concentric cylinders and an intermediate cooling channel. The only supplier for beryllium in such a configuration was Electrofusion in California. Because of its toxicity, it was only with considerable difficulty that the import of beryllium was allowed by Japan Customs officers.

Silicon: The silicon detector — a key component for the success of a B Factory experiment — was originally planned to use a custom designed Application Specific Integrated Circuit (ASIC), however as discussed in Section 1.4.4.2, the then-standard Honeywell technology for radiation-hard ASIC design could not be used for a project in Japan. As a result, the choice of which ASIC to use had to be changed to allow a working vertex detector to be assembled and installed in time for data taking, while a suitable radiation-hard design was developed for a subsequent detector.

Drift chamber: The Central Drift Chamber (CDC) design originally envisaged two chambers: an inner "precision chamber" with two wire layers and three cathode-strip readout surfaces that focused on high spatial resolution and the provision of z-direction information for triggering and an outer 48-layer closed-cell drift chamber for momentum and dE/dx measurements.
Since most of the particles produced in B meson decays have relatively low momentum, multiple scattering is a major contributor to momentum measurement precision. Because of this, and in order to maximize the chamber's transparency to synchrotron X-rays, considerable effort was made to increase the effective radiation length of the chamber. This included the use of a helium-based chamber gas and aluminum field wires with no gold plating, both unique features at that time (Uno et al., 1993). Eventually, the inner precision chamber and the outer tracker were both incorporated into a single, common gas vessel and their intervening gas barrier was eliminated.

Particle identification: A number of technologies were investigated for an efficient charged particle identification system for higher momentum tracks. These included a Time-Of-Flight (TOF) system, an array of aerogel radiators (ACC) developed in collaboration with Matsushita Electric (Enomoto et al., 1993), and DIRC for the barrel region following the design concept developed for *BABAR* (Ratcliff, 1993) and a focusing DIRC for the forward end-cap region (Kamae et al., 1996; Lu et al., 1996). The choice of aerogel for both the barrel and end-cap was finally made by an ad-hoc task force appointed by the spokespersons. Their main reason for the selection of the aerogel option was its overall simplicity and minimal impact on the design of the accelerator and other detector components. The aerogel system served the Belle experiment well.
In addition to a cylindrical array of 128 4-cm-thick scintillators as a TOF system, for additional charged particle identification capability, it was also decided to include a second layer of 64 4-mm-thick counters (the TSC) to form a track-trigger. The TSC-TOF was initially considered to be a unnecessary redundancy. The subsequent issues with regard to de-scoping the SVX trigger capability (Section 1.4.4.2) meant that

the provision of this redundancy proved to be a wise choice. The fast L0 triggers generated from TSC-TOF coincidences are an essential part of the Belle DAQ system.

K_L^0-muon detector: For the detection technology of the "KLM" (Belle's instrumented return yoke) LST's and RPC's were considered; RPCs were finally selected because of their robustness and simplicity. The key components in an RPC are the highly resistive planar electrodes that require very smooth surfaces in order to avoid non-particle induced electromagnetic discharges. Various electrode materials were studied including oil-covered Bakelite, dry Bakelite, ABS and PVC plastic, and float glass. It was found that ABS plastic and float glass had acceptable efficiency and lifetime properties and glass electrodes were selected because of their availability and low price (Morgan, 1995). This was the first use of glass electrodes in a large-scale RPC system. These worked well as long as care was taken to avoid any moisture contamination in the operating gas.

1.4.4.2 Belle construction: two major crises

The Belle and KEKB Letters of Intent, submitted in April 1994, resulted in the approval of the project by the Japanese government, and construction started soon thereafter. The detector construction had two major crises: the failure of the initially planned technology for the silicon vertex detector and the collapse of the support structure for the CsI crystals of the barrel electromagnetic calorimeter.

SVX failure

A complication arose in the design of the ASIC chip, called SMAASH (with both analog and digital pipelines, on-board data sparsification, and trigger signals derived from 32-bit digital OR circuits; Yokoyama et al., 1997), intended for front-end readout of the SVX detector. US export restrictions meant that the chip design program also had to incorporate the development of the required radiation-hard techniques for the SMAASH ASIC chip. In early 1997, technical problems with the chip development caused the SVX subsystem project to fall well behind the schedule needed to be ready in time for the August 1998 installation date. Following a June 1997 recommendation of a review panel of international experts chaired by P. Weilhammer of CERN, Belle abandoned the SVX and redesigned the entire system, settling for a more modest arrangement, SVD1, based on commercially available, non-radiation-hard components, that met the angular acceptance and signal-to-noise requirements, but with no triggering capability and a marginally acceptable data acquisition rate. SVD1 (Alimonti, 2000) was a three-layer array of double-sided silicon detectors (DSSD) that were fabricated by Hamamatsu Photonics using a design that was originally developed for the DELPHI experiment's micro-vertex detector. The readout was based on the VA1 front-end chip that was commercially available from the IDE AS company in Oslo, Norway. In a crash program involving a close collaboration among thirteen different groups in Belle and the KEK mechanical shop, SVD1 was designed and constructed and ready to be installed in Belle by the beginning of October 1998. By that time, the Belle roll-in date had been shifted to February 1999. To compensate for SVD1's lack of internal trigger capabilities, a fast L0 trigger derived from TSC-TOF coincidences was used to latch the SVD response for potentially interesting beam-crossings while the slower L1 trigger decision was being made.

Because it was a relatively primitive system, enough spare parts and a prototype frame were available to permit the assembly of a spare device, SVD1.1. During all of the data-taking prior to the installation of SVD2 in 2003 (Natkaniec, 2006), Belle maintained a spare, replacement vertex detector that was ready to be installed. The original version was eventually replaced after radiation damage in summer 1999, and was replaced again by a more radiation-hard version a year later.

Collapse of the CsI crystal support frame

In the Belle calorimeter design, the crystals are supported by a honeycomb cell structure formed by 0.5-mm-thick aluminum fins stretched between a 1.6-mm-thick aluminum inner cylinder and an 8-mm-thick stainless steel outer cylinder. The fins and the inner cylinder were originally welded together and bolted to the outer supporting cylinder.

In May 1998, when the loading of the crystals into the structure and the associated cabling was nearly complete, and just weeks before the scheduled date for installation of the ECL into the Belle structure, severe deformations to the structure were evident and loud ominous sounds were heard when the partially filled support structure was rotated. These were caused by failures of many of the welds between the thin aluminum vanes and the inner cylinder. After removing all of the crystals and cables, a major renovation of the structure was undertaken that stiffened the outer support cylinder and used bolts and washers to connect the aluminum vanes to the inner cylinder. This required a delay of the Belle roll-in date from August 1998 until February 1999. The modifications to the support structure were completed by mid-August and crystal re-installation and re-cabling were completed in September.

1.4.4.3 KEKB/Belle commissioning and early running

The original schedule, in which Belle and KEKB were commissioned at the same time, was changed. The initial KEKB commissioning occurred without Belle in place. Instead, a modest commissioning detector, called BEAST, was installed to provide feedback to KEKB on background

conditions during the machine study and tuning period. During the initial KEKB beam commissioning period, the fully assembled Belle was commissioned in the rolled-out position using cosmic rays.

KEKB commissioning run

The initial KEKB commissioning run started in December 1998 and was reasonably successful, but not without mishap. The injection system, including the positron source, worked well, although sometimes positron injection produced large radiation doses in BEAST. The closed-orbit deviations in both rings were corrected to less than 1 mm, which indicated that the magnets were well aligned. In the high-energy ring (HER), a 250 mA electron beam ($\sim$ 0.25 times the design value) was stored with a respectable 60 minute lifetime. In the low-energy ring (LER), a 370 mA positron beam was stored ($\sim$ 0.15 times the design value).

In February, during high-current operation of the HER, the intense synchrotron radiation fan generated in the downstream superconducting IR quadrupoles — through which the exiting electron beam passes off-axis and, thus, in a region of high field — burned a hole through a downstream section of the aluminium beam-pipe, causing a catastrophic vacuum system failure. A replacement pipe section, made from aluminum, was quickly fabricated and installed. Subsequent simultaneous running of both the LER and HER produced collisions with a luminosity that was estimated to be $\sim 10^{30}$ cm^2 s^{-1}. BEAST measurements indicated that the SVD occupancy rates would probably be tolerable, but the large radiation doses that sometimes occurred during positron injection posed some danger. In addition, BEAST results indicated that the CDC occupancy levels and CsI pedestal widths would be very high during high-current operation of the HER.

Belle commissioning run

The commissioning of the fully assembled Belle detector and solenoid with cosmic rays in the rolled-out position also started in December 1998. This allowed for a complete relative alignment in space and time of all the detector subsystems and exposed some problems with the detector and the data acquisition system. The SVD1 and CDC spatial resolutions and the overall p_T resolution of the CDC were measured to be near the design value. The other subsystems, including the trigger and the DAQ software, also performed well. One major problem was an efficiency drop in the resistive-plate chambers of the K_L^0-muon detector, which was caused by minute levels of water vapor contamination in the chamber gas. This was cured by replacing all 5 km of polyolefin tubing in the gas distribution system with copper.

1.4.4.4 Early operation

Belle rolled into place on May 1, 1999 and saw first collisions (25 mA positron beam on a 9 mA electron beam) on June 1. Early running was plagued by high occupancy in the CDC caused by synchrotron radiation produced by the electron beam. The origin of this problem was traced to back-scattered X-rays from the aluminum section of the down-stream beam-pipe that was installed during the KEKB commissioning run. In addition, in July, there was an abrupt deterioration in the performance of the inner-most layer of SVD1.0. This was found to be due to low-energy synchrotron X-rays produced in one of the upstream correction magnets in the HER.

The first run managed to map out the $\Upsilon(4S)$ peak, and was then terminated in August. In the ensuing two-month shutdown, the downstream aluminum pipe was replaced with a copper version, SVD1 was replaced by the SVD1.1 spare, the CDC grounding was improved and additional beam halo masks were incorporated inside the HER to reduce backgrounds from spent electrons. Software current limits were established on the upstream correction magnets to prevent a repetition of the conditions that destroyed SVD1.0. Although the front-end electronics for SVD1.1 were not radiation hard, subsequent versions of the VA1 chip were fabricated with smaller feature sizes, and these were found to be quite radiation hard (Taylor, 2003).

Electron cloud instability

These fixes were effective and in the next run—Belle's first physics run—Belle collected a 28 pb^{-1} data sample at the $\Upsilon(4S)$ peak containing 76k hadronic events with all detector sub-systems operating at near-design performance levels. The peak machine luminosity was 3.1×10^{32} cm^{2}s^{-1} but attempts to go above this level were stymied by a blow-up of the positron beam size. This was traced to the electron cloud instability, in which photo-electrons from the vacuum chamber wall produced by synchrotron X-rays from one positron bunch experience a Coulomb attraction to the following positron bunch. The cure for this was the establishment of a weak magnetic field near the vacuum chamber wall that bends the photo-electrons back into the wall. The first attempt at doing this in the LER involved attaching a large number of small permanent magnets to the beam pipe, which was only modestly successful. The real cure to the problem was achieved by the painstaking wrapping of solenoidal coils around all exposed sections of the LER beam pipe, as was the case with PEP-II.

1.5 Physics at last

The KEK and SLAC B Factories were under constant examination to improve the respective accelerator teams' understanding of beam optics, accelerator controls, and all aspects of collider operations; the instantaneous luminosity increased gradually and steadily with the passage of time. Both machines quickly passed their design luminosities. The PEP II luminosity passed 1×10^{33} cm^2 s^{-1} in 1999, and reached 2×10^{33} cm^2 s^{-1} early in 2000. The

KEKB peak luminosity passed 1×10^{33} cm^2 s^{-1} in February 2000 and reached 2×10^{33} cm^2 s^{-1} by the summer, later reaching 3.4×10^{33} cm^2 s^{-1} in April 2001, the largest luminosity then achieved in colliders. Over the life of the B Factories there was a further improvement by a factor of six at both facilities: see Table 1.3.1.

There were two very different kind of collaborations going on between the two B Factory communities: the collaboration between the accelerator groups, and that between the detector and physics analysis groups. The accelerator collaboration was both close and collegial. On each occasion when one or the other group were faced with a new phenomenon on their suite of accelerators or control systems or simulation systems, they would be in touch, and most often a small crew of experts from the "other team" would appear in their control room trying to help diagnose the new behavior. This joint facing of each new problem was certainly a component of the increased performance of both machines. The competition between the two teams was also very important in motivating careful attention to up-time, and to optimum performance. The detector/physics teams, by contrast, were relatively separate. One explanation of this comes from the desire not to share "too much" the details of data analysis, so that any discovery made would be independently verified by the other experiment. A secondary concern was to ensure that knowledge of analysis techniques and systematic uncertainties from one experiment did not unintentionally lead to a bias on the results, and "too good" agreement between Belle and *BABAR*. In any case, while there were occasional requests for help or advice on problems, details of on-going analyses were treated as confidential.

The initial aim of both experiments was to present first results at the ICHEP 2000 meeting in Osaka, Japan. Belle submitted 17 papers to this conference, most of these using 5.6 fb^{-1} of data, whereas *BABAR* submitted 15 papers based on a data sample of 9.8 fb^{-1}. Belle's first journal paper, a measurement of the $B^0 - \overline{B}^0$ mixing parameter Δm_d, was submitted to Physical Review Letters in November 2000 (Abe, 2001b) and the first *BABAR* paper accepted for publication was measurement of time-dependent *CP* asymmetries in B^0 meson decay and was submitted to Physical Review Letters in February 2001 (Aubert, 2001a). These first publications were a taste of things to come.

1.5.1 Establishing *CP* violation in B meson decay

Following the initial results shown in Osaka, the two B Factories continued to work in competition with one another toward the goal of determining the level of *CP* violation manifest in B meson decay. The two experiments had similar strategies: to accumulate as much data as possible in time for the next summer conference season. By the time of the 2001 summer conference season *BABAR* and Belle had accumulated, and processed for physics analysis, approximately 29 fb^{-1} of data each at the $\Upsilon(4S)$ peak.

At the 2001 Europhysics Conference on HEP *BABAR* announced the result $\sin 2\beta = 0.59 \pm 0.14(\text{stat}) \pm 0.05(\text{syst})$, a 4.1σ deviation from the *CP* conserving solution of $\sin 2\beta = \sin 2\phi_1 = 0$. At the same time this result was submitted for publication. A few weeks later at the 2001 Lepton-Photon conference, Belle announced their result $\sin 2\phi_1 = 0.99 \pm 0.14(\text{stat}) \pm 0.06(\text{syst})$, a 6σ deviation from the *CP* conserving solution. These *BABAR* (Aubert, 2001e) and Belle (Abe, 2001g) results were published as back-to-back articles in the August 27, 2001 issue of Physical Review Letters. The Belle and *BABAR* central values straddled predictions based on the KM model — and they were consistent with each other. Together the B Factory results clearly established the existence of *CP* violation in the B meson system. More details of these and subsequent measurements of $\phi_1 = \beta$ can be found in Chapter 17.6.

1.5.2 The premature end of BABAR data taking

As a result of budgetary decisions within the US, data taking with *BABAR* was curtailed and the experiment stopped running in 2008. However, the *BABAR* management, supported by SLAC, was able to work with the funding agency representatives in order to ensure that a series of planned special runs at center-of-mass energies away from the $\Upsilon(4S)$ would be allowed to go ahead before the shut-down. As a result *BABAR* accumulated data at the $\Upsilon(3S)$ and $\Upsilon(2S)$, and performed an energy scan above the $\Upsilon(4S)$. The most significant result from these runs was the discovery of the η_b, the long-sought-after ground state of the $b\bar{b}$ system (Section 18.4). The measurement of the ratio of hadrons to di-lepton pairs can be used to obtain a precision determination of the b quark mass as discussed in the same section.

1.5.3 The final Belle data taking runs

The final beam abort ceremony of KEKB/Belle took place at KEK on June 30, 2010. The last data taking period was devoted mainly to an energy scan around the $\Upsilon(5S)$, collecting more than 21 fb^{-1} of data (see Section 3.2 for details on data taking).

The end of Belle data taking was triggered by two considerations. First, Belle accumulated data in excess of 1 ab^{-1} in accordance with the plan put forward before the start of operation. Second, it was time to start work on the upgrade of the facility, both the accelerator (to SuperKEKB) and the detector (to Belle II).

Chapter 2
The collaborations and detectors

Editors:
Nicolas Arnaud (BABAR)
Hiroaki Aihara, Simon Eidelman (Belle)

Additional section writers:
I. Adachi, D. Epifanov, R. Itoh, Y. Iwasaki, A. Kuzmin, L. Piilonen, S. Uno, T. Tsuboyama

2.1 Introduction

The *BABAR* and Belle detectors have been primarily designed to study *CP* violation in the B meson sector. In addition, they aimed to precisely measure decays of bottom mesons, charm mesons and τ leptons. They also searched for rare or forbidden processes in the Standard Model. As described in detail in this book, all these original goals have been reached and in many cases exceeded, thanks to the very high integrated luminosity delivered by the two B Factories (PEP-II and KEKB, see Chapter 1), to the quality of the physics analysis stimulated by the fruitful competition between the two experiments, and, last but not least, to the excellent performance of the two detectors, maintained over almost a full decade-long operation period. In the following, the main characteristics of *BABAR* and Belle are reviewed and compared, while the main information about the evolution of these detectors during the data taking period can be found in Section 3.2. These two chapters, however, only provide an introduction to the two B Factory detectors and to their years of operation. For more details, the reader should consult specific detector papers from *BABAR* (Aubert, 2002j, 2013) and Belle (Abashian, 2002b; Brodzicka, 2012), as well as the references therein. A summary of the two detector main characteristics can be found in Table 2.2.1 located at the end of this chapter.

Both e^+e^- colliders operated mainly at the center-of-mass energy of 10.58 GeV which corresponds to the mass of the $\Upsilon(4S)$ resonance which decays almost exclusively (with branching fraction greater than 96%) to charged or neutral B meson pairs (Beringer et al., 2012).

In a $\Upsilon(4S)$ decay, neutral B mesons are produced in a coherent quantum state $|B^0, \overline{B}^0\rangle = (|B^0\rangle|\overline{B}^0\rangle - |\overline{B}^0\rangle|B^0\rangle)/\sqrt{2}$, which means that, until one meson decays, there is always one B^0 and one $\overline{B}^0$ in spite of $B^0 - \overline{B}^0$ mixing. Studying their decays often requires one to reconstruct B decay vertices and to measure the flight times of these mesons – in particular for time-dependent *CP* violation analysis. As they are produced almost at rest in the $\Upsilon(4S)$ rest frame – the mass of the resonance is just above the $B\overline{B}$ production threshold – the only way to have B vertices displaced from the e^+e^- collision point is to boost these particles. This is achieved by choosing different energies for the two beams – see Table 2.1.1.

Neglecting a very small beam crossing angle (in KEKB), the kinematic parameters of $\Upsilon(4S)$ in the laboratory frame (*i.e.* detector rest frame) are:

$$\beta = \frac{p_{\Upsilon(4S)} \times c}{E_{\Upsilon(4S)}} = \frac{E_- - E_+}{E_- + E_+} \tag{2.1.1}$$

$$\gamma = \frac{1}{\sqrt{1-\beta^2}} = \frac{E_- + E_+}{2\sqrt{E_- E_+}} \tag{2.1.2}$$

$$\beta\gamma = \frac{E_- - E_+}{2\sqrt{E_- E_+}} \tag{2.1.3}$$

Asymmetric colliders require asymmetric detectors, designed to maximize their acceptance. By convention, their 'forward' and 'backward' sides are defined relative to the high energy beam. With the large boost, more particles are produced on average in the forward direction, as shown on the *BABAR* and Belle protractors displayed in Figure 2.1.1. Therefore, both detectors have more instrumentation on the forward side (extended polar angle coverage including a forward electromagnetic calorimeter) and they are offset relative to the interaction point (IP) by a few tens of centimeters in the direction of the low energy beam.

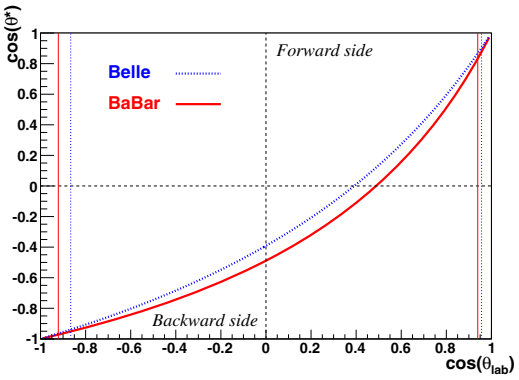

Figure 2.1.1. This plot shows the relationship between polar angles in the center-of-mass and laboratory frames for *BABAR* (red curve, solid line) and Belle (blue curve, dotted line). The corresponding vertical lines define the angular acceptance of the two detectors.

The Belle and *BABAR* detectors must fulfill stringent requirements imposed by the physics goals of the two experiments.

- An acceptance close to 4π and extended in the forward region, as explained above.
- An excellent vertex resolution ($\sim$100 μm), both along the beam direction and in the transverse plane.
- Very high reconstruction efficiencies for charged particles and photons, down to momenta of a few tens of MeV/c.
- Very good momentum resolution for a wide range of momenta, to help separating signal from background.

Table 2.1.1. Beam energies, corresponding Lorentz factor, and beam crossing angle of the B Factories for the nominal $\Upsilon(4S)$ running.

B Factory	e^- beam energy E_- (GeV)	e^+ beam energy E_+ (GeV)	Lorentz factor $\beta\gamma$	crossing angle φ (mrad)
PEP-II	9.0	3.1	0.56	0
KEKB	8.0	3.5	0.425	22

- Precise measurements of photon energy and position, from 20 MeV to 8 GeV in order to reconstruct π^0 mesons or radiative decays.
- Highly efficient particle identification for electrons and muons, as well as a π/K separation over a wide range of momenta – from ∼0.6 GeV/c to ∼4 GeV/c.
- A fast and reliable trigger, and online data acquisition system able to acquire good quality data, to process the data live, and finally to store it pending offline reconstruction
- A high radiation tolerance and the capability to operate efficiently in the presence of high-background levels.

Both detectors have the same structure with a cylindrical symmetry around the beam axis. They are of compact design with their size being a trade-off between the need for a large tracking system and the need to minimize the volume of the calorimeter, by far the most expensive single component of the detector. The forward and backward acceptances are constrained by the beamline geometry. Although the *BABAR* and Belle collaborations made different technological choices for their detector components, they have similar subdetectors, each with well-defined functions. Going from the inside to the outside of the *BABAR* and Belle detectors, one finds successively:

- A charged particle tracking system, made of two components.
  - A silicon detector, known as the SVT ('Silicon Vertex Tracker') in *BABAR*, and the SVD ('Silicon Vertex Detector') in Belle, made of double-sided strip layers to measure charged particle tracks just outside the beam pipe. This detector is used to reconstruct vertices (both primary and secondary), measures the momentum of low-energy charged particles which do not reach the outer detectors due to the strong longitudinal magnetic field and provide inputs (angles and positions) to the second tracking detector, a drift chamber, which lies just beyond its outer radius – see below for details.
  - A drift chamber, known in *BABAR* as DCH ('Drift CHamber') and in Belle as the CDC ('Central Drift Chamber'), which measures the momentum and the energy loss (dE/dx) of the charged particles which cross its sensitive volume. The latter information is useful for particle identification (PID).
- A solenoid cryostat located between the electromagnetic calorimeter and the instrumented flux return – these two detectors are described below. The cryostat is needed by the superconducting solenoid that provides a 1.5 T longitudinal magnetic field in which both tracking devices are embedded.
- PID detectors designed to distinguish the numerous pions from the rarer kaons from a momentum of about 500 MeV/c to the kinematic limit of 4.5 GeV/c.
  - *BABAR* is using a novel device called DIRC (Adam, 2005) – 'Detector of Internally Reflected Cherenkov light' – which covers the barrel region.
  - Belle has two types of PID detectors: Aerogel Cherenkov Counters ('ACC') covering both the barrel and the forward regions; additional Time-Of-Flight ('TOF') counters in the barrel region with a ∼100 ps resolution which makes them efficient in separating charged particles up to 1.2 GeV/c, as the particle flight path from the IP to the TOF counters is about 1.2 m.
- The *BABAR* (EMC) and Belle (ECL) calorimeters; these are highly-segmented arrays of thallium-doped cesium iodide – in short CsI(Tl) – crystals assembled in a projective geometry. The *BABAR* EMC consists of a barrel and a forward end cap while the Belle ECL includes a barrel, a forward end cap and a backward end cap. Both calorimeters cover about 90% of the total solid angle. In addition to the ECL, Belle developed a special extreme forward calorimeter (the EFC), made of radiation-hard BGO (Bismuth Germanate Oxide or $Bi_4Ge_3O_{12}$) crystals. Mounted on the final quadrupoles close to the beam pipe, it provided information on the instantaneous luminosity and the machine background which helped optimize KEKB operation.
- An instrumented flux return, designed to identify muons and to detect neutral hadrons (primarily K_L^0 and neutrons), and divided into three regions: central barrel, forward and backward end caps. The *BABAR* IFR ('Instrumented Flux Return') consists of alternative layers of glass-electrode-resistive plate chambers (RPC's) and steel of the magnet flux return. Originally, there were 19 RPC layers in the barrel and 18 in the end caps. Second-generation RPCs were installed in the forward end cap in 2002 while RPCs were replaced by Limited Streamer Tubes (LSTs) in the barrel in the period 2004-2006. Belle K_L^0 and Muon detection system (KLM) was designed designed similarly and employed alternating layers of RPC's (15 in the barrel and 14 in the end caps) and 4.7 cm-thick iron plates.
- A two-level trigger with a hardware Level-1 (L1) followed by a software Level-3 (L3). The L1 trigger com-

bines track and energy triggers with information from the muon detectors and the decision to accept/reject an event is taken by a central trigger system called GLT ('GLobal Trigger') by *BABAR* and GDL ('Global Decision Logic') by Belle. The L3 trigger level runs on the online computer farm. The two trigger systems have similar design characteristics: a L1-accepted rate of O(kHz) and L3-accepted rate of O(100 Hz), for a few percent dead time and an event size of about 30 kB. Obviously these parameters have evolved during the data taking as luminosity and backgrounds increased. Both the *BABAR* and Belle triggers have been found to be robust, reliable and efficient in a wide range of data taking conditions, including runs at lighter Υ resonances or at $\Upsilon(5S)$ and above.

2.1.1 The BABAR and Belle collaborations

BABAR

The size of the *BABAR* collaboration reached a maximum in 2004-2005 with more than 600 collaborators. At the end of 2012, there were still 325 *BABAR* collaborators belonging to 73 institutions.

The *BABAR* collaboration is led by a spokesperson whose term is three years. He/she is selected by an *ad hoc* search committee whose choice is then validated by the *BABAR* Council. The Council is the main body of the collaboration and gathers representatives from all *BABAR* institutions. All important decisions (changes in the *BABAR* management, turnovers in the various *BABAR* committees, application of a new institution wishing to join *BABAR*, etc.) are subject to ratification by the Council. During the first year following his/her election, the spokesperson-elect works in the senior management team with the current spokesperson who is ending his/her term. The other members of the senior management are the technical coordinator, the physics analysis coordinator (PAC) and the computing coordinator. The PAC and computing coordinator are usually aided by a deputy who is expected to become the head of the corresponding office later. The two other *BABAR* boards are the Executive Board which includes representatives from the different countries involved in *BABAR* and the Technical Board (TB). The TB focuses on the detector running; each *BABAR* system (the various sub-detectors, the online and trigger groups, the machine detector interface, etc.) is represented there by two system managers, at least one of whom is based at SLAC.

The physics analysis organization is led by a PAC and a deputy-PAC (DPAC). The PAC term is two years: one as DPAC, the other as PAC on charge. Analysis Working Groups (AWGs), led by up to three people depending on the workload, gather together analysis topics which belong to the same field, *e.g.* 'charmonium' or 'charmless B-decays'. Analysts regularly report the progress of their work at AWG meetings during which group discussions help the analysis to move forward. Analysis developments and details are described in *BABAR* Analysis Documents (a.k.a. 'BADs') stored in the *BABAR* CVS repository. Usually, an analysis has one or more 'supporting BADs' (which are private *BABAR* documents) and one journal draft BAD which will ultimately be submitted for publication. Readers from within the AWG are chosen to read in detail the supporting BAD(s) of an analysis once it is in an advanced stage. When this part is completed, a Review Committee (RC) made up of three people (not all from the AWG) is formed. The RC and the analysts then work in close contact (phone or in-person meetings, exchanges on internal forums, etc.) to finalize the analysis, validate its results and complete the journal draft.

The *BABAR* collaboration as a whole has two main ways to get involved with the review of an analysis which is close to completion. One is the 'Collaboration Wide Talk' (CWT) which is held during either a physics meeting or a plenary session of a *BABAR* quarterly collaboration meeting. The CWT describes the whole analysis, usually including systematic uncertainties and the unblinded results – the permission for unblinding is given by the RC (see Chapter 14 about blind analysis). The last global step is the 'Collaboration Wide Review' (CWR), a two week-period during which *BABAR* collaborators proof read the draft of the written document which summarizes the whole analysis – either a journal paper or a physics note if the result is initially only to be shown at conferences. Finally, a journal draft is examined by two 'Final Readers' (FR) prior to being submitted. The PAC and the DPAC follow all the on going analyses in parallel and can step in at any time to request more information, clarify a potential issue, remind about the coming deadlines, etc. The CWR and FR steps are managed by the 'Publication Board' which also follows the correspondence between analysts and journal referees. Finally, the assignment of *BABAR* talks (obtained by the PAC who is in direct contact with conference organizers) is the responsibility of the 'Speakers Bureau'.

The analysis review process described above has been continued since the completion of the data taking so as to maintain the high quality of the *BABAR* scientific production. An internal forum system and various databases provide permanent documentation of the on-going analyses and of their review process, to the whole collaboration. The Authorship of each paper is automatically granted to all current members of the *BABAR* collaboration; people who contributed significantly to this paper without being official *BABAR* members are added to that particular author list. People usually start signing *BABAR* papers one year after becoming a *BABAR* member, and remain author one year after leaving the collaboration.

Belle

The size of the Belle collaboration grew with time and reached a maximum in 2012, two years after data taking ended, with about 470 collaborators from 72 institutions in 16 countries.

The Belle collaboration is led by three spokespersons whose term is two years with a maximum of three con-

secutive terms. One spokesperson is from KEK, one from Japanese Universities and one from the non-Japanese institutions. The spokespersons are elected by the staff members of the whole collaboration. Spokespersons are responsible for running the collaboration, representing its interests in the institutions and with national funding agencies, and for allocating the available resources among the different subgroups.

The main body of the collaboration assembles three times a year at the Belle General Meeting (BGM), and between BGMs, decisions are enacted by the spokespersons and the Executive Board (EB). The role of the Executive Board, which is made up of the three spokespersons, three members from KEK, three members from Japanese institutions, and three members from institutions outside Japan, is to advise the spokespersons on scientific and technical matters, and to ratify all important decisions. The EB usually meets monthly.

Each collaborating institution selects a representative to sit on the The Institutional Board (IB), which meets at each BGM. The IB deals with organizational, management, and personnel issues, including admitting new collaborators, modifications of the group's organization, initiating the spokespersons' selection process, etc. The IB also makes recommendations concerning potential new members during a general meeting. The resignation of members or institutions is treated similarly. The IB also functions as a "KEKB users' organization". It gathers complaints and/or suggestions regarding KEK and asks KEK for improvements. Various institutional matters are also discussed by the IB, *i.e.* items concerning each institution's interest, such as students' thesis topics, etc. The Belle management also includes two physics analysis coordinators and the computing coordinator.

The organization of the physics analysis is similar to *BABAR*. Working Groups (WG) led by one or two persons gather together analyses that belong to the same field, *e.g.*, charmonium or charmless B decays. Analysts report regularly the progress of their work at WG meetings during which group discussions help the analysis to move forward. Analysis developments and details are described in written documents - so called Belle Notes. Usually, an analysis has one or more supporting Belle Note resulting in a journal draft to be submitted for publication. When an analysis is judged to be mature enough, a refereeing committee (RC) of three collaboration members is formed. The RC and the analysts then work in close contact (phone or in-person meetings, E-mail exchanges, videoconferences etc.) to finalize the analysis, validate its results and complete the journal draft.

In addition to BGMs the results of analyses close to completion are discussed at Belle Analysis Meetings (BAM) usually held three times a year. When the RC and the analysts decide that the analysis is complete, a collaboration-wide review starts, a two week-period during which Belle colleagues proof read the final document, a draft of a journal publication. These steps are managed by the Publication Council which follows up on the correspondence between analysts and journal referees and has the general task of maintaining high quality of the Belle papers. Finally, a so called authorship confirmation procedure is started by the general consent of the referees. Authorship of each paper is not automatic in Belle. Those eligible for authorship are supposed to read the final draft and choose one of the three possibilities: agreement with the paper conclusions and willingness to become an author, non-authorship because of disagreement with the conclusions or because of insufficient contribution.

The assignment of Belle talks is the responsibility of the spokespersons who are in direct contact with conference organizers and inform the collaboration about the forthcoming scientific meetings.

2.1.2 The BABAR detector

Figure 2.1.2 (Aubert, 2002j) shows longitudinal and end views of the *BABAR* detector. The end view shows the forward side of *BABAR*; on the backward side one would see the toroidal water tank (also called 'StandOff Box', in short SOB) which contains the 10,752 DIRC photomultipliers (PMTs) detecting the Cherenkov photons created in the quartz bars. The right-handed *BABAR* coordinate system is shown on both pictures: the z-axis coincides with the axis of the DCH, which is offset by about 20 mrad relative to the beam axis in the horizontal plane – this rotation helps to minimize the perturbation of the beams by the *BABAR* solenoidal field which is parallel to the axis of the DCH. The y-axis is vertical and points upward while the x-axis points away from the center of the PEP-II rings. One commonly uses another coordinate system as well, with z unchanged, θ the polar angle defined with respect to this axis ($\theta = 0$ corresponds to the most forward direction), and ϕ the azimuthal angle – unless otherwise stated, the *BABAR* detector is assumed to have a cylindrical symmetry. Figure 2.1.3 shows photographs of the *BABAR* detector seen from the backward end (left picture) and of the SVT (right picture).

2.1.3 The Belle detector

The schematic longitudinal cross section of the Belle detector is shown in Figure 2.1.4. Individual subdetectors as listed in Section 2.1 are denoted in the figure. The full detector is composed of the barrel part and of the forward (in the direction of the incoming e^- beam) and the backward (in the direction of the incoming e^+ beam) endcaps. The coordinate system used is similar to that of *BABAR*; the z-axis is in the opposite direction of the e^+ beam (note that this is not exactly the same as the direction of the e^- beam due to a finite crossing-angle of the beams), the y-axis is vertical and the x-axis horizontal away from the center of the KEKB ring.

Photographs of the Belle detector are shown in Figure 2.1.5.

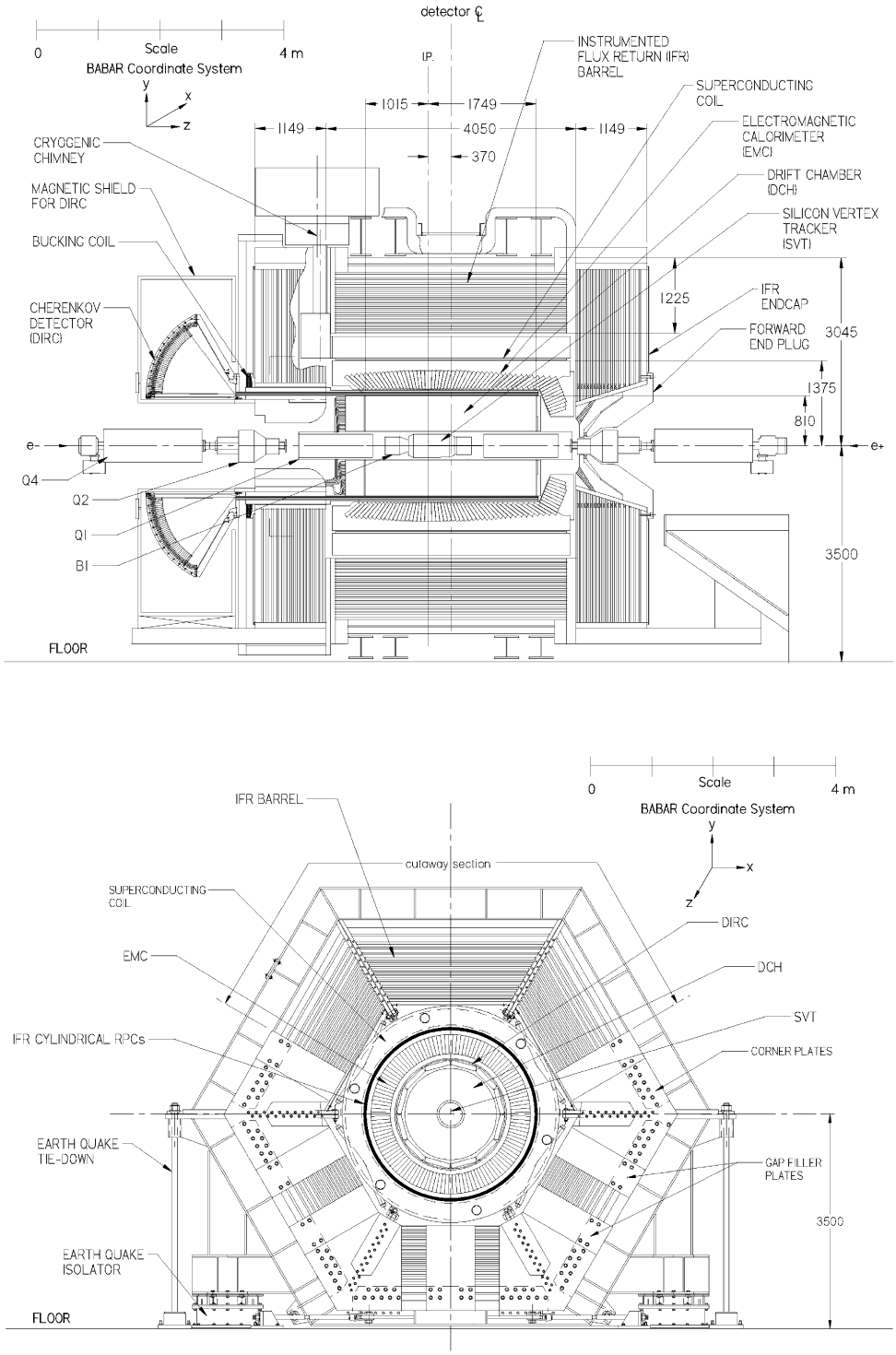

Figure 2.1.2. (top) Longitudinal and (bottom) end view of the *BABAR* detector (Aubert, 2002j).

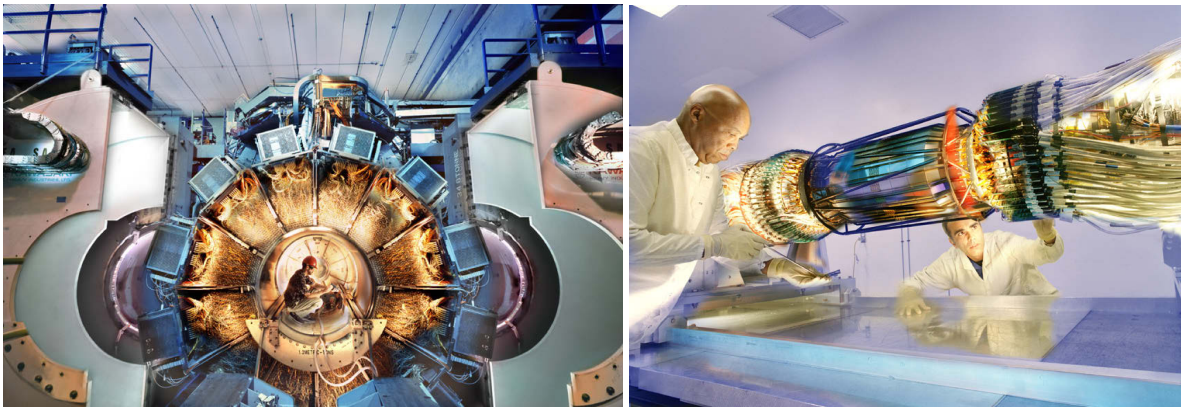

Figure 2.1.3. (left) View of the *BABAR* detector from the backward end, with the magnetic shield rolled out of the way to reveal the PMTs of the DIRC. The central support tube, with the SVT as well as the B1 and Q1 (dipole and quadrupole) magnets of the interaction region beam delivery system (right) was removed from the detector for maintenance at the time this photograph was taken.

2.2 BABAR and Belle comparative descriptions

This section provides a comparison of the different *BABAR* and Belle components, classified by function: first the subdetectors, then the trigger, the online and Data AcQuisition (DAQ) systems and finally the background protection system. As previously mentioned, the detector journal publications from each collaboration should be consulted for more detailed explanations of the detectors discussed below. Information about the PEP-II trickle injection system can be found in Section 3.2.2. Also, a casual reader not interested in the technical details of the detector setup and performances can move directly to Section 2.2.9 in which a summary of the comparison between the two detectors is provided.

2.2.1 Silicon detector

BABAR

As shown on Figure 2.2.1, the *BABAR* SVT is made of five layers: three close to the beryllium beam pipe to perform impact parameter measurements and two at a larger radius to help pattern recognition in the tracking system (SVT and DCH) and to perform stand-alone low-p_T tracking: only tracks with momentum greater than 120 MeV/c can be reliably measured in the DCH. The inner three layers are primarily used for vertex measurements while the outer two, located much further away, help the track extrapolation to the DCH. The end view in Fig. 2.2.1 shows the number of SVT modules: 6, 6, 6, 16 and 18 for layers 1 to 5 respectively. It also shows that the two outer layers are divided into two sub-layers each, located at slightly different radii to ensure a small azimuthal overlap between modules. A similar overlap exists for the inner 3 layers which are tilted by 5°. The three inner layers are straight while the outer two are arch-shaped to minimize the amount of silicon required to cover the solid angle and hence the amount of silicon that a track would have to pass through in the forward or backward regions of the SVT: only about 4% X_0.[13] The angular coverage is from 20 degrees to 150 degrees in the laboratory frame: 90% of the solid angle is covered in the center-of-mass frame. The total active area of silicon is close to 1 m^2 for about 150,000 channels. Each SVT module is divided electrically in two half-modules which are readout at the ends. All sensors are double-sided: on one side, the strips are parallel

[13] The quantity X_0 is called the radiation length.

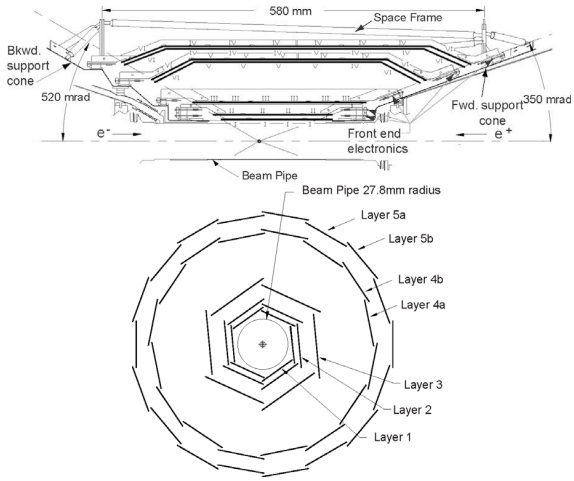

Figure 2.2.1. Longitudinal – unless otherwise mentioned, all subdetectors are axially symmetric around the detector principle axis – and transverse sections of the 5-layer *BABAR* SVT (Aubert, 2002j). The 27.9 mm diameter beampipe visible in the center of the SVT is composed of two beryllium layers with a water channel between them for cooling purpose.

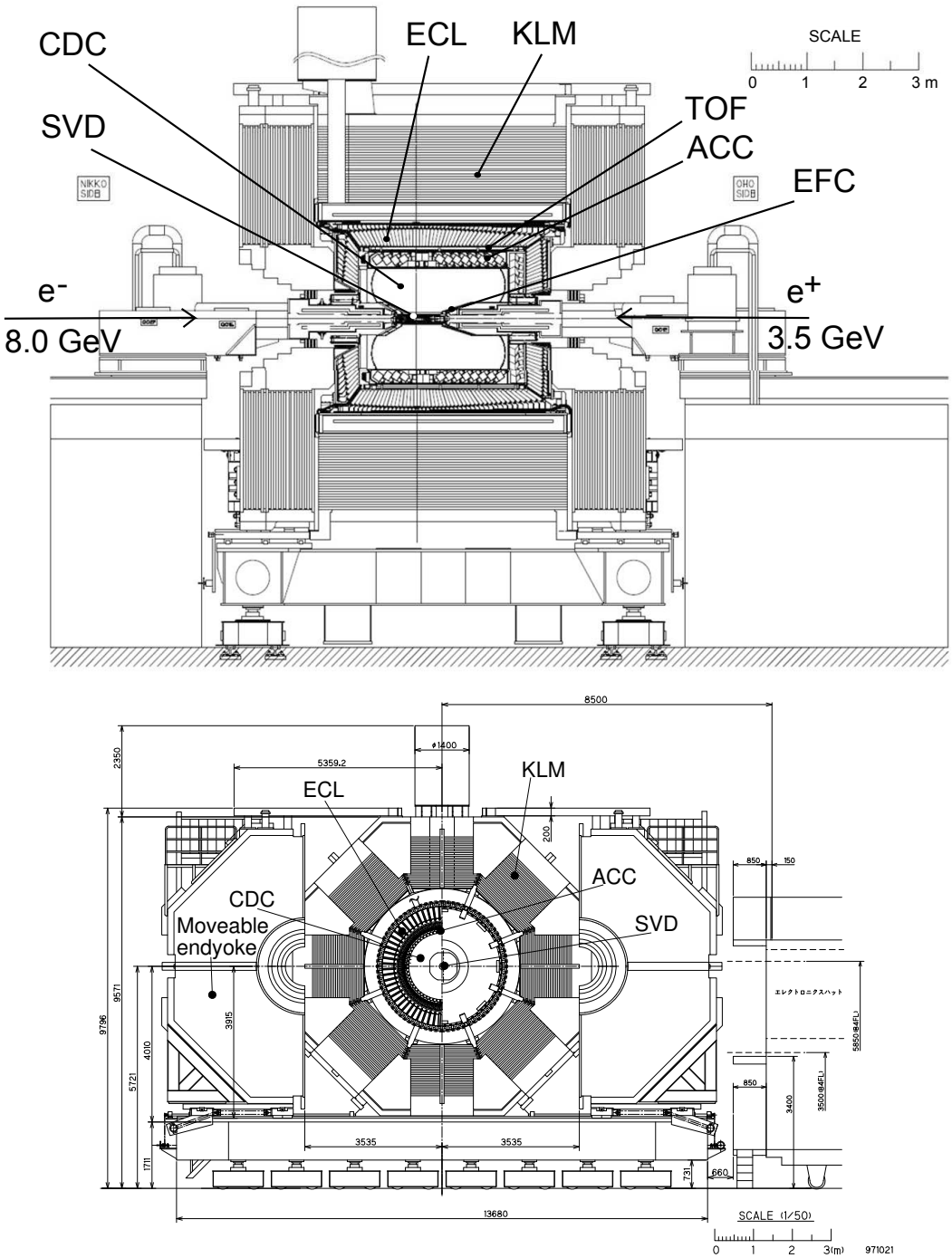

Figure 2.1.4. Longitudinal (top), adapted from (Abashian, 2002b), and transverse (bottom) cross sections of the Belle detector.

to the beam and measure the azimuthal angle ϕ and the radius of the hit r; on the other side the strips are transverse and measure the z coordinate. The SVT consists of 340 sensors which are aligned *in situ* relative one-another using dimuon and cosmic ray events. This local alignment is quite stable over time: it only needs to be updated when something 'significant' occurs in the *BABAR* detector hall: a detector access or a quench of the superconducting coil

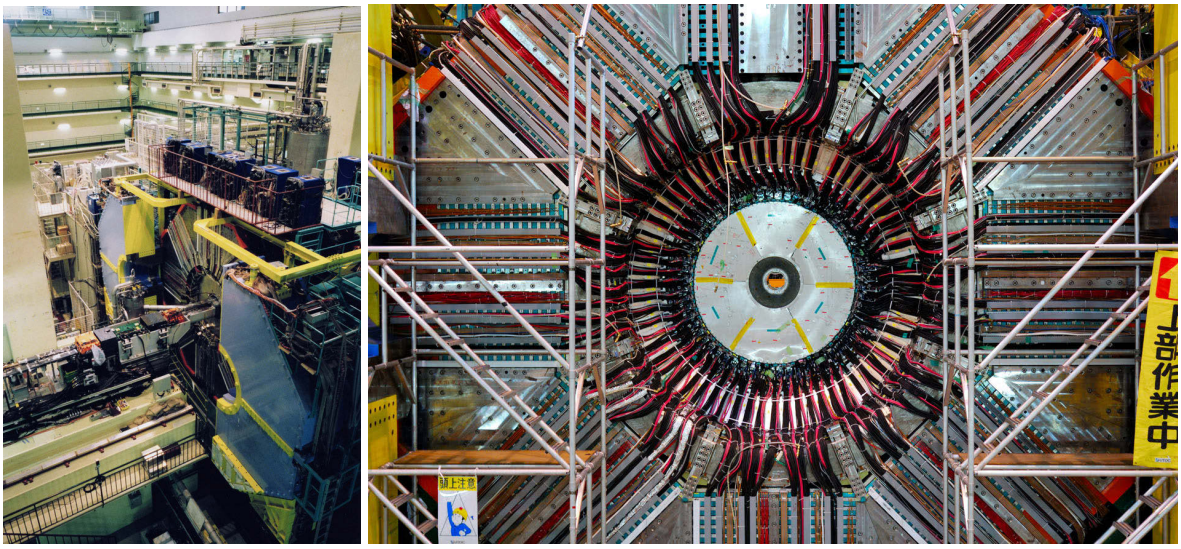

Figure 2.1.5. Left: View of the Tsukuba detector hall with the Belle detector. The beamline enters from the bottom left through the detector end cap. Right: Beamline view of the detector. From the outer to the inner part the KLM modules, ECL modules, ACC PMT's and the CDC end flange can be seen (see the text for description of subdetectors).

for instance. Once this is done, the SVT is considered as a rigid single body and one can check its alignment with respect to the DCH. This global alignment is updated after every run (about once an hour): the newly computed alignment constants are then used to reconstruct tracks during the following run, data from which a new set of constants is extracted and so on. This procedure, called rolling calibration, is used by most of the *BABAR* systems and allows one to monitor changes in detector calibration which occur for the whole detector about once a day, between two successive periods of data taking.

Obviously the SVT is a very sensitive device which could be damaged by radiation as it is very close to the IP. Damage could come from two effects: either a huge burst of radiation destroying instantaneously some channels, or the integrated dose exceeding the SVT radiation budget and leading to permanent damage. To mitigate such problems, a dedicated system called SVTRAD has been developed: this continuously monitors the radiation levels in the SVT and can either temporarily inhibit the injection or even force a beam abort if the instantaneous dose is deemed to be too high. More information about the SVTRAD system can be found in Section 2.2.8 below.

During the whole data taking period, the SVT performance was constantly monitored while studies were done regularly to predict future performance based on the expected increase of the beam currents and of the luminosity. The main effects of the evolving running conditions to the SVT were twofold: occupancy-induced damage and radiation damage. While the former is an instantaneous effect which can be mitigated by limiting the occupancy in the most affected layers, the latter gets integrated over time. Both the modules and the front-end electronics suffer from this degradation. There is no way to recover the lost performance, except by replacing any damaged components – which was not attempted on the SVT. The consequences of these effects are the reduction of the collected charge and the increase of the noise. Both effects limit the SVT performance and have been taken into account to define the operating mode of this sub-system.

Over the nine years of operation, the average efficiency of the SVT modules (computed for each half-module by dividing the number of hits associated to tracks with the number of tracks crossing that particular module) was above 95%, excluding a few percent of defective half-modules. Some half-modules had issues with individual channels; however, these had no significant impact on the overall efficiency as usually two or more strips are used to detect charge in a given layer crossed by a charged particle. The z and $r\phi$ resolutions range from $\sim$15 to $\sim$40 μm depending on the layer and on the measured quantity. The best results are obtained for tracks with a polar angle close to 90° while resolution degrades slowly in the forward and backward directions. Measurements of $\mathrm{d}E/\mathrm{d}x$ allow the SVT to achieve a 2σ separation between kaons and pions up to a momentum of 500 MeV/c.

Belle

The Belle SVD has been improved step by step after the commissioning of the Belle detector in 1999. In the first 3 years, the first system, called SVD1, which consisted of 3 layers of AC coupled double-sided silicon-strip detectors (DSSD) read out with VA1 readout chip (Gamma-Medica, 1999), was used. As SVD1 was the first silicon vertex detector built at KEK, a conservative design was chosen. Its coverage was $23° < \theta < 140°$ while the full acceptance of the Belle detector was $17° < \theta < 150°$. The limited radiation hardness of the VA1 chip AMS 1.2 μm (200 krad)

and its long shaping time (2.8 μsec) discouraged aggressive operation of the KEKB collider. In addition, since the Belle readout electronics were set to the ground level, and the bias voltage was applied across the dielectric in the coupling capacitor of the DSSD, a few pinholes appeared in the dielectric each year.

Because of these problems, the Belle collaboration started the upgrade of the SVD before the start of KEKB operation. In 2000, all SVD ladders were replaced utilizing an upgraded VA1 AMS 0.8 μm chip (Aihara, 2000b) whose radiation tolerance improved to 1 Mrad.

A major upgrade was done in summer 2003. The second generation silicon vertex detector, SVD2 (Natkaniec, 2006), consisting of 4 layers of DSSD and covering the full angular acceptance ($17° < \theta < 150°$), was installed (Fig. 2.2.2). The inner radius of the beam pipe was reduced from 20 mm to 15 mm (Abe, 2004i). The radii of the SVD2 layers are 20 mm, 44 mm, 70 mm and 88 mm. As the KEKB luminosity increased after SVD2 was installed, 85 % of Belle data were taken with SVD2.

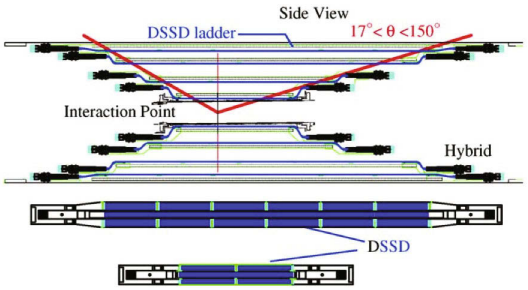

Figure 2.2.2. The longitudinal cross section of Belle's SVD2 (Natkaniec, 2006). The layer 1 and layer 4 ladders are also depicted. The radii of layers 1 to 4 are 20, 44, 70 and 88 mm, respectively. SVD2 covers the whole Belle acceptance ($17° < \theta < 150°$) shown by dashed lines.

SVD2 also utilized a newly-developed chip, VA1TA, which had a 0.8 μsec peaking time and a radiation tolerance of 20 Mrad (AMS 0.35 μm technology) (Yokoyama, 2001). The control register was made of triple-module-redundancy logic to avoid and detect single-event upsets (SEUs). Thanks to the short shaping time, the contribution of the dark current to the overall noise was not substantial. The voltage from the low-voltage power supply was increased to be above the bias voltage and the rate of pinhole appearance was reduced dramatically. SVD2 was operated for eight years without major problems.

The material in front of the CDC innermost layer is the beam pipe (0.62% X_0), four layers of strip sensors (1.71% X_0), the SVD CFRP (carbon fiber reinforced polymer) cover (0.23% X_0) and the CDC inner CFRP cylinder (0.17% X_0) totaling 2.73% X_0. The SVD sensor alignment is done among DSSDs (internal) and with respect to the CDC (global). Both internal and global alignment parameters are determined for every KEKB run period. No significant change in alignment parameters was observed throughout the experiment.

The impact parameter resolution in r-ϕ and r-Z was measured to be $\sigma_r = 21.9 \oplus 35.5/p$ μm and $\sigma_Z = 27.8 \oplus 31.9/p$ μm, respectively, where p represents the track momentum in GeV/c and the $\oplus$ sign denotes summation in quadrature (Abe, 2004h).

The hit occupancy in the inner most layer remained in the range 5-7% at the highest luminosity of 2×10^{34}/ s/ cm^2 without degradation of the detector performance.

There is an important difference in the positioning of the silicon detector and hence its role as a part of the tracking system between *BABAR* and Belle. In the case of *BABAR* the SVT is installed inside a support tube. As a result, the innermost radius of DCH is 236 mm and the radius of the outermost layer of the SVT is 140 mm. Therefore, efficient low-momentum track-reconstruction capability of the SVT was required and the 5-layer design was a natural choice. In the case of Belle, the SVD is supported by the CDC, with the radii of the outermost SVD layer and the innermost CDC layer being 90mm and 110mm, respectively. The reconstruction of low p_t tracks can be done by the CDC. Thus, the main purpose of the Belle SVD is to extrapolate the tracks reconstructed in the CDC to the decay vertices inside the beam pipe. The reconstruction of low p_T tracks with the CDC is efficient down to 70 MeV/c (Dungel, 2007).

2.2.2 Drift chamber

BABAR

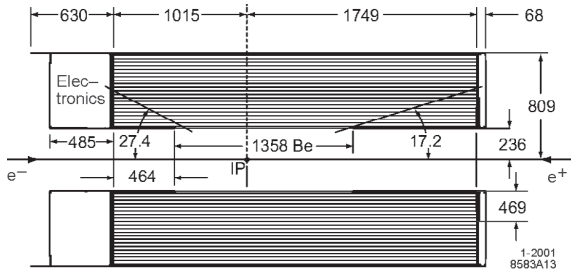

Figure 2.2.3. Longitudinal section of the *BABAR* DCH (Aubert, 2002j) with the principal dimensions given in millimeters. Like the whole *BABAR* detector, the 40-layer drift chamber is offset by 370 mm from the IP. The electronics are located behind the backward end plate. The DCH coverage, defined by requiring that at least half of the layers are traversed by the tracks, extends from 17.2° to 152.6° in polar angle.

Figure 2.2.3 shows a longitudinal section of the *BABAR* DCH which performs both the tracking and part of the PID for charged particles – the latter is possible thanks to measurements of track ionization losses (dE/dx). Indeed, low momentum tracks do not reach the DIRC and so only the tracking system can help identify them. Moreover, the

DIRC only covers the *BABAR* barrel section which means that the DCH is the only detector available to perform PID on the forward side of *BABAR*. The DCH is also a key component of the L1-trigger level. The DCH readout electronics, mounted on the backward end plate of the chamber, were upgraded in 2004-2005 to cope with the trigger rate increase associated with the increase of the PEP-II luminosity and with the corresponding increase of background. In particular, the new readout boards included FPGAs responsible for performing the feature extraction step (extraction of physical signals from the raw data; gain and pedestal corrections; data sparsification and data formatting) prior to transferring the data from the front-end boards to the DAQ modules. Previously, feature extraction was performed in the DAQ modules. These new chips were sensitive to SEUs occurring at a rate of a few per day in the whole DCH electronics. Therefore, a dedicated system was set up to monitor the behavior of the new DCH front-end boards and to reload in a few seconds the chip firmware, should errors be detected.

The DCH counts 40 layers of small hexagonal cells of which 24 are placed at small stereo angles (about 50-70 mrad) to provide z information. The field wires are made of aluminum and the gas mixture is 80:20 Helium:Isobutane in order to minimize multiple scattering inside the DCH (the material inside the chamber only counts for 0.2% X_0). The 40 layers are gathered in 10 'superlayers' in which all layers have the same orientation. Labeling 'A' an axial DCH superlayer (which stereo angle is null), 'U' a superlayer with positive stereo angle and 'V' a superlayer with negative stereo angle, the pattern of the *BABAR* DCH can be written: 'AUVAUVAUVA'. This particular alternation optimizes the performance and the reliability of the DCH.

Like the SVT, the DCH is a delicate system which must be monitored continuously and carefully to detect any unsafe condition and mitigate it in the appropriate way. Particular examples of monitoring (with hardware and software systems) included the DCH gas mixture composition and potential gas leakage, and the high-voltage (HV) settings of each group of wires. The monitoring systems were continuously improved over the years to minimize the dead time of the DCH without bypassing safety requirements. In the final implementation, if the current of a given channel was found to be too high, the corresponding voltage was reduced until the current fell below a safe threshold, at which point the HV would be ramped up again. During this process, all the other HV settings were unchanged, allowing data taking to proceed. In addition, a real time software process was able to predict the DCH current during running, using several monitoring variables that were independent (beam currents, various background levels readout by sensors, etc.). In this way, the DCH would only switch from the injectable voltage level to the running one if the beam conditions were good enough to ensure a safe operation of the chamber when it would reach its working point. Apart from a small number of wires which were damaged by a HV incident during the *BABAR* commissioning phase, the whole DCH worked well during the whole data taking period. The DCH nominal HV was regularly raised during the data taking to correct for gain losses due to aging: while the nominal HV level was 1960 V, the initial setting was 1900 V; by the end of data taking, it had been raised to 1945 V – one volt corresponds to about 1% on the gain. Loss of gain due to wire aging was 11% over the life of the chamber. The DCH performed as expected during all the *BABAR* data taking, both as the main component of the tracking system and as an important contributor to *BABAR* PID, with a measured dE/dx resolution of about 8%, close to the design value of 7%.

Belle

The Belle Central Drift Chamber (CDC) plays several important roles. First, it reconstructs charged particle tracks, precisely measures their hit coordinates in the detector volume, and enables reconstruction of their momenta. Second, it provides particle identification information using measurements of dE/dx within its gas volume. Low-momentum tracks, which do not reach the particle identification system, can be identified using the CDC alone. Finally, it provides efficient and reliable trigger signals for charged particles.

Since the majority of the particles in B meson decays have momenta lower than 1 GeV/c, minimization of multiple scattering is important for improving the momentum resolution. Therefore, a gas mixture of 50% He and 50% C_2H_6 was chosen, which, because of the low Z nature of the gases, provided optimal momentum resolution while retaining good energy loss resolution.

The structure of the CDC is shown in Fig. 2.2.4. It is asymmetric in the z direction with an angular coverage of $17^\circ \leq \theta \leq 150^\circ$ and has a maximum wire length of 2400 mm. The inner radius of the CDC lies at 80mm, and the detector has no inner wall in order to minimize multiple scattering in the material that lies within the radius of the first wire layer and to ensure good tracking efficiency for low-p_t tracks. The outer radius is 880 mm. In the forward and backward directions at small r, the CDC has the shape of a truncated cone. This allows for the necessary space to accommodate the accelerator components while keeping the maximum available acceptance. The chamber has 50 cylindrical layers, each containing between three and six either axial or small-angle stereo layers, and three cathode strip layers. The CDC has total of 8400 drift cells. The two innermost super-layers are composed of three layers each and the three outer stereo super-layers are composed of four layers each. When combined with the cathode strips, this provides a high-efficiency fast z-trigger. For each stereo super-layer, the stereo angle was determined by maximizing the z-measurement capability while keeping the gain variations along the wire below 10%. The sense wires are made of gold-plated tungsten and have the diameter of 30 μm, while the aluminum field shaping wires have the diameter of 126 μm.

In all layers, except the three innermost, the maximum drift distance is between 8 mm and 10 mm. In the radial

direction the thickness of drift cells ranges from 15.5 mm to 17 mm. In the innermost layers the cells are smaller and signals are read out by cathode strips. Staggering of the neighboring radial layers within a super-layer in the ϕ direction by half cell helps in resolving left-right ambiguities.

The CDC read-out electronics consists of Radeka-type pre-amplifiers which amplify the signal and send it to modules performing shaping, discrimination and charge(Q)-to-time(T) conversion. These modules are placed in the electronics hut and are connected to pre-amplifiers via ∼30 m long twisted pair cables. The technique used is a simple extension of the ordinary TDC/ADC readout scheme, but allows Belle to measure both, timing and charge of the signals, using multi-hit TDC's only.

In summer 2003, the cathode part, which corresponds to the inner most three layers, was replaced with a new chamber in order to provide space for SVD2. The new chamber consists of two layers with smaller cells about 5 mm × 5 mm due to limited space and reducing the occupancy. The maximum drift time becomes shorter; less than 100 nsec in the 1.5 T magnetic field.

The high voltage applied to the sense wires was kept for 11-years of operation without serious radiation damage. After detailed alignment and calibration, the overall spatial resolution is around 130 μm, as expected. The tracking system consisting of the SVD and CDC provides rather good momentum resolution, especially for low-momentum tracks thanks to the minimization of material inside the inner radius of the CDC:

$\sigma p_T/p_T = 0.0019 p_T \oplus 0.0030/\beta$ $[p_T : \text{GeV}/c]$.

The resolution on dE/dx, which is important for PID, was 7% for minimum-ionizing particles. The $r-\phi$ trigger of the CDC provides a highly efficient and reliable trigger signal. The z trigger that uses the cathode strips works well in reducing the rate of the charged trigger by a factor of three without sacrificing any physics events.

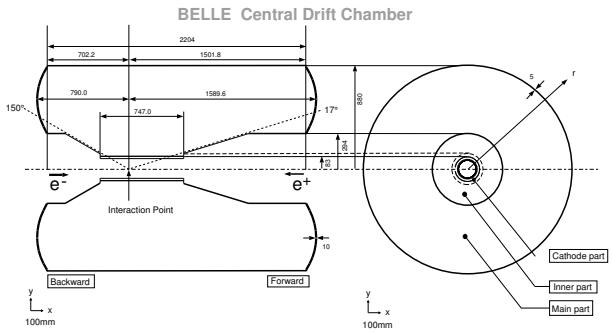

Figure 2.2.4. Belle CDC structure.

2.2.3 Charged particle identification

Principles of the charged particle identification and their technological realization used in both detectors are described in the following. Readers interested mainly in the methods and performance of the PID systems may obtain more details from a separate chapter on charged particle identification, Chapter 5.

2.2.3.1 *BABAR*

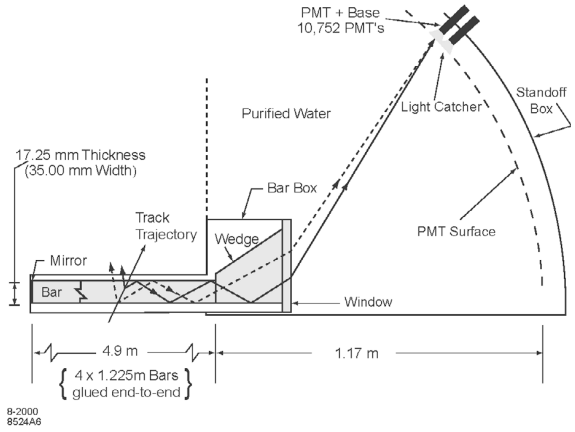

Figure 2.2.5. Principle of the *BABAR* DIRC (Aubert, 2002j) – note that this schematic is inverted with respect to the other pictures showing longitudinal sections of *BABAR* or of one of its components: the forward (backward) side of the detector is on the left (right) side of the picture.

Many detectors contribute to the *BABAR* PID system: the SVT and DCH via measurements of the specific energy loss $\mathrm{d}E/\mathrm{d}x$ for charged particles crossing their active area; the EMC for electron identification and the IFR for the muons. But its main component is the DIRC which dominates the π/K separation power at high momentum by measuring the emission angle θ_C of the Cherenkov light produced by a charged particle crossing a quartz bar radiator (see Fig. 2.2.5). The dimension of each quartz bar is 4.9 m × 6 cm^2.

Charged tracks crossing a quartz bar at a velocity greater than the speed of light in that medium produce light through the Cherenkov effect. A fraction of these photons propagate to the backward bar end through total internal reflection – the forward bar end is instrumented with a mirror to reflect forward photons backward. Then, they exit the quartz bar through the quartz wedge which reflects them at a large angle with respect to the bar axis. Traveling through the ultra-pure water contained in the SOB, they are finally detected by one of the 10,752 PMTs located about 1.2 m away from the bar end (located beyond the backward end of the magnet). Not only the positions of the detected photons but also their arrival times are used to reconstruct the Cherenkov angle at which they were emitted.

The large water tank of the *BABAR* DIRC was sensitive to backgrounds resulting mainly from neutrons interacting with the H_2O molecules. Moreover, it was a permanent

concern as water could leak in the boxes containing the DIRC quartz bars (called 'barboxes') and from there reach other parts of the *BABAR* detector, causing serious and permanent damage to the apparatus. Therefore, the DIRC group had to design a sophisticated system monitoring in real time the humidity outside the SOB and triggering a quick water dump, should a leak be detected. In addition, N_2 was continuously flowing in the DIRC barboxes to keep the quartz bars dry – drops of water would have spoiled the quartz optical properties. Lastly, the SOB was full of ultra-pure water (a potential environmental hazard) running in closed circuit and which had to be continuously purified by a dedicated water plant.

The DIRC reconstruction associates PMT hits with charged tracks crossing the quartz bars with a momentum above the Cherenkov threshold. In addition to background hits which can potentially 'hide' the image of the Cherenkov ring on the PMT array, a complication arises from the fact that the actual path of a given photon between its origin, somewhere along the charged particle track in the quartz, and its detection is unknown. For each detected photon, there are 16 ambiguities coming from our ignorance in the number and of the nature of the reflections undergone by the photon in the quartz. Fortunately, most of them can be rejected as un-physical or leading to an inconsistent timing for the hit – the DIRC is truly a 3D-imaging device, which uses both the position and timing information to reconstruct its data. The ambiguities reduce typically to three and are used in the reconstruction algorithms based on an unbinned maximum likelihood formalism – see Chapter 11. Their outputs are usually a likelihood value for each of the five 'stable' charged particle types (e, μ, π, K and p) plus an estimation of the Cherenkov angle θ_C and of the number of signal and background photons, if enough photons have been found for that particular track. The angle resolutions achieved are typically 10 mrad per photon and 2.5 mrad per track, a level only 10% larger than the DIRC design goal. This is sufficient to separate kaons from pions by more than 4 σ at 3 GeV/c.

2.2.3.2 Belle

Particle identification at Belle, in particular for kaons and pions, is performed by combined information from three detector elements; the time-of-flight detector (TOF), aerogel Cherenkov counter (ACC) and dE/dx in the CDC. In this section, brief specifications of two of these detectors (TOF and ACC) are summarized. A description of the CDC is given in Section 2.2.2.

Time-of-flight system

The time-of-flight (TOF) system consists of a barrel of 128 plastic scintillator counters and can distinguish between kaons and pions for tracks with momenta below 1.2 GeV/c. The system is designed to have time resolution of 100 ps for muon tracks (Kichimi, 2000).

One TOF module (the entire system comprises 64 modules) is shown in Figure 2.2.6. Each module consists of two TOF counters and one thin trigger scintillation counter (TSC). Fine-mesh PMTs are attached to the both ends of the TOF counter and the backward end of the TSC counter. The acceptance is 33° - 121° in the laboratory polar angle, and the minimum transverse momentum to reach a TOF counter is 0.28 GeV/c. The two-layer configuration of TSC and TOF counters with 1.5 cm air gap removes photon-conversion triggers due to a huge photon background caused by spent particle hits on the beam pipe near the interaction region.

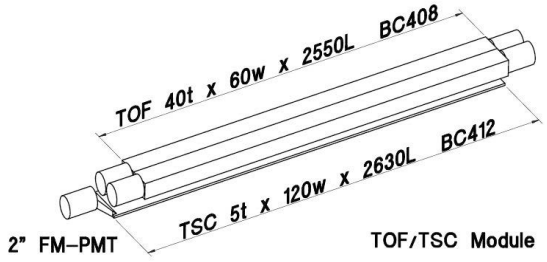

Figure 2.2.6. One TOF module consisting of two TOF counters and one TSC counter. The scales are in mm.

The TOF readout system records a set of charges Q_i and timings T_i from the rising edges of discriminator outputs for each PMT signal from the TOF detector. Figure 2.2.7 shows the block diagram of the timing measurement utilizing the Time Stretcher (TS) circuit. The circuit finds the first rising edge T_2 of the TS reference clock (reduced radio-frequency - RF - signal of the KEKB accelerator with a frequency of 508.9 MHz) following the rising edge T_1 of the TOF signal, and expands the time interval $(T_2 - T_1)$ by a factor of 20, for the timing of the following pulse $(T_3 - T_2)$. These measured times are read out with Belle standard FASTBUS TDCs with a 0.5 ns least significant bit (LSB), providing a 25 ps LSB as a result. A further time-walk correction is applied for timing variation due to a pulse charge, $\Delta T_i \sim 1/\sqrt{Q_i}$.

The TOF system measures time of flight for charged tracks reconstructed by the CDC and requires additionally the beam collision time for each event, $t_{\rm IP}$. It is determined by the RF clock signal used as a reference, and the time offset is calibrated offline on a run-by-run basis using a large sample of μ-pair events ($\gamma\gamma \to \mu^+\mu^-$) with a purity better than 98%. The expected TOF for each muon track is calculated, taking into account its flight length measured by the CDC, and the offset is tuned to give a zero deviation on average between the calculation and the TOF measurement for each PMT.

Determination of the collision timing for TOF measurement has an ambiguity of an integer multiple of 1.96 ns in each event corresponding to the period of the RF clock. This ambiguity can be solved in almost all cases, assigning the velocity of light to high momentum tracks in an event

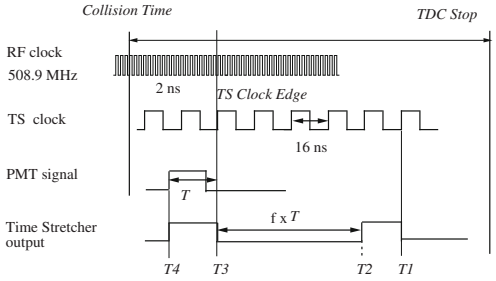

Figure 2.2.7. Time Stretcher TDC scheme for Belle's TOF sub-system. The TS reference clock of approximately 8 ns is generated from the KEKB RF signal of 508.9 MHz (Abashian, 2002b).

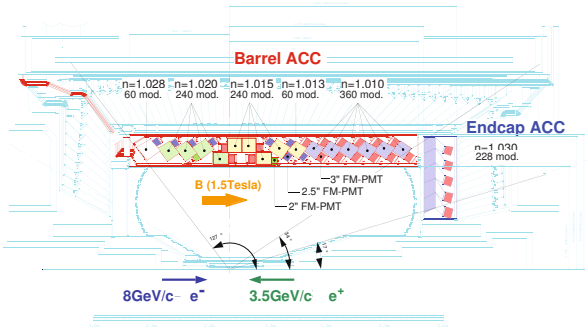

Figure 2.2.8. From (Abashian, 2002b). Layout of the ACC system consisting of 16-module lineup for the barrel and 5-layer modules for the end cap regions of the Belle detector.

(or, equivalently, assigning the pion mass to the tracks). When the pion-mass assumption fails, the kaon or proton mass is tried.

Long-term variation of the time resolution of the TOF system was monitored using the μ-pair samples. The resolution of 110 ps measured in 2008 (Kichimi, 2010) was degraded from the initial resolution of 96 ps obtained in 1999. The 110 ps resolution includes a systematic error of 40 ps in total from timing jitters in the detector and accelerator electronics, calculation from μ-track information, and the collision position spread due to a beam bunch length. The degradation in timing performance is mainly due to aging, a reduction of the attenuation length and light yield in the TOF scintillation counters over the ten year running period. Pion tracks have a slightly worse average time resolution, typically by 10 ps, due to a nuclear scattering effect.

Aerogel Cherenkov counters

Figure 2.2.8 shows the configuration of the Belle Aerogel Cherenkov counter (ACC; Iijima, 2000). The polar angle coverage is $33.3° < \theta < 127.9°$ in the barrel, and $13.6° < \theta < 33.4°$ in the forward endcap. The detector is built from aerogel modules of ten distinct types, varying in refractive index ($n = 1.010, 1.013, 1.015, 1.020, 1.028$, or 1.030), and in the number (one or two) and size (2-, 2.5-, or 3-inch diameter) of photomultiplier tubes used to detect photons, according to their position in polar angle.

The barrel device consists of 60 identical sectors in the ϕ direction, and 16 modules are arranged in each sector. The typical size of one module is approximately $120 \times 120 \times 120\ \mathrm{mm}^3$, occupied with a silica aerogel radiator. The aerogel radiator volume is covered with a white reflector with high reflectivity (larger than 93%); it is supported by a 0.1 mm thick aluminum wall.

Each counter is viewed by one or two fine-mesh PMT(s) to detect Cherenkov light in an axial magnetic field of 1.5 T. The PMT diameters were chosen to be either 2", 2.5", or 3", depending on refractive indices since larger index aerogel generates more photons and the acceptance of a PMT can be smaller as a result.

The end cap device is divided into 12 identical sectors in ϕ, and each sector contains 19 modules, which are configured to have 5-layer structure in the radial direction. Each counter module contains a $\sim 100 \times 100 \times 100\ \mathrm{mm}^3$ radiator volume followed by an air light-guide, and then one 3" PMT is attached. This module is made of 0.5 mm-thick CFRP to reduce material while remaining rigid. The CFRP inner wall is covered with the same white reflector as used for the barrel. As there is no TOF coverage in the endcap regions, in order to achieve the required K–π separation for tracks with momenta $< 1.5\,\mathrm{GeV}/c$, the ACC endcap aerogel system has a refractive index of 1.03.

Output signals are amplified by front-end electronics attached to the PMT backplane and are sent to a charge-to-time conversion circuit and subsequently digitized using a TDC.

The calibration constants for all PMTs are obtained by μ-pair events collected in the beam collisions and daily PMT responses during experiments are monitored by the illuminating LED system, which is installed on all counter modules. The effective number of photoelectrons extracted from LED data as a function of the integrated luminosity for a typical PMT is plotted in Figure 2.2.9. The luminosity range plotted (up to 300 fb^{-1}) corresponds to almost 6 years from the beginning of operation. The variation is less than 5% over this period and this stability is found to be sufficient.

2.2.4 Electromagnetic calorimeter

BABAR

Figure 2.2.10 shows the longitudinal cross-section of the *BABAR* EMC. Its polar angle coverage ranges from 15.8° to 141.8° which corresponds to around 90% of the solid angle in the center-of-mass system. The cylindrical barrel is divided into 48 rings of 120 CsI(Tl) crystals each while the end cap holds 820 crystals assembled in eight rings. These

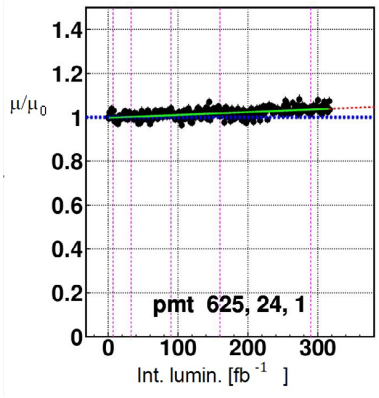

Figure 2.2.9. The relative pulse height as a function of integrated luminosity for a typical PMT of ACC.

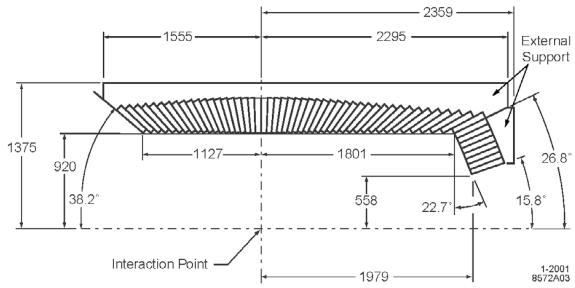

Figure 2.2.10. Longitudinal section of the *BABAR* EMC (Aubert, 2002j) showing the arrangement of the 56 CsI(Tl) crystal rings: 48 for the barrel and 8 for the forward end cap. All dimensions quoted on the drawing are in mm.

add up to a total of 6,580 crystals among which only three had their readout chain permanently broken by the end of the data taking period. The penetrating particles – in particular electrons and photons – initiate showers in crystals and cause the CsI to scintillate; the amount of light depends on the energy deposited in the calorimeter by each particle. The crystals are supported at the outer radius to avoid pre-showers (*i.e.* particles producing showers in the material in front of the calorimeter). It is worth noting that the crystals are organized in a quasi-projective geometry: they all point to a position near the IP, offset just enough to avoid the possibility of having particles going completely through non-instrumented gaps of the EMC. The amount of material between the IP and the EMC ranges between 0.3 and 0.6 X_0 except for the 3 most forward rings of the forward end cap, which see elements of the beamline and of the SVT readout system. These rings are shadowed by up to 3 X_0 and have been mainly included to ensure shower containment close to the end of the calorimeter acceptance.

There are two kinds of calibration for the EMC: a low-energy calibration using a 6.13 MeV radioactive photon source (fluorinert irradiated by neutrons) and a high-energy calibration using reconstructed Bhabha events. The source (Bhabha) calibration was performed about once every 1-2 weeks (a few times a year). In addition, a light pulser was used to monitor the light response of each individual crystal on a daily basis in order to identify potential problematic areas. The radiation dose received by the EMC over the years of data taking had no significant impact on its performance.

The EMC energy resolution σ_E/E varies from 5% at 6.13 MeV to about 2% at 7.5 GeV, an energy probed using Bhabha events. The angular resolution is 12 mrad (3 mrad) at low (high) energy. The π^0 measured mass is in agreement with the PDG value and has a resolution of about 7 MeV/c^2. Finally, the EMC provides the main discrimination variable to identify electrons: the ratio E/p of the shower energy to the track momentum – other PID inputs are the DCH $\mathrm{d}E/\mathrm{d}x$ and the θ_C value measured by the DIRC. The electron identification probability is around 90% on average with a pion contamination of $15-30$%, depending on the track momentum and polar angle.

Belle

The overall configuration of the Belle calorimeter, ECL, is shown in Figure 2.2.11.

The ECL consists of a barrel section and two end caps of segmented arrays of CsI(Tl) crystals. The former part is 3.0 m long and has an inner radius of 1.25 m. The end caps are located at $z = +2.0$ m and $z = -1.0$ m. The ECL is composed of 8736 CsI(Tl) crystals in total. The scintillation light produced by particles in the crystals is detected with silicon photodiodes.

Each crystal has a tower-like shape and points almost to the interaction point. The crystals are tilted by a small angle in the θ and ϕ directions to prevent photons escaping through the gaps between the crystals. The angular coverage of the ECL is $17.0° < \theta < 150.0°$ (total solid-angle coverage of 91% of 4π). Small gaps are left intentionally between the barrel and end cap crystals providing the necessary space for cables and supporting parts of the inner detector (these gaps result in a loss of acceptance at the level of 3%).

The amount of material in front of the ECL ranges between 0.3 to 0.8 X_0.

The calorimeter is calibrated using Bhabha scattering and $e^+e^- \to \gamma\gamma$ events. For the two innermost layers of crystals in the forward and backward end caps, cosmic ray interactions are used for calibration. The Bhabha calibration is performed once every 1-2 months. The electronic channel transition coefficients are monitored every day with a test pulse generator.

The radiation dose received by the ECL varies from 100 rads for barrel crystals to about 700 rads for forward end cap crystals. The degradation of the light output due to the overall dose was less than 5% and had no significant impact on ECL performance.

The ECL energy resolution varies from 4% at 100 MeV to about 1.6% at 8 GeV. The angular resolution is about 13 mrad (3 mrad) at low (high) energies. Such an energy and angular resolution provides a π^0 mass resolution of

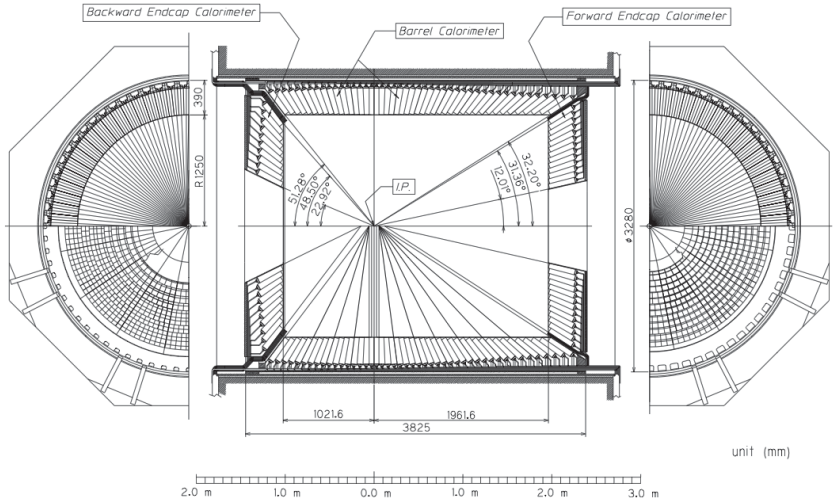

Figure 2.2.11. From (Abashian, 2002b). Overall configuration of the Belle ECL.

about $4.5\,\mathrm{MeV}/c^2$. The ECL provides the main parameter for electron/hadron separation: the ratio E/p of the shower energy to the track momentum.

In addition the ECL is used to provide the Belle online luminosity monitoring system. The rate of Bhabha events is measured using geometrical coincidences of high energy deposits in the forward and backward ECL. This system provides a stable accurate luminosity measurement during an experimental run as well as during injection periods.

2.2.5 Muon detector

BABAR

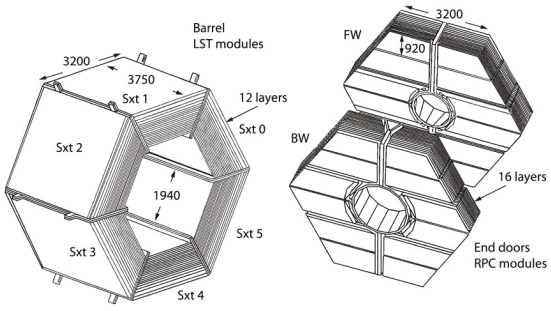

Figure 2.2.12. Overview of the *BABAR* IFR at the end of the data taking period (Aubert, 2013): the barrel sextants made of 12 LST layers are visible in the left picture while the forward and backward end doors appear on the right. The forward RPCs (16 layers) have all been changed whereas the backward ones are still the original detectors.

The final layout of the *BABAR* IFR – with, in particular, LST modules in all sextants of the barrel region – is shown in Figure 2.2.12.

The steel of the magnet flux return is finely segmented into 18 plates of increasing thickness: from 2 cm for the nine inner plates to 10 cm for the outermost ones. When data taking started, the *BABAR* IFR was instrumented with more than 800 RPCs, organized in 19 layers in the barrel region (divided itself into six sextants) and 18 in the end doors. These detectors quickly showed serious aging problems (Anulli, 2002, 2003; Piccolo, 2002, 2003) and the deterioration of their performance lead directly to a reduction of the *BABAR* muon identification capability. Overall, 6-17% of the muons were lost due to problems in the IFR. Although several attempts were made to fix the RPCs and to limit the rate of degradation, it was finally decided to replace most of these detectors. This was by far the largest *BABAR* upgrade and it was successfully completed in a 4-year period in various steps.

The RPCs in the backward end cap were never replaced. Due to the boost, they had low rates and covered a small solid angle. In 2002, more than 200 new RPCs were installed in the forward end cap (Anulli, 2005a). Their performance was significantly improved with respect to the original RPCs (Anulli, 2005b). These detectors nevertheless required constant maintenance and upgrades (Band, 2006; Ferroni, 2009) until the end of the data taking, in order to maintain their efficiency and their reliability while the luminosity was increasing. In particular, the chambers with the highest rates were operated in avalanche mode from 2006.

The first two barrel sextants were replaced during the summer 2004 shutdown, only one and a half years after the decision to proceed with this upgrade had been taken. An extensive review process lead to the choice of the Limited Streamer Tube (LST) (Andreotti, 2003) technology

to replace the existing RPCs. The procedure consisted of replacing 12 RPC layers by LSTs and to fill the remaining gaps with brass – the outermost layer (#19) could not be instrumented due to a geometrical interference. Increasing the total absorber thickness allowed the improvement of the pion rejection of the muon PID algorithms. The last four barrel sextants were replaced during the fall 2006 shutdown.

The LST efficiency was measured using di-muon events. On average, it was 88% at the end of the data taking, slightly below the geometrical acceptance of 92%. The difference was mainly due to a few misfunctioning or broken channels.

Belle

The muon and K_L detector subsystem of Belle identifies K_L mesons and muons above 600 MeV/c with high efficiency. The barrel-shaped region around the interaction point covers a polar angular range of 45° to 125° while the forward and backward end caps extend this range to between 20° and 155°.

This system consists of alternating layers of double-gap resistive plate counters and 4.7 cm thick iron plates. There are 15 detector layers and 14 iron layers in the octagonal barrel region and 14 detector layers and 14 iron layers in each end cap. The iron plates provide a total of 3.9 interaction lengths of material (in addition to the 0.8 interaction lengths in the ECL) for a hadron traveling normal to the detector planes. The hadronic shower from a K_L interaction determines its direction (assuming an origin at the e^+e^- interaction point) but not its energy. The range and transverse deflection of a non-showering charged particle discriminates between muons and hadrons ($\pi^\pm$ or $K^\pm$).

The active elements are double-gap glass-electrode RPCs operating in limited streamer mode. Each 2 mm gas gap is sandwiched between float-glass electrodes with a bulk resistivity of $10^{12-13}\,\Omega\cdot$cm (Figure 2.2.13). The non flammable gas mixture consists of 62% HFC-134a, 30% argon, and 8% butane-silver.[14] An ionizing particle traversing the gap initiates a streamer in the gas that results in a local discharge of the electrodes. This discharge is limited by the high resistivity of the glass and the quenching characteristics of the gas. A discharge in either gas gap induces signals on both of the orthogonal external copper-strip planes. Each ∼5 cm wide strip forms a ∼50 Ω transmission line with an adjacent ground plane. In the barrel (but not the end caps), a 100 Ω resistor connects the pickup strip to ground at the readout end to minimize reflections; it also reduces the pulse height into the front-end electronics by a factor of two.

The barrel RPCs, made in the US, use 2.4 mm thick float glass (73% SiO_2, 14% Na_2O, 9% CaO, and 4% trace elements). The end cap RPCs, made in Japan, use 2.0 mm thick float glass (70–74% SiO_2, 12–16% Na_2O, 6–12% CaO, 0–2% Al_2O_3, and 0–4% MgO).

[14] Butane-silver is a mixture of approximately 70% n-butane and 30% iso-butane.

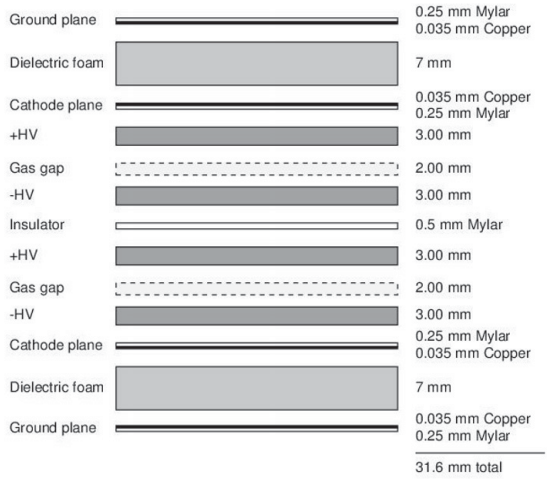

Figure 2.2.13. Exploded cross section of a Belle superlayer double-gap RPC module.

The VISyN system by LeCroy (now Universal Voltronics) is used to distribute high voltage, with Model 1458 mainframes and 1468P and 1469N modules. For each RPC, a positive voltage of +4.7 kV (+4.5 kV) is applied to the barrel (end cap) anode plates and −3.5 kV to the cathode plates. Eight (five) anode plates in the barrel (end cap) are driven by a common HV channel while each cathode plane is driven by its own HV channel. The dark current is approximately $\sim 1\,\mu\text{A/m}^2$ or 5 mA total; most of this flows through the noryl spacers.

Pulses travel from the 38,000 RPC cathode strips along twisted-pair cables, between 3 and 6 meters long, to front-end electronics on the magnet yoke periphery. The typical 100 mV pulse has a FWHM of under 50 ns and a rise time of under 5 ns. The dark rate in a typical detector module is under 0.03 Hz/cm^2 with few spurious discharges or after pulses. The signal threshold for discriminating these pulses is 40 mV (70 mV) in the barrel (end caps). The double-gap design results in a superlayer efficiency of over 98% despite the lower (90% to 95%) efficiency of a single RPC layer. Robustness against several failure modes is achieved by having independent gas and high voltage supplies for each RPC layer within a module. Hit position is resolved to about 1.1 cm when either one or two adjacent strips fire, resulting in an angular resolution of under 10 mrad from the interaction point.

The Belle RPCs have performed reliably and without evidence of failures or physical deterioration throughout Belle's lifespan. However, the RPCs are rate-limited by the glass-electrode resistivity, so the efficiency of the modestly shielded end cap RPCs suffered during high-luminosity operation from soft neutrons produced in beamline structures. This was mitigated by the addition of external polyethylene shielding outside the end caps in Belle's later years, but more such shielding would have been needed to eliminate the efficiency drop.

2.2.6 Trigger

BABAR

As already discussed above, the *BABAR* trigger is implemented as a two-level hierarchy, with the L1 (hardware) followed by the L3 (software). Its combined efficiency at the $\Upsilon(4S)$ resonance energy matches its requirements: more than 99% for $B\overline{B}$ decays, more than 95% for continuum decays ($u\overline{u}$, $d\overline{d}$, $s\overline{s}$ $c\overline{c}$) and still around 92% for $\tau\tau$ events. This trigger was very flexible, as illustrated by the quick and complex modifications of the L3 trigger lines implemented during the last few months of the *BABAR* running, when data were taken at the $\Upsilon(2S)$ and $\Upsilon(3S)$ resonances and a final energy scan above the $\Upsilon(4S)$ was performed. It was also robust against background: trigger rates much higher than the design values for both L1 and L3 were achieved as luminosity was increasing, while the dead-time remained relatively constant, around the 1% design value.

The *BABAR* L1-trigger uses information coming from the DCH for charged tracks, from showers in EMC and from the IFR. The corresponding first two triggers – Drift Chamber Trigger (DCT) and ElectroMagnetic Trigger (EMT) – fulfill all trigger requirements independently and are highly redundant, which boosts the global L1 efficiency and allows one to measure the efficiency of these components using data. Originally, the DCT only provided r and ϕ information; in 2005, 3D-tracking was implemented in L1 to add z-information which allowed one to reject background events (scattered beam-gas particles hitting the beam pipe) where tracks were produced tens of centimeters away from the IP. This upgrade gave the system more headroom to follow the increases of luminosity and background without generating a significant dead time, especially during the final period of data taking. The third L1 input trigger, the IFR Trigger (IFT), is mostly used for tests: IFR plateau measurements, cosmics trigger, etc. Some work was required after the IFR barrel upgrade to align in time the RPC and LST signals, the latter coming in about 0.6 μs later.

Information coming from the three components described above are received by the GLT which processes all these primitives and sends out some triggers to the central *BABAR* DAQ system. At this stage, a trigger can be masked (for instance if it corresponds to a known temporarily noisy EMC crystal) or prescaled (meaning that not all selected events are registered; in particular, events identified as Bhabha at the trigger level are prescaled). If a valid trigger remains at this stage, the DAQ system issues a *L1 Accept* signal and the entire event is readout.

The *BABAR* L3-trigger refines and augments the L1 selection methods. It has been implemented in such a way that a wide range of algorithms can be used to select events independently of one another. Their logic and their parameters are set in software and these filters have access to the full event to make their decision. First, L3 input lines are defined by using a logical OR of any number of L1 output lines. Then, one or more scripts are executed for each firing L3 input line and return a yes/no flag depending on whether the event passes this step. Finally, L3 output lines are the logical OR of selected L3 script flags; these flags can also be used as vetoes, for instance to reject Bhabha events which would have been accepted otherwise. Thanks to the spare capacity planned for at the time the L3 system was designed, it could log data at a much higher rate than anticipated: close to 800 Hz at the end of the $\Upsilon(3S)$ data taking, to be compared with the initial expectation of 120 Hz.

Moving from the regular $\Upsilon(4S)$ data taking to the $\Upsilon(3S)$ run during which new physics (NP) decays were sought after, the trigger had to identify completely different topologies of events. Indeed, part of the signal decays were containing particles invisible to *BABAR* which would take away a significant fraction of the energy-momentum available for the collision. Whereas $B\overline{B}$ events exhibit large visible energy, high multiplicity or high transverse activity, the decays of interest of the $\Upsilon(3S)$ are characterized by low visible energy and low multiplicity. This new approach was implemented in three successive steps which required the design of new L1 and L3 trigger lines, such as new L3 filters. These updates were done carefully, checking at each step that the trigger rates would not exceed the capabilities of the system. They were successful, allowing the *BABAR* collaboration to collect large datasets at the $\Upsilon(2S)$ and $\Upsilon(3S)$ resonances.

Belle

The trigger system of the Belle detector consists of subtriggers and the global decision logic (GDL) - constituents of the Level 1 (L1) hardware trigger - and of Level 3 (L3) software trigger. The sub-triggers are formed by signals from the CDC, ECL, TOF, and KLM sub-detectors. The GDL receives summary information from each sub-trigger, then makes a logical combination of sub-trigger information to trigger on hadronic ($B\overline{B}$ and continuum) events, Bhabha and $\mu^+\mu^-$ pair events, etc. Three independent triggers are prepared for the hadronic events; they require either three or more charged track candidates, high levels of deposited energy in the ECL (with a veto on the ECL trigger for Bhabha events) or four isolated neutral clusters in the ECL. The L3 software trigger ran on the online computer farm (see Section 2.2.7). Events triggered by L1 as Bhabha, $\mu^+\mu^-$ pairs, two-photon events, cosmic rays or events with high deposited energy in the ECL, bypass the L3 trigger decision. The events triggered by the presence of charged track candidates are passed to the L3 trigger to determine the presence of actual good charged particle tracks, thus reducing the size of the raw data being recorded.

The efficiencies of the L1 triggers for hadronic events can be measured using the redundancy of the three selection requirements mentioned above because they are almost independent. The overall efficiency for hadronic events is estimated to be more than 99%.

At the beginning of the experiment Belle experienced a high trigger rate caused by the beam background. Signals

arising from this background caused the trigger rate to be nearly the DAQ upper limit of 200 Hz even while running at very low luminosity. The rate of the two-charged-track trigger was especially high because of the low p_t tracks originating from the beam-nucleus interactions. To reduce such a high trigger rate, the requirement of coincidence with outer sub-triggers, such as a TOF hit and/or an ECL isolated cluster, was added. Figure 2.2.14 shows the average trigger rate as a function of the experiment number.[15] The green curve shows the average total current of KEKB. The highest total current was 3000 mA around experiment 50. The sudden drop of the total current at experiment 57 was due to the crab cavity installation at KEKB. The red curve shows the average trigger rate. It was as high as 500 Hz around experiment 50, which corresponds to the highest total current and luminosity. In early experiments, high background was indicated by the normalized trigger rate, the blue curve in Figure 2.2.14, defined as the the average trigger rate divided by the average luminosity (called the effective cross section). This

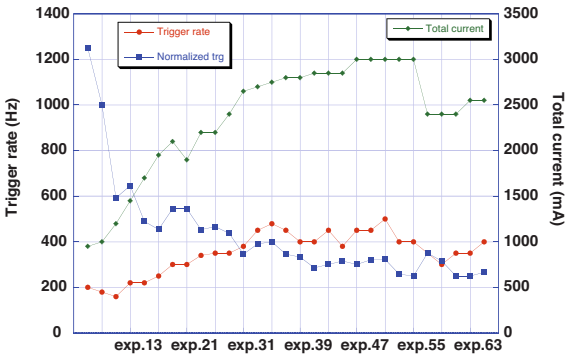

Figure 2.2.14. Average trigger rate as a function of the experiment number for Belle.

rate is normalized to the trigger rate with the luminosity 1×10^{34} cm^{-2} s^{-1}. It was higher than 1200 Hz at the beginning of operation, and dropped dramatically as the total current increased (and hence the luminosity increased). After experiment 33 the rate was stable below 400 Hz, which was interpreted as an amelioration of the vacuum around the IP with the higher beam current. In a special run in experiment 47, the luminosity components in the trigger rate were measured to be about 190 Hz in the normalized trigger rate. The noise-to-signal ratio (N/S) was calculated to be about 5.6 in experiment 7, and about 1 or smaller after experiment 37, an indication of the cleaner environment of KEKB operation.

[15] An extended period of operation is referred to as an experiment within Belle, see Chapter 3. The corresponding nomenclature on *BABAR* is a Run.

2.2.7 Online and DAQ

BABAR

The high-level design of the *BABAR* online system (Aubert, 2002j) remained unchanged during the whole data taking period. The DAQ chain starts from the common front-end electronics, includes the embedded processors in the readout modules (which start processing the data fragments coming from the detector after a Level 1 accept), the network event builder, the Level 3 trigger and the event logging system. While the design remained constant, the system itself evolved significantly over the time to follow the progress in hardware technology, and to cope with the changes in data taking conditions: higher luminosity, larger backgrounds, longer periods of data taking thanks to the trickle injection mode (see Section 3.2.2 for details), and so on. Several other developments were made with the intent of making the overall system more robust, better performing, and easier to use. For all upgrades, the philosophy was first to maximize the performance of the existing hardware, and only then to plan a hardware upgrade.

With PEP-II operated in trickle injection mode, data taking could occur continuously during one day or more. Therefore special emphasis was put on the data taking efficiency. The aim was to minimize the time spent by the detector in any non-data-taking state (calibration, error recovery, transition from 'injectable' mode to 'runnable' mode, procedure to begin a new run, etc.). Maximizing the *BABAR* duty cycle required a continuous monitoring of the whole system and attention to detail. While the online system had already been designed to minimize the DAQ dead time, new features were introduced, parts of the system were improved, and procedures modified to increase the detector uptime despite the more challenging environment. One concrete example of this evolution was the reduction of staffing for the detector operation, as the online control and monitoring system was simplified and automated.

Moreover, as explained in Chapter 3, the PEP-II operation in trickle injection mode required developments in the trigger and the DAQ, in order to make the detector insensitive to the background bursts associated with the continuous injection. Dedicated monitoring was added to allow detailed data quality analysis in real time.

The CPUs and the operating system used by the *BABAR* online system evolved over the years, switching from vendor-specific products to commodity systems. This allowed control of the cost of the upgrades of the online system and to provide enough headroom to anticipate the increase of luminosity and background. Most of the online software was written in C++; various scripting languages were used as well, such as Java for graphical tools.

An important evolution of the online system was the replacement of Objectivity-based databases by `Root`-based ones. Several reasons explain this migration, which culminated in 2006 with the decision to stop using Objectivity in *BABAR*. Indeed, there were many concerns regarding the support and the maintenance cost of this software,

plus some technical issues. All these changes were carefully planned to make sure they would have no impact on the data taking.

Belle

The original requirement for the Belle Data Acquisition System (Belle DAQ) was to read out event fragments from 8 detector subsystems with a total data size of 40 kbytes at a maximum rate of 500 Hz, and to record the data after event building and data reduction by real time processing.

Figure 2.2.15 shows the configuration of the DAQ system at the beginning of the experiment. The readout system is designed to utilize the unified technology based on the Q-to-T conversion combined with the common FASTBUS multi-hit TDC (LeCroy 1877S), except for the SVD readout. The data are read by the VME processor and collected by the specially-designed event builder, and then processed by the online computer farm equipped with a large number of VME processor modules where high level software triggering is performed. The data are finally sent to the KEK Computer Center via ∼2 km optical fiber links and recorded on digital video tapes.[16]

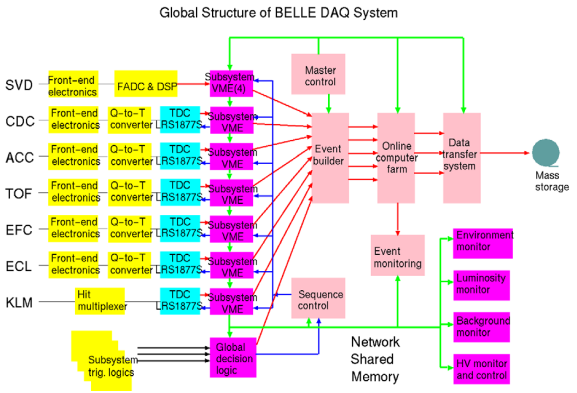

Figure 2.2.15. The configuration of the Belle DAQ system at the beginning of the experiment.

However, since the system was implemented using 1990's-era information technology, maintenance of the system was difficult in the long run. In addition, the FASTBUS based readout system is not pipelined and it has a readout dead time of more than 10% at the design maximum trigger rate of 500 Hz. The trigger rate at the beginning of data taking was 200 Hz and the dead time was manageable, but the rate increase was foreseen as the luminosity improves.

Belle started the 'continuous' upgrade of the system to keep up with the luminosity increase. The first step was made in 2001 to replace the event builder and VME based online computer farm with a set of Linux PC servers (EFARM) connected via Fast Ethernet fibers. The level 3 data reduction which was performed in VME processors was ported to the EFARM. The system became more maintainable for a longer term operation as a result of this upgrade.

In 2003, the real time reconstruction farm (RFARM) was introduced. The system is a large scale PC farm directly fed by the event builder, and real time full event reconstruction is performed utilizing parallel processing of events. The processing results such as the reconstructed IP position were also fed back to the accelerator control, which greatly contributed to the improvement of luminosity. In the same year, the improvement of the FASTBUS readout was also made so as to reduce the readout dead time by a factor of four.

An improvement to the back-end system was made in 2005, when a second EFARM and RFARM were added in order to have sufficient bandwidth and processing power to cope with the expected increase in luminosity.

For further reduction of the readout dead time, an upgrade of the FASTBUS readout system, to a pipelined version, was started. A new TDC was developed based on COPPER, a common pipeline readout module developed at KEK (Figure 2.2.16). The TDC is designed to be plug-compatible with LeCroy 1877S, allowing the use of the same detector front-end electronics without any modifications. The upgrade was performed detector by detector starting from the CDC in 2007 utilizing the short shutdown time during summer and winter. By 2009, five detector subsystems were upgraded resulting in a reduction in dead time to less than 1%. Figure 2.2.17 shows the Belle DAQ configuration at the end of data taking.

2.2.8 Background and mitigation

BABAR

Predicting accurately the background level using dedicated simulations is not an easy task, whether the detector plans to run at the intensity or at the energy frontier. Yet, background is a major concern for any HEP experiment as it can severely impact the data taking: first, by slowing down the acquisition system and creating dead time; then, by decreasing the quality of the logged data when signal signatures get lost in a mass of random hits; finally, by degrading or even destroying detector components. Therefore, special care is given to design detectors able to handle background levels corresponding to the predictions (with significant safety margins added), while numerous probes monitor the background during the data taking. When the conditions become unsafe for the detector, automated systems make its HV ramp down to safer levels and can even dump the beams.

Figure 2.2.18 shows an overview of the *BABAR* background monitoring system: several probes monitor quantities sensitive to background (radiation doses, rates recorded by scaler boards, channel currents, etc.) in real time and compare the measured values with pre-defined alarm levels. The status of each variable (in alarm or not) is indi-

[16] These are the same tape format as previously used by some TV broadcasting companies.

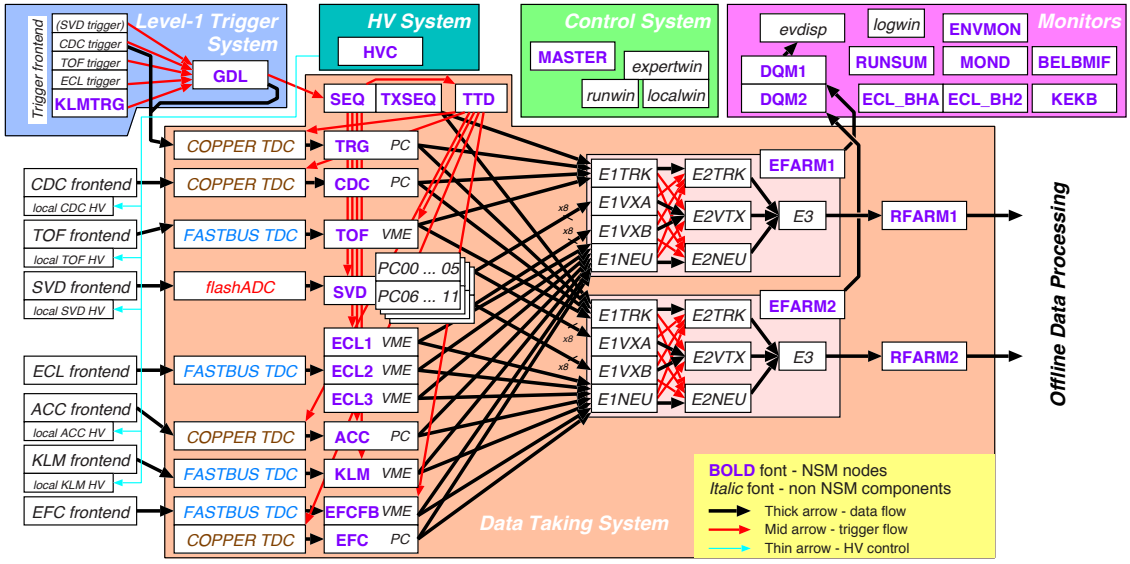

Figure 2.2.17. The configuration of the Belle DAQ system at the end of data taking.

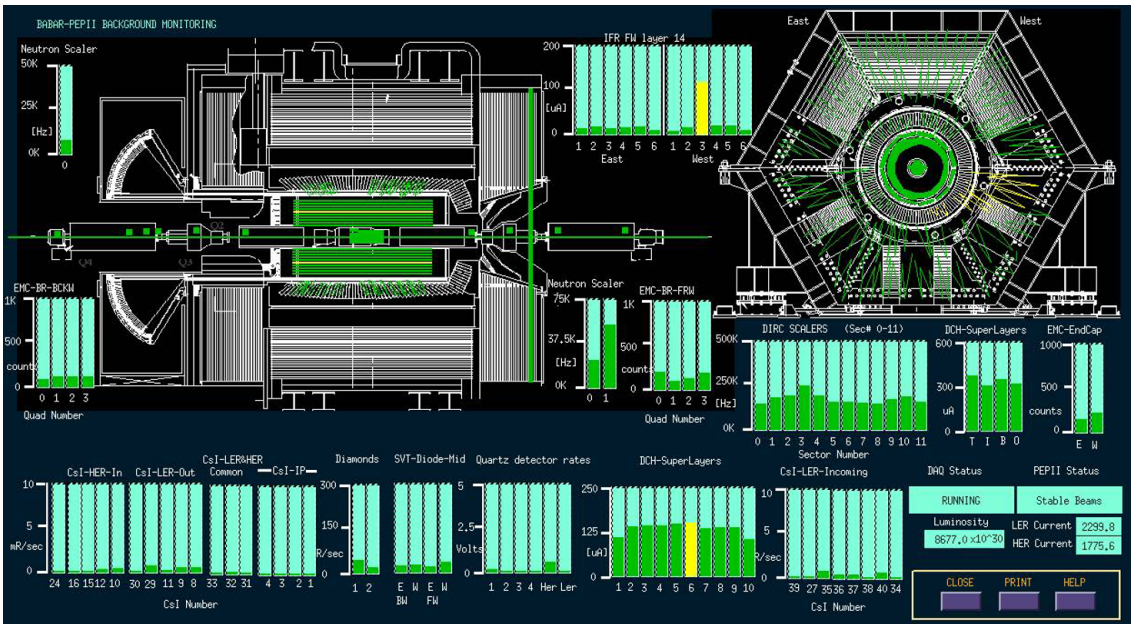

Figure 2.2.18. Snapshot of the global *BABAR* background display (Aubert, 2013) taken at a time when the background was low: all but a couple of probes are green which, in the *BABAR* framework, means 'safe level' – alarm states are indicated by yellow (warning level reached) and red (concern) colors. This display was available 24/7 in the control room to help shifters get a real time overview of the background levels around the *BABAR* detector. The longitudinal and end cross-sections show the locations of the background probes which survey all systems: SVT radiation monitors, current levels in the DCH superlayers, rates in the DIRC, EMC and IFR or neutron rates on both ends of the beampipe.

cated by the color of the display. New alarms produce visual and audio alerts in the control room while automated systems can modify the detector state or even abort the beams if the background becomes worrisome.

There were two main active detector protection systems in *BABAR* to ensure a safe operation of the sensitive tracking system. First, the SVTRAD which monitored both the instantaneous and the integrated radiation doses received by the SVT. Originally, rates were measured by 12 PIN diodes located on both ends of the SVT in three horizontal planes (one at the beam level, the other two 3 cm above/below it) and on the inside and outside of

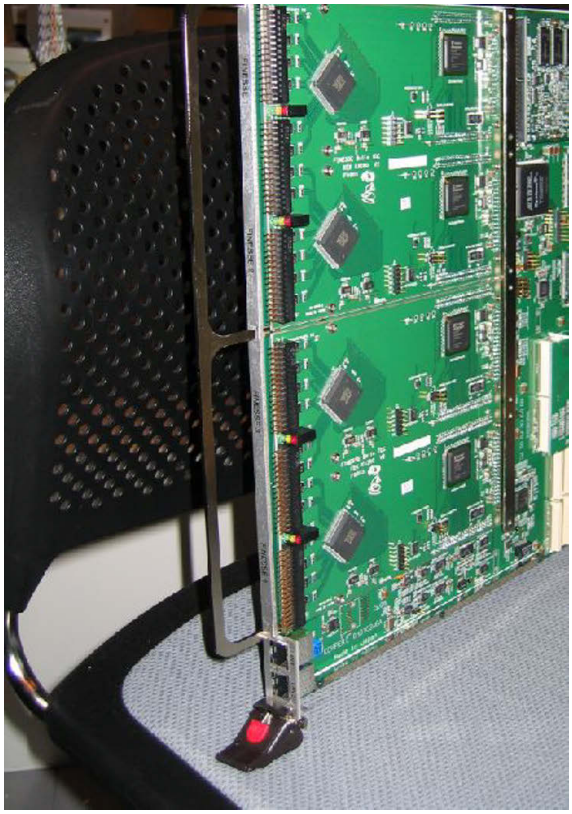

Figure 2.2.16. A pipeline TDC module based on COPPER.

the PEP-II rings. As expected, the middle-plane diodes accumulated the highest radiation doses and started to become less reliable due to damage. Therefore, in 2002 two diamond sensors were added to the SVTRAD system – this was the first time such sensors were used in a HEP experiment – and they worked well until the end of the data taking. Another advantage of these detectors with respect to the PIN diodes is that they are insensitive to temperature fluctuations. The maximum total dose after nine years of operations was measured to be around 4 MRad, *i.e.* less than the SVT radiation budget, set to 5 MRad. The SVTRAD was also able to abort the beams, either when instantaneous doses were too high or because the integrated dose was consistently above some threshold during 10 consecutive minutes. Beam aborts induced by the SVTRAD protection system occurred a few times a day on average. When PEP-II started to deliver beams in trickle injection mode (particles are injected in existing bunches at a few Hz frequency, see Section 3.2.2 for details), the SVTRAD was modified to monitor in addition the dose associated with each injection of particles in the collider rings. This provided a complementary feedback on the trickle injection quality. The second active protection system was based on the monitoring of the DCH currents and was used to prevent damage to the drift chamber wires and the associated front-end electronics; it is described above in Section 2.2.2.

The main *BABAR* background probes were also displayed in the accelerator control room, providing valuable information about the beam status and helping operators reduce the background levels. For instance, the accelerator crew was notified when the SVTRAD 10-minute counter was enabled; this signal would tell them that the beams were to be tuned and that they also had some time to try and fix the problem before a beam abort would be issued.

In addition to the real-time monitoring and protection system, various shieldings around *BABAR* have been built and improved over the years. The main additions with respect to the original detector design have been a DIRC shielding around the beamline components at the backward end and shielding walls on the forward side of *BABAR* to protect the outer IFR layers.

2.2.9 Conclusion: main common points, main differences

Table 2.2.1 summarizes in a single page the typical performances of the *BABAR* and Belle detectors. Of course the signals detected by the individual subdetectors need to be combined and converted into data used for physics measurements. Various methods and tools are used for this data reconstruction which are beyond the scope of this book. Typical performances of combined tracking, charged particle identification and neutral particle reconstruction are also given in Table 2.2.1. More information can be found in the detector articles published by the two collaborations and in this book, in particular for PID – see Chapter 5 – and for tracking and vertexing – see Chapter 6.

Both detectors reached their design performance and were robust enough to keep them almost constant while the luminosity delivered by the colliders was increasing. Both data taking periods were about a decade long, allowing *BABAR* and Belle to collect huge datasets which made possible the impressive harvest of physics results achieved by the two collaborations. The detector upgrades described in Section 3.2 were mainly driven by the luminosity increase although both experiments had a subdetector weaker than the others: the silicon tracker for Belle and the muon detector for *BABAR*. Several technological and conceptual breakthroughs were made by the *B* Factories, among which the *BABAR* DIRC (a new concept of ring-imaging Cherenkov PID detector), the use of the object-oriented language C++ for the experiment software, or the development of distributing computing. Now, they all are well-established in the HEP community.

Table 2.2.1. Summary of the *BABAR* and Belle detector main characteristics. The *BABAR* numbers provided in this table are representative of the detector performances; they vary with the type of events reconstructed. Moreover, the PID selectors can be tuned depending on the analysis requirements – looser or tighter cuts. [a]Until summer 2003 Belle used a 3 layer SVD. [b]Number of photo-electrons. [c]For Bhabha events. [d]L3 trigger was operated partially from 2004 to 2007. [e]The maximal trigger rate is determined at the end of the DAQ chain. [f]For $B\overline{B}$ events. [g]For momenta above 0.8 GeV/c. [h]For π^0's reconstructed from photons in hadronic events.

Detector type	Belle				*BABAR*			
	abbreviation	Type	θ Coverage	Illustrative Performance	abbreviation	Type	θ Coverage	Illustrative Performance
Tracking	SVD	Silicon 3/4 layers[a] Two-sided	$[17°; 150°]$	Single hit resolution: 12 μm ($R\phi$) 19 μm (z)	SVT	Silicon 5 layers Two-sided	$[20.1°; 150.2°]$	Single hit resolution: $\sim$10-15 μm (inner) $\sim$40 μm (outer)
	CDC	Drift chamber	$[17°; 150°]$	Single hit resolution: 130 μm ($R\phi$) 200-1400 μm (z) $\sigma(\mathrm{d}E/\mathrm{d}x)\sim$7%	DCH	Drift chamber	$[17.2°; 152.6°]$	Single-cell hit resolution: $\sim$100 μm (center of the cell) $\sigma(\mathrm{d}E/\mathrm{d}x)\sim$8%
Particle ID	TOF	Time of flight scintillator	$[34°; 130°]$	$\sigma_t = 100$ ps	DIRC	Cherenkov	$[25.5°; 141.4°]$	$\sigma_{\theta_C}\sim$2.4 mrad
	ACC	Threshold Cherenkov with aerogel	$[17°; 127°]$	$N_{\mathrm{p.e.}} \geq 6$[b]	–	–	–	–
					–	–	–	–
Calorimetry	ECL	CsI(Tl)	$[12.4°; 31.4°]$ $[32.2°; 128.7°]$ $[130.7°; 155.1°]$	$\sigma_E/E\sim$1.7%[c]	EMC	CsI(Tl)	$[15.8°; 140.8°]$	$\sigma_E/E\sim$3%
Muon and K_L^0 detector	KLM	RPC	$[20°; 155°]$	$\sigma_\theta = \sigma_\phi = 30$ mrad for K_L^0	IFR	RPC, LST	$[20°; 154°]$	LST layer eff. $\sim$88%
Trigger	L1	Hardware	Full		L1	Hardware	Full	Max. rate $\sim$5 kHz
	L3[d]	Software	Belle		L3	Software	*BABAR*	Max. rate $\sim$1 kHz
	L1+L3		acceptance	Max. rate $\sim$0.5 kHz[e] Physics mode eff. $> 99\%$[f]	L1+L3		Acceptance	Physics mode eff. $\sim$99%
PID Algorithms	$\mu^\pm$ (KLM)			$\langle\mu$ eff$\rangle = 90\%$[g] $\langle\pi$ misID$\rangle = 2\%$	$\mu^\pm$			$\langle\mu$ eff$\rangle = 59 - 65\%$ $\langle\pi$ misID$\rangle = 1.4 - 0.8\%$
	K/π (TOF,ACC,CDC)			$\langle K$ eff$\rangle \geq 85\%$ $\langle\pi$ misID$\rangle \leq 10\%$	K/π			$\langle K$ eff$\rangle = 84\%$ $\langle\pi$ misID$\rangle = 1.1\%$
	$e^\pm$ (CDC,ECL)			$\langle e$ eff$\rangle = 90\%$ $\langle\pi$ misID$\rangle \sim 0.3\%$	$e^\pm$			$\langle e$ eff$\rangle = 90 - 95\%$ $\langle\pi$ misID$\rangle < 0.2\%$
Tracking	(CDC,SVD)			$\sigma_{p_T}/p_T = 0.0019 p_t$ [GeV/c] $\oplus$ 0.0030/β	SVT + DCH			$\sigma_{p_T}/p_T\sim$0.5%
Neutrals	(ECL)			$\sigma(m_{\pi^0}) = 4.8$ MeV/c^2 [h]	EMC			

Chapter 3
Data processing and Monte Carlo production

Editors:
Fabrizio Bianchi and Nicolas Arnaud (BABAR)
Shoji Uno (Belle)

Additional section writers:
Concetta Cartaro, Christopher Hearty, Ryosuke Itoh, Leo Piilonen, Teela Pulliam, Dennis Wright

3.1 Introduction: general organization of the data taking, data reconstruction and MC production

The *BABAR* and Belle experiments have collected around one Petabyte of raw data each. These data have been calibrated, the events reconstructed, and collections of selected events produced. Monte Carlo events (MC) have been generated and reconstructed with the same code used for the detector data. The total amount of data produced by *BABAR* and Belle were over six Petabytes and over three Petabytes respectively. Over the years, both collaborations have developed computing models that have proven to be highly successful in handling the amount of data produced, and in supporting the physics analysis activities. The main elements of the two computing models are outlined in this introductory section and will be described in more detail in the remainder of this chapter.

The 'raw data' coming from the detectors have been permanently stored on tape, calibrated, and reconstructed usually within 48 hours of the actual data taking. Reconstructed data have been permanently stored in a format suitable for subsequent physics analysis.

Many samples of Monte Carlo events, corresponding to different sets of physics channels, have been generated and reconstructed in the same way. In addition to the physics triggers, the data acquisition also recorded random triggers that have been used to create 'background frames' that have been superimposed on the generated Monte Carlo events to account for the effects of the machine background and of electronic noise, before the reconstruction step.

Detector and Monte Carlo data have been centrally 'skimmed' to produce subsets of selected events, the 'skims', designed for a specific area of analysis. Skims are very convenient for physics analysis, but they increase the storage requirements because the same event can be present in more than one skim.

The quality of the detector data and of the simulated events has been monitored through all the steps of processing.

From time to time, as improvements in detector calibration constants and/or in the code were implemented, the detector data have been reprocessed and new samples of simulated data generated. When sets of new skims become available, an additional skim cycle has been run on all the events.

BABAR has been one of the first experiments to adopt the C++ programming language to write offline and online software. In the mid-nineties, when this decision was taken, the dominant language in the High Energy Physics (HEP) community was `Fortran 77`. However, problems and limitations associated with this language were becoming very clear and *BABAR* chose early to commit to the C++ technology because there was the perception that the HEP computing model was a very good match to an object-oriented design. At first, the C++ expertise was limited to few collaborators, who started offering tutorials. Starting in 1996, formal training courses were offered to the collaboration members and rapidly produced a shared vocabulary and set of concepts that were immensely helpful in the actual software development. The final outcome of this effort was the over 3 million lines of code that today constitutes the *BABAR* offline software.

Belle data processing and analysis code (called Belle AnalysiS Framework - `basf`) was developed in C++ with an extensive use of adjoined tools (*e.g.* the CLHEP library (CLHEP, 2008) for which some of the Belle members were the initial developers). The simulation tool, `GEANT3` (Brun, Bruyant, Maire, McPherson, and Zanarini, 1987), on the other hand, was written in `Fortran`.

Belle data were stored using the `PANTHER` banks event store based on the entity-relationship model (Putzer, 1989) and developed specifically for this experiment. `PANTHER` banks (Adachi, 2004) offered a satisfactory storage throughout the data taking and reliable usage in the data analysis process. Due to the large volume of recorded data centralized skimming was used (see Section 3.5) in order to facilitate subsequent analysis of events. Furthermore, at the level of specific analysis, additional skimming was performed, resulting in the so called index files, providing unique event identifiers that enable processing of selected events only.

Similarly large data volumes produced by *BABAR* were anticipated to make it impossible to routinely run on all the data. At first, *BABAR* decided to use an event store based on the object-oriented database technology that was expected to solve the problem of an efficient and scalable access to the data. The end result of this work was what, at the time, was the world's largest object-oriented database. Unfortunately, it soon became clear that data volumes and usage patterns were exceeding the capabilities of the technologies that were available at that time. A lot of effort went into mitigating these problems. Finally, the working solution identified was to handle data persistency using `Root` I/O which offers the advantages of its lightweight interface and built-in data compression. In this context, client/server data access was a very important issue and the bundled data server, `rootd`, was insufficient for *BABAR*'s need. A better performing solution was developed starting from `rootd` and taking advantage of the experience made with the object-oriented database.

The result of this effort was a data server named `XRootD` (Furano and Hanushevsky, 2010).

BABAR was the first HEP experiment to effectively use geographically distributed resources, because the amount of computing needed to satisfy the production and analysis requirements exceeded what was possible at SLAC. Grid computing tools became available too late for the B Factories and *BABAR* solved the problem by assigning specific production tasks and datasets to different computing centers. Only 20-30% of Monte Carlo data where produced using Grid resources with the aid of specific software tools.

Belle (re-)processed the recorded data centrally at KEK while the production of simulation was dispersed among the collaborating institutions. As with *BABAR*, a significant part of MC simulation was produced at remote sites.

3.2 Data taking

BABAR started taking physics data in October 1999 after an extensive period of commissioning of both the collider and the detector. The data taking ended on April 7^{th} 2008, about six months earlier than planned, due to budget constraints at the US Department Of Energy (DOE) level. The *BABAR* data taking can be divided into seven main periods, called 'Runs',[17] for which details are given below. The equivalent of the *BABAR* Run is called 'Experiment' at Belle.

Two consecutive *BABAR* Runs are separated by a shutdown period usually lasting a few months and during which various operations are performed by the PEP-II and *BABAR* teams: repairs, fixes and maintenance, both at the hardware and software levels. The longest *BABAR* shutdown took place between Runs 4 and 5 (from August 2004 to April 2005) as the start of the new data taking period was delayed due to an electrical accident at SLAC: all work procedures had to be reviewed and improved in order to reinforce the site-wide safety best practice.

BABAR Runs 1 to 6 data were taken at (or near) the energy of the $\Upsilon(4S)$ resonance (10.58 GeV). About 90% of these data were taken at the peak of the resonance ('on-resonance' data) to maximize the number of produced $B\overline{B}$ pairs. The remaining ∼10% were taken about 40 MeV below ('off-resonance' data) to study non-B backgrounds, in particular the production of light quark and τ pairs called 'continuum'. Taking advantage of years of continuous improvements and upgrades, both on the machine and detector sides, Run 7 was expected to increase the size of the *BABAR* dataset by 50% in about a year. Once this goal would have been achieved, it was planned to end the data taking by running at other energies, below and above the $\Upsilon(4S)$ resonance. When it became clear shortly before Christmas 2007 that Run 7 was going to be much shorter than anticipated due to the lack of funding, the *BABAR* management reacted quickly and decided to stop the $\Upsilon(4S)$ resonance data taking – which had just restarted a week earlier. Instead, data were taken at the $\Upsilon(3S)$ resonance during two months; then, the collision energy was moved to the $\Upsilon(2S)$ resonance for about a month. In both cases, on- and off-resonance data were recorded. Finally, the energy region above the $\Upsilon(4S)$ resonance up to 11.2 GeV was scanned during the last 10 days of data taking.

Although originally designed to be a fixed-energy machine, PEP-II performed remarkably well during Run 7 and all of the CM energy changes were done by moving the energy of the HER beam, keeping the LER one fixed. At the $\Upsilon(2S)$ energy (10.02 GeV), the HER orbit was quite close to the vacuum beam pipe in the interaction region (IR), leading to a trade-off between luminosity and background. At 11 GeV and above, synchrotron radiation became the dominant issue and the HER current had to be decreased, which had a direct impact on the delivered luminosity. On the *BABAR* side, the trigger was the main system impacted by the changes of the running energy as the data taking goal moved from selecting $B\overline{B}$ events with large visible energy, high multiplicity and/or high transverse energy to looking for decays with low visible energy and low multiplicity. These changes had to be made while the data taking was ongoing and occurred thanks to the flexibility of the *BABAR* trigger design.

Belle started taking data on June 1^{st} 1999. After that, data taking has been continuous for 6-9 months every year until the final shutdown on June 30^{th} 2010. After each major shutdown a new "Experiment" started. Hence the Belle data are grouped into experiments 7 to 73, where only odd numbers are used.[18] Experiments 7 - 27 are recorded using the first Silicon Vertex Detector (SVD1) and the rest with the second (SVD2) detector (see Section 2.2.1). There were two scheduled shutdowns every year, in summer and winter. The summer shutdown took about three months or more for maintenance and hardware replacements within the Belle detector as well as in the KEKB accelerator. The winter shutdowns were shorter, typically one month long. In the last three years of operation, the winter shutdowns were slightly extended due to budget constraints. Beside these shutdowns one day every two weeks was devoted to maintenance of the accelerator and detector. Typically after each experiment cosmic ray data was taken with the Belle solenoid turned off for the purpose of detector alignments. Belle took data mostly at the energy of the $\Upsilon(4S)$ resonance in order to study B meson decays. For the purpose of the background estimation arising from the non-B meson events the off-resonance data was collected 60 MeV below the resonance peak energy, for around 10% of the running time, approximately every two months. Similar off-resonance data taking was performed also for the data taken at other Υ resonances. Note that the *BABAR* off-resonance data taking was performed 40 MeV below the $\Upsilon(4S)$ mass, a difference which has no impact on the usage of this data.

[17] In the following the word "run" is used to identify a small data acquisition batch up to a few hours long, *i.e.* the basic unit of the *BABAR* and Belle data taking system, not to be confused with the "Run" defined here.

[18] For various reasons some experiment numbers are not used: experiment 29, 57 and 59.

The first Belle non-$\Upsilon(4S)$ data was taken at the energy of $\Upsilon(5S)$ resonance for 3 days in 2005. During the following year in the last week of February, $\Upsilon(3S)$ resonance data was taken to enable the search for invisible particles from decays of the $\Upsilon(1S)$ resonance. The last $\Upsilon(4S)$ resonance data was taken in June 2008. After that, $\Upsilon(1S)$ (second half of June 2008), $\Upsilon(2S)$ (December 2008 and November 2009) and $\Upsilon(5S)$ resonance data were taken, and energy scans between the $\Upsilon(4S)$ and $\Upsilon(6S)$ were carried out in the last two years of operation. The $\Upsilon(1S)$ The CM energy change was rather smoothly performed, keeping the same ratio of the beam energies in the KEKB rings. During that time, the magnetic fields of the Belle solenoid and super-conducting final focusing magnet were kept at the same values. The luminosity decreased at lower CM energies for reasons which have not been well understood. The beam background did not change by a large amount when running at different energies. The same was true for the trigger rates, where the increase of the cross-section at lower energy resonances was canceled by a lower luminosity. Looser trigger requirements were adopted for two charged track events in the case of the $\Upsilon(3S)$ data taking to achieve the physics goals of the $\Upsilon(3S)$ programme.

3.2.1 Integrated luminosity vs. time; luminosity counting

The integrated luminosity collected by Belle for each CM energy is listed in Table 3.2.1 and is calculated using Bhabha events, where the final state electrons are detected in the barrel part of the detector, and after removing runs deemed to be unusable for physics studies (so-called bad runs) because of detector-related issues. The Belle integrated luminosity as a function of time is shown in Fig 3.2.1. As well as the luminosity measurement, the counting of recorded $\Upsilon(nS)$ events is done using the method described in Section 3.6.2. The yields obtained are presented in Table 3.2.2.

The systematic error on the luminosity measurement is about 1.4% and the statistical error is usually small compared to the systematic error. The latter is dominated by the uncertainty of the Monte Carlo generator used to calculate the cross-section for Bhabha events. The $\Upsilon(4S)$ dataset is split into two periods, named SVD1 and SVD2, which correspond to different configurations of the Silicon Vertex Detector, as explained in the following section. All other resonance and scan data were taken in the SVD2 configuration.

Lees (2013i) describes the methods used to measure the *BABAR* time-integrated luminosities at the $\Upsilon(2S)$, $\Upsilon(3S)$, and $\Upsilon(4S)$ resonances, as well as in the continuum regions below each of these resonances. For each running period at fixed energy, the luminosity was computed offline, using Bhabha ($e^+e^- \to e^+e^-$) and dimuon ($e^+e^- \to \mu^+\mu^-$) events for Runs 1-6 and only Bhabha events for Run 7 – due to uncertainties in the large $\Upsilon \to \mu^+\mu^-$ background. No detailed analysis could be performed for the final scan data because of the short duration of the running at each scan point (only about 5 pb^{-1}). Therefore, the corresponding luminosity is only an estimation taken from (Aubert, 2009x). The systematic error on the luminosity measurement is about 0.5% for the data collected at the $\Upsilon(4S)$ and 0.6% (0.7%) for data collected at the $\Upsilon(3S)$ ($\Upsilon(2S)$). Table 3.2.1 and Fig. 3.2.2 show the luminosity integrated by *BABAR*, broken down by CM energy.

In addition to measuring the luminosity, the number of Υ particles in the different datasets is also computed using a common method referred to as 'B-counting' for the $\Upsilon(4S)$ running. This number is found by counting the hadronic events in the on-resonance dataset and subtracting the contribution coming from the continuum, estimated using off-resonance data and properly scaled to the peak energy – see Section 3.6.2 for details. The final results are shown in Table 3.2.2.

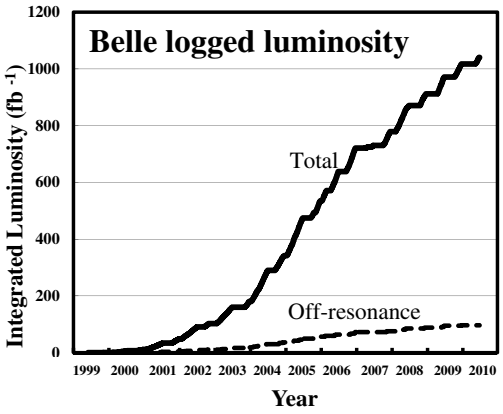

Figure 3.2.1. Evolution of the Belle integrated luminosity. A detailed breakdown of datasets is given in Table 3.2.1.

Table 3.2.2. Number of Υ particles in the different *BABAR* and Belle datasets

Experiment	Resonance	Υ number
BABAR	$\Upsilon(4S)$	$(471.0 \pm 2.8) \times 10^6$
	$\Upsilon(3S)$	$(121.3 \pm 1.2) \times 10^6$
	$\Upsilon(2S)$	$(98.3 \pm 0.9) \times 10^6$
Belle	$\Upsilon(5S)$	$(7.1 \pm 1.3) \times 10^6$
	$\Upsilon(4S)$ - SVD1	$(152 \pm 1) \times 10^6$
	$\Upsilon(4S)$ - SVD2	$(620 \pm 9) \times 10^6$
	$\Upsilon(3S)$	$(11 \pm 0.3) \times 10^6$
	$\Upsilon(2S)$	$(158 \pm 4) \times 10^6$
	$\Upsilon(1S)$	$(102 \pm 2) \times 10^6$

Table 3.2.1. Summary of the luminosity integrated by *BABAR* and Belle, broken down by CM energy.

Experiment	Resonance	On-resonance Luminosity (fb^{-1})	Off-resonance Luminosity (fb^{-1})
BABAR	$\Upsilon(4S)$	424.2	43.9
	$\Upsilon(3S)$	28.0	2.6
	$\Upsilon(2S)$	13.6	1.4
	Scan > $\Upsilon(4S)$	n/a	∼4
Belle	$\Upsilon(5S)$	121.4	1.7
	$\Upsilon(4S)$ - SVD1	140.0	15.6
	$\Upsilon(4S)$ - SVD2	571.0	73.8
	$\Upsilon(3S)$	2.9	0.2
	$\Upsilon(2S)$	24.9	1.7
	$\Upsilon(1S)$	5.7	1.8
	Scan > $\Upsilon(4S)$	n/a	27.6

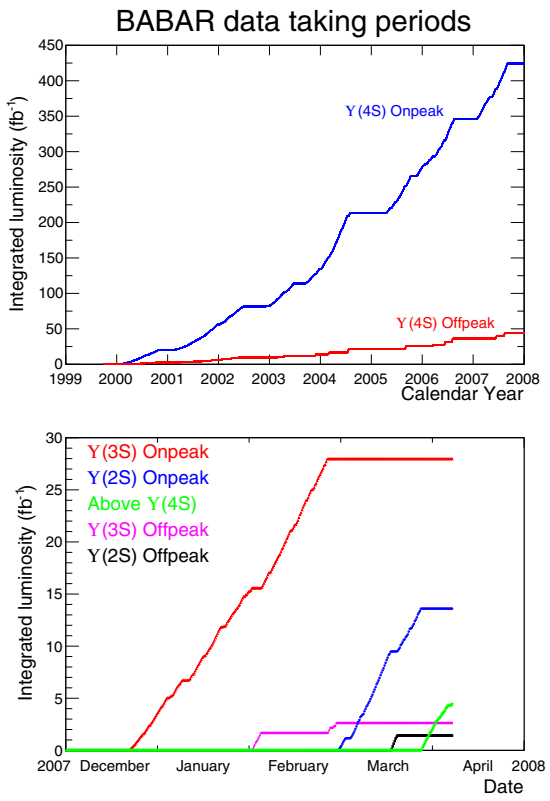

Figure 3.2.2. Evolution of the different *BABAR* datasets with time. The top plot shows the luminosity integrated during the $\Upsilon(4S)$ running periods, on-resonance (blue curve) and off-resonance (red curve) operation. The bottom plot focuses on the last *BABAR* running period (Run 7) which lasted less than four months and during which three different data taking phases occurred: $\Upsilon(3S)$ (red curve shows the on-resonance dataset; the purple one the off-resonance), $\Upsilon(2S)$ (blue curve for the on-resonance data, black for the off-resonance) and finally a scan between the $\Upsilon(4S)$ energy and 11.2 GeV (green curve).

3.2.2 Major hardware/online upgrades which modified the quality of BABAR data

This section summarizes the upgrades to the *BABAR* detector and also describes the 'trickle injection' mode which allowed PEP-II to keep the luminosity (and hence the detector data taking conditions) stable during most of the run. In the following, the 'forward' and 'backward' sides of the detector are defined relative to the high energy beam.

Detector upgrades

Over the years, the main *BABAR* activities during the shutdowns between Runs were related to the Instrumented Flux Return (IFR). Indeed, from the very beginning of the data taking, the resistive plate chambers (RPCs) showed severe aging all around the detector. Attempts were made to slow down the performance degradation but it became clear soon enough that the whole system needed an upgrade involving the replacement of most of the muon chambers. This project was completed with the following sequence:

- 12 forward RPCs were replaced between Run 1 and Run 2.
- The remaining forward RPCs were replaced between Runs 2 and 3. Brass was installed in the forward IFR to increase the total absorber thickness.
- The first two Limited Streamer Tube (LST) sextants were installed between Runs 4 and 5 and the last four between Runs 5 and 6.

Another important area of detector-related work was background mitigation and system upgrades, to cope with the instantaneous luminosity increase over the years – PEP-II exceeded its design luminosity goal by a factor four. These issues were addressed in various ways:

- Addition of shielding in various places around the detector (inside the PEP-II tunnel entrance on the backward side, in front of the IFR end-cap, etc.).
- Replacement of the Detector of Internally Reflected Cherenkov light (DIRC) and Drift Chamber (DCH)

front-end electronics to deal with the increase of the instantaneous luminosity over time.
– Online software developments (mainly for the Silicon Vertex Tracker (SVT), the DIRC and the EMC) to speed up the readout of the detector after a L1-accept and hence to be able to run at higher trigger rate while keeping the DAQ dead time low.

The trigger system also underwent upgrades, primarily the inclusion of 3D-tracking information in the L1 DCT trigger to remove background events in which scattered beam-gas particles would hit the beam pipe about 20 cm away from the IP. This new system was tested in parallel to the old one at the end of Run 4 and was used from Run 5 onwards. The IFR component of the trigger also had to be updated when RPCs were replaced by LSTs which had a different latency. Finally, as explained above, several changes were made to the trigger system (both to L1 and L3) in early 2008 during Run 7, as the characteristics of the events needed for the physics analysis during this period were completely different from those recorded at the $\Upsilon(4S)$ resonance.

Trickle injection

When *BABAR* started taking data, PEP-II was operating in fill-and-coast mode during which the injection and data taking periods were clearly separated. No attempt was made to inject the beams during a data taking run. Therefore, both currents (and consequently the instantaneous luminosity) were slowly decreasing over time. When they had dropped by about 30-50%, data taking was ended and the detector HV ramped down. Once *BABAR* was in a safe mode insensitive to the potentially-high injection backgrounds, the beams were replenished. Then, the HV were raised again and the DAQ restarted when they had reached their nominal values. The whole procedure (end of the actual run; *BABAR* transition from runnable to injectable states; beam injection; *BABAR* transition from injectable to runnable; beginning of a new run) would take around 5 minutes. The duration of each fill was adjusted depending on the machine conditions, in order to maximize the amount of integrated data. But the average luminosity delivered by PEP-II was only ∼70% of the peak luminosity.

A major improvement took place in 2004 when a new mode of operation called 'trickle injection' was introduced. The beam currents were kept constant thanks to a continuous injection of particles into the least filled bunches, without interrupting the data taking. The average luminosity immediately grew up by about 40% and the increase of the integrated luminosity was even larger than the gain directly provided by improving the duty cycle of the machine. Indeed, operating the accelerator near the peak luminosity at all times and with constant currents, allowed the PEP-II crew to improve the tuning of the beams and to reach new standards of performance and stability from which *BABAR* benefited as well.

The main challenge of this new running mode (first established with one beam, some months later with both) was to inject enough particles into the rings, while keeping the background levels low for *BABAR*. Quickly, it became clear that the newly-injected bunches were causing background bursts: events with many hits in all detector components were saturating the DAQ and causing high dead time. This background in phase with the injected bunch lasted up to a few thousands revolutions after the injection, until the excitations induced by the particles added to the bunch got damped. As it was possible to know exactly which bunches had been recently refilled and where they were located in the ring at any time (technically speaking, the *BABAR* clock was locked to the PEP-II timing system and markers were recorded for each injected bunch), the solution to this problem was to inhibit the trigger when one such bunch was close enough to the detector. These online vetoes were extended offline when the data were reconstructed, to make sure that the trickle injection background would not impact the physics. Indeed, no significant difference was ever found between events recorded just outside the trickle injection inhibit windows and those selected far away from any injected bunch. The trickle injection frequency was 5 Hz for the HER and 10 Hz for the LER, resulting in a dead time of 1.4% for the HER and 1.9% for the LER, 3.3% in total.

At the end of the commissioning phase which lasted a few months in total, the trickle injection mode became the default configuration for PEP-II. A constant and detailed monitoring, both on the detector and machine sides, allowed to operate the B Factory safely in these conditions until the end of the data taking, not only at the $\Upsilon(4S)$ resonance, but also from the $\Upsilon(2S)$ energy up to 11.2 GeV. The veto regions did not change over time and induced a dead time of ∼1% (∼0.5%) for the LER (HER) beam. As the HER and LER inhibit windows did not overlap due to the low injection frequencies, the total dead time was the sum of the two contributions, a small price to pay for the significant increase in integrated luminosity described above. As described in Section 2.2.7, the *BABAR* online system had to be significantly modified to follow this significant change of the machine operations: not only had the detector control system to allow injection during data taking, but the DAQ system also had to accommodate much longer periods of continuous data taking.

Summary

Both the detector improvements and the PEP-II trickle injection mode allowed *BABAR* to accumulate good data at a rate which increased over the years. More information about these different types of upgrades can be found in (Aubert, 2013).

3.2.3 Major hardware/online upgrades which modified the quality of Belle data

Detector upgrades

Belle encountered serious beam background in the beginning of the experiment. The radiation damage on the read-

out electronics chips of the silicon vertex detector (SVD1) was serious and the detector was replaced several times. Finally, the second type of silicon vertex detector (SVD2), which used so-called radiation hard electronics, was installed during the summer of 2003. At the same time, the inner part of the central drift chamber was also replaced with a compact small cell type drift chamber in order to make space for four instead of only three SVD layers. The diameter of the beam pipe was changed from 40 mm to 30 mm enabling the radius of the innermost SVD layer to be reduced to 20 mm in order to achieve a better vertex resolution; also the angular coverage of the silicon vertex detector was matched to that of other detectors ($17° \leq \theta \leq 150°$). This was the only major hardware change in the whole running period of the Belle detector and more information can be found in Chapter 2.

Other detector modules have been used without any major replacement. Unfortunately, the outermost two layers of the 14 resistive plate chambers used in the muon and K_L detector could not be operated due to the neutron background created by the radiative Bhabha events. However, the muon identification capability was not significantly affected. After the summer of 2003 the beam background was not so serious despite an increase of the luminosity to twice the design value.

Apart from the silicon vertex detector, the Belle data acquisition system used one type of multi-hit TDC module. The module did not have a pipe-line readout scheme. Therefore, the readout dead time was larger than at *BABAR*. Several efforts have been made in order to reduce the dead time. Finally, the readout modules were replaced gradually with a pipe-line TDC for most of the sub-detectors rather late in the running period.

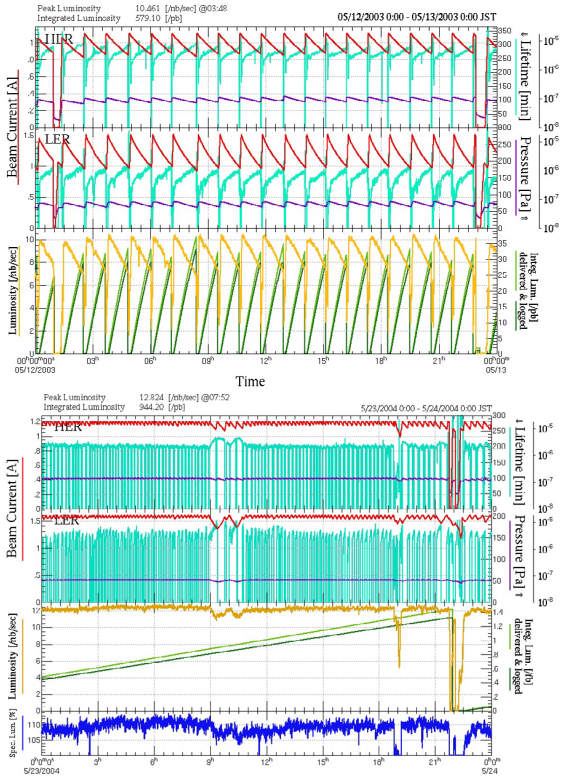

Figure 3.2.3. Comparison of beam currents and luminosity of KEKB before (top) and after (bottom) adoption of the continuous injection scheme. The top two panels of each plot show the electron and positron beam currents (red) and the third panel shows the luminosity (yellow). From (Abe et al., 2013).

Continuous injection and Crab cavities

Belle turned off the detector high voltage during beam injection as commonly done at other experiments. The injection time took slightly longer than at PEP-II causing a slightly lower average luminosity. In order to reduce such a time loss, a continuous injection scheme was adopted from January of 2004. The detector high voltage was kept on and the trigger signals were vetoed for 3.5 ms just after each beam injection. The scheme caused 3.5% dead time only in the case of a 10 Hz injection rate. After adopting continuous injection, the KEKB machine beams became stable and the peak luminosity was improved due to the constant beam currents. The obvious difference in the beam currents and luminosity before and after adoption of the continuous injection scheme is shown in Fig. 3.2.3 (Abe et al., 2013). The effect of the scheme can also be seen in Fig. 3.2.1 as an increased slope of the integrated luminosity after the beginning of 2004.

Another important upgrade of the beam optics took place in February 2007. At that time Crab cavities (Yamamoto et al., 2010) were introduced. These are RF deflectors providing the electron and positron bunches inside the KEKB accelerator rings, which at the interaction point have a crossing angle of 22 mrad, with a rotational kick in order to undergo a head-on collision. The schematic principle of the Crab cavities operation is shown in Fig. 3.2.4. The installation of the cavities into the KEKB was not without problems, as can be also observed by a short-lasting plateau at the beginning of 2007 in the integrated luminosity curve (Fig. 3.2.1). While the increase in the luminosity after the installation was modest, the beam induced backgrounds were reduced.

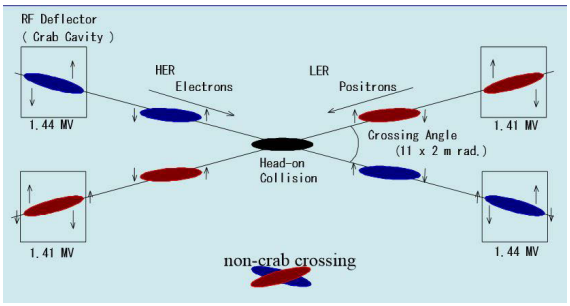

Figure 3.2.4. Schematic principle of Crab cavities operation leading to head-on collisions in KEKB despite the finite crossing-angle of electron and positron bunches.

3.3 Data Reconstruction

3.3.1 Introduction

Both *BABAR* and Belle developed tools to process raw data in a timely way. The reconstruction also provides another layer of data quality checks besides those performed in the control room by looking at strip charts and histograms filled during data collection.

3.3.2 The BABAR prompt reconstruction

3.3.2.1 Data processing

The *BABAR* data are processed in a two pass Prompt Reconstruction (PR) system. The raw data (XTC files) are read in each pass, once to compute time-dependent or detector specific calibration constants, and then again to fully reconstruct the data. The system is named Prompt since the calibration pass is done within a few hours of collecting data and the reconstruction pass is completed within 12 hours.

The first pass, the Prompt Calibration (PC) fully reconstructs a representative subset of the raw data. The actual percentage of data used depends on the number of events in the XTC file. The PC pass computes various calibration constants which are recorded in the Conditions Database (CDB). The CDB tracks information related to the detector systems and the beam conditions as a function of data-collecting time. Most calibrations are calculated for each run, but a subset of these calibrations needs information collected over multiple runs and were then called Rolling Calibrations. A separate database was used to collect inputs from each run for the Rolling Calibrations. When enough statistics were collected, or some other criteria met, a Rolling Calibration was performed. An example of this procedure is the determination of the beamspot rolling calibrations described in Section 6.4. The output of both single run and rolling calibrations are written to the CDB with a validity period corresponding to the span of runs used. A copy of the updated conditions database is made available for the full event reconstruction (the second PR pass), for more specific physics event selection (skimming) and for general data analysis.

The second pass, the Event Reconstruction (ER), reads the raw data from the XTC files, the conditions and calibrations from the CDB, and performs the full physics event reconstruction; track finding, vertexing, PID, etc. Interleaved with this processing are two stages of event-filtering. The first uses only L3 output-line information (Section 2.2.6) to reduce the contribution of events collected solely for diagnostic or detector-calibration purposes (*e.g.*, Bhabha events, used for EMC calibration, etc., are reduced by a factor of 15 beyond the factors already applied in L3). The second, which follows DCH-track and EMC-cluster reconstruction, tests events against about a dozen physics-motivated filters. One filter is highly efficient for $B\overline{B}$ final states, but much less efficient for some other processes. Hence additional filters address particular low-multiplicity states relevant to tau physics, two-photon physics, and so on. If an event satisfies any of these filters, or the earlier L3-based filter stage, it is saved. Reasons for saving it are recorded with the event.

The output of the ER pass, the reconstructed events, is written to data collections which are archived and then made accessible to the skimming system and to the analysts. *BABAR* originally used an object-oriented database technology (Objectivity/DB) to store both the conditions and the reconstructed events, but later switched to a file-based `Root` I/O system (`XRootD`), first migrating the data storage (2003) and then also the conditions database (2007).

3.3.2.2 Reprocessing

During the life of *BABAR*, as in any active experiment, the data reconstruction algorithms and the detector calibrations are constantly being improved. In order for the physics analysis to benefit from these improvements, it is necessary to reprocess the accumulated dataset, starting from the raw data. In *BABAR*, this reprocessing was done about once a year, in parallel with the prompt processing of the incoming data. The total throughput and resources needed for the reprocessing often exceeded the corresponding need for the current data. The allocation of resources needed to perform a reprocessing of the *BABAR* dataset was driven by several facts: first, the moment when a stable and improved reconstruction framework was available; then, the deadline by which to make the reprocessed data available for physics analysis, in order to prepare results for the next round of conferences; finally, the size of the particular dataset to reprocess.

The optimization of resources for the reprocessing is accomplished by breaking the conditions time-line into intervals and running separate instance of the two-pass processing system for each interval. The calibrations are computed within each separate interval and data run ranges corresponding to each interval can be processed in parallel. The reprocessed condition intervals are then merged into the Master CDB covering the whole time-line. The Master CDB is then used for accessing the current and reprocessed data.

A comprehensive bookkeeping system, based on a relational SQL database (Oracle or MYSQL), keeps track of all processing and reprocessing jobs indexed by run number. It records the date, time, software release and calibration used for that (re)processing of the data run, as well as status of the job (completed, failed, etc.) and other statistical quantities.

3.3.3 The Belle data reconstruction

3.3.3.1 Data processing

There are three major periods in the Belle data processing scheme, designed to cope with increasing event rate as well as to monitor data quality more reliably.

In the 1^{st} period from 1999 to 2003, raw data acquired in the Belle DAQ system are recorded to tape. Then, once a tape becomes full and is released from the drive, offline processing starts reading raw data to perform event reconstruction (Adachi, 2004). This method only allows one to monitor data quality with a delay of several hours since one has to wait for a tape release to trigger the processing. In this first processing step, detector calibration constants are not updated and are usually taken from the previous experimental period with some necessary extrapolations applied. If one needs to process a run immediately after it has finished, that is possible, but only by forcing a change of tape. The delay in having processed data is reduced for that run at a cost of adding an overall delay, corresponding to the tape change, for processing all data. The reconstructed data are written to tape as a data summary tape (DST). Then the next step called "skimming" is done by reading DST (see Section 3.5.3), where one creates datasets containing physics events such as Bhabha events, μ-pair events, and hadronic events on disk which can be accessed by users. Those physics datasets are used for checking detector response and producing calibration constants.

To improve the reconstruction chain, a computing cluster (PC farm) for a real-time reconstruction (RFARM) was introduced in 2003. Data sent by the DAQ system are received by the PC farm and reconstruction is done in parallel to the data acquisition (Itoh, 2005a). Output data are written in a hierarchy mass storage system (HSM) consisting of disks with a tape library as backend (Katayama, 2005). This upgrade enables Belle to obtain reconstructed events shortly after online data-taking, and precise data monitoring becomes much more reliable. The data quality assurance is one of the duties of persons on shift during the data taking. The skimming to select physics events is also carried out in the same way as before to provide calibration data for detector experts.

Following the initial success of the first RFARM system, the computing power in the RFARM doubled in order to be able to keep up with increasing luminosities in 2005. This configuration can process events at the highest KEKB luminosity without delay.

The Belle experiment employs a unique software framework `basf` (Belle AnalysiS Framework) and traditional data manipulation system with a `zlib` compression capability (`PANTHER`) throughout for all phases in event processing and this simple management was scalable using the processing scheme mentioned above (Adachi, 2004). The software has been widely used not only for event reconstruction, but for all physics analyses without any serious issues.

3.3.3.2 Reprocessing

Belle reprocesses all of the raw data once the detector calibration constants are obtained (Ronga, Adachi, and Katayama, 2004). Usually the first half of the annual data recorded from spring to summer is reprocessed to produce analysis datasets used to obtain new results to be presented in the summer conferences and the rest of raw data from autumn to winter is reprocessed for the winter conferences. The calibration constants used for reprocessing are computed by the detector experts using the physics events described above, once the experimental period (a couple of months) is completed, and another set of constants computed directly from data. Once constants for all detector elements are updated in the database (based on PostgreSQL) the reprocessing is carried out. In this step, output data are recorded in a compact form effectively used for physics analysis (mini-DST, MDST) on disk. Major physics analysis skims such as events containing J/ψ candidates from B decays are produced in an organized fashion to speed up individual analysis. More background-tolerant tracking algorithms (combination of Hough and conformal transformation) and improved calibration constants (polar angle dependent threshold for shower clusters in the ECL, new SVD alignment resulting in smaller Δz bias for several experiments - see Section 6) are developed using a large amount of data, making detailed studies of detector response possible. These new features are applied in a consistent way by reprocessing the raw data sample of $\sim 560\,\text{fb}^{-1}$ (experiment 31 to 55) taken with the SVD2 vertex detector (see Section 2.2.1), in the so called "grand reprocessing", and the data processing of later experiments. The "grand reprocessing" was started in July 2009 and completed (including the calibration part) by February 2010. Due to lack of time and manpower available, many shorter runs of the earlier part of the Belle data sample, taken with the SVD1 vertex detector, were not included in this effort. At the same time new sets of Monte Carlo events are simulated with up-to-date decay information to improve the understanding of the nature of background. All Belle final physics results are in principle obtained from datasets produced in the grand reprocessing.

3.4 Monte Carlo simulation production

3.4.1 Introduction

Several Monte Carlo event generators are used to simulate the final states of e^+e^- collisions. A final state is represented by a set of four-vectors originating from a common vertex near the e^+e^- interaction point or from the source of a particular background. Once produced, the four-vectors are passed by the software framework to the detector simulation where they are tracked in the detector, taking into account the interaction between the particles and the different materials, and the electronic signals which mimic the detector response are computed.

In the following sections the Monte Carlo simulation production at *BABAR* is described, followed by Section 3.4.5 detailing some differences in the approach taken by Belle.

3.4.2 Event generators

The generators depend on theoretical models of interactions to calculate the four-vectors. A combination of events from both signal and background generators is required in order to produce a simulated event stream realistic enough to be essentially indistinguishable from real data. A variety of generators makes this possible, as well as allowing individual sources of signal or background to be studied independently.

3.4.2.1 Signal generators

The production of hadronic events from the e^+e^- collision through the decay of the Upsilon resonances and the direct production of $u\overline{u}$, $d\overline{d}$, $s\overline{s}$ and $c\overline{c}$ pairs, is handled by the `EvtGen` (Lange, 2001) package and the `Jetset` generator, otherwise known as `Pythia` (Sjöstrand, 1995). Collision vertices are sampled from beam parameters in the PEP conditions database or ASCII files. These parameters include beam energies, boosts and spot sizes.

B decays, including CP-violating and other complex sequential decays are simulated using `EvtGen`. `EvtGen` is a framework in which new decay simulations can be added as modules. It uses decay amplitudes instead of probabilities for each node in the decay tree in order to simulate the entire decay chain, including all angular correlations. It also has detailed models for semileptonic decays and an interface to `Jetset` for the generation of continuum events ($u\overline{u}$, $d\overline{d}$, $s\overline{s}$ and $c\overline{c}$ production), and for generic hadronic decays including those of B mesons.

Lepton pair events were simulated with `KK2F` (Jadach, Ward, and Was, 2000), which is a high precision electroweak Standard Model generator for $e^+e^- \to \tau^+\tau^-$ and $e^+e^- \to \mu^+\mu^-$ events, amongst others. It takes into account QED radiative corrections (up to second order), including hard bremsstrahlung. When τ pair events are produced, the τ decays are handled by the `TAUOLA` generator (Davidson, Nanava, Przedzinski, Richter-Was, and Was, 2012).

`AfkQed` (Czyz and Kühn, 2001) was used to generate hard photons from initial and final state radiation using lowest-order QED calculations. Other generators used included `Gamgam`, which produces exclusive 2-photon decays of B^0's, `Diag36` (Berends, Daverveldt, and Kleiss, 1986), which generates 4-lepton final states, and `SingleParticle`, which generates one particle per event, using user-specified parameters.

To compute the PEP luminosity and the Bhabha scattering cross section `BHWIDE` (Jadach, Placzek, and Ward, 1997), a wide-angle Bhabha generator which has a theoretical accuracy of 0.5%, and `BHLUMI` (Jadach, Placzek, Richter-Was, Ward, and Was, 1997), a small-angle Bhabha generator, were used.

3.4.2.2 Background generators

In real data, several background processes contribute to events and mimic (or hide) real signals. Some of these backgrounds may be removed during the data analysis, while others may not. In either case, it is necessary to simulate them in order to aid background subtraction or to mix them with the simulated signal. These backgrounds include Bhabha scattering, bremsstrahlung, QED background, initial state radiation, machine background, and cosmic rays.

Luminosity backgrounds from electrons or positrons striking the beamline or other machine elements outside the nominal detector acceptance, were simulated using `BHWIDE` and `BHLUMI` .

Lepton pair and two-photon events from QED background were generated by `Bkqed` (Berends and Kleiss, 1981) which also includes effects from radiative photons.

Machine backgrounds due to electrons and positrons striking apertures and photons from Compton scattering and bremsstrahlung from beam gas are simulated by `TurtleRead` (Barlow et al., 2005) which reads ASCII files written by the `Decay Turtle` ray-tracing program.

Cosmic ray muons were another source of background triggers for *BABAR*. To estimate this, the `HemiCosm` code shot muons inward from the upper hemisphere surrounding the volume of the simulated detector. The muons were sampled from the usual zenith angle distribution and one of three available momentum spectra.

All these background generators where mostly used during the design and construction phase of the *BABAR* detector. After the start of the data-taking the effect of the different backgrounds processes, including machine background and background hits from the detector electronic noise, was simulated by superimposing recorded random triggers to the signal events.

3.4.3 Detector Simulation

The purpose of the *BABAR* detector simulation is to take four-vectors from the generator stage and transport them through the detector geometry, where energy loss, production of secondaries, multiple scattering and decays can occur. As these particles pass through sensitive regions of the detector, their energy, charge and angle information is collected in order to generate raw, idealized hits, which consist of positions and energy deposits in the detector. These quantities are stored in persistent containers in the database for later use in the simulation of the detector response where idealized information is converted to realistic detector hits, blended with background data, and digitized. The resulting realistic hits are then passed to the reconstruction code where the full simulated event is built for later comparison with real events.

3.4.3.1 `Bogus`, `SimApp`, and `GEANT4`

The software package which handled the generation of the raw hits on *BABAR* is called `Bogus`. It was an application layer built on top of the `GEANT4` simulation toolkit (Agostinelli et al., 2003) and was designed to model the

BABAR detector geometry and materials, propagate particles through a varying magnetic field, perform particle interactions and decays, and provide scoring of detector hits.

`Bogus` was integrated into the *BABAR* software framework and designed to be fully compatible with its event scheme, allowing Monte-Carlo truth information to be added to the simulated *BABAR* event. The code which accomplished this, `BfmModule`, initialized the `GEANT4` kernel, extracted event generator tracks from the framework event, invoked `GEANT4` to propagate these tracks through the detector and wrote the propagated tracks and produced secondaries into the event framework.

This event was then passed to `SimApp`, the package responsible for simulating the detector response. Beginning with hits from `Bogus`, it converted them to digitizations which mimicked the real electronic output of the detector, that is, the ADC and TDC words. These were then mixed with corresponding digitizations from background frames obtained from random triggers recorded by the data acquisition.

Trigger conditions corresponding to a particular month of data-taking (see Section 3.4.4) were finally applied to the full event which was then sent to the reconstruction.

3.4.3.2 Physics and transport processes

The physics of the initial e^+e^- collisions and the decays of short-lived hadrons were handled by the event generators discussed above. All other physics processes, including K_s and Λ decays, and π and K decays in flight, were supplied by `GEANT4`. In terms of shower development in the detector, by far the most important are the standard electromagnetic processes of multiple scattering, ionization, bremsstrahlung, pair production, Compton scattering and photoelectric effect. These processes are sufficient to describe accurately the energy distribution in the EMC. Hadronic processes, though less frequent, are important for the propagation of hadrons produced in the initial interaction and the hadronic secondaries they in turn produce. The processes used included elastic scattering and capture, as implemented by the `GEANT4` version of the `Gheisha` hadronic code (Fesefeldt, 1985), and inelastic scattering as implemented by the `GEANT4` version of the Bertini cascade (Bertini and Guthrie, 1971). The latter was especially useful for a reasonable propagation of kaons from B decays.

The decay of long-lived particles was also handled by `GEANT4`, which used PDG (Beringer et al., 2012) branching ratios to determine the final state of the decays.

The default particle transport code in `GEANT4` is a Runge-Kutta stepper, but for *BABAR* this was deemed too slow. It was replaced by a specialized helical stepper which took advantage of the near-uniform *BABAR* magnetic field by taking large steps and using exact calculations of the intersection of helical tracks and volume boundaries.

3.4.4 MC production systems

Quite early in the history of the *BABAR* experiment, the simulation production used computing resources coming from over 17 production sites across the globe. Such distributed production was possible because the only data that needed to be available at the production sites were the background event collections and the conditions. Moreover, a missing production due to failed jobs was simply replaced with a new production of the same decay mode, but with different random number generation seeds. All this resulted in simple production management tools that were easy to install at production sites.

In *BABAR*, simulation production is done on a 'per month' basis, using background frames and conditions and calibrations corresponding to a specific month of data taking. Conditions and calibrations are read from the MySQL conditions database and were previously computed during the prompt calibration pass of the reconstruction of raw data or with a special offline analysis of the raw data for those conditions that require data samples larger than a single run.

The production is carried out in cycles corresponding to major updates in the simulation or reconstruction code. In all cycles, the number of Monte Carlo events was much larger than the number of events collected by *BABAR*. In the final cycle, the number of $b\bar{b}$ and $c\bar{c}$ events corresponded to a luminosity ten times higher than the luminosity of the detector data and to a luminosity three times higher for continuum events.

Unlike the detector data, the simulated data are automatically marked 'good' in the bookkeeping database.

Before simulation production at a site can start, a test production must be run and compared to the exact same production performed at SLAC. This tests the release installation, the accuracy of the conditions exported to the site, and the availability of the background collections. Recently, most of the major simulation productions have been done off-site while specialized productions were mostly done at SLAC (for maximum control). However, having multiple sites has been very useful when several varieties of production needed to be done at the same time.

All the Monte Carlo event collections are imported at SLAC and stored in a High Performance Storage System (HPSS, a large tape storage robot). From SLAC, they are exported to the remote sites according to the requests of the Analysis Working Groups (AWGs) that are doing their analysis at that site.

Currently, simulation production remains distributed although an eventual collapse back onto SLAC is foreseen.

3.4.5 Differences between BABAR and Belle simulations

Rather than implement stand-alone programs for event generation and simulation in Belle, these codes were integrated into the `basf` as user modules. In this way, a user could run an entire Monte Carlo production sequence — generation, simulation, reconstruction, skimming, and

analysis — in one basf job and therefore is able to take advantage of the parallel-processing of events built into basf if desired.

In practice, event generation in Belle was done in single-processing mode to avoid inadvertent repetition or overlap of random number sequences. The output files from this generation step were fed to the subsequent parallel-processing job for simulation and analysis (generated events were processed by several processors, one event at a time by each processor).

3.4.5.1 Generators

In addition to EvtGen (Lange, 2001), Belle used the qq98 (CLEO, 1996) event generator in the early years for B decays. Other generators used by Belle included CTOY (written for Belle based on the HemiCosm code) for cosmic ray muons, SG for single tracks (including cosmic rays), BHLUMI (Jadach, Placzek, Richter-Was, Ward, and Was, 1997) for lepton pairs (with TAUOLA (Davidson, Nanava, Przedzinski, Richter-Was, and Was, 2012) for subsequent τ decays), KK (Jadach, Ward, and Was, 2000) for fermion pairs, and AAFH (Berends, Daverveldt, and Kleiss, 1986) for two-photon production of fermion pairs.

3.4.5.2 Detector simulation

Belle used the Fortran-based GEANT3 (Brun, Bruyant, Maire, McPherson, and Zanarini, 1987) toolkit for detector simulation (this was the dominant motivation for Belle's continued support of Fortran, alongside C++, in its software library). C++ wrappers were incorporated around the GEANT3 toolkit to embed it within the basf. GEANT3 was supplemented with a Cherenkov-light simulation (written in C++) to model light propagation within the Aerogel Cherenkov Counters (ACC). Four-vectors of the generated particles in an event were passed to GEANT3, which then pass them through the model of the Belle geometry and generate hits in the sensitive elements. Decays of long-lived particles such as K_S^0 mesons were handled by GEANT3. The simulation accounted for the evolution of the real detector's behavior (dead or hot channels, efficiency changes, geometry changes, and trigger-parameter tuning) via information tabulated in the master database by experiment and run number. Through user hooks provided in GEANT3, these hits were digitized (simulated ADC, TDC and latch responses) tailored to the detector element so that the output data stream would mimic the appearance of the real data, supplemented with the additional "truth" information from the simulation. At the conclusion of the simulation of each event, additional hits from real background events (recorded with a random trigger and filtered to avoid any events with reconstructed tracks or clusters) were superimposed on the event to mimic the background activity in each detector element. The method developed consists of overlaying a random-triggered real beam background event to a simulated signal event. The random-triggered event is taken during a beam run with a typical rate of 1-2 Hz. The beam background file, the collection of the random-triggered events, is created for each run. The beam background overlay procedure is applied to the output after the detector simulation. Thanks to this method, the run-dependent beam background effects can be reproduced in the simulation. However, because this overlay process is done after the digitization step, it is not possible to consider a pile-up effect of electric charge before the digitization. A data file containing these background events was recorded for each run. Background events were selected at random from the files for a given Experiment when simulating Monte Carlo data early on within Belle. Later in the life of the experiment background events were selected sequentially from the corresponding background file for a given run.

3.4.5.3 Geometry

The detailed Belle detector geometry was modeled for GEANT3 in a manner similar to that of *BABAR* for GEANT4. The magnetic field in Belle's interior was obtained from a tabulated map of the field's radial and axial components that extended from the beamlines to the yoke's exterior surface; this field was used by GEANT3 for charged particle propagation. No uniform-field approximations were made in the Belle simulation.

3.4.5.4 Physics and transport processes

Propagation, decay and interactions of all particles except the Cherenkov photons in the ACC were handled by the GEANT3 toolkit. Also for the most demanding part, the Belle electromagnetic-calorimeter (ECL) simulation, no fast (*i.e.*, parametric) simulations were used. The Fluka (Fasso, Ferrari, Ranft, and Sala, 1993) code embedded in GEANT3 was used to simulate hadronic interactions.

3.4.5.5 Post-simulation track extrapolation

In the analysis phase of each event, whether simulated or real, Belle utilized the GEANT track-extrapolation package distributed with GEANT3 to extrapolate each reconstructed charged track from the outer surface of the Central Drift Chamber (CDC) through the outer detectors; ACC, Time-of-Flight (TOF), ECL, and K_L^0 and μ detector (KLM). This proved quite useful in matching tracks to hits in these outer detectors.

3.4.5.6 MC production systems on Belle

Generation, simulation, and reconstruction of $e^+e^- \to \tau^+\tau^-(\gamma)$ was done for the most part at Nagoya University and the output data files were stored there.

Monte Carlo production of generic $B\overline{B}$ decays, continuum ($e^+e^- \to q\overline{q}$) processes, and other specific signal

processes were handled by KEK and the other institutions with significant computing resources. Grid computing became available for Belle's use fairly late in its lifetime and therefore did not play a significant role in Monte Carlo production. In Belle, the Monte Carlo Production Manager utilized a web-based production scheme that harnessed the CPU and storage capabilities at the remote institutions; the grid was treated as one of these 22 remote sites.

Each production cycle was defined by a set of experiments (and all of the real-data runs within each experiment) and the Belle software library that had been used to process the real data therein. Ten times the real integrated luminosity in $b\bar{b}$ events and six times that in continuum events (with $c\bar{c}$ handled separately from the lighter quarks) were produced in each MC production cycle. For data samples taken at energies other than $\Upsilon(4S)$ six times the accumulated luminosity in the data were simulated.

The Production Manager would first coordinate with each of the Site Managers to ensure that the remote site had the proper Belle software library installed and operating properly; this was done by exercising the remote library via several test jobs and then comparing several thousand output histograms with the reference histograms at KEK. The Site Manager at each validated site was then permitted to request the simulation of a sequence of experiments and runs via the web interface, upon which the KEK-generated event files and the corresponding background-event files were delivered to the remote site for MC production. Each job's simulated, reconstructed, analyzed and filtered outputs were delivered to KEK and tracked by the Site Manager, who was responsible for restarting any failed jobs. Each output file was read back in entirety upon delivery to KEK to verify its integrity. Once all jobs in the requested sequence were completed and delivered successfully, the Site Manager would record this via the web interface. On rare occasions when a site fell behind significantly in its commitment to deliver the requested sequence, the Production Manager would consult with the other Site Managers and then transfer the sequence to another site with spare capacity. KEK produced about half of Belle's generic-MC events; the other institutions produced the remainder (see Fig. 3.4.1).

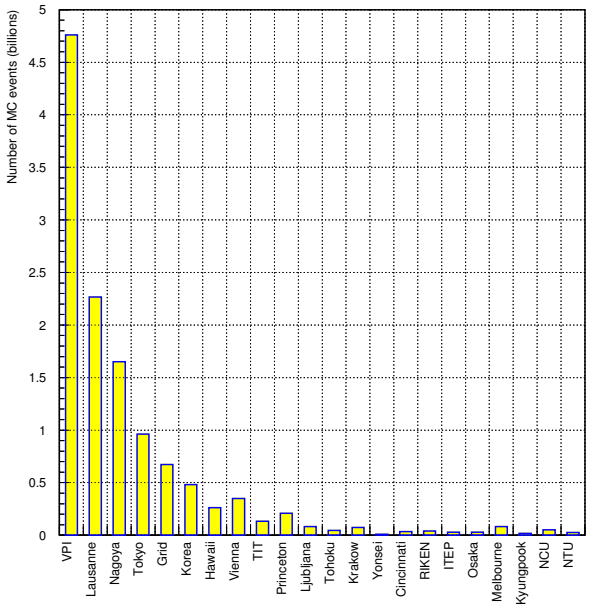

Figure 3.4.1. Generic MC production in Belle at remote sites (circa 2008).

3.5 Event skimming

3.5.1 Introduction: purpose of event skimming

The amount of detector and Monte Carlo data is such that it would be highly inefficient to have all analysts reading the full data sample. The identified solution was to centrally run an extra production step, the skimming, where events passing different sets of physics-motivated criteria were written to separate streams, the skims.

Each skim was optimized for a group of analyses using common sets of selected events as input. The fact that some analyses reached completion and new analyses started, resulted in skim definitions that were changing with time, new skims being added to production while others became obsolete and were removed. The two experiments adopted different skimming philosophies, *BABAR* introduced a large number of skims specific to analysis topics, whereas Belle had a limited number of skims strongly related to the selection of events produced in a type of process. The *BABAR* methodology is described below, and is followed by a more detailed description of the Belle skims as an illustration of how one can identify events of a given type.

3.5.2 Skimming in BABAR

BABAR analysis effort is organized into AWGs and each AWG is assigned to a particular site for the bulk of their analysis work. The skims relevant to a specific AWG are exported to the site of the AWG.

Events are organized into lists referred to as 'collections'. Events from the full reconstruction steps go into the 'AllEvent' collections. The outputs of the skimming step consist of the 'AllEventSkim' collections (with all the events that passed the skimming step) and of a set of collections for each skim. Skims can either be a full copy of the selected events (deep copy skims) or pointers to the events in the 'AllEventSkim' collections (pointer skims). The choice of the type of skims used depends on the fraction of selected events, on the need for detailed detector data, and on the availability of the 'AllEventSkim' collections at the AWG site.

Skim production was done in Skim Cycles and a couple of cycles had more than 200 output streams. Each 'AllEvents' collection, corresponding to a single run, was bro-

ken into pieces and each piece was skimmed. The output streams coming from the pieces of the same 'AllEvents' collection are then merged. Finally, in order to create skimmed collections with a reasonable number of events, streams coming from different AllEvents collections were merged.

Only the 'AllEvents' collections declared 'good' by the 'Data Quality Group' (see Section 3.6) were used as input for the skimming procedure. All the skim jobs must have been completed and the output streams merged successfully to declare the skimming of several AllEvents collections which are part of the same skimming job as good. To have an efficient skimming production, monitoring, job crash recovery, disk clean up, and efficient data distribution are all critical elements. A set of software tools was developed to make this production possible.

As mentioned above, the level of analysis pre-selection that is available in skimming depends on the AWG requirements. To illustrate this one can consider the example a number of different Charmless B decays to four-particle final states (where each particle is one of the following: $\pi^{\pm}$, $K^{\pm}$, π^0, K^0_S) which are studied within the so-called Quasi-Two-Body AWG within *BABAR*. A set of skims associated with these final states was developed by members of that working group to isolate B decays of particular interest. While each of the possible final states is topologically similar, and in turn the analysis strategies for these decays are similar, there are different requirements placed on different channels. Hence analyses would use dedicated skims for a given combination of topology and final state. The decay $B^0 \to \rho^+\rho^-$ has two charged and two neutral pions in the final state. This used the 'BFourHHPP' skim variant, where H denotes a charged hadron (without any PID constraints imposed), while P denotes a neutral pion decaying into two photons. Similarly the decays to the four charged track final states $B^0 \to \rho^0\rho^0$ and $B^0 \to K^*K^*$ (with subsequent $K^* \to K\pi$ decay) used the 'BFourHHHH' skim. In this way each of these skims can be used to study a number of similar final states minimizing the time required by the data analyst to process the data. The ensemble of similar four body skims was also made available as the 'BFourBody' skim. This skim methodology is applied across the *BABAR* AWG system, where some skims are specific to the analysis of a given decay, while others are usable for a set of similar decays.

3.5.3 Skimming in Belle

After data processing, events taken by Belle are classified into several categories. Some of the categories such as Bhabha events, muon pair events and γ pair events are used for detector calibration, while the following three categories are used for physics analyses:

1. a skim for hadronic events, called *HadronBJ*, which is mainly used for analyses of B and charm mesons,
2. a skim for τ-pair events, called *TauSkim*, which is mainly used for analyses of τ leptons, and
3. a skim for low multiplicity events, called *LowMult*, which is mainly used for two photon analyses

Further skims that contain smaller categories of physics events are made from these three basic skims and provided to individual analyses, so that users usually do not need to run over a huge number of events in the basic skim. Details of the second stage skim are described in the section of each analysis. Classification conditions for the three basic skims are described in the rest of this subsection.

Hadronic event skim:

HadronBJ events are selected primarily based on track multiplicity and visible energy: the event must have at least three charged tracks with a transverse momentum greater than 0.1 GeV/c that originate from the vicinity of interaction point ($|\Delta r| < 2\,\text{cm}$ and $|\Delta z| < 4\,\text{cm}$), and the sum of the energy of charged tracks and reconstructed photons (E^*_{vis}) must be greater than 20% of $\sqrt{s}$. Note that all observables denoted by an asterix are measured in the CM frame.

These two selection criteria remove the majority of beam gas background and two-photon events. Beam gas background is further reduced by requiring the primary vertex position of the event, when the vertex is well-reconstructed, to be $|\Delta r| \leq 3.5\,\text{cm}$ and $|\Delta z| \leq 1.5\,\text{cm}$. Background events from radiative Bhabha and higher multiplicity QED processes are suppressed by requiring that two or more ECL clusters are detected at large angle ($-0.7 < \cos\theta^* < 0.9$), the average ECL cluster energy below 1 GeV, and the total ECL cluster energy (E^*_{sum}) to be below 80% of $\sqrt{s}$. E^*_{sum} is also required to be greater than 18% of $\sqrt{s}$ since there are τ-pair, beam gas and two photon events that have low energy sum. However, this condition is rather tight for light quark pair production events ($e^+e^- \to q\,\overline{q}$ with $q = u, d, s, c$), and hence a conditional selection is applied: $E^*_{sum} > 0.18\sqrt{s}$ or $HJM > 1.8\ \text{GeV}/c^2$, where HJM stands for heavy jet mass, which is the invariant mass of particles found in hemispheres perpendicular to the event thrust axis. The HJM is the most effective variable to remove τ-pair events, and it is required to exceed 25% of E^*_{vis}. However, in order to regain $q\overline{q}$ events, a conditional selection is required: $HJM/E^*_{vis} > 0.25$ or $HJM > 1.8\ \text{GeV}/c^2$. These general conditions to select hadronic events turned out not to be very efficient for inclusive ψ events. Therefore, the events with J/ψ and $\psi(2S)$ candidates are explicitly added to *HadronBJ*.

Tau pair events: TauSkim

Signatures of the τ-pair production, $e^+e^- \to \tau^+\tau^-(\gamma)$, are low-multiplicity and missing-momentum. Since at least two-neutrinos are missing in τ-pair events, tight kinematic constraints can not be applied. So *TauSkim* is designed to reduce well defined Bhabha, $q\overline{q}/B\overline{B}$, two-photon and beam-gas background.

TauSkim events are selected primarily based on track multiplicity and the position of the event vertex: the number of charged tracks in an event must be at least two

and less than 8, where each track must have a transverse momentum greater than 0.1 GeV/c and originate from the vicinity of the interaction point ($|\Delta r| < 2\,\text{cm}$ and $|\Delta z| < 5\,\text{cm}$). The net charge of the event Q must be $|Q| \leq 2$. Beam gas background is reduced by requiring the primary vertex position of the event to be $|\Delta r_{\text{v}}| \leq 1.0\,\text{cm}$ and $|\Delta z_{\text{v}}| \leq 3.0\,\text{cm}$.

Background from (radiative) Bhabha events is suppressed by requiring the sum of ECL clusters in CM (E^*_{sum}) to be below 11 GeV, and the polar angle of the missing momentum in the CM frame to be between 5° and 175° for two track events.

Background from two-photon events is reduced by requiring the maximum of the transverse momentum of the charged tracks ($P_t^{\max}$) to be greater than $0.5\,\text{GeV}/c$ and the sum of the visible energy E^*_{vis} greater than 3 GeV, where E^*_{vis} is the sum of the absolute momentum of charged tracks multiplied by c and the photon-cluster energies in the CM: the photon cluster is the ECL cluster to which no charged tracks are associated. Even if E^*_{vis} is less than 3 GeV, the events are accepted if $P_t^{\max} > 1.0\,\text{GeV}/c$.

In order to further reduce the (radiative) Bhabha events, events with 2-4 charged tracks are rejected if the total energy E^*_{tot} is greater than 9 GeV and the number of clusters in the barrel region ($30° < \theta^* < 130°$) is less than two, where E^*_{tot} is the sum of of the visible energy and the absolute value of the missing momentum ($E^*_{tot} = E^*_{vis} + c|p^*_{miss}|$). This condition reduces (radiative) Bhabha events where one electron or positron is detected in the Barrel calorimeter, but the energies of the other electron or photons are not measured correctly either by starting to shower in the tracking volume or missing energy from the shower in the gap between the barrel and end cap of the calorimeter.

With these selection criteria, about 80% of tau-pair events are kept while Bhabha and two-photon events are reduced to an acceptable level. If the events are passed by both the *TauSkim* and *HadronBJ* conditions, the events are kept in *HadronBJ*, while the remaining ones are kept in *TauSkim*. As a result both *HadronBJ* and *TauSkim* events are processed in physics analyses using the *TauSkim* sample.

The low-multiplicity skim

The low-multiplicity (LowMult) skimming of Belle data processing provides event-data collections mainly for analyses of zero-tag two-photon processes with an exclusive final-state system, $\gamma\gamma \to X$, including charged tracks in the final state (see Chapter 22 for the description of two-photon processes). The charged multiplicity of the target events is required to be two or four because of charge conservation, and the total visible energy is expected to be much smaller than the energy of the e^+e^- collision.

The minimum requirement of the transverse momentum p_t for charged tracks in two track events is chosen to be 0.3 GeV/c. Tracks must originate from the vicinity of the interaction point, which is $|\Delta r| < 1\,\text{cm}$ and $|\Delta z| < 5\,\text{cm}$. For the four track events the additional two tracks are required to satisfy looser selection criteria, $p_t > 0.1$ GeV/c, $|\Delta r| < 5\,\text{cm}$ and $|\Delta z| < 5\,\text{cm}$. For the four-track events, a looser constraint for the impact parameter of tracks is adopted to collect the $K^0_S K^0_S$ final-state events.

Only events with smaller visible energy, with the sum of absolute momentum of tracks $\Sigma|p| < 6$ GeV/c and the sum of calorimeter cluster energies $E^*_{sum} < 6$ GeV, are collected, thus rejecting QED backgrounds with the full energy of beam collision deposited in the detector.

A further requirement on the missing-mass squared $MM^2 > 2\,\text{GeV}^2/c^4$ is imposed to reject radiative events such as $\mu\mu\gamma$ where the photon travels in the forward direction and remains undetected. Any constraints originating from the trigger or particle-identification are not included in the requirements, in order to avoid introducing systematic uncertainties on the skimming efficiency from these sources.

In two photon events an approximate transverse-momentum (p_t) balance is expected. This was used in skimming of events with two charged tracks, applying loose selection on p_t balance (where in the calculation of p_t one also takes into account the calorimeter energy deposits for any number of γ or π^0 candidates).

In addition, to salvage physics events where a track is mis-reconstructed or originates from noise (or from secondary interactions), a sub-category of events is skimmed using a condition on the visible energy $E^*_{vis} < 4$ GeV, when the event has at least two tracks. Processes with six tracks, such as D^+D^- production, can be explored in this sub-category, although the skimmed data must be used together with the TauSkim and/or HadronBJ skims to recuperate events with the visible energy exceeding the above condition.

3.6 Data quality and B counting

3.6.1 The control of data quality

Data quality control is crucial at each step of the data acquisition, from the initial readout of the detector following a positive trigger, to the final physics analysis. Therefore, *BABAR* and Belle have defined detailed procedures to validate each step of the data processing and to identify as quickly as possible any new hardware or software problem. These prescriptions have evolved over the years while the experiments were gaining experience. In the following, we will mainly focus on the final versions of the data quality procedures which were in use at the end of the data taking.

3.6.1.1 Online data quality control in *BABAR*

The first level of data quality control is done in the control room. The shift crew relies on information from the slow control monitoring and DAQ systems to make sure that the detector is taking good data in a smooth way. Should an unexpected event occur, the diagnostics of the situation

and the following actions are guided by well-established recovery procedures. If needed, the shift crew can also seek help by contacting a team of on-call experts – at least one per critical system of the experiment.

In *BABAR*, the standard shift crew was made of two people: the 'pilot', in charge of controlling the flow of the main data acquisition elements, and the 'Data Quality Manager' (DQM), whose main task was to check monitoring plots continuously. These histograms, classified by subsystem (SVT, DCH, etc.), accumulated data in real time during a run (usually about an hour long, unless a beam abort or some hardware problem ended it prematurely). About 15-20% of the events accepted by the L1 (hardware) trigger level were used for this fast monitoring. Most histograms could be directly compared with reference ones, automatically selected by the control system depending on the data taking conditions (colliding beams, single beam or cosmic events). Detailed guidance was also provided by each *BABAR* system to help the shift crew assess the quality of the runs. Therefore, it was very easy to spot a change in the behavior of a given hardware component (readout section with an occupancy unusually low or high, noisy channels, etc.) and to react appropriately. This information, combined with the detector status provided by the slow monitoring system (high voltage, low voltage, gas flow, temperature, etc.), allowed the shift crew to flag each run after it had ended. Flags assigned at the subsystem level included 'good', 'bad', 'unknown', and 'flawed'. The first three have obvious meanings while the fourth one was used to mark data in which the quality was not perfect, but would be worth processing for offline checks by experts. The global run flag was the worst among the subsystem flags: for instance, one subsystem flagged 'flawed' while the other ones got the mark 'good' would result with the run being assigned 'flawed' as global flag. Shift crews had two hours to flag a run after its end. This delay gave shifters the opportunity to get expert advice when needed. To avoid PC processing delays, it was crucial to give the right flag to each run in a timely manner as only colliding beam runs with 'good' or 'flawed' flag were automatically processed. Runs initially marked 'bad' and re-qualified as 'good' later could only be processed during the next round of reprocessing; in the meantime, their data were unavailable.

Most of the raw data that was marked 'bad' suffered from hardware failure. Although such a failure may have occurred in the final part of a run, all its data were potentially lost as the entire run would not be processed. In the worst case, up to an hour of *BABAR* data would be declared unusable, even if the failure occurred only in the last few seconds of data taking. Therefore, a software tool was developed during the final reprocessing to truncate these problematic runs and recover some good data. This procedure was conceptually simple, but involved significant bookkeeping subtleties. Ultimately, this tool added about $1\,\mathrm{fb}^{-1}$ to the final $\Upsilon(4S)$ dataset.

3.6.1.2 Control of the data processing quality in *BABAR*

Data processing procedures could be subject to various problems, even when working with raw data designated as 'good'. To handle such complexities, this stage required dedicated quality assurance (QA) procedures which had to be (re)done for a given run each time it was (re)processed. Only runs that were declared good after data processing were included in the datasets used for physics analysis.

The two steps of the *BABAR* processing (PC and ER) generated a large number of `Root` histograms. The Data Quality Group (DQG), led by an experienced *BABAR* member, analyzed the primary histograms produced by the processing, and was responsible for the quality control of data produced by the experiment. This group also checked the consistency of the skimmed data, and validated software releases used to generate Monte-Carlo events. The DQG met weekly at SLAC – to facilitate face-to-face collaboration between the online and offline teams – to assess the quality of the runs processed in the past week. Experts (one per subsystem) used logbook entries and QA histograms to flag each processed run. They could also look at stripcharts showing the run-by-run evolution of key QA quantities (both at the detector level and after the event reconstruction) versus time. These were very useful to help identify trends which could indicate a developing problem. The processing classification was similar to the one used for online data: a run could be declared 'good', 'flawed' (meaning worth reprocessing, either immediately or after some further data correction) or 'bad'. This global flag, with optional related comments, was added to a database which kept track of all these checks and ensured that at most a single processing of a given run was used by analysts. Selecting good runs was of course a key task for the DQG group; but experts were also working hard to distinguish runs which were bad for well-identified and permanent reasons from those which might be later reprocessed successfully. To give an idea of the amount of work performed by the DQG, one can note that the whole *BABAR* dataset ($\Upsilon(4S)$, $\Upsilon(2S)$, $\Upsilon(3S)$ and the final energy scan) contains more than 35,000 physics runs in total. Only the common and constant efforts of both the operations and computing teams allowed *BABAR* to log 95% of the luminosity delivered by PEP-II and to give the analysts 99% of this dataset for physics. Indeed, a few fb^{-1} of data were recovered during the final reprocessing of the $\Upsilon(4S)$ dataset in 2008.

3.6.1.3 Data quality monitoring in Belle

The monitoring of data quality was done in two levels at Belle. The first was the real time monitoring of detector signals based on sampled level 1 triggered events, which is called the Data Quality Monitor (DQM). The data of 10-20% of triggered events were sampled at the event builder and sent to the monitor PCs. The data were analyzed to examine the detailed operating status of each detector, and histograms were accumulated including the detector hit-map, the gain variation, etc. The histograms

were placed in a shared memory so that the contents could be referred to without interrupting the data taking and are transferred to the browsing PC on request over the network. The task of monitoring the data was performed every 15 minutes by one member of the Belle shift crew, the so called "non-expert" shifter. Of course the title is misleading since the physicist on shift needed to be well acquainted with the detector in order to observe any deviation of the monitored distributions of recorded events from the expected ones. However it is true that the second shift member, the "expert" shifter, was usually a more senior member of the collaboration responsible for the data acquisition and the slow control monitors. In case of deviations evident in the DQM which the "expert" shifter was unable to resolve the corresponding detector experts were called in order to resolve any issues.

The second level of data quality check is the monitoring of data quality of the full event reconstruction and event classification. During the DST production, various higher level quantities were accumulated in histograms to facilitate maintaining a high data quality for physics analysis. This system is called the Quality Assurance Monitor (QAM), and is maintained by the QAM group. The histograms are checked whenever the DST for one run was made. At the beginning of the experiment, the DST production was performed offline and it took a few days to to obtain the result from the QAM. Therefore, timely feedback to the team responsible for data taking was difficult. After the introduction of RFARM in 2003, the DST production was fully integrated as a real time processing step, and the QAM was merged with the DQM. The RFARM was capable of full event reconstruction together with the event type classification, and the versatile monitoring of specific physics quantities became possible.

A mechanism to collect histograms from nodes processing data in parallel was implemented in RFARM and the histograms were collected and merged every 3 minutes during data taking. The resulting histograms were sent to the monitor PC of the DQM over the network so that they could be treated as a part of DQM histograms. The shifters checked both of DQM and QAM histograms in real time to verify and ensure the high quality of data being recorded.

The real time monitoring of QAM provided by RFARM was a powerful tool for the special runs such as the energy scan. For example, the distribution of the Fox-Wolfram moment ratio (R_2, see Chapter 9) could be obtained for hadronic events during data taking, giving the fraction of $B\overline{B}$ events in the sample in real time, and it was possible to know the beam energy of the current scan point precisely. It enabled "on-the-fly" determination of next scanning point so that the energy scan could be performed efficiently.

3.6.2 B-counting techniques

Knowing with the best possible precision and with well understood errors the number of B meson pairs in the used data sample is of paramount importance for many of the analyses performed at the B Factories. The techniques developed by *BABAR* and Belle to compute this number for a given set of data were made part of the central production activities to enforce quality control and consistency of the results.

3.6.2.1 B-counting in *BABAR*

For the $\Upsilon(4S)$ running periods, the number of $B\overline{B}$ events in *BABAR* was computed by subtracting the number of hadronic events due to continuum interactions from the total number of the events in the on-resonance data set:

$$N_{B\overline{B}} = (N_H - N_\mu \cdot R_{off} \cdot \kappa)/\epsilon_{B\overline{B}} \tag{3.6.1}$$

where

- N_H is the number of events satisfying the hadronic event selection in the on-resonance data;
- N_μ is the number of events satisfying muon pair selection criteria in the on-resonance data;
- R_{off} is the ratio of selected hadronic events to selected muon pair events in the off-resonance (continuum) data;
- $\kappa \equiv \frac{\epsilon'_\mu \cdot \sigma'_\mu}{\epsilon_\mu \cdot \sigma_\mu} \cdot \frac{\sum_i \epsilon_i \cdot \sigma_i}{\sum_i \epsilon'_i \cdot \sigma'_i}$ corrects for the changes in continuum production cross section (σ) and efficiency for satisfying the selection criteria (ϵ) between on and off-resonance center-of-mass energies. Off-resonance quantities are denoted by a prime. The subscript μ refers to muon pair events; the various contributions to the continuum hadronic cross section, primarily $e^+e^- \to q\overline{q}$, are denoted by the subscript i. Since the muon pair and $q\overline{q}$ cross sections vary similarly with $\sqrt{s}$ (0.7% difference between on- and off-resonance), κ has a value close to 1. The quantity $N_\mu \cdot R_{off} \cdot \kappa$ is then the number of continuum hadronic events in the on-resonance dataset.
- $\epsilon_{B\overline{B}} = 0.940$ is the efficiency for produced $B\overline{B}$ events to satisfy the hadronic event selection, calculated under the assumption that

$$\mathcal{B}(\Upsilon(4S) \to B^+B^-) = \mathcal{B}(\Upsilon(4S) \to B^0\overline{B}^0) = 0.5. \tag{3.6.2}$$

  Variations in the amount of non-$B\overline{B}$ decays of the $\Upsilon(4S)$, and in the branching ratios of B^+B^- and $B^0\overline{B}^0$, are included in the systematic error, but are not significant.

The numbers of hadronic events and muon pairs for each run was found as part of the skimming process (see Section 3.5 above). The hadronic event selection was based on the number of charged tracks (≥ 3), the total measured energy, the event shape, the location of the event vertex, and the momentum of the highest momentum track. Muon pair events were selected using the invariant mass of the two tracks, the angle between them, and the energy associated with each track in the calorimeter. When no energy was associated with either track, at least one of the tracks was required to be identified as a muon in the IFR. This happened in roughly the 0.5% of the events,

when backgrounds in the calorimeter (such as out-of-time Bhabha events) would cause a timing mismatch between the calorimeter and the tracking system.

The selection criteria were tuned to maximize efficiency for $B\overline{B}$ and $\mu^+\mu^-$ events while minimizing sensitivity to beam backgrounds. In particular, the analysis minimized the time variation of the efficiency for simulated $q\overline{q}$ and $\mu^+\mu^-$ events.

The residual non-statistical time variations of the efficiencies result in an uncertainty in κ and a corresponding 0.27% systematic error on $N_{B\overline{B}}$. The other significant contributions to the overall 0.6% uncertainty on $N_{B\overline{B}}$ include 0.36% from the uncertainty in the fraction of events that fail the selection criteria, mostly low multiplicity $B\overline{B}$ decays that fail the requirement on the number of charged tracks, and 0.40% from the uncertainty in the modeling of the total energy distribution that translates into an uncertainty on the fraction of the events that fail the energy cut.

The total number of $B\overline{B}$ events (McGregor, 2008) in the nominal full dataset is $N_{B\overline{B}} = (471.0 \pm 2.8) \times 10^6$. In addition to the overall number quoted above, $N_{B\overline{B}}$ was tabulated for each run so that analysts could obtain B-counting and luminosity values for any subset of the full $\Upsilon(4S)$ dataset.

The numbers of $\Upsilon(3S)$ and $\Upsilon(2S)$ mesons produced in data sets collected at these resonances have been found using a similar analysis. In this case, the off-resonance continuum scaling was performed using $e^+e^- \to \gamma\gamma$ events, due to the non-negligible $\Upsilon \to \mu^+\mu^-$ branching fraction. The hadronic selection criteria were also modified for these analyses.

The $\Upsilon(3S)$ and $\Upsilon(2S)$ datasets contain $(121.3 \pm 1.2) \times 10^6$ and $(98.3 \pm 0.9) \times 10^6$ Upsilons, respectively. These numbers are calculated using hadronic events, with a correction for the fraction of leptonic decays that fail the hadronic selection.

The primary contributions to the systematic errors are uncertainties on the efficiency of the total energy selection (0.6%), the requirement on the number of tracks (0.4%), and the uncertainty on the $\Upsilon \to \ell^+\ell^-$ branching fractions (0.5%).

3.6.2.2 B-counting in Belle

The final Belle $\Upsilon(4S)$ dataset contains $(771.6 \pm 10.6) \times 10^6$ $B\overline{B}$ events. As in the *BABAR* B-counting scheme, this number is obtained by a subtraction of off-resonance hadronic contributions, as measured by the number of events in the previously described $HadronBJ$ skim, from the total number of on-resonance hadronic events. In the Belle case, this is calculated as:

$$N_{B\overline{B}} = \frac{N_{on} - r(\epsilon_{q\bar{q}})\alpha N_{q\bar{q}}^{off}}{\epsilon_{B\overline{B}}} \tag{3.6.3}$$

where

- N_{on} is the number of events satisfying the hadronic event selection in the on-resonance data;
- $r(\epsilon_{q\bar{q}})$ is the ratio of efficiency for $q\bar{q}$ events off-resonance to the efficiency for those on-resonance;
- α is the ratio of the number of Bhabha (e^+e^-) events or μ-pair events observed on-resonance to those observed off-resonance. This is described in more detail below;
- $N_{q\bar{q}}^{off}$ is the number of events satisfying the hadronic event selection in the off-resonance data;
- $\epsilon_{B\overline{B}}$ is the efficiency of the $\Upsilon(4S) \to B\overline{B}$ event selection criteria for on-resonance data.

The values of $\epsilon_{B\overline{B}}$ remained relatively stable throughout the lifetime of Belle. Although it was evaluated on an experiment-by-experiment basis, typical values were around 99% and differed by less than 0.5% over all experiments. The efficiency for $q\bar{q}$ events showed no strong dependence on energy, so $r(\epsilon_{q\bar{q}})$ was determined to be very near to 1, with variations of less than 0.3% over all data taking periods.

Aside from differences in these numerical constants, there is a notable difference from the *BABAR* approach. For most data taking periods, the off-resonance contributions are scaled using Bhabha events, rather than μ-pair events. Originally, the average of α as calculated with Bhabha events and μ-pair events was used for the final calculation. However, for data taken after spring of 2003, the μ-pair efficiency became significantly less stable. This is attributed multiple effects, including changes to the trigger masks used in the dimuon event identification, as well as some inherent instability due to intrinsic timing variations in a subset of these trigger masks. For data following this period, only Bhabha events are used to calculate the value of α.

Since the rate of fermion pair production is identical regardless of the type of fermion produced, the approach is effectively equivalent, regardless of whether e^+e^- or $\mu^+\mu^-$ events are considered. However, the periods when both methods can be used to calculate α allow an estimate of systematic uncertainty on this value. This was determined to be a 0.5% uncertainty. This value is considered representative of the uncertainty on α, even during data taking periods when μ-pair events were not used for this calculation.

Systematic uncertainties are also assigned on the value of $r(\epsilon_{q\bar{q}})$, but these are a minor contribution to the overall error, less than 0.2% for all experiments. This uncertainty is consistent with the level of variation seen in $q\bar{q}$ efficiency as a function of run range during a single experiment, as evaluated by Monte Carlo events generated with conditions matched to those of the corresponding running period. A sideband in the z-position of the measured event vertex is used to study systematic uncertainties due to the inclusion of beam gas events, but such uncertainties are below 0.1%.

Ultimately, the uncertainty on $N_{B\overline{B}}$ is dominated by the systematic uncertainty from α, and is approximately 1.5% for most of the Belle data.

The B-counting and $\overline{b}$ cross section measurement methodology used by Belle in the context of B_s^0 mesons collected at the $\Upsilon(5S)$ is discussed in detail Chapter 23.

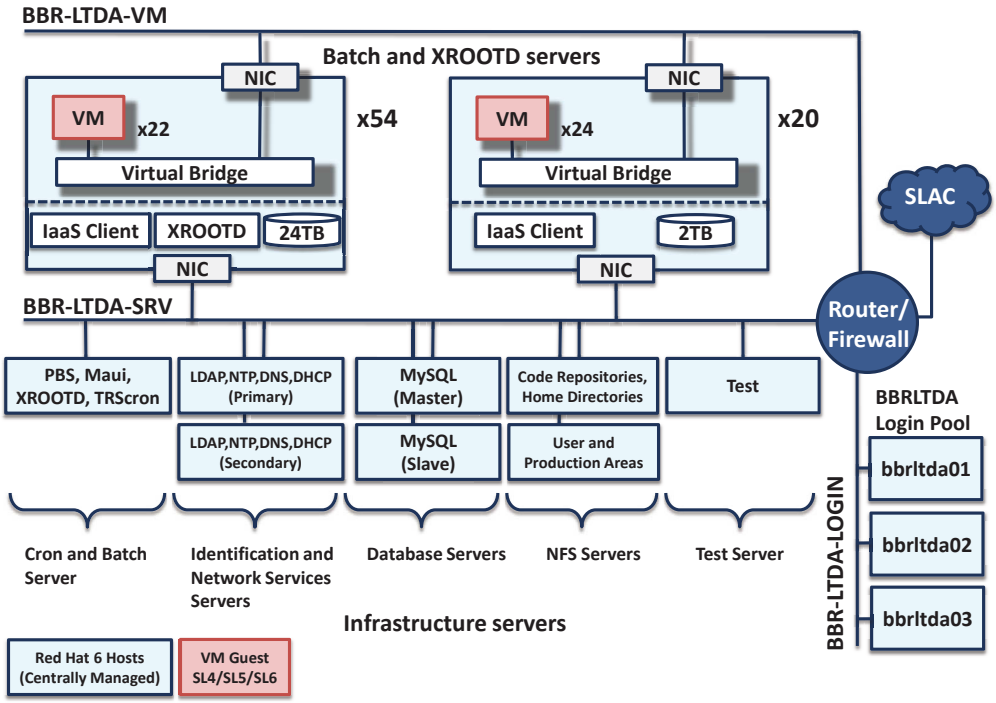

Figure 3.7.1. The LTDA cluster provides both storage and CPU resources in order to support analysis of *BABAR* data in the future. It includes database servers, code repositories, user home directories, working areas, production areas, and `XRootD` disk space. The isolation of back versioned components running on the batch system is implemented with firewall rules: virtual machines (VM's) are not allowed to connect to either the SLAC network or the world, and only well defined services are allowed between the VM network and the service network – see text for details.

3.7 Long Term Data Access system

3.7.1 The BABAR approach

The Long Term Data Access (LTDA) system is designed to preserve the capability of analyzing the *BABAR* data until at least the end of 2018. This requires the support of code, repositories, data, databases, storage, and CPU capacity. Special attention has to be devoted to the documentation. The system maintenance effort has to be minimized, including hardware maintenance, operating systems (OS) upgrades, tool upgrades, code validation, etc. The use of a contained system offers a controlled environment and simplifies documentation and user support. The *BABAR* analysis environment is supported with a frozen operating system infrastructure rather than actively migrating to future software environment as needed. The *BABAR* framework preserves its full capability of expansion and development, and is able to support future new analyses.

A long-lived frozen *BABAR* environment has to be maintained despite the evolving nature of hardware and OS. Also the support of back versioned OS is difficult, because future security exploits will require unknown patches. Hardware virtualization solves the hardware support problem for the foreseeable future and the use of OS images on virtual machines (VM's) solves the system administration problem, replacing it with the easier management of a small number of OS images.

The design of the LTDA cluster architecture takes into account the possibility that systems can be compromised from the security point of view and, in order to reduce risk to an acceptable level, a risk-based approach has been taken:

- Assume that systems that can be compromised, are actually compromised.
- Compromised components of the LTDA will be detectable by logging and monitoring.
- The LTDA will prevent accidental modification or deletion of the data.
- The dynamic creation of VM's from read-only images adds a small layer of security, by avoiding the compromised elements from being persisted beyond the destruction of the VM.

A representation of the cluster together with the layout of the network is shown in Figure 3.7.1. All sessions requiring back versioned platforms, including interactive sessions for debugging, run in VM's on the batch system. The isolation of the back versioned components is realized

through firewall rules that are implemented in the LTDA switch. The LTDA network is composed of three subnets to which different elements of the cluster are attached. All the back versioned components (VM's) are connected to a VM subnet (BBR-LTDA-VM) and connection rules are enforced with the service network, (BBR-LTDA-SRV) including the VM's physical hosts and other infrastructure servers (always patched and up to date), and the login network (BBR-LTDA-LOGIN, always patched and up to date). The login pool is the only point of access for the users.

The LTDA batch resources are managed by PBS Torque (Torque, 2012) and Maui Scheduler (Adaptive Computing, 2012) is used as the job scheduler. The virtualization layer is implemented using QEMU (Qemu, 2012) and KVM (KVM, 2012). The data to which the user jobs need to access are managed by `XRootD` and staged on the disks of the batch servers on demand. Each batch and `XRootD` server has 12 disks of 2 TB, 11 of which are dedicated to `XRootD`. The last 2 TB disk of each server is used as a scratch area by the VM's running on the node. Each batch server has 12 physical cores of which one is dedicated to the host itself and the `XRootD` service. The other 11 cores are used to run virtual machines. With hyper-threading on, each node can run up to 22 VM's. The cluster also includes 20 servers used uniquely as a batch resource.

The LTDA cluster has been running in production mode since March 2012. All the active *BABAR* users have an account on the cluster with a 1GB NFS home directory. So far about 50 users have run jobs on the system while about 15 of them have made heavy use of the system. About 2 million jobs have been completed in the last year.

In almost one year of active use some fine tuning has been necessary. NFS connection parameters have been adapted to handle the high number of NFS accesses occurring when the queues are filled to their maximum capacity. On two occasions an upgrade of the host kernels has disrupted the system network. We have now established a validation procedure which allows us to test all the upgrades on a test machine, configured exactly like a batch server, before they are deployed to the entire cluster.

Monitoring of the servers, the services and the batch queues is also implemented. So far the cluster has met and exceeded the expectations.

3.7.2 The Belle approach

The Belle group recently discussed their policy on data preservation (Akopov et al., 2012). It was decided that the Belle data will not be released to the public domain until the time the statistics of Belle II supersedes the Belle data and all Belle members (and Belle II members) lose interest in Belle data. This situation will likely occur around 2017-2018, a couple of years after the commissioning of the SuperKEKB accelerator. Two approaches are considered to provide an environment to access Belle data even in the Belle II experiment period. One is porting the Belle software to the new computing system for the Belle II experiment. The other is converting the Belle data to the data format adopted in Belle II so that it can be read in the Belle II software framework. The former approach does not require significant modifications of the current software. However, every time the computing system is replaced with a new one (which typically takes place every three or four years at KEK) the portability of the data has to be confirmed. For the latter case, one needs to prepare conversion software from the Belle data format to the Belle II one. Furthermore, the Belle data conversion has to be done in a systematic manner considering the available hardware and human resource. But once it is converted, Belle users can keep using it in the Belle II software framework. In both cases, the current Belle data has to be migrated to a new format.

Part B
Tools and methods

Chapter 4
Multivariate methods and analysis optimization

Editors:
Frank Porter (BABAR)

Additional section writers:
Piti Ongmonkolkul

Multivariate analysis (MVA) is widely used to extract discriminating information from data. This chapter provides a general discussion of the most relevant MVA tools used by *BABAR* and Belle, their mathematical properties, and optimization methods. Specific multivariate algorithms used for charged particle identification (PID), B-flavor tagging and discrimination against background are described in Chapters 5, 8, and 9, respectively.

4.1 Introduction

The goal of analysis optimization is to make optimal use of the available data to perform a measurement of physical interest. Depending on the circumstance, the exact meaning of "optimal" may differ. However, the essential notions are those of efficiency (minimizing variance) and robustness. The goal of efficiency must be interpreted in the context of being unbiased, or negligibly biased. Robustness is used here in the broader sense, including both sensitivity to model errors and sensitivity to statistical outliers. An analysis that minimizes statistical uncertainties may not be optimal if the systematic uncertainties are large.

With the large, complex event samples from present experiments, plus the improvements in computing technology, analysis methods have evolved. This evolution has been aided by advances in the available statistical methodologies.

The optimization problem may be viewed as a problem in classification: For example, we wish to classify a set of events according to "signal" or "background". Thus, we have the problem of optimizing a binary decision process. This may be generalized to more than two classes, but the binary decision covers much of what we do. Another possible approach is to define some weight, or probability for each event to belong to the various classes. The technique of ${}_s\mathcal{P}lots$, discussed in Chapter 11, provides such an example.

It should be remarked that there are many variations on the methods presented. The discussion here is introductory rather than comprehensive. The reader is referred to the text by Hastie, Tibshirani, and Friedman (2009) for a more complete treatment of most of this material.

4.2 Notation

As is common in physics, we adopt an informal notation eschewing a notational distinction between a random variable and an instance. Our variables may be discrete or continuous, but for convenience the treatment here is in terms of continuous variables. The particle physics notion of an "event" maps easily onto the statistical concept of "event".

We suppose that each event corresponds to an independent identical random sampling in an ℓ-dimensional sampling space. An event is described by the vector $\boldsymbol{x} = (x_1, \ldots, x_\ell)$. The variables used to optimize the selection of events are called "selection variables". We'll denote these with the symbol $\boldsymbol{s} = (s_1, \ldots, s_k)$. These are functions of the sampling vector, $\boldsymbol{s} = \boldsymbol{s}(\boldsymbol{x})$. In some cases, $\boldsymbol{s}$ is simply a subset of the $\boldsymbol{x}$ variables. The dimension, k, of $\boldsymbol{s}$ may itself be varied during the optimization process. The term multivariate is used to describe situations where we analyse a multi-dimensional hyperspace $\boldsymbol{s}$, using some well defined methodology.

The means of the selection variables are denoted $\boldsymbol{\xi} = (\xi_1, \ldots, \xi_k)$. The covariance matrix is

$$\Sigma = E\left[(\boldsymbol{s} - \boldsymbol{\xi})(\boldsymbol{s} - \boldsymbol{\xi})^T\right], \tag{4.2.1}$$

where the "E" denotes expectation value. Uncertain parameters of the distribution of the selection variables are denoted with $\boldsymbol{\theta}$. If there are r such parameters, we denote them as $\boldsymbol{\theta} = (\theta_1, \ldots, \theta_r)$. The quantities $\boldsymbol{\xi}$ and Σ may be functions of $\boldsymbol{\theta}$. Estimators for $\boldsymbol{\theta}$ are denoted $\widehat{\boldsymbol{\theta}}$. If the sampling distribution for the selection variables is multivariate normal, the corresponding density is

$$N(\boldsymbol{s}; \boldsymbol{\xi}, \Sigma) \equiv \frac{1}{\sqrt{(2\pi)^k \det \Sigma}} \exp\left[-\frac{1}{2}(\boldsymbol{s} - \boldsymbol{\xi})^T \Sigma^{-1} (\boldsymbol{s} - \boldsymbol{\xi})\right]. \tag{4.2.2}$$

4.3 Figures of merit

We often reduce the optimization of an analysis to the problem of maximizing or minimizing the expected value of a figure of merit (FOM). "Loss functions", typically making some estimate of error rate, are often used for this, and are discussed, for example, in Hastie, Tibshirani, and Friedman (2009). Here, we mention some of the more common FOMs used specifically in particle physics.

If we are looking for some yet unobserved new effect, we might optimize on the expected significance of that new effect. Suppose S is the expected number of signal events after selection (depending on the analysis), and B is the expected number of background events, which we assume we can estimate from known processes. The total number of events observed is N, including both signal

and background. The size of a possible signal is estimated according to $\widehat{S} = N - B$. An estimate for the size of fluctuations in background is $\sqrt{B}$. Thus, $S/\sqrt{B}$ is related to the significance of a possible signal. In such a measurement, this provides a figure of merit to be maximized. The left side of Fig. 4.3.1 shows an example of this (with detection efficiency substituting for S, that is, the efficiency is S divided by expected number of produced signal events in the dataset) in the Belle analysis searching for $\tau \to \ell hh'$ lepton flavor violating decays (Miyazaki, 2013). Another example can be found in Section 18.4.4.2, where the analyses that resulted in the observation of $\eta_b(1S)$ and $\eta_b(2S)$ mesons used the test statistic $S/\sqrt{B}$ to optimize event selection criteria.

Another approach to a figure of merit for the case of a search for a new effect has been suggested by Punzi (2003b). This approach defines a "sensitivity region" for the possible parameters, m, of the new effect. This definition is based on the confidence level of the region for m that will be quoted if evidence for a new effect is not claimed. The figure of merit then corresponds to maximizing the size of the sensitivity region. A simple form of this figure of merit is

$$\frac{\epsilon}{n_\sigma/2 + \sqrt{B}}, \tag{4.3.1}$$

where ϵ is the efficiency to observe a signal event, B is the expected background, and n_σ is the desired one-tailed significance (in order to claim a discovery) of an observation expressed in standard deviations of a Gaussian probability distribution. This FOM has been used in some analyses, for example, in *BABAR*'s search for for $B^+ \to \ell^+ \nu_\ell$ recoiling against $B^- \to D^0 \ell^- \bar{\nu} X$ (Aubert, 2010a).

On the other hand, we may wish to get the most precise measurement of some known process. In this case, the signal is proportional to S, and the estimated error on the signal is $\sqrt{S+B}$ (*i.e.*, the expected fluctuation on the total number of events). Thus, to optimize on precision (of signal yield), we wish to maximize the expected value of $S/\sqrt{S+B}$. This can be viewed in an equivalent form: suppose that there are a total of N_S signal events in the dataset before event selection. Selection involves some efficiency, ϵ, to select signal events, so that we expect $S = \epsilon N_S$. Then this FOM may be expressed as $\sqrt{N_S}\sqrt{\epsilon \cdot S/(S+B)}$, where the factor $S/(S+B)$ is the signal purity in the selected sample. This makes explicit the trade-off between efficiency and purity in the optimization.

Of course, the idea of optimizing precision applies more generally than measurements of signal strength, for example in the measurement of *CP* asymmetries. An example of optimizing on expected precision is shown in the right side of Fig. 4.3.1, for the Belle analysis measuring y_{CP} in $D^0 - \overline{D}^0$ mixing (Staric, 2007).

In practice, in a complicated analysis, the optimization process is usually broken into more-or-less disjoint aspects, such as topological background suppression (*e.g.*, Chapter 9) or particle identification (Chapter 5). For these situations we often optimize on the signal purity, $S/(S+B)$, or equivalently, the "signal-to-noise": S/B. For example, in the optimization of PID, the goal is to get the best efficiency for the desired particle type for a given contamination probability, or variations on this idea. A useful graphical tool is known (from its engineering origins) as the "receiver operating characteristic", a plot showing the trade-off between efficiency and purity, or variants. Fig. 4.4.1 provides an example in the context of PID, discussed later in this chapter. The idea is used as well in B meson reconstruction, for example in Fig. 7.4.3. Depending on the application, it may be acceptable to have a greater or lesser contamination. That is, we may not optimize strictly on the particle identification purity in the context of a given analysis. This leads to the provision of several PID selectors. In principle, the particle identification could be optimized along with the subsequent analysis, but this is unwieldy, and the provision of a choice of selectors approximates this. Providing pre-defined selectors also facilitates re-use of work done to estimate systematic uncertainties.

There are still other figures of merit that may be used in classification problems. The misclassification error, equal to the fraction of the sample that is incorrectly classified may be used. In building decision trees, two variants of this idea are commonly adopted, the "Gini index" and the "cross-entropy". These FOMs are available in most multivariate classification packages in use in HEP and are defined below in the discussion on decision trees, although their application is not limited to decision trees.

4.4 Methods

Statistical methods and tools of increasing sophistication used to optimize analyzes are described in the remainder of this chapter. Beforehand, it is important to stress that for many methods to be successful, two mandatory steps are required : training and validation. There are a few exceptions to this rule, where one can analytically compute the parameters required to perform an optimization.

It is dangerous to optimize a selection with the actual data that is to be used in the measurement. Such an approach is prone to tuning on fluctuations and the production of biases. For a simple example, suppose we are tuning an analysis for a particular signal, using the actual data. If we try to optimize S/B, say, we will find selection criteria that tend to favor signal-like events, tuning on any upward fluctuations. This will tend to bias our measurement of the signal strength toward high values. Nevertheless, this has been done extensively in particle physics, sometimes successfully, but sometimes with disastrous results. With an awareness of the issues, *BABAR* and Belle have gone to some length to avoid relying on the measurement data for the optimization. Note that these issues are discussed in a somewhat different context in Chapter 14.

Thus, *BABAR* and Belle take the approach of using a training dataset for the optimization. This could be simulated data, sidebands to the data that will not be used in the measurement, or a dataset that has similarities with the measurement data. A feature of the training dataset is

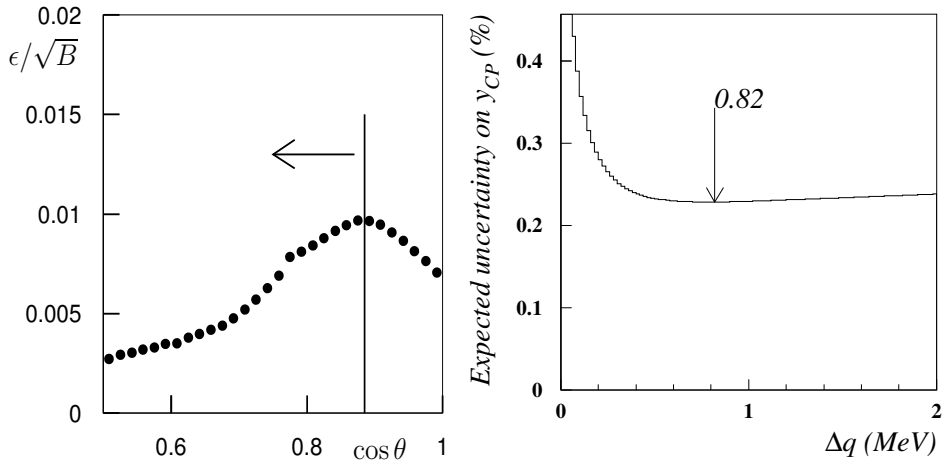

Figure 4.3.1. Examples of figures of merit used in optimization of Belle analyses. Left: Optimization on $\epsilon/\sqrt{B}$ in the search for the lepton flavor violating decay $\tau \to \mu\pi\pi$ (see Chapter 20). The horizontal axis is the cosine of the angle between the missing momentum vector and the direction of the tagging charged particle, in the CM frame. Belle internal, from the (Miyazaki, 2013) analysis. Right: Optimization on expected uncertainty in the measurement of the y_{CP} parameter in $D^0 - \overline{D}^0$, see Section 19.2.3. The horizontal axis is the measured kinetic energy released in the candidate D^* decay. Belle internal, from the (Staric, 2007) analysis.

that it is known (or known well enough) which class each event belongs to, so that the FOM may be computed. The selection criteria are optimized using the training dataset, then applied to perform the desired measurement.

A further refinement in method is the notion of validation. It is possible that the training dataset contains fluctuations that result in criteria that are not broadly optimal. This is related to the problem of "over-training", in which the training provides a model exquisitely tuned to the training sample, but with no real advantage on an independent sample. Effectively, the model is made very complicated when the underlying distribution is simpler. Since the training must be useful on an independent sample (it has to "generalize"), this erratic tendency has to be regularized in some way. For example, another dataset may be used to "validate" the selection and stop the optimization procedure (training) when no further improvement is obtained. This helps to avoid the phenomenon of over-training. A variant on this is "cross-validation", in which the training dataset is split into multiple equal subsets, and each of the subsets is used to validate the training on the remaining (aggregated) subsets.

The estimate of the efficiency obtained using the training/validation datasets may be biased too high. This is because the final selection criteria actually depend on both the training and validation datasets, and fluctuations in either dataset may affect the tuning in the optimization. To avoid this, a further independent "test" dataset, not used in the optimization process, may be used to obtain an unbiased efficiency estimate.

Some classification methods lend themselves more easily than others to interpretation, for example, in deciding how important the various inputs are. However, for a complicated problem a dedicated procedure may be required to understand which variables are most important, and perhaps eliminate ones that are not useful. A simple approach is to remove one or more variables at a time to see the effect of this on the classifier performance.

4.4.1 Rectangular cuts

When variables are uncorrelated, a selection may be optimized by looking at the effect of each variable in turn. This gives a selection region that is a hyper-rectangle in the space of selection variables, with sides aligned with the coordinate axes of the selection variables. Such selection criteria are known as rectangular cuts. They have the merits of ease of application, optimization, and interpretation. They are widely used, especially in "pre-selection" (*e.g.*, skim production) where the selection is still relatively inclusive, and more sophisticated optimization is not essential.

This simple approach may be used even if variables are correlated, however the result may no longer be optimal. In this case it may be possible to do considerably better with more sophisticated methods. For example, a refinement is possible, in which arbitrary regions of sample space may be approximated by sequences of rectangular cuts. A form of this approach is the technique of the decision tree, described further below.

When there are correlations among variables, we may also look for transformations that produce a set of uncorrelated variables, and then apply rectangular cuts in the transformed space.

4.4.2 Likelihood method

The likelihood function provides a mapping of the observations with often beneficial properties. This is employed,

for example, in the "likelihood method" for particle identification (Chapter 5). In this approach, detector measurements such as dE/dx, time-of-flight, calorimeter response, and muon detector response are combined by multiplying their likelihoods for a given particle type interpretation. Then rectangular cuts are applied to ratios of these likelihoods for different particle hypotheses. This approach to combining the available information has the merits of ease of application and interpretation. It also has some motivation from the fact that the likelihood ratio provides a uniformly most powerful test in the case of simple hypotheses. Table 5.2.1 shows a comparison of "cut-based" (that is, making rectangular cuts on the basic detector quantities) and "likelihood based" muon selection: for an efficiency loss of less than 10%, the likelihood method decreases the pion contamination by approximately 30%.

The likelihood function is constructed from the sampling *p.d.f.*, so the form of the distribution must be known including any correlations among variables. This can be a difficulty with this approach if this information is not readily available. The "supervised learning" methods (neural networks and decision trees) described below have an advantage in this respect, because subtle features, including correlations, are usually included automatically in the training samples. Maximum likelihood fits have been used widely at the B Factories and are discussed in Chapter 11.

4.4.3 Linear discriminants

A linear discriminant is some linear function of the sample event variables:

$$L = A + \boldsymbol{B} \cdot \boldsymbol{s}, \tag{4.4.1}$$

where A and $\boldsymbol{B}$ are independent of $\boldsymbol{s}$. The idea here is that L may be such that it tends to take on different values for different classes (*i.e.*, signal or background) of event. Thus, L may be useful for event classification. The optimization process here is to select those values of A and $\boldsymbol{B}$ that produce the best FOM.

The most commonly used linear discriminant is the "Fisher discriminant" (Fisher, 1936), motivated in the case of multivariate normal sampling. If signal is described by $f_S(\boldsymbol{s}) = N(\boldsymbol{s}; \boldsymbol{\xi_S}, \Sigma_S)$ and background by $f_B(\boldsymbol{s}) = N(\boldsymbol{s}; \boldsymbol{\xi_B}, \Sigma_B)$, we may form the logarithm of the likelihood ratio for an event to be signal or background:

$$\begin{aligned}\ln\lambda &= \ln\frac{w_S f_S(\boldsymbol{s})}{w_B f_B(\boldsymbol{s})} \\ &= \ln\frac{w_S}{w_B} - \frac{1}{2}\ln\frac{\det\Sigma_S}{\det\Sigma_B} - \frac{1}{2}\left(\boldsymbol{\xi}_S^T\Sigma_S^{-1}\boldsymbol{\xi}_S - \boldsymbol{\xi}_B^T\Sigma_B^{-1}\boldsymbol{\xi}_B\right) \\ &\quad + \boldsymbol{s}^T\left(\Sigma_S^{-1}\boldsymbol{\xi}_S - \Sigma_B^{-1}\boldsymbol{\xi}_B\right) - \frac{1}{2}\boldsymbol{s}^T\left(\Sigma_S^{-1} - \Sigma_B^{-1}\right)\boldsymbol{s},\end{aligned} \tag{4.4.2}$$

where w_S and w_B are the probabilities (weights) for an event to be signal or background, respectively. If the covariance matrices for signal and background are the same, $\Sigma_S = \Sigma_B = \Sigma$, then

$$\begin{aligned}\ln\lambda = \ln\frac{w_S}{w_B} &- \frac{1}{2}\left(\boldsymbol{\xi}_S^T\Sigma^{-1}\boldsymbol{\xi}_S - \boldsymbol{\xi}_B^T\Sigma^{-1}\boldsymbol{\xi}_B\right) \\ &+ \left(\boldsymbol{\xi}_S - \boldsymbol{\xi}_B\right)^T\Sigma^{-1}\boldsymbol{s}.\end{aligned} \tag{4.4.3}$$

This is now a linear expression in $\boldsymbol{s}$, referred to as the "Fisher discriminant".

If any of $\boldsymbol{\xi}_{B,S}$ or $\Sigma_{B,S}$ are unknown, they must be estimated, for example with a least-squares or maximum likelihood fit to the entire dataset. It is important to remember the assumption that $\Sigma_B = \Sigma_S$. There is no general reason why this should be true. If not equal, improvement (possibly substantial) in the analysis may sometimes be obtained with the full "quadratic discriminant" of Eq. (4.4.2). This is discussed and demonstrated with a simple example in Narsky (2005b, Section 2.1). Linear discriminants have been used widely at the B Factories, for example see Section 9.5 which contains a detailed description of the Belle strategy for continuum background suppression for B meson decay analyses.

4.4.4 Neural nets

The basis of the neural net (see, for example, Haykin (2009); MacKay (2003) for thorough developments) is a model for biological neurons, in which the firing of a neuron occurs once the summed "inputs" cross some threshold. In practice, this discontinuous behavior is smoothed out to a continuous function such as the sigmoid:

$$\sigma(X) = \frac{1}{1+e^{-X}}, \tag{4.4.4}$$

where X is a parameterized function of the inputs (for example, Eq. (4.4.5) below). As with other classification methods, the neural net is trained, validated, and tested on datasets with known outcomes. The training involves optimizing the values of parameters in the net to, for example, minimize classification error.

The simplest neural net consists of one "neuron". Suppose the function X is of the linear form $X = \sum_{i=1}^{k} w_i s_i + b$ (which is the same form as a Fisher discriminant). To use this net as a binary classifier, we choose a threshold X_c such that if $X > X_c$, the net returns a one, otherwise it returns a zero. Such a basic element is called a "perceptron", which represents a decision boundary in the problem space. Complex networks may be built out of these. Note that the function of the parameters $\boldsymbol{w}$ is to assign weights to the different inputs, and the parameter b acts as a "bias", changing the location of the decision threshold but not the relative weightings.

A feed-forward neural net (or "multilayer perceptron") consists of layers – an input layer, an output layer, and any number of "hidden" layers in between. Each layer has a number of nodes that take inputs from the next lower layer and provide outputs to the next higher layer. The input layer consists simply of the k selection variables $s_i, i = 1, \ldots, k$, each variable represented by a node. Let

us suppose for this discussion that our network has a single hidden layer. Each node in the hidden layer represents a numeric value obtained by a non-linear transformation on a linear combination of the input nodes. For example, using the sigmoid, the hidden nodes $h_1, \ldots, h_p$ compute the values:

$$h_i = \sigma\left(\sum_{j=1}^{k} w_{ij} s_j + b_i\right), \quad i = 1, \ldots, p. \tag{4.4.5}$$

The inclusion of a constant bias term, b_i, may be thought of as including a linear term corresponding to an additional input equal to the constant one.

The output layer may consist of multiple nodes for multiple classes; often we have two output nodes, which logically may be taken as a single output, as appropriate for the two-class "signal" vs "background" selection. We will assume this case here. The output is computed from the hidden layer by taking linear combinations of the hidden layer results,

$$y_j = a_j + \sum_{i=1}^{p} c_{ji} h_i, \quad j = 1, 2. \tag{4.4.6}$$

We may then obtain a number between 0 and 1 expressing the output of the neural net, for example, by

$$t = e^{y_1} / \left(e^{y_1} + e^{y_2}\right), \tag{4.4.7}$$

where y_1 is the "signal" class output. In the two class problem, a single output is often taken using the sigmoid where $t \equiv \sigma(y_2 - y_1)$; Eq. (4.4.7) is a generalization that may be extended to an arbitrary number of classes. Once the neural net is trained, large values of t indicate signal; an analysis can make an event selection based on t. It may be remarked that the difference between the neural net and a linear model is the use of non-linear "activation functions"; in the present example, the sigmoid.

Training of the neural net consists in searching for optimal values of the net parameters, where optimal is defined in terms of minimizing a measure of the classification error rate. For the example net, this training corresponds to finding values for the $p \times k$ parameters $\boldsymbol{w}$, the p parameters $\boldsymbol{b}$, the two parameters $\boldsymbol{a}$, and the $2 \times p$ parameters $\boldsymbol{c}$. The optimal values are often found by a gradient descent method, referred to as "back propagation" in this context.

A popular methodology is the Bayesian neural network (for example see the discussion on hadronic tag reconstruction for Belle in Section 7.4.1). In this case, the output of the net is interpreted as a posterior probability to be, *e.g.*, signal. Regularization of the network may be achieved with the help of prior distributions (often Gaussian) in the parameters.

4.4.5 Binary decision trees

The idea of a binary decision tree [see for example Hastie, Tibshirani, and Friedman (2009, Chapter 9)] is a recursive search for the best binary selection over the set of variables. Given a (training) dataset, we search for the variable and a selection (or "cut") value which provides the best FOM. This split results in two "nodes", one classified as "signal", the other as "background". A new search is applied to each of these nodes, resulting in two further splits. The process is repeated until further splits do not improve the FOM or fall below a specified minimum number of events. Trees that are grown by the latter criteria may be "pruned" to eliminate splits that fail some worthiness criterion. The result is a set of rectangular regions in our selection variable space, each classified as either signal or background. In the tree analogy, the set of final nodes at the end of the chain are called "leaves"'.

In binary decision trees, a commonly used FOM, besides simply computing the average error (misclassification error), is the "Gini index", $G(p) = -2p(1-p)$, where p is the fraction of correctly classified events at the given node. For example this FOM has been used in a number of inclusive $B \to X\ell^+\ell^-$ analyses described in Section 17.9. A similar alternative is the "cross-entropy", $Q(p) = p \log p + (1-p)\log(1-p)$. At each split, the values of Q of the two daughter nodes are added, weighted by the numbers of events (or other weights). The split that maximizes this sum is chosen. However, these FOMs are not necessarily the ones we really wish to optimize on, and some available tools permit user-defined FOMs.

An individual decision tree is a "weak" classifier (or "weak learner") in general. That is, it has a probability greater than random of making a correct classification, but possibly not much greater. It has been trained with a particular set of assumptions, such as the relative importance of training events. Better predictive power may be obtained with methods that combine decision trees trained in different ways. We introduce some of these techniques below.

A feature of decision trees is that they are intuitive. We can follow the progress along the tree and see how decisions are being made as well as see the relative importance of the different inputs as discriminators. By studying the trees produced in a given problem, we may eliminate variables that have little separation power, or are redundant with other variables.

4.4.6 Boosting

The idea of boosting [see for example Hastie, Tibshirani, and Friedman (2009, Chapter 10)] is to take a set of weak learners and combine them in such a way as to obtain a "strong learner": roughly, a classifier whose output error can be made arbitrarily small in a computationally efficient manner. Here, we introduce the technique in the context of boosting decision trees, although it can be used as well with other classifiers, such as neural nets.

In boosting trees, we take the results of training a tree and increase the weight ("boost") of misclassified events in forming a new tree. This process is repeated, and the outputs of the trees combined. For example, we consider the popular adaptive "AdAboost" methodology (Freund and Schapire, 1997; Hastie, Tibshirani, and Friedman, 2009):

- Start by assigning an equal weight to each event.
- Train a tree with these weights.
- Compute the weighted average error ϵ over all events.
- Compute $\alpha = \log[(1-\epsilon)/\epsilon]$.
- Increase the weight of misclassified events by a factor of e^{α}.
- Repeat the training with these weights, using the same classification algorithm.

After some desired number of iterations, the classification of an event is computed as an average over all of the trees, weighted by their values of α. The AdAboost is set as a default option within Toolkit for Multivariate Analysis (TMVA) and is used for the final *BABAR* PID algorithm discussed in Chapter 5.

4.4.7 Bagging and random forest

In "bagging" [Bootstrap AGGregatING; see, *e.g.*, Hastie, Tibshirani, and Friedman (2009, Chapter 8)] decision trees (or other classifiers in general) are constructed many times on bootstrap replicas of the training data. A bootstrap replica is a sampling, with replacement (that is, the datum is "returned" to the sample before the next sampling), of events from the training dataset. An event may appear multiple times in the replica. The point of the bootstrap is that the dataset itself is used as an empirical estimator for the underlying sampling distribution. Hence, multiple occurrences of an event are simply a consequence of identically distributed, independent samplings from this density estimator. The bootstrap replication results in another training dataset of the same size as the original. The final classifier is obtained by taking the majority vote of the individual classifiers.

If each bagging replica is passed through the same training algorithm, there will generally be significant correlations among the resulting decision trees. This tendency can be mitigated by the "random forest". In a random forest, each decision begins with choosing a random subset of the selection variables to be used in determining the split for that node. The sum of exclusive $b \to s\gamma$ analysis from *BABAR* described in Section 17.9.2.4 uses two random forest classifiers, one to perform best candidate selection and a second to provide background suppression.

4.4.8 Error correcting output code

We may consider the situation with multiple output classes, but where one is still interested in the binary question of determining whether the event belongs to a particular class or not. For example, suppose we have the classes e, π, K, p. There may be discriminants among all of these, and we may train classifiers to distinguish among binary partitions of this set of classes. That is, we might have a classifier that preferentially returns a 1 for classes e or π and a -1 for K, or p. We could train different classifiers for every such partition of the classes, resulting in an "exhaustive matrix". The aggregate of these classifiers is used in classifying an event. The technology of digital error correction may be used for this, in a method referred to as "error-correcting output codes" (ECOC) (Dietterich and Bakiri, 1995).

An event is classified by evaluating each of the classifiers to give a vector consisting of the numbers -1 and 1 for the event. The soft Hamming distances (Hamming, 1950) between this vector and the expected vectors for each class are calculated, where the soft Hamming distance between two binary strings of equal length is the sum of squares of the differences at each position of the vector. This yields a vector of numbers with length equal to the number of classes. In the simplest case we can take the class with minimum soft Hamming distance to be the resulting class. The idea is that an individual classifier might make an error, but this error may be corrected by the redundancy in the combination of the classifiers. For instance in *BABAR* many analyses have different PID requirements on the efficiency and mis-identification rate implying different levels of tightness in the selection. Instead of assigning the class with the minimum soft Hamming distance, a cut is applied based on the soft Hamming for the particular class and the ratios of soft Hamming distance of the particular class to those of the other classes. For example, for electron selection, we cut on S_e and S_e/S_K, S_e/S_π, S_e/S_p where S_x is the soft Hamming distance for class x. The disadvantage of the ECOC approach is in the need to build the classifiers for the exhaustive matrix, which becomes daunting if the number of classes becomes large.

BABAR eventually applied the ECOC approach in the evolution of its particle identification algorithm (Chapter 5), where the results of several bagged decision tree classifiers are combined. We may get an idea of the impact from Fig. 4.4.1, which compares three methods for particle identification: a likelihood-based selector (Section 4.4.2); a selector using bagged decision trees (Section 4.4.7) with a non-exhaustive error correction matrix; and a selector using bagged decision trees with an exhaustive error correction matrix. In the case of the non-exhaustive matrix, the classifiers used are one-vs-one classifiers, comparing the pion with kaon hypothesis, pion with electron, etc.

In Fig. 4.4.1, top (for $\pi - K$ separation), we see that the non-exhaustive ECOC performs similarly with the likelihood selector. When we go to an exhaustive ECOC selection we find a notable improvement in mis-identification for the same efficiency. In the bottom plot (for $e - \pi$ separation) the non-exhaustive ECOC is tuned to somewhat higher efficiency, but yields much poorer mis-identification than the likelihood selector. Note that this is in contrast with the situation for the $\pi - K$ separation: relative classifier performance can depend substantially on the problem. Finding the optimal approach may require extensive study, including consideration of systematics as well as performance. However, in this case tuning an exhaustive ECOC to the same efficiency as the likelihood selector again provides a lower misidentification for the same efficiency.

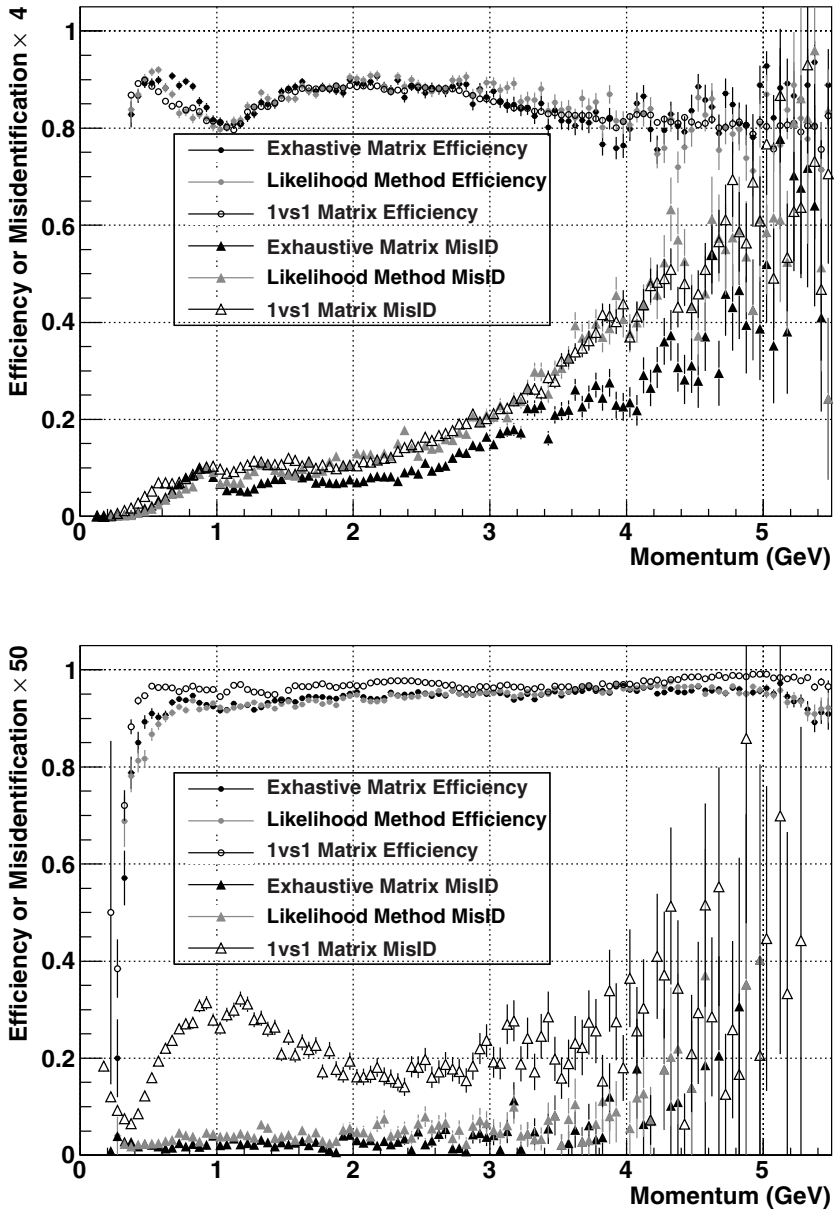

Figure 4.4.1. Performance of various particle identification selections in *BABAR*. The horizontal axis is momentum, and the vertical axis is either efficiency (circles) or a factor (for visibility) times the mis-identification probability (triangles). Gray symbols indicate a selector based on a likelihoods; open symbols indicate a selector based on bagged decision trees with a non-exhaustive error correction matrix (see text); black symbols indicate a selector based on bagged decision trees with an exhaustive error correction matrix. Top: Performance of kaon selection. The pion mis-identification probabilities are multiplied by four. Bottom: Performance of electron selection. The pion mis-identification probabilities are multiplied by fifty.

4.5 Available tools

There are two general purpose toolkits implementing many of these algorithms that have become the most widely used in our analyses:

- StatPatternRecognition (Narsky, 2005b)
- TMVA ("Toolkit for Multivariate Analysis"; Hoecker et al., 2007)

For neural nets, popular packages are:

- Stuttgart Neural Network Simulator (SNNS; Zell et al., 1995)
- NeuroBayes (Feindt and Kerzel, 2006; Phi-T, 2008)

Implementations of various classifiers may be found as well in the broader toolkits:

- The R project (R Project Contributors, 1997)
- S-PLUS (TIBCO, 2008) (a commercial alternative to R)
- MATLAB (MathWorks, 1984)

These should not be taken as exhaustive lists, only providing those packages most commonly seen in the present context.

Chapter 5
Charged particle identification

Editors:
Alessandro Gaz (BABAR)
Shohei Nishida (Belle)

5.1 Introduction

In this chapter we present the implementation and performance of charged particle identification (PID) at Belle and *BABAR*.

After a brief introduction, the algorithms and statistical tools used by the two experiments are discussed (Section 5.2). The PID algorithms that give the ultimate performance are based on multivariate techniques, described in detail in Chapter 4. Some examples of the typical performance of the particle identification algorithms (PID selectors) are then given, along with a discussion on PID-related error sources, for both *BABAR* (Section 5.3) and Belle (Section 5.4).

The identification of charged particles stable enough to be detected (electrons, muons, pions, kaons, and protons) plays a central role in the physics program of the *BABAR* and Belle experiments. Not only are very good PID capabilities required for separating hadronic final states of B decays such as $\pi^+\pi^-$, $K^\pm\pi^\mp$, K^+K^-, and many others, but the PID performance is crucial for the flavor-tagging of the B mesons (see Chapter 8). B^0 candidates are distinguished from $\overline{B}^0$ candidates based on the identification of their decay products such as high-momentum charged leptons (e or μ) or charged kaons. More generally PID very often provides powerful tools to reduce the backgrounds arising from final states which differ from that under study by swapping one of its particles with one of different flavor.

5.1.1 Definitions

The performance of a PID selector dedicated to the identification of charged particles of type α ($\alpha = e$, μ, π, K, p) is characterized by an efficiency and a set of mis-identification probabilities.

The PID efficiency of particle type α is computed as the fraction of successfully identified α tracks among all the α tracks reconstructed and selected for a particular analysis, while the mis-identification probabilities are the probabilities that particles of type $\beta, \gamma, \ldots$, are incorrectly identified as α.

In many cases the quantities defined above depend on the momentum and on the polar and azimuthal angles of the tracks. Therefore the performance of PID selectors is studied and determined in bins of (p, θ, ϕ).

5.1.2 Subdetectors providing PID information

BABAR uses the information from all of its subdetectors as inputs for the PID selectors. Measurements of the energy loss $\mathrm{d}E/\mathrm{d}x$ of a charged track are provided by the SVT and the DCH. The number of Cherenkov photons and the measurement of their angle with respect to the incident track are provided by the DIRC, while the EMC is responsible for the measurement of the deposited energy and of quantities describing the shape of the shower associated with a track (such as the lateral and the Zernike moments (Zernike, 1934)), which can be used to distinguish leptonic and hadronic tracks. Finally most information (such as the number of iron layers traversed by the candidate track, and variables related to the shape of the cluster) relevant to the identification of muons is provided by the IFR.

Belle uses similar input information. Measurements of the $\mathrm{d}E/\mathrm{d}x$ of a charged track are provided by the CDC. A TOF counter measures the time of flight of a charged particle from the interaction point to the counter, from which the velocity of the particle can be measured (Kichimi, 2000). The number of Cherenkov photons at the ACC provides separation for higher momenta (Iijima, 2000). Information from the ECL, together with that from the CDC and ACC, is used for electron identification (Hanagaki, Kakuno, Ikeda, Iijima, and Tsukamoto, 2002). The KLM is responsible for muon identification (Abashian, 2002a).

5.2 PID algorithms and multivariate methods

In the most simple method, PID selectors are based on cuts applied to the most relevant variables for every particle type (*e.g.* E/p for electrons, the distance traveled in the return yoke for muons, the Cherenkov angle for K/π separation, ...). Better performance is obtained with the use of likelihood based selectors, in which the information from the various subdetectors is used to compute a set of likelihoods L_k that the measured properties of the charged track in question would be produced by a true k-particle. For an example of implementation of a selector based on likelihood ratios, see Eq. (5.2.1). Belle has always used selectors based on likelihood ratios throughout the whole life of the experiment.

Cut and likelihood based selectors are very stable over the data-taking periods and do not need re-tuning to compensate for the aging of the detectors and the changes introduced by the reprocessing of the data. However, significant improvements can be achieved by considering a larger set of variables, even some with very mild discrimination power, in the implementation of PID selectors. *BABAR* uses more sophisticated statistical tools such as *Neural Networks* (NN), *Bagged Decision Trees* (BDT), and *Error Correcting Output Code* (ECOC) algorithms, to accommodate a large number of input variables (up to 36) and the significant correlations among them.

Due to their higher sensitivity to variations in the performance of the detector, the selectors based on multivariate methods need to be re-trained on data control samples (see Section 5.3) after every major change in the reconstruction algorithms. Particularly important for *BABAR*, which was affected by large variations in the performance of the IFR, is the inclusion of the data taking period as

one of the input variables, in order to take into account the loss of efficiency in specific regions of the detector.

In the following sections the more refined algorithms implemented at Belle and *BABAR* will be described.

5.2.1 Belle algorithms

The PID at Belle is based on likelihood ratios. For hadron identification, likelihoods for a candidate particle α are calculated based on $\mathrm{d}E/\mathrm{d}x$ information from the CDC (L_α^{CDC}), time of flight from the TOF (L_α^{TOF}) and the number of photons from the ACC (L_α^{ACC}), respectively. Then, the likelihood ratios

$$L(\alpha:\beta)=\frac{L_\alpha^{\mathrm{CDC}}L_\alpha^{\mathrm{TOF}}L_\alpha^{\mathrm{ACC}}}{L_\alpha^{\mathrm{CDC}}L_\alpha^{\mathrm{TOF}}L_\alpha^{\mathrm{ACC}}+L_\beta^{\mathrm{CDC}}L_\beta^{\mathrm{TOF}}L_\beta^{\mathrm{ACC}}} \quad (5.2.1)$$

are calculated and used for identification. For example, pions (kaons) can be selected by requiring a low (high) value of $L(K:\pi)$, and protons are typically identified with requirements on both $L(p:K)$ and $L(p:\pi)$. The cut value applied to the likelihood ratios can be optimized depending on the analysis.

For electron identification, in addition to L_α^{CDC} and L_α^{ACC}, information from the ECL (matching of the positions of the track and the energy cluster, E/p, and transverse shower shape) is used to form likelihood ratios. There is a small region around $\theta\sim 125^\circ$ with low electron identification performance because of a small gap between the barrel ECL and backward endcap ECL. For muon identification, reconstructed hits in the KLM are compared to the extrapolation of the CDC track, using the difference ΔR between the measured and expected range of the track, and the statistic χ_r^2 constructed from the transverse deviations of all hits associated to the track, normalized by the number of hits. Likelihoods for the muon, pion, and kaon hypotheses are formed based on *p.d.f.*s in ΔR and χ_r^2. The likelihood ratio $L_\mu/(L_\mu+L_\pi+L_K)$ is then used as a discriminating variable.

5.2.2 BABAR algorithms

In *BABAR*, the ultimate performance in the selection of muons is achieved with an algorithm based on *Bagged Decision Trees* (Narsky, 2005a; also discussed in Section 4.4.7 of this Book). The algorithm takes as input 30 variables: in addition to variables related to the length and the shape of the IFR cluster associated to the candidate track and the measurement of the energy deposited in the EMC, the variables related to the shape of the cluster in the calorimeter, the number of Cherenkov photons, the opening angle of the Cherenkov cone, and the number of DCH hits and the $\mathrm{d}E/\mathrm{d}x$ measured in the DCH are also used.

The training of the selectors is performed on high purity data samples of muons and pions, subdivided in 720 bins of p, θ, and charge. Candidate tracks are randomly discarded in order to have the same number of muons and pions in the same bin. This allows the use of the p, θ, and charge variables in the tree without introducing any bias due to the different (p,θ) spectrum of the source sample. The source sample is then randomly split into a training and a testing sample. Four different levels of tightness are designed for the muon selector (VeryLoose, Loose, Tight, and VeryTight); the cuts on the output of the classifier are designed such that either the muon selection efficiency or the pion mis-identification probability are kept constant. The target efficiencies (besides the very low-momentum part of the spectrum, where few muons can be identified) are 90%, 80%, 70%, and 60% and the target pion mis-identification probabilities are 5%, 3%, 2%, and 1.2%. Two additional selectors, optimized for muons in the momentum range [0.3, 0.7] GeV/c, with a target efficiency of 70% and 60% have been developed. With roughly the same efficiency, the BDT based muon selectors are significantly more effective in rejecting the pion contamination with respect to the selectors based on Neural Networks, as can be seen from Table 5.2.1.

For the other charged particles (electrons, pions, kaons, and protons), a class of selectors based on the *Error Correcting Output Code* algorithms (Dietterich and Bakiri, 1995) is used. The discrimination is based on 36 variables from the four inner subdetectors: SVT, DCH, DIRC, and EMC. Candidate e, π, K, and p are separated by means of several binary classifiers (in our case BDT's) combined through an *exhaustive matrix* (see Chapter 4). The use of the exhaustive matrix ensures the robustness of this type of selector against potential mis-classifications of some of the binary classifiers. The selectors are trained on high purity data samples (see Section 5.3) and the cuts on the outputs of the binary classifiers are tuned in such a way that the selection efficiency matches that of the analogous likelihood based selectors. Six levels of tightness are provided (SuperLoose, VeryLoose, Loose, Tight, VeryTight, and SuperTight). At the same level of efficiency, the mis-identification rate for the ECOC algorithms is significantly lower than that of the likelihood based selectors (see Table 5.2.1).

Table 5.2.1. Efficiencies and mis-identification rates (averaged over the momentum and polar angle spectra) for different kinds of muon and kaon *BABAR* PID selectors, all using Tight requirements. The quoted uncertainty represents the typical statistical uncertainty in each bin of the tables that measures the performance of the supported selectors. No systematic uncertainty has been included.

Muon selector	efficiency (%)	π mis-id rate (%)
Cut based	65.0 ± 0.5	1.43 ± 0.05
NN	60.5 ± 0.5	0.97 ± 0.05
BDT	59.4 ± 0.5	0.76 ± 0.05
Kaon selector	efficiency (%)	π mis-id rate (%)
Cut based	80.2 ± 0.2	1.39 ± 0.07
Likelihood based	83.0 ± 0.2	1.47 ± 0.07
ECOC	84.2 ± 0.2	1.10 ± 0.07

5.3 BABAR PID performance and systematics

The tuning of the PID selectors and the assessment of their performance takes advantage of high purity samples of tracks selected from the data. A large number of electron and muon tracks is selected from $e^+e^- \to e^+e^-(\gamma)$, $\mu^+\mu^-(\gamma)$ processes, with minimal cuts on the kinematics of the event, on the quality of both the candidate track and of the other track in the event, and on the basic PID properties (to distinguish electrons from muons). For some low-statistics cross-checks, a sample of electrons (muons) from the decays $B \to J/\psi K^{(*)}$, $J/\psi \to e^+e^-$ $(\mu^+\mu^-)$ has also been used.

K and π candidates are selected from $D^{*+} \to D^0\pi^+$, $D^0 \to K^-\pi^+$. The K/π assignment is done based on the charge of the soft pion from the D^{*+} decay. The purity of the sample is increased by applying quality cuts on the reconstructed tracks, and rejecting fake D^0's using cuts on the invariant mass of the reconstructed D^0 candidate and on the likelihood that the K and π tracks originate from a common vertex. Additional π samples, especially important for measuring the mistagging of pions as muons at high momentum (where the population of $D^0 \to K^-\pi^+$ is low) are obtained from $K^0_S \to \pi^+\pi^-$ decays and from $e^+e^- \to \tau^+\tau^-$ events where one τ (tag) has one charged particle among its decay products and the other decays to a final state with three charged particles. Finally a high-purity sample of protons is obtained from $\Lambda^0 \to p\pi^-$ decays, by taking advantage of the long lifetime of the Λ^0 baryon. The purity of the sample is enhanced by applying cuts on the quality of the candidate tracks and on the probability that the proton and pion tracks are consistent with originating from the same displaced vertex. Some examples of performance of the *BABAR* selectors are displayed in Table 5.2.1 and in Figure 5.3.1.

These high purity samples are utilized in the training of the more advanced PID algorithms and in establishing the performance of all the selectors. Depending on the available statistics, the control samples are divided into several bins with different (p, θ). In the case of the muon selectors at *BABAR*, the samples are also subdivided in 6 bins of ϕ, to better characterize the degradation of the RPC chambers and the staged upgrade of the barrel section with LST detectors (see Chapter 2). Each of the selectors is applied to every bin of the control samples and the efficiencies for both the data ($\varepsilon_{\text{data}}$) and the simulation ($\varepsilon_{\text{MC}}$) are computed. The tables of efficiencies thus built are then used to correct the simulation so that its PID performance matches that of the data. One of the most widely used algorithms to apply this correction in *BABAR* is the so-called *PID-tweaking*. In the case where $\varepsilon_{\text{data}} = \varepsilon_{\text{MC}}$, no correction is applied, whereas if $\varepsilon_{\text{data}} < \varepsilon_{\text{MC}}$ a MC track that passes the selector is randomly discarded with probability

$$\frac{\varepsilon_{\text{data}}}{\varepsilon_{\text{MC}}}. \tag{5.3.1}$$

In the case $\varepsilon_{\text{data}} > \varepsilon_{\text{MC}}$, a MC track that does not pass the selection is accepted with probability

$$(\varepsilon_{\text{data}} - \varepsilon_{\text{MC}})\frac{1}{\varepsilon_{\text{MC}}}. \tag{5.3.2}$$

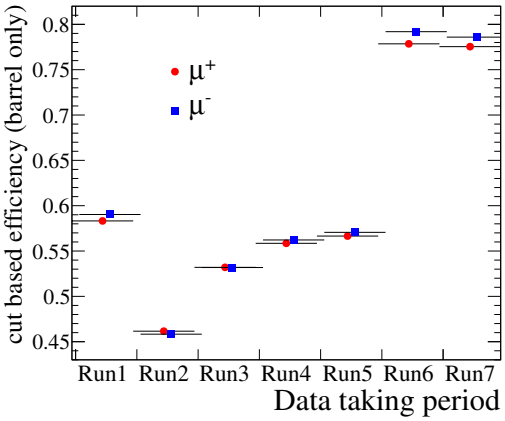

Figure 5.3.2. Muon selection efficiencies for a typical *BABAR* cut-based muon selector as a function of the data taking period. The efficiencies are computed only for the barrel region. The loss in performance due to the degradation of the RPC detector during the early phases of the data taking is evident, as is the full recovery with the installation of the LST's, completed after the end of Run5.

At the end of the *BABAR* experiment, the size of the typical correction applied by the PID-tweaking algorithm was about one percent.

5.3.1 History of PID performance in BABAR

For the *BABAR* experiment, the most important issue affecting the stability of PID performance was the degradation of the efficiency of the RPC chambers (see Chapter 2). This is visible from Fig. 5.3.2, which shows the efficiency of one of the cut-based muon selectors as a function of the data-taking period. This loss of performance was also one of the main motivations to develop muon selectors relying on variables in addition to those measured by the IFR.

5.3.2 Systematic effects

Both experiments rely on high-purity data samples to assess the performance of PID selectors and correct the simulation so that it matches the data as much as possible. Several ways exist to estimate the systematic uncertainty in a measurement related to PID requirements. It is not possible to establish a recommended way to proceed for all analyses, since in general the performance of each selector can be sensitive to the charged and neutral multiplicity of the events studied. For example, the performance of electron and muon selectors is studied in low multiplicity events, thus some care must be taken when applying these selectors to B-decays, where the multiplicity of the final states is substantially higher.

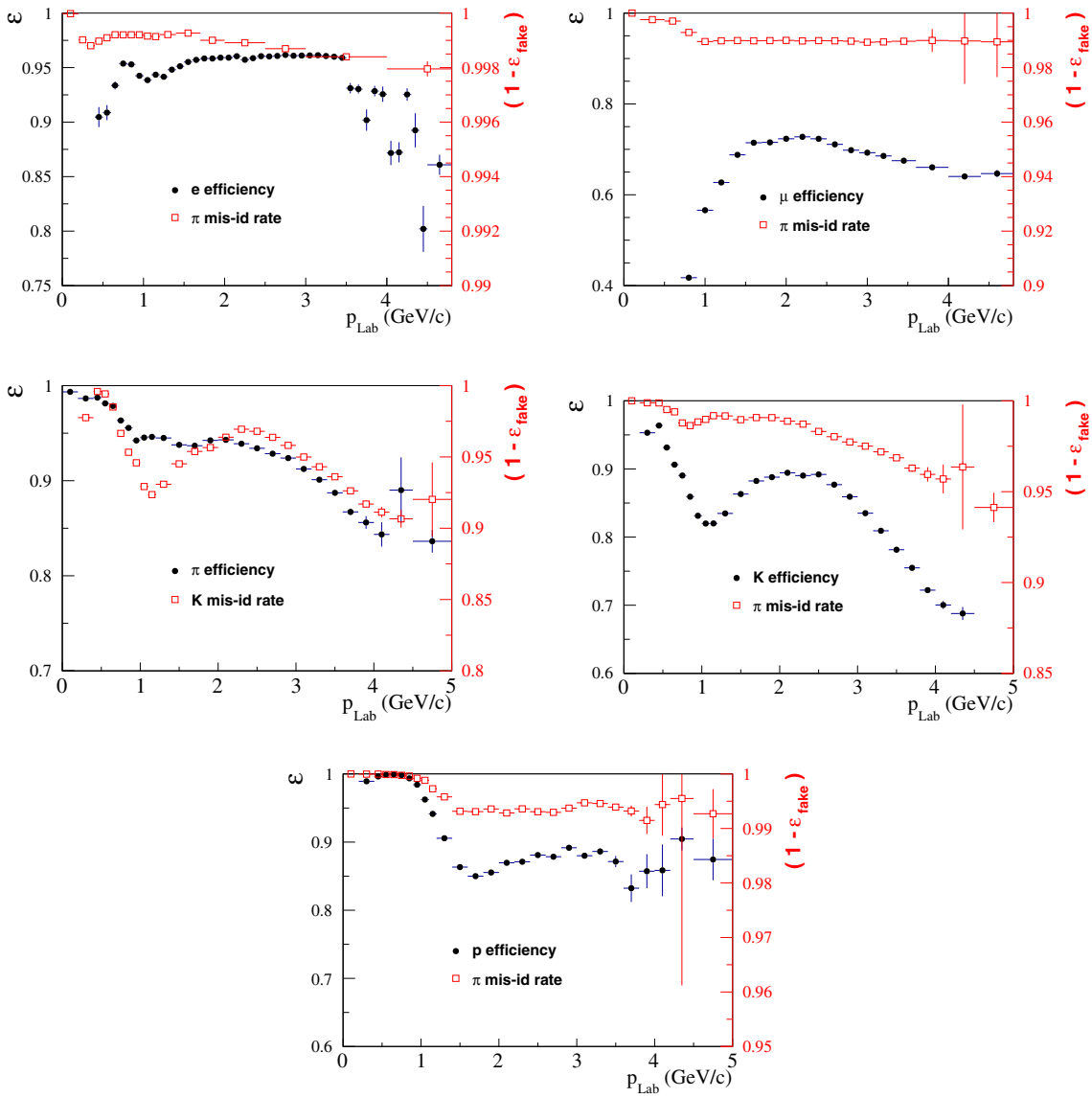

Figure 5.3.1. Performance of some typical *BABAR* PID selectors for electrons (top left plot), muons (top right), pions (middle left), kaons (middle right), and protons (bottom) as a function of the momentum of the candidate charged track. The solid (black) dots represent the efficiency, which can be read off the left axis, of the particular selectors, while the empty (red) squares show the complement (*e.g.* kaon for the pion selector, and pion for all other selectors) mis-identification probability (right axis). Note that the vertical scale differs from plot to plot.

In *BABAR*, many of the analyses estimate the systematic uncertainty on the PID performance by taking the difference of the signal reconstruction efficiency in the simulation obtained by applying or not applying the correction (usually the PID-tweaking) based on the efficiency tables described above. For some analyses where the relative contribution of the PID to the total systematic uncertainty is large, or there is a sizable dependence on the multiplicities and the topologies of the events, alternative strategies have been applied, and where possible the performance of the chosen selector(s) has been checked in control samples with similar track multiplicities and topologies of the channel under study.

5.4 Belle PID performance and systematics

In Belle, the PID performance of the kaon and pion identification algorithm is estimated using the decay $D^{*+} \rightarrow$

$D^0\pi^+$ followed by $D^0 \to K^-\pi^+$, similar to *BABAR*. Figure 5.4.1 (a) and (b) shows typical curves of the efficiencies and mis-identification rates for the kaon and pion identification in the barrel region, studied with this control sample. Discrepancies between data and MC can be seen, especially in the mis-identification.

In the study of the kaon and pion identification, the control sample is divided into 384 bins, *i.e.* 32 momentum (p) bins and 12 polar angle (θ) bins. The momentum range is divided into 100 (200) MeV/c bins below (above) 3 GeV/c. The polar angle subdivision is based on the structure of the ACC: one θ bin for the backward endcap (with no ACC), and one bin for each of the ten types of aerogel counter module in the barrel and forward endcap, except for the large polar angle range covered by the $n = 1.010$ modules, which is divided in two (see Figure 2.2.8, and the accompanying text in Section 2.2.3).

For each bin, the efficiency and mis-identification rate for K and π are estimated both for the data and the MC for different PID selections. The relevant value for general analyses is the ratio of the efficiency or mis-identification rate between the data and the MC: $R_l = \epsilon_l^{\rm data}/\epsilon_l^{\rm MC}$ and its uncertainty, where l is the bin index. These quantities are provided as a look-up table for general use in Belle analyses. The efficiency (mis-identification rate) ratio and its uncertainty for a given analysis, which is quoted as the systematic uncertainty from PID, can then be calculated by

$$R = \frac{1}{N}\sum_l n_l R_l, \tag{5.4.1}$$

and

$$\delta R = \frac{1}{N}\left(\sqrt{\sum_l \left(n_l \delta R_l^{\rm stat}\right)^2} + \sum_l n_l \delta R_l^{\rm syst}\right) + \delta R_{\rm const}, \tag{5.4.2}$$

where R_l is the efficiency ratio in bin l, n_l is the number of tracks in that bin (analysis dependent), and $N = \sum n_l$. The parameters $\delta R_l^{\rm stat}$ and $\delta R_l^{\rm syst}$ are respectively the statistical and systematic uncertainties in bin l obtained from the control sample study; $\delta R_{\rm const}$ is an additional systematic uncertainty, independent of (p, θ), based on variations in efficiency between different data taking periods ("experiments" in Belle nomenclature: see Section 3.2). In this way, the correction factor and the systematic error can be automatically calculated. The typical systematic uncertainty δR for kaon and pion identification at Belle is 0.8%. In physics analyses that measure a direct *CP* asymmetry, the systematic error due to an asymmetry in the PID efficiency between positive and negative charged tracks needs to be estimated. This error can be calculated by using the tables for R_l, $\delta R_l^{\rm stat}$, and $\delta R_l^{\rm syst}$, which are provided separately for positive and negative particles.

The study of the proton identification is performed with $\Lambda \to p\pi^-$, using the same binning for θ as above, but with only 12 bins for momentum. The typical proton efficiency is shown in Fig. 5.4.1 (c).

For the study of the lepton identification, the two-photon process $e^+e^- \to e^+e^-\ell^+\ell^-$ ($\ell = e, \mu$) is used to obtain high statistics electron and muon samples. The control sample is divided into 70 bins (10 momentum bins in 500 MeV/c steps and 7 polar angle bins). The efficiencies of the lepton identifications estimated using this process are shown in Fig. 5.4.1 (d) and (e). Since the above process leads to low track-multiplicity events, inclusive J/ψ events ($J/\psi \to \ell^+\ell^-$) are also used as a control sample, mainly for the estimation of a possible performance difference between low-multiplicity events and hadronic events. The mis-identification rates of the lepton identification for pions and kaons, are studied using a control sample of $K^0_S \to \pi\pi$ and $D^{*+} \to D^0\pi^+ \to K^-\pi^+\pi^+$.

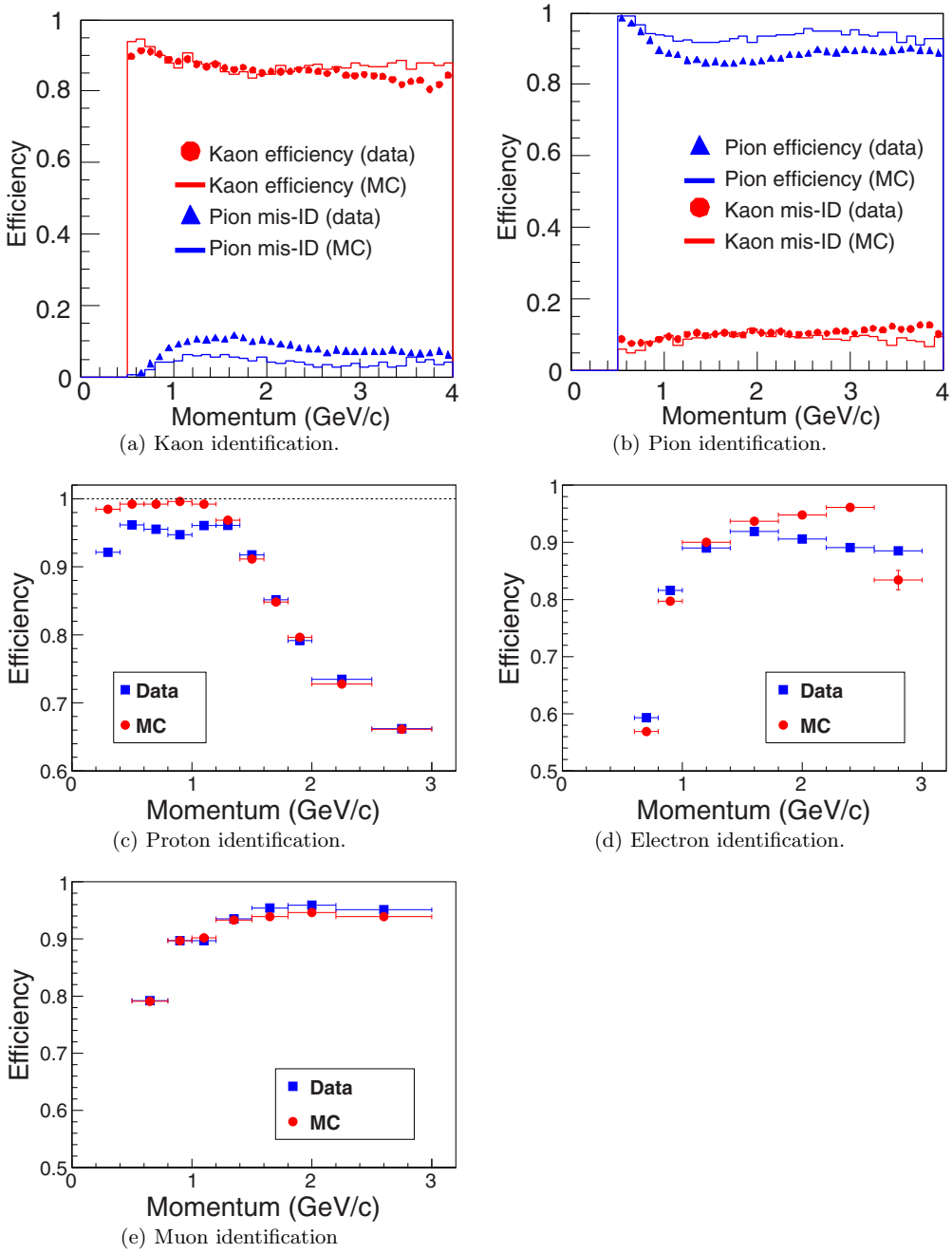

(a) Kaon identification.

(b) Pion identification.

(c) Proton identification.

(d) Electron identification.

(e) Muon identification

Figure 5.4.1. Performance of the PID at Belle as a function of the momentum of the candidate charged track for the data and MC-simulated events. (a) Performance of kaon identification: kaon efficiency and pion mis-identification rate. (b) Performance of pion identification: pion efficiency and kaon mis-identification rate. (c) Performance of proton identification. (d) Performance of electron identification. (e) Performance of muon identification. In (c), (d) and (e), only efficiencies respectively for protons, electrons and muons are shown for the data and MC simulated events.

Chapter 6
Vertexing

Editors:
Wouter Hulsbergen (BABAR)
Takeo Higuchi (Belle)

Additional section writers:
Maurizio Martinelli

6.1 The role of vertexing in the B Factories

A vertex algorithm is a procedure by which the parameters of a decay vertex or interaction vertex are determined from the reconstructed parameters of the outgoing particles. In the simplest case the outgoing particles are charged particles that are either stable or have a large $c\tau$ (where τ is the particle lifetime) compared to the dimensions of the detector, namely electrons, muons, protons and charged pions and kaons. These particles are reconstructed as charged particle trajectories (or 'tracks') in the tracking detectors and their reconstructed parameters are the track parameters. More complicated vertex algorithms involve final states that include not only tracks, but also photons or other decaying particles.

The role of vertexing algorithms in the B Factory experiments can roughly be divided in three parts. First, vertex fits are used to obtain the parameters of reconstructed 'composite' particles from their decay products, *i.e.* charged particle trajectories and photon calorimeter clusters. These parameters are usually the vertex position, momentum and invariant mass of the decaying particle. However, also the decay length of an unstable particle inside a decay chain (such as the D meson in a $B \to D\pi$ decay), or the decay time difference Δt of the two B mesons from an $\Upsilon(4S)$ decay, can be computed with a vertex fit.

Second, the χ^2 of a vertex fit is used to suppress combinatorial background in the selection of composite particles. Apart from a few cases of decays in flight (pions and long lived strange hadrons), the decay products from most composite particles all originate from a small region around the interaction point. The track parameter resolution of B Factories is just sufficient to separate the decay vertices of bottom and charm mesons. When searching for exclusive decays a requirement on the vertex χ^2 provides an efficient way to reject wrong combinations from the composite particle candidates. The χ^2 plays a similar role in the reconstruction of the primary interaction vertex or in the reconstruction of the 'second' B vertex for the determination of B meson decay time difference. In that case the contribution of individual tracks to the vertex χ^2 is used to select the subset of tracks that best determines the vertex position.

Finally, vertexing is used in the calibration and monitoring of the position and size of the interaction region. As we shall see, information on the average position of the primary vertex can be used as a constraint in vertex fits. In the *BABAR* and Belle experiments the beam parameters are also fed back in real time to the accelerator for diagnostics.

This chapter is organized as follows. The parameterization of reconstructed tracks, which defines the input to the vertex algorithms, is described in Section 6.2. Vertex fitting algorithms are discussed in Section 6.3. The calibration of the interaction region for use in vertex fits is described in Section 6.4. An important application of vertex fits is the determination of decay times, in particular the B meson decay time difference Δt. The demands on vertex resolution in the B Factory experiments are primarily determined by the requirement that Δt be measured with sufficient precision to probe $B^0\overline{B}^0$ oscillations. The procedures by which the decay time difference is estimated and its resolution calibrated are discussed in Sections 6.5.

6.2 Track parameterization and resolution

If stochastic processes like energy loss and multiple scattering in detector material are ignored, the trajectory of a charged particle in a magnetic field can be described by five parameters. In a uniform magnetic field the trajectory follows a helix. The helix axis is parallel to the magnetic field, which in the B Factory solenoids is almost parallel to the e^+-e^- beam axis.

Even in the case that the field is not uniform or material effects cannot be ignored, the track can locally be parameterized as a helix. With respect to a conveniently chosen pivot point, the parameters can be defined as (see Chapter 2 for the definition of the coordinate system)

d_ρ or d_0	signed distance in the x-y plane from the pivotal point to the helix,
ϕ_0	azimuthal angle from the pivotal point to the helix center,
κ or ω	inverse of the track transverse momentum times charge of the track, $\kappa = e/p_t$
d_z or z_0	signed distance along the z axis from the pivotal point to the helix,
$\tan\lambda$	tangent of the dip angle.

The two experiments follow a slightly different notation and definition. When two names are shown in the first column of the table above, the first is for Belle and the second for *BABAR* . The sign of the inverse transverse momentum κ coincides with the sign of the charge of the particle. If the pivot point is the origin, then d_ρ is the (signed)[19] minimum distance to the z-axis and d_z is the z-coordinate of the point-of-closest approach to the origin. The azimuthal coordinate ϕ is the angle of the transverse momentum vector with the x axis in *BABAR* while the coordinate $\phi + \phi_0$ is the angle of the transverse momentum vector with the y axis in Belle. In the following we use the Belle definition, illustrated in Fig. 6.2.1. The *BABAR* definition can be found in (Hulsbergen, 2005).

[19] Sign of d_ρ: for $e > 0$ and the pivot point lying outside the helix projection to the (x, y) plane then $d_\rho > 0$; for the pivot point inside the helix projection $d_\rho < 0$. For $e < 0$ this definition is reversed.

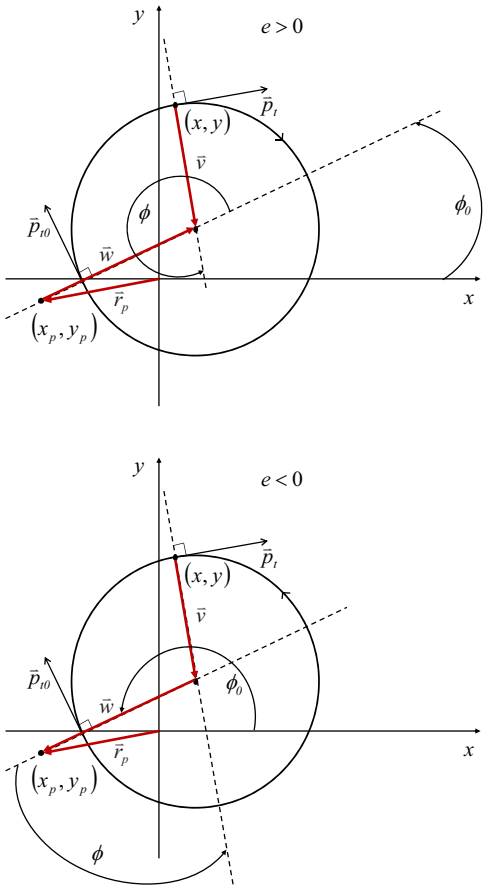

Figure 6.2.1. Schematic representations of the helix parameterization for a positively (top) and negatively (bottom) charged track in the (x, y) plane used at Belle. Magnetic field is in the direction of the z-axis. Vector $\boldsymbol{r}_p$ determines position of the pivot point. Other vectors in the figure are defined as $\boldsymbol{r} = \boldsymbol{r}_p + \mathrm{sgn}(e)\boldsymbol{w} - \boldsymbol{v}$, where $\boldsymbol{w} = \mathrm{sgn}(e)(d_\rho + \rho)(\cos\phi_0, \sin\phi_0)$, $\boldsymbol{v} = \rho(\cos(\phi_0 + \phi), \sin(\phi_0 + \phi))$.

The charged particle position along the track trajectory can be represented using a running parameter ϕ as

$$\begin{aligned} x(\phi) &= x_p + d_\rho \cos\phi_0 + \rho\{\cos\phi_0 - \cos(\phi_0 + \phi)\}, \\ y(\phi) &= y_p + d_\rho \sin\phi_0 + \rho\{\sin\phi_0 - \sin(\phi_0 + \phi)\}, \\ z(\phi) &= z_p + d_z - r\phi\tan\lambda, \end{aligned} \tag{6.2.1}$$

where (x_p, y_p, z_p) is the pivot point and $\rho = 1/B_z\kappa$ is the (signed) curvature radius with B_z representing the strength of the magnetic field. Using $p_\mathrm{t} = e/\kappa$ the momentum vector along the trajectory is given by

$$\begin{aligned} p_x(\phi) &= -p_\mathrm{t}\sin(\phi_0 + \phi), \\ p_y(\phi) &= \ p_\mathrm{t}\cos(\phi_0 + \phi), \\ p_z(\phi) &= \ p_\mathrm{t}\tan\lambda. \end{aligned} \tag{6.2.2}$$

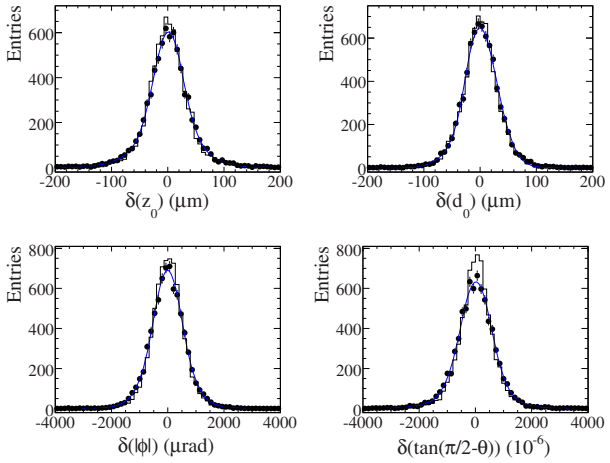

Figure 6.2.2. Measurements of the differences between the fitted track parameters of the top and bottom stubs of cosmic ray muons with a momentum above 2 GeV/c in *BABAR*. The data are shown as points, Monte Carlo simulation as histograms. The (blue) smooth curves are the results of a Gaussian fit to the data. From (Brown, Gritsan, Guo, and Roberts, 2009).

Expressions for the inverse transformation — from position and momentum vector to helix parameters — and the corresponding Jacobian can be found in (Hulsbergen, 2005).

The helix track parameters are determined by a fit to the measured hit coordinates along the track. Both Belle and *BABAR* use a track fit based on a Kalman filter (Fruhwirth, 1987). The *BABAR* track fit is described in (Brown, 1997). The track parameter resolution is determined by the number of hits and the hit resolution, and by multiple scattering and energy loss. For the resolution on the direction and position of the track the first two layers in the vertex detector are most important. However, for the extrapolation to the interaction point the curvature resolution is relevant as well. Both B Factory experiments feature a multi-layer vertex detector (Section 2.2.1) with a hit resolution in the range $10 - 50$ μm to precisely measure impact parameters. A precise curvature resolution is facilitated by a large drift chamber.

An estimate of the track resolution in data can be obtained from cosmic ray events. The muon trajectory is reconstructed as two separate segments in the top and bottom halves of the tracking detector. The difference or 'residual' between the reconstructed parameter of the segments at their point of closest approach is representative for the actual parameter resolution, after a correction with a factor $\sqrt{2}$. The distribution of the residuals is shown in Figure 6.2.2 for muons with momenta above 2 GeV/c in *BABAR* data and Monte Carlo. From a fit with a single Gaussian to these distributions the single-track resolution in data is estimated as 29 μm for z_0, 24 μm for d_0, 0.45 mrad for ϕ_0 and $0.53 \cdot 10^{-3}$ for $\tan\lambda$ (Brown, Gritsan, Guo, and Roberts, 2009) (see Chapter 2 for a discussion of the p_T resolution). The parameter resolution in Belle

is similar. It should be noted, however, that due to the contribution from multiple scattering the resolutions are a rather strong function of momentum. For example, in *BABAR* the d_0 resolution at $p_T \approx 0.1$ GeV/c^2 is over a factor 5 worse than at $p_T \approx 3$ GeV/c^2 (Aubert, 2002j).

Besides the track parameters the track fit also computes a track parameter covariance matrix, which can be used in vertex fits. The covariance matrix is among others a function of the estimated uncertainty in the hit coordinates and the estimated RMS of the scattering angle distribution. Due to pattern recognition mistakes and simplifications in the track model, the estimated track parameter uncertainty may not perfectly reflect the RMS of the error distribution. In Belle these imperfections are compensated by scale factors that depend on track p_T and $\tan\lambda$. The scale factors are calibrated with cosmic ray events and simulations. In Babar such scale factors are not used.

6.3 Vertex fitting by χ^2 minimization

The B Factory experiments have deployed several implementations of vertex fits. A complete description of these algorithms is outside the scope of this book. In the following we sketch the formalism of a generic minimum χ^2 vertex algorithm. A pedagogical introduction to vertex fitting can be found in the lectures by P. Avery (Avery, 1991, 1998).

To start, we consider a collection of N charged tracks and use a χ^2 minimization algorithm to determine the best vertex out of which they emerge. Once that is done, the vertex can be improved by adding neutral particles, enforcing mass constraints to the in-going or some of the outgoing composite particles, and requiring consistency of the vertex location with the collider luminous region. The goodness of a fit is measured by testing the compatibility of the minimum χ^2 with the expected probability distribution of a χ^2 with the relevant number of degrees of freedom.

Following the notation in (Fruhwirth, 1987) we denote the reconstructed helix parameters of track i by $\boldsymbol{p}_i$ and the corresponding covariance matrix by V_i. Given a set of N outgoing tracks each labeled with an index i, the χ^2 of the vertex can be generically written as

$$\chi^2 \;=\; \sum_{i=1}^{N} \left[\boldsymbol{p}_i - \boldsymbol{h}_i(\boldsymbol{x}, \boldsymbol{q}_i)\right]^T V_i^{-1} \left[\boldsymbol{p}_i - \boldsymbol{h}_i(\boldsymbol{x}, \boldsymbol{q}_i)\right] \quad (6.3.1)$$

where $\boldsymbol{x}$ is a 3D vector representing the fitted vertex position, $\boldsymbol{q}_i$ is the fitted momentum vector of the outgoing track and $\boldsymbol{h}_i$, the measurement model, is a function of $\boldsymbol{x}$ and $\boldsymbol{q}_i$ that expresses the parameters of the helical trajectory of the charged particle emerging from the vertex with momentum $\boldsymbol{q}_i$.

The solution to the vertex fit is the set of parameters $\widehat{\boldsymbol{\xi}} \equiv (\boldsymbol{x}, \boldsymbol{q}_1 \ldots \boldsymbol{q}_N)$ that minimizes the χ^2. In case the function $\boldsymbol{h}_i$ is linear in the parameters $\boldsymbol{\xi}$, the solution can be expressed generically as

$$\widehat{\boldsymbol{\xi}} \;=\; \boldsymbol{\xi}_0 - \left[\frac{d^2\chi^2}{d\boldsymbol{\xi}^2}(\boldsymbol{\xi}_0)\right]^{-1} \frac{d\chi^2}{d\boldsymbol{\xi}}(\boldsymbol{\xi}_0) \quad (6.3.2)$$

where $\boldsymbol{\xi}_0$ is an arbitrary starting point for $\boldsymbol{\xi}$. The inverse of the second derivative matrix on the right hand side is also half the covariance matrix for $\widehat{\boldsymbol{\xi}}$. If the derivative of $\boldsymbol{h}_i$ is denoted by $\boldsymbol{H}_i$, this leads to the well known expression for the linear least squares estimator,

$$\widehat{\boldsymbol{\xi}} \;=\; \boldsymbol{\xi}_0 - C \sum_i \boldsymbol{H}_i^T V_i^{-1} \left[\boldsymbol{p}_i - \boldsymbol{h}_i(\boldsymbol{x}, \boldsymbol{q}_i)\right] \quad (6.3.3)$$

with the covariance matrix

$$C \;=\; \left(\sum_i \boldsymbol{H}_i^T V_i^{-1} \boldsymbol{H}_i\right)^{-1}. \quad (6.3.4)$$

For vertex fits to helix trajectories the function $\boldsymbol{h}_i$ is not linear and hence its derivative $\boldsymbol{H}_i$ not constant. In that case the minimum is obtained by starting from a suitable expansion point $\boldsymbol{\xi}_0$ and iteratively applying Eq. (6.3.2) until a certain convergence criterion is met, usually a minimum change in the χ^2.

There are two flavors of measurement models for tracks in vertex fits: If the parameters $\boldsymbol{p}_i$ are helix parameters, the measurement model is given by the inverse of Eq. (6.2.1) and Eq. (6.2.2) above. Alternatively, the track parameters can also be translated into position and momentum space using Eq. (6.2.1) and Eq. (6.2.2). In this case the measurement model is trivial, but has one dimension more than the original five parameter helix. Furthermore, since the transformation only applies to a particular point on the helix, it needs to be repeated if the vertex position estimate changes between iterations.

The number of degrees of freedom of the computed χ^2 is $N_{DOF} \equiv 2N - 3$, *i.e.* the difference between the number of measurements, $5N$ (5 helix parameters per track) and the number of fitted parameters $3(N + 1)$ (3 vertex coordinates and 3 momentum components per track). Assuming that the uncertainties on the track parameters are correctly estimated *i.e.* that they are representative of the RMS of the error distribution, the minimum χ^2 follows the probability distribution of a χ^2 variate with N_{DOF} degrees of freedom whose expectation value equals N_{DOF}. A goodness of fit requirement is usually derived from χ^2 and N_{DOF} to retain the acceptable N-prong vertices *e.g.* in the selection of event data samples.

The vertex fitting formalism can be extended with additional constraints, such as prior knowledge of the vertex position (for example from knowledge of the interaction point, IP) or the known mass of the decaying particle. Such constraints always take the form of a constraint equation

$$f(\boldsymbol{\xi}) \;=\; 0. \quad (6.3.5)$$

A distinction can be made between exact constraints and constraints that have an associated uncertainty. The latter are sometimes called 'χ^2 constraints'. Mass constraints are

usually (but not always) implemented as exact constraints while IP constraints are an example of a χ^2 constraint. Exact constraints can be implemented by using a Lagrange multiplier. They add a term to the χ^2

$$\Delta\chi^2 \;=\; \lambda f(\boldsymbol{\xi}) \tag{6.3.6}$$

where the Lagrange multiplier λ is treated as an additional parameter in the vertex fit. An alternative (more efficient) method to deal with exact constraints is discussed in (Hulsbergen, 2005). For one-dimensional constraints with an uncertainty σ the χ^2 contribution is

$$\Delta\chi^2 \;=\; \frac{f(\boldsymbol{\xi})^2}{\sigma^2}. \tag{6.3.7}$$

This expression can be generalized to more than one dimension by writing it in a matrix notation. Note that each independent constraint adds one degree of freedom to the χ^2.

The vertex fit can also be extended to include reconstructed neutral particles. Photons reconstructed as calorimeter clusters do not add position information to the vertex, but they contribute to the momentum, and affect the χ^2 minimization once mass constraints are applied.

Several vertex fits are implemented in sequence to reconstruct decay trees that involve more than one decay vertex, *e.g.* $B \to DX$ transitions. Such decay trees are usually reconstructed by starting from the most downstream vertex and working towards the mother of the decay trees: first fit the D vertex, then use the result to fit the B (this approach is sometimes called leaf-by-leaf fitting). Other more global associations of constraints are implemented for decay trees with leaves or branches with many neutral particles (Hulsbergen, 2005).

The vertex fits applied in the B Factory experiments are essentially extensions of the scheme above – see in particular (Tanaka, 2001) for Belle and (Hulsbergen, 2005) for *BABAR*. Implementations of the vertex fitting algorithm differ both in the parameterization of the problem and in the way the χ^2 is minimized. As outlined above, tracks can be parameterized in terms of helix coordinates or (locally) in terms of Cartesian coordinates. The latter leads to simpler expressions for derivatives, but may lead to slower convergence because derivatives vary more rapidly along the track.

For the minimization both the global χ^2 fit technique described above and the Kalman filter are used. Even for algorithms that seemingly use the same minimization scheme, the implementations may differ. To our knowledge, the most efficient method to fit tracks to a common vertex is the algorithm developed by Billoir, Fruhwirth, and Regler (1985), presented in slightly different from in (Fruhwirth, 1987). This algorithm was extended with a mass constraint in (Amoraal et al., 2013).

Not all algorithms are applicable to all vertexing problems. The general leaf-by-leaf approach for decay tree fitting cannot easily be applied to the reconstruction of *e.g.* $K^0_S \to \pi^0\pi^0$ or $B^0 \to K^0_S\pi^0$. For these types of decay trees a 'global' decay tree fit can be used (Hulsbergen, 2005). The latter also has the advantage that one has access to the vertex-constrained parameters of all particles in the decay tree. However, this algorithm computes a single covariance matrix for all of the parameters in the decay tree, making it noticeably slower than a leaf-by-leaf approach. The CPU consumption of vertex algorithms is often a concern because of the combinatoric background in the reconstruction and selection of composite particles.

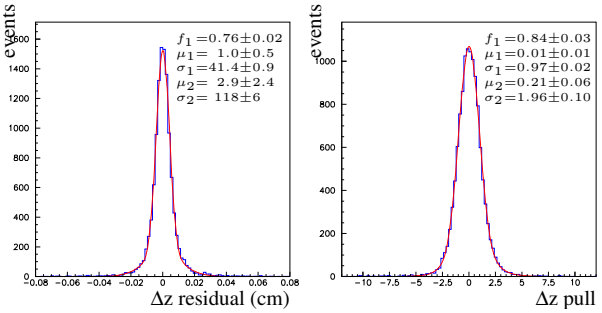

Figure 6.3.1. Residual (left) and pull (right) of the decay vertex z position of reconstructed $B^0 \to J/\psi K^0_S$ candidates in a *BABAR* simulated data sample. Fits to a double Gaussian are superimposed.

A strict control on the accuracy of the vertex reconstruction is mandatory for the B Factory experiments where the primary goal is to determine time-dependent *CP* asymmetries from the distance between two vertices. This is illustrated in Figure 6.3.1 which shows the residuals and pull[20] for the decay vertex z position of reconstructed $B^0 \to J/\psi K^0_S$ ($J/\psi \to \mu^+\mu^-$) candidates from a sample of simulated data taken from *BABAR*. The vertex resolution depends on the topology of the decay and the direction and momenta of the final state particles and especially on whether the K^0_S particles decays inside or outside the vertex detector volume. These effects are accounted for in the per-event reconstruction uncertainty, the estimate of which is computed by the vertex fit algorithm. Due to spread in the estimated uncertainty, the vertex resolution is not a Gaussian distribution. However, the pull distribution is reasonably Gaussian with an RMS value close to unity, indicating that the uncertainties are correctly estimated.

For this decay the z residual distribution has an RMS of about 70 μm. A double Gaussian fit returns a core component, which corresponds to about three quarters of the distribution, with a standard deviation equal to 40 μm. The resolution in the transverse coordinates is comparable to that in z: about 50 μm.

Figure 6.3.2 shows the reconstructed mass of $B^\pm \to J/\psi K^\pm$ decays in data, from *BABAR*, fitted both with and without a mass constraint on the $J/\psi \to \mu^+\mu^-$ decay. The mass constraint improves the accuracy of the derived J/ψ momentum and this leads to a large improvement in the $B^\pm$ invariant mass resolution. The improvement in mass resolution is comparable to what one would obtain

[20] A 'pull' is a residual divided by its estimated uncertainty. See also Section 11.5.2.

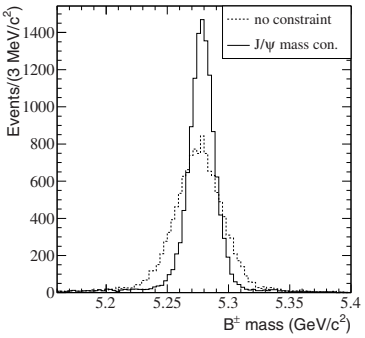

Figure 6.3.2. Distribution of the reconstructed invariant mass of $B^{\pm} \to J/\psi K^{\pm}$ decays in *BABAR* data with and without enforcement of a mass constraint on the $J/\psi \to \mu^+\mu^-$ decay vertex leaf.

by considering the $B^{\pm}$-J/ψ mass difference instead of the $B^{\pm}$ mass. However, the advantage of applying the mass-constrained vertex fit is that the resolution on both the vertex position and on the B momentum are improved.

6.4 Primary vertex reconstruction and beamspot calibration

The majority of beam-beam collisions occur in a tiny region in the center of the detectors, the interaction region or *beamspot*. The size of the interaction region is determined by beam optics and has varied through the B Factory runs. It is typically 1 mm along the beam (z), 100 μm in the horizontal direction (x) and a few μm in the vertical direction (y).

The position and size of the beamspot are used as a constraint in the reconstruction of the $B^0\overline{B}^0$ decay time difference Δt. Since the beamspot is smallest in the vertical plane, the vertical coordinate is the most constraining. In the directions along x and z the beamspot is not smaller than a typical B decay length, which is about 25 μm in the transverse plane and about 200 μm along the z-axis, and its constraint plays a marginal role.

The position and shape of the interaction region vary with time and needs to be carefully calibrated and monitored. The calibration is based on the spatial distribution of reconstructed primary vertices (PVs). In the production of a $B^0\overline{B}^0$ or B^+B^- pair at the $\Upsilon(4S)$ resonance there are no particles originating from the primary collision point other than the B mesons themselves. Consequently, the primary vertex cannot be directly reconstructed in these decays and the beamspot calibration instead relies on continuum events. Bhabha and di-muon events have the advantage that there are only two tracks in the event, that have both relatively high momentum and are guaranteed to originate from the PV. Hadronic events have more tracks and consequently a smaller statistical per-event uncertainty on the vertex position, but they are polluted by a $b\bar{b}$ contribution. The calibration

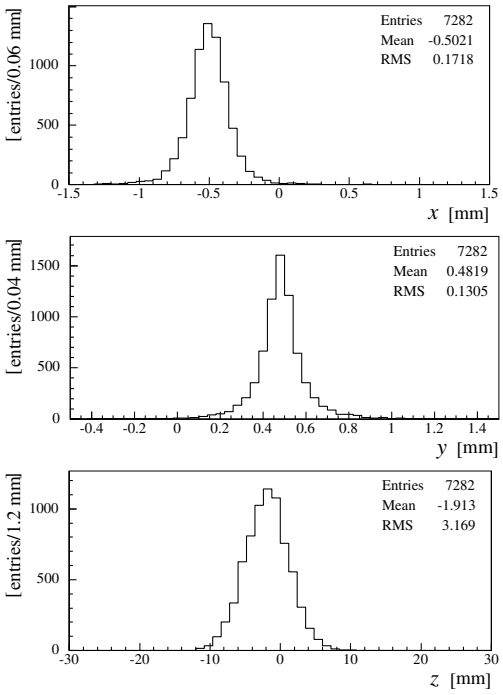

Figure 6.4.1. Distribution of the x (top), y (middle), and z (bottom) position of reconstructed primary vertices in a typical Belle run (Exp. 5, run 333). From (Tomura, 2002a).

in *BABAR* relies both on two-prong events and on multi-hadron events with at least 5 tracks. The calibration procedure in Belle uses only multi-hadron events (Tomura, 2002a).

An example of the distribution of the position of reconstructed primary vertices in hadronic events in a typical Belle run is shown in Figure 6.4.1. In the y direction the RMS of the distribution is dominated by the vertex resolution. In the z direction it is dominated by the beamspot size, while in the x direction it is a combination of both.

The distribution of PV positions is characterized by an average position, the direction of its three principal axes (which are close, but not identical to the x, y and z axis; see Chapter 2) and the RMS along each axis. The calibrated position, rotation and sizes are determined from moments of (*BABAR*) or fits to (Belle) the (x, y, z) distribution of PVs.

To determine the size of the beamspot the vertex resolution must be 'subtracted'. In the vertical direction since the resolution is so much wider than the beam size, the beam spread must be estimated by other means. In *BABAR* the size in y is computed from the luminosity reported by the accelerator (Chapter 1). In Belle it is obtained from measurements of the size of the HER and LER beams by the accelerator (Tomura, 2002a). When the beamspot is used as a constraint in vertex fits, its size always appears in quadrature with the actual vertex resolution. Hence, it is important to know the size in the vertical direction precisely.

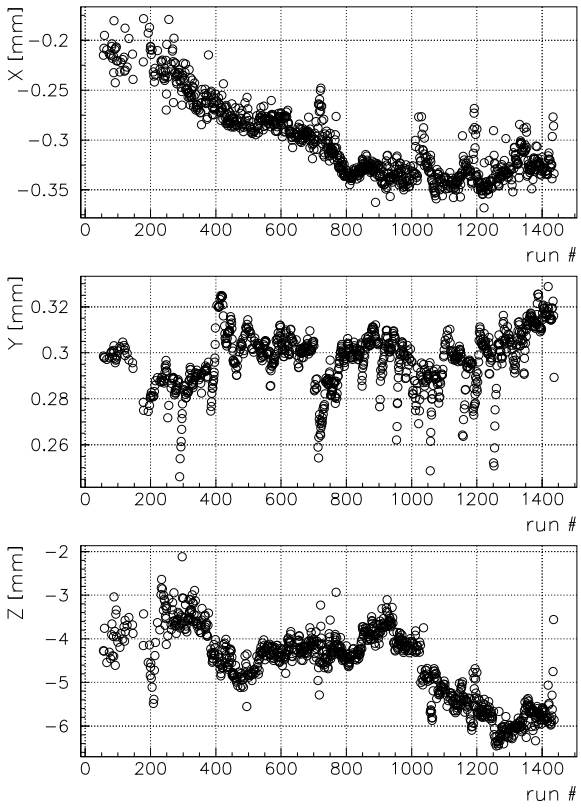

Figure 6.4.2. Average primary vertex position in x (top), y (center) and z (bottom) as a function of run number in Belle data. From (Tomura, 2002a).

To accommodate variations over time the calibration procedure is performed in time slices. Belle fits the mean position with the other parameters (the widths and the rotation angles) fixed for every $\mathcal{O}(10^4)$ events. *BABAR* updates all parameters every $\sim$ 10 minute interval, corresponding to approximately the same number of selected events. Figure 6.4.2 shows the average primary vertex position as a function of run number in the early days of Belle. In this period the typical duration of a run was about 2 hours. Under stable conditions, the variation of the position within a run is much smaller, typically of the order of 10 μm in x, 1 μm in y and 100 μm in z in both experiments.

In vertex reconstruction the average beamspot can be used as a constraint on the *production* vertex of the B (or D, or τ) particle. The χ^2 contribution takes the form, *cf.* Eq. (6.3.7),

$$\Delta\chi^2 \;=\; \begin{pmatrix} x_\mathrm{p} - x_\mathrm{IP} \\ y_\mathrm{p} - y_\mathrm{IP} \\ z_\mathrm{p} - z_\mathrm{IP} \end{pmatrix}^T V_\mathrm{IP}^{-1} \begin{pmatrix} x_\mathrm{p} - x_\mathrm{IP} \\ y_\mathrm{p} - y_\mathrm{IP} \\ z_\mathrm{p} - z_\mathrm{IP} \end{pmatrix} \qquad (6.4.1)$$

where $\boldsymbol{x}_\mathrm{p}$ are the parameters of the production vertex in the vertex fit, $\boldsymbol{x}_\mathrm{IP}$ is the position of the center of the beamspot and V_IP is a 3×3 covariance matrix, representative of the size of the beamspot. In Belle the constraint is only applied to the coordinates in the transverse plane; in *BABAR* both the 2D and 3D constraint are used, depending on the vertex algorithm. Figure 6.4.3 shows the $D^{*+} - D^0$ mass difference in $e^+e^- \to D^{*+}X$ continuum events where we have selected $D^{*+} \to D^0\pi^+$ decays with $D^0 \to K^-\pi^+$ with and without the constraint that the D^{*+} originates from the beamspot. Due to its low momentum the direction of the soft pion is very sensitive to multiple scattering. Requiring it to originate from the interaction region substantially improves the mass resolution.

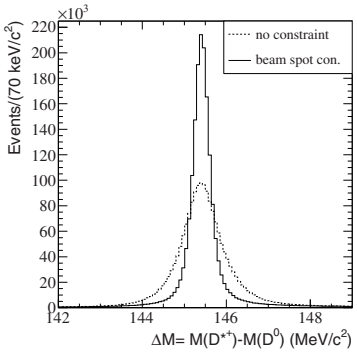

Figure 6.4.3. Distribution of the reconstructed $D^{*+} - D^0$ mass difference in $D^{*+} \to D^0\pi^+$ decays with $D^0 \to K^-\pi^+$ from *BABAR* continuum data with and without a primary vertex constraint.

In some applications, such as for D^* from B decays or the reconstruction of the associated B vertex for Δt reconstruction in Belle, the beamspot is used as a constraint on a *decay* vertex. In this case the size of the beamspot must be increased with the effective width of the decay length distribution of the (mother) particle, schematically,

$$V_\mathrm{IP,tot} \;=\; V_\mathrm{IP} \;+\; V_\mathrm{flight}\,. \qquad (6.4.2)$$

Both experiments add the RMS of the B decay length distribution in the transverse plane (about 25 μm, see Figure 6.4.4) in quadrature with the calibrated beamspot size to obtain an effective size appropriate for B decay products. This mostly affects the size in y.

Finally, although these quantities do not directly pertain to the vertex algorithms, it is convenient in the characterization of the beamspot, to mention the calibration of the beam kinematics. The beam energies are used in the computation of *e.g.* the beam-energy-constrained mass (Chapter 9) and the proper decay time. In principle, there are six unknown parameters related to the incident beams, namely the 3-momenta of the electron and positron beam. In practice, the beam-directions are close enough to their nominal direction that only the relative direction matters, reducing the number of degrees of freedom to four. These are parameterized by the center-of-momentum energy $\sqrt{s}$ and by the boost vector.

Both experiments calibrate $\sqrt{s}$ with the kinematics of fully reconstructed hadronic B decays. In particular, a

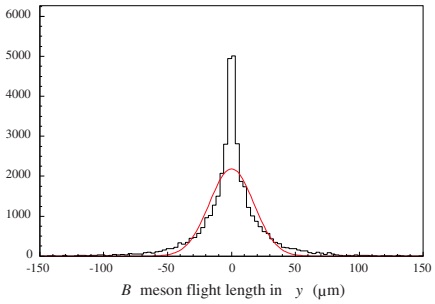

Figure 6.4.4. Distribution of the B meson flight length in the y direction in Belle simulated data. A fit to a single Gaussian (red), with a width of 25 μm, is superimposed.

deviation of $\sqrt{s}$ from nominal can be directly inferred from a shift of the beam-energy-constrained mass relative to the nominal B mass. The uncertainty is dominated by the uncertainty on the nominal B mass.

In Belle the boost vector is sufficiently constant that it has been fixed to its nominal value for the entire period of data taking. In *BABAR* the boost vector is calibrated on a run-by-run basis using the four-momentum sum in dimuon events. Note that due to effects of initial and final state radiation, the latter is not a very sensitive probe of $\sqrt{s}$.

6.5 Δt determination

The analysis of time-dependent *CP* violation in decays of neutral B mesons at the e^+e^- B Factories requires measurement of the decay time difference Δt of the two B mesons in the event (see Chapter 10). The procedures to reconstruct the vertex of the 'tagging' B and extract the decay time difference are described in (Tajima, 2004) for Belle and (Aubert, 2001c, 2002a) for *BABAR*, to which the reader is referred for details.

We denote the reconstructed B meson that decays to the final state of interest as $B_{\rm rec}$. We label the other B meson by $B_{\rm tag}$, because its decay products are used to determine the flavor of $B_{\rm rec}$ at $\Delta t = 0$. In an asymmetric e^+e^- B Factory the determination of Δt is derived from the measurement of the difference in the decay vertex positions of $B_{\rm rec}$ and $B_{\rm tag}$ along the boost axis, which is approximately the z axis. Consequently, we talk about the Δz *measurement* and the Δz *to* Δt *conversion*.

By far the dominant contribution to the resolution on Δt is the Δz resolution. For most analyses the latter is in turn dominated by the $B_{\rm tag}$ vertex resolution. The determination of the $B_{\rm rec}$ vertex position is performed with a standard vertex fit, as described above. The reconstruction of the $B_{\rm tag}$ vertex position is more complicated since it requires the selection of the subset of tracks that directly originate from the $B_{\rm tag}$ vertex.

6.5.1 Reconstruction of the $B_{\rm tag}$ vertex

Figure 6.5.1 shows schematically the topology of an event with the $B_{\rm rec}$ and $B_{\rm tag}$ decays. Since there are no other particles in the event beside the two B mesons, all tracks that are not associated to $B_{\rm rec}$, *i.e.* tracks from the *rest of the event* (ROE), necessarily originate from the $B_{\rm tag}$ decay. However, a couple of experimental complications make the reconstruction of the $B_{\rm tag}$ vertex position non-trivial. First, in only a small fraction of events, are all the decay products of the $B_{\rm tag}$ inside the acceptance of the detector, hence a strategy based on a full reconstruction is excluded.[21]

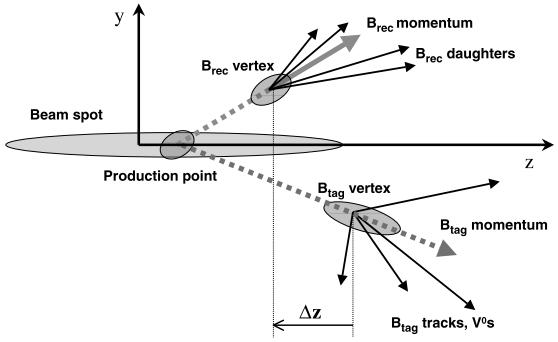

Figure 6.5.1. Schematic view of the geometry in the yz plane for a $\Upsilon(4S) \to B\overline{B}$ decay. For fully reconstructed decay modes, the line of flight of the $B_{\rm tag}$ can be estimated from the (reverse) momentum vector and the vertex position of $B_{\rm rec}$, and from the beamspot position in the xy plane and the $\Upsilon(4S)$ average boost. Note that the scale in the y direction is substantially magnified compared to that in the z direction. From (Aubert, 2002a).

Second, most $B_{\rm tag}$ mesons decay to an open-charmed particle with at least one additional vertex after a flight length comparable to the decay length of a B meson. The confusion in the assignment of the tracks between these vertices biases the measurement of the $B_{\rm tag}$ position and degrades the $B_{\rm tag}$ vertex resolution.

The strategy to select the optimal set of tracks is similar in both experiments. First, from the tracks in the ROE a subset is selected that satisfies requirements like a minimum number of vertex detector hits and a maximum transverse distance to the interaction region. Tracks from reconstructed photon conversions and V^0 decays (a neutral particle decaying into two charged tracks, for example $K^0_S \to \pi^+\pi^-$) are either removed or replaced with the mother particle. Subsequently, all tracks are combined in a single vertex using the interaction region as a constraint. If the χ^2 of the vertex is larger than a certain criterion, the worst track is removed and the vertex refitted. This procedure is repeated until the criterion is satisfied or no tracks are left. In *BABAR* the criterion is a maximum contribution to the χ^2 of 6 for each track, while in Belle the

[21] Also the sum of branching fractions of decays used in typical full reconstruction, see Chapter 7, is small.

criterion is a maximum vertex χ^2 of 20 per degree of freedom (since a track contributes two degrees of freedom, the *BABAR* criterion is substantially tighter than the Belle criterion). In Belle tracks that have been identified as high p_T leptons by the flavor tagging algorithm are always kept since those have a large probability to originate from the $B_{\rm tag}$ vertex.

If the beamspot is used as a constraint in the $B_{\rm tag}$ vertex reconstruction, even vertices with a single track can be reconstructed. The experiments exploit the beamspot differently. In Belle the constraint is an ellipsoid in the xy plane, increased in size to account for the $B_{\rm tag}$ transverse motion, as explained in Section 6.4. This use of the beamspot leads to a small bias that is proportional to the $B_{\rm tag}$ decay time and is treated as a systematic uncertainty. In *BABAR* the $B_{\rm tag}$ direction and origin are reconstructed with a vertex fit using the $B_{\rm rec}$ vertex and momentum and the calibrated beamspot position and $\Upsilon(4S)$ momentum. This $B_{\rm tag}$ 'pseudo-particle' is subsequently used as any other track in the $B_{\rm tag}$ vertex reconstruction. The advantage of this approach is that there is no bias due to the beamspot constraint. However, it can only be applied to analyses with a fully reconstructed $B_{\rm rec}$.

Since the $B_{\rm tag}$ vertex has in general fewer tracks than the $B_{\rm rec}$ vertex and may be contaminated by D daughter tracks, the Δz resolution is dominated by the $B_{\rm tag}$ z position resolution. The latter is in the range $100-200$ μm, which has to be compared to a typical resolution of the $B_{\rm rec}$ vertex of 50 μm. As the total resolution is of the order of the B mixing period, accurate knowledge of the resolution is essential when Δt is used in maximum likelihood fits to extract the parameters for time-dependent *CP* violation. The calibration of the so-called *resolution function* is discussed below.

6.5.2 From vertex positions to Δt

To be sensitive to time-dependent *CP* violating effects the vertex resolution must be sufficient to resolve the oscillations due to $B^0\overline{B}^0$ mixing in the decay time distribution. Given a proper decay time t and a momentum vector $\boldsymbol{p}$, the difference between the production and decay vertex positions of a B meson is given by

$$\boldsymbol{x}_{\rm decay}-\boldsymbol{x}_{\rm prod} \;=\; \frac{\boldsymbol{p}c}{mc^2}\,c\,t \qquad (6.5.1)$$

where we have explicitly included factors c to express momentum and mass in units of energy. At the $\Upsilon(4S)$ resonance the B momentum in the $\Upsilon(4S)$ rest frame is $p_B^*\approx 340\,{\rm MeV}/c$. With a lifetime of 1.5 ps, the B^0 decay length in the $\Upsilon(4S)$ frame is only ~ 30 μm, small compared to the typical resolution of vertex detectors. This is the main motivation for constructing an asymmetric B Factory: the boost of the $\Upsilon(4S)$ system increases the decay length, making the measurement of the decay time possible.

If the z-axis is chosen along the boost direction, the experimental resolution on the B meson decay time difference is dominated by the resolution on the decay vertex z position. The displacement in z of one of the B mesons is related to its proper decay time t by

$$z_{\rm decay}-z_{\rm prod} \;=\; \gamma\left(\alpha\cos\theta+\beta\sqrt{1+\alpha^2}\right)ct \qquad (6.5.2)$$

where γ and β are the boost parameters from the $\Upsilon(4S)$ frame to the lab frame and θ and $\alpha=p_B^*c/m_Bc^2$ are the polar angle and boost factor of the B in the $\Upsilon(4S)$ frame.

Since no tracks originate from the production vertex, the sensitivity to the decay time difference of the B mesons comes mainly through the difference in the z positions of the decay vertices. As the polar angles of the two B mesons are exactly opposite, the difference in the z positions can be expressed as

$$z_1-z_2 \;=\; \gamma\beta\sqrt{1+\alpha^2}c(t_1-t_2)+\gamma\alpha\cos\theta c(t_1+t_2). \qquad (6.5.3)$$

If the small parameter $\alpha\approx 0.06$ is ignored, one obtains the well known approximation

$$\Delta t \;=\; \Delta z/\gamma\beta c. \qquad (6.5.4)$$

This expression is used for all time-dependent analyses in Belle and for those without a fully reconstructed $B_{\rm rec}$ in *BABAR*. The average value for the boost factor is $\beta\gamma=0.55$ in *BABAR* and $\beta\gamma=0.42$ in Belle. It is calculated directly from the beam energies and has a typical uncertainty of 0.1%. For a typical Δz resolution of 100 μm, the Δt resolution is 0.6 ps, a bit less than half the B lifetime and small compared to the B^0 oscillation period of ~ 12.5 ps.

Ignoring the second term in Eq. (6.5.3) leads to a $\cos\theta$ and decay time dependent bias. If the detection efficiency is symmetric in $\cos\theta$, the expectation value of the bias is zero.[22] Ignoring the acceptance and taking $P(\cos\theta)\propto 1-\cos^2\theta$, the RMS of this term is $2\gamma\alpha c\tau_{B^0}/\sqrt{5}$, or about 30 μm (taking $\langle t_1+t_2\rangle\sim 2\tau_{B^0}$). Consequently, its contribution to the resolution is small but not negligible.

In the case of a fully reconstructed $B_{\rm rec}$ the momentum direction is measured with sufficient precision to correct for the B momentum in the $\Upsilon(4S)$ frame. However, as can be seen in Eq. (6.5.3) the correction depends on the sum of the decay times, t_1+t_2, which can only be determined with very poor resolution. *BABAR* has used the estimate $t_1+t_2=\tau_B+|\Delta t|$ to correct for the measured $B_{\rm rec}$ momentum direction and extract Δt from Eq. (6.5.3), giving

$$\Delta t \;=\; \frac{\Delta z/c \;-\; \gamma\alpha\cos\theta\,\tau_B}{\gamma\beta+s\gamma\alpha\cos\theta} \qquad (6.5.5)$$

where s is the sign of Δz and terms quadratic in α have been ignored. The distribution of the event-by-event difference between Δt computed with Eq. (6.5.4) and Eq. (6.5.5) has an RMS of 0.20 ps. Therefore, for a typical resolution of 0.6 ps, the $\cos\theta$ correction improves the Δt resolution by about 5% (Aubert, 2002a).

Equation (6.5.5) is used for most B decays to hadronic final states in *BABAR*, while Eq (6.5.4) is used for semileptonic modes. In Belle the correction is not applied, but

[22] Assuming that also the distribution of events is symmetric in $\cos\theta$, which is valid in the case of $B\overline{B}$ events.

included in the resolution model. The contribution to the resolution is computed on a per-event basis for fully reconstructed final states and empirically parameterized from simulated events for the semi-leptonic modes.

The time-dependent analysis of decays $B^0 \to K^0_S\pi^0$ and $B^0 \to K^0_S\pi^0\gamma$ is particularly challenging because there are no tracks directly originating from the $B_{\rm rec}$ vertex. In early analyses in *BABAR* (Aubert, 2004q), the $B_{\rm rec}$ vertex position was estimated from the intersection of the trajectories of one or both K^0_S daughters with the beamspot. The implementation was similar to the reconstruction of $B_{\rm tag}$ vertices with a single track and the standard Δz to Δt conversion (see above) was used. This method suffers from a bias, small compared to the resolution, but irreducible.

Eventually *BABAR* developed a third method that makes use of a decay tree fit (Hulsbergen, 2005) which was applied to a number of decays including $B^0 \to K^0_S K^0_S K^0_S$. In this algorithm the decay time difference Δt is extracted from a single vertex fit to the $\Upsilon(4S) \to B^0\overline{B}^0$ decay tree, using all reconstructed particles associated with $B_{\rm rec}$ and $B_{\rm tag}$ and knowledge of the average interaction point and $\Upsilon(4S)$ momentum. The particles missing from the $B_{\rm tag}$ vertex are parameterized as a single unconstrained four-vector at the $B_{\rm tag}$ vertex. This algorithm maximally exploits all available information from reconstruction and beam parameter calibration. It is interesting that it obtains a competitive resolution only if a constraint on the B decay time sum is applied. The latter is implemented as a χ^2 constraint $t_1 + t_2 = 2\tau_B$ with (RMS) uncertainty $\sqrt{2}\tau_B$. Note that this approach is similar but not identical to the substitution $t_1 + t_2 = \tau_B + |\Delta t|$ applied in the 'momentum corrected' method described above. It has been verified that such a constraint does not bias the Δt measurement. However, since this method does not lead to a significant improvement in resolution, it has only been applied to studies of $B^0 \to K^0_S\pi^0$ and alike.

6.5.3 Δt resolution function

To account for the finite decay time resolution the *p.d.f.* describing the physical time evolution in a time-dependent analysis is convolved with a *r*esolution function which is the response function that describes the distribution of the observed decay time as a function of the true decay time $\Delta t_{\rm true}$. To first order the resolution function is a Gaussian function with zero mean and a width corresponding to the average resolution. In practice, the deviations from a Gaussian are important. The parameterization and calibration of the resolution function is described in detail in Section 10.4. Here, we briefly emphasize features of the vertex resolution that impact the Δt resolution in time-dependent analyses.

The estimated uncertainty in the $B_{\rm tag}$ vertex z position is a function of the number of tracks assigned to the vertex and the direction and momentum of those tracks. It differs substantially between events, leading to a large variation in the estimated uncertainty on Δt, as shown in

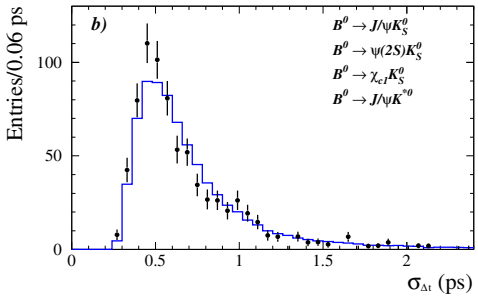

Figure 6.5.2. Distribution of event-by-event uncertainty on Δt for the $J/\psi K^0_S$, $\psi(2S)K^0_S$, $\chi_{c1}K^0_S$ and $J/\psi K^{*0}$ events. The histogram corresponds to Monte Carlo simulation and the points with error bars to *BABAR* data. From (Aubert, 2002a).

Fig. 6.5.2. The estimated event-by-event uncertainty on Δt is denoted by $\sigma_{\Delta t}$.

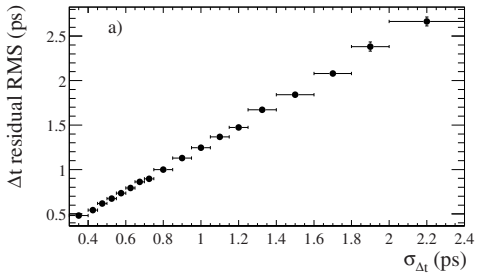

Figure 6.5.3. RMS of the $\delta t = \Delta t - \Delta t_{\rm true}$ distribution in *BABAR* simulated events as a function of the estimated event-by-event uncertainty in Δt. From (Aubert, 2002a).

To benefit statistically from this variation the estimated uncertainty is used in the parameterization of the resolution function. Fig. 6.5.3 shows the actual Δt resolution — defined as the RMS of the error distribution — in simulated *BABAR* events as a function of the estimated uncertainty $\sigma_{\Delta t}$. The linear correlation illustrates that $\sigma_{\Delta t}$ is a good measure for the actual resolution, although a scaling factor of approximately 1.1 must be applied to obtain pulls with unit RMS. Therefore, the parameterization of the resolution function typically uses a width that is proportional to $\sigma_{\Delta t}$. The proportionality factor is derived from the data.

The bias due to tracks from D daughters depends on the direction of the D meson in the B rest frame: If the D meson moves approximately perpendicular to the z axis, the z positions of D and B vertices coincide and the bias is small. Due to the boost of the D meson in the B frame, in such events the D daughter trajectories also have a relatively large angle with respect to the beam direction, leading to a small vertex position uncertainty. It is for this reason that both experiments observe that the bias from D daughter tracks is roughly proportional to the per-event estimated uncertainty on the $B_{\rm tag}$ vertex z position, as il-

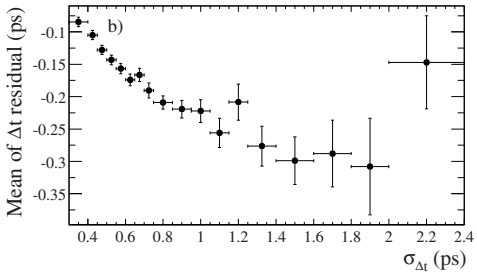

Figure 6.5.4. Mean of the $\delta t = \Delta t - \Delta t_{\rm true}$ distribution in *BABAR* simulated events as a function of the estimated event-by-event uncertainty in Δt. From (Aubert, 2002a).

lustrated in Figure 6.5.4. Therefore, the parameterization of the resolution function for B decays often also uses a mean that is proportional to $\sigma_{\Delta t}$.

Chapter 7
B-meson reconstruction

Editors:
Paul Jackson (BABAR)
Anže Zupanc (Belle)

Additional section writers:
José Ocariz

The *BABAR* and Belle detectors were designed and built to detect and reconstruct particles produced in e^+e^- collisions and their decay products. Particles with long enough lifetimes or stable particles that deposit signals in subdetectors which in turn allow the measurements of their momenta or energies and consequently their four-momenta (see Chapters 2 and 5 for more details) are: $e^\pm$, $\mu^\pm$, $\pi^\pm$, $K^\pm$, p, $\overline{p}$, γ, and K^0_L and are commonly collectively referred to as final state particles. Particles such as B mesons and charm mesons decay inside the beam pipe close to the interaction point. In order to study the properties of B mesons, or other short-lived particles, they must first be reconstructed from their final state particles.

Reconstruction of B mesons proceeds via summing the momenta of all final state particles to check for consistency with specific exclusive B-meson decays. The goal is to measure the four-momentum vector of a reconstructed B meson, or to at least identify particles in an event arising from the same B meson. Candidates are identified by utilizing discriminating variables sensitive to the B-meson properties. The building of these candidates from their final state particle momenta is referred to as exclusive B-meson reconstruction or also full hadronic reconstruction and is described in detail in Section 7.1. Full reconstruction of (semi-) leptonic B-meson decays is not possible because the neutrinos leave the detectors undetected and hence the momentum they carry is not measured directly. However, due to the experimental setup of B Factories additional kinematic constraints can be applied which allow us to infer the neutrino or semi-leptonically decaying B-meson momentum indirectly. The constraints and methods are described in more detail in Sections 7.2 and 7.4. As explained in Section 7.3 the unique kinematic properties of B-meson decays to $D^{*\pm}$ mesons permit a partial reconstruction approach, without recourse to constraining the entirety of the B decay. As a consequence the partial reconstruction efficiency of B mesons is much higher than that achieved by more exclusive techniques. The choice of the most suitable reconstruction method in any given analysis depends on the studied decay mode and the physics parameters of interest.

The rest of this chapter describes the methods – procedures and main kinematical constraints – used by *BABAR* and Belle to reconstruct and identify decays of B mesons. In each subsection example B-meson decay modes are used for illustration of the reconstruction procedures. The techniques relevant to the reconstruction of charm, tau and other events are described in other chapters.

7.1 Full hadronic B-meson reconstruction

In most of the analyses we wish to extract some physics parameters of interest for a given specific exclusive B-meson decay mode, meaning that the entire B-meson decay chain from intermediate particles to all final state particles is reconstructed. For example, $B^0 \to D^{*-}\pi^+$ decays can be reconstructed from final state particles produced in the following exclusive decay chain:

$$\begin{aligned} B^0 &\to D^{*-}\pi^+ \\ &\hookrightarrow \overline{D}^0\pi^- \\ &\hookrightarrow K^+\pi^-\pi^0 \\ &\hookrightarrow \gamma\gamma. \end{aligned} \tag{7.1.1}$$

In exclusive reconstruction the reconstruction of the decay chain proceeds from bottom up. First the selection of tracks and clusters not associated with any track is performed. The former are used to construct final state charged particle candidates (*i.e.* to determine their four-momentum vector), $K^\pm$ and $\pi^\pm$ in the above example, and the latter to construct photon candidates as described in Chapter 2. In the next stages all decaying particles in the decay chain are reconstructed: two photon candidates are combined to form π^0 meson candidates; $\overline{D}^0$ candidates are formed by combining K^+, π^- and π^0 candidates; D^{*-} by pairing $\overline{D}^0$ candidates from the previous level and a negatively charged pion; and finally the D^{*-} and π^+ candidates are combined to form the B^0 candidates. At each stage the four-momentum of a decaying particle is given by the sum of the four-momenta of its decay products following the momentum conservation rule.

Not all combinations of two or more particles which form the 'mother' particle candidates are correct. Wrong combinations (or background candidates) can be roughly divided into two categories:[23] combinatorial background and physics background. Combinatorial background candidates are random combinations of particles which are not produced in a decay of the same particle. For example, in an event two π^0 mesons are produced and both decay into two photons. If all four photons are detected then six different π^0 candidates (two photon combinations) can be reconstructed in total – two of them represent correctly reconstructed π^0 mesons (signal candidates) while the other four represent combinatorial background candidates. Similarly, the B^0 candidate in our example can be a combination of correctly reconstructed D^{*-} and π^+ candidates, where the former originates from one B-meson decay and the latter from the decay of the second B meson produced in the same event. Another large source of combinatorial background are events in which a light quark–anti-quark pair is produced instead of a pair of B mesons – so called continuum events (see Chapter 9). The 'continuum' background is usually the dominant background for rare B-meson decay studies (decays of B mesons that do not proceed through the dominant $b \to c$ transition). Much effort has therefore been invested in the development of

[23] Background composition strongly depends on the studied B-meson decay mode. Here only a general overview is given.

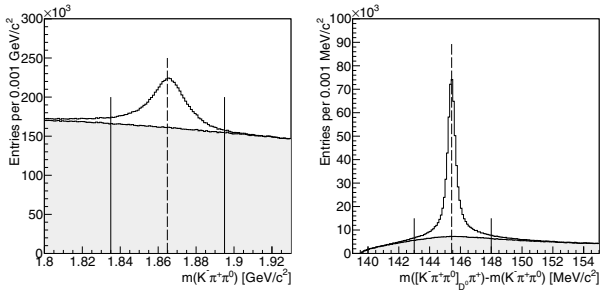

Figure 7.1.1. Invariant mass distribution of D^0 candidates reconstructed in $K^-\pi^+\pi^0$ (left) and $D^{*+} - D^0$ mass difference for D^{*+} candidates reconstructed in $D^0\pi^+$ and D^0 in $K^-\pi^+\pi^0$ decay modes (right) in simulated events. The correctly reconstructed D^0 (D^{*+}) candidates peak at the nominal D^0 mass ($D^{*+} - D^0$ mass difference) indicated by vertical dashed lines. Full histograms show the contribution of background candidates. The signal regions are indicated by the two vertical lines.

continuum suppression techniques. They are described in detail in Chapter 9.

The physics background originates from specific B-meson decays to final states which can be easily misidentified as the final state under study. For example, consider the charmless $B^+ \to K^+\pi^-\pi^+$ decays. The same or a very similar final state can also be achieved in many other B-meson decays, like for example: the $B^+ \to \overline{D}{}^0\pi^+ \to K^+\pi^-\pi^+$ decay chain leads to the same final state; $B^+ \to \overline{D}{}^0\pi^+ \to K^+K^-\pi^+$ and $B^+ \to K^+J/\psi \to K^+\mu^-\mu^+$, where in the former case the K^- from the $\overline{D}{}^0$ decay is mis-identified as π^- and in the latter the two muons as pions, respectively; $B^+ \to \overline{D}{}^0\pi^+ \to K^+\pi^-\pi^+\pi^0$, $B^+ \to \overline{D}{}^0\rho^+ \to K^+\pi^-\pi^+\pi^0$ and $B^+ \to K^+\eta' \to K^+\pi^-\pi^+\gamma$ decays have four-body final states but can still contaminate signal candidates when the π^0 or γ are not reconstructed. Physics backgrounds are potentially more dangerous than combinatorial background because their distributions often peak around same values as distributions of the signal decay mode.

In the rest of this section most commonly used kinematical constraints which can help to reduce the contribution of combinatorial as well as physics backgrounds are discussed.

7.1.1 Kinematical discrimination of B mesons

7.1.1.1 Invariant mass and mass difference

In the case of B-meson decays via intermediate resonances, as shown in Equation (7.1.1), the most straightforward way to suppress the contribution of combinatorial background is to select only candidates populating the regions around the nominal masses (signal regions) of the decaying particles in the invariant mass distributions. Figure 7.1.1 shows for example the invariant mass distribution of D^0 candidates reconstructed in the $K^-\pi^+\pi^0$ decay mode (charge conjugation is implied). In this example a clear signal peak is visible over the smooth contribution of combinatorial background candidates. By selecting candidates that populate the signal region, indicated by two vertical lines, large amounts of combinatorial background are rejected while retaining almost all signal D^0 candidates. The signal region varies for different particles and even for the same particle reconstructed in different decay modes. In general, the invariant mass distribution of signal candidates is given by a convolution of the particle's true lineshape (usually a relativistic Breit-Wigner) and a detector resolution (usually described by the Gaussian function) stemming from the experimental uncertainty in the determination of momenta of the particle's decay products. It therefore depends on the resolution achieved in a given decay mode and the natural width of the reconstructed particle, if it's comparable or larger to the resolution. In case of D^0 mesons the natural width is negligible compared to the detector resolution which ranges from around 5-6 MeV/c^2 in decay modes to charged final state particles only (*e.g.* $K^-\pi^+$, $K^-\pi^+\pi^+\pi^-$) and up to around 12 MeV/c^2 in decay modes with one neutral pion. Composite particles whose natural width is much larger than the invariant mass resolution are for example $K^*(892)$ and $\rho(770)$ with natural widths around 50 and 150 MeV/c^2, respectively.

In the example B-meson decay the D^{*+} mesons are reconstructed in the $D^0\pi^+$ decay mode. The energy release in the $D^{*+} \to D^0\pi^+$ decay is very small (The D^{*+} mass is only about 6 MeV/c^2 above the $D^0\pi^+$ threshold). The D^{*+} momentum measurement is dominated by the D^0 momentum. The pion has low momentum, whose magnitude and direction are well measured. Therefore, most of the uncertainty in the D^*'s momentum results from the measurement resolution of the D^0 momentum. This introduces a correlation between the measured D^0 and D^* invariant masses. Due to this correlation, the experimental smearing of the D^0 momentum (partly) cancels in the $D^{*+} - D^0$ mass difference, $\Delta m = m(D^{*+}) - m(D^0)$. The mass difference has a much better resolution and discriminates more effectively between signal D^{*+} and background than the D^{*+} invariant mass. Figure 7.1.1 shows the mass difference distribution for $D^{*+} \to D^0\pi^+$ decays, where the D^0 is reconstructed in the $K^-\pi^+\pi^0$ mode. As can be seen the mass difference is about an order of magnitude better resolved than the mass of the D^0. The mass difference is commonly used to discriminate between the signal and background for particles reconstructed from composite particles with small energy released in the decay; apart from D^* mesons, such cases include also excited charm baryons decaying to Λ_c, charmonium(-like) states decaying to J/ψ, etc.

Kinematic fitting can improve the momentum (invariant mass) resolution of reconstructed particles and therefore also the signal and background discrimination. Details of kinematic fitting and performance improvements that can be achieved are described in Chapter 6.

7.1.1.2 Energy difference ΔE and beam-energy substituted mass $m_{\rm ES}$

In principle, the invariant mass of B mesons could also be used to distinguish between signal and background B-meson candidates. However, as it will be explained in what follows, the experimental setup of the B Factories allows one to set additional kinematical constraints which improve the knowledge of the B-meson's momentum and hence allow for better signal and background discrimination.

The $\Upsilon(4S)$ decays in two same-mass particles, B and $\overline{B}$, thus imposing two constraints in the CM frame. If the B meson is correctly reconstructed, the energy of its decay products has to be equal to half the CM energy or equal to the beam energy in the $\Upsilon(4S)$ rest frame,[24] and its reconstructed mass has to be equal to that of the B meson:

$$E^{\star}_{\rm rec} = E^{\star}_{\rm beam} = \sqrt{s}/2, \tag{7.1.2}$$

$$m_{\rm rec} = m_B. \tag{7.1.3}$$

In order to exploit the specifics of B-meson decay kinematics, two variables are defined, the beam-energy substituted mass, $m_{\rm ES}$, and the energy difference, ΔE. They together exploit in an optimal way the information contained in the equations above.

The energy difference ΔE can be expressed in a Lorentz-invariant form as

$$\Delta E = \left(2q_B q_0 - s\right)/2\sqrt{s}, \tag{7.1.4}$$

where $\sqrt{s} = 2E^{\star}_{\rm beam}$ is the total energy of the e^+e^- system in the CM frame, and q_B and $q_0 = (E_0, \boldsymbol{p}_0)$ are the Lorentz four-vectors representing the energy-momentum of the B candidate and of the e^+e^- system, $q_0 = q_{e^+} + q_{e^-}$. In the CM frame, ΔE takes the more familiar form

$$\Delta E = E^{\star}_B - E^{\star}_{\rm beam}, \tag{7.1.5}$$

where $E^{\star}_B$ is the reconstructed energy of the B meson. The uncertainty of ΔE originates from the error in the B-meson energy measurement, $\sigma^2_{E^{\star}_B}$, and the beam energy spread, $\sigma^2_{E^{\star}_{\rm beam}}$:

$$\sigma^2_{\Delta E} = \sigma^2_{E^{\star}_B} + \sigma^2_{E^{\star}_{\rm beam}}. \tag{7.1.6}$$

The ΔE resolution receives a sizable contribution from the beam energy spread, but is generally dominated by detector energy resolution (this being the dominant term for modes involving photons). Figure 7.1.2 (a and b) shows the ΔE distributions for two cases: $B^+ \to K^0_S\pi^+$, $K^0_S \to \pi^+\pi^-$ and $B^+ \to K^+\pi^0$, $\pi^0 \to \gamma\gamma$. A clear difference in the ΔE resolution is seen between decay modes with and without photons in the final state. The long tail at low ΔE for the $B^0 \to K^+\pi^0$ signals comes from the photon shower leakage in the calorimeter crystals.

The measurement error $\sigma_{E^{\star}_B}$ receives contributions from the errors in the absolute values of the momenta of the decay products. The momenta of the B-meson decay products can be combined in a second variable that is only weakly correlated to ΔE. This is possible if the variable depends on the small three-momentum of the B meson to which the larger momenta of the B decay products contribute with opposing signs in the CM frame. The pioneering experiments invented for this purpose a beam-energy constrained mass. While ARGUS did actually a fit of the B-meson four momentum with the B-meson energy constrained to the beam energy, CLEO used a simpler approach adopted also at Belle, substituting the B energy with the beam energy, which is what we call the beam-energy substituted mass or beam-energy constrained mass[25]

$$m^{\rm CLEO}_{\rm ES} = m_{\rm bc} = \sqrt{E^{\star 2}_{\rm beam} - \boldsymbol{p}^{\star 2}_B}, \tag{7.1.7}$$

where $p^{\star}_B$ is the CM momentum of the B meson, derived from the momenta of their decay products, and the B-meson energy is substituted by $E^{\star}_{\rm beam}$.

The idea behind ΔE is different and complementary to that of $m_{\rm ES}$. Whereas the latter is by construction independent of the mass hypothesis for each of the particles, ΔE depends strongly on them. If, for example, a kaon is misidentified as a pion, its energy, and consequently that of the B candidate, will be smaller than its true energy. The event then will be shifted towards negative values of ΔE. In contrast, the distribution for signal events peaks

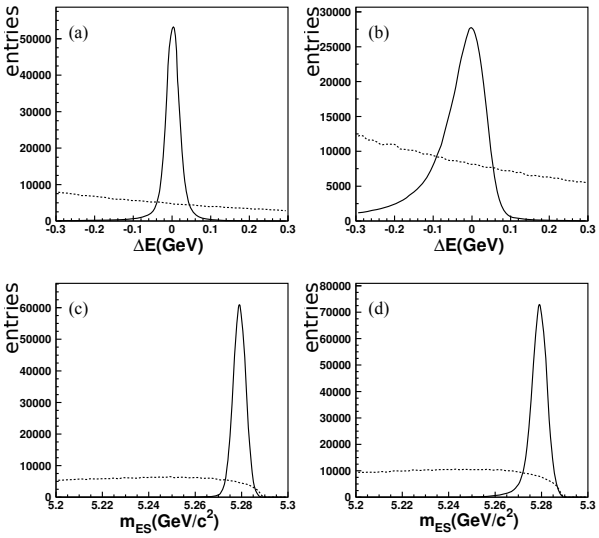

Figure 7.1.2. The ΔE and $m_{\rm ES}$ distributions for (a and c) $B^+ \to K^0_S\pi^+$ and (b and d) $B^+ \to K^+\pi^0$. Solid line histograms are signal events generated using GEANT Monte Carlo and dotted histograms are from the continuum MC. The signal resolution in ΔE is much worse for $B^+ \to K^+\pi^0$, due to the neutral pion present in the final state, but the difference is less pronounced in $m_{\rm ES}$ as explained in the text.

[24] All quantities with a star symbol ($\star$) are estimated in the CM frame unless otherwise stated.

[25] Since only the three-momentum of the B-meson candidate is used, this quantity is not Lorentz-invariant.

at zero as expected, making ΔE especially helpful for discriminating from physics background events involving misidentification. On the other hand, $m_{\rm ES}$ will not change if a particle is misidentified, leading to peaking background from true B decays with incorrectly assigned particle identities.

While this is true for symmetric-energy e^+e^- colliders operating at the Y(4S) (such as CLEO), where the laboratory system and the CM system are identical, it does not hold for the asymmetric B Factories. The B momentum vector can only be boosted to the CM frame after masses have been assigned, and the result depends on these mass assignments, although much weaker than for ΔE. To strictly keep mass independence, *BABAR* is using a modified variable, which makes use of the three-momenta in the laboratory system and of the beam energy in the CM system:

$$m_{\rm ES} = \sqrt{\left(s/2 + \boldsymbol{p}_B \boldsymbol{p}_0\right)^2 / E_0^2 - \boldsymbol{p}_B^2}. \qquad (7.1.8)$$

where $(E_0, \boldsymbol{p}_0)$ is the four-momentum of the CM system in the laboratory. This definition is identical with Eq. (7.1.7) if the laboratory system is the CM system, *i.e.*, at a symmetric-energy collider. But due to the weak mass dependence, the behavior of $m_{\rm ES}$ and $m_{\rm bc}$ are largely the same even at asymmetric colliders and therefore throughout this book the common notation $m_{\rm ES}$ will be used for both of them. When presenting beam-energy substituted mass or beam-energy constrained mass distributions the reader should keep in mind that Belle uses the definition given in Eq. (7.1.7) while *BABAR* uses the definition given in Eq. (7.1.8).[26]

To appreciate this subtlety, we approximate $m_{\rm ES} \approx m_{\rm bc}$, where the approximation arises from the uncertainty in the B momentum measurement (boosted to the CM frame), $\sigma^2_{p^\star_B}$, and the beam energy spread, $\sigma^2_{E^\star_{\rm beam}}$:

$$\sigma^2_{m_{\rm ES}} \approx \sigma^2_{E^\star_{\rm beam}} + \left(\frac{p^\star_B}{m_B}\right)^2 \sigma^2_{p^\star_B}. \qquad (7.1.9)$$

As the B mesons are almost at rest in the CM frame, $p^\star_B/m_B \approx 0.06$, the second term in the above equation gets small and the resolution in $m_{\rm ES}$ is dominated by the spread in the beam energy. This is illustrated in Figure 7.1.2 (c and d) which shows the $m_{\rm ES}$ distributions for $B^+ \to K^0_S\pi^+$ and $B^+ \to K^+\pi^0$. The signal resolution in $m_{\rm ES}$ is much less affected by the uncertainty in the measured B-meson four-momentum compared to ΔE. For signal events, $m_{\rm ES}$ yields the mass of the B meson and shows a clean peak. For continuum events, composed of light quarks, the only way of reaching the B rest mass is by artificially associating random particles. As a consequence, their distribution displays a slowly varying shape, as expected from their combinatorial nature.

The $m_{\rm ES}$ resolution is around 3 MeV/c^2 when no neutral particles contribute to the final state. The resolution for ΔE more strongly depends on the B-meson decay mode: it is much larger for low mass final states such as $\pi^+\pi^-$ (Lees (2013b) quotes $\sigma_{\Delta E} \sim 29$ MeV) than for high mass final states such as $\overline{D}^{(*)}D^{(*)}K$ (del Amo Sanchez (2011e) quotes $\sigma_{\Delta E}$ between 6 and 14 MeV for modes with zero or one D^{*0} meson in the final state).

The energy difference and beam substituted mass, defined in Eqs (7.1.5) and (7.1.8), exploit optimally the kinematical constraints from the $\Upsilon(4S)$ decay to two B mesons. A small correlation between the ΔE and $m_{\rm ES}$ variables follows from their common inputs – the beam energy, measured momentum of charged particles and energy of neutrals. The correlation from the energy measurement becomes severe if the final state particles contain high energy photons, as shown in the top scatter plot in Figure 7.1.3. The correlation coefficient is +18% for $m_{\rm ES}$ and ΔE in $B^+ \to K^+\pi^0$. The correlation can be reduced by calculating $m_{\rm ES}$ after modifying the magnitude of the π^0 momentum but retaining its direction to constrain the reconstructed B energy to be the beam energy.[27] The bottom scatter plot in Figure 7.1.3 shows that the correlation between the modified $m_{\rm ES}$ and ΔE is reduced and the corresponding correlation coefficient is −4% (Duh, 2012). This technique is found useful only for two-body B decays with a hard photon, π^0 or $\eta \to \gamma\gamma$ meson in the final state. For other B decays with soft photons only, the modified $m_{\rm ES}$ has similar distribution as that of $m_{\rm ES}$ because the $m_{\rm ES}$ resolution is dominated by the beam-energy spread. Furthermore, the modification does not artificially create an enhancement in $m_{\rm ES}$ for the continuum background.

For final states with heavy particles, in particular B decays to baryons, the correlation becomes strong since the beam energy spread $\sigma_{E^\star_{\rm beam}}$ dominates in both variables. The difference between the mean beam energy used in the calculation of ΔE and $m_{\rm ES}$ and the true beam energy of the event is the same, hence this contribution alone would lead to 100% correlation. Therefore, in these analyses other pairs of variables are preferred. If ΔE is replaced by the invariant mass

$$m_B = \sqrt{E_B^2 - \boldsymbol{p}_B^2} \qquad (7.1.10)$$

of the reconstructed B candidate, this variable will not depend on the beam energy at all and the correlation with $m_{\rm ES}$ becomes again very small, as shown in Fig. 7.1.4: distributions from simulated events $\overline{B}^0 \to \Lambda_c^+\overline{p}\pi^+\pi^-$ in ΔE vs $m_{\rm ES}$ with a correlation coefficient of −29% compared to m_B vs $m_{\rm ES}$ with a correlation coefficient of (-2.3 ± 0.5)% (Lees, 2013h).

[26] As to any rule there is also an exception to this one: In the measurement reported by Belle in Abe (2001f) the definition Eq. (7.1.8) is used.

[27] In the calculation of the modified $m_{\rm ES}$ (using Eq. 7.1.7) the momentum of the B meson given as $\boldsymbol{p}_B = \boldsymbol{p}_{K^+} + \boldsymbol{p}_{\pi^0}$ is replaced with $\boldsymbol{p}_B = \boldsymbol{p}_{K^+} + \sqrt{(E^2_{\rm beam} - E_{K^+})^2 - M^2_{\pi^0}} \cdot \frac{\boldsymbol{p}_{\pi^0}}{|\boldsymbol{p}_{\pi^0}|}$, where M_{π^0} is the nominal mass of π^0, and $\boldsymbol{p}_{K^+}$ ($\boldsymbol{p}_{\pi^0}$) is the measured K^+ (π^0) momentum.

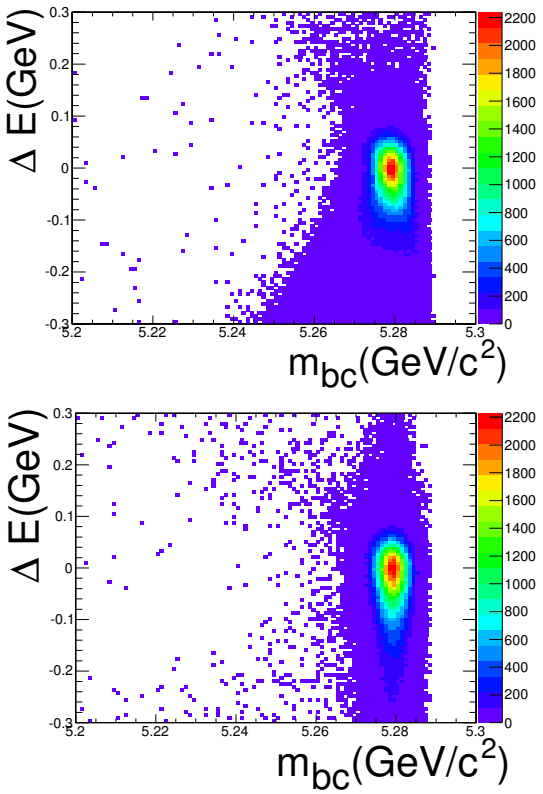

Figure 7.1.3. The ΔE vs $m_{\rm ES}$ $(= m_{\rm bc})$ distributions for the $B^+ \to K^+\pi^0$ signals. The top plot is for the original $m_{\rm ES}$ definition and the bottom is for the modified $m_{\rm ES}$ case. Belle internal, from the Duh (2012) analysis.

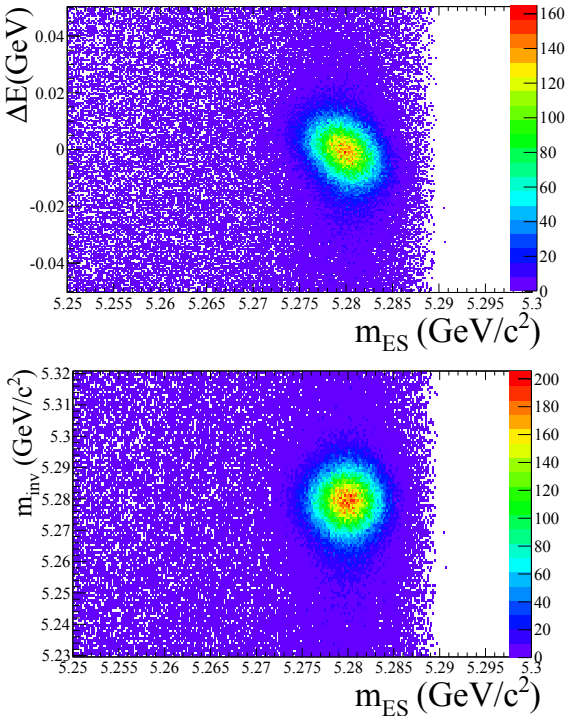

Figure 7.1.4. Distributions from $\overline{B}^0 \to \Lambda_c^+ \overline{p}\pi^+\pi^-$ events (Monte Carlo). The top plot is for ΔE vs $m_{\rm ES}$ showing a strong correlation, and the bottom is for the invariant mass m_B vs $m_{\rm ES}$ which is only weakly correlated through measurement errors. *BABAR* internal, from the Lees (2013h) analysis.

7.1.1.3 Signal yield extraction

After the reconstruction and selection of a specific exclusive B-meson decay is performed the next step is to determine the number of correctly reconstructed B-meson candidates. Most often the signal yield is extracted by performing an extended maximum likelihood fit to the two dimensional ΔE-$m_{\rm ES}$ distribution. In studies in which there is negligible correlation between the two variables the distribution of events can be modeled by a product of two one dimensional probability density functions. The ΔE and $m_{\rm ES}$ distributions of signal B-meson candidates are often modeled with a Gaussian function (or sum of two or more Gaussian functions). The background candidates are modeled in $m_{\rm ES}$ with an empirical function introduced by the ARGUS collaboration (Albrecht et al., 1990a):

$$\begin{aligned}\text{Argus}(m_{\rm ES}|m_{\rm thr},c) &= m_{\rm ES}\sqrt{1-\left(\frac{m_{\rm ES}}{m_{\rm thr}}\right)^2}\times \\ &\exp\left[-c\left(1-\left(\frac{m_{\rm ES}}{m_{\rm thr}}\right)^2\right)\right], \quad (7.1.11)\end{aligned}$$

where $m_{\rm thr}$ represents the endpoint in $m_{\rm ES}$ distribution and c is a free shape parameter. Background in ΔE is usually modeled with a polynomial function. The choice of signal and background models given above is very general and depends on the properties of the studied decay mode and background composition. The models used in specific studies are provided in relevant sections and details about maximum likelihood fitting are provided in Chapter 11.

7.2 Semileptonic B-meson reconstruction

Analyses of B-meson decay modes containing leptons present one of the richest means of extracting information about the CKM matrix, along with an understanding of properties of the b quark bound in a meson. These probes are used in a variety of final states where the measurement strategy can be more or less inclusive. Decays of the form: $B \to X\ell\nu$, are used to measure $|V_{cb}|$, $|V_{ub}|$ and to extract branching fractions of B transitions to charm-type and up-type mesons. For semileptonic decays involving charm states (denoted $B \to X_c\ell\nu$), the final state can be reconstructed from the particles produced in a typical exclusive

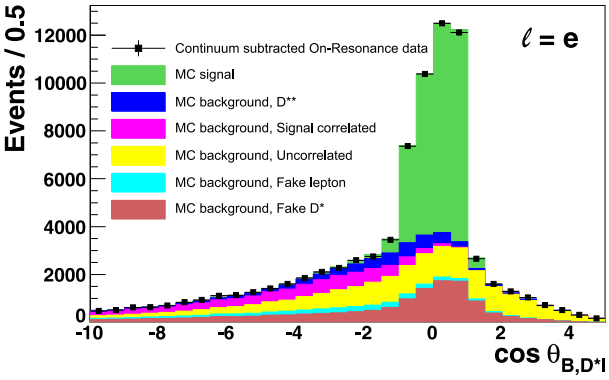

Figure 7.2.1. The $\cos\theta_{B,D^*\ell}$ distribution for $B^0 \to D^{*-}e^+\nu_e$ decays (Dungel, 2010). The points with error bars are data and full histograms are, top to bottom, the signal component and different types of background. Signal decays are constrained to lie in the interval $(-1, 1)$, while background decays populate a much wider region.

decay chain:

$$\begin{aligned} B^0 &\to D^{*-}\ell^+\nu \\ &\hookrightarrow \overline{D}^0\pi^- \\ &\hookrightarrow K^+\pi^-\pi^0 \\ &\hookrightarrow \gamma\gamma. \end{aligned} \tag{7.2.1}$$

The reconstruction of the decay chain proceeds from the identification of the charged lepton. In tandem with this, the reconstruction of a D meson occurs, most commonly a suitable ground state neutral or charged meson (D^0, $\overline{D}^0$, D^+, D^-). This ground state D meson may then be combined with soft a $\pi^\pm$ or π^0 in an attempt to form a $D^{*\pm}$ or D^{*0}. A tight constraint on Δm is applied to evidence such transitions. Higher resonant states of charm mesons (*e.g.* D^{**}) are usually examined in a combination of angular and mass distributions.

Under the assumption that the neutrino is the only missing particle, the cosine of the angle between the inferred direction of the reconstructed B and that of the $D^{(*)}\ell$ system is

$$\cos\theta_{B,D^{(*)}\ell} = \frac{2E_B^* E^*_{D^{(*)}\ell} - m_B^2 - m^2_{D^{(*)}\ell}}{2|\boldsymbol{p}_B^*||\boldsymbol{p}^*_{D^{(*)}\ell}|}\ , \tag{7.2.2}$$

where E_B^* is half of the CM energy and $|\boldsymbol{p}_B^*|$ is $\sqrt{E_B^{*2} - m_B^2}$. The quantities $E^*_{D^{(*)}\ell}$, $\boldsymbol{p}^*_{D^{(*)}\ell}$ and $m_{D^{(*)}\ell}$ are calculated from the reconstructed $D^{(*)}\ell$ system. This cosine is also a powerful discriminator between signal and background: signal events should strictly lie in the interval $(-1, 1)$, although – due to finite detector resolution – about 5% of the signal is reconstructed outside this interval. The background on the other hand does not have this restriction and populates a much wider region (see Fig. 7.2.1).

The experimental techniques used in reconstruction of semileptonic B-meson decays are described in more details in Section 17.1.1.3.

7.3 Partial B-meson reconstruction

The term partial reconstruction refers to a reconstruction technique in which not all of the final state particles are required to be detected and identified, as is the case in exclusive (full) reconstruction described in Section 7.1. Partial reconstruction of the B meson can therefore result in substantially larger efficiency, albeit with reduced purity resulting from higher backgrounds.

BABAR and Belle use the partial reconstruction technique mainly in time-dependent studies of $B^0 \to D^{*-}X^+$ (where X represents some hadronic state like π, ρ or D) and $B^0 \to D^{*-}\ell^+\nu_\ell$ decays. In these measurements the B mesons are reconstructed using only the hadronic state X (or charged lepton) and the soft pion from the $D^{*-} \to \overline{D}^0\pi^-$ decay. The $\overline{D}^0$ decay is not reconstructed which increases the acceptance.

The remainder of this section describes the kinematic constraints and variables used to distinguish between partially reconstructed signal and background $B^0 \to D^{*-}X^+$ and $B^0 \to D^{*-}\ell^+\nu_\ell$ candidates. Physics use cases are described in Sections 17.5 and 17.8.

7.3.1 $B \to D^{*\pm}X$ decays

The partial reconstruction technique was originally applied by CLEO (Brandenburg et al., 1998; Giles et al., 1984) to

$$\begin{aligned} B^0 &\to D^{*-}\pi_f^+ \\ &\hookrightarrow \overline{D}^0\pi_s^- \end{aligned} \tag{7.3.1}$$

decays, where π_f and π_s are referred to as "fast" and "slow" pions, respectively. *BABAR* and Belle applied this technique to generic $B \to D^{*\pm}X$ decays. In principle, X may be any single-particle state (*e.g.* π, ρ, D, $D_s^{(*)}$) as long as it can be exclusively reconstructed. For simplicity the discussion is restricted only to $B \to D^{*\pm}\pi$ decays. In this mode the $D^{*\pm}$ meson is created in a helicity zero state and the characteristic angular distributions of the D^{*+} decay products (see Chapter 12 for more details) can be exploited for background suppression.

7.3.1.1 Kinematic Variables

The decay chain given in Eq. (7.3.1) involves 5 particles (B^0, D^*, D^0, π_s and π_f), each determined by it's four-momentum. There are thus 20 parameters in total which describe the entire decay chain. The experimentally measured inputs to the partial reconstruction are only the three-momenta of the fast and slow pion, $\boldsymbol{p}_{\pi_f}$ and $\boldsymbol{p}_{\pi_s}$, respectively. In principle, it is possible to determine all five four-momenta from the measured $\boldsymbol{p}_{\pi_f}$ and $\boldsymbol{p}_{\pi_s}$ using energy-momentum conservation in the B^0 and D^* decays (8 constraints), the known particle masses of B^0, D^{*-}, $\overline{D}^0$, π_s and π_f (5 constraints), and the fact that the energy of the B^0 in the CM frame is equal to the half of

the beam energy (1 constraint). However, since the B-meson mass and the beam-energy constraints are imposed to determine the B-meson four-momentum the signal and background B-meson candidates cannot be separated by kinematic variables used in exclusive studies, like ΔE and $m_{\rm ES}$ given in Eqs (7.1.5) and (7.1.8), respectively. Instead, variables which can be used to identify signal events from the decay kinematics are utilized. Many different possible kinematic variables have been used in analyses of partially reconstructed $B^0 \to D^*\pi$ decays performed by *BABAR* and Belle.

The measured[28] $\boldsymbol{p}_{\pi_f}$ and $\boldsymbol{p}_{\pi_s}$ represent six independent variables which can be used to distinguish signal events from background. Consider three of these as $\boldsymbol{p}_{\pi_f}$ in spherical polar coordinates: magnitude (p_{π_f}), polar (θ_{π_f}) and azimuthal (ϕ_{π_f}) angle. Since the fast pion has no preferred direction (distribution of signal decays is uniform in θ_{π_f} and ϕ_{π_f}), only the magnitude, p_{π_f}, is useful. Signal decays are uniformly distributed within a small window in p_{π_f}, smeared by the B^0 momentum in the CM frame, as the fast pion is mono-energetic in the B rest frame. Background events are distributed predominantly outside this window. The three remaining degrees of freedom can be considered as the magnitude of the slow pion momentum, p_{π_s}, the angle between the slow pion direction and the opposite of the fast pion direction, δ_{fs}, and the azimuthal angle of the slow pion direction around the fast pion direction. The last of these three provides no useful information. The $\cos\delta_{fs}$ peaks sharply at $+1$ for signal, as the slow pion follows the D^* direction due to the small energy released in the D^* decay, while the background events populate the entire physical region. Instead of the slow pion magnitude the cosine of the angle between the slow pion direction in D^* rest frame and the D^* direction in CM frame, $\cos\theta_{\rm hel}$, is used since the former is correlated with the p_{π_f} for signal events, while the latter is not. For partially reconstructed $D^*\pi$ events the $\cos\theta_{\rm hel}$ is given by

$$\cos\theta_{\rm hel} = \frac{1}{p^\star_{\pi_s}}\left(\frac{E_{\pi_s}E_{D^*} - E^\star_{\pi_s}m_{D^*}}{p_{D^*}\gamma_{D^*}} - \beta_{D^*}E^\star_{\pi_s}\right), \tag{7.3.2}$$

where the energy and magnitude of the D^* momentum are given by $E_{D^*} = E_B - \sqrt{|\boldsymbol{p}_{\pi_f}|^2 + m^2_{\pi_f}}$ and $p_{D^*} = \sqrt{E^2_{D^*} - m^2_{D^*}}$, respectively, and $\gamma_{D^*} = E_{D^*}/m_{D^*}$ and $\beta_{D^*} = \sqrt{1 - 1/\gamma^2_{D^*}}$. The B-meson energy is taken to be half of the CM energy, $E_B = \sqrt{s}/2$. The quantities denoted with asterisks in the above equation are calculated in the D^* rest frame. The distribution for signal events in $\cos\theta_{\rm hel}$ is proportional to $\cos^2\theta_{\rm hel}$, as the $B^0 \to D^*\pi$ decay is a pseudoscalar to vector pseudoscalar transition. The $\cos\theta_{\rm hel}$ is calculated using kinematic constraints valid only for signal decays so the background events can populate also the unphysical region $|\cos\theta_{\rm hel}| > 1$. Figure 7.3.1 illustrates the discriminating power of the p_{π_f}, $\cos\delta_{fs}$ and $\cos\theta_{\rm hel}$ kinematic variables for partially reconstructed $B^0 \to D^{*-}\pi^+$ decays (Ronga, 2006).

[28] All momenta in the partial reconstruction section are evaluated in the CM frame unless stated otherwise.

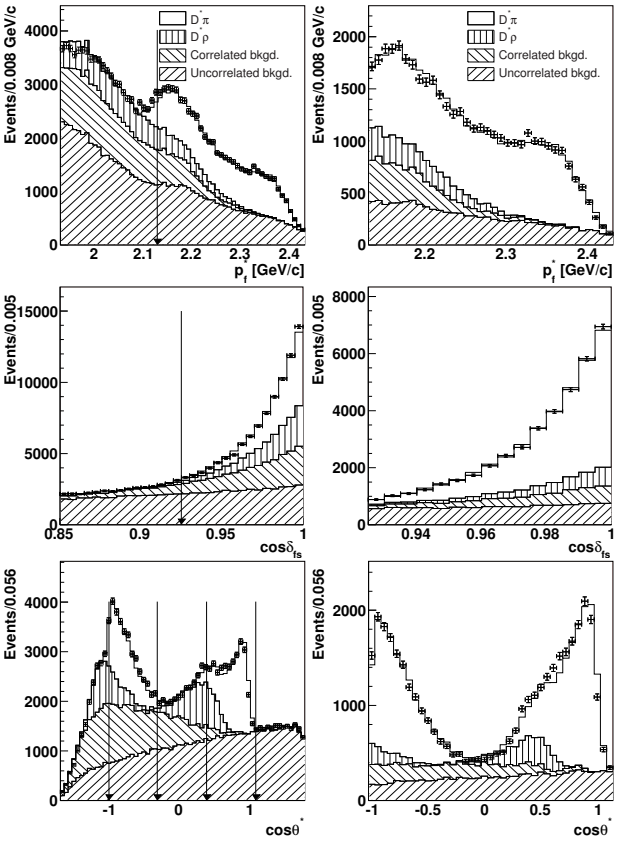

Figure 7.3.1. The p_{π_f} (top), $\cos\delta_{fs}$ (middle), and $\cos\theta_{\rm hel}$ (bottom) distributions of partially reconstructed $D^*\pi$ candidates showing selection regions (left) and signal region (right). The arrows indicate the borders of the signal region. Points with error bars show the observed data distribution, while the empty histograms show the distribution of signal $D^*\pi$ candidates, and the hatched histograms show the contributions of background candidates originating from different sources (Ronga, 2006).

In quite few measurements, the $\cos\delta_{fs}$ variable is replaced by the 'missing mass',[29] $m_{\rm miss}$, which should be equal to the D^0 meson mass for signal $B^0 \to D^*\pi$ decays. The four-momentum of the missing D^0, p_{D^0}, can be obtained from the four-momentum conservation in the decay of the B^0 and D^*. The magnitude of the B-meson momentum in the CM frame, p_B, is given by the known B-meson energy, $E_B = \sqrt{s}/2$, and the known B-meson mass: $p_B = \sqrt{E^2_B - m^2_B}$. From the angle between the B and π_f, given by,

$$\cos\theta_{B\pi_f} = \frac{m^2_B + m^2_{\pi^\pm} - m^2_{D^{*\pm}} - 2E_BE_{\pi_f}}{2p_Bp_{\pi_f}}, \tag{7.3.3}$$

and the measured slow and fast pion momenta, the B four-momentum may be calculated up to an unknown azimuthal angle ϕ around $\boldsymbol{p}_{\boldsymbol{\pi_f}}$. Depending on the value of

[29] The variables $m_{\rm miss}$ and $\cos\delta_{fs}$ are strongly correlated.

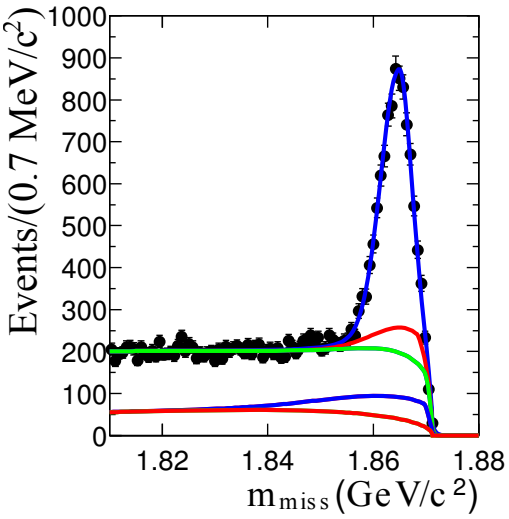

Figure 7.3.2. The $m_{\rm miss}$ distributions. The curves show, from bottom to top, the cumulative contributions of continuum, peaking $B\overline{B}$, combinatorial $B\overline{B}$, and $B^0 \to D^{*-}\rho^+$ background, and $B^0 \to D^{*-}\pi^+$ signal events (Aubert, 2004p).

ϕ, the expected D^0 momentum can then be calculated as

$$p^2_{D^0}(\phi) = m_B^2 + (p_{\pi_f} + p_{\pi_s})^2 - 2E_B(E_{\pi_f} + E_{\pi_s}) + 2p_B p_{\pi_f}\cos\theta_{B\pi_f} + 2p_B p_{\pi_s}\cos\theta_{B\pi_f}\cos\theta_{fs} + 2p_B p_{\pi_s}\sin\theta_{B\pi_f}\sin\theta_{fs}\cos\phi. \quad (7.3.4)$$

The ϕ-dependent missing mass is then calculated as, $m(\phi) = \sqrt{p^2_{D^0}(\phi)}$. The value of ϕ is not constrained by kinematics and may be chosen arbitrarily: *BABAR* defines in Aubert (2004p) the missing mass for partially reconstructed $B^0 \to D^{*-}\pi^+$ decays to be $m_{\rm miss} = \frac{1}{2}[m_{\rm max} + m_{\rm min}]$, where $m_{\rm max}$ and $m_{\rm min}$ are the maximum and minimum values of $m(\phi)$, while in analysis of partially reconstructed $B^0 \to D^{*+}D^{*-}$ decays *BABAR* chooses the value for which $\cos\phi = 0.62$, which is the median of the corresponding Monte Carlo distribution for signal events obtained using generated momenta, and defines the missing mass $m_{\rm miss} = m_{\rm miss}(\cos\phi = 0.62)$ (Lees, 2012k). For signal candidates, the $m_{\rm miss}$ variable peaks at the nominal D^0 mass m_{D^0}, with a spread of about 3 MeV/c^2, while the background is smoothly distributed, dropping off just above the D mass due to lack of phase space. The distribution of $m_{\rm miss}$ for partially reconstructed $B^0 \to D^{*-}\pi^+$ decays is shown in Fig. 7.3.2 (Aubert, 2004p).

7.3.2 $B \to D^{*\pm}\ell\nu_\ell$ decays

The partial reconstruction technique of semileptonic

$$B^0 \to D^{*-}\ell^+\nu_\ell \quad (7.3.5)$$
$$\hookrightarrow \overline{D}^0\pi_s^-$$

decays was first applied by ARGUS (Albrecht et al., 1987a, 1994a) and later used by other experiments, including *BABAR* and Belle. The signal events are selected using only the charged lepton from the B^0 decay and the slow pion from the D^* decay. Due to the undetected neutrino in the final state, the kinematics of these decays differ from the partial reconstruction of hadronic $B \to D^{*\pm}X$ decays.

As a consequence of the limited phase space available in the D^* decay, the slow pion is emitted within a one-radian wide cone centered about the D^* direction in $\Upsilon(4S)$ rest frame. The D^* four-momentum can therefore be computed by approximating its direction as that of the slow pion, and parameterizing its momentum as a linear[30] function of the slow pion's momentum, p_{π_s}:

$$p_{D^*} = \alpha + \beta p_{\pi_s}, \quad (7.3.6)$$
$$E_{D^*} = \sqrt{p^2_{D^*} + m^2_{D^*}}, \quad (7.3.7)$$

where the offset and slope parameters α and β are taken from the simulation. The approximations used in the determination of the D^* four-momentum result in an uncertainty in the D^* energy of about 400 MeV. The missing momentum carried by the neutrino is then given by energy-momentum conservation in the $B \to D^*\ell\nu_\ell$ decays

$$p_\nu = p_B - p_{D^*} - p_\ell.$$

One requires knowledge of the B-meson four-momentum, p_B, to solve this equation. The direction of the motion of the B is not known, but it's momentum is sufficiently small (on average 0.34 GeV/c) compared to the typical values of the magnitudes of lepton and D^* momenta so that the three-momentum of the B meson can be set to zero. The neutrino invariant mass can then be computed as

$$M_\nu^2 = \left(\frac{\sqrt{s}}{2} - E_{D^*} - E_\ell\right)^2 - (\boldsymbol{p}_{D^*} + \boldsymbol{p}_\ell)^2, \quad (7.3.8)$$

where the energy of the B meson is taken to be half of the CM energy. Figure 7.3.3 shows the distribution of partially reconstructed $B^0 \to D^{*-}\ell^+\nu_\ell$ decays ($\pi_s\ell$ combinations) from Aubert (2006s). The signal events produce a prominent peak at $M_\nu^2 \approx 0$ with spread around $0.850\,{\rm GeV}^2/c^4$ while background events are distributed in a wide range, dropping sharply to zero where there is a lack of phase space.

7.4 Recoil B-meson reconstruction

B-meson decays to a final state with one or more neutrinos offer very little or even no kinematic constraints which are usually exploited in B decay searches in order to distinguish these decays from continuum and $B\overline{B}$ backgrounds, as described in Sections 7.1 and 7.3 and Chapter 9. Prominent examples of such decays are:

$$B^0 \to \nu\overline{\nu},$$
$$B^+ \to K^+\nu\overline{\nu},$$
$$B^0 \to D^-\ell^+\nu_\ell.$$

[30] *BABAR* uses in (Aubert, 2006s) a third order polynomial.

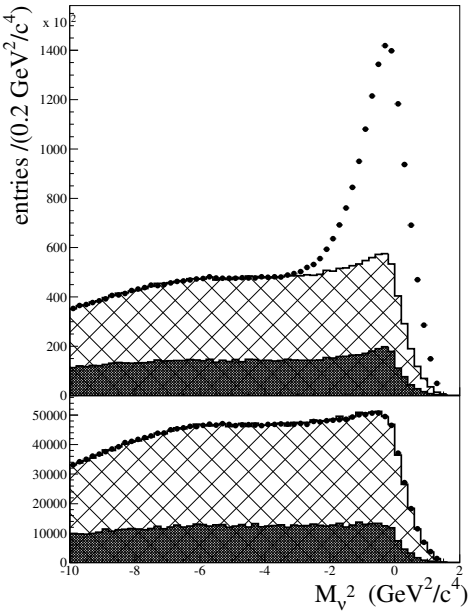

Figure 7.3.3. M_ν^2 distribution for right-charge, $\ell^\pm\pi_s^\mp$, (top) and wrong-charge, $\ell^\pm\pi_s^\pm$, (bottom) events. The points correspond to on resonance data. The distributions of continuum events (dark histogram), obtained from luminosity-rescaled off-resonance events, and $B\overline{B}$ combinatorial background events (hatched area), obtained from the simulation, are overlaid. Monte Carlo events are normalized to the difference between on-resonance and rescaled off peak data in the region $M_\nu^2 < -4.5\,\mathrm{GeV}^2/c^4$ (Aubert, 2006s).

The above decays cannot be measured by reconstructing all the decay products since the neutrinos cannot be detected in detectors like *BABAR* and Belle. A different approach is taken instead, which is referred to as recoil B-meson reconstruction and is described in detail in the rest of this subsection. Herein, specific reference will be made to the searches for above example decays, to elucidate the necessity of the recoil method, although the techniques of studying the system recoiling against a reconstructed B meson, referred to as the "tag"-B (B_{tag}[31]), can be applied to any analysis. The full list of measurements utilizing the recoil method performed by *BABAR* and Belle is given in Table 7.4.1.

Several different approaches are used in the recoil B-meson reconstruction technique. These can be separated according to the method used to reconstruct the decay of the B meson accompanying the signal B-meson decay. The accompanying B meson can be reconstructed either inclusively or exclusively. In the exclusive reconstruction the accompanying B meson is reconstructed in several specific decay modes. It is further divided into the hadronic and semileptonic reconstruction, depending whether the decay modes used are hadronic or semileptonic, respectively. In the inclusive reconstruction all detected particles which are not assigned to the signal B-meson are used to reconstruct the accompanying B-meson, without testing whether the assigned particles are consistent with a specific B-meson decay chain. In all cases the recoil B-meson reconstruction relies on the following unique properties of experimental setup of the B Factories (see Chapters 1 and 2 for more details):

- the $B\overline{B}$ pairs are produced without any additional particles,
- the detectors enclose the interaction region almost hermetically,
- the collision energy (or initial state energy) is precisely known.

The most commonly used strategy in the recoil B-meson reconstruction is to reconstruct exclusively the decay of one of the B mesons (B_{tag}) in the event. The remaining particle(s) in the event (detected as tracks or energy deposits in the calorimeter) must therefore originate from the other B-meson decay, referred to as the

[31] The same notation, B_{tag}, is also used in Chapter 8 where it represents a flavor tagged B-meson.

Table 7.4.1. List of measurements performed by *BABAR* and Belle using the B recoil techniques.

Hadronic B_{tag}	
$B \to X_u \ell\nu$	(Bizjak, 2005; Urquijo, 2010)
	(Aubert, 2008ac)
$B \to X_c \ell\nu$	(Schwanda, 2007; Urquijo, 2007)
	(Aubert, 2010c,e)
$B \to D^{(*)}\pi\ell\nu$	(Abe, 2005d)
$B \to D^{**}\ell\nu$	(Liventsev, 2008)
	(Aubert, 2007z, 2008s)
$B \to \pi\ell\nu$	(Aubert, 2006r)
$B \to X_s\gamma$	(Aubert, 2008q)
$B \to \tau\nu$	(Adachi, 2012b; Ikado, 2006)
	(Aubert, 2005ae, 2008c; Lees, 2013a)
$B \to h^{(*)}\nu\overline{\nu}$	(Chen, 2007b)
	(Aubert, 2008an)
$B \to$ invisible	(Hsu, 2012)
$B \to D^{(*)}\ell\nu_\ell$	(Aubert, 2008h,y, 2010e)
$B \to D^{(*)}\tau\nu_\tau$	(Aubert, 2008al; Lees, 2012e)
$B \to K\tau\mu$	(Aubert, 2007au)
$B \to \ell\tau/\ell\nu$	(Aubert, 2008az)
$B \to \tau\tau$	(Aubert, 2006b)
Semileptonic B_{tag}	
$B \to K\nu\overline{\nu}$	(Aubert, 2005b, 2008an)
	(del Amo Sanchez, 2010p)
$B \to$ invisible $(+\gamma)$	(Aubert, 2004y)
$B \to \pi\ell\nu$	(Hokuue, 2007)
$B \to \rho\ell\nu$	(Hokuue, 2007)
$B \to \tau\nu$	(Hara, 2010)
	(Aubert, 2005ae, 2006a, 2007a, 2010a)
$B \to \ell\nu$	(Aubert, 2010a)
Inclusive B_{tag}	
$B \to D^{(*)}\tau\nu_\tau$	(Bozek, 2010; Matyja, 2007)
$B \to D_s^{(*)}K\ell\nu_\ell$	(Stypula, 2012)

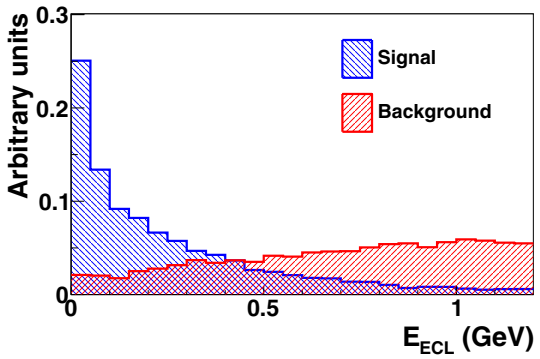

Figure 7.4.1. The $E_{\rm extra}(= E_{\rm ECL})$ distribution of simulated signal and background events. Belle internal, from the $B^+ \to \tau^+\nu_\tau$ Adachi (2012b) analysis.

"recoil"-B ($B_{\rm recoil}$) or "signal"-B ($B_{\rm sig}$),[32] and are compared with the signature expected for the signal mode. In studies of the example decay, $B^+ \to K^+\nu\overline{\nu}$ the presence of exactly one charged track (positively identified as a kaon) not used in the reconstruction of the $B_{\rm tag}$ is required. An additional powerful variable which allows for separation of signal and background is the remaining energy in the calorimeter, denoted as $E_{\rm extra}$ at *BABAR* or as $E_{\rm ECL}$ at Belle. It is defined as the sum of the energy deposits in the calorimeter that cannot be directly associated with the reconstructed daughters of the $B_{\rm tag}$ or the $B_{\rm recoil}$. Figure 7.4.1 shows a typical distribution of simulated signal and background events. For signal events (*e.g.* example decays given in beginning of this subsection), $E_{\rm extra}$ must be either zero or a small value arising from beam background hits and detector noise, since neutrinos do not loose any energy in the calorimeter. On the other hand, background events are distributed toward higher $E_{\rm extra}$ due to the contribution from additional clusters, produced by unassigned tracks and neutrals from the mis-reconstructed tag and recoil B mesons. For signal B-meson decays to a final state with only one neutrino (like the example decay $B^0 \to D^-\ell\nu_\ell$) where the $B_{\rm tag}$ is reconstructed in a hadronic decay mode, the neutrino momentum can be inferred using the momentum conservation relation from the measured momenta of $B_{\rm tag}$, D^- and ℓ, and known initial state: $p_{\nu_\ell} = p_{e^-} + p_{e^+} - p_{B_{\rm tag}} - p_{D^-} - p_\ell$. This allows for the construction of a powerful kinematic constraint – missing mass squared, defined as $MM^2 = |p_\nu|^2$, which peaks at the neutrino mass ($MM^2 = 0$) for correctly reconstructed events.

In studies of B-meson decay modes using the exclusive recoil B-meson reconstruction technique the number of reconstructed signal decays is linearly proportional to the efficiency of the $B_{\rm tag}$ reconstruction, which is given by

$$\varepsilon_{B_{\rm tag}} = \sum_f \varepsilon_f \mathcal{B}_f, \qquad (7.4.1)$$

and the sum runs over the B-meson decays to the exclusively reconstructed final states f. The ε_f are the corresponding reconstruction efficiencies and the $\mathcal{B}_f$ are the branching fractions of the $B \to f$ decays. In order to achieve as high efficiency as possible a large number of B-meson decay modes are used for the $B_{\rm tag}$ reconstruction. On the quark level B mesons decay dominantly via $\overline{b} \to \overline{c}W^+$ transitions, where the virtual W materializes either into a pair of leptons $\ell\nu_\ell$ (semileptonic decay), or into a pair of quarks, $u\overline{d}$ or $c\overline{s}$, which then hadronize. The most common choice for exclusive $B_{\rm tag}$ reconstruction are therefore semileptonic $B \to \overline{D}^{(*)}\ell^-\nu_\ell$ decays (semileptonic $B_{\rm tag}$ reconstruction) and hadronic $B \to \overline{D}^{(*)}n\pi$, $\overline{D}^{(*)}D_s^{(*)}$ or $B \to J/\psi K m\pi$ (hadronic $B_{\rm tag}$ reconstruction), where n and m indicate any number ($n,\ m \leq 10$) of charged or neutral pions and kaons, respectively. The branching fractions of these hadronic decay modes are between 10^{-3} and up to 10^{-2}, and the branching fraction for inclusive semileptonic decays[33] of a B meson to a D meson plus anything else is around 20%. The two analysis techniques are complimentary and non-overlapping and, as such, can be readily combined to improve the sensitivity of any recoil B analysis. This essentially doubles the size of the available $B_{\rm tag}$ sample.

Many decay modes for which the B meson cannot be exclusively reconstructed rely on these methods to make measurements feasible. For the proposed high luminosity asymmetric e^+e^- super flavor factories, measurements of B decays, not related to *CP* violation or the CKM picture of the Standard Model, will benefit from recoil methods. This corresponds to a wide program of purely leptonic, semileptonic and radiative penguin[34] B decays. Furthermore, with a huge dataset the recoil methods will provide a clean "single B beam" which will permit the extraction of hadronic B decay branching fractions using a missing mass technique.

In this section the general idea behind the recoil B-meson reconstruction has been presented. In addition the variables or constraints which can be imposed in studies of B-meson decays involving one or more neutrinos with recoil B-meson technique have been briefly described. The rest of this section is devoted to the description of different approaches to $B_{\rm tag}$ reconstruction. More details on analyses of decay modes utilizing the recoil B-meson reconstruction (given in Table 7.4.1) can be found in Sections 17.9, 17.10 and 17.11.

7.4.1 Hadronic tag B reconstruction

The full reconstruction of one B meson, decaying hadronically, has been utilized in a multitude of analyses by the B Factories (see Table 7.4.1). The approaches of *BABAR* and Belle differ somewhat, providing samples which vary

[32] The terms used for this B meson in the various *BABAR* and Belle papers are not consistent. Elsewhere in this book we use the term $B_{\rm sig}$.

[33] Semitauonic decays are not included in this case.

[34] A penguin decay is represented by a higher order Feynman diagram including a loop with a W or Z boson; a quark in the loop undergoes a tree process - either a strong interaction one, or electroweak one.

in efficiency and purity. The optimization of these choices depends primarily on the signal mode in the recoil system and the available kinematic constraints which can be imposed.

7.4.1.1 *BABAR*

BABAR opts for a semi-exclusive approach where hadronic B decays are reconstructed by *seeding* the event with a charm meson, and combining it with a number of pions and kaons. The algorithm underwent a major expansion in 2008 doubling its reconstruction efficiency. The starting point is the creation of a list with all the possible seeds in the event. In the original algorithm, D^0, D^+, D^{*0} and D^{*+} mesons were used as seeds, reconstructed in the following decay chains: $D^- \to K^+\pi^-\pi^-$, $K^+\pi^-\pi^-\pi^0$, $K^0_S\pi^-$, $K^0_S\pi^-\pi^0$, $K^0_S\pi^-\pi^-\pi^+$; $\overline{D}^0 \to K^+\pi^-$, $K^+\pi^-\pi^0$, $K^+\pi^-\pi^-\pi^+$, $K^0_S\pi^+\pi^-$; $D^{*-} \to \overline{D}^0\pi^-$; and $\overline{D}^{*0} \to \overline{D}^0\pi^0$, $\overline{D}^0\gamma$. The 2008 expansion added the decay chains $D^- \to K^+K^-\pi^-$, $K^+K^-\pi^-\pi^0$; $D^0 \to K^0_S\pi^-\pi^-\pi^0$, K^+K^-, $K^0_S\pi^0$, $\pi^+\pi^-\pi^0$, $\pi^+\pi^-$; $D^{*-} \to D^-\pi^0$, and the new seeds $D_s^+ \to \phi\pi^0$, $K^0_SK^+$; $D_s^{*+} \to D_s^+\gamma$ and $J/\psi \to e^+e^-$, $\mu^+\mu^-$.

Subsequently, each one of the reconstructed seeds is combined with up to 5 charmless particles to form a $B_{\rm tag} \to D_{\rm seed}\,Y$ candidate, where $D_{\rm seed}$ refers to the charm meson used to seed events. The Y system represents a collection of hadrons composed of $n_1\pi^\pm + n_2K^\pm + n_3\pi^0 + n_4K^0_S$ ($n_1 = 1,...,5$, $n_2 = 0,...,2$, $n_3 = 0,...,2$ and $n_4 = 0,1$) and having total charge equal to ±1. In the expansion, four neutral Y systems, $K^+\pi^-$, $\pi^+\pi^-$, K^+K^- and π^0, were added. Overall, the original algorithm reconstructs $B_{\rm tag}$ candidates in 630 different decay chains, and the expansion in 1768.

The $B_{\rm tag}$ candidates thus formed are accepted if they satisfy some loose requirements that ensure kinematic consistency with a B meson: the beam-energy substituted mass, $m_{\rm ES}$, has to be greater than 5.18 GeV/c^2, and ΔE has to satisfy $-0.12 < \Delta E < 0.12$ GeV. Correctly reconstructed events should have the $m_{\rm ES}$ and ΔE distributions peak at the B-meson mass and at zero, respectively.

These algorithms provide several $B_{\rm tag}$ candidates per event. One of the most extended methods to choose a unique candidate selects the decay chain with the highest *purity*, defined as the fraction of B candidates that are correctly reconstructed for $m_{\rm ES} > 5.27$ GeV/c^2 in each particular chain. The purity is determined from a fit to the $m_{\rm ES}$ spectrum of a data sample, where the signal distribution is described by a Crystal Ball function (Skwarnicki, 1986), named after the Crystal Ball collaboration, defined as

$$\mathrm{CB}(m|\alpha,n,m_0,\sigma) = \begin{cases} e^{-(m-m_0)^2/2\sigma^2}, & \text{if } \frac{m-m_0}{\sigma} < -\alpha \\ A\left(B - \frac{m-m_0}{\sigma}\right)^{-n}, & \text{otherwise,} \end{cases} \tag{7.4.2}$$

where $A = (n/|\alpha|)^n e^{-|\alpha|^2/2}$ and $B = n/|\alpha| - |\alpha|$. The background distribution is described by an ARGUS function as defined in Eq. (7.1.11). The purity can also be used to reject combinatorial background by selecting only decay chains with a minimum value of purity, typically between 30% and 55%.

In more recent analyses, the best $B_{\rm tag}$ candidate tends to be selected together with the rest of the event. For instance, in $B \to D^*\ell\nu$, each $B_{\rm tag}$ candidate is combined with D^* and ℓ candidates. The best $B_{\rm tag}D^*\ell$ candidate is selected maximizing the energy measured in the calorimeter that is used in the reconstruction.

In the final selection the kinematic requirements on $B_{\rm tag}$ are tightened, candidates are selected with $m_{\rm ES} > 5.27$ GeV/c^2 and narrower ΔE windows ($-90 < \Delta E < 60$ MeV is typically used). Events outside these regions may be used to study the combinatorial background.

When all the $B_{\rm tag}$ decay chains are used in the analysis, the efficiencies of the original algorithm, defined as

$$\varepsilon_{B^0_{\rm tag}} = \frac{N(B^0_{\rm tag})}{N(B\overline{B})}, \tag{7.4.3}$$

$$\varepsilon_{B^+_{\rm tag}} = \frac{N(B^+_{\rm tag})}{N(B\overline{B})}, \tag{7.4.4}$$

reaches typically 0.2% ($B^0\overline{B}^0$) and 0.4% (B^+B^-).

7.4.1.2 Belle

Belle developed two versions of hadronic $B_{\rm tag}$ reconstruction algorithms in the course of its history. In both versions the $B_{\rm tag}$ mesons are reconstructed in a set of exclusive final states, although the approach is slightly different from the one used by *BABAR* described above. The difference between the two versions is in the selection of $B_{\rm tag}$ candidates. In the first version a set of rectangular cuts is imposed on $B_{\rm tag}$ candidates (referred to as cut-based selection), while in the second the selection of $B_{\rm tag}$ candidates is made using a NeuroBayes neural network (referred to as NB selection) (Feindt, 2004) (see Section 4.4.4 for more details on neural nets). The latter version is mostly used in the measurements using the full data sample collected by Belle at the $\Upsilon(4S)$. At the end of this section a comparison between the two versions in terms of performance is provided.

In the cut-based approach Belle reconstructs a set of the following exclusive decay modes: $B^+ \to \overline{D}^{(*)0}(\pi,\ \rho,\ a_1,\ D_s^{(*)})^+$ and $B^0 \to D^{(*)-}(\pi,\ \rho,\ a_1,\ D_s^{(*)})^+$. $\overline{D}^0$ mesons are reconstructed in 7 decay modes: $K^+\pi^-$, $K^+\pi^-\pi^0$, $K^+\pi^-\pi^-\pi^+$, $K^0_S\pi^0$, $K^0_S\pi^-\pi^+$, $K^0_S\pi^-\pi^+\pi^0$ and K^-K^+. D^- mesons are reconstructed in 6 decay modes: $D^- \to K^+\pi^-\pi^-$, $K^+\pi^-\pi^-\pi^0$, $K^0_S\pi^-$, $K^0_S\pi^-\pi^0$, $K^0_S\pi^-\pi^-\pi^+$ and $K^+K^-\pi^-$, and the D_s^+ mesons are reconstructed in two decay modes: $K^0_SK^+$ and $K^+K^-\pi^+$. The D candidates are required to have an invariant mass m_D within $(4-5)\sigma$ of the nominal D mass value depending on the decay mode, where σ represents the D mass resolution. The $\overline{D}^{*0}$, D^{*-} and D_s^{*+} mesons are reconstructed in $\overline{D}^{*0} \to \overline{D}^0\pi^0$, $\overline{D}^0\gamma$, $D^{*-} \to \overline{D}^0\pi^-$, $D^-\pi^0$ and $D_s^{*+} \to D_s^+\gamma$ modes, respectively. $D^*_{(s)}$ candidates are required to have a mass difference $\Delta m = m_{D\pi} - m_D$ within ±5 MeV/c^2 of its nominal mass or $\Delta m = m_{D_{(s)}\gamma} - m_{D_{(s)}}$ within ±20 MeV/c^2.

The ρ^0, ρ^+ and a_1^+ are reconstructed in $\pi^+\pi^-$, $\pi^+\pi^0$ and $\rho^0\pi^+$ modes, respectively. The invariant mass of the $\pi\pi$ pairs is required to be within ± 225 MeV/c^2 of the nominal ρ mass, and the $\rho\pi$ combinations are required to have invariant mass between 0.7 and 1.6 GeV/c^2 (a_1 mass region). In order to obtain reasonable purity of the $B_{\rm tag}$ sample (*e.g.* above 20% in the $m_{\rm ES} > 5.27$ GeV/c^2 region) the decay chains with a high multiplicity of tracks and neutrals (and hence with a large contribution of combinatorial background) in the final state are excluded. Therefore in the $B \to \overline{D}^{(*)} a_1$ decay modes only the $D^- \to K^+\pi^-\pi^-$, $K_S^0\pi^-$ and $\overline{D}^0 \to K^+\pi^-$ modes are used. The selection of $B_{\rm tag}$ candidates is based on $m_{\rm ES}$ and ΔE. The definition of the signal region in the $\Delta E - m_{\rm ES}$ plane depends on the studied signal decay mode. If an event has multiple $B_{\rm tag}$ candidates the one with the smallest χ^2 is selected based on deviations from the nominal values of ΔE, the $D_{(s)}$ candidate mass and the $D^*_{(s)} - D_{(s)}$ mass difference, if applicable. The efficiencies as defined in Eqs (7.4.4) and (7.4.3) of $B^0_{\rm tag}$ and $B^+_{\rm tag}$ are found to be 0.10% and 0.14%, respectively.

In the second approach Belle increased the number of reconstructed exclusive B decay modes and used a neural network in their selection in order to increase the hadronic $B_{\rm tag}$ reconstruction efficiency (Feindt et al., 2011). In addition to the decay modes used in the cut-based selection the $B_{\rm tag}$ candidates are reconstructed also in the following decay modes: $B^+ \to \overline{D}^{*0}\pi^+\pi^+\pi^-\pi^0$, $D^-\pi^+\pi^+$, $\overline{D}^0K^+$, $J/\psi K^+$, $K^+\pi^0$, $K_S^0\pi^+$, $K^+\pi^+\pi^-$, and for neutral B mesons via $B^0 \to D^{*-}\pi^+\pi^+\pi^-\pi^0$, $\overline{D}^0\pi^0$, $J/\psi K_S^0$, $K^+\pi^-$, and $K_S^0\pi^+\pi^-$.[35] The D meson decay modes used in the reconstruction of $B_{\rm tag}$ are $\overline{D}^0 \to \pi^-\pi^+$, $K_S^0K^-K^+$, $D^- \to K^+K^-\pi^-\pi^0$ and $D_s^+ \to K^+\pi^+\pi^-$, $K^+K^-\pi^+\pi^0$, $K_S^0K^+\pi^+\pi^-$, $K_S^0K^-\pi^+\pi^+$, $K^+K^-\pi^+\pi^+\pi^-$ and $\pi^+\pi^+\pi^-$ in addition to the modes used by Belle in the cut-based reconstruction, given above. The J/ψ is reconstructed in e^+e^- and $\mu^+\mu^-$ modes. The sum of branching ratios of reconstructed decay modes adds up to around 12% for B^+, 10% for B^0 (not taking into account branching fractions of $D^{(*)}$, J/ψ, and other intermediate states), 38% for D^0, 29% for D^+, 18% for D_s^+ and 12% for J/ψ. The reconstruction and selection proceeds in four stages. At each stage all available information on a given candidate is used to calculate a single scalar variable (referred to as network output) using the NeuroBayes neural network which can be by construction interpreted as a probability that a given candidate is correctly reconstructed (Feindt, 2004). The network output for each reconstructed particle is used as an input to other neural networks in the later stage(s). In the first stage $\pi^\pm$, $K^\pm$, K_S^0, γ and π^0 candidates are reconstructed and classified, in the second D^0, $D^\pm_{(s)}$ and J/ψ, in the third D^{*0} and $D^{*\pm}_{(s)}$, and finally in the last, fourth stage the $B^\pm$ and B^0 candidates are reconstructed and classified. The neural networks of the first stage particles include measurements of time-of-flight, the energy loss in the CDC and Cherenkov light in the ACC for the charged particles, and shower shape variables for photons (see Chapter 2 for subdetectors description). The variables with the largest separation power in the second stage, *e.g.* classification of $D_{(s)}$ mesons, are the network outputs of the daughters (charged or neutral kaons and pions), the invariant masses of daughter pairs (in case of multi-body decay modes), the angle between the momentum of the $D_{(s)}$ meson and the vector joining the $D_{(s)}$ decay vertex and interaction point and the significance of the distance between the decay vertex and the interaction point. In the last stage, the B-meson stage, the variables providing good discrimination between correctly reconstructed B mesons and background candidates are again the network outputs of the daughters ($D^{(*)}$, J/ψ, pions, kaons), the mass of the $D_{(s)}$ or mass difference between $D^*_{(s)}$ and $D_{(s)}$, ΔE, and the angle between the B-meson momentum and the beam. A large fraction of $B_{\rm tag}$ candidates are background candidates from continuum events. As explained in detail in Chapter 9 continuum background can be quite successfully suppressed at B Factories by exploiting event shape variables, such as the reduced second Fox-Wolfram moment, R_2, thrust angle and super Fox-Wolfram moments. In the default $B_{\rm tag}$ networks these variables are excluded, but outputs of some additional neural networks, which take also the continuum suppression variables into account (with R_2 and thrust angle only, or with R_2, thrust angle and super Fox-Wolfram moments), are provided.

In an ideal case, one would reconstruct all possible $B_{\rm tag}$ candidates in the given decay modes without making any selections (cuts) between the stages. No signal candidates would be lost, *i.e.* the efficiency is maximized. Postponing the moment of the selection to the latest possible stage is always the preferred strategy in data analyses, since at the end more information is available which can be used to more successfully separate signal and background candidates. However this procedure is limited by combinatorics and computing resources. Events with many reconstructed particles lead to a large number of possible $B_{\rm tag}$ candidates which of course require more computing time. Loose cuts between the reconstruction stages are therefore required in order to keep computing time at a bearable level. These cuts on the network output for a given candidate are not performed at the end of each stage in which the candidate is reconstructed and classified but it is performed at the next stage and depends on the complexity of the decay mode in the next stage. As an example, the amount of combinations of the decay $B \to \overline{D}\pi\pi\pi$ is much higher then that of the decay $B \to \overline{D}\pi$ given the same number of $\overline{D}$ candidates. Therefore, a tighter cut on the signal probability of $\overline{D}$ candidates is performed only when necessary, *e.g.* when the reconstruction of all candidates would require too many resources, as in the case of $B \to \overline{D}\pi\pi\pi$ decays.

At the end the kinematic consistency of a $B_{\rm tag}$ candidate with a B-meson decay is checked using the beam constrained mass, $m_{\rm ES}$, as described previously. Since the

[35] The $B \to D^{(*)}(\rho, a_1)^+$ modes are reconstructed as $B \to D^{(*)}(\pi^0\pi^+, \pi^+\pi^-\pi^+)$ in the network based $B_{\rm tag}$ selection meaning that there are no explicit restrictions made on the invariant masses of the two or three pion systems.

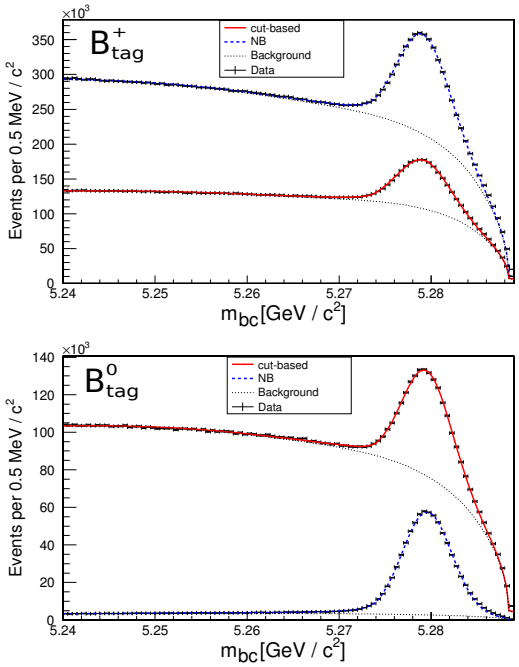

Figure 7.4.2. The $m_{\rm ES}$ ($= m_{\rm bc}$) distribution of hadronic $B^+_{\rm tag}$ (top) and $B^0_{\rm tag}$ (bottom) samples obtained by Belle with cut-based (red) and NB selection (blue) (Feindt et al., 2011). In case of the $B^+_{\rm tag}$ sample the cut on the network output in the NB selection is chosen to give equal purity as the cut-based selection in $m_{\rm ES} > 5.27$ GeV/c^2. In case of the $B^0_{\rm tag}$ sample the cut on the network output in the NB selection is chosen to give equal B-meson signal yield as the cut-based selection. These cuts are arbitrary and are chosen only for the purpose of comparing the NB and cut-based $B_{\rm tag}$ selections.

network output can be interpreted as signal probability the candidates which are reconstructed in different decay modes can be easily compared to one another. In case multiple $B_{\rm tag}$ candidates are found in an event the one with highest signal probability is taken as the best one. The $m_{\rm ES}$ distributions of $B^+_{\rm tag}$ and $B^0_{\rm tag}$ samples obtained by Belle with cut-based and NB selections are shown in Fig. 7.4.2. In order to compare the performance in terms of $B_{\rm tag}$ efficiencies and purities of the NB and cut-based selections the network output cuts in the NB selection are chosen is such a way that equal purities (in $m_{\rm ES} > 5.27$ GeV/c^2 region) or equal efficiencies are obtained in both selections. As can be seen from Fig. 7.4.2 at the same purity the signal yield (and hence efficiency) is approximately two times larger. The NB selection with efficiency equal to the cut-based selection will result in a much purer sample: nearly 90% versus 25% (reducing the background level by more than a factor of 20). The NB selection used in Fig. 7.4.2 is arbitrary and is chosen only for the purpose of comparing the NB and cut-based $B_{\rm tag}$ selections. The final selection depends on the studied decay mode and can be selected either to give maximal possible $B_{\rm tag}$ efficiency or high purity. Figure 7.4.3 shows purity-efficiency plots for $B^+_{\rm tag}$ and $B^0_{\rm tag}$ for the default NB selection and the one including continuum suppression. The highest possible efficiency that can be achieved with the NB selection at Belle is around 0.18% for $B^0_{\rm tag}$ and 0.28% for $B^+_{\rm tag}$ with around 10% purity. This corresponds to an improvement in efficiency by roughly a factor of two comparing to Belle's cut-based $B_{\rm tag}$ selection.

7.4.2 Semileptonic tag B reconstruction

This method of semi–exclusive B reconstruction involves the selection of a D meson and suitable lepton candidate, ℓ, which are then combined into a $D\ell$ candidate.

The $B_{\rm tag}$ is reconstructed in the set of semileptonic B decay modes $B^- \to D^0\ell^-\overline{\nu}_\ell X$, where ℓ denotes an e or μ, and X can be either nothing or a transition particle from a higher mass charm state decay, which one does not necessarily need to reconstruct. This methodology naturally includes the $B^- \to D^0\ell^-\overline{\nu}_\ell$ and $B^- \to D^{*0}\ell^-\overline{\nu}_\ell$ modes and also retains those modes with excited D meson states which decay, via the emission of soft transitions particles, to a D^0. The technique can be similarly applied to the tagging of neutral B mesons where one would reconstruct $\overline{B}^0 \to D^{(*)+}\ell^-\overline{\nu}_\ell$ for a combination of all possible $\overline{B}^0 \to D^+\ell^-\overline{\nu}_\ell$ and $\overline{B}^0 \to D^{*+}\ell^-\overline{\nu}_\ell$ states reconstructed exclusively. The main loss in efficiency arises from the B and charm decay branching fractions while further selection criteria must be applied in order to suppress non-B decay backgrounds (continuum) and fakes from hadronic B decays.

The D^0 decay is reconstructed by *BABAR* in the four cleanest hadronic modes: $K^-\pi^+$, $K^-\pi^+\pi^-\pi^+$, $K^-\pi^+\pi^0$, and $K^0_s\pi^+\pi^-$. The K^0_s is reconstructed only in the mode $K^0_s \to \pi^+\pi^-$. Belle reconstructs D^0 candidates in ten decay modes (Hokuue, 2007): in addition to the four decay modes above, the $K^0_s\pi^0$, $K^0_s\pi^+\pi^-\pi^0$, $K^-\pi^+\pi^+\pi^-\pi^0$, K^+K^-, $K^0_sK^+K^-$ and $K^0_sK^-\pi^+$ modes are also included. The added benefit of reconstructing the low momentum transition daughter in D^{*0} decays is to provide a more complete and exclusive tag B selection. Indeed if one neglects to reconstruct these π^0 or γ daughters (from $D^{*0} \to D^0\pi^0/\gamma$) then they will be considered in the reconstruction of the signal B target mode. However, it is observed that the semi-exclusive reconstruction of $B \to D^0\ell\nu X$ provides a higher efficiency with some loss of purity.

For neutral B tags the selection becomes that of either $\overline{B}^0 \to D^+\ell^-\overline{\nu}_\ell$ or $\overline{B}^0 \to D^{*+}\ell^-\overline{\nu}_\ell$. The D^+ decays are reconstructed at Belle in seven decay modes $K^-\pi^+\pi^+$, $K^0_S\pi^+$, $K^-\pi^+\pi^+\pi^0$, $K^0_S\pi^+\pi^0$, $K^0_S\pi^+\pi^+\pi^-$, $K^0_SK^+$ and $K^+K^-\pi^+$ (Hokuue, 2007), while *BABAR* uses only the first two decay modes. The D^{*+} decays can be reconstructed as both $D^0\pi^+$ and $D^+\pi^0$. The mass difference between D^* and D provides a powerful constraint as does the invariant mass of the D^0 or D^+ candidate.

The center-of-mass lepton momentum (p^*_ℓ) for both electrons and muons is selected to be greater than 0.8 (1.0) GeV/c at *BABAR* (Belle). This is the lower end of muon identification for the current B Factories and there is commonly non-B background below $p^*_\ell \sim 1$ GeV/c. The

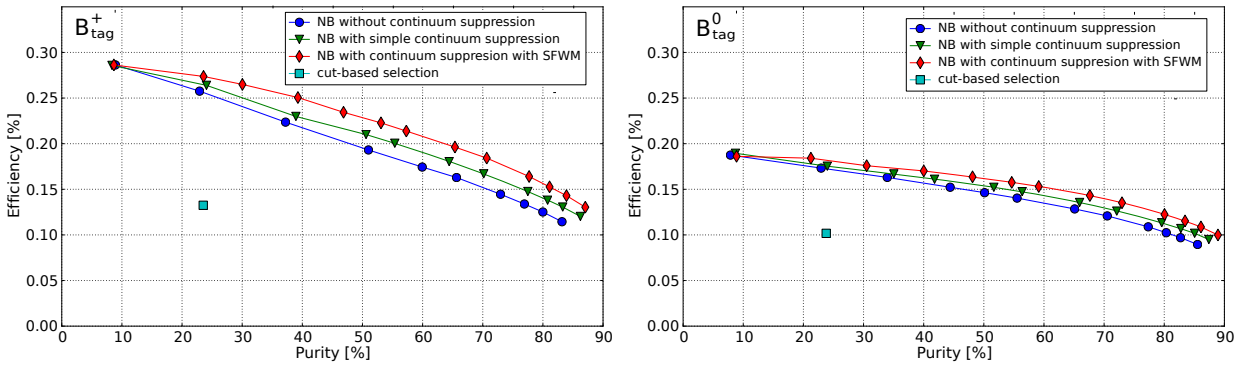

Figure 7.4.3. Purity-efficiency plots for hadronic $B^+_{\rm tag}$ (left) and $B^0_{\rm tag}$ (right) as obtained by Belle with neural network based selection (NB) and cut-based selection (Feindt et al., 2011). The network based selection can include no continuum suppression variables (blue), only simple ones (green) or Super-Fox-Wolfram moments (SFWM; red).

reconstructed D mesons are required to be within $\pm 3\sigma$ ($\pm 2.5\sigma$) at *BABAR* (Belle) of their nominal mass value. As explained in Section 7.2 the cosine of the angle between the B meson and the $D^{(*)}\ell$ candidate momenta, $\cos\theta_{B,D\ell}$ defined in Eq. (7.2.2), is a powerful discriminant. In case the $D\ell$ and the neutrino are the only decay products of the B then $\cos\theta_{B,D\ell}$ must lie in the physical region between ± 1. If additional decay products from the cascade of a higher mass charm state down to the D^0 go unreconstructed then this will force the value of $\cos\theta_{B,D\ell}$ to be smaller. In order to keep such candidates events with $\cos\theta_{B,D\ell}$ between -2.5 and $+1.1$ are usually accepted. The positive limit is allowed to be slightly outside of the physical region to account for detector and reconstruction effects. Of course, for the reconstruction of exclusive channels ($B^- \to D^0\ell^-\overline{\nu}_\ell$, $B^- \to D^{*0}\ell^-\overline{\nu}_\ell$, $\overline{B}^0 \to D^+\ell^-\overline{\nu}_\ell$ and $\overline{B}^0 \to D^{*+}\ell^-\overline{\nu}_\ell$), the selection is tightened to only consider the physical region.

A typical $B^- \to D^0\ell^-\overline{\nu}_\ell X$ selection at *BABAR* yields an efficiency of approximately 6×10^{-3} with a mode dependent purity which averages to $\sim 60\%$. For the neutral B reconstruction the efficiency is typical half that of a similar charged B selection.

The loss of a neutrino in the semileptonic tagging mode limits the constraints that can be imposed compared to the case when all of the B meson decay products are reconstructed. For example the signal B direction cannot be found as is possible for hadronic B reconstruction. However, this constraint is not of paramount importance in the analysis of signal decay modes to final state with more than one neutrino like for example $B^+ \to \tau^+\nu_\tau$ or $B^0 \to \nu\overline{\nu}$). The knowledge of signal B momentum enables calculation of missing mass which is a very powerful variable to separate signal B decays with a single neutrino in the final state from background decays, but becomes weak when multiple neutrinos are present in the signal B decay.

7.4.3 Inclusive $B_{\rm tag}$ reconstruction

As discussed in the previous two sections the reconstruction of the recoil B meson using the hadronic and semileptonic $B_{\rm tag}$ samples has many benefits, however suffers from low reconstruction efficiencies. To increase the statistics Belle adopted an inclusive $B_{\rm tag}$ reconstruction (Bozek, 2010; Matyja, 2007) in studies of semitauonic $B \to D^{(*)}\tau^-\nu$ decays (see Section 17.10). In contrast to the measurements utilizing the hadronic or semileptonic recoil $B_{\rm tag}$ reconstruction technique the procedure in this case is first to reconstruct the signal side (pairs of a $D^{(*)}$ and a lepton or pion from tau decay). In the second step the $B_{\rm tag}$ is inclusively reconstructed from all remaining particles passing certain selection criteria however without checking consistency with any specific B-meson decays. The number of neutral particles on the tagging side $N_{\pi^0} + N_\gamma < 6$ and $N_\gamma < 3$. The quality of $B_{\rm tag}$ reconstruction and suppression of background is further improved by requiring zero total charge and net proton/antiproton number, no leptons on the tagging side and extra energy to be close to zero (less then 350 MeV). These criteria reject events in which some particles from the signal or tagging side were undetected and suppress events with a large number of spurious showers. The consistency of $B_{\rm tag}$ with a B-meson decay is checked using the beam constrained mass, $m_{\rm ES}$, and the energy difference, ΔE. The simulation and reconstruction of the inclusive $B_{\rm tag}$ sample is checked using a control sample of events, where the $B \to D^{*-}\pi^+$ decays (followed by $D^{*-}\pi^-$, $\overline{D}^0 \to K^+\pi^-$) are reconstructed on the signal side. Figure 7.4.4 shows the $m_{\rm ES}$ and ΔE distributions of the control sample for data and the MC simulation. The good agreement of the shapes and of the absolute normalization demonstrates the validity of the MC-simulations for $B_{\rm tag}$ decays. While the $m_{\rm ES}$ distribution shows a clear peak at the B-meson mass, the ΔE distribution is very broad. On the negative side events with undetected particles contribute and the main source of the events with $\Delta E > 0$ are spurious showers in the electromagnetic calorimeter from secondary interactions of hadrons. These clusters add linearly to ΔE, but tend to average in the vector sum of their momenta that enters the calculation of $m_{\rm ES}$, see Eq. (7.1.8).

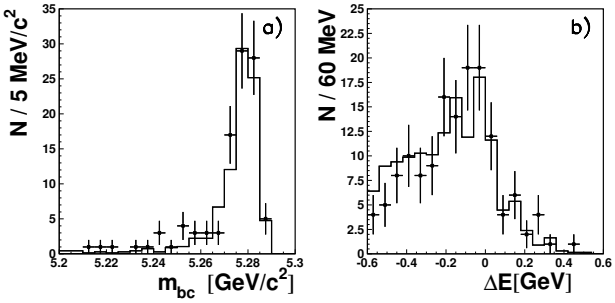

Figure 7.4.4. The $m_{\rm ES}$ ($= m_{\rm bc}$) (a) and ΔE (b) distributions for inclusively reconstructed $B_{\rm tag}$ using a $B^0 \to D^{*-}\pi^+$ recoil control sample from data (points with error bars) and MC (histograms) (Matyja, 2007). The ΔE ($m_{\rm ES}$) of $B_{\rm tag}$ candidates is required to be between -0.25 and 0.05 GeV (larger then 5.27 GeV/c^2) when plotting $m_{\rm ES}$ (ΔE).

7.4.4 Double tagging

There are two assumptions made when using the recoil method: the first is that the B reconstruction efficiency is well modeled by the Monte Carlo simulations of generic B decays and continuum events. The hadronic $B_{\rm tag}$ reconstruction efficiencies defined in Eqs (7.4.4) and (7.4.3) depend on the decay rates of B-meson decays to final state included in the reconstruction. Some of them are poorly known and hence the $B_{\rm tag}$ reconstruction efficiencies determined on simulated samples need to be validated or calibrated using the real data sample. The second is that for analyses with few reconstructed particles from the signal B, the extra energy used to discriminate signal from background events is also well-modeled. These assumptions can be checked by using control samples which test both the tag B reconstruction efficiency and the description of extra energy in a fully-reconstructed event. Both *BABAR* and Belle use double-tagged samples, in which both B mesons are fully reconstructed either in semileptonic or hadronic final states, as such a control.

The crosscheck using the double-tag approach was first applied by *BABAR* (Aubert, 2004y), using double semileptonic B decays. For the semileptonic $B_{\rm tag}$ technique described in Section 7.4.2 this means the reconstruction of two oppositely charged and non-overlapping $B \to D^0\ell\nu_\ell X$ candidates with little other detector activity. Both *BABAR* and Belle have also used "hybrid double-tags", where one B is reconstructed in a hadronic final state while the second B is reconstructed in a semileptonic final state ($B \to D^{(*)}\ell\nu_\ell$). These samples vary in size, depending on the final states used, but given a semileptonic tag reconstruction efficiency (quoted by *BABAR*) of $\sim 0.7\%$ and a hadronic tag efficiency of $\sim 0.2\%$, one expects to find approximately 50 semileptonic double-tagged events per fb^{-1}, 30 hybrid tags per fb^{-1}, and 4 hadronic double-tagged events per fb^{-1}. Given the large datasets of the B Factories, and the expected dataset at future super flavor factories, these are significant samples which can be used as important cross-checks of the assumptions in the recoil method.

The double-tagged events have two important features. The first is that one expects naïvely the yield to be proportional to $\varepsilon_{\rm tag}^2$, which is the basis of the cross-check of the tag efficiency. The second is that the complete reconstruction of both B mesons creates an environment in which the extra energy in a given event should represent the effect of energy deposits unassociated with the B decays themselves. This latter feature is an important ingredient in the cross-check of the extra energy modeling in signal events, where it is also assumed that all detected particles associated with the B decays have been reconstructed.

The cross-check of the tag efficiency is currently only used in the semileptonic approach, and only by *BABAR*. The early approach to the double-tag sample (Aubert, 2006a) made two assumptions. Given an efficiency, $\varepsilon_{\rm tag}$, for reconstructing one of the two Bs in an event in a semileptonic final state, the number of double tags (N_2) is given simply by

$$N_2 = \varepsilon_{\rm tag}^2 \times N_{B^+B^-} \tag{7.4.5}$$

where $N_{B^+B^-}$ is the number of charged B pairs originally produced by the B Factory or generated in Monte Carlo simulations. The tag efficiency cross-check was performed by taking the ratio of the above equation in data and in MC simulation and assuming that the double-tag sample is dominated by charged B mesons so that $N_{B^+B^-}$ cancels, yielding the correction factor ($c_{\rm tag}$) for the tagging efficiency in MC,

$$c_{\rm tag} = \frac{\varepsilon_{\rm tag}^{\rm data}}{\varepsilon_{\rm tag}^{\rm MC}} = \sqrt{\frac{N_2^{\rm data}}{N_2^{\rm MC}}}. \tag{7.4.6}$$

While MC studies of the double-tags suggest that the contamination from neutral B decays, or other backgrounds, is very small, the second assumption - that the reconstruction of the first B does not bias the reconstruction of the second - is not addressed. The closeness of the correction to 1.0, as cited by *BABAR*, does suggest that also the second assumption is essentially correct.

A second approach to the efficiency correction attempts to address some of the potential deficiencies of the first method outlined above. In the alternative approach (Aubert, 2007a), the data/MC comparison is performed using the ratio of single-tagged to double-tagged events. If the efficiency of reconstructing the first tag is $\varepsilon_{\rm tag,1}$ and the efficiency of reconstructing the second tag is $\varepsilon_{\rm tag,2}$, then the single-tag and double-tag yields, N_1 and N_2, are given by

$$N_1 = \varepsilon_{\rm tag,1} \times N_{B^+B^-} \tag{7.4.7}$$

$$N_2 = \varepsilon_{\rm tag,1} \times \varepsilon_{\rm tag,2} \times N_{B^+B^-}. \tag{7.4.8}$$

The ratio of the two cancels some of the common factors, yielding the following quantity to be determined in both data and MC simulations,

$$\varepsilon_{\rm tag,2} = \frac{N_2}{N_1} \tag{7.4.9}$$

BABAR determines the number of single-tagged events by subtracting the combinatorial component under the D^0

mass distribution using an extrapolation of events from the D^0 mass sideband. This leaves a sample of events containing correctly reconstructed events, mis-reconstructed events from neutral B semileptonic decay, and events from $e^+e^- \to c\bar{c}$ continuum background events with real D^0 mesons paired with a combinatorial lepton. The correction to the tag efficiency is assumed to be equal for either the first or second tag, and is computed from the data and MC as,

$$c_{\rm tag} = \frac{\varepsilon^{\rm data}_{\rm tag,2}}{\varepsilon^{\rm MC}_{\rm tag,2}} = \frac{N^{\rm data}_2/N^{\rm data}_1}{N^{\rm MC}_2/N^{\rm MC}_1} \tag{7.4.10}$$

The correction is computed using only events in which the D^0 meson in the first $B_{\rm tag}$ decays into the $K^-\pi^+$ final state. This is cross-checked using a sample in which the D^0 meson from the first tag decays into the $K^-\pi^+\pi^-\pi^+$ final state only, yielding complementary results.

In both of the above methods, and across several iterations of semileptonic recoil-based analyses, *BABAR* has found the correction to be very close to 1.0. This suggests both that the assumptions in the above two methods are largely accurate, and also that existing simulations of these and the background decays are adequate for the purposes of modeling the decays. The correction has an associated systematic error, which is typically determined by propagating the statistical uncertainty due to the finite sample sizes of the double-tag and single-tag samples. The uncertainty of the correction is about 4%.

Belle (Sibidanov, 2013) uses fully reconstructed events to calibrate the efficiency of the NB-based $B_{\rm tag}$ reconstruction. One of the produced B mesons is reconstructed as hadronic $B_{\rm tag}$ while the other B meson is reconstructed in the semileptonic decay mode $B_{sl} \to D^{(*)}\ell\nu$. The number of double tagged events is therefore given by:

$$N(B_{\rm tag}B_{sl}) = N_{B\bar{B}} \times \mathcal{B}(B_{\rm tag} \to f)\varepsilon_{B_{\rm tag}\to f} \times \mathcal{B}(B_{sl} \to D^{(*)}\ell\nu)\varepsilon_{B_{sl}}, \tag{7.4.11}$$

where $\mathcal{B}(B_{\rm tag} \to f)\varepsilon_{B_{\rm tag}\to f}$ is the product of branching fraction and reconstruction efficiency of the specific decay $B_{\rm tag} \to f$ and $\mathcal{B}(B_{sl} \to D^{(*)}\ell\nu)\varepsilon_{B_{sl}}$ is the corresponding product for the semileptonically decaying B meson, which is well modeled in the simulation. The correction factor for $B_{\rm tag} \to f$ is then obtained by measuring the ratio of the numbers of reconstructed double tagged events in real data and MC samples

$$c^f_{\rm tag} = \frac{\mathcal{B}^{\rm data}(B_{\rm tag} \to f)\varepsilon^{\rm data}_{B_{\rm tag}\to f}}{\mathcal{B}^{\rm MC}(B_{\rm tag} \to f)\varepsilon^{\rm MC}_{B_{\rm tag}\to f}} = \frac{N^{\rm data}(B_{\rm tag}B_{sl})}{N^{\rm MC}(B_{\rm tag}B_{sl})} \cdot \frac{N^{\rm MC}_{B\bar{B}}\mathcal{B}^{\rm MC}(B_{sl} \to D^{(*)}\ell\nu)}{N^{\rm data}_{B\bar{B}}\mathcal{B}^{\rm data}(B_{sl} \to D^{(*)}\ell\nu)}. \tag{7.4.12}$$

In this method of the $B_{\rm tag}$ efficiency calibration it is assumed that the $B_{sl} \to D^{(*)}\ell\nu$ modes are well modeled in the MC sample and hence the $\varepsilon^{\rm data}_{B_{sl}} = \varepsilon^{\rm MC}_{B_{sl}}$. The overall correction factor (averaged over all $B_{\rm tag}$ modes) is found to be around 0.7 and consistent between different B_{sl} decay modes. The total uncertainty of the calibration is estimated to be 4.2% for $B^+_{\rm tag}$ and 4.5% for $B^0_{\rm tag}$.

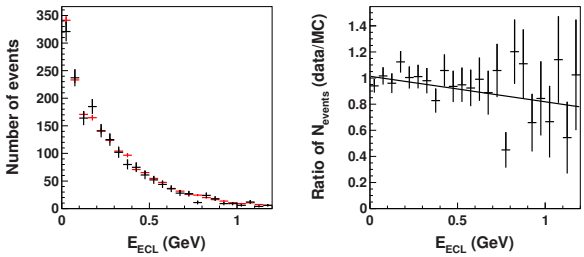

Figure 7.4.5. Extra energy distribution for double-tagged $B^+_{\rm tag}B^-_{sl}$ events (left plot), where the semileptonically decaying B meson is reconstructed in the $D^{*0}\ell^-\overline{\nu}_\ell$ decay mode. Black and red data points show the distribution obtained in data and in a sample of simulated events, respectively. The right plot shows the ratio of the two distributions fitted with a linear function. Belle internal, from the Adachi (2012b) analysis.

The second application of the double-tagged sample is to test the modeling of extra particles left in the detector after both B mesons have been reconstructed. In the case of signal events, this typically means that the tag B is reconstructed up to any neutrinos in the final state (as in semileptonic tags), and that the signal B is also reconstructed up to possible neutrinos in its final state. After reconstruction of both B mesons the remaining particles left in the event are assumed to come from several sources: neutrals, such as photons, which arise from the electron-positron beams but not the interaction point; some low momentum charged particles associated with interactions between the beam and the beampipe; neutral clusters from hadronic showering in the calorimeter which fail to associate with a track; and detector noise. These sources would typically lead to a few extra neutral particles left in a signal event in about 20-30% of the reconstructed events.

Double-tagged events are used to test the simulation of these extra neutral particles by fully reconstructing both B mesons either semileptonically, hadronically, or in a hybrid configuration. An example of the use of the double-tags to test the extra energy simulation is the Belle collaboration's hadronic-tagged search for $B^+ \to \tau^+\nu_\tau$. Belle constructs a hybrid double-tag sample (one hadronic B and one semileptonic B per event in the sample), and assumes that the extra neutral clusters remaining in these events comes from the same sources as in signal events. They compare the extra energy in data and MC (Fig. 7.4.5) and use the difference as a variation on their *p.d.f.* model for signal events. Comparisons show that existing detector simulations at the B Factories handle the variety of sources of extra neutral clusters fairly well, even in moderate to high multiplicity final states of B decay.

7.5 Summary

B-meson reconstruction is crucial for the broad physics program performed at Belle and *BABAR*. All of the techniques presented in this chapter utilize unique constraints provided by the experimental setup of B Factories. They either improve the resolution (*e.g.* $m_{\rm ES}$ and ΔE versus B-meson invariant mass in full hadronic reconstruction), increase reconstruction efficiency (partial reconstruction) or make possible studies of B-meson decays with multiple neutrinos in the final state (recoil reconstruction). Some of the B reconstruction methods presented herein were already used by experiments prior to Belle and *BABAR*. Others, in particular recoil techniques using fully- or semi-exclusive B-meson reconstruction, were pioneered in the B Factories era and proved invaluable to access rare processes where the kinematics of the signal B meson could not be fully constrained. Together with background discrimination (see Chapter 9) B reconstruction techniques have been constantly improved over the past ten years which has enabled studies of less clean modes and increased sensitivity to rare decays.

Chapter 8
B-flavor tagging

Editors:
Juerg Beringer (BABAR)
Kazutaka Sumisawa (Belle)

Additional section writers:
Robert Cahn, Simone Stracka

8.1 Introduction

The goal of B-flavor tagging is to determine the flavor of a B meson (*i.e.* whether it contains a b or a $\overline{b}$ quark) at the time of its decay. At the B Factories, flavor tagging is needed for most measurements of time-dependent CP asymmetries and B meson mixing. As will be discussed in Chapter 10, these measurements usually require full reconstruction of the decay of one of the B mesons (referred to as $B_{\rm rec}$ or "signal" B), measurement of the decay time difference Δt between the two B meson decays, and flavor tagging of the other B meson (referred to as $B_{\rm tag}$ in the following).

At the B Factories, in contrast to hadron colliders, B meson pairs are produced in isolation (apart from any initial-state radiation), since there is no "underlying event" and the fraction of events with multiple e^+e^- interactions ("pile-up") is negligible. Therefore, if a $B_{\rm rec}$ decay is fully reconstructed, the remaining tracks in the event can be assumed to come from the $B_{\rm tag}$ decay. In this case flavor tagging is to a good approximation independent of the specific $B_{\rm rec}$ decay mode reconstructed (but of course still depends on whether decays of $B^0/\overline{B}^0$, B^+/B^- or, when running at the $\Upsilon(5S)$, $B_s^0/\overline{B}_s^0$ are tagged), and the flavor tagging performance can be measured using fully reconstructed flavor-specific $B_{\rm rec}$ decays. For inclusive reconstruction of the signal B, flavor tagging in general depends on the specific $B_{\rm rec}$ reconstruction since the remaining tracks in the event cannot be unambiguously assigned to either the $B_{\rm rec}$ or $B_{\rm tag}$ meson.

The tagging of neutral $B^0/\overline{B}^0$ mesons from $\Upsilon(4S)$ decays assuming a fully reconstructed $B_{\rm rec}$ decay is the primary use case for flavor tagging at the B Factories. This is the situation considered in the following.

Flavor tagging relies on the fact that a large fraction of B mesons decay to a final state that is flavor specific, *i.e.* to good approximation, can only be reached either through the decay of a b quark, or through the decay of a $\overline{b}$ quark. Because of the large number of decay channels, full reconstruction of a sufficiently large number of flavor-specific $B_{\rm tag}$ decays is not feasible. Instead inclusive techniques are employed that make use of different flavor-specific signatures of B decays. For example, in semileptonic decays $B^0 \to D^{*-}\ell^+\nu_\ell$ the charge of the lepton unambiguously identifies the flavor of the decaying B meson as long as the lepton can be clearly associated with the semileptonic B decay and does not come from a secondary D meson decay.

The flavor tagging algorithms developed by *BABAR* and Belle proceed in two stages. In the first stage, individual flavor-specific signatures are analyzed, each of which provides a signature-specific flavor tag that by itself could be used for flavor tagging. In the second stage, the results from the first stage signatures are combined into a final flavor tag. Both stages rely on multivariate methods in order to optimally combine all available information.

The outline of this chapter is as follows. After defining the relevant quantities characterizing the performance of B-flavor tagging and discussing the choice of tagging categories, the different sources of flavor information and the corresponding discriminating variables are reviewed. Section 8.6 describes the specific flavor tagging algorithms used by the *BABAR* and Belle experiments and quotes the performance of these algorithms. The method used to measure the flavor tagging performance is described elsewhere (see Section 10.6).

8.2 Definitions

The figure of merit for the performance of a tagging algorithm is the effective tagging efficiency Q,

$$Q = \varepsilon_{\rm tag}(1-2w)^2, \tag{8.2.1}$$

where $\varepsilon_{\rm tag}$ denotes the fraction of events to which a flavor tag can be assigned, and the mistag probability w is the fraction of events with an incorrectly assigned tag. The term

$$D = 1-2w \tag{8.2.2}$$

is called the dilution and is the factor by which measured CP and mixing asymmetries are reduced from their physical values due to incorrectly assigned flavor tags. The definition of Q is motivated by the fact that the statistical uncertainties σ on such asymmetry measurements generally scale approximately as (see Section 8.4)

$$\sigma \propto \frac{1}{\sqrt{Q}}. \tag{8.2.3}$$

Tagging efficiencies and mistag fractions are not a priori the same for tagging B^0 and $\overline{B}^0$ decays because the detector performance may not be completely charge symmetric. Therefore the averages

$$\varepsilon_{\rm tag} = \frac{\varepsilon_{B^0} + \varepsilon_{\overline{B}^0}}{2} \tag{8.2.4}$$

$$w = \frac{w_{B^0} + w_{\overline{B}^0}}{2} \tag{8.2.5}$$

and differences

$$\Delta\varepsilon_{\rm tag} = \varepsilon_{B^0} - \varepsilon_{\overline{B}^0} \tag{8.2.6}$$

$$\Delta w = w_{B^0} - w_{\overline{B}^0} \tag{8.2.7}$$

are defined where the subscript refers to the true decay. For example, w_{B^0} refers to the fraction of neutral $B_{\rm tag}$ mesons that decay as B^0 but are tagged as $\overline{B}^0$.

8.3 Tagging categories

The effective tagging efficiency Q can be improved (and hence the statistical uncertainty of a measurement decreased) by grouping events into mutually exclusive tagging categories according to their mistag probabilities w (or dilutions D). For tagging categories c with fractions of events ε_c, dilutions D_c, total tagging efficiency $\varepsilon = \sum_c \varepsilon_c$ and average dilution $D = \sum_c \varepsilon_c D_c/\varepsilon$ one finds

$$Q = \sum_c \varepsilon_c D_c^2 = \varepsilon D^2 + \sum_c \varepsilon_c (D_c - D)^2. \tag{8.3.1}$$

Thus the resulting Q is always larger or equal to the one obtained when all events are treated as a single category. One gains most from dividing events into categories when the differences in dilution (or mistag fraction) between categories can be made large. However, the characteristics and any systematic effects, such as correlations with the tag vertex resolution, tag-side interference (see Section 15.3.6), or background levels, are expected to be determined by the different flavor-specific signatures. For this reason one would prefer a grouping of events according to different signatures over a category definition based on w.

The mistag probability w that can be achieved for a given set of $B_{\rm tag}$ decay modes is determined by the flavor-specific signatures present in these decays. Fortunately, the mistag probabilities of different flavor-specific signatures tend to be different. For example, in semileptonic decays the charge of a reconstructed high-momentum electron or muon gives a much better indication of the correct tag than the charge of a low momentum pion ("slow pion") from a secondary D^* decay.

Therefore a grouping of events into tagging categories according to the mistag probability naturally provides a grouping according to the different signatures of the corresponding $B_{\rm tag}$ decays. Conversely, a grouping according to different signatures leads to an approximate grouping according to mistag probabilities. As a result it is possible to define tagging categories that both optimize the tagging performance and group events according to different signatures.

8.4 Dilution factor and effective tagging efficiency

As mentioned above, a *CP* asymmetry $A^{\rm rec}$ measured using flavor tagging is reduced from the physical asymmetry by a factor D due to incorrectly assigned flavor tags. This scaling is easy to see by writing the measured asymmetry $A^{\rm rec}$ as

$$A^{\rm rec} = \frac{N - \overline{N}}{N + \overline{N}}, \tag{8.4.1}$$

where N and $\overline{N}$ denote the number of reconstructed B decays

$$\begin{aligned} N &= \varepsilon_{\rm tag}(1-w)N_0 + \varepsilon_{\rm tag} w \overline{N}_0 \\ \overline{N} &= \varepsilon_{\rm tag}(1-w)\overline{N}_0 + \varepsilon_{\rm tag} w N_0 \end{aligned} \tag{8.4.2}$$

tagged as B^0 and $\overline{B}^0$, respectively. N_0 and $\overline{N}_0$ are the corresponding number of reconstructed B decays of a certain type before tagging is applied. Substituting Eq. (8.4.2) into (8.4.1) one directly obtains

$$A^{\rm rec} = (1-2w)A^0 = DA^0, \tag{8.4.3}$$

where $A^0 = (N_0 - \overline{N}_0)/(N_0 + \overline{N}_0)$ denotes the true physical asymmetry.

The statistical uncertainty in A^0 is

$$\sigma_{A^0} = \frac{\sigma_{A^{\rm rec}}}{1-2w}\ . \tag{8.4.4}$$

Using Eq. (8.4.1) and denoting the total number of tagged events by $N_{\rm tag} = N + \overline{N}$, assuming a small asymmetry (*i.e.* $N \approx \overline{N} = N_{\rm tag}/2$), one finds

$$\sigma_{A^{\rm rec}} \propto \frac{1}{\sqrt{N_{\rm tag}}}\ . \tag{8.4.5}$$

Together with Eq. (8.4.4) it follows

$$\sigma_{A^0} \propto \frac{1}{\sqrt{\varepsilon_{\rm tag}}(1-2w)} = \frac{1}{\sqrt{Q}}\ . \tag{8.4.6}$$

In general, this scaling of σ_{A^0} with Q is only approximate. For a likelihood-based analysis and assuming a sufficiently large number of events, the expected uncertainty in an estimated *CP* or mixing asymmetry $\widehat{A}$ can be obtained from the maximum-likelihood estimator for the variance on $\widehat{A}$ (see Section 11.1.3),

$$\sigma(\widehat{A})^2 = V(\widehat{A}) = \left(\frac{d^2 \log(L(A))}{d^2 A} \right)^{-1}_{A=\widehat{A}}. \tag{8.4.7}$$

This was calculated (Cahn, 2000; Le Diberder, 1990) for the case of a measurement of a time-dependent *CP* asymmetry with no direct *CP* violation such as *e.g.* the measurement of $A = \sin 2\phi_1$. Using several tagging categories c, ignoring effects of resolution and background, and with $x_d = \Delta m/\Gamma$, the approximation

$$\sigma(\widehat{A}) \approx \left[N \frac{2x_d^2}{1+4x_d^2} \sum_c \epsilon_c D_c^2 \left(1 + \frac{12 x_d^2 D_c^2 A^2}{1+16x_d^2} \right) \right]^{-1/2}, \tag{8.4.8}$$

was derived. This leads to an improved definition Q' of the effective tagging efficiency,

$$Q' = \sum_c \varepsilon_c D_c^2 \left(1 + \frac{12 x_d^2 D_c^2 A^2}{1+16x_d^2} \right) \tag{8.4.9}$$

with $\sigma(\widehat{A}) \propto 1/\sqrt{Q'}$.

Q' depends on the true asymmetry A and reduces to the standard definition of Q for $A = 0$. For large asymmetries ($A \approx 1$) and for the most powerful tagging categories used by the *BABAR* or Belle tagging algorithms with $w_c \approx 2\%$, the factor

$$1 + \frac{12 x_d^2 D_c^2 A^2}{1+16x_d^2} \tag{8.4.10}$$

amounts to a correction of more than 60%. This effect was clearly observed when the scaling of the uncertainties of different *BABAR* $\sin 2\phi_1$ results with effective tagging efficiency was analyzed.

8.5 Physics sources of flavor information

In the following the different flavor-specific signatures are discussed in more detail. Since the focus of this chapter is on tagging for fully reconstructed $B_{\rm rec}$ decays, it is assumed that only tracks from the $B_{\rm tag}$ decays are considered in the calculation of any of the discriminating variables described below.

8.5.1 Leptons

Electrons and muons produced directly in semileptonic B decays (primary leptons) provide excellent tagging information. The charge of a lepton from a $b \to c\,\ell^-\,\overline{\nu}$ transition is directly associated to the flavor of the B^0 meson: a positively charged lepton indicates a B^0, a negatively charged lepton indicates a $\overline{B}^0$.

Leptons from cascade decays (secondary leptons) occurring via the transition $b \to W^- c\,(\to s\,\ell^+\,\nu)$ carry tagging information as well: their charge is opposite to that of primary leptons from $B_{\rm tag}$ and they are characterized by a much softer momentum spectrum.

The following kinematical variables are useful to identify primary and secondary leptons:

- q, the charge of the track.
- p^*, the center-of-mass momentum of the candidate track. Combined with the charge of the track this is the most powerful discriminating variable.
- $\theta_{\rm lab}$, the polar angle in the laboratory frame.
- E_{90}^W, the energy in the hemisphere defined by the direction of the virtual $W^\pm$ in the semi-leptonic $B_{\rm tag}$ decay. E_{90}^W is calculated in the center-of-mass frame under the assumption that the $B_{\rm tag}$ is produced at rest. The sum of energies for E_{90}^W extends over all charged and neutral candidates of the recoiling charm system X that are in the same hemisphere (with respect to the direction of the virtual $W^\pm$) as the lepton candidate:

$$\begin{aligned} p_B^\mu &= p_W^\mu + p_X^\mu \approx (m_{B^0}, \mathbf{0}) \\ p_W^\mu &= p_\ell^\mu + p_\nu^\mu \\ p_X^\mu &= \sum_{i \neq \ell} p_i^\mu \\ E_{90}^W &= \sum_{i \in X,\ \boldsymbol{p}_i \cdot \boldsymbol{p}_W > 0} E_i \end{aligned} \tag{8.5.1}$$

- $\boldsymbol{p}_{\rm miss}$, the missing momentum given by:

$$\boldsymbol{p}_{\rm miss} = \boldsymbol{p}_B - \boldsymbol{p}_X - \boldsymbol{p}_\ell \approx -(\boldsymbol{p}_X + \boldsymbol{p}_\ell). \tag{8.5.2}$$

- $\cos\theta_{\rm miss}$, the cosine of the angle between the lepton candidate's momentum $\boldsymbol{p}_\ell$ and the missing momentum $\boldsymbol{p}_{\rm miss}$ is calculated in the $\Upsilon(4S)$ center-of-mass frame (again with the approximation of the $B_{\rm tag}$ being produced at rest).
- $M_{\rm recoil}$, mass recoiling against $\boldsymbol{p}_{\rm miss} + \boldsymbol{p}_\ell$ in the $B_{\rm tag}$ frame. The $M_{\rm recoil}$ distribution for semileptonic B decays peaks around the D mass and has a tail toward the lower side due to missing particles, while that for semileptonic D decays is more broad with a tail up to 5 GeV/c^2.

The above kinematical variables can be combined with particle identification (PID) information and applied only to selected electron or muon candidate tracks. Or they can be applied to all tracks in order to recover the tagging information from leptons that fail the PID selection ("kinematically identified leptons").

8.5.2 Kaons

The dominant source of charged kaons are $b \to c \to s$ transitions ($B^0 \to \overline{D}(\to K^+ X')X$ decays), where the charge of the kaon tags the flavor of $B_{\rm tag}$. Kaons from such decays are referred to as "right sign" kaons (a K^+ indicates a B^0 decay). The high average multiplicity of charged kaons of 0.78 ± 0.08 (Beringer et al., 2012), combined with the higher multiplicity of right sign vs wrong sign kaons of $0.58 \pm 0.01 \pm 0.08$ vs. $0.13 \pm 0.01 \pm 0.05$ (Albrecht et al., 1994b) make kaons overall the most powerful source of tagging information.

The following discriminating variables are useful for flavor tagging with kaons:

- q, the charge of the track.
- $\mathcal{L}_K$, the kaon likelihood obtained from PID information.
- If more than one charged kaon is identified, it is useful to combine the information $(q \cdot \mathcal{L}_K)$ from up to three charged kaons.
- $n_{K_S^0}$, the number of K_S^0 mesons reconstructed on the tag side. A kaon produced together with one or more K_S^0 tends to originate from a strange quark in a $b \to c\overline{c}(d, s)$ decay or from the appearance of $s\overline{s}$ out of the vacuum, while one without an accompanying K_S^0 has a higher probability to come from the $b \to c \to s$ cascade decay.
- The sum of the squared transverse momenta of charged tracks on the tag side. A large total transverse momentum squared increases the likelihood that a charged kaon was produced from a $b \to cW^-, c \to s \to K^-$ transition, rather than the transition $b \to XW^-, W^- \to \overline{c}s/d, \overline{c} \to \overline{s} \to K^+$, which would give a "wrong-sign" kaon.
- p^*, the center-of-mass momentum of the candidate track.
- $\theta_{\rm lab}$, the polar angle in the laboratory frame.

8.5.3 Slow pions

Low momentum $\pi^\pm$ from $D^{*\pm}$ decays (slow pions) provide another source of tagging information. The substan-

tial background from low momentum tracks can be reduced by correlating the direction of the slow pion and the remaining tracks from the $B_{\rm tag}$ decay. Since the slow pion and the D^0 are emitted nearly at rest in the $D^{*\pm}$ frame, the slow pion direction in the $B_{\rm tag}$ rest frame will be along the direction of the D^0 decay products and opposite to the remainder of the $B_{\rm tag}$ decay products. This direction can be approximately determined by calculating the thrust axis of the $B_{\rm tag}$ decay products. The thrust is calculated using both charged tracks and neutral clusters not used in the reconstruction of $B_{\rm rec}$.

The following variables provide useful discriminating power:

- q, the charge of the track.
- p^*, the momentum of the slow pion candidate in the $\Upsilon(4S)$ center-of-mass frame.
- $p^{\rm lab}$, the momentum of the slow pion candidate in the laboratory frame.
- $\theta_{\rm lab}$, the polar angle in the laboratory frame.
- $\cos\theta_{\pi\rm T}$, the cosine of the angle between the slow pion direction and the $B_{\rm tag}$ thrust axis in the $\Upsilon(4S)$ center-of-mass frame.
- $\mathcal{L}_K$, the PID likelihood of the track to be a kaon. PID information helps to reject the contribution from low momentum kaons flying in the thrust direction.
- $\mathcal{L}_e$, the PID likelihood of the track to be a electron. This helps to reject background from electrons produced in photon conversions and π^0 Dalitz decays.

8.5.4 Correlation of kaons and slow pions

In events where both a charged kaon and a slow pion candidate (*e.g.* from a $D^{*+} \to D^0(\to K^- X)\pi^+$ decay) are found, the corresponding flavor tagging information can potentially be improved by using the angular correlation between the kaon and slow pion. A kaon and a slow pion of opposite charge (*i.e.* agreeing flavor tag) that are emitted in approximately the same direction in the $\Upsilon(4S)$ center-of-mass frame can provide a combined tag with a relatively low mistag fraction.

In addition to the information used to identify kaons and slow pions, the following discriminating variable can be used:

- $\cos\theta_{K,\pi}$, the cosine of the angle between the kaon and the slow pion momentum calculated in the $\Upsilon(4S)$ center-of-mass frame.

8.5.5 High-momentum particles

A very inclusive tag can be obtained by selecting tracks with the highest momentum in the $\Upsilon(4S)$ center-of-mass frame and using their charge as a tag. Given the other signatures discussed above, the aim of such a tag is to identify fast particles coming from the hadronization of the W boson produced in the decay $b \to c W^-$ (for example fast pions from $\overline{B}^0 \to D^{*+}\pi^-$) as well as high momentum leptons that may have failed the selection for the lepton tag signature. Direct hadrons or leptons with a positive (negative) charge indicate a B^0 ($\overline{B}^0$) tag. These particles are produced at the $B_{\rm tag}$ decay vertex and, in the $\Upsilon(4S)$ center-of-mass frame, are energetic and fly in a direction opposite to the charm decay products of $B_{\rm tag}$.

Useful discriminating variables are:

- q, the charge of the track.
- p^*, the momentum of the track in the $\Upsilon(4S)$ center-of-mass frame.
- d_0, the impact parameter in the xy plane.
- The angle between the particle and the $B_{\rm tag}$ thrust axis in the $\Upsilon(4S)$ center-of-mass frame.

8.5.6 Correlation of fast and slow particles

The angular correlations between slow charged pions from $D^{*\pm}$ decays and fast, oppositely charged particles originating from the $W^\mp$ hadronization in the decay $b \to c W$ can be exploited for flavor tagging. Since the $W^\mp$ and the $D^{*\pm}$ are emitted back-to-back in the $B_{\rm tag}$ center-of-mass frame, the slow pion and the fast tracks are expected to be emitted at a large angle.

The following discriminating variables are useful:

- $p^*_{\rm Slow}$, the center-of-mass momentum of the slow track.
- $p^*_{\rm Fast}$, the center-of-mass momentum of the fast track.
- $\cos\theta_{\rm SlowFast}$, the cosine of the angle between the slow and the fast track.
- $\cos\theta_{\rm SlowT}$, the cosine of the angle between the slow track and $B_{\rm tag}$ thrust axis.
- $\cos\theta_{\rm FastT}$, the cosine of the angle between the fast track and $B_{\rm tag}$ thrust axis.
- $\mathcal{L}_{K\rm Slow}$, the PID likelihood for the slow track to be a kaon.

8.5.7 Λ baryons

The flavor of a Λ baryon produced in $B_{\rm tag}$ decays carries tagging information because it contains an s quark that was likely produced in the cascade decay $b \to c \to s$. Therefore, the presence of a Λ ($\overline{\Lambda}$) will indicate a $\overline{B}^0$ (B^0).

$\Lambda \to p\pi$ decays on the tag side are reconstructed by combining charged tracks with tracks that are identified as protons (or antiprotons). Although Λ candidates are found in a small fraction of events, they provide relatively clean flavor tags that are fully complementary to the other signatures.

Useful discriminating variables include:

- q, the flavor of Λ (Λ or $\overline{\Lambda}$).
- M_Λ, the reconstructed mass of the Λ.
- χ^2_Λ, the χ^2 probability of the fitted Λ decay vertex.
- $\cos\theta_\Lambda$, the cosine of the angle between the Λ momentum and the direction from the primary vertex to the Λ decay vertex.
- s_Λ, the flight length of the Λ candidate before decay.
- p_Λ, the momentum of the Λ candidate.
- $p_{\rm proton}$, the momentum of the proton candidate used for the Λ reconstruction.

– $n_{K_S^0}$, the number of K_S^0 mesons reconstructed on the tag side.
– Δz, difference between the z coordinate of the two tracks at the Λ vertex point.

8.6 Specific flavor tagging algorithms

In this section the tagging algorithms developed by *BABAR* and Belle are discussed. In both experiments these algorithms have been improved greatly during the lifetime of the experiment, resulting in a substantial performance increase. In the following only the final versions of the tagging algorithms are discussed.

8.6.1 Multivariate tagging methods

The *BABAR* and Belle tagging algorithms both use multivariate methods: *BABAR* uses an artificial neural network, while Belle's tagger is based on a multi-dimensional look-up table. Both algorithms provide not only a flavor tag but also an estimated mistag probability for each event.

Both tagging algorithms were trained using large samples of simulated events. Imperfections in the simulation of particle decays (*e.g.* due to incomplete knowledge of branching fractions) or detector response may lead to inaccurate estimates of the per-event mistag probability by the tagging algorithm. Therefore both algorithms use the estimated per-event mistag probabilities only when separating events into tagging categories. For each category, w and Δw are measured using a sample of events where the signal B decays into a self-tagging decay mode (B_{flav} control sample, see Section 10.6). As a result, inaccuracies in the simulation of the training sample can only lead to a non-optimal tagging performance but will not introduce any systematic errors. The loss in tagging performance that results from using tagging categories rather than per-event mistag probabilities was found to be small both for the *BABAR* and the Belle tagging algorithms.

8.6.2 Systematic effects

Systematic effects associated with tagging are discussed in Chapter 15; only a brief overview is given here. As discussed above, by using tagging categories whose w and Δw are measured on data, systematic effects that could arise from imperfections in the tagging algorithm or its training are replaced by the statistical uncertainties of the measurements of w and Δw. The remaining systematic effects associated with flavor tagging arise from

– potential differences in the tagging performance for signal events and for the B_{flav} control sample used to measure w and Δw, and
– tag-side interference (see Section 15.3.6).

8.6.3 Flavor tagging in BABAR

The *BABAR* tagging algorithm (Aubert, 2005i, 2009z; Lees, 2013c) is a modular, multivariate flavor-tagging algorithm that analyses charged tracks on the tag side in order to provide a flavor tag and a mistag probability w. The flavor of B_{tag} is determined from a combination of nine different flavor-specific signatures, which include charged leptons, kaons, pions and Λ baryons (see Section 8.5).

For each of these signatures, properties such as charge, momentum, and decay angles are used as input to a specific neural network (NN) or "sub-tagger". Three sub-taggers are dedicated to charged leptons, making use of identified electrons (Electron), muons (Muon) and kinematically identified leptons (Kin. Lepton). The Kaon sub-tagger combines the information from up to three kaons into a single tag. Slow pions are used both by a dedicated slow pion sub-tagger (Slow Pion) and in correlation with kaons (K-Pi). The Max p* sub-tagger analyzes high-momentum particles. The correlation of fast and slow particles is exploited by the FSC sub-tagger. The Lambda sub-tagger looks at Λ baryons.

These sub-taggers are combined by a single final neural network (BTagger) that is trained to determine the correct flavor of B_{tag}. Based on the output of this NN and the contributing sub-taggers, each event is assigned to one of six mutually exclusive tagging categories. The overall structure of the *BABAR* tagging neural network is shown in Figure 8.6.1.

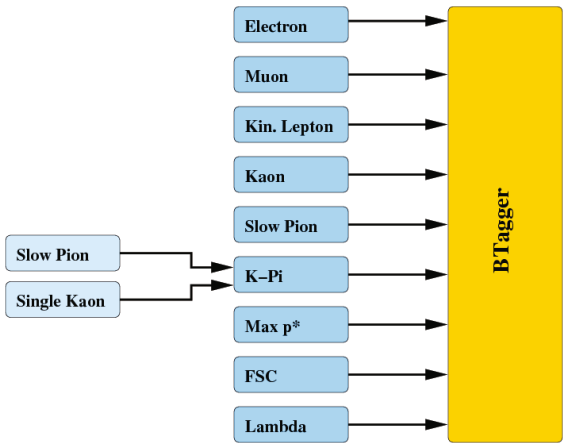

Figure 8.6.1. Schematic overview of the *BABAR* tagging algorithm. Each box corresponds to a separate neural network.

The use of sub-taggers dedicated to specific signatures allows one to keep track of the underlying physics of each event and simplifies studies of systematics. For example, events with an identified electron or muon from a semi-leptonic B_{tag} decay can be separated from other decays and assigned to the `Lepton` tagging category. The `Lepton` category does not only have a low w but also more precisely reconstructed B_{tag} vertices, is less sensi-

tive to the bias from charm on the tag side, and is immune to the intrinsic mistagging associated with doubly Cabibbo-suppressed decays (see tag-side interference in Section 15.3.6).

The training and validation of each of the sub-tagger NNs is based on the Stuttgart Neural Network Simulator (Zell et al., 1995). Extensive studies have been performed for each sub-tagger, including a wide search for the most discriminating input variables. NN architectures and the number of training cycles are optimized to yield the most efficient flavor assignment. The NNs are feed-forward networks with one hidden layer. The weights and bias values of the logistic activation functions are optimized during training using standard back-propagation.

The NNs are trained using a simulated sample of about 500,000 $B^0\overline{B}^0$ pairs in which one meson ($B_{\rm rec}$) decays to a $\pi^+\pi^-$ final state while the other ($B_{\rm tag}$) decays to any possible final state according to known or expected branching fractions. Half of this sample is used for training the NN, while the other half is used as a test sample for an unbiased evaluation of the performance. Each sub-tagger is trained separately before the training of the BTagger network.[36]

Details of the architecture of the different neural networks used by the *BABAR* tagging algorithm are given in Table 8.6.1. For each of the nine sub-taggers and for the final BTagger NN the table lists all input variables and the training target. Some of the sub-taggers are trained to separate B^0 from $\overline{B}^0$ decays, while others are trained to discriminate true from fake signatures.

The output $y_{\rm BTagger}$ of the final BTagger NN is mapped to values between -1 (for a perfectly tagged $\overline{B}^0$) and $+1$ (B^0). The distribution of this output for the $B_{\rm flav}$ control sample is shown in Figure 8.6.2. Excellent agreement is observed between data and simulation.

The estimated probability p of a correct tag assignment is given by the BTagger NN output

$$p = 1 - w = (1 + |y_{\rm BTagger}|)/2, \tag{8.6.1}$$

and the probability of a given $B_{\rm tag}$ being a B^0 is

$$p_{B_{\rm tag}=B^0} = (1 + y_{\rm BTagger})/2. \tag{8.6.2}$$

The correctness of these probabilities can be checked with the $B_{\rm flav}$ control sample. For example, one can plot the probability of observing a $\overline{B}^0$ on the $B_{\rm flav}$ side as a function of the estimated probability $p_{B_{\rm tag}=B^0}$. Taking into account the time-integrated mixing probability $\chi_d = 0.1862 \pm 0.0023$ (Beringer et al. (2012)), one expects for a perfectly trained tagging algorithm

$$p_{B_{\rm flav}=\overline{B}^0} = (1 - 2\chi_d)p_{B_{\rm tag}=B^0} + \chi_d \tag{8.6.3}$$

$$= (1 - 2\chi_d)(1 + y_{\rm BTagger})/2 + \chi_d. \tag{8.6.4}$$

[36] Simultaneous training of all sub-taggers and the BTagger NN has been shown not to result in a significantly better classification performance.

As can be seen from Figure 8.6.3, the probabilities obtained from the BTagger NN output are in very good agreement with the expectations for both data and simulation. Nevertheless, as discussed in Section 8.6.1, these estimated probabilities are only used to separate events into tagging categories.

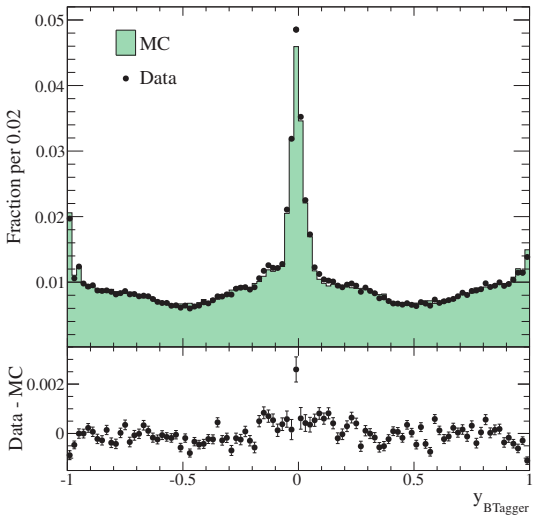

Figure 8.6.2. Distribution of the output of the final BTagger NN ($y_{\rm BTagger}$) on the $B_{\rm flav}$ control sample for data and simulation, using the full *BABAR* data sample. A contribution of up to 22% from combinatorial background is subtracted in each bin based on a fit to the $m_{\rm ES}$ distribution. The difference between data and simulation (with statistical uncertainties added in quadrature) is also shown.

The tagging algorithm assigns each event to one of six hierarchical and mutually exclusive tagging categories: `Lepton`, `Kaon I`, `Kaon II`, `Kaon-Pion`, `Pion` or `Other`. The name given to each category indicates the dominant physics processes (or sub-tagger) contributing to the flavor identification. For most categories, this classification is based on $y_{\rm BTagger}$. For the `Lepton` category, which singles out events with a cleanly identified primary lepton, additional cuts are made on the output of the electron or muon sub-taggers. Over 95% of events in the `Lepton` category contain a semileptonic $B_{\rm tag}$ decay. The definition of the tagging categories is summarized in Table 8.6.2.

The final version of the *BABAR* tagging algorithm[37] (Lees, 2013c) achieves an effective tagging efficiency $Q = (33.1 \pm 0.3)\%$ on the full *BABAR* data set. The breakdown of this performance into the different tagging categories is shown in Table 8.6.3.

[37] Improvements in the particle identification algorithms used for the final version of the *BABAR* tagging algorithm (Lees, 2013c) lead to a higher Q value of $(33.1 \pm 0.3)\%$, compared to $Q \approx 31\%$ achieved by the previous version (Aubert, 2005i). The tagging algorithm itself did not change.

Table 8.6.1. Overview of the neural networks used by the *BABAR* BTagger and its sub-taggers. For each sub-tagger the network architecture is shown in the second column according to the notation $N_{\text{inputs}} : N_{\text{hidden nodes}} : N_{\text{outputs}}$. The input variables are listed in the third column while the fourth column describes the goal of the NN training.

(Sub-)Tagger	Network architecture	Discriminating input variables	Training goal
Electron	4:12:1	q, p^*, E_{90}^W, $\cos\theta_{\text{miss}}$	Classify B^0 versus $\overline{B}^0$
Muon	4:12:1	q, p^*, E_{90}^W, $\cos\theta_{\text{miss}}$	Classify B^0 versus $\overline{B}^0$
Kin. Lepton	3:3:1	p^*, E_{90}^W, $\cos\theta_{\text{miss}}$	Recognize primary leptons
Kaon	5:10:1	$(q\mathcal{L}_K)_1$, $(q\mathcal{L}_K)_2$, $(q\mathcal{L}_K)_3$, $n_{K_S^0}$, $\Sigma p_\perp$	Classify B^0 versus $\overline{B}^0$
Slow Pion	3:10:1	p^*, $\cos\theta_{\pi\text{T}}$, $\mathcal{L}_K$	Recognize slow pions from $D^{*\pm}$ decays
Max p^*	3:6:1	p^*, d_0, $\cos\theta$	Recognize direct B daughters
K–Pi	3:10:1	$(q\mathcal{L}_K)$, SlowPion tag, $\cos\theta_{K,\pi}$	Recognize K-π pairs from $D^{*\pm}$ decays
FSC	6:12:1	$\cos\theta_{\text{SlowFast}}$, p^*_{Slow}, p^*_{Fast}, $\cos\theta_{\text{SlowT}}$, $\cos\theta_{\text{FastT}}$, $\mathcal{L}_{K\text{Slow}}$	Recognize fast-slow correlated tracks
Lambda	6:14:1	M_Λ, χ^2, $\cos\theta_\Lambda$, s_Λ, p_Λ, p_{proton}	Recognize Λ decays
BTagger	9:20:1	All of the above tags	Classify B^0 versus $\overline{B}^0$

Table 8.6.2. Definition of tagging categories for the *BABAR* flavor tagging algorithm. Events with $|y_{\text{BTagger}}| < 0.1$ are classified as `Untagged` and are not used to extract time-dependent information from data.

Category	Definition
`Lepton`	($\lvert y_{\text{Electron}}\rvert > 0.8$ or $\lvert y_{\text{Muon}}\rvert > 0.8$) and $\lvert y_{\text{BTagger}}\rvert > 0.8$
`Kaon I`	$\lvert y_{\text{BTagger}}\rvert > 0.8$
`Kaon II`	$0.6 < \lvert y_{\text{BTagger}}\rvert < 0.8$
`Kaon-Pion`	$0.4 < \lvert y_{\text{BTagger}}\rvert < 0.6$
`Pion`	$0.2 < \lvert y_{\text{BTagger}}\rvert < 0.4$
`Other`	$0.1 < \lvert y_{\text{BTagger}}\rvert < 0.2$

Table 8.6.3. Performance of the final *BABAR* tagging algorithm on data.

Category	$\varepsilon_{\text{tag}}(\%)$	$\Delta\varepsilon_{\text{tag}}(\%)$	$w(\%)$	$\Delta w(\%)$	$Q(\%)$	$\Delta Q(\%)$
`Lepton`	9.7 ± 0.1	0.2 ± 0.2	2.1 ± 0.2	0.2 ± 0.5	8.9 ± 0.1	0.1 ± 0.4
`Kaon I`	11.3 ± 0.1	-0.1 ± 0.2	4.1 ± 0.3	0.2 ± 0.6	9.6 ± 0.1	-0.1 ± 0.4
`Kaon II`	15.9 ± 0.1	-0.1 ± 0.2	13.0 ± 0.3	-0.2 ± 0.6	8.7 ± 0.2	0.0 ± 0.5
`Kaon-Pion`	13.2 ± 0.1	0.4 ± 0.2	23.0 ± 0.4	-1.3 ± 0.7	3.9 ± 0.1	0.5 ± 0.3
`Pion`	16.8 ± 0.1	-0.3 ± 0.3	33.3 ± 0.4	-2.7 ± 0.6	1.9 ± 0.1	0.6 ± 0.2
`Other`	10.6 ± 0.1	-0.5 ± 0.2	41.8 ± 0.5	5.9 ± 0.7	0.28 ± 0.03	-0.4 ± 0.1
Total	77.5 ± 0.1	-0.3 ± 0.5			33.1 ± 0.3	0.7 ± 0.8

The contribution of each of the nine sub-taggers to the overall tagging performance can be evaluated in two ways:

- the absolute effective tagging efficiency obtained by using only one sub-tagger (Q_{abs});
- the incremental effective tagging efficiency (Q_{incr}), defined as the improvement in Q associated with adding a single sub-tagger on top of all the others.

Table 8.6.4 shows Q_{abs} and Q_{incr} for the nine sub-taggers. In most events multiple flavor tagging signatures are present and contribute to the final tag as can be seen from the fact that Q_{incr} is small for most sub-taggers. The exception is the Kaon sub-tagger which is the only tagger whose presence is essential to maintain a high tagging performance. The fact that in most cases several sub-taggers contribute to the final tag helps to ensure the robustness of the tagging algorithm.

8.6.4 Flavor tagging in Belle

The flavor tagging method used by Belle (Kakuno, 2004) is based on a multi-dimensional look-up table. A schematic diagram of the algorithm is shown in Figure 8.6.4.

The algorithm provides two parameters as the flavor tagging outputs: q denoting the flavor of B_{tag} ($+1$ for B^0, -1 for $\overline{B}^0$), and r is an expected flavor dilution factor that ranges from zero for no flavor information ($w \simeq 0.5$)

Table 8.6.4. Contribution of the nine sub-taggers to the *BABAR* tagging algorithm for the version of the algorithm used in 2004. The final version of the algorithm has the same architecture of the sub-taggers and BTagger but uses an improved kaon identification, leading to a slightly larger tagging performance. The determination of $Q_{\rm abs}$ on data was made using the $B_{\rm flav}$ control sample, assuming a time-integrated mixing probability of $\chi_d = 0.182$ and correcting for background. See text for the definition of $Q_{\rm abs}$ and $Q_{\rm incr}$.

Sub-tagger	$Q_{\rm abs}$ on MC (%)	$Q_{\rm abs}$ on data (%)	$Q_{\rm incr}$ on MC (%)
Electron	6.1 ± 0.1	5.0 ± 0.2	1.14
Muon	4.0 ± 0.1	3.3 ± 0.2	1.0
Kin. Lepton	2.9 ± 0.1	2.6 ± 0.2	0.36
Kaon	18.8 ± 0.1	18.3 ± 0.4	9.91
Slow Pions	5.2 ± 0.1	6.1 ± 0.4	0.47
K-Pi	9.3 ± 0.1	10.0 ± 0.4	0.25
Max p^*	11.0 ± 0.3	9.7 ± 0.5	0.06
FSC	6.0 ± 0.1	6.6 ± 0.4	0.08
Lambda	0.3 ± 0.1	0.2 ± 0.1	0.38

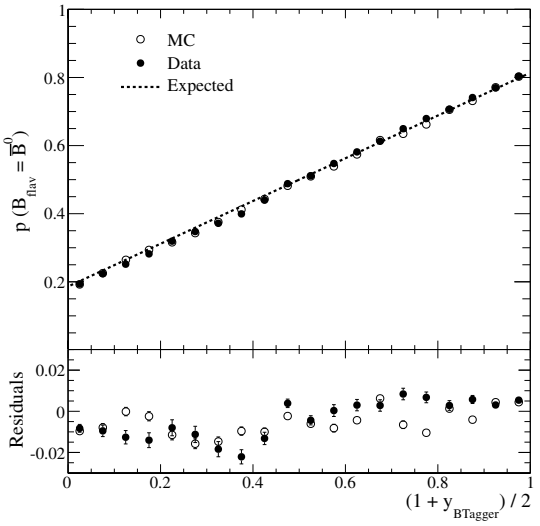

Figure 8.6.3. Probability of observing a fully reconstructed $\overline{B}^0$ on the $B_{\rm flav}$ side as a function of the probability $p_{B_{\rm tag}=B^0} = (1 + y_{\rm BTagger})/2$ of having a B^0 on the $B_{\rm tag}$ side. The dotted line shows the dependence expected for a perfectly trained tagging algorithm. The solid points are from the full *BABAR* $B_{\rm flav}$ control sample, the open circles are obtained from simulation. A contribution of up to 22% from combinatorial background is subtracted in each bin based on a fit to the $m_{\rm ES}$ distribution. The residuals with respect to the expectation are shown at the bottom.

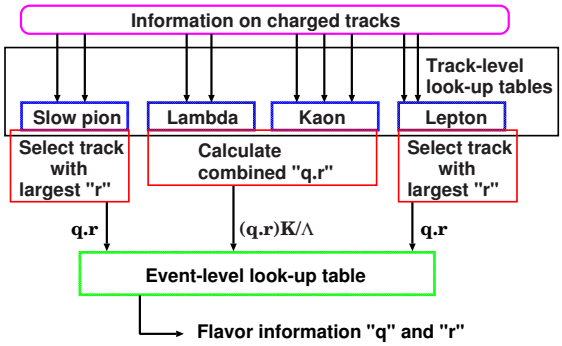

Figure 8.6.4. Schematic diagram of Belle's two-stage flavor tagging algorithm. See the text for the definition of the parameters "q" and "r".

to unity for an unambiguous flavor assignment ($w \simeq 0$). In order to obtain a high overall effective tagging efficiency Q, an estimated flavor dilution factor is assigned to each event based on multiple discriminants. Using a multi-dimensional look-up table prepared from a large sample of simulated events and binned by the values of the discriminants, the signed probability, $q \cdot r$, is given by

$$q \cdot r = \frac{N(B^0) - N(\overline{B}^0)}{N(B^0) + N(\overline{B}^0)}, \tag{8.6.5}$$

where $N(B^0)$ and $N(\overline{B}^0)$ are the numbers of B^0 and $\overline{B}^0$ in the corresponding bin of the look-up table.

The flavor tagging algorithm proceeds in two stages: the track stage and the event stage. In the track stage, each pair of oppositely charged tracks is examined to satisfy criteria for the Λ-like particle category. The remaining charged tracks are sorted into slow-pion-like, lepton-like and kaon-like particle categories. The b flavor and its dilution factor of each particle, $q \cdot r$, in the four categories is estimated using the discriminants shown in Table 8.6.5.

In the second stage, the results from the first stage are combined to obtain the event-level value of $q \cdot r$. From the lepton-like and slow-pion-like track categories, the track with the highest r value from each category is chosen as the input to the event level look-up table. The flavor dilution factors of the kaon-like and Λ-like particle candidates are combined by calculating the product of the flavor dilution factors in order to account for the cases with multiple

Table 8.6.5. Discriminants used in the Belle tagging algorithm.

(Sub-)Stage	Variables	Number of bins
Lepton	q, e or $\mu, \mathcal{L}_\ell, p^*, \theta_{\rm lab}, M_{\rm recoil}, p^*_{\rm miss}$	31680
Kaon	$q, n_{K^0_S}, p^*, \theta_{\rm lab}, \mathcal{L}_K$	19656
Lambda	$q, n_{K^0_S}, M_\Lambda, \theta_\Lambda, \Delta z$	32
Slow pion	$q, p^{\rm lab}, \theta_{\rm lab}, \cos\theta_{\pi\rm T}, \mathcal{L}_e$	7000
Event	$(q\cdot r)_\ell, (q\cdot r)_{K/\Lambda}, (q\cdot r)_{\pi_s}$	16625

s quarks in an event. The product of flavor dilution factors gives better effective efficiency than taking the track with the highest r. Using the flavor dilution factor r determined from Monte Carlo (MC) simulation as a measure of the tagging quality is a straightforward and powerful way of taking into account correlations among various tagging discriminants.

By using two stages, the look-up tables can be kept small enough to provide sufficient statistics for each bin. Four million $B^0\overline{B}^0$ MC events are used to generate the particle-level look-up tables. To reduce statistical fluctuations of the r values in the particle-level look-up tables, the r value in each bin is calculated by including events in nearby bins with small weights. The event-level look-up table is prepared using MC samples that are statistically independent of those used to generate the track-level tables to avoid any bias from a statistical correlation between the two stages. Seven million $B^0\overline{B}^0$ MC events are used to create the event-level look-up table. The performance of individual tagging categories as obtained in MC simulation is shown for illustration in Table 8.6.6.

Table 8.6.6. Performance of sub-taggers in the Belle flavor tagging algorithm in terms of effective tagging efficiency $Q_{\rm abs}$ in simulated events.

Sub-tagger	$Q_{\rm abs}$ on MC
Leptons	12%
Kaons and Λ's	18%
Slow Pions	6%

All tagged events are sorted into seven subsamples according to the value of r: $0 \le r \le 0.1$, $0.1 < r \le 0.25$, $0.25 < r \le 0.5$, $0.5 < r \le 0.625$, $0.625 < r \le 0.75$, $0.75 < r \le 0.875$ and $0.875 < r \le 1$. For each subsample l, the corresponding average wrong tag fraction w_l is determined. For events with $r \le 0.1$, there is negligible flavor discrimination available and w_0 is set to 0.5. For the other six subsamples, the average wrong tag fractions w_l ($l = 1, 6$) are measured directly from data using samples of semi-leptonic ($B^0 \to D^{*-}\ell^+\nu$) and hadronic ($B^0 \to D^{(*)-}\pi^+$ with $D^{*-}\rho^+$) B meson decays. These decays are fully reconstructed and the flavor of the associated B mesons is tagged. A total of 1461983 events are used to evaluate the performance of the tagging algorithm. An effective tagging efficiency of $Q = (30.1 \pm 0.4)\%$ is obtained. The wrong tag fractions, differences and tagging efficiencies for each subsample are shown in Table 8.6.7.

The average value of r for each region (r_l) and the measured wrong tag fraction (w_l) should satisfy $r_l \simeq 1 - 2w_l$ if the MC simulation used for constructing the look-up tables simulates generic B decays correctly. The degradation from the subdivision into r bins and use of the corresponding measured wrong tag fractions w_l is estimated to be about $\sim 0.5\%$, according to a Monte Carlo study.

Table 8.6.7. Tagging efficiencies ($\varepsilon_{\rm tag}$), wrong tag fractions (w) and their differences (Δw) for each r-interval for data taking with the SVD2 by Belle.

$r-$interval	$\varepsilon_{\rm tag}$	w	Δw
$0.000 - 0.100$	0.222 ± 0.004	0.5	0.0
$0.100 - 0.250$	0.145 ± 0.003	0.419 ± 0.004	-0.009 ± 0.004
$0.250 - 0.500$	0.177 ± 0.004	0.319 ± 0.003	$+0.010 \pm 0.004$
$0.500 - 0.625$	0.115 ± 0.003	0.223 ± 0.004	-0.011 ± 0.004
$0.625 - 0.750$	0.102 ± 0.003	0.163 ± 0.004	-0.019 ± 0.005
$0.750 - 0.875$	0.087 ± 0.003	0.104 ± 0.004	$+0.017 \pm 0.004$
$0.875 - 1.000$	0.153 ± 0.003	0.025 ± 0.003	-0.004 ± 0.002

Chapter 9
Background suppression for B decays

Editors:
José Ocariz (BABAR)
Paoti Chang (Belle)

Additional section writers:
Jacques Chauveau

9.1 Introduction

While the physics program of the B Factories is not limited to B physics, this chapter focuses on the techniques used to discriminate B decay events from backgrounds: details on specific background-suppression techniques for charm, τ lepton and other decay modes are described in the relevant chapters of this book. For both *BABAR* and Belle, most analyses of B decays use the kinematical constraints from the e^+e^- collision at the $\Upsilon(4S)$ resonance to identify signal events; additional discrimination can be obtained from information based on the "event shape", that is the phase-space distribution of decay particles detected in the event, and are the main topic of this chapter.

9.2 Main backgrounds to B decays

The production cross-section from e^+e^- collisions at the $\Upsilon(4S)$ resonance receives sizable contributions other than $B\overline{B}$, and so the event rate is dominated by non-B events. The identification of specific B decay channels therefore has to deal with a potentially large number of backgrounds from various sources. The dominant source of combinatorial background comes from $e^+e^- \to q\bar{q}$ events, which are usually referred to as "continuum background". To study this background using real data, in addition to using signal sidebands (for example by requiring $m_{\rm ES}$ to lie safely below the B mass peak), the B Factories have also dedicated a significant fraction of off-resonance data-taking, at a center-of-mass energy slightly below the $\Upsilon(4S)$ peak: 40 MeV for *BABAR*, 60 MeV for Belle (see Chapter 3). Also depending on the decay channel under consideration, other backgrounds (either from other B decays or from other processes) may also contribute, and need to be addressed correspondingly. For example, B decay modes with only charged particles suffer backgrounds from QED processes (Bhabha scattering $e^+e^- \to e^+e^-$, $e^+e^- \to \mu^+\mu^-$, and $e^+e^- \to \tau^+\tau^-$) which can usually be suppressed by taking advantage of their clean leptonic signatures.

In the case of charmless $b \to u$ and $b \to s$ decay channels, background rates outnumber the signal by orders of magnitude, so combinatorial background from continuum events is most often the dominant source of background: random combinations of particles in the final state may mimic the kinematical signatures of the signal. Thus background suppression is a crucial issue in the analysis techniques. While the signal-to-background rates are usually more favorable in $b \to c$ decay modes, background suppression can play an important role in controlling potential systematic uncertainties in precision measurements of charmed B decays. Also, rejection of backgrounds from other B decay modes can play a significant role in the analysis results, as decay rates of such backgrounds, or their CP nature, can be poorly known.

9.3 Topological discrimination

For simplicity, the discussion in this chapter is restricted to fully-reconstructed B decays; while most of the tools and techniques described here can be easily implemented or adapted to partly-reconstructed B modes, for a discussion of specific issues related to such modes, the reader is referred to the relevant chapters.

As discussed in Chapter 7, one fundamental difference between B meson signal and combinatorial background is the kinematics of their underlying production at the B Factories, so essentially all B meson analyses performed by *BABAR* and Belle take advantage of this information to identify the signal decay modes. After kinematic selection, additional background rejection is ensured by exploiting differences in the angular distributions of the particles produced in $e^+e^- \to \Upsilon(4S) \to B\overline{B}$ and background processes. For instance in a $B\overline{B}$ event, both B mesons are produced almost at rest in the $\Upsilon(4S)$ frame, as the $\Upsilon(4S)$ mass is barely above the $B\overline{B}$ production threshold; as a result, the B decay products are distributed isotropically in the $e^+e^- \to \Upsilon(4S) \to B\overline{B}$ rest frame. In contrast for $q\bar{q}$ events, the quarks are produced with a large initial momentum, and yield a back-to-back fragmentation into two jets of light hadrons. For the same reason in $B\overline{B}$ events, the angular distribution of decay products from the two B mesons are uncorrelated, while for continuum a sizeable correlation arises, as the decay particles from each B candidate tend to align with the direction of its jet.

Information based on the phase-space distribution of decay particles can be quantified in many different ways. Early *BABAR* and Belle physics analyses used methods initially developed by the ARGUS and CLEO collaborations; they then moved to develop more refined background-suppression techniques. We recall these methods in this section, and proceed to the description of those developed by *BABAR* and Belle in the next two sections. The *BABAR* Physics Book (Harrison and Quinn, 1998) is a useful reference for background suppression tools and methods available on the eve of B Factories; for consistency, a few definitions and variables inherited prior to the advent of the B Factories are summarized here:

- *Variables related to the B meson direction:* the spin-1 $\Upsilon(4S)$ decaying into two spin-0 B mesons results in a $\sin^2\theta_{\rm B}$ angular distribution with respect to the beam axis; in contrast for $e^+e^- \to f\bar{f}$ events, the spin-1/2 fermions f, and its two resulting jets, are distributed

following a $1+\cos^2\theta_{\rm B}$ distribution. Using the angle $\theta_{\rm B}$ between the reconstructed momentum of the B candidate (computed in the $\Upsilon(4S)$ reference frame) and the beam axis, the variable $|\cos\theta_{\rm B}|$ allows one to discriminate between signal B decays and the B candidates from continuum background.

– *Thrust and related variables:* for a collection of N momenta $\boldsymbol{p}_i$ $(i=1,\cdots N)$, the thrust axis $\boldsymbol{T}$ is defined as the unit vector along which their total projection is maximal; the thrust scalar T (or thrust) is a derived quantity defined as

$$T=\frac{\sum_{i=1}^{N}|\boldsymbol{T}\cdot\boldsymbol{p}_i|}{\sum_{i=1}^{N}|\boldsymbol{p}_i|}. \tag{9.3.1}$$

A useful related variable is $|\cos\theta_{\rm T}|$, where $\theta_{\rm T}$ is the angle between the thrust axis of the momenta of the B candidate decay particles (all evaluated in the $\Upsilon(4S)$ rest frame), and the thrust axis of all the other particles in the event (we call the set of those particles not associated with the B candidate, "the rest-of-the-event", or ROE). For a $B\overline{B}$ event, both B mesons are produced almost at rest in the $\Upsilon(4S)$ rest frame, so their decay particles are isotropically distributed, their thrust axes are randomly distributed, and thus $|\cos\theta_{\rm T}|$ follows a uniform distribution in the range $[0,1]$. In contrast for $q\bar{q}$ events, the momenta of particles follow the direction of the jets in the event, and as a consequence the thrusts of both the B candidate and the ROE are strongly directional and collimated, yielding a $|\cos\theta_{\rm T}|$ distribution strongly peaked at large values. Altogether, these arguments bring a qualitative description of the discriminating power provided by $|\cos\theta_{\rm T}|$.
Another thrust-related variable is $\theta_{T,B}$ the angle between the thrust axis of the B decay particles and the beam axis; for signal, $|\cos\theta_{\rm T,B}|$ is uniformly distributed, while for continuum events, the thrust of particle momenta from the B candidate tends to be aligned with the $1+\cos^2\theta_{\rm T,B}$ distribution followed by the jets.

– *Sphericity and related variables:* sphericity and thrust are strongly correlated concepts, nonetheless both are commonly used. For a collection of momenta $\boldsymbol{p}_i$, the sphericity tensor S is defined as

$$S^{\alpha,\beta}=\frac{\sum_{i=1}^{N}p_i^{\alpha}p_i^{\beta}}{\sum_{i=1}^{N}|\boldsymbol{p}_i|^2}, \tag{9.3.2}$$

(with $\alpha,\beta=x,y,z$) and provides a three-dimensional representation of the spatial distribution of the $\boldsymbol{p}_i$ collection. For an isotropic distribution, its three eigenvalues λ_k have similar magnitude; while for a planar distribution, one of the eigenvalues is significantly smaller, with its eigenvector orthogonal to that plane; and finally for a very directional distribution, the eigenvector oriented in that preferred direction has an eigenvalue considerably larger than the two others. Useful quantities derived from sphericity are the sphericity scalar (or sphericity), and the sphericity axis. The sphericity scalar S is defined as

$$S=\frac{3}{2}\left(\lambda_2+\lambda_3\right), \tag{9.3.3}$$

λ_2 and λ_3 being the two lowest eigenvalues; values of S close to 1 correspond to isotropically distributed momentum collections, while very collimated distributions yield sphericity values close to zero. The sphericity axis is collinear with the sphericity eigenvector having the largest eigenvalue. In the same spirit as $|\cos\theta_{\rm T}|$, the variable $|\cos\theta_{\rm S}|$ is often used, where $\theta_{\rm S}$ is the angle between the sphericity axes of the B candidate and the ROE.

– *The Fox-Wolfram moments:* another useful parameterization of phase-space distribution of momentum and energy flow in an event, was introduced in (Fox and Wolfram, 1978): for a collection of N particles with momenta $\boldsymbol{p}_i$, the k-th order Fox-Wolfram moment H_k is defined as

$$H_k=\sum_{i,j}^{N}|\boldsymbol{p}_i|\,|\boldsymbol{p}_j|\,P_k\left(\cos\theta_{ij}\right), \tag{9.3.4}$$

where θ_{ij} is the angle between $\boldsymbol{p_i}$ and $\boldsymbol{p_j}$, and P_k is the k-th order Legendre polynomial. Notice that in the limit of vanishing particle masses, $H_0=1$; that is why the normalized ratio $R_k=H_k/H_0$ is often used, so that for events with two strongly collimated jets, R_k takes values close to zero (one) for odd (even) values of k. These sharp signatures provide a convenient discrimination between events with different topologies.

The variables and tools described in the list above do not necessarily provide the optimal background discriminating power, and for channels suffering from large background rates, additional specific tools are developed. One such example is provided by a multivariate discriminant variable introduced by the CLEO collaboration (Asner et al., 1996) in the context of charmless B decays; it is a Fisher combination (see Chapter 4 for the description of the Fisher discriminant) of nine variables corresponding to the momentum flow around the thrust axis of the B candidate, binned in nine cones of 10° around the thrust axis as illustrated in Figure 9.3.1. The linear coefficients assigned to the combination of these nine variables are extracted from MC generated events for the signal, and either B mass sidebands or events collected off-resonance for continuum. The Fisher used by CLEO has often been referred to as "the CLEO Fisher" by the B Factories.

9.4 BABAR strategy

For *BABAR*, a typical analysis strategy is based on a two-step approach: first, variables using the complete set of particles in the event are built to reject copious backgrounds while maintaining high efficiency for signal. In the second step, variables are built separately, using information from the decay particles of the signal B candidate

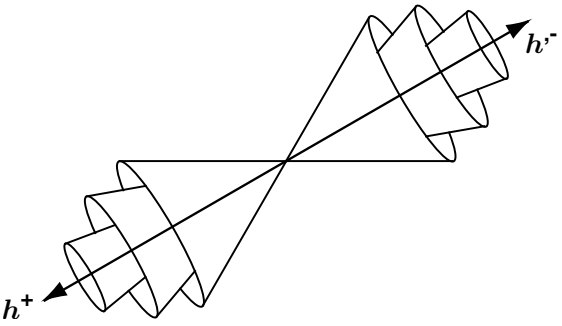

Figure 9.3.1. A graphical illustration of the CLEO Fisher discriminant, from (Asner et al., 1996). The h^+, h'^- arrows indicate the momenta of the two charged hadronic tracks in a $B^0 \to h^+h'^-$ candidate; the momentum of ROE particles within each cone (the first three cones around its thrust axis being drawn in the figure) are summed and combined to give the Fisher discriminant.

and of the ROE, to further reject backgrounds through additional requirements on the selection, and/or as inputs to a maximum-likelihood fit (see Chapter 11 for the description of maximum-likelihood fits) at later stages in the analysis.

Figure 9.4.1 illustrates two typical variables used in the first step. A simple requirement on the number of charged tracks per event can provide highly efficient background suppression. Also, in this first step, a simple requirement on the normalized second Fox-Wolfram moment ratio R_2 is applied; a loose cut on the value of R_2 has negligible impact on signal, while efficiently removing a substantial fraction of diphoton or dilepton backgrounds. In this first step, typical *BABAR* analyses also combine information both from the decay particles of the B meson candidate and from the ROE, and use them to achieve additional background rejection. For example, Figure 9.4.2 shows the distributions of $|\cos\theta_S|$, both for signal (from simulated B decays) and for continuum events (from sidebands on data, by requiring m_{ES} to be in the $5.20 - 5.26$ GeV/c^2 range). A simple per-event requirement on the value of $|\cos\theta_S|$ is applied to define the final analysis sample.

An important advantage of variables based on the ROE is that for the signal B decays, their correlation is small or negligible with the variables built out of the B candidate observables. Therefore it is appropriate to construct a joint likelihood function from the product of their $p.d.f.$s to use in a fit.

9.4.1 Linear discriminants

For typical *BABAR* analyses, several combinations of variables from the ROE are built, and combined in multivariate discriminants. A general description of linear discriminants in the optimization of the analyses is given in

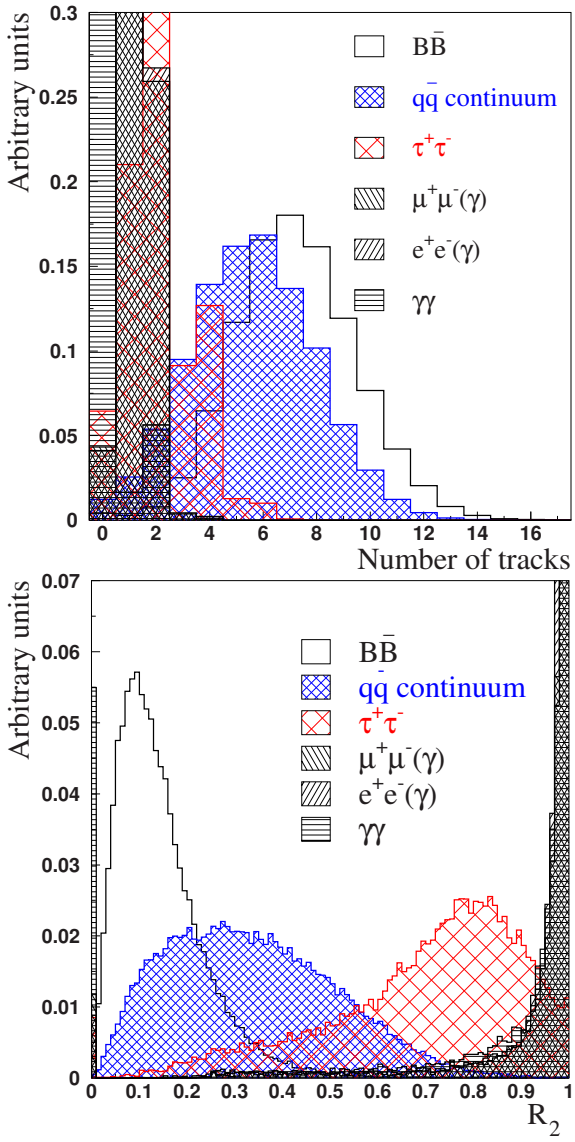

Figure 9.4.1. Two examples of global variables, used as a first step in background suppression in most *BABAR* analyses of B decays. The top plot shows the number of charged tracks per event for various processes; the bottom plot is the distribution of the normalized second Fox-Wolfram moment ratio R_2, for various processes. The figures are from a *BABAR* Thesis (Rahatlou, 2002).

Chapter 4. Many of these discriminants use the so-called "monomials" L_n, defined as

$$L_n = \sum_{i \in ROE} p_i \times |\cos\theta_i|^n \,, \tag{9.4.1}$$

where p_i is the momentum (computed in the $\Upsilon(4S)$ reference frame) of particle i belonging to the ROE, and θ_i is the angle between its momentum and the thrust axis of the B candidate. Dedicated studies concluded that the L_0

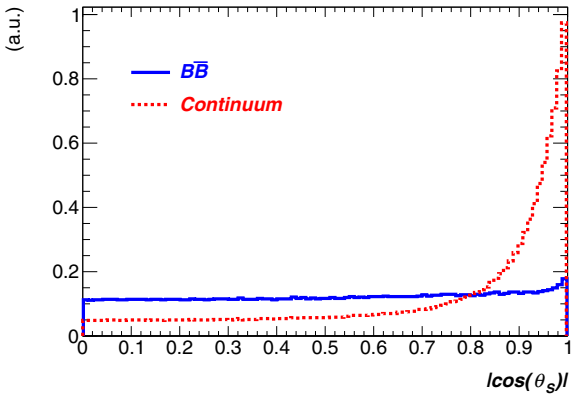

Figure 9.4.2. The signal (solid blue line) and continuum background (dashed red line) distributions of $|\cos\theta_S|$, a variable often used as a first step in background suppression for charmless two-body B decays. $|\cos\theta_S|$ is uniformly distributed for the signal, while for continuum it is sharply peaked at large values. The figure is adapted from a *BABAR* Thesis (Malclès, 2006). The vertical scale is in arbitrary units (a.u.).

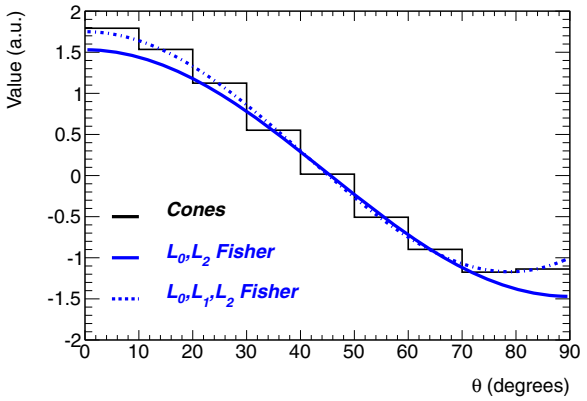

Figure 9.4.3. The contribution to the *BABAR* and CLEO Fisher discriminants, for a single 1 GeV particle, as a function of the angle of its momentum and the thrust axis of the B candidate. The nine-step line indicates the values of the nine cone coefficients in 10° bins for the CLEO Fisher, while the continuous blue line is the resulting function for the $\mathcal{F}$ used by *BABAR*. The dash-dotted line corresponds to a three-variable Fisher (shown for illustration only, not used in actual *BABAR* analyses). The coefficients for these Fisher discriminants were optimized using samples of charmless two-body B decays for signal, and data events from $m_{\rm ES}$ sidebands for background. The figure is adapted from a *BABAR* Thesis (Pivk, 2003). The vertical scale is in arbitrary units (a.u.).

and L_2 pair provides most of the discriminating power to separate signal from continuum background; for instance, a bi-variate linear (Fisher) combination $\mathcal{F} = c_0 L_0 + c_2 L_2$ (using L_0 and L_2 only) reaches a signal-to-background separation comparable to a Fisher using the nine variables in the CLEO Fisher. Figure 9.4.3 illustrates the contribution from a single 1 GeV particle to both discriminants, as a function of its angle with respect to the thrust axis. That same figure shows the contribution from a three-variable Fisher discriminant (including also the L_1 monomial), that exhibits an almost equivalent angular dependence to the nine-variable CLEO discriminant, thus showing that a comparable discriminating power can be achieved with a smaller number of variables.

For most charmless B decay analyses, the optimization algorithm returns values very close to $\mathcal{F} = L_2 - 2 \times L_0$ (*i.e.* $c_0 = -2c_2$, up to arbitrary offset and scale parameters) for the Fisher coefficients. To a certain extent, this two-variable Fisher discriminant can be thought of as a simple, continuous extension of the CLEO discriminant, that can be explained in terms of the relative sign and ratio of the c_0 and c_2 coefficients described above. For an isotropically distributed collection of particles, the total $\mathcal{F}$ value will be close to zero, as particles with angles collinear/orthogonal to the B candidate thrust axis contribute with opposite signs, and tend to cancel out in the sum. In contrast, contributions from a collection of particles collinear with the thrust axis will mostly sum up to give a positive value.

Figure 9.4.4 shows the distributions of this bi-variate $\mathcal{F}$ discriminant, with coefficients evaluated both before and after a first-step cut on $|\cos\theta_S| < 0.8$ (c.f. Figure 9.4.2). Before the first-step selection, the $\mathcal{F}$ discriminant provides a $\sim 1.6\sigma$ separation between signal and background. The first-step cut on $|\cos\theta_S|$ rejects $\sim$ 65% of all continuum background, while retaining $\sim$ 80% of signal; for the significantly signal-enriched remaining selected events, $\mathcal{F}$ still provides a $\sim 1.2\sigma$ separation. This remaining discriminating power is efficiently exploited in the maximum-likelihood analysis.

The monomial L_0 is the total momentum flow observed in the detector, and L_2 is a direction-weighted sum of contributions to the total momentum flow. Hence the ratio L_2/L_0 is expected to be rather insensitive to the actual per-event value of the total momentum flow, which largely cancels in the ratio. The relative sign of the c_0, c_2 coefficients in $\mathcal{F}$ expresses the same cancellation. As a result, the simulated distributions of both $\mathcal{F}$ and L_2/L_0 are found to be in excellent agreement with data. Some *BABAR* analyses have therefore preferred to use the simpler L_2/L_0 ratio. Simplicity over complexity (*i.e.* adding L_1 or splitting the ROE between charged and neutral particles) has been privileged by most *BABAR* analyses because the discriminating gain was found to be marginal.

9.4.2 Nonlinear discriminants

Many *BABAR* analyses combine the information from the monomials with other variables to further enhance their discriminating power and the resulting performance in background suppression. As already mentioned, there are significant correlations among event-shape variables (since they all quantify in different ways the spatial distribution of momentum flow). To better exploit such potentially

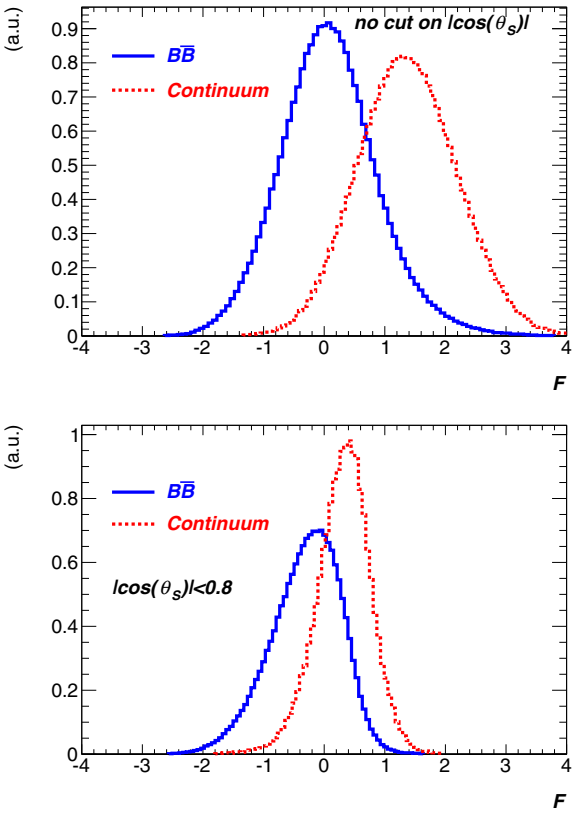

Figure 9.4.4. The signal (solid blue line) and background (dashed red line) distributions of the Fisher discriminant $\mathcal{F}$ based on the L_0 and L_2 monomials, used for continuum background suppression in several *BABAR* charmless B decay analyses. To illustrate the two-step procedure, the distributions are shown both before (top) and after (bottom) a first-step cut of $|\cos\theta_S| < 0.8$. The figures are adapted from a *BABAR* Thesis (Malclès, 2006). The vertical scale is in arbitrary units (a.u.).

nonlinear correlations, neural networks (NN, see Chapter 4 for a description of multivariate methods) and other nonlinear discriminant algorithms are used. As an illustration, typical charmless 3-body analyses use, in addition to the L_0 and L_2 monomials, variables such as $|\cos\theta_B|$ and $|\cos\theta_T|$ in their final MVA. Figure 9.4.5 illustrates the discriminating power achieved with a NN based on these four variables, used in several Dalitz-plot analyses of charmless 3-body B decays in *BABAR* (see Chapter 13 for a description of Dalitz-plot analyses). In these analyses, the NN output is used both for selection and in the maximum-likelihood fit. At the first stage, this NN provides a $\sim 1.9\sigma$ separation between signal and background. A cut at NN > -0.4 is then applied to remove roughly 75% of continuum background while retaining a 90% signal efficiency; on top of enhancing its signal-to-background content, this cut also reduces the sample size to a value that is suitable for the CPU constraints affecting multidimensional amplitude fits in Dalitz-plot analyses. Then, at the amplitude analysis stage, the NN is implemented in the likelihood function, where its remaining $\sim 1.4\sigma$ separation is exploited in the maximum-likelihood fit. Two specific features, relevant to the implementation of a NN in a Dalitz analyses are worth mentioning:

- For continuum background, the NN is correlated with the Dalitz variables. This feature can be qualitatively described as follows: for continuum event candidates passing all selection criteria, and belonging to the center of the Dalitz plot, the angular distribution of particles tends to exhibit a more isotropic distribution, since already the three particles composing the signal candidate have similar momenta and roughly equidistant angular separation. In order to include the NN in the likelihood function, a parameterization of this correlation as a function of Dalitz masses, has to be effectively implemented for its continuum component.
- In light of the aforementioned systematic sensitivity to the simulation of the total momentum flow, some *BABAR* analyses have opted for not allowing the L_0 and L_2 monomials to be independently optimized in the training stage of the NN, and used instead a linear combination with fixed coefficients or the L_2/L_0 ratio in the NN training.

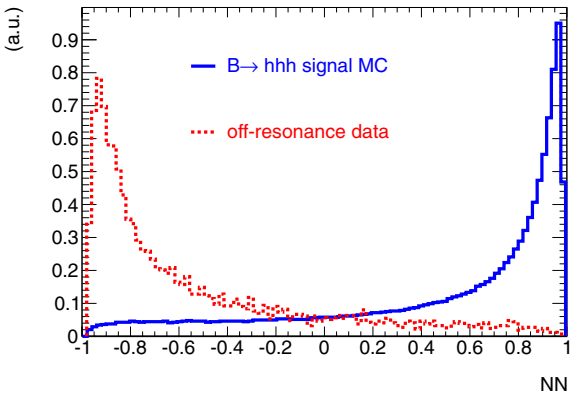

Figure 9.4.5. An example of a multilayer perceptron output NN, used to discriminate between the signal B decay and continuum background in the charmless 3-body analysis of $B^0 \to K^0_S\pi^+\pi^-$ decays. The solid blue histogram is the NN output evaluated on signal Monte-Carlo, and the dashed red histogram uses off-resonance data. This neural network uses four variables as inputs : L_0, L_2, $|\cos\theta_B|$ and $|\cos\theta_T|$. The figure is adapted from a *BABAR* Thesis (Pérez, 2008). The vertical scale is in arbitrary units (a.u.).

9.4.3 Including additional sources of background suppression

In addition to the "event-shape" variables discussed in the previous sections, various other sources of discriminating

information are also available in B decay analyses: in particular, decay-time information extracted from vertexing (discussed in Chapter 6), kinematical variables extracted from B meson reconstruction (Chapter 7), and the output of B-flavor tagging (Chapter 8), can all contribute to background suppression. As described in more detail in Chapter 11, a generic time-dependent analysis combines all this information in a maximum-likelihood analysis.

For specific analyses, only a subsample of this information is effectively used in the likelihood function; for instance, timing information is not necessary to perform a time-independent fit, and analysis of a flavor-specific decay (like charged B modes, or "self-tagging" neutral decay modes), does not require tagging. In such scenarios, some *BABAR* analyses (particularly in searches of rare decay channels) exploit this available background-suppressing power, by combining event-shape variables with the tagging index output and/or the time difference significance $\Delta t/\sigma(\Delta t)$ into a linear Fisher discriminant, which is in turn used in the likelihood function.

9.5 Belle strategy

For Belle, the correlated shape variables are first combined to form a Fisher discriminant and then other uncorrelated variables are included with the Fisher variable to form a signal-to-background likelihood ratio $\mathcal{R}$. The numbers of signal and background events can be extracted by either applying a cut on the likelihood ratio and then performing a fit using $m_{\rm ES}$ and ΔE, or by requiring a loose cut on $\mathcal{R}$, and then performing a fit using the variables $m_{\rm ES}$, ΔE and $\mathcal{R}$. Later in the lifetime of Belle, more analyses employ the neural network technique to combine correlated variables with the Fisher discriminant and other uncorrelated variables. One can make a requirement on the neural network output to suppress the background or include the output after a loose requirement in a multi-dimensional likelihood fit to extract the signal.

9.5.1 *SFW*

There are two kinds of Fisher discriminant used to study charmless B decays on Belle. All reconstructed particles in an event are divided into two categories: B candidate daughters (denoted as s) and the ROE (denoted as o). Two Fisher discriminants are constructed using the energy and momentum of each particle in the e^+e^- center-of-mass frame. The first Fisher discriminant is composed of several Fox-Wolfram moments h_j^{kl} and is defined as

$$SFW = a_2 h_2^{so} + a_4 h_4^{so} + \sum_{j=1}^{4} b_j h_j^{oo}, \qquad (9.5.1)$$

where a_2, a_4 and b_j are the Fisher coefficients determined to separate signal and backgrounds in an optimal way using the signal and continuum MC events. The SFW variable is colloquially referred to as the "Super Fox-Wolfram Moment". In order to avoid the data-MC discrepancy in event shapes, data in regions dominated by continuum are often used to determine the coefficients. Variables $h_i^{so}(i = 2, 4)$ and h_j^{oo} are the normalized Fox-Wolfram moments, defined as

$$h_l^k = \frac{\sum_{m,n} |\vec{p_m}||\vec{p_n}| P_l(\cos\theta_{mn})}{\sum_{m,n} |\vec{p_m}||\vec{p_n}|}, \qquad (9.5.2)$$

where $\vec{p_m}$ and $\vec{p_n}$ are the momenta of particles m and n; $P_l(\cos\theta_{mn})$ is the l-th order Legendre polynomial of cosine of the angle (θ_{mn}) between $\vec{p_m}$ and $\vec{p_n}$; k categorizes the type of Fox-Wolfram moment, so and oo, where m is from B signal daughters and n is from the ROE for so, and both m and n are from the ROE for oo. If B daughter particles themselves decay into several particles, the event shape is more isotropically distributed. However, the B candidates from the continuum are also more isotropically distributed to mimic the $B\overline{B}$ events. For two-body or three-body B decays, the signal-to-background separation is therefore better if the SFW variable is computed using the particles directly from B decays. For instance, in the decay $B \to \omega K$ with $\omega \to \pi^+\pi^-\pi^0$, the Fox-Wolfram moment h_l^{so} in Eq. (9.5.2) is calculated using the ω momentum instead of the momenta of its daughter pions. The difference of the separation power between the two different treatments is less pronounced for multi-body B decays.

9.5.2 *KSFW*

To further improve the continuum suppression, a second Fisher discriminant was developed by Belle:

$$KSFW = \sum_{l=0}^{4} R_l^{so} + \sum_{l=0}^{4} R_l^{oo} + \gamma \sum_{n=1}^{N_t} |(P_t)_n|, \qquad (9.5.3)$$

where R_l^{so} and R_l^{oo} are modified Fox-Wolfram moments similar to h_l^{so} and h_l^{oo} in Eq. (9.5.2), respectively; the third term is the scalar sum of the transverse momentum of each particle multiplied by a free parameter γ and N_t is the total number of particles. The expressions of R_l^{so} and R_l^{oo} are described as follows:

- R_l^{so}
  In constructing R_l^{so}, the missing momentum of an event is treated as an additional particle and the moment is decomposed into three categories: a charged particle part (c), neutral particle part (n), and missing particle part (m). The variable R_l^{so} is expressed as

$$R_l^{so} = \frac{\alpha_{\rm cl} H_{\rm cl}^{so} + \alpha_{\rm nl} H_{\rm nl}^{so} + \alpha_{\rm ml} H_{\rm ml}^{so}}{E^*_{\rm beam} - \Delta E}. \qquad (9.5.4)$$

  For odd l, we have

$$H_{\rm nl}^{so} = H_{\rm ml}^{so} = 0 \qquad \text{and} \qquad (9.5.5)$$

$$H_{\rm cl}^{so} = \sum_i \sum_{j\rm x} Q_i Q_{j\rm x} |p_{j\rm x}| P_l(\cos\theta_{i,j\rm x}), \qquad (9.5.6)$$

where i runs over the B daughters; jx indexes the ROE in the category x (x = c, n, m); Q_i and $Q_{j\mathrm{x}}$ are the charges of particle i and jx, respectively; $p_{j\mathrm{x}}$ is the momentum of particle jx; and $P_l(\cos\theta_{i,j\mathrm{x}})$ is the l-th order Legendre polynomial of the cosine of the angle between particles i and jx.
For even l,

$$H^{so}_{\mathrm{x}l} = \sum_i \sum_{j\mathrm{x}} |p_{j\mathrm{x}}| P_l(\cos\theta_{i,j\mathrm{x}}), \qquad (9.5.7)$$

which is similar to Eq. (9.5.6) except for the charge factors. There are two free parameters for $l = 1, 3$ and nine (3×3) for $l = 0, 2, 4$.

– R^{oo}_l
The definition of the second term of Eq. (9.5.3) is simpler.
For odd l, we have

$$R^{oo}_l = \sum_j \sum_k \beta_l Q_j Q_k |p_j||p_k| P_l(\cos\theta_{j,k}), \qquad (9.5.8)$$

where j and k run over the ROE and other variables are the same as used in Eq. (9.5.6).
For even l, we have

$$R^{oo}_l = \sum_j \sum_k \beta_l |p_j||p_k| P_l(\cos\theta_{j,k}). \qquad (9.5.9)$$

There are five Fisher coefficients (β_l) to be determined.

The total number of Fisher coefficients in $KSFW$ is 17, determined using the signal and continuum MC events. To further improve the background suppression, the 17 coefficients are obtained in seven missing mass squared (M^2_{miss}) bins, where M^2_{miss} is defined as

$$M^2_{\mathrm{miss}} = \left(E_{\Upsilon(4S)} - \sum_{n=1}^{N_t} E_n \right)^2 - \sum_{n=1}^{N_t} |p_n|^2, \qquad (9.5.10)$$

where $E_{\Upsilon(4S)}$ is the energy of $\Upsilon(4S)$ and E_n and p_n are the energy and momentum of particle n, respectively. Therefore, there are seven sets of 17 Fisher coefficients in $KSFW$. In general $KSFW$, compared to SFW, provides better signal-background separation for charmless two-body and three-body B decays, but the improvement is less pronounced for the B decays into a final state with more than three particles.

Two other variables that can distinguish between signal and continuum are $\cos\theta_{\mathrm{B}}$ (as mentioned in Section 9.3) and ΔZ, where the former is the cosine of the angle between the B momentum and the beam direction in the CM frame and the latter is the distance in the beam direction between the B vertex and the vertex from the ROE. Figure 9.5.1 shows the $\cos\theta_{\mathrm{B}}$ and ΔZ distributions for the $B^+ \to K^+\pi^0$ signal and the continuum events. Since $\Upsilon(4S)$ produced at e^+e^- resonance is transversely polarized, the B moving distribution behaves as $\sin^2\theta_{\mathrm{B}}$ while it is more or less flat for the continuum background.[38] The ΔZ distribution is broader for $B\overline{B}$ events due to the relatively longer lifetime of B mesons. Signal B vertices are constructed using the charged tracks of the B daughters. For a decay mode with only one charged track in the final state, for instance $B^+ \to K^+\pi^0$, the z vertex position is obtained by projecting the single track trajectory to the beam axis. Obviously the ΔZ resolution is better if there is more than one charged particle used to reconstruct the decay vertex. The ΔZ variable is not applicable for the decay modes with only photons in the final state, for instance $B^0 \to \pi^0\pi^0$. It is possible to use photon conversions to obtain the B vertex in a future super flavor factory. The primary aim for this case is to perform a time-dependent measurement.

Finally all the shape information is combined to form a signal-to-background likelihood ratio ($\mathcal{R}$), defined as

$$\mathcal{R} = \frac{\mathcal{L}_S}{\mathcal{L}_S + \mathcal{L}_B}, \qquad (9.5.11)$$

$$\mathcal{L}_{S/B} = P(KSFW)_{S/B} \times P(\cos\theta_{\mathrm{B}})_{S/B} \times P(\Delta Z)_{S/B}, \qquad (9.5.12)$$

where $P_{S/B}$ is the probability density function for signal (S) and background (B). Continuum suppression can be achieved by applying a cut selection on $\mathcal{R}$ based on a figure of merit or requiring a loose selection and including $\mathcal{R}$ in a multi-dimensional likelihood fit. To avoid poor modeling of the rising edges as shown in the top plot of Fig. 9.5.2, in some analyses a modified likelihood ratio $\mathcal{R}'$ can be defined as

$$\mathcal{R}' = \log \frac{\mathcal{R} - lb}{ub - \mathcal{R}}, \qquad (9.5.13)$$

where lb is the lower bound of $\mathcal{R}$, which is the loose $\mathcal{R}$ selection value to reduce the background, and ub is the upper bound (usually 1.0). The bottom plot of Fig. 9.5.2 shows the $\mathcal{R}'$ distribution with lower $\mathcal{R}$ bound at 0.2 for $B^+ \to K^+\pi^0$ signal and the continuum background. The signal and background $\mathcal{R}'$ distributions may be described by a single or double Gaussian, which can be used as *p.d.f.* representations of $\mathcal{R}'$ in the multi-dimensional fit.

9.5.3 Additional variables and neural network

Additional background discrimination is provided by B-flavor tagging. As described in Chapter 8, events with good flavor tags usually contain high momentum leptons and are more likely to be $B\overline{B}$ events. The top plot of Fig. 9.5.3 shows the normalized signed probability $(q \cdot r)$ distributions for B signal and the continuum background from MC. Note that the $q \cdot r$ definition for the tag B

[38] The distribution of the angle between f and the beam axis for $e^+e^- \to f\bar{f}$ (continuum) events has a $1 + \cos^2\theta_{\mathrm{B}}$ shape. However, the reconstructed θ_{B} in continuum events is a consequence of random combinations of tracks. The distribution is also affected by acceptance effects. The resulting distribution turns out to be almost uniform.

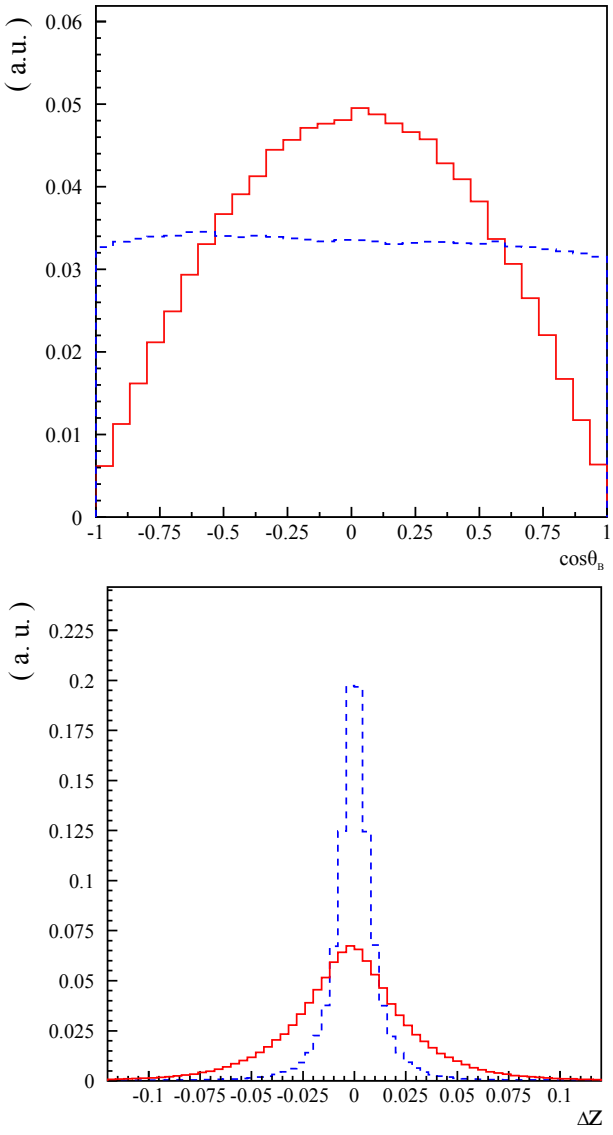

Figure 9.5.1. The $\cos\theta_{\rm B}$ (top) and ΔZ (bottom) distributions for the $B^+ \to K^+\pi^0$ and continuum MC events. Solid red lines are B signal candidates and dashed blue lines are the continuum background. These figures are Belle internal, from the (Duh, 2012) analysis. The vertical scale is in arbitrary units (a.u.).

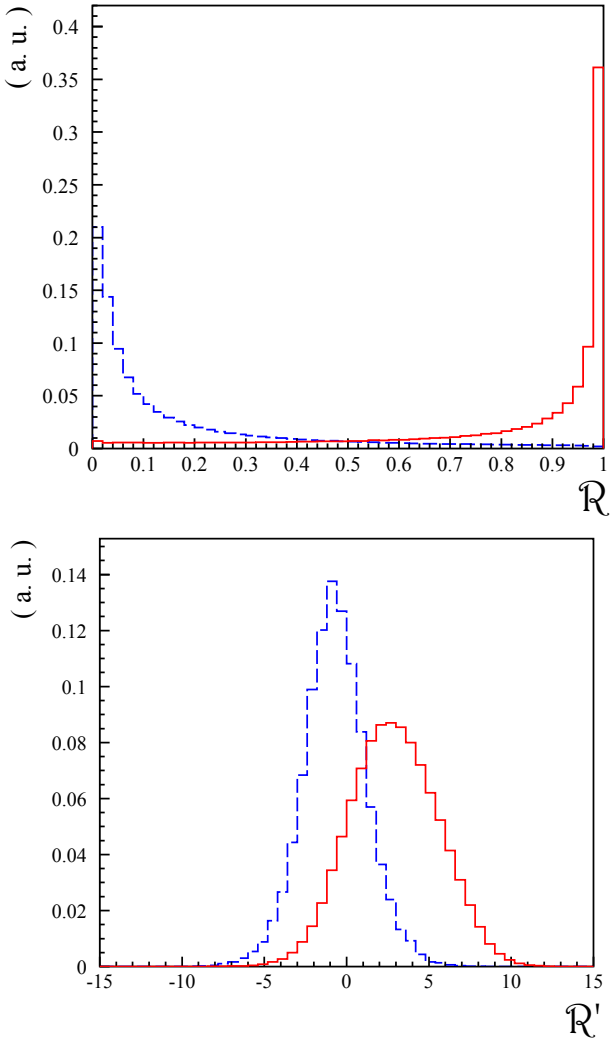

Figure 9.5.2. The $\mathcal{R}$ (top) and modified $\mathcal{R}$ (bottom) distributions for the $B^+ \to K^+\pi^0$ and continuum MC events. Solid red lines are B signal candidates and dashed blue lines are the continuum background. The modified $\mathcal{R}$ ($\mathcal{R}'$) is defined after requiring $\mathcal{R} > 0.2$. These figures are Belle internal, from the (Duh, 2012) analysis. The vertical scale is in arbitrary units (a.u.).

described in Eq. 8.6.5 is also valid for the charged B meson system by replacing $B^0(\overline{B}^0)$ with $B^+(B^-)$. It is easy to understand that the majority of the continuum events populate the central $q \cdot r$ region, where the flavor information is poorly known, while sizable fractions of B signal events have $q \cdot r \sim \pm 1$. If the signal B decays into a flavor specific state, one can use the product of the signal B-flavor (q_B) and $q \cdot r$ to distinguish between signal and background. As shown in the bottom plot of Fig. 9.5.3, a large fraction of signal events populate the region around $q_B \cdot q \cdot r = -1$ and the distributions for both signal and the continuum events in the $B^+ \to K^+ l^+ l^-$ study become asymmetric. The asymmetric $q_B \cdot q \cdot r$ distribution for the continuum is due to the correlation of strangeness between the tag and signal sides. To utilize all available information, the quantity $q_B \cdot q \cdot r$ ($q \cdot r$ for the CP eigenmodes) can be used in the likelihood for background suppression, or alternatively the original $\mathcal{R}$ selections can be optimized depending on the value of $q_B \cdot q \cdot r$. The latter method has been used in many Belle analyses.

To utilize all the available information, in some Belle analyses the variables described above were combined us-

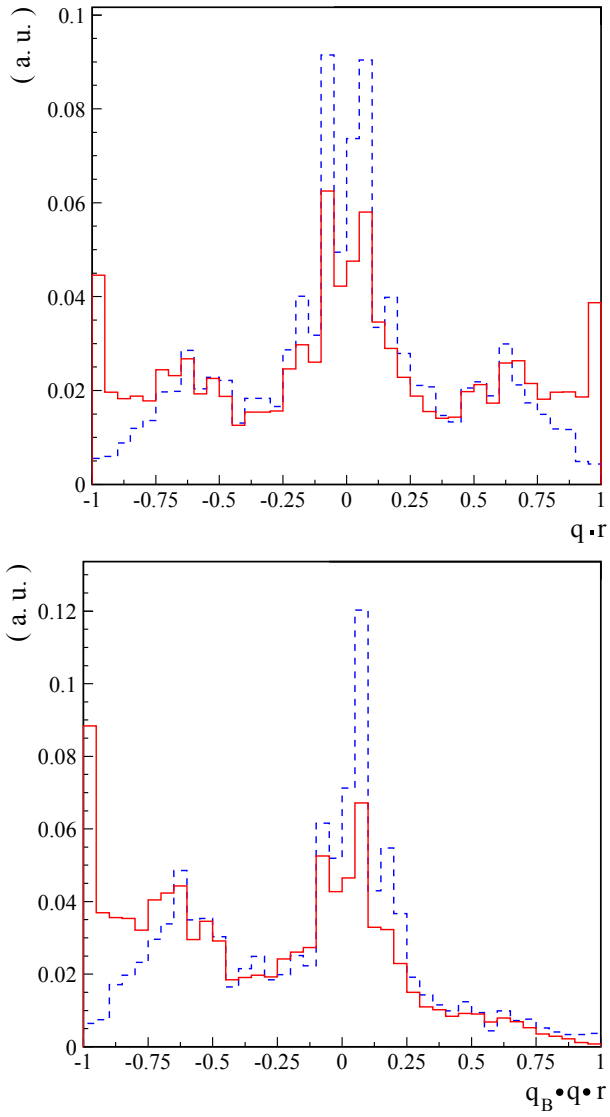

Figure 9.5.3. The $q{\cdot}r$ (top) and $q_B{\cdot}q{\cdot}r$ (bottom) distributions for signal (solid red) and continuum MC (dashed blue) events. Signal B events are generated to decay into a flavor specific state. These figures are Belle internal, from the (Wei, 2009) analysis. The vertical scale is in arbitrary units (a.u.).

ing the neural network technique. One of the popular packages used in Belle is the NeuroBayes package (Feindt and Kerzel, 2006; Phi-T, 2008). For instance, the suppression of the continuum background in the Belle analyses of $B^0 \to D^0K^{*0}, D^0 \to K^-\pi^+$ (Negishi, 2012) and $B^- \to DK^-, D \to K^+\pi^-$ (Horii, 2011) was achieved using several variables as the NeuroBayes inputs: such as KSFW, $\cos\theta_{\rm T}$, $\cos\theta_{\rm B}$, ΔZ, flavor tagging information $q{\cdot}r$, and the cosine of the angle between the momentum of the kaon candidate from the D decay and the B momentum in the D rest frame. Three more variables are included in the $B^0 \to D^0K^{*0}$ search: (1) the distance of closest approach between the trajectories of the K^* and D candidates; (2) the difference between the sum of the particle charges in the D hemisphere and the sum in the opposite hemisphere, excluding those used in the reconstruction of the B meson; and (3) the angle between the D and $\Upsilon(4S)$ directions in the rest frame of the B candidate. The advantage of employing the neural network technique is that variables having correlations with each other can be added and their correlations are considered non-linearly. As with the signal-background likelihood ratio, one can make a requirement on the NeuroBayes output to suppress the continuum background or include it in a multi-dimensional likelihood fit to extract the signal yield.

NeuroBayes is widely used in many high energy experiments. The application, to name a few, ranges from Higgs search (Aaltonen et al., 2009d), studies of single top production (Aaltonen et al., 2010; Chatrchyan et al., 2012a), measuring B and D meson properties (Aaij et al., 2012l; Aaltonen et al., 2011d), and full B meson reconstruction at B factories (Feindt et al., 2011).

9.6 Summary

In summary, various techniques of background suppression, mostly inspired by charmless B decay analyses suffering from huge backgrounds, are described in this chapter.

As an illustration, for an analysis of $B \to \eta' h$ ($h = \rho, K^*, \omega, \phi$) (Schumann, 2007) in Belle, the continuum background is suppressed by imposing $q \cdot r$ dependent selections on $\mathcal{R}$. The signal efficiency due to the suppression is (42–88)% and the background is reduced by (98–45)%, depending on the decay mode. The possible improvement by including the variable $\mathcal{R}'$ in the fit for signal extraction is investigated in the $B^+ \to K^+\pi^0$ analysis in Belle. With a lower bound (lb) value chosen to be 0.2, the significance (the signal yield from the fit divided by its uncertainty) of the extracted signal is improved by 15%. Note that there may be correlations between $\mathcal{R}'$ and other variables. For instance, the variables $\mathcal{R}'$ and ΔE for the continuum background is found to be correlated in the $B \to hh'$ analysis (Duh, 2012). Hence, different ΔE *p.d.f.*s in different $\mathcal{R}'$ regions are implemented in the analysis. Examples of using the NeuroBayes package to include various correlated variables are described in Section 9.5.3. A requirement on the NeuroBayes output in the analysis of $B^- \to DK^-, D \to K^+\pi^-$ (Horii, 2011) retains 96% of the signal and rejects 74% of the background. In the search of $B^0 \to DK^{*0}, D \to K^-\pi^+$, the NeuroBayes output, ranging from -1 to 1, is first required to be greater than -0.6 to suppress the background, and is then included in the multi-likelihood fit after being transformed using Eq. (9.5.13) with the NeuroBayes output $\mathcal{R}$, $lb = -0.6$ and $ub = 1.0$. The loose cut ($lb = -0.6$) rejects 70.5% of the background, while the signal loss is 3.9%.

For *BABAR*, most analyses of $B \to hh$ channels ($h = \pi, K$) (see Chapter 17.4) followed strategies in line with the generic approach described in Section 9.4.1: a two-step background suppression, starting with simple loose cuts on

strongly discriminating variables, then using Fisher discriminants as a discriminating variable in a likelihood fit. At the selection step, signal efficiencies were often adapted to the specific signal-to-background rates for the final state being considered; for example in (Aubert, 2007ay), the cut on the $|\cos\theta_S|$ value applied in the $B^+ \to h^+\pi^0$ study was chosen to retain about $\sim 80\%$ of signal while rejecting $\sim 65\%$ of continuum; in contrast, a tighter selection was applied for $B^0 \to \pi^0\pi^0$, as a consequence of its smaller signal-to-background rate. In the same spirit, the final update of the $B^0 \to \pi^+\pi^-$, $K^+\pi^-$ study (Lees, 2013b) applied a looser cut on $|\cos\theta_S|$, achieving close to $\sim 90\%$ signal efficiency. Owing to its larger signal purity, in this study both the signal and background parameters of the Fisher *p.d.f.* were extracted from the signal sample itself in the maximum-likelihood fit (instead of being extrapolated from sidebands or simulation control samples), thus minimizing the corresponding systematic uncertainties. The observation of the rare $B^+ \to K^+\overline{K}^0$ and $B^0 \to K^0\overline{K}^0$ decays (Aubert, 2006ai) is another useful illustration of linear discriminants in *BABAR*; the enhancement of signal sensitivity provided by a similar Fisher discriminant was instrumental in establishing the observation of these two rare channels. Concerning nonlinear discriminants, most *BABAR* analyses of charmless $B \to hhh$ decays ($h = \pi, K$) implemented NN discriminants in line with the generic strategy discussed in Section 9.4.2; at the selection level, typical cuts on the NN value were chosen to retain some $\sim 90\%$ of signal, while rejecting up to $\sim 75\%$ of continuum. For Dalitz-plot analyses such as (Aubert, 2009av), non-negligible correlations between the NN and the Dalitz variables for continuum events were observed, and addressed with a dedicated parameterization; in this way, the $\sim 1.4\sigma$ separation provided by these NN discriminants could be implemented in the likelihood function, and used in the amplitude fits.

Chapter 10
Mixing and time-dependent analyses

Editors:
Adrian Bevan (BABAR)
Thomas Mannel (theory)

This Chapter introduces neutral meson mixing, as well as the principles and methods underlying time-dependent analyses in B meson decays. A detailed discussion of experimental concerns for a time-dependent analysis follows on from a theoretical introduction of mixing and time-dependent formalism (Sections 10.1 and 10.2). The experimental aspects discussed here include the use of flavor tagging methods introduced in Chapter 8 and the inevitable dilution of information when the tagging assignment is incorrect (Section 10.3). The impact of the detector resolution on the reconstructed value of the proper time difference between the decays of two neutral mesons and on the measurement of physical observables is raised in Section 10.4. The corresponding time evolution of background events is discussed in Section 10.5. The final part of this chapter discusses how parameters required to describe the mixing and time-evolution of B mesons can be extracted from the data (Section 10.6). Systematic uncertainties common to all time-dependent analyses of B decays are discussed in Section 15.3.

Mixing in the neutral B meson system was discovered by the ARGUS Collaboration (Albrecht et al., 1987b), and Section 17.5 summarizes the measurements of B mixing performed by *BABAR* and Belle. An understanding of mixing in B mesons is one of the ingredients in the study of time-dependent *CP* asymmetries: in particular, it is crucial for the measurement of the angles of the Unitarity Triangle introduced in Chapter 16, and discussion of measurements of the angles can be found in Sections 17.6 through 17.8. Tests of quantum entanglement, the *CPT* symmetry, and Lorentz covariance using neutral B mesons, discussed in Sections 17.5.3 through 17.5.5, also rely on a good understanding of mixing. Neutral meson mixing in charm decays was discovered at the B Factories: this is discussed in Section 19.2.

10.1 Neutral meson mixing

Meson mixing is a phenomenon that only occurs for the weakly-decaying, open-flavor (*i.e.* not $q\overline{q}$ pairs) neutral K, D, and $B^0_{d,s}$ mesons. Collectively we can refer to these mesons as P when describing the formalism common to all three systems. The effective Hamiltonian describing neutral meson mixing is given by

$$\mathcal{H}_{\text{eff}} = \mathbf{M} - \frac{i\mathbf{\Gamma}}{2} = \left[\begin{pmatrix} M_{11} & M_{12} \\ M_{21} & M_{22} \end{pmatrix} - \frac{i}{2}\begin{pmatrix} \Gamma_{11} & \Gamma_{12} \\ \Gamma_{21} & \Gamma_{22} \end{pmatrix}\right], \quad (10.1.1)$$

where $\mathbf{M}$ and $\mathbf{\Gamma}$ are two-by-two Hermitian matrices describing the mass and decay rate components of $\mathcal{H}_{\text{eff}}$, respectively.

The *CPT* symmetry imposes that the matrix elements in Eq. (10.1.1) satisfy $M_{11} = M_{22}$ and $\Gamma_{11} = \Gamma_{22}$. In the limit of *CP* or T invariance in mixing, $\Gamma_{12}/M_{12} = \Gamma_{21}/M_{21}$ is real. Figure 10.1.1 shows the short-distance box diagrams responsible for (top) D and (bottom) $B^0_{d,s}$ mixing transitions in the SM. For the cases of kaons and D mesons these diagrams are dominated by long-distance contributions that are difficult to compute. The long-distance pieces are strongly CKM suppressed only in the case of B mesons for which M_{12} can be computed in perturbation theory. Long-distance contributions are due to real intermediate states whereas the short-distance contributions arise from heavy quark transitions (in particular, the top quark).

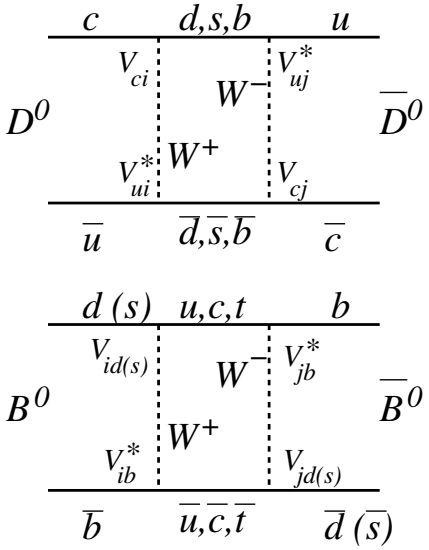

Figure 10.1.1. Box diagrams corresponding to the short-distance contributions to neutral meson mixing for (top) D and (bottom) $B^0_{d,s}$ mesons. Each of these contributions is matched by a diagram where the quark triplet, and W bosons are interchanged. The V_{ij} are CKM matrix elements discussed in Chapter 16.

Solving the time evolution represented by the effective Hamiltonian of Eq. (10.1.1) amounts to determining its eigenstates; however, the eigenvalue problem is non-Hermitian, hence the eigenvalues will be complex and the eigenstates will not be orthogonal. This non-Hermiticity and thus the imaginary parts of the eigenvalues lead to a non-unitary time evolution in the two-dimensional subspace spanned by the B_d and the $\overline{B}_d$. As a consequence, probability is not conserved in this subspace, which describes the fact that both mesons will eventually decay and hence disappear from this two-dimensional space.

The eigenstates of the effective Hamiltonian can be represented as an admixture of the flavor eigenstates via

$$|P_{1,2}\rangle = p|P^0\rangle \pm q|\overline{P}^0\rangle, \tag{10.1.2}$$

where $|q|^2 + |p|^2 = 1$ to normalize the wave function, and

$$\frac{q}{p} = \sqrt{\frac{M_{12}^* - \frac{i}{2}\Gamma_{12}^*}{M_{12} - \frac{i}{2}\Gamma_{12}}}, \tag{10.1.3}$$

and the corresponding eigenvalues read

$$m_1 - \frac{i}{2}\Gamma_1 = M_{11} - \frac{i}{2}\Gamma_{11} + \frac{p}{q}\left(M_{12} - \frac{i}{2}\Gamma_{12}\right) \tag{10.1.4}$$

$$m_2 - \frac{i}{2}\Gamma_2 = M_{11} - \frac{i}{2}\Gamma_{11} - \frac{p}{q}\left(M_{12} - \frac{i}{2}\Gamma_{12}\right) \tag{10.1.5}$$

where $m_{1,2}$ are the masses and $\Gamma_{1,2}$ are the widths of the two effective Hamiltonian eigenstates. These states are graphically depicted for various neutral meson systems in Fig. 10.1.2, illustrating their mass and width differences. These two parameters determine the time evolution of a neutral meson that oscillates between the particle and the anti-particle state, as explained in more detail below.

Assuming $m_2 > m_1$ we define $\Delta m = m_2 - m_1 > 0$ and $\Delta\Gamma = \Gamma_2 - \Gamma_1$, and then write the time evolved state that had been a $|P^0\rangle$ at $t = 0$ as

$$|P^0(t)\rangle = g_+(t)|P^0\rangle + \frac{q}{p}g_-(t)|\overline{P}^0\rangle \tag{10.1.6}$$

with

$$g_\pm(t) = e^{-im_1 t}e^{-\frac{1}{2}\Gamma_1 t}\frac{1}{2}\left[1 \pm e^{-i\Delta m\, t}e^{\frac{1}{2}\Delta\Gamma\, t}\right]. \tag{10.1.7}$$

From these relations we can compute the time-dependent decay rates for both P^0 and $\overline{P}^0$. If $|f_{CP}\rangle$ is a common final state for both P^0 and $\overline{P}^0$, we denote the corresponding decay amplitudes as

$$A_f = \langle f|H_{\Delta F=1}|P^0\rangle \tag{10.1.8}$$

$$\overline{A}_f = \langle f|H_{\Delta F=1}|\overline{P}^0\rangle \tag{10.1.9}$$

where $H_{\Delta F=1}$ is the Hamiltonian for transitions involving a flavor change of one unit. Defining

$$\lambda = \frac{q}{p}\frac{\overline{A}_f}{A_f} \tag{10.1.10}$$

and — following the textbook (Bigi and Sanda, 2000) — the auxiliary variables $K_\pm(t)$ and $L(t)$

$$K_\pm(t) = 4\,e^{\Gamma_1 t}|g_\pm(t)|^2 \tag{10.1.11}$$
$$= 1 + e^{\Delta\Gamma\, t} \pm 2e^{\frac{1}{2}\Delta\Gamma\, t}\cos(\Delta m\, t)$$

$$L(t) = 4\,e^{\Gamma_1 t}g_-^*(t)g_+(t) \tag{10.1.12}$$
$$= 1 - e^{\Delta\Gamma\, t} - 2i\,e^{\frac{1}{2}\Delta\Gamma\, t}\sin(\Delta m\, t)$$

one arrives at

$$\Gamma(P^0(t) \to f) \propto |\langle f|H_{\Delta F=1}|P^0(t)\rangle|^2 \tag{10.1.13}$$
$$= e^{-\Gamma_1 t}|A_f|^2\left[K_+(t) + |\lambda|^2 K_-(t) + 2\mathrm{Re}\left\{\lambda L^*(t)\right\}\right]$$

$$\Gamma(\overline{P}^0(t) \to f) \propto |\langle f|H_{\Delta F=1}|\overline{P}^0(t)\rangle|^2 \tag{10.1.14}$$
$$= e^{-\Gamma_1 t}|\overline{A}_f|^2\left[K_+(t) + \frac{1}{|\lambda|^2}K_-(t) + 2\mathrm{Re}\left\{\frac{1}{\lambda}L^*(t)\right\}\right].$$

These expressions — as well as the resulting CP asymmetries — simplify considerably in the cases where some of the parameters are small. For comparison we list the values for the relevant parameters for the various neutral meson systems in Table 10.1.1 The width difference $\Delta\Gamma$ in the kaon system is large compared to the average decay width Γ $(= (\Gamma_1 + \Gamma_2)/2 = 1/\tau)$ and the mass difference Δm; hence, the above expressions are typically expanded in a different way. In the system of neutral D mesons, both the oscillation frequency Δm and the width difference $\Delta\Gamma$ are very small compared to the average decay width Γ. The resulting expressions are given in Section 19.2.

Furthermore, for kaons and D mesons, the expressions for M_{12} and Γ_{12} are dominated by long-distance contributions. This makes the theoretical estimates of Δm and $\Delta\Gamma$ in these systems difficult to compute.

The situation is simpler for B mesons. The matrix element Γ_{12} is strongly CKM suppressed, and thus $\Delta\Gamma$ is small compared to Δm, and can be set to zero. Furthermore, Δm is dominated by the short-distance top quark contribution. We relate Δm and $\Delta\Gamma$ to M_{12} and Γ_{12} using Eqs (10.1.4) and (10.1.5)

$$\Delta m_{d,s}^2 - (\Delta\Gamma_{d,s}/2)^2 = 4\left[|M_{12}|^2 - |\Gamma_{12}/2|^2\right]$$
$$\Delta m_{d,s}\Delta\Gamma_{d,s} = 4\mathrm{Re}(M_{12}\Gamma_{12}^*)\,. \tag{10.1.15}$$

Neglecting $|\Gamma_{12}|$ in the above expressions and explicitly calculating the box diagram amplitude for B_d leads to

$$\Delta m_d \simeq 2|M_{12}| \tag{10.1.16}$$
$$= 2\frac{G_F^2 M_W^2}{16\pi^2 m_{B_d}}S_0|V_{td}V_{tb}^*|\eta_B\langle B_d|(\bar{b}d)(\bar{b}d)|\overline{B}_d\rangle \tag{10.1.17}$$

where S_0 is a function of m_t^2/M_W^2 whose leading term behaves as m_t^2/M_W^2, reflecting the Glashow-Iliopoulos-Maiani (GIM) mechanism (Buras and Fleischer, 1998; Inami and Lim, 1981), η_B are the perturbative QCD corrections known to next to leading order (NLO) precision, and $(\bar{b}d)(\bar{b}d)$ is a local $(V-A)\times(V-A)$ operator with $\Delta B = 2$.

For the small width difference $\Delta\Gamma_d$, it follows from Eqs (10.1.15) that

$$\Delta\Gamma_d \simeq 2|M_{12}|\,\mathrm{Re}\left(\frac{\Gamma_{12}}{M_{12}}\right). \tag{10.1.18}$$

Recall that Δm_d was defined to be positive; the sign of $\Delta\Gamma_d$ must be determined by experiment.

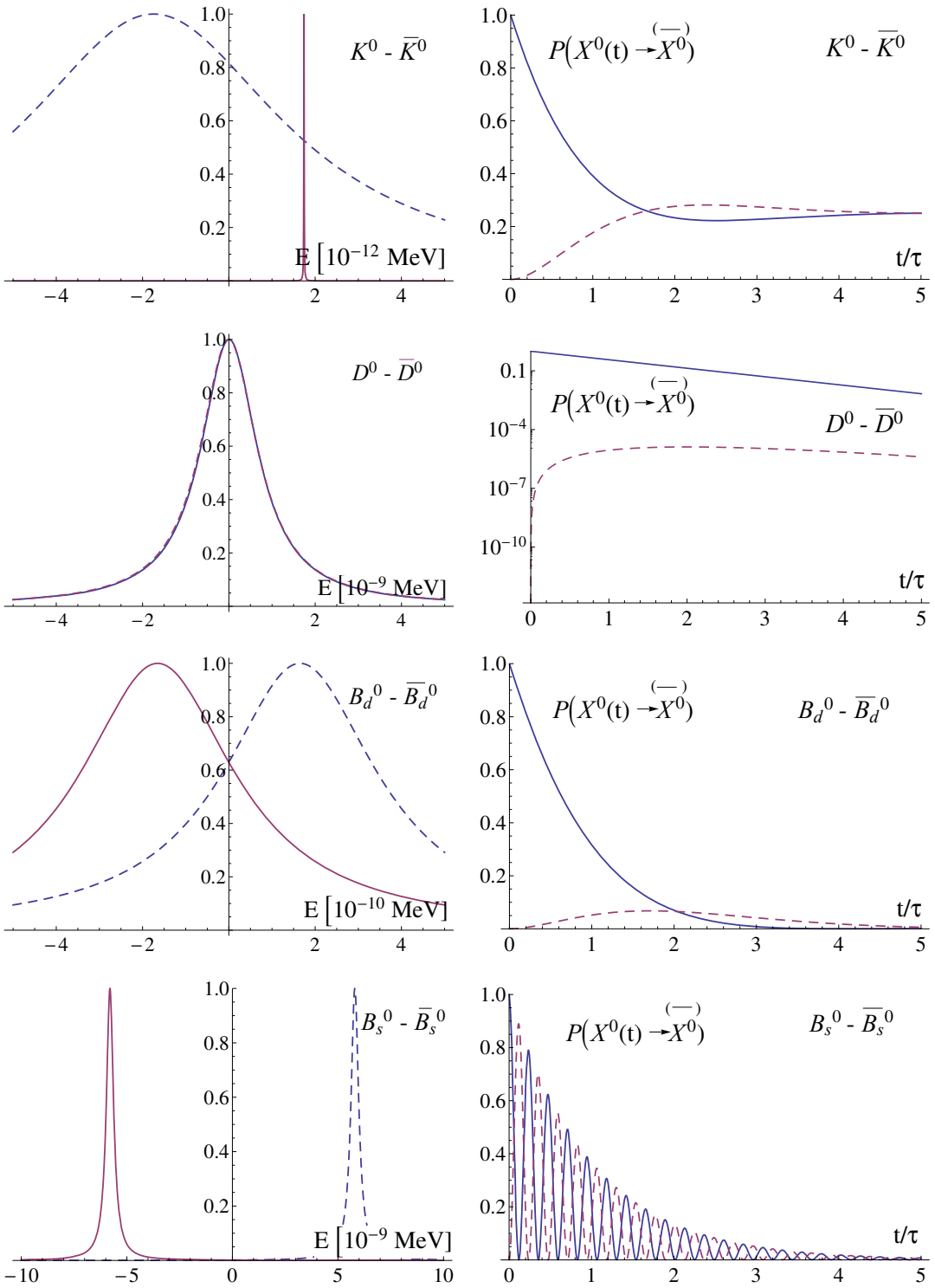

Figure 10.1.2. Left: Illustration of mass and width differences of the eigenstates (one denoted by full (red) line and the other by dashed (blue) line) for various neutral meson systems. Right: Probabilities for an initially produced neutral meson to be found after the time t in a particle (full (blue) line) or an anti-particle state (dashed (red) line).

Table 10.1.1. Values of the mixing parameters for the different neutral mesons. All numbers are approximate to illustrate the relative sizes.

Meson	M/MeV	Δm/MeV	Γ/MeV	$\Delta\Gamma$/MeV
K^0	497.6	3.48×10^{-12}	3.68×10^{-12}	7.34×10^{-12}
D^0	1864.9	9.45×10^{-12}	1.6×10^{-9}	2.57×10^{-11}
B_d	5279.6	3.34×10^{-10}	4.43×10^{-10}	~ 0
B_s	5366.8	1.16×10^{-8}	4.39×10^{-10}	6.58×10^{-11}

With the same assumption $|\Gamma_{12}| \ll |M_{12}|$, it also follows from Eq. (10.1.3) that

$$\left(\frac{q}{p}\right)_d = e^{-i\phi_{M_{12}}}, \tag{10.1.19}$$

where $\phi_{M_{12}}$ is the complex phase of M_{12}.

10.2 Time-dependent evolution

Neutral B_d mesons (from now on referred to as B^0 mesons) are produced via $e^+e^- \to \Upsilon(4S) \to B^0\overline{B}^0$ transitions at *BABAR* and Belle. The wave function for the final state B meson pair is prepared in an anti-symmetric coherent P-wave ($L = 1$) state Ψ, where

$$\Psi = \frac{1}{\sqrt{2}}\left(|B^0\rangle|\overline{B}^0\rangle - |\overline{B}^0\rangle|B^0\rangle\right). \tag{10.2.1}$$

The B_d mesons remain in this coherent state, where there is always exactly one B^0 and one $\overline{B}^0$, until one of them decays. When the first B meson decays, the wave function collapses and the remaining un-decayed B meson will continue to propagate through space-time and oscillate between a B^0 and $\overline{B}^0$ state, with a characteristic frequency Δm_d, until it also decays. This assumes that the $B\overline{B}$ pair is successfully described by quantum mechanics, despite the macroscopic extent of the state; aspects of this assumption can be tested at the B Factories, as discussed in Section 17.5.3.

If one of the B mesons decays into a final state that can be used to unambiguously determine the flavor of the B at the time it decayed, we refer to that as a $B_{\rm tag}$. The set of decay modes of interest as a $B_{\rm tag}$ candidate are referred to as flavor-specific final states. An example of a flavor-specific decay is $B^0 \to D^{(*)-}\ell^+\nu_\ell$, where $\ell = e, \mu$. The *CP*-conjugate process has a ℓ^- in the final state, so the charge of the final-state lepton is used to identify the flavor of the $B_{\rm tag}$ with a B^0 ($\overline{B}^0$) tag originating from a decay with a ℓ^+ (ℓ^-). Similarly, if the other B decays into a *CP*-eigenstate or admixture thereof, we refer to that as the B_{CP}. Events with one $B_{\rm tag}$ and one B_{CP} are of interest in the study of time-dependent *CP* violation. This sequence is illustrated in Fig. 10.2.1 as seen from the laboratory frame of reference: in this frame, the center-of-mass frame is boosted forward in the direction of the electron (high energy) beam. The B mesons are created almost at rest in the center-of-mass frame.

Having identified the flavor of $B_{\rm tag}$, one can infer the flavor of B_{CP} at the instant the first B meson decays, and the correlated wave function collapses, using the time evolution of the $B^0\overline{B}^0$ system. The detailed study of this system leads to the measurement of so-called time-dependent asymmetries.

The decay times of B_{CP} and $B_{\rm tag}$ in the center-of-mass frame of reference can be labeled as t_1 and t_2, respectively, and the time evolution of the $B^0\overline{B}^0$ system is a function of $t_1 + t_2$ and $t_1 - t_2$ in general. Assuming a negligible difference between the decay rates of the mass eigenstates (*i.e.* $\Delta\Gamma_d = 0$), the B_{CP} decay rate distribution for B_{CP} decaying into a *CP* eigenstate for a B^0 ($\overline{B}^0$) tagged event is given by f_+ (f_-), following from $g_\pm$ defined in Eq. (10.1.7)

$$f_\pm(\Delta t) = \frac{e^{-|\Delta t|/\tau_{B^0}}}{4\tau_{B^0}}\left[1 \pm \frac{2{\rm Im}\lambda}{1+|\lambda|^2}\sin(\Delta m_d \Delta t) \mp \frac{1-|\lambda|^2}{1+|\lambda|^2}\cos(\Delta m_d \Delta t)\right], \tag{10.2.2}$$

where $\tau_{B^0} \equiv 1/\Gamma_d$ is the B^0 meson lifetime and λ is given in Eq. (10.1.10). The sign of sine and cosine terms indicated in Eq. (10.2.2) is for a *CP* odd final state such as $J/\psi K^0_S$. *CP* even final states, such as $\pi^+\pi^-$ have the opposite sign conventions for the sinusoidal terms. The proper time difference $t_1 - t_2$ between the decay times of the two B mesons is denoted by Δt (see Section 6.5), and terms involving $t_1 + t_2$ drop out. One can compute the time dependence of neutral mesons decaying into flavor-specific final states (so called $B_{\rm flav}$ events), where $\lambda = 0$. These events are used to provide an experimental cross check of the time-dependent measurement and input parameters required to perform time-dependent fits to data (see Section 10.6). Analysis of such decays enables one to measure Δm_d, where the time dependence becomes

$$h_\pm(\Delta t) = \frac{e^{-|\Delta t|/\tau_{B^0}}}{4\tau_{B^0}}\left[1 \mp \cos(\Delta m_d \Delta t)\right]. \tag{10.2.3}$$

It has been pointed out that, while the assumption $\Delta\Gamma_d = 0$ is valid at the B Factories, improved constraints on this will be required at future experiments in order to verify if one can continue to use this approximation (Bevan, Inguglia, and Meadows, 2011).

The coefficients of the sine and cosine terms in equation (10.2.2) are often referred to in terms of the parameters S and C by the *BABAR* experiment and in terms of

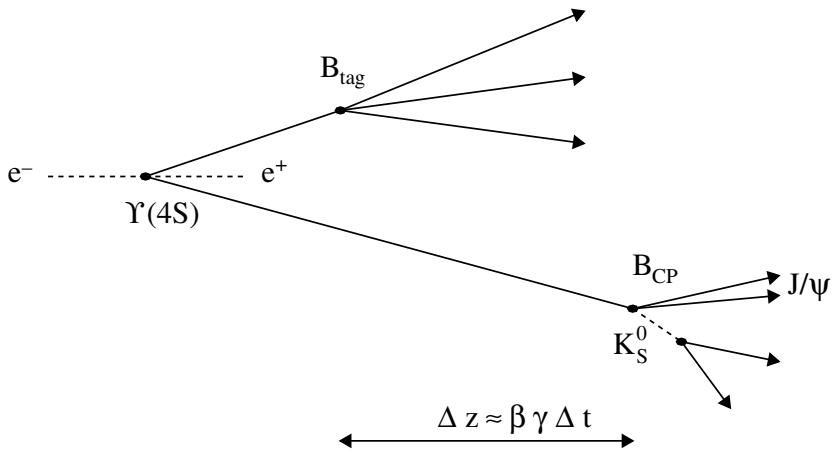

Figure 10.2.1. An illustration (not to scale) of a B meson pair decaying in the laboratory frame of reference. On the left hand side of the figure, the initial e^+e^- pair collides producing an $\Upsilon(4S)$. This subsequently decays into two B mesons described by the wave function given in Eq. (10.2.1), one decaying into a $B_{\rm tag}$ final state and the other into a B_{CP} final state. Once the first B meson decays, the remaining one oscillates with the characteristic frequency Δm_d before finally decaying. The spatial distance Δz between the decay vertices of the $B_{\rm tag}$ and B_{CP} as measured in the laboratory frame of reference is related to the proper time difference Δt between the decays of these particles in the center-of-mass frame of reference (see Section 6.5). In this example the B_{CP} final state is $J/\psi K^0_S$.

S and $-A$ by Belle, where

$$S = \frac{2\ \mathrm{Im}\lambda}{1+|\lambda|^2}, \tag{10.2.4}$$

$$C = -A = \frac{1-|\lambda|^2}{1+|\lambda|^2}. \tag{10.2.5}$$

Note that S and C are related through

$$\left(\frac{S}{\sin\theta}\right)^2 + \left(C\right)^2 = 1\ , \tag{10.2.6}$$

where θ is the phase of λ.[39] For brevity, we use the notation S and C to refer to these coefficients in the remainder of this book.

An asymmetry between $f_+(\Delta t)$ and $f_-(\Delta t)$ is constructed in order visualize possible *CP* violation. If we neglect experimental effects for the moment, this time-dependent decay-rate asymmetry is given by

$$\mathcal{A}(\Delta t) = \frac{f_+(\Delta t) - f_-(\Delta t)}{f_+(\Delta t) + f_-(\Delta t)}, \tag{10.2.7}$$

which reduces to the form

$$\mathcal{A}(\Delta t) = S\sin(\Delta m_d \Delta t) - C\cos(\Delta m_d \Delta t). \tag{10.2.8}$$

[39] Often the relation between parameters S and C is written in a form of inequality $S^2 + C^2 \leq 1$.

In certain modes, the fitted parameters S and C are related to fundamental parameters of the SM, the angles of the Unitarity Triangle. As discussed in Chapter 16, two notations are used in the literature for these angles. The *BABAR* experiment uses β, α, and γ to denote the angles, whereas the Belle experiment reports results in terms of ϕ_1, ϕ_2, and ϕ_3, respectively. In this book, we use the second notation for brevity.

10.3 Use of flavor tagging

The purpose of flavor tagging is to classify the $B_{\rm tag}$ either as a B^0 or as a $\overline{B}^0$ (see Chapter 8). The performance of the flavor tagging algorithm determines how well the values of S and C can be extracted from the data.

The *BABAR* experiment classifies events according to the information content used in determining the flavor of the $B_{\rm tag}$ meson. These categories of events are ranked in order of decreasing contribution to the total tagging efficiency Q (see Eq. 8.2.1). Thus, the *BABAR* classification is effectively one based on the $B_{\rm tag}$ decay mode. The Belle experiment's algorithm uses the same information but, instead of having distinct categories of events, that algorithm computes a continuous variable that assigns a dilution factor for a given event.

As discussed in Section 8.2, the algorithm for assigning a flavor tag to an event, thus categorizing the tag-side B meson as a B^0 or as a $\overline{B}^0$, is not perfect. There is a finite probability to incorrectly tag an event and thus dilute measurements that rely on this information. The mistag probability is denoted by w_{B^0} ($w_{\overline{B}^0}$) for a B^0 ($\overline{B}^0$)-tagged event. The value of the mistag probability depends on the $B_{\rm tag}$ final state used, and results in a dilution factor $\langle D\rangle = 1-2\langle w\rangle$ given by Eq. (8.2.2), where $\langle w\rangle$ is the average mistag probability for B^0 and $\overline{B}^0$ events (which is often just written as w). This dilution factor reduces the amplitude of oscillation from the ideal level (with $D = 1$ when $w_{B^0,\overline{B}^0} = 0$) by some value $D < 1$ for a non-zero mistag probability. The time-dependent formalism developed in Section 10.2 needs to be modified to account for the dilution; indeed one should also account for possible differences in mistag probability between B^0- and $\overline{B}^0$-tagged events, denoted by $\Delta w = w_{B^0} - w_{\overline{B}^0}$. Such a difference could be manifest through asymmetries in particle identification, as well as the intrinsic difference in cross section between particles and anti-particles interacting with the matter of the detector. On allowing for dilution effects, the rates of tagged B^0 and $\overline{B}^0$ events are given by

$$\begin{aligned} f_+^{\rm Phys} &= (1 - w_{B^0})f_+ + w_{\overline{B}^0} f_-, \\ f_-^{\rm Phys} &= (1 - w_{\overline{B}^0})f_- + w_{B^0} f_+. \end{aligned} \tag{10.3.1}$$

Taking dilution into account, the time dependence of the physical states given by Eq. (10.3.1) becomes

$$\begin{aligned} f_\pm^{\rm Phys}(\Delta t) = \frac{e^{-|\Delta t|/\tau_{B^0}}}{4\tau_{B^0}} \,[\, 1 \mp \Delta w \\ \pm\langle D\rangle S \sin(\Delta m_d \Delta t) \\ \mp\langle D\rangle C \cos(\Delta m_d \Delta t)]. \end{aligned} \tag{10.3.2}$$

The observed amplitudes of the sine and cosine terms in the time-dependent asymmetry are suppressed by the average dilution factor $\langle D\rangle$ for B and $\overline{B}$. As Δw is small, this factor is sometimes omitted for analyses with a low number of signal events. The analog of the asymmetry given by Eq. (10.2.8) is

$$\mathcal{A}(\Delta t) = \frac{f_+^{\rm Phys}(\Delta t) - f_-^{\rm Phys}(\Delta t)}{f_+^{\rm Phys}(\Delta t) + f_-^{\rm Phys}(\Delta t)} \tag{10.3.3}$$

$$\begin{aligned} &= -\Delta w + \langle D\rangle [S \sin(\Delta m_d \Delta t) \\ &\qquad - C \cos(\Delta m_d \Delta t)]. \end{aligned} \tag{10.3.4}$$

Thus, a non-zero mistag probability Δw results in a small offset in $\mathcal{A}(\Delta t)$ at $\Delta t = 0$. Figure 10.3.1 shows the distribution of $\mathcal{A}(\Delta t)$ for $S = 0.7$, $C = 0.0$, and $\Delta w = 0.0$. The amplitude of the sinusoidal oscillation is given by the magnitude of S in the case of a perfectly tagged asymmetry. In reality, dilution effects reduce the measured amplitude relative to the physical one, as illustrated in the figure below with the case of $\langle w\rangle = 0.2$.

The time dependence of events that one typically uses to study mixing ($C = 1$, $S = 0$), allowing for mistagged events, is given by

$$\begin{aligned} h_\pm^{\rm Phys}(\Delta t) = \frac{e^{-|\Delta t|/\tau_{B^0}}}{4\tau_{B^0}} [1 \mp \Delta w \\ \pm\langle D\rangle \cos(\Delta m_d \Delta t)], \end{aligned} \tag{10.3.5}$$

where the $\pm$ index refers to mixed ($-$) and unmixed ($+$) events. Unmixed events have a $B^0\overline{B}^0$ final state whereas mixed events are either B^0B^0 or $\overline{B}^0\overline{B}^0$ final states. Given that the distribution is symmetric about $\Delta t = 0$, the modulus of this distribution is shown sometimes when illustrating neutral meson oscillation.

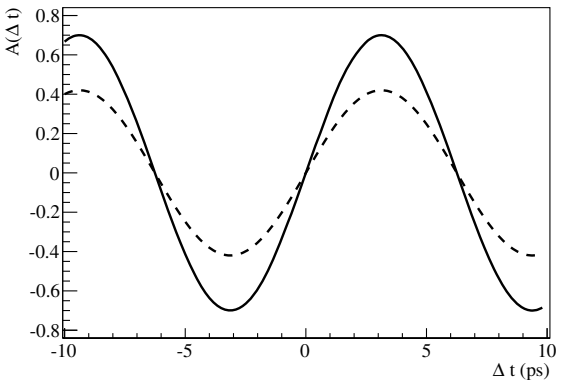

Figure 10.3.1. Distributions of the time-dependent *CP* asymmetry with $S = 0.7$, $C = 0$, and $\Delta w = 0$ for (solid) perfect tagging, and (dashed) the corresponding distributions after taking into account dilution with $\langle w\rangle = 0.2$.

10.4 Resolution of Δt

A number of factors contribute to the resolution of the reconstructed value of Δz, and hence to that of the computed value of $\Delta t \simeq \Delta z/\beta\gamma$. The experimental resolution $R(\delta t, \sigma_{\Delta t})$, as a function of $\delta t = \Delta t - \Delta t_{\rm true}$ and the uncertainty on Δt, $\sigma_{\Delta t}$, can be accounted for when measuring time-dependent *CP* asymmetry parameters by convoluting $R(\delta t, \sigma_{\Delta t})$ with $f_\pm^{\rm Phys}(\Delta t)$, giving

$$\begin{aligned} F_\pm^{\rm Phys}(\Delta t) &= \int_{-\infty}^{\infty} f_\pm^{\rm Phys}(\Delta t_{\rm true}) R(\delta t, \sigma_{\Delta t}) {\rm d}\Delta t_{\rm true}, \\ &= f_\pm^{\rm Phys}(\Delta t) \otimes R(\delta t, \sigma_{\Delta t}). \end{aligned} \tag{10.4.1}$$

Therefore, one can replace $f_\pm^{\rm Phys}$ with $F_\pm^{\rm Phys}$ in Eqs (10.3.3) and (10.3.4) to obtain the corresponding equations that account for both dilution and resolution effects. Factors contributing to the resolution of Δt include:

- $B_{\rm tag}$ vertex resolution, which is a combination of tracking effects and, for a sub-sample of $B_{\rm tag}$ mesons, the finite lifetime of D mesons;
- B_{CP} vertex resolution, which is a superposition of tracking effects; and

– resolution of the measurement of the boost factor $\beta\gamma$ determined from the energy of the e^+ and e^- beams.

It is important to understand the Δt resolution in detail as this is of a similar magnitude to the average separation between the B_{CP} and $B_{\rm tag}$ proper decay times. Thus, this resolution has a significant effect on the extraction of S and C from a time-dependent analysis.

Different approaches are used to understand resolution effects at the B Factories. *BABAR* adopts a parametric approach to describe the Δt resolution, whereas Belle characterizes resolution effects according to their physical source. Both approaches work well and provide a good description of resolution for use in time-dependent analyses.

The nominal *BABAR* Δt resolution function has a triple Gaussian form, where the mean μ_i and width s_i of the two central Gaussian components are scaled by $\sigma_{\Delta t}$ on an event-by-event basis. The three Gaussians are denoted by G_i, where $i =$ core, tail, and outlier, in order of increasing width. The resolution function is given by

$$\begin{aligned}\mathcal{R}_{\rm sig}(\delta t,\sigma_{\Delta t}) = {} & f_{\rm core}G_{\rm core}\left(\delta t,\mu_{\rm core}\sigma_{\Delta t},s_{\rm core}\sigma_{\Delta t}\right)+\\ & f_{\rm tail}G_{\rm tail}\left(\delta t,\mu_{\rm tail}\sigma_{\Delta t},s_{\rm tail}\sigma_{\Delta t}\right)+\\ & f_{\rm outlier}G_{\rm outlier}\left(\delta t,\mu_{\rm outlier},s_{\rm outlier}\right).\end{aligned} \tag{10.4.2}$$

The parameters $s_{\rm tail}$, $s_{\rm outlier}$ and $\mu_{\rm outlier}$ are set to 3.0, 8.0 ps and 0.0 ps, respectively, and the other parameters are determined from reference samples of fully reconstructed B meson decays as described in Section 10.6. The tail width was determined from Monte Carlo simulated data, and the outlier mean was taken as unbiased, with a width varying from $4-12$ ps. The mean of this range was taken as the nominal value for $s_{\rm outlier}$. As the physical tagging categories for *BABAR* have different purities and dilutions, the values of μ_i and s_i for the core Gaussian contribution to the resolution function depend on the flavor category of an event. This difference is taken into account when analyzing data. For early analyses, each of the *BABAR* flavor tagging categories had a separate value for $\mu_{\rm core}$ and $s_{\rm core}$; in later iterations, the distinction was only made between `Lepton` and non-`Lepton` tagging categories. For *BABAR* data, $s_{\rm core}$ is typically 1.01 ± 0.04 (1.10 ± 0.02) for `Lepton` (non-`Lepton`) events.

The Belle Δt resolution function (Tajima, 2004) accounts for four different physical effects

– $B_{\rm tag}$ vertex resolution,
– B_{CP} vertex resolution,
– shift in the $B_{\rm tag}$ vertex position resulting from secondary tracks from charm meson decays, and
– kinematic approximation that the B mesons are at rest in the center-of-mass frame.

The $B_{\rm tag}$ and B_{CP} vertices are described by (i) a Gaussian resolution function in the case of multi-track vertices, and (ii) a sum of two Gaussians in the case of single-track vertices. The widths of these Gaussians are scaled by the uncertainty on the reconstructed vertex being described. The resolution function resulting from non-prompt tracks associated with a decay in flight of charm mesons is described by the sum of a delta function and exponentials. The kinematic approximation is described by a resolution function dependent on the polar angle of $B_{\rm tag}$ as reconstructed in the center-of-mass frame of reference. Given that a B_{CP} or $B_{\rm flav}$ candidate is fully reconstructed, and decays opposite the $B_{\rm tag}$ in the center-of-mass frame of reference, whereas the $B_{\rm tag}$ may not be, the polar angle of the $B_{\rm tag}$ candidate is determined from the fully reconstructed B_{CP} or $B_{\rm flav}$ decay. The physical time dependence $f_\pm^{\rm Phys}$ is convoluted by each of these resolution functions in turn in order to obtain the resultant $F_\pm^{\rm Phys}$.

Figure 10.4.1 shows the $f_\pm^{\rm Phys}$ and $F_\pm^{\rm Phys}$ distributions for $S=0.7$ and $C=0.0$, where both dilution and resolution effects are considered. The distribution $f_\pm^{\rm Phys}$ is smeared out considerably as a result of experimental resolution when computing $F_\pm^{\rm Phys}$. The effect of dilution serves to reduce the reconstructed asymmetry between B^0- and $\overline{B}^0$-tagged events. This can be seen as a reduction in the asymmetry between F_+ and F_- in comparison with the true distributions f_+ and f_-.

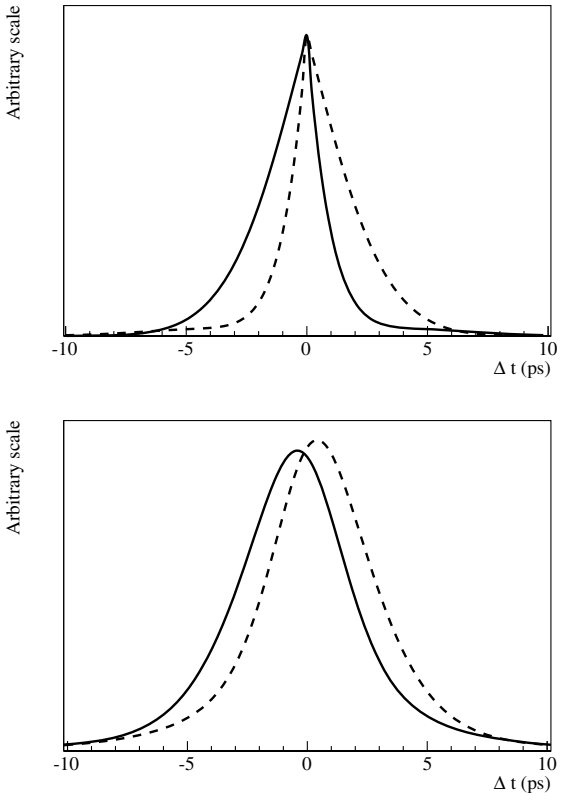

Figure 10.4.1. Distributions of (top) $f_\pm^{\rm Phys}(\Delta t)$ with $S=0.7$, and $C=0.0$ for (solid) B^0- and (dashed) $\overline{B}^0$-tagged events for perfectly reconstructed decays, and (bottom) the corresponding distributions $F_\pm^{\rm Phys}$ after taking into account typical dilution and resolution effects.

10.5 Modeling the Δt distribution for background events

Generically, one can categorize three types of background that are encountered in time-dependent analyses at the B Factories: (i) continuum events, (ii) B background including charm mesons that decay in flight, and (iii) other B background categories. The effect on the time-evolution of each of these types of events from the resolution of Δt needs to be considered. The following describes the general approach adopted for each of these types of background.

- The hadronization processes resulting from continuum $e^+e^- \to q\bar{q}$ background, where $q = u, d, s$, or c, occur on a time scale too small to measure. As a result, the time dependence for this type of background is assumed to be a prompt distribution modeled using a δ function convoluted with the resolution function. The resolution function typically adopted for continuum background is a simplified version of Eq. (10.4.2), where the scale factors $s_{\rm tail}$ and $s_{\rm outlier}$ are set to 2.0 ps and 8.0 ps, respectively, and only the core Gaussian mean and scale factor are weighted by $\sigma_{\Delta t}$. The remaining parameters of the background resolution function are obtained from fits to data.
- The time evolution of B background events that contain charm particles is biased as a result of the assumption that all tracks in the B_{CP} vertex originate from the same point whereas, in reality, the tracks from the charm meson in the event originate from a secondary vertex that is displaced from the B_{CP} vertex. This type of background can occur in the analysis of charmless B decays and, where necessary, the time dependence is assumed to be similar to the signal one, except that the lifetime is taken to be different from τ_{B^0}. An effective lifetime is extracted from samples of Monte Carlo simulated data and used in place of τ_{B^0} for this type of background. Cross checks using control fits to data validate the approximation of using Monte Carlo simulated data to determine the effective lifetime. A signal resolution function is assumed to be valid for this category of events.
- The time evolution of B background events that do not contain charm particles is assumed to be the same as that for signal. Such backgrounds occur in time-dependent measurements of charmless B decay processes. While these events will be mis-reconstructed as a given hypothesized signal mode, the differences observed between the resolution functions for signal Monte Carlo simulated data and B background Monte Carlo simulated data are small. Some analyses perform systematic cross checks where the time dependence is given by a kernel estimation *p.d.f.* corresponding to the Δt distribution observed for Monte Carlo simulated data in order to account for any bias. Such a distribution is formed from the sum of kernels, one for each event in a control sample. In this case Gaussian kernels are used with a mean corresponding to the value of Δt of a given event, and a width given by the RMS of the ensemble of data in the control sample. As such a model neglects the per-event uncertainty on Δt, when this approach is used, a systematic cross check is performed where the kernel estimation *p.d.f.* is replaced with a signal-like time dependence.

Both B Factories categorize continuum background with a prompt distribution as described above. *BABAR* treats background from different types of B decays as indicated above, whereas Belle assigns an exponentially decaying distribution convoluted with the resolution function as the *p.d.f.* for B background events. The lifetime assumed for the Belle B background *p.d.f.* is an effective one determined from Monte Carlo simulated data.

It is possible that background events may themselves be *CP* violating. In such cases, one can account for the level of *CP* violation by ensuring that the time dependence incorporates the asymmetry given in Eq. (10.2.8) for neutral B decays, or the corresponding time-integrated asymmetry for charged B decays. This issue is discussed in Section 15.3.5.

10.6 Parameter extraction from data

In order to perform a time-dependent analysis, one needs to determine the values of w, Δw, and the tagging efficiencies, which are collectively referred to as tagging parameters, and the resolution function parameters required to evaluate the convolution of $f_\pm(\Delta t)$ with $R(\delta t, \sigma_{\Delta t})$. A sample of neutral B mesons decaying into flavor-specific final states is used to determine these parameters. Several hundred thousand events were in the control samples used by the B Factories. The set of modes used by *BABAR* for this is $B^0 \to D^{(*)-}(\pi^+, \rho^+, a_1^+)$, whereas Belle uses $B^0 \to D^{(*)-}\pi^+$, $D^{*-}\rho^+$, $D^{*-}\ell^+\nu$ as well as the charmonium decays $J/\psi K_S^0$, and $J/\psi K^*(892)^0$. No flavor tag information is used by Belle when extracting the parameters using the charmonium decays. *BABAR* only uses the $B \to D^*\ell^-\nu$ sample to perform a cross-check as there is a larger background in that mode than the other control sample channels. Collectively, this ensemble of flavor-specific decay modes is referred to as the $B_{\rm flav}$ control sample in the following. In addition to determining tagging and resolution function parameters for use in extracting information on *CP* asymmetries from neutral $B_{\rm flav}$ modes, a set of charged control samples is also used to perform a number of independent validation checks. One of these validations is the determination of S for a sample of charged B decays. As S is physically related to the $B^0 - \overline{B}^0$ mixing amplitude, the fitted value for this parameter in a sample of charged B decays should be consistent with zero. The charged B control sample is formed using $B^+ \to J/\psi K^+$, $J/\psi K^*(892)$, $\psi(2S)K^+$, $\chi_{c1}K^+$, and $\eta_c K^+$ in the case of *BABAR*, while $B^+ \to J/\psi K^+$ and $\overline{D}^0\pi^+$ are used by Belle. The corollary of using a set of control modes is that, for each mode used to determine the parameters of interest, one introduces additional parameters relating to the shape of distributions of signal and background events, and the purity of each control channel in the signal region. Having determined the purities for each $B_{\rm flav}$ mode, one can use

these events to extract estimates of tagging and resolution parameters. This procedure implicitly assumes that there is no significant interference on the tag side of the event (see Section 15.3.6), so that the mistag probabilities computed from the $B_{\rm flav}$ sample are the same as those on the B_{CP} side of the event. While this assumption was valid for the B Factories, the precision of measurements at a super flavor factory may require that one formally accounts for tag-side interference in the time dependence of the neutral meson system.

In order to determine tagging efficiencies, one simply needs to determine the fractions of the $B_{\rm flav}$ sample reconstructed in each of the physical categories; to determine the mistag probabilities and differences, one needs to account for $B^0 - \overline{B}^0$ mixing in the $B_{\rm flav}$ control sample. The time evolution of these decays, neglecting resolution effects, is given by Eq. (10.3.5). One can account for experimental resolution by convoluting $h_\pm$ with a resolution function as described in Section 10.4:

$$H_\pm^{\rm Phys}(\Delta t) = \int_{-\infty}^{\infty} h_\pm^{\rm Phys}(\Delta t_{\rm true}) R(\delta t, \sigma_{\Delta t}) {\rm d}\Delta t_{\rm true}, \\ = h_\pm^{\rm Phys}(\Delta t) \otimes R(\delta t, \sigma_{\Delta t}). \qquad (10.6.1)$$

Therefore, it is possible to not only extract the tagging parameters but also the resolution function parameters from the $B_{\rm flav}$ sample, where one assumes that the Δt resolution function is the same for the $B_{\rm flav}$ and B_{CP} events. There are many more events in the $B_{\rm flav}$ sample than the B_{CP} sample; hence, a more precise determination of the resolution function parameters can be obtained using the $B_{\rm flav}$ data. Tagging performance is discussed in Chapter 8, and vertex resolution is discussed in Chapter 6.

Given the complexity of the situation, the extraction of parameters related to the tagging performance and Δt resolution is done in a two-step process. The first step involves extracting the purity of each of the $B_{\rm flav}$ decay modes used. Having done this, one determines the tagging and resolution function parameters from the ensemble of $B_{\rm flav}$ modes. The result of this process is a set of parameters and the corresponding error matrix that can be subsequently used as input parameters for the time-dependent analyses described in Chapter 17. In a number of cases, the time-dependent asymmetry parameters are extracted from a simultaneous fit to both the B_{CP} and $B_{\rm flav}$ samples so that tagging and resolution parameters are transparently propagated into the *CP* analysis.

Chapter 11
Maximum likelihood fitting

Editors:
Wouter Verkerke (BABAR)

11.1 Formalism of maximum likelihood fits

The final step in a physics analysis, after appropriate event selection and reconstruction steps have been performed, is extracting a statement on a physics parameter of interest from the observed distribution of events in the data. To make such an estimation, a model must be formulated that describes the expected distribution of the observable quantities $\boldsymbol{x}$ for a given set of physics parameters of interest $\boldsymbol{p}$. Then, given an observed data sample $\boldsymbol{x_0}$ one uses the relation between $\boldsymbol{x}$ and $\boldsymbol{p}$ described by the model to infer a statement on the value $\boldsymbol{p}$ for which the observed data is most likely. A standard technique to make such an inference is a maximum likelihood estimator. In this section the basics of this technique are described, starting with a description of probability density function as a means to model the observed data density, followed by a brief description of the maximum likelihood formalism and a discussion on the structure of typical models used for B-physics data modeling.

11.1.1 Probability Density Functions

For many analyses, the models of observable distributions are described with a *probability density function* (p.d.f.) for the observable quantities $\boldsymbol{x}$:

$$f(\boldsymbol{x};\boldsymbol{p}). \tag{11.1.1}$$

Such a probability density function is positive definite, and normalized to unity over the allowed range of the observable $\boldsymbol{x}$ for any value of $\boldsymbol{p}$, i. e.

$$\forall \boldsymbol{p} : \int f(\boldsymbol{x};\boldsymbol{p}) d\boldsymbol{x} \equiv 1, \tag{11.1.2}$$

where the integral is over the allowed domain of the observables $\boldsymbol{x}$.

In addition to the parameter(s) of interest $\boldsymbol{p}$, realistic models often incorporate a set of additional 'nuisance parameters' $\boldsymbol{q}$ that represent quantities that affect the relation between $\boldsymbol{p}$ and $\boldsymbol{x}$ that are not a priori known and must be simultaneously inferred from the data. Examples of such nuisance parameters are resolution parameters and flavor tagging efficiencies (see Section 10 for details). The model is thus defined as

$$f(\boldsymbol{x};\boldsymbol{p},\boldsymbol{q}). \tag{11.1.3}$$

11.1.2 Maximum Likelihood estimation of model parameters

The basis of parameter inference using a model F and observed data is the *likelihood*, defined as the probability density function evaluated at the measured data point $\boldsymbol{x_0}$:

$$L(\boldsymbol{p},\boldsymbol{q}) = f(\boldsymbol{x_0};\boldsymbol{p},\boldsymbol{q}). \tag{11.1.4}$$

The likelihood is then treated as a function of the parameters $\boldsymbol{p}$ and $\boldsymbol{q}$.

For measurements consisting of an ensemble of data points the likelihood of the ensemble is simply the product of the likelihood of each observation:

$$L(\boldsymbol{p},\boldsymbol{q}) = \prod_{i=0,\ldots,N} f(\boldsymbol{x_i};\boldsymbol{p},\boldsymbol{q}), \tag{11.1.5}$$

where $\boldsymbol{x_i}$ represent independent and identically distributed measurements of the observable x. In practice one often uses the negative log-likelihood

$$-\log L(\boldsymbol{p},\boldsymbol{q}) = -\sum_{i=0,\ldots,N} \log f(\boldsymbol{x_i};\boldsymbol{p},\boldsymbol{q}), \tag{11.1.6}$$

instead of the likelihood as this is numerically easier to calculate.

Equation (11.1.5) defines an *unbinned* likelihood - the likelihood is evaluated at each data point and no binning of the data is needed. The (unbinned) maximum likelihood estimator $\widehat{\boldsymbol{p}}$ for a parameter vector $\boldsymbol{p}$ is defined as the value of $\boldsymbol{p}$ for which the likelihood is maximal or, equivalently, the negative log-likelihood is minimal.

For an analysis with a very large number of observed events and a small number of observables, it can be efficient to minimize a binned log-likelihood instead, defined as

$$-\log L(\boldsymbol{p},\boldsymbol{q}) = -\sum_{i=0\ldots N} n_i \cdot \log f(\boldsymbol{x_i};\boldsymbol{p},\boldsymbol{q}), \tag{11.1.7}$$

where x_i and n_i represent the bin center and event count of bin i of a histogram with N bins. The computation time scales with the number of bins N rather than the number of events. A binned likelihood is a priori less precise than an unbinned likelihood as the information of the precise position of the event in each bin is discarded, but at small bin sizes this may be a negligible loss of precision. In practice, the prediction $f(\boldsymbol{x_i};\boldsymbol{p},\boldsymbol{q})$ in each bin is often approximated with the value of the probability density function at the bin center, where the integral of the p.d.f. over the bin volume should be used. This approximation has little impact if the bin size is chosen sufficiently small, but can otherwise result in biases in sharply falling or rising distributions, e. g. in the fitted lifetime of exponential decay distributions.

The traditional χ^2 fit is related to the binned maximum likelihood (ML) fit by inserting the additional assumption that the uncertainty can be interpreted as Gaussian, however, this assumption is a poor approximation of reality for bins with low statistics (roughly $n < 10$).

The properties of likelihood estimators are extensively described in the literature (Edwards, 1992). In the asymptotic limit of infinite statistics maximum likelihood estimators (ML estimators) are so-called ideal estimators: they are *consistent*, meaning that they give the correct answer in the limit of infinite statistics, *unbiased*, meaning that they give the correct answer on average for finite statistics, and *efficient*, meaning that the variance of the estimated parameter values is equal to the bound of the expectation value of the variance predicted by the second derivative of the log-likelihood. On finite samples, ML estimators are not ideal, but nevertheless generally well behaved if samples statistics are sufficiently large. However, some particular care must be exercised when using ML estimators for problems with very small (signal) event counts: in these cases bias terms appear in the likelihood, which are generally proportional to $1/N_{obs}$, where N_{obs} is the number of observed events, and may be non-negligible compared to the statistical uncertainty, which is approximately proportional to $1/\sqrt{N_{obs}}$.

11.1.3 Estimating the statistical uncertainty using the likelihood

The simplest way to measure the statistical uncertainty $\sigma(\widehat{p})$ on the estimate of a single parameter $\widehat{p}$ is to estimate the variance $V(\widehat{p})$ of that parameter and calculate the uncertainty as the square-root of the variance. The ML estimator for the variance on $\widehat{p}$ is given by the second derivative of the log-likelihood at $p = \widehat{p}$:

$$\sigma(\widehat{p})^2 = V(\widehat{p}) = \left(\frac{d^2 \log(L(p))}{d^2 p} \right)^{-1}_{p=\widehat{p}} . \tag{11.1.8}$$

In case there are multiple parameters, the variance of the ensemble of parameters is represented by the covariance matrix defined as

$$V(p, p') = \langle pp' \rangle - \langle p \rangle \langle p' \rangle , \tag{11.1.9}$$

and can be estimated as

$$\widehat{V}(p, p') = \left(\frac{\partial^2 \log(L(p, p')}{\partial p \partial p'} \right)^{-1}_{p=\widehat{p}, p'=\widehat{p}'} , \tag{11.1.10}$$

A multivariate covariance can also be expressed in terms of scalar variances and a correlation matrix

$$V(p, p') = \sqrt{V(p) V(p')} \cdot \rho(p, p'). \tag{11.1.11}$$

Here $\rho(p, p')$ expresses the linear correlation between parameters p and p' and has values in the range $[-1, 1]$ by construction.

An alternative estimator for the uncertainty on a parameter is based on an interval defined by the log-likelihood ratio

$$\lambda(p) = \log \frac{L(p)}{L(\widehat{p})}, \tag{11.1.12}$$

where $L(p)$ is the likelihood for a given value p, $\widehat{p}$ is the value of p for which the likelihood is maximal and $L(\widehat{p})$ is therefore the maximum value of the likelihood. An interval in p defined by a rise in the log-likelihood-ratio of half a unit from zero corresponds to nominally a 68% confidence interval. Intervals defined this way are related to classic frequentist confidence intervals — under the condition that Wilks' theorem[40] (Wilks, 1938) holds.

When nuisance parameters are present, an interval can be defined for each parameter replacing the likelihood ratio with the profile likelihood ratio

$$\lambda_P(p) = \log \frac{L(p, \widehat{\widehat{\boldsymbol{q}}}(p))}{L(\widehat{p}, \widehat{\boldsymbol{q}})}, \tag{11.1.13}$$

where $\widehat{p}$ and $\widehat{\boldsymbol{q}}$ represent again the ML estimates of parameters p and $\boldsymbol{q}$ and $\widehat{\widehat{\boldsymbol{q}}}(p)$ represents the *conditional* ML estimate of parameters $\widehat{\boldsymbol{q}}$ for a given value of p.

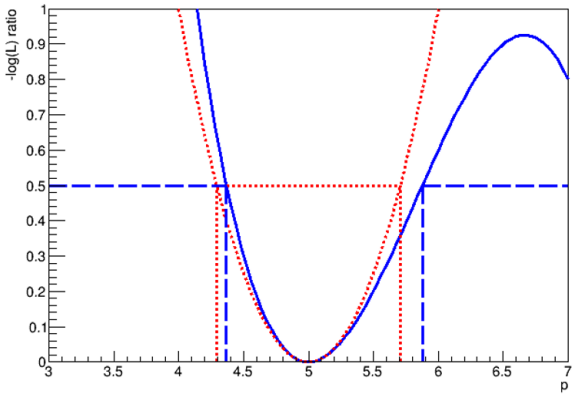

Figure 11.1.1. Illustration of the definition of parameter uncertainties in an example log-likelihood ratio (blue solid curve). The variance estimator (`HESSE` , see Section 11.1.5.2) of Eq. (11.1.8) uses the second derivative at $\widehat{p}$ (here $\widehat{p} = 5$) and corresponds to assuming a parabolic log-likelihood ratio shape (red dashed curve) and defining the interval by the intersection points of the parabola with the horizontal line at +0.5 units. The likelihood ratio estimator (`MINOS` , see Section 11.1.5.2) of Eq. (11.1.12) defines the interval using the intersection of the actual log-likelihood ratio curve with a horizontal line at +0.5 units (blue curve, long dashes).

The difference between the variance-based uncertainty and the likelihood-ratio-based uncertainty is visualized in Fig. 11.1.1. If the log-likelihood has a perfectly parabolic shape, as is expected in the limit of infinite statistics (under certain regularity conditions), both uncertainty estimates will give the same interval.[41] At low statistics differences may occur due to the different methods of estimating

[40] Wilks' theorem states that the likelihood ratio $\lambda(p)$ will be asymptotically χ^2 distributed under certain regularity conditions as the samples sizes approaches infinity.

[41] The 2nd derivative will perfectly predict the value of the parameter where the log of the likelihood ratio has increased by half a unit from zero in this case.

the uncertainty. In particular, the profile likelihood-based intervals can yield asymmetric intervals around the central values.

11.1.4 Hypothesis testing and significance

Most measurements of CP-violating parameters are expressed as interval estimates. Conversely, the result of a search for a rare signal is usually not expressed as an interval on a signal (strength) parameter, but rather as a test of the background-only hypothesis.

The *significance* of the observation is the probability of the background-only hypothesis to result in the observed signal strength, or larger. This probability is known as the p-value. A p-value threshold of $1.2{\cdot}10^{-7}$ – corresponding to the probability of a 5σ Gaussian fluctuation – is conventionally taken to reject the background-only hypothesis, and to declare the discovery of a new signal.

To calculate the p-value one must construct a test statistic as function of the data that distinguishes the background-only hypothesis (the 'null hypothesis') from the signal-plus-background hypothesis (the 'alternate hypothesis'). A common choice is $\lambda_P(0)$ of Eq. (11.1.13), where p is the signal strength, so that $\lambda_P(0)$ becomes the ratio of the maximum likelihood of the background-only model and the maximum likelihood of the signal-plus-background model. A dataset that is perfectly consistent with the background-only hypothesis will thus have $\lambda_P(0) = 0$, as the numerator and denominator of Eq. (11.1.13) are equal, whereas datasets with increasing signal strength will result in increasing values of $\lambda_P(0)$. The p-value is then calculated as the fraction of experiments sampled from the background-only hypothesis that result in a value $\lambda_P(0)$ that is as large as the observed value or larger:

$$p = \int_{\lambda_P^{obs}(0)}^{\infty} f(\lambda_P(0)|p=0)d\lambda_P(0), \tag{11.1.14}$$

where $\lambda_P^{obs}(0)$ is the value of $\lambda_P(0)$ observed in the data, and $f(\lambda_P(0)|p=0)$ is the expected distribution of $\lambda_P(0)$ values for the background-only hypothesis.

Customarily the significance is re-expressed as a Gaussian fluctuation of $Z\sigma$ that results in the same p-value, where Z is defined as

$$p = \int_{-\infty}^{Z\sigma} \frac{1}{\sqrt{2\pi}\sigma} e^{-x^2/(2\sigma^2)} dx, \tag{11.1.15}$$

and can be calculated from p using the inverse of the error function.[42]

In the asymptotic regime of large statistics, and under certain regularity conditions (Wilks' theorem), $f(\lambda_P(0)|0)$ becomes a $\log(\chi^2)$ distribution with one degree of freedom for each parameter-of-interest. The significance expressed in Gaussian standard deviations can in that case be directly related to the value of $\lambda_P^{obs}(0)$:

$$\lambda_P^{obs}(0) = \frac{1}{2}Z^2. \tag{11.1.16}$$

Finally, for the specific and simple case of a likelihood describing a counting experiment with an expected signal count s and background count b, both with Gaussian uncertainties, the value of Z can be directly expressed as

$$Z_{sb} = \frac{s}{\sqrt{s+b}}, \tag{11.1.17}$$

but it should be noted that the assumption of Gaussian uncertainties for $s < 10$ or $b < 10$ is poor.

11.1.5 Computational aspects of maximum likelihood estimates

For all but a handful of textbook examples, the expression for maximum likelihood estimator for $\widehat{p}$ cannot be expressed analytically, hence the maximum likelihood estimate is computed numerically. The computational problem factorizes into two pieces: definition of the likelihood function for a given problem, and heuristic searches for the maximum of the likelihood function.

11.1.5.1 Likelihood definition

The definition of the likelihood involves coding the definition of the probability density function that is used to model the data, and then evaluating the natural log of this p.d.f. for each observed data point.

The `Root` framework (Brun and Rademakers, 1997) implements definitions of basic functional shapes such as polynomials and Gaussian distributions, but the complexity of models used in typical B Factory analyses is such that they cannot be expressed in terms of this limited set of basic functions. For the first round of B Factory measurements custom software packages were developed that implemented the probability density functions representing the physics models as `Fortran`, `LISP`, or C++ functions.

In the next iteration, the `RooFit` toolkit (Verkerke and Kirkby, 2003) was developed by the *BABAR* collaboration that allowed one to build probability density functions of arbitrary complexity inside the `Root` framework with a minimum amount of custom code. To this end, `RooFit` defines generic software objects that represent observables, probability density functions defining basic shapes as well as B-physics specific shapes, and operator objects that allow a user to combine basic shapes through addition, multiplication and convolution. Over time a large number of analyses have migrated to using `RooFit` to encode their likelihood functions. The package has been available in the `Root` framework since 2005. Such models were either coded 'by hand', or for certain complicated models constructed by higher level packages that automate building of `RooFit` p.d.f.s with a certain structure from an configuration file.

[42] In `Root` this calculation is easily accessible as function `RooStats::PValueToSignificance(double pvalue)`

11.1.5.2 Likelihood minimization

The standard tool used by the HEP community for nearly forty years for minimization and uncertainty estimation is the `Minuit` package (James and Roos, 1975), originally written in `Fortran`. A version translated in C++ is now available in the `Root` analysis framework, as well as a new version, `Minuit2`, that was written from scratch in C++ by the original authors. The main components of the `Minuit` package are three algorithms that operate on an user-defined (likelihood) function: `MIGRAD` , `HESSE` , and `MINOS` .

`MIGRAD` is a heuristic algorithm that searches for minima in externally provided multi-variate functions and follows mostly a strategy based on a steepest descent algorithm following a numerically calculated gradient of the input function. Convergence is declared when the input function is within a preset estimated distance from the function value in the nearest minimum assuming a quadratic form. The algorithm has been demonstrated to work well on problems with a very large number of dimensions (> 100), but computational cost increases with the dimensionality.[43] An inherent difficulty with a heuristic search algorithm is distinguishing between local minima and the global minimum. In most cases, the algorithm will settle on the first minimum it finds along its search trajectory, even if this is not the true global minimum. The odds of finding the true global minimum increase if the search is started at a point close to where it is expected to be, putting a premium on an educated guess by the analyzer for the starting values of the algorithm. It is almost impossible to prevent the finding of local minima.

`HESSE` calculates the covariance matrix by sampling the likelihood in small steps around the minimum found by `MIGRAD` and calculating the second derivative from these samples. Its output is the covariance matrix as defined in Eq. (11.1.10). The calculation takes $\frac{1}{2}N^2$ likelihood samplings, where N is the number of parameters allowed to vary, which for large N may exceed the calculation spent in `MIGRAD` minimization.

`MINOS` performs the calculation of the uncertainty interval defined by an increase in the negative log-likelihood of half a unit[44] with respect to the assumed global minimum. When a `MINOS` error calculation is requested for all N parameters of a fit, a $N-1$ dimensional hypersurface is first reconstructed that is defined by $\lambda(\boldsymbol{p}) = 0.5$. The N-dimensional hyper-cube that encloses this hypersurface defines the `MINOS` uncertainty on each parameter. Through geometrical arguments it can be shown that the uncertainty defined this way is identical to that of Eq. (11.1.13) for each parameter. `MINOS` calculations can be prohibitively time consuming for a large number of parameters (roughly $N > 30$), but it is also possible to perform a `MINOS` calculation on any subset of the parameters. In such cases `MINOS` uses Eq. (11.1.13) to reduce the parameter space to the desired subset.

[43] The cost of numeric derivative calculations increases linearly with the number of parameters. The number of descent steps required to find the minimum typically increases also with the number of parameters, but is strongly dependent on the shape of the likelihood.

[44] The default `MINOS` value of the increase is 1 unit, as built-in `Root` fitting functions pass two times the value of the negative log-likelihood. Conversely, `Minuit` instances owned by `RooFit` reconfigure the `MINOS` error definition to half a unit.

11.2 Structure of models for signal yield measurements and rare decay searches

The probability density functions used as models in B Factory analyses serve two main goals: analysis of the data in terms of a signal and a background component, and if needed inference of the physics parameters of interest. This section covers techniques used to describe the data in terms of signal and background.

The simplest model M to extract a signal yield from the data in the presence of background is a model that describes the data sample as a sum of a signal and background components.

$$m(\boldsymbol{x};\boldsymbol{p},\boldsymbol{q}) = f \cdot s(\boldsymbol{x};\boldsymbol{p}) + (1-f)\cdot b(\boldsymbol{x};\boldsymbol{q}). \qquad (11.2.1)$$

In this equation, $s(\boldsymbol{x};\boldsymbol{p})$ is the model of a signal distribution in the observables $\boldsymbol{x}$, $b(\boldsymbol{x};\boldsymbol{q})$ is a model of the background distribution, and f is the fraction of signal in the data.

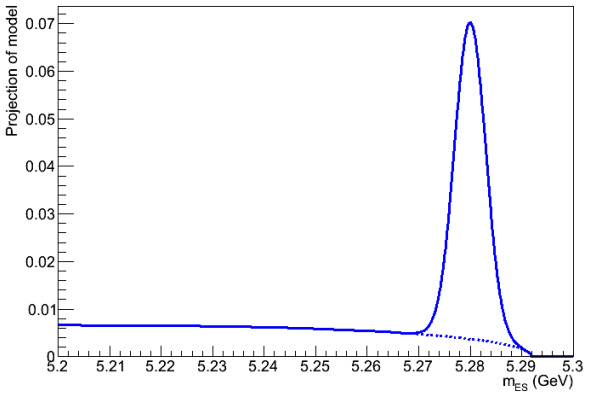

Figure 11.2.1. A simple composite probability density model (solid line) consisting of a background component defined by an Argus function (dashed line) plus a signal component defined by a Gaussian function.

Figure 11.2.1 shows an example of a simple version of such a model where the signal is described by a Gaussian distribution of the energy-substituted mass m_{ES} and the background by an Argus function (Albrecht et al., 1990a) that models the kinematics of continuum background events for this observable. See Section 9 for more details on p.d.f. choices to describe signal and background.

With sufficient statistics, the shape parameters $\boldsymbol{p}$ and $\boldsymbol{q}$ of both signal and background can be constrained from the data, in addition to the parameter of interest f: the fraction of signal events in the data. The estimate of the number of signal events in data is then f times the total number of observed events.

In the model of Eq. (11.2.1) the p.d.f. only models the shape of the distribution of the observed events and not its count, hence the parameter of interest can only be a fraction, and not a yield. As one is usually interested in the latter in the context of a measurement, the likelihood formalism can be extended to also include the event count of the sample so that a yield can be obtained straight from the fit.

11.2.1 Extended ML formalism

In the extended maximum likelihood formalism (EML) (Barlow, 1990) the normalization of the model is not fixed to one, but to a parameter N_{exp}, so that the likelihood expression effectively becomes

$$L(\boldsymbol{p},\boldsymbol{q}) = \left(\prod_{i=0\ldots N_{obs}} f(\boldsymbol{x_i};\boldsymbol{p},\boldsymbol{q})\right)\cdot\text{Poisson}(N_{\text{obs}}|N_{\text{exp}}(\boldsymbol{p},\boldsymbol{q})), \tag{11.2.2}$$

where N_{obs} is the observed event count, modeled by a Poisson distribution with the expected event count $N_{\text{exp}}(\boldsymbol{p},\boldsymbol{q})$ as mean. The likelihood of a composite model with a signal and background term can then be rewritten in the EML formalism taking

$$m(\boldsymbol{x};\boldsymbol{p},\boldsymbol{q}) = \frac{N_S}{N_S+N_B}\cdot s(\boldsymbol{x};\boldsymbol{p}) + \frac{N_B}{N_S+N_B}\cdot b(\boldsymbol{x};\boldsymbol{q}), \tag{11.2.3}$$

as the probability density function and

$$N_{\text{exp}} = N_S + N_B, \tag{11.2.4}$$

as the expression for the expected event count. A minimization of the extended likelihood will now directly return the estimates for the signal and background event yields N_S and N_B.

Often, we may assume that the shapes of the component distributions and the numbers of events are uncorrelated. That is, N_S etc are not dependent on $\boldsymbol{p}$ and $\boldsymbol{q}$. In this case the extended likelihood information does not improve the precision of the measurement of N_S and N_B, as the fit can always tune N_{exp} to match N_{obs} exactly for every possible value of $\boldsymbol{p}$, $\boldsymbol{q}$ and $f \equiv N_S/(N_S+N_B)$.

The extended ML formalism in this form is thus mostly used for notational convenience in B Factory analyses, allowing one to directly extract signal event yields from the fits, and to write sums of more than two components in a straightforward form with yield parameters for every component

$$m(\boldsymbol{x};...) = N_S\cdot s(\boldsymbol{x};\boldsymbol{p}) + \sum_i N_B^i b^i(\boldsymbol{x};\boldsymbol{q^i}), \tag{11.2.5}$$

where the index i runs over all background components and b^i denotes the model for background component i, with parameters $\boldsymbol{q^i}$.

11.2.2 Extending a model to multiple dimensions

In searches for rare decays, a single observable often does not contain sufficient information to distinguish signal from background and the information of multiple observables must be used. Several strategies can be followed to include the information contained in additional observables. One way is to preselect events using cuts in these additional observables in order to obtain a subsample enriched in signal events, and to restrict the signal extraction fit to the original observable. Another strategy – one that is often used for B Factory analyses and which maximizes the statistical precision – is to extend the signal and background models to describe the distributions in these additional observables, effectively constructing a multidimensional probability density function that is fit to the full event sample.

For observables that are uncorrelated, a multidimensional model can be constructed as a simple product of one-dimensional p.d.f.s, *e.g.*

$$f(x,y,z;\boldsymbol{p}) = f_1(x;\boldsymbol{p_1})\cdot f_2(y;\boldsymbol{p_2})\cdot f_3(z;\boldsymbol{p_3}), \tag{11.2.6}$$

where the f_1, f_2, f_3 represent normalized one-dimensional probability density functions. In case there are expected correlations between observables, *e.g.* between x and y, these must be modeled inside a higher-dimensional p.d.f. $f(x,y)$. This may be accomplished, for example, through the inclusion of conditional probability density functions

$$f(x,y;\boldsymbol{p}) = f_1(x|y;\boldsymbol{p_1})\cdot f_2(y;\boldsymbol{p_2}), \tag{11.2.7}$$

where $f_1(x|y)$ is the conditional probability density in x for a given value of y, *i.e.*

$$\forall y,\boldsymbol{p_1} : \int f_1(x|y;\boldsymbol{p_1})dx \equiv 1, \tag{11.2.8}$$

which describes the distribution of x for each given value of y, and $f_2(y)$ describes the distribution in y. Advantages of the formalism with conditional p.d.f.s are that correlations are often easier to formulate in this way and that all normalization integrals remain one-dimensional. The latter is of particular importance if numeric integration is needed, which is substantially more difficult in two or more dimensions at the level of precision required for `Minuit` minimization. The downside of conditional p.d.f.s is that the normalization integral must be calculated for each value of y separately, which may be computationally expensive, in case the integration needs to be performed numerically.

Apart from their construction, the use of multidimensional probability density functions presents no new technical or conceptual issues in ML estimation, but visualization and validation of multidimensional p.d.f.s introduce some additional issues.

A multi-dimensional model can be most simply visualized by projecting it on one of its observables:

$$P_{yz}(x) = \int f(x,y,z)dydz. \tag{11.2.9}$$

In the case of a factorizing model as defined in Eq. (11.2.6) the projection integral simply reduces to $f_1(x)$ and is trivial to calculate. If correlations are present, the integral must be explicitly calculated.

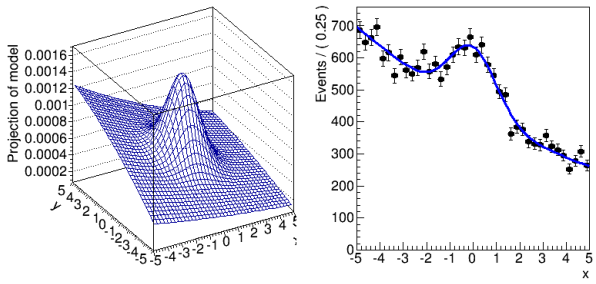

Figure 11.2.2. A two-dimensional probability density function consisting of a linear background and a Gaussian signal. On the left the probability density of the model is shown as a function of x and y. On the right the projection of the model on the observable x is overlaid on the distribution of a simulated data sample.

A conceptual issue with plain projection plots is that they include the full background and are not suitable to visualize the presence of a small signal in the data that is concentrated in a restricted region of the observable phase space. This is demonstrated in Fig. 11.2.2, which visualizes a two-dimensional model with a linear background and a Gaussian signal concentrated in the central region: while the signal is clearly visible in the central region, it is washed out in the projection plot. This can be mitigated by only projecting a 'signal region' defined in the projected observable x

$$P_{y^{SR}}(x) = \int_{y_{SR}^{min}}^{y_{SR}^{max}} F(x,y)dy, \tag{11.2.10}$$

where the interval y_{SR}^{min} to y_{SR}^{max} represents the region in the observable y that is enhanced in the signal.

Likelihood ratio plots. In the search for rare decays many observables are typically used and the signal may not be confined to an easily definable signal region as was possible in the example of Fig. 11.2.2. In these cases, projections of the data and model on a single observable can be defined using a likelihood ratio, rather than a series of cuts on each of the projected observables.

For such a plot, the signal and background models are first integrated over the plotted observable x to obtain the signal and background probabilities according to these models using *only* the information contained in the projected observables $\boldsymbol{y}$ and then combined in a likelihood ratio as follows:

$$LR(\boldsymbol{y}) = \frac{\int S(x,\boldsymbol{y})dx}{\int \left(f \cdot S(x,\boldsymbol{y}) + (1-f)B(x,\boldsymbol{y})\right)dx}. \tag{11.2.11}$$

A likelihood ratio projection plot is then constructed by taking all parameters (f in the example above) at their estimated values from the data, and by only plotting the data that meet a criterion $LR(\boldsymbol{y}) > \alpha$, where α is a threshold in the predicted signal probability (between 0 and 1), and projecting the model with corresponding selection

$$P_{\boldsymbol{y}}^{LR}(x) = \int_{LR(\boldsymbol{y})>\alpha} F(x,\boldsymbol{y})d\boldsymbol{y}. \tag{11.2.12}$$

The integral over the region defined by $LR(\boldsymbol{y}) > \alpha$ is clearly not calculable analytically, even if the model itself is, but can be approximated with a Monte Carlo integration technique as follows

$$C(x;\boldsymbol{p},\boldsymbol{q}) = 1/N_D \sum_{D_{LR}(\boldsymbol{y})} F(x;\boldsymbol{y},\boldsymbol{p},\boldsymbol{q}), \tag{11.2.13}$$

where $D_{LR}(\boldsymbol{y})$ is a pseudo-experiment dataset with N_D events, sampled from the p.d.f. $F(x,\boldsymbol{y})$ from which all events that fail the requirement $LR(\boldsymbol{y}) > \alpha$ have been removed. Figure 11.2.3 shows an example of a likelihood ratio plot defined using a three-dimensional extension of the model shown in Fig. 11.2.2 projecting over the y and z dimensions using a likelihood ratio cut with a value of 0.7.

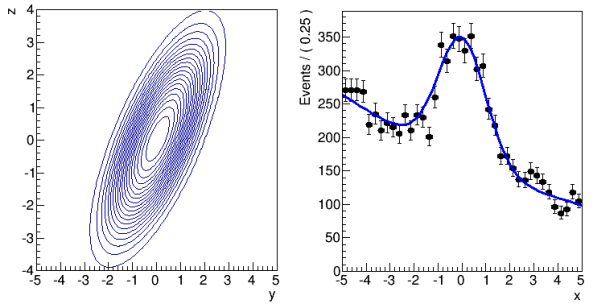

Figure 11.2.3. Visualization of a three-dimensional model, similar to that of Fig. 11.2.2. On the left a contour plot with constant values of likelihood ratio defined by Eq. (11.2.11) of a model in the observables y and z is shown. On the right the projection of the model on the observable x is shown, requiring $LR(y,z) > 0.7$ for both data and model to enhance the visibility of the signal.

11.2.3 *${}_s\mathcal{P}lots$*

A challenge in multi-dimensional models with a large number of observables is to verify that each component describes the data well in all observables. For factorizing p.d.f.s, Eq. (11.2.6), a new technique named *${}_s\mathcal{P}lot$* has been developed at the B Factories (Pivk and Le Diberder, 2005) to facilitate such studies.

In the *${}_s\mathcal{P}lot$* technique the distribution in observable x is predicted using the distribution in all of the other variables, $\boldsymbol{y}$, which must be uncorrelated to $\boldsymbol{y}$, and can be

compared to the direct model prediction in x. The central concept in ${}_s\mathcal{P}lot$ is the definition of the ${}_sWeight$

$$ {}_s\mathcal{P}_n(\boldsymbol{y}) = \frac{\sum_{j=1}^{n_c} V_{nj}^{-1} \cdot F_j(\boldsymbol{y})}{\sum_{k=1}^{n_c} N_k \cdot F_k(\boldsymbol{y})}, \tag{11.2.14} $$

where n is the selected component of a model consisting of n_c components (*e.g.* signal and one or more backgrounds). In this expression the indices j, k run over the n_c model components, F_j is the p.d.f. for component j in the observables $\boldsymbol{y}$, N_k is the expected number of events for the k^{th} component, and V_{nj}^{-1} is the inverse of the covariance matrix V_{nj} in these yield parameters. The matrix V_{nj} is obtained from the data, either through a numeric summation over the per-event contributions using Eq. (11.1.10), or from `HESSE` following a maximum likelihood fit to the data. Note that ${}_sWeights$ can be negative, as V_{nj} is not positive definite. The predicted distribution for any component j in observable x is given by the histogram of events in x where each event contributes with a weight ${}_s\mathcal{P}_n(\boldsymbol{y})$.

An example is shown in Figure 11.2.4, where for a 3-dimensional model in observables $m_{ES}, \Delta E, \mathcal{F}$, the p.d.f. in m_{ES} for signal and background are compared with the ${}_s\mathcal{P}lots$ in this observable, calculated using ${}_sWeights$ that use exclusively the data and the model prediction in observables $\Delta E, \mathcal{F}$. In this example the data was simulated and has been sampled from the model itself and perfect agreement is observed between the p.d.f. and the ${}_s\mathcal{P}lot$ prediction. When applied on samples of observed data, discrepancies between the ${}_s\mathcal{P}lot$ and the direct model prediction may occur, which may be indicative of disagreements between data and model.

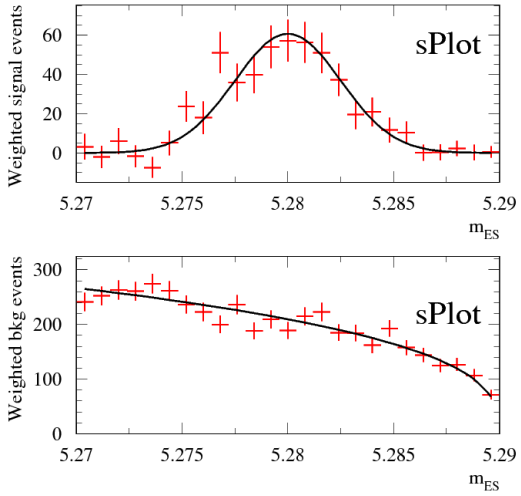

Figure 11.2.4. Demonstration of ${}_s\mathcal{P}lot$ concept using a model in three observables $m_{ES}, \Delta E, \mathcal{F}$ with a signal and background component. The top and bottom plot show the estimated signal and background shape in m_{ES}, respectively. In either plot the line represents the model prediction in the observable m_{ES}, and the histogram is the ${}_s\mathcal{P}lot$ defined as weighted sum over the data using ${}_sWeight$ ${}_s\mathcal{P}_n(\boldsymbol{y})$ calculated from the model prediction using only the observables ΔE and $\mathcal{F}$.

11.3 Structure of models for decay time-dependent measurements

Much of the interesting physics of the B-analyses is encoded in the distribution of the decay-time difference Δt between B^0 and $\overline{B}^0$ mesons, and connected to the phenomena of $B^0 - \overline{B}^0$ flavor oscillations (see also Chapter 10 and Section 6.5). The time scale of flavor oscillations is close to the decay time of B^0 mesons and to the experimental resolution of the B Factory detectors. Thus it is important to precisely model both the physics effects encoded in the decay time distribution, as well as the effect of the detector resolution on this distribution, of which the effect may vary on an event-by-event basis.

A priori, the observed inclusive decay-time distribution is expected to be modeled by the convolution of the physics distribution, a pure exponential decay law, and a detector resolution function:

$$ f(\Delta t; \tau, \boldsymbol{q}) = \frac{\exp(-|\Delta t_{\text{tr}}|/\tau) \otimes r(\Delta t - \Delta t_{\text{tr}}; \boldsymbol{q})}{\int \exp(-|\Delta t_{\text{tr}}|/\tau) \otimes r(\Delta t - \Delta t_{\text{tr}}; \boldsymbol{q}) d\Delta t}, \tag{11.3.1} $$

where Δt is observed decay time difference, Δt_{tr} is the true decay time difference, which is the integration variable of the convolution integral, and τ is the lifetime of B^0 mesons. Fig. 11.3.1 illustrates the shape of the convoluted p.d.f. of Eq. (11.3.1) and of its components.

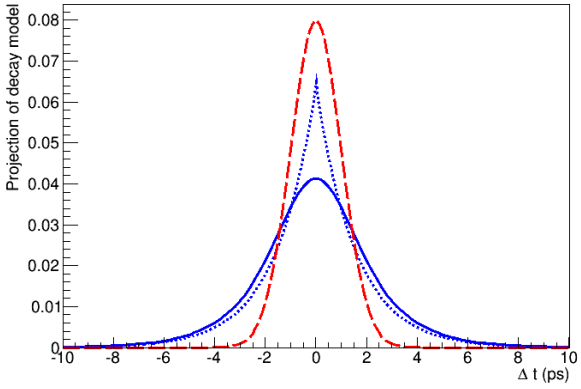

Figure 11.3.1. Visualization of exponential decay time difference distribution before (blue dashed) and after (blue solid) convolution with a Gaussian resolution function (red, long dashes).

The resolution model of Eq. (11.3.1) is usually empirically described as a sum of Gaussians, describing a 'core' (C) and a 'tail' (T) resolution, and often includes a very wide 'outlier' (O) term to account for the possibility that

outlier events can occur in the data:

$$r(\Delta t;\boldsymbol{\mu},\boldsymbol{\sigma}) = f_C \cdot \text{Gauss}(\Delta t;\mu_C,\sigma_C) + (1-f_C-f_O)\cdot \text{Gauss}(\Delta t;\mu_T,\sigma_T) + f_O \cdot \text{Gauss}(\Delta t;0,\sigma_O), \tag{11.3.2}$$

where $\mu_{C,T}$ and $\sigma_{C,T,O}$ represent the means and widths of the corresponding Gaussian distributions, respectively, and f_C and f_O represent the fraction of events in the core and outlier component, respectively. While very few events are expected that are not described by the convolution of the physics model with a core and tail Gaussian resolution term, it is important to include a wide outlier term in the resolution model, as otherwise a single event that is 'far' from both core and tail models has the potential to contribute disproportionally to the likelihood and can strongly and unduly influence the fit result, even when outliers only contribute at the permille level to the event sample. A common pragmatic choice for the outlier term is a very broad Gaussian distribution, as shown in the example of Eq. (11.3.2), but other shapes have also been used.

The resolution model of the previous example describes the average performance of the decay-time reconstruction. Since the decay-time difference is calculated from the distance between two decay vertices, the resolution in the time difference will depend on the number of tracks used in the vertex fits as well as their configuration, and the vertex fit procedure returns an estimate of the uncertainty on the decay-time difference for each event.

A more precise inference on the physics parameter τ of the model f can be made by taking into account this per-event uncertainty on the decay time difference – weighting events with a precise measurement of $\sigma_{\Delta t}$ more strongly than those with a poorer measurement by modifying the resolution model as follows

$$r'(\Delta t|\sigma_{\Delta t};\boldsymbol{\mu},\boldsymbol{\sigma}) = \text{Gauss}(\Delta t;\mu_C, S\cdot\sigma_{\Delta t}), \tag{11.3.3}$$

where $\sigma_{\Delta t}$ is the estimate of the uncertainty on Δt for each event. In this form the mean and width parameters of the resolution model r' describes an a posteriori shift μ_C and scaling S of the per-event error $\sigma_{\Delta t}$ that is needed to match the model to the data. If the per-event uncertainty estimated by the vertex fit is correct, the mean and width will be 0 and 1, respectively, and r' will be a unit Gaussian. In practice, this is often not the case due to the complexity of the underlying vertex fitting procedure and a more complex p.d.f. is needed to describe the shape of the resolution function. Here one can either take an empirical form for r', *e.g.* a sum of two or three Gaussians, or try to construct a form that parameterizes the effect of the leading underlying causes explicitly. Various choices of resolution models used for time-dependent analyses at the B Factories are described in more detail in Section 6.5. Inserting r' in Eq. (11.3.1) results in a conditional probability density function

$$f(\Delta t|\sigma_{\Delta t};\tau,\boldsymbol{q}) = \frac{e^{-|\Delta t_{\text{tr}}|/\tau} \otimes r'(\Delta t - \Delta t_{\text{tr}};\sigma_{\Delta t},\boldsymbol{q})}{\int e^{-|\Delta t_{\text{tr}}|/\tau} \otimes r'(\Delta t - \Delta t_{\text{tr}};\sigma_{\Delta t},\boldsymbol{q}) d\Delta t}, \tag{11.3.4}$$

where Δt_{tr} is again the integration variable of the convolution integral, and which describes the distribution of Δt for a *given* value of $\sigma_{\Delta t}$, but not the distribution of $\sigma_{\Delta t}$ itself. Such a conditional p.d.f. can be fit directly to the data, or be multiplied with another (empirical) p.d.f. that describes the distribution of the per-event uncertainty on Δt:

$$F'(\Delta t,\sigma_{\Delta t}|\tau;\boldsymbol{q}) = F(\Delta t|\sigma_{\Delta t};\tau,\boldsymbol{q})\cdot\text{Gauss}(\sigma_{\Delta t};\boldsymbol{q}). \tag{11.3.5}$$

In realistic models that account for the presence of background in the data, a separate decay-time distribution is defined for signal and background, each multiplied with one or more probability density functions in other observables that primarily serve to distinguish signal from background events. This approach to model building is straightforward except for one aspect related to conditional models: The p.d.f. of Eq. (11.3.4) makes no assumptions on the distribution of $\sigma_{\Delta t}$ in the data, but does assume that signal and background events have the same distribution, whereas the p.d.f. of Eq. (11.3.5) allows for different distributions of $\sigma_{\Delta t}$ for signal and background, but requires an explicit description of both. The most appropriate form depends on the specifics of the analysis. Using Eq. (11.3.4) in cases where it is not appropriate, *e.g.* when distributions of $\sigma_{\Delta t}$ for signal and background are expected to be different, is referred to as the "Punzi problem" (Punzi, 2003a) in HEP statistics literature, and may lead to biased fit results.

Finally, the physics of interest in the decay time distribution is exposed by splitting the event sample in two more categories, *e.g.* same-flavor and opposite-flavor B^0 meson pairs to expose flavor oscillations:

$$F(\Delta t, f;\tau,\boldsymbol{q}) = \begin{cases} \frac{\left(e^{-|\Delta t_{\text{tr}}|/\tau}\cos(\Delta m\Delta t_{\text{tr}})\right)\otimes R(\ldots)}{\int\left(e^{-|\Delta t_{\text{tr}}|/\tau}\cos(\Delta m\Delta t_{\text{tr}})\right)\otimes R(\ldots)d\Delta t} : f\equiv -1 \\ \frac{\left(e^{-|\Delta t_{\text{tr}}|/\tau}(1-\cos(\Delta m\Delta t_{\text{tr}})\right)\otimes R(\ldots)}{\int\left(e^{-|\Delta t_{\text{tr}}|/\tau}(1-\cos(\Delta m\Delta t_{\text{tr}})\right)\otimes R(\ldots)d\Delta t} : f\equiv +1 \end{cases} \tag{11.3.6}$$

defining a two-dimensional p.d.f. in a continuous observable Δt and a discrete observable f that distinguishes same-flavor from opposite-flavor events. The techniques illustrated on inclusive decay time distributions apply transparently to models modified in this way.

11.3.1 Visualization of p.d.f.s of decay time distributions

Models describing measurements of time-dependent *CP*-violating decay processes commonly have two or three continuous observables: the decay time and one or two kinematic variables, such as m_{ES} or ΔE, to distinguish

B decays from continuum background. These observables are usually uncorrelated and the kinematic variables have a well-defined 'signal' range that allows one to plot the decay time distribution of these events inside this signal range only, using Eq. (11.2.10).

In the case that the p.d.f. contains a conditional observable, such as $\sigma_{\Delta t}$, a different technique is required to project the conditional observable, as the p.d.f. does not contain information on the distribution of that observable. An average curve C is constructed from curves representing the projection over the non-conditional observables taken at the values $\sigma_{\Delta t}$ found in the data:

$$C(\Delta t; \boldsymbol{p}, \boldsymbol{q}) = \frac{1}{n} \sum_{i=0,\ldots,n} \int d\boldsymbol{y} F(\Delta t; \sigma^i_{\Delta t}, \boldsymbol{y}, \boldsymbol{p}, \boldsymbol{q}). \tag{11.3.7}$$

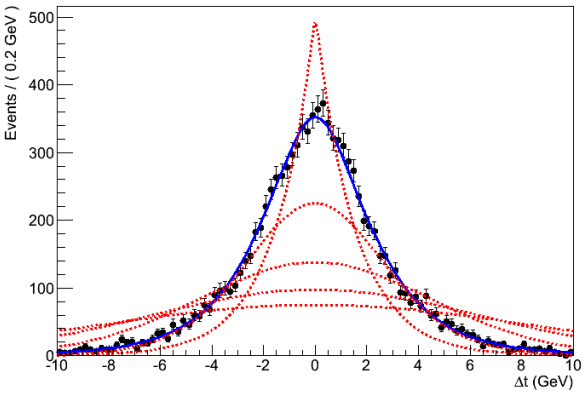

Figure 11.3.2. Distribution of the conditional decay time model $F(\Delta t|\sigma_{\Delta t})$ of Eq. (11.3.4) with values of $\sigma_{\Delta t}$ of 0, 2, 4, 6, 8 ps (red dashed, ordered high to low at $\Delta t = 0$) and distribution of the data overlayed with the weighted average of the conditional model using the $\sigma_{\Delta t}$ values of the data sample.

where n is the number of events in the data. Figure 11.3.2 shows an example of a decay-time distribution: the red dashed curves illustrate the shape of the model at various values of $\sigma_{\Delta t}$, and the blue curve represents the weighted average using the $\sigma_{\Delta t}$ values of the dataset. Note that in the limit of the data $\sigma^i_{\Delta t}$ describing the true distribution of $\sigma_{\Delta t}$ Eq. (11.3.7) amounts to the Monte-Carlo integral (given by Eq. 11.2.13) over observable $\sigma_{\Delta t}$. For computational efficiency the summation of the data $\sigma^i_{\Delta t}$ is sometimes approximated by a summation over a histogram of the data.

11.4 Techniques used for constraining nuisance parameters from control samples

11.4.1 Simultaneous fits to control regions

As a general analysis strategy it is preferable to constrain the nuisance parameters $\boldsymbol{q}$, such as the decay time resolution model parameters, as much as possible from the data itself, instead of inferring them from simulation studies. In many cases this can be accomplished by simply floating the nuisance parameters in the ML fit. This will worsen the estimated uncertainty on the physics parameter of interest, as the values of nuisance parameters are no longer assumed to be known exactly, instead their statistical uncertainties, as inferred by the ML fit from the data, are propagated to the uncertainty on the physics parameter of interest.

In many B-physics analyses additional high-statistics control samples exist that can constrain these nuisance parameters with greater precision than the signal sample. For example, for decay-time dependent CP violation measurements high statistics control samples from the B^0 flavor tagged samples can be used to measure the nuisance parameters originating from the description of the flavor tagging performance as well as the modeling of the detector decay time resolution.

The most straightforward way to incorporate the knowledge on nuisance parameters – their uncertainties and their correlations – in a measurement is to perform a joint likelihood minimization:

$$-\log L(\boldsymbol{p}, \boldsymbol{q}, \boldsymbol{q'}) = -\log L_{\mathrm{SIG}}(\boldsymbol{p}, \boldsymbol{q}) - \log L_{\mathrm{CTL}}(\boldsymbol{q}, \boldsymbol{q'}), \tag{11.4.1}$$

where $L_{\mathrm{SIG}}(\boldsymbol{p}, \boldsymbol{q})$ is the likelihood for the signal region in terms of parameters of interest $\boldsymbol{p}$ and nuisance parameters $\boldsymbol{q}$ and $L_{\mathrm{CTL}}(\boldsymbol{q}, \boldsymbol{q'})$ is the likelihood for the control region in terms of nuisance parameters $\boldsymbol{q}$ that are shared with the signal region and nuisance parameters $\boldsymbol{q'}$ that are unique to the control region. Equivalently, this construction can be expressed as a joint probability density function

$$F(x|i; \boldsymbol{p}, \boldsymbol{q}, \boldsymbol{q'}) = \begin{cases} F_{\mathrm{SIG}}(x; \boldsymbol{p}, \boldsymbol{q}) & \text{if } (i = \mathrm{SIG}) \\ F_{\mathrm{CTL}}(x; \boldsymbol{q}, \boldsymbol{q'}) & \text{if } (i = \mathrm{CTL}) \end{cases} \tag{11.4.2}$$

that is conditional on a newly introduced discrete observable i that has states SIG and CTL, which label the events in the signal and control samples respectively.

A minimization of a joint likelihood ensures that the full information in both samples is taken into account, and the estimated uncertainty of parameters and their correlations reflect the information from both samples, as is illustrated in Fig. 11.4.1. The p.d.f.s describing the signal and control sample can be very dissimilar in shape and structure, the only requirement is that the common parameters have the same physics interpretation in both models.

11.4.2 Simultaneous fits to multiple signal regions

A mathematically similar, but conceptually different application of joint fits is to perform a joint likelihood fit to multiple signal regions, with similar p.d.f.s. If a signal region can be split into regions with different expected signal purities, a split into these regions will exploit this difference in purity without the need to provide an explicit parameterization of the change in purity over the phase space of the original signal sample.

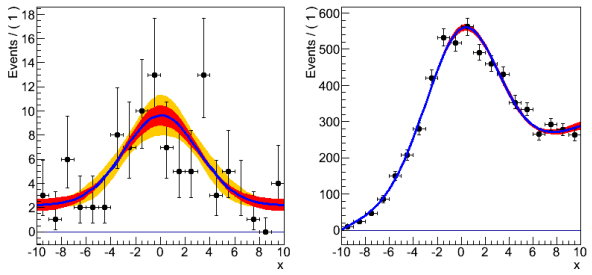

Figure 11.4.1. Visualization of the effect of a simultaneous fit. On the left a fictitious low statistics signal sample is shown (modeled by a flat background and a Gaussian signal). The model uncertainty from the fit to the signal sample only is visualized with the light orange band. On the right a fictitious high statistics control sample is shown (modeled by a sloped background and the same Gaussian signal). The uncertainty on the control sample model is visualized with the dark red band. The reduced uncertainty on the signal sample by performing a joint fit with the control sample is shown also in dark red in the left plot.

A prime example of this technique is splitting a signal model according to the flavor tagging technique (see also Chapter 8) that was used to tag a particular event. Different tagging techniques are expected to result in quite different purities. The original model

$$F(x;\boldsymbol{p},\boldsymbol{q}) = F(x;\boldsymbol{p},\boldsymbol{q},w_{tag}) \tag{11.4.3}$$

is substituted with

$$F(x|c;\boldsymbol{p},\boldsymbol{q}) = \begin{cases} F_{\text{tag1}}(x;\boldsymbol{p},\boldsymbol{q},w_{\text{tag1}}) & \text{if } (c=\text{tag1}) \\ F_{\text{tag2}}(x;\boldsymbol{p},\boldsymbol{q},w_{\text{tag2}}) & \text{if } (c=\text{tag2}) \\ F_{\text{tag3}}(x;\boldsymbol{p},\boldsymbol{q},w_{\text{tag3}}) & \text{if } (c=\text{tag3}) \\ \ldots & \\ F_{\text{tag}n}(x;\boldsymbol{p},\boldsymbol{q},w_{\text{tag}n}) & \text{if } (c=\text{tag}n) \end{cases}, \tag{11.4.4}$$

where c is a discrete observable that labels which flavor tagging technique was used (here these are labeled tag1 through tag$n$, for illustration). The component models $F_{\text{tag}i}(x;\boldsymbol{p},\boldsymbol{q},w_{\text{tag}i})$ are structurally identical to the original $F(x;\boldsymbol{p},\boldsymbol{q},w_{\text{tag}})$, and expressed in terms of the same observables and parameters, *except* for the parameter w that describes the mistag probability, which is now uniquely defined by $w_{\text{tag}i}$ for each state tag$i$ rather than being a global parameter w. At the likelihood level, the original likelihood $L(\boldsymbol{p},\boldsymbol{q},w_{\text{tag}})$ is now reparameterized for each region as $L(\boldsymbol{p},\boldsymbol{q},w_{\text{tag1}},w_{\text{tag2}},w_{\text{tag3}},\ldots,w_{\text{tag}n})$.

Since the model of Eq. (11.4.4) is defined conditionally on the discrete split observable c, the model makes no assumptions on the distribution of events over the defined subsets, and since each subset is equipped with its own nuisance parameter $w_{\text{tag}i}$, also no assumption is made on the variation of the mistag rates over the subsets. The split likelihood is generally expected to improve the statistical uncertainty on the parameter of interest: in the above example, events with better than average mistag properties will now weigh more strongly in the likelihood than events with less than average mistag properties, when compared to the original likelihood definition.

While the signal splitting technique can quickly increase the number of parameters allowed to vary in the fit, the likelihood tends to be uncorrelated between the 'split' parameters and the minimization stability in `Minuit` is not as strongly impacted as one might a priori expect. The calculation of the covariance matrix by `HESSE` will nevertheless be more time consuming, as `HESSE` is not aware of this block-diagonal form and will simply calculate all covariance matrix elements.

11.5 Miscellaneous issues

11.5.1 Background subtraction and weighted events

An alternative approach to extracting signal properties from a data sample with a known background contribution is to subtract the background in the data, using an estimate from a sideband region, and then fitting the background subtracted data samples with a signal-only model.

An advantage of the subtraction approach is that no parametric form is needed to describe the distribution of the background. Background subtraction can be applied in both binned and unbinned ML estimates. In the latter case, background events are added to the unbinned dataset with negative weights. Another form of background subtraction is to reweight the data, using the ${}_sWeights$ defined in Eq. (11.2.14), in such a way that the sum of weights reflects only the signal component. ${}_sWeights$ can be either positive or negative.

In all cases of event weighting the distribution of the expected event count in any given region is modified from a Poisson distribution to a distribution that reflects the effect of the subtracted background distribution. In a χ^2 fit, the (squared) uncertainty associated with each bin is the calculated with the sum of the squares of the weights of the events in the bin, using the prescription for the variance with weighted events:

$$\sigma^2 = V = \sum_{i=1}^{N} w_i^2, \tag{11.5.1}$$

where w_i is the weight of the i-th of N events contributing to a given bin. For example in a bin containing 20 events with weight $+1$ and 10 events of weight -1, the uncertainty on the weighted sum of 10 events is estimated as $\sqrt{30}$, compared to $\sqrt{10}$ for a bin containing 10 events with only positive weights.

In the likelihood formalism, the definition of the likelihood of Eq. (11.1.6) can be modified to include event weights

$$-\log L(\boldsymbol{p},\boldsymbol{q}) = -\sum_{i=0,\ldots,n} w_i \cdot \log F(\boldsymbol{x_i};\boldsymbol{p},\boldsymbol{q}), \tag{11.5.2}$$

so that the ML estimators for the parameters $\boldsymbol{p},\boldsymbol{q}$ will take the weights into account. The likelihood of Eq. (11.5.2) is

however not directly suitable for variance estimators: unlike a χ^2 fit, where the uncertainty associated with each data point can be externally specified according to Eq. (11.5.1), the variance estimator for these parameters will *not* reflect the increased uncertainty and will simply (incorrectly) assume Poisson uncertainties with $\mu = \sum w_i$. and will thus – in case of datasets with events that have weights less than unity – underestimate the uncertainty.

Nevertheless it is possible to extract an approximately correct covariance matrix by combining the ML estimate of variance V given by Eq. (11.5.2) with another ML estimate of the variance (C) for which the weight w_i in Eq. (11.5.2) was substituted by w_i^2 :

$$V' = V \cdot C^{-1} \cdot V. \tag{11.5.3}$$

The estimation of errors using Eqs (11.5.2) and (11.5.3) is not restricted to cases where event weights are ± 1, but can also be more generally applied to event samples with arbitrary event weights.

11.5.2 Validation of ML fits on complex models

Maximum likelihood fits on complex models can be validated by studying their behavior on simulated data that are sampled from the model itself. A typical study consists of simulating many (of order 1000) data samples according to the model under study, and fitting the model to each of these datasets. For every estimated parameter in the fit, the distribution of its pull, defined as

$$\text{pull}(p) = \frac{\widehat{p} - p_{\text{true}}}{\sigma(\widehat{p})} \tag{11.5.4}$$

can be examined. If the estimator $\widehat{p}$ is free of bias, *i.e.* it will estimate the true value correctly on average, the mean of the pull distribution will be consistent with zero. If the estimator $\widehat{\sigma}(p)$ represents the uncertainty correctly the variance of the pull distribution will be consistent with one. A too narrow pull distribution indicates that $\widehat{\sigma}(p)$ overestimates the uncertainty. Conversely, a too wide pull distribution indicates that $\widehat{\sigma}(p)$ underestimates the uncertainty. Verification of the absence of bias is of particular importance for estimators of small yields for which ML estimators can be rather imperfect. Studies on simulated data can also be used to determine the expected spread in (statistical) uncertainties on the physics parameter-of-interest, indicating whether the uncertainty obtained on the measured data was 'lucky' or not. For these studies, in particular when studying the aspect of expected statistical uncertainties, it is important to draw event samples from a conditional model evaluated at the observed values of the conditional observables (such as $\sigma_{\Delta t}$ in decay time dependent fits), to get a maximally relevant answer.

Another aspect of validation of ML estimates is to measure the goodness-of-fit of the model $f(x)$ with respect to the data x. To do so, a test statistic $T(x)$ must be defined to quantify the agreement between data and model in some way. A common test statistic for this purpose is Pearson's χ^2, which divides the data in bins and measures the distance between the model prediction and the data in each bin. The goodness-of-fit is then expressed by the p-value of the hypothesis that model $f(x)$ is true, calculating Eq. (11.1.14) using the chosen test statistic. If the p-value is low, one may need to reject the model f as a valid model.[45] The χ^2 test statistic is popular, despite its requirement that the data must be binned, because this test statistic is *distribution-free*: in the limit of sufficient event counts in all bins the distribution of χ^2 values is independent of the distribution of the data predicted by model f, simplifying the interpretation of χ^2 values in terms of probabilities.

Estimating the goodness-of-fit for complex likelihood models with multiple observables constitutes a more difficult problem: due to the large number of empty bins that arise in binning multi-dimensional observables distributions the χ^2 test statistic is no longer in the distribution-free regime. Various unbinned multidimensional goodness-of-fit tests have been developed over the years (Aslan and Zech, 2002), but are not as easy to use as the χ^2 test in the high-statistics regime for various reasons, *e.g.* because they are not distribution-free either, and have not been routinely used at the B Factories.

It should be noted that the unbinned maximum likelihood itself is *not* a reliable goodness-of-fit estimator. One reason for this is that this test statistic does not generally provide a sane definition of agreement between data and model. For example, for a likelihood assuming an exponential decay law distribution, the maximum log-likelihood is simply proportional to average lifetime of the events in the data. Thus, all data samples with the same average lifetime will result in the same goodness-of-fit independent of the observed distribution of events. Another problem with the maximum likelihood as goodness-of-fit test statistic is in obtaining the distribution of the test statistic: ML estimates are not distribution free, unlike likelihood ratios, so the expected distribution of ML values under the hypothesis that model f is true, must be obtained from an ensemble of pseudo-experiments. For models $f(\boldsymbol{\theta})$ with parameters $\boldsymbol{\theta}$ this poses a challenge as the true values of the parameters are unknown. Instead, the distribution is usually obtained from pseudo-experiments sampled from the model $f(\widehat{\boldsymbol{\theta}})$ using the ML estimates of the parameters $\widehat{\boldsymbol{\theta}}$. In the example of the decay law distribution, where the maximum likelihood is simply proportional to the estimated lifetime $\widehat{\tau}$, the p-value for the hypothesis $f(\widehat{\tau})$ will then be close to 50% by construction and thus not provide meaningful information on the goodness-of-fit.

[45] Note that since a goodness-of-fit test is a hypothesis test in which the alternate hypothesis is the set of all possible alternatives to the hypothesis f being tested, one cannot formulate the alternate hypothesis, and thus not quantify the *power* of the test: the probability that the hypothesis f is false and the alternate hypothesis is true. One should therefore not conclude from a high p-value that the hypothesis f is true.

11.5.3 Computational optimizations of likelihood calculations

Unbinned maximum likelihood fits are computationally intensive, and the fits underlying many of the B Factory results have taken many hours or even days to complete. Efficient computation of the likelihood is thus important. In this section we discuss a number of the techniques that are applied in many of the B Factory likelihood fits to optimize computational efficiency. The techniques discussed here are applied automatically in all `RooFit`-based likelihood implementations and have often been applied by hand in custom likelihood implementations.

Constant term pre-calculation. In many models (partial) expressions occur that do not depend on any floating model parameter. These terms can be identified and precalculated once at the beginning of the fit.

Caching and lazy evaluation. Expensive objects such as numeric integrals over functions, may not need to be recalculated every time their value is needed. By explicitly tracking if input variables have changed and caching the value of the previous outcome of the calculation, unnecessary repeated calculations can be prevented. For simultaneous fits, this strategy is also applied to components of the likelihood, so that these are only recalculated if a parameter on which the component actually depends is changed.

Analytical (partial) integrals. For many functions, analytical expressions are known for their integrals. By using the analytical forms, expensive numeric integration can be avoided. For multi-dimensional functions, knowledge of partial analytical integrals can be used to reduce the dimensionality of the numeric integration that is needed. This is particularly efficient in cases where the dimension of the numeric integral is reduced to one, as numeric integrals in one dimension can be calculated much more efficiently and with accurate convergence estimates than multi-dimensional integrals.

Approximation of the complex error function. Many time-dependent B-physics models that involve convolution with Gaussian resolution models are expressed in terms of the complex error function. Standard calculation of the complex error function can take $\mathcal{O}(100)$ complex number multiplications to estimate its value. Instead, inside p.d.f.s interpolation in a 2-dimensional lookup table is used to speed up the calculation.

Parallelization of the likelihood calculation. The calculation of the likelihood is by its nature very suitable for parallelized calculation. The wall-time of execution of ML fits can be decreased by roughly a factor N by parallelizing the likelihood calculation over all N available cores on a multi-core host, or alternatively over multiple hosts.

Chapter 12
Angular analysis

Editors:
Georges Vasseur (BABAR)

An angular analysis uses the information coming from the angular distributions of the final state particles. These distributions depend on the spin and polarization of all the particles involved in the decay chain. Consequently an angular analysis may determine the spin of a particle if unknown, and the polarization of the particles in a given decay chain.

Furthermore, the angles of the Unitarity Triangle have been determined, in several B-meson decay modes, through the measurement of time-dependent CP asymmetries in vector-vector final states, such as $J/\psi K^*$, D^*D^*, and $\rho\rho$, which have both CP-even and CP-odd components. These components need to be disentangled in order to extract the value of the CP asymmetry. This can be achieved by performing an angular analysis.

In this chapter the angular analysis is described. The formalism is presented in Section 12.1. An overview of the main modes studied at the B Factories that require an angular analysis is given in Section 12.2. Several analysis details are discussed in Section 12.3. Finally angular fits are described in Section 12.4.

12.1 Formalism

12.1.1 Spin and helicity

The spin is a quantum number characterizing a particle. It is a positive half-integer for particles called fermions (for example, electrons, muons, and protons have a spin of $\frac{1}{2}$) or integer for particles called bosons (for example, mesons). The spin J of a given particle and its parity P are often given using the notation J^P. According to the values of J^P, particles are referred to as scalars (0^+: f_0, a_0, K_0^*, ...), pseudoscalars (0^-: π, η, η', K, D, η_c, B, ...), vectors (1^-: ρ, ω, ϕ, K^*, D^*, ψ, ...), axial vectors (1^+: a_1, K_1, ...), or tensors (2^+: a_2, K_2^*, ...).

The helicity h of a particle of spin J corresponds to the projection of its spin along its momentum. For particles with mass, it can be one of $2J+1$ values: $-J$, $-J+1$, ..., $J-1$, J. For massless particles, only two values are allowed: $-J$ and J. For example, photons, of spin 1, can have two helicities, -1 and $+1$. More information on the helicity formalism can be found in (Jacob and Wick, 1959).

12.1.2 Angular bases

Let us consider a spin 0 particle M_0 (for example a B meson or a D meson) decaying to two particles M_1 and M_2. Since the spin of M_0 is zero, the spin projection of the final state on the decay axis in the M_0 rest frame has to be zero. In other words, M_1 and M_2 must have the same helicity. For example, if one of the final state particles has spin 0 and hence its helicity is 0, the helicity of the other final state particle must also be equal to 0: it is longitudinally polarized.

Let us now focus on the case where at least one of the direct decay products of M_0 has spin 1 (a vector or axial vector particle) and the other a spin greater or equal to 1. If M_1 or M_2 is of spin 1, h can take three values: -1, 0, and $+1$. There is one complex amplitude A_h associated with each case: the longitudinal amplitude A_0 and the transverse ones A_{+1} and A_{-1}. The three amplitudes (A_0, A_{+1}, A_{-1}) correspond to helicity eigenstates and define the helicity basis.

For a CP eigenstate, the longitudinal amplitude is CP-even, while the transverse ones are an admixture of CP-even and CP-odd components. In the transversity basis (A_L, $A_\parallel$, $A_\perp$), the amplitudes correspond to CP eigenstates:

$$\begin{array}{lll} CP\text{-even longitudinal} & : A_L & = A_0 \quad , \\ CP\text{-even transverse} & : A_\parallel & = \frac{A_{+1}+A_{-1}}{\sqrt{2}} \quad , \\ CP\text{-odd transverse} & : A_\perp & = \frac{A_{+1}-A_{-1}}{\sqrt{2}} \quad . \end{array}$$

Both "0" and "L" subscripts are commonly used for the longitudinal amplitude. In what follows, the latter notation is used. Additional information on the subject can be found in (Kramer and Palmer, 1992), in (Dunietz, Quinn, Snyder, Toki, and Lipkin, 1991), and in the review of polarization in B decays of (Beringer et al., 2012).

The fractions of each polarization amplitude are defined as $f_{L,\parallel,\perp} = \frac{|A_{L,\parallel,\perp}|^2}{\Sigma|A_h|^2}$, where h runs on the three polarization eigenstates. They satisfy the relation $f_L + f_\parallel + f_\perp = 1$. The phase differences of the two transverse amplitudes with respect to the longitudinal one are defined as $\phi_{\parallel,\perp} = \mathrm{Arg}(A_{\parallel,\perp}/A_L)$. As the decay is described by three independent complex amplitudes, A_L, $A_\parallel$, and $A_\perp$, there are six independent real parameters, often chosen as f_L, $f_\perp$, $\phi_\parallel$, $\phi_\perp$, the total decay rate Γ, and an overall phase δ_0.

This overall phase is meaningless in most cases. It is relevant when there exists an external amplitude which can be used as a reference to measure it. This is the case, for example, if one of the B-meson daughters is a K^*. In addition to the three amplitudes, $A_L, A_\parallel, A_\perp$, describing the decay mode with the K^*, there is another amplitude A_{00} associated with the related decay mode where the K^* is replaced by the $J=0$ ($K\pi$) wave, K_0^*. The overall phase can be defined as $\delta_0 = \mathrm{Arg}(A_{00}/A_L)$. As both the K^* and K_0^* decay to the same final state $K\pi$, the δ_0 phase can be measured through interference between the $B \to M_1 K^*$ and $B \to M_1 K_0^*$ decays (Aubert, 2008bf).

The total amplitude may also be expressed as a function of S, P, or D partial waves, characterized by the relative orbital angular momentum L between M_1 and M_2, L being equal to 0, 1, and 2 for S, P, and D waves respectively. The partial wave basis is used for example in (Chung, 1997).

The expressions for the angular dependence are relatively simple in the helicity and transversity bases. They are given in the next subsections.

12.1.3 Angular distributions in the helicity basis

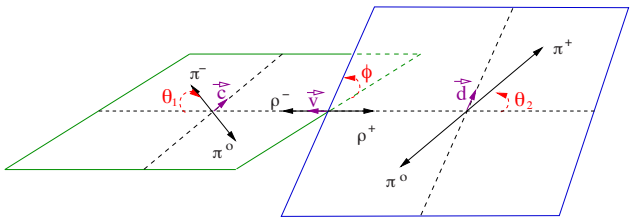

Figure 12.1.1. The three angles in the helicity frame: θ_1, θ_2, and ϕ, shown in the example of $B \to \rho^-\rho^+$ decays. The $B \to \rho^-\rho^+$, $\rho^- \to \pi^-\pi^0$, and $\rho^+ \to \pi^+\pi^0$ decays are represented in the B, ρ^-, and ρ^+ rest frames respectively. The unit vector $\boldsymbol{v}$ defines the direction of the ρ^- in the B rest frame, or equivalently the direction of (opposite to) the line of flight of the B in the ρ^+ (ρ^-) rest frame. The decay plane of the ρ^- (ρ^+) is defined by the $\boldsymbol{c}$ ($\boldsymbol{d}$) and $\boldsymbol{v}$ unit vectors. Here ϕ is the angle between the two decay planes and θ_1 (θ_2) is the polar angle of the π^- (π^+) with $\boldsymbol{v}$ ($-\boldsymbol{v}$).

In the helicity frame, in the case of the $M_0 \to M_1 M_2$ decay with M_1 and M_2 each subsequently undergoing a two-body decay, the relevant angles are the polar angle θ_1 of a decay product of M_1 with respect to the direction opposite to the line of flight of M_0 in the M_1 rest frame, the angle θ_2 for M_2 (same as θ_1 for M_1), and the angle ϕ between the decay planes of M_1 and M_2 in the M_0 rest frame. The choice of the decay product of M_1 (M_2) used to define θ_1 (θ_2) is arbitrary, but it must be consistent throughout the analysis. Figure 12.1.1 shows the three angles in the case of $B \to \rho^-\rho^+$ decays, with $\rho^- \to \pi^-\pi^0$ and $\rho^+ \to \pi^+\pi^0$. If M_i ($i = 1$ or 2) undergoes a three-body decay, θ_i is defined as the angle between the normal of the decay plane of M_i with respect to the direction opposite to the line of flight of M_0 in the M_i rest frame.

The differential decay rate in the helicity frame can be expressed as:

$$\frac{1}{\Gamma}\,\frac{d^3\Gamma}{d\cos\theta_1\, d\cos\theta_2\, d\phi} = \frac{9}{8\pi}\,\Sigma\,\alpha_i\, g_i(\cos\theta_1, \cos\theta_2, \phi)\,. \tag{12.1.1}$$

The g_i functions depend on the quantum numbers of the particles in the decay chain and are given for the most common cases in the next section. The α_i are real parameters, which can be expressed as functions of the fractions f_L, $f_\parallel$, $f_\perp$ and of the phase differences $\phi_\parallel$, $\phi_\perp$ Beringer et al. (2012):

$$\begin{aligned}
\alpha_1 &= \frac{|A_L|^2}{\Sigma|A_h|^2} = f_L\,,\\
\alpha_2 &= \frac{|A_\parallel|^2 + |A_\perp|^2}{\Sigma|A_h|^2} = 1 - f_L\,,\\
\alpha_3 &= \frac{|A_\parallel|^2 - |A_\perp|^2}{\Sigma|A_h|^2} = f_\parallel - f_\perp\,,\\
\alpha_4 &= \frac{\mathrm{Im}(A_\perp A_\parallel^*)}{\Sigma|A_h|^2} = \sqrt{f_\perp f_\parallel}\,\sin(\phi_\perp - \phi_\parallel)\,,\\
\alpha_5 &= \frac{\mathrm{Re}(A_\parallel A_L^*)}{\Sigma|A_h|^2} = \sqrt{f_\parallel f_L}\,\cos(\phi_\parallel)\,,\\
\alpha_6 &= \frac{\mathrm{Im}(A_\perp A_L^*)}{\Sigma|A_h|^2} = \sqrt{f_\perp f_L}\,\sin(\phi_\perp)\,.
\end{aligned} \tag{12.1.2}$$

12.1.4 Angular distributions in the transversity basis

The angles used in the transversity frame are illustrated in Figure 12.1.2 for the decay mode $B \to \rho^+\rho^-$. The angle θ_1 has the same definition as in the helicity frame. In the M_2 rest frame, the axes (x,y,z) are defined such that the x-axis has the direction opposite to the momentum of the M_1 particle, the z-axis is normal to the decay plane of the M_1 particle, and the projection of the momentum along the y-axis is positive for the decay product of M_1 that is used to define θ_1 (the π^- in the example of Figure 12.1.2). Then θ_{tr} and ϕ_{tr} are the polar and azimuthal angles of one decay product of M_2. They are called the transversity angles.

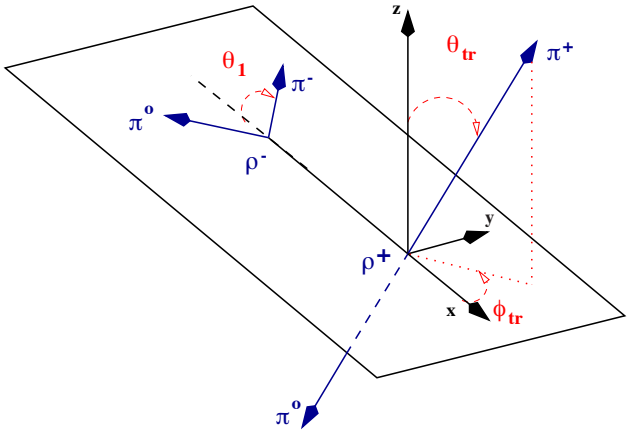

Figure 12.1.2. The three angles in the transversity frame: θ_1, θ_{tr}, and ϕ_{tr}, shown in the example of $B \to \rho^+\rho^-$ decays. Here θ_1 is the angle of the π^- with the ρ^- direction. And θ_{tr} (ϕ_{tr}) is the polar (azimuthal) angle of the π^+ in the ρ^+ rest frame.

It is convenient to write the differential decay rate, as in the helicity frame, as the sum of six terms:

$$\frac{1}{\Gamma}\,\frac{d^3\Gamma}{d\cos\theta_1\, d\cos\theta_{tr}\, d\phi_{tr}} = \frac{9}{8\pi}\,\Sigma\,\alpha_i^{tr}\, g_i^{tr}(\cos\theta_1, \cos\theta_{tr}, \phi_{tr})\,, \qquad (12.1.3)$$

with $\alpha_i^{tr} = \alpha_i$, except for

$$\alpha_2^{tr} = \frac{\alpha_2+\alpha_3}{2} = \frac{|A_\parallel|^2}{\Sigma|A_h|^2} = f_\parallel\,,$$
$$\alpha_3^{tr} = \frac{\alpha_2-\alpha_3}{2} = \frac{|A_\perp|^2}{\Sigma|A_h|^2} = f_\perp\,. \qquad (12.1.4)$$

12.1.5 *CP* violation

If both the M_0 decay and its charge conjugate $\overline{M}_0$ decay are considered, there are now six complex amplitudes or twelve real parameters to describe the two decays. They can be chosen as the six parameters, Γ, f_L, $f_\perp$, $\phi_\parallel$, $\phi_\perp$, and δ_0, already given for the M_0 decay, and the corresponding ones, $\overline{\Gamma}$, $\overline{f}_L$, $\overline{f}_\perp$, $\overline{\phi}_\parallel$, $\overline{\phi}_\perp$, and $\overline{\delta}_0$, for the $\overline{M}_0$ decay. Alternatively they can be defined as the six averages of the M_0 and $\overline{M}_0$ parameters and the six differences between M_0 and $\overline{M}_0$ parameters, written below:

$$A_{CP} = \frac{\overline{\Gamma}-\Gamma}{\overline{\Gamma}+\Gamma}\,,$$
$$A_{CP}^L = \frac{\overline{f}_L - f_L}{\overline{f}_L + f_L}\,,$$
$$A_{CP}^\perp = \frac{\overline{f}_\perp - f_\perp}{\overline{f}_\perp + f_\perp}\,, \qquad (12.1.5)$$
$$\Delta\phi_\parallel = \frac{1}{2}(\overline{\phi}_\parallel - \phi_\parallel)\,,$$
$$\Delta\phi_\perp = \frac{1}{2}(\overline{\phi}_\perp - \phi_\perp - \pi)\,,$$
$$\Delta\delta_0 = \frac{1}{2}(\overline{\delta}_0 - \delta_0)\,.$$

The quantity π, introduced in the definition of $\Delta\phi_\perp$, is the phase difference between $A_\perp$ and $\overline{A}_\perp$ if *CP* were conserved. *CP* violation can be established in an angular analysis if one measures a non-zero value for any of these last six parameters.

12.1.6 Time dependence

The transversity basis is most suited to study *CP* violation in time-dependent asymmetries in neutral B decays. Where τ is the B^0 lifetime, Δm_d is the mass difference responsible for the B^0-$\overline{B}^0$ oscillations, and Δt is the proper time difference between the decay times of the two B mesons (see Section 10), the time-evolution for each amplitude is given by:

$$A_L(\Delta t) = A_L(0)\, e^{-im\Delta t}\; e^{-|\Delta t|/2\tau} \times \left(\cos\frac{\Delta m_d \Delta t}{2} + i\eta\lambda_L \sin\frac{\Delta m_d \Delta t}{2}\right),$$
$$A_\parallel(\Delta t) = A_\parallel(0)\, e^{-im\Delta t}\; e^{-|\Delta t|/2\tau} \times \left(\cos\frac{\Delta m_d \Delta t}{2} + i\eta\lambda_\parallel \sin\frac{\Delta m_d \Delta t}{2}\right), \qquad (12.1.6)$$
$$A_\perp(\Delta t) = A_\perp(0)\, e^{-im\Delta t}\; e^{-|\Delta t|/2\tau} \times \left(\cos\frac{\Delta m_d \Delta t}{2} - i\eta\lambda_\perp \sin\frac{\Delta m_d \Delta t}{2}\right).$$

The η parameter equals 1 for B decays and -1 for $\overline{B}$ decays. The parameter λ, introduced in Section 10, may have three values, λ_L, $\lambda_\parallel$, and $\lambda_\perp$, which are in general different from each other. The total amplitude is the sum of the three amplitudes, and the time-dependent total neutral B-meson decay rate is expressed as:

$$\Gamma(\Delta t) = |A_L(\Delta t) + A_\parallel(\Delta t) + A_\perp(\Delta t)|^2 \qquad (12.1.7)$$
$$= |A_L(\Delta t)|^2 + |A_\parallel(\Delta t)|^2 + |A_\perp(\Delta t)|^2 + 2\mathrm{Re}(A_\parallel(\Delta t)A_L^*(\Delta t) + A_\perp(\Delta t)A_L^*(\Delta t) + A_\perp(\Delta t)A_\parallel^*(\Delta t))\,.$$

Thus the time-dependence of the various terms entering the differential decay rate needs to be obtained. Since equivalent expressions describe the two *CP*-even amplitudes A_L and $A_\parallel$, the "+" subscript is used to denote both "L" and "$\parallel$" to minimize the number of relations to be used:

$$
\begin{aligned}
|A_+(\Delta t)|^2 &= |A_+(0)|^2\, e^{-|\Delta t|/\tau}\left(\frac{1+|\lambda_+|^2}{2}\right.\\
&\quad +\frac{1-|\lambda_+|^2}{2}\cos(\Delta m_d\Delta t)\\
&\quad \left.-\eta\,\mathrm{Im}\lambda_+\sin(\Delta m_d\Delta t)\right),\\
|A_\perp(\Delta t)|^2 &= |A_\perp(0)|^2\, e^{-|\Delta t|/\tau}\left(\frac{1+|\lambda_\perp|^2}{2}\right.\\
&\quad +\frac{1-|\lambda_\perp|^2}{2}\cos(\Delta m_d\Delta t)\\
&\quad \left.+\eta\,\mathrm{Im}\lambda_\perp\sin(\Delta m_d\Delta t)\right),\\
A_\parallel(\Delta t)A_L^*(\Delta t) &= A_\parallel(0)A_L^*(0)\, e^{-|\Delta t|/\tau}\left(\frac{1+\lambda_\parallel\lambda_L^*}{2}\right.\\
&\quad +\frac{1-\lambda_\parallel\lambda_L^*}{2}\cos(\Delta m_d\Delta t)\\
&\quad \left.+\frac{i\eta}{2}(\lambda_\parallel-\lambda_L^*)\sin(\Delta m_d\Delta t)\right),\\
A_\perp(\Delta t)A_+^*(\Delta t) &= A_\perp(0)A_+^*(0)\, e^{-|\Delta t|/\tau}\left(\frac{1-\lambda_\perp\lambda_+^*}{2}\right.\\
&\quad +\frac{1+\lambda_\perp\lambda_+^*}{2}\cos(\Delta m_d\Delta t)\\
&\quad \left.-\frac{i\eta}{2}(\lambda_\perp+\lambda_+^*)\sin(\Delta m_d\Delta t)\right).
\end{aligned}
\tag{12.1.8}
$$

These general expressions are rather complex. However, they can be simplified under certain assumptions. If the final state interactions can be neglected, the three parameters, λ_L, $\lambda_\parallel$ and $\lambda_\perp$ are equal to a common value λ. If direct *CP*-violation effects can also be neglected, λ satisfies $|\lambda| = 1$. The expressions for the time-dependent terms then become:

$$
\begin{aligned}
&|A_+(\Delta t)|^2 = |A_+(0)|^2\, e^{-|\Delta t|/\tau}\,(1-\eta\,\mathrm{Im}\lambda\sin(\Delta m_d\Delta t))\,,\\
&|A_\perp(\Delta t)|^2 = |A_\perp(0)|^2\, e^{-|\Delta t|/\tau}\,(1+\eta\,\mathrm{Im}\lambda\sin(\Delta m_d\Delta t))\,,\\
&\mathrm{Re}(A_\parallel(\Delta t)A_L^*(\Delta t)) =\\
&\quad \mathrm{Re}(A_\parallel(0)A_L^*(0))\, e^{-|\Delta t|/\tau}\,(1-\eta\,\mathrm{Im}\lambda\sin(\Delta m_d\Delta t))\,,\\
&\mathrm{Im}(A_\perp(\Delta t)A_+^*(\Delta t)) =\\
&\quad \mathrm{Im}(A_\perp(0)A_+^*(0))\, e^{-|\Delta t|/\tau}\cos(\Delta m_d\Delta t)\\
&\quad -\mathrm{Re}(A_\perp(0)A_+^*(0))\, e^{-|\Delta t|/\tau}\eta\mathrm{Re}\lambda\sin(\Delta m_d\Delta t)\,.
\end{aligned}
\tag{12.1.9}
$$

In the case of the $B \to K^*J/\psi$ decay mode, where $\lambda = e^{2i\beta}$, the first three terms of Eq. (12.1.9) have the usual $\mathrm{Im}\lambda = \sin 2\beta$ coefficient in front of $\sin(\Delta m_d\Delta t)$, while the last term introduces a $\mathrm{Re}\lambda = \cos 2\beta$ coefficient, allowing one to resolve an ambiguity on the measurement of β (Aubert, 2005c), as discussed in Section 17.6.

12.2 List of modes

The common decay modes are reviewed here according to the type of the particles M_0, M_1, M_2 and, when relevant, the daughters of M_1 and M_2. In the title of the subsections, P, V, and T stand for pseudoscalar, vector, and tensor mesons, respectively, while $l(\gamma)$ is for a lepton (photon). When two vector mesons with different decay types are present, they are labeled V_1 and V_2.

For each mode, the expressions governing the angular distributions are given. The procedure to derive the formulae can be found elsewhere (Chung, 1971; Richman, 1984).

12.2.1 $V \to PP$

Let us start with the simple case of a vector meson decaying to two pseudoscalar mesons. The distribution of the helicity angle θ_1 of the vector meson depends upon the polarization of the vector meson.

For longitudinal polarization, the distribution is given by:

$$\frac{1}{\Gamma}\,\frac{d\Gamma}{d\cos\theta_1} = \frac{3}{2}\cos^2\theta_1\,. \tag{12.2.1}$$

For transverse polarization, the expression is the following:

$$\frac{1}{\Gamma}\,\frac{d\Gamma}{d\cos\theta_1} = \frac{3}{4}\sin^2\theta_1\,. \tag{12.2.2}$$

The latter case applies to the decay $\Upsilon(4S) \to B\overline{B}$, as the $\Upsilon(4S)$ vector meson produced in e^+e^- collisions through a virtual photon is transversely polarized. Hence the angle of the B-meson direction with respect to the beam axis at the B Factories is governed by Eq. (12.2.2).

12.2.2 $P \to VP$, $V \to PP$

The case of a pseudoscalar meson decaying to a pseudoscalar meson and a vector meson, which then decays to two pseudoscalar mesons, is found for example in the following modes:

- $B \to \rho\pi$, with $\rho \to \pi\pi$,
- $B \to D^*\pi$, with $D^* \to D\pi$,
- $B \to D^*D$, with $D^* \to D\pi$.

This case was briefly mentioned in Section 12.1. Here there is no degree of freedom. As the helicity of the pseudoscalar meson is 0, the helicity of the vector meson must also be 0: it is then known that the vector meson is longitudinally polarized. Hence the distribution of the θ_1 angle is determined: it follows Eq. (12.2.1). In such modes, where the angular distribution is known, the helicity angle can be used in the selection for background rejection.

12.2.3 $P \to V\gamma$, $V \to PP$ and $P \to T\gamma$, $T \to PP$

Similarly, if a pseudoscalar meson decays to a photon and a vector meson, which then decays to two pseudoscalar mesons, as in the mode:

– $B \to K^*\gamma$, with $K^* \to K\pi$,

the vector meson can only have an helicity which is allowed for the photon, *i.e.* ± 1. So it is transversely polarized. Consequently the distribution of the θ_1 angle is given by Eq. (12.2.2).

When applying the same argument to a pseudoscalar meson decaying to a photon and a tensor meson, which then decays to two pseudoscalar mesons, such as:

– $B \to K_2^*(1430)\gamma$, with $K_2^*(1430) \to K\pi$,

it is found that the tensor meson can only have helicity ± 1. In this case the θ_1 angle is distributed according to:

$$\frac{1}{\Gamma}\,\frac{d\Gamma}{d\cos\theta_1} = \frac{15}{4}\sin^2\theta_1\cos^2\theta_1 \ . \tag{12.2.3}$$

12.2.4 $P \to VV$, $V \to PP$

The case of a pseudoscalar meson decaying to two vector mesons, each of them decaying to two pseudoscalar mesons, can be illustrated by the following decay modes:

– $B \to \rho\rho$, with $\rho \to \pi\pi$,
– $B \to K^*\rho$, with $K^* \to K\pi$ and $\rho \to \pi\pi$,
– $B \to K^*\phi$, with $K^* \to K\pi$ and $\phi \to K^+K^-$,
– $B \to D^*K^*$, with $D^* \to D\pi$ and $K^* \to K\pi$,
– $B \to D^*D^*$, with $D^* \to D\pi$.

Both bases have been used to analyse this type of decay. In the helicity basis, the g_i functions of Eq. (12.1.1) have the following angular dependence:

$$\begin{aligned}
g_1 &= \cos^2\theta_1\cos^2\theta_2\,,\\
g_2 &= \frac{1}{4}\sin^2\theta_1\sin^2\theta_2\,,\\
g_3 &= \frac{1}{4}\sin^2\theta_1\sin^2\theta_2\cos 2\phi\,,\\
g_4 &= -\eta\frac{1}{2}\sin^2\theta_1\sin^2\theta_2\sin 2\phi\,,\\
g_5 &= \frac{1}{2\sqrt{2}}\sin 2\theta_1\sin 2\theta_2\cos\phi\,,\\
g_6 &= -\eta\frac{1}{2\sqrt{2}}\sin 2\theta_1\sin 2\theta_2\sin\phi\,.
\end{aligned} \tag{12.2.4}$$

When integrating over the ϕ angle, the last four terms $g_3 - g_6$ disappear and the differential decay rate reduces to the following expression, with f_L as the single parameter:

$$\frac{1}{\Gamma}\,\frac{d^2\Gamma}{d\cos\theta_1 d\cos\theta_2} = \frac{9}{4}\left(f_L\cos^2\theta_1\cos^2\theta_2 + (1-f_L)\frac{1}{4}\sin^2\theta_1\sin^2\theta_2\right)\ . \tag{12.2.5}$$

In the transversity basis the corresponding g_i^{tr} functions appearing in Eq. (12.1.3) are:

$$\begin{aligned}
g_1^{tr} &= \cos^2\theta_1\sin^2\theta_{tr}\cos^2\phi_{tr}\,,\\
g_2^{tr} &= \frac{1}{2}\sin^2\theta_1\sin^2\theta_{tr}\sin^2\phi_{tr}\,,\\
g_3^{tr} &= \frac{1}{2}\sin^2\theta_1\cos^2\theta_{tr}\,,\\
g_4^{tr} &= -\eta\frac{1}{2}\sin^2\theta_1\sin 2\theta_{tr}\sin\phi_{tr}\,,\\
g_5^{tr} &= \frac{1}{2\sqrt{2}}\sin 2\theta_1\sin^2\theta_{tr}\sin 2\phi_{tr}\,,\\
g_6^{tr} &= -\eta\frac{1}{2\sqrt{2}}\sin 2\theta_1\sin 2\theta_{tr}\cos\phi_{tr}\,.
\end{aligned} \tag{12.2.6}$$

After integrating over the ϕ_{tr} angle, the last three terms disappear and the differential decay rate simplifies to:

$$\frac{1}{\Gamma}\,\frac{d^2\Gamma}{d\cos\theta_1 d\cos\theta_{tr}} = \frac{9}{8}\Big(f_L\cos^2\theta_1\sin^2\theta_{tr} + f_\parallel\frac{1}{2}\sin^2\theta_1\sin^2\theta_{tr} + f_\perp\sin^2\theta_1\cos^2\theta_{tr}\Big)\,. \tag{12.2.7}$$

This expression allows the extraction of the fraction of the three amplitudes. Figure 12.2.1 illustrates, in the case of the $B^0 \to D^{*+}D^{*-}$ analysis (Miyake, 2005), the sine square (cosine square) dependence on θ_{tr} of the A_L and $A_\parallel$ amplitudes ($A_\perp$ amplitude) and the cosine square (sine square) dependence on θ_1 of the A_L amplitude ($A_\parallel$ and $A_\perp$ amplitudes).

The following expression, depending only on the fraction $f_\perp$ of the *CP*-odd amplitude, is obtained by integrating also over the θ_1 angle:

$$\frac{1}{\Gamma}\,\frac{d\Gamma}{d\cos\theta_{tr}} = \frac{3}{4}\Big((1-f_\perp)\sin^2\theta_{tr} + 2f_\perp\cos^2\theta_{tr}\Big)\,. \tag{12.2.8}$$

12.2.5 $P \to VV$, $V_1 \to P\gamma$, $V_2 \to PP$

Vector-vector final states, where one vector meson decays to a pseudoscalar meson and a photon and the other one to two pseudoscalar mesons, include:

– $B \to D^*K^*$, with $D^* \to D\gamma$ and $K^* \to K\pi$,
– $B \to D_s^*\rho$, with $D_s^* \to D_s\gamma$ and $\rho \to \pi\pi$,
– $B \to D_s^*D^*$, with $D_s^* \to D_s\gamma$ and $D^* \to D\pi$,
– $B_s \to D_s^*\rho$, with $D_s^* \to D_s\gamma$ and $\rho \to \pi\pi$.

Here the helicity basis is used and the differential decay rate, integrated over the ϕ angle, is expressed as:

$$\frac{1}{\Gamma}\,\frac{d^2\Gamma}{d\cos\theta_1 d\cos\theta_2} = \frac{9}{4}\left(f_L\sin^2\theta_1\cos^2\theta_2 + (1-f_L)\frac{1}{4}(1+\cos^2\theta_1)\sin^2\theta_2\right)\,. \tag{12.2.9}$$

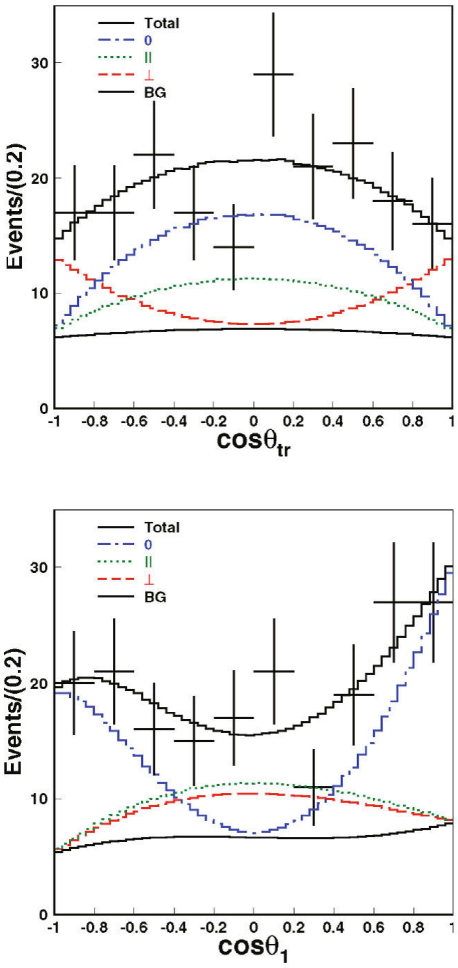

Figure 12.2.1. Angular distributions in the transversity frame for (top) $\cos\theta_{tr}$ and (bottom) $\cos\theta_1$, shown in the example of the $B^0 \to D^{*+}D^{*-}$ analysis (Miyake, 2005). The points with error bars represent the data. The dot-dashed, dotted, and dashed lines correspond to the A_L, $A_\parallel$, and $A_\perp$ amplitudes respectively. The lower solid line is the background (BG), while the upper solid line shows the sum of all contributions. The asymmetry in the $\cos\theta_1$ distribution is due to an inefficiency for low momentum track reconstruction.

12.2.6 $P \to VV$, $V \to P\gamma$

An example of a vector-vector final state, where both vector mesons decay to a pseudoscalar meson and a photon, is:

– $B_s \to D_s^* D_s^*$, with $D_s^* \to D_s\gamma$.

The differential decay rate in the helicity basis, integrated over the ϕ angle, is:

$$\frac{1}{\Gamma}\,\frac{d^2\Gamma}{d\cos\theta_1 d\cos\theta_2} = \frac{9}{4}\Big(f_L \sin^2\theta_1 \sin^2\theta_2 + (1-f_L)\frac{1}{4}(1+\cos^2\theta_1)(1+\cos^2\theta_2)\Big)\,. \tag{12.2.10}$$

12.2.7 $P \to VV$, $V_1 \to PP$, $V_2 \to ll$

In the case of a B-meson decay to two vector mesons, where M_1 decays to two pseudoscalar mesons and M_2 decays to two leptons, the transversity basis is used. An example of this is $B \to K^*\psi$, with $K^* \to K\pi$ and $\psi \to e^+e^-$, where ψ is either J/ψ or $\psi(2S)$. The g_i^{tr} functions have the following angular dependence:

$$\begin{aligned}
g_1^{tr} &= \frac{1}{2}\cos^2\theta_1(1-\sin^2\theta_{tr}\cos^2\phi_{tr})\,,\\
g_2^{tr} &= \frac{1}{4}\sin^2\theta_1(1-\sin^2\theta_{tr}\sin^2\phi_{tr})\,,\\
g_3^{tr} &= \frac{1}{4}\sin^2\theta_1\sin^2\theta_{tr}\,,\\
g_4^{tr} &= \eta\frac{1}{4}\sin^2\theta_1\sin 2\theta_{tr}\sin\phi_{tr}\,,\\
g_5^{tr} &= -\frac{1}{4\sqrt{2}}\sin 2\theta_1\sin^2\theta_{tr}\sin 2\phi_{tr}\,,\\
g_6^{tr} &= \eta\frac{1}{4\sqrt{2}}\sin 2\theta_1\sin 2\theta_{tr}\cos\phi_{tr}\,.
\end{aligned} \tag{12.2.11}$$

12.2.8 $P \to VV$, $V_1 \to PP$, $V_2 \to V\gamma$

The case of a B-meson decay to two vector mesons, where M_1 decays to two pseudoscalar mesons and M_2 decays to a vector meson and a photon, is illustrated by the decay $B \to K^*\chi_{c1}$, with $K^* \to K\pi$ and $\chi_{c1} \to J/\psi\gamma$. The transversity basis is used in this case. The g_i^{tr} functions have the following angular dependence:

$$\begin{aligned}
g_1^{tr} &= \frac{1}{2}\cos^2\theta_1(1+\sin^2\theta_{tr}\cos^2\phi_{tr})\,,\\
g_2^{tr} &= \frac{1}{4}\sin^2\theta_1(1+\sin^2\theta_{tr}\sin^2\phi_{tr})\,,\\
g_3^{tr} &= \frac{1}{4}\sin^2\theta_1(2\cos^2\theta_{tr}+\sin^2\theta_{tr})\,,\\
g_4^{tr} &= -\eta\frac{1}{4}\sin^2\theta_1\sin 2\theta_{tr}\sin\phi_{tr}\,,\\
g_5^{tr} &= -\frac{1}{4\sqrt{2}}\sin 2\theta_1\sin^2\theta_{tr}\sin 2\phi_{tr}\,,\\
g_6^{tr} &= -\eta\frac{1}{4\sqrt{2}}\sin 2\theta_1\sin 2\theta_{tr}\cos\phi_{tr}\,.
\end{aligned} \tag{12.2.12}$$

12.2.9 $P \to TV$, $T \to PP$, $V \to PP$

The mode $B \to K_2^*(1430)\phi$, with $K_2^*(1430) \to K\pi$ and $\phi \to K^+K^-$, is an example of a pseudoscalar meson decaying to a tensor and a vector meson, each of them decaying to two pseudoscalar mesons. In the helicity basis the g_i functions have the following angular dependence (Datta et al., 2008):

$$\begin{aligned} g_1 &= \frac{5}{12}(3\cos^2\theta_1 - 1)^2\cos^2\theta_2\,, \\ g_2 &= \frac{5}{4}\cos^2\theta_1\sin^2\theta_1\sin^2\theta_2\,, \\ g_3 &= \frac{5}{4}\cos^2\theta_1\sin^2\theta_1\sin^2\theta_2\cos 2\phi\,, \\ g_4 &= -\eta\frac{5}{2}\cos^2\theta_1\sin^2\theta_1\sin^2\theta_2\sin 2\phi\,, \\ g_5 &= \frac{5}{8\sqrt{6}}(3\cos^2\theta_1 - 1)\sin 2\theta_1\sin 2\theta_2\cos\phi\,, \\ g_6 &= -\eta\frac{5}{8\sqrt{6}}(3\cos^2\theta_1 - 1)\sin 2\theta_1\sin 2\theta_2\sin\phi\,. \end{aligned} \tag{12.2.13}$$

After integrating over the ϕ angle, the four last terms disappear and the differential decay rate depends simply on the parameter f_L:

$$\frac{1}{\Gamma}\,\frac{d^2\Gamma}{d\cos\theta_1 d\cos\theta_2} = \frac{15}{16}\Big(f_L(3\cos^2\theta_1 - 1)^2\cos^2\theta_2 + 3(1 - f_L)\cos^2\theta_1\sin^2\theta_1\sin^2\theta_2\Big)\,. \tag{12.2.14}$$

12.3 Analysis details

12.3.1 Generators

In order to perform an angular analysis it is important to have simulated data with the correct angular distributions. This allows one to calculate, for example, the correct efficiencies on the signal (see the next subsection) and to study how well (with how much bias) the angular fits described in Section 12.4 can extract the fitted parameters.

Here is a brief explanation of how this is achieved in the `EvtGen` event generator (Lange, 2001) introduced in Chapter 3. The crucial point is that decay amplitudes, and not probabilities, are used for each step in the generation of a decay chain. This allows one to include all angular correlations in the entire decay chain. Each particle is described according to the value of its spin and mass by an object with the corresponding number of degrees of freedom. Each decay in the decay chain is handled by a specific model taking into account the spin of the initial and final state particles. Relevant parameters can be given as arguments to the decay model. For example in the case of the model describing the decay of a scalar to two vector mesons, the six arguments are the magnitude and the phase of the three helicity amplitudes.

12.3.2 Experimental effects

A large number of angular analyses require cuts on the helicity angles, θ_i ($i = 1$ or 2), as the region at high values of $|\cos\theta_i|$, which usually corresponds to soft decay products, has a rapidly changing efficiency and may be dominated by background. The cut may be asymmetric if the decay products are different. For example, if one of the decay products is a ρ^+ vector meson, decaying subsequently into $\pi^+\pi^0$, the kinematics of the ρ^+-meson decay are strongly correlated with the value of the relevant helicity angle θ_i. Assuming θ_i was defined with respect to the π^+, high ($\cos\theta_i \sim 1$), medium ($\cos\theta_i \sim 0$), and low ($\cos\theta_i \sim -1$) values correspond respectively to a decay with a hard π^+ and a soft π^0, two pions of similar momentum, and a hard π^0 and a soft π^+ in the laboratory frame. Since there is usually a huge background of low momentum π^0s, an upper cut on $\cos\theta_i$ in this case sould be tighter than a lower cut in order to reduce the soft π^0 background.

For the same reason, the reconstruction efficiency depends upon the fraction of longitudinal polarization. Defining ϵ_L (ϵ_T) as the reconstruction efficiency obtained if the signal was completely longitudinally (transversely) polarized, *i.e.* $f_L = 1$ ($f_L = 0$), ϵ_L and ϵ_T would be different, usually with $\epsilon_L < \epsilon_T$. This effect has to be taken into account to correct the measured raw value $f_L^{\rm meas}$ of the fraction of longitudinal polarization to obtain the true longitudinal polarization fraction:

$$f_L = \frac{f_L^{\rm meas}}{f_L^{\rm meas} + (1 - f_L^{\rm meas})\frac{\epsilon_L}{\epsilon_T}}\,. \tag{12.3.1}$$

Similarly, the rate of mis-reconstructed signal events depends on the value of the fraction of longitudinal polarization.

In the various analyses, the efficiency is often modeled as a function of $\cos\theta_i$ ($i = 1$ or 2) with an appropriate function $A(\cos\theta_i)$. Figure 12.3.1 illustrates the efficiency function in the case of the $B^0 \to \phi K^{*0}$ analysis (Aubert, 2008bf). This otherwise smooth function shows some sharp dips due to D meson vetoes (special cuts applied in the analysis in order to reject the background coming from a D meson decay), as seen in Figure 12.3.1(a) near $\cos\theta_1 = 0.8$.

12.3.3 Caveats

Here is a discussion of some technical points that should be considered in specific angular analyses.

When studying decays with identical particles in the final state, the formulae need to be symmetrized. For example the $B^0 \to \rho^0\rho^0 \to (\pi^+\pi^-)(\pi^+\pi^-)$ decay has four bosons, identical by pairs, in the final state. In this case the amplitude $A(p_1^+, p_1^-, p_2^+, p_2^-)$, as a function of the four-momenta, p_1^+, p_2^+, p_1^-, and p_2^-, of the two π^+ and the two π^-, has to be replaced by the symmetrized amplitude under the permutations $p_1^+ \to p_2^+$ and $p_1^- \to p_2^-$.

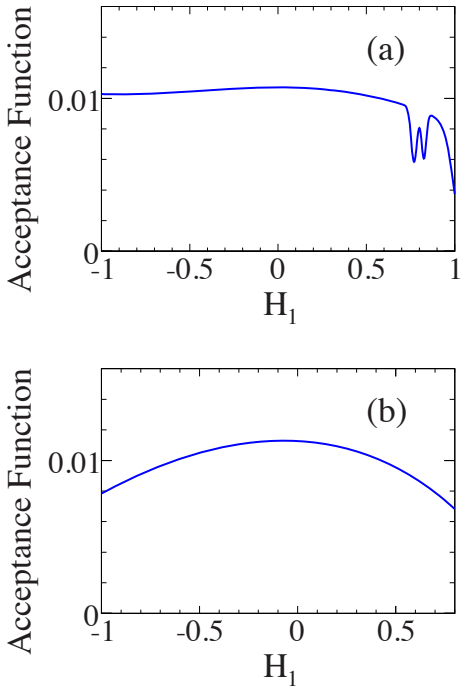

Figure 12.3.1. Angular efficiency functions for $H_1 = \cos\theta_1$ (here θ_1 is the angle associated with the $K\pi$ system) in the cases of (a) $B^0 \to \phi K^{\pm}\pi^{\mp}$ and (b) $B^0 \to \phi K^0_s\pi^0$ (Aubert, 2008bf). The wiggles in the upper plot are due to the D meson vetoes.

When performing a multi-variable maximum likelihood fit, care has to be taken for correlations between variables. In particular, continuum events tend to have correlations between the masses of the reconstructed M_i ($i = 1$ or 2) candidates and the cosine of their helicity angles. A solution is to use a two-dimensional probability density function in this case.

12.4 Angular fits

In this section, the various types of angular fits which have been performed are quickly reviewed.

12.4.1 Dedicated or global fits

Two strategies are possible:

- The signal yield is first extracted using variables such as $m_{\rm ES}$ and ΔE. Second, only the angular variables are fitted to extract the polarization information. Where appropriate, time-dependent information can be obtained in a third step.
- A single maximum likelihood fit is performed using the signal selection variables, as well as the angular variables, and any relevant time-dependence. The polarization parameters are determined in the fit at the same time as other parameters such as signal yields.

The angular parameters can usually be extracted in time-integrated analyses. Numerous results in various decay modes are given in this book, in particular in Section 17.4. The time-dependence, when used, is added essentially to study *CP* violation, as shown in Sections 17.6 and 17.7.

The angular information is also used in Dalitz analyses, through either the helicity formalism or Zemach tensors, as described in Chapter 13.

12.4.2 Partial and complete angular analyses

Most angular analyses integrate over the angle ϕ, for which the acceptance in the B Factory detectors is uniform, to determine the fraction of longitudinally polarized events: f_L. The helicity basis is the natural one to use in this case, as the two daughters are treated symmetrically. The formulae to fit have been given in Section 12.2 for different cases:

- Eq. (12.2.5) for $P \to VV$, $V \to PP$,
- Eq. (12.2.9) for $P \to VV$, $V_1 \to P\gamma$, $V_2 \to PP$,
- Eq. (12.2.10) for $P \to VV$, $V \to P\gamma$,
- Eq. (12.2.14) for $P \to TV$, $T \to PP, V \to PP$.

Partial angular analyses have been performed to measure f_L in a large number of decay modes, such as $B \to \rho\rho$, $B \to K^*\rho$, and $B \to D^*K^*$. In some cases, the angular analysis is performed to disentangle the *CP*-even and *CP*-odd components. In that case, $f_\perp$ has to be measured and the transversity basis is more suited for such a partial angular analysis. If the decay is dominated by the *CP*-even longitudinal polarization, however, one can effectively use either basis and deal with the small transverse component when addressing systematic uncertainties. If no attempt is made to disentangle the *CP*-even and *CP*-odd components, the mixture of these two components results in a dilution of the *CP* asymmetry.

Finally, in a limited number of channels, a complete angular fit has been performed to measure not only the fractions of the three amplitudes, but also the relative phases between them. Of course, the complete angular analysis is more difficult than the partial one, as it implies fitting more free parameters. Consequently it requires sufficiently large data samples. Such an analysis has been performed in the B-meson decays to ϕK^*, both in the vector-vector modes ($B^+ \to \phi K^{*+}$ and $B^0 \to \phi K^{*0}$) using either Eq. (12.2.4) or Eq. (12.2.6), and in the vector-tensor mode ($B^0 \to \phi K^{*0}_2(1430)$) using Eq. (12.2.13). More details can be found in (Chen, 2005a), (Aubert, 2007c), and (Aubert, 2008bf). A complete angular analysis was also performed in the B-meson decays to charmonium K^*, according to Eq. (12.2.11) when the charmonium decays to two leptons ($B^+ \to J/\psi K^{*+}$, $B^0 \to J/\psi K^{*0}$, and $B^0 \to \psi(2S)K^{*0}$), and to Eq. (12.2.12) when the charmonium decays to a vector meson and a photon ($B^0 \to \chi_{c1}K^{*0}$). They are documented in (Aubert, 2005c), (Itoh, 2005b), and (Aubert, 2007x).

12.4.3 Other angular analyses

Not all the types of angular analyses have been covered in this chapter and other kinds of angular analyses have also been performed at B Factories. The goal may be to determine the unknown spin of a particle by studying the angular distribution of its decay products. Examples can be found in charmed meson spectroscopy (Section 19.3) and in charmed baryon spectroscopy (Section 19.4). Angular analyses also allow one to study angular asymmetries or correlations, in particular in the case of baryonic decay modes which are presented in Section 17.12, in order to investigate the underlying dynamics of the decay. Finally, in two-photon physics, described in Chapter 22, the angular dependence of the differential cross section for various processes is studied.

Chapter 13
Dalitz-plot analysis

Editors:
Thomas Latham (BABAR)
Anton Poluektov (Belle)

Additional section writers:
Eli Ben-Haim, Mathew Graham, Fernando Martinez-Vidal

13.1 Introduction

Dalitz-plot analysis is a powerful technique that involves studying the amplitude for the decay of a parent particle into a three-body final state. Compared to two-body decays, the three-body decay possesses intrinsic degrees of freedom that permit the determination of the relative magnitudes and phases of interfering amplitudes. The types of measurements that can benefit from using the Dalitz-plot analysis technique include:

- Searches for new states;
- Measurements of properties of resonances — masses, widths, quantum numbers;
- *CP* violation searches and measurements of the associated parameters;
- Studies of flavor mixing.

This chapter starts with a discussion of the kinematics of three-body decays (Sections 13.1.1 and 13.1.2) before describing the formalisms commonly used to model the three-body decay amplitude (Section 13.2). This is followed by an outline of the experimental effects that must also be accounted for in order to successfully describe the distribution of the data over the Dalitz plot (Section 13.3). Technical details of the implementation are presented in Section 13.4 before a discussion of the uncertainties arising from the chosen model (Section 13.5).

13.1.1 Three-body decay phase space

In the case of a two-body decay, the energies of the final state particles in the center-of-mass frame are fully determined by the conservation of energy and momentum, up to an overall rotation. In contrast, the kinematics of three-body decays are not similarly constrained: after requiring energy and momentum conservation in the system of three final state particles, there are five remaining degrees of freedom. In the case where the initial and final state particles all have spin zero, after taking into account arbitrary rotations, two degrees of freedom remain. The amplitude of the decay can thus be represented as a function of two parameters; the scatter plot of this pair of parameters is called the Dalitz plot (Dalitz distribution).

There is freedom in the choice of which two parameters one uses to describe the amplitude of a three-body decay. It is often convenient to choose a pair of parameters where the phase-space term is constant within the kinematically allowed region in the two-dimensional space spanned by these variables. In this case the structure of the amplitude becomes apparent. This can be achieved by taking either the kinetic energies of two of the final-state particles, or the squares of the invariant masses of two pairs of final-state particles. The former parameterization is convenient for nonrelativistic decays and was originally proposed by R. H. Dalitz to study the decay of charged kaons to three pions (Dalitz, 1953). The corresponding relativistic formulation was first introduced in Fabri (1954). However, the latter approach is generally more suitable for relativistic decays and has an additional advantage that it allows for easy determination of the masses of intermediate states. For a particle of mass M decaying into three particles denoted as a, b and c, the differential decay probability is

$$d\Gamma = \frac{1}{(2\pi)^3}\frac{1}{32M^3}|\mathcal{A}|^2 dm_{ab}^2 dm_{bc}^2\,, \tag{13.1.1}$$

where m_{ab} and m_{bc} are the invariant masses of the pairs of particles ab and bc, respectively. Thus, any nonuniformity observed in the distribution of the variables m_{ab}^2 and m_{bc}^2 is due to the dynamical structure of the decay amplitude $\mathcal{A}$. Most of the analyses performed at the B Factories deal with the Dalitz plot expressed this way; the exception to this will be considered in Section 13.4.1.

13.1.2 Boundaries, kinematic constraints

The invariant masses of pairs of final-state particles are related by the linear dependence:

$$m_{ab}^2 + m_{bc}^2 + m_{ac}^2 = M^2 + m_a^2 + m_b^2 + m_c^2. \tag{13.1.2}$$

The range of invariant masses m_{bc}^2 can be written in terms of either one of the other squared invariant masses (*e.g.*, m_{ab}^2):

$$\begin{aligned}(m_{bc}^2)_{\max} &= (E_b^* + E_c^*)^2 - (p_b^* - p_c^*)^2\,,\\ (m_{bc}^2)_{\min} &= (E_b^* + E_c^*)^2 - (p_b^* + p_c^*)^2\,,\end{aligned} \tag{13.1.3}$$

where

$$E_b^* = \frac{m_{ab}^2 - m_a^2 + m_b^2}{2m_{ab}}\,,\quad E_c^* = \frac{M^2 - m_{ab}^2 - m_c^2}{2m_{ab}}\,, \tag{13.1.4}$$

are the energies of particles b and c in the ab rest frame and

$$p_b^* = \sqrt{E_b^{*2} - m_b^2}\,,\quad p_c^* = \sqrt{E_c^{*2} - m_c^2}\,, \tag{13.1.5}$$

are the corresponding momenta.

The region of kinematically allowed phase space described by these constraints is shown in Fig. 13.1.1. The points on the boundary of the phase space correspond to the configurations where the final state particles are collinear. In particular, three extreme points where m_{ab}^2, m_{bc}^2, or m_{ac}^2 are maximal, correspond to the configurations with one of the particles produced at rest (in the frame of the decaying particle).

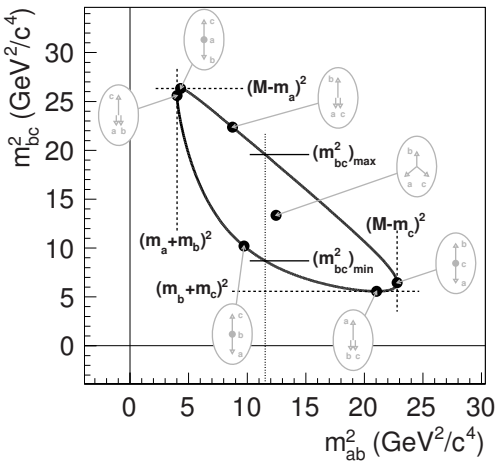

Figure 13.1.1. Kinematic boundaries of the three-body decay phase space and illustration of various kinematic configurations of the final-state particles for characteristic Dalitz plot points. In this example, the $B^0 \to \pi^- \overline{D}{}^0 K^+$ phase space is shown; $a = \pi^-$, $b = \overline{D}{}^0$, $c = K^+$.

13.2 Amplitude description

Experimental data show that nonleptonic three-body B and D decays proceed predominantly through resonant two-body decays. For three-body decays of a spin-zero particle P (*e.g.*, a D or B meson) to pseudoscalar final-state particles abc, the baseline model commonly adopted to describe the decay amplitude $\mathcal{A}(m^2_{ab}, m^2_{bc})$ consists of a coherent sum of two-body amplitudes (subscript r) and a "nonresonant" (subscript NR) contribution (Beringer et al., 2012),

$$\mathcal{A}(\mathbf{m}) = \sum_r a_r e^{i\phi_r} \mathcal{A}_r(\mathbf{m}) + a_{\rm NR} e^{i\phi_{\rm NR}} \mathcal{A}_{\rm NR}(\mathbf{m})\,. \quad (13.2.1)$$

The parameters a_r ($a_{\rm NR}$) and ϕ_r ($\phi_{\rm NR}$) are the magnitude and phase of the amplitude for component r (NR). The functions $\mathcal{A}_r$ and $\mathcal{A}_{\rm NR}$ are Lorentz-invariant expressions that describe the dynamical properties of the decay into the multi-body final state as a function of position in the Dalitz plot $\mathbf{m} \equiv (m^2_{ab}, m^2_{bc})$. When the final state contains identical particles, *e.g.* $D^+ \to \pi^+\pi^+\pi^-$ or $B^0 \to K^0_S K^0_S K^0_S$, it is important that the total amplitude $\mathcal{A}(\mathbf{m})$ is correctly symmetrized with respect to exchange of those particles.

The most common ways to parameterize the functions $\mathcal{A}_r$ are reviewed in the following Sections 13.2.1 and 13.2.2. The parameterizations of nonresonant amplitude are discussed in Section 13.2.3. Section 13.2.4 discusses a special case of time-dependent amplitude analyses.

13.2.1 Isobar formalism

The isobar formalism (or isobar model) is so-called because it was first used to describe pion-nucleon, nucleon-nucleon, and antinucleon-nucleon interactions (Sternheimer and Lindenbaum, 1961). In such reactions the intermediate resonances are isobars of a particular nuclear state. The isobar model was later generalized to any three-body final state (Herndon, Soding, and Cashmore, 1975).

In this formalism, the function $\mathcal{A}_r$ describes the decay through a single intermediate resonance r and takes the form

$$\mathcal{A}_r = F_P \times F_r \times T_r \times W_r, \quad (13.2.2)$$

where $T_r \times W_r$ is the resonance propagator (T_r is the dynamical function for the resonance r, while W_r describes the angular distribution of the decay), F_P and F_r are the transition form factors of the parent particle and resonance, respectively. In what follows, we assume that the resonance is produced in the ab channel. In that case the particle c will be referred to as the bachelor particle. Naturally, the full amplitude $\mathcal{A}$ may contain contributions of resonances in any of the ab, ac, and bc channels.

The dynamical function T_r is commonly described using a relativistic Breit-Wigner (BW) parameterization with mass-dependent width (see, *e.g.*, review on Dalitz plot analysis formalism on p. 889 in Beringer et al. (2012))

$$T_r = \frac{1}{m_r^2 - m_{ab}^2 - i m_r \Gamma_{ab}}\,. \quad (13.2.3)$$

Here m_r is the mass of the resonance, and the mass-dependent width Γ_{ab} is given by

$$\Gamma_{ab} = \Gamma_r \left(\frac{q_{ab}}{q_r}\right)^{2J+1} \left(\frac{m_r}{m_{ab}}\right) F_r^2\,, \quad (13.2.4)$$

where Γ_r and J are the width and spin of the resonance, q_{ab} is the momentum of the daughter particles in the center-of-mass frame of a and b, and q_r is the momentum the decay products would have in the rest frame of a resonance with mass m_r.

Strictly speaking, the Breit-Wigner parameterization works well only in the case of narrow states. The use of the mass-dependent width results in the amplitude T_r becoming a non-analytic function. An alternative parametrization proposed by Gounaris and Sakurai (GS) (Gounaris and Sakurai, 1968) recovers the analyticity of the amplitude and provides a better description for broad vector resonances such as $\rho(770)$ and $\rho(1450)$.

For resonances such as the $f_0(980) \to \pi\pi$ that lie close to the threshold of another channel ($f_0(980) \to KK$ in this case), the effect of the opening of the second channel must be taken into account, for example, by employing the Flatté coupled-channel form (Flatte, 1976),

$$T_r = \frac{g_1}{m_r^2 - m_{ab}^2 - i(\rho_1 g_1^2 + \rho_2 g_2^2)}\,, \quad (13.2.5)$$

where ρ_1, ρ_2 and g_1, g_2 are the phase-space factors and coupling constants of the $\pi\pi$ and KK channels, respectively.

Values of the mass and width of resonances are in general taken from world averages (Beringer et al., 2012).

Since different parameterizations of the resonance lineshapes, especially for broad resonances, often give different values, one has to make sure that the values used in the fit were extracted using the same parameterization as in the model. If the resonance is apparent and systematic biases (or external errors) of its parameters are expected to be larger than their statistical errors from the fit, the mass and width can be left unconstrained.

The angular dependence W_r is described using either Zemach tensors (Zemach, 1964, 1965), where transversality is enforced, or the helicity formalism (Bonvicini et al., 2008; Jacob and Wick, 1959), which allows for a longitudinal component in the resonance propagator (see Beringer et al. (2012) for a comprehensive summary). The expressions for scalar, vector and tensor states are

$$\begin{aligned} J=0: &\quad W_r = 1\,, \\ J=1: &\quad W_r = m_{ac}^2 - m_{bc}^2 - \frac{(M^2-m_c^2)(m_a^2-m_b^2)}{m_r^2}\,, \\ J=2: &\quad W_r = \left[m_{bc}^2 - m_{ac}^2 + \frac{(M^2-m_c^2)(m_a^2-m_b^2)}{m_r^2}\right]^2 - \\ &\qquad \frac{1}{3}\left[m_{ab}^2 - 2M^2 - 2m_c^2 + \frac{(M^2-m_c^2)^2}{m_r^2}\right]\times \\ &\qquad \left[m_{ab}^2 - 2m_a^2 - 2m_b^2 + \frac{(m_a^2-m_b^2)^2}{m_r^2}\right]. \end{aligned} \tag{13.2.6}$$

Transversality is enforced by substituting m_{ab}^2 for m_r^2 in the denominators of the previous expressions. This leads to the alternative expressions

$$\begin{aligned} J=0: &\quad W_r = 1, \\ J=1: &\quad W_r = -2\,(\boldsymbol{p}\cdot\boldsymbol{q})\,, \\ J=2: &\quad W_r = \frac{4}{3}\left[3\,(\boldsymbol{p}\cdot\boldsymbol{q})^2 - (|\boldsymbol{p}|\,|\boldsymbol{q}|)^2\right], \end{aligned} \tag{13.2.7}$$

where $\boldsymbol{q}$ and $\boldsymbol{p}$ are the momenta of one of the resonance daughters and the bachelor particle, respectively, evaluated in the rest frame of the resonance. The decision as to which daughter to choose is a matter of convention and it is very important that this choice be documented since it affects the interpretation of the relative phases. The angle between $\boldsymbol{q}$ and $\boldsymbol{p}$ is known as the helicity angle (see also Section 12.1) and $\boldsymbol{p}\cdot\boldsymbol{q}$ is proportional to the cosine of the helicity angle $\cos\theta_H$. The Zemach expressions are essentially Legendre polynomials of $\cos\theta_H$ multiplied by coefficients that contain the momenta of the daughter and bachelor particles raised to the power J.

The form factors F_P and F_r usually use the Blatt-Weisskopf parameterization for the decay vertex (Blatt and Weisskopf, 1952). The expressions for the Blatt-Weisskopf penetration factors depend on the spin J of the intermediate resonance

$$\begin{aligned} J=0: &\quad F = 1 \\ J=1: &\quad F = \sqrt{\frac{1+R^2q_r^2}{1+R^2q_{ab}^2}} \\ J=2: &\quad F = \sqrt{\frac{9+3R^2q_r^2+R^4q_r^4}{9+3R^2q_{ab}^2+R^4q_{ab}^4}}\,, \end{aligned} \tag{13.2.8}$$

where R is the radial parameter of the decaying meson and typically takes values between 1 and 5 $(\mathrm{GeV})^{-1}$. In this prescription, F is normalized so that $F=1$ for $q_r = q_{ab}$.

While the P- and D-waves of the decay amplitude are usually well described using a certain number of BW or GS propagators, the actual number depending on the specific decay, the S-wave typically contains a number of broad overlapping states, for which the isobar model gives a poor description. In that case, more complex alternatives have been adopted, which are reviewed in Section 13.2.2.

Figure 13.2.1 illustrates how various intermediate two-body states appear in the Dalitz plot. Unlike the uniform distribution of the phase-space decay (Fig. 13.2.1(a)), scalar resonances appear as bands in the Dalitz plot, as shown in Fig. 13.2.1(b-d) for resonances in bc, ac, and ab channels, respectively. Angular distributions for vector and tensor intermediate states introduce characteristic non-uniformity of the event density along the resonance bands (Fig. 13.2.1(e,f)). Finally, the region where the amplitudes of two resonances overlap is sensitive to the phase difference between the two amplitudes (Fig. 13.2.1(g,h)).

13.2.2 K-matrix formalism

The complex S-wave dynamics, which can also include the presence of several broad and overlapping scalar resonances, can alternatively be described through the use of a K-matrix formalism (Chung et al., 1995; Wigner, 1946) with the production vector (P-vector) approximation (Aitchison, 1972). Within this formalism, the production process described by the P-vector can be viewed as the initial formation of several states, which are then propagated by the K-matrix term into the final state that is observed. This approach ensures that the two-body scattering matrix respects unitarity, which is not guaranteed in the case of the isobar model. At the B Factories this approach is most commonly used to describe the $\pi^+\pi^-$ S-wave contribution to the Dalitz-plot amplitude, *e.g.* in the *BABAR* analyses (Aubert, 2008l, 2009h; del Amo Sanchez, 2010a,b) and Belle analysis (Abe, 2007b). In such cases the amplitude is given by

$$\mathcal{A}_u(s) = \sum_v \left[I - iK(s)\rho(s)\right]^{-1}_{uv} P_v(s)\,, \tag{13.2.9}$$

where $s \equiv m_{ab}^2$ is the $\pi^+\pi^-$ invariant mass, I is the identity matrix, K is the matrix describing the scattering process, ρ is the diagonal phase-space matrix, and P is the production vector. The indices u and v represent the production and scattering channels, respectively, and take the values 1 to 5, where $1=\pi\pi$, $2=K\overline{K}$, $3=\pi\pi\pi\pi$, $4=\eta\eta$, $5=\eta\eta'$. Hence in the case of describing the $\pi^+\pi^-$ amplitude $u=1$. The propagator can be described using scattering data, provided that the two-body system in the final state is isolated and does not interact with the rest of the final state in the production process.

The parameterizations adopted for the K, ρ, and P terms in Eq. (13.2.9) by the B Factories are the same as those used by previous analyses (Anisovich and Sarantsev,

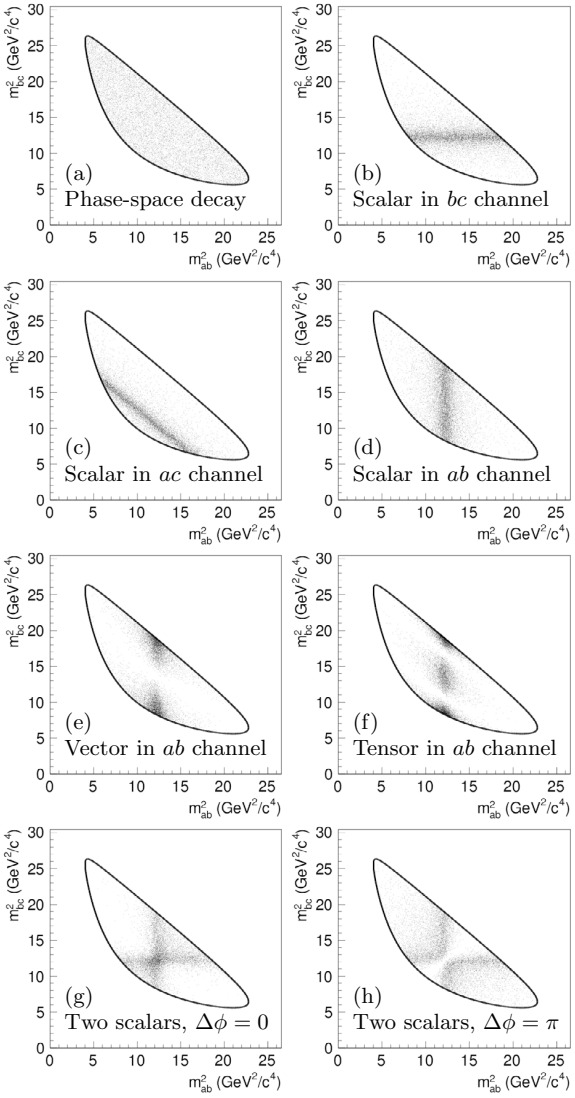

Figure 13.2.1. Example Dalitz plots with (a) phase-space decay, (b-d) one scalar resonance appearing in various decay channels, (e, f) vector and tensor resonances, and (g, h) the interference of two scalar resonances with different values of the relative phase $\Delta\phi$.

2003; Link et al., 2004a), up to some sign conventions and constant terms. The K-matrix is formulated as

$$K_{uv}(s) = \left(\sum_{\alpha} \frac{g_u^{\alpha} g_v^{\alpha}}{m_{\alpha}^2 - s} + f_{uv}^{\text{scatt}} \frac{1 - s_0^{\text{scatt}}}{s - s_0^{\text{scatt}}} \right) f_{A0}(s), \tag{13.2.10}$$

where g_u^{α} is the coupling constant of the K-matrix pole at m_{α} to the u^{th} channel. The parameters f_{uv}^{scatt} and s_0^{scatt} describe the slowly varying part of the K-matrix. The factor

$$f_{A0}(s) = \frac{1 - s_{A0}}{s - s_{A0}} \left(s - s_A \frac{m_{\pi}^2}{2} \right) \tag{13.2.11}$$

suppresses the false kinematic singularity at $s = 0$ in the physical region near threshold, the Adler zero (Adler, 1965). For example, the parameter values used in the *BABAR* analysis of $D^0 \to K_S^0 \pi^+ \pi^-$ (Aubert, 2008l) are listed in Table 13.2.1, and are adapted from a global analysis of the available $\pi\pi$ scattering data from threshold up to 1900 MeV/c^2 (Anisovich and Sarantsev, 2003). The parameters f_{uv}^{scatt}, for $u \neq 1$, are all set to zero since they are not related to the $\pi\pi$ scattering process. Similarly, the parameterization for the P-vector is

$$P_v(s) = \sum_{\alpha} \frac{\beta_{\alpha} g_v^{\alpha}}{m_{\alpha}^2 - s} + f_{1v}^{\text{prod}} \frac{1 - s_0^{\text{prod}}}{s - s_0^{\text{prod}}}. \tag{13.2.12}$$

Note that the P-vector has the same poles as the K-matrix, otherwise the $\mathcal{A}_1$ amplitude would vanish (diverge) at the K-matrix (P-vector) poles. The parameters β_{α}, f_{1v}^{prod}, and s_0^{prod} of the initial P-vector depend on the production mechanism and cannot be extrapolated from scattering data. Thus they have to be determined directly from the D or B meson decay data sample. They are complex numbers analogous to the $a_r e^{i\phi_r}$ coefficients in Eq. (13.2.1), hence they can be fitted in the same way.

For the $K\pi$ S-wave, the B Factories generally have either used a simple $K_0^*(1430)$ BW that neglects a possible nonresonant contribution or a $K_0^*(1430)$ BW together with an effective-range nonresonant component with a phase shift derived from scattering data (Aston et al., 1988),

$$\mathcal{A}_{K\pi, L=0}(\mathbf{m}) = T_{K\pi, L=0}(s)/\rho(s). \tag{13.2.13}$$

Here $s \equiv m_{K\pi}^2$, $\rho(s) = 2q/\sqrt{s}$ is the phase-space factor, q is the momentum of the kaon and pion in the $K\pi$ rest frame, and

$$T_{K\pi, L=0}(s) = B \sin(\delta_B + \phi_B) e^{i(\delta_B + \phi_B)} + R \sin\delta_R e^{i(\delta_R + \phi_R)} e^{i2(\delta_B + \phi_B)}, \tag{13.2.14}$$

where the phases δ_B and δ_R have a dependence on s and q given by

$$\begin{aligned} \tan\delta_R &= M\Gamma(s)/(M^2 - s), \\ \cot\delta_B &= 1/(aq) + rq/2. \end{aligned} \tag{13.2.15}$$

The parameters a and r play the role of a scattering length and effective interaction length, respectively, and B (ϕ_B) and R (ϕ_R) are the magnitudes (phases) for the nonresonant and resonant terms. M and $\Gamma(s)$ are the mass and mass-dependent width, see Eq. (13.2.4), of the $K_0^*(1430)$ resonance. This parametrization in fact corresponds to a K-matrix approach describing a rapid phase shift coming from the resonant term and a slowly rising phase shift governed by the nonresonant term, with relative strengths R

Table 13.2.1. K-matrix parameters used in the *BABAR* analysis of $D^0 \to K^0_S\pi^+\pi^-$ (Aubert, 2008l). They are adapted from the results of a global analysis of the available $\pi\pi$ scattering data from threshold up to 1900 MeV/c^2 (Anisovich and Sarantsev, 2003). Masses and coupling constants are given in GeV/c^2.

m_α	$g^\alpha_{\pi^+\pi^-}$	$g^\alpha_{K\bar{K}}$	$g^\alpha_{4\pi}$	$g^\alpha_{\eta\eta}$	$g^\alpha_{\eta\eta'}$
0.65100	0.22889	−0.55377	0.00000	−0.39899	−0.34639
1.20360	0.94128	0.55095	0.00000	0.39065	0.31503
1.55817	0.36856	0.23888	0.55639	0.18340	0.18681
1.21000	0.33650	0.40907	0.85679	0.19906	−0.00984
1.82206	0.18171	−0.17558	−0.79658	−0.00355	0.22358
$s_0^{\rm scatt}$	$f_{11}^{\rm scatt}$	$f_{12}^{\rm scatt}$	$f_{13}^{\rm scatt}$	$f_{14}^{\rm scatt}$	$f_{15}^{\rm scatt}$
−3.92637	0.23399	0.15044	−0.20545	0.32825	0.35412
s_{A0}	s_A				
−0.15	1				

and B. The parameters B, ϕ_B, R, ϕ_R, a, and r can be determined from the fit to data as with the P-vector parameters and isobar coefficients. Or, in the case of limited data sample, they can be taken from fits to the LASS scattering data (Aston et al., 1988). Other recent experimental efforts to improve the description of the $K\pi$ S-wave using K-matrix and model independent parameterizations from large samples of $D^+ \to K^-\pi^+\pi^+$ decays are described in Aitala et al. (2006); Bonvicini et al. (2008); Link et al. (2007).

13.2.3 Nonresonant description

In many analyses the nonresonant amplitude is taken to be a uniform phase-space distribution, *i.e.* a constant magnitude and phase. Indeed, such a constant matrix element is the most strict definition of a nonresonant amplitude. However, final-state interactions and other effects are likely to change this behavior, meaning that a uniform amplitude is not fully motivated. In addition, it is found in many cases not to give a good description of the data. This has been seen both in analyses of charm decays with very large event yields and in analyses of B decays where, although the event yields are generally much smaller, the phase space is considerably larger and so there is greater sensitivity to the nonresonant description. This has led analysts either to adopt various empirical forms or to attempt to use information from scattering data to describe the entire S-wave amplitude. The latter approach is described in the previous Section 13.2.2.

An example of one of the empirical forms that has been adopted by Garmash (2005) is

$$\mathcal{A}_{\rm NR} = e^{-\alpha m^2_{ab}}\,, \tag{13.2.16}$$

where α is a free parameter of the fit. This modification of the uniform amplitude allows for enhancements of the magnitude at lower m^2_{ab} values while the phase remains constant over the Dalitz plot. In most cases more than one such term is employed, often for each neutral or singly charged m^2_{ij} combination. The recent *BABAR* analysis of $B \to KKK$ decays (Lees, 2012y) uses a model that has polynomial dependence on the invariant mass and includes an explicit P-wave term.

In recent years there has been an increasing amount of theoretical work towards an understanding of the dynamics of nonresonant three-body amplitudes, see for example Lesniak et al. (2009) and Kamano, Nakamura, Lee, and Sato (2011). In particular, the work focuses on both the effects of final-state interactions and the requirement that two- and three-body prescriptions respect unitarity in the Dalitz-plot model. However, these developments are, in general, yet to be put into practice in the analysis of experimental data.

13.2.4 Time-dependent analyses

Performing a time-dependent Dalitz-plot analysis of neutral B decays allows the extraction of the CP-violating parameters along with the parameters of the isobar model. A full time- and tag-dependent Dalitz-plot analysis has the following advantages compared to a quasi-two-body analysis:

- determines weak and strong phases simultaneously, alleviating ambiguities from different amplitude contributions;
- provides sensitivity to $\cos 2\phi$ (where ϕ is the appropriate weak phase), alleviating the degeneracy of the trigonometric ambiguities;
- correctly accounts for contamination between different resonant contributions.

See Chapters 8 and 10 for details of the techniques of flavor tagging and time-dependent analyses. Here we will give a brief description of how the time dependence and the Dalitz-plot dependence are combined.

With $\Delta t \equiv t_{\rm rec} - t_{\rm tag}$ defined as the proper time interval between the decay of the fully reconstructed $B_{\rm rec}$ and that of the other meson $B_{\rm tag}$ from the $\Upsilon(4S)$ decay, the

time-dependent decay rate $|\mathcal{A}^+(\Delta t)|^2$ ($|\mathcal{A}^-(\Delta t)|^2$) when the $B_{\rm tag}$ is a B^0 ($\overline{B}^0$) is given by

$$|\mathcal{A}^{\pm}(\Delta t)|^2 = \frac{e^{-|\Delta t|/\tau_{B^0}}}{4\tau_{B^0}}\Big[|\mathcal{A}|^2 + |\overline{\mathcal{A}}|^2 \mp \left(|\mathcal{A}|^2 - |\overline{\mathcal{A}}|^2\right)\cos(\Delta m_d \Delta t) \pm 2\mathrm{Im}\left[\frac{q}{p}\overline{\mathcal{A}}\mathcal{A}^*\right]\sin(\Delta m_d \Delta t)\Big], \quad (13.2.17)$$

where τ_{B^0} is the mean neutral B lifetime and Δm_d is the mass difference between B_H and B_L. The time distribution is convolved with the Δt resolution function in the typical way. Here, we have assumed that *CP* is conserved in $B^0\overline{B}^0$ mixing ($|q/p| = 1$) and that the lifetime difference between B_H and B_L is negligible ($\Delta\Gamma_d = 0$). The decay rate, Eq. (13.2.17), is used as a *p.d.f.* in a maximum-likelihood fit and must therefore be normalized:

$$|\mathcal{A}^{\pm}(\Delta t)|^2 \longrightarrow \frac{1}{\langle|\mathcal{A}|^2 + |\overline{\mathcal{A}}|^2\rangle}|\mathcal{A}^{\pm}(\Delta t)|^2\,, \quad (13.2.18)$$

where $\langle ...\rangle$ denotes the value of the integral over the Dalitz plot.

13.3 Experimental effects

The amplitude formalisms outlined above provide a model of the underlying physics of the three-body decay. However, these descriptions may have to be modified or augmented to account for the imperfections of experimental measurements. Broadly, these modifications fall into two categories, one accounting for candidates from background processes (see Section 13.3.1) and the other for effects of reconstruction of signal candidates. The latter category incorporates two main effects: efficiency (Section 13.3.2) and misreconstruction (Section 13.3.3).

13.3.1 Backgrounds

At the B Factories, the dominant source of background in most three-body analyses is from combinatorics, *i.e.* where three random particles in an event happen to fake the signal decay under consideration. This is largely due to the cross-section for light quark production being two to three times higher than that for charm or bottom. Additionally, in searches for rare decays (such as charmless B decays) the branching fraction of the decay of interest is small, $\mathcal{O}\left(10^{-7} - 10^{-5}\right)$. Therefore the relative rate of particles from other B decays combining to fake the signal is correspondingly greater. While these types of backgrounds can be greatly suppressed using the multivariate techniques described in Chapter 4, the Dalitz-plot distribution of the events that remain must still be modeled. In general, such random combinations of particles tend to populate the edges and corners of the Dalitz plot, since they are most frequently formed from collinear and anti-collinear particles in the predominantly jet-like continuum events.

In addition to the combinatoric backgrounds, there exist fully or partially reconstructed backgrounds that originate from decays of the same class of parent meson to a final state similar to the one under consideration. For example, in an analysis of the decay $B^0 \to K^0_S\pi^+\pi^-$ there are potentially large backgrounds from many other B decays including $B^0 \to \eta'(\to \rho^0\gamma)K^0_S$, $B^0 \to D^-(\to K^0_S\pi^-)K^+$, and $B^+ \to K^0_S\pi^+$. In the first of these examples the decay has been partially reconstructed but the energy of the missing photon is sufficiently small that the reconstructed B^0 candidate passes selection criteria. In the second case the decay is fully reconstructed but a kaon/pion misidentification occurs. In the third case the decay is again fully reconstructed and combined with an additional soft pion from the rest of the event to form a signal candidate. Each of these scenarios can lead to very different distributions of events in the Dalitz plot.

In general, the distributions of backgrounds across the Dalitz plot are rather difficult to model with parametric functions. Additionally, the precise nature of the backgrounds can vary dramatically from one analysis to another. Thus, the most common approach for modeling the Dalitz-plot distributions of the backgrounds is to use histograms obtained from either Monte Carlo simulation or sidebands in data. Often some form of smoothing or interpolation is applied to the histograms in order to limit the effect of statistical fluctuations in the input data sample. In B decay analyses, it is found that most backgrounds (particularly the dominant combinatoric backgrounds) preferentially populate the corners and edges of the Dalitz plot. In order to increase the resolution of the histograms in these regions, adaptive binning techniques can be used and/or the histograms can be formed in the so-called "square Dalitz plot", which is discussed in detail in Section 13.4.1.

13.3.2 Efficiency

The most obvious effect of detector acceptance is a reduction in the number of events detected. In three-body decays this is complicated by the fact that the kinematic properties of the decay products differ accross the Dalitz plot. Thus, the acceptance as a function of the Dalitz plot variables is, in general, nonuniform.

The typical acceptance function drops at the corners of the phase space, which correspond to the kinematic configuration where one of the final state particles is produced at rest in the frame of the decaying particle. Reconstruction efficiency is typically smaller for such particles, especially if the decaying particle has a small boost in the laboratory frame.

At *BABAR* and Belle, the efficiency profile is usually well modeled by the full detector simulation. The profile is then modeled either by a parameterized form, such as a two-dimensional polynomial, or by a histogram. Either way, this allows the efficiency as a function of the position in phase space, $\varepsilon(\mathbf{m})$, to be included in the signal Dalitz-plot model, where it multiplies the squared absolute value of the amplitude. When histograms are used they often

utilize adaptive binning techniques and/or are formed in the "square Dalitz plot" (see Section 13.4.1) to improve the resolution in the areas of most rapidly changing efficiency or of greatest importance for the signal model. Interpolation or smoothing techniques can be employed to reduce the effect of statistical fluctuations.

Another, nonparametric, technique to include the efficiency profile in the Dalitz plot fit was used in some Belle analyses (Abe, 2004f; Kuzmin, 2007). The method uses the fact that in the unbinned maximum likelihood fit the efficiency profile enters only the normalization term. The normalization of the *p.d.f.* over the Dalitz plot is calculated using the Monte-Carlo integration technique, but instead of a uniformly distributed sample in the phase-space variables, a large number of simulated events is used that pass the same selection as applied to data.

13.3.3 Misreconstructed signal

Another extremely important effect of reconstruction for a Dalitz-plot analysis is the potential migration of an event from its true coordinate on the Dalitz plot to its reconstructed position. In reality, these effects of reconstruction lie on a continuum, but in order to produce a reasonable model they are most often classified into two types. The first type consists of so-called "correctly reconstructed" events, where the migration is negligible relative to the widths of the resonances under consideration. In this case the amplitude models are used without alteration. In very few cases the migration is not negligible but can be modeled using a simple Gaussian resolution. This class of correctly reconstructed signal events will not be discussed further here. The second type contains events which have more pronounced migration and are sometimes called "self cross feed" in *BABAR* and Belle publications; they form the main topic of this section, and will be referred to as "misreconstructed signal".

For many three-body decay modes, there is a significant fraction of signal events that are incorrectly reconstructed yet still satisfy the selection criteria. Such events typically occur when one low-energy particle from the signal decay is replaced by another in the same event. This behavior is especially prevalent in decays containing neutral pions, where another photon in the event is incorrectly assigned as one of the low-energy photons used to reconstruct the π^0.

In order to correctly model this behavior, it is necessary to determine both the frequency of the misreconstruction (including the variation of that frequency over the Dalitz plot) and the precise migration effects that occur. This can only be achieved with full detector simulation, where both the generated and reconstructed Dalitz-plot positions are known.

Consider an event that is generated with Dalitz-plot coordinate $\mathbf{m}^t$. The probability that this event passes the selection criteria is given by the efficiency as a function of the true position, $\varepsilon(\mathbf{m}^t)$. If the event is selected then there is a further chance that it is misreconstructed. Since such misreconstructions are dependent on the kinematic configuration, this probability is also a function of the true position, $f_{\rm MR}(\mathbf{m}^t)$. The resulting migration probability from true coordinate $\mathbf{m}^t$ to the reconstructed one, $\mathbf{m}^r$, can be described by the four-dimensional function $R_{\rm MR}(\mathbf{m}^r, \mathbf{m}^t)$, which obeys the unitary condition

$$\iint R_{\rm MR}\left(\mathbf{m}^r, \mathbf{m}^t\right)\, d\mathbf{m}^r = 1 \;\forall\, \mathbf{m}^t\,. \tag{13.3.1}$$

Consequently, for an event reconstructed at $\mathbf{m}^r$ the probability for it to be a well-reconstructed signal event is

$$P_{\rm sig}^{\rm WR} \propto \left[1 - f_{\rm MR}(\mathbf{m}^r)\right]\, \varepsilon(\mathbf{m}^r)\, \left|\mathcal{A}(\mathbf{m}^r)\right|^2\,, \tag{13.3.2}$$

while the corresponding probability for a misreconstructed signal event is

$$P_{\rm sig}^{\rm MR} \propto \iint f_{\rm MR}\left(\mathbf{m}^t\right) \varepsilon\left(\mathbf{m}^t\right) \left|\mathcal{A}\left(\mathbf{m}^t\right)\right|^2 \times R_{\rm MR}\left(\mathbf{m}^r, \mathbf{m}^t\right)\, d\mathbf{m}^t\,. \tag{13.3.3}$$

Typically, this integration is implemented as a summation over binned distributions. Therefore, it is essential to include factors that account for the amount of phase space contained within each bin in both the generated and reconstructed histograms.

13.4 Technical details

This part of the chapter describes various technical issues not related to the physics processes involved, but aimed to improve or simplify analyses or presentation of their results. These include the square Dalitz plot transformation (Section 13.4.1), various parameterizations of the complex coefficients for amplitude components (Section 13.4.2), fitting techniques (Section 13.4.3), and the concept of fit fractions, which are used in the presentation of fit results (Section 13.4.4).

13.4.1 Square Dalitz plot

A common feature of Dalitz-plot analyses of B-meson decays to charmless final states is that both the signal events and the combinatorial $e^+e^- \to q\bar{q}$ ($q = u, d, s, c$) continuum background events populate the kinematic boundaries of the Dalitz plot. This is due to the low masses of the final state particles compared with the B mass. Large variations occurring over small areas of the Dalitz plot are difficult to describe in detail. As a result, the typical representation of the Dalitz plot may be inconvenient when using empirical reference shapes in a maximum-likelihood fit. The boundaries of the Dalitz plot are particularly important since it is here that the interference between light meson resonances occurs. These are the regions with the greatest sensitivity to relative phases. A solution that was adopted by some analyses is to apply a transformation to the kinematic variables that maps the

Dalitz plot into a rectangle: the so-called *square Dalitz plot* (SDP). Such a transformation avoids the curved kinematic boundary, which simplifies the use of nonparametric *p.d.f.*s (histograms) to model the distribution of events over the Dalitz plot. Moreover, the transformation is required to expand the regions of interference and simplify parameterization; for instance, the Dalitz plot can be tiled by equally sized bins.

A common definition of the SDP first appeared in the analysis of $B^+ \to \pi^+\pi^+\pi^-$ by *BABAR* (Aubert, 2005d), where the SDP is obtained by the transformation:

$$dm_{ab}^2\, dm_{bc}^2 \longrightarrow |\det J|\, dm'\, d\theta'. \tag{13.4.1}$$

The new coordinates are

$$m' \equiv \frac{1}{\pi} \arccos\left(2\frac{m_{ac} - m_{ac}^{\min}}{m_{ac}^{\max} - m_{ac}^{\min}} - 1\right), \tag{13.4.2}$$

$$\theta' \equiv \frac{1}{\pi}\theta_{ac}, \tag{13.4.3}$$

where $m_{ac}^{\max} = M - m_b$ and $m_{ac}^{\min} = m_a + m_c$ are the kinematic limits of m_{ac}, θ_{ac} is the helicity angle of the ac combination, and J is the Jacobian of the transformation. Both new variables range between 0 and 1. The determinant of the Jacobian is given by

$$|\det J| \;=\; 4\,|\mathbf{p}_a^*||\mathbf{p}_b^*|\, m_{ac} \cdot \frac{\partial m_{ac}}{\partial m'} \cdot \frac{\partial \cos\theta_{ac}}{\partial \theta'}, \tag{13.4.4}$$

where $|\mathbf{p}_a^*| = \sqrt{E_a^{*} - m_a^2}$, $|\mathbf{p}_b^*| = \sqrt{E_b^{*} - m_b^2}$, and the energies are defined in the ac rest frame. Figure 13.4.1 shows the determinant of the Jacobian as a function of the SDP parameters m' and θ'. If the events in the nominal Dalitz plot were distributed according to a uniform three-body phase space, their distribution in the SDP would match the plot of $|\det J|$.

The effect of the transformation, Eq. (13.4.1), is illustrated in Fig. 13.4.2, which shows the nominal and square Dalitz plots for Monte Carlo simulated $B^0 \to \pi^+\pi^-\pi^0$ signal events, where the Dalitz-plot model contains only $\rho^+\pi^-$, $\rho^-\pi^+$, and $\rho^0\pi^0$ amplitudes. The benefits of the SDP explained above are clearly visible in this figure. This simulation does not take into account any detector effects and corresponds to a particular choice of the decay amplitudes for which destructive interferences occur in regions where the ρ resonances overlap. To simplify the comparison, hatched areas showing the interference regions between ρ bands and dashed isocontours $m_{ij} = 1.5\,\mathrm{GeV}/c^2$ have been superimposed on both Dalitz plots.

Another transformation of the phase space was used in the recent *BABAR* amplitude analysis of $B^0 \to K_S^0 K_S^0 K_S^0$ decays (Lees, 2012c). In this particular case, due to the presence of identical particles in the final state, symmetrization of the amplitude under exchange of the identical particles is required. The square Dalitz plot transformation described above would result in curved boundaries. On the other hand, mapping the invariant masses to the plane defined by two helicity angles results in a rectangle.

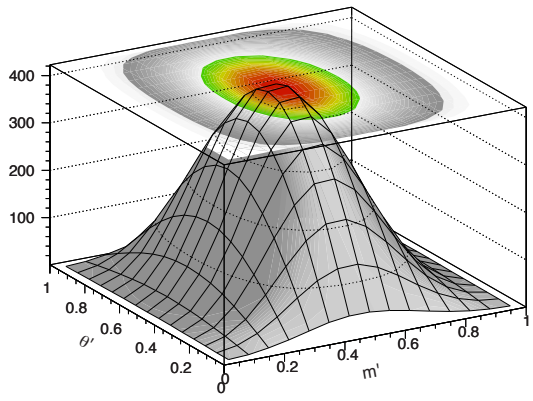

Figure 13.4.1. Jacobian determinant, Eq. (13.4.4), of the transformation, Eq. (13.4.1), defining the square Dalitz plot (SDP). Such a distribution would be obtained in the SDP if events were uniformly distributed over the nominal Dalitz plot.

13.4.2 Complex coefficients

The complex coefficients of each contribution to the amplitude are expressed in Eq. (13.2.1) in terms of a magnitude and a phase,

$$c_r = a_r e^{i\phi_r}, \tag{13.4.5}$$

which is arguably the most intuitive formulation. However, it is also possible to use the real and imaginary parts as the fit parameters

$$c_r = x_r + iy_r. \tag{13.4.6}$$

This latter form has the advantage that the parameters are well behaved when the magnitude of the contribution is small, while the former expression can exhibit biases under these circumstances. One caveat is that, conversely, when the magnitude is large the latter form can appear to exhibit bias. Since the magnitude of a contribution is, in general, better constrained than the phase, the fitted values from a group of pseudo experiments tend to lie on an arc in the complex plane. When projecting this arc onto the real and imaginary axes the distributions can appear skewed. This behavior is not generally indicative of a true bias in the fit; indeed the distributions of the magnitudes and phases (calculated from the fitted x_r and y_r parameters) can be perfectly centered on the true values. However, care should be taken when interpreting the errors on the fit parameters due to their large correlation.

The choice of formulations is much broader when parametrizing *CP* violation. Perhaps the simplest approach is to assign the B (or D) one set of parameters and the $\overline{B}$ (or $\overline{D}$) another set

$$\begin{aligned} c_r &= a_r e^{i\phi_r} \\ \bar{c}_r &= \bar{a}_r e^{i\bar{\phi}_r}, \end{aligned} \tag{13.4.7}$$

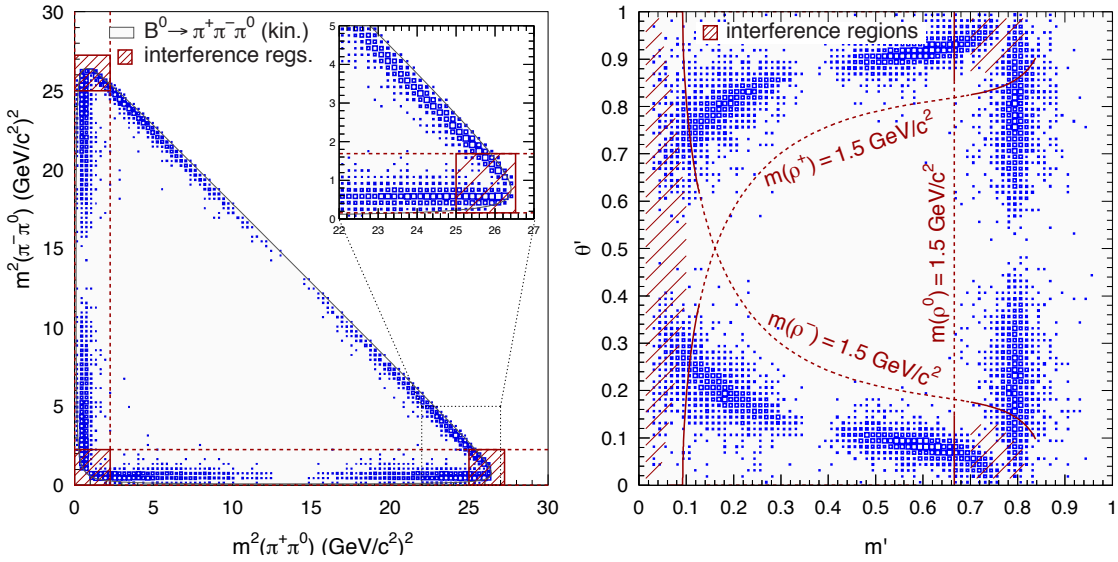

Figure 13.4.2. Nominal (left) and square (right) Dalitz plots for Monte Carlo generated $B^0 \to \pi^+\pi^-\pi^0$ decays (Aubert, 2007v). The comparison of the two Dalitz plots shows that the transformation, Eq. (13.4.1), indeed homogenizes the distribution of events, which are no longer near the plot boundaries but rather cover a larger fraction of the physical region. The decays have been simulated without any detector effects and the three $\rho\pi$ amplitudes have been chosen in order to have destructive interference where the ρ bands overlap. The main overlap regions between the ρ bands are indicated by the hatched areas. Dashed lines in both plots correspond to $m_{ij} = 1.5\,\mathrm{GeV}/c^2$.

or

$$c_r = x_r + iy_r \qquad (13.4.8)$$
$$\bar{c}_r = \bar{x}_r + i\bar{y}_r\,.$$

Alternatively, one can use sets of *CP*-conserving and *CP*-violating parameters, such as those used in the *BABAR* analysis of $B^+ \to K^+\pi^+\pi^-$ (Aubert, 2008j)

$$c_r = (x_r + \Delta x_r) + i(y_r + \Delta y_r) \qquad (13.4.9)$$
$$\bar{c}_r = (x_r - \Delta x_r) + i(y_r - \Delta y_r)\,,$$

or those used in the Belle analysis of the same decay (Garmash, 2006)

$$c_r = a_r e^{i\delta_r}\left(1 + b_j e^{i\phi_j}\right) \qquad (13.4.10)$$
$$\bar{c}_r = a_r e^{i\delta_r}\left(1 - b_j e^{i\phi_j}\right)\,,$$

or those used in the CLEO analysis of $D^0 \to K^0_S\pi^+\pi^-$ (Asner et al., 2004b)

$$c_r = a_r e^{i(\delta_r+\phi_r)}\left(1 + \frac{b_j}{a_j}\right) \qquad (13.4.11)$$
$$\bar{c}_r = a_r e^{i(\delta_r-\phi_r)}\left(1 - \frac{b_j}{a_j}\right)\,.$$

Each of these formulations has advantages and disadvantages. For example, there can be ambiguities in the phases in the CLEO prescription. While the formulation in terms of real and imaginary parts is generally better behaved when the magnitude of the *CP* violation is small, it is less intuitive in terms of interpretation of the results. Hence it is advisable to try several forms and to choose that which best suits the particular measurement being attempted.

13.4.3 Fitting

Once the model of the Dalitz-plot distribution has been formed for all event categories (signal and backgrounds) it is necessary to fit the data to determine the values of the parameters of the model. This is generally achieved using the technique of maximum-likelihood fitting, which is discussed in detail in Chapter 11. As such, only the details specific to Dalitz-plot analyses will be discussed here. Both binned and unbinned fits are used, the former being more common in the analysis of charm decays where the signal yields and purities are greater.

One of the key issues is the normalization of the signal Dalitz-plot *p.d.f.*. There is, in general, no analytic solution to the integral of such a function and so numerical techniques must be employed. The two most commonly used approaches are Monte Carlo and Gauss-Legendre estimation. When a Dalitz-plot model contains narrow resonances such as $\phi(1020)$ or χ_{c0}, it can be useful to perform an integration with higher resolution in the region of those structures. This can involve dividing the Dalitz plot into a number of regions, performing the integration with different resolutions in each region, and finally combining the results.

Since the calculation of the normalization integrals can be computationally expensive, it is desirable to calculate them only once and to cache the values for later use. From Eq. (13.2.1), it is clear that while the complex coefficients factorize from the integral, the parameters of the resonance dynamics, *e.g.*, the mass and width, do not. It is thus possible to cache the integrals only if the parameters

of the resonances are fixed in the fit. Under these circumstances, the integrals of each of the $\mathcal{A}_r\mathcal{A}^\star_{r'}$ terms can be calculated prior to the fit. The *p.d.f.* normalization can then be calculated by combining these cached terms and the current values of the complex coefficients at each iteration of the fit. Consequently, it is a common procedure to fix the resonance parameters in the fit. Where necessary, likelihood scans are used to determine the values of any less well-known parameters.

Due to the complexity of the likelihood function and the large numbers of parameters involved in Dalitz-plot fits it is quite common for several local minima to appear in the parameter space. This can cause problems for the minimization routine in finding the global minimum. In addition, these local minima can be almost degenerate with the global minimum, leading to the need to quote multiple solutions. This can occur, for example, when ambiguities arise from broad overlapping states. The data can often be well described by two or more configurations of the magnitudes and phases of these states. The problem of finding the global minimum is usually overcome by performing multiple fits to a given data sample, each with different (often randomized) starting values for the various parameters. One can then choose the case where the best likelihood was obtained as the global solution. This method also permits the exploration of the other local minima, which allows the results from other solutions to be quoted if they are not significantly separated in likelihood from the global minimum.

13.4.4 Fit fractions

The choice of normalization, phase convention, and amplitude formalism may not always be the same for different experiments or indeed among the different fitting packages used within a single experiment. Consequently, it is extremely important to provide as much convention-independent information as possible to allow a more meaningful comparison of results. Fit fractions are quite commonly used, both for this purpose and for providing a means to estimate the branching fractions of the various decay modes involved. The fit fraction for a component j is defined as the integral of the square of the decay amplitude for that component divided by the integral of the square of the entire matrix element over the Dalitz plot:

$$FF_j = \frac{\int\int_{\rm DP} |c_j\mathcal{A}_j(\mathbf{m})|^2\, d\mathbf{m}}{\int\int_{\rm DP} \left|\sum_k c_k\mathcal{A}_k(\mathbf{m})\right|^2 d\mathbf{m}}\,. \tag{13.4.12}$$

Similarly, the fit fraction for the conjugate process is defined to be:

$$\overline{FF}_j = \frac{\int\int_{\rm DP} \left|\bar{c}_j\overline{\mathcal{A}}_j(\mathbf{m})\right|^2 d\mathbf{m}}{\int\int_{\rm DP} \left|\sum_k \bar{c}_k\overline{\mathcal{A}}_k(\mathbf{m})\right|^2 d\mathbf{m}}\,. \tag{13.4.13}$$

Furthermore, the fit fraction asymmetry is defined to be

$$A_j^{FF} = \frac{\overline{FF}_j - FF_j}{\overline{FF}_j + FF_j}\,, \tag{13.4.14}$$

and the *CP*-conserving (*CP*-violating) fit fraction is given by the sum (difference) of the numerators of Eq. (13.4.12) and Eq. (13.4.13) divided by the sum of the denominators of the same equations. These definitions follow those in Asner et al. (2004b). Note that the sum of the fit fractions is not necessarily unity due to the presence of net constructive or destructive interference.

While the fit fractions can be very useful in comparing results for a given channel, there is additional information in the interference between the contributing decay modes. In order to allow such comparisons one can define interference fit fractions by (del Amo Sanchez, 2010a)

$$FF_{ij} = \frac{\int\int_{\rm DP} 2{\rm Re}\left[c_i c_j^*\mathcal{A}_i(\mathbf{m})\mathcal{A}_j^*(\mathbf{m})\right] d\mathbf{m}}{\int\int_{\rm DP} \left|\sum_k c_k\mathcal{A}_k(\mathbf{m})\right|^2 d\mathbf{m}}\,, \tag{13.4.15}$$

for $i < j$ only. Note that, with this definition, $FF_{jj} = 2FF_j$.

13.5 Model uncertainties

While most of the experimental uncertainties in the measurements involving Dalitz-plot analyses can, in principle, be controlled with Monte Carlo simulation and control samples, there is an essential contribution to the systematic error which is usually hard to quantify. This is the uncertainty on the amplitude arising from model assumptions in its description. This section will describe the possible sources of model uncertainties and outline some methods by which they can be estimated (Section 13.5.1), before discussing the various approaches towards model-independent analysis that have been adopted by the B Factories (Sections 13.5.2 and 13.5.3).

13.5.1 Estimation of model uncertainties

The sources of model uncertainty and common methods to estimate them are listed below.

- Isobar description:
  The isobar formalism is valid only in the case of narrow and non-overlapping resonances, otherwise the unitarity of the amplitude is violated. In contrast, most of the Dalitz-plot analyses have to deal with wide states that interfere with each other. If the use of the isobar model is not implied by the nature of the measurement, more accurate results can be obtained (or at least, the uncertainty due to the use of the isobar description can be quantified) by using an alternative approach, such as the K-matrix.
- Lineshapes of two-body amplitudes:
  Reasonable theoretical description of broad resonances requires corrections to be applied to the Breit-Wigner lineshape, discussed in Section 13.2. Those corrections (*i.e.* Blatt-Weisskopf form factors and mass-dependent widths) depend on a number of poorly constrained parameters, such as radial parameters of the decaying particle and intermediate resonances. The uncertainty

due to these parameters can be estimated by variation within their errors, if known, or otherwise within some reasonable range.
- Identification of intermediate states:
  While the presence of narrow states is usually apparent, some broad states can be misinterpreted as reflections of other two-body channels or as nonresonant structures. In addition, a good description of the amplitude requires that broad states beyond the kinematically allowed region of phase space are properly accounted for. Thus, the model uncertainty estimation often involves variation of the list of intermediate resonances.
- Parameters of the intermediate states:
  Uncertainty due to the finite precision on, for example, the masses and widths of resonances, can be evaluated in a straightforward way by varying the parameters within their errors.
- Uncertainty of the nonresonant amplitude:
  A range of different parameterizations of the nonresonant amplitude is available. Analyses involving D decays, where the phase space of the decay is reasonably small, often parameterize the nonresonant amplitude with the constant complex term, while in B decays more complicated parameterizations, discussed in Section 13.2.3, are necessary. Comparison of the fit results when using alternative parameterizations can give an estimate of the associated uncertainty.

13.5.2 Model-independent analysis

Some applications of Dalitz-plot analyses require a model description of the amplitude, such as searches for intermediate states and measurements of their parameters. Other applications need only that the three-body amplitude (or part of it) is described as a certain function of the phase space variables. In the latter case, the model-independent (MI) Dalitz-plot analysis is a possible option. Below we give two examples of MI approaches: binned analysis and MI partial-wave analysis.

One example of the type of analysis that does not require a model description of the amplitude is the search for *CP* violation in the three-body decays of B or D mesons. While the *CP* asymmetry integrated over the phase space can be small, the local asymmetries in some areas of the phase space can be significant. The understanding of these local asymmetries requires a Dalitz-plot analysis. On the other hand, establishing the existence of *CP* violation does not require a full amplitude analysis. One can therefore divide the phase space into a large number of bins and search for asymmetries in the number of events reconstructed in each bin (Bediaga et al., 2009). The drawback of such an approach is that if *CP* violation is observed, its interpretation will require a full amplitude analysis.

There is, however, a quantitative measurement that uses a model-independent binned Dalitz-plot analysis approach — it is the measurement of the angle ϕ_3 in $B \to DK$, $D \to K^0_S\pi\pi$ decays. In this measurement, the Dalitz-plot analysis is a tool to obtain the parameters of the admixture of D^0 and $\overline{D}^0$ states: their relative amplitude and phase difference. This is possible in the binned approach. The average amplitude and $D^0 - \overline{D}^0$ strong phase difference over the bin is described by a few coefficients. The analysis of the binned $D \to K^0_S\pi\pi$ Dalitz plot from $B \to DK$ allows the extraction of ϕ_3 once the amplitude coefficients are known. These coefficients can be extracted from other measurements: flavor-tagged $D^0 \to K^0_S\pi\pi$ decays, and quantum-correlated decays of pairs of D mesons from $e^+e^- \to \psi(3770) \to D^0\overline{D}^0$ processes. This analysis, performed by the Belle collaboration (Aihara, 2012) using the strong phase parameters measured by CLEO (Libby et al., 2010), is described in detail in Section 17.8.

13.5.3 Model independent partial wave analysis

Another kind of model-independent Dalitz-plot analysis is possible in cases when the data sample is large: the (quasi) model-independent partial wave analysis (MI-PWA). The basic idea behind MI-PWA is that most of the model uncertainty in Dalitz-plot analyses usually comes from the scalar component. One can deal with the scalar component in a model-independent way while keeping the model description for the rest of the amplitude. The scalar component can be parameterized as

$$\mathcal{A}_0(s) = f(s)e^{i\phi(s)}\,, \tag{13.5.1}$$

where the functions $f(s)$ and $\phi(s)$ are defined by interpolation of the values f_j and ϕ_j in each bin j. The values f_j and ϕ_j are treated as free parameters in the amplitude fit. The interference with the non-scalar (reference) part of the amplitude allows one to obtain not only the absolute value of the scalar amplitude, but also its phase as a function of s. The MI-PWA analysis was proposed in the E791 collaboration (Aitala et al., 2006) and used by *BABAR* for the analysis of the $D_s^+ \to \pi^+\pi^-\pi^+$ Dalitz plot (Aubert, 2009i).

In cases where the size of the data sample is insufficient to use a full MI-PWA, it is still possible to study the contributions of each partial wave using an angular-moments analysis. This can then inform the choice of model to be used. Such an approach can be highly informative when a number of overlapping contributions are present. A recent example of this approach is the *BABAR* analysis of $B \to KKK$ decays (Lees, 2012y).

Chapter 14
Blind analysis

Editors:
Aaron Roodman (BABAR)
Alan Schwartz (Belle)

In developing an analysis, it is important not to optimize the analysis procedure on the data that will be used for the measurement (known colloquially as "tuning on the data"). This point is discussed above in Section 4. In this chapter we discuss the method of a blind analysis, which aims to exclude the possibility of even *unintentional* optimization based on the data. Blind analyses have become widespread in particle physics in recent years, and the blind analysis method has been used extensively at the B Factories. Some of the jargon of blind analyses ("opening the box" for a measurement) has also entered into widespread use, even for measurements that are not blind analyses in the strict sense; there has been an increased awareness of the general requirement to avoid tuning on the data.

Here we present the blind analysis method, introducing its definition and history (Section 14.1), and giving pedagogical examples for the cases of upper limits (Section 14.2) and precision measurements (Section 14.3). We then provide some examples of the use of the method at Belle (Section 14.4) and *BABAR* (Section 14.5). For an in-depth discussion of the blind analysis method, see the review article by Klein and Roodman (2005).

14.1 Definition and brief history

A *blind analysis* is a measurement such as that of a branching fraction or upper limit that is performed without looking at the data result until most or all analysis criteria are finalized. The purpose is to eliminate the possibility of an experimenter biasing the result in a particular direction. For example, if all previous measurements of a parameter had obtained positive values, then one might be tempted to keep adjusting analysis criteria until a positive value is obtained. This, however, yields a result biased positive. An early example of a blind analysis is the measurement of the e/m ratio of the electron performed by Dunnington (1933). In this measurement, the e/m value was proportional to the angle between the electron source and the detector. Dunnington asked his machinist to arbitrarily label this angle around 340°; only when the analysis was completed did Dunnington accurately measure this angle to obtain the final result.

Within high energy physics, the blind analysis technique was motivated by a number of positive results that were later found to be due to faulty analysis methods (for examples see Harrison (2002)). It was originally championed by rare kaon decay experiments running at Brookhaven National Laboratory (BNL) in the mid-1980s. Probably the first experiment to use this technique was BNL E791 (Arisaka et al., 1993), which searched for the forbidden decay $K_L^0 \to \mu^\pm e^\mp$. The experiment defined a signal region in two kinematic variables, the $\mu^\pm e^\mp$ invariant mass ($M_{\mu e}$) and the K_L^0 candidate's transverse momentum squared (P_T^2). The signal region was subsequently "blinded," *i.e.*, events falling within this region were not selected for viewing, while all selection criteria were finalized. Only after these criteria were finalized was this region unblinded and signal events counted. A similar technique was used by BNL E787 (Adler et al., 1996), which searched for the rare decay $K^+ \to \pi^+ \nu\overline{\nu}$, and by BNL E888 (Belz et al., 1996a,b), which searched for a long-lived H dibaryon. The method was subsequently adopted by the Fermilab KTeV experiment (Alavi-Harati et al., 1999), which measured ϵ'/ϵ in the K^0-$\overline{K}^0$ system; Fermilab E791 (Aitala et al., 1999b, 2001a), which measured rare/forbidden D meson decays; and the CERN NOMAD experiment (Astier et al., 1999), which searched for neutrino oscillations.

As mentioned, the principle of a blind analysis is to *not* look at potential signal events before finalizing analysis criteria in order to avoid biasing the result. There are three main types of measurements this applies to: setting an upper limit, in which one wants to avoid selection criteria that bias one against signal events; measuring a branching fraction, in which one wants to avoid selections that bias one against background events (this can "sculpt" a signal peak); and precision measurements such as that of measuring mixing or *CP*-violation parameters, in which one wants to avoid selections or fitting procedures that bias the result in a preferred direction. Some general examples of these cases are discussed below, followed by specific examples from Belle and *BABAR*. Not every measurement requires a blind analysis: usually when one searches for new particles and does not know *a priori* where to look, one inspects relevant distributions in an unblind manner. However, one still must be careful not to adjust selection criteria to increase or decrease the signal yield while looking at the signal events for feedback. A blind analysis is typically more time-consuming than an unblind one and, in the case of setting an upper limit, can produce a poor result (see below).

14.2 Setting upper limits: a quantitative example

An upper limit can become biased when one searches for a decay that is not expected to occur and observes one or more signal candidates; one tends to assume they are background and tighten one or more selection cuts to eliminate them. The problem with this procedure is that one may eliminate a *real* signal event, in which case the upper limit obtained for the rate of the rare process is biased low and has statistical undercoverage.

To illustrate this bias quantitatively, consider the following example. An ensemble of 1000 identical experiments search for the rare decay $D \to X$, which we postulate to have a branching fraction of 2.5×10^{-5}. If the experiments have a single-event-sensitivity (S.E.S.) of $1.0 \times$

10^{-5}, then the expected number of observed events is 2.5 (The S.E.S. of an experiment is the branching fraction that would produce, given the experiment's data set and efficiency, an average over a statistical ensemble of one detected event). From Poisson statistics for $\mu = 2.5$, we calculate that the ensemble obtains the following results:

- about 82 experiments observe no events;
- about 205 experiments observe one event;
- about 257 experiments observe two events;
- the remainder, about 456 experiments, observe ≥ 3 events.

For simplicity we assume that the experiments observe no background (this is typically the case for rare K and τ decay searches). This assumption does not change our final conclusions. The experiments that observe no events will set a 90% C.L. upper limit of 2.30 times the S.E.S. [see Section 36.3.2.5 and Table 36.3 of Beringer et al. (2012)] or 2.30×10^{-5}, which is below the true value. The experiments observing one, two, three, etc., events will set upper limits of 3.89, 5.32, 6.68, etc., times the S.E.S., which are above the true value. In this manner 8.2% of experiments obtain "incorrect" upper limits, which is less than 10% of the ensemble and thus consistent with the definition of a 90% C.L. limit.

Now suppose that each experiment that observed events looks at their candidate(s) and that some find a kinematic or particle identification variable (for at least one of the candidates) that is more than 2σ away from the value expected for a signal event. These experiments then impose a 2σ cut on that variable to eliminate the event(s) and adjust the S.E.S. upwards to account for the 4.6% loss in sensitivity. However, if up to 20 variables are potentially considered to be cut on, then the chance of an event surviving this procedure is only $(0.9545)^{20} = 0.394$. Therefore, after experiments observing events adjust a single cut value, approximately $82 + (1 - 0.394)(205) + [1 - (0.394)^2](1 - 0.954)(257) = 216$ experiments observe no events and set an upper limit of either 2.30×10^{-5} (no events originally observed) or $2.30 \times (\text{S.E.S.})/0.954 = 2.41 \times 10^{-5}$. Both limits are below the true value. The fraction of experiments is 22%, which is larger than 10% and thus inconsistent with the definition of a 90% C.L. limit. The bias of the procedure has resulted in undercoverage. To avoid such bias, the decision whether to cut on a variable or not must be made *before* looking at signal candidate events.

While a blind analysis does yield unbiased upper limits, it has a serious drawback in that it is possible to miss an obvious background, observe a large number of events in the signal region, and end up setting a poor upper limit. This situation does a disservice to the experiment, as the full "discriminating power" of the detector has not been utilized. Thus in practice, experiments carefully study signal candidates after all cuts have been finalized to check whether there are any due to a trivial background or instrumental problem such as the high voltage having been tripped off. If such events are found, it usually is preferable to eliminate them and set a biased but useful upper limit rather than leave them and set an unbiased but not useful limit.

Here we have discussed only bias introduced in the signal acceptance, not bias potentially introduced when estimating backgrounds. The latter depends upon the background sample used and the method of estimation. For example, if one is estimating background by counting events in a sideband and extrapolating, then to avoid bias one must blind that part of the sideband used to estimate background when finalizing cuts, or at least not "tune" cuts to explicitly remove events from that sideband region.

14.3 Precision measurements

For precision measurements of parameters in which one typically performs a fit rather than simply counts events, a different technique for avoiding bias must be used. In this case *hiding the answer* is often the appropriate method. For example, the KTeV experiment used this technique for its measurement of ϵ'/ϵ. The value of ϵ'/ϵ was obtained from a fit to the data, and to avoid bias KTeV inserted an unknown offset into the fitting program such that the fit yielded the "hidden" value

$$\left(\frac{\epsilon'}{\epsilon}\right)_{\text{hidden}} \equiv \left\{\begin{matrix}+1\\-1\end{matrix}\right\} \times \left(\frac{\epsilon'}{\epsilon}\right)_{\text{true}} + c\,. \quad (14.3.1)$$

In this expression, c is a hidden random constant, and the choice of the factor ± 1 is also hidden. The values of c and ± 1 were made by a pseudo-random number generator. Thus KTeV could finalize its data samples, analysis cuts, Monte-Carlo corrections, and fitting technique while remaining unaffected by the (hidden) true value of ϵ'/ϵ. The use of the factor ± 1 prevented KTeV from knowing the direction in which the result moved as changes to the analysis were applied.

When performing a blind analysis using the "hidden answer" technique, one must consider whether there exists figures, tables, or other ancillary results that could inadvertently reveal the blinded result. Only if the measurement result is not readily apparent from such information should the figure, table, etc. be presented.

14.4 Examples from Belle

The Belle experiment used blind analysis methods extensively: in measuring branching fractions, *CP* asymmetries, in fitting Dalitz plots, and in searching for rare and forbidden decays. Only after selection criteria and the fitting procedure were finalized, and the background estimated, were the results unblinded. To unblind a result required approval from one's internal review committee. If a committee member felt that more studies were needed before unblinding, then the analyzer could not proceed. If an analysis was an update to a previous Belle result, then before unblinding the analyzer was usually required to run his/her analysis code on the previous data set used and compare the result obtained with that obtained previously. If there were a discrepancy, it had to be understood before continuing. After unblinding, the only steps

remaining in the analysis were finalizing the systematic errors and, occasionally, refining the background estimate.

This methodology yielded unbiased results but also occasional surprises such as:

- significant direct *CP* violation in $B^0 \to K^+\pi^-$ decays (Chao, 2004);
- large direct *CP* violation in $B^0 \to \pi^+\pi^-$ decays, and values of *CP* parameters $C_{\pi\pi}$ and $S_{\pi\pi}$ outside the physical region (Abe, 2004b, 2005b);
- the value of $\sin 2\phi_1$ and *CP* asymmetries measured in $b \to sq\overline{q}$ transitions such as $B^0 \to \phi K^0_S$ and $B^0 \to f_0(980)K^0_S$ differed substantially from that expected based on measurements of the $b \to c\bar{c}s$ transition $B^0 \to J/\psi K^0_S$ (Chen, 2005b); and
- the branching fraction for $B^+ \to \tau^+\nu$ measured with 414 fb^{-1} was much larger than that expected based on the value of $|V_{ub}|$ determined from B semileptonic decays (Ikado, 2006).

A typical example of a blind analysis is a search for the lepton-number-violating decays $\tau^- \to \mu^- V^0$ and $\tau^- \to e^- V^0$, where V^0 is a neutral vector meson ρ^0, ϕ, ω, or K^{*0} (Miyazaki, 2011). These mesons were reconstructed via $\rho^0 \to \pi^+\pi^-$, $\phi \to K^+K^-$, $\omega \to \pi^+\pi^-\pi^0$, and $K^{*0} \to K^+\pi^-$. The analysis selected candidate events based on the variables $M_{\ell V}$ and ΔE, where $M_{\ell V}$ is the invariant mass of the $\ell^- V^0$ pair ($\ell = e, \mu$), and ΔE is the difference in energy between the $\ell^- V^0$ system and the beam energy in the e^+e^- center-of-mass frame. Events were first selected by dividing the reconstructed tracks and calorimeter hits for each event into two azimuthal hemispheres and requiring that, in one of the hemispheres, there be only a single track. This topology corresponds to a $\tau^- \to \ell^-\nu\overline{\nu}$, $\tau^- \to \pi^-\nu$, or $\tau^- \to \rho^-(\to \pi^-\pi^0)\nu$ decay; the presence of this "tagging" decay indicates $e^+e^- \to \tau^+\tau^-$ production.

From this tagged sample, events were selected that have three tracks in the "signal hemisphere". Two of the tracks were required to reconstruct to a ρ^0, ϕ, ω, or K^{*0} meson and satisfy particle identification criteria. The third track was required to satisfy muon or electron identification criteria. At this point an elliptical signal region in the $M_{\ell V}$-ΔE plane was blinded while topological and kinematic selection criteria were optimized using MC-simulated events and applied. The blinded signal ellipse was centered near $M_{\ell V} = m_\tau$ and $\Delta E = 0$ and had semi-major and semi-minor axes equal to 3σ in resolution.

After the cut optimization procedure, the background in the signal region was estimated by extrapolating from the number of events observed in a larger $M_{\ell V}$-ΔE region surrounding the blinded ellipse. The backgrounds ranged from 0.06 to 1.5 events. After selection criteria were finalized and the backgrounds estimated, the signal regions were unblinded and the signal yields obtained. The results for four modes are shown in Fig. 14.4.1. From the observed signal yields along with the background estimates, reconstruction efficiencies, and systematic uncertainties, upper limits were calculated using a frequentist approach (Conrad, Botner, Hallgren, and Perez de los Heros, 2003).

It should be noted that in performing a blind analysis one doesn't have to rely solely on the simulated data. Any

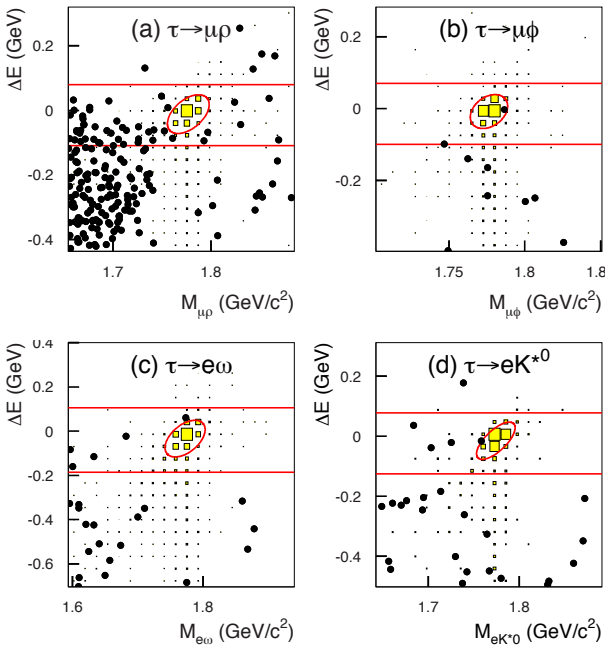

Figure 14.4.1. $M_{\ell V}$-ΔE signal region (see text) for four typical lepton-number-violating decays: *(a)* $\tau^- \to \mu^-\rho^0$ *(b)* $\tau^- \to \mu^-\phi$ *(c)* $\tau^- \to e^-\omega$, and *(d)* $\tau^- \to e^-K^{*0}$ from Miyazaki (2011). Data points are shown as solid circles, and MC signal distributions are shown as yellow boxes (with arbitrary normalization). Red ellipses denote blinded regions, and horizontal lines denote the regions used for estimating background within the blinded ellipses.

data sample statistically independent from the data used for the evaluation of the measurement result can be used. This includes (real) data samples with decay modes exhibiting similarities with the studied one, or even samples of the studied decay mode on a distinct (typically smaller) data set. For example, in Belle study of $D^+ \to K^0_S K^+$ and $D^+_s \to K^0_S\pi^+$ decays (Won, 2009) a smaller sample of selected decays obtained in the off-resonance data sample was used to optimize the selection, subsequently applied to the larger on-resonance data sample.

14.5 Examples from BABAR

The *BABAR* collaboration extensively discussed the use of the blind analysis method prior to data taking, and wrote a document describing possible methods (Ford, 2000) which recommended their use whenever possible. Most *BABAR* results that could make use of a blind analysis technique did in fact do so.

For certain measurements, hiding the answer is not sufficient; it may also be necessary to hide the visual aspect of the measurement. One example is the *CP*-violation measurements performed by *BABAR*. In this case the approximate size and sign of the CP asymmetry can be seen by looking at the Δt distributions for B^0 and $\overline{B}^0$ decays

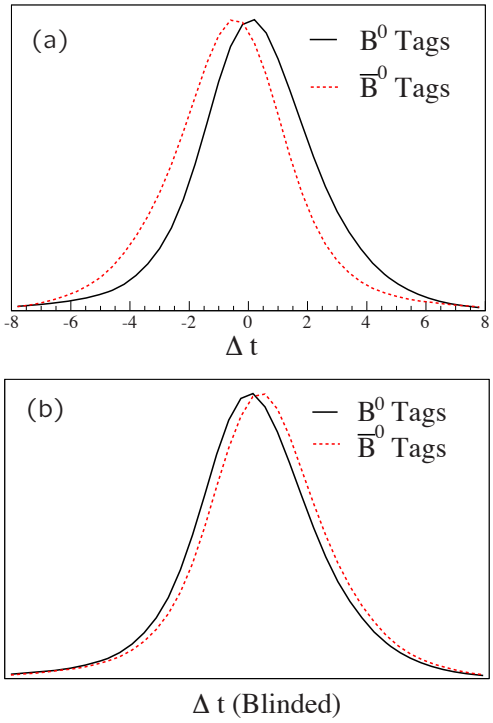

Figure 14.5.1. The Δt distributions for B decays into *CP* eigenstates, for $\sin 2\phi_1 = 0.75$ with the B^0 flavor tagging and vertex resolution that are typical for *BABAR*. *(a)* The true number of B^0-tagged (solid line) and $\overline{B}^0$-tagged (dashed line) decays into *CP* eigenstates as a function of Δt. *(b)* The Δt_{Blind} distributions for B^0-tagged (solid) and $\overline{B}^0$-tagged (dashed) decays.

into *CP* eigenstates, as shown in Figure 14.5.1a (see also Chapter 10). Before *CP* violation had been established, and to avoid any chance of bias, a blind analysis was developed to hide both the answer and the visual asymmetry (Roodman, 2000).

In *BABAR*'s initial *CP*-violation measurement (Aubert, 2001a), the result (obtained from fitting the data) was hidden as in Eq. (14.3.1). In addition, the visual asymmetry was hidden by altering the Δt distribution used to display the data. This was achieved by using the variable

$$\Delta t_{\text{Blind}} \equiv \left\{ \begin{matrix} +1 \\ -1 \end{matrix} \right\} \times s_{\text{tag}} \times \Delta t \; + \; c\,. \qquad (14.5.1)$$

The parameter s_{tag} equals $+1$ or -1 for B^0 or $\overline{B}^0$ flavor tags, respectively. Since the asymmetry is nearly equal and opposite for the two B flavors, *BABAR* hid the asymmetry by flipping one of the distributions. In addition, *CP*-violation can be manifest by the asymmetry about $\Delta t = 0$ of an individual B^0 or $\overline{B}^0$ distribution. This feature was hidden by the offset term c in Eq. (14.5.1), which has the affect of hiding the $\Delta t = 0$ point. The result is shown in Fig. 14.5.1b, where the amount of *CP*-violation is no longer visible.

This technique allowed *BABAR* to use the Δt_{Blind} distribution and blinded fit results to validate the analysis and study systematic effects while remaining blind to the presence of any asymmetry. There was one additional restriction: that the fit result could not be superimposed on the data, since the smooth fit curve would show the asymmetry. Instead, to assess the agreement of the fit curve and the data, a distribution of only the residuals was used. In practice, this added only a small complication to the measurement. In fact, after the second iteration of the analysis (Aubert, 2001e), it was realized that the asymmetry would remain blinded if the only Δt distribution used was that of the sum of B^0 and $\overline{B}^0$ events. Subsequently, no additional checks were done (or needed) using individual B^0 and $\overline{B}^0$ Δt distributions.

BABAR developed other methods for blinding an analysis, depending on its nature (upper limit, branching fraction, or precision measurement). For example, fit results were sometimes blinded directly within the `RooFit` package (Verkerke and Kirkby, 2003), and so `Root`-based fits to data could be subjected to a blind analysis methodology with relative ease. An alternative to a `RooFit`-based blinding method was to set up an analysis chain whereby one performs a fit to data using `Minuit` (James and Roos, 1975) and writes the output to a log file, removing any reference to signal observables while writing the log file. In this manner the output of the fit can be viewed in order to study issues such as the convergence of the fit, the values of ancillary fit parameters, and the covariance matrix.

Lastly, *BABAR* often worked the blind analysis strategy into its internal review process. For many, but not all analyses, the three-person review committee's approval was required before the authors could unblind their analysis (as done in Belle).

Chapter 15
Systematic error estimation

Editors:
Wolfgang Gradl (BABAR)
Pao-Ti Chang (Belle)

Additional section writers:
Adrian Bevan, Chih-hsiang Cheng, Andreas Hafner, Kenkichi Miyabayashi

For most measurements at the B Factories, the estimation of systematic uncertainties is a very important and challenging part of the analysis. There are a number of effects which can systematically influence the result. The ones which are frequently encountered in measurements performed by the B Factories are discussed in the present chapter.

Sources of systematic effects include the difference between data and simulation, the uncertainty on external input needed to convert a directly measured value (*e.g.* the number of signal events) to the desired quantity (*e.g.* a branching fraction), and the analysis procedure chosen to extract the signal (*e.g.* background model, fit bias). In addition, physics processes can introduce discrepancies between the measured value and the parameter of interest. This is often the case because the signal model used is only an approximation of the true, underlying process. An example of this type of systematic uncertainty is the effect of tag-side interference in measurements of time-dependent *CP* asymmetries.

Where possible, measured values are corrected for such systematic shifts, and there is a systematic uncertainty associated with the correction. Some of the systematic corrections are derived from control sample studies; their associated uncertainty is essentially statistical in nature and scales with the size of the corresponding control sample and therefore with the data sample available for analysis.

Careful design of the analysis strategy can help to minimize the effect of systematic errors on the final result. A particular systematic effect might cancel in the ratio of two observable quantities, such as the total number of produced B mesons in the measurements of rate asymmetries. Similarly, if the branching fraction of a decay is measured relative to a well-known decay mode with similar final state topology, systematic uncertainties due to reconstruction or PID efficiency cancel to a certain extent.

15.1 Differences between data and simulation

Most analyses at the B Factories are designed and optimized using simulated data ('Monte Carlo'). Collected data are only looked at after the analysis procedure has been thoroughly tested and validated (see Chapter 14 for a rationale and methods). Quantities such as the event selection efficiency and mis-tag or mis-identification rates are needed for measurements of branching fractions or absolute cross sections, and they are typically obtained from simulated data. If the simulation does not describe the detector perfectly, the efficiency of the selection as applied to real data differs from the efficiency derived from simulated events; this difference needs to be quantified and corrected. The correction factors to be applied to efficiencies obtained from simulation are derived from independent control samples and their simulated counterparts and have their own statistical and systematic uncertainties. The total uncertainty in the correction factor is taken as a systematic uncertainty for the selection efficiency. Correlations between systematic uncertainties need to be taken into account; for example, for a final state with multiple π^0, the efficiency correction has to be applied for each π^0 in the final state, and the systematic uncertainties are added linearly.

15.1.1 Track reconstruction

Many analyses performed at the B Factories require a precise simulation of the charged track finding and reconstruction efficiency in order to determine absolute rates or cross sections. The way to measure the tracking efficiency is by predicting the presence of a charged particle unambiguously (*e.g.* using kinematic constraints on a series of particle decays) and checking if a reconstructed track matches the prediction. Once the method is validated, one can study the tracking efficiency as a function of the track momentum and polar angle. The same procedure is applied to Monte Carlo events to estimate the tracking efficiency in simulation. From the tracking efficiencies in data and Monte Carlo, one produces a look-up table of correction factors and their uncertainties to correct for the data-MC discrepancy in terms of track momentum and polar angle. This table is used to correct for the signal efficiency estimated from Monte Carlo simulation and to calculate the systematic uncertainty from track reconstruction.

15.1.1.1 Methods at *BABAR*

At *BABAR* several methods are exploited to study possible efficiency differences between the data and simulation over a wide range of particle momenta and production environments relevant to most analyses. They are discussed in detail in (Allmendinger, 2012).

These methods rely on distinct data samples, where additional constraints are applied to select specific event topologies. The primary method to study the charged track reconstruction efficiency in the data and simulation uses $e^+e^- \to \tau^+\tau^-$ events. Events of interest for the efficiency study involve one leptonic τ decay $\tau^\pm \to \mu^\pm\nu_\mu\nu_\tau$ ('tag side'), $\mathcal{B}(\tau^\pm \to \mu^\pm\nu_\mu\nu_\tau) = (17.36 \pm 0.05)\%$ (Beringer et al., 2012), back-to-back with a semi-leptonic decay $\tau^\mp \to h^\mp h^\mp h^\pm \nu_\tau (\geq 0n)$ ('signal side') with a branching fraction of $\mathcal{B}(\tau^\mp \to h^\mp h^\mp h^\pm \nu_\tau(\geq 0n)) = (14.56 \pm 0.08)\%$, (Beringer et al., 2012). Here, h denotes a charged hadron, and at least two tracks are required to fail a loose electron selection. The presence of one or more neutral particles, denoted by $\geq 1n$, *e.g.* π^0, but excluding $K^0_S \to \pi^+\pi^-$, is

allowed in the final state. This data sample is referred to as 'Tau31' sample. The primary selection for τ pair candidates requires one isolated muon track in combination with at least two tracks consistent with being hadrons. Through charge conservation, the existence of an additional track is inferred.

Due to the presence of multiple neutrinos in the event, however, the direction of the additional track cannot be determined exactly. Using the measured trajectories of the muon and the two hadrons, kinematic regions can be defined which are correlated with the polar angle θ and transverse momentum p_T of the missing track. The variation of the agreement between data and simulation as a function of θ and p_T is conservatively quantified using these estimator quantities.

This variation is the largest uncertainty when applying the results to a physics analysis, where the events typically have distributions in θ and p_T different from the τ pair events. The other main uncertainties include both τ and non-τ backgrounds: radiative Bhabha events with a converted photon (*i.e.*, $e^+e^- \to e^+e^-\gamma, \gamma \to e^+e^-$), τ pair events with a converted photon or a $K^0_S \to \pi^-\pi^+$, 2-γ events, and continuum events ($q\bar{q}$, with $q = u, d, s, c$). Control samples are used to estimate the levels and/or shapes of the most important backgrounds. This study shows no difference in the track finding efficiency between the data and simulation with an uncertainty of (0.13-0.24)% per track, depending on the exact requirements on the track quality. This method is also used to investigate the stability of track reconstruction over the diverse *BABAR* running periods. No time-dependent effects in the difference between the data and simulation have been observed.

Initial-state radiation (ISR) events in the reaction channel $e^+e^- \to \pi^+\pi^-\pi^+\pi^-\gamma_{\rm ISR}$ are used to cross-check the systematic uncertainties in track reconstruction determined from $\tau^+\tau^-$ events. The absence of neutrinos in this reaction allows to apply a fit with kinematic constraints to events with at least three detected pions. Hereby the kinematic parameters of the possibly missing track are determined using energy and momentum conservation, and the track reconstruction efficiency can be measured as a function of track momentum and angles. In these events, the high-energy ISR photon is emitted back-to-back to the collimated hadronic system in the center-of-mass frame. Because the analysis only selects events with photon energy $E_\gamma > 3\,\text{GeV}$, this back-to-back topology is approximately preserved in the laboratory frame. This leads to an environment with a slightly higher track overlap probability. In this environment, the track reconstruction efficiency difference between the data and simulation is found to be $(0.7 \pm 0.4)\%$ per track, compatible with the result of the τ based study of no significant bias.

Low momentum tracks are studied in $D^{*\pm} \to D^0\pi^\pm_s$ decays, using inclusively selected $D^{*\pm}$. π_s denotes the low momentum pion ("slow pion") from the D^* decay. The relative reconstruction efficiency for the slow pions as a function of the pion momentum is measured using their angular distribution, following a method developed by CLEO (Menary, 1992). This method exploits the fact that in the decay of a vector meson to two pseudoscalar mesons the expected distribution of events is an even function of the cosine of the π_s helicity angle θ^*. Furthermore, $\cos\theta^*$ is related to the slow pion momentum in the lab frame: $p_{\pi_s} = \gamma(p^*_{\pi_s}\cos\theta^* - \beta E^*_{\pi_s})$. Any observed asymmetry in $dN/d\cos\theta^*$ can be therefore mapped to a relative efficiency difference as a function of p_{π_s} (see Allmendinger (2012) for a more complete discussion). Repeating the study on data and simulation, a relative difference between the slow π reconstruction efficiencies is extracted, which is then ascribed as a systematic uncertainty. Using the full *BABAR* dataset, this study results in a systematic uncertainty of 1.5% per track with a transverse momentum of $p_T < 180\,\text{MeV}/c$. This systematic uncertainty includes the effects from both reconstruction efficiency and detector acceptance.

An asymmetry in the track reconstruction efficiency between positively and negatively charged tracks can arise from a charge dependence of the interaction with the detector material; such a detector-induced asymmetry can introduce a bias when measuring small *CP* rate asymmetries. The asymmetry in reconstruction efficiency has to be determined directly from data with a precision of $\mathcal{O}(10^{-3})$. Like the overall tracking efficiency, it can also be measured using the above mentioned Tau31 sample by comparing the number of (2+1)-track events (in which one track was not reconstructed) to the number of (3+1)-track events. The asymmetry in the reconstruction efficiency is found to be $(\varepsilon(\pi^+) - \varepsilon(\pi^-))/(\varepsilon(\pi^+) + \varepsilon(\pi^-)) = (0.10 \pm 0.26)\%$, thus consistent with zero within its uncertainty. This high-statistics measurement is cross-checked and validated with a high purity sample of $D^0 \to \pi^+\pi^-$ events tagged by the decay $D^{*+} \to D^0\pi^+_s$; the charge-dependent reconstruction asymmetry as measured in this decay is also consistent with zero asymmetry, but has a larger uncertainty.

Very sensitive measurements of charge asymmetries, such as A_{CP} in charm meson decays, require a much better control of any detector-induced charge asymmetry. These analyses rely on data-driven methods to determine the charge asymmetry in the track reconstruction with a systematic uncertainty as small as 0.08% (see Section 19.2.6).

Finally, the effect of a vertex of the charged tracks that is displaced from the primary event origin is investigated in $B \to h^+h^-K^0_S$ (with $h = \pi, K$) decays with $K^0_S \to \pi^+\pi^-$. Here the finite lifetime of the K^0_S leads to a displacement of the vertex of the two daughter pions. For these tracks a difference of $(0.5 \pm 0.8)\%$ in the reconstruction efficiency between data and simulation has been observed.

The results of these studies show that at *BABAR* the track finding efficiency in data agrees within uncertainties with the simulated data. Thus, in a *BABAR* analysis, simulated track finding efficiencies can be applied to data. The appropriate systematic errors depending on the number of tracks involved need to be propagated, taking into account that the systematic errors are fully correlated *i.e.*, the systematic uncertainties per track are added linearly.

15.1.1.2 Methods at Belle

The track finding efficiency for charged particles with momenta above 200 MeV/c is studied using the decay chain $D^* \to D^0\pi_s, D^0 \to \pi^+\pi^- K^0_S$ and $K^0_S \to \pi^+\pi^-$.[46] Partially reconstructed D^* decays provide a clean sample with sufficient statistics to perform the tracking study. The decay chain can be reconstructed without actually detecting one of the pions from the K^0_S decay. The four-momentum of this pion can be inferred from the kinematic constraints of the decay chain.

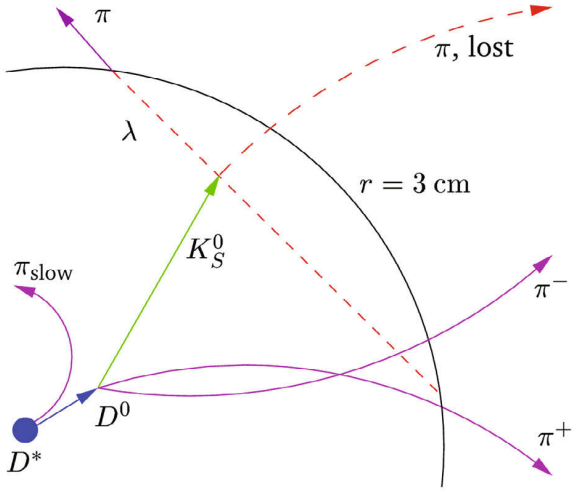

Figure 15.1.1. Illustration of the Belle method to determine the efficiency of tracking.

The method is illustrated in Fig. 15.1.1. The D^* meson partial reconstruction starts from the reconstruction of the common vertex of the two charged pions from the D^0 decay (the D^0 decay vertex; see Chapter 6 about vertexing). Following is the determination of possible K^0_S decay vertex positions, which are constrained to lie on the trajectory of the detected pion and within a certain radius (specifically this is chosen to be 3 cm) from the interaction region to limit the amount of possible points. The segment of the pion track on which the K^0_S vertex is searched for is discretely scanned and for each discrete part of the track the momentum magnitude and direction of the K^0_S is calculated (the latter is determined by the line joining the D^0 and K^0_S decay vertices, and the former from the requirement that the K^0_S together with the detected charged pion pair yields the invariant mass of the D^0). For each possible value of K^0_S four-momentum (corresponding to each possible K^0_S decay vertex position) a corresponding un-detected pion four-momentum can be calculated by subtracting the momentum of the detected daughter pion. The correct K^0_S momentum (*i.e.* the correct position of the K^0_S decay vertex) is then determined by requiring that the resulting pion four-momentum magnitude corresponds to the pion nominal mass. A slow pion candidate is added to the D^0 and the signal of partially reconstructed D^*'s is determined from the $D^0\pi_s$ invariant mass distribution (Fig. 15.1.2).

Practically, several selection requirements are implemented to improve the signal-to-background ratio. For instance, the D^0 momentum must be larger than 2 GeV/c in the laboratory frame to reduce combinatorial background. The K^0_S vertex should be inside the innermost layer of the silicon vertex detector to ensure silicon hits for the K^0_S daughter tracks, and the missing pions are required to be in the tracking fiducial region. The ratio of the yield of fully reconstructed D^*'s to those partially reconstructed with one pion from the K^0_S not required is the track reconstruction efficiency.

Finally the ratio of the tracking efficiencies of data and MC can be obtained as a function of other variables, such as track total momentum and polar angle. The efficiency as a function of particle's transverse momenta for real and simulated data is shown in Fig. 15.1.3. Since the ratio of the data-MC efficiencies is found to be consistent with unity the difference and its uncertainties are assigned as the tracking uncertainty. For Belle, the systematic error for charged-track reconstruction is 0.35% on average for high momentum tracks ($p > 200$ MeV/c).

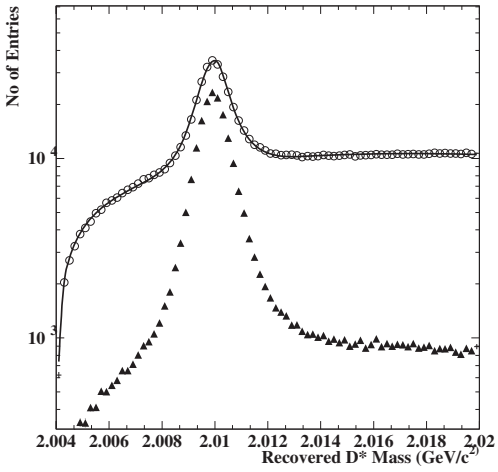

Figure 15.1.2. D^* mass distribution for partially (circle) and fully (triangle) reconstructed candidates in Belle data. A similar reconstruction in the simulated data yields the ratio of data-MC simulation tracking efficiencies. The solid line represents a fit to the partially reconstructed candidates.

The efficiency difference of low momentum tracks ($p <$ 200 MeV/c) is studied using the decay chain, $B^0 \to D^{*-}\pi^+$ and $D^{*-} \to \overline{D}^0\pi^-_s$. The large $B^0 \to D^{*-}\pi^+$ branching fraction provides a sample of slow pions large enough to investigate possible track reconstruction discrepancies be-

[46] For particles with $p < 200$ MeV/c a different method is used as described below.

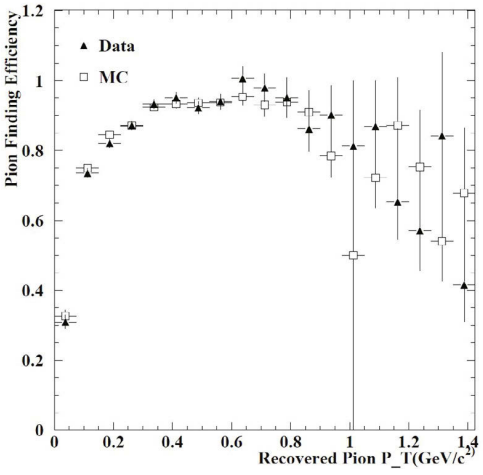

Figure 15.1.3. Reconstruction efficiency for charged tracks as a function of the particle's transverse momentum for simulated and real Belle data.

tween data and simulation. Since the tracking difference between data and the MC expectation at higher momenta is known, the data-MC ratios are normalized according to the data-MC ratio obtained using the D^* partial reconstruction method for track momenta above 200 MeV/c. For events with lower π_s momentum, the difference between the reconstructed yields in data and MC simulation is ascribed to a difference in the low momentum track reconstruction efficiency. Experimentally $\overline{D}^0$ candidates are reconstructed using several sub-decay modes. A slow pion (π_s) and a high momentum pion with opposite charge are included to form a B candidate. The sample is divided in terms of the momentum of the slow pion, and the number of B events in each momentum bin can be extracted using a fit to $m_{\rm ES}$ and Δm (mass difference between D^{*-} and $\overline{D}^0$). The yield ratio of data and MC is thus obtained in each π_s momentum bin. The normalized ratios and their uncertainties at low momentum are used to correct for data-MC differences and to estimate the corresponding uncertainties. In Belle the tracking efficiency in simulation agrees well with that in data for track momenta above 125 MeV/c and the simulation may over-estimate the reconstruction efficiency for tracks with momentum below 100 MeV/c. On average the systematic uncertainty for low momentum tracks is 1.3% per track.

15.1.2 K_S^0 and Λ reconstruction

Experimentally, K_S^0 and Λ usually are reconstructed through $K_S^0 \to \pi^+\pi^-$ and $\Lambda \to p\pi^-$ decays. Both particles have a long lifetime. They are identified by the requirement that their decay vertex is displaced from the interaction point and that their reconstructed mass is close to their corresponding nominal mass. For long-lived particles systematic uncertainties in addition to the tracking uncertainties of their daughter particles need to be taken into account. The tracks may originate far from the interaction point, and also the reconstruction of the secondary vertex may show differences between simulation and data. Several studies are performed to investigate the K_S^0/Λ reconstruction.

15.1.2.1 Exclusive $D^* \to D^0\pi_s, D^0 \to \pi^+\pi^- K_S^0$

Similar to the study of track reconstruction systematics, the K_S^0 reconstruction is studied using the exclusive decays of $D^* \to D^0\pi_s, D^0 \to \pi^+\pi^- K_S^0$. One measures the efficiency of the displaced vertex requirement for the K_S^0 reconstruction by obtaining the numbers of K_S^0 candidates with and without reconstructing a K_S^0 vertex. The Belle method is described as follows. Two oppositely charged tracks that are identified as pions are selected and their invariant mass is computed without applying a vertex constraint. A pair with invariant mass close to the nominal K_S^0 mass is selected as a K_S^0 candidate. Every K_S^0 candidate is combined with another $\pi^+\pi^-$ pair to form a D^0 candidate, which is required to pair with a slow charged pion to form a D^*. To reduce the combinatorial background, a suitable mass range, estimated using simulations, is selected in the D^0 mass and $\Delta m' = m_{D^*} - m_D - m_{\pi_s}$. The uncertainty in $\Delta m'$ is significantly reduced with respect to m_{D^*} because the contribution from the K_S^0 candidate momentum largely cancels in the subtraction and hence a tighter signal window can be applied due to a better resolution. Finally, the numbers of all K_S^0 particles and of those passing a displaced vertex selection are estimated by fitting the candidate K_S^0 mass with and without requiring a displaced vertex, respectively.

The control sample has sufficiently high statistics so that the study is extended to measure the efficiency in terms of K_S^0 momentum and polar angle similar to the charged track study described in Section 15.1.1. Likewise the efficiency of requiring a displaced vertex for Monte Carlo events can be estimated. Hence, the data-MC efficiency ratio can be obtained. The systematic uncertainty that arises from the reconstruction of the two K_S^0 daughter pion tracks has to be added to the efficiency uncertainty of the displaced vertex for the total K_S^0 systematic uncertainty. Since Λ and K_S^0 decays have a similar topology, the Λ systematic uncertainty can be estimated using the K_S^0 results. For the Belle full data sample, the total systematic uncertainty of the K_S^0 reconstruction is on average around 1% including track reconstruction systematic uncertainties.

15.1.2.2 Ratio of two D decays

The performance of the K_S^0 reconstruction in data can be checked using the double ratio

$$\eta(K_S^0) = \frac{N(D^+ \to K_S^0\pi^+)^{\rm data}}{N(D^+ \to K^-\pi^+\pi^+)^{\rm data}} \Big/ \frac{N(D^+ \to K_S^0\pi^+)^{\rm MC}}{N(D^+ \to K^-\pi^+\pi^+)^{\rm MC}} \,. \tag{15.1.1}$$

In order to obtain a higher purity sample one can demand a high enough momentum of the D^+ candidates.

The disadvantages of this method are: the uncertainty in the $D^+ \to K^+\pi^+\pi^-$ branching fraction is large, the resonant substructure in these D^+ decays needs to be properly implemented in the simulation of $K^+\pi^+\pi^-$ decays, and the systematic uncertainty from particle identification needs to be included.

15.1.2.3 K^0_S decay length distribution

Another method to check the data-MC discrepancy in the K^0_S reconstruction is to compare the K^0_S decay length distribution. The D^* decay mode $D^* \to D^0\pi_s, D^0 \to \pi^+\pi^- K^0_S$ used for the K^0_S efficiency study above provides a clean sample to measure the K^0_S decay length. Assuming that decays with short decay length are inside the fiducial region of the silicon vertex detector and are well simulated based on the tracking study, one can compare the fraction of reconstructed K^0_S with longer decay length between data and MC events. The K^0_S data-MC efficiency correction and the corresponding systematic uncertainty are thus obtained.

15.1.3 Particle identification

The performance of particle identification (PID) for *BABAR* and Belle is described in Chapter 5, with the related systematic uncertainties briefly discussed in Sections 5.3.2 and 5.4. The PID efficiency and its uncertainty are studied by choosing low-background samples in which the type of charged particles is identified without using the PID information. Then one can examine if the PID gives the correct identification. The PID efficiency and uncertainty can be estimated by counting the number of particles that are correctly identified. For instance, K^0_S and Λ are relatively long-lived and can fly a measurable distance before they decay into $\pi^+\pi^-$ or $p\pi^-$; requiring a distinct vertex and the appropriate mass range for the two-track mass provides clean samples of pions and protons. As for kaons, the sample of $D^{*+} \to D^0\pi^+_s$ and $D^0 \to K^-\pi^+$ is used. For electrons and muons, samples of $e^+e^- \to e^+e^-l^+l^-, e^+e^- \to l^+l^-(\gamma)$ and $J/\psi \to l^+l^-$ ($l = e$ or μ) are chosen to study the performance of lepton identification; by positively identifying one of the leptons, the PID efficiency for the other can be studied.

The correction and systematic uncertainty for the signal efficiency due to PID can be estimated using the data-MC ratios of the PID efficiency and their uncertainties in different momentum, polar angle and azimuthal angle bins, similar to what is described for tracking systematics in Section 15.1.1. An alternative way to obtain the PID efficiency and its systematic uncertainty is to use signal MC events without applying any PID selection and weight each event according to the PID efficiency obtained in data. For sufficiently large Monte Carlo samples, the uncertainty due to the size of the sample for understanding the PID performance can be omitted. Typical systematic uncertainties per charged track in *BABAR* and Belle measurements are 0.8%-1.0%. The uncertainty due to the PID efficiency is treated as correlated among several tracks.

15.1.4 π^0 reconstruction

The reconstruction efficiency of π^0's in the decay channel $\pi^0 \to \gamma\gamma$ can differ between data and simulation mainly for the following reasons (see Section 2.2.4 for the description of the electromagnetic calorimeters):

- *Imperfect modeling of the material distribution in the detector.* A photon can undergo pair production in the material of the detector before reaching the calorimeter. If the produced tracks are reconstructed in the tracking detectors, the corresponding clusters in the calorimeter, if any, are tagged as being produced by a charged track and the photon candidate is lost. Even if the reconstruction algorithms still find a photon candidate, the energy resolution might be degraded, leading to a π^0 candidate with an incorrectly reconstructed energy or mass.
- *Imperfect modeling of photon shower shape.* In order to discriminate electromagnetic from hadronic showers, shower shape variables such as the lateral moment,[47] the number of crystals in a shower etc. are used. Showers tend to be somewhat narrower in simulation than in data, creating a small efficiency difference between data and MC.
- *Split-offs.* The particle showers created by hadrons interacting with the material in the calorimeter contain a fraction of neutral hadrons. Such secondary hadrons can travel a sizable distance in the calorimeter before interacting with the material and depositing (a part of) their energy. These so-called *split-offs* leave the signature of a calorimeter cluster without an associated track pointing to it, which is hard to distinguish from a real photon. Cluster split-offs occur close to tracks, and the secondary showers usually have low energies. Detailed modeling of hadronic showers is difficult, thus split-offs present a further potential source of systematic difference between data and simulation.
- *Additional background in data.* Real data events typically contain more (soft) photon candidates, most of which originate from beam-related background. This background consists primarily of electrons and positrons from radiative Bhabha scattering which hit elements of the detector or the beam line, producing neutrons with energies in the MeV range, which then can produce low energy showers in the calorimeter. These additional photon candidates increase the number of $\gamma\gamma$ combinations in data, giving rise to more π^0 candidates, especially at low π^0 momentum.

The data-MC efficiency ratio is first measured in very clean events in which the presence of a π^0 can be predicted with little background. Possible differences between the π^0 reconstruction efficiency in such events and high-multiplicity events with higher background must then be

[47] The lateral moment of a cluster in the calorimeter is defined as $LAT \equiv \sum_{i=3}^{N} r^2_{\perp i} E_i / (25(E_1 + E_2) + \sum_{i=3}^{N} r^2_{\perp i} E_i)$, where the N crystals which belong to a cluster are sorted by their energy E_i, and $r_{\perp i}$ is the (transverse) distance between the cluster centroid and the ith crystal.

also estimated. The data-MC efficiency ratio is measured using τ (Belle, *BABAR*) and η (Belle) decays and multihadronic events with a photon radiated from the initial state (*BABAR*). An important step is the validation of the efficiency correction which is derived from this class of events and to make sure the correction is applicable to B or charm decays, which tend to produce substantially more activity in the detector. In the following, we present some of the methods used to determine the π^0 efficiency correction and the associated systematic uncertainty.

15.1.4.1 Methods using τ decays

A clean way to extract the π^0 reconstruction efficiency is provided by comparing the observed rates of $\tau^- \to \pi^-\pi^0\nu_\tau$ to $\tau^- \to \pi^-\nu_\tau$ with the respective ratio of the branching fractions. The branching fractions of the two decays are known with sub-percent precision, allowing a measurement of the π^0 reconstruction efficiency with an uncertainty of the order of 1%.

In *BABAR*, $e^+e^- \to \tau^+\tau^-$ events are tagged with one τ decaying into $e^\pm\nu_e\nu_\tau$ (tag). On the signal side, a charged track incompatible with either the electron or the muon hypothesis is required. π^0 candidates are reconstructed from two photon candidates; events with more than two photon candidates (*i.e.* those with extra activity in the calorimeter) are removed.

The efficiency correction $\eta \equiv \varepsilon^{\rm data}/\varepsilon^{\rm MC}$ is computed as a function of the π^0 momentum p_{π^0} as the double ratio

$$\eta(p_{\pi^0}) = \frac{N(\tau \to \pi\pi^0\nu)^{\rm data}(p_{\pi^0})}{N(\tau \to \pi\nu)^{\rm data}} \Big/ \frac{N(\tau \to \pi\pi^0\nu)^{\rm MC}(p_{\pi^0})}{N(\tau \to \pi\nu)^{\rm MC}} \tag{15.1.2}$$

$$= \frac{N(\tau \to \pi\pi^0\nu)^{\rm data}(p_{\pi^0})}{N(\tau \to \pi\pi^0\nu)^{\rm MC}(p_{\pi^0})} \Big/ \frac{N(\tau \to \pi\nu)^{\rm data}}{N(\tau \to \pi\nu)^{\rm MC}} \,. \tag{15.1.3}$$

In this double ratio, the track reconstruction and PID efficiencies (used on the tag side track) largely cancel provided there are no correlations between the tag and the signal side of the event:

$$\frac{N(\tau \to \pi\pi^0\nu)^{\rm data}}{N(\tau \to \pi\nu)^{\rm data}} = \frac{N_{\tau\tau}\, \mathcal{B}(\tau \to \pi\pi^0\nu)\, \varepsilon^{\rm data}_{\rm tag}\, \varepsilon^{\rm data}_{\rm track}\, \varepsilon^{\rm data}_{\pi^0}}{N_{\tau\tau}\, \mathcal{B}(\tau \to \pi\nu)\, \varepsilon^{\rm data}_{\rm tag}\, \varepsilon^{\rm data}_{\rm track}}$$
$$\approx \varepsilon^{\rm data}_{\pi^0} \frac{\mathcal{B}(\tau \to \pi\pi^0\nu)}{\mathcal{B}(\tau \to \pi\nu)} \tag{15.1.4}$$

Using the well-measured branching fractions (and the corresponding values for simulated data), the double ratio directly measures the ratio of π^0 reconstruction efficiencies in data and simulation, modulo a few small corrections for split-offs and the mis-modeling of the high-energy tail of the $\pi^0\pi^-$ mass spectrum. The resulting correction factor depends on the π^0 momentum in the laboratory frame. For a typical π^0 momentum spectrum, the correction factor is around 0.97 with a statistical uncertainty well below 1%.

The result of the τ based study is combined with the results from ω production in events with hard initial state radiation (see below, Section 15.1.4.2) to obtain an overall momentum dependent π^0 efficiency correction. A systematic uncertainty of about 1.5% is assigned to cover the systematic differences between the two methods.

Belle also uses $\tau^+\tau^-$ events where one of the τ leptons decays leptonically and the other into $\pi^\pm\pi^0\nu$ (single π^0 events), and events where both decay into $\pi^\pm\pi^0\nu$ (double π^0 events). The ratio of data and MC simulation π^0 reconstruction efficiencies can be expressed as

$$\frac{\varepsilon^{\rm data}_{\pi^0}}{\varepsilon^{\rm MC}_{\pi^0}} = 2 \cdot \frac{N_2^{\rm data}}{N_1^{\rm data}} \cdot \frac{\mathcal{B}(\tau \to \ell\nu\bar{\nu})}{\mathcal{B}(\tau \to \pi\pi^0\nu)} \cdot \frac{\varepsilon_1^{\rm MC}}{\varepsilon_2^{\rm MC}} \cdot \frac{(\varepsilon^{\rm data}_{1'}/\varepsilon^{\rm MC}_{1'})}{(\varepsilon^{\rm data}_{2'}/\varepsilon^{\rm MC}_{2'})}, \tag{15.1.5}$$

where $N_{1,2}^{\rm data}$ are the numbers of reconstructed single and double π^0 events, and $\varepsilon_{1,2}^{\rm MC}$ are the efficiencies to reconstruct these events in the Monte Carlo; writing $\varepsilon_1 = \varepsilon_{\pi^0}\varepsilon_{1'}$ and $\varepsilon_2 = \varepsilon^2_{\pi^0}\varepsilon_{2'}$, Belle separates the efficiency for each class of event into the π^0 reconstruction efficiency, and a remainder term. The final double-ratio expression in Eq. (15.1.5) is assumed to be unity. Such a study reveals a correction factor of around 0.96 to be applied to the simulated reconstruction efficiency, with an uncertainty of 2.4%.

A comparison of $\eta \to 3\pi^0$ and $\eta \to \pi^+\pi^-\pi^0$ decays also yields the π^0 reconstruction efficiency directly from the data, and the systematic uncertainty at Belle is found to be 4%.

15.1.4.2 Methods using ω-ISR and $\omega\pi^0$-ISR events

Another approach to measure the difference in the π^0 reconstruction efficiency between data and Monte Carlo is to use the low-background processes $e^+e^- \to \gamma_{\rm ISR}\omega$ and $e^+e^- \to \gamma_{\rm ISR}\omega\pi^0$, where the ω decays to $\pi^+\pi^-\pi^0$ and the initial state radiation photon is required to have a laboratory energy above 3 GeV. As in the case of the tracking efficiency study, one can exploit the fact that the kinematics of the reaction are fully known: both energy and momentum vector of the π^0 are predicted by a kinematic fit, using only the information of the initial state particles, the ISR photon and the two pion tracks. In the reaction $e^+e^- \to \gamma_{\rm ISR}\omega\pi^0$ the directly produced π^0 is required to be reconstructed while the efficiency study is performed with the π^0 from the ω decay. This method allows to study the π^0 efficiency as a function of the π^0 momentum and flight direction.

This method, in both reaction channels, makes use of the rather narrow width of the ω. Signal events in which the π^0 momentum and energy were correctly inferred by the kinematic fit peak strongly close to the nominal ω mass; a fit to this mass spectrum yields the number of produced events which should contain a π^0. The number of events with a reconstructed π^0 is extracted from testing all π^0 candidates in the event with a $5C$ kinematic fit under the hypothesis $e^+e^- \to \omega\gamma \to \pi^+\pi^-\pi^0\gamma$. The classification of events into the categories 'π^0 found' or 'π^0 lost' is quite sensitive to the presence of extra π^0 candidates due to background photons, which is different in data and simulation.

At *BABAR*, the π^0 efficiency corrections derived from τ and ω-ISR events as described above are combined into an overall efficiency correction with an associated systematic uncertainty which also accounts for the remaining differences between the two methods. The π^0 efficiency correction factors as a function of the π^0 lab momentum for both analyses as well as the combined correction factor which is recommended for general analyses are shown as a function of the π^0 lab momentum in Fig. 15.1.4.

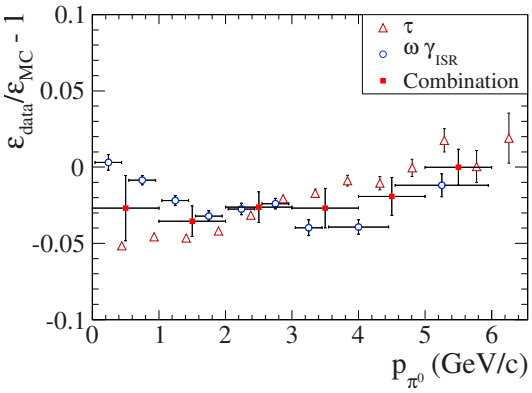

Figure 15.1.4. *BABAR* π^0 efficiency correction factors as a function of the π^0 lab momentum. The closed squares show the combination of the two analyses described in the text, with the error bars indicating the total systematic uncertainty associated with the efficiency correction (Aubert, 2013).

15.1.4.3 Slow π^0, and π^0 efficiency in multi-hadronic decays

As described above, the π^0 efficiency correction is primarily measured in very clean events with few tracks and few or no additional neutrals. Typical B decays, however, contain more tracks and neutral candidates, which can affect the probability to correctly reconstruct a π^0. To ensure that the efficiency correction is applicable to this class of multi-hadron events, an inclusive measurement of the ratio of $D^0 \to K\pi\pi^0$ to $D^0 \to K\pi$ decays has been performed at *BABAR*. The π^0 efficiency correction derived from this analysis suffers from a larger statistical uncertainty due to background subtraction and is less precise than the one derived from τ or ISR events. Within the given uncertainties, the π^0 efficiency corrections agree.

A dedicated study of low-momentum π^0's has been performed using the decay chain $B^0 \to D^{*-}\pi^+, D^{*-} \to D^-\pi^0$. The method is similar to the one used for low-momentum tracks described in Section 15.1.1.2.

Similar to the study for the tracking efficiency, the data-MC efficiency ratio can also be computed using the double ratio

$$\eta(p_{\pi^0}) = \frac{N(D^0 \to K^+\pi^-\pi^0)^{\rm data}}{N(D^0 \to K^+\pi^-)^{\rm data}} \Big/ \frac{N(D^0 \to K^+\pi^-\pi^0)^{\rm MC}}{N(D^0 \to K^+\pi^-)^{\rm MC}} \,. \tag{15.1.6}$$

This π^0 efficiency correction is thus obtained in hadronic events, as opposed to the efficiency in clean $e^+e^- \to \tau^+\tau^-$ events. To reduce the D^0 combinatorial background, one can demand a soft π^+ that combines with a D^0 candidate to form a D^{*+} and the reconstruction uncertainty for slow pions cancels in the ratio. The dominant systematic error in the correction is the branching fraction uncertainty of $D^0 \to K^+\pi^-\pi^0$, which results in a common scale factor across the full momentum range. If the data-simulation efficiency ratio for the π^0 reconstruction is known from other studies in a typical momentum range, one can normalize the double ratio in that momentum range to obtain the correction factors and the corresponding uncertainties in other momentum ranges. For neutral pions with momenta below 200 MeV/c the data-MC simulation correction factor at Belle is found to be 1.023±0.024 for the data recorded with the SVD2 vertex detector (see Chapter 2). For *BABAR*, a similar study results in a correction factor for low-momentum π^0 of 0.98 ± 0.07.

15.1.5 High-energy photons

The detection efficiency of high energy photons (with typical energies above $E_\gamma \approx 2\,\text{GeV}$) is measured using radiative Bhabha events: $e^+e^- \to e^+e^-\gamma$ (Belle) and $e^+e^- \to \mu^+\mu^-\gamma$ (*BABAR*). After requiring exactly two tracks in an event that are identified as an e^+e^- or $\mu^+\mu^-$ pair, the missing energy direction can be computed. The photon efficiency is estimated from the fraction of events that have a reconstructed photon matching the magnitude and direction of the missing energy, which is required to point to the electromagnetic calorimeter fiducial region. The precise value of the efficiency correction depends on the details of the criteria to select photon candidates and the decision whether a photon candidate matches the prediction from the kinematic fit.

For recent *BABAR* analyses of ISR events (Lees, 2012h), the difference in the reconstruction efficiency of high-energy photons between data and simulation was determined to be $\varepsilon_{\rm data} - \varepsilon_{\rm MC} = (-1.00 \pm 0.02\ (\text{stat}) \pm 0.55\ (\text{syst})) \times 10^{-2}$.

15.2 Analysis procedure

A second, important group of systematic uncertainties is related to the analysis procedure. This includes the use of external parameters as well as the use of specific models to separate signal from background and to extract the quantity of interest from the data. In a typical analysis at the B Factories, multi-dimensional maximum likelihood fits are often used to separate signal and background on a statistical basis (see Section 11). This procedure needs to be carefully checked and validated and systematic uncertainties assigned where appropriate. The most important sources of these systematic uncertainties are discussed in this section.

15.2.1 External input

In many analyses, the physics observables are extracted from a fit with some of the parameters fixed to values based on external information. Using external information is necessary if for example the statistical power of the selected sample under consideration is not large enough to determine all relevant parameters with sufficient accuracy. For instance, in rare B decay searches the peak positions and resolutions of $m_{\rm ES}$ and ΔE of signal events are often fixed; in Dalitz plot analyses the masses and natural widths of intermediate resonances are fixed to their PDG values; the mixing parameter Δm_d and the B^0 meson lifetime are not allowed to vary in fits for time-dependent *CP* asymmetries. The systematic uncertainties that arise from using external input parameters are obtained by checking the deviations in the fitted values after varying the external parameters according to their uncertainties.

Unlike the PDG values used as the external parameters, some of the *p.d.f.* parameters explicitly depend on the detector resolution, and the corresponding uncertainties are determined using data. For instance, the uncertainty of $m_{\rm ES}$ is dominated by the beam energy spread and the $m_{\rm ES}$ peak position and resolution are determined using high-statistics control samples such as $B \to D^0\pi$ and $D^0 \to K^+\pi^-(\pi^0)$ for decay modes without (with) photons in the final state. The corrections between data and simulation and their uncertainties are obtained from these control samples and applied to the decay modes of interest. The same procedure is applied to estimate the correction and uncertainty for the ΔE *p.d.f.* parameters obtained in simulation. It is preferred to choose a control decay mode with high statistics that has the same numbers of charged and neutral particles in the final state as the mode under study. The same consideration can be applied to estimate systematic uncertainties related to flavor tagging, vertexing, mass resolutions and other external parameters.

Most analyses also rely on external input to derive the quantity of interest from directly measured quantities. Examples of such external parameters are the integrated luminosity (or, alternatively, the number of $B\overline{B}$ pairs produced), branching fractions of daughter decays, particle masses and their lifetimes, etc. These quantities and their uncertainties are typically taken from averages calculated by the Particle Data Group, with the exception of the luminosities, which are measured by the B Factories (see Sections 3.2.1 and 3.6.2). At both experiments, the precision of the luminosity measurement is limited by systematic uncertainties, mainly by uncertainties of the Monte Carlo generator(s) used to calculate the cross-sections of the physics processes used to measure luminosity. At Belle, the luminosity is measured using Bhabha scattering to a precision of about 1.4%. *BABAR* uses both Bhabha scattering and $e^+e^- \to \mu^+\mu^-$ (Lees, 2013i); the systematic uncertainty of the luminosity is about 0.5% for the data collected at the $\Upsilon(4S)$.

The uncertainties from these external parameters are propagated to the final result using either Gaussian error propagation in the simplest cases, or by varying the parameters within their uncertainties and repeating the analysis.

15.2.2 Modeling of background

Background distributions are often modeled using events from simulation or sidebands of *e.g.* mass distributions. A typical example is modeling the background distributions in the Dalitz plot for B or D decays. One can assume that the Dalitz plot distributions for the combinatorial background are the same as those obtained using events outside the $m_{\rm ES} - \Delta E$ signal region or in the D mass sideband region. The background model can be cross-checked by comparing the distributions of simulated background events in the signal and sideband regions or by comparing the data distributions in different sideband regions. The systematic uncertainty due to the background modeling is then estimated by using the *p.d.f.*s obtained from different sideband regions and by varying the *p.d.f.* parameters according to the uncertainties.

In many cases the background is sufficiently large so that the background *p.d.f.* parameters can be determined directly from a fit to data. This procedure moves the uncertainty originating from the background *p.d.f.* parameters into the overall statistical uncertainty returned by the fit. However, in many cases the actual shape of the background distribution is not known from first principles, and there may be several different parameterizations which describe, within the given uncertainties of the data, the background shape equally well. The systematic uncertainty related to this is determined by choosing different functions for the background *p.d.f.*s and repeating the fit. For example, B yields in many rare decay searches are extracted with an unbinned maximum likelihood fit to the distributions of $m_{\rm ES}$, ΔE and other variables (see Chapter 9). The *p.d.f.*s of the B decay background are usually estimated from simulations, while the continuum *p.d.f.*s are modeled as a polynomial function for ΔE and an ARGUS function (see Eq. 7.1.11) for $m_{\rm ES}$ with their parameters allowed to vary in the fit. Systematic uncertainties of the fit can be evaluated using other function models that provide an acceptable goodness of the fit.

15.2.3 Fit bias

The results of multi-dimensional maximum likelihood fits (see Chapter 11) can be systematically biased when the correlations between various discriminating variables are not considered or several components have similar *p.d.f.*s, so that the fit cannot completely distinguish between those components. The fit bias can be examined using large ensembles of simulated experiments ('toy MC', see Section 11.5.2); a bias correction is then derived from these studies. There is no unique method of assigning a systematic uncertainty to this bias correction, and analyst discretion is required. As a conservative approach, the systematic uncertainty associated with the bias correction is often taken to be half or even all of the correction.

15.3 Systematic effects for time-dependent analyses

A number of systematic effects need to be understood in order to verify that one is able to correctly extract time-dependent information from fits to data. The general methodology for performing a time-dependent *CP* asymmetry analysis at the B Factories is outlined in Chapter 10. In addition there are special cases that have been considered over the course of these experiments including time-dependent analyses of modes requiring a full angular analysis (Chapter 12), and time-dependent Dalitz plot analyses (Chapter 13).

In the following we discuss systematic uncertainties arising from detector and reconstruction effects (see Sections 15.3.1 through 15.3.3), uncertainties from physics parameters (see Section 15.3.4), and uncertainties arising from approximations made in the analyses (see Sections 15.3.5 through 15.3.6). The systematic uncertainties quoted on S and C (see Chapter 10) in the remainder of this chapter are typical values obtained by the B Factories.

15.3.1 Alignment of the vertex detector

In order to precisely reconstruct the decay vertex position of both B mesons in an event and the value of the proper time difference Δt between the decays of both mesons (see Chapter 6 for a detailed discussion on these matters), accurate information is required on the position of the reconstructed *hits* that correspond to the signature of charged particles traveling through the tracking volume. The silicon detectors at the B Factories dominate our understanding of the vertex positions by virtue of their proximity to the interaction point, and hence the B decay vertices. The first few measurement points of each track originating from a B decay will be recorded in the silicon detector, and hence one must precisely know the position of the strips embedded in the silicon. This position changes slightly with time, and if not corrected for, will smear out the knowledge of each hit position, and hence fitted track and computed vertex. The purpose of the silicon detector calibration is to correct for variations in the alignment as a function of run period, and in the case of Belle, the differences between the different SVDs installed during operation (see Chapter 2).

While the detector calibration is extremely effective at correcting for variations in detector position as a function of time, there is an uncertainty arising from any residual lack of knowledge in the position and orientation of each double-sided silicon sensor module that provides a measurement of r, ϕ and z within the detector. The local alignment procedure adopted by *BABAR* is described in detail in (Brown, Gritsan, Guo, and Roberts, 2009). In order to estimate the magnitude of the uncertainty arising from the alignment of the silicon detector, different sets of alignment constants are applied to simulated Monte Carlo data for signal events or equivalently the silicon detector positions are intentionally modified in a plausible range in both global displacement and rotation as well as random misalignment for each silicon sensor, and the change in fitted values of the *CP*-violating parameters S and C (see Section 10.2) from the nominal value is assigned as an uncertainty from this source of systematic. The magnitude of this uncertainty on S and C is at most a few per mille. In extreme cases, for example modes such as $B^0 \to \rho^+\rho^-$ that suffer from a significant contribution from mis-reconstructed signal in the final state, the effect of the silicon detector alignment is somewhat larger: ~ 0.01. The reason for this is that some of the mis-reconstructed signal in this final state has a biased reconstructed vertex position, resulting from the inclusion of low-momentum tracks reconstructed at the extremities of the helicity angle distributions (see Chapter 12). Sometimes these low momentum tracks are incorrectly assigned from the rest of the event to a signal B candidate, rather than including the correct tracks from the signal side. Different alignment sets change the reconstruction rate of this component of mis-reconstructed signal, and thus induce a bias on the measured observables S and C.

15.3.2 Beamspot position, z scale and boost

As discussed in Chapter 6, the beamspot location can be used to improve constraints on vertex reconstruction, and is used when reconstructing the tagging B meson vertex. The dominant contribution to the systematic uncertainty when adding this constraint comes from the limited knowledge of the vertical position of the beamspot. The knowledge of the beamspot is included in the vertex fit via the addition of an extra term in the χ^2 of the track fit. The limitation in the absolute knowledge of the beamspot location therefore translates into a systematic uncertainty on the reconstructed value of Δt, and hence propagates through onto the measured observables S and C in a time-dependent *CP* asymmetry analysis. Detailed studies of the beam-spot position calibration were performed at the B Factories (see Section 6.4).

Knowledge of the mean vertical position is the dominant systematic uncertainty from the use of the beamspot in *BABAR*, while its spread is found to give a much larger effect in Belle. The corresponding systematic uncertainties in the measured values of S and C are estimated by modifying the position and uncertainty on the vertical beamspot position according to the variations seen in data. For example, *BABAR* varies this position by $\pm 20\mu$m, as well as increase the uncertainty on this quantity by 20μm to evaluate the systematic uncertainty arising from the use of the beamspot in vertex reconstruction. Belle changes the beamspot position uncertainty to a factor of 2 larger or smaller value than the nominal one, 21μm. The relative change in S (C) from its nominal value ($S \sim \sin 2\phi_1$, $C \sim 0$) is found to be 0.13% (0.06%) in *BABAR* and 0.3% (0.08%) in Belle for B decays to $c\bar{c}s$ final states.

Other important factors impacting the measurement of S and C are the z scale determined from the vertex detector, and the boost factor. Detailed studies of control

samples show that the z scale uncertainty is the dominant of these two effects, and to account for these uncertainties Δt and $\sigma_{\Delta t}$ are scaled by 0.6%. This results in negligible systematic shifts, of the order of 4.7×10^{-4} in S and 2.3×10^{-4} in C, for B decays to $c\bar{c}s$ final states. These are interpreted as systematic uncertainties from the z scale and boost determination.

15.3.3 Resolution function and flavor tagging parameters

Both the Δt resolution function parameters and flavor tagging performance parameters are integral inputs to a time-dependent analysis. There are two conceptual ways to incorporate systematic uncertainties from these parameters into the extracted values of S and C. Firstly one can perform a simultaneous fit to the so-called $B_{\rm flav}$ sample of events (see Section 10.2) and the selected signal candidates. In this approach the uncertainties on and correlations between resolution function and tagging model parameters are automatically folded into the statistical uncertainty reported for the asymmetry parameters. This approach is adopted by *BABAR*. The second approach is to take the results of a reference fit to the $B_{\rm flav}$ data sample, and incorporate the variations of S and C from the nominal result when varying the resolution and tagging parameters by their uncertainties. This approach results in a number of contributions that are added in quadrature ignoring the correlations that exist between them. Belle uses the second approach as there are only small correlations between the parameters describing the resolution and tagging performance. As a result this second approach provides a conservative and still proper estimation of the systematic uncertainty from the knowledge of these parameters. The typical uncertainty on S and C obtained for the resolution function and tagging parameters using the second approach is ≤ 0.01.

15.3.4 The effect of physics parameters

Time-dependent *CP* asymmetry measurements at the B Factories follow the method described in Chapter 10. In particular, these analyses assume $\Delta\Gamma_d = 0$, unlike the situation for time-dependent measurement for B_s (and eventually D) meson decays. No systematic uncertainty is ascribed for the use of this assumption, which is well motivated by theoretical arguments for the statistics available at *BABAR* and Belle. A non-zero value of $\Delta\Gamma_d = 0$ would give rise to hyperbolic sine and cosine terms in the time-dependent asymmetries as discussed in Section 17.5.2.6, and one can estimate the magnitude of any systematic uncertainty from neglecting these hyperbolic terms by comparing results obtained using an ensemble of simulated Monte Carlo experiments with $\Delta\Gamma_d \neq 0$, and observing the bias introduced on the fitted values of S and C. If one assumes that $\Delta\Gamma_d \leq 0.01$, the systematic uncertainties in S and C would be negligible, if one were to use the existing experimental limit on the value of $\Delta\Gamma_d$ the bias on S would be 0.005.

The physics parameters τ_{B^0} and Δm_d are required inputs for time-dependent measurements. During the ML fitting procedure used to extract S and C from data, the B^0 lifetime and mixing frequency are fixed to their nominal values. The uncertainty on the measured values of τ_{B^0} and Δm_d are propagated through the fitting procedure, assuming that they are uncorrelated, and the resulting variation of S and C from the nominal fitted values is assigned as an uncertainty. This source of uncertainty is found to be at most a few per-mille.

15.3.5 *CP* violation in background components

A subtlety raised in Chapter 10 is the issue of correctly accounting for any *CP* asymmetry (time-dependent or time-integrated) in background modes when performing a time-dependent analysis. This issue is not significant for the case of charmonium decays such as $B^0 \to J/\psi K^0_S$, where there is very little background, however it should be considered when analyzing modes with significant levels of background such as $B^0 \to \rho^+\rho^-$.

There are two types of *CP* violating background that may occur (*i.e.* direct and mixing-induced *CP* violation, see Chapter 16) from neutral B mesons, and charged B mesons may only violate *CP* via direct decay. In addition one may need to consider the $B\overline{B}$ background, where the B signal candidates are formed by combining the daughter particles of the true $B_{\rm tag}$ and $B_{\rm rec}$. In general the reconstructed $|\Delta t|$ values of these background events are smaller than the true ones as the reconstructed $B_{\rm tag}$ and B_{CP} vertices tend to be closer to each other.

Such an effect can be taken into account by replacing the B lifetime in the exponential decay of Eq. (10.2.2) with an effective lifetime. This is particularly relevant for final states with charm mesons in them as discussed in Chapter 10, but is also manifest at a lower level for B backgrounds without charm decays. Generally one assumes that any bias for the latter class of B decays is negligible.

Having corrected for the above reconstruction effects one is faced with having to address the issue of a physical asymmetry in the background decay channel. In the case of a neutral B decay the asymmetry will be of the form of Eq. (10.2.8). One has to account for tagging and resolution effects, and typically it is assumed that it is valid to use the same tagging and resolution parameters for the background channels as for the correctly reconstructed signal. Ideally one should generate samples of Monte Carlo simulated data for each *CP* violating background mode with the values of S and C as measured in data. This way any dilution from mis-reconstructing a given channel is taken into account when setting the values of the effective S and C required to model the *CP* asymmetry of a given background mode. In cases where there is no measurement of the asymmetry parameters, but it is reasonable to expect a non-zero asymmetry, one varies the effective values of S and C between $+1$ and -1 to estimate the maximal effect a given background would have on the signal. *CP* violation

in charged decay modes can be accounted for in an analogous way, where one uses the time-integrated asymmetry to allow for any possible direct *CP* violation.

Typical systematic uncertainties in the values of the *CP* asymmetry parameters measured for the high-background decay $B \to \rho^+\rho^-$ arising from possible *CP* violation in the background are $\leq 0.2\%$ for S and $1-2\%$ for C, see Aubert (2007b). This uncertainty is dominated by contributions from $B \to a_1\pi$ decays, assuming that *CP* violation could be large, as the example discussed predates *CP* asymmetry measurements of $B \to a_1^{\pm}\pi^{\mp}$.

15.3.6 Tag-side interference

In order for a decay channel to have non-zero *CP* asymmetry, it must have at least two interfering amplitudes with different weak phases. This is a necessary condition, but it is not sufficient to guarantee that there will be an observable *CP* violation effect in that final state. The discussion so far has focused on interfering amplitudes on the $B_{\rm rec}$ side of the event leading to a measurable *CP* violation effect. However it was pointed out by Long, Baak, Cahn, and Kirkby (2003) that in addition to interference on the $B_{\rm rec}$ side, one has to consider possible effects of interference on the $B_{\rm tag}$ side, where more than one amplitude contributes to the final state. If neglected, interference effects on the $B_{\rm tag}$ side of the event could result in an undesired contribution to the measured *CP* asymmetry for the $B_{\rm rec}$. Many different final states are included in the (inclusive) reconstruction of the $B_{\rm tag}$ with different contributions to the so-called tag-side interference effect.

As discussed in Section 8, the dominant contributions to the tagging efficiency come from semi-leptonic decays with final state leptons, and hadronic decays such as $B \to D^{(*)-}\pi^+$. Since the semi-leptonic decays proceed via a single amplitude in the SM, semi-leptonic tagged decays do not suffer from tag-side interference. However possible interference effects need to be considered when performing a time-dependent analysis, where $B_{\rm tag}$ decays to a hadronic final state as the decay can proceed by more than one amplitude.

If one considers the decay $B \to D^-\pi^+$, with subsequent $D^- \to K^+\pi^-\pi^-$ decay as an example, the final state can be reached via the CKM preferred $b \to c\overline{u}d$ transition of a $\overline{B}^0$. The same final state can also be reached from a B^0 through $B^0 - \overline{B}^0$ mixing followed by a doubly-CKM suppressed $\overline{b} \to \overline{u}c\overline{d}$ transition. The ratio of these two amplitudes is given approximately by the ratio of CKM matrix elements $|(V_{ub}^* V_{cd})/(V_{cb} V_{ud}^*)| \simeq 0.02$.

The strength of the amplitude of the doubly-CKM suppressed relative to the allowed decay can be parameterized as

$$\frac{\overline{A}_f}{A_f} = r_f e^{-i\phi_3 + i\delta_f}, \tag{15.3.1}$$

where r_f is the ratio of suppressed to favored decays, and δ_f is the relative strong phase difference between the B^0 and $\overline{B}^0$ decay proceeding via $\overline{b} \to \overline{c}u\overline{d}$ and $b \to u\overline{c}d$ transitions, respectively. In practice a number of modes are summed over on the tag-side of the event, and we replace r_f and δ_f with primed variants to represent the effective ratio of amplitudes and phase difference of an ensemble of modes.

It is possible to compute a correction on the time-dependent asymmetry parameters S and C resulting from the use of hadronic tag modes, either for a given mode, or an ensemble of modes. These corrections are a function of Δt and have the effect of slightly reducing the amplitude and broadening the time distribution, or increasing the amplitude and narrowing the distribution as discussed in Section VI and Fig. 3 of Long, Baak, Cahn, and Kirkby (2003). The effect depends on the values of r'_f and δ'_f. Thus one can expect the measured values of S and C in a time-dependent analysis to differ from the true values for hadronically tagged events.

The semileptonic decay, $B^0 \to D^{*-}\ell^+\nu_\ell$ is a high purity $B_{\rm flav}$ mode and free from doubly-CKM suppressed diagram as already discussed. Thus applying the proper flavor tagging algorithm on the $B_{\rm tag}$ decay products in this sample gives an estimation of the possible range of the effective ratio of the amplitudes and phase difference for an ensemble of the tag-side modes. This estimation is used to see the effects on S and C as described in more detail later.

If a time-dependent analysis were limited by systematic uncertainties arising from tag-side interference, there are two possible approaches that may be considered to mitigate this uncertainty: (i) only use semi-leptonic tagged events, thus removing the affected data from the analysis, and (ii) given sufficient data, to measure the ratio of CKM allowed to suppressed decays, and the corresponding phase difference between the amplitudes using control samples. In the following discussion the true values of these time-dependent asymmetry parameters are represented by S_0 and C_0, whereas the measured values of these observables are denoted by $S_{\rm fit}$ and $C_{\rm fit}$.

15.3.6.1 The tree dominated $B^0 \to J/\psi K_S^0$ decay

The prime example of a time-dependent measurement made by the B Factories is that of $B^0 \to J/\psi K_S^0$, which is described in Section 17.6. The biases on the true values of measured time-dependent asymmetries in this decay arising from tag-side interference can be treated as a perturbation on the measurement, *i.e.* a systematic shift with an associated uncertainty. It is possible to relate the true values of the *CP* asymmetry parameters S_0 and C_0 to the fitted values $S_{\rm fit}$ and $C_{\rm fit}$ up to some correction related to the additional amplitudes interfering on the tag side of the event. The correction depends on $\Phi = 2\phi_1 + \phi_3$ resulting from the phase difference between the doubly CKM suppressed and CKM allowed amplitudes on the tag side of the decay and the short distance $B^0 - \overline{B}^0$ mixing box contributions. The corrections to the fitted *CP* asymmetry parameters are related to the magnitude of the effective ratio of CKM suppressed to allowed amplitudes for the tag-side decay given by r'_f, as shown in the following

$$C_{\rm fit} = C_0 + 2C_0 r'_f \cos\delta'_f \{G\cos(\Phi) - S_0 \sin(\Phi)\} \\ -2r'_f \sin\delta'_f \{S_0 \cos(\Phi) + G\sin(\Phi)\}, \quad (15.3.2)$$

$$S_{\rm fit} = S_0 + 2S_0 r'_f \cos\delta'_f G\cos(\Phi) \\ +2r'_f \sin\delta'_f C_0 \cos(\Phi). \quad (15.3.3)$$

Here the factor G is $2{\rm Re}\lambda_{CP}/(|\lambda_{CP}|^2+1)$, and λ_{CP} is the quantity given in Eq. (10.1.10) evaluated for the $B_{\rm rec}$ reconstructed in a *CP* eigenstate.

Using a Monte Carlo simulation based approach, one can estimate the magnitude of the effect on the value of $S_{\rm fit}$ and $C_{\rm fit}$ extracted from data, and hence determine S_0 and C_0. In order to do this one has to determine r'_f and δ'_f. The value of r'_f is given by $|(V^*_{ub}V_{cd})/(V_{cb}V^*_{ud})|$ and an estimate of the uncertainty on this can be derived from a comparison of rates for allowed to suppressed $D \to K\pi$ transitions. This comparison indicates that the error on r'_f is about 25%. As there is no knowledge of the phase difference, one assumes that this parameter is uniformly distributed in the simulated pseudo-experiments. This approach of evaluating the effect of tag-side interference for $B^0 \to J/\psi K^0_S$ has been broadly applied to $b \to c\bar{c}s$, $c\bar{c}d$, and $q\bar{q}s$ final states. The magnitude of the systematic uncertainty ascribed to the measurement of S (C) in this set of channels is typically 0.001 (0.014). The systematic uncertainty is negligible for the extraction of $\sin 2\phi_1$ from the golden $b \to c\bar{c}s$ measurements. However this source of systematic uncertainty is significant for some of the precision measurements of C, and in fact dominant for the golden channel $B^0 \to J/\psi K^0_S$ discussed in Section 17.6. For the measurement of ϕ_1 from an ensemble of *CP*-even and odd states (*i.e.* $J/\psi K^0_L$ and $c\bar{c}K^0_S$) *BABAR* ascribes a systematic uncertainty as described above. However, Belle note that there may be some cancellation between the even and odd states and account for this in their estimation of the systematic uncertainty from this source on the combined measurements of S and C (Adachi, 2012c).

There is no indication of a significant shift in the measured values of S and C found via this Monte Carlo simulation based approach, hence no corrections are applied to the results obtained by the B Factories.

15.3.6.2 The complication of loop amplitudes in $B^0 \to \pi^+\pi^-$

An example of a decay with both tree and loop (penguin) amplitudes used in a time-dependent analysis is $B^0 \to \pi^+\pi^-$ which is discussed further in Section 17.7. The decay amplitude for the reconstructed B meson depends on ϕ_3, as does the tag-side. Thus the situation encountered with $B^0 \to \pi^+\pi^-$ is therefore much more complicated than the previous case. The uncertainty from tag-side interference can be as large as $2r'_f$. This complication for calculating tag-side interference applies not only to $B^0 \to \pi^+\pi^-$ decays, but more generally to the set of $b \to u\bar{u}d$ transitions related to ϕ_2 where there are significant penguin contributions. The least problematic of these decays being $B^0 \to \rho^+\rho^-$, which is known to have a small penguin contribution, relative to other $b \to u\bar{u}d$ transitions.

The magnitude of the systematic uncertainty ascribed to the measurement of S (C) in this set of channels is typically $0.007 - 0.010$ ($0.016 - 0.04$) depending on the final state. While small, compared to the overall experimental uncertainty, this is the dominant source of systematic uncertainty for the extraction of C from the $B^0 \to \pi^+\pi^-$ and $\rho^+\rho^-$ channels discussed in Section 17.7. The systematic uncertainty is negligible on the extraction of ϕ_2 for the golden $b \to u\bar{u}d$ measurements given the statistics available at the B Factories.

15.3.6.3 Time-dependent measurement of $\sin(2\phi_1 + \phi_3)$

The measurement of $\sin(2\phi_1 + \phi_3)$ using $B \to D^{*\pm}\pi^{\mp}$ decays is discussed in Section 17.8. The manifestation of tag-side interference in this time-dependent measurement differs from that discussed for the previous two examples as described below. As with the $b \to u\bar{u}d$ transition case the reconstructed B meson depends on ϕ_3, so it is not straightforward to extract an estimate of tag-side interference for $B \to D^{*\pm}\pi^{\mp}$ decays. Furthermore, the amplitude of the $\sin(\Delta m_d \Delta t)$ term in the time-evolution of this decay is $2r\sin(2\phi_1 + \phi_3)$. Here the parameter r is the ratio of doubly-CKM suppressed to allowed decays for the reconstructed B meson (the $B \to D^{*\pm}\pi^{\mp}$) and has nothing to do with the tag-side of the event.[48] The magnitudes of both r_f and r'_f are expected to be comparable and of the order of 0.02, thus there is the potential for tag-side interference to obscure the signal measurement. It is possible to perform an analysis of the time-dependence of $B \to D^{*\pm}\pi^{\mp}$ explicitly taking into account the effect of tag-side interference while doing so. In contrast to the discussion of B decays to $J/\psi K^0_S$ or $\pi^+\pi^-$ final states where the effect of tag-side interference is treated as a perturbation on a measurement, for $\sin(2\phi_1 + \phi_3)$ one attempts to formally incorporate the full time-dependence of both B mesons decaying in an event, allowing for *CP* violation for both the signal and tag sides. A scheme for doing this is outlined by Long, Baak, Cahn, and Kirkby (2003) and this approach has been adopted by the B Factories.

15.4 Summary

In order to provide for very precise measurements of various observables the systematic uncertainties of the measurements must be kept under control. In an ideal case the systematic uncertainty should not exceed the statistical one by a large margin. At the B Factories several ingenious methods were developed to estimate the remaining systematic errors as precisely as possible. Whenever possible the uncertainties are obtained using real data control

[48] The parameter r should not be confused with either the ratio r_f in Eq. (15.3.1), or the effective parameter r'_f for an ensemble of modes on the tag-side of the event.

samples, thus avoiding systematic effects due to possible discrepancies between MC simulation and data. For some sources of systematic uncertainties encountered in several measurements performed at the B Factories the estimation methods and representative values are summarized in Table 15.4.1.

Table 15.4.1. Summary of typical *BABAR* and Belle systematic uncertainties appearing in various measurements. $\Delta\varepsilon$ denotes the difference between the efficiency as estimated in the MC simulation and in the real data, σ_ε denotes the uncertainty on the efficiency. $\sigma_{S,C}$ denotes the uncertainty of *CP* violating parameters S, C (see Chapter 10).

Measurement	*BABAR*		Belle		Comment
	Method	Typical value	Method	Typical value	
Tracking	$e^+e^- \to \tau^\pm\tau^\mp$,	$\sigma_\varepsilon/\varepsilon = (0.13 - 0.24)\%$	$D^{*+} \to D^0(\to \pi^+\pi^- K_s^0)\pi^+$	$\sigma_\varepsilon/\varepsilon = 0.35\%$	Uncertainty per charged track
	$\tau^\pm \to h^\pm h^\pm h^\mp \nu$, $\tau^\mp \to \mu^\mp \bar{\nu}$	$\Delta\varepsilon'/2\varepsilon = (0.10 - 0.26)\%$			Asymmetry for h^+/h^-
	$e^+e^- \to 2\pi^+2\pi^-\gamma_{\rm ISR}$	$\Delta\varepsilon/\varepsilon = (0.7 - 0.4)\%$			Uncertainty per charged track
	$B \to h^+h^- K_s^0(\to \pi^+\pi^-)$	$\Delta\varepsilon/\varepsilon = (0.5 \pm 0.8)\%$			Uncertainty for tracks with displaced vertex
	$D^{*+} \to D^0\pi_s^+$	$\sigma_\varepsilon/\varepsilon = 1.5\%$	$B^0 \to D^{*-}(\to \overline{D}^0\pi_s^-)\pi^+$	$\sigma_\varepsilon/\varepsilon = 1.3\%$	Uncertainty for low momentum tracks ($p \lesssim 200$ MeV/c)
			$D^{*+} \to D^0(\to \pi^+\pi^- K_s^0)\pi^+$	$\sigma_\varepsilon/\varepsilon = 1\%$	Uncertainty for K_s^0 reconstruction (including tracking uncertainty for $\pi^+\pi^-$)
PID	$D^{*+} \to D^0(\to K^-\pi^+)\pi^+$ $e^+e^- \to e^+e^-(\gamma)$ $e^+e^- \to e^+e^-\ell^+\ell^-$ $J/\psi \to \ell^+\ell^-$	$\sigma_\varepsilon/\varepsilon = (0.8 - 1.0)\%$	$D^{*+} \to D^0(\to K^-\pi^+)\pi^+$ $e^+e^- \to e^+e^-(\gamma)$ $e^+e^- \to e^+e^-\ell^+\ell^-$ $J/\psi \to \ell^+\ell^-$	$\sigma_\varepsilon/\varepsilon = (0.8 - 1.0)\%$	Uncertainty per charged track
π^0 reconstruction	$e^+e^- \to \tau^+\tau^-$, $\tau^+ \to e^+\nu\bar{\nu}$, $\tau^- \to \pi^-(\pi^0)\nu$ $e^+e^- \to \gamma_{\rm ISR}\omega(\to \pi^+\pi^-\pi^0)$	$\varepsilon_{\rm data}/\varepsilon_{\rm MC} \sim 0.970 \pm 0.015$	$e^+e^- \to \tau^+\tau^-$, $\tau^+ \to \ell^+\nu\bar{\nu}$ or $\pi^+\pi^0\bar{\nu}$, $\tau^- \to \pi^-\pi^0\nu$ $\eta \to 3\pi^0/\eta \to \pi^+\pi^-\pi^0$	$\varepsilon_{\rm data}/\varepsilon_{\rm MC} = 0.960 \pm 0.024$ $\sigma_\varepsilon/\varepsilon = 4\%$	Efficiency correction per π^0 ($p \geq 200$ MeV/c)
	$B^0 \to D^{*-}\pi^+ \to D^0\pi^0\pi^+$	$\varepsilon_{\rm data}/\varepsilon_{\rm MC} = 0.98 \pm 0.07$	$B^0 \to D^{*-}\pi^+ \to D^0\pi^0\pi^+$	$\varepsilon_{\rm data}/\varepsilon_{\rm MC} = 1.024 \pm 0.027$	Efficiency correction per π^0 ($p < 200$ MeV/c)
High energy photons	$e^+e^- \to \mu^+\mu^-\gamma$	$\Delta\varepsilon = (1.00 \pm 0.55) \cdot 10^{-2}$			
t-dependent	MC	$\sigma_{S,C} \lesssim 0.01$	MC	$\sigma_{S,C} \lesssim 0.01$	vertex detector alignment
	changing beam spot position	$\sigma_S/S \sim 0.13\%$ $\sigma_C/C \sim 0.06\%$	changing beam spot position	$\sigma_S/S \sim 0.3\%$ $\sigma_C/C \sim 0.08\%$	beam spot position
	varying parameters from $B_{\rm flav}$ sample	$\sigma_{S,C} \lesssim 0.01$	varying parameters from $B_{\rm flav}$ sample	$\sigma_{S,C} \lesssim 0.01$	resolution function, flavor tag
	varying parameters	$\sigma_{S,C} \sim \mathcal{O}(10^{-3})$	varying parameters	$\sigma_{S,C} \sim \mathcal{O}(10^{-3})$	physics parameters ($\Delta\Gamma_d, \Delta m_d, ...$)
	varying possible S, C for background	$\sigma_C/C \lesssim (1 - 2)\%$	varying possible S, C for background	$\sigma_C/C \lesssim (1 - 2)\%$	CP violation in background
	$B^0 \to D^{*-}\ell^+\nu$	$\sigma_{S,C} \sim (0.1, 1.4) \cdot 10^{-2}$ $\sigma_S \sim 1.0 \cdot 10^{-2}$ $\sigma_C \sim (1.6 - 4.0) \cdot 10^{-2}$	$B^0 \to D^{*-}\ell^+\nu$	$\sigma_{S,C} \sim (0.1, 0.8) \cdot 10^{-2}$ $\sigma_S \sim 1.0 \cdot 10^{-2}$ $\sigma_C \sim (1.6 - 4.0) \cdot 10^{-2}$	tag-side interference in $B \to J/\psi K_s^0$ } tag-side interference in $b \to u\bar{u}d$

Part C
The results and their interpretation

Chapter 16
The CKM matrix and the Kobayashi-Maskawa mechanism

Editors:
Adrian Bevan and Soeren Prell (BABAR)
Boštjan Golob and Bruce Yabsley (Belle)
Thomas Mannel (theory)

16.1 Historical background

Fundamentals

In the early twentieth century the "elementary" particles known were the proton, the electron and the photon. The first extension of this set of particles occurred with the neutrino hypothesis, first formulated by W. Pauli in his famous letter to his "radioactive friends" in 1924. From the theoretical side, the formulation of a theory of weak interactions by Fermi in 1934 marked another milestone in the development of our understanding. This set up for the first time a framework, in which some of the fundamental questions on the role of hadrons versus leptons and on the properties of particles and their interactions could be formulated. This also resulted in a clear formulation of "weak" versus "strong" interactions and the understanding of interactions as an exchange of mediating particles. In particular, Yukawa postulated the existence of such a particle and triggered the search for what we now know as the pion. At about the same time the muon was discovered, and initially called the "μ meson", however this soon turned out to be distinct from the pion.

Although the the term "flavor" came much later, one may mark the beginning of (quark) flavor physics by the discovery of strange particles (Rochester and Butler, 1947). Their decays into non-strange particles had lifetimes too long to be classified as strong decays: this led to the introduction of the strangeness quantum number (Gell-Mann, 1953), which is conserved in strong decays but may change in a weak decay.

The subsequent proliferation of new particles could nicely be classified and ordered by Gell Mann's "eightfold way" (Gell-Mann, 1962), which was an extension of the isospin symmetry to a symmetry based on the group $SU(3)$. However, none of the particles fitted into the fundamental representation of this group, although there were various attempts such as Sakata's model, in which the proton, the neutron and the Λ baryon formed the fundamental representation. Eventually this puzzle was resolved by the postulate of quarks as the fundamental building blocks of matter.

Strangeness, parity violation, and charm

The decays of the strange particles, in particular of the kaons, paved the way for the further development of our understanding. Before 1954, the three discrete symmetries C (charge conjugation), P (parity) and T (time reversal) were believed to be conserved individually, a conclusion drawn from the well known electromagnetic interaction. Based on this assumption, the so called θ-τ puzzle emerged: Two particles (at that time called θ and τ, where the latter is not to be confused with the third generation lepton) were observed, which had identical masses and lifetimes. However, they obviously had different parities, since the θ particle decayed into two pions (a state with even parity), and the τ particle decays into three pions (a state with odd parity).

The resolution was provided by the bold assumption by Lee and Yang (1956) that parity is not conserved in weak interactions, and θ and τ are in fact the same particle, which we now call the charged kaon. Subsequently the parity violating $V-A$ structure of the weak interaction was established and, on the experimental side, parity violation was confirmed directly in β decays (Garwin, Lederman, and Weinrich, 1957; Wu, Ambler, Hayward, Hoppes, and Hudson, 1957). However, the combination of two discrete transformations, namely *CP*, still seemed to be conserved.

Another puzzle related to kaon decays was the relative coupling strength. It tuned out that the coupling strength of strangeness-changing processes is much smaller than that of strangeness-conserving transitions. This finding eventually led to the parameterization of quark mixing by Cabibbo (1963). In modern language, the up quark u couples to a combination $d\cos\theta_C + s\sin\theta_C$ of the down quark d and the strange quark s. The value $\theta_C \sim 13^\circ$ for the Cabibbo angle explained the observed pattern of branching ratios in baryon decays.

Experiments at that time only probed the three lightest quarks, and there was no known reason for the extreme suppression of the flavor changing neutral current (FCNC) decay $K^+ \to \pi^+\ell^+\ell^-$ with respect to the charged current decay $K^+ \to \pi^0\ell^+\overline{\nu}$, $\Gamma(K^+ \to \pi^+\ell^+\ell^-)/\Gamma(K^+ \to \pi^0\ell^+\overline{\nu}) \sim 10^{-6}$. The resolution of this puzzle was found by Glashow, Iliopoulos, and Maiani (1970): one includes the charm quark, with the same quantum numbers as the up quark, and coupling to the orthogonal combination $-d\sin\theta_C + s\cos\theta_C$.

FCNC processes are suppressed by this "GIM mechanism". In fact, FCNC's in the kaon system involve a transition of an s quark into a d quark. This can be achieved by two successive charged current processes involving (in the two-family picture) either the up or the charm quark as an intermediate state. Taking Cabibbo mixing into ac-

count, these amplitudes are

$$\mathcal{A}(s \to d) = \mathcal{A}(s \to u \to d) + \mathcal{A}(s \to c \to d) = \sin\theta_C \cos\theta_C [f(m_u) - f(m_c)], \quad (16.1.1)$$

where $f(m)$ is some smooth function of the mass m. Hence, if the up and charm quark masses were degenerate, $K^0 - \overline{K}^0$ mixing and other kaon FCNC processes would not occur.

However, the up and charm masses are not degenerate and thus $K^0 - \overline{K}^0$ mixing can occur. Neglecting the small up-quark mass, the mixing amplitude turns out to be

$$\mathcal{A}(K \to \overline{K}) \propto \sin^2\theta_C \cos^2\theta_C \frac{m_c^2}{M_W^2}. \quad (16.1.2)$$

This implies that a mass difference Δm_K appears in the neutral kaon system. From this mass difference (an expression analogous to Eq. 10.1.17) Gaillard and Lee (1974b) could extract the prediction that the charm-quark mass should be about $m_c \sim 1.5$ GeV, and it was one of the great triumphs of particle physics when narrow resonances with masses of about 3 GeV were discovered a few months later (Aubert et al., 1974; Augustin et al., 1974): these were identified as $c\overline{c}$ bound states. Around this time the term "particle family" was coined, and the discovery of the charm quark completed the second particle family; it also introduced a 2×2 quark mixing matrix into the phenomenology of weak interactions.

CP violation and the Kobayashi-Maskawa mechanism

Almost ten years before the discovery of charm, *CP* violation was observed in the study of rare kaon decays by Christenson, Cronin, Fitch, and Turlay (1964). This effect is difficult to accommodate for two families, but an extension to three families allows it to be taken into account naturally. The "six-quark model" was proposed by Kobayashi and Maskawa (1973), extending Cabibbo's 2×2 quark mixing matrix into the 3×3 Cabibbo-Kobayashi-Maskawa (CKM) matrix. The GIM mechanism for the six quark model is implemented by the unitarity of the CKM matrix.

While the observation of decays $K_L^0 \to 2\pi$ meant that *CP* was violated, the data at that time only required *CP* violation in mixing (see Section 16.6 for the classification of *CP*-violating effects). The observed strength of *CP* violation in mixing, $\varepsilon_K \simeq 2.3 \times 10^{-3}$, was consistent with the Kobayashi-Maskawa (KM) mechanism (Ellis, Gaillard, and Nanopoulos, 1976; Pakvasa and Sugawara, 1976). However, this did not constitute a proof that the KM mechanism was really the origin of the observed *CP* violation; the measurement of the single parameter ε_K could not be used to test the KM mechanism. One alternative explanation was offered by the super-weak model of Wolfenstein (1964), where *CP* violation was due to a new, very weak four-fermion interaction that changed strangeness by 2 units ($\Delta S = 2$). This possibility was ruled out by the observation of direct *CP* violation in $K_L \to \pi\pi$ decays, $\mathrm{Re}(\varepsilon'_K/\varepsilon_K) = (1.65 \pm 0.26) \times 10^{-3}$ (Alavi-Harati et al., 1999; Burkhardt et al., 1988; Fanti et al., 1999). Nonetheless, convincing evidence for the KM mechanism required the measurement of $\sin(2\phi_1)$ at the B Factories.

With the discovery of the τ lepton in 1975 (Perl et al., 1975) and of the bottom quark in 1977 (Herb et al., 1977) it became clear that there is a third generation of quarks and leptons. Furthermore, the bottom quark turned out to be quite long-lived, indicating a small mixing angle between the first and second generation. This fact is the experimental foundation of using B decays to study *CP* violation, as well as for b tagging in high-p_t physics.

The third generation remained incomplete for many decades, since the top quark turned out to be quite heavy, and a direct discovery had to wait until 1995, when it was discovered at the Tevatron at Fermilab (Abachi et al., 1995a; Abe et al., 1994). However, the first hint of the large top-quark mass was the discovery of $B^0 - \overline{B}^0$ oscillations (also known as mixing) by ARGUS (Albrecht et al., 1987b). The measured Δm_d implied a heavy top with a mass m_t above $50 - 70$ GeV, if the standard six quark model was assumed (Bigi and Sanda, 1987; Ellis, Hagelin, and Rudaz, 1987). The phenomenon of neutral meson mixing is discussed in Chapter 10, while Section 17.5 discusses results on B mixing from the B Factories.

In fact, if the top mass had been significantly smaller, ARGUS could not have observed $B^0 - \overline{B}^0$ oscillations. The GIM mechanism for down-type quarks leads generally to suppression factors of the form

$$\text{CKM Factor} \times \frac{1}{16\pi^2} \frac{m_t^2 - m_u^2}{M_W^2} \quad (16.1.3)$$

and hence the GIM suppression for the bottom quark is much weaker than in the up-quark sector, where the corresponding factor is

$$\text{CKM Factor} \times \frac{1}{16\pi^2} \frac{m_b^2 - m_d^2}{M_W^2}. \quad (16.1.4)$$

Hence FCNC decays of B-mesons have branching ratios in the measurable region, while FCNC processes for D-mesons are heavily suppressed.

The third particle family was completed by the discovery of the τ neutrino as a particle distinct from the electron and the muon neutrino by the DONUT collaboration (Kodama et al., 2001). Although models with a fourth particle generation are frequently considered as benchmark models for physics beyond the Standard Model, there is no indication of a fourth family. On the contrary, from the width of the Z boson precisely measured at LEP it can be inferred that there is no further family with a neutrino lighter than 40 GeV, and the recent discovery of a Higgs boson in the mass range of 125 GeV (Aad et al., 2012; Chatrchyan et al., 2012b) rules out a large class of fourth-generation models.

16.2 *CP* violation and baryogenesis

Particle physics experiments of the past thirty years have confirmed the Standard Model (SM) even at the quantum level, including quark mixing and *CP* violation. However, the observed matter-antimatter asymmetry of the universe indicates that there must be additional sources of *CP* violation, since the amount of *CP* violation implied by the CKM mechanism is insufficient to create the observed matter-antimatter asymmetry.

In fact, the excess of baryons over antibaryons in the universe

$$\Delta = n_{\mathfrak{B}} - n_{\overline{\mathfrak{B}}} \tag{16.2.1}$$

is small compared to the number of photons: the ratio is measured to be $\Delta/n_\gamma \sim 10^{-10}$. Although it is conceivable that there might be regions in the universe consisting of antimatter, just as our neighborhood consists of matter, no mechanism is known which could, from the Big Bang, produce regions of matter (or antimatter) as large as we observe today. Furthermore, searches have been performed for sources of photons indicative of regions of matter and antimatter colliding. These searches failed to find any large regions of antimatter.

The conditions under which a non-vanishing Δ can emerge dynamically from the symmetric situation $\Delta = 0$ have been discussed by Sakharov (1967). He identified three ingredients

1. There must be baryon number violating interactions $H_{\text{eff}}(\Delta\mathfrak{B} \neq 0) \neq 0$.
2. There must be *CP* violating interactions. If *CP* were unbroken, then we would have for every process $i \to f$ mediated by $H_{\text{eff}}(\Delta\mathfrak{B} \neq 0)$ the *CP* conjugate one with the same probability

$$\Gamma(i \to f) = \Gamma(\bar{i} \to \overline{f}) \tag{16.2.2}$$

   which would erase any matter-antimatter asymmetry.
3. The universe must have been out of thermal equilibrium. Under the assumption of locality, causality, and Lorentz invariance, *CPT* is conserved. Since in an equilibrium state time becomes irrelevant on the global scale, *CPT* reduces to *CP*, and the argument of point 2 applies.

In order to illustrate the first two Saharov conditions, we employ a very simplistic example. Assume that in the early universe, there was a particle X that could decay to only two final states $|f_1\rangle$ and $|f_2\rangle$, with baryon numbers $N_{\mathfrak{B}}^{(1)}$ and $N_{\mathfrak{B}}^{(2)}$ respectively, and decay rates

$$\Gamma(X \to f_1) = \Gamma_0 r \quad \text{and} \quad \Gamma(X \to f_2) = \Gamma_0(1-r)\,, \tag{16.2.3}$$

where Γ_0 is the total width of X. Taking the *CP* conjugate, the particle $\overline{X}$ decays to the state $\overline{f}_1$ with baryon number $-N_{\mathfrak{B}}^{(1)}$ and $\overline{f}_2$ with baryon number $-N_{\mathfrak{B}}^{(2)}$; the rates are

$$\Gamma(\overline{X} \to \overline{f}_1) = \Gamma_0 \overline{r} \quad \text{and} \quad \Gamma(\overline{X} \to \overline{f}_2) = \Gamma_0(1-\overline{r}), \tag{16.2.4}$$

where Γ_0 is the same as for X due to *CPT* invariance.

The overall change $\Delta N_{\mathfrak{B}}$ in baryon number induced by the decay of an equal number of X and $\overline{X}$ particles is

$$\begin{aligned}\Delta N_{\mathfrak{B}} &= r N_{\mathfrak{B}}^{(1)} + (1-r) N_{\mathfrak{B}}^{(2)} - \overline{r} N_{\mathfrak{B}}^{(1)} - (1-\overline{r}) N_{\mathfrak{B}}^{(2)} \\ &= (r-\overline{r})\left(N_{\mathfrak{B}}^{(1)} - N_{\mathfrak{B}}^{(2)}\right)\end{aligned} \tag{16.2.5}$$

Thus $\Delta N_{\mathfrak{B}} \neq 0$ means that we have to have *CP* violation ($r \neq \overline{r}$) and a violation of baryon number ($N_{\mathfrak{B}}^{(1)} \neq N_{\mathfrak{B}}^{(2)}$), illustrating the first two conditions.

Sakharov's paper remained mostly unnoticed until the first formulation of Grand Unified Theories (GUTs). In these theories, for the first time, all the necessary ingredients were present. In particular, baryon number violation appears naturally since quarks and leptons appear in the same multiplets of the GUT symmetry group. Furthermore, there are additional sources of *CP* violation, and a phase transition takes place at the scale M_{GUT}, which has to be quite high to prevent proton decay.

One may also consider electroweak baryogenesis. The electroweak interaction provides *CP* violation through the CKM mechanism, and the electroweak phase transition has been thoroughly studied. The first ingredient is also present, as the current corresponding to baryon number is conserved only at the classical level: electroweak quantum effects violate baryon number, but still conserve the difference $\mathfrak{B} - L$ of baryon and lepton number. However, although all the ingredients are present, this cannot explain Δ. In particular, the CKM *CP* violation is too small by several orders of magnitude.

Given the firm evidence for non-vanishing neutrino masses, there could be new sources of *CP* violation in the lepton sector, and even (although there is no evidence for this as yet) lepton-number violation. This could lead to violation of baryon number via leptogenesis, with the surplus of leptons transferred to the baryonic sector through $(\mathfrak{B} - L)$-conserving interactions.

In any case, an additional source(s) of *CP* violation is needed, beyond the phase of the CKM matrix (which is explained in the next section), in order to explain the matter-antimatter asymmetry of the universe. The search for this new interaction is one of the main motivations for flavor-physics experiments.

16.3 *CP* violation in a Lagrangian field theory

The SM is formulated as a quantum field theory based on a Lagrangian derived from symmetry principles. To this end, the (hermitian) Lagrangian of the SM is given in terms of scalar operators $\mathcal{O}_i$ with couplings a_i

$$\mathcal{L}(x) = \sum_i \left(a_i \mathcal{O}_i(x) + a_i^* \mathcal{O}_i^\dagger(x)\right)\,, \tag{16.3.1}$$

where the $\mathcal{O}_i$ are composed of the SM quark, lepton, and gauge fields. It is straightforward to verify that *CP* conservation implies that all couplings a_i can be made real by suitable phase redefinitions of the fields composing the

$\mathcal{O}_i$. In turn, *CP* is violated in a Lagrangian field theory if there is no choice of phases that renders all a_i real.

In the SM there are in principle two sources of *CP* violation. The so-called "strong *CP* violation" originates from special features of the QCD vacuum, resulting in a contribution of the form

$$\mathcal{L}_{\text{strong } CP} = \theta \frac{\alpha_S}{8\pi} G^{\mu\nu,a} \tilde{G}^a_{\mu\nu} \tag{16.3.2}$$

where $G_{\mu\nu}$ ($\tilde{G}_{\mu\nu}$) is the (dual) strength of the gluon field. This term is P and *CP* violating due to its pseudoscalar nature. However, a term such as Eq. (16.3.2) will have a strong impact on the electric dipole moment (EDM) of the neutron, $d_N \sim \theta \times 10^{-15}$ e cm. In combination with the current limit on the neutron EDM of $d_N < 0.29 \times 10^{-25}$ e cm, this yields a stringent limit, $\theta \leq 10^{-10}$. However, the theoretical reason for its smallness has not yet been discovered. This is known as the "strong *CP* problem" (see for example Cheng, 1988; Kim and Carosi, 2010); we shall ignore this in what follows by setting $\theta = 0$.

The second source of *CP* violation is the CKM matrix. It turns out that all terms in the SM Lagrangian are *CP* invariant except for the charged current interaction term

$$H_{\text{cc}} = \frac{g}{\sqrt{2}} \left(\overline{u}_L\, \overline{c}_L\, \overline{t}_L\right) V_{\text{CKM}} \gamma^\mu \begin{pmatrix} d_L \\ s_L \\ b_L \end{pmatrix} W^+_\mu . \tag{16.3.3}$$

Under a *CP* transformation we have

$$\left(\overline{u}_L\, \overline{c}_L\, \overline{t}_L\right) V_{\text{CKM}} \gamma^\mu \begin{pmatrix} d_L \\ s_L \\ b_L \end{pmatrix} W^+_\mu \tag{16.3.4}$$

$$\xrightarrow{CP} \left(\overline{d}_L\, \overline{s}_L\, \overline{b}_L\right) V^T_{\text{CKM}} \gamma^\mu \begin{pmatrix} u_L \\ c_L \\ t_L \end{pmatrix} W^-_\mu \tag{16.3.5}$$

and hence the combination $H_{\text{cc}} + H^\dagger_{\text{cc}}$ appearing in the SM Lagrangian is *CP* invariant, if

$$V^T_{\text{CKM}} = V^\dagger_{\text{CKM}} \quad \text{or} \quad V_{\text{CKM}} = V^*_{\text{CKM}}. \tag{16.3.6}$$

This statement refers to a specific phase convention for the quark fields; in general terms it implies that in the *CP*-invariant case, the CKM matrix can be made real by an appropriate phase redefinition of the quark fields.

16.4 The CKM matrix

The CKM matrix V_{CKM} appearing in Eq. (16.3.3) is explicitly written as

$$V_{\text{CKM}} = \begin{pmatrix} V_{ud} & V_{us} & V_{ub} \\ V_{cd} & V_{cs} & V_{cb} \\ V_{td} & V_{ts} & V_{tb} \end{pmatrix}. \tag{16.4.1}$$

Here the V_{ij} are the couplings of quark mixing transitions from an up-type quark $i = u, c, t$ to a down-type quark $j = d, s, b$.

In the SM the CKM matrix is unitary by construction. Using the freedom of phase redefinitions for the quark fields, the CKM matrix has $(n-1)^2$ physical parameters for the case of n families. Out of these, $n(n-1)/2$ are (real) rotation angles, and $((n-3)n+2)/2$ are phases, which induce *CP* violation. For $n = 2$, no *CP* violation is possible, while for $n = 3$ a single phase appears. This is the unique source of *CP* violation in the SM, once the possibility of strong *CP* violation is ignored.

The CKM matrix for 3 families may be represented by three rotations and a matrix generating the phase

$$\begin{aligned} U_{12} &= \begin{bmatrix} c_{12} & s_{12} & 0 \\ -s_{12} & c_{12} & 0 \\ 0 & 0 & 1 \end{bmatrix}, \\ U_{13} &= \begin{bmatrix} c_{13} & 0 & s_{13} \\ 0 & 1 & 0 \\ -s_{13} & 0 & c_{13} \end{bmatrix}, \\ U_{23} &= \begin{bmatrix} 1 & 0 & 0 \\ 0 & c_{23} & s_{23} \\ 0 & -s_{23} & c_{23} \end{bmatrix}, \\ U_\delta &= \begin{bmatrix} 1 & 0 & 0 \\ 0 & 1 & 0 \\ 0 & 0 & e^{-i\delta_{13}} \end{bmatrix}, \end{aligned} \tag{16.4.2}$$

where $c_{ij} = \cos\theta_{ij}$, $s_{ij} = \sin\theta_{ij}$, and δ is the complex phase responsible for *CP* violation; by convention the mixing angles θ_{ij} are chosen to lie in the first quadrant so that the s_{ij} and c_{ij} are positive. Then (Chau and Keung, 1984)

$$\begin{aligned} V_{\text{CKM}} &= U_{23} U^\dagger_\delta U_{13} U_\delta U_{12} \\ &= \begin{pmatrix} c_{12}c_{13} & s_{12}c_{13} & s_{13}e^{-i\delta} \\ -s_{12}c_{23} - c_{12}s_{23}s_{13}e^{i\delta} & c_{12}c_{23} - s_{12}s_{23}s_{13}e^{i\delta} & s_{23}c_{13} \\ s_{12}s_{23} - c_{12}c_{23}s_{13}e^{i\delta} & -c_{12}s_{23} - s_{12}c_{23}s_{13}e^{i\delta} & c_{23}c_{13} \end{pmatrix}. \end{aligned} \tag{16.4.3}$$

This is the representation used by the PDG (Beringer et al., 2012).

The elements of the CKM matrix exhibit a pronounced hierarchy. While the diagonal elements are close to unity, the off-diagonal elements are small, such that *e.g.* $V_{ud} \gg V_{us} \gg V_{ub}$. In terms of the angles θ_{ij} we have $\theta_{12} \gg \theta_{23} \gg \theta_{13}$. This fact is usually expressed in terms of the Wolfenstein parameterization (Wolfenstein, 1983), which can be understood as an expansion in $\lambda = |V_{us}|$. It reads up to order λ^3

$$V_{\text{CKM}} = \begin{pmatrix} 1 - \lambda^2/2 & \lambda & A\lambda^3(\rho - i\eta) \\ -\lambda & 1 - \lambda^2/2 & A\lambda^2 \\ A\lambda^3(1 - \rho - i\eta) & -A\lambda^2 & 1 \end{pmatrix} + \mathcal{O}(\lambda^4). \tag{16.4.4}$$

The parameters A, ρ and η are assumed to be of order one. When using this parameterization, one has to keep in mind that unitarity is satisfied only up to order λ^4. As it turns out that both ρ and η are also of order λ, the

extension to higher orders becomes non-trivial, and one has to consider redefining the parameters accordingly; this has been studied by Ahn, Cheng, and Oh (2011).

One can obtain an exact parameterization of the CKM matrix in terms of A, λ, ρ, and η, for example, by following the convention of Buras, Lautenbacher, and Ostermaier (1994), where

$$\lambda = s_{12}, \tag{16.4.5}$$
$$A = s_{23}/\lambda^2, \tag{16.4.6}$$
$$A\lambda^3(\rho - i\eta) = s_{13}e^{-i\delta}, \tag{16.4.7}$$

and by substituting Eqs (16.4.5) through (16.4.7) into Eq. (16.4.3), while noting that $\sin^2\theta = 1 - \cos^2\theta$. Such a parameterization is described in Section 19.2.1.3 to illustrate *CP* violation in the charm sector.

Sometimes a slightly different convention for the Wolfenstein parameters is used, with parameters denoted $\overline{\rho}$ and $\overline{\eta}$. These parameters were defined at fixed order by Buras, Lautenbacher, and Ostermaier (1994); the modern definition (Charles et al., 2005),

$$\overline{\rho} + i\overline{\eta} = -\frac{V_{ud}V_{ub}^*}{V_{cd}V_{cb}^*}, \tag{16.4.8}$$

holds to all orders. The difference with the parameterization defined above appears only at higher orders in the Wolfenstein expansion; the relation between this scheme and the one defined in (16.4.5–16.4.7) is given by

$$\rho + i\eta = (\overline{\rho} + i\overline{\eta})\frac{\sqrt{1 - A^2\lambda^4}}{\sqrt{1 - \lambda^2}[1 - A^2\lambda^4(\overline{\rho} + i\overline{\eta})]}. \tag{16.4.9}$$

16.5 The Unitarity Triangle

The unitarity relations $V_{\rm CKM} \cdot V_{\rm CKM}^\dagger = 1$ and $V_{\rm CKM}^\dagger \cdot V_{\rm CKM} = 1$ yield six independent relations corresponding to the off-diagonal zeros in the unit matrix. They can be represented as triangles in the complex plane; each triangle has the same area, reflecting the fact that (with three families) there is only one irreducible phase. A non-trivial triangle — one with angles other than 0 or π — indicates *CP* violation, proportional to the triangles' common area. Bigi and Sanda (2000) provide a detailed discussion of the various triangles, their interpretation, and the possibilities to probe them. Only two triangles have sides of comparable length, which means that they are of the same order in the Wolfenstein parameter λ. The corresponding relations are

$$V_{ud}V_{ub}^* + V_{cd}V_{cb}^* + V_{td}V_{tb}^* = 0 \tag{16.5.1}$$
$$V_{ud}V_{td}^* + V_{us}V_{ts}^* + V_{ub}V_{tb}^* = 0. \tag{16.5.2}$$

Inserting the Wolfenstein parameterization, both relations turn out to be identical, up to terms of order λ^5; the apex of the Unitarity Triangle is given by the coordinate $(\overline{\rho}, \overline{\eta})$. The three sides of this triangle (Fig. 16.5.1) — usually referred to as "the" Unitarity Triangle— control semi-leptonic and non-leptonic B_d transitions, including $B_d - \overline{B}_d$ oscillations. In order to obtain the triangle shown in Fig 16.5.1, Eq. (16.5.1) is divided by $V_{cd}V_{cb}^*$ so that the base of the triangle is of unit length. Due to the sizable angles, one expects large *CP* asymmetries in B decays in the SM; this was actually realized *before* the discovery of "long" B lifetimes. Note that in both unitarity-triangle relations CKM matrix elements related to the top quark appear; in particular V_{td} and V_{ts} can be accessed only indirectly via FCNC decays of bottom quarks.

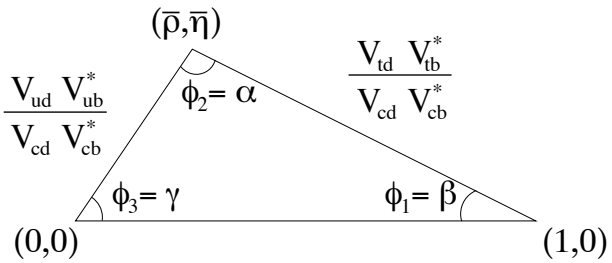

Figure 16.5.1. The Unitarity Triangle.

The angles of the Unitarity Triangle are defined as

$$\phi_1 = \beta \equiv \arg\left[-V_{cd}V_{cb}^*/V_{td}V_{tb}^*\right], \tag{16.5.3}$$
$$\phi_2 = \alpha \equiv \arg\left[-V_{td}V_{tb}^*/V_{ud}V_{ub}^*\right], \tag{16.5.4}$$
$$\phi_3 = \gamma \equiv \arg\left[-V_{ud}V_{ub}^*/V_{cd}V_{cb}^*\right], \tag{16.5.5}$$

where this definition is independent of the specific phase choice expressed in Eq. (16.4.3). Different notation conventions have been used in the literature for these angles. In particular the *BABAR* experiment has used α, β, and γ, whereas the Belle experiment has reported results in terms of ϕ_2, ϕ_1, and ϕ_3, respectively. We use the latter for brevity when discussing results in later sections.

The presence of *CP* violation in the CKM matrix implies non-trivial values for these angles ($\phi_i \neq 0°, 180°$), corresponding to a non-vanishing area for the Unitarity Triangle. In fact, all the triangles that can be formed from the unitarity relation have the same area, which is proportional to the quantity

$$\Delta = \mathrm{Im}\, V_{cs}^* V_{us} V_{cd} V_{ud}^* \tag{16.5.6}$$

which is independent of the phase convention. Note that all other, rephasing invariant fourth order combinations of CKM matrix elements, which cannot be reduced to products of second order invariants, can be related to Δ, which is thus unique.

Furthermore, the phase in the CKM matrix could also be removed, if the masses of either two up-type quarks or two down-type quarks were degenerate. In summary, the presence of *CP* violation is equivalent to (Jarlskog, 1985)

$$\begin{aligned} J &= \det[M_u\,,\, M_d] \\ &= 2i\Delta \times (m_u - m_c)(m_u - m_t)(m_c - m_t) \\ &\quad \times (m_d - m_s)(m_d - m_b)(m_s - m_b) \end{aligned} \tag{16.5.7}$$

being non-vanishing.

The SM allows us to construct "the" Unitarity Triangle by measuring its angles or its sides or any combinations of them. Any discrepancy between the observed and predicted values indicates a manifestation of dynamics beyond the SM. Clearly this requires good control of experimental and theoretical uncertainties, both in their *CP* sensitive and insensitive rates.

Measurements of the magnitudes of CKM matrix elements V_{ub} and V_{cb} can be found in Section 17.1, and measurements of V_{td} and V_{ts} in Section 17.2. Measurements of the angles ϕ_1, ϕ_2, and ϕ_3 are discussed in Sections 17.6, 17.7, and 17.8 respectively. It is possible to perform *global fits*, using data from many decay processes to over-constrain our knowledge of the CKM mechanism. Given the lack of knowledge of the determination of the apex of the Unitarity Triangle, these global fits are often expressed in terms of constraints on the $(\overline{\rho}, \overline{\eta})$ plane. Some experimental results require input from Lattice QCD calculations in order to be used in a global fit. These global fits are discussed in Chapter 25, both in the context of the SM (Section 25.1) and allowing for physics beyond the SM (Section 25.2).

It is exactly some of the measurements described in Chapter 17 and further in Section 25.1 which were addressed in (Nobelprize.org, 2010) among experimental verifications of the Kobayashi-Maskawa mechanism in the scientific background to the 2008 Nobel Prize in Physics awarded to M. Kobayashi and T. Maskawa: "The respective collaborations BABAR and BELLE have now measured the *CP* violation in remarkable agreement with the model ... and all experimental data are now in impressive agreement with the model ...".

16.6 *CP* violation phenomenology for B mesons

Since *CP* violation is due to irreducible phases of coupling constants, it becomes observable through interference effects. The simplest example is an amplitude consisting of two distinct contributions

$$A_f = \lambda_1 \langle f|O_1|B\rangle + \lambda_2 \langle f|O_2|B\rangle \tag{16.6.1}$$

where $\lambda_{1,2}$ are (complex) coupling constants (in our case combinations of CKM matrix elements) and $\langle f|O_{1,2}|B\rangle$ are matrix elements of interaction operators between the initial and final state.

The *CP* conjugate is the process $\overline{B} \to \overline{f}$, yielding

$$\overline{A}_{\overline{f}} = \lambda_1^* \langle \overline{f}|O_1^\dagger|\overline{B}\rangle + \lambda_2^* \langle \overline{f}|O_2^\dagger|\overline{B}\rangle. \tag{16.6.2}$$

The matrix elements of $\mathcal{O}_{1,2}^{(\dagger)}$ involve only strong interactions, which we assume to be *CP*-invariant. Hence we have

$$\langle \overline{f}|O_1^\dagger|\overline{B}\rangle = \langle f|O_1|B\rangle \quad \text{and} \quad \langle \overline{f}|O_2^\dagger|\overline{B}\rangle = \langle f|O_2|B\rangle. \tag{16.6.3}$$

Thus for the *CP* asymmetry we find

$$\begin{aligned}\mathcal{A}_{CP}(B \to f) &\equiv \frac{\Gamma(B \to f) - \Gamma(\overline{B} \to \overline{f})}{\Gamma(B \to f) + \Gamma(\overline{B} \to \overline{f})} \\ &\propto 2\,\mathrm{Im}[\lambda_1 \lambda_2^*]\,\mathrm{Im}[\langle f|O_1|B\rangle \langle f|O_2|B\rangle^*].\end{aligned} \tag{16.6.4}$$

Consequently, in order to create *CP* violation, there has to be — aside from the "weak phase" due to the complex phases of the CKM matrix — also a "strong phase", *i.e.* a phase difference between the matrix elements $\langle f|O_1|B\rangle$ and $\langle f|O_2|B\rangle$. In the SM these two contributions correspond to different diagram topologies. In many cases, one can identify tree-level contributions which carry different CKM factors compared to loop (penguin) contributions. *CP* violation then emerges from the interference of "trees" and "penguins".

In the following we are going to consider decays into CP eigenstates f in which case we have $f = \overline{f}$. For a quantum-coherent pair of neutral B-mesons (like the color-singlet $B^0\overline{B}^0$ pair from $\Upsilon(4S)$ decay) the time evolution generates a phase difference $\Delta m\,\Delta t$, which acts like the strong phase difference between the amplitudes for $B \to f$ and for $B \to \overline{B} \to f$. Hence we make use of the time-dependent *CP* asymmetry

$$\begin{aligned}\mathcal{A}_{\mathrm{CP}}^{B\to f}(\Delta t) &\equiv \frac{\Gamma(B^0(\Delta t) \to f) - \Gamma(\overline{B}^0(\Delta t) \to f)}{\Gamma(B^0(\Delta t) \to f) + \Gamma(\overline{B}^0(\Delta t) \to f)} \\ &= S^{B\to f}\,\sin(\Delta m_d\,\Delta t) - C^{B\to f}\,\cos(\Delta m_d\,\Delta t)\,.\end{aligned} \tag{16.6.5}$$

The derivation (see the discussion in Chapter 10 leading to Eq. 10.2.8) neglects the small lifetime difference $\Delta\Gamma$ in the B_d system; the expressions for S and C can be found in Eqs (10.2.4) and (10.2.5).

We may distinguish three different types of *CP* violation according to the various sources from which it emerges. *CP violation in decays*, sometimes referred to as *direct CP violation*, stems from different rates for a process and for its *CP* conjugate: hence we have $|\overline{A}_f/A_f| \neq 1$. This contribution leads to $C^{B\to f} \neq 0$: it is already present at $\Delta t = 0$, and remains in time-integrated measurements. *CP violation in the mixing* emerges in cases where we have $|p/q| \neq 1$.[49] One observable related to this is the semileptonic decay asymmetry a_{SL}, which is the asymmetry between the decay rate of $B^0 \to X^-\ell^+\nu_\ell$ and the *CP* conjugate process. Finally, *mixing-induced CP violation*, sometimes also called *CP violation in interference between a decay without mixing and a decay with mixing* occurs for $\mathrm{Im}\lambda \neq 0$, in which case interference of the amplitudes $B \to f$ and $B \to \overline{B} \to f$ leads to *CP* violation.[50]

[49] For a definition of the quantities p, q, and λ, we refer to Chapter 10, where time evolution is considered.

[50] In kaon physics sometimes the notion *indirect CP violation* is used for saying that the parameter ϵ is non-vanishing. Comparing this with the definitions given here, non-vanishing ϵ corresponds to a combination of $|q/p| \neq 1$ and $|\overline{A}_f/A_f| \neq 1$.

In the B_d system we have to a very good approximation[51]

$$\frac{q}{p} = \exp(-2i\phi_1) \ . \tag{16.6.6}$$

This follows from Eq. (10.1.19) and by inspection of the box diagram contributing to the B_d mixing (Fig. 10.1.1), from which it can be seen that the CKM matrix elements appearing in the amplitude yield $\phi_{M_{12}} = 2\phi_1$. Hence in all cases where $A = \overline{A}$, we find $|\lambda| = 1$ and $\mathrm{Im}\lambda = -\sin(2\phi_1)$, leading to

$$C^{B\to f} = 0 \quad \text{and} \quad S^{B\to f} = -\sin(2\phi_1). \tag{16.6.7}$$

This holds for the golden mode $B \to J/\psi K_s$ where there is no relative weak phase between A and $\overline{A}$. However, if there appears a relative weak phase in the decay amplitudes, then we may still have $|A| = |\overline{A}|$ and hence $|\lambda| = 1$, and thus no direct *CP* violation. For example, the tree amplitude in $B \to \pi\pi$ carries a weak phase $e^{-i\phi_3}$ which (neglecting penguin contributions) would lead to

$$\lambda = \exp(-2i(\phi_1 + \phi_3)) = \exp(+2i\phi_2). \tag{16.6.8}$$

However, the penguin contribution in $B \to \pi\pi$ cannot be neglected; in particular it leads to $|\lambda| \neq 1$ and to direct *CP* violation in these decays.

In general we have the "unitarity relation" between the quantities $S^{B\to f}$ and $C^{B\to f}$,

$$\left(C^{B\to f}\right)^2 + \left(S^{B\to f}\right)^2 = 1 - \left(D^{B\to f}\right)^2 \leq 1 \tag{16.6.9}$$

where

$$D^{B\to f} = \frac{2\,\mathrm{Re}\lambda}{1+|\lambda|^2}. \tag{16.6.10}$$

However, in the limit of vanishing lifetime difference the time-dependent *CP* asymmetry does not depend on $D^{B\to f}$, and hence a direct measurement of this quantity in the B_d system is difficult.

[51] This relation depends on the phase conventions used. It holds in the convention used in (16.4.3).

Chapter 17
B physics

The main objective of the B Factories was to perform measurements of the decays and CP asymmetries of B mesons. While the asymmetric set-up and high luminosities of the B Factories allowed us for the first time to perform statistically significant measurements of time-dependent CP asymmetries, the symmetric predecessors of the B Factories, DORIS and CESR, had already produced some data on B decays. Experiments at LEP and the Tevatron had provided a proof of principle of the time-dependent CP asymmetry measurement in the golden mode $B^0 \to J/\psi K^0_S$, and improved our knowledge of B^0_d mixing.

Most of the time, the B Factories took data near the $\Upsilon(4S)$ resonance, which decays almost exclusively into $B^0\overline{B}^0$ and B^+B^- pairs. As a consequence, the overwhelming majority of B Factory measurements relate to these states: these measurements are described in the following sections. However, some data has been taken at the $\Upsilon(5S)$ resonance, which also decays into $B_s^{(*)0}\overline{B}_s^{(*)0}$ pairs. Measurements of B^0_s decays performed with this data are discussed in Chapter 23.

There are many ways to arrange this vast amount of material. The scheme adopted for this book uses the Unitarity Triangle as an organizing principle. We start from a discussion of the ways the sides of the triangle are constrained, including theoretical methods as well as experimental results in the corresponding sections. Hence we start with the measurements determining the magnitude of the CKM matrix elements V_{cb}, V_{ub}, V_{ts}, and V_{td}. This is followed by a discussion of the decay rates of charmed and charmless non-leptonic processes, including a comparison with theoretical expectations. The reason for this is that many charmed and charmless non-leptonic decay modes are used in the measurement of CP asymmetries, and therefore should be discussed before moving on to review work related to the angles of the Unitarity Triangle.

Before treating the CP asymmetries related to the angles of the Unitarity Triangle, we discuss measurements of B lifetimes and $B^0 - \overline{B}^0$ mixing, which are needed to understand the time-dependent analyses performed for the extraction of the angles. Searches for CPT and other symmetry violations which are based on the lifetime- and mixing-measurement techniques are then presented. Following on from this one will find the description of measurements of CP violation, *i.e.* the extraction of the angles ϕ_1, ϕ_2, and ϕ_3.

The end of this chapter is devoted to special processes. These are either rare decays related to flavor changing neutral current transitions of the b quark, processes involving τ leptons or baryons in the final state, or decays which are very rare or forbidden in the Standard Model.

17.1 V_{ub} and V_{cb}

Editors:
Vera Luth (BABAR)
Christoph Schwanda (Belle)
Paolo Gambino [V_{cb}]; Frank Tackmann [V_{ub}] (theory)

Additional section writers:
Christine Davies, Jochen Dingfelder, Alexander Khodjamirian, Andreas Kronfeld, Matthias Steinhauser, and Ruth Van de Water

17.1.1 Overview of semileptonic B decays

17.1.1.1 Motivation

Semileptonic decays of B^+ and B^0 mesons proceed via leading-order weak interactions. In the following, only decays involving low-mass charged leptons, $\ell = e^{\pm}$ or $\mu^{\pm}$, are considered. They are expected to be free of non-Standard Model contributions, and therefore play a critical role in the determination of the magnitudes of the CKM-matrix elements V_{cb} and V_{ub}. $|V_{cb}|$ normalizes the Unitarity Triangle, and the ratio $|V_{ub}|/|V_{cb}|$ determines the side opposite to the angle ϕ_1. Thus, their values impact most studies of flavor physics and CP-violation in the quark sector. Leptonic and semileptonic decays involving $\tau^{\pm}$ leptons are sensitive to couplings to the charged Higgs boson and are discussed in Section 17.10.

There are two methods to determine $|V_{cb}|$ and $|V_{ub}|$, one based on the study of exclusive semileptonic B decays where the hadron in the final state is a D, D^*, D^{**}, π or ρ meson, the other based on the study of inclusive decays of the form $B \to X\ell^+\nu_\ell$, where X refers to either X_c or X_u, *i.e.*, to any hadronic final state with charm or without charm, respectively.

To extract $|V_{cb}|$ or $|V_{ub}|$ from the measured partial decay rates, both inclusive and exclusive determinations rely on theoretical descriptions of the QCD contributions to the underlying weak decay process. Since both methods rely on different experimental techniques and involve different theoretical approximations, they complement each other and provide largely independent determinations (of comparable accuracy) of $|V_{cb}|$ and $|V_{ub}|$. This in turn provides a crucial cross check of the methods and our understanding of semileptonic B decays in general.

17.1.1.2 Theoretical Overview

Semileptonic decays of B mesons, $B \to X\ell\nu$, proceed through the electroweak transitions $b \to c\ell\nu$ and $b \to u\ell\nu$, as illustrated in Figure 17.1.1. These are governed by the CKM-matrix elements V_{cb} and V_{ub}, and since the intermediate W boson decays leptonically, do not involve any other CKM matrix elements. Hence, measurements of the $B \to X\ell\nu$ decay rate can be used to directly measure $|V_{cb}|$ and $|V_{ub}|$.

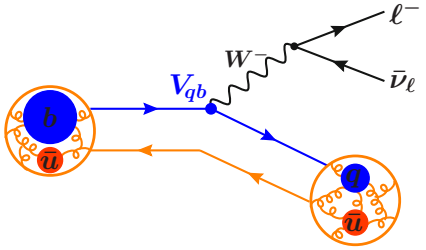

Figure 17.1.1. Illustration of semileptonic decay $B^- \to X\ell^-\overline{\nu}_\ell$.

The theoretical description of semileptonic B decays starts from the electroweak effective Hamiltonian,

$$\mathcal{H}_{\text{eff}} = \frac{4G_F}{\sqrt{2}} \sum_{q=u,c} V_{qb}\,(\overline{q}\gamma_\mu P_L b)(\ell\gamma^\mu P_L \nu_\ell)\,, \qquad (17.1.1)$$

where $P_L = (1-\gamma_5)/2$, and G_F is the Fermi constant as extracted from muon decay. The W boson has been integrated out at tree level using the hierarchy $m_b \ll m_W$, and higher-order electroweak corrections are suppressed by additional powers of G_F and are thus very small. The differential B decay rates take the form

$$d\Gamma \propto G_F^2 |V_{qb}|^2 \left| L^\mu \langle X|\overline{q}\gamma_\mu P_L b|B\rangle \right|^2 . \qquad (17.1.2)$$

An important feature of semileptonic decays is that the leptonic part in the effective Hamiltonian and the decay matrix element factorizes from the hadronic part, and that QCD corrections can only occur in the $b \to q$ current. The latter do not affect Eq. (17.1.1) and are fully contained in the hadronic matrix element $\langle X|\overline{q}\gamma_\mu P_L b|B\rangle$ in Eq. (17.1.2). This factorization is violated by small electromagnetic corrections, for example by photon exchange between the quarks and leptons, which must be taken into account in situations where high precision is required.

The challenge in the extraction of $|V_{cb}|$ and $|V_{ub}|$ is the determination of the hadronic matrix element of the quark current in Eq. (17.1.2). For this purpose, different theoretical methods have been developed, depending on the specific decay mode under consideration. In almost all cases, the large mass of the b-quark, $m_b \sim 5\,\text{GeV}$ is exploited.

In exclusive semileptonic decays, one considers the decay of the B meson into a specific final state $X = D, D^*, \pi$, or ρ. In this case, one parameterizes the hadronic matrix element in terms of form factors, which are non-perturbative functions of the momentum transfer q^2. This is discussed in Sections 17.1.2 and 17.1.4. The two methods commonly used to determine the form factors are lattice QCD (LQCD) and light-cone sum rules (LCSR). In LQCD, the QCD functional integrals for the matrix elements are computed numerically from first principles. Heavy quark effective theory (HQET), and non-relativistic QCD (NRQCD), were first introduced, at least in part, to enable lattice-QCD calculations with heavy quarks. Even when these formalisms are not explicitly used, heavy-quark dynamics are usually used to control discretization

effects. An exception are the most recent determinations of m_c and m_b from lattice QCD, discussed below, which use a fine lattice in combination with a highly improved lattice action such that heavy quarks with masses almost up to m_b can be treated with a light-quark formalism. A complementary method is based on LCSR which use hadronic dispersion relations to approximate the form factor in terms of quark-current correlators and can be calculated in an operator product expansion (OPE).

In inclusive semileptonic decays, one considers the sum over all possible final states X that are kinematically allowed. Employing parton-hadron duality one can replace the sum over hadronic final states with a sum over partonic final states. This eliminates any long-distance sensitivity to the final state, while the short-distance QCD corrections, which appear at the typical scale $\mu \sim m_b$ of the decay, can be computed in perturbation theory in terms of the strong coupling constant $\alpha_s(m_b) \sim 0.2$. The remaining long-distance corrections related to the initial B meson can be expanded in powers of $\Lambda_{\rm QCD}/m_b \sim 0.1$, where $\Lambda_{\rm QCD}$ is the hadronic scale of order $m_B - m_b \sim 0.5\,\text{GeV}$. This is called *heavy quark expansion* (HQE), and it systematically expresses the decay rate in terms of nonperturbative parameters that describe universal properties of the B meson. This is discussed in Sections 17.1.3 and 17.1.5.

17.1.1.3 Experimental Techniques

As in other analyses of $B\overline{B}$ data recorded at B Factories, the two dominant sources of background for the reconstruction of semileptonic B decays are the combinatorial $B\overline{B}$ and the continuum backgrounds (see Chapter 9).

The suppression of the continuum processes, $e^+e^- \to \ell^+\ell^-(\gamma)$ with $\ell = e, \mu$, or τ, and quark-antiquark pair production, $e^+e^- \to q\overline{q}(\gamma)$ with $q = u, d, s, c$, is achieved by requiring at least four charged particles in the event and by imposing restrictions on several event shape variables, either sequentially on individual variables or by constructing multivariable discriminants. Among these variables are thrust, the maximum sum of the longitudinal momenta of all particles relative to a chosen axis, $\Delta\theta_{\rm thrust}$, the angle between the thrust axis of all particles associated with the signal decay and the thrust axis of the rest of the event, R_2, the ratio of the second to the zeroth Fox-Wolfram moments, and L_0 and L_2, the normalized angular moments.

The separation of semileptonic B decays from $B\overline{B}$ backgrounds is very challenging because they result in one or more undetected neutrinos. The energy and momentum of the missing particles can be inferred from the sum of all other particles in the event,

$$(E_{\rm miss}, \mathbf{p}_{\rm miss}) = (E_0, \mathbf{p}_0) - \left(\sum_i E_i, \sum_i \mathbf{p}_i\right), \quad (17.1.3)$$

where $(E_0, \mathbf{p}_0)$ is the four-vector of the colliding beams. If the only undetected particle in the event is a single neutrino, the missing mass should be close to zero and the missing momentum should be non-zero. Figure 17.1.2 shows examples of missing mass squared distributions, $m^2_{\rm miss} = E^2_{\rm miss} - |\mathbf{p}_{\rm miss}|^2$, for selected $B^- \to X_c\ell^-\overline{\nu}$ candidates. There are narrow peaks at zero for correctly reconstructed decays and in most cases rather small backgrounds from other decays modes. In Figure 17.1.2a there is a broad enhancement above the peak due to $B^- \to D^{*0}\ell^-\overline{\nu}$ decays, in which the low energy pion or photon from the decay $D^{*0} \to D^0\pi^0$ or $D^{*0} \to D^0\gamma$ escaped detection. To reduce the impact of the dependence of the $m^2_{\rm miss}$ resolution on the neutrino energy, the variable $E_{\rm miss} - p_{\rm miss} = m^2_{\rm miss}/(E_{\rm miss} + p_{\rm miss})$ is often preferred.

A variable first introduced by the CLEO Collaboration (Bartelt et al., 1999) to select exclusive semileptonic decays $B \to D\ell\nu$ is

$$\cos\theta_{BY} = (2E_BE_Y - m_B^2 - m_Y^2)/2|\mathbf{p}_B||\mathbf{p}_Y|, \quad (17.1.4)$$

where m_Y and $|\mathbf{p}_Y|$ refer to the invariant mass and momentum sum of the hadron X and the charged lepton ℓ. If the only missing particle is the neutrino, θ_{BY} corresponds to the angle between the momentum vectors $\mathbf{p}_B$ and $\mathbf{p}_Y = \mathbf{p}_X + \mathbf{p}_\ell$, and the condition $|\cos\theta_{BY}| \leq 1.0$ should be fulfilled, while for background events or incompletely reconstructed semileptonic decays the distribution extends to values well beyond this range, thus enabling a separation from the signal decays.

For the isolation of the exclusive signal decay the kinematic variables

$$\Delta E = E_B^* - E_{\rm beam}^* \ \text{ and } \ m_{\rm ES} = \sqrt{E^{*2}_{\rm beam} - \mathbf{p}^{*2}_B} \quad (17.1.5)$$

are used. A comparison of ΔE and $m_{\rm ES}$ distributions for selected samples of hadronic and semileptonic B decays is given in Figure 17.1.3. ΔE is centered on zero and the $m_{\rm ES}$ distribution peaks at the B-meson mass. For hadronic decays the ΔE resolution is dominated by the detector resolution. The resolution in $m_{\rm ES}$ is determined by the spread in the energy of the colliding beams, typically less than 3 MeV. For semileptonic decays both variables are affected by the measurement of the neutrino momentum and energy. The size of the continuum and combinatorial $B\overline{B}$ background depends on the decay mode and the overall event selection. Backgrounds with kinematics very similar to the signal B decays may contribute to the peak region defined as $|\Delta E| < 0.125\,\text{GeV}, m_{\rm ES} > 5.27\,\text{GeV}$.

There are several variables that are commonly used to describe the kinematics of semileptonic decays, both for exclusive and inclusive decays: the momentum transfer squared q^2, the momentum of the charged lepton p_ℓ, and the hadronic mass m_X. The last two are of particular importance for analyses of inclusive decays, summing over all possible hadronic states X. They are used to separate charmless decays from the dominant decays to charm hadrons.

There are two ways to define and measure q^2, either as the invariant mass squared of the four-vector sum of the reconstructed lepton and neutrino, or as the momentum transfer squared from the B meson to the final state hadron X, $q^2 = (p_\ell + p_{\rm miss})^2 = (p_B - p_{\rm X})^2$. In the first

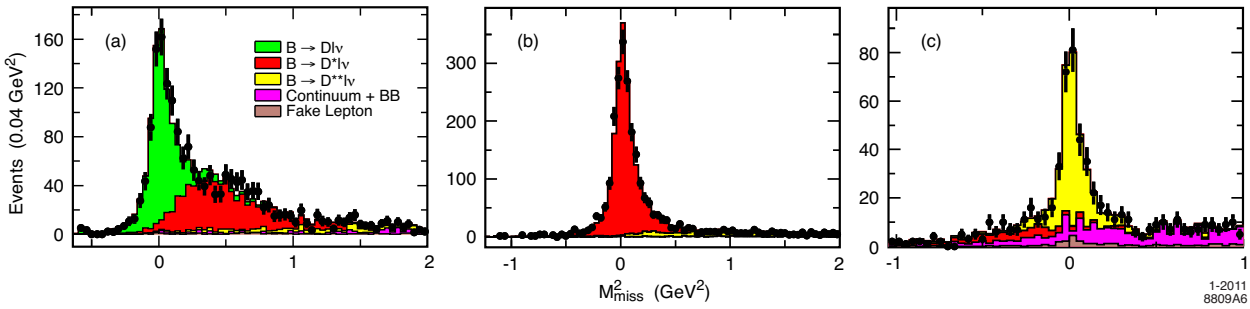

Figure 17.1.2. Distributions of the missing mass squared for exclusive $B \to X_c \ell \nu$ candidates in $B\overline{B}$ events tagged by a hadronic decay of the second B meson (Aubert, 2008b), a) $B^- \to D^0 \ell^- \overline{\nu}_\ell$, b) $\overline{B}^0 \to D^{*+} \ell^- \overline{\nu}_\ell$, and c) $B^- \to D^{*+} \pi^- \ell^- \overline{\nu}_\ell$. The contributions from various exclusive decay modes are marked by color shading.

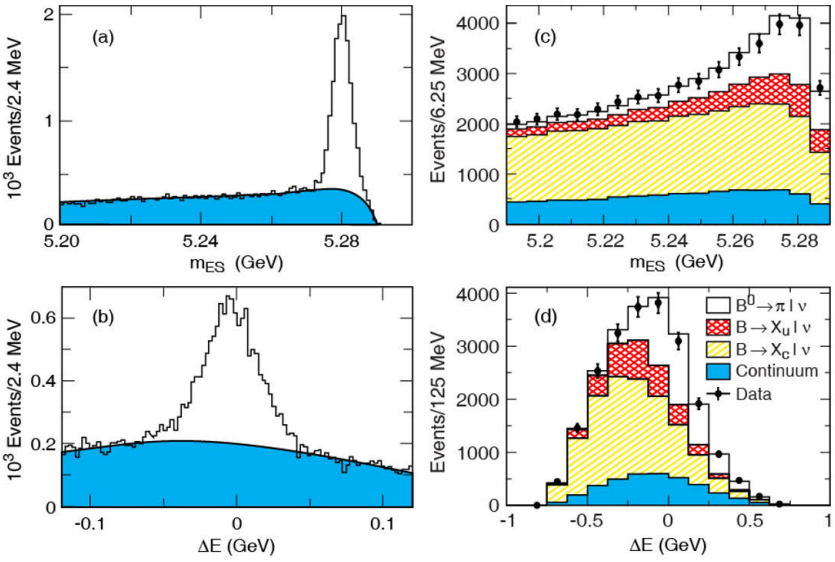

Figure 17.1.3. Distributions of $m_{\rm ES}$ and ΔE for (a, b) hadronic B decays above combinatorial continuum and $B\overline{B}$ background (blue) (Mazur, 2007), and (c, d) selected $B^0 \to \pi^- \ell^+ \nu$ decays (Ha, 2011) in the q^2 range of $0 - 16\,\mathrm{GeV}^2$, above a variety of backgrounds contributions, specifically $B \to X_u \ell \nu$ (red), various $B \to X_c \ell \nu$ decays (yellow), and continuum background (blue). For both samples, the distributions are restricted to events in the signal bands, *i.e.*, $m_{\rm ES}$ is shown for events in the peak region for ΔE, $|\Delta E| < 0.125\,\mathrm{GeV}$, and ΔE is restricted to events in the peak region for $m_{\rm ES}$, $m_{\rm ES} > 5.27\,\mathrm{GeV}$.

case, the resolution in q^2 is dominated by the measurement of the missing energy which tends to have a poorer resolution than the measured missing momentum, because the missing momentum is a vector sum and contributions from particle losses (or additional tracks and EMC showers) do not add linearly as is the case for $E_{\rm miss}$. Thus it is advantageous to replace $E_{\rm miss}$ by $|\mathbf{p}|_{\rm miss}$, the absolute value of the measured missing momentum, $q^2 = [(E_\ell, \boldsymbol{p}_\ell) + (p_{\rm miss}, \boldsymbol{p}_{\rm miss})]^2$.

In the second case, the q^2 measurement is not affected by the measurement of the missing momentum, but the direction of the B meson momentum is not known. Therefore the B momentum vector is estimated as the average over four or more possible directions of the B meson. The two methods have different sensitivity to combinatorial background: the first has the best resolution at high q^2, whereas the second method shows the best resolution at low q^2 where the hadron background is smaller. The width of the core resolution is in the range $(0.18 - 0.34)\,\mathrm{GeV}^2$, and the tails can be approximated by a second Gaussian function with widths in the range $(0.6 - 0.8)\,\mathrm{GeV}^2$. Figure 17.1.4 shows the resolution for selected $B \to \pi \ell \nu$ candidates. The q^2 resolution is important for many analyses of semileptonic decays.

With increasing data samples, more recent analyses have employed $B\overline{B}$ tagging techniques to substantially reduce continuum and combinatorial $B\overline{B}$ backgrounds. The detection of the decay of one of the B mesons produced at the $\Upsilon(4S)$ not only identifies the second B decay, but it uniquely determines its momentum, mass, charge and flavor. Furthermore, the kinematics of the final state are constrained such that an undetectable neutrino from the

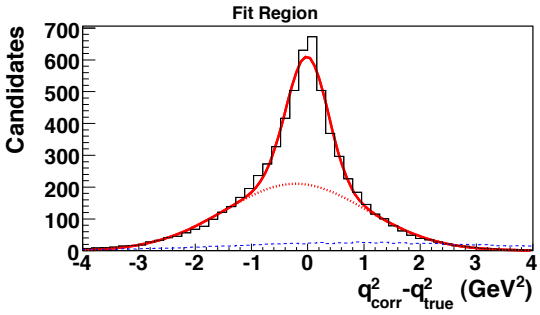

Figure 17.1.4. q^2 resolution for selected $B^0 \to \pi^-\ell^+\nu$ decays (del Amo Sanchez, 2011n) for true signal (black, solid histogram) and combinatorial signal (blue, dashed histogram) as obtained from simulation. The result of the fit to the signal with the sum of two Gaussian functions is shown (solid and dotted lines).

second decay can be identified from the missing momentum and missing energy of the rest of the event.

The cleanest samples of $B\overline{B}$ events are obtained with hadronic tags. Tag efficiencies and purities vary considerably, depending on the number of charged and neutral particles in the tag decay and the associated signal decay. Given the low branching fractions for individual hadronic decays and their high final-state particle multiplicity, the average achievable tagging efficiency is typically 0.3% for purities of $\simeq 0.5$. Recently, tag efficiencies have been increased as much as a factor of three by the addition of other hadronic decay modes, and by simultaneous constraints on the semileptonic signal decay in a given event, and by effectively selecting the best of several candidates per event (see Chapter 7).

Tag efficiencies in the range of $1-3\%$ can be obtained using semileptonic B decays. As for hadronic tags, the achievable tag efficiencies and purities are strongly dependent on both the tag decay and the decay of the signal B recoiling against the tag. In comparison with fully reconstructed hadronic tags, events tagged by semileptonic decays provide looser kinematic constraints on the recoiling B and result in a less accurate measurement of the missing neutrino and higher combinatorial backgrounds.

17.1.2 Exclusive decays $B \to D^{(*)}\ell\nu$

17.1.2.1 Theoretical Overview

In the following, we discuss exclusive B decays to a D or D^* meson. The transition matrix elements of the weak current given in Eq. (17.1.2) are decomposed into Lorentz-covariant forms, built from the independent four-vectors of the decay and form factors. For a pseudoscalar final state, only the vector current contributes,

$$\langle P|\overline{q}\gamma^\mu b|\overline{B}\rangle = f_+(q^2)\left(p_B^\mu + p_P^\mu - \frac{m_B^2 - m_P^2}{q^2}q^\mu\right) + f_0(q^2)\,\frac{m_B^2 - m_P^2}{q^2}q^\mu, \quad (17.1.6)$$

where p_B and p_P denote the four-vector momenta of the mesons, $q = p_B - p_P$ is the momentum transfer, and $f_{+,0}(q^2)$ are two form factors. For a vector final state, both the vector and axial currents contribute:

$$\langle V|\overline{q}\gamma^\mu b|\overline{B}\rangle = V(q^2)\,\varepsilon^{\mu\sigma}{}_{\nu\rho}\epsilon^*_\sigma\frac{2p_B^\nu p_V^\rho}{m_B + m_V}, \quad (17.1.7)$$

$$\langle V|\overline{q}\gamma^\mu\gamma^5 b|\overline{B}\rangle = i\epsilon^*_\nu\left[A_0(q^2)\,\frac{2m_V q^\mu q^\nu}{q^2} + A_1(q^2)\,(m_B + m_V)\eta^{\mu\nu} - A_2(q^2)\,\frac{(p_B + p_V)_\sigma q^\nu}{m_B + m_V}\eta^{\mu\sigma}\right], \quad (17.1.8)$$

where ϵ_ν is the polarization vector of the vector meson, $\eta^{\mu\nu} = g^{\mu\nu} - q^\mu q^\nu/q^2$, $\varepsilon^{\alpha\beta\gamma\delta}$ is the Levi-Civita tensor, and $V(q^2)$ and $A_i(q^2)$ are form factors. These form-factor decompositions are general: to determine $|V_{cb}|$, $\overline{q} = \overline{c}$, $P = D$, and $V = D^*$; to determine $|V_{ub}|$, $\overline{q} = \overline{u}$, $P = \pi$, and $V = \rho$.

The key feature of $B \to D^{(*)}$ decays is that the masses of both the charm and bottom quarks are large compared to the energy scale of non-perturbative QCD. Therefore, in both cases the heavy quark is nearly static, surrounded by a cloud of gluons, the light valence quark, and virtual quark-antiquark pairs. In particular, the effects of spin and flavor are suppressed by powers of $\Lambda_{\rm QCD}/m_Q$ ($Q = c, b$). In turn, approximate heavy-quark symmetries impose constraints on the form factors. These constraints become more transparent with a different basis of form factors,

$$\frac{\langle D|\overline{c}\gamma^\mu b|B\rangle}{\sqrt{m_B m_D}} = h_+(w)\,(v_B + v_D)^\mu + h_-(w)\,(v_B - v_D)^\mu, \quad (17.1.9)$$

$$\frac{\langle D^*|\overline{c}\gamma^\mu b|B\rangle}{\sqrt{m_B m_{D^*}}} = h_V(w)\,\varepsilon^{\mu\nu\rho\sigma}v_{B,\nu}v_{D^*,\rho}\epsilon^*_\sigma, \quad (17.1.10)$$

$$\frac{\langle D^*|\overline{c}\gamma^\mu\gamma^5 b|B\rangle}{\sqrt{m_B m_{D^*}}} = ih_{A_1}(w)\,(1+w)\epsilon^{*\mu} - i\,[h_{A_2}(w)v_B^\mu + h_{A_3}(w)v_{D^*}^\mu]\,\epsilon^*\cdot v_B, \quad (17.1.11)$$

where the velocities (for hadrons $H = B, D, D^*$) are $v_H = p_H/m_H$, the velocity transfer is $w = v_B \cdot v_{D^{(*)}} = (m_B^2 + m_{D^{(*)}}^2 - q^2)/2m_B m_{D^{(*)}}$. Again, these decompositions are completely general.

At zero recoil $w = 1$, heavy-quark dynamics requires (Isgur and Wise, 1989, 1990b; Shifman and Voloshin, 1987)

$$h_+(1) = 1 + {\rm O}(\alpha_s) + {\rm O}\left((\Lambda_{\rm QCD}/m_q)^2\right), \quad (17.1.12)$$

$$h_-(1) = 0 + {\rm O}(\alpha_s) + {\rm O}(\Lambda_{\rm QCD}/m_q), \quad (17.1.13)$$

$$h_{A_1}(1) = 1 + {\rm O}(\alpha_s) + {\rm O}\left((\Lambda_{\rm QCD}/m_q)^2\right). \quad (17.1.14)$$

The other zero-recoil form factors are not crucial to the extraction of $|V_{cb}|$. The task is to compute the corrections to heavy-quark symmetry; this is usually done in a way that aims to have the error scale with the deviation from the symmetry limit. The long-distance corrections of order $(\Lambda_{\rm QCD}/m_q)^n$ must be obtained non-perturbatively; the short-distance corrections of order α_s^l may be obtained perturbatively or non-perturbatively. It is, however, important to ensure that the separation of long- and short-distance effects is done in a consistent way. At nonzero recoil, all form factors receive contributions at first order in $\Lambda_{\rm QCD}/m_q$. Calculations of the form factors dependence on w require more effort.

The differential decay rates for $B^- \to D^{0(*)}\ell^-\overline{\nu}$ are

$$\frac{d\Gamma_{B^-\to D^0\ell^-\overline{\nu}}}{dw} = \frac{G_F^2 m_D^3}{48\pi^3}(m_B+m_D)^2(w^2-1)^{3/2} \times |\eta_{\rm EW}|^2|V_{cb}|^2|\mathcal{G}(w)|^2, \quad (17.1.15)$$

$$\frac{d\Gamma_{B^-\to D^{0*}\ell^-\overline{\nu}}}{dw} = \frac{G_F^2 m_{D^*}^3}{4\pi^3}(m_B-m_{D^*})^2(w^2-1)^{1/2} \times |\eta_{\rm EW}|^2|V_{cb}|^2\chi(w)|\mathcal{F}(w)|^2, \quad (17.1.16)$$

where $\eta_{\rm EW} = 1.0066$ is the one-loop electroweak correction (Sirlin, 1982) defined relative to G_F as extracted from muon decay.[52] The form factor $\mathcal{G}(w)$ is a function of $h_+(w)$ and $h_-(w)$ and in $\chi(w)|\mathcal{F}(w)|^2$, $\mathcal{F}(w)$ contains all four $B \to D^*$ form factors that enter Eqs (17.1.10) and (17.1.11). The full expressions can be found in Section 5.2 of Antonelli et al. (2010a). At zero recoil, $\mathcal{G}(1) = 1$ and $\mathcal{F}(1) = h_{A_1}(1)$. For decays of neutral mesons, $\overline{B}^0 \to D^{+(*)}\ell^-\overline{\nu}$, Coulomb attraction in the final state leads to an additional factor $1+\alpha\pi$ (Atwood and Marciano, 1990; Ginsberg, 1968) on the right-hand sides of Eqs (17.1.15) and (17.1.16).

For the determination of $|V_{cb}|$, the decay $B \to D^*\ell\nu$ is preferred over $B \to D\ell\nu$ for three reasons: First, theoretical predictions are simplest at zero recoil, where the rates are phase-space suppressed, but less so for the D^* final state $[(w^2-1)^{1/2}$ versus $(w^2-1)^{3/2}]$. Second, at zero recoil, the form factor $\mathcal{G}(1)$ receives corrections of order $\Lambda_{\rm QCD}/m_Q$, instead of $(\Lambda_{\rm QCD}/m_Q)^2$ for $\mathcal{F}(1)$. On the other hand, for $B \to D\ell\nu$ only the vector current contributes, resulting in a single form factor $\mathcal{G}(1)$, for low-mass leptons. Finally, and less crucially, the three polarization states of D^* increase the rate.

For these reasons let us first consider $\mathcal{F}(1) = h_{A_1}(1)$. One can show that the optical theorem and the OPE imply

$$|h_{A_1}(1)|^2 + \frac{1}{2\pi}\int_0 d\epsilon\, w(\epsilon) = 1 - \Delta_{1/m_Q^2} - \Delta_{1/m_Q^3}, \quad (17.1.17)$$

where $\epsilon = E - m_{D^*}$ is the excess energy of charmed states with $J^{PC} = 1^{-+}$, $w(\epsilon)$ is a structure function, and the upper limit of integration may be considered large for the moment. The contributions Δ_{1/m^n} describe corrections to the axial vector current for finite-mass quarks. The Δ_{1/m_Q^2} contributions can be conveniently written as

$$\Delta_{1/m_Q^2} = \frac{\mu_G^2}{3m_c^2} + \frac{\mu_\pi^2(\mu)-\mu_G^2}{4}\left(\frac{1}{m_c^2} + \frac{2/3}{m_c m_b} + \frac{1}{m_b^2}\right), \quad (17.1.18)$$

where $\mu_G^2 \simeq 3(m_{B^*}^2 - m_B^2)/4$ and $\mu_\pi^2(\mu)$ are matrix elements of the chromomagnetic energy and kinetic energy of the b quark in the B meson. The meaning of the scale μ in $\mu_\pi^2(\mu)$ is explained below. The $1/m_Q^3$ contributions have a similar expression (see, *e.g.*, Gambino, Mannel, and Uraltsev (2010)) with analogs of μ_G^2 and μ_π^2 that are related to moments of the inclusive semileptonic distribution.

For $\epsilon \gg \Lambda_{\rm QCD}$, the hadronic states in the excitation integral are dual to quark-gluon states. Introducing a scale μ to separate this short-distance part from the long-distance part (which must be treated non-perturbatively), one writes

$$\frac{1}{2\pi}\int_0 d\epsilon\, w(\epsilon) = \frac{1}{2\pi}\int_0^\mu d\epsilon\, w(\epsilon) + [1-\eta_A(\mu)^2]. \quad (17.1.19)$$

Here the quantity $\eta_A(\mu)$ combines the short-distance ($\epsilon > \mu$) contributions. It has been calculated to two loops in perturbation theory (Czarnecki, Melnikov, and Uraltsev, 1998); its μ dependence is compensated by $\mu_\pi^2(\mu)$. Rearranging Eq. (17.1.17) results in

$$h_{A_1}(1) \simeq \eta_A(\mu) - \frac{1}{2}\Delta_{1/m_Q^2} - \frac{1}{2}\Delta_{1/m_Q^3} - \frac{1}{4\pi}\int_0^\mu d\epsilon\, w(\epsilon). \quad (17.1.20)$$

The last term from higher hadronic excitations is not directly constrained by data.

Using recent data to compute $\Delta_{1/m_Q^2} + \Delta_{1/m_Q^3}$, Gambino, Mannel, and Uraltsev (2010) find

$$\Delta_{1/m_Q^2} + \Delta_{1/m_Q^3} = 0.11 \pm 0.03 \quad (17.1.21)$$

in the kinetic scheme with $\mu = 0.75\,\text{GeV}$. Combining this with the two-loop result of $\eta_A(0.75\,\text{GeV}) = 0.985 \pm 0.010$, Eq. (17.1.20) implies

$$\mathcal{F}(1) < 0.93, \quad (17.1.22)$$

since the excitation integral is positive. They further estimate the excitation contribution to be (in the notation used here)

$$\frac{1}{4\pi}\int_0^{0.75\ \text{GeV}} d\epsilon\, w(\epsilon) \approx 0.065, \quad (17.1.23)$$

leading to

$$\mathcal{F}(1) = 0.86 \pm 0.02. \quad (17.1.24)$$

One should note, however, that the estimate in Eq. (17.1.23) entails the application of the OPE at scales of 1 GeV or lower, and consequently the error is difficult to assess.

[52] This is just the QED running of the semileptonic form fermion operator from the W mass to the m_b scale. The leading bremsstrahlung part of the QED corrections is subtracted by experiments using approximate methods. Structure dependent corrections are still poorly understood (Becirevic and Kosnik, 2010; Bernlochner and Schonherr, 2010), but are unlikely to give non-negligible corrections.

With lattice QCD, the QCD action is discretized on an Euclidean space-time lattice, and calculations are performed numerically using Monte Carlo methods and importance sampling (see, *e.g.*, Bazavov et al., 2010; DeGrand and Detar, 2006; Hashimoto and Onogi, 2004; Kronfeld, 2002). Physical results are recovered in the limit of zero lattice spacing. Since lattice results are obtained from first principles in QCD, they can be improved to arbitrary precision, given sufficient computing resources. In recent years, LQCD has made substantial progress, particularly in flavor physics. The most computationally demanding part of QCD calculations, namely the treatment of the sea of virtual quark-antiquark pairs, has become feasible.

The Fermilab-MILC calculations (Bernard et al., 2009a) are based on $2+1$ flavors of sea quarks, two corresponding to up and down quarks (Bazavov et al., 2010) and one for the strange sea. The former two have masses larger than in nature, $m_l > 0.1 m_s$, but calculations at a sequence of light-quark masses are guided to the physical limit with chiral perturbation theory (Laiho and Van de Water, 2006).The uncertainties of these calculations can be reliably estimated, because a HQET analysis of the form factor follows through on the lattice (Harada, Hashimoto, Kronfeld, and Onogi, 2002; Kronfeld, 2000), and in this way, the error scales as $1-\mathcal{F}(1)$, rather than as $\mathcal{F}(1)$.

The current value (Bailey et al., 2010),

$$\eta_{\rm EW}\mathcal{F}(1) = 0.9077(51)(88)(84)(90)(30)(33), \quad (17.1.25)$$

includes the electroweak correction $\eta_{\rm EW} = 1.0066$. The stated uncertainties stem, respectively, from Monte-Carlo statistics, the $D^* \to D\pi$ coupling, the chiral extrapolation, discretization errors, perturbative matching, and tuning the bare quark masses. This result is an update of earlier calculations by Bernard et al. (2009a) that were based on a smaller set of LQCD data. Adding the errors in quadrature, we obtain

$$\eta_{\rm EW}\mathcal{F}(1) = 0.908 \pm 0.017, \quad (17.1.26)$$

which agrees well with the bound in Eq. (17.1.22).

The difference between the value in Eq. (17.1.24) and the LQCD result of $\mathcal{F}(1) = 0.902 \pm 0.017$ (without $\eta_{\rm EW}$), though not large, might be due to a breakdown of the OPE in the estimate the low-energy excitation integral, although this appears to be unlikely in view of our present understanding of heavy quark physics. LQCD form-factor calculations have passed several very challenging tests, including predictions of the shapes of $D \to \pi\ell\nu$ and $D \to K\ell\nu$ form factors (Aubin et al., 2005; Bernard et al., 2009b) and agreement to high precision for the normalization of these form factors with experiment (Na, Davies, Follana, Lepage, and Shigemitsu, 2010; Na et al., 2011).

Let us now turn, more briefly, to $B \to D\ell\nu$ and $\mathcal{G}(1)$. Unquenched LQCD calculations (Okamoto et al., 2005) result in

$$\mathcal{G}(1) = 1.074 \pm 0.024\ , \quad (17.1.27)$$

and are compatible with the HQE calculation (Uraltsev, 2004),

$$\mathcal{G}(1) = 1.04 \pm 0.02\ , \quad (17.1.28)$$

within the stated uncertainties.

17.1.2.2 Measurements of Branching Fractions and Differential Distributions

The decay $B \to D^*\ell\nu$ was measured at Belle (Dungel, 2010) and *BABAR* (Aubert, 2008h,v, 2009ab) assuming the HQET parameterization of the form factor $\eta_{\rm EW}\mathcal{F}(w)$ given by (Caprini, Lellouch, and Neubert, 1998) in terms of the four quantities: the normalization $\eta_{\rm EW}\mathcal{F}(1)|V_{cb}|$, the slope $\rho^2_{D^*}$, and the form-factor ratios $R_1(1) = R^{*2}V(1)/A_1(1)$ and $R_2(1) = R^{*2}A_2(1)/A_1(1)$, where

$$R^* = (2\sqrt{m_B m_{D^*}})/(m_B + m_{D^*}). \quad (17.1.29)$$

In some analyses (Aubert, 2008v, 2009ab) the partial width $d\Gamma/dw$ was measured as a function of the velocity transfer $w = v_B \cdot v_{D^*}$ to determine the normalization $\eta_{\rm EW}\mathcal{F}(1)|V_{cb}|$ and the slope $\rho^2_{D^*}$, with form-factor ratios $R_1(1)$ and $R_2(1)$ taken as input from other measurements. In the analyses by Dungel (2010) and Aubert (2008h) the differential decay rate of $B \to D^*\ell\nu$ with $D^* \to D\pi$ is measured as a function of four variables, w and the angles θ_ℓ, θ_V and χ (Figure 17.1.5), where

- θ_ℓ is the angle between the direction of the lepton and the direction opposite the B meson in the rest frame of the virtual W,
- θ_V is the angle between the direction of the D meson and the direction opposite the B meson in the D^* rest frame, and
- χ is the angle between the decay planes of the D^* and the W, defined in the B meson rest frame.

The differential rate in terms of these four kinematic variables gives access to all four HQET parameters of the $B \to D^*\ell\nu$ decay.

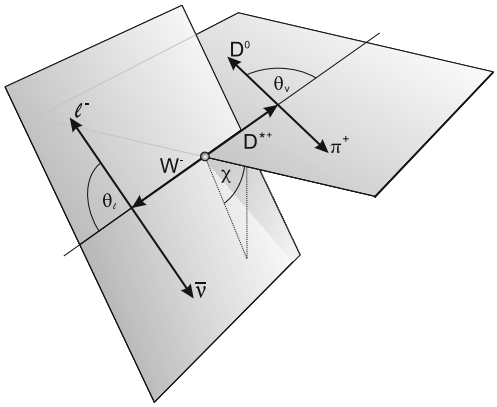

Figure 17.1.5. Definition of the angles θ_ℓ, θ_V and χ for the decay $\overline{B}^0 \to D^{*+}\ell^-\overline{\nu}$ with $D^{*+} \to D^0\pi^+$ (Dungel, 2010).

The Belle measurement (Dungel, 2010) is based on 711 fb^{-1} of $\Upsilon(4S)$ data resulting in about 120,000 reconstructed $B^0 \to D^{*-}\ell^+\nu$ decays. In this analysis the decay chain $D^{*-} \to \overline{D}^0\pi^-$ followed by $\overline{D}^0 \to K^+\pi^-$ is reconstructed and D^* candidates are combined with a charged

lepton ℓ ($\ell = e, \mu$) with momentum between 0.8 GeV and 2.4 GeV. As the analysis is untagged, the direction of the neutrino is not precisely known. However, using the $\cos\theta_{BY}$ variable with $Y = D^*\ell$ (see Section 17.1.1.3), the B momentum vector is constrained to a cone centered on the $D^*\ell$ direction. By averaging over the possible B directions one can approximate the neutrino momentum and calculate the kinematic variables of the decay, w, $\cos\theta_\ell$, $\cos\theta_V$ and χ. The typical 1σ resolutions for these variables are 0.025, 0.049, 0.050 and 13.5°, respectively. Figure 17.1.6 shows the result of the simultaneous fit to the one-dimensional projections of the four variables for the selected $B^0 \to D^{*-}\ell^+\nu$ sample. A feature of this method is that the same events enter into the four projections and the resulting correlations are accounted for by combining separate covariance matrices for the data and the simulated signal and background distributions.

BABAR performed a similar analysis of the decay $B^0 \to D^{*-}\ell^+\nu$ based on a sample of 79 fb^{-1} (Aubert, 2008h). Several D^0 decay modes are analyzed and the selected sample contains about 52,800 $B^0 \to D^{*-}\ell^+\nu$ decays. The results extracted from the fit to the four one-dimensional decay distributions were combined with another *BABAR* analysis of $B^0 \to D^{*-}\ell^+\nu$ which performed a fit to the four-dimensional decay rate $\Gamma(w, \theta_\ell, \theta_V, \chi)$ (Aubert, 2006af), thereby enhancing the sensitivity to $R_1(1)$, $R_2(1)$ and $|V_{cb}|$.

BABAR also analyzed the isospin conjugated decay mode $B^+ \to \bar{D}^{*0}e^+\nu$ in a sample of 205 fb^{-1}, with the neutral D^* meson decaying to $\bar{D}^{*0} \to \bar{D}^0\pi^0$ and $\bar{D}^0 \to K^+\pi^-$ (Aubert, 2008v). The reconstruction of the neutral D^* meson involves a low momentum π^0 rather than a charged pion, thus it is sensitive to different detection efficiencies and provides an independent check of the D^* reconstruction. In this analysis the HQET form-factor ratios $R_1(1)$ and $R_2(1)$, are taken as external parameters from other measurements.

The results of the $B \to D^*\ell\nu$ form-factor measurements, with common input parameters (mainly B lifetimes and D meson branching ratios) rescaled to the values available by the end of the year 2011 (Beringer et al., 2012), are summarized in Table 17.1.1. The $B^0 \to D^{*-}\ell^+\nu$ branching ratios calculated by using these form-factor parameters are given in Table 17.1.2.

The HQET parameterization of the $B \to D\ell\nu$ form factor $\eta_{\rm EW}\mathcal{G}(w)$ (Caprini, Lellouch, and Neubert, 1998) has only two free parameters: the normalization given by $\eta_{\rm EW}\mathcal{G}(1)|V_{cb}|$ and the slope ρ^2_D. These parameters are adopted for the Belle (Abe, 2002c) and *BABAR* (Aubert, 2009ab, 2010e) measurements of this decay.

Untagged analyses of $B \to D\ell\nu$ are limited by large backgrounds and related large irreducible uncertainties. Based on a sample of 417 fb^{-1}, *BABAR* performed a study of $B \to D\ell\nu$ decays, in which the second B meson in the event is reconstructed in a hadronic decay mode (Aubert, 2010e). This tagging technique results in a sizable background reduction and a more precise measurement of w. With a tagging efficiency of about 0.5%, 16 D meson decay modes and with a lower limit on the lepton momentum at 0.6 GeV yields of 2147 ± 69 $B^+ \to \bar{D}^0\ell^+\nu$ and 1108 ± 45 $B^0 \to D^-\ell^+\nu$ decays are obtained. These signal yields are determined by a fit to the missing-mass-squared distribution, $m^2_{\rm miss} = (p_B - p_D - p_\ell)^2$ (see Figure 17.1.2). The normalization $\eta_{\rm EW}\mathcal{G}(1)|V_{cb}|$ and the slope ρ^2_D are extracted from a fit to the efficiency-corrected signal yields in ten bins of w (see Figure 17.1.7).

Table 17.1.2. The $B^0 \to D^{*-}\ell^+\nu$ branching ratio, calculated using the HQET parameterization of the form factor $\eta_{\rm EW}\mathcal{F}(w)$ (Caprini, Lellouch, and Neubert, 1998) and the parameter values in Table 17.1.1. For measurements that do not determine $R_1(1)$ and $R_2(1)$, we assume the average values of these parameters (Section 17.1.2.3). The errors quoted correspond to the statistical and systematic uncertainties, respectively.

Analysis	$\mathcal{B}(B^0 \to D^{*-}\ell^+\nu)$ (%)
Belle (Dungel, 2010)	$4.59 \pm 0.03 \pm 0.26$
BABAR $D^{*-}\ell^+\nu$ (Aubert, 2008h)	$4.58 \pm 0.04 \pm 0.25$
BABAR $\bar{D}^{*0}e^+\nu$ (Aubert, 2008v)	$4.95 \pm 0.07 \pm 0.34$
BABAR $DX l\nu$ (Aubert, 2009ab)	$4.96 \pm 0.02 \pm 0.20$
Average	$4.83 \pm 0.01 \pm 0.12$

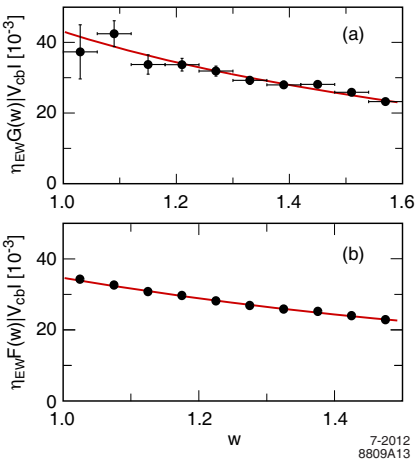

Figure 17.1.7. *BABAR* measurements, corrected for the reconstruction efficiency, of the w dependence of the form factors, with fit results superimposed (solid line): (a) $\eta_{EW}\mathcal{G}(w)|V_{cb}|$ for $B \to D\ell\nu$ decays from tagged events (Aubert, 2010e), and for comparison (b) $\eta_{EW}\mathcal{F}(w)|V_{cb}|$ for $B \to D^*\ell\nu$ decays from untagged events (Aubert, 2008h).

The results of the $B \to D\ell\nu$ form-factor measurements at the B Factories, rescaled to common input parameters (Beringer et al., 2012), are summarized in Table 17.1.3. We also calculate the $B^0 \to D^-\ell^+\nu$ branching fraction from these values (Table 17.1.4).

BABAR also published a measurement of $B \to D^*\ell\nu$ and $B \to D\ell\nu$ adopting an innovative approach. Using a sample of 207 fb^{-1}, this analysis is based on an inclusive selection of $B \to DX\ell\nu$ decays, where only the D meson and the charged lepton are reconstructed (Au-

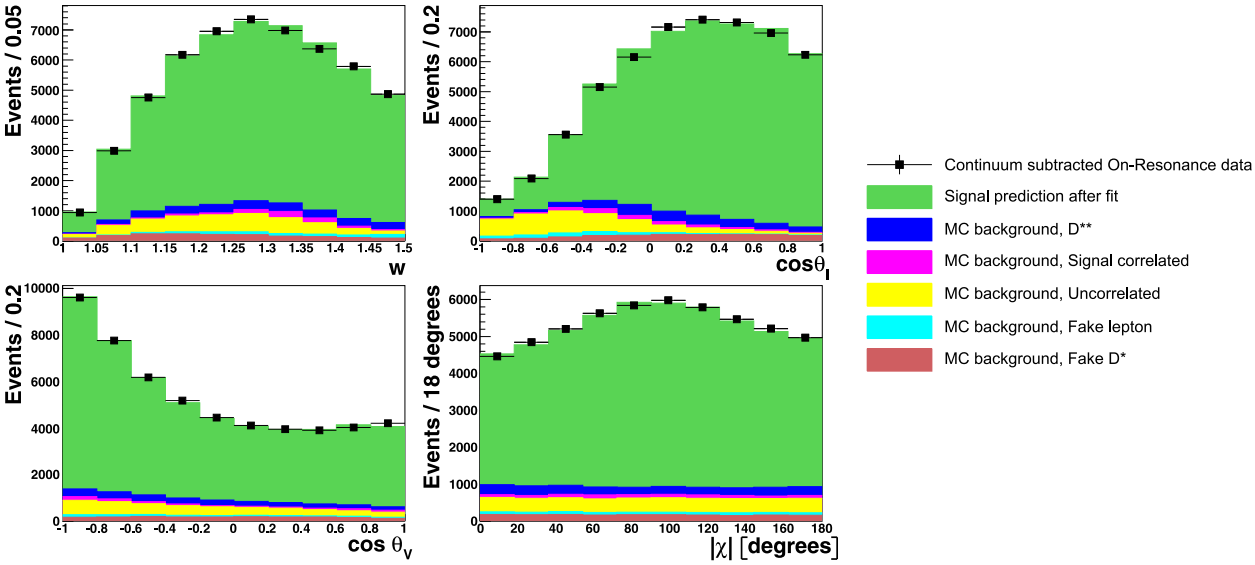

Figure 17.1.6. Belle analysis of $B \to D^*\ell\nu$ (Dungel, 2010): Result of the simultaneous fit to four one-dimensional projections of selected $B^0 \to D^{*-}\ell^+\nu$ events: w (top-left), $\cos\theta_\ell$ (top-right), $\cos\theta_V$ (botton-left) and χ (bottom-right). The data points represent continuum subtracted event yields. The histograms represent the signal component and different background contributions.

Table 17.1.1. Summary of the B Factory results for the $B \to D^*\ell\nu$ form-factor parameters $\eta_{\rm EW}\mathcal{F}(1)|V_{cb}|$, $\rho^2_{D^*}$, $R_1(1)$ and $R_2(1)$. The measurements have been rescaled to the end of year 2011 values of the common input parameters (Beringer et al., 2012). The errors quoted for each parameter correspond to the statistical and systematic uncertainties, respectively. The average is obtained by a four dimensional fit to these values taking into account correlated systematic uncertainties.

Analysis	$\eta_{\rm EW}\mathcal{F}(1)\lvert V_{cb}\rvert$ (10^{-3})	$\rho^2_{D^*}$	$R_1(1)$	$R_2(1)$
Belle (Dungel, 2010)	$34.7 \pm 0.2 \pm 1.0$	$1.21 \pm 0.03 \pm 0.01$	$1.40 \pm 0.03 \pm 0.02$	$0.86 \pm 0.02 \pm 0.01$
BABAR $D^{*-}\ell^+\nu$ (Aubert, 2008h)	$34.1 \pm 0.3 \pm 1.0$	$1.18 \pm 0.05 \pm 0.03$	$1.43 \pm 0.06 \pm 0.04$	$0.83 \pm 0.04 \pm 0.02$
BABAR $\bar{D}^{*0}e^+\nu$ (Aubert, 2008v)	$35.1 \pm 0.6 \pm 1.3$	$1.12 \pm 0.06 \pm 0.06$		
BABAR $DX l\nu$ (Aubert, 2009ab)	$35.8 \pm 0.2 \pm 1.1$	$1.19 \pm 0.02 \pm 0.06$		
Average	$35.5 \pm 0.1 \pm 0.5$	$1.20 \pm 0.02 \pm 0.02$	$1.40 \pm 0.03 \pm 0.01$	$0.86 \pm 0.02 \pm 0.01$

Table 17.1.3. Summary of the B Factory results for the $B \to D\ell\nu$ form-factor parameters $\eta_{\rm EW}\mathcal{G}(1)|V_{cb}|$ and ρ^2_D. The measurements have been rescaled to the end of year 2011 values of the common input parameters (Beringer et al., 2012). The errors quoted for each parameter correspond to the statistical and systematic uncertainties, respectively. The average is obtained by a two dimensional fit to these values taking into account correlated systematic uncertainties.

Analysis	$\eta_{\rm EW}\mathcal{G}(1)\lvert V_{cb}\rvert$ (10^{-3})	ρ^2_D
Belle (Abe, 2002c)	$40.8 \pm 4.4 \pm 5.0$	$1.12 \pm 0.22 \pm 0.14$
BABAR $DX l\nu$ (Aubert, 2009ab)	$43.4 \pm 0.8 \pm 2.1$	$1.20 \pm 0.04 \pm 0.06$
BABAR tagged (Aubert, 2010e)	$42.5 \pm 1.9 \pm 1.1$	$1.18 \pm 0.09 \pm 0.05$
Average	$42.7 \pm 0.7 \pm 1.5$	$1.19 \pm 0.04 \pm 0.04$

bert, 2009ab). To reduce background from $D^{**}\ell\nu$ decays and other background sources, the lepton momentum is restricted to $p_\ell > 1.2$ GeV, and the D mesons are reconstructed only in the two cleanest decay modes, $D^0 \to K^-\pi^+$ and $D^+ \to K^-\pi^+\pi^+$. The $D^{(*)}\ell\nu$ signal and background yields, the values of ρ^2_D, $\rho^2_{D^*}$, $\eta_{\rm EW}\mathcal{G}(1)|V_{cb}|$ and $\eta_{\rm EW}\mathcal{F}(1)|V_{cb}|$ are obtained from a binned χ^2 fit to the three-dimensional distributions of the lepton momentum p_ℓ, the D momentum p_D, and $\cos\theta_{BY}$. The results of this analysis are listed in Tables 17.1.1 and 17.1.3. The statistical errors are less than those of the tagged analysis which was based on a larger overall event sample, but the systematic uncertainty of the $B \to D\ell\nu$ measurement is larger by a factor of two.

Table 17.1.4. The $B^0 \to D^- \ell^+ \nu$ branching ratio, calculated using the HQET parameterization of the form factor $\eta_{\rm EW}\mathcal{G}(w)$ (Caprini, Lellouch, and Neubert, 1998) and the parameter values in Table 17.1.3. The errors quoted correspond to the statistical and systematic uncertainties, respectively.

Analysis	$\mathcal{B}(B^0 \to D^- \ell^+ \nu)$ (%)
Belle (Abe, 2002c)	$2.07 \pm 0.12 \pm 0.52$
BABAR $DX l\nu$ (Aubert, 2009ab)	$2.18 \pm 0.03 \pm 0.13$
BABAR tagged (Aubert, 2010e)	$2.12 \pm 0.10 \pm 0.06$
Average	$2.14 \pm 0.03 \pm 0.10$

17.1.2.3 Extraction of $|V_{cb}|$ and the Decay Form Factors

We combine the results of four measurements of $B \to D^* \ell\nu$ decays, three obtained by *BABAR* (Aubert, 2008h,v, 2009ab) and one by Belle (Dungel, 2010), by performing a four-dimensional fit to the HQET parameters $\eta_{\rm EW}\mathcal{F}(1)|V_{cb}|$, $\rho^2_{D^*}$, $R_1(1)$ and $R_2(1)$ taking into account systematic error correlations. The results are

$$\begin{aligned} \eta_{\rm EW}\mathcal{F}(1)|V_{cb}| &= (35.45 \pm 0.50) \times 10^{-3}\ , \\ \rho^2_{D^*} &= 1.199 \pm 0.027, \\ R_1(1) &= 1.396 \pm 0.033, \\ R_2(1) &= 0.860 \pm 0.020. \end{aligned} \tag{17.1.30}$$

The correlations between the different fit parameters are

$$\begin{aligned} \rho_{\eta_{\rm EW}\mathcal{F}(1)|V_{cb}|,\rho^2_{D^*}} &= \ \ 0.326, \\ \rho_{\eta_{\rm EW}\mathcal{F}(1)|V_{cb}|,R_1(1)} &= -0.084, \\ \rho_{\eta_{\rm EW}\mathcal{F}(1)|V_{cb}|,R_2(1)} &= -0.064, \\ \rho_{\rho^2_{D^*},R_1(1)} &= \ \ 0.563, \\ \rho_{\rho^2_{D^*},R_2(1)} &= -0.804, \\ \rho_{R_1(1),R_2(1)} &= -0.761. \end{aligned} \tag{17.1.31}$$

The χ^2 of the combination is 8.0 for 8 degrees of freedom. For $B \to D\ell\nu$, there are three measurements, one by Belle (Abe, 2002c) and two by *BABAR* (Aubert, 2009ab, 2010e). The results of the fit to $\eta_{\rm EW}\mathcal{G}(1)|V_{cb}|$ and ρ^2_D are

$$\begin{aligned} \eta_{\rm EW}\mathcal{G}(1)|V_{cb}| &= (42.68 \pm 1.67) \times 10^{-3}, \\ \rho^2_D &= 1.186 \pm 0.057, \end{aligned} \tag{17.1.32}$$

with a correlation of

$$\rho_{\eta_{\rm EW}\mathcal{G}(1)|V_{cb}|,\rho^2_D} = 0.839. \tag{17.1.33}$$

The χ^2 of the average is 0.3 for 4 degrees of freedom. The measured values and the averages are shown in Figure 17.1.8.

Using the form-factor normalization from the latest LQCD calculation of Eq. (17.1.26), we obtain for $|V_{cb}|$ from $B \to D^* \ell\nu$ decays,

$$|V_{cb}| = (39.04 \pm 0.55_{\rm exp} \pm 0.73_{\rm th}) \times 10^{-3}\ . \tag{17.1.34}$$

Based on an earlier LQCD calculations, Eq. (17.1.27), we derive $|V_{cb}|$ from $B \to D\ell\nu$ decays,

$$|V_{cb}| = (39.46 \pm 1.54_{\rm exp} \pm 0.88_{\rm th}) \times 10^{-3}\ . \tag{17.1.35}$$

On the other hand, we obtain values for $|V_{cb}|$ that are about 5% larger if we rely on heavy flavor sum rule calculations, Eq. (17.1.24), for $B \to D^* \ell\nu$ decays

$$|V_{cb}| = (40.93 \pm 0.58_{\rm exp} \pm 0.95_{\rm th}) \times 10^{-3}\ , \tag{17.1.36}$$

or on HQE calculations, Eq. (17.1.28), for $B \to D\ell\nu$ decays,

$$|V_{cb}| = (40.75 \pm 1.59_{\rm exp} \pm 0.78_{\rm th}) \times 10^{-3}\ . \tag{17.1.37}$$

While the results for the two decay modes agree well, $|V_{cb}|$ measured in $B \to D^* \ell\nu$ decays is more precise and will be considered as the main result.

17.1.3 Inclusive Cabibbo-favored B decays

17.1.3.1 Theoretical Overview

Our understanding of inclusive semileptonic B decays rests on a simple idea: since inclusive decays include all possible hadronic final states, the final state quark hadronizes with unit probability and the transition amplitude is sensitive only to the long-distance dynamics of the initial B meson. Thanks to the large hierarchy between the typical energy release, of $O(m_b)$, and the hadronic scale $\Lambda_{\rm QCD}$, and to asymptotic freedom, any residual sensitivity to non-perturbative effects is suppressed by powers of $\Lambda_{\rm QCD}/m_b$.

An OPE allows us to express the non-perturbative physics in terms of B meson matrix elements of local operators of dimension $d \geq 5$, while the Wilson coefficients can be expressed as a perturbative series in α_s (Bigi, Shifman, Uraltsev, and Vainshtein, 1993; Bigi, Uraltsev, and Vainshtein, 1992; Blok, Koyrakh, Shifman, and Vainshtein, 1994; Manohar and Wise, 1994). The OPE disentangles the physics associated with *soft* scales of order $\Lambda_{\rm QCD}$ (parameterized by the matrix elements of the local operators) from that associated with *hard* scales $\sim m_b$ (in the Wilson coefficients). The total semileptonic width and the moments of the kinematic distributions are therefore double expansions in α_s and $\Lambda_{\rm QCD}/m_b$, with a leading term that is given by the free b quark decay. Quite importantly, the power corrections start at $O(\Lambda^2_{\rm QCD}/m_b^2)$ and are comparatively suppressed. At higher orders in the OPE, terms suppressed by powers of m_c also appear, starting with $O(\Lambda^3_{\rm QCD}/m_b^3 \times \Lambda^2_{\rm QCD}/m_c^2)$ (Bigi, Mannel, Turczyk, and Uraltsev, 2010).

The relevant parameters in the double series are the heavy quark masses m_b and m_c, the strong coupling α_s, and the matrix elements of the local operators. As there are only two dimension five operators, two matrix elements appear at $O(1/m_b^2)$:

$$\mu^2_\pi(\mu) = \frac{1}{2m_B}\langle B|\bar{b}\,\boldsymbol{\pi}^2\, b|B\rangle_\mu, \tag{17.1.38}$$

$$\mu^2_G(\mu) = \frac{1}{2m_B}\langle B|\bar{b}\frac{i}{2}\sigma_{\mu\nu}G^{\mu\nu}b|B\rangle_\mu, \tag{17.1.39}$$

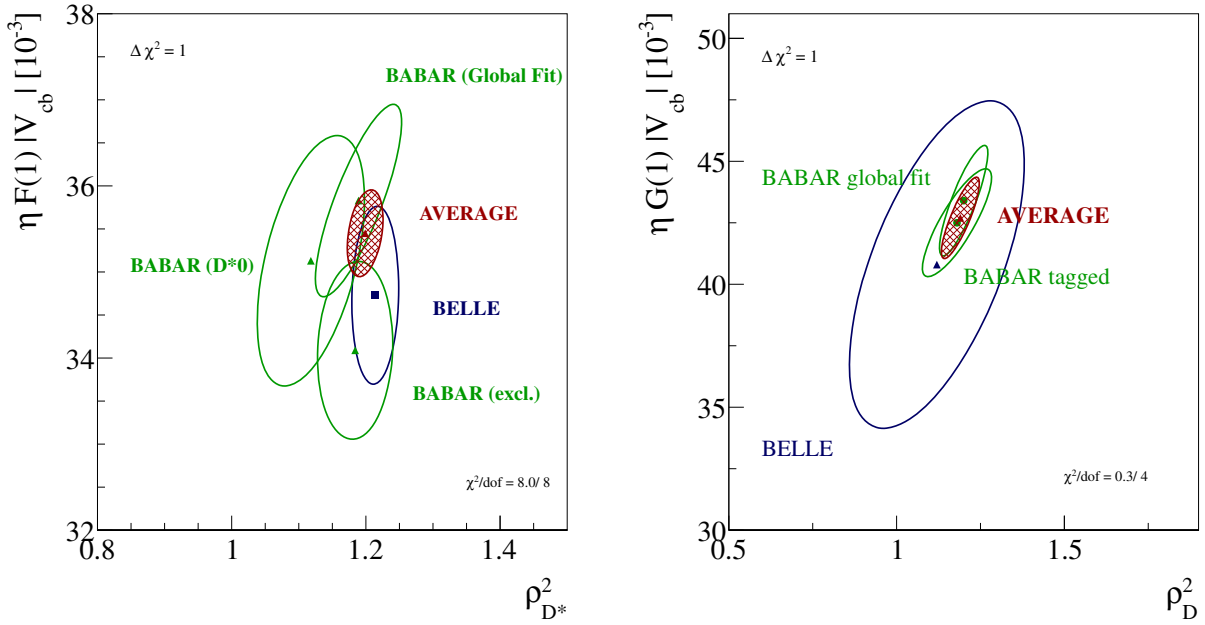

Figure 17.1.8. One sigma contour plots of the averages of $\eta_{\rm EW}\mathcal{F}(1)|V_{cb}|$ and $\rho^2_{D^*}$ (left), and of $\eta_{\rm EW}\mathcal{G}(1)|V_{cb}|$ and ρ^2_D.

where $\boldsymbol{\pi} = -i\boldsymbol{D}$ with $\boldsymbol{D}$ the space component of the covariant derivative, $\sigma^{\mu\nu} = i/2[\gamma^\mu, \gamma^\nu]$, and $G^{\mu\nu}$ the gluon field tensor. The matrix element of the kinetic operator, μ_π^2, is naturally associated with the average kinetic energy of the b quark in the B meson, while that of the chromomagnetic operator, μ_G^2, is related to the B^*-B hyperfine mass splitting. They generally depend on a cutoff $\mu = O(1\,\text{GeV})$ chosen to separate soft and hard physics. The cutoff can be implemented in different ways. In the kinetic scheme (Bigi et al., 1995, 1997), a Wilson cutoff on the gluon momentum is employed in the b quark rest frame: all soft gluon contributions are attributed to the expectation values of the higher dimensional operators, while hard gluons with momentum $|\boldsymbol{k}| > \mu$ contribute to the perturbative corrections to the Wilson coefficients. In the HQET a different notation is usually employed: at leading order in $1/m_Q$ one can identify μ_π^2 with $-\lambda_1$ and μ_G^2 with $3\lambda_2$. Most current applications of the OPE involve $O(1/m_b^3)$ effects (Gremm and Kapustin, 1997) as well, parameterized in terms of two additional parameters, generally indicated by ρ_D^3 and ρ_{LS}^3 or by their HQET counterparts $\rho_{1,2}$. These OPE parameters describe universal properties of the B meson and of the quarks and are useful in several applications.

The interesting quantities to be measured are the total rate and some global shape parameters, such as the first few moments of the lepton energy spectrum or of the hadronic invariant mass distribution. The lepton energy moments are defined as

$$\langle E_\ell^n \rangle = \frac{1}{\Gamma_{E>E_{\rm cut}}} \int_{E>E_{\rm cut}} dE_\ell E_\ell^n \frac{d\Gamma}{dE_\ell}, \quad (17.1.40)$$

where E_ℓ is the lepton energy in $B \to X_c \ell \nu$, $\Gamma_{E>E_{\rm cut}}$ is the semileptonic width above the energy threshold $E_{\rm cut}$ and $d\Gamma/dE_\ell$ is the differential semileptonic width as a function of E_ℓ. The hadronic mass moments are similarly defined as

$$\langle m_X^{2n} \rangle = \frac{1}{\Gamma_{E>E_{\rm cut}}} \int_{E>E_{\rm cut}} dm_X^2 m_X^{2n} \frac{d\Gamma}{dm_X^2}. \quad (17.1.41)$$

Here, $d\Gamma/dm_X^2$ is the differential width as a function of the mass squared of the hadronic system X. For both types, n is the order of the moment. For $n > 1$, the moments can also be defined relative to $\langle E_\ell \rangle$ and $\langle m_X^2 \rangle$, respectively, in which case they are called central moments.

The OPE cannot be expected to converge in regions of phase space where the momentum of the final hadronic state is $O(\Lambda_{\rm QCD})$ and where perturbation theory has singularities. This is because what actually controls the expansion is not m_b but the energy release, which is $O(\Lambda_{\rm QCD})$ in those cases. The OPE is therefore valid only for sufficiently inclusive measurements and in general cannot describe differential distributions. The lepton energy moments can be measured very precisely, while the hadronic mass moments are directly sensitive to higher dimensional matrix elements such as μ_π^2 and ρ_D^3. In most cases, one has to take into account an experimental lower threshold on the lepton momentum. The leptonic and hadronic moments give information on the quark masses and on the non-perturbative OPE matrix elements, while the total rate allows for the extraction of $|V_{cb}|$.

The reliability of the inclusive method rests on our ability to control the higher order contributions in the double series and to constrain quark-hadron duality violation, *i.e.* effects beyond the OPE, which exist but are expected

to be rather suppressed in semileptonic decays. The calculation of higher order effects allows us to verify the convergence of the double series and to reduce and properly estimate the residual theoretical uncertainty. Duality violation effects (see Bigi and Uraltsev, 2001a, for a review) can be constrained *a posteriori*, by checking whether the OPE predictions fit the experimental data. This in turn depends on precise measurements and precise OPE predictions. As the experimental accuracy reached at the B Factories is better than the theoretical accuracy for all the measured moments, any effort to improve the latter is strongly motivated.

The main ingredients for an accurate analysis of the experimental data on the moments and the subsequent extraction of $|V_{cb}|$ have been known for some time. Two implementations are currently employed in global analyses; they are based on either the kinetic scheme (Benson, Bigi, Mannel, and Uraltsev, 2003; Gambino and Uraltsev, 2004) or the $1S$ mass scheme for the b quark (Bauer, Ligeti, Luke, Manohar, and Trott, 2004). They both include terms through $O(\alpha_s^2\beta_0)$ and $O(1/m_b^3)$ ($\beta_0 = 11 - 2n_l/3$ is the first coefficient of the QCD beta function) but they use different perturbative schemes, include a somewhat different choice of experimental data under specific assumptions, and estimate the theoretical uncertainties in two distinct ways. Nevertheless, the two methods yield similar results for $|V_{cb}|$.

An important component of the OPE calculation are the purely perturbative contributions. Although the $O(\alpha_s)$ perturbative corrections to various kinematic distributions and to the rate have been computed long ago, the triple differential distribution was first computed at $O(\alpha_s)$ only recently by Aquila, Gambino, Ridolfi, and Uraltsev (2005); Trott (2004). The so-called BLM corrections, *i.e.* those of $O(\alpha_s^2\beta_0)$, are usually the dominant source of two-loop corrections in B decays. They can be found in complete form in Aquila, Gambino, Ridolfi, and Uraltsev (2005). The complete two-loop perturbative corrections to the width and moments of the lepton energy and hadronic mass distributions have been recently computed (Biswas and Melnikov, 2010; Melnikov, 2008; Pak and Czarnecki, 2008) by both numerical and analytic methods. The kinetic scheme implementation for actual observables can be found in Gambino (2011). In general, using $\alpha_s(m_b)$ in the on-shell scheme, the non-BLM corrections amount to about -20% of the two-loop BLM corrections and give small contributions to normalized moments. In the kinetic scheme with cutoff $\mu = 1\,\text{GeV}$, the perturbative expansion of the total width is

$$\Gamma[\overline{B} \to X_c e\overline{\nu}] \propto 1 - 0.96\,\frac{\alpha_s(m_b)}{\pi} - 0.48\,\beta_0\left(\frac{\alpha_s}{\pi}\right)^2 + 0.82\left(\frac{\alpha_s}{\pi}\right)^2 + O(\alpha_s^3) \approx 0.916. \tag{17.1.42}$$

Higher order BLM corrections of $O(\alpha_s^n\beta_0^{n-1})$ to the width and moments are also known (Aquila, Gambino, Ridolfi, and Uraltsev, 2005; Benson, Bigi, Mannel, and Uraltsev, 2003). The resummed BLM result is numerically very close to that from NNLO calculations (Benson, Bigi, Mannel, and Uraltsev, 2003). The residual perturbative error in the total width is therefore about 1%.

The global fit to moments can be performed to NNLO to extract the OPE parameters and $|V_{cb}|$. In the normalized leptonic moments the perturbative corrections cancel to a large extent, independently of the mass scheme, because hard gluon emission is comparatively suppressed. This pattern of cancellations, crucial for an accurate estimate of the theoretical uncertainties, is confirmed by the complete $O(\alpha_s^2)$ calculation, although the numerical precision of the available results is not sufficient to improve the overall accuracy for the higher central leptonic moments (Gambino, 2011). The non-BLM corrections turn out to be more important for the hadronic moments. Even though it improves the overall theoretical uncertainty only moderately, the complete NNLO calculation leads to the meaningful inclusion of precise mass constraints, such as those discussed in Section 17.1.3.2, in various perturbative schemes (Gambino, 2011).

Sources of significant residual theoretical uncertainty are the perturbative corrections to the Wilson coefficients of the power-suppressed operators. They induce corrections of $O(\alpha_s\Lambda_{\text{QCD}}^2/m_b^2)$ to the width and to the moments. Only the $O(\alpha_s\mu_\pi^2/m_b^2)$ terms are presently known (Becher, Boos, and Lunghi, 2007). A complete calculation of these effects has recently been performed for inclusive radiative decays (Ewerth, Gambino, and Nandi, 2010), where the $O(\alpha_s)$ corrections increase the coefficient of μ_G^2 in the rate by almost 20%. The extension of this calculation to the semileptonic decay rate is in progress. In view of the importance of $O(1/m_b^3)$ corrections, if a theoretical precision of 1% in the decay rate is to be reached, the $O(\alpha_s/m_b^3)$ effects may need to be calculated.

As to the higher order power corrections, a first analysis of $O(1/m_b^4)$ and $O(1/m_Q^5)$ effects is given in Mannel, Turczyk, and Uraltsev (2010). The main problem is the proliferation of non-perturbative parameters: *e.g.* as many as nine new expectation values appear at $O(1/m_b^4)$ and more at the next order. Because they cannot all be extracted from experiment, they are estimated in the ground state saturation approximation, thus reducing them to the known $O(1/m_b^{2,3})$ parameters. In this approximation, the total $O(1/m_Q^{4,5})$ correction to the width is about $+1.3\%$. The $O(1/m_Q^5)$ effects are dominated by $O(1/m_b^3m_c^2)$ intrinsic charm contributions, amounting to $+0.7\%$ (Bigi, Mannel, Turczyk, and Uraltsev, 2010). The net effect on $|V_{cb}|$ also depends on the corrections to the moments. Mannel, Turczyk, and Uraltsev (2010) estimate that the overall effect on $|V_{cb}|$ is a 0.4% increase. While this sets the scale of higher order power corrections, it is as yet unclear how much the result depends on the assumptions made for the expectation values.

It is worth stressing that the semileptonic moments are sensitive to the values of the heavy quark masses and in particular to a specific linear combination of m_c and m_b (Voloshin, 1995), which to a good approximation is the one needed for the extraction of $|V_{cb}|$ (Gambino and Schwanda, 2011). Checking the consistency of the con-

straints on m_c and m_b from semileptonic moments with the precise determinations of these quark masses (see Section 17.1.3.2) is an important step in the effort to improve our theoretical description of inclusive semileptonic decays. The inclusion of these constraints in the semileptonic fits will eventually improve the accuracy of the $|V_{ub}|$ and $|V_{cb}|$ determinations. Indeed, the b quark mass and the OPE expectation values obtained from the moments are crucial inputs in the determination of $|V_{ub}|$ from inclusive semileptonic decays (see Section 17.1.5 and Antonelli et al., 2010a). The heavy quark masses and the OPE parameters are also relevant for a precise calculation of other inclusive decay rates such as that of $B \to X_s\gamma$ (Gambino and Giordano, 2008).

The first two moments of the photon energy distribution in $B \to X_s\gamma$ are also often included in the semileptonic fits. They are sensitive to m_b and μ_π^2 and play the same role as a loose constraint on m_b ($\delta m_b \sim 90$ MeV). However, as discussed in Section 17.9, experiments place a lower limit on the photon energy, which introduces a sensitivity to the Fermi motion of the b-quark inside the B meson and tends to disrupt the OPE. One can still re-sum the higher-order terms into a non-local distribution function and since the lowest integer moments of this function are given in terms of the local OPE parameters, one can parameterize it assuming different functional forms (Benson, Bigi, and Uraltsev, 2005). Another serious problem is that only the leading operator contributing to inclusive radiative decays can be described by an OPE. Therefore, unknown $O(\alpha_s \Lambda_{\rm QCD}/m_b)$ contributions should be expected (Paz, 2010) and radiative moments, though interesting in their own respect, should be considered with care in the context of precision moment analyses.

17.1.3.2 Recent charm and bottom quark mass determinations (other than from semileptonic B decays)

In the following, we discuss recent determinations of m_c and m_b, excluding those from semileptonic B decays, and only including results since 2007 (except for the use of non-relativistic sum rules). All quark mass values are presented in the $\overline{\rm MS}$ scheme where the renormalization scale is set to $\mu = m_b$ for the bottom and $\mu = 3$ GeV for the charm quark. For convenience we also provide results for $m_c(m_c)$, even though the scale $\mu = m_c$ is too small considering the current level of precision.

Low-energy sum rules (LESR)

The theoretical prediction of moments of the vector current correlator depend on the heavy quark mass and thus the latter can be extracted from the comparison to moments evaluated with the help of experimental data for the total cross section $\sigma(e^+e^- \to \text{hadrons})$. The method is restricted to the first few moments which permits using the fixed-order polarization function. In Kühn, Steinhauser, and Sturm (2007) the charm quark mass has been determined with an uncertainty of 13 MeV. The extraction of the bottom quark mass has been updated (Chetyrkin et al., 2009) using new experimental input. More recently, LESR have also been used to extract the charm quark mass (Dehnadi, Hoang, Mateu, and Zebarjad, 2011).

Non-relativistic sum rules (NRSR)

This method requires the evaluation of the polarization function in the non-relativistic limit and is therefore not restricted to lower moments. The most advanced analysis (Pineda and Signer, 2006) uses an almost complete next-to-next-to-leading logarithmic approximation to determine the bottom quark mass.

In Signer (2009) non-relativistic sum rules have been used to extract the charm-quark mass in an approach which combines fixed-order and non-relativistic calculations.

Finite-energy sum rules (FESR)

The residue theorem can be used to relate the (appropriately weighted) experimental cross section $\sigma(e^+e^- \to \text{hadrons})$ to a contour integral of the vector current correlation function. The freedom to choose the integration kernel can be used to extract a precise value for the charm quark mass. The most recent analysis was published in Bodenstein, Bordes, Dominguez, Penarrocha, and Schilcher (2011).

Lattice QCD (LQCD)

Each quark mass in the lattice QCD Lagrangian must be tuned at each value of the lattice spacing by calibrating to the experimentally-measured value of a 'gold-plated' hadron mass. For m_c and m_b the best choices are ground-state heavy quarkonium or heavy-strange mesons, because they allow very precise tuning. Direct conversion to the $\overline{\rm MS}$ scheme using $m_c(\mu) = Z m_{c,\rm latt}$ is possible using lattice or continuum QCD perturbation theory, but this introduces a significant source of error. The most recent determination of $m_c(m_c)$ using this approach (Blossier et al., 2010) gives a value of 1.28(4) GeV. Since the stated uncertainty includes only the impact of working with only u and d quarks in the sea, it is omitted from Table 17.1.5.

For the b quark, it is also possible to use non-relativistic or even static quark methods to determine the binding energy of a heavy-light meson, and thereby m_b. These calculations are currently underway with gluon configurations that include the full effect of sea quarks.

The most precise results from full lattice QCD instead use time-moments of charmonium or bottomonium current-current correlators, extrapolated to the continuum limit and compared to the high-order continuum QCD perturbation theory developed for LESR (Allison et al., 2008; McNeile, Davies, Follana, Hornbostel, and Lepage, 2010). The pseudoscalar current in a highly improved relativistic quark formalism with an exact Partially Conserved

Axial Current (PCAC) relation produces the smallest errors, although reaching bottomonium also requires an extrapolation in the heavy quark mass to the b on current lattices. This method also allows for a completely non-perturbative determination of the ratio of $m_b(\mu)/m_c(\mu) = 4.51(4)$, which can be used to test other determinations.

In Tables 17.1.5 and 17.1.6 the results for m_c and m_b mentioned in the text are listed in chronological order. One observes that the method based on NRSR is not (yet) competitive which is probably due to missing third-order corrections. They are available for the other analyses. For both m_b and m_c the results from LESR and LQCD are very precise and in excellent agreement. They use similar perturbative analyses, but very different input data, with different sources of systematic errors. The recent LESR result (Dehnadi, Hoang, Mateu, and Zebarjad, 2011) gives an error on m_c, which is two to four times larger than for other analyses. This has sparked a debate on the theoretical uncertainties of LESR, and in particular on the use of renormalization scales as low as 1 GeV in their estimation, and on the uncertainty of the perturbative QCD prediction for $R(s) = \sigma(e^+e^- \to hadrons, s)/\sigma(e^+e^- \to \mu^+\mu^-, s)$ above 5 GeV. Tables 17.1.5 and 17.1.6 also include the results from Narison (2012), where m_c and m_b have been extracted together with the gluon condensates. In contrast to other determinations based on LESRs and LQCD, a significant influence of the gluon condensate on the quark masses is observed which is quite surprising. Furthermore, the energy region between 3.73 GeV and 4.6 GeV has been parameterized using ψ resonances in the narrow-width approximation, instead of precise experimental data. This might explain the 1.5σ difference in the central value of $m_c(m_c)$ compared to, for example, the LQCD result. An analogous treatment for bottom quarks seems to have a smaller effect.

We conclude that m_b and m_c can be reliably and precisely extracted using a variety of methods. The results in Tables 17.1.5 and 17.1.6 have correlated errors, so we do not average them. They are well encompassed, however, by $m_c(3\ \text{GeV}) = 0.99(1)\,\text{GeV}$ and $m_b(m_b) = 4.16(2)\,\text{GeV}$.

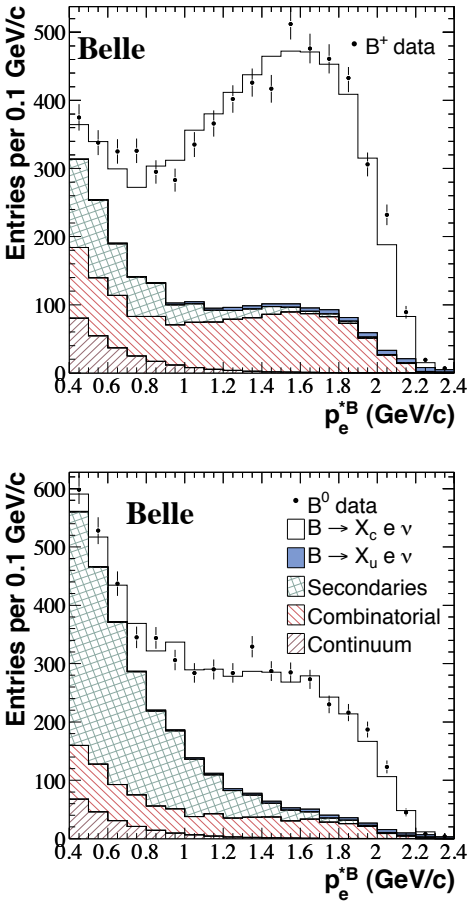

Figure 17.1.9. Belle analysis of the electron momentum spectrum for B^+ and B^0 decays (Urquijo, 2007) before background subtraction, overlaid with the sum of various background contributions and the signal.

17.1.3.3 Moment Measurements

Moments of inclusive observables in $B \to X_c\ell\nu$ decays have been measured by the Belle (Schwanda, 2007; Urquijo, 2007) and *BABAR* (Aubert, 2004c,n,r, 2010c) collaborations.

The Belle collaboration has measured spectra of the lepton energy E_ℓ and the hadronic mass m_X in $B \to X_c\ell\nu$ using 152 million $\Upsilon(4S) \to B\overline{B}$ events (Schwanda, 2007; Urquijo, 2007). These analyses proceed as follows: first, the decay of one B meson in the event is fully reconstructed in a hadronic mode (B_{tag}). Next, the semileptonic decay of the second B meson in the event (B_{sig}) is identified by searching for a charged lepton among the remaining particles in the event. In Urquijo (2007), the electron momentum spectrum p_e^* in the B meson rest frame is measured down to 0.4 GeV (Figure 17.1.9). In Schwanda (2007), all remaining particles in the event, excluding the charged lepton (electron or muon), are combined to reconstruct the hadronic X system. The m_X spectrum is measured for different lepton energy thresholds in the B meson rest frame (Figure 17.1.10).

The observed spectra are distorted by resolution and acceptance effects and cannot be used directly to obtain the moments. In the Belle analyses, acceptance and finite resolution effects are corrected by unfolding the observed spectra using the Singular Value Decomposition (SVD) algorithm (Höcker and Kartvelishvili, 1996). Belle measures the energy moments $\langle E_\ell^k \rangle$ for $k = 0, 1, 2, 3, 4$ and minimum lepton energies ranging from 0.4 to 2.0 GeV. Moments of the hadronic mass $\langle m_X^k \rangle$ are measured for $k = 2, 4$ and minimum lepton energies from 0.7 to 1.9 GeV.

To determine $|V_{cb}|$, Belle performs fits to 14 lepton energy moments, 7 hadronic mass moments and 4 moments of the photon energy spectrum in $B \to X_s\gamma$ (Schwanda, 2008) based on OPE expressions derived in the kinetic (Benson, Bigi, Mannel, and Uraltsev, 2003; Benson, Bigi, and Uraltsev, 2005; Gambino and Uraltsev, 2004) and

Table 17.1.5. Recent results for the charm-quark mass. An asterisk indicates that we have obtained this number from the value of m_c quoted as the main result of the paper using four-loop accuracy (together with $\alpha_S(m_Z) = 0.1184$ (Nakamura et al., 2010)).

$m_c(3\ \text{GeV})$ (GeV)	$m_c(m_c)$ (GeV)	Method	Reference
0.986 ± 0.013	$1.275 \pm 0.013^*$	LESR	Kühn, Steinhauser, and Sturm (2007)
$0.96 \pm 0.04^*$	1.25 ± 0.04	NRSR	Signer (2009)
0.986 ± 0.006	$1.275 \pm 0.006^*$	LQCD	McNeile, Davies, Follana, Hornbostel, and Lepage (2010)
0.998 ± 0.029	1.277 ± 0.026	LESR	Dehnadi, Hoang, Mateu, and Zebarjad (2011)
0.987 ± 0.009	1.278 ± 0.009	FESR	Bodenstein, Bordes, Dominguez, Penarrocha, and Schilcher (2011)
$0.972 \pm 0.006^*$	1.262 ± 0.006	FESR	Narison (2012)

Table 17.1.6. Recent results for the bottom-quark mass.

$m_b(m_b)$ (GeV)	Method	Reference
4.19 ± 0.06	NRSR	Pineda and Signer (2006)
4.163 ± 0.016	LESR	Chetyrkin et al. (2009)
4.164 ± 0.023	LQCD	McNeile, Davies, Follana, Hornbostel, and Lepage (2010)
4.167 ± 0.013	LESR	Narison (2012)

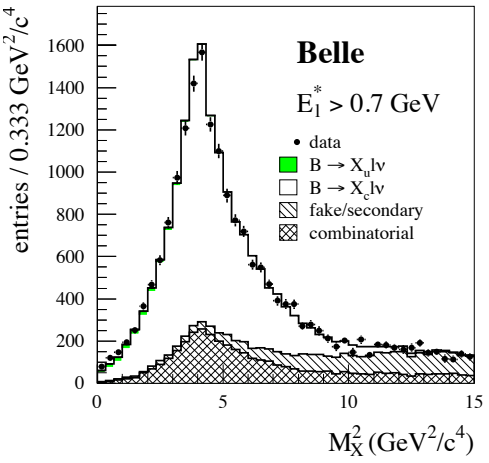

Figure 17.1.10. Belle analysis of the hadronic mass distribution for $B \to X_c\ell\nu$ decays (Schwanda, 2007). The data after continuum subtraction are compared with the sum of simulated $X_c\ell\nu$ signal and background contributions.

Table 17.1.7. Results of the OPE fits in the kinetic and 1S schemes to moments measured by Belle (Schwanda, 2008): $|V_{cb}|$ and the inclusive branching fractions for $B \to X_c\ell\nu$ decays, plus χ^2 per degree of freedom.

	Kinetic scheme	1S scheme
$\lvert V_{cb}\rvert$ (10^{-3})	41.58 ± 0.90	41.56 ± 0.68
$\mathcal{B}_{X_c\ell\nu}$ (%)	10.49 ± 0.23	10.60 ± 0.28
χ^2/ndf.	4.7/18	7.3/18

1S schemes (Bauer, Ligeti, Luke, Manohar, and Trott, 2004). Both theoretical frameworks are considered independently and yield very consistent results (see Table 17.1.7).

BABAR has measured the hadronic mass spectrum m_X in $B \to X_c\ell\nu$ using a data sample of 232 million $\Upsilon(4S) \to B\overline{B}$ events (Aubert, 2010c). The experimental method is similar to the Belle analysis discussed previously, *i.e.*, one B meson is fully reconstructed in a hadronic mode and a charged lepton with momentum above 0.8 GeV in the B meson frame identifies the semileptonic decays of the second B. The remaining particles in the event are combined to reconstruct the hadronic system X. The resolution in m_X is improved by a kinematic fit to the whole event, taking into account 4-momentum conservation and constraining the missing mass to zero.

To derive the true moments from the reconstructed ones, *BABAR* applies a set of linear corrections. These corrections depend on the charged particle multiplicity of the X system, the normalized missing mass, $E_{\text{miss}} - p_{\text{miss}}$, and the lepton momentum. In this way, *BABAR* measures the moments of the hadronic mass spectrum up to $\langle m_X^6 \rangle$ for minimum lepton energies ranging from 0.8 to 1.9 GeV.

This study also updates the previous *BABAR* measurement of the lepton energy moments in $B \to X_c\ell\nu$ (Aubert, 2004n) using new branching fraction measurements for background decays and improving the evaluation of systematic uncertainties. Furthermore, first measurements of combined hadronic mass and energy moments of the form $\langle n_X^k \rangle$ with $k = 2, 4, 6$ are presented. They are defined as $n_X^2 = m_X^2 - 2\widetilde{\Lambda}E_X + \widetilde{\Lambda}^2$, where m_X and E_X are the mass and the energy of the X system and the constant $\widetilde{\Lambda}$ is taken to be 0.65 GeV.

BABAR performs a simultaneous fit to 12 hadronic mass moments (or 12 combined mass-energy moments), 13 lepton energy moments (including partial branching fractions as zero order moments), and 3 photon energy moments in $B \to X_s\gamma$ (Aubert, 2005x, 2006t), and based on OPE calculations in the kinetic scheme (Benson, Bigi, Mannel, and Uraltsev, 2003; Benson, Bigi, and Uraltsev, 2005; Gambino and Uraltsev, 2004) extracts $|V_{cb}|$, the total branching

Table 17.1.8. Results of the OPE fits in the kinetic scheme to moments measured by *BABAR* (Aubert, 2010c). $|V_{cb}|$ and the inclusive branching fractions for $B \to X_c \ell\nu$ decays, plus χ^2 per degree of freedom. The first uncertainty is experimental, the second theoretical.

	Hadronic moment	Mass-energy moment
$\lvert V_{cb}\rvert$ (10^{-3})	$42.05 \pm 0.45 \pm 0.70$	$41.91 \pm 0.48 \pm 0.70$
m_b (GeV)	$4.549 \pm 0.031 \pm 0.038$	$4.556 \pm 0.034 \pm 0.041$
$\mathcal{B}_{X_c\ell\nu}$ (%)	$10.64 \pm 0.17 \pm 0.06$	$10.64 \pm 0.17 \pm 0.06$
χ^2/ndf.	10.9/28	8.2/28

fractions, m_b and m_c, and OPE parameters. The results are given in Table 17.1.8.

17.1.3.4 Global Fit and Determination of $|V_{cb}|$

We perform a global analysis of the B Factory measurements using the full $\mathcal{O}(\alpha_s^2)$ calculations of the moments in the kinetic scheme (Gambino, 2011). This fit combines the 54 moment measurements shown in Table 17.1.9 and determines $|V_{cb}|$, the b-quark mass m_b and the higher order parameters in the OPE description of semileptonic decays. The only external input is the average B^0 and B^+ lifetime, assumed to be (1.582 ± 0.007) ps (Beringer et al., 2012).

From the fits to moments in $B \to X_c\ell\nu$ we obtain a linear combination of the b- and c-quark masses. To enhance the precision on m_b, we make two choices to gain additional constraints: we either include photon energy moments from $B \to X_s\gamma$ decays in the fit, or use as a precise constraint on the c-quark mass $m_c(3\ \text{GeV}) = 0.998 \pm 0.029$ GeV, as derived with low-energy sum rules (Dehnadi, Hoang, Mateu, and Zebarjad, 2011). The results for the kinetic scheme based on the Belle and *BABAR* moments are shown in Table 17.1.10 and Figure 17.1.11.

The same moments are fit with expressions derived in the 1S scheme (Bauer, Ligeti, Luke, Manohar, and Trott, 2004). In this framework, we cannot introduce a c-quark mass constraint. Results are thus presented for the entire set of 54 moment measurements and for the $X_c\ell\nu$ moments only (Table 17.1.11).

The fit results shown in the first rows of Tables 17.1.10 and 17.1.11 are based on the same set of measurements and can thus be compared directly. For $|V_{cb}|$, the result obtained in the kinetic scheme, $(42.09 \pm 0.75) \times 10^{-3}$, agrees very well with the 1S result, $(42.01 \pm 0.49) \times 10^{-3}$. The uncertainty on $|V_{cb}|$ in the kinetic scheme is 1.8% compared to 1.2% is the 1S scheme. Note however that the assumptions on the dominant theory error are significantly different in the two frameworks. The results for the b-quark mass cannot be compared directly due to different mass definitions.

We adopt the results of the fit in the kinetic scheme with the constraint on the c-quark mass as currently the most precise result, based on inclusive $B \to X_c\ell\nu$ decays,

$$|V_{cb}|_{\text{incl}} = (42.01 \pm 0.47_{\text{exp}} \pm 0.59_{\text{th}}) \times 10^{-3}. \quad (17.1.43)$$

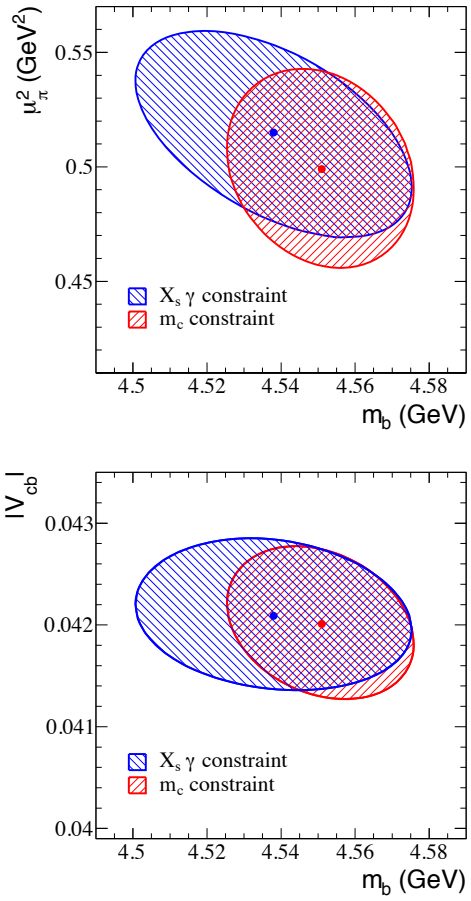

Figure 17.1.11. $\Delta\chi^2 = 1$ contours for the global fit to Belle and *BABAR* moments in the kinetic mass scheme, for details see the text.

17.1.4 Exclusive decays $B \to \pi\ell\nu$

17.1.4.1 Theoretical Overview

The decay rate for $B \to \pi\ell\nu$ semileptonic decay is given by:

$$\frac{d\Gamma}{dq^2} = \frac{G_F^2 |V_{ub}|^2}{24\pi^3} \frac{(q^2 - m_\ell^2)^2\, \mathbf{p}_\pi}{q^4 m_B^2} \times \left\{ \left(1 + \frac{m_\ell^2}{2q^2}\right) m_B^2\, \mathbf{p}_\pi^2 \left[f_+^{B\pi}(q^2)\right]^2 + \frac{3m_\ell^2}{8q^2}(m_B^2 - m_\pi^2)^2 \left[f_0^{B\pi}(q^2)\right]^2 \right\}, \quad (17.1.44)$$

where $q \equiv p_B - p_\pi$ is the 4-momentum transferred to the lepton-neutrino pair and

$$\mathbf{p}_\pi = \left[(m_B^2 + m_\pi^2 - q^2)^2 - 4m_B^2 m_\pi^2\right]^{1/2} / (2m_B)$$

is the pion 3-momentum in the B rest frame. The form factors $f_+^{B\pi}(q^2)$ and $f_0^{B\pi}(q^2)$ are defined in Eq. (17.1.6).

Table 17.1.9. Experimental inputs used in the global analysis of $B \to X_c \ell\nu$. n is the order of the moment, c is the threshold value in GeV. In total, there are 29 measurements from *BABAR* and 25 from Belle.

Experiment	Hadron moments $\langle m_X^n \rangle$	Lepton moments $\langle E_\ell^n \rangle$	Photon moment $\langle E_\gamma^n \rangle$
BABAR	$n = 2$, $c = 0.9, 1.1, 1.3, 1.5$ $n = 4$, $c = 0.8, 1.0, 1.2, 1.4$ $n = 6$, $c = 0.9, 1.3$ (Aubert, 2010c)	$n = 0$, $c = 0.6, 1.2, 1.5$ $n = 1$, $c = 0.6, 0.8, 1.0, 1.2, 1.5$ $n = 2$, $c = 0.6, 1.0, 1.5$ $n = 3$, $c = 0.8, 1.2$ (Aubert, 2004n, 2010c)	$n = 1$, $c = 1.9, 2.0$ $n = 2$, $c = 1.9$ (Aubert, 2005x, 2006t)
Belle	$n = 2$, $c = 0.7, 1.1, 1.3, 1.5$ $n = 4$, $c = 0.7, 0.9, 1.3$ (Schwanda, 2007)	$n = 0$, $c = 0.6, 1.0, 1.4$ $n = 1$, $c = 0.6, 0.8, 1.0, 1.2, 1.4$ $n = 2$, $c = 0.6, 1.0, 1.4$ $n = 3$, $c = 0.8, 1.0, 1.2$ (Urquijo, 2007)	$n = 1$, $c = 1.8, 1.9$ $n = 2$, $c = 1.8, 2.0$ (Limosani, 2009)

Table 17.1.10. Results of the OPE global fit to $B \to X_c \ell\nu$ moments in the kinetic scheme: the first row refers to the fit including $B \to X_s\gamma$ moments, the second row gives the results obtained with the charm-quark mass constraint. In all cases, the first error is the uncertainty of the global fit. For $|V_{cb}|$ the second error is an additional theoretical uncertainty arising from the calculation of $|V_{cb}|$. The χ^2/ndf. is $17.1/(54-7)$ for the $B \to X_s\gamma$ and $23.3/(44-7)$ for the m_c constrained fit.

Constraint	$\lvert V_{cb}\rvert$ (10^{-3})	$m_b^{\rm kin}$ (GeV)	μ_π^2 (GeV^2)	ρ_D^3 (GeV^3)	μ_G^2 (GeV^2)	ρ_{LS}^3 (GeV^3)
$B \to X_s\gamma$	$42.09 \pm 0.46 \pm 0.59$	4.538 ± 0.038	0.515 ± 0.045	0.209 ± 0.021	0.263 ± 0.047	-0.121 ± 0.090
$m_c(3\ \text{GeV})$	$42.01 \pm 0.47 \pm 0.59$	4.551 ± 0.025	0.499 ± 0.044	0.177 ± 0.021	0.227 ± 0.048	-0.081 ± 0.092

Table 17.1.11. Results of the OPE global fit to $B \to X_c \ell\nu$ moments in the 1S scheme: the first row refers to the fit including $B \to X_s\gamma$ moments, the second row gives the results obtained with $B \to X_c \ell\nu$ moments only.

Input	$\lvert V_{cb}\rvert$ (10^{-3})	m_b^{1S} (GeV)	λ_1 (GeV^2)	ρ_1 (GeV^3)	τ_1 (GeV^3)	τ_2 (GeV^3)	τ_3 (GeV^3)
all moments	42.01 ± 0.49	4.696 ± 0.043	-0.354 ± 0.072	0.057 ± 0.060	0.154 ± 0.122	-0.039 ± 0.078	0.194 ± 0.105
$X_c \ell\nu$ only	42.58 ± 0.78	4.595 ± 0.110	-0.428 ± 0.099	0.080 ± 0.062	0.150 ± 0.124	-0.023 ± 0.086	0.204 ± 0.112

In the limit of zero momentum-transfer the form factors must satisfy the kinematic constraint $f_+^{B\pi}(0) = f_0^{B\pi}(0)$. Furthermore, in the limit $m_\ell \to 0$, which is a good approximation for $\ell = e, \mu$, the scalar form factor $f_0^{B\pi}(q^2)$ becomes negligible:

$$\frac{d\Gamma}{dq^2} = \frac{G_F^2 |V_{ub}|^2}{24\pi^3} \mathbf{p}_\pi^3 |f_+^{B\pi}(q^2)|^2. \tag{17.1.45}$$

Hence precise experimental measurements of the $B \to \pi\ell\nu$ branching fraction along with reliable theoretical calculations of the form factor $f_+^{B\pi}(q^2)$ enable a clean determination of the CKM matrix element $|V_{ub}|$.[53]

The form factors encode the non-perturbative dynamics of binding quarks into hadrons and therefore they cannot be calculated perturbatively. In practice, two methods are available for computing QCD form factors with controlled uncertainties: lattice QCD and light-cone sum rules. As discussed in Section 17.1.2, LQCD is a first-principles approach providing results with steadily improvable errors. LCSR is derived from the correlator of quark currents calculated in terms of the OPE. Matching the result of this calculation to the hadronic dispersion relation yields an analytical expression for the form factor. The precision of LCSR is limited by the accuracy of OPE and by the quark-hadron duality approximation used in the dispersion relation. Lattice QCD and light-cone sum rule form-factor calculations are complementary in that they work in different kinematical regions: LQCD is best at high q^2 while LCSR are applicable at low q^2-values.

Heavy-to-light form-factor parameterizations

It is useful for comparing different theoretical calculations or theory with experiment to parameterize the form factor $f_+^{B\pi}(q^2)$ as a function of q^2. Many parameterizations are available in the literature, but here we focus on the model-independent parameterization of Boyd, Grinstein, and Lebed (1995), hereafter "BGL", and its variants, which is based on the general properties of analyticity, unitarity and crossing-symmetry. All form factors are analytic functions of q^2, except at physical poles and threshold branch points. Hence, given an appropriate

[53] In principle, the exclusive semileptonic decay channel $B \to \rho\ell\nu$ can also be used to determine $|V_{ub}|$ (see, *e.g.*, Flynn, Nakagawa, Nieves, and Toki, 2009). In practice, however, systematic uncertainties are not under control in current lattice QCD calculations of the ρ meson because the ρ is unstable and is not described within the framework of chiral perturbation theory; these concerns will be addressed in future LQCD calculations when more computing resources are available. Light-cone sum rule determinations of the $B \to \rho\ell\nu$ form factor are available, such as in Ball and Zwicky (2005b), but there has not been any recent work on this channel.

change of variables, they can be expressed in a particularly useful manner as a convergent power series (see, *e.g.*, Arnesen, Grinstein, Rothstein, and Stewart, 2005; Bourrely, Machet, and de Rafael, 1981; Boyd and Savage, 1997; Lellouch, 1996).

Consider the following change of variables:

$$z(q^2,t_0)=\frac{\sqrt{1-q^2/t_+}-\sqrt{1-t_0/t_+}}{\sqrt{1-q^2/t_+}+\sqrt{1-t_0/t_+}}, \qquad (17.1.46)$$

where $t_+\equiv(m_B+m_\pi)^2$, and $t_0<t_+$ is an arbitrary parameter to be discussed later. This transformation maps the semileptonic region of q^2 onto a unit circle in the complex z plane. In terms of the new variable z, the $B\to\pi$ form factor takes a simple form:

$$P_+(q^2)\phi_+(q^2,t_0)f_+(q^2)=\sum_{k=0}^{\infty}a_k(t_0)z(q^2,t_0)^k. \quad (17.1.47)$$

(A similar function can be derived for the scalar form factor $f_0(q^2)$.) The function $P_+(q^2)$ must be chosen to vanish at the B^* pole in order to preserve the correct analytic structure of $f_+(q^2)$:

$$P_+^{B\pi}(q^2)=z(q^2,m_B^*)\,, \qquad (17.1.48)$$

while the function $\phi_+(q^2,t_0)$ can be any analytic function. It is helpful, however, to choose $\phi_+(q^2,t_0)$ so that the unitarity constraint on the series coefficients (a_k's) obeys a simple form. The choice for $\phi_+(q^2,t_0)$ corresponding to the BGL parameterization is given in Arnesen, Grinstein, Rothstein, and Stewart (2005):

$$\begin{aligned}\phi_+(q^2,t_0)=&\sqrt{\frac{3}{96\pi\chi_J^{(0)}}}\left(\sqrt{t_+-q^2}+\sqrt{t_+-t_0}\right)\\&\times\left(\sqrt{t_+-q^2}+\sqrt{t_+-t_-}\right)^{3/2}\\&\times\left(\sqrt{t_+-q^2}+\sqrt{t_+}\right)^{-5}\frac{(t_+-q^2)}{(t_+-t_0)^{1/4}},\end{aligned} \qquad (17.1.49)$$

where the numerical factor $\chi_J^{(0)}$ can be calculated using perturbation theory and the OPE.

Unitarity constrains the size of the BGL series coefficients:

$$\sum_{k=0}^{N}a_k^2\lesssim 1, \qquad (17.1.50)$$

where this holds for any value of N. In the case of the $B\to\pi$ form factor, Becher and Hill (2006) use the heavy-quark power-counting to argue that the sizes of the series coefficients should in fact be much less than one:

$$\sum_{k=0}^{N}a_k^2\le\left(\frac{\Lambda}{m_Q}\right)^3\ll 1, \qquad (17.1.51)$$

where Λ is a typical hadronic scale; this is consistent with lattice calculations by Bailey et al. (2009) and experimental measurements by *BABAR* in del Amo Sanchez (2011n) and Belle in Ha (2011). The free parameter t_0 appearing in Eq. (17.1.46) determines the range of $|z|$ in the semileptonic region, and hence can be chosen to accelerate the series convergence. For example, Arnesen, Grinstein, Rothstein, and Stewart (2005) use the value $t_0=0.65t_-$ such that $-0.34<z<0.22$ for $B\to\pi l\nu$ decay. The small magnitude of $|z|$, in conjunction with the tight heavy-quark bound on the size of the series coefficients, ensures that only the first few terms in the series are needed to describe the $B\to\pi$ form factor to sub-percent accuracy.

Bourrely, Caprini, and Lellouch (2009) (BCL) use the same series expansion of Eq. (17.1.47), but without an outer function ϕ_+ and with a different Blashke factor P_+:

$$f_+(q^2)=\frac{1}{1-q^2/m_{B^*}^2}\sum_{k=0}^{K}b_k(t_0)z(q^2,t_0)^k. \qquad (17.1.52)$$

Their choice avoids unphysical singularities which are generated at $q^2=t_+$ by the outer function in a truncated BGL parameterization. Further, Bourrely, Caprini, and Lellouch (2009) optimize the parameter t_0 such that the semileptonic domain is mapped onto a symmetric interval in z. With the choice $t_0=(m_B+m_\pi)(\sqrt{m_B}-\sqrt{m_\pi})^2$, the value of $|z|<0.279$. Although the BCL parameterization has a simpler functional form, the constraint on the series is more complicated than Eq. (17.1.50) in that it is no longer diagonal in the series index k. We use the BCL parameterization to obtain $|V_{ub}|$ in Section 17.1.4.3.

A different approach suggested by Flynn and Nieves (2007a,b) uses the Omnès parameterization, allowing one to express the form-factor shape in terms of the elastic B-π scattering phase shift and the value of $f_+(q^2)$ at a few subtraction points below the $B\pi$ production threshold.

Lattice QCD form-factor calculations

State-of-the-art LQCD computations now regularly include the effects of three light dynamical quarks. Often calculations are done in the isospin limit with two lighter degenerate quarks and one heavier quark with a mass close to the physical strange quark; these are referred to as "2+1" flavor simulations.

In practice, limited computational resources prohibit calculations with simulated values of the u- and d-quark as light as those in the real world. LQCD calculations must also be done at fixed, nonzero values of the lattice spacing. Hence one generates data with a sequence of light-quark masses (down to $\sim m_{\rm strange}/10$ for current $B\to\pi$ calculations) and a sequence of lattice spacings (down to $a\sim 0.09$ fm for current $B\to\pi$ calculations) and extrapolates the remainder of the way to the physical masses and zero lattice spacing. Because these limits are interrelated, it is now standard to use model-independent functional forms derived in Chiral Perturbation Theory (χPT) for the specific lattice quark formulation being used (*i.e.* including discretization corrections) to guide the extrapolation (see, *e.g.*, Aubin and Bernard, 2007, for the case of $B\to\pi$). This procedure leaves a remaining systematic uncertainty in the physical matrix element due

to truncation of the chiral expansion that is typically included in error budgets as a "chiral extrapolation error." This, in combination with statistical errors, is currently the largest source of uncertainty in lattice calculations of the $B \to \pi$ form factor. Fortunately, increasing computational resources are allowing this error to be reduced in a straightforward manner.

The next-largest uncertainty in current lattice $B \to \pi$ form-factor calculations is due to perturbative operator matching. Numerical lattice simulations evaluate the hadronic matrix element of the vector current $V_\mu = i\overline{u}\gamma_\mu b$ written in terms of the discretized versions of the heavy-quark (b) and light anti-quark ($\overline{u}$) fields that appear in the lattice actions. Hence one must compute matching factors to relate the continuum vector current to its lattice counterpart. Current $B \to \pi$ form-factor calculations rely on either a combination of perturbative and non-perturbative methods or on one-loop lattice perturbation theory; the residual uncertainties from neglected 2-loop and higher-order terms in the perturbative series can be approximately as large as the chiral-continuum extrapolation error. Hence new methods are being developed and new actions are being used in order to reduce the renormalization error in the future.

Currently there are two realistic "2+1" flavor LQCD calculations of the $B \to \pi$ form factor – one by the HPQCD Collaboration (Dalgic et al., 2006) and one by the Fermilab Lattice and MILC collaborations (Bailey et al., 2009). These calculations were both performed on gauge configurations made publicly available by the MILC Collaboration (see Aubin et al., 2004) and include the effects of three flavors of dynamical staggered light quarks; hence the statistical errors are somewhat correlated among the two results. The two calculations use different heavy-quark formalisms, however, for the b quark. The Fermilab and MILC collaborations use the Fermilab formalism developed by El-Khadra, Kronfeld, and Mackenzie (1997) in which one uses knowledge of the heavy-quark limit of QCD to systematically remove heavy-quark discretization errors order-by-order in $1/m_b$. The HPQCD Collaboration uses the formulation of the NRQCD action from Lepage, Magnea, Nakhleh, Magnea, and Hornbostel (1992), in which the b-quark is a non-relativistic field and the action is expanded in powers of $\boldsymbol{v_b}/c$, where $\boldsymbol{v_b}$ is the spatial velocity of the b quark. Both heavy-quark formulations work well for b quarks at currently available values of the lattice spacing. The Fermilab formalism, however, has two advantages in that it possesses a continuum limit and that it can also be used for c quarks, thereby providing a cross check of the method. Future calculations using other lattice formulations for the light and heavy quarks, such the relativistic heavy-quark action developed by Christ, Li, and Lin (2007) and used by the RBC and UKQCD Collaborations for B-meson leptonic decays and mixing (see Van de Water and Witzel, 2010), will provide valuable independent cross checks of the $B \to \pi$ form factor in the next few years.

The Fermilab Lattice and MILC Collaborations present their form-factor results in terms of the BGL series coefficients and the correlation matrix; these are given in Table 17.1.12. The series coefficients can be used to obtain the form factor over the entire q^2 range, and are therefore a useful way to present the data, as pointed out by Bernard et al. (2009b). This is particularly helpful for state-of-the art extractions of $|V_{ub}|$ that rely on simultaneous BGL fits of the lattice and experimental data including correlations (see del Amo Sanchez, 2011n; Ha, 2011). Alternatively one can present the integrated decay rate over a q^2 range for which the lattice calculation is most reliable, typically from $q^2 = 16\ \mathrm{GeV}^2$ to $q^2_{\mathrm{max}} = (m_B - m_\pi)^2$:

$$\Delta\zeta \equiv \frac{G_F^2}{24\pi^3} \int_{q_\mathrm{i}^2}^{q_\mathrm{f}^2} dq^2 \mathbf{p}_\pi^3 |f_+^{B\pi}(q^2)|^2 \,. \qquad (17.1.53)$$

The quantity $\Delta\zeta$ is given for both the Fermilab/MILC and HPQCD calculations in Table 17.1.13.

The 2006 HPQCD $B \to \pi$ form-factor calculation relies on the parameterization of Ball and Zwicky (2005a) (BZ) during an intermediate step to interpolate their data to fiducial values of the pion energy before performing the chiral extrapolation. Use of models such as the one in Becirevic and Kaidalov (2000), hereafter "BK"; or the BZ parameterization can lead to an underestimation in the quoted form-factor errors, particularly at low values of q^2 where the lattice data are poor or nonexistent and the shape is constrained primarily by the model function. Moreover, any comparisons between different theoretical or experimental determinations of the BK or BZ fit parameters are not necessarily meaningful, since any observed discrepancies could simply be due to limitations of the model. Hence only lattice QCD form factor determinations based on BGL-like series (such as also the BCL parameterization) should be considered model-independent.

Table 17.1.12. Coefficients a_k and correlation matrix ρ_{kl} of a 3-parameter BGL series expansion of $f_+^{B\pi}$ from Bernard et al. (2009b). Statistical and systematic errors are added in quadrature.

Fit:	0.0216(27)	−0.0378(191)	−0.113(27)
ρ	a_0	a_1	a_2
a_0	1.000	0.640	0.475
a_1	0.640	1.000	0.964
a_2	0.474	0.964	1.000

Light-cone sum rule form-factor calculations

The method of QCD light-cone sum rules allows one to calculate the $B \to \pi$ form factors at small and intermediate q^2 (see, *e.g.*, Bagan, Ball, and Braun, 1998; Ball and Zwicky, 2005c; Belyaev, Khodjamirian, and Ruckl, 1993; Duplancic, Khodjamirian, Mannel, Melic, and Offen, 2008; Khodjamirian, Ruckl, Weinzierl, and Yakovlev, 1997). The key element of the calculational procedure is

Table 17.1.13. Results for the integrated decay rate $\Delta\zeta = \Delta\Gamma^{B\to\pi l\nu}/|V_{ub}|^2$ from lattice QCD and light-cone sum rules. Statistical and systematic errors are added in quadrature.

	q^2 (GeV^2)	$\Delta\zeta$ (ps^{-1})
HPQCD (Dalgic et al., 2006)	> 16	2.02 ± 0.55
Fermilab/MILC (Bailey et al., 2009)	> 16	$2.21^{+0.47}_{-0.42}$
LCSR (Khodjamirian, Mannel, Offen, and Wang, 2011)	< 12	$4.59^{+1.00}_{-0.85}$

the correlator of the two heavy-light quark currents:

$$i\int d^4x e^{iqx}\langle\pi^+(p)|\, T\{\overline{u}\gamma_\mu b(x), m_b\bar{b}i\gamma_5 d(0)\}\,|0\rangle \equiv F((p+q)^2,q^2)p_\mu + \widetilde{F}((p+q)^2,q^2)q_\mu\,, \tag{17.1.54}$$

$$F((p+q)^2,q^2) = \frac{2m_B^2 f_B f_+^{B\pi}(q^2)}{m_B^2-(p+q)^2} + \ldots\,, \tag{17.1.55}$$

where Eq. (17.1.55) represents the hadronic dispersion relation for the amplitude F, with the ground-state B-meson contribution containing the vector $B\to\pi$ form factor multiplied by the B decay constant. The remaining hadronic sum in Eq. (17.1.55) is indicated by ellipses. The amplitude $\widetilde{F}$ is used to calculate the scalar form factor $f_0^{B\pi}(q^2)$. At $(p+q)^2 \ll m_b^2$ and $q^2 \ll m_b^2$, the T-product in Eq. (17.1.54) is expanded near the light-cone $x^2\sim 0$, yielding process-independent nonlocal vacuum-pion matrix elements, such as $\langle\pi(p)|\overline{u}_\alpha(x)d_\beta(0)|0\rangle$. The light-cone OPE yields

$$F((p+q)^2,q^2) = \sum_{t=2,3,4,\ldots}\int Du_i \sum_{k=0,1,\ldots}\left(\frac{\alpha_S}{\pi}\right)^k T_k^{(t)}((p+q)^2,q^2,u_i,m_b,\mu)\varphi_\pi^{(t)}(u_i,\mu)\,, \tag{17.1.56}$$

a convolution (at the factorization scale μ) of calculable short-distance coefficient functions $T_k^{(t)}$ and universal pion light-cone distribution amplitudes (DA's) $\varphi_\pi^{(t)}(u_i,\mu)$ of growing twist $t\geq 2$. The integration goes over the momentum fractions $u_i = u_1, u_2, \ldots$ of quarks and gluons in the pion. The terms in Eq. (17.1.56) corresponding to higher-twist pion DA's are suppressed by inverse powers of the b-quark virtuality $((p+q)^2-m_b^2)\sim \overline{\Lambda} m_b$, where $\overline{\Lambda}\gg \Lambda_{\rm QCD}$ does not scale with m_b. Currently Eq. (17.1.54) includes all LO contributions of the twist 2, 3, 4 quark-antiquark and quark-antiquark-gluon DA's of the pion and the NLO, $O(\alpha_S)$ corrections to the twist-2 and twist-3 two-particle coefficient functions.

Furthermore, one uses quark-hadron duality and approximates the sum over excited B-states in the hadronic dispersion relation by the quark-gluon spectral density $\mathrm{Im}\, F^{(\rm OPE)}(s,q^2)$ calculated from the OPE, Eq. (17.1.56), introducing the effective threshold parameter s_0^B. The final step involves a Borel transformation $(p+q)^2\to m^2\sim \overline{\Lambda} m_b$. The resulting LCSR for the $B\to\pi$ form factor has the following form

$$f_+^{B\pi}(q^2) = \left(\frac{e^{m_B^2/m^2}}{2m_B^2 f_B}\right)\frac{1}{\pi}\int_{m_b^2}^{s_0^B} ds\,\mathrm{Im}\, F^{(\rm OPE)}(s,q^2)\, e^{-s/m^2}. \tag{17.1.57}$$

The uncertainty introduced by the quark-hadron duality approximation is minimized by calculating the B meson mass from the derivative of the same LCSR, thereby fixing s_0^B. Details of the method can be found in Duplancic, Khodjamirian, Mannel, Melic, and Offen (2008); an introductory review is in Colangelo and Khodjamirian (2000). The LCSR method and input was also successfully tested for $D\to\pi, K$ form factors by Khodjamirian, Klein, Mannel, and Offen (2009). The input includes α_S and the b quark mass (in the $\overline{\rm MS}$ scheme), as well as the nonperturbative parameters of the pion DA's, *e.g.*, f_π and the shape parameters (Gegenbauer moments) for the twist-2 pion DA $\varphi_\pi^{(2)}$. For the decay constant f_B the QCD sum rule for the two-point correlator of $\bar{b}i\gamma_5 q$ currents is employed. More details on the numerical results and their uncertainties can be found in the most recent LCSR analysis by Khodjamirian, Mannel, Offen, and Wang (2011), predicting $f_+^{B\pi}(q^2)$ at $0\leq q^2 < 12\,\mathrm{GeV}^2$, in particular, $f_+^{B\pi}(0) = 0.28\pm 0.03$. Extrapolation to larger q^2 reveals a reasonable agreement with the lattice QCD results (see Figure 17.1.12). The most convenient quantity for the $|V_{ub}|$ determination is the integrated decay rate $\Delta\zeta$ defined in Eq. (17.1.53); the most recent LCSR result from Khodjamirian, Mannel, Offen, and Wang (2011) is given in Table 17.1.13. The estimated error corresponds to the quadratic sum of the uncertainties due to variations of the input parameters in LCSR. The largest individual errors originate from the uncertainties of the $\overline{\rm MS}$ quark masses ($m_{u,d}$ and m_b) and of the shape parameters in the pion twist-2 DA, as well as from the renormalization scale uncertainty. There is still room for improvement of the OPE in the future, *e.g.*, if one calculates the $O(\alpha_S^2)$ and twist-5, 6 corrections and gains a better control over the pion DA's. On the other hand, the systematic error due to the quark-hadron duality approximation cannot be completely eliminated from the LCSR calculation. Hence, with this method it seems not feasible to reach a precision at a few percent level foreseeable with the future improvements of the lattice QCD calculations.

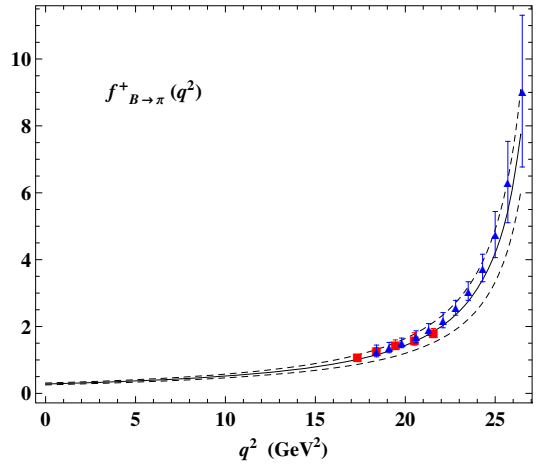

Figure 17.1.12. The vector form factor $f_+^{B\pi}(q^2)$ (in arbitrary units) calculated from LCSR (Khodjamirian, Mannel, Offen, and Wang, 2011) and fitted to the BCL parameterization from Bourrely, Caprini, and Lellouch (2009) (solid line) with uncertainties (dashed lines), compared to the LQCD results by HPQCD (Dalgic et al., 2006) (squares) and by FNAL/MILC (Bailey et al., 2009) (triangles with error bars).

17.1.4.2 Measurements of Branching Fractions and q^2 Distributions

The semileptonic decay $B \to \pi\ell\nu$ has been studied with different experimental approaches at the B Factories. The goal is a precise measurement of the branching fraction and the spectrum of the squared momentum transfer, q^2, to allow for a determination of the q^2 dependence of the $B \to \pi$ form factor. The main experimental challenge is the reduction of the much more abundant background from $B \to X_c\ell\nu$ decays, where X_c is any hadronic final state with a charm quark. It is also difficult to separate $B \to \pi\ell\nu$ decays from the other $B \to X_u\ell\nu$ decays, where X_u is a charmless hadronic final state, due to very similar decay kinematics. The $B \to \pi\ell\nu$ analyses are based on event samples with a tagged B meson or on untagged event samples. In the tagged analyses, one of the two B mesons in the $B\overline{B}$ event is either fully reconstructed in a hadronic decay mode or partially reconstructed in a semileptonic decay mode. While the tagged analyses provide a very clean environment, they are statistically limited for the B Factory data samples. At present, untagged analyses, which were first performed by the CLEO collaboration (Athar et al., 2003), still provide the most precise results for $B \to \pi\ell\nu$.

In untagged analyses, the four-momentum of the undetected neutrino is inferred from the missing energy and momentum in the whole event. The reconstructed neutrino is combined with a charged lepton ($\ell = e, \mu$) and a pion to form a $B \to \pi\ell\nu$ candidate. The dominant background at low q^2 is due to $e^+e^- \to q\overline{q}$ ($q = u, d, s, c$) continuum events, where the charged lepton originates from a semileptonic decay of a produced hadron (mostly from $e^+e^- \to c\bar{c}$ events) or the misidentification of a charged hadron as a lepton. Continuum events produce jet-like event topologies and can thus be efficiently separated from the more isotropic $B\overline{B}$ events with selection criteria on event shape variables (*e.g.* R_2, L_2, $\cos\Delta\theta_{\rm thrust}$, see Chapter 9). The overall largest background comes from $B \to X_c\ell\nu$ decays. It is reduced by selection criteria on variables that are related to the neutrino reconstruction, *e.g.* the missing mass squared in the event or the polar angle of the missing momentum vector, or on kinematic variables, *e.g.* the helicity angle of the lepton. These variables also help to partially suppress the $B \to X_u\ell\nu$ background, which has a large uncertainty and limits the measurement at high q^2.

Three untagged analyses have been performed by the *BABAR* (del Amo Sanchez, 2011d,n) and Belle collaborations (Ha, 2011). The background suppression based on event shape, neutrino reconstruction and kinematical variables is optimized as a function of q^2 to allow for a precise measurement over the full q^2 range. While the Belle (Ha, 2011) and one of the *BABAR* (del Amo Sanchez, 2011d) analyses use one-dimensional selection criteria, the other *BABAR* measurement (del Amo Sanchez, 2011n) makes use of neural-network discriminators, which have been trained individually for each background class and q^2 interval, yielding an improved background suppression. In contrast to the other two analyses that focus on $B^0 \to \pi^-\ell^+\nu$ decays, this analysis includes a simultaneous measurement of $B^0 \to \pi^-\ell^+\nu$, $B^+ \to \pi^0\ell^+\nu$, $B^0 \to \rho^-\ell^+\nu$ and $B^+ \to \rho^0\ell^+\nu$ decays. By measuring these four decay modes, the uncertainties due to cross feed between these modes and various background contributions are reduced. In all three analyses the signal is extracted from a fit to the two-dimensional ΔE-$m_{\rm ES}$ distribution. The fit is performed in several intervals of q^2 to measure the shape of the q^2 spectrum. The Belle analysis uses 13 q^2 intervals (Ha, 2011), the *BABAR* analyses 6 (del Amo Sanchez, 2011n) or 12 (del Amo Sanchez, 2011d) q^2 intervals. The shapes of the signal and background contributions are taken from simulation whereas the yields for the signal and the dominant background contributions are obtained from the fit. Figures 17.1.3 and 17.1.13 show the $m_{\rm ES}$ and ΔE projections from *BABAR* and Belle for a specific q^2 range, indicating the signal above the sum of backgrounds from several sources.

A number of tagged measurements have been performed by *BABAR* (Aubert, 2006r, 2008y) and Belle (Adachi, 2008a; Hokuue, 2007). They have led to a simpler and more precise reconstruction of the neutrino momentum and have low backgrounds and a uniform acceptance in q^2. This is achieved at the expense of much smaller signal samples which limit the statistical precision of the form-factor measurement. The semileptonic-tag measurements from *BABAR* and Belle use $B \to D^{(*)}\ell\nu$ decays to partially reconstruct one of the two B mesons. They have a signal-to-background ratio of ~ 2 and yield ~ 0.5 signal decays per fb^{-1}. The signal is extracted from the distribution of the variable $\cos^2\phi_B$, where ϕ_B is the angle between the direction of either B meson and the plane containing the momentum vectors of the tag-side $D^*\ell$ system

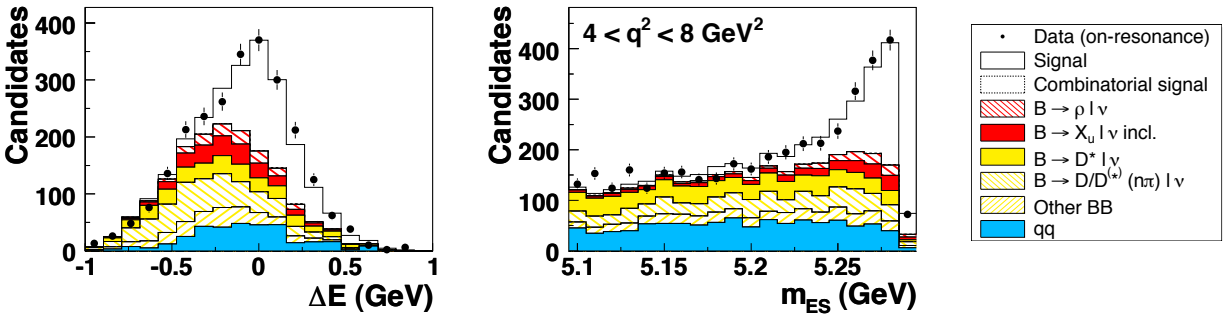

Figure 17.1.13. $m_{\rm ES}$ and ΔE distributions for the q^2 interval $4 < q^2 < 8\,{\rm GeV}^2$ from the *BABAR* untagged $B \to \pi\ell\nu$ measurement (del Amo Sanchez, 2011n).

and the signal-side $\pi\ell$ system (Aubert, 2008y; Hokuue, 2007). The hadronic-tag measurements yield fewer signal events, ~ 0.1 signal decays per fb^{-1}, but reach signal-to-background ratios of up to ~ 10. The signal is extracted from the missing mass squared distribution, where the signal is expected to be located in a narrow peak near zero, as shown in Figure 17.1.14.

Table 17.1.14 summarizes the signal yields, approximate signal-to-background ratios and integrated luminosities of the various measurements.

The leading experimental systematic uncertainties are associated with the reconstruction of charged and neutral particles, which affect the reconstruction of the missing momentum, with backgrounds from continuum events at low q^2 and from $B \to X_u\ell\nu$ decays at high q^2. Due to the feed-down from $B \to \rho\ell\nu$ decays, the uncertainties on the branching fraction and form factors for this decay mode also contribute to the systematic uncertainty. For the tagged measurements, the systematic uncertainties are about a factor of two smaller. They contribute to the knowledge of the total branching fraction, but their statistical precision is not yet sufficient to provide significant information on the shape of the q^2 spectrum.

Table 17.1.15 summarizes all $B \to \pi\ell\nu$ branching fraction measurements. Shown are the total branching fraction as well as the partial branching fractions for $q^2 < 12$ GeV^2 and $q^2 > 16$ GeV^2. Overall the individual measurements are in a good agreement, though for the tagged measurements the partial branching fractions at intermediate q^2 are somewhat smaller. A combination of all untagged $B \to \pi\ell\nu$ measurements from the B Factories results in an average total branching fraction of $(1.44 \pm 0.03 \pm 0.05) \times 10^{-4}$, with a precision of $3-4\%$ (2% statistical and 3% systematic).

Figure 17.1.15 shows a fit of the z-expansion introduced in Section 17.1.4.1 to the measured q^2 spectra from all untagged $B \to \pi\ell\nu$ analyses, using the BCL parameterization with three parameters (b_0, b_1, b_2). The results are summarized in Table 17.1.16. The χ^2 probability of this fit is 1.1%. An inclusion of the tagged measurements would decrease the probability to 0.02%. This low probability is mostly due to the lower branching fractions from the tagged measurements. The *BABAR* measurement in 12 q^2 bins prefers a larger (negative) quadratic term and a smaller linear term in the z expansion compared to the other two untagged analyses. The fitted function also determines the product $f_+(0)|V_{ub}|$, which for a given value of $|V_{ub}|$ can be compared with LCSR predictions of $f_+(0)$, the $B \to \pi$ form factor at $q^2 = 0$. The largest value of $f_+(0)|V_{ub}|$ from the individual measurements comes from the untagged *BABAR* measurement in 6 q^2 bins. For the combination of all untagged measurements, a value of $f_+(0)|V_{ub}| = (0.940 \pm 0.029) \times 10^{-3}$ is obtained. Combining this value with the $|V_{ub}|$ result obtained using the LCSR calculation (see Table 17.1.17) gives $f_+(0) = (0.27 \pm 0.03)$, in good agreement with the LCSR result, $f_+(0) = (0.28 \pm 0.02)$. A comparison of the fitted BCL parameterization with the shapes predicted by form-factor calculations from LQCD, LCSR or quark models like ISGW2. is presented in Figure 17.1.15 (right). It agrees best with the recent LCSR calculation (Khodjamirian, Mannel, Offen, and Wang, 2011) and deviates significantly from the ISGW2 quark model prediction.

17.1.4.3 Determination of $|V_{ub}|$

Two different methods have been used to determine $|V_{ub}|$ from the measured $B \to \pi\ell\nu$ differential decay rates. The more traditional approach relates the measured partial branching fractions, $\Delta\mathcal{B}(q^2_{\rm min}, q^2_{\rm max})$, with the normalized partial decay rate, $\Delta\zeta(q^2_{\rm min}, q^2_{\rm max})$, predicted by form-factor calculations integrated over a certain q^2 range. For LQCD calculations (Bailey et al., 2009; Dalgic et al., 2006), the range $q^2 > 16\,{\rm GeV}^2$ is used, and for the recent LCSR (Khodjamirian, Mannel, Offen, and Wang, 2011) calculation the range is $q^2 < 12\,{\rm GeV}^2$. $|V_{ub}|$ is obtained from the relation

$$|V_{ub}| = \sqrt{\frac{\Delta B(q^2_{\rm min}, q^2_{\rm max})}{\tau_0 \Delta\zeta(q^2_{\rm min}, q^2_{\rm max})}}, \qquad (17.1.58)$$

where $\tau_0 = (1.519 \pm 0.007)$ ps is the B^0 lifetime (Beringer et al., 2012). Table 17.1.17 shows the values of $\Delta B(q^2_{\rm min}, q^2_{\rm max})$, $\Delta\zeta(q^2_{\rm min}, q^2_{\rm max})$ and the $|V_{ub}|$ results for

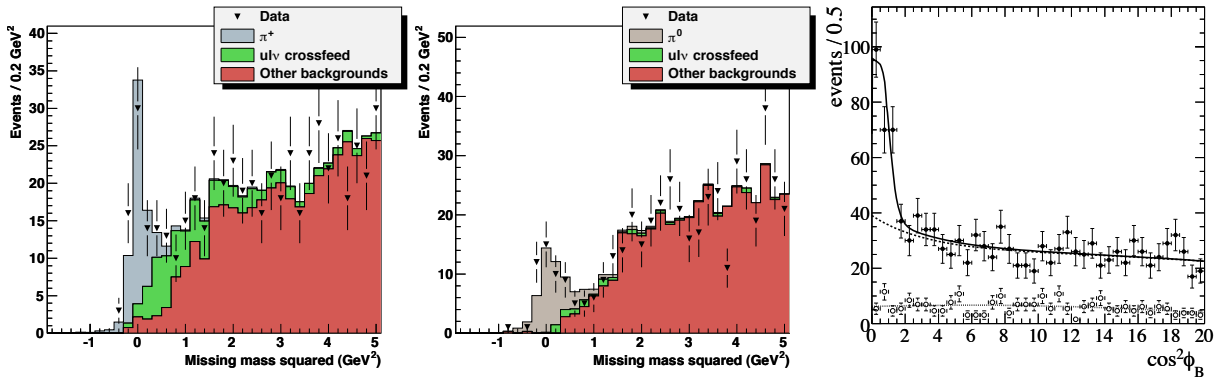

Figure 17.1.14. Missing mass squared distributions from the Belle tagged $B^0 \to \pi^-\ell^+\nu$ (left) and $B^+ \to \pi^0\ell^+\nu$ (center) measurements (Adachi, 2008a) and $\cos^2\phi_B$ distribution from the *BABAR* semileptonic-tag $B^0 \to \pi^-\ell^+\nu$ measurement (Aubert, 2008y) (right). In the right figure, the solid line represents the signal and the dotted and dashed lines represent the backgrounds with combinatorial and with correctly reconstructed D mesons in the semileptonic tag, respectively.

Table 17.1.14. Integrated luminosity, signal yield and approximate signal-to-background ratio, S/B, for the $B \to \pi\ell\nu$ measurements.

Measurement	Int. lumi. (fb^{-1})	$N_{\rm sig}(B^0 \to \pi^-\ell^+\nu)$	$N_{\rm sig}(B^+ \to \pi^0\ell^+\nu)$	S/B
BABAR untagged (6 bins) (del Amo Sanchez, 2011n)	349	7181	3446	~ 0.2
BABAR untagged (12 bins) (del Amo Sanchez, 2011d)	423	11778	–	~ 0.1
Belle untagged (Ha, 2011)	605	21486	–	~ 0.1
BABAR semileptonic tag (Aubert, 2008y)	348	150	134	~ 2
Belle semileptonic tag (Hokuue, 2007)	253	156	69	~ 2
BABAR hadronic tag (Aubert, 2006r)	211	31	26	~ 10
Belle hadronic tag (Adachi, 2008a)	605	59	49	~ 10

Table 17.1.15. Branching fractions for $B^0 \to \pi^-\ell^+\nu$. The two untagged *BABAR* measurements are assumed to be statistically independent since the selected data samples have less than 1% of the events in common (del Amo Sanchez, 2011d).

Measurement	$\mathcal{B}_{\rm tot}$ (10^{-4})	$\Delta\mathcal{B}(q^2 < 12\,{\rm GeV}^2)$ (10^{-4})	$\Delta\mathcal{B}(q^2 > 16\,{\rm GeV}^2)$ (10^{-4})
BABAR untagged (6 bins)	$1.41 \pm 0.05 \pm 0.07$	$0.88 \pm 0.03 \pm 0.05$	$0.32 \pm 0.02 \pm 0.02$
BABAR untagged (12 bins)	$1.42 \pm 0.05 \pm 0.07$	$0.84 \pm 0.03 \pm 0.04$	$0.33 \pm 0.02 \pm 0.03$
Belle untagged	$1.49 \pm 0.04 \pm 0.07$	$0.83 \pm 0.02 \pm 0.04$	$0.40 \pm 0.02 \pm 0.02$
Average untagged	$1.44 \pm 0.03 \pm 0.05$	$0.84 \pm 0.02 \pm 0.03$	$0.36 \pm 0.01 \pm 0.02$
Average tagged	$1.31 \pm 0.08 \pm 0.06$	$0.67 \pm 0.06 \pm 0.03$	$0.37 \pm 0.04 \pm 0.02$
Average	$1.42 \pm 0.03 \pm 0.05$	$0.81 \pm 0.02 \pm 0.03$	$0.36 \pm 0.01 \pm 0.02$

Table 17.1.16. Results of the fits of the BCL parameterization with 3 parameters to the measured $\Delta B/\Delta q^2$ distribution.

Measurement	χ^2/ndf	Prob(χ^2/ndf)	Fit parameters	$f_+(0)\lvert V_{ub}\rvert$ (10^{-3})
BABAR (6 bins)	6.0/3	11.2%	$b_1/b_0 = -0.90 \pm 0.45$	1.090 ± 0.055
			$b_2/b_0 = +0.47 \pm 1.49$	
BABAR (12 bins)	4.1/9	90.5%	$b_1/b_0 = +0.09 \pm 0.53$	0.863 ± 0.044
			$b_2/b_0 = -4.65 \pm 1.55$	
Belle	11.9/10	29.4%	$b_1/b_0 = -1.31 \pm 0.27$	0.914 ± 0.040
			$b_2/b_0 = -0.79 \pm 0.91$	
BABAR +Belle	48.0/28	1.1%	$b_1/b_0 = -0.75 \pm 0.22$	0.940 ± 0.029
			$b_2/b_0 = -1.84 \pm 0.69$	

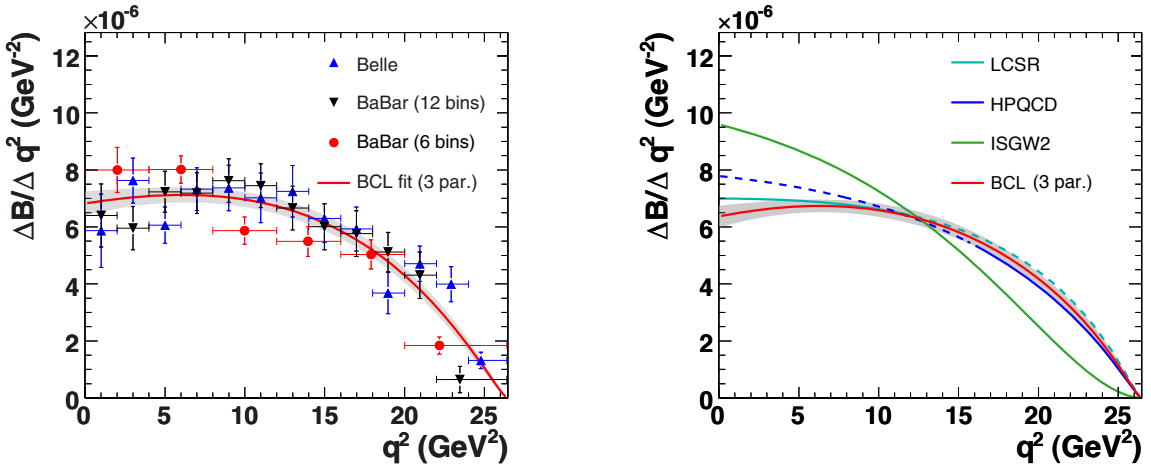

Figure 17.1.15. Left: Fit of the BCL parameterization with 3 parameters to the measured $B \to \pi\ell\nu$ q^2 distribution. The uncertainty of the fit is shown as shaded error band. Right: Comparison of the fit result with form-factor predictions from HPQCD (Dalgic et al., 2006), LCSR (Khodjamirian, Mannel, Offen, and Wang, 2011) and ISGW2 (Scora and Isgur, 1995). The extrapolations of the predictions to the full q^2 range are shown as dashed lines.

the three untagged $B \to \pi\ell\nu$ measurements and the averages of the untagged and tagged measurements, and for three form-factor calculations. The uncertainty on $|V_{ub}|$ is dominated by the theoretical form-factor uncertainty.

The more recent method is based on a simultaneous fit to the measured q^2 spectra and the LQCD predictions. The BCL parameterization is used as parameterization for $f_+(q^2)$ over the whole q^2 range to minimize the model dependence of the form factor. This method makes use of the full shape information from data and the shape and normalization from theory, which results in a reduced uncertainty on $|V_{ub}|$.

The combined fit to the FNAL/MILC lattice calculations and the data from the three untagged measurements yields $|V_{ub}| = (3.23 \pm 0.30) \times 10^{-3}$. Figure 17.1.16 and Table 17.1.17 show the results of the fit. Only four of the twelve FNAL/MILC points have been included in the fit, avoiding LQCD points with a correlation higher than 80%. This reduction of the theoretical input does not change the $|V_{ub}|$ result but leads to a better agreement of the fitted curve with the lattice points. The fit results for the parameters in the BCL parameterization are $b_1/b_0 = -0.82 \pm 0.20$ and $b_2/b_0 = -1.63 \pm 0.62$, and a value of $f_+(0)|V_{ub}| = 0.945 \pm 0.028$ is obtained. The χ^2 probability of the fit is 2.2% ($\chi^2/ndf = 58.9/31$). The $|V_{ub}|$ values obtained from fits to the individual untagged measurements agree with each other within about one standard deviation. The total uncertainty of $|V_{ub}|$ is about 9%. The contributions to this uncertainty have been estimated to be 3% from the branching fraction measurements, 4% from the shapes of the q^2 spectra determined from data, and 8% from the form-factor normalization obtained from theory. Using the HPQCD lattice calculation gives similar fit results. However, at present no information on the correlation of the HPQCD points is available and therefore only one point can be used in the fit to determine the normalization of the decay rate, which results in larger uncertainties.

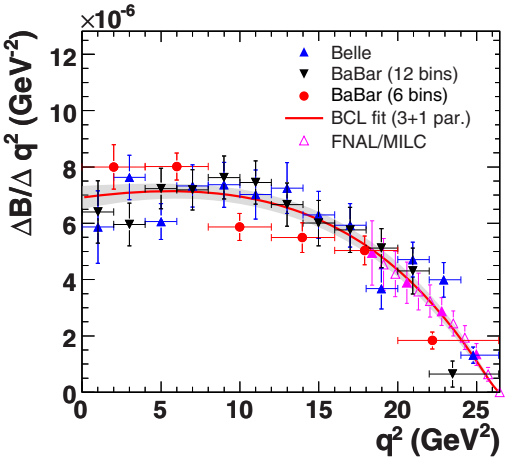

Figure 17.1.16. Simultaneous fit of the BCL parameterization to the measured q^2 spectra and to four of the twelve points of the FNAL/MILC calculation (magenta, closed triangles). The FNAL/MILC prediction has been rescaled to the data according to the $|V_{ub}|$ value obtained in the fit.

As a final result for $|V_{ub}|$ from $B \to \pi\ell\nu$ decays we quote the value obtained from the simultaneous fit to the three untagged measurements from *BABAR* and Belle, combined with the FNAL/MILC calculation:

$$|V_{ub}|_{\text{excl}} = (3.23 \pm 0.30) \times 10^{-3}. \qquad (17.1.59)$$

Future improvements for $|V_{ub}|$ will rely on progress in form-factor calculations based on LQCD or LCSR and

Table 17.1.17. $|V_{ub}|$ derived from $B \to \pi\ell\nu$ decays for various q^2 regions and form-factor calculations: LCSR (Khodjamirian, Mannel, Offen, and Wang, 2011), HPQCD (Dalgic et al., 2006), FNAL/MILC (Bailey et al., 2009). The quoted errors on $|V_{ub}|$ are due to experimental uncertainties and theoretical uncertainties on $\Delta\zeta$. The last column shows the $|V_{ub}|$ results of the simultaneous fits to data and the FNAL/MILC prediction. Here the stated error represents the combined experimental and theoretical uncertainty.

	LCSR	HPQCD	FNAL/MILC	FNAL/MILC fit
$\Delta\zeta$ (ps^{-1})	$4.59^{+1.00}_{-0.85}$	2.02 ± 0.55	$2.21^{+0.47}_{-0.42}$	$2.21^{+0.47}_{-0.42}$
q^2 range (GeV^2)	$0-12$	$16-26.4$	$16-26.4$	$16-26.4$
Experiment		$\|V_{ub}\|$ (10^{-3})		
BABAR (6 bins)	$3.54\pm0.12^{+0.38}_{-0.33}$	$3.22\pm0.15^{+0.55}_{-0.37}$	$3.08\pm0.14^{+0.34}_{-0.28}$	2.98 ± 0.31
BABAR (12 bins)	$3.46\pm0.10^{+0.37}_{-0.32}$	$3.26\pm0.19^{+0.56}_{-0.37}$	$3.12\pm0.18^{+0.35}_{-0.29}$	3.22 ± 0.31
Belle	$3.44\pm0.10^{+0.37}_{-0.32}$	$3.60\pm0.13^{+0.61}_{-0.41}$	$3.44\pm0.13^{+0.38}_{-0.32}$	3.52 ± 0.34
BABAR +Belle	$3.47\pm0.06^{+0.37}_{-0.32}$	$3.43\pm0.09^{+0.59}_{-0.39}$	$3.27\pm0.09^{+0.36}_{-0.30}$	3.23 ± 0.30
Tagged	$3.10\pm0.16^{+0.33}_{-0.29}$	$3.47\pm0.23^{+0.60}_{-0.39}$	$3.32\pm0.22^{+0.37}_{-0.31}$	3.33 ± 0.39

on more precise experimental determinations of the q^2 spectrum in $B \to \pi\ell\nu$ decays. In particular an improved precision in the high q^2 region, where LQCD predictions exist, would be important. This will require a better understanding of the composition and dynamics of the $B \to X_u\ell\nu$ background and significantly larger data samples for tagged event samples expected at the next generation of B Factories.

17.1.5 Inclusive Cabibbo-suppressed B decays

17.1.5.1 Theoretical Overview

The theoretical description of inclusive $B \to X_u\ell\nu$ decays rests on the same basic principles as that of inclusive $B \to X_c\ell\nu$ decays described in Section 17.1.3.1. Due to the inclusive nature of the process, the only sensitivity to long-distance dynamics comes from the B meson in the initial state. The total $B \to X_u\ell\nu$ rate is given by an OPE in terms of local operators, which has a similar structure as that for the $B \to X_c\ell\nu$ rate, with non-perturbative corrections first appearing at $O(1/m_b^2)$.

In practice, the experimental sensitivity to $B \to X_u\ell\nu$ and $|V_{ub}|$ is highest in the region of phase space that is less impacted by the dominant $B \to X_c\ell\nu$ background, namely the region where the hadronic X_u system has invariant mass m_X below the mass of the lightest charm meson, $m_X \lesssim m_D$. In this phase-space region non-perturbative corrections are kinematically enhanced, and as a result the non-perturbative dynamics of the decaying b quark inside the B meson becomes an $O(1)$ effect.

In addition to the lepton energy, E_ℓ, convenient variables to describe the decay kinematics are the hadronic variables

$$p_X^+ = E_X - |\boldsymbol{p}_X|\,, \qquad p_X^- = E_X + |\boldsymbol{p}_X|\,, \tag{17.1.60}$$

where E_X and $\boldsymbol{p}_X$ are the energy and momentum of the hadronic system in the B-meson rest frame. In terms of these variables, the total hadronic and leptonic invariant masses are given by

$$m_X^2 = p_X^+ p_X^-\,, \quad q^2 = (m_B - p_X^+)(m_B - p_X^-)\,. \tag{17.1.61}$$

The fully differential decay rate is given by

$$\frac{d^3\Gamma}{dp_X^+\,dp_X^-\,dE_\ell} = \frac{G_F^2|V_{ub}|^2}{192\pi^3}\int dk\, C(E_\ell, p_X^-, p_X^+, k)\, F(k) + O\Big(\frac{\Lambda_{\rm QCD}}{m_b}\Big)\,. \tag{17.1.62}$$

The coefficient $C(E_\ell, p_X^-, p_X^+, k)$ describes the quark decay $b \to u\ell\nu$ and can be computed in QCD perturbation theory. The "shape-function" $F(k)$ is a non-perturbative function. It describes the momentum distribution of the b quark in the B meson (Bigi, Shifman, Uraltsev, and Vainshtein, 1994; Neubert, 1994a). For $p_X^+ \sim k \sim \Lambda_{\rm QCD}$, which includes a large portion of the small m_X region, the full non-perturbative shape of $F(k)$ is necessary to obtain an accurate description of the differential decay rate. On the other hand, in the limit $p_X^+ \gg k \sim \Lambda_{\rm QCD}$, only the first few moments of $F(k)$ are needed. Typically, the experimental measurements can lie anywhere between these two kinematic regimes.

There are several sources of uncertainties in the theoretical predictions that must be considered. First, there are perturbative uncertainties in the calculation of C due to unknown higher-order corrections. Second, there are parametric uncertainties due to the imprecise knowledge of inputs, in particular the b-quark mass and $F(k)$. The total decay rate scales like m_b^5, while partial rates restricted to the small m_X region typically exhibit an even stronger dependence on m_b. The first few moments of $F(k)$ are determined by m_b and the expectation values of local operators that are constrained by fits to $B \to X_c\ell\nu$ moments. A substantial part of the m_b dependence enters indirectly via the first moment of $F(k)$. Depending on the kinematic cuts, the shape of $F(k)$ (beyond what is encoded in its first few moments) can also have a significant influence on the

predictions. An important consistency check for the overall shape of $F(k)$ is to give a reasonable description of the measured shape of the photon-energy spectrum in inclusive $B \to X_s\gamma$ decays (see Section 17.9), which at leading order in $1/m_b$ is given in terms of the same function $F(k)$ via an expression analogous to Eq. (17.1.62).

In addition to the leading shape function $F(k)$, several additional shape functions appear at $O(\Lambda_{\rm QCD}/m_b)$ (Bauer, Luke, and Mannel, 2003). Apart from their first few moments, very little is known about the form of these subleading shape functions. They thus introduce an uncertainty in the theoretical predictions that is hard to quantify in a systematic fashion. An even larger number of unknown shape functions appears at $O(\alpha_s\Lambda_{\rm QCD}/m_b)$ (Lee and Stewart, 2005).

Weak annihilation contributions could have a large impact at large q^2 and might be another source of theoretical uncertainties. However, recent analyses (Bigi, Mannel, Turczyk, and Uraltsev, 2010; Gambino and Kamenik, 2010; Ligeti, Luke, and Manohar, 2010) have used CLEO-c data to constrain contributions from weak annihilation, resulting in a rather small impact. The corresponding uncertainty is below 2% for the total rate, translating into an uncertainty of less than 1% on $|V_{ub}|$ for the most inclusive analyses.

For the determination of $|V_{ub}|$ theoretical predictions by different groups are in use. A more detailed summary and comparison can be found elsewhere (Antonelli et al., 2010a). At their core, the different calculations are all based on Eq. (17.1.62), but they differ in the treatment of the perturbative and non-perturbative contributions.

The BLNP approach (Bosch, Lange, Neubert, and Paz, 2004; Lange, Neubert, and Paz, 2005) preferentially treats the kinematic region $p_X^+ \ll p_X^-$ where the p_X^+ and p_X^- dependences of C factorize. This allows for the resummation of Sudakov double logarithms of p_X^+/p_X^- and p_X^+/m_B to NNLL. They also include the full $O(\alpha_s)$ corrections, for which the perturbative expansions are performed using the so-called shape-function scheme for m_b, and a subset of the perturbative corrections in C are absorbed into $F(k)$. The subleading shape functions are separately modeled and included in the predictions.

The GGOU approach (Gambino, Giordano, Ossola, and Uraltsev, 2007) treats the $p_X^+ \ll p_X^-$ and $p_X^+ \sim p_X^-$ regions on the same footing. The coefficient C is computed at fixed order to $O(\alpha_s)$ and $O(\alpha_s^2\beta_0)$ (Gambino, Gardi, and Ridolfi, 2006), where the perturbative expansion is performed using the kinetic scheme for m_b. In this case no resummation effects at small p_X^+ are included. The effect of resummation as well as all contributions from subleading shape functions are absorbed into $F(k)$. This results in three non-universal distribution functions $F_i(k, q^2)$, which have subleading dependence on q^2.

In the dressed-gluon exponentiation (DGE) approach (Andersen and Gardi, 2006; Gardi, 2008) the perturbative expansion includes the NNLL resummation in moment space as well as the full $O(\alpha_s)$ and $O(\alpha_s^2\beta_0)$ corrections. It also incorporates an internal resummation of running coupling corrections in the Sudakov exponent. This approach effectively corresponds to a perturbative model for the leading shape function, with non-perturbative corrections only included via its moments. Therefore, it tends to be more predictive than the other approaches, resulting in smaller theoretical uncertainties within the framework. However, the intrinsic uncertainties due the assumptions inherent in the framework are not estimated. Another approach based on Sudakov resummation has been proposed in (Aglietti, Di Lodovico, Ferrera, and Ricciardi, 2009). It employs the so-called analytic coupling in the infrared.

The full $O(\alpha_s^2)$ corrections to the $b \to u\ell\nu$ spectrum are only known in the limit $p_X^+ \ll p_X^-$ (Greub, Neubert, and Pecjak, 2010), and are currently not included in the determination of $|V_{ub}|$. In case of BLNP, their effect turns out to be much larger than expected from the perturbative uncertainties at $O(\alpha_s)$, resulting in an increase of $|V_{ub}|$ by 8%. On the other hand, the $O(\alpha_s^2\beta_0)$ terms often dominate the $O(\alpha_s^2)$ corrections, and their inclusion in the GGOU and DGE approaches does not lead to similarly large corrections. A resolution of this apparent discrepancy will probably have to await a calculation of the complete $O(\alpha_s^2)$ corrections.

All the above approaches choose specific model parameterizations of the shape function(s), and it is unclear to what extent the model variations used to estimate the shape function uncertainties reflect the actual limited knowledge of their form, particularly at subleading order in $1/m_b$. Also, the theoretical uncertainties do not include explicit estimates of the possible size of $O(\alpha_s\Lambda_{\rm QCD}/m_b)$ corrections.

Given all the above, it is possible that the theoretical uncertainties currently quoted for $|V_{ub}|$ might be underestimated. On the other hand, the different theoretical frameworks yield values of $|V_{ub}|$ that are compatible within uncertainties with each other and across a variety of different experimental cuts.

Imposing an additional lower cut on q^2 restricts the decay kinematics to the part of the small m_X region where $p_X^+ \sim p_X^-$. Formally, this allows the application of the OPE in terms of local operators (Bauer, Ligeti, and Luke, 2001). In practice, the resulting OPE still has rather large $1/m_b^2$ and higher order corrections, and some residual shape-function effects must be included. Nevertheless, this approach provides an important cross check on the extracted value of $|V_{ub}|$.

In some recent experimental analyses the phase-space restrictions have been relaxed and up to 90% of the total inclusive $B \to X_u\ell\nu$ rate is measured. In principle, this makes it possible to use a simpler theoretical description based on the local OPE only. Consequently, the main theoretical uncertainties are due to m_b and higher-order perturbative corrections. In practice, these analyses still make explicit use of the theoretical description of the signal shape in the shape-function region to determine the experimental reconstruction efficiencies, and the associated theoretical uncertainties contribute via the experimental systematic uncertainties. Nevertheless, the fact that the resulting values of $|V_{ub}|$ are consistent with the other anal-

yses enhances the confidence in our current understanding of inclusive $B \to X_u \ell\nu$ decays.

Recently, an improved treatment of the shape function has been developed (Ligeti, Stewart, and Tackmann, 2008), which combines the advantages of the BLNP and GGOU approaches and uses appropriate basis functions to approximate the shape function. It is expected that this procedure will allow for a combined global fit to all available inclusive $B \to X_s\gamma$ and $B \to X_u\ell\nu$ measurements (Bernlochner et al., 2011). As in the determination of $|V_{cb}|$ from inclusive $B \to X_c\ell\nu$ decays, a global fit has the advantage that the input parameters, such as $F(k)$ and m_b, are directly constrained by data and are determined together with $|V_{ub}|$.

17.1.5.2 Measurements of Partial Branching Fractions

The observation of charged leptons with momenta exceeding the kinematic limit for $B \to X_c\ell\nu$ decays by the CLEO Collaboration (Bartelt et al., 1993) was the first evidence for charmless semileptonic decays. Since then, a series of measurements near the kinematic limit have been performed (Bornheim et al., 2002; Limosani, 2005; Aubert, 2006x); they differ in the kinematic selection and the size of the data sample. At lower lepton momenta, the background from $B \to X_c\ell\nu$ increases sharply to more than 10 times the signal and the dominant uncertainty arises from the subtraction of the sum of lepton spectra from exclusive $B \to X_c\ell\nu$ decays, for which the branching fractions and form factors are known to different degrees. The signal-to-background ratio can be substantially improved by combining the high energy lepton with a measurement of the missing neutrino in the event, but this can only be achieved with a substantial reduction in the selection efficiency (Aubert, 2005h).

Experimenters simulate the charmless semileptonic $B \to X_u\ell\nu$ decays as a hybrid, *i.e.*, a combination of two components: three-body decays involving a single low-mass charmless meson, π, ρ, η, η', or ω, and decays to non-resonant multi-body hadronic final states. The three-body decays make up about the 20% of the charmless semileptonic decay rate, and their simulation is based on OPE calculations and form-factor measurements and measured branching fractions (Beringer et al., 2012). The generated mass distribution and kinematics of multi-body hadronic states X_u are based on the prescription by De Fazio and Neubert (De Fazio and Neubert, 1999). The fragmentation of X_u into final state hadrons are simulated by using `Jetset` (Sjöstrand, 1994). The two components are combined so that the cumulative distributions of the hadronic mass, the momentum transfer squared, and the lepton momentum reproduce OPE predictions. The generated distributions are often reweighted to accommodate specific choices of the parameters for the inclusive and exclusive decays. The overall normalization is adjusted to reproduce the measured inclusive charmless branching fraction (Beringer et al., 2012).

An example of the extraction of the signal yield is illustrated in Figure 17.1.17 (Aubert, 2006x), showing the observed spectra of the highest momentum electron in events recorded on and below the $\Upsilon(4S)$ resonance. The data collected on the $\Upsilon(4S)$ resonance include contributions from $B\overline{B}$ events and continuum events. The latter is subtracted using off-resonance data, collected below the $B\overline{B}$ production threshold, and on-resonance data with lepton momenta above 2.8 GeV, *i.e.*, well above the endpoint for semileptonic B decays. The principal challenge is the subtraction of the electron spectrum from B-meson decays which is dominated by various $B \to X_c\ell\nu$ decays. Hadronic B decays contribute mostly via hadron misidentification and secondary electrons from decays of D, J/ψ, and $\psi(2S)$ mesons. The signal contribution is determined from a χ^2 fit of the observed inclusive electron spectrum to the sum of Monte Carlo (MC) simulated signal and individual background contributions. The relative normalization factors for signal and background distributions are free parameters of the fit.

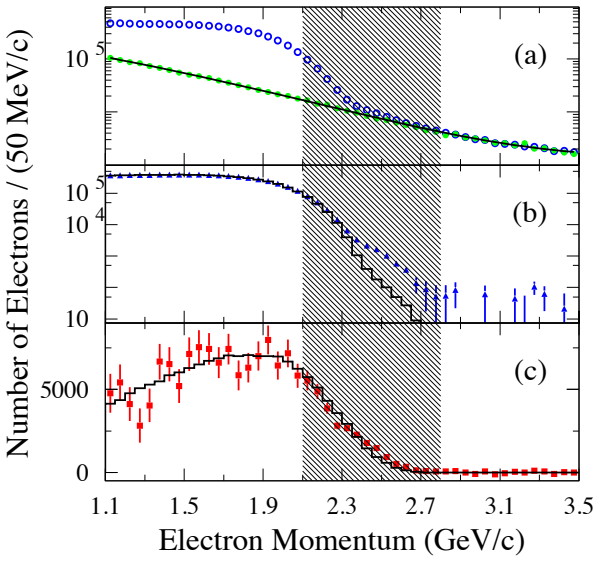

Figure 17.1.17. *BABAR* analysis of the electron momentum spectra in the $\Upsilon(4S)$ rest frame (Aubert, 2006x): (a) on-resonance data (open circles - blue), scaled off-resonance data (solid circles - green); the solid line shows the result of the fit to the non-$B\overline{B}$ events using both on- and off-resonance data; (b) on-resonance data after subtraction of the fitted non-$B\overline{B}$ background (triangles - blue) compared to simulated $B\overline{B}$ background (histogram) that is adjusted by a combined fit to the on- and off-resonance data; (c) on-resonance data after subtraction of all backgrounds (data point - red), compared to the simulated $B \to X_u e\nu$ signal spectrum (histogram); the error bars indicate errors from the fit, which include the uncertainties in the fitted yields for continuum and $X_c e\nu$ backgrounds. The shaded area indicates the momentum interval for which the on-resonance data are combined into a single bin for the purpose of reducing the sensitivity of the fit to the simulated shape of the signal spectrum in this region.

In this analysis, a potential bias of the fitted yield from the assumed shape of the signal spectrum is reduced by combining the on-resonance data for the interval from 2.1 to 2.8 GeV in a single bin. The lower limit of this bin is chosen so as to retain the sensitivity to the steeply falling $B\overline{B}$ background distributions, while containing a large fraction of the signal events in a region where the background is low.

In total, the selected sample includes 610×10^3 electrons, from which roughly 6.5% have been extracted as the signal yield in the momentum interval $2.0 - 2.6$ GeV. This translates to a partial branching fraction of $\Delta\mathcal{B}(B \to X_u e\nu) = (0.572 \pm 0.041 \pm 0.051) \times 10^{-3}$. Here the first error is statistical and the second is the total systematic error. The systematic error includes the uncertainty in the assumed shape of the signal spectrum. The gain in precision compared to earlier analyses of the lepton spectrum near the kinematic endpoint can be attributed to higher statistics, and to improved background estimates. While earlier measurements were restricted to lepton energies close to the kinematic endpoint for $B \to X_c\ell\nu$ decays at 2.3 GeV and covered only 10% of the $B \to X_u\ell\nu$ spectrum, this and other more recent measurements have been extended to lower momenta, thus covering about 25% to 35% of the spectrum (see Table 17.1.18).

More recently, the large data samples accumulated at the B Factories have enabled studies of $B\overline{B}$ event samples tagged by the full reconstruction of the hadronic decays of one of the B mesons. An electron or muon with momentum $p_\ell^* > 1\,\text{GeV}$ in the CM system is taken as a signature for a semileptonic decay of the second B meson. The overall event rate is low due to the low tag efficiency, but the combinatorial backgrounds are substantially reduced allowing the extension of the acceptance for signal events to 90% of the remaining phase space. The tag decay determines the CM momentum and charge of the recoiling signal B decay, and permits the reconstruction of hadronic observables with good resolution. Of particular relevance are q^2 and m_X, the mass of the hadronic state X. The systematic uncertainties related to the tag efficiency largely cancel in the measurement of the ratio of event yields for selected charmless semileptonic decays relative to all $B \to X\ell\nu$ decays. Corrections to the signal yield account for a possible difference in the tagging efficiency in the presence of a signal $B \to X_u\ell\nu$ decay or generic semileptonic decay. The combinatorial background of the tag decay is subtracted by fits to the m_{ES} distributions. Other backgrounds originate from secondary $B \to X \to \ell$ decays and hadron misidentified as leptons, primarily muons. The dominant $B \to X_c\ell\nu$ background is reduced by vetoing kaons from charm particle decays and low-momentum pions from $D^* \to D\pi$ decays. Events with additional missing particles result in large values of the missing mass squared m^2_{miss} and are rejected. This not only reduces the backgrounds, but also improves the resolution of the reconstructed variables describing the signal decays. In particular, the hadronic variable $P_+ = p_X^+$ is sensitive to detector resolution and the background modeling. The normalization of the remaining $B \to X_c\ell\nu$ background is determined from fits to the observed inclusive spectra of different kinematic variables.

Using the hadron-tagged $B\overline{B}$ events, Belle (Bizjak, 2005; Urquijo, 2010) and *BABAR* (Aubert, 2008ac; Lees, 2012x) have measured partial decay rates. The *BABAR* measurements are based on the full dataset of 467 million produced $B\overline{B}$ events, whereas the Belle results are based on 275 million (Bizjak, 2005) and 657 million (Urquijo, 2010) produced $B\overline{B}$ pairs, respectively. Figure 17.1.18 shows *BABAR* data and results of fits (Lees, 2012x) to four different kinematic distributions of $B \to X_u\ell\nu$ decays, performed to extract the partial branching fractions. These branching fractions are listed in Table 17.1.19 for tagged data samples from *BABAR* and Belle. Unless stated otherwise, the minimum lepton momentum is 1 GeV. The listed branching fractions and extraction of $|V_{ub}|$ are based on fits to the distributions of the variables listed in the first column with the specific restrictions imposed. For the *BABAR* and Belle results listed in the last line, no additional restriction is imposed, and the results agree very well within the stated errors.

These most recent analyses by Belle (Urquijo, 2010) and *BABAR* (Lees, 2012x), based on their full data samples, use a two-dimensional fit to m_X versus q^2 to extract the branching fraction. Figures 17.1.19 and 17.1.20 show the Belle and *BABAR* data and fit results. The *BABAR* selection of the signal candidates is cut-based, whereas Belle employs a nonlinear multivariate discriminator, a boosted decision tree. For the two analyses, the statistical and systematic errors on the branching fractions are comparable in size ($\simeq 7 - 9\%$). The systematic uncertainties are dominated by the simulation of the signal decays; in particular, they are sensitive to the shape function and the b-quark mass. The average of these two branching fraction measurements, assuming full correlation of the uncertainty in the predicted signal spectrum, is $\Delta\mathcal{B}(p_\ell^* > 1\,\text{GeV}) = (1.87 \pm 0.10 \pm 0.11) \times 10^{-3}$.

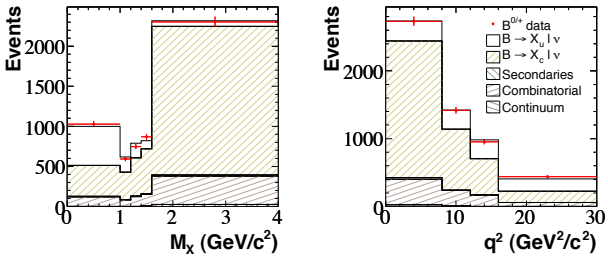

Figure 17.1.19. Belle (Urquijo, 2010): Projections of measured distributions (data points) of (a) m_X and (b) q^2 with varying bin size, compared to results of a two-dimensional $m_X - q^2$ distribution for the sum of scaled MC contributions. The data are not efficiency corrected.

Table 17.1.18. Overview of partial branching fraction measurements with statistical and systematic errors, based on measurements of the inclusive lepton spectrum for $B \to X_u \ell\nu$ decays using untagged data samples. $s_{\rm h}^{\rm max}$ refers to the maximum kinematically allowed hadronic mass squared for a given electron energy and q^2.

Experiment	Selection	$\Delta\mathcal{B}$ (10^{-3})
CLEO (Bornheim et al., 2002)	$p_\ell^* > 2.1\,\text{GeV}$	$0.328 \pm 0.023 \pm 0.073$
Belle (Limosani, 2005)	$p_\ell^* > 1.9\,\text{GeV}$	$0.847 \pm 0.037 \pm 0.153$
BABAR (Aubert, 2006x)	$p_\ell^* > 2.0\,\text{GeV}$	$0.572 \pm 0.041 \pm 0.051$
BABAR (Aubert, 2005h)	$p_\ell^* > 2.0\,\text{GeV}, s_{\rm h}^{\rm max} > 3.5\,\text{GeV}^2$	$0.441 \pm 0.042 \pm 0.042$

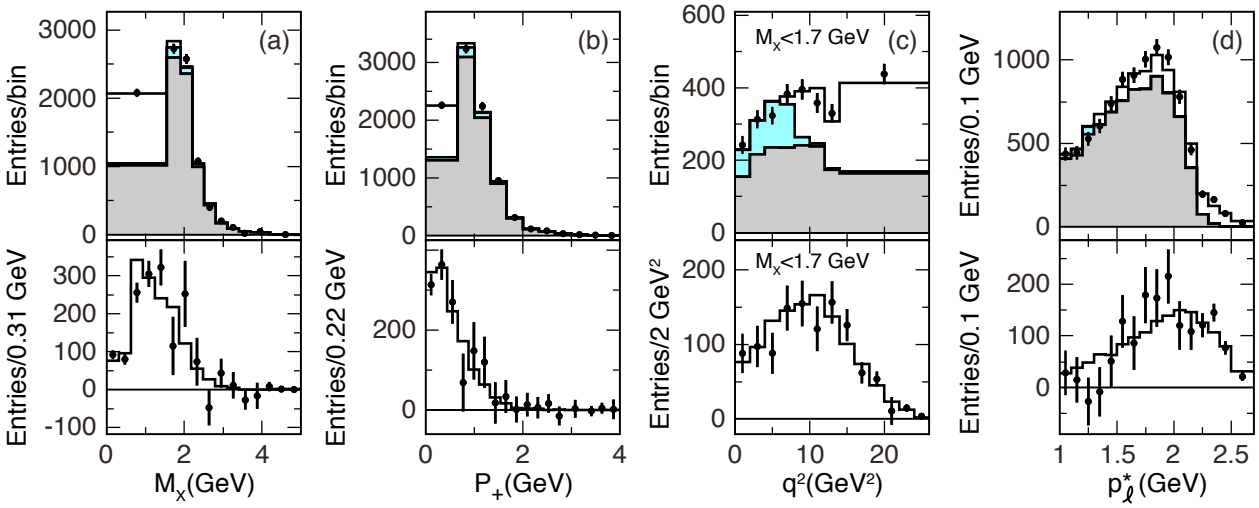

Figure 17.1.18. *BABAR* (Lees, 2012x): Extraction of $|V_{ub}|$ from selected samples of inclusive $B \to X_u \ell\nu$ decays: (a) hadronic mass m_X, (b) P_+, (c) q^2 with restriction $m_X \leq 1.7\,\text{GeV}$, and (d) lepton momentum p_ℓ^*. upper row: comparison of data (points with statistical errors) with results of χ^2 fit with varying bin size for the sum of scaled MC distributions (histograms) of signal inside (white) and outside (blue) the selected kinematic region and background (gray); lower row: background subtracted distributions, compared to the results of the fit with finer binning. The data are not efficiency corrected.

Table 17.1.19. Partial $B \to X_u \ell\nu$ branching fractions (Bizjak, 2005; Urquijo, 2010; Lees, 2012x) and values of $|V_{ub}|$ (Lees, 2012x) based on BLNP calculations for different kinematic regions in tagged $B\overline{B}$ events. The stated errors are statistical and systematic, and for $|V_{ub}|$ the third error refers to the theoretical uncertainty.

Selection	Belle: $\Delta\mathcal{B}$ (10^{-3})	*BABAR*: $\Delta\mathcal{B}$ (10^{-3})	*BABAR*: $\lvert V_{ub}\rvert$ (10^{-3})
$m_X \leq 1.55\,\text{GeV}$	—	$1.08 \pm 0.08 \pm 0.06$	$4.17 \pm 0.15 \pm 0.12^{+0.24}_{-0.24}$
$m_X \leq 1.70\,\text{GeV}$	$1.24 \pm 0.11 \pm 0.12$	$1.15 \pm 0.06 \pm 0.08$	$3.97 \pm 0.17 \pm 0.14^{+0.20}_{-0.20}$
$P_+ \leq 0.66\,\text{GeV}$	$1.11 \pm 0.10 \pm 0.16$	$0.98 \pm 0.09 \pm 0.08$	$4.02 \pm 0.18 \pm 0.16^{+0.24}_{-0.23}$
$m_X \leq 1.70\,\text{GeV}, q^2 \geq 8\,\text{GeV}^2$	$0.84 \pm 0.08 \pm 0.10$	$0.68 \pm 0.06 \pm 0.04$	$4.25 \pm 0.19 \pm 0.13^{+0.23}_{-0.25}$
$p_\ell^* > 1.3\,\text{GeV}$	—	$1.52 \pm 0.16 \pm 0.14$	$4.29 \pm 0.22 \pm 0.20^{+0.19}_{-0.20}$
$p_\ell^* > 1.0\,\text{GeV}, m_X - q^2$	$1.96 \pm 0.17 \pm 0.16$	$1.80 \pm 0.13 \pm 0.15$	$4.28 \pm 0.15 \pm 0.18^{+0.18}_{-0.20}$

17.1.5.3 Determination of $|V_{ub}|$

The measured partial branching fractions $\Delta\mathcal{B}$ can be related to $|V_{ub}|$ in the following way,

$$|V_{ub}| = \sqrt{\Delta\mathcal{B}/(\tau_B\,\Delta\Gamma_{\rm theory})}, \tag{17.1.63}$$

where $\Delta\Gamma_{\rm theory}$ is the theoretically predicted partial rate (in units of ps^{-1}) for a selected phase space region.

The extracted values of $|V_{ub}|$ are presented in Table 17.1.20 for both untagged and tagged $B\overline{B}$ samples. The $|V_{ub}|$ results have been adjusted by HFAG to include updates of input parameters and reflect the latest understanding of the theoretical uncertainties. The averages of the various available measurements have been obtained by taking correlations into account. In particular, all theoretical uncertainties are considered to be correlated, as are the uncertainties on the modeling of $B \to X_c \ell\nu$ and $B \to X_u \ell\nu$ decays. Experimental uncertainties due to particle identification and reconstruction efficiencies are fully correlated for measurements from the same experi-

Table 17.1.20. Overview of $|V_{ub}|$ measurements based on inclusive $B \to X_u \ell\nu$ decays. The critical input parameters m_b and μ_π^2 depend on the different mass schemes and have been obtained from the OPE fits to $B \to X_c \ell\nu$ hadronic mass and lepton energy moments in the kinetic mass scheme. For the BLNP and the DGE calculations, they have been subsequently translated from the kinetic to the shape function and $\overline{\text{MS}}$ schemes, respectively. The additional uncertainties m_b and μ_π^2 are due to these scheme translations. The first error is experimental and the second reflects the uncertainties of the QCD calculations and the HQE parameters (Asner et al., 2011).

	BLNP	GGOU	DGE
m_b scheme	SF scheme	Kinetic scheme	$\overline{\text{MS}}$ scheme
m_b (GeV)	$4.588 \pm 0.023 \pm 0.011$	4.560 ± 0.023	4.194 ± 0.043
μ_π^2 (GeV^2)	$0.189^{+0.041}_{-0.040} \pm 0.020$	0.453 ± 0.036	—
Experiment		$\|V_{ub}\|$ (10^{-3})	
CLEO (Bornheim et al., 2002)	$4.19 \pm 0.49^{+0.26}_{-0.34}$	$3.93 \pm 0.46^{+0.22}_{-0.29}$	$3.82 \pm 0.43^{+0.23}_{-0.26}$
Belle (Limosani, 2005)	$4.88 \pm 0.45^{+0.24}_{-0.27}$	$4.75 \pm 0.44^{+0.17}_{-0.22}$	$4.79 \pm 0.44^{+0.21}_{-0.24}$
BABAR (Aubert, 2006x)	$4.48 \pm 0.25^{+0.27}_{-0.28}$	$4.29 \pm 0.24^{+0.18}_{-0.24}$	$4.28 \pm 0.24^{+0.22}_{-0.24}$
BABAR (Aubert, 2005h)	$4.66 \pm 0.31^{+0.31}_{-0.36}$	—	$4.32 \pm 0.29^{+0.24}_{-0.29}$
Average untagged	$4.65 \pm 0.22^{+0.26}_{-0.29}$	$4.39 \pm 0.22^{+0.18}_{-0.24}$	$4.44 \pm 0.21^{+0.21}_{-0.25}$
Belle (Urquijo, 2010)	$4.47 \pm 0.27^{+0.19}_{-0.21}$	$4.54 \pm 0.27^{+0.10}_{-0.11}$	$4.60 \pm 0.27^{+0.11}_{-0.13}$
BABAR (Lees, 2012x)	$4.28 \pm 0.24^{+0.18}_{-0.20}$	$4.35 \pm 0.24^{+0.09}_{-0.11}$	$4.40 \pm 0.24^{+0.12}_{-0.13}$
Average tagged	$4.35 \pm 0.19^{+0.19}_{-0.20}$	$4.43 \pm 0.21^{+0.09}_{-0.11}$	$4.49 \pm 0.21^{+0.13}_{-0.13}$
Average all	$4.40 \pm 0.15^{+0.19}_{-0.21}$	$4.39 \pm 0.15^{+0.12}_{-0.14}$	$4.45 \pm 0.15^{+0.15}_{-0.16}$

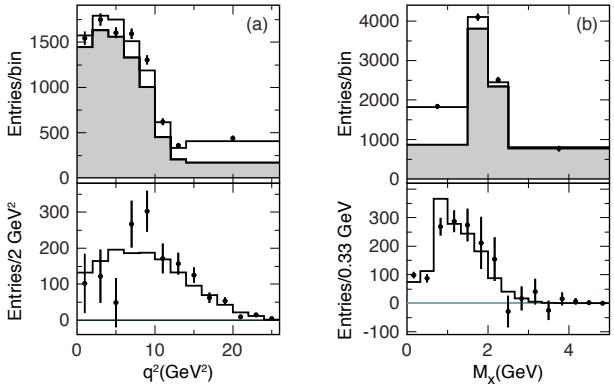

Figure 17.1.20. *BABAR* (Lees, 2012x): Projection of measured distributions (data points) of (a) q^2 and (b) m_X with varying bin size. Upper row: comparison with the result of the χ^2 fit to the two-dimensional $m_X - q^2$ distribution for the sum of two scaled MC contributions. Lower row: corresponding spectra with equal bin size after background subtraction based on the fit. The data are not efficiency corrected.

ment, and uncorrelated for different experiments. Statistical correlations are also taken into account, whenever available. The averaging procedure used is documented by the HFAG Collaboration (Asner et al., 2010). The earlier measurements near the kinematic limit of the lepton spectrum covered limited fractions of the total phase space and had sizable experimental and theoretical uncertainties. The more recent measurements based on the tagged $B\overline{B}$ samples of the full *BABAR* and Belle data sets have reduced backgrounds and cover a much larger fraction of the phase space.

The extracted values of $|V_{ub}|$ based on the different QCD calculations agree well. The estimated theoretical errors are dominated by the uncertainty on m_b, and by other non-perturbative corrections. For BLNP there are sizable contributions from the leading and subleading shape functions and the matching scales. For GGOU the uncertainties in the parameterization of the different shape functions are important. For the DGE calculation, the main uncertainty comes from α_s and m_b for which the $\overline{\text{MS}}$ renormalization scheme is used. The uncertainty in the weak annihilation process is included. It contributes asymmetrically to the error for the three QCD calculations.

Values of $|V_{ub}|$ based on partial branching fractions (Lees, 2012x) for different regions of phase space are presented in Table 17.1.19 for the BLNP calculation. The resulting uncertainties are highly correlated. For the different kinematic regions, the variations of $|V_{ub}|$ are consistent within the experimental uncertainties. Similar results were also obtained for other QCD calculations. The analysis based on the restricted region $m_X < 1.7\,\text{GeV}$ combined with $q^2 > 8\,\text{GeV}^2$, is expected to be less affected by non-perturbative contributions to the shape functions. Therefore, the use of a more HQE inspired approach (Bauer, Ligeti, and Luke, 2001) is appropriate. It results in a value of $|V_{ub}|$ that is in good agreement with the results based on the three QCD calculations presented here. As discussed in Section 17.1.5, NNLO effects in the BLNP calculation would lead to an increase of about 8% in $|V_{ub}|$ in some of the BLNP values reported above, but not in those related to tagged measurements with looser signal selection criteria. Further investigation is necessary to clarify this unexpected indication.

There is a high degree of consistency among the measurements and results for different QCD calculations show

little variation. Based on results in Table 17.1.20, we quote the unweighted arithmetic average of the results and uncertainties from the tagged data analyses as the overall result,

$$|V_{ub}|_{\rm incl} = (4.42 \pm 0.20_{\rm exp} \pm 0.15_{\rm th}) \times 10^{-3}. \quad (17.1.64)$$

17.1.6 Evaluation of the results

As a result of joint efforts by theorists and experimentalists our understanding of semileptonic B-meson decays has substantially advanced over the last decade. Here we summarize the present situation.

17.1.6.1 Summary on $|V_{cb}|$

Substantial progress has been made in the application of HQE calculations to extract $|V_{cb}|$ and m_b from fits to measured moments from $B \to X_c \ell\nu$ decays. The total error quoted on $|V_{cb}|$ is 1.8% and the introduction of a c-quark mass constraint, $m_c(3\,{\rm GeV}) = (0.998 \pm 0.029)\,{\rm GeV}$, has reduced the overall uncertainty on m_b to only 25 MeV.

The measurement of $|V_{cb}|$ based on the exclusive decay $B \to D^* \ell\nu_\ell$ now has a combined experimental and theoretical uncertainty of 2.3%, still dominated by the form-factor normalization. The measurement based on $B \to D\ell\nu_\ell$ has substantially improved and now provides a very useful cross check on the more precise $B \to D^*\ell\nu_\ell$ determination. However, the values of $|V_{cb}|$ based on the latter differ by about 5%, depending on the choice of the QCD calculation for the normalization of the form factors; lattice calculations lead to lower values of $|V_{cb}|$ than heavy flavor sum rules.

Consequently the comparison of the inclusive and exclusive determinations of $|V_{cb}|$ depends on the choice of the normalization of the form factors. For the LQCD calculations, the values of the inclusive and exclusive determination of $|V_{cb}|$ differ at the level of 2.5σ,

$$\begin{aligned} |V_{cb}|_{\rm excl} &= [39.04\ (1 \pm 0.014_{\rm exp} \pm 0.019_{\rm th})] \times 10^{-3} \\ |V_{cb}|_{\rm incl} &= [42.01\ (1 \pm 0.011_{\rm exp} \pm 0.014_{\rm th})] \times 10^{-3}\ . \end{aligned} \quad (17.1.65)$$

The average has a probability of $P(\chi^2) = 0.015$. We therefore scale the errors by $\sqrt{\chi^2} = 2.51$ and arrive at

$$|V_{cb}| = [40.81\ (1 \pm 0.022_{\rm exp} \pm 0.028_{\rm th})] \times 10^{-3}\ . \quad (17.1.66)$$

For the heavy flavor sum rule calculations, the value is

$$|V_{cb}|_{\rm excl} = [40.93\ (1 \pm 0.014_{\rm exp} \pm 0.023_{\rm th})] \times 10^{-3} \quad (17.1.67)$$

and agrees very well with the inclusive measurement. The average value with unscaled uncertainties is

$$|V_{cb}| = [41.67\ (1 \pm 0.009_{\rm exp} \pm 0.012_{\rm th})] \times 10^{-3}\ . \quad (17.1.68)$$

17.1.6.2 Summary on $|V_{ub}|$

For inclusive measurements of $|V_{ub}|$ experimental and theoretical errors are comparable in size. The dominant experimental uncertainties are related to the limited size of the tagged samples, the signal simulation, and background subtraction. The theoretical uncertainties are dominated by the error on the b-quark mass; a 20-30 MeV uncertainty in m_b impacts $|V_{ub}|$ by 2-3%.

Measurements of the differential decay rate as a function of q^2 for $B^0 \to \pi^- \ell^+ \nu_\ell$ provide valuable information on the shape of the form factor, though with sizable errors due to large backgrounds. Results based on different QCD calculations agree within the stated theoretical uncertainties. While the traditional method of normalizing to QCD calculations in different ranges of q^2 results in uncertainties of $^{+17\%}_{-10\%}$, combined fits to LQCD predictions and the measured spectrum using a theoretically motivated ansatz (Becher and Hill, 2006; Bourrely, Caprini, and Lellouch, 2009; Boyd, Grinstein, and Lebed, 1995) have resulted in a reduction of the theoretical uncertainties to about 8%.

The values of the inclusive and exclusive determinations of $|V_{ub}|$ are only marginally consistent, they differ at a level of 3σ,

$$\begin{aligned} |V_{ub}|_{\rm excl} &= [3.23\ (1 \pm 0.05_{\rm exp} \pm 0.08_{\rm th})] \times 10^{-3} \\ |V_{ub}|_{\rm incl} &= [4.42\ (1 \pm 0.045_{\rm exp} \pm 0.034_{\rm th})] \times 10^{-3}. \end{aligned} \quad (17.1.69)$$

This average has a probability of $P(\chi^2) = 0.003$. Thus we scale the error by $\sqrt{\chi^2} = 3.0$ and arrive at

$$|V_{ub}| = [3.95\ (1 \pm 0.096_{\rm exp} \pm 0.099_{\rm th})] \times 10^{-3}. \quad (17.1.70)$$

17.1.6.3 Conclusions and Outlook

While there has been tremendous progress, we have not achieved the precision of 1% for $|V_{cb}|$ or 5% on $|V_{ub}|$, goals many of us had hoped to reach by now, based on the final results of the Belle and *BABAR* experiments. The puzzling differences in the results of exclusive and inclusive measurements of $|V_{ub}|$, and to a lesser extent of $|V_{cb}|$ if we rely on non-lattice calculations, challenge our current understanding of the experimental and theoretical techniques. To resolve this puzzle a major effort will be required. It will take much larger tagged data samples and a more detailed assessment of the detector performance and the background composition to reduce experimental errors. It will also require further progress in QCD calculations, based on lattice or heavy flavor sum rules or other methods, to reduce the uncertainties of form-factor predictions for exclusive decays, to adopt precision determinations of the heavy quark masses, and to improve the detailed predictions of inclusive processes.

17.2 V_{td} and V_{ts}

Editors:
Kevin Flood (BABAR)
Tobias Hurth (theory)

The CKM matrix elements $|V_{td}|$ and $|V_{ts}|$ are fundamental parameters of the Standard Model that can only be determined experimentally using rare radiative B or K decays (Fig. 17.2.1), or B^0 and $\overline{B}^0$ oscillations involving top quarks through a box diagram (Fig. 17.2.2). A discussion of kaon decays is beyond the scope of this article; see, *e.g.*, (Donoghue, Golowich, and Holstein, 1982; Gaillard and Lee, 1974b; Gilman and Wise, 1983). Measurement of the single top quark production cross-section allows for a model-independent direct determination of $|V_{tb}|$, but the magnitudes of $|V_{td}|$ and $|V_{ts}|$ cannot be similarly extracted from tree-level decays. However, a recent paper (Ali, Barreiro, and Lagouri, 2010) speculates that $\sim 10\%$ precision for the signal $t \to Ws$ can be achieved at the LHC with an integrated luminosity of 10fb^{-1}, despite the presence of a nearly three orders of magnitude larger background from single top production of $t \to Wb$. Derivation of $|V_{td}|$ and $|V_{ts}|$ from the experimental observables necessarily assumes the SM although the FCNC observables used, *e.g.* from $B_{d,s}$ mixing, $B \to X(s,d)\gamma$, or ϵ in the kaon sector, may receive new physics contributions from unrelated sources (with the term new physics - NP - one addresses experimentally yet unconfirmed processes and particles beyond those included in the Standard Model). Independent determination of the magnitudes of $|V_{td}|$ and $|V_{ts}|$ from several different sources, along with V_{tb} from single top measurements, can provide a robust model-independent check of the unitarity of the CKM matrix or, conversely, offer a sensitive probe for the possible presence of physics beyond the SM.

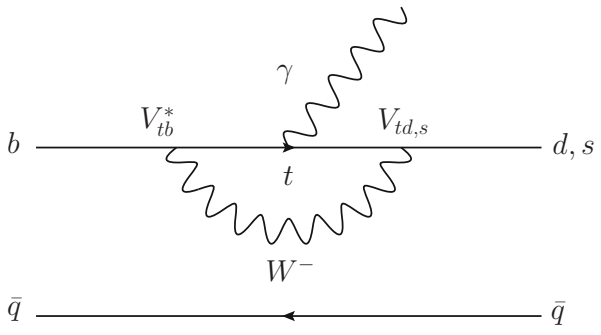

Figure 17.2.1. Lowest order SM Feynman diagram for a loop-mediated radiative B decay.

In the past few years, the experimental and lattice QCD inputs necessary to calculate $|V_{td}|$ and $|V_{ts}|$ to good precision have become available. The B Factories have contributed measurements of Δm_d, the mass difference between the neutral B_d mass eigenstates, and branching fractions from the inclusive and exclusive one-loop radiative penguin processes $B \to X(s,d)\gamma$, while the CDF, DØ and LHCb collaborations have measured Δm_s, the mass difference between the neutral B_s mass eigenstates, to subpercent precision. These results have been matched by progress in lattice QCD calculations leading to increased precision in the additional parameters required to extract $|V_{td}|$ and $|V_{ts}|$ from the experimental results.

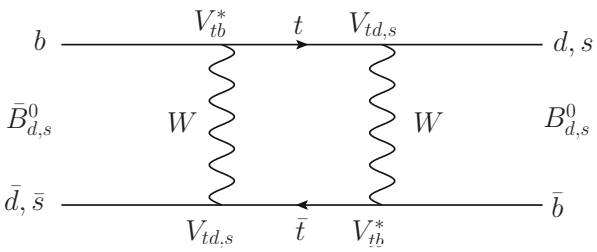

Figure 17.2.2. Lowest order SM Feynman diagram describing B^0 and $\overline{B}^0$ oscillations.

17.2.1 $B_{d,s}$ mixing

Equation (17.2.1) relates Δm_d to $|V_{td}|$ (Bigi and Sanda, 2000):

$$\Delta m_d = \frac{G_F^2}{6\pi^2} f_B^2 m_B M_W^2 \eta_B S_0 |V_{tb}^* V_{td}|^2 \widehat{B}_B \ , \qquad (17.2.1)$$

where we have inserted

$$\langle B^0 | (\bar{b}d)(\bar{b}d) | \overline{B}^0 \rangle = \frac{4}{3} f_B^2 m_{B_d}^2 \widehat{B}_B \qquad (17.2.2)$$

for the hadronic matrix element in Eq. (10.1.17). Here, m_B and M_W are respectively the B^0 and W masses; G_F is the Fermi constant; η_B is a QCD correction (Buras, Jamin, and Weisz, 1990); S_0 is a function of m_t^2/m_W^2 (Buras, 1981; Inami and Lim, 1981); f_B is the B-meson decay constant; and $\widehat{B}_B$ is the B-meson bag parameter (Donoghue, Golowich, and Holstein, 1992). A discussion of the experimental techniques used at the B Factories to measure Δm_d is given in Section 17.5.

In order to extract $|V_{td}|$ using Eq. (17.2.1), we adopt the latest combination of lattice QCD results available from "www.latticeaverages.org" (Laiho, Lunghi, and Van de Water, 2010), who report $f_b\sqrt{\widehat{B}_B} = 227 \pm 19\,\text{MeV}$. This result is obtained by combining the average decay constant f_b obtained from the MILC and HPQCD collaborations, along with the HPQCD determination of the bag parameter $\widehat{B}_B$, which reduces the total uncertainty with respect to taking the two parameters separately. Other required inputs are taken from Tables 25.1.2 and 25.1.3, as well as the PDG (Beringer et al., 2012). We additionally assume that $|V_{tb}| = 1$. Using the B Factory results given in Table 17.5.2, which are averaged by the

Heavy Flavor Averaging Group (HFAG) to obtain a final value of $\Delta m_d = 0.508 \pm 0.003 \pm 0.003$ ps^{-1}, we find $V_{td} = (9.5 \pm 0.7) \times 10^{-3}$.

The uncertainty in $|V_{td}|$ induced by the uncertainty in $f_b\sqrt{\widehat{B}_B}$ can be reduced by rewriting this factor as $f_b\sqrt{\widehat{B}_B} = f_s\sqrt{\widehat{B}_{B_s}}/\xi$, where $\xi = f_s\sqrt{\widehat{B}_{B_s}}/f_b\sqrt{\widehat{B}_B}$. The factor ξ can be more accurately determined in lattice QCD calculations than its individual terms because of the inclusion of $f_s\sqrt{\widehat{B}_{B_s}}$, which is obtained directly at the physical strange quark mass rather than by extrapolation to the down quark mass, and approximate cancellation of some uncertainties in the ratio. Using the values $\xi = 1.237 \pm 0.032$ and $f_s\sqrt{\widehat{B}_{B_s}} = 279 \pm 15$ MeV, we find $V_{td} = (9.6 \pm 0.5) \times 10^{-3}$, with a reduction in the uncertainty of $\sim 30\%$ relative to the result based solely on $f_b\sqrt{\widehat{B}_B}$. The lattice parameter uncertainties can be further controlled by taking the ratio $|V_{td}/V_{ts}|$, which directly uses ξ^{-1}, and incorporating the PDG combination of the $B_s^0\overline{B}_s^0$ oscillation frequency results from CDF (Abulencia et al., 2006b) and LHCb (Aaij et al., 2012f), $\Delta m_s = 17.69 \pm 0.08$ ps^{-1}. Using an expression for $|V_{ts}|$ analogous to Eq. (17.2.1), we obtain $|V_{td}/V_{ts}| = 0.208 \pm 0.005$.

17.2.2 $B \to X(s,d)\gamma$

Loop-mediated radiative decays provide a set of processes complementary to B^0 and $\overline{B}^0$ oscillations from which the value of $|V_{td}/V_{ts}|$ can be derived using experimental branching fraction results together with inputs from lattice QCD. Since new physics may enter each type of process differently, a comparison of $|V_{td}/V_{ts}|$ extracted from both mixing and radiative decays provides a robust test of the consistency of the SM CKM paradigm or, conversely, offers a powerful probe for the presence of new physics (Descotes-Genon, Ghosh, Matias, and Ramon, 2011; Lenz et al., 2011). Amplitudes for the rare $\Delta F = 1$ decays $b \to d\gamma$ and $b \to s\gamma$, essentially proportional to V_{td} and V_{ts} respectively, have been measured using both inclusive and exclusive final states at the B Factories. These provide the experimental inputs necessary to calculate the ratio of CKM elements $|V_{td}/V_{ts}|$.

The details of the various experimental techniques used to measure the branching fractions for the radiative penguin $B \to X(s,d)\gamma$ processes are addressed in Section 17.9. Here, we discuss the calculation of the ratio $|V_{td}/V_{ts}|$ using a combination of the latest branching fraction results from *BABAR* (Aubert, 2008z, 2009r) and Belle (Nakao, 2004; Taniguchi, 2008) in the exclusive $B \to (\rho,\omega,K^*)\gamma$ modes, followed by calculation of the ratio using *BABAR*'s latest $B \to X_d\gamma$ semi-inclusive results (del Amo Sanchez, 2010q). Belle has no comparable semi-inclusive analysis as of the time of publication of this review. The exclusive and inclusive *BABAR* results use the same *BABAR* dataset as well as a similar event selection, and are thus highly correlated; they cannot be averaged easily. Since there are correlated inputs to both the inclusive and exclusive calculations, as well as non-trivial correlations in the theory assumptions, we forego any attempt here to make any combination of the exclusive and inclusive results.

In their measurements of combinations of the exclusive mode branching fractions, both *BABAR* (Aubert, 2008z) and Belle (Taniguchi, 2008) assume an exact isospin symmetry, *i.e.* $\Gamma(B^\pm \to \rho^\pm\gamma) \equiv 2\overline{\Gamma}(B^0 \to \rho^0\gamma)$, as well as $2\overline{\Gamma}(B^0 \to \rho^0\gamma) \equiv 2\overline{\Gamma}(B^0 \to \omega\gamma)$ However, these relations are not exact and symmetry-breaking corrections have been calculated (Ball, Jones, and Zwicky, 2007; Ball and Zwicky, 2006b). The asymmetry expected between ρ^0 and ω predominantly arises from the different form factors for these decays, while the principal contribution to symmetry breaking between neutral and charged ρ mesons is the presence of a weak annihilation diagram with photon emission from the spectator quark. Both collaborations report *CP*- and isospin-averaged results for $B \to (\rho,\omega)\gamma$ and $B \to \rho\gamma$, as well as branching fractions for contributing individual modes. *BABAR* and Belle have searched for isospin asymmetries in these modes, and no statistically significant asymmetry is observed in either the $\rho\gamma$ or $(\rho,\omega)\gamma$ modes. A discussion of the experimental measurements themselves, as well as related theoretical background, can be found below in Section 17.9.

Belle (Taniguchi, 2008) calculates the ratio of branching fractions from products of likelihoods for each of the individual $B \to (\rho,\omega)\gamma$ and $B \to K^*\gamma$ final states, which are convolved with residual systematics that do not cancel in the ratio of branching fractions, and finds

$$R_{\rho^0} = \frac{\mathcal{B}(B^0 \to \rho^0\gamma)}{\mathcal{B}(B^0 \to K^{*0}\gamma)} = 0.0206^{+0.0045+0.0014}_{-0.0043-0.0016}, \quad (17.2.3)$$

$$R_{\rho} = \frac{\mathcal{B}(B \to \rho\gamma)}{\mathcal{B}(B \to K^*\gamma)} = 0.0302^{+0.0060+0.0026}_{-0.0055-0.0028}, \quad (17.2.4)$$

$$R_{\rho/\omega} = \frac{\mathcal{B}(B \to (\rho,\omega)\gamma)}{\mathcal{B}(B \to K^*\gamma)} = 0.0284 \pm 0.0050^{+0.0027}_{-0.0029}, \quad (17.2.5)$$

where the first and second errors are statistical and systematic, respectively.

The *BABAR* result for the exclusive modes (Aubert, 2008z) employs a different strategy, first concatenating all $B \to (\rho,\omega)\gamma$ final states into a single dataset which is then simultaneously fit over all modes with an isospin constraint applied in order to extract the isospin-averaged $B \to (\rho,\omega)\gamma$ branching fraction. A similar procedure omitting the $\omega\gamma$ final state is used to produce the $B \to \rho\gamma$ branching fraction. The $B \to K^*\gamma$ branching fraction used in *BABAR*'s calculation of the ratio is taken from HFAG, and thus it is not possible to account for systematic experimental effects which may be common to both numerator and denominator in the ratio of branching fractions, and they quote only a total uncertainty for the branching frac-

tion ratio results,

$$R_{\rho^+} = \frac{\mathcal{B}(B^+ \to \rho^+\gamma)}{\mathcal{B}(B^+ \to K^{*+}\gamma)} = 0.030^{+0.012}_{-0.011}, \quad (17.2.6)$$

$$R_{\rho^0} = \frac{\mathcal{B}(B^0 \to \rho^0\gamma)}{\mathcal{B}(B^0 \to K^{*0}\gamma)} = 0.024 \pm 0.006, \quad (17.2.7)$$

$$R_{\omega} = \frac{\mathcal{B}(B^0 \to \omega\gamma)}{\mathcal{B}(B^0 \to K^{*0}\gamma)} = 0.012^{+0.007}_{-0.006}, \quad (17.2.8)$$

$$R_{\rho} = \frac{\mathcal{B}(B \to \rho\gamma)}{\mathcal{B}(B \to K^{*}\gamma)} = 0.042 \pm 0.009, \quad (17.2.9)$$

$$R_{\rho/\omega} = \frac{\mathcal{B}[B \to (\rho/\omega)\gamma]}{\mathcal{B}(B \to K^{*}\gamma)} = 0.039 \pm 0.008. \quad (17.2.10)$$

We use a weighted average of the common central values reported by each collaboration, given the total uncertainty for each measurement and symmetrizing uncertainties where applicable, to arrive at averaged values subsequently used in the calculation of $|V_{td}/V_{ts}|$,

$$\begin{aligned} R_{\rho^0} &= \frac{\mathcal{B}(B^0 \to \rho^0\gamma)}{\mathcal{B}(B^0 \to K^{*0}\gamma)} = 0.0219 \pm 0.0037, \\ R_{\rho} &= \frac{\mathcal{B}(B \to \rho\gamma)}{\mathcal{B}(B \to K^{*}\gamma)} = 0.0341 \pm 0.0052, \\ R_{\rho/\omega} &= \frac{\mathcal{B}(B \to (\rho,\omega)\gamma)}{\mathcal{B}(B \to K^{*}\gamma)} = 0.0320 \pm 0.0047. \end{aligned} \quad (17.2.11)$$

Both collaborations adopt similar formalisms to derive the ratio of CKM elements from the underlying experimental results, with the ratio $R_{\rm th}(\rho\gamma/K^*\gamma)$ (and similarly $R_{\rm th}(\omega\gamma/K^*\gamma)$) given by (Ali, Lunghi, and Parkhomenko, 2004; Ball, Jones, and Zwicky, 2007; Beneke, Feldmann, and Seidel, 2005; Bosch and Buchalla, 2005):

$$R_{\rm th}(\rho\gamma/K^*\gamma) = \frac{\mathcal{B}_{\rm th}(B \to \rho\gamma)}{\mathcal{B}_{\rm th}(B \to K^{*}\gamma)} \quad (17.2.12)$$

$$\equiv S_\rho \left|\frac{V_{td}}{V_{ts}}\right|^2 \frac{(M_B^2 - m_\rho^2)^3}{(M_B^2 - m_{K^*}^2)^3} \zeta^2 \left[1 + \Delta R(\rho/K^*)\right], \quad (17.2.13)$$

where m_ρ is the mass of the ρ meson, ζ is the ratio of the transition form factors, $\zeta = \overline{T}_1^\rho(0)/\overline{T}_1^{K^*}(0)$ and $S_\rho = 1$ and 1/2 for the $\rho^\pm$ and ρ^0 mesons, respectively. A similar expression applies for $B \to (\rho,\omega)\gamma$ with the substitution $\rho \to (\rho,\omega)$ based on the symmetries defined above. These theoretical relations are based on the method of QCD factorization; the application of this method to radiative decays is discussed in Section 17.9. Within such factorization formulae, process-independent non-perturbative functions like form factors are separated from perturbatively calculable functions. Here, the main sources of theoretical uncertainties are the form factors and the Λ/m_b corrections. The former is expected to be reduced by taking ratios of the observables. The α_S corrections to the hard kernels and the power corrections, both included in the ratio in Eq. (17.2.13) via the factor $(1 + \Delta R)$, introduce further dependences on the CKM matrix elements, namely ϕ_2 as given in Eq. (16.5.4) and $R_{ut} = |V_{ud}V_{ub}^*/V_{td}V_{tb}^*|$, and one finds numerically (Beneke, Feldmann, and Seidel, 2005):

$$\Delta R(\rho^\pm/K^{*\pm}) = \left\{1 - 2R_{ut}\cos\phi_2\,[0.24^{+0.18}_{-0.18}] + R_{ut}^2\,[0.07^{+0.12}_{-0.07}]\right\}, \quad (17.2.14)$$

$$\Delta R(\rho^0/K^{*0}) = \left\{1 - 2R_{ut}\cos\phi_2\,[-0.06^{+0.06}_{-0.06}] + R_{ut}^2\,[0.02^{+0.02}_{-0.01}]\right\}. \quad (17.2.15)$$

These results are consistent with the predictions given in the literature (Ali, Lunghi, and Parkhomenko, 2004; Ball, Jones, and Zwicky, 2007; Bosch and Buchalla, 2005). The neutral mode is better suited for the determination of $|V_{td}/V_{ts}|$ than the charged mode, in which the function ΔR is dominated by the weak annihilation contribution, which leads to a larger error. The most recent determination of the ratio ζ within the light-cone QCD sum rule approach (Ball and Zwicky, 2006b), $1/\zeta = 1.17 \pm 0.09$, leads to the determination of $|V_{td}/V_{ts}|$ via Eq. (17.2.13). However, the experimental data on the branching fractions of $B \to K^*\gamma$ and $B \to \rho\gamma$ calls for a larger error on ζ, if one assumes no large power corrections beyond the known annihilation terms (Beneke, Feldmann, and Seidel, 2005) (see also Section 17.9.4.1).

Using the combined results from both experiments, we obtain

$$\left|\frac{V_{td}}{V_{ts}}\right|_{\rho^0} = 0.26 \pm 0.02 \pm 0.03, \quad (17.2.16)$$

$$\left|\frac{V_{td}}{V_{ts}}\right|_{\rho} = 0.22 \pm 0.02 \pm 0.02, \quad (17.2.17)$$

$$\left|\frac{V_{td}}{V_{ts}}\right|_{\rho,\omega} = 0.21 \pm 0.02 \pm 0.02, \quad (17.2.18)$$

where the first error is the total experimental uncertainty and the second is the theory uncertainty. *BABAR* additionally reports the ratio for the two exclusive modes not measured by Belle:

$$\left|\frac{V_{td}}{V_{ts}}\right|_{\rho^+} = 0.198^{+0.039}_{-0.035} \pm 0.016, \quad (17.2.19)$$

$$\left|\frac{V_{td}}{V_{ts}}\right|_{\omega} = 0.202^{+0.058}_{-0.050} \pm 0.016. \quad (17.2.20)$$

Although experimental uncertainties on the exclusive branching fractions may be substantially reduced in the future, irreducible theory uncertainties can complicate interpretation of any observed discrepancy in $|V_{td}/V_{ts}|$ with values from other processes. Such uncertainties are generally under better control for inclusive radiative penguin decays, where $|V_{td}/V_{ts}|$ has been calculated to next-to-leading-log (NLL) precision (Ali, Asatrian, and Greub, 1998). Following this formalism, the ratio of the inclusive branching fractions can be written as a function of

the Wolfenstein parameters λ, $\overline{\rho}$, $\overline{\eta}$

$$\begin{aligned} R(d\gamma/s\gamma) = & \\ & \lambda^2[1+\lambda^2(1-2\overline{\rho})]\,[(1-\overline{\rho})^2+\overline{\eta}^2+ \\ & \frac{D_u}{D_t}(\overline{\rho}^2+\overline{\eta}^2)+\frac{D_r}{D_t}(\overline{\rho}(1-\overline{\rho})-\overline{\eta}^2)]\,, \\ & \simeq 0.046 \;\; [\text{for } (\rho,\eta)=(0.11,0.33), \\ & \qquad\qquad \text{or } (\overline{\rho},\overline{\eta})=(0.107,0.322)]\,, \end{aligned} \quad (17.2.21)$$

where the quantities D_i, which depend on several input parameters such as m_t, m_b, m_c, must be calculated numerically. As with the exclusive decays, care must be taken to use a set of input parameters determined independently from $|V_{td}|$ and $|V_{ts}|$. For the *BABAR* result, this was done by re-expressing the Unitarity Triangle apex $(\overline{\rho}, \overline{\eta})$ as a function of ϕ_1 and using the HFAG world-average for ϕ_1. Given the current HFAG world-average values of the CKM inputs, the theory uncertainty on the ratio $R(d\gamma/s\gamma)$ is expected to be $< 0.2\%$, an order of magnitude smaller than the uncertainty for the exclusive modes prediction.

The *BABAR* analysis (del Amo Sanchez, 2010q) of the $b \to d\gamma$ and $b \to s\gamma$ inclusive rates used in the calculation of $|V_{td}/V_{ts}|$ are extrapolated from measurements of the partial decay rates to seven exclusive hadronic final states, shown in Table 17.9.6, in the mass ranges $0.5 < M(X_d) < 1.0\,\text{GeV}/c^2$ and $1.0 < M(X_d) < 2.0\,\text{GeV}/c^2$. The low-mass region contains contributions that are highly correlated with the dataset used for the *BABAR* exclusive modes analysis and, in the inclusive analysis, it is assumed that there is no non-resonant signal component in this mass range.

To obtain the inclusive rates, the experimentally determined partial rates must be corrected for the fraction of missing final states, as well as for hadronic systems with $M(X) > 2.0\,\text{GeV}/c^2$. Well-characterized corrections for final states with neutral kaons and non-reconstructed ω final states are made in the low-mass region. In the high-mass region, the missing fractions depend on the details of the fragmentation of the hadronic system, which is modeled using `Jetset` (Sjöstrand, 1995) and expected to be different for X_d and X_s. The Kagan-Neubert photon spectrum model (Kagan and Neubert, 1998) is used to correct for the mass region above $2.0\,\text{GeV}/c^2$ that is not measured. The photon spectra for $b \to d\gamma$ and $b \to s\gamma$ are expected to be nearly identical, and the uncertainty in the extrapolation is mainly from lack of knowledge of the details of the underlying fragmentation process. In the high-mass region, this is the largest contribution to the total systematic uncertainty. *BABAR* finds

$$\frac{\mathcal{B}(b\to d\gamma)}{\mathcal{B}(b\to s\gamma)} = 0.040 \pm 0.009 \pm 0.010\,, \quad (17.2.22)$$

and determines

$$\left|\frac{V_{td}}{V_{ts}}\right| = 0.199 \pm 0.022 \pm 0.024 \pm 0.002\,, \quad (17.2.23)$$

where the first error is purely statistical, the second accounts for systematic effects including the uncertainty in the extrapolation for the missing mass and final states, and the third uncertainty is purely from theory considerations.

There is good agreement among the values of $|V_{td}/V_{ts}|$ obtained from exclusive and inclusive analyses of radiative penguin processes. The farthest outlier from the central value of $|V_{td}/V_{ts}|$ is obtained from the average of the ρ^0 mode. However, all results are in reasonable agreement with each other. While the total uncertainty in the current results for the exclusive and inclusive approaches is comparable, the relatively very small inclusive theory uncertainty will make it a more sensitive observable at future flavor facilities that plan to integrate much larger datasets than available at Belle or *BABAR*. Comparing these results with the $|V_{td}/V_{ts}|$ value from mixing, there is also good agreement, albeit with substantially larger uncertainties for the radiative decays results. For any future Belle inclusive analysis, it seems reasonable to assume that the uncertainty will be similar to that for their exclusive analysis, just as at *BABAR*. This would allow for more precise comparisons between $|V_{td}/V_{ts}|$ from rare radiative decays and from mixing.

17.2.3 Summary

A direct determination of $|V_{ts}|$ and $|V_{td}|$ from a measurement of the decays $t \to s$ and $t \to d$ at LHC is difficult, and will likely remain so at least in the near future. Indirect methods involving virtual top quarks are therefore required to measure these CKM matrix elements. At the B Factories, the FCNC transitions $b \to s$ and $b \to d$ in radiative penguin processes have been used to obtain measurements of the ratio $|V_{td}/V_{ts}|$, while the value of $|V_{td}|$ has been obtained from measurements of B_d mixing. Extracting the values of the CKM elements from these processes necessarily assumes there are no contributions from physics beyond the SM and it is difficult to distinguish possible NP contributions, which may enter at the same order as the lowest order SM processes.

The major uncertainties in the existing measurements originate from ignorance of the hadronic matrix elements. The current method for extracting $|V_{td}|$ and $|V_{ts}|$ from $\Delta B = \pm 2$ processes relies heavily on lattice calculations, and any further experimental improvements in $\Delta m_{s/d}$ measurements will need to be matched by corresponding improvements in the lattice calculations. Likewise, for improvement in the precision of $|V_{td}|$ and $|V_{ts}|$ extracted from radiative penguin processes, significant advances in the theoretical methods will be necessary.

Experimentally, it may be possible at future super flavor factories to make a fully inclusive branching fraction measurement of $b \to d\gamma$, as well as $b \to s\ell^+\ell^-$ and $b \to d\ell^+\ell^-$, which will help to reduce theory and model dependences. In $b \to s\ell^+\ell^-$ and $b \to d\ell^+\ell^-$ decays, additional amplitudes arise from diagrams similar to Fig. 17.2.1 but with a Z boson replacing the photon (see Section 17.9 for a discussion of these modes). Because the contribution of these additional electroweak amplitudes becomes greater, and the contribution from the photon pole decreases, with increasing invariant mass of the di-lepton

final state, extracting $|V_{td}/V_{ts}|$ as a function of dilepton mass using these decays may allow one to disentangle any underlying new physics contributions from those of the SM CKM matrix elements. Finally, if such future facilities obtain enough data at the $\Upsilon(5S)$, it may also be possible to very cleanly determine $|V_{td}/V_{ts}|$ from the ratio of branching fractions for the annihilation penguin processes $B_d \to \gamma\gamma$ and $B_s \to \gamma\gamma$ (Bosch and Buchalla, 2002a). These di-photon modes are further discussed below in Section 17.11.

17.3 Hadronic B to charm decays

Editors:
Richard Kass (BABAR)
Martin Beneke (theory)

Additional section writers:
Justin Albert, Vincent Poireau, Stephen Schrenk

17.3.1 Introduction

B meson decays into all hadronic final states containing open charm or charmonium account for almost three quarters of all B decays. Despite constituting the majority of final states, these decays pose a challenge to both experiment and theory. The large available phase space in a B meson decay means that there are hundreds of possible final states all with rather small branching fractions, typically a few tenths of a percent. Therefore to study in detail any particular final state a very large sample of B mesons is necessary as well as a detector capable of measuring the energy, momentum, and identity of the final state particles to high precision. Since these are all hadronic final states, decay rate calculations must be done using non-perturbative QCD. For the majority of final states, a quantitative prediction with controlled theoretical uncertainties remains out of reach. Only the decay rates of the simplest hadronic decays to charm, such as $\overline{B}^0 \to D^+\pi^-$, can be calculated from first principles using QCD.

In spite of the above drawbacks, hadronic B decays to charm play an important role in the more glamorous aspects of B physics, *i.e.* the determination of the CKM parameters, measurements of *CP* violation, and search for physics beyond the Standard Model. If for no other reason these decay modes must be measured in order to understand the possible backgrounds involved in a measurement of a CKM parameter. Although the branching fractions here are small, it is still possible to collect very clean samples of B events using modes such as $B \to D\pi$, $B \to D^*\pi$, etc. Two-body decays such as $\overline{D}^0\pi^+$ and $D^-\pi^+$ provide important detector calibration tools for determining momentum resolution ($\pi^\pm$, $K^\pm$; see Sections 2.2.2, 6.2), electromagnetic energy resolution (π^0, η; see Section 2.2.4), mass resolution (D, B; see Chapter 7), secondary vertex location (D, K^0_s; see Chapter 6), and particle identification efficiency and rejection (π/K; see Chapter 5). Finally, precision measurements of modes such as $B \to D^{(*)}\pi$, $D^{(*)}\pi\pi$ may serve as standard candles for QCD calculations.

In this section we are mainly concerned with decay rates and not the specifics of how the final states are reconstructed and the techniques involved. These techniques are described in detail in Chapters 7 (B reconstruction), 12 (angular analysis), and 13 (Dalitz analysis).

17.3.2 Theory overview

A first principles calculation of the decay rate of the full set of B decays to charm, and even the two-body final states only, is still beyond our capabilities. Instead a variety of approaches to these calculations have been tried with various levels of success. An excellent and still relevant discussion of these techniques can be found in Chapters 2 and 10 of (Harrison and Quinn, 1998). In the following overview we cover the generalized factorization approach of Bauer, Stech, and Wirbel (1987) (BSW) and Neubert and Stech (1998) (NS), and the QCD factorization approach (Beneke, Buchalla, Neubert, and Sachrajda, 2000), which provides a first principles calculation for a limited class of final states.

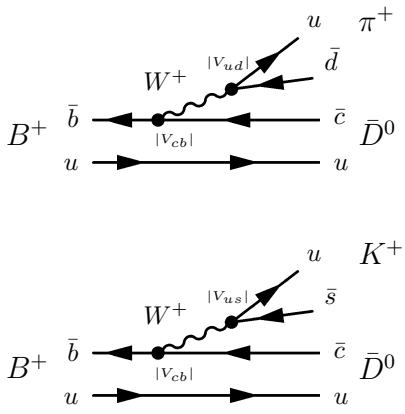

Figure 17.3.1. Dominant Feynman diagrams contributing to the decays $B^+ \to \overline{D}^0\pi^+$ (top) and $B^+ \to \overline{D}^0K^+$ (bottom).

We begin our discussion with $b \to c\bar{u}d$ transitions. The case of $b \to c\bar{u}s$ is completely analogous. Examples for these transitions are shown in Fig. 17.3.1. A popular and useful approach to calculate decay rates (especially for two-body B decays) is the factorization ansatz. To understand this technique, consider the decays that are shown in Fig. 17.3.2. In this figure only the electroweak contributions to the decay amplitudes are shown. A naïve attempt to calculate the decay rate would write the matrix element in terms of the usual currents, *e.g.*, $\bar{c}\gamma_u(1-\gamma_5)b$. However, this is clearly a drastic approximation as it neglects the all important role of gluons in the production of the final state hadrons. Nevertheless, at this early stage of calculation an important distinction becomes apparent. The decay $B^+ \to \overline{D}^0\pi^+$ can proceed through two amplitudes as shown in Figs 17.3.2a) and b). Since all final state particles must be color singlets, diagram b) will be suppressed due to color matching relative to a) by $1/N_c$, with N_c the number of colors. Amplitudes such as Fig. 17.3.2 a) are known as "color-allowed" while an amplitude such as Fig. 17.3.2 b) is often called "color-suppressed". The decay

$B^0 \to D^-\pi^+$ shown in Fig. 17.3.2 c) is color-allowed, while $B^0 \to \overline{D}^0\pi^0$, Fig. 17.3.2 d), is color-suppressed. Although not suitable for a quantitative prediction, the notion of color suppression provides a useful guide to the hierarchies in the branching fractions of B to charm decays, in addition to the hierarchies caused by the CKM elements.

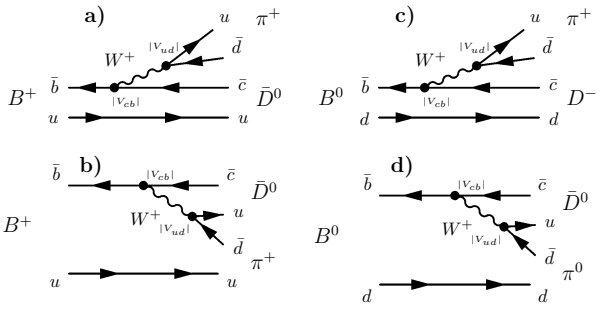

Figure 17.3.2. Two-body Feynman diagrams contributing to the $B^+ \to \overline{D}^0\pi^+$ (a, b) and $B^0 \to D\pi$ (c, d) decays.

For a more detailed discussion we recall the effective Hamiltonian

$$H_{\rm eff} = \frac{G_F}{\sqrt{2}} V_{cb}V_{ud}^* \Bigg\{ \left(C_1 + \frac{C_2}{N_c}\right) [\bar{c}_i b_i]_{\rm V-A} [\bar{d}_k u_k]_{\rm V-A} + 2C_2\, [\bar{c}_i T^a_{ij} b_j]_{\rm V-A} [\bar{d}_k T^a_{kl} u_l]_{\rm V-A} \Bigg\} \tag{17.3.1}$$

for the $b \to c\bar{u}d$ transition. Here C_1 and C_2 are Wilson coefficients that account for short-distance QCD effects and Eq. (17.3.1) includes the color indices i, j, k, l. In the naïve factorization approach the $\langle D^+\pi^-|H_{\rm eff}|\overline{B}^0\rangle$ matrix element is separated into currents by inserting the QCD vacuum state, which ignores all long-distance QCD interactions between the currents. Applied to $\overline{B}^0 \to D^+\pi^-$ ($B^0 \to D^-\pi^+$ in Fig. 17.3.2c) the "factorized" matrix element is now:

$$\frac{G_F}{\sqrt{2}} V_{cb}V_{ud}^*\, a_1\, \langle D^+|\bar{c}\gamma_\mu(1-\gamma_5)b|\overline{B}^0\rangle \langle \pi^-|\bar{d}\gamma^\mu(1-\gamma_5)u|0\rangle \tag{17.3.2}$$

with $a_1 = C_1 + C_2/N_c$. The matrix element of the color-octet operator is set to zero in the factorization approximation. Decays which involve this combination of Wilson coefficients are often called color-allowed or Type I transitions. In addition there are also color-suppressed (or Type II) transitions. As an example $B^0 \to \overline{D}^0\pi^0$ is illustrated in Fig. 17.3.2 d). Here one first uses a so-called Fierz identity $[\overline{\psi}_1\psi_2]_{\rm V-A}[\overline{\psi}_3\psi_4]_{\rm V-A} = [\overline{\psi}_3\psi_2]_{\rm V-A}[\overline{\psi}_1\psi_4]_{\rm V-A}$ to rearrange the four-fermion operators in $H_{\rm eff}$ into the form $[\bar{d}b]_{\rm V-A}[\bar{c}u]_{\rm V-A}$. Then the factorized amplitude similar to Eq. (17.3.2) for this process is

$$\frac{G_F}{\sqrt{2}} V_{cb}V_{ud}^*\, a_2\, \langle \pi^0|\bar{d}\gamma_\mu(1-\gamma_5)b|\overline{B}^0\rangle \langle D^0|\bar{c}\gamma^\mu(1-\gamma_5)u|0\rangle, \tag{17.3.3}$$

where now $a_2 = C_2 + C_1/N_c$. Finally there are decay modes such as $B^+ \to \overline{D}^0\pi^+$ (Fig. 17.3.2 a) and b)) which are a combination of color-allowed and color-suppressed amplitudes. These decays are called "Type III" processes.

In the absence of any QCD effects, $C_1 = 1$ and $C_2 = 0$, and we recover the estimate based on color-matching. Short-distance QCD effects renormalize the Wilson coefficients, such that at the mass scale $\mu = m_b = 4.8$ GeV we have $a_1 \approx 1$ and $a_2 \approx 0.2$. The value of a_2 is strongly scale-dependent. The uncanceled scale-dependence of the physical amplitude is a clear manifestation of the shortcomings of the naïve factorization approach. As we discuss below, factorization is expected to work more reliably for the color-allowed amplitude.

In applying Eqs (17.3.2) and (17.3.3) the matrix elements with the quarks are usually written in the familiar forms:

$$\langle \pi|\bar{d}\gamma_\mu\gamma_5 u|0\rangle = -if_\pi q_\mu \tag{17.3.4}$$

$$\langle D|\bar{c}\gamma_\mu b|B\rangle = f_+(q^2)(p_B + p_D)_\mu + f_-(q^2)q_\mu. \tag{17.3.5}$$

Here $q = p_B - p_D$ where p_D and p_B are the D and B 4-momentum respectively and $q^2 = m_\pi^2$. The parameterization of the matrix elements in terms of the pion decay constant f_π and two $B \to D$ transition form factors follows from the spin and parity transformations of the meson states and current operators, and Lorentz invariance. Thus using the factorization approach, the amplitude Eq. (17.3.2) for $\overline{B}^0 \to D^+\pi^-$ can now be written conveniently as:

$$-i\frac{G_F}{\sqrt{2}} V_{cb}V_{ud}^* a_1 f_\pi f_+(m_\pi^2)(m_B^2 - m_D^2). \tag{17.3.6}$$

The pion decay constant and $B \to D$ form factor must be determined by other methods or from data (for the latter see Section 17.1.2).

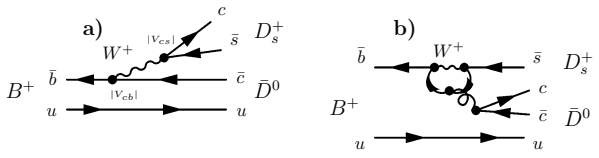

Figure 17.3.3. Spectator a) and penguin b) diagrams contributing to $B^+ \to D_s^+\overline{D}$.

This formalism can also be applied to $b \to c\bar{c}s$ (and the Cabibbo-suppressed $b \to c\bar{c}d$) transitions. The color-allowed amplitude leads to final states such as $B \to DD$

and $B \to DD_s$ with two charmed mesons. The color-suppressed amplitude produces a charmonium. The momentum transfer q^2 is now large, approximately m_D^2, and therefore both form factors (f_+, f_-) appear in the decay amplitude, which, *e.g.*, for $B^+ \to \overline{D}^0 D_s^+$ is now given by:

$$A_{\rm tree} = -i\frac{G_F}{\sqrt{2}} V_{cb}V_{cs}^* a_1\, f_{D_s} f_+(m_{D_s}^2)(m_B^2 - m_D^2)\,\mathcal{F}$$
$$\text{with} \quad \mathcal{F} = 1 + \frac{f_-(m_{D_s}^2)m_{D_s}^2}{(m_B^2 - m_D^2)f_+(m_{D_s}^2)}\,. \tag{17.3.7}$$

As shown in Fig. 17.3.3, these decays include contributions from penguin diagrams, since they contain two quarks with identical flavor. However, the penguin operator coefficients (C_3, C_4, C_5, C_6) in the effective Hamiltonian are all small, of the order of a few percent. The amplitude can be written as the sum of two pieces, $A_{\rm tree}$ and $A_{\rm peng}$:

$$\mathcal{A}(B \to DD) = A_{\rm tree} + A_{\rm peng}, \tag{17.3.8}$$

with an estimate $|A_{\rm peng}| < 0.1|A_{\rm tree}|$. It is important to note that while the decay rate is hardly changed by including the penguin contributions they are essential for the observation of direct *CP*-violating asymmetries (see Section 16.6).

A phenomenological approach to predict the branching fractions of hadronic B decays that incorporates factorization is followed in Bauer, Stech, and Wirbel (1987) (BSW) and Neubert and Stech (1998) (NS). In this approach the QCD effects and Wilson coefficients are captured by two phenomenological parameters, a_1 and a_2. Here a_1 represents the factor for decay modes that proceed via Type I (color-favored) amplitudes while a_2 is the corresponding factor for Type II (color-suppressed) amplitudes. Decay amplitudes that have contributions from both Type I and II amplitudes (Type III) contain a linear combination of a_1 and a_2. The values of a_1 and a_2 are determined from fits to measured B decay rates. For B meson decays the relative phase between a_1 and a_2 turns out to be positive, which implies constructive interference in the Type III decays. These constants, once determined, are assumed to apply universally to all two-body hadronic B final states.

Table 17.3.1 gives predictions from this model for several Type I, II, and III B decay modes as well as the current PDG (Beringer et al., 2012) values (dominated by *BABAR* and Belle results) for the corresponding branching fractions. The model reproduces well the Type I (color-favored) measurements as well as the Type III where the a_1 term dominates the amplitude. Not surprisingly, the Type II predictions differ considerably for some of the decay modes. In particular, the NS model predictions for the $K^{(*)}\psi'$ differ by a factor of two from the experimental measurements. For the $K\psi'$ modes, the prediction is half the measurement while for the $K^*\psi'$ modes the prediction is twice the measurement.

A generalization of factorization can indeed be rigorously derived from the first principles of QCD for the color-allowed amplitude of final states with one charmed meson (Beneke, Buchalla, Neubert, and Sachrajda, 2000). The physical picture is that of color transparency (Bjorken, 1989): in the heavy-quark mass limit, the light meson (*e.g.* the pion) is emitted as a compact color-singlet object with large momentum from the $B \to D$ transition region. In the QCD factorization approach of BBNS (Beneke, Buchalla, Neubert, and Sachrajda, 2000) the coefficient a_1 is written as

$$a_1(M) = \sum_{i=1,2} C_i \int_0^1 du\, T_i(u)\Phi_M(u), \tag{17.3.9}$$

up to $1/m_b$ corrections, where Φ_M denotes the light-cone distribution amplitude of the light meson, which, roughly speaking, describe how the longitudinal momentum of the energetic meson M is shared between the quark and antiquark in the meson, and $T_i(u)$ is a function that can be calculated order by order in the strong coupling $\alpha_s(m_b)$. At tree level, the QCD factorization result reproduces naïve factorization. At the one-loop order, the previously neglected matrix element of the color-octet operator in Eq. (17.3.1) is now non-zero, and leads to a consistent cancellation of the renormalization scale dependence. A consequence of this is that a_1 is non-universal, and depends on the light final state meson M. However, the non-universality is small, a few percent, as is the correction to naïve factorization. In Table 17.3.1, the decay modes labeled "Type I" receive small corrections to factorization, see (Beneke, Buchalla, Neubert, and Sachrajda, 2000).

Unfortunately, the color-suppressed amplitude a_2 in heavy-light final states and the color-allowed amplitude in all final states with two charmed mesons, are not accessible to a rigorous factorization treatment. Counting powers of the small quantity $\Lambda_{\rm QCD}/m_b$ shows that the color-suppressed amplitude in $B \to D\pi$ and related decays is $1/m_b$ suppressed, but the parametric suppression from the form factors and decay constants is not operative in practice. This implies that contrary to the Type I decays, there are no first-principles calculations of Type II and III modes. The same statement applies to the calculation of *CP*-violating charge asymmetries in decays to two charmed mesons.

It is instructive to compare the Type I, II, and III amplitudes for the $B \to D\pi$ final states. In complete generality, we may write

$$\mathcal{A}(\overline{B}^0 \to D^+\pi^-) = T + A, \tag{17.3.10}$$
$$\sqrt{2}\,\mathcal{A}(\overline{B}^0 \to D^0\pi^0) = C - A, \tag{17.3.11}$$
$$\mathcal{A}(B^- \to D^0\pi^-) = T + C, \tag{17.3.12}$$

where T stands for the "color-allowed tree topology", C for "color-suppressed tree topology", and A for "annihilation topology". Since the three final states are related by exchanges of up and down quark, and since the corresponding $SU(2)$ isospin symmetry is a very good approximate symmetry of the QCD Lagrangian, only two of the three amplitudes are independent. The isospin relation $\mathcal{A}(\overline{B}^0 \to D^+\pi^-) + \sqrt{2}\,\mathcal{A}(\overline{B}^0 \to D^0\pi^0) + \mathcal{A}(B^- \to D^0\pi^-) = 0$ allows one to regard $(T + A)$ and $(C - A)$

Table 17.3.1. Predictions of branching fractions of the Neubert & Stech (NS) model (Neubert and Stech, 1998) using $a_1 = 0.98$ and $a_2 = 0.29$ and comparisons with the PDG (Beringer et al., 2012) values.

Decay mode	NS Model	$\mathcal{B}_{\rm theo}(\times 10^{-3})$	PDG $\mathcal{B}(\times 10^{-3})$
	Type I		
$D^-\pi^+$	$0.318a_1^2$	3.0	2.68±0.13
D^-K^+	$0.025a_1^2$	0.2	0.197±0.021
$D^-\rho^+$	$0.778a_1^2$	7.5	7.8±1.3
D^-K^{*+}	$0.041a_1^2$	0.4	0.45±0.07
$D^-a_1^+$	$0.844a_1^2$	8.1	6.0±2.2±2.4
$D^{*-}\pi^+$	$0.296a_1^2$	2.8	2.76±0.13
$D^{*-}K^+$	$0.022a_1^2$	0.2	0.214±0.016
$D^{*-}\rho^+$	$0.870a_1^2$	8.4	6.8±0.9
$D^{*-}K^{*+}$	$0.049a_1^2$	0.5	0.33±0.06
$D^{*-}a_1^+$	$12.17a_1^2$	11.6	13.0±2.7
	Type II		
$\overline{D}^0\pi^0$	$0.084a_2^2$	0.07	0.263±0.014
K^0J/ψ	$0.800a_2^2$	0.7	0.871±0.032
K^+J/ψ	$0.852a_2^2$	0.7	1.013±0.034
$K^0\psi'$	$0.326a_2^2$	0.3	0.62±0.05
$K^+\psi'$	$0.347a_2^2$	0.3	0.639±0.033
$K^{*0}J/\psi$	$2.518a_2^2$	2.1	1.33±0.06
$K^{*+}J/\psi$	$2.680a_2^2$	2.3	1.43±0.08
$K^{*0}\psi'$	$1.424a_2^2$	1.2	0.61±0.05
$K^{*+}\psi'$	$1.516a_2^2$	1.3	0.67±0.14
π^0J/ψ	$0.018a_2^2$	0.02	0.0176±0.0016
π^+J/ψ	$0.038a_2^2$	0.03	0.049±0.004
ρ^0J/ψ	$0.050a_2^2$	0.04	0.027±0.004
ρ^+J/ψ	$0.107a_2^2$	0.09	0.050±0.008
	Type III		
$\overline{D}^0\pi^+$	$0.338(a_1 + 0.729a_2(f_D/200\,\text{MeV}))^2$	4.8	4.84±0.15
$\overline{D}^0\rho^+$	$0.828(a_1 + 0.450a_2(f_D/200\,\text{MeV}))^2$	10.2	13.4±1.8
$\overline{D}^{*0}\pi^+$	$0.315(a_1 + 0.886a_2(f_{D^*}/230\,\text{MeV}))^2$	4.8	5.19±0.26
$\overline{D}^{*0}\rho^+$	$0.926(a_1^2 + 0.456a_2^2(f_{D^*}/230\,\text{MeV})^2 + 1.291a_1a_2(f_{D^*}/230\,\text{MeV}))$	12.6	9.8±1.7
$\overline{D}^{*0}a_1^+$	$1.296(a_1^2 + 0.128a_2^2(f_{D^*}/230\,\text{MeV})^2 + 0.269a_1a_2(f_{D^*}/230\,\text{MeV}))$	13.6	19±5

as the two independent amplitudes. These amplitudes are complex due to strong-interaction phases from final-state interactions. Only the relative phase of the two independent amplitudes is an observable. We define δ_{TC} to be the relative phase of $(T + A)$ and $(C - A)$. The QCD factorization formula implies that (Beneke, Buchalla, Neubert, and Sachrajda, 2000)

$$\left|\frac{C-A}{T+A}\right| = O(\Lambda_{\rm QCD}/m_b), \qquad \delta_{TC} = O(1). \quad (17.3.13)$$

Treating the charm meson as a light meson compared to the scale m_b, one finds that it is not difficult to accommodate $|C - A|/|T + A| \sim 0.2 - 0.3$ and a large phase $\delta_{TC} \sim 40°$, which is in qualitative agreement with experimental results. The large phase shows that large corrections to naïve factorization must be expected for the color-suppressed amplitude in heavy-light decays.

The situation for B decays to charmonium is ambiguous. QCD factorization formally holds for these decays despite their color suppression, since the "emitted" charmonium is a compact object (Beneke, Buchalla, Neubert, and Sachrajda, 2000). However, various corrections from soft gluon reconnections (Melic, 2004) and color-octet contributions (Beneke and Vernazza, 2009) turn out to be very large relative to the formally dominant color-suppressed amplitude, and prevent a reliable prediction. One should therefore expect large corrections to the naïve factorization and generalized factorization (BSW) estimates of these decay modes, as is indeed observed. Again, these uncertainties prevent a reliable calculation of the (small) *CP*-violating charge asymmetries for final states such as $K\psi$.

While the BSW/NS approach to factorization and the QCD factorization approach (where applicable) provides estimates in agreement with many measured branching fractions, extending this technique to decays with more than two particles in the final state (*e.g.* $B \to D\pi\pi$ or $B^0 \to D^{*-}\pi^+\pi^+\pi^-\pi^0$) is not nearly as successful. A fundamental problem here is that some of the final state particles are the result of gluons and therefore the role of QCD can not be ignored. In (Reader and Isgur, 1993) the problem of multi-body decays with D's and π's in the final state is discussed using results from heavy-quark symmetry and factorization. Here the decay process proceeds through intermediate states such as $D\rho$ or $D_2^*\pi$ and the contributions are summed to obtain the total branching fraction. Unfortunately, for many of the modes mentioned in (Reader and Isgur, 1993) and Table 17.3.2, precision measurements are lacking, making a detailed comparison not possible. In Table 17.3.2 the entries with a ">" indicate modes where only an intermediate state and not the explicit final state has been measured. In these cases the measured branching fraction of the intermediate state is taken as the lower limit of the branching fraction of the mode of interest. An example of such a mode is $\overline{D}^0\pi^+\pi^0$ where only the intermediate state $\overline{D}^0\rho^+$ has been measured. For this mode we note that their model's prediction for $B^+ \to \overline{D}^0\pi^+\pi^0$ of 0.59% is significantly lower than the measured $1.34 \pm 0.18\%$ for $\overline{D}^0\rho^+$.

Table 17.3.2. Branching fraction predictions of the RI model (Reader and Isgur, 1993) and comparisons with the PDG (Beringer et al., 2012) values. The entries with a ">" indicate modes where only an intermediate state and not the explicit final state has been measured. The measured branching fraction of the intermediate state is taken as the lower limit of the branching fraction of the mode of interest.

Decay mode	RI Model $\mathcal{B}$ ($\times 10^{-3}$)	PDG $\mathcal{B}$ ($\times 10^{-3}$)
$D^-\pi^+\pi^0$	5.9	$> 7.8\pm0.13$
$D^-\pi^+\pi^-$	0.7	0.84 ± 0.09
$\overline{D}^0\pi^+\pi^0$	5.9	$> 13.4\pm1.8$
$D^-\pi^+\pi^+$	0.7	1.07 ± 0.05
$D^{*-}\pi^+\pi^0$	7.5	15 ± 5
$D^{*0}\pi^+\pi^-$	1.1	0.62 ± 0.22
$D^{*0}\pi^+\pi^0$	7.5	$> 9.8\pm1.7$
$D^{*-}\pi^+\pi^+$	1.1	1.35 ± 0.22
$D^-\pi^+\pi^+\pi^-$	2.1	8.0 ± 2.5
$\overline{D}^0\pi^+\pi^+\pi^-$	2.1	11 ± 4
$D^{*-}\pi^+\pi^+\pi^-$	2.9	$> 13\pm3$
$D^{*-}\pi^+\pi^+\pi^0$	2.2	15 ± 7

17.3.3 Decays with a single D decay (D, D^*, D_s)

Due to the experiments at the B Factories there has been an enormous increase in both the number of single charm modes reconstructed and the precision of their branching fractions. As shown in Tables 17.3.3 and 17.3.4 the typical branching fractions for decay modes in this category are in the few tenths of a percent for the modes with a $W \to u\bar{d}$ transition and an order of magnitude smaller for modes with a $W \to u\bar{s}$ transition. In Fig. 17.3.1 the simplest diagrams for $B^+ \to \overline{D}^0\pi^+$ and $B^+ \to \overline{D}^0K^+$ are shown. Including the CKM factors V_{ud} and V_{us} at the relevant vertices explains the dominance of the pion modes over the kaon modes. Other mechanisms such as color-suppression can play an important role in simple two-body final states such as $\overline{D}^0\pi^0$ (Fig. 17.3.2 d). It is important to note that although these diagrams contain only pseudoscalars in the final state it is also likely that the quarks will hadronize into vector particles. Thus the D's can be replaced with D^*'s, π's with ρ's, K's with K^*'s, etc. Finally, the hadronization process also allows for more complicated final states such as $\overline{D}^0K^+K^*$, $D^{*-}3\pi^+\pi^-$, etc.

17.3.3.1 Two body final states

In this section we do not consider the kaon final states (*e.g.* $\overline{D}^0K^+$) as they are discussed in detail in Section 17.8 due to their important role in determining ϕ_3.

Color-favored two-body decay modes, $D^{(*)-}\pi^+$, $\overline{D}^{(*)0}\pi^+$, were studied in (Aubert, 2007g) using approximately one quarter of the final *BABAR* $\Upsilon(4S)$ data sample. These final states are such that even with relatively simple selection criteria (*e.g.* only using $\overline{D}^0 \to K^+\pi^-$ and $D^- \to K^+\pi^-\pi^-$), high purity samples are obtained. To illustrate the quality (*i.e.* very large signal to background) possible in hadronic B decays into charm we show the beam-energy-substituted mass plots ($m_{\rm ES}$) from (Aubert, 2007g) in Fig. 17.3.4. In all modes the systematic errors are at least a factor of two larger than the statistical errors. In general, there is good agreement between the model predictions in Table 17.3.1 and the branching fraction measurements from this study.

Color-suppressed two-body decay modes have been extensively studied in (Lees, 2011b; Blyth, 2006; Kuzmin, 2007; Schumann, 2005). In the most comprehensive study (Lees, 2011b) eight modes ($\overline{D}^{(*)0}X$, $X = \pi^0$, η, ω, η') are analyzed and their branching fractions measured. The results of this study are in agreement with previous *BABAR* and Belle measurements, although with higher precision. The improved precision in the branching fractions allows for a detailed comparison with predictions from factorization models (Chua, Hou, and Yang, 2002; Deandrea and Polosa, 2002; Eeg, Hiorth, and Polosa, 2002; Neubert and Stech, 1998) and perturbative QCD (pQCD) (Keum, Kurimoto, Li, Lu, and Sanda, 2004; Lu, 2003). There is poor agreement with the factorization predictions; in most cases the measurements are significantly larger than the expectation. In contrast, with the exception of $D^0\omega$ where the measurement is significantly lower than the prediction,

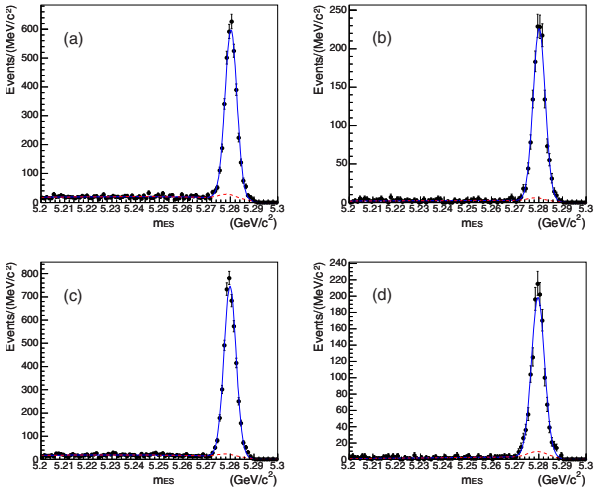

Figure 17.3.4. The $m_{\rm ES}$ distributions for (a) $B^0 \to D^- \pi^+$, (b) $B^0 \to D^{*-} \pi^+$, (c) $B^+ \to \overline{D}^0 \pi^+$, and (d) $B^+ \to \overline{D}^{*0} \pi^+$ (from Aubert, 2007g). In the figures the solid line is the fit to the data while the background component (including peaking background) is shown as a dashed line.

experiment and pQCD are close. These differences should not come as a surprise since there is no rigorous QCD approach to the color-suppressed amplitude, as discussed in the theory overview of this chapter. The experimental results along with the model predictions are given in Table VII of Lees (2011b).

B meson decay provides a convenient laboratory to study orbitally excited states of the D meson. For the case where a light quark is bound to a c quark, heavy quark effective theory (HQET) suggests that $\boldsymbol{j} = \boldsymbol{L} + \boldsymbol{s}_l$ with $\boldsymbol{s}_l$ the total angular momentum of the light quark and $\boldsymbol{L}$ the orbital angular momentum of the $c\overline{q}$ system will be a good quantum number. As a result, four $L = 1$ states are expected with total angular momentum and parity (J^P), and j values of 0^+ $(j = 1/2)$, 1^+ $(j = 1/2)$, 1^+ $(j = 3/2)$, and 2^+ $(j = 3/2)$. These states are known as the D_0^*, D_1', D_1, and D_2^* respectively. The states in the mass range of 2.2-2.8 GeV/c^2 are often collectively referred to as the D^{**}. Both *BABAR* and Belle have studied these states in detail using both specific decay channels (Aubert, 2006p; Abe, 2005i) and Dalitz plot analyses of $B^+ \to D^- \pi^+ \pi^+$ and $\overline{B}^0 \to D^0 \pi^+ \pi^-$ (Abe, 2004f; Kuzmin, 2007; Aubert, 2009g). In addition to branching fraction measurements these studies have also determined the masses and widths of these states. The results are in good agreement with the expectations of HQET. More details on those measurements can be found in Section 19.3.

A variety of final states with a D_s or D_s^* in addition to a scalar or vector meson were the subject of several studies by *BABAR* (Aubert, 2007l, 2008u) and Belle (Das, 2010; Joshi, 2010). These decays are of interest as they can proceed via color-suppressed W exchange (*e.g.* $B^0 \to D_s^{(*)-} K^{(*)+}$), and assuming $SU(3)$ flavor symmetry can be used to calculate the amplitude ratio $r(D^{(*)}\pi) = |A(B^0 \to D^{(*)+}\pi^-)|/|A(B^0 \to D^{(*)-}\pi^+)|$, an important parameter for the determination of $\sin(2\phi_1 + \phi_3)$ using $B^0 \to D^{\mp}\pi^{\pm}$. As shown in Tables 17.3.3 and 17.3.4 the branching fractions into $D_s^{(*)}X$ states are small, a few times 10^{-5}, as expected from CKM factors and the evident lack of rescattering in the W exchange modes. As predicted in Mantry, Pirjol, and Stewart (2003) the ratios $\mathcal{B}(B^0 \to D_s^- K^+)/\mathcal{B}(B^0 \to D_s^{*-} K^+)$ and $\mathcal{B}(B^0 \to D_s^- K^{*+})/\mathcal{B}(B^0 \to D_s^{*-} K^{*+})$ are consistent with one within the experimental uncertainties.

17.3.3.2 Three or more body final states

Given the large phase space available and mean charged multiplicity of almost six in B meson decay, final states with three or more particles make up a sizable amount of hadronic B decays. The branching fractions for many of the modes of the form $B \to \overline{D}^{(*)}(n\pi)$, $n = 2 - 5$ charged pions have been measured in (Aubert, 2009g) and (Abe, 2005i; Majumder, 2004). The analysis in (Majumder, 2004) illustrates a difficulty with final states involving a large number of particles, *i.e.* systematic errors from track finding dominate in such high multiplicity decays. It is also interesting to note the absence of branching fraction measurements with multiple π^0s (*i.e.* not a decay product of a $D^{(*)}$) in the final state.

The three-body decay, $B^0 \to D^{*-}\omega\pi^+$, has been used to study factorization in Aubert (2006ay). As discussed in Reader and Isgur (1993) and Ligeti, Luke, and Wise (2001) the factorization approach allows data from $\tau \to X\nu$ to be used to predict the properties of decays such as $B \to D^* X$, where X is the same hadronic system in both decays. The invariant mass spectrum of the $\omega\pi$ system was found to be in good agreement with the theoretical expectations based on factorization and τ decay data. In addition, a Dalitz plot analysis shows a non uniform distribution with a preference for $\omega\pi$ at low mass. A broad enhancement in the $D^*\pi$ system at about 2.5 GeV/c^2 may indicate the presence of $B^0 \to D_1'\omega$. Finally, the longitudinal polarization of the D^* was found to be in agreement with expectations of HQET.

Three-body decays with charged and neutral kaons as well as K^*s in the final state were studied in (Drutskoy, 2002). Even though only 29.4 fb^{-1} of data was used here (a small fraction of Belle's final data sample) five modes of the form $B \to D^{(0)} K K^{(*)0}$ were observed for the first time. An angular analysis of the KK^* system is consistent with the assignment $J^P = 1^+$ and that the decay mainly proceeds through an $a_1(1260)$ intermediate state.

The branching fraction and resonant substructure of the CKM-favored mode $B^0 \to \overline{D}^0 K^+ \pi^-$ (not including the D^*) was determined in (Aubert, 2006n). A motivation for studying this decay was to gain access to ϕ_3 through the interference of the $\overline{b} \to \overline{c}u\overline{s}$ and $\overline{b} \to \overline{u}c\overline{s}$ amplitudes and use the Dalitz plot to reduce the ambiguity in the strong phase. Unfortunately, the branching fraction turned out to be too small to be of practical use

in determining ϕ_3 with the final *BABAR* and Belle data samples.

Decays of the type $B \to D_s^{(*)} K\pi$ can proceed through the production of an $s\bar{s}$ pair "popping" out of the vacuum. Three such modes ($D_s^- K^+\pi^+$, $D_s^{*-} K^+\pi^+$, and $D_s^- K_s^0\pi^+$) as well as the CKM suppressed $D_s^- K^+ K^+$ mode were observed in (Aubert, 2008ai). The first two modes were also studied by Belle (Wiechczynski, 2009). Both groups find that the invariant mass distributions of the $D_s^{(*)} K^+$ subsystem are incompatible with three-body phase space and with enhancements near 2.7 GeV/c^2, suggestive of charm resonances below the $D_s^{(*)} K^+$ threshold.

17.3.4 Decays with 2 D's

17.3.4.1 $W \to c\bar{d}$

In the neutral $B \to D^{(*)+} D^{(*)-}$ decays, the interference of the dominant tree diagram (see Fig. 17.3.5 a) with the $B^0\overline{B}^0$ mixing diagram is sensitive to the CKM phase ϕ_1 . However, the theoretically uncertain contributions of penguin diagrams (Fig. 17.3.5 b) with different weak phases are potentially significant and may shift both the observed *CP* asymmetries and the branching fractions by amounts that depend on the ratios of the penguin to tree contributions and their relative phases.

The penguin-tree interference in neutral and charged $B \to D^{(*)} \overline{D}^{(*)}$ decays can also provide some sensitivity to the angle ϕ_3, with additional information on the branching fractions of $B \to D_s^{(*)} \overline{D}^{(*)}$ decays, assuming $SU(3)$ flavor symmetry between $B \to D^{(*)} \overline{D}^{(*)}$ and $B \to D_s^{(*)} \overline{D}^{(*)}$.

The color-suppressed decay modes $B^0 \to D^{(*)0} \overline{D}^{(*)0}$, if observed, would provide evidence of W-exchange or annihilation contributions (see Fig. 17.3.5 c, 17.3.5 d). In principle, these decays could also provide sensitivity to the CKM phase ϕ_1, if sufficient data were available.

The most precise published results on $D^{(*)} \overline{D}^{(*)}$ decays from the B Factories use exclusive reconstruction of these decays: all tracks and neutral energy from each of the decay chain products is reconstructed, and the reconstructed B meson is ultimately composed from these charged tracks and clusters. The D mesons are reconstructed in their decays to some or all of the following: $D^0 \to K^-\pi^+$, $K^-\pi^+\pi^0$, $K^-\pi^+\pi^+\pi^-$, K^+K^-, $K_S^0\pi^+\pi^-$, $K_S^0\pi^+\pi^-\pi^0$; and $D^+ \to K_S^0\pi^+$, $K_S^0\pi^+\pi^0$, $K_S^0 K^+$, $K^-\pi^+\pi^+$, $K^-K^+\pi^+$. The D^{*+} mesons are then reconstructed in their decays to $D^0\pi^+$ or $D^+\pi^0$. Charge conjugate decays are of course implied throughout. As the product branching fractions of these decays are small ($\mathcal{O}(10^{-7} - 10^{-6})$) particular attention must be paid to particle identification as well as background rejection, details of which can be found in Chapters 5 (charged particle identification) and 9 (background suppression). An example of an $m_{\rm ES}$ distribution with good signal-to-background is shown in Fig. 17.3.6.

Both *BABAR* and Belle have several results for these decays. The branching fraction results, as well as corresponding theoretical predictions, are summarized in Table 17.3.5.

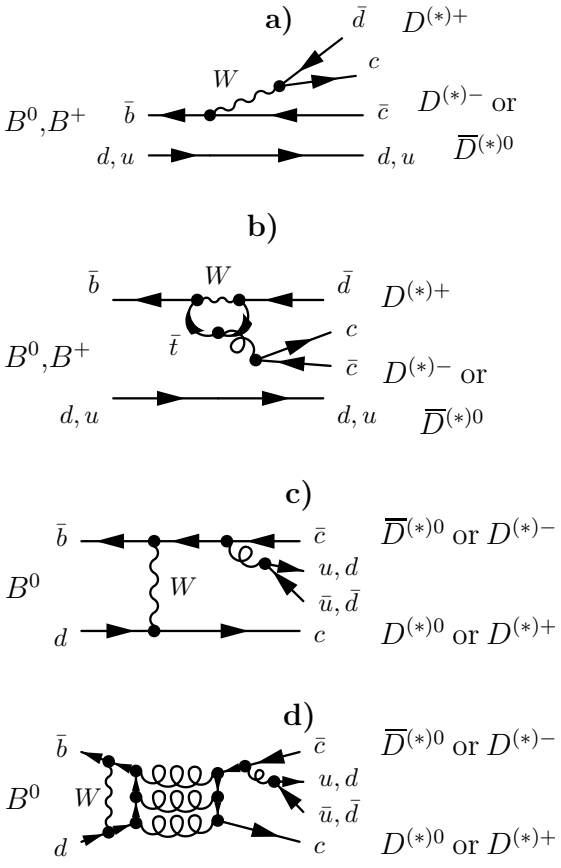

Figure 17.3.5. Feynman graphs for $B \to D^{(*)} \overline{D}^{(*)}$ decays: the tree (a) and penguin (b) diagrams are the leading terms for both $B^0 \to D^{(*)+} D^{(*)-}$ and $B^+ \to D^{(*)+} \overline{D}^{(*)0}$ decays, whereas the exchange (c) and annihilation (d) diagrams (the latter of which is OZI-suppressed) are the lowest-order terms for $B^0 \to D^{(*)0} \overline{D}^{(*)0}$ decays.

In addition to the branching fractions (and to the time-dependent *CP* asymmetries, detailed in Section 17.6), *CP*-violating charge asymmetries can be measured in the four charged $B \to D^{(*)} \overline{D}^{(*)}$ decays as well as in $B^0 \to D^{*\pm} D^{\mp}$, and also polarization can be measured in the vector-vector decays $B^0 \to D^{*+} D^{*-}$ and $B^+ \to D^{*+} \overline{D}^{*0}$. Those results are summarized in Tables 17.3.6 and 17.3.7 respectively.

The Cabibbo-favored $D_s^{(*)} \overline{D}^{(*)}$ decays (which can occur via tree and penguin diagrams analogous to those in Fig. 17.3.5a and b, each with the upper $\bar{d}$ replaced with an $\bar{s}$) typically have branching fractions an order of magnitude higher than their $D^{(*)} \overline{D}^{(*)}$ analogues, *i.e.* in the $\mathcal{O}(10^{-3} - 10^{-2})$ range rather than $\mathcal{O}(10^{-4} - 10^{-3})$. The measured and predicted branching fractions for these modes can be found in Table 17.3.8, and measured and predicted polarizations can be found in Table 17.3.9.

Table 17.3.3. Measured single charm B^+ branching fractions ($\mathcal{B}$) from *BABAR*, Belle, and the PDG (Beringer et al., 2012) (average). The PDG value may use measurements from other experiments when calculating the average.

	BABAR results		Belle results		PDG Averages
Final state	$\mathcal{B}$ ($\times 10^{-3}$)	Ref.	$\mathcal{B}$ ($\times 10^{-3}$)	Ref.	$\mathcal{B}$ ($\times 10^{-3}$)
$\overline{D}^0\pi^+$	$4.90 \pm 0.07 \pm 0.22$	(Aubert, 2007g)			4.84 ± 0.15
$\overline{D}^0K^+/\mathcal{B}(\overline{D}^0\pi^+)$	$83.1 \pm 3.5 \pm 2.0$	(Aubert, 2004l)	$67.7 \pm 2.3 \pm 3.0$	(Horii, 2008)	76 ± 6
$\overline{D}^0K^*(892)^+$	$0.529 \pm 0.030 \pm 0.034$	(Aubert, 2006q)			0.53 ± 0.04
$\overline{D}^0K^+\overline{K}^0$			$0.55 \pm 0.14 \pm 0.08$	(Drutskoy, 2002)	$0.55 \pm 0.14 \pm 0.08$
$\overline{D}^0K^+\overline{K}^*(892)^0$			$0.75 \pm 0.13 \pm 0.11$	(Drutskoy, 2002)	$0.75 \pm 0.13 \pm 0.11$
$D^*(2010)^-\pi^+\pi^+$			$1.25 \pm 0.08 \pm 0.22$	(Abe, 2004f)	1.35 ± 0.22
$D^-\pi^+\pi^+$	$1.08 \pm 0.03 \pm 0.05$	(Aubert, 2009g)	$1.02 \pm 0.04 \pm 0.15$	(Abe, 2004f)	1.07 ± 0.05
$\overline{D}^*(2007)^0\pi^+$	$5.52 \pm 0.17 \pm 0.42$	(Aubert, 2007g)			5.18 ± 0.26
$\overline{D}^*(2007)^0K^+$	$0.421^{+0.030}_{-0.026} \pm 0.021$	(Aubert, 2005t)	$0.40 \pm 0.11 \pm 0.02$	(Abe, 2001f)	0.420 ± 0.034
$\overline{D}^*(2007)^0K^*(892)^+$	$0.83 \pm 0.11 \pm 0.10$	(Aubert, 2004k)			0.81 ± 0.14
$\overline{D}^*(2007)^0K^+\overline{K}^*(892)^0$			$1.53 \pm 0.31 \pm 0.29$	(Drutskoy, 2002)	$1.53 \pm 0.31 \pm 0.29$
$\overline{D}^*(2007)^0\pi^+\pi^+\pi^-$			$10.55 \pm 0.47 \pm 1.29$	(Majumder, 2004)	10.3 ± 1.2
$\overline{D}^{*0}3\pi^+2\pi^-$			$5.67 \pm 0.91 \pm 0.85$	(Majumder, 2004)	$5.67 \pm 0.91 \pm 0.85$
$D^*(2010)^-3\pi^+\pi^-$			$2.56 \pm 0.26 \pm 0.33$	(Majumder, 2004)	$2.56 \pm 0.26 \pm 0.33$
$\overline{D}^{**0}\pi^+$	$5.9 \pm 1.3 \pm 0.2$	(Aubert, 2006p)			$5.9 \pm 1.3 \pm 0.2$
$\overline{D}_1(2420)^0\pi^+ \times \mathcal{B}(\overline{D}_1^0 \to \overline{D}^0\pi^+\pi^-)$			$0.185 \pm 0.029^{+0.035}_{-0.055}$	(Abe, 2005i)	$0.185 \pm 0.029^{+0.035}_{-0.055}$
$\overline{D}_1(2421)^0\pi^+ \times \mathcal{B}(\overline{D}_1^0 \to D^{*-}\pi^+)$			$0.68 \pm 0.07 \pm 0.13$	(Abe, 2004f)	$0.68 \pm 0.07 \pm 0.13$
$\overline{D}_2^*(2462)^0\pi^+ \times \mathcal{B}(\overline{D}_2^{*0} \to D^-\pi^+)$	$0.35 \pm 0.02 \pm 0.04$	(Aubert, 2009g)	$0.34 \pm 0.03 \pm 0.072$	(Abe, 2004f)	0.35 ± 0.04
$\overline{D}_2^*(2462)^0\pi^+ \times \mathcal{B}(\overline{D}_2^{*0} \to D^{*-}\pi^+)$			$0.18 \pm 0.03 \pm 0.04$	(Abe, 2004f)	$0.18 \pm 0.03 \pm 0.04$
$\overline{D}_0^*(2400)^0\pi^+ \times \mathcal{B}(\overline{D}_0^{*0} \to D^-\pi^+)$	$0.68 \pm 0.03 \pm 0.2$	(Aubert, 2009g)	$0.61 \pm 0.06 \pm 0.18$	(Abe, 2004f)	0.64 ± 0.14
$\overline{D}_1'(2427)^0\pi^+ \times \mathcal{B}(\overline{D}_1'^0 \to D^{*-}\pi^+)$			$0.50 \pm 0.04 \pm 0.11$	(Abe, 2004f)	$0.50 \pm 0.04 \pm 0.11$
$D_s^+\pi^0$	$0.016^{+0.006}_{-0.005} \pm 0.001$	(Aubert, 2007l)			$0.016^{+0.006}_{-0.005} \pm 0.001$
$D_s^-\pi^+K^+$	$0.202 \pm 0.013 \pm 0.038$	(Aubert, 2008ai)	$0.171^{+0.008}_{-0.007} \pm 0.025$	(Wiechczynski, 2009)	0.180 ± 0.022
$D_s^{*-}\pi^+K^+$	$0.167 \pm 0.016 \pm 0.035$	(Aubert, 2008ai)	$0.131^{+0.013}_{-0.012} \pm 0.028$	(Wiechczynski, 2009)	0.145 ± 0.024
$D_s^-K^+K^+$	$0.011 \pm 0.004 \pm 0.002$	(Aubert, 2008ai)			$0.011 \pm 0.004 \pm 0.002$

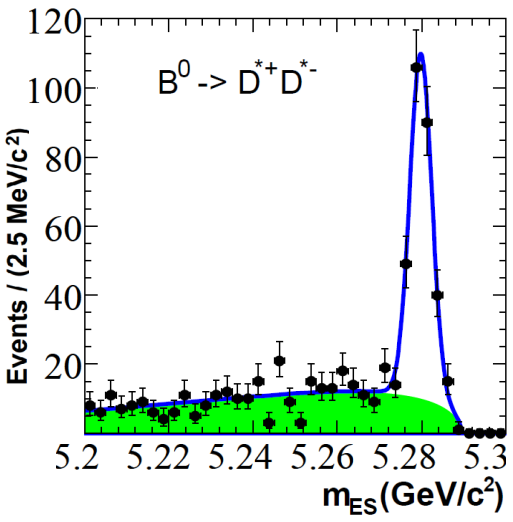

Figure 17.3.6. The $m_{\rm ES}$ distribution for $D^{*+}D^{*-}$ candidates from (Aubert, 2006m).

B mesons can also decay to $D_{sJ}^{(*)}\overline{D}^{(*)}$ states, with the multiple $D_{sJ}^{(*)}$ states having been discovered at the B Factories since the original observation of $D_{sJ}^*(2317)^+$ at *BABAR* in 2002. These decays are described in Section 19.3 of this Book, and specifically B decays to $D_{sJ}^{(*)}\overline{D}^{(*)}$ are described in Section 19.3.4.

17.3.4.2 $W \to c\bar{s}$

Diagrams similar to Fig. 17.3.2 with $W \to c\bar{s}$ and $u\bar{u}/d\bar{d}$ popping lead to $B \to \overline{D}^{(*)}D^{(*)}K$ final states. These final states play a substantial role in the B decays since they account for about 4% of their total branching fraction. Here, $D^{(*)}$ is either a D^0, D^{*0}, D^+ or D^{*+}, $\overline{D}^{(*)}$ is the charge conjugate of $D^{(*)}$ and K is either a K^+ or a K^0. Twenty-two decay modes are possible with this configuration. The decays of B mesons to $\overline{D}^{(*)}D^{(*)}K$ final states are interesting for many different reasons. For example, in the past (*i.e.* early 1990's), the hadronic decays of the B meson were in theoretical conflict with the B semileptonic branching fraction due to the inconsistency originating from the number of charmed hadrons per B decay (Bigi, Blok, Shifman, and Vainshtein, 1994). At the time, the measured semileptonic branching fraction, $\approx 10\%$, was in

Table 17.3.4. Measured single charm B^0 branching fractions ($\mathcal{B}$) from *BABAR*, Belle, and the PDG (Beringer et al., 2012) (average). The PDG value may use measurements from other experiments when calculating the average.

	BABAR results		Belle results		PDG Averages
Final state	$\mathcal{B}$ ($\times 10^{-3}$)	Ref.	$\mathcal{B}$ ($\times 10^{-3}$)	Ref.	$\mathcal{B}$ ($\times 10^{-3}$)
$D^-\pi^+$	$2.55 \pm 0.05 \pm 0.16$	(Aubert, 2007g)			2.68 ± 0.13
$D^-K^0\pi^+$	$0.49 \pm 0.07 \pm 0.05$	(Aubert, 2005aa)			$0.49 \pm 0.07 \pm 0.05$
$D^-K^*(892)^+$	$0.46 \pm 0.06 \pm 0.05$	(Aubert, 2005aa)			0.45 ± 0.07
D^-K^+			$0.18 \pm 0.04 \pm 0.01$	(Abe, 2001f)	0.197 ± 0.021
$D^-K^+\overline{K}^*(892)^0$			$0.88 \pm 0.11 \pm 0.15$	(Drutskoy, 2002)	$0.88 \pm 0.11 \pm 0.15$
$\overline{D}^0\pi^+\pi^-$			$0.84 \pm 0.04 \pm 0.08$	(Kuzmin, 2007)	$0.84 \pm 0.04 \pm 0.08$
$D^*(2010)^-\pi^+$	$2.79 \pm 0.08 \pm 0.17$	(Aubert, 2007g)			2.76 ± 0.13
$D^*(2010)^-K^+$	$0.214 \pm 0.012 \pm 0.010$	(Aubert, 2006n)	$0.20 \pm 0.04 \pm 0.01$	(Abe, 2001f)	0.214 ± 0.016
$D^*(2010)^-K^0\pi^+$	$0.30 \pm 0.07 \pm 0.03$	(Aubert, 2005aa)			$0.30 \pm 0.07 \pm 0.03$
$D^*(2010)^-K^*(892)^+$	$0.32 \pm 0.06 \pm 0.03$	(Aubert, 2005aa)			0.33 ± 0.06
$D^*(2010)^-K^+\overline{K}^*(892)^0$			$1.29 \pm 0.22 \pm 0.25$	(Drutskoy, 2002)	$1.29 \pm 0.22 \pm 0.25$
$D^*(2010)^-\pi^+\pi^+\pi^-$			$6.81 \pm 0.23 \pm 0.72$	(Majumder, 2004)	7.0 ± 0.8
$D^{*-}3\pi^+2\pi^-$			$4.72 \pm 0.59 \pm 0.71$	(Majumder, 2004)	$4.72 \pm 0.59 \pm 0.71$
$\overline{D}^*(2010)^-\omega\pi^+$	$2.88 \pm 0.21 \pm 0.31$	(Aubert, 2006k)			2.89 ± 0.30
$D_1(2430)^0\omega$ $\times\mathcal{B}(D_1(2430)^0 \to D^{*+}\pi^+)$	$0.41 \pm 0.12 \pm 0.11$	(Aubert, 2006k)			$0.41 \pm 0.12 \pm 0.11$
$\overline{D}^{**-}\pi^+$	$2.1 \pm 1.0 \pm 0.1$	(Aubert, 2006p)			$2.1 \pm 1.0 \pm 0.1$
$D_1(2420)^-\pi^+$ $\times\mathcal{B}(\overline{D}_1^- \to D^-\pi^+\pi^-)$			$0.089 \pm 0.015^{+0.017}_{-0.032}$	(Abe, 2005i)	$0.100^{+0.021}_{-0.025}$
$\overline{D}_2^*(2460)^-\pi^+$ $\times\mathcal{B}(D_2^*(2460) \to D^0\pi^-)$			$0.215 \pm 0.017 \pm 0.031$	(Kuzmin, 2007)	$0.215 \pm 0.017 \pm 0.031$
$\overline{D}_0^*(2400)^-\pi^+$ $\times\mathcal{B}(D_0^*(2400) \to D^0\pi^-)$			$0.060 \pm 0.013 \pm 0.027$	(Kuzmin, 2007)	$0.060 \pm 0.013 \pm 0.027$
$D_{s0}(2317)^-K^+$ $\times\mathcal{B}(D_{s0}(2317) \to D_s\pi^0)$			$0.042^{+0.014}_{-0.013} \pm 0.004$	(Drutskoy, 2005)	$0.042^{+0.014}_{-0.013} \pm 0.004$
$D^+\pi^-$			$(7.8 \pm 1.3 \pm 0.4) \times 10^{-4}$	(Das, 2010)	$(7.8 \pm 1.3 \pm 0.4) \times 10^{-4}$
$D_s^+\pi^-$	$0.025 \pm 0.004 \pm 0.002$	(Aubert, 2008u)	$0.0199 \pm 0.0026 \pm 0.0018$	(Das, 2010)	0.0216 ± 0.0026
$D_s^{*+}\pi^-$	$0.026^{+0.005}_{-0.004} \pm 0.002$	(Aubert, 2008u)	$0.0175 \pm 0.0034 \pm 0.0020$	(Joshi, 2010)	0.021 ± 0.004
$D_s^{*+}\rho^-$	$0.041^{+0.013}_{-0.012} \pm 0.004$	(Aubert, 2008u)			$0.041^{+0.013}_{-0.012} \pm 0.004$
$D_s^-K^+$	$0.029 \pm 0.004 \pm 0.002$	(Aubert, 2008u)	$0.0191 \pm 0.0024 \pm 0.0017$	(Das, 2010)	0.022 ± 0.005
$D_s^{*-}K^+$	$0.024 \pm 0.004 \pm 0.002$	(Aubert, 2008u)	$0.0202 \pm 0.0033 \pm 0.0022$	(Joshi, 2010)	0.0219 ± 0.0030
$D_s^-K^*(892)^+$	$0.035^{+0.01}_{-0.009} \pm 0.004$	(Aubert, 2008u)			$0.035^{+0.01}_{-0.009} \pm 0.004$
$D_s^{*-}K^*(892)^+$	$0.032^{+0.014}_{-0.012} \pm 0.004$	(Aubert, 2008u)			$0.032^{+0.014}_{-0.012} \pm 0.004$
$D_s^-\pi^+K^0$	$0.110 \pm 0.026 \pm 0.020$	(Aubert, 2008ai)			$0.110 \pm 0.026 \pm 0.020$
$\overline{D}^0K^0$	$0.053 \pm 0.007 \pm 0.003$	(Aubert, 2006k)	$0.050^{+0.013}_{-0.012} \pm 0.006$	(Krokovny, 2003a)	0.052 ± 0.007
$\overline{D}^0K^+\pi^-$	$0.088 \pm 0.015 \pm 0.009$	(Aubert, 2006n)			$0.088 \pm 0.015 \pm 0.009$
$\overline{D}^0K^*(892)^0$	$0.040 \pm 0.007 \pm 0.003$	(Aubert, 2006k)	$0.048^{+0.013}_{-0.010} \pm 0.005$	(Krokovny, 2003a)	0.042 ± 0.006
$D_2^*(2460)^-K^+$ $\times\mathcal{B}(D_2^*(2460)^- \to \overline{D}^0\pi^-)$	$0.0183 \pm 0.0040 \pm 0.0031$	(Aubert, 2006n)			$0.0183 \pm 0.0040 \pm 0.0031$
$\overline{D}^0\pi^0$	$0.269 \pm 0.009 \pm 0.013$	(Lees, 2011b)	$0.225 \pm 0.014 \pm 0.035$	(Blyth, 2006)	0.263 ± 0.014
$\overline{D}^0\rho^0$			$0.319 \pm 0.020 \pm 0.045$	(Kuzmin, 2007)	$0.319 \pm 0.020 \pm 0.045$
$\overline{D}^0f_2$			$0.120 \pm 0.018 \pm 0.038$	(Kuzmin, 2007)	$0.120 \pm 0.018 \pm 0.038$
$\overline{D}^0\eta$	$0.253 \pm 0.009 \pm 0.011$	(Lees, 2011b)	$0.177 \pm 0.016 \pm 0.021$	(Blyth, 2006)	0.236 ± 0.032
$\overline{D}^0\eta'$	$0.148 \pm 0.013 \pm 0.007$	(Lees, 2011b)	$0.114 \pm 0.020^{+0.010}_{-0.013}$	(Schumann, 2005)	0.138 ± 0.016
$\overline{D}^0\omega$	$0.257 \pm 0.011 \pm 0.014$	(Lees, 2011b)	$0.237 \pm 0.023 \pm 0.028$	(Blyth, 2006)	0.253 ± 0.016
$\overline{D}^*(2007)^0\pi^0$	$0.305 \pm 0.014 \pm 0.028$	(Lees, 2011b)	$0.139 \pm 0.018 \pm 0.026$	(Blyth, 2006)	0.22 ± 0.06
$\overline{D}^*(2007)^0\eta$	$0.269 \pm 0.014 \pm 0.023$	(Lees, 2011b)	$0.140 \pm 0.028 \pm 0.026$	(Blyth, 2006)	0.23 ± 0.06
$\overline{D}^*(2007)^0\eta'$	$0.148 \pm 0.022 \pm 0.013$	(Lees, 2011b)	$0.121 \pm 0.034 \pm 0.022$	(Schumann, 2005)	0.140 ± 0.022
$\overline{D}^*(2007)^0\pi^+\pi^-$			$0.62 \pm 0.012 \pm 0.018$	(Satpathy, 2003)	$0.62 \pm 0.012 \pm 0.018$
$\overline{D}^*(2007)^0K^0$	$0.036 \pm 0.012 \pm 0.003$	(Aubert, 2006k)			$0.036 \pm 0.012 \pm 0.003$
$\overline{D}^*(2007)^0\pi^+\pi^+\pi^-\pi^-$			$2.60 \pm 0.47 \pm 0.37$	(Majumder, 2004)	2.7 ± 0.5
$\overline{D}^*(2007)^0\omega$	$0.455 \pm 0.024 \pm 0.0039$	(Lees, 2011b)	$0.229 \pm 0.039 \pm 0.040$	(Blyth, 2006)	0.36 ± 0.11

Table 17.3.5. Results of the measured branching fractions for the ten $B \to D^{(*)}\overline{D}^{(*)}$ decay modes from *BABAR* and Belle: the number of events for fitted signal $N^{\rm sig}$, the branching fractions $\mathcal{B}$ (and where appropriate 90% C.L. upper limits on branching fractions), as compared with theoretical predictions. All *BABAR* measurements are from (Aubert, 2006m). (Empty entries indicate no measurement from the given experiment, or no prediction.)

Mode	$N^{\rm sig}_{BABAR}$	$N^{\rm sig}_{\rm Belle}$	$\mathcal{B}_{BABAR}$ (10^{-4})	$\mathcal{B}_{\rm Belle}$ (10^{-4})	$\mathcal{B}^{\rm theory}_{\rm predict}$ (10^{-4})
$B^0 \to D^{*+}D^{*-}$	270±19	1225±59	8.1 ±0.6± 1.0	7.82 ±0.38± 0.63 (Kronenbitter, 2012)	6.0 (Rosner, 1990)
$B^0 \to D^{*\pm}D^{\mp}$	156±17	887±39	5.7 ±0.7± 0.7	6.14 ±0.29± 0.50 (Rohrken, 2012)	
$B^0 \to D^{+}D^{-}$	63±9	221±19	2.8 ±0.4± 0.5	2.12 ±0.16± 0.18 (Rohrken, 2012)	
$B^0 \to D^{*0}\overline{D}^{*0}$	0±6		−1.3 ±1.1± 0.4 (< 0.9)		
$B^0 \to D^{*0}\overline{D}^{0}$	10±8		1.0 ±1.1± 0.4 (< 2.9)		
$B^0 \to D^{0}\overline{D}^{0}$	−11±12	0±25	−0.1 ±0.5± 0.2 (< 0.6)	< 0.43 (Adachi, 2008b)	
$B^+ \to D^{*+}\overline{D}^{*0}$	185±20		8.1 ±1.2± 1.2		7.1 (Sanda and Xing, 1997)
$B^+ \to D^{*+}\overline{D}^{0}$	115±16	74±12	3.6 ±0.5± 0.4	4.57 ±0.71± 0.56 (Majumder, 2005)	3.7 (Sanda and Xing, 1997)
$B^+ \to D^{+}\overline{D}^{*0}$	63±11		6.3 ±1.4± 1.0		3.1 (Sanda and Xing, 1997)
$B^+ \to D^{+}\overline{D}^{0}$	129±20	370±29	3.8 ±0.6± 0.5	3.85 ±0.31± 0.38 (Adachi, 2008b)	5.3 (Sanda and Xing, 1997)

Table 17.3.6. Results of measured *CP*-violating charge asymmetries $\mathcal{A}_{CP}$ for $D^{*\pm}D^{\mp}$ and the four charged B modes, as compared with theoretical predictions (where $\mathcal{A}_{CP}$ is defined as $(\Gamma^- - \Gamma^+)/(\Gamma^- + \Gamma^+)$, where the superscript refers to the sign of the $B^{\pm}$ meson in the case of the charged B decays, and for $D^{*\pm}D^{\mp}$, Γ^+ refers to $D^{*-}D^{+}$ and Γ^- to $D^{*+}D^{-}$. Empty entries indicate no measurement from the given experiment, or no prediction.)

Mode	$\mathcal{A}^{BABAR}_{CP}$	$\mathcal{A}^{\rm Belle}_{CP}$	Theoretical predictions
$B^0 \to D^{*\pm}D^{\mp}$	$0.008 \pm 0.048 \pm 0.013$ (Aubert, 2009ad)	$0.06 \pm 0.05 \pm 0.02$ (Rohrken, 2012)	
$B^+ \to D^{*+}\overline{D}^{*0}$	$-0.15 \pm 0.11 \pm 0.02$ (Aubert, 2006m)		0.012 (Xing, 2000)
$B^+ \to D^{*+}\overline{D}^{0}$	$-0.06 \pm 0.13 \pm 0.02$ (Aubert, 2006m)		0.012 (Xing, 2000)
$B^+ \to D^{+}\overline{D}^{*0}$	$0.13 \pm 0.18 \pm 0.04$ (Aubert, 2006m)		0.002 (Xing, 2000)
$B^+ \to D^{+}\overline{D}^{0}$	$-0.13 \pm 0.14 \pm 0.02$ (Aubert, 2006m)	$0.00 \pm 0.08 \pm 0.02$ (Adachi, 2008b)	0.030 (Xing, 2000)

Table 17.3.7. Results of measured polarization parameters for the two $D^*\overline{D}^*$ vector-vector decays, as compared with theoretical predictions. Here R_L is the fraction of longitudinal polarization and $R_\perp$ is the *CP*-odd fraction. (Empty entries indicate no measurement from the given experiment, or no prediction. There are presently no published measurements of, or predictions for, polarization in the $D^{*+}\overline{D}^{*0}$ mode.)

Mode	$\begin{pmatrix} R_\perp \\ R_L \end{pmatrix}^{BABAR}$	$\begin{pmatrix} R_\perp \\ R_L \end{pmatrix}^{\rm Belle}$	Theoretical predictions
$B^0 \to D^{*+}D^{*-}$	$0.158 \pm 0.028 \pm 0.006$ (Aubert, 2009ad)	$0.138 \pm 0.024 \pm 0.006$ (Kronenbitter, 2012)	0.06 (Rosner, 1990)
		$0.624 \pm 0.029 \pm 0.011$ (Kronenbitter, 2012)	0.55 (Rosner, 1990)

conflict with expectations from parton model calculations, 15 − 16%. It was realized (Buchalla, Dunietz, and Yamamoto, 1995) that an enhancement in the $b \to c\bar{c}s$ transition was needed to resolve the theoretical discrepancy with the B semileptonic branching fraction. Buchalla *et al.* predicted sizable branching fractions for decays of the form $B \to \overline{D}^{(*)}D^{(*)}K\,(X)$. Furthermore, the $\overline{D}^{(*)}D^{(*)}K$ events have been used to investigate isospin relations and to extract a measurement of the ratio of $\Upsilon(4S) \to B^+B^-$ and $\Upsilon(4S) \to B^0\overline{B}^0$ decays (Poireau and Zito, 2011). Likewise, the mode $B^0 \to D^{*-}D^{*+}K^0_S$ has been used to perform a time-dependent *CP* asymmetry measurement to determine the sign of $\cos 2\phi_1$ (see Section 17.6). It is also worth recalling that many $D^{(*)}K$ and $\overline{D}^{(*)}D^{(*)}$ resonant processes are at play in the studied decay channels. Using $B \to \overline{D}^{(*)}D^{(*)}K$ final states, *BABAR* and Belle observed and measured properties of the resonances $D^+_{s1}(2536)$ (see Section 19.3), $D_{sJ}(2700)$ (see also Section 19.3), $\psi(3770)$ (see Section 18.2), and $X(3872)$ (see Section 18.3).

BABAR reconstructs the B^0 and B^+ mesons in the 22 $\overline{D}^{(*)}D^{(*)}K$ modes using 429 fb^{-1} (del Amo Sanchez, 2011e), while Belle studies only the modes $B^0 \to D^{*-}D^{*+}K^0$ and $B^+ \to \overline{D}^0D^0K^+$ with 414 fb^{-1} (Brodzicka, 2008; Dalseno, 2007). The collaborations use the decays of particles into $K^0_S \to \pi^+\pi^-$, $D^0 \to K^-\pi^+$, $K^-\pi^+\pi^0$, and $K^-\pi^+\pi^-\pi^+$, $D^+ \to K^-\pi^+\pi^+$, $D^{*+} \to D^0\pi^+$, and $D^+\pi^0$, $D^{*0} \to D^0\pi^0$, and $D^0\gamma$ final states. Additionally, Belle uses the decays $D^0 \to K^0_S\pi^+\pi^-$ and $D^0 \to K^-K^+$. The selection of these particles is based on mass cuts, energies of the decay products, vertexing and particle identification to name a few. The B candidates are reconstructed by combining a $\overline{D}^{(*)}$, a $D^{(*)}$ and a K candidate in a subset of the 22 modes. To suppress the background, topological variables are used which dis-

Table 17.3.8. Results of the measured branching fractions for the eight $B \to D_s^{(*)}\overline{D}^{(*)}$ decay modes from *BABAR* and Belle: the number of events for fitted signal $N^{\rm sig}$, and the branching fractions $\mathcal{B}$, as compared with theoretical predictions. (Empty entries indicate no measurement from the given experiment, or no prediction.)

Mode	Analysis technique	$\mathcal{B}_{BABAR}$ (10^{-3})	$\mathcal{B}_{\rm Belle}$ (10^{-3})	$\mathcal{B}^{\rm theory}_{\rm predict}$ (10^{-3})
$B^0 \to D_s^{*+}D^{*-}$	Semi-exclusive tag	17.3 ±1.8± 1.5 (Aubert, 2006aw)		
	D_s^* partial reco.	18.8 ±0.9± 1.7 (Aubert, 2005q)		24.0 ± 6.7 (Luo and Rosner, 2001)
	D^* partial reco.	15.8 ±1.7± 1.4 (Aubert, 2003d)		
$B^0 \to D_s^{*+}D^-$	Semi-exclusive tag	7.1 ±1.6± 0.6 (Aubert, 2006aw)		10.0 ± 2.8 (Luo and Rosner, 2001)
$B^0 \to D_s^{+}D^{*-}$	Semi-exclusive tag	7.3 ±1.3± 0.7 (Aubert, 2006aw)		8.6 ± 2.4 (Luo and Rosner, 2001)
	D^* partial reco.	8.3 ±1.5± 0.7 (Aubert, 2003d)		
$B^0 \to D_s^{+}D^-$	Semi-exclusive tag	6.6 ±1.4± 0.6 (Aubert, 2006aw)		14.9 ± 4.1 (Luo and Rosner, 2001)
	Full reconstruction		7.3 ±0.4± 0.7 (Zupanc, 2007)	
$B^+ \to D_s^{*+}\overline{D}^{*0}$	Semi-exclusive tag	16.7 ±1.9± 1.5 (Aubert, 2006aw)		
$B^+ \to D_s^{*+}\overline{D}^{0}$	Semi-exclusive tag	7.9 ±1.7± 0.7 (Aubert, 2006aw)		
$B^+ \to D_s^{+}\overline{D}^{*0}$	Semi-exclusive tag	7.8 ±1.8± 0.7 (Aubert, 2006aw)		
$B^+ \to D_s^{+}\overline{D}^{0}$	Semi-exclusive tag	9.5 ±2.0± 0.8 (Aubert, 2006aw)		

Table 17.3.9. Results of measured polarization parameters for the $D_s^*\overline{D}^*$ vector-vector decays, as compared with theoretical predictions. Here R_L is the fraction of longitudinal polarization and $R_\perp$ is the *CP*-odd fraction. (Empty entries indicate no measurement from the given experiment, or no prediction. There are presently no published measurements of, or predictions for, polarization in the $D_s^{*+}\overline{D}^{*0}$ mode.)

Mode	$\begin{pmatrix} R_\perp \\ R_L \end{pmatrix}^{BABAR}$	Theoretical Predictions
$B^0 \to D_s^{*+}D^{*-}$		0.06 (Rosner, 1990)
	$0.519 \pm 0.050 \pm 0.028$ (Aubert, 2003d)	0.55 (Rosner, 1990)

criminate against continuum background (see Chapter 4). Signal events have $m_{\rm ES}$ compatible with the known B meson mass, and a difference between the candidate energy and the beam energy in the center-of-mass, ΔE (see Chapter 9), compatible with zero.

For each mode, *BABAR* fits the $m_{\rm ES}$ distribution to get the signal yield. According to their physical origin, four categories of events with differently shaped $m_{\rm ES}$ distributions are separately considered: $\overline{D}^{(*)}D^{(*)}K$ signal events, "cross-feed" events, combinatorial background events, and peaking background events. To determine the yields and the branching fractions, the shape of each of these contributions are determined. The cross-feed events are from all the $\overline{D}^{(*)}D^{(*)}K$ modes, except the one we reconstruct, that pass the complete selection, and which are reconstructed in the signal mode; the peaking background is the part of the combinatorial background that is peaking in the signal region. *BABAR* observes from the analysis of simulated samples that most of the cross-feed originates from the combination of an unrelated soft π^0 or γ with the D^0 from a D^{*+} decay to form a wrong D^{*0} candidate. A part of the combinatorial $B\overline{B}$ background is peaking in the signal region, and is fitted separately from generic MC samples $e^+e^- \to q\overline{q}$ $(q = u, d, s, c, b)$ satisfying the $\overline{D}^{(*)}D^{(*)}K$ selection. For the modes $B^+ \to \overline{D}^{*0}D^{*0}K^+$ and $B^+ \to \overline{D}^0D^0K^+$, the cross-feed events and the peaking background are negligible, and Belle performs a two dimensional fit on $m_{\rm ES}$ and ΔE to obtain the signal yield.

Due to the presence of cross-feed events, the fit for the branching fraction for any one channel uses as inputs the branching fractions from the other channels. Since these branching fractions are not a priori known, *BABAR* employs an iterative procedure to obtain the 22 branching fractions. It has been shown that $\overline{D}^{(*)}D^{(*)}K$ events contain resonant contributions (Aubert, 2008bd). In order to measure the branching fractions inclusively without any assumptions on the resonance structure of the signal, *BABAR* estimates the efficiency as a function of location in the Dalitz plane of the data. *BABAR* uses this efficiency at the event position in the Dalitz plane to reweight the signal contribution. To isolate the signal contribution event-per-event, *BABAR* uses the ${}_s\mathcal{P}lots$ technique (Pivk and Le Diberder, 2005) (see Chapter 11). The ${}_s\mathcal{P}lots$ technique exploits the result of the $m_{\rm ES}$ fit (yield and covariance matrix) and the *p.d.f.*s of this fit to compute an event-per-event weight for the signal category and background category.

Both experiments consider several sources of systematic uncertainties on the branching fraction measurements: signal shape, cross-feed determination, peaking background, combinatorial background, fit bias, iterative procedure, limited MC statistics, efficiency mapping, difference between data and MC, number of B mesons in the data sample, and secondary branching fractions.

The combination from the *BABAR* and Belle results can be found in Table 17.3.10. Summing the 10 neutral modes and the 12 charged modes, the $\overline{D}^{(*)}D^{(*)}K$ events represent $(3.65\pm0.10\pm0.24)\%$ of the B^0 decays and $(4.06\pm 0.11\pm 0.28)\%$ of the B^+ decays.

17.3.5 Decays to charmonium

Decays of B mesons to charmonium modes are color suppressed. In all they consist of a few percent of B decays. Despite their small branching fractions, these decays play a major role in *CP* studies due to the ability to reconstruct many charmonium modes cleanly with little background as well as the simplicity in interpreting the results theoretically. B^0 meson decays to charmonium are used to measure the *CP* violation parameter $\sin 2\phi_1$ as well as $\cos 2\phi_1$ (see Sections 17.6.3 and 17.6.8). The relevant decay diagrams for charmonium modes are shown in Fig. 17.3.7.

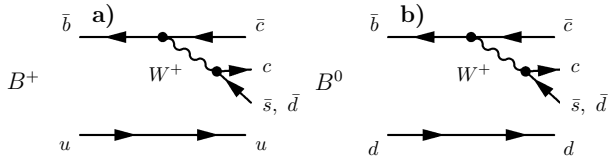

Figure 17.3.7. Color-suppressed Feynman diagrams for B meson decays to charmonium.

The easiest way to reconstruct decays to charmonium is via the dileptonic decays of J/ψ or $\psi(2S)$ to electrons or muons. The relatively high energy and topology of the leptons allows a clean sample of charmonium to be reconstructed (which helped in earning the decay to the *CP* state $B^0 \to J/\psi K^0_s$ the title of "Golden Mode"). The χ_{c1} and χ_{c2} states can be reconstructed through their radiative decays to $J/\psi\gamma$. $\psi(2S)$ can also be reconstructed through the decay $\psi(2S) \to J/\psi\pi\pi$. The lower mass states η_c and χ_{c0} do not decay to two leptons and the χ_{c0} branching fraction to $J/\psi\gamma$ is small thus these states must be reconstructed through their decay to hadrons. The higher mass "exotic" charmonium-like X states are reconstructed through decays to $J/\psi\pi\pi$, radiative decays to J/ψ or $\psi(2S)$, or through decays that include two D mesons. They are covered in Section 18.3. Inclusive decays of B mesons to charmonium are covered in Section 18.2.4.1.

17.3.5.1 Reconstruction of charmonium via dileptons

There are several factors that must be taken into account when reconstructing B decays to charmonium where the charmonium are reconstructed via dileptons. The first is that the invariant mass of the two leptons is often significantly below the nominal J/ψ or $\psi(2S)$ mass. This is the result of both final state radiation and energy loss in the detector via bremsstrahlung. This is particularly true for the dielectron mode. Analyses often correct for this energy loss by adding in the energy of photon showers that are within a small angle (typically 50 mrad) of the initial electron direction (*e.g.* Aubert, 2009m; Guler, 2011) to the invariant mass calculation.

The second is that for fully reconstructed B mesons, it is important to perform a mass-constrained fit of the J/ψ or $\psi(2S)$. This improves the energy resolution of the reconstructed B significantly as most of the energy of a charmonium meson coming from a B decay is in its mass.[54] This fit or a global fit for the B meson usually includes the well-measured dilepton vertex.

For charmonium states with radiative decay to J/ψ or $\psi(2S)$, radiative γ candidates must pass a minimum energy cut, typically 30 MeV. A common additional requirement is that the γ candidate not be a part of a $\pi^0 \to \gamma\gamma$ candidate.

17.3.5.2 Reconstruction of charmonium via hadrons

The η_c is reconstructed via $KK\pi$ modes (Fang, 2003; Aubert, 2008ba) in addition to the $p\overline{p}$ mode (Fang, 2003; Aubert, 2007k). The $\eta_c(2S)$ is reconstructed via $KK\pi$ (Vinokurova, 2011; Aubert, 2008ba), as well as via $\eta_c\gamma$.

17.3.5.3 Reconstruction of B candidates

B mesons are reconstructed by combining charmonium candidates with the appropriate other particle candidates. Typically a vertex-constrained fit is done at this point. Both Belle and *BABAR* use kinematic variables to discriminate signal candidates from background. These variables are discussed in Section 7.1.

17.3.5.4 $W \to c\overline{d}$

Decays of B mesons to charmonium $c\overline{d}$ are Cabibbo suppressed and thus are expected to have decay rates of about 5% of the equivalent Cabibbo-allowed $c\overline{s}$ modes. In these modes, the tree and penguin contributions have different phases (unlike the Cabibbo-allowed modes where they are the same) and thus charge asymmetries of a few percent may occur. See Section 17.6.4 for more details.

[54] A key variable for B reconstruction is $\Delta E = E^*_B - E^*_{\rm beam}$ where * refers to the center-of-mass system, E_B is the B candidate's energy, and $E^*_{\rm beam}$ is the beam energy.

Table 17.3.10. Branching fractions of $B \to \overline{D}^{(*)} D^{(*)} K$ decays in units of 10^{-4}. The first uncertainties are statistical and the second are systematic. The results from the modes $B^0 \to D^{*-} D^{*+} K^0$ and $B^+ \to \overline{D}^0 D^0 K^+$ are a combination between the *BABAR* (del Amo Sanchez, 2011e) and Belle (Brodzicka, 2008; Dalseno, 2007) measurements.

Mode	$\mathcal{B}$ (10^{-4})	Mode	$\mathcal{B}$ (10^{-4})
B decays through external W-emission amplitudes			
$B^0 \to D^- D^0 K^+$	$10.7 \pm 0.7 \pm 0.9$	$B^+ \to \overline{D}^0 D^+ K^0$	$15.5 \pm 1.7 \pm 1.3$
$B^0 \to D^- D^{*0} K^+$	$34.6 \pm 1.8 \pm 3.7$	$B^+ \to \overline{D}^0 D^{*+} K^0$	$38.1 \pm 3.1 \pm 2.3$
$B^0 \to D^{*-} D^0 K^+$	$24.7 \pm 1.0 \pm 1.8$	$B^+ \to \overline{D}^{*0} D^+ K^0$	$20.6 \pm 3.8 \pm 3.0$
$B^0 \to D^{*-} D^{*0} K^+$	$106.0 \pm 3.3 \pm 8.6$	$B^+ \to \overline{D}^{*0} D^{*+} K^0$	$91.7 \pm 8.3 \pm 9.0$
B decays through external+internal W-emission amplitudes			
$B^0 \to D^- D^+ K^0$	$7.5 \pm 1.2 \pm 1.2$	$B^+ \to \overline{D}^0 D^0 K^+$	$14.0 \pm 0.7 \pm 1.2$
$B^0 \to D^{*-} D^+ K^0$	$64.1 \pm 3.6 \pm 3.9$	$B^+ \to \overline{D}^0 D^{*0} K^+$	$63.2 \pm 1.9 \pm 4.5$
$+ D^- D^{*+} K^0$		$B^+ \to \overline{D}^{*0} D^0 K^+$	$22.6 \pm 1.6 \pm 1.7$
$B^0 \to D^{*-} D^{*+} K^0$	$79.3 \pm 3.8 \pm 6.7$	$B^+ \to \overline{D}^{*0} D^{*0} K^+$	$112.3 \pm 3.6 \pm 12.6$
B decays through internal W-emission amplitudes			
$B^0 \to \overline{D}^0 D^0 K^0$	$2.7 \pm 1.0 \pm 0.5$	$B^+ \to D^- D^+ K^+$	$2.2 \pm 0.5 \pm 0.5$
$B^0 \to \overline{D}^0 D^{*0} K^0$	$10.8 \pm 3.2 \pm 3.6$	$B^+ \to D^- D^{*+} K^+$	$6.3 \pm 0.9 \pm 0.6$
$+ \overline{D}^{*0} D^0 K^0$		$B^+ \to D^{*-} D^+ K^+$	$6.0 \pm 1.0 \pm 0.8$
$B^0 \to \overline{D}^{*0} D^{*0} K^0$	$24.0 \pm 5.5 \pm 6.7$	$B^+ \to D^{*-} D^{*+} K^+$	$13.2 \pm 1.3 \pm 1.2$

Table 17.3.11. Measured B^0 to charmonium $c\overline{d}$ branching fractions ($\mathcal{B}$) from *BABAR*, Belle, and the PDG (Beringer et al., 2012) (average). The PDG value may use measurements from other experiments when calculating the average.

	BABAR results		Belle results		PDG Averages
Final state	$\mathcal{B}$ $(\times 10^{-6})$	Ref.	$\mathcal{B}$ $(\times 10^{-6})$	Ref.	$\mathcal{B}$ $(\times 10^{-6})$
$J/\psi\,\pi^0$	$16.9 \pm 1.4 \pm 0.7$	(Aubert, 2008i)	$23 \pm 5 \pm 2$	(Abe, 2003c)	17.6 ± 1.6
$J/\psi\,\eta$			$12.3^{+1.8}_{-1.7} \pm 0.7$	(Chang, 2012)	12.3 ± 1.9
$J/\psi\,\pi^+\pi^-$	$46 \pm 7 \pm 6$	(Aubert, 2003a)			46 ± 9
$J/\psi\,\rho^0$	$27 \pm 3 \pm 2$	(Aubert, 2007e)			27 ± 4
$\chi_{c1}\pi^0$			$11.2 \pm 2.5 \pm 1.2$	(Kumar, 2008)	11.2 ± 2.8

Table 17.3.12. Measured B^+ to charmonium $c\overline{d}$ branching fractions ($\mathcal{B}$) from *BABAR*, Belle, and the PDG (Beringer et al., 2012) (average). The PDG value may use measurements from other experiments when calculating the average. Note: in (Aubert, 2004ae) *BABAR* measures the ratio $\mathcal{B}(J/\psi\pi^+)/\mathcal{B}(J/\psi K^+)$.

	BABAR results		Belle results		PDG Averages
Final state	$\mathcal{B}$ $(\times 10^{-6})$	Ref.	$\mathcal{B}$ $(\times 10^{-6})$	Ref.	$\mathcal{B}$ $(\times 10^{-6})$
$J/\psi\,\pi^+$			$38 \pm 6 \pm 3$	(Abe, 2003c)	49 ± 4
$J/\psi\,\rho^+$	$50 \pm 7 \pm 3$	(Aubert, 2007e)			50 ± 8
$\psi(2S)\pi^+$			$24.4 \pm 2.2 \pm 2.0$	(Bhardwaj, 2008)	24.4 ± 3.0
$\chi_{c1}\pi^+$			$22 \pm 4 \pm 3$	(Kumar, 2006)	22 ± 5

Measured branching fractions for these modes are given in Tables 17.3.11 and 17.3.12. In Table 17.3.1 the measured branching fractions of the $J/\psi\pi$ and $J/\psi\rho$ modes are compared with the predictions from the NS model. Among the four measured modes only the $J/\psi\pi^0$ is consistent with the model's prediction. Both of the ρ modes are overestimated by the model while the $J/\psi\pi^+$ is underestimated.

17.3.5.5 $W \to c\overline{s}$

Measured branching fractions for these modes are given in Tables 17.3.13 and 17.3.14.

The measured branching fractions of the $J/\psi K$ and $J/\psi K^*$ modes are compared in Table 17.3.1 with the predictions from the NS model. All of the $J/\psi K$ measurements are higher than the predictions from the model while for the K^* modes the situation is reversed. The mea-

Table 17.3.13. Measured B^0 to charmonium $c\bar{s}$ branching fractions ($\mathcal{B}$) from *BABAR*, Belle, and the PDG (Beringer et al., 2012) (average). The PDG value may use measurements from other experiments when calculating the average.

	BABAR results		Belle results		PDG Averages
Final state	$\mathcal{B}$ ($\times 10^{-3}$)	Ref.	$\mathcal{B}$ ($\times 10^{-3}$)	Ref.	$\mathcal{B}$ ($\times 10^{-3}$)
$\eta_c K^0$	$0.64^{+0.22}_{-0.20} \pm 0.20$	(Aubert, 2007k)	$1.23 \pm 0.23^{+0.40}_{-0.41}$	(Fang, 2003)	0.83 ± 0.12
$\eta_c K^{*0}$	$0.57 \pm 0.07 \pm 0.8$	(Aubert, 2007k)	$1.62 \pm 0.32^{+0.55}_{-0.60}$	(Fang, 2003)	0.64 ± 0.09
$J/\psi K^0$	$0.869 \pm 0.022 \pm 0.030$	(Aubert, 2007k)	$0.79 \pm 0.04 \pm 0.09$	(Abe, 2003c)	0.874 ± 0.032
$J/\psi K^{*0}$	$1.309 \pm 0.026 \pm 0.077$	(Aubert, 2005k)	$1.29 \pm 0.05 \pm 0.013$	(Abe, 2002d)	1.34 ± 0.06
$J/\psi K_1(1270)^0$			$1.30 \pm 0.34 \pm 0.32$	(Abe, 2001e)	1.30 ± 0.5
$J/\psi \eta K_S^0$	$0.084 \pm 0.026 \pm 0.027$	(Aubert, 2004v)			0.08 ± 0.04
$J/\psi \phi K^0$	$0.102 \pm 0.038 \pm 0.010$	(Aubert, 2003l)			0.094 ± 0.026
$J/\psi \omega K^0$	$0.23 \pm 0.03 \pm 0.03$	(del Amo Sanchez, 2010c)			0.23 ± 0.04
$\psi(2S)K^0$	$0.646 \pm 0.065 \pm 0.051$	(Aubert, 2005k)	0.67 ± 0.011	(Abe, 2003c)	0.62 ± 0.05
$\psi(2S)K^{*0}$	$0.592 \pm 0.085 \pm 0.089$	(Aubert, 2005k)	$0.552^{+0.035+0.053}_{-0.032-0.058}$	(Mizuk, 2009)	0.61 ± 0.05
$\chi_{c0} K^0$	$0.142^{+0.055}_{-0.044} \pm 0.022$	(Aubert, 2009av)			$0.14^{+0.06}_{-0.04}$
$\chi_{c0} K^{*0}$	$0.17 \pm 0.03 \pm 0.02$	(Aubert, 2008ag)			0.17 ± 0.04
$\chi_{c1} K^0$	$0.42 \pm 0.03 \pm 0.03$	(Aubert, 2009m)	$0.351 \pm 0.033 \pm 0.045$	(Soni, 2006)	0.393 ± 0.027
$\chi_{c1} K^{*0}$	$0.25 \pm 0.02 \pm 0.02$	(Aubert, 2009m)	$0.173^{+0.015+0.034}_{-0.012-0.022}$	(Mizuk, 2008)	$0.222^{+0.040}_{-0.031}$
$\chi_{c2}\ K^{*0}$	$0.066 \pm 0.018 \pm 0.005$	(Aubert, 2009m)			0.066 ± 0.019

Table 17.3.14. Measured B^+ to charmonium $c\bar{s}$ branching fractions ($\mathcal{B}$) from *BABAR*, Belle, and the PDG (Beringer et al., 2012) (average). The PDG value may use measurements from other experiments when calculating the average.

	BABAR results		Belle results		PDG Averages
Final state	$\mathcal{B}$ ($\times 10^{-3}$)	Ref.	$\mathcal{B}$ ($\times 10^{-3}$)	Ref.	$\mathcal{B}$ ($\times 10^{-3}$)
$\eta_c K^+$	0.87 ± 0.15	(Aubert, 2006ae)	$1.25 \pm 0.14^{+0.39}_{-0.40}$	(Fang, 2003)	0.96 ± 0.12
$\eta_c K^{*+}$	$1.1^{+0.5}_{-0.4} \pm 0.1$	(Aubert, 2007k)			$1.1^{+0.5}_{-0.4}$
$\eta_c(2S)K^+$	$0.34 \pm 0.18 \pm 0.03$	(Aubert, 2007k)			0.34 ± 0.18
$J/\psi K^+$	$1.061 \pm 0.015 \pm 0.048$	(Aubert, 2007k)	$1.01 \pm 0.02 \pm 0.07$	(Abe, 2003c)	1.016 ± 0.033
$J/\psi K^+\pi^+\pi^-$	$1.16 \pm 0.07 \pm 0.09$	(Aubert, 2008d)	$0.716 \pm 0.010 \pm 0.060$	(Guler, 2011)	0.81 ± 0.013
$J/\psi K^{*+}$	$1.454 \pm 0.047 \pm 0.097$	(Aubert, 2005k)	$1.28 \pm 0.07 \pm 0.014$	(Abe, 2002d)	1.43 ± 0.08
$J/\psi K_1(1270)^+$			$1.80 \pm 0.34 \pm 0.39$	(Abe, 2001e)	1.80 ± 0.5
$J/\psi \eta K^+$	$0.108 \pm 0.023 \pm 0.024$	(Aubert, 2004v)			0.108 ± 0.033
$J/\psi \phi K^+$	$0.044 \pm 0.014 \pm 0.005$	(Aubert, 2003l)			0.052 ± 0.017
$J/\psi \omega K^+$	$0.32 \pm 0.01^{+0.06}_{-0.03}$	(del Amo Sanchez, 2010c)			$0.320^{+0.060}_{-0.032}$
$\psi(2S)K^+$	$0.617 \pm 0.032 \pm 0.044$	(Aubert, 2005k)	$0.665 \pm 0.017 \pm 0.055$	(Guler, 2011)	0.639 ± 0.033
$\psi(2S)K^{*+}$	$0.592 \pm 0.085 \pm 0.089$	(Aubert, 2005k)			0.67 ± 0.14
$\psi(2S)K^+\pi^+\pi^-$			$0.431 \pm 0.020 \pm 0.050$	(Guler, 2011)	0.43 ± 0.05
$\psi(3370)K^+$	$3.5 \pm 2.5 \pm 0.3$	(Aubert, 2006ae)	$0.48 \pm 0.11 \pm 0.07$	(Chistov, 2004)	0.49 ± 0.13
$\chi_{c0} K^+$	$0.123^{+0.027}_{-0.025} \pm 0.006$	(Aubert, 2008l)	$0.112 \pm 0.012^{+0.030}_{-0.020}$	(Garmash, 2006)	$0.134^{+0.019}_{-0.016}$
$\chi_{c1} K^+$	$0.45 \pm 0.01 \pm 0.03$	(Aubert, 2009m)	$0.449 \pm 0.019 \pm 0.053$	(Garmash, 2006)	0.479 ± 0.023
$\chi_{c1} K^{*+}$	$0.26 \pm 0.05 \pm 0.04$	(Aubert, 2009m)	$0.405 \pm 0.059 \pm 0.095$	(Soni, 2006)	0.30 ± 0.06
$\chi_{c2} K^+$			$0.0111^{+0.0036}_{-0.0034} \pm 0.0009$	(Bhardwaj, 2011)	0.011 ± 0.004

surements are all lower than the predictions. The level of disagreement is typically about a factor of two.

As discussed in Colangelo, De Fazio, and Pham (2002) naïve factorization would predict a zero branching fraction for decays such as $B \to \chi_{c0} K^{(*)}$ and $B \to \chi_{c2} K^{(*)}$ [55]. However, as seen in Tables 17.3.13 and 17.3.14 this is not the case. There are non-zero branching fraction measurements for five of the eight possible final states. In fact, the $B \to \chi_{c0} K^{(*)}$ branching fractions are the same order of magnitude as the factorization allowed $B \to \chi_{c1} K^{(*)}$ decays. In Beneke and Vernazza (2009) it is shown that including color-octet contributions leads to a "correction" to naïve factorization that may even dominate the entire decay amplitude. The calculation is, however, highly uncertain and formally valid only, when the charmonium is a truly non-relativistic bound state. It qualitatively describes correctly the hierarchies of charmonium branching fractions with a sizable $\chi_{c0} K$ one, and a suppression of

[55] Note that in the amplitude for $\overline{B} \to \chi_{c0(2)} \overline{K}$ decays one encounters the $\langle \chi_{c0(2)} | (\overline{c}c)_{V-A} | 0 \rangle$ matrix element, as can be seen following the examples given in Eqs 17.3.2 and 17.3.3. This matrix element includes the (axial-)vector operator between states with spin 0 and 0 (2) and hence equals to zero.

$\chi_{c2}K$ and h_cK, although the suppression of the latter two is not as strong as seen in the data.

17.3.6 Summary

Hadronic decays of B mesons into charm make up the largest category of final states. From the point of view of an experimentalist many of these final states are easy to reconstruct as the hardware and software capabilities of both Belle and *BABAR* are well matched to the demands made by final states such as $D\pi$, $D^*\pi$, and DDK to name a few. A glance at the PDG (Beringer et al., 2012) reveals the enormous progress made by *BABAR* and Belle in the number of final states observed and the precision of the measurement of their branching fractions. However there are still some challenges left for experimentalists in this area. To date, no radiative B decays have been observed, there is only an upper limit for $B^0 \to \overline{D}^{*0}\gamma$ (Aubert, 2005ad). There is also much work to be done reconstructing final states with multiple π^0s.

Since all of these final states rely on QCD to turn quarks into hadrons, gluons play an important role in the dynamics of the decay. At the moment a comprehensive theoretical picture capable of first principle calculations of decay rates is still an elusive goal. The precision data now available on a large number of decay modes will make it easier to achieve this goal. It is also important to keep in mind that the glory in B physics lies not with the QCD component of these decay modes but with the electroweak role in the transition to the final state. Much of what we have learned about *CP* violation in the b sector of the CKM model has come from hadronic final states with charm such as ψK^0_S (ϕ_1) and DK^- (ϕ_3). Looking to the upcoming era of super flavor factories it is clear that this category of final state will continue to play an important role in many aspects of the physics program.

17.4 Charmless B decays

Editors:
Fergus Wilson (BABAR)
Peter Krizan (Belle)
Martin Beneke (theory)

17.4.1 Introduction

In 1964, indirect *CP* violation was discovered in the mixing of the neutral kaon system (Christenson, Cronin, Fitch, and Turlay, 1964) with a value that is currently $|\epsilon| = (2.228 \pm 0.011) \times 10^{-3}$ (Beringer et al., 2012). It took another 30 years before direct *CP* violation was fully established in the kaon system. The absence of direct *CP* violation in the meantime led to the super-weak theory that suggested that *CP* violation would only occur in mixing with a change of two units of flavor ($\Delta S = 2$) and that *CP* violation in the B system would be negligible. At the same time, the discovery of neutral currents in the 1970s and the suggestion that there were six quarks meant that a *CP* violating phase could be introduced into what became the CKM matrix. This would allow flavor to change by one unit ($\Delta S = 1$) and lead to direct *CP* violation in decays. It wasn't until 1999, six years after the start of the construction of the B Factories, that direct *CP* in the kaon system was finally found to be non-zero, $\mathrm{Re}(\epsilon'/\epsilon) = (1.65 \pm 0.26) \times 10^{-3}$ (Fanti et al. (1999)). This result appeared just as the B Factories hoped to establish *CP* violation in the B meson sector. This was achieved through the observation of the angle ϕ_1 in $B^0 \to J/\psi K^0_S$ in 2001 (see Section 17.6).

Although *CP* violation was initially measured in a $b \to c\bar{c}s$ quark transition, the decays of B mesons to final states without a charm quark are equally as important for the thorough understanding of *CP* violation. The study of the branching fractions and angular distributions (see Chapter 12) probes the dynamics of both weak and strong interactions. In many cases, the measurement of the weak phases can be directly related to the CKM angles (ϕ_1, ϕ_2, ϕ_3). Since the CKM element $|V_{ub}|$ is much smaller than $|V_{cb}|$, the branching fractions for these charmless modes are typically less than 10^{-5}, and so are only feasible in the era of large integrated luminosities. The accumulated datasets has made it possible to measure branching fractions, direct and indirect *CP* asymmetries, G-parity conservation, longitudinal polarization f_L, weak and strong phases. This has enabled comprehensive comparison with theoretical predictions and models.

Figure 17.4.1 shows six of the main amplitudes that contribute to the hadronic B meson decays (there are a number of other less important diagrams that are not shown). The color-allowed tree diagram (T) dominates in $b \to c$ decays but the color-suppressed diagram (C) can also contribute. If the c quark is replaced by a u quark, the tree diagrams are suppressed and the one-loop flavor-changing neutral current (FCNC) penguin diagrams (P) become more or equally important. For example, decays

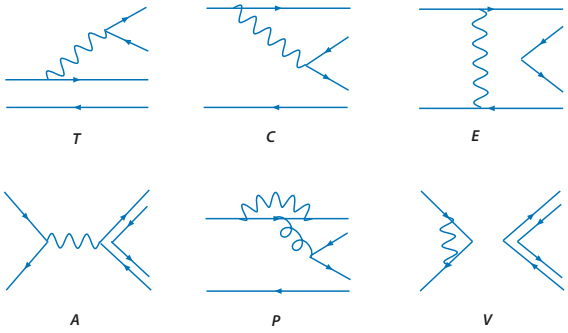

Figure 17.4.1. The dominant amplitudes contributing to charmless B meson decays: T) color-allowed external W-emission tree diagram; C) color-suppressed internal W-emission tree diagram; E) W-exchange diagram; A) W-annihilation diagram; P) penguin diagram with gluon exchange; and V) W-loop diagram.

such as $B \to \pi\pi, \pi\rho, \rho\rho$, proceed through $b \to u$ tree diagram but also have a non-negligible $b \to d$ penguin loop contribution. Transitions of $b \to s$ can only occur through the penguin diagrams (P) and CKM suppressed tree decays ($b \to u\bar{u}s$). The former have approximately the same weak phase ϕ_1 as the $b \to c\bar{c}s$ modes (see Chapter 17.6). Penguin diagrams in B meson decays can be relatively large as they involve the CKM elements $|V_{tb}|$ and $|V_{ts}|$. This is in contrast to D meson decays which require $|V_{cb}|$ and $|V_{ub}|$. As a result D meson decays are a good place to study tree-level, SM-dominated *CP* violation (such as ϕ_3) while B meson charmless decays have the potential to reveal non-SM physics through heavy virtual particles in the penguin loops.

In B meson decays with an odd number of kaons, the penguin loop (P) will dominate as the $b \to u$ tree diagram is suppressed by the $|V_{ub}|$ coupling. If there are an even number of kaons, the $b \to u$ color-allowed tree diagram (T) again becomes possible and start to contribute a noticeable level.

In the search for indirect *CP* violation, any decay with a $b \to du\bar{u}$ transition is useful as it provides a possible source of measurement of ϕ_2, through interference between the decay and the B meson mixing. Examples include $B \to \pi\pi, \pi\rho, \rho\rho$ as discussed in Chapter 17.7. However the presence of the penguin loop as an alternative decay channel complicates the interpretation. Similarly, transitions $b \to q\bar{q}s$ (where q is not a charm quark) provide a precise measurement of ϕ_1 but in this case there is one dominant penguin decay. Since penguin loops are sensitive to new virtual heavy particles, discrepancies in the value of ϕ_1 measured in different decay modes could be a sign of new physics. This chapter does not explicitly discuss the CKM angles and more information on the extraction of ϕ_1 (*e.g.* $B \to \eta' K^0_S$), ϕ_2 (*e.g.* $B \to \rho\rho$), and ϕ_3 (*e.g.* $B \to K\pi\pi$) from charmless decays can be found in Chapters 17.6, 17.7, and 17.8, respectively. For information on charmless baryonic decays, please see Chapter 17.12.

Direct *CP* violation is observed as an asymmetry in the yields between a decay and its *CP* conjugate when at least two contributing decay amplitudes A_i carry different weak ϕ_i and strong phases δ_i as explained in detail in Chapter 16:

$$A_{CP} = \frac{2\sin(\phi_i - \phi_j)\sin(\delta_i - \delta_j)}{R + R^{-1} + \cos(\phi_i - \phi_j)\cos(\delta_i - \delta_j)}, R \equiv \left|\frac{A_i}{A_j}\right| \tag{17.4.1}$$

Neutral and charged B meson decays involving both tree and penguin amplitudes are a natural place to look for this effect and charmless meson decays have provided evidence for direct *CP* violation in $B^0 \to K^+\pi^-$, $B^0 \to \pi^+\pi^-$, $B^0 \to \eta K^{*0}$, and $B^+ \to \rho^0 K^+$ (see below).

The diagrams in Fig. 17.4.1 give a simplistic view of the decays. The weak decays of the B meson are subject to both short and long distance QCD effects. The calculation of these properties is challenging as it involves both short-distance perturbative and long-distance non-perturbative QCD. The various models, techniques and successes are the subject of the next section.

17.4.2 Theoretical overview

Theoretical calculations of charmless decays of B mesons are based on an effective description of the weak interaction valid at scales below the scale M_W. Extracting the CKM elements $\lambda_p^{(D)} \equiv V_{pb}V_{pD}^*$ ($p = u, c$, $D = d, s$), the effective Hamiltonian for $\Delta B = 1$ transitions is

$$H_{\rm eff} = \frac{G_F}{\sqrt{2}} \sum_{p=u,c} \lambda_p^{(D)} \sum_i C_i\, Q_i^p, \tag{17.4.2}$$

where Q_i^p denotes the so-called tree, QCD and electroweak penguin, and dipole operators. The Wilson coefficients C_i include the physics from the highest scales, including M_W, down to the scale m_b, and their calculation is under complete theoretical control, provided the underlying short-distance physics is known. Eq. 17.4.2 assumes the Standard Model, and the convention that $\lambda_t^{(D)}$ is eliminated by the unitarity relation $\lambda_u^{(D)} + \lambda_c^{(D)} + \lambda_t^{(D)} = 0$. The structure of the operators Q_i, the values of their Wilson coefficients, and the flavor structures can be modified in extensions of the SM.

It is sufficient to work to first order in the weak interaction. The decay amplitude $A(\bar{B} \to f) = \langle f|H_{\rm eff}|\bar{B}\rangle$ can be written as

$$A(\bar{B} \to f) = \lambda_u^{(D)} A_f^u + \lambda_c^{(D)} A_f^c\,. \tag{17.4.3}$$

The larger of the two partial amplitudes determines the branching fraction, while the interference with the subleading one causes the direct *CP* asymmetry, provided there is a relative strong phase between the hadronic amplitudes A_f^u and A_f^c. For a first estimate, the size of an amplitude is governed by three factors:

- the size of the Wilson coefficients, which divides the amplitudes into tree ($C_i \sim 1$) and penguin ($C_i \sim 0.1$) which are loop-suppressed. Tree amplitudes can be color-allowed or color-suppressed (see the introduction to the section on B decays to charm, 17.3).
- the size of the CKM factors is $\lambda_u^{(d)} \sim \lambda_c^{(d)} \sim \lambda^3$ for $b \to d$ transitions. For these transitions the penguin amplitude A_f^c is typically sub-leading on account of its smaller Wilson coefficient. For $b \to s$ transitions $\lambda_c^{(s)} \sim \lambda^2 \gg \lambda_u^{(s)} \sim \lambda^4$, hence these transitions are dominated by the loop-induced penguin amplitude despite their smaller Wilson coefficient.
- the size of the hadronic matrix elements $\langle f|Q_i^p|\bar{B}\rangle$, which can vary substantially depending on the spin and parity of the final state particles, and whether the final state can only be reached by annihilation of the B meson constituents. The direct *CP* asymmetry depends crucially on the phases of these matrix elements.

The three factors in combination lead to a fascinating variety of decay patterns, which are summarized in this section.

From the theoretical point of view, the basic problem for the quantitative prediction of charmless B decays is the computation of the hadronic matrix elements $\langle f|Q_i^p|\bar{B}\rangle$. The difficulty resides in the strong interaction, which cannot be treated perturbatively at the hadronic scale $\Lambda \approx 0.5\,\text{GeV}$ relevant to the formation of the hadronic final state f, and to the initial bound state. An extreme point of view ("non-perturbative anarchy") would declare the matrix elements to be non-perturbative and unpredictable. In this case, large phases and large direct *CP* asymmetries in charmless B decays would be expected. The other extreme is the assumption of naïve factorization. The operators Q_i can mostly be written as local products of two bilinear quark currents $J_i^a J_i^b$. In the decay of a B meson to two light mesons M, naïve factorization sets

$$\langle M_1 M_2|Q_i|\bar{B}\rangle \approx \langle M_1|J_i^a|\bar{B}\rangle\langle M_2|J_i^b|0\rangle \tag{17.4.4}$$

(with $M_1 \leftrightarrow M_2$ added where appropriate). With this assumption all direct *CP* asymmetries vanish.

A direct computation of the matrix elements $\langle f|Q_i^p|\bar{B}\rangle$ with numerical simulations of QCD is neither conceptually nor practically within reach. The available theoretical methods therefore exploit (approximate) flavor symmetries of QCD, or the existence of several scales, which allows for an expansion in Λ/m_b. The two methods are complementary to a large extent. While the $SU(3)$ approach does not allow the computation of any individual decay from first principles of QCD, its virtue lies in relating groups of decays by expressing them in terms of only a few reduced matrix elements. The second method, the factorization approach, begins with the identification of m_b, $\sqrt{m_b\Lambda}$, and Λ as relevant scales in $\langle f|Q_i^p|\bar{B}\rangle$. Only the scale Λ requires a non-perturbative treatment of the strong interaction. By computing the strong interaction effects at the other two scales perturbatively, a great deal of simplification of the matrix elements can be achieved. Most of the analytical progress in the theory of hadronic B

decays achieved over the past few years can be attributed to a systematic implementation of factorization and the heavy-quark expansion. The conclusion is that the truth for B decays lies in between the two above extremes, but closer to naïve factorization than non-perturbative anarchy. In the remainder of this section we provide a brief overview of the different methods and some generic results.

17.4.2.1 $SU(3)$ approach

The $SU(3)$ approach is based on an approximation to QCD, where the up, down, and strange quark masses are equal. In practice, this amounts to an expansion in m_s/Λ, or, since only the first term is kept, to the approximation $m_s \simeq 0$. In this approximation, QCD acquires an $SU(3)$ flavor symmetry. The quark fields, meson states and the weak interaction Hamiltonian are decomposed into $SU(3)$ representations, and the matrix elements $\langle f|H_{\rm eff}|\bar{B}\rangle$ are expressed in terms of reduced matrix elements and $SU(3)$ Clebsch-Gordan coefficients (Zeppenfeld, 1981). The generic accuracy of this approach is determined by the size of $SU(3)$-breaking corrections, which cannot be calculated. A typical estimate for the ratio of K and π decay constants $f_K/f_\pi - 1 \simeq 25\%$ at the amplitude level, though it appears that the non-factorizable $SU(3)$-breaking effects may be smaller than those in decay constants and form factors.

For applications it is more intuitive to work with topological or flavor amplitudes rather than the abstract reduced matrix elements, and hence this notation is widely used. These amplitudes arise naturally in factorization-based calculations of $\langle f|H_{\rm eff}|\bar{B}\rangle$ as well. The "color-allowed tree amplitude" T stands for an amplitude $\langle M_1M_2|\bar{B}\rangle$ with quark flavors $\langle[\bar{q}_s u][\bar{u}D]|[\bar{q}_s b]\rangle$ ($q_s = u, d, s$ the spectator quark, $D = d, s$); the "color-suppressed tree amplitude" C is related to $\langle[\bar{q}_s D][\bar{u}u]|[\bar{q}_s b]\rangle$. The terminology comes from the structure of the effective Hamiltonian $H_{\rm eff}$ and the naïve factorization approximation, where T (C) contains a large (small) combination of Wilson coefficients, giving rise to the naïve expectation that $C/T \simeq 0.2$. The "tree" amplitudes are distinguished from the QCD and electroweak "penguin" amplitudes, in which $u\bar{u}$ is replaced by $\sum_q q\bar{q}$ ($q = u, d, s$) and $\sum_q e_q q\bar{q}$, respectively .

The amplitudes for a given set of B decays are written in terms of the independent $SU(3)$ (or topological) amplitudes and CKM parameters, all of which are then fitted to the relevant data. There are often too many amplitude parameters to carry out this program to completion. Possible ways to proceed consist of marginalizing over the phases of amplitudes, resulting in "$SU(3)$ bounds" for the other parameters, or of making further simplifying assumptions beyond the $SU(3)$ limit. The most common additional assumptions are a particular implementation of meson-mixing for η, η' (ω, ϕ), and neglecting weak annihilation amplitudes.

For instance, with the latter assumption, the $B \to \pi\pi$ and $B \to \pi K$ decay amplitudes are parameterized as follows

$$
\begin{aligned}
\sqrt{2}\,\mathcal{A}_{B^-\to\pi^-\pi^0} &= \lambda_u^{(d)}[T + C + P_u^{EW} + P_u^{C,EW}] \\
&\quad + \lambda_c^{(d)}[P_c^{EW} + P_c^{C,EW}] \\
\mathcal{A}_{\bar{B}^0\to\pi^+\pi^-} &= \lambda_u^{(d)}[T + P_u + \frac{2}{3}P_u^{C,EW}] \\
&\quad + \lambda_c^{(d)}[P_c + \frac{2}{3}P_c^{C,EW}] \\
-\mathcal{A}_{\bar{B}^0\to\pi^0\pi^0} &= \lambda_u^{(d)}[C - P_u + P_u^{EW} + \frac{1}{3}P_c^{C,EW}] \\
&\quad + \lambda_c^{(d)}[-P_c + P_c^{EW} - \frac{1}{3}P_c^{C,EW}], \\
\\
\mathcal{A}_{B^-\to\pi^-\bar{K}^0} &= \lambda_c^{(s)}[P_c - \frac{1}{3}P_c^{C,EW}] \\
&\quad + \lambda_u^{(s)}[P_u - \frac{1}{3}P_u^{C,EW}] \\
\sqrt{2}\,\mathcal{A}_{B^-\to\pi^0 K^-} &= \lambda_c^{(s)}[P_c + P_c^{EW} + \frac{2}{3}P_c^{C,EW}] \\
&\quad + \lambda_u^{(s)}[T + C + P_u + P_u^{EW} + \frac{2}{3}P_u^{C,EW}] \\
\mathcal{A}_{\bar{B}^0\to\pi^+ K^-} &= \lambda_c^{(s)}[P_c + \frac{2}{3}P_c^{C,EW}] \\
&\quad + \lambda_u^{(s)}[T + P_u + \frac{2}{3}P_u^{C,EW}] \\
\sqrt{2}\,\mathcal{A}_{\bar{B}^0\to\pi^0\bar{K}^0} &= \lambda_c^{(s)}[-P_c + P_c^{EW} + \frac{1}{3}P_c^{C,EW}] \\
&\quad + \lambda_u^{(s)}[C - P_u + P_u^{EW} + \frac{1}{3}P_u^{C,EW}],
\end{aligned}
\tag{17.4.5}
$$

in terms of T, C, the two penguin amplitudes P_p, and four electroweak (EW) penguin amplitudes (the superscript "C" indicates color-suppressed). Since T, C, P_u, P_u^{EW} and $P_u^{C,EW}$ appear only as $T + P_u^{C,EW}$, $C + P_u^{EW}$, and $P_u - P_u^{C,EW}/3$ the parameterization contains six complex strong interaction amplitudes. Assuming only $SU(2)$ isospin symmetry, the most general parameterization of the $\pi\pi$ (πK) amplitudes requires four (six) complex numbers, so $SU(3)$ symmetry has eliminated four of the 10 independent amplitudes. The full power of $SU(3)$ symmetry becomes apparent, when one adds the analogous decomposition of the $B \to KK$ decays and all the $B_s \to \pi\pi$, πK, KK decays. The parameterization can be extended to include η and η' (requiring two singlet penguin amplitudes S_p and an assumption on meson-mixing), and to final states including vector mesons (requiring a larger number of new parameters).

The $SU(3)$ approach is primarily data-driven. No attempt is undertaken to predict the decay amplitudes from QCD dynamics. Where enough experimental information is available, $SU(3)$ relations can give direct access to CKM angles. In particular, if only the more accurate relations of $SU(2)$ isospin are required, this leads to strategies to determine angles almost free of theoretical uncertainties, as discussed elsewhere in this book. $SU(3)$ fits of large sets of final states have been performed (Chiang, Gronau, Luo, Rosner, and Suprun, 2004; Chiang, Gronau, Rosner,

and Suprun, 2004; Chiang and Zhou, 2006, 2009; Soni and Suprun, 2007).

17.4.2.2 QCD-based factorization

The factorization approach is more ambitious than the $SU(3)$ approach as it attempts the calculation of individual decays directly from the Lagrangian of the theory in terms of only a few remaining hadronic parameters. In the following, we outline the factorization structure of the matrix elements of hadronic two-body decays, and discuss some general results. The discussion applies to (quasi) two-body final states of mesons. A theoretical description of multi-body final states with similar rigour is not yet available.

The concept of factorization has a long history in B physics as an approximation of $\langle f|H_{\rm eff}|\bar{B}\rangle$ as a product of a decay constant, form factor and a Wilson coefficient (Bauer, Stech, and Wirbel, 1987; Wirbel, Stech, and Bauer, 1985). The term "QCD factorization" refers to a systematic separation of scales in $\langle f|H_{\rm eff}|\bar{B}\rangle$. Contrary to the (useful but ad-hoc) approximation of "naïve" factorization, QCD factorization implies an expansion of the matrix element in the small parameters $\alpha_s(\mu)$ and Λ/m_b, with $\mu = m_b$ or $\sqrt{m_b\Lambda}$ one of the perturbative scales. Since the α_s series can be calculated (with some effort), but only the leading term in the $1/m_b$ expansion assumes a simple form, the generic accuracy of this approach is limited by power corrections $\Lambda/m_b \simeq 20\%$ at the amplitude level.

The QCD factorization approach developed in (Beneke, Buchalla, Neubert, and Sachrajda, 1999, 2000, 2001) replaces the naïve factorization ansatz by a factorization formula that includes radiative corrections and spectator-scattering effects. Where it can be justified, the naïve factorization ansatz emerges in the simultaneous limit, when m_b becomes large and when radiative corrections are neglected. The basic formula for the hadronic matrix elements is

$$\begin{aligned}\langle M_1M_2|Q_i|\bar{B}\rangle &= F^{BM_1}(0)\int_0^1 du\, T_i^I(u)\Phi_{M_2}(u)\\ &\quad+\int_0^1 d\xi du dv\, T_i^{II}(\xi,u,v)\,\Phi_B(\xi)\Phi_{M_1}(v)\Phi_{M_2}(u)\\ &= F^{BM_1}\,T_i^{\rm I}\star\Phi_{M_2}+\Phi_B\star[H_i^{\rm II}\star J^{\rm II}]\star\Phi_{M_1}\star\Phi_{M_2}\,,\end{aligned}\tag{17.4.6}$$

where $F^{BM_1}(0)$ is a (non-perturbative) B to light-meson transition form factor, Φ_{M_i} and Φ_B are light-cone distribution amplitudes, and $T_i^{\rm I,II}$ are perturbatively calculable hard-scattering kernels. M_1 is the meson that picks up the spectator quark from the B meson, as illustrated in Fig. 17.4.2. The third line uses a short-hand notation $\star$ for convolutions and indicates that the spectator-scattering effect in the second line is a convolution of physics at the hard scale m_b, encoded in $H_i^{\rm II}$, and the hard-collinear scale $\sqrt{m_b\Lambda}$, encoded in the jet function $J^{\rm II}$. Eq. 17.4.6 shows

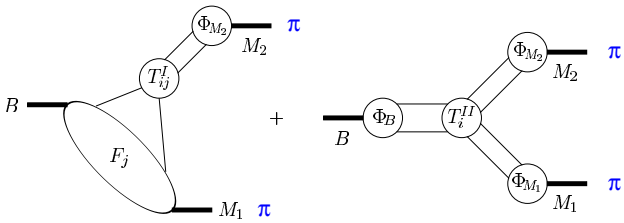

Figure 17.4.2. Graphical representation of the factorization formula given Eq. 17.4.6 (Beneke, Buchalla, Neubert, and Sachrajda, 2000).

that there is no long-distance interaction between the constituents of the meson M_2 and the (BM_1) system at leading order in $1/m_b$. This is the precise meaning of factorization. Strong interaction scattering phases are generated at leading order in the heavy-quark expansion only by perturbative loop diagrams contributing to the kernels $T_i^{\rm I}$ and $H_i^{\rm II}$. Thus the phases are of order $\delta\sim\mathcal{O}(\alpha_s(m_b),\Lambda/m_b)$.

Factorization as embodied by Eq. 17.4.6 is not expected to hold at sub-leading order in $1/m_b$. Some power corrections related to scalar currents are enhanced by factors such as $m_\pi^2/((m_u+m_d)\Lambda)$. Some corrections of this type, in particular those related to scalar penguin amplitudes, nevertheless appear to be calculable and turn out to be numerically important. On the other hand, attempts to compute sub-leading power corrections to hard spectator-scattering in perturbation theory usually result in infrared divergences, which signal the breakdown of factorization. These effects are usually estimated and included into the error budget. All weak annihilation contributions belong to this class of effects and often constitute the dominant source of theoretical error, in particular for the direct CP asymmetries. Factorization as above applies to pseudoscalar flavor-non-singlet final states and to the longitudinal polarization amplitudes for vector mesons. Final states with η and η' require additional considerations, but can be included (Beneke and Neubert, 2003a). The transverse helicity amplitudes for vector mesons are formally power-suppressed but can be sizeable, and do not factorize in a simple form (Beneke, Rohrer, and Yang, 2007; Kagan, 2004). The description of polarization is therefore more model-dependent than branching fractions and CP asymmetries. QCD factorization results are available for a variety of complete sets of final states. (Beneke and Neubert, 2003b; Beneke, Rohrer, and Yang, 2007) contain the theoretical predictions for pseudoscalar and vector meson final states (PP, PV, VV). A similar analysis has been performed for final states with a scalar meson (Cheng, Chua, and Yang, 2008), axial-vector mesons (Cheng and Yang, 2007, 2008), and a tensor meson (Cheng and Yang, 2011).

Several variations of factorization have been considered in the literature and applied to the calculation of branching fractions, CP asymmetries and polarization observables. The perturbative QCD (PQCD) framework (Keum, Li, and Sanda, 2001; Lu, Ukai, and Yang, 2001) makes the stronger (and controversial) additional assumption that the B meson transition form factors $F^{B\to M_1}(0)$

are also dominated by short-distance physics and factorize into light-cone distribution amplitudes. Both terms in Eq. 17.4.6 can then be combined to

$$\langle M_1 M_2|Q_i|\bar{B}\rangle = \phi_B \star [T^{\rm PQCD} \star J^{\rm PQCD}] \star \phi_{M_1} \star \phi_{M_2}. \quad (17.4.7)$$

PQCD needs fewer non-perturbative input parameters, but there is a larger dependence on unknown light-cone distribution amplitudes. Since the approach relies on regularizing the infrared sensitivity by intrinsic transverse momentum, there is a larger sensitivity to perturbative corrections at low scales, where the strong coupling is large and perturbation theory is potentially unreliable. From a phenomenological perspective, the principal difference between the PQCD and all other approaches is the relative importance of the weak annihilation mechanism. In QCD factorization the strong interaction phases arise at the scale m_b from loop diagrams, that have yet to be included in the PQCD approach, and from the model for weak annihilation. In the most widely used implementation of PQCD, the strong phases originate only from a weak annihilation tree diagram. As a consequence, the predicted direct *CP* asymmetries can be rather different in the two approaches. There is a large literature covering individual or few decay modes in PQCD. Large sets of final states were analyzed in (Ali et al., 2007; Li and Mishima, 2006). We note that the PQCD factorization formula Eq. 17.4.7 was recently revised due to infrared divergences in loop effects (Li and Mishima, 2011), which weakens its predictive power. Most phenomenological analyses predate this revision.

Alternative to the diagrammatic arguments put forward in the BBNS approach in (Beneke, Buchalla, Neubert, and Sachrajda, 1999, 2000, 2001), factorization of charmless B decays can be elegantly derived in the framework of soft-collinear effective theory (SCET) (Bauer, Pirjol, Rothstein, and Stewart, 2004; Beneke and Feldmann, 2004; Chay and Kim, 2004). It is important to stress that the theoretical basis of QCD factorization and SCET is exactly the same. However, the phenomenological implementation of factorization put forward in (Bauer, Pirjol, Rothstein, and Stewart, 2004) differs in two respects from the BBNS approach. First, perturbation theory at the intermediate scale $\sqrt{m_b \Lambda}$ is avoided by not factorizing the spectator-scattering term into a hard and jet function. Eq. 17.4.6 then takes the form

$$\langle M_1 M_2|Q_i|\bar{B}\rangle = F^{BM_1}\, T_i^{\rm I} \star \Phi_{M_2} + \Xi^{BM_1} \star H_i^{\rm II} \star \Phi_{M_2}\,, \quad (17.4.8)$$

where Ξ^{BM_1} is a generalized, non-local B meson form factor related to the matrix element $\langle M_1|\bar{q} A_\perp b|\bar{B}\rangle$ (Beneke and Feldmann, 2004), which depends on momentum transfer q^2 and an additional convolution variable. Second, penguin diagrams with charm loops (Ciuchini, Franco, Martinelli, Pierini, and Silvestrini, 2001) are supposed to be non-factorizable, hence non-perturbative. From the phenomenological perspective, the principal difference to the BBNS approach concerns again the generation of strong interaction phases. Since the non-local form factor is unknown, Eq. 17.4.8 can be used only at the tree level, hence the amplitudes, including the color-suppressed tree amplitude C, have no phases. The only exception is the charm penguin amplitude P_c, which is considered as an unknown complex number and is therefore the only source of direct *CP* violation. The approach proposed in (Bauer, Pirjol, Rothstein, and Stewart, 2004) assumes that scalar penguin and weak annihilation power corrections are zero, but since P_c is a phenomenological parameter, this has no effect on the analysis. Because of the need to fit the dominant penguin amplitudes to data, the "SCET" approach, unlike the QCD factorization or PQCD approach, shares many features of other data-driven approaches such as the $SU(3)$ amplitude approach. It uses the fewest theoretical assumptions of the three factorization-based methods, at the price of having less predictive power. Large sets of final states have been analyzed with this method in (Bauer, Rothstein, and Stewart, 2006; Wang, Wang, Yang, and Lu, 2008; Williamson and Zupan, 2006). We mention that the question whether the penguin loops with charm factorize or not, which for some time has been a point of controversy, has meanwhile been resolved in favor of factorization (Beneke, Buchalla, Neubert, and Sachrajda, 2009).

For a more detailed comparison of the various QCD-based factorization approaches we refer to the short review in (Artuso et al., 2008). This review also provides an overview of the status of the calculation of radiative corrections, which up to now are computed at next-to-leading order (NLO), and partly even at next-to-next-to-leading order (NNLO) (Bell, 2008, 2009; Beneke, Huber, and Li, 2010; Beneke and Jager, 2006, 2007), only in the QCD factorization (BBNS) approach.

17.4.2.3 Generic results

To conclude this overview we summarize a few general results that emerged from comparing theoretical calculations to data. The remainder of this section contains a more specific mode-by-mode analysis. The comparison still suffers from a lack of precise knowledge of quantities such as $|V_{ub}|$, B meson form factors, and light-cone distributions amplitudes, which cause a significant theoretical uncertainty.

1. The *color-allowed tree amplitude* T that governs the branching fractions of decays to final states such as $\pi^+\pi^-$ and its vector-meson relatives is well described by factorization, and even close to its naïve factorization value. The main uncertainty in color-allowed tree-dominated decays comes from $F^{BM_1}(0)$, the B meson form factor.
2. The *color-suppressed tree amplitude* C that governs branching fractions of decays to final states such as $\pi^0\pi^0$ and its vector-meson relatives is often underestimated. Its value depends strongly on the precise magnitude of the spectator-scattering effect. This can be seen from the numerical representation (Beneke, Huber, and Li, 2010) of the NNLO color-suppressed tree amplitude:

$$\alpha_2(\pi\pi) = 0.220 - [0.179 + 0.077\, i]_{\rm NLO}$$

$$
\begin{aligned}
&- [0.031 + 0.050\,i]_{\rm NNLO} \\
&+ \left[\frac{r_{\rm sp}}{0.445}\right] \Big\{ [0.114]_{\rm LOsp} \\
&+ [0.049 + 0.051 i\,]_{\rm NLOsp} + [0.067]_{\rm tw3} \Big\} \\
&= 0.240^{+0.217}_{-0.125} + (-0.077^{+0.115}_{-0.078}) i\,. \qquad (17.4.9)
\end{aligned}
$$

Here 0.220 represents the naïve factorization value. Loop corrections to the form-factor-like term in the first line of Eq. 17.4.6 and the first two lines of Eq. 17.4.9 almost cancel this number, but generate a sizable imaginary part, *i.e.* scattering phase. The real part of the amplitude is regenerated by spectator-scattering in the second line of Eq. 17.4.6 and the third and fourth line of Eq. 17.4.9. It is evident that the strong interaction dynamics of the color-suppressed tree amplitude is far from the naïve factorization picture, and is governed by quantum effects. The theoretical uncertainty is correspondingly large.

3. The *QCD penguin amplitude* P that governs branching fractions of decays to final states such as πK and its vector-meson relatives is certainly underestimated in leading order in the heavy-quark expansion. The power-suppressed but chirally-enhanced scalar penguin amplitude, and perhaps a (difficult to disentangle) weak annihilation contribution, is required to explain the penguin-dominated PP final states. While the scalar penguin amplitude is calculable, some uncertainty remains. An important observation is the smaller size of the PV, VP and VV penguin amplitudes as compared to PP final states, which can be inferred from the measured branching fractions of hadronic $b \to s$ transitions. This is a clear indication of the relevance of factorization, which predicts this pattern as a consequence of the quantum numbers of the operators Q_i. If the penguin amplitude were entirely non-perturbative, no pattern of this form would be expected. A similar statement applies to the $\eta^{(\prime)} K^{(*)}$ final states, where factorization explains naturally the strikingly large differences in branching fractions, including the large $\eta' K$ branching fraction, through the interference of penguin amplitudes, although sizeable theoretical uncertainties remain. A flavor-singlet penguin amplitude seems to play a sub-ordinate role in these decays.
4. The situation is much less clear for the *strong phases and direct CP asymmetries*. A generic qualitative prediction is that the strong phases are small, since they arise through either loop effects ($\alpha_s(m_b)$) or power corrections (Λ/m_b). Enhancements may arise, when the leading-order term is suppressed, for instance by small Wilson coefficients. This pattern is indeed observed. Quantitative predictions have met only partial success. The observed direct *CP* asymmetry in the decay to $\pi^+\pi^-$, and the asymmetry difference in the decays to $\pi^0 K^+$ and $\pi^- K^+$ are prominently larger than predicted. A comparison of all *CP* asymmetry results shows a pattern of quantitative agreements and disagreements that are not presently understood. Since $\alpha_s(m_b)$ and Λ/m_b are roughly of the same order, it is quite possible that power corrections are $\mathcal{O}(1)$ effects relative to the perturbative calculation, preventing a reliable quantitative estimate. However, the direct *CP* asymmetry calculations are still LO calculations, contrary to the branching fractions, so the final verdict must await the completion of the NLO asymmetry calculation. Contrary to direct *CP* asymmetries, the S parameter that appears in time-dependent *CP* asymmetries is predicted more reliably, since it does not require the computation of a strong phase. This is exploited in computations of the difference between $\sin 2\phi_1$ from $b \to s$ penguin dominated and $b \to c\bar{c}s$ tree decays (Beneke, 2005; Cheng, Chua, and Soni, 2005b).
5. *Polarization in $B \to VV$ decays* was expected to be predominantly longitudinal, since the transverse helicity amplitudes are Λ/m_b suppressed due to the V-A structure of the weak interaction and helicity conservation in short-distance QCD. While this is parametrically true (with one exception (Beneke, Rohrer, and Yang, 2006)), a closer inspection shows that the parametric suppression is hardly realized in practice for the penguin amplitudes (Beneke, Rohrer, and Yang, 2007; Kagan, 2004). This leads to the qualitative prediction (or rather, in this case, postdiction) that the longitudinal polarization fraction should be close to 1 in tree-dominated decays, but can be much less, even less than 0.5, in penguin-dominated decays, as is indeed observed. However, quantitative predictions of polarization fractions for penguin-dominated decays must be taken with a grain of salt, since they rely on model-dependent or universality-inspired assumptions of the non-factorizing transverse helicity amplitudes.

The remainder of this chapter is devoted to an overview of experimental techniques of importance to charmless B decay measurements and provides a summary of two-body and three-body final state data collected by the *BABAR* and Belle experiments. A detailed comparison and interpretation of the data in the light of theoretical approaches as discussed above is beyond the scope of this review. For this reason we will generally refrain from making reference to specific theoretical papers in the following.

17.4.3 Experimental techniques

The decays of B mesons to final states with two or three hadrons without a charm quark are loosely broken down into "two-body", "quasi-two-body" and "three-body" decays. The "two-body" analyses concentrate on long-lived final states such as $\pi\pi$, $K\pi$, KK, etc. As these modes can be used to access the CKM angle ϕ_2, they are covered in Chapter 17.7; only the observation of direct *CP* violation is discussed here. The "quasi-two-body" category includes decays where one or both of the decay products is a resonance. Final state particles that have been measured include scalar (S) particles (a_0 (980), $f_0(980)$, $f_0(1370)$, $f_0(1500)$, $K_0^*(1430)$); pseudoscalar (P) particles ($K^\pm$, K^0, $\pi^\pm$,π^0, η, η'); vector (V) particles (ρ, ϕ, ω, K^*); tensor (T) particles ($K_2^*(1430)$, $f_2(1270)$); and axial-vector (A)

mesons, which can be classified into two groups as the $^3P_1$ nonet ($a_1(1260)$, $f_1(1285)$, $f_1(1420)$, K_{1A}) and the $^1P_1$ nonet (b_1, $b_1(1170)$, $b_1(1380)$, K_{1B}).[56] Three-body charmless decays concentrate on final states with π or K but can sometimes branch out to include protons and resonances such as K^* *e.g.* $B^+ \to \bar{p}pK^+$ (see Chapter 17.12) and $B^+ \to K^{*0}K^{*0}K^+$.

The "quasi-two-body" decays are traditionally reconstructed assuming that the resonances decaying to the same final state (such as ρ and $f_0(980)$ decaying to $\pi\pi$) do not interfere. This has the advantage that branching fractions can be compared to measurements from earlier experiments but the effect of interference is then considered as a systematic. The main differences between the ways that decays are analysed are usually dictated by the extent and nature of the background, as the B meson charmless decays have a low signal-to-background ratio. This can be compared to D meson decays which are typically selected with very high purity.

Whatever the final state, the candidate selection process follows a broadly similar path (see Chapter 7 for more details on B meson reconstruction). The B meson candidates are reconstructed through their decays. The intermediate resonance will be formed first and then combined with a third particle to form the B meson. The reconstructed mass will usually be required to be less than ~ 3 times the width from the nominal central value. If the natural widths of the resonances are smaller than the detector resolution, the resonance masses (including π^0's) are constrained to their nominal PDG values in the fit for the B meson candidate (Beringer et al., 2012); this improves the precision of the parameters obtained in the fit. Quality criteria are applied to the tracks before fitting, such as demanding the tracks are well-measured, have a minimum p_T, and originate from close to the beam spot. The momenta of the charged tracks will usually be extracted assuming a particular mass hypothesis determined by the particle type (*e.g.* pion versus kaon, see Chapter 5). However, in some analyses, such as $B^0 \to h^+h^-$ (with $h = K, \pi$), the B meson will be fitted under one mass hypothesis (usually a pion), and any shift in the value of ΔE is used to differentiate between decays with one or more kaons. The shift is of the order of $\sim 50\,\text{MeV}$ per kaon. The vertexing will apply various constraints to improve the resolution (see Chapter 6) and to take into account the flight distance of long lived particles such as the K^0_S meson. These constraints become more important as the number of neutral particles in the decay increases. A further criterion that is sometimes applied is to require that there is at least one additional charged track from the beam spot region; this is a crude indicator that there has been at least one other decay in the event, which is assumed to be the other B meson.

Two kinematic variables, m_{ES} and ΔE, are used to select the events (see Eqs 7.1.8 and 7.1.5 for definitions). Any linear correlation between these variables can be removed by rotating them in the (m_{ES}, ΔE) plane or a two dimensional *p.d.f.* can be used in the maximum likelihood (ML) fit. Events with $|\Delta E| < 300\,\text{MeV}$ are typically accepted, although an asymmetric acceptance region is used if there is a chance of energy loss from photon emission or π^0 reconstruction. The minimum value of m_{ES} is set to allow a good fit to the m_{ES} background distribution and is rarely set less than $5.220\,\text{GeV}/c^2$ (below this value, other selection criteria start to distort the selection efficiency).

The (m_{ES}, ΔE) plane is divided into regions to aid analysis. A signal region is defined around the point $m_{\text{ES}} = m_B, \Delta E = 0$ with a width roughly 3 times the resolution on m_{ES} ($\sim 3\,\text{MeV}/c^2$) and ΔE ($\sim 20-50\,\text{MeV}$, depending on the number of neutral particles). Although the signal region is usually rectangular in shape, elliptical signal regions have been used *e.g.* Fig. 3 in (Garmash, 2005). Two sidebands are defined above and below the ΔE signal region, the upper region allowing for the study of two-body decays that have been combined with a random track and the lower region to study four-body decays that have lost a track. A further sideband below the signal region in m_{ES} can be used to study the continuum background, although care must be taken to account for any decays from B mesons.

In the center-of-mass (CM) frame, the continuum background is characterized by a jet-like, back-to-back structure while the $B\overline{B}$ events have a more spherical distribution since they are produced close to rest (see Chapter 9 for details). Therefore, event shape variables are used to separate signal from this background. Many different criteria have been used over the years including sphericity, spherocity, planarity, acoplanarity and thrust (see the Glossary and Chapter 9). In addition, angles are often measured between the direction of the B meson decay and a reference axis, such as the beam line or the direction of the rest of the event (ROE). An important example is the thrust angle in the CM frame, defined as the angle θ_T between the thrust axis of the B meson candidate and that of the rest of the particles in an event. Signal events are uniformly distributed in $\cos\theta_T$, while continuum events are peaked near $\cos\theta_T = \pm 1$. A requirement on $\cos\theta_T$ or $|\cos\theta_T|$ of less than $0.7 - 0.9$ is usually applied.

Any remaining event shape variables are combined into a multivariate discriminant that can either be used as selection criteria or as a *p.d.f.* observable in a ML fit. Fisher discriminants and neural networks are popular but Boosted Decision Trees (or Forests) have also been applied (see Chapter 4 for details). The number of variables is typically about six. Although discriminants with many more variables have been tried, they rarely bring any additional discrimination. The choice of variables depends on the mode under consideration, consistency with previously used discriminants, and ultimately on the prejudice of the analyst. It is important to check for correlations between the input variables and any other variables used in the ML fit. Variables that have been used over the years include (see Chapter 9 for many definitions): CLEO cones (momentum distribution in nine angular cones about the thrust vector); modified Fox-Wolfram moments (Abe, 2001c); the variable S_T, the scalar sum of the transverse momenta, calculated with respect to the

[56] $K_1(1270)$ and $K_1(1400)$ are admixtures of K_{1A} and K_{1B}

thrust axis, of particles outside a 45° cone around the B thrust axis, divided by the scalar sum of their momenta (Jen, 2006); the polar angles of the B meson momentum vector and the B meson thrust axis with respect to the beam axis; the angle between the B meson thrust axis and the thrust axis of the rest of the event; and the ratio of the second- and zeroth-order momentum-weighted polynomial moments of the energy flow around the B meson thrust axis (Aubert, 2004a). Although not strictly event shape variables, some success has been achieved by using two additional inputs to the neural network: the flavor of the other B meson as reported by a multivariate tagging algorithm (Aubert, 2005i); and the boost-corrected proper-time difference between the decay vertices of the two B mesons divided by its error. The multivariate discriminant can be trained with Monte Carlo (MC) simulation for the signal, and $q\overline{q}$ continuum MC, off-resonance data or sideband data for the background. The discriminant can sometimes be used as a selection criterion as well as a *p.d.f.* as a simple cut on the output can eliminate a substantial part of the background (of the order of 20%-40%) with little signal loss. Instead of using the tagging information in the event-shape, Belle have sometimes used the B meson flavor tagging output (Kakuno, 2004) to calculate a figure of merit; signal retention of greater than 60% with background rejection greater than 90% has been achieved (Jen, 2006).

B meson decays to charm have large branching fractions and final states that are either the same as the mode under consideration or easily mis-reconstructed. These charm backgrounds can be suppressed by reconstructing the charm candidate from combinations of tracks and applying a veto around the nominal mass (typically $\sim 40\,\mathrm{MeV}/c^2$ for the D meson).

The helicity distribution is an important variable that can be used to identify particles of a particular spin, extract the longitudinal polarization f_L, or simply as a selection criterion. The helicity angle θ_H of the resonance is defined as the angle between the momentum vector of one of the resonance's daughter particles and the direction opposite to the B meson momentum in the resonance rest frame (Kramer and Palmer (1992)). The choice of daughter must be consistent from event to event (either based on charge or flavor) and care must be taken to avoid any unexpected ordering in momentum or azimuthal angle introduced by the track finding algorithms.

It is often necessary to limit the range of the helicity angle. At values of $|\cos\theta_H| > 0.9$ the signal reconstruction efficiency starts to fall off, as one of the daughter tracks of the resonance has a low momentum. At the same time, backgrounds created from combinations of tracks start to increase. If the resonance decays to particles of differing mass, then the momentum selection criteria on the daughter particles will cause the $\cos\theta_H$ distribution to be skewed, requiring careful compensation for the change in efficiency. The allowed range of $\cos\theta_H$ is mode dependent but typically events are rejected if $\cos\theta_H$ is greater than $0.7 - 0.9$, with different ranges for negative and positive $\cos\theta_H$. In Vector-Vector (VV) decays, the longitudinal component is typically dominant and causes the helicity angle distribution to be enhanced near ± 1. For these decays, careful consideration of the $\cos\theta_H$ rejection criterion is required to optimize the signal and background ratio. The value of the longitudinal component is an important measurement (see Section 17.4.5.3) so care must be taken to limit any bias in the acceptance.

There can be multiple B meson candidates in an event. The average number of candidates per accepted event ranges up to ~ 1.5, with more mis-reconstructed candidates expected in decays with more neutrals (such as π^0) due to low-energy photons or noise in the electromagnetic calorimeter. Resonances with large widths (such as ρ^0) also have more mis-reconstructed candidates due increased combinatorics. One approach to dealing with multiple candidates is to accept all N candidates in an event with a weight $1/N$ applied to each, but usually a criterion is used to select the best one. This is sometimes a random choice but more common methods rely on a χ^2 based on the pull of the fitted resonance mass from the nominal value or the B meson vertex probability. The accuracy of the selection depends on the mass width of the resonance and the number of neutral particles in the fit. The true candidate is selected with an accuracy that is rarely below 75% and often greater than 95%, based on MC simulation. If the number of mis-reconstructed candidates is large then these "self-crossfeed" candidates are sometimes included as a separate hypothesis category in the ML fit. There is no agreed point at which this happens but it is typically considered as an option when the true candidate selection accuracy falls below $\sim 85\%$.

After the application of all the selection criteria, there will still be a number of backgrounds from B meson decays either from decays via a charm particle that have not been rejected by the D meson mass requirement or B meson decays that have been mis-reconstructed. Unlike the continuum background, these $B\overline{B}$ backgrounds are likely to have a peaking distribution in one or more of the observables used in a ML fit. The contribution to the background from $B\overline{B}$ decays is identified by running the selection on generic $B\overline{B}$ background MC decays, where all the known decay channels have been included. Decays that have not been observed are often included assuming some estimated branching fraction $(10^{-6} - 10^{-5})$ that allows a small number to be selected and characterized. If a decay is observed to pass the selection, the analysis is rerun on the exclusive MC events to extract an estimate of the number of events expected in the final sample. If there are many modes (~ 20 are not uncommon) an attempt is often made to group them into a smaller number based on similarities in the distributions of the observables. The combined sample must be correctly weighted by the expected branching fractions and reconstruction efficiencies for each individual mode. This is a problem for decays that have not been measured yet and in these cases it is typical to assume a branching fraction that is about half the reported branching fraction upper limit. If no upper limit has been reported, a branching fraction is chosen

such that only a few events can be expected to appear in the data.

Higher mass resonances that peak outside the invariant mass selection region can still feed-down to the signal region because: they have a large width, such as $f_0(1370)$; through reflection, where a daughter particle is mis-identified, such as in $B \to \omega\pi^+$; or where a resonance has a long range component *e.g.* the S-wave component of the $K_0^*(1430)$. These backgrounds are often treated in a separate analysis that looks in the mass region above the resonance under consideration (since this is still blinded) and performs a ML fit to the higher mass region using $m_{\rm ES}$, ΔE, the multivariate discriminant, and the reconstructed mass. Once the yield is extracted, the number of events in the resonance signal region is estimated by extrapolating the fitted mass *p.d.f.* (or a fit to the extracted ${}_sWeights$, see Chapter 4) down to the low mass region and integrating.

A further category of background occurs when the B meson decays to the same final state without passing through a resonance, such as $B^+ \to \pi^+\,\pi^-\,\pi^+$ when looking for $B^+ \to \rho^0\,\pi^+$ or $B^0 \to \pi^+\,\pi^-\,\rho^0$ when looking for $B^0 \to \rho^0\,\rho^0$. These backgrounds also become important when D mesons are used as calibration channels as these "non-resonant" decays can be responsible for a significant number of the events underneath the calibration channel of interest. Strictly speaking, "non-resonant" means a decay in a Dalitz Plot that is uniformly distributed in phase space (see later and Chapter 13). However, this distinction is generally ignored and any final state which cannot be represented by a peaking structure is usually categorized as non-resonant. This has practical benefits when performing a fit as it is often difficult to identify the source of smoothly varying distributions. A fit which uses more than one such distribution is likely to find that the background events flow between the different distributions without affecting the significance of the signal. As a result, some papers will report a non-resonant measurement while others will simply consider it as part of the background.

The signal modes, mis-reconstructed signal modes (if used), continuum background and $B\overline{B}$ backgrounds distributions are used in a ML fit to extract the signal yield, branching fraction, A_{CP}, and longitudinal polarization f_L. The observables used are usually $m_{\rm ES}$, ΔE, the multivariate discriminant and the intermediate resonance masses. If an angular analysis is required, the helicity $\cos\theta_H$ of the resonances is also used. In this later case, the reconstruction efficiency as a function of $\cos\theta_H$ must be taken into account, often by multiplying the expected true distribution by a polynomial of a suitable order. The efficiency for the other variables is usually treated as uniform.

The observables used in the *p.d.f.*s are usually assumed to be uncorrelated and the total *p.d.f.* is taken to be the product of the separate individual *p.d.f.*s. However, in some cases this assumption is invalid and the correlations need to be taken into account explicitly. If the correlation only exists between two observables and is reasonably linear, then the correlation can be reduced by using rotated variables derived from the observables in the *p.d.f.*s. Sometimes, a two-dimensional *p.d.f.* is used. A third option is to create a *p.d.f.* based on one of the observables, where the *p.d.f.* parameters (*e.g.* means and widths) are dependent on the other observable.

A standard set of cross-checks on the fit is performed. The *p.d.f.*s are used to generate a series of simulated data samples that are then fitted with the ML method. This reveals any problems with minimization, pulls and biases. The tests are repeated with data samples generated from the full MC simulated data; this can reveal problems with correlations between observables. The ML fit is sometimes performed on a calibration channel taken from the data, such as a charm decay to the same or similar final state as the B meson decay under consideration. In this case, the ML model is simplified (*e.g.* no angular observables are used), any charm vetoes are removed, and all the model parameters are floated, if possible. This can reveal any differences between the MC simulation and data in the $m_{\rm ES}$ and ΔE signal distributions, which can then be corrected for in the final fit.

The systematic uncertainties for the result are often separated into two categories and will depend on the measurement under consideration. Additive systematics affect the fit yield and hence the significance of a branching fraction measurement. Multiplicative systematics affect the central value of the result but not the significance. In the additive category, we place uncertainties on the accuracy of the fixed parameters in the *p.d.f.*s, any ML fit biases in extracting the yields, model-dependent parameters (such as the mean and width of poorly known resonances), the presence or absence of uncertain resonances (such as the $\sigma(600)$), interference, $B\overline{B}$ background yields, and uncertainty on the longitudinal polarization f_L. In a large number of modes, the uncertainty on the fixed parameters extracted from the MC simulation is the dominant systematic (see Chapter 15 for more details on systematic error estimation). In the multiplicative category falls the reconstruction efficiency uncertainties arising from differences between data and MC simulation from tracking, uncertainties in the branching fractions of any intermediate decays, charged particle identification, neutral particle (π^0) identification, and long-lived particle (K_S^0) identification. Also, the accuracy of the known $B\overline{B}$ cross-section, luminosity and limited MC statistics can contribute. If various sub-decays are combined (*e.g.* $K^{*+} \to K_S^0\,\pi^+$ or $K^+\,\pi^0$) to form an overall measurement, the multiplicative systematics are correlated and must be added linearly.

Many of the systematic errors associated with f_L and A_{CP} cancel since these two measurements are based on ratios of signal yields. The systematic uncertainty on A_{CP} caused by the detector responding differently to positive and negative tracks or the presence of s and $\overline{s}$ in K^- and K^+ respectively is generally considered to be 0.5% at most.

Once calculated, the systematic error is convolved with the likelihood function with a Gaussian distribution with a variance equal to the total systematic error (see Chapter 15). The signal significance is then defined as $\sqrt{2\Delta \ln \mathcal{L}}$,

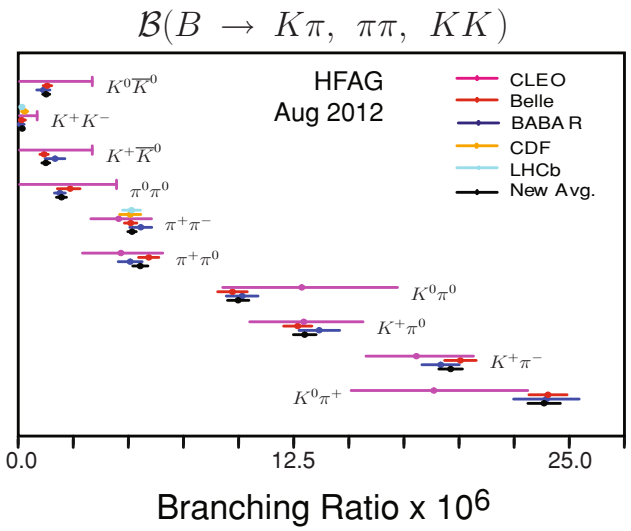

Figure 17.4.3. Summary of branching fraction measurements ($\times 10^{-6}$) and HFAG averages for two-body decays to $K\pi$,$\pi\pi$ and KK (Amhis et al. (2012)).

where $\Delta \ln \mathcal{L}$ is the change in log-likelihood $\ln \mathcal{L}$ from the maximum value to the value when the number of signal events is set to zero. If multiple signal resonances are extracted in the same fit it is often helpful to state the linear correlation coefficient between the results.

17.4.4 Two-body decays

In this section, we just report on branching fractions and A_{CP} measurements; further details are covered in Chapter 17.7. Table 17.4.1 summarises the branching fraction and direct CP measurements made for charmless two-body decays, while Figure 17.4.3 illustrates the branching fraction measurements made so far.

The final state particles in B meson decays to two long-lived particles benefit from having relatively larger momenta than most B decays, leading to a cleaner analysis environment. Decays such as $B \to K\pi$ and $B \to \pi\pi$ are therefore good places to look for new physics and CP violation, both direct and indirect. The first observations of QCD penguin $b \to d$ transitions were made in $B^+ \to \overline{K}^0 K^+$ (Aubert, 2006ai) and $B^0 \to K^0 \overline{K}^0$ (Abe, 2005e).

The decay $B^0 \to K^+\pi^-$ proceeds via both $b \to u$ tree and $b \to s$ transitions, which can interfere, leading to a direct CP violating asymmetry (Lin, 2008). The two dominant decay diagrams are shown in Fig. 17.4.4. The world average is now $A_{CP}(K^+\pi^-) = -0.098 \pm 0.013$. The four $K\pi$ asymmetries can be related through sum rules. From Eq. 17.4.5 it follows that

$$\mathcal{A}_{B^- \to \pi^- \bar{K}^0} - \sqrt{2}\,\mathcal{A}_{B^- \to \pi^0 K^-} + \mathcal{A}_{\bar{B}^0 \to \pi^+ K^-} + \sqrt{2}\,\mathcal{A}_{\bar{B}^0 \to \pi^0 \bar{K}^0} = 0 \qquad (17.4.10)$$

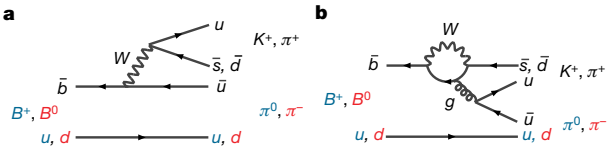

Figure 17.4.4. The dominant Tree-level (a) and Penguin-loop (b) Feynman diagrams in the two-body decays $B \to K\pi$ and $B \to \pi\pi$ (Lin, 2008).

This, together with the fact that penguin decays dominate, leads to the prediction (Gronau, 2005)

$$\Delta(K^+\pi^-) + \Delta(K^0\pi^+) = 2\,(\Delta(K^+\pi^0) + \Delta(K^0\pi^0)) \times (1 + \mathcal{O}(5\%)) \qquad (17.4.11)$$

where $\Delta(K\pi) = \Gamma(\overline{B} \to \bar{K}\bar{\pi}) - \Gamma(B \to K\pi)$. Consequently, it is expected that:

$$A_{CP}(K^+\pi^-) + A_{CP}(K^0\pi^+) \approx A_{CP}(K^+\pi^0) + A_{CP}(K^0\pi^0) \qquad (17.4.12)$$

The sum rule prediction for the width agrees quite well with experimental results. If $A_{CP}(K^0\ \pi^+)$ and $A_{CP}(K^0\ \pi^0)$ are small then the predicted values for $A_{CP}(K^+\ \pi^0)$ and $A_{CP}(K^+\ \pi^-)$ are very similar. However the measured values for $A_{CP}(K^+\ \pi^0)$ and $A_{CP}(K^+\ \pi^-)$ differ by about five standard deviations. This is shown in Fig. 17.4.5 where the difference in the number of events is clearly visible and the sign of the difference between the number of events in $B^0 \to K^+\pi^-$ is opposite to that of $B^+ \to K^+\pi^0$. This could be a sign of new physics but other effects, including enhancements in sub-dominant decay diagrams or strong interaction effects, have also been suggested as an explanation.

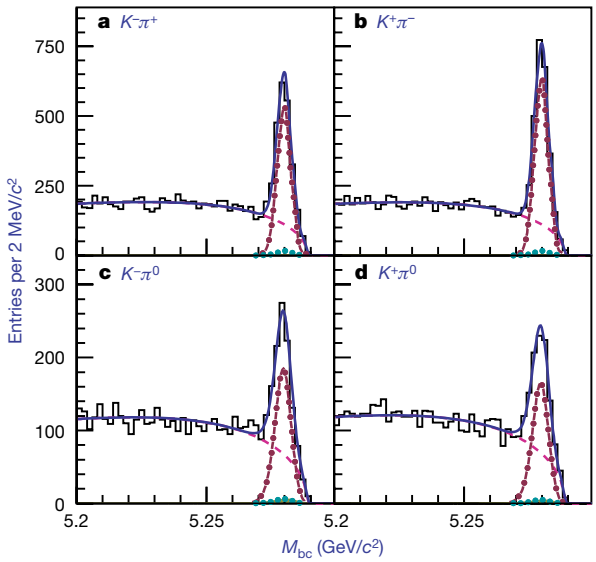

Figure 17.4.5. The direct *CP* violation in $B \to K^{\mp}\pi^{\pm}$ (top) and $B^{\pm} \to K^{\pm}\pi^0$ (bottom) can be seen in the difference between the heights of signal distributions (red/points) in the left and right plots (Lin, 2008).

Table 17.4.1. Charmless B decays branching fractions $\mathcal{B}$ and CP asymmetries A_{CP} for *BABAR* and Belle for decays $B \to KK, K\pi, \pi\pi$. The averages come from HFAG and may include measurements from other experiments such as CLEO and CDF (Amhis et al. (2012)).

	BABAR results			Belle results			Averages	
Final state	$\mathcal{B}$ ($\times 10^{-6}$)	A_{CP}	Ref.	$\mathcal{B}$ ($\times 10^{-6}$)	A_{CP}	Ref.	$\mathcal{B}$ ($\times 10^{-6}$)	A_{CP}
K^+K^-	$0.04 \pm 0.15 \pm 0.08$		(Aubert, 2007o)	$0.09^{+0.18}_{-0.13} \pm 0.01$		(Abe, 2007g)	$0.15^{+0.11}_{-0.10}$	
$K^+\overline{K}^0$	$1.61 \pm 0.44 \pm 0.09$	$0.10 \pm 0.26 \pm 0.03$	(Aubert, 2006ai)	$1.11^{+0.19}_{-0.18} \pm 0.05$	$0.017 \pm 0.168 \pm 0.002$	(Chang, 2011)	1.19 ± 0.18	0.041 ± 0.141
$K^+\pi^-$	$19.1 \pm 0.6 \pm 0.6$	$-0.107 \pm 0.016^{+0.006}_{-0.004}$	(Aubert, 2007o)	$20.0 \pm 0.34 \pm 0.63$	$-0.069 \pm 0.014 \pm 0.007$	(Chang, 2011)	$19.55^{+0.54}_{-0.53}$	-0.086 ± 0.007
$K^+\pi^0$	$13.6 \pm 0.6 \pm 0.7$	$0.030 \pm 0.039 \pm 0.010$	(Aubert, 2007ay)	$12.62 \pm 0.31 \pm 0.56$	$0.043 \pm 0.024 \pm 0.002$	(Chang, 2011)	$12.94^{+0.52}_{-0.51}$	0.037 ± 0.021
$K^0\overline{K}^0$	$1.08 \pm 0.28 \pm 0.11$		(Aubert, 2006ai)	$1.26^{+0.19}_{-0.18} \pm 0.06$		(Chang, 2011)	1.21 ± 0.16	
$K^0\pi^+$	$23.9 \pm 1.1 \pm 1.0$	$-0.029 \pm 0.039 \pm 0.010$	(Aubert, 2006ai)	$23.97^{+0.53}_{-0.52} \pm 0.69$	$-0.014 \pm 0.012 \pm 0.006$	(Chang, 2011)	23.80 ± 0.74	-0.015 ± 0.012
$K^0\pi^0$	$10.1 \pm 0.6 \pm 0.4$		(Aubert, 2008m)	$9.66 \pm 0.46 \pm 0.49$		(Chang, 2011)	$9.92^{+0.49}_{-0.48}$	
$\pi^+\pi^-$	$5.5 \pm 0.4 \pm 0.3$		(Aubert, 2007o)	$5.04 \pm 0.21 \pm 0.19$		(Chang, 2011)	5.11 ± 0.22	
$\pi^+\pi^0$	$5.02 \pm 0.46 \pm 0.29$	$0.03 \pm 0.08 \pm 0.01$	(Aubert, 2007ay)	$5.86 \pm 0.26 \pm 0.38$	$0.025 \pm 0.043 \pm 0.007$	(Chang, 2011)	$5.48^{+0.35}_{-0.34}$	0.026 ± 0.039
$\pi^0\pi^0$	$1.83 \pm 0.21 \pm 0.13$	$0.43 \pm 0.26 \pm 0.05$	(Aubert, 2008m)	$2.3^{+0.4+0.2}_{-0.5-0.3}$	$0.44^{+0.53}_{-0.52} \pm 0.17$	(Abe, 2005h)	$1.91^{+0.22}_{-0.23}$	0.43 ± 0.24

The branching fractions of two-body decays to $\pi\pi$ final states are of interest to understand the so-called penguin pollution in $B^0 \to \pi^+\pi^-$ (discussed in Section 17.7). It was observed that in the $\pi^+\pi^-$ final state there appeared to be evidence for a significant tail in the ΔE distribution for selected events that was not apparent in the Monte Carlo simulation used at that time. After some investigation it was realised that the tail in ΔE was the result of final state radiation (FSR) which needed to be accounted for properly in the simulation in order to continue to improve the precision of branching fraction measurements in an un-biased way. The first $B^0 \to \pi^+\pi^-$ branching fraction measurement that attempted to account for this FSR effect appropriately was performed by *BABAR* (Aubert, 2007o). Subsequent results account for this effect.

Initial expectations for the decay $B^0 \to \pi^0\pi^0$ were that the branching fraction would be small, led in part by theoretical calculations indicating that this process would be dominated by a color suppressed tree. In the summer of 2002, preliminary results from the B Factories started to show hints of a relatively large signal with a branching fraction central value of a few 10^{-6}. Subsequent results published by *BABAR* and Belle led to the observation of this channel. The world average branching fraction is currently $(1.91^{+0.22}_{-0.23}) \times 10^{-6}$.

17.4.5 Quasi-two-body decays

In the sections that follow, the quasi-two-body decays have been grouped according to the spins of their final state particles. For each grouping of spin, the results for the branching fractions are itemized in tables and are shown in the plots to enable convenient comparison.

17.4.5.1 $B \to$ two Pseudoscalars, Pseudoscalar Vector, Pseudoscalar Scalar, Pseudoscalar Tensor with $\eta^{(\prime)}$

A number of searches have been performed with a Pseudoscalar η or η' in the final state together with one other particle. For Pseudoscalar-Pseudoscalar (PP) modes, the other particle is an $\eta^{(\prime)}$, K, or π; for Pseudoscalar-Vector (PV) modes, a K^*, ρ, ω, or ϕ; for Pseudoscalar-Scalar (PS) modes, an $f_0(980)$ or $K_0^*(1430)$; for Pseudoscalar-Tensor (PT), $K_2^*(1430)$. The branching fractions and asymmetries reported by Belle and *BABAR*, and their HFAG averages, are given in Table 17.4.2. Figure 17.4.6 shows the branching fractions. The HFAG averages represent a snapshot of the field in late 2012 (Amhis et al. (2012)) but are being annually updated on the website (see Asner et al. (2011)).

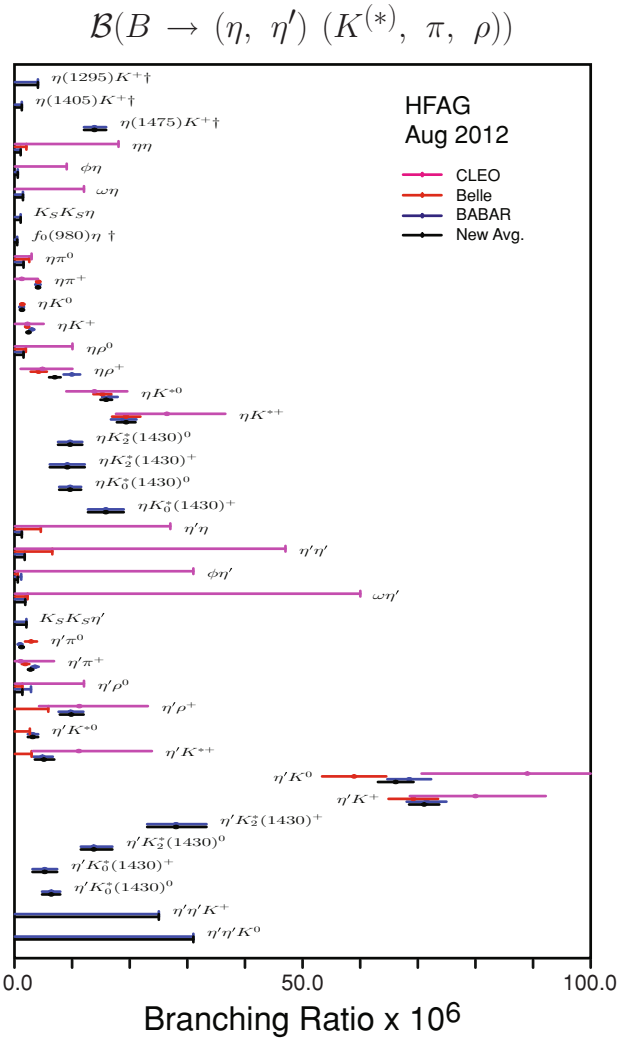

Figure 17.4.6. Summary of branching fraction measurements ($\times 10^{-6}$) and HFAG averages for decays with an η or η' meson combined with a pseudoscalar, vector, scalar or tensor particle (Amhis et al. (2012)).

Table 17.4.2. Charmless B decays branching fractions $\mathcal{B}$ and CP asymmetries A_{CP} for *BABAR* and Belle for decays with an η or η' in the final state. The averages come from HFAG. The decays are arranged from top to bottom, as Pseudoscalar-Pseudoscalar (PP), Pseudoscalar-Vector (PV), Pseudoscalar-Scalar (PS), Pseudoscalar-Tensor (PT), and three-body decays (Amhis et al. (2012)).

	BABAR results			Belle results			Averages	
Final state	$\mathcal{B}$ ($\times 10^{-6}$)	A_{CP}	Ref.	$\mathcal{B}$ ($\times 10^{-6}$)	A_{CP}	Ref.	$\mathcal{B}$ ($\times 10^{-6}$)	A_{CP}
ηK^+	$2.94^{+0.39}_{-0.34} \pm 0.21$	$-0.36 \pm 0.11 \pm 0.03$	(Aubert, 2009d)	$2.12 \pm 0.23 \pm 0.11$	$-0.38 \pm 0.11 \pm 0.01$	(Hoi, 2012)	$2.36^{+0.22}_{-0.21}$	-0.37 ± 0.09
ηK^0	$1.15^{+0.43}_{-0.38} \pm 0.09$		(Aubert, 2009d)	$1.27^{+0.33}_{-0.29} \pm 0.08$		(Hoi, 2012)	$1.23^{+0.27}_{-0.24}$	
$\eta\eta$	< 1.0		(Aubert, 2009d)	< 2.0		(Chang, 2005)	< 1.0	
$\eta\pi^+$	$4.00 \pm 0.40 \pm 0.24$	$-0.03 \pm 0.09 \pm 0.03$	(Aubert, 2009d)	$4.07 \pm 0.26 \pm 0.21$	$-0.19 \pm 0.06 \pm 0.01$	(Hoi, 2012)	4.02 ± 0.27	-0.13 ± 0.10
$\eta\pi^0$	< 1.5		(Aubert, 2008af)	< 2.5		(Chang, 2005)	< 1.5	
$\eta(1295)K^+$	< 4.0		(Aubert, 2008bb)				< 4.0	
$\eta(1405)K^+$	< 1.2		(Aubert, 2008bb)				< 1.2	
$\eta(1475)K^+$	$13.8^{+1.8+1.0}_{-1.7-0.6}$		(Aubert, 2008bb)				$13.8^{+2.1}_{-1.8}$	
$\eta' K^+$	$71.5 \pm 1.3 \pm 3.2$	$0.008^{+0.017}_{-0.018} \pm 0.009$	(Aubert, 2009d)	$69.2 \pm 2.2 \pm 3.7$	$0.028 \pm 0.028 \pm 0.021$	(Schumann, 2006)	71.1 ± 2.6	0.013 ± 0.017
$\eta' K^0$	$68.5 \pm 2.2 \pm 3.1$		(Aubert, 2009d)	$58.9^{+3.6}_{-3.5} \pm 4.3$		(Schumann, 2006)	66.1 ± 3.1	
$\eta'\eta$	< 1.2		(Aubert, 2008af)	< 4.5		(Schumann, 2007)	< 1.2	
$\eta'\eta'$	< 1.7		(Aubert, 2009d)	< 6.5		(Schumann, 2007)	< 1.7	
$\eta'\pi^+$	$3.5 \pm 0.6 \pm 0.2$	$0.03 \pm 0.17 \pm 0.02$	(Aubert, 2009d)	$1.8^{+0.7}_{-0.6} \pm 0.1$	$0.20^{+0.37}_{-0.36} \pm 0.04$	(Schumann, 2006)	$2.7^{+0.5}_{-0.4}$	0.06 ± 0.16
$\eta'\pi^0$	$0.9 \pm 0.4 \pm 0.1$		(Aubert, 2008af)	$2.8 \pm 1.0 \pm 0.3$		(Schumann, 2006)	1.2 ± 0.4	
ηK^{*+}	$18.9 \pm 1.8 \pm 1.3$	$0.01 \pm 0.08 \pm 0.02$	(Aubert, 2006l)	$19.3^{+2.0}_{-1.9} \pm 1.5$	$0.03 \pm 0.10 \pm 0.01$	(Wang, 2007a)	19.3 ± 1.6	0.02 ± 0.06
ηK^{*0}	$16.5 \pm 1.1 \pm 0.8$	$0.21 \pm 0.06 \pm 0.02$	(Aubert, 2006l)	$15.2 \pm 1.2 \pm 1.0$	$0.17 \pm 0.08 \pm 0.01$	(Wang, 2007a)	15.9 ± 1.0	0.19 ± 0.05
$\eta\rho^+$	$9.9 \pm 1.2 \pm 0.8$	$0.13 \pm 0.11 \pm 0.02$	(Aubert, 2008af)	$4.1^{+1.4}_{-1.3} \pm 0.4$	$-0.04^{+0.34}_{-0.32} \pm 0.01$	(Wang, 2007a)	6.9 ± 1.0	0.11 ± 0.11
$\eta\rho^0$	< 1.5		(Aubert, 2007as)	< 1.9		(Wang, 2007a)	< 1.5	
$\eta' K^{*+}$	$4.8^{+1.6}_{-1.4} \pm 0.8$	$-0.26 \pm 0.27 \pm 0.02$	(del Amo Sanchez, 2010h)	< 2.9		(Schumann, 2007)	$5.0^{+1.8}_{-1.6}$	$-0.30^{+0.33}_{-0.37} \pm 0.02$
$\eta' K^{*0}$	$3.1^{+0.9}_{-0.8} \pm 0.3$	$0.02 \pm 0.23 \pm 0.02$	(del Amo Sanchez, 2010h)	< 2.6		(Schumann, 2007)	3.1 ± 0.9	$0.08 \pm 0.25 \pm 0.02$
$\eta'\rho^+$	$9.7^{+1.9}_{-1.8} \pm 1.1$	$0.26 \pm 0.17 \pm 0.02$	(del Amo Sanchez, 2010h)	< 5.8		(Schumann, 2007)	$9.8^{+2.1}_{-2.0}$	$0.04 \pm 0.28 \pm 0.02$
$\eta'\rho^0$	< 2.8		(del Amo Sanchez, 2010h)	< 1.3		(Schumann, 2007)	< 1.3	
$\omega\eta$	< 1.4		(Aubert, 2009d)				< 1.4	
$\omega\eta'$	< 1.8		(Aubert, 2009d)	< 2.2		(Schumann, 2007)	< 1.8	
$\phi\eta$	< 0.5		(Aubert, 2009d)				< 0.5	
$\phi\eta'$	< 1.1		(Aubert, 2009d)	< 0.5		(Schumann, 2007)	< 0.5	
$f_0(980)\eta$	< 0.4		(Aubert, 2007as)				< 0.4	
$f_0(980)\eta'$	< 0.9		(del Amo Sanchez, 2010h)				< 0.9	
$\eta K_0^*(1430)^+$	$15.8 \pm 2.2 \pm 2.2$	$0.05 \pm 0.13 \pm 0.02$	(Aubert, 2006l)				15.8 ± 3.1	$0.05 \pm 0.13 \pm 0.02$
$\eta K_0^*(1430)^0$	$9.6 \pm 1.4 \pm 1.3$	$0.06 \pm 0.13 \pm 0.02$	(Aubert, 2006l)				9.6 ± 1.9	$0.06 \pm 0.13 \pm 0.02$
$\eta' K_0^*(1430)^+$	$5.2 \pm 1.9 \pm 1.0$	$0.06 \pm 0.20 \pm 0.02$	(del Amo Sanchez, 2010h)				5.2 ± 2.1	
$\eta' K_0^*(1430)^0$	$6.3 \pm 1.3 \pm 0.9$	$-0.19 \pm 0.17 \pm 0.02$	(del Amo Sanchez, 2010h)				6.3 ± 1.6	
$\eta K_2^*(1430)^+$	$9.1 \pm 2.7 \pm 1.4$	$-0.45 \pm 0.30 \pm 0.02$	(Aubert, 2006l)				9.1 ± 3.0	$-0.45 \pm 0.30 \pm 0.02$
$\eta K_2^*(1430)^0$	$9.6 \pm 1.8 \pm 1.1$	$-0.07 \pm 0.19 \pm 0.02$	(Aubert, 2006l)				9.6 ± 2.1	$-0.07 \pm 0.19 \pm 0.02$
$\eta' K_2^*(1430)^+$	$28.0^{+4.6}_{-4.3} \pm 2.6$	$0.15 \pm 0.13 \pm 0.02$	(del Amo Sanchez, 2010h)				$28.0^{+5.3}_{-5.0}$	
$\eta' K_2^*(1430)^0$	$13.7^{+3.0}_{-1.9} \pm 1.2$	$0.14 \pm 0.18 \pm 0.02$	(del Amo Sanchez, 2010h)				$13.7^{+3.2}_{-2.2}$	
$K_S^0 K_S^0 \eta$	< 1.0		(Aubert, 2009am)				< 1.0	
$K_S^0 K_S^0 \eta'$	< 2.0		(Aubert, 2009am)				< 2.0	
$\eta'\eta' K^+$	< 25		(Aubert, 2006al)				< 25	
$\eta'\eta' K^0$	< 31		(Aubert, 2006al)				< 31	

Theory predictions for PP and PV branching fractions are typically in the low parts per million. In leading order SM calculations, the time dependent *CP* violation asymmetry parameter $S = \sin 2\phi_1$ in decays such as $B^0 \to \eta' K^0_S$, $B^0 \to KKK^0_S$ and $B^0 \to \phi K^0_S$ is expected to be the same as in the golden mode $B^0 \to J/\psi K^0_S$ and provide a useful comparison between decays mediated by $b \to s\bar{s}u$, $b \to su\bar{u}$, $b \to sd\bar{d}$ and $b \to c\bar{c}s$ (see Section 17.6 for details), provided the decays are dominated by a single weak phase. Within the standard model (SM), the decay $B \to \eta' K$ proceeds through $b \to s$ penguin loops with only a small contribution from $b \to u$ tree diagrams (Chen, 2002). Corrections can be estimated in QCD factorization and turn out to be small. Therefore a significant deviation would be a sign of new physics (Abe, 2003e). The decay rates of $\eta\eta$, $\eta'\eta'$, $\eta\phi$ and $\eta'\phi$ can be related to any deviation in ΔS from the charmonium measured ϕ_1 via $SU(3)$ flavor symmetry (Aubert, 2006av, 2007am).

In charged decays such as $B^+ \to \eta' K^+$ and $B^+ \to \eta'\pi^+$ (Abe, 2001d; Schumann, 2006), the *CP* charge asymmetry A_{CP} is expected to be small in $\eta' K^+$. A large direct *CP* asymmetry is expected in $B^+ \to \eta K^+$ but not in $B^+ \to \eta' K^+$ because the overall penguin amplitudes in $B^+ \to \eta K^+$ are of the same order as the tree amplitude, while in $B^+ \to \eta' K^+$ the penguin dominates. This is confirmed by the experiments, which measure $A_{CP} = -0.37 \pm 0.09$ for $B^+ \to \eta K^+$ but only $A_{CP} = 0.013 \pm 0.017$ for $B^+ \to \eta' K^+$. In $\eta\rho^+$, $\eta\pi^+$ and $\eta'\pi^+$, the $b \to u$ and $b \to s$ amplitudes are of similar size possibly leading to large direct *CP* violation (Aubert, 2005l).

Any sub-leading terms in $B^0 \to \eta' K^0_S$ can be constrained by measuring the decays $\eta'\eta$, $\eta\pi^0$ and $\eta'\pi^0$. $B^0 \to \eta\pi^0$ and $B^0 \to \eta'\pi^0$ may also constrain isospin breaking effects on the value of $\sin 2\phi_2$ in $B^0 \to \pi^+\pi^-$ decays. The branching fractions are a useful test of predictions from QCD factorization, perturbative QCD (for $\eta'\pi^0$) and flavor-$SU(3)$ symmetry (Aubert, 2006g). These limit the deviation ΔS of the measured S from the value seen in charmonium decays, with bounds on $|\Delta S| < 0.05$.

Mixing-induced *CP* violation has been observed in $B^0 \to \eta' K^0$ (Aubert, 2007am) and (Chen, 2007a). The $\eta' K^*$ and ηK branching fractions are suppressed while $\eta' K$ and ηK^* are enhanced, since the two $b \to s$ penguins that contribute interfere constructively in $\eta' K$ decays and destructively in ηK, while the situation is reversed for $\eta' K^*$ and ηK^* (Beneke and Neubert, 2003a; Lipkin, 1991) as is observed (Abe, 2007a; Chang, 2005). Searches for $\eta' h$ can improve the understanding of flavor-singlet penguin amplitudes with intermediate up-type (u,c,t) quarks (Schumann, 2007).

Searches for excited η and η' mesons (*e.g.* the $J^P = 0^-$ states $\eta(1295)$, $\eta(1405)$, $\eta(1475)$) with a kaon have also been performed (Aubert, 2008bb). They decay strongly to at least three pseudoscalar mesons but their exact nature is uncertain and they could be gluonium admixtures (*i.e.* a state with additional gg components). Partial wave analysis suggests that the meson spectrum is a linear combination of the resonant state and a non-resonant phase-space contribution. The $J^P = 1^+$ states $f_1(1285)$ and $f_1(1420)$, and the $J^P = 1^-$ state $\phi(1680)$ have a similar mass and final decay states as the $J^P = 0^-$ states so have to be included in any search for excited η and η' mesons.

Penguin (tree) diagrams dominate in the B decay to ηK^* ($\eta\rho$) (Wang, 2007a). The decays $\eta'\rho$ are suppressed due to the small value of the CKM matrix element, even though they proceed via tree diagrams (Aubert, 2007ak). The expected branching fraction for $B^0 \to \eta'\rho^0$ is of the order $10^{-8} - 10^{-7}$ and a few times 10^{-6} for $B^+ \to \eta'\rho^+$. The measured values for $\mathcal{B}(B^+ \to \eta^{(\prime)}\rho^+)$ are $\sim 10 \times 10^{-6}$ while only upper limits (UL) of $< (1.5 - 2.8) \times 10^{-6}$ have been placed on $B^0 \to \eta^{(\prime)}\rho^0$ decays.

Upper limits of 0.4×10^{-6} and 0.9×10^{-6} have been found for $B^0 \to f_0(980)\eta$ and $B^0 \to f_0(980)\eta'$, respectively (Aubert, 2007as; del Amo Sanchez, 2010h). Measurements also exist for $B \to \eta^{(\prime)} K^*_0(1430)$ and $B \to \eta^{(\prime)} K^*_2(1430)$; the measured values of A_{CP} are compatible with zero.

Decays involving two identical neutral spin zero particles and another spin zero particle can be used to add important information on time-dependent *CP* violation and hadronic B decays (Aubert, 2006al). Examples of such decays include $B \to \eta'\eta' K$ and $B^0 \to K^0_S K^0_S \eta^{(\prime)}$. There are no theoretical predictions for the branching fractions for these SM-suppressed modes.

17.4.5.2 $B \to$ PV excluding $\eta^{(\prime)}$

The branching fractions and asymmetries for the remaining PV modes without an η or η' are given in Table 17.4.3 and the hierarchy of the branching fraction values are shown in Fig. 17.4.7. The decays $B \to \omega\pi^-$ and $B \to \omega K^-$ are dominated by $b \to u$ tree and $b \to s$ QCD penguin diagrams. They can therefore give an insight into gluonic penguin diagrams (Lu, 2002; Wang, 2004a), (Aubert, 2006ad) and direct *CP* (Lu, 2002).

Charmless B meson decays to final states with an odd number of kaons are usually expected to be dominated by $b \to s$ penguin loops while $b \to u$ tree amplitudes are typically large for final states with π and ρ but ηK decays are suppressed relative to the abundant $\eta' K$.

The $B \to \omega K^0$ decay is a $b \to u\bar{u}s$ process dominated by a single penguin loop amplitude with the same weak phase ϕ_1 as ϕK^0, $K^+K^-K^0$, $\eta' K^0$, $\pi^0 K^0$, and $f_0(980)K^0$, but additional amplitudes and multiple particles in the loop complicate the situation by introducing non-negligible weak phases. B meson decays to *CP* eigenstates ωK^0_S (together with $\eta' K^0_S$, $\eta' K^0_L$ and $\pi^0 K^0_S$) can be used to extract S and C (Aubert, 2009aa). The maximum deviation ΔS from the value of $S = \sin 2\phi_1$ measured in charmonium K^0_S decays is ~ 0.1. The charged decay modes are expected to have a direct *CP* violation value consistent with zero (Aubert, 2006ad).

In the Standard Model, $B \to K^* K$ decays are dominated by $b \to ds\bar{s}$ gluonic penguin diagrams; for the charged $B^\pm$ decay, the spectator $\bar{d}$ is replaced with $\bar{u}$. Such transitions provide a valuable tool with which to test the quark-flavor sector of the SM. The mode $B^+ \to \overline{K}^{*0} K^+$ is

Table 17.4.3. Charmless B decays branching fractions $\mathcal{B}$ and CP asymmetries A_{CP} for *BABAR* and Belle for Pseudoscalar-Vector (PV) final states. The averages come from HFAG and may include measurements from other experiments such as CLEO and CDF (Amhis et al. (2012)).

	BABAR results			Belle results			Averages	
Final state	$\mathcal{B}$ ($\times 10^{-6}$)	A_{CP}	Ref.	$\mathcal{B}$ ($\times 10^{-6}$)	A_{CP}	Ref.	$\mathcal{B}$ ($\times 10^{-6}$)	A_{CP}
$K^*(1410)^+\pi^-$				< 86		(Garmash, 2007)	< 86	
$K^*(1410)^0\pi^+$				< 45		(Garmash, 2005)	< 45	
$K^*(1680)^+\pi^-$	< 25		(Aubert, 2008g)	< 10.1		(Garmash, 2007)	< 10.1	
$K^*(1680)^0\pi^+$	< 15		(Aubert, 2005g)	< 12		(Garmash, 2005)	< 12	
$K^*(1680)^0\pi^0$	< 7.5		(Aubert, 2008g)				< 7.5	
$K^{*+}\pi^-$	$8.3^{+0.9}_{-0.8} \pm 0.8$	$-0.24 \pm 0.07 \pm 0.02$	(Aubert, 2009av)	$8.4 \pm 1.1^{+1.0}_{-0.9}$	$-0.21 \pm 0.11 \pm 0.07$	(Garmash, 2007)	8.6 ± 0.9	-0.19 $\pm$ 0.07
$K^{*+}\pi^0$	$8.2 \pm 1.5 \pm 1.1$	$-0.06 \pm 0.24 \pm 0.04$	(Lees, 2011g)				8.2 ± 1.8	$0.04 \pm 0.29 \pm 0.05$
$K^{*0}\overline{K}^0$	< 1.9		(Aubert, 2006au)				< 1.9	
$K^{*0}\pi^+$	$10.8 \pm 0.6^{+1.2}_{-1.4}$	$0.032 \pm 0.052^{+0.016}_{-0.013}$	(Aubert, 2008j)	$9.7 \pm 0.6^{+0.8}_{-0.9}$	$-0.149 \pm 0.064 \pm 0.022$	(Garmash, 2006)	$9.9^{+0.8}_{-0.9}$	-0.04 ± 0.09
$K^{*0}\pi^0$	$3.3 \pm 0.5 \pm 0.4$	$-0.15 \pm 0.12 \pm 0.04$	(Lees, 2011a)	$0.4^{+1.9}_{-1.7} \pm 0.1$		(Chang, 2004)	2.5 ± 0.6	$-0.09^{+0.23}_{-0.26}$
ωK^+	$6.3 \pm 0.5 \pm 0.3$	$-0.01 \pm 0.07 \pm 0.01$	(Aubert, 2007f)	$8.1 \pm 0.6 \pm 0.6$	$0.05^{+0.08}_{-0.07} \pm 0.01$	(Jen, 2006)	6.7 ± 0.5	0.02 ± 0.05
ωK^0	$5.4 \pm 0.8 \pm 0.3$		(Aubert, 2007f)	$4.4^{+0.8}_{-0.7} \pm 0.4$		(Jen, 2006)	5.0 ± 0.6	
$\omega\pi^+$	$6.7 \pm 0.5 \pm 0.4$	$-0.02 \pm 0.08 \pm 0.01$	(Aubert, 2007f)	$6.9 \pm 0.6 \pm 0.5$	$-0.02 \pm 0.09 \pm 0.01$	(Jen, 2006)	6.9 ± 0.5	-0.04 ± 0.06
$\omega\pi^0$	< 0.5		(Aubert, 2008af)	< 2.0		(Jen, 2006)	< 0.5	
$\overline{K}^{*0}K^+$	< 1.1		(Aubert, 2007av)				< 1.1	
ϕK^+	$9.2 \pm 0.4^{+0.7}_{-0.5}$	$0.128 \pm 0.044 \pm 0.013$	(Lees, 2012y)	$9.60 \pm 0.92^{+1.05}_{-0.84}$	$0.01 \pm 0.12 \pm 0.05$	(Garmash, 2005)	8.8 ± 0.5	-0.01 ± 0.06
ϕK^0	$7.1 \pm 0.6^{+0.4}_{-0.3}$	$-0.05 \pm 0.18 \pm 0.05$	(Lees, 2012y)	$9.0^{+2.2}_{-1.8} \pm 0.7$		(Chen, 2003)	$7.3^{+0.7}_{-0.6}$	
$\phi\pi^+$	< 0.24		(Aubert, 2006am)	< 0.33		(Kim, 2012)	< 0.24	
$\phi\pi^0$	< 0.28		(Aubert, 2006am)				< 0.28	
$\phi(1680)K^+$				< 0.8		(Garmash, 2005)	< 0.8	
$\rho(1450)^-K^+$	$2.4 \pm 1.0 \pm 0.6$		(Lees, 2011a)				2.4 ± 1.2	
$\rho(1450)^0\pi^+$	$1.4 \pm 0.4^{+0.5}_{-0.8}$	$-0.06 \pm 0.28^{+0.23}_{-0.32}$	(Aubert, 2009h)				$1.4^{+0.6}_{-0.9}$	$-0.06^{+0.36}_{-0.42}$
$\rho(1700)^-K^+$	$0.6 \pm 0.6 \pm 0.4$		(Lees, 2011a)				0.6 ± 0.7	
ρ^+K^0	$8.0^{+1.4}_{-1.3} \pm 0.6$	$-0.12 \pm 0.17 \pm 0.02$	(Aubert, 2007al)				$8.0^{+1.5}_{-1.4}$	$-0.12 \pm 0.17 \pm 0.02$
$\rho^+\pi^0$	$10.2 \pm 1.4 \pm 0.9$	$-0.01 \pm 0.13 \pm 0.02$	(Aubert, 2007y)	$13.2 \pm 2.3^{+1.4}_{-1.9}$	$0.06 \pm 0.17^{+0.04}_{-0.05}$	(Zhang, 2005)	$10.9^{+1.4}_{-1.5}$	0.02 ± 0.11
ρ^-K^+	$6.6 \pm 0.5 \pm 0.8$	$0.20 \pm 0.09 \pm 0.08$	(Lees, 2011a)	$15.1^{+3.4+2.4}_{-3.3-2.6}$	$0.22^{+0.22+0.06}_{-0.23-0.02}$	(Chang, 2004)	7.2 ± 0.9	0.15 ± 0.13
ρ^0K^+	$3.56 \pm 0.45^{+0.57}_{-0.46}$	$0.44 \pm 0.10^{+0.06}_{-0.14}$	(Aubert, 2008j)	$3.89 \pm 0.47^{+0.43}_{-0.41}$	$0.30 \pm 0.11^{+0.11}_{-0.05}$	(Garmash, 2006)	$3.81^{+0.48}_{-0.46}$	0.37 ± 0.10
ρ^0K^0	$4.4 \pm 0.7 \pm 0.3$		(Aubert, 2009av)	$6.1 \pm 1.0^{+1.1}_{-1.2}$		(Garmash, 2007)	4.7 ± 0.7	
$\rho^0\pi^+$	$8.1 \pm 0.7^{+1.3}_{-1.6}$	$0.18 \pm 0.07^{+0.05}_{-0.15}$	(Aubert, 2009h)	$8.0^{+2.3}_{-2.0} \pm 0.7$		(Gordon, 2002)	$8.3^{+1.2}_{-1.3}$	$0.18^{+0.09}_{-0.17}$
$\rho^0\pi^0$	$1.4 \pm 0.6 \pm 0.3$		(Aubert, 2004g)	$3.0 \pm 0.5 \pm 0.7$		(Kusaka, 2008)	2.0 ± 0.5	
$\rho^0(1450)K^+$	< 11.7		(Aubert, 2005g)				< 11.7	
$\rho^\mp\pi^\pm$	$22.6 \pm 1.8 \pm 2.2$		(Aubert, 2002g)	$22.6 \pm 1.1 \pm 4.4$		(Kusaka, 2008)	23.0 ± 2.3	

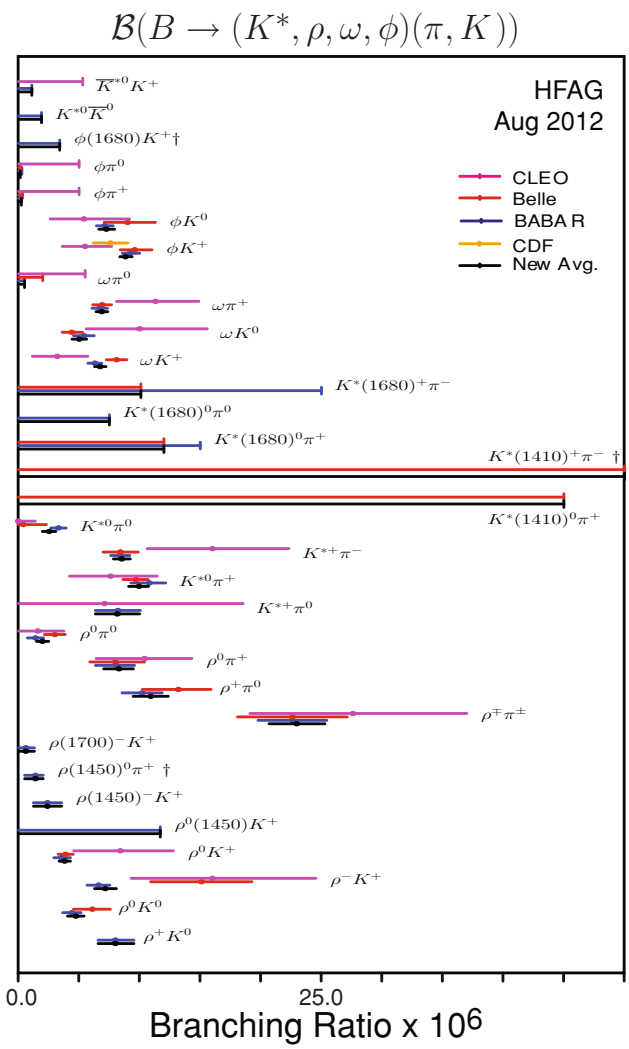

Figure 17.4.7. Summary of branching fraction measurements ($\times 10^{-6}$) and HFAG averages for Pseudovector-Vector (PV) decays (Amhis et al. (2012)).

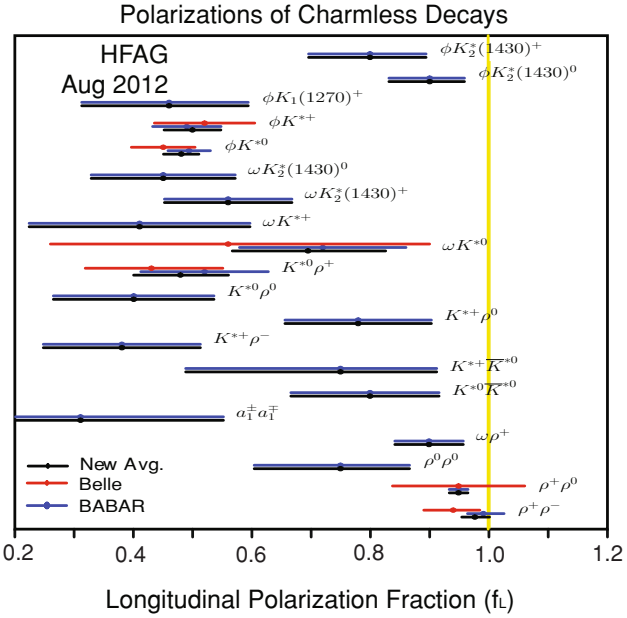

Figure 17.4.8. The longitudinal polarization fractions f_L for charmless B decays at *BABAR* and Belle. The average is from the HFAG group (Amhis et al. (2012)).

also relevant for the interpretation of the time dependent *CP* asymmetry obtained with the $B^0 \to \phi K_S^0$ mode. To leading order, the *CP* asymmetry equals $\sin 2\phi_1$ for this mode. However, sub-dominant amplitudes proportional to $V_{ub}^* V_{us}$ could produce a deviation $\Delta S_{\phi K_S^0}$ from $\sin 2\phi_1$. Bounds can be placed on $\Delta S_{\phi K_S^0}$ by exploiting $SU(3)$ flavor symmetry and combining measured rates for relevant $b \to s$ and $b \to d$ processes (including $B^+ \to \overline{K}^{*0}K^+$). Measurements yielding a significant deviation in excess of such a bound would be a strong indication of physics beyond the SM. Furthermore, $B^+ \to \overline{K}^{*0}K^+$ is one of several charmless decays that can be used, together with U-spin symmetry, to extract the angle ϕ_3 (Aubert, 2007av). Only upper limits exist on $B^0 \to \overline{K}^{*0}K^0$ (Aubert, 2006au), which can be used to constrain certain extensions of the Standard Model.

17.4.5.3 $B \to$ VV

Decays to a Vector-Vector (VV) final state with pairs formed from ω, K^*, ρ, and ϕ can, in principle, be used to determine the helicity amplitudes of the decay. However, this requires a complete angular analysis and in general the number of reconstructed events currently restricts any analysis to integrating over two of the helicity angles and simply reporting the longitudinal polarization f_L. A full angular analysis *has* been done for low-background decays such as $B^0 \to \phi K^{*0}$. Further details of the angular analysis process can be found in Chapter 12, where the angular distributions for the VV final states is given in Eq. 12.2.5.

As discussed in Section 17.4.2, the $B \to VV$ decays are naïvely predicted to be dominated by the longitudinal polarization since $f_L \approx 1 - 4m_V/m_B \sim 0.9$, but the naïve factorization expectation is not born out by the QCD factorization analysis for the penguin-dominated decays.

The measured f_L from a number of VV decays are given in Table 17.4.4. Figure 17.4.8 shows the reported results from Belle and *BABAR* and their HFAG averages. There is an apparent hierarchy with $\rho\rho$ modes near $f_L = 1$, K^*K^* and $\phi K_2^*(1430)$ near 0.75, and ϕK^*, ωK^*, and $a_1^\pm(1260)a_1^\mp(1260)$ near 0.5. Modes dominated by tree decays have $f_L \sim 1$ while penguin-dominated decays are closer to 0.5. There is also a hierarchy based on the masses of the vector mesons, with larger masses having smaller values of f_L. However, this is more evident when comparing decays with a D^* as one or both of the daughter vector mesons.

Table 17.4.4. Longitudinal Polarization fractions f_L for *BABAR* and Belle. The average is from the HFAG group (Amhis et al. (2012)).

	BABAR results		Belle results		Average
Final state	f_L	Ref.	f_L	Ref.	f_L
$K^{*+}\overline{K}^{*0}$	$0.75^{+0.16}_{-0.26} \pm 0.03$	(Aubert, 2009k)			$0.75^{+0.16}_{-0.26} \pm 0.03$
$K^{*0}\overline{K}^{*0}$	$0.80^{+0.10}_{-0.12} \pm 0.06$	(Aubert, 2008ah)			$0.80^{+0.10}_{-0.12} \pm 0.06$
$K^{*+}\rho^-$	$0.38 \pm 0.13 \pm 0.03$	(Lees, 2012l)			$0.38 \pm 0.13 \pm 0.03$
$K^{*+}\rho^0$	$0.78 \pm 0.12 \pm 0.03$	(del Amo Sanchez, 2011g)			$0.78 \pm 0.12 \pm 0.03$
$K^{*0}\rho^+$	$0.52 \pm 0.10 \pm 0.04$	(Aubert, 2006ab)	$0.43 \pm 0.11^{+0.05}_{-0.02}$	(Abe, 2005f)	0.48 ± 0.08
$K^{*0}\rho^0$	$0.40 \pm 0.08 \pm 0.11$	(Lees, 2012l)			$0.40 \pm 0.08 \pm 0.11$
ωK^{*+}	$0.41 \pm 0.18 \pm 0.05$	(Aubert, 2009af)			$0.41 \pm 0.18 \pm 0.05$
ωK^{*0}	$0.72 \pm 0.14 \pm 0.02$	(Aubert, 2009af)	$0.56 \pm 0.29^{+0.18}_{-0.08}$	(Goldenzweig, 2008)	0.69 ± 0.13
$\omega K_2^*(1430)^+$	$0.56 \pm 0.10 \pm 0.04$	(Aubert, 2009af)			$0.56 \pm 0.10 \pm 0.04$
$\omega K_2^*(1430)^0$	$0.45 \pm 0.12 \pm 0.02$	(Aubert, 2009af)			$0.45 \pm 0.12 \pm 0.02$
$\omega\rho^+$	$0.90 \pm 0.05 \pm 0.03$	(Aubert, 2009af)			0.90 ± 0.06
ϕK^{*+}	$0.49 \pm 0.05 \pm 0.03$	(Aubert, 2007c)	$0.52 \pm 0.08 \pm 0.03$	(Chen, 2005a)	0.50 ± 0.05
ϕK^{*0}	$0.494 \pm 0.034 \pm 0.013$	(Aubert, 2008bf)	$0.45 \pm 0.05 \pm 0.02$	(Chen, 2005a)	0.480 ± 0.030
$\phi K_1(1270)^+$	$0.46^{+0.12+0.06}_{-0.13-0.07}$	(Aubert, 2008ad)			$0.46^{+0.12+0.06}_{-0.13-0.07}$
$\phi K_2^*(1430)^+$	$0.80^{+0.09}_{-0.10} \pm 0.03$	(Aubert, 2008ad)			$0.80^{+0.09}_{-0.10} \pm 0.03$
$\phi K_2^*(1430)^0$	$0.901^{+0.046}_{-0.058} \pm 0.037$	(Aubert, 2008bf)			$0.901^{+0.046}_{-0.058} \pm 0.037$
$\rho^+\rho^-$	$0.992 \pm 0.024^{+0.026}_{-0.013}$	(Aubert, 2007b)	$0.941^{+0.034}_{-0.040} \pm 0.030$	(Somov, 2006)	$0.977^{+0.028}_{-0.024}$
$\rho^+\rho^0$	$0.950 \pm 0.015 \pm 0.006$	(Aubert, 2009p)	$0.95 \pm 0.11 \pm 0.02$	(Zhang, 2003)	0.950 ± 0.016
$\rho^0\rho^0$	$0.75^{+0.11}_{-0.14} \pm 0.04$	(Aubert, 2008r)			$0.75^{+0.11}_{-0.14} \pm 0.04$
$a_1^\pm a_1^\mp$	$0.31 \pm 0.22 \pm 0.10$	(Aubert, 2009ae)			$0.31 \pm 0.22 \pm 0.10$

The branching fractions and asymmetries are given in Table 17.4.5 and the hierarchy of measured branching fractions is shown in Fig. 17.4.9.

The decay to ωK^* is penguin dominated but the tree diagrams are more important for the other decays (Aubert (2006f) and Goldenzweig (2008)). The branching fraction hierarchy of the decays to ωK^* and $\omega\phi$ is a useful determination of the contribution of electro-weak penguins and so potentially helpful for the understanding of ϕ_2. The ωK^* final state can also be used to look at branching fractions and f_L in Vector-Tensor (VT) decays ($B \to \omega K_2^*(1430)$) and Scalar-Vector (SV) decays ($B \to \omega K^{*0}(1430)$) and compared to other VT decays such as $B \to \phi K_2^*(1430)$ (Aubert, 2009af).

Decays proceeding via electro-weak and gluonic $b \to d$ penguin diagrams have been measured in the decays $B \to \rho\gamma$ and $B^0 \to K^0\overline{K}^0$. The charmless decay $B^0 \to K^{*0}\overline{K}^{*0}$ proceeds through both electro-weak and gluonic $b \to d$ penguin loops to two vector particles (VV). The standard model suppressed decay $B^0 \to K^{*0}K^{*0}$ could appear via an intermediate heavy boson (Aubert (2008ah,ao, 2009k) and Chiang (2010)).

17.4.5.4 $B \to$ SP, SV, SS

The modes involving a B meson decay to Pseudoscalar-Scalar (PS), Vector-Scalar (VS) and Scalar-Scalar (SS) are summarized in Table 17.4.6 with branching fractions plotted in Fig. 17.4.10.

Table 17.4.5. Charmless B decays branching fractions $\mathcal{B}$ and CP Asymmetries A_{CP} for *BABAR* and Belle for mode Vector-Vector (VV) final states. The averages come from HFAG and may include measurements from other experiments such as CLEO (Amhis et al. (2012)).

	BABAR results			Belle results			Averages	
Final state	$\mathcal{B}$ ($\times 10^{-6}$)	A_{CP}	Ref.	$\mathcal{B}$ ($\times 10^{-6}$)	A_{CP}	Ref.	$\mathcal{B}$ ($\times 10^{-6}$)	A_{CP}
$K^{*+}K^{*-}$	< 2.0		(Aubert, 2008ao)				< 2.0	
$K^{*+}\overline{K}^{*0}$	$1.2 \pm 0.5 \pm 0.1$		(Aubert, 2009k)				1.2 ± 0.5	
$K^{*0}K^{*0}$	< 0.41		(Aubert, 2008y)	< 0.2		(Chiang, 2010)	< 0.2	
$K^{*0}\overline{K}^{*0}$	$1.28^{+0.35}_{-0.30} \pm 0.11$		(Aubert, 2008y)	$0.26^{+0.33+0.10}_{-0.29-0.08}$		(Chiang, 2010)	0.81 ± 0.23	
$K^{*+}\rho^-$	$10.3 \pm 2.3 \pm 1.3$	$0.21 \pm 0.15 \pm 0.02$	(Lees, 2012l)				10.3 ± 2.6	
$K^{*0}\rho^+$	$9.6 \pm 1.7 \pm 1.5$	$-0.01 \pm 0.16 \pm 0.02$	(Aubert, 2006ab)	$8.9 \pm 1.7 \pm 1.2$		(Abe, 2005f)	9.2 ± 1.5	-0.01 ± 0.16
$K^{*0}\rho^0$	$5.1 \pm 0.6^{+0.6}_{-0.8}$	$-0.06 \pm 0.09 \pm 0.02$	(Lees, 2012l)	$2.1^{+0.8+0.9}_{-0.7-0.5}$		(Kyeong, 2009)	3.9 ± 0.8	-0.06 ± 0.09
$K^{*+}\rho^0$	$4.6 \pm 1.1 \pm 0.4$	$0.31 \pm 0.13 \pm 0.03$	(del Amo Sanchez, 2011g)				4.6 ± 1.1	0.31 ± 0.13
ωK^{*+}	< 7.4	$0.29 \pm 0.35 \pm 0.02$	(Aubert, 2009af)				< 7.4	0.29 ± 0.35
ωK^{*0}	$2.2 \pm 0.6 \pm 0.2$	$0.45 \pm 0.25 \pm 0.02$	(Aubert, 2009af)	$1.8 \pm 0.7^{+0.3}_{-0.2}$		(Goldenzweig, 2008)	2.0 ± 0.5	0.45 ± 0.25
$\omega\omega$	< 4.0		(Aubert, 2006f)				< 4.0	
$\omega\phi$	< 1.2		(Aubert, 2006f)				< 1.2	
$\omega\rho^+$	$15.9 \pm 1.6 \pm 1.4$	$-0.20 \pm 0.09 \pm 0.02$	(Aubert, 2009af)				15.9 ± 2.1	-0.20 ± 0.09
$\omega\rho^0$	< 1.6		(Aubert, 2009af)				< 1.6	
$\phi K^*(1410)^+$	< 4.3		(Aubert, 2008ad)				< 4.3	
$\phi K^*(1680)^0$	< 3.5		(Aubert, 2007ap)				< 3.5	
ϕK^{*+}	$11.2 \pm 1.0 \pm 0.9$	$0.00 \pm 0.09 \pm 0.04$	(Aubert, 2007c)	$6.7^{+2.1+0.7}_{-1.9-1.0}$	$-0.02 \pm 0.14 \pm 0.03$	(Chen, 2003)	10.0 ± 1.1	-0.01 ± 0.08
ϕK^{*0}	$9.7 \pm 0.5 \pm 0.6$	$0.01 \pm 0.06 \pm 0.03$	(Aubert, 2008bf)	$10.0^{+1.6+0.7}_{-1.5-0.8}$	$0.02 \pm 0.09 \pm 0.02$	(Chen, 2003)	9.8 ± 0.7	0.01 ± 0.05
$\phi\phi$	< 0.2		(Aubert, 2008ay)				< 0.2	
$\phi\rho^+$	< 3.0		(Aubert, 2008ay)				< 3.0	
$\phi\rho^0$	< 0.33		(Aubert, 2008ay)				< 0.33	
$\rho^+\rho^-$	$25.5 \pm 2.1^{+3.6}_{-3.9}$		(Aubert, 2007b)	$22.8 \pm 3.8^{+2.3}_{-2.6}$		(Somov, 2006)	$24.2^{+3.1}_{-3.2}$	
$\rho^+\rho^0$	$23.7 \pm 1.4 \pm 1.4$	$-0.054 \pm 0.055 \pm 0.010$	(Aubert, 2009p)	$31.7 \pm 7.1^{+3.8}_{-6.7}$	$0.00 \pm 0.22 \pm 0.03$	(Zhang, 2003)	$24.0^{+1.9}_{-2.0}$	-0.05 ± 0.05
$\rho^0\rho^0$	$0.92 \pm 0.32 \pm 0.14$		(Aubert, 2008r)	$0.4 \pm 0.4^{+0.2}_{-0.3}$		(Chiang, 2008)	$0.73^{+0.27}_{-0.28}$	

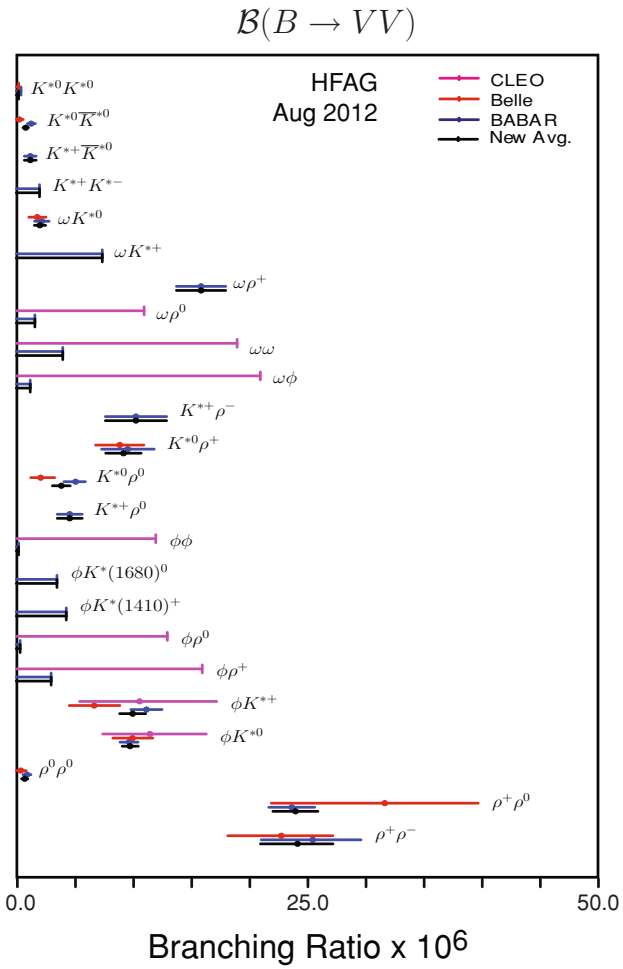

Figure 17.4.9. Summary of branching fraction measurements ($\times 10^{-6}$) and HFAG averages for Vector-Vector (VV) decays (Amhis et al. (2012)).

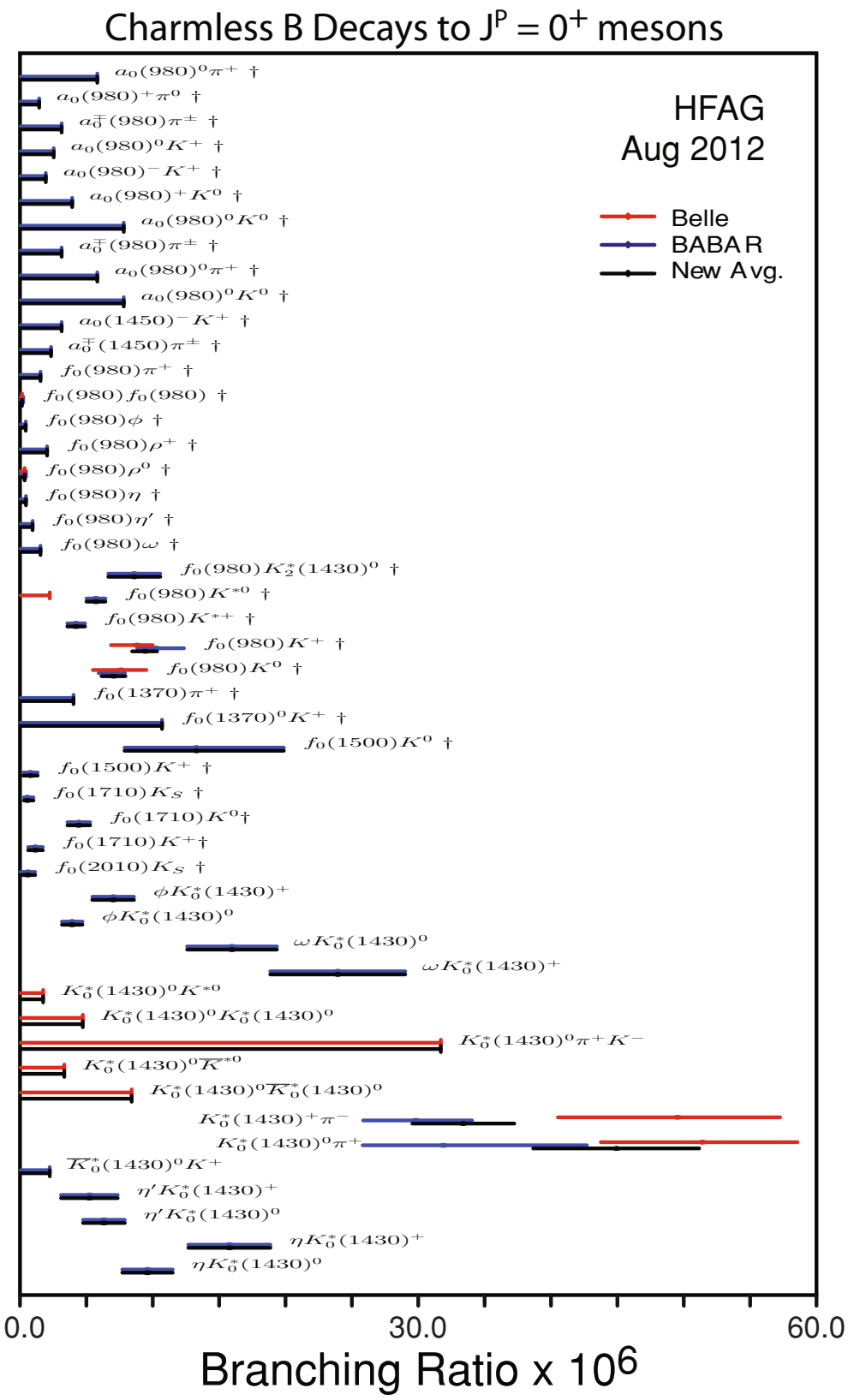

Figure 17.4.10. Summary of branching fraction measurements ($\times 10^{-6}$) and HFAG averages for $J^P = 0^+$ final states, including Scalar-Pseudoscalar (SP), Scalar-Vector (SV) and Scalar-Scalar (SS) decays (Amhis et al. (2012)).

Table 17.4.6. Charmless B decays branching fractions $\mathcal{B}$ and CP asymmetries A_{CP} for *BABAR* and Belle for $J^P = 0^+$ final states, including Scalar-Pseudoscalar (SP), Scalar-Vector (SV) and Scalar-Scalar (SS) decays. The averages come from HFAG (Amhis et al. (2012)).

	BABAR results			Belle results			Averages	
Final state	$\mathcal{B}$ ($\times 10^{-6}$)	A_{CP}	Ref.	$\mathcal{B}$ ($\times 10^{-6}$)	A_{CP}	Ref.	$\mathcal{B}$ ($\times 10^{-6}$)	A_{CP}
$\overline{K}_0^*(1430)^0 K^+$	< 2.2		(Aubert, 2007av)				< 2.2	
$K_0^*(1430)^+ \pi^-$	$29.9^{+2.3}_{-1.7} \pm 3.6$	$0.07 \pm 0.14 \pm 0.01$	(Aubert, 2009av)	$49.7 \pm 3.8^{+6.8}_{-8.2}$		(Garmash, 2007)	$33.5^{+3.9}_{-3.8}$	0.10 ± 0.07
$K_0^*(1430)^0 \pi^+ K^-$				< 31.8		(Chiang, 2010)	< 31.8	
$K_0^*(1430)^0 \pi^+$	$32.0 \pm 1.2^{+10.8}_{-6.0}$	$0.032 \pm 0.035^{+0.034}_{-0.028}$	(Aubert, 2008j)	$51.6 \pm 1.7^{+7.0}_{-7.5}$	$0.076 \pm 0.038^{+0.028}_{-0.022}$	(Garmash, 2006)	45.1 ± 6.3	0.55 ± 0.33
$\eta K_0^*(1430)^+$	$15.8 \pm 2.2 \pm 2.2$	$0.05 \pm 0.13 \pm 0.02$	(Aubert, 2006l)				15.8 ± 3.1	0.05 ± 0.13
$\eta K_0^*(1430)^0$	$9.6 \pm 1.4 \pm 1.3$	$0.06 \pm 0.13 \pm 0.02$	(Aubert, 2006l)				9.6 ± 1.9	0.06 ± 0.13
$\eta' K_0^*(1430)^+$	$5.2 \pm 1.9 \pm 1.0$	$0.06 \pm 0.20 \pm 0.02$	(del Amo Sanchez, 2010h)				5.2 ± 2.1	
$\eta' K_0^*(1430)^0$	$6.3 \pm 1.3 \pm 0.9$	$-0.19 \pm 0.17 \pm 0.02$	(del Amo Sanchez, 2010h)				6.3 ± 1.6	
$a_0(1450)^- K^+$	< 3.1		(Aubert, 2007as)				< 3.1	
$a_0(980)^+ K^0$	< 3.9		(Aubert, 2004x)				< 3.9	
$a_0(980)^+ \pi^0$	< 1.4		(Aubert, 2008ax)				< 1.4	
$a_0(980)^- K^+$	< 1.9		(Aubert, 2007as)				< 1.9	
$a_0(980)^0 K^+$	< 2.5		(Aubert, 2004x)				< 2.5	
$a_0(980)^0 K^0$	< 7.8		(Aubert, 2004x)				< 7.8	
$a_0(980)^0 \pi^+$	< 5.8		(Aubert, 2004x)				< 5.8	
$a_0^\mp(1450)\pi^\pm$	< 2.3		(Aubert, 2007as)				< 2.3	
$a_0^\mp(980)\pi^\pm$	< 3.1		(Aubert, 2007as)				< 3.1	
$f_0(1370)\pi^+$	< 4.0		(Aubert, 2009h)				< 4.0	
$f_0(1370)^0 K^+$	< 10.7		(Aubert, 2005g)				< 10.7	
$f_0(1500)K^+$	$0.74 \pm 0.18 \pm 0.52$		(Lees, 2012y)				0.74 ± 0.55	
$f_0(1500)K^0$	$13.3^{+5.8}_{-4.4} \pm 3.2$		(Lees, 2012y)				$13.3^{+6.6}_{-5.4}$	
$f_0(1710)K_S^0$	$0.50^{+0.46}_{-0.24} \pm 0.11$		(Lees, 2012c)				$0.5^{+0.5}_{-0.3}$	
$f_0(1710)K^+$	$1.12 \pm 0.25 \pm 0.50$		(Lees, 2012y)				1.12 ± 0.56	
$f_0(2010)K_S^0$	$0.54^{+0.21}_{-0.20} \pm 0.52$		(Lees, 2012c)				0.54 ± 0.56	
$f_0(980)K^+$	$10.3 \pm 0.5^{+2.0}_{-1.4}$	$-0.106 \pm 0.050^{+0.036}_{-0.015}$	(Aubert, 2008j)	$8.8 \pm 0.8^{+0.9}_{-1.8}$	$-0.077 \pm 0.065^{+0.046}_{-0.026}$	(Garmash, 2006)	$9.4^{+0.9}_{-1.0}$	$-0.10^{+0.05}_{-0.04}$
$f_0(980)K^0$	$6.9 \pm 0.8 \pm 0.6$	$-0.28 \pm 0.24 \pm 0.09$	(Lees, 2012y)	$7.6 \pm 1.7^{+0.9}_{-1.3}$		(Garmash, 2007)	7.0 ± 0.9	
$f_0(980)K^{*+}$	$4.2 \pm 0.6 \pm 0.3$	$-0.15 \pm 0.12 \pm 0.03$	(del Amo Sanchez, 2011g)				4.2 ± 0.7	-0.15 ± 0.12
$f_0(980)K^{*0}$	$5.7 \pm 0.6 \pm 0.4$	$0.07 \pm 0.10 \pm 0.02$	(Lees, 2012l)	< 2.2		(Kyeong, 2009)	5.7 ± 0.7	0.07 ± 0.10
$f_0(980)\eta$	< 0.4		(Aubert, 2007as)				< 0.4	
$f_0(980)\eta'$	< 0.9		(del Amo Sanchez, 2010h)				< 0.9	
$f_0(980)\omega$	< 1.5		(Aubert, 2009af)				< 1.5	
$f_0(980)\phi$	< 0.38		(Aubert, 2008ay)				< 0.38	
$f_0(980)\pi^+$	< 1.5		(Aubert, 2009h)				< 1.5	
$K_0^*(1430)^0 K^{*0}$				< 1.7		(Chiang, 2010)	< 1.7	
$K_0^*(1430)^0 \overline{K}^{*0}$				< 3.3		(Chiang, 2010)	< 3.3	
$K_0^*(1430)^0 \rho^0$	$27 \pm 4 \pm 2 \pm 3$		(Lees, 2012l)					
$K_0^*(1430)^+ \rho^-$	$28 \pm 10 \pm 5 \pm 3$		(Lees, 2012l)					
$K_0^*(1430)^+ \omega$	$24.0 \pm 2.6 \pm 4.4$	$-0.10 \pm 0.09 \pm 0.02$	(Aubert, 2009af)				24.0 ± 5.1	-0.10 ± 0.09
$K_0^*(1430)^0 \omega$	$16.0 \pm 1.6 \pm 3.0$	$-0.07 \pm 0.09 \pm 0.02$	(Aubert, 2009af)				16.0 ± 3.4	-0.07 ± 0.09
$K_0^*(1430)^+ \phi$	$7.0 \pm 1.3 \pm 0.9$	$0.04 \pm 0.15 \pm 0.04$	(Aubert, 2008ad)				7.0 ± 1.6	0.04 ± 0.15
$K_0^*(1430)^0 \phi$	$3.9 \pm 0.5 \pm 0.6$	$0.20 \pm 0.14 \pm 0.06$	(Aubert, 2008bf)				3.9 ± 0.8	0.20 ± 0.15
$f_0(980)\rho^+$	< 2.0		(Aubert, 2009p)				< 2.0	
$f_0(980)\rho^0$	< 0.40		(Aubert, 2008r)	< 0.3		(Chiang, 2008)	< 0.3	
$f_0(980)f_0(980)$	< 0.19		(Aubert, 2008r)	< 0.1		(Chiang, 2008)	< 0.1	
$f_0(980)K_2^*(1430)^0$	$8.6 \pm 1.7 \pm 1.0$		(Lees, 2012l)			(Kyeong, 2009)	8.6 ± 2.0	
$K_0^*(1430)^0 K_0^*(1430)^0$				< 4.7		(Chiang, 2010)	< 4.7	
$K_0^*(1430)^0 \overline{K}_0^*(1430)^0$				< 8.4		(Chiang, 2010)	< 8.4	

The exact structure of scalar mesons is not clear with various models proposed such as two-quark and four-quark states with potential contributions from glueballs and molecules (compare with the search for exotic states in Chapter 18.3). The experimental measurement of scalars is also complicated as they are often quite broad, decay to pions (and so can be faked by combining the relatively large number of unrelated pions), and have an angular decay structure that is very similar to the non-resonant background. The $a_0(980)$ (along with the $a_1(1260)$ and b_1) is an ideal candidate for a four-quark structure as it lies near the $K\bar{K}$ threshold and so could be a $q\bar{q}$ state with a $K\bar{K}$ admixture. As an example, the decay $B^+ \to a_0^+\pi^0$ can differentiate between two- and four-quark models as the two-body branching fraction could be as high as 2×10^{-7} while the four-quark model is an order of magnitude lower. The branching fraction however is only measured to a precision of $\mathcal{B}(B^+ \to a_0^+\pi^0) < 1.4\times10^{-6}$ (Aubert, 2008ax). The current experimental upper limits on $\mathcal{B}(B^0 \to a_0^\pm\pi^\mp)$ and $\mathcal{B}(B^0 \to a_0^- K^+)$ are 3.1×10^{-6} and 1.9×10^{-6}, respectively (Aubert, 2007as). Vector-current considerations and G-parity conservation suppress the color-allowed electroweak tree decay, leading to the small predicted branching fractions. G-parity $G = Ce^{i\pi I_2}$ is a product of charge conjugation C and a rotation about the second Isospin axis I_2; it is expected to be conserved by strong interactions (as the strong force conserves both C and Isospin) but not in electro-weak interactions.

The a_0, including the $a_0(980)$ and $a_0(1450)$, decays to $\eta\pi$ but the exact branching fraction is not well known (roughly 85%). The decay $B^\pm \to a_0\pi^\pm$ has the benefit of being self-tagging as the pion charge identifies the B meson flavor (Aubert, 2004x).

The averaged decay rates for $B^+ \to f_0(980)K^+$ and $B^0 \to f_0(980)K^0$ have been measured to be 9.4×10^{-6} (Aubert, 2008j), (Garmash, 2006) and 7.0×10^{-6} (Aubert, 2009av) (Garmash, 2007), respectively. These are compatible with expectations that the $b \to ss\bar{s}$ penguin dominates over the $b \to su\bar{u}$ penguin.

The SV mode $\phi K_0^*(1430)^0$ has been measured as part of a time-dependent and time-integrated analysis of $B \to \phi K_S^0\pi^0$ and $B \to \phi K^\pm\pi^\mp$ decays (Aubert, 2008bf), which also include VV and VT decays (see Tables 17.4.5 and 17.4.8). The decay $B \to \omega f_0(980)$ naturally forms part of a search for $\omega\rho$.

17.4.5.5 $B \to$ AP, AV, AA

Figure 17.4.11 and Table 17.4.7 show the reported results from Belle and *BABAR*, and their HFAG averages, for modes involving Axial-Pseudovector (AP), Axial-Vector (AV) and Axial-Axial (AA) decays.

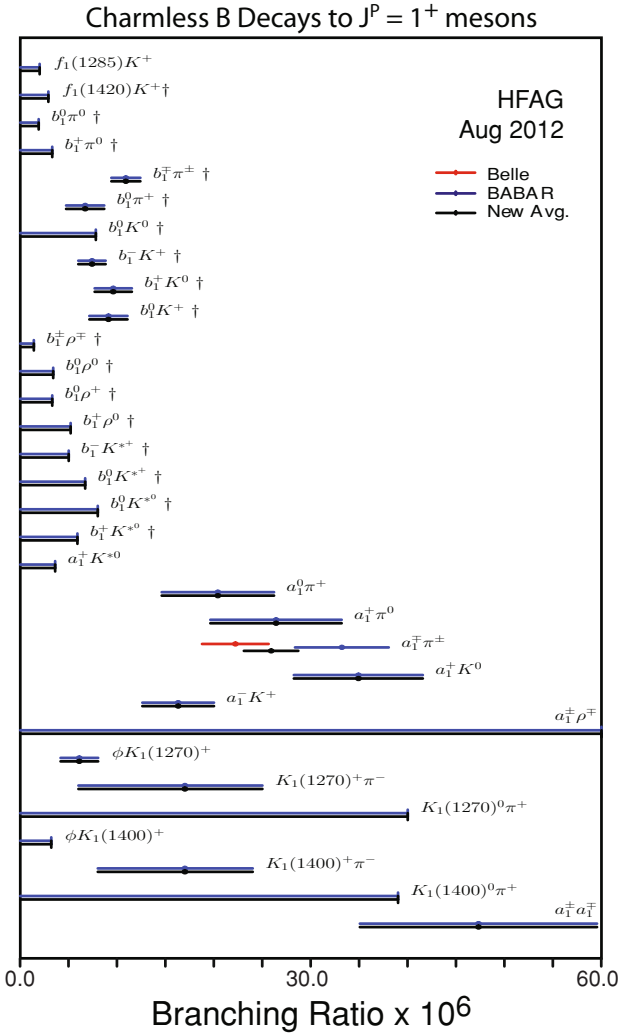

Figure 17.4.11. Summary of branching fraction measurements ($\times10^{-6}$) and HFAG averages for $J^P = 1^+$ final states, including Axial-Pseudovector (AP), Axial-Vector (AV) and Axial-Axial (AA) decays (Amhis et al. (2012)).

Table 17.4.7. Charmless B decays branching fractions $\mathcal{B}$ and CP asymmetries A_{CP} for *BABAR* and Belle for $J^P = 1^+$ final states, including Axial-Pseudovector (AP), Axial-Vector (AV) and Axial-Axial (AA) decays. The averages come from HFAG (Amhis et al. (2012)).

	BABAR results			Belle results			Averages	
Final state	$\mathcal{B}$ ($\times 10^{-6}$)	A_{CP}	Ref.	$\mathcal{B}$ ($\times 10^{-6}$)	A_{CP}	Ref.	$\mathcal{B}$ ($\times 10^{-6}$)	A_{CP}
$K_1(1270)^+\pi^-$	17^{+8}_{-11}		(Aubert, 2010d)				17^{+8}_{-11}	
$K_1(1270)^0\pi^+$	< 40		(Aubert, 2010d)				< 40	
$K_1(1400)^+\pi^-$	17^{+7}_{-9}		(Aubert, 2010d)				17^{+7}_{-9}	
$K_1(1400)^0\pi^+$	< 39		(Aubert, 2010d)				< 39	
$a_1^+K^0$	$34.9 \pm 5.0 \pm 4.4$	$0.12 \pm 0.11 \pm 0.02$	(Aubert, 2008ae)				34.9 ± 6.7	$0.12 \pm 0.11 \pm 0.02$
$a_1^+\pi^0$	$26.4 \pm 5.4 \pm 4.1$		(Aubert, 2007i)				26.4 ± 6.8	
$a_1^-K^+$	$16.3 \pm 2.9 \pm 2.3$	$-0.16 \pm 0.12 \pm 0.01$	(Aubert, 2008ae)				16.3 ± 3.7	$-0.16 \pm 0.12 \pm 0.01$
$a_1^0\pi^+$	$20.4 \pm 4.7 \pm 3.4$		(Aubert, 2007i)				20.4 ± 5.8	
$a_1^\mp\pi^\pm$	$33.2 \pm 3.8 \pm 3.0$		(Aubert, 2006aj)				33.2 ± 4.8	
$b_1^+K^0$	$9.6 \pm 1.7 \pm 0.9$	$-0.03 \pm 0.15 \pm 0.02$	(Aubert, 2008aj)				9.6 ± 1.9	-0.03 ± 0.15
$b_1^+\pi^0$	< 3.3		(Aubert, 2008aj)				< 3.3	
$b_1^-K^+$	$7.4 \pm 1.0 \pm 1.0$	$0.07 \pm 0.12 \pm 0.02$	(Aubert, 2007aj)				7.4 ± 1.4	$0.07 \pm 0.12 \pm 0.02$
$b_1^0K^+$	$9.1 \pm 1.7 \pm 1.0$	$-0.46 \pm 0.20 \pm 0.02$	(Aubert, 2007aj)				9.1 ± 2.0	$-0.46 \pm 0.20 \pm 0.02$
$b_1^0K^0$	< 7.8		(Aubert, 2008aj)				< 7.8	
$b_1^0\pi^+$	$6.7 \pm 1.7 \pm 1.0$	$0.05 \pm 0.16 \pm 0.02$	(Aubert, 2007aj)				6.7 ± 2.0	$0.05 \pm 0.16 \pm 0.02$
$b_1^0\pi^0$	< 1.9		(Aubert, 2008aj)				< 1.9	
$b_1^\mp\pi^\pm$	$10.9 \pm 1.2 \pm 0.9$	$-0.05 \pm 0.10 \pm 0.02$	(Aubert, 2007aj)				10.9 ± 1.5	$-0.05 \pm 0.10 \pm 0.02$
$b_1^\pm\rho^\mp$	< 1.4		(Aubert, 2009ak)				< 1.4	
$f_1(1285)K^+$	< 2.0		(Aubert, 2008bb)				< 2.0	
$f_1(1420)K^+$	< 2.9		(Aubert, 2008bb)				< 2.9	
$\phi K_1(1270)^+$	$6.1 \pm 1.6 \pm 1.1$	$0.15 \pm 0.19 \pm 0.05$	(Aubert, 2008ad)				6.1 ± 1.9	0.15 ± 0.20
$\phi K_1(1400)^+$	< 3.2		(Aubert, 2008ad)				< 3.2	
$a_1^+K^{*0}$	< 3.6		(del Amo Sanchez, 2010l)				< 3.6	
$a_1^\pm\rho^\mp$	< 61		(Aubert, 2006as)				< 61	
$b_1^+K^{*0}$	< 5.9		(Aubert, 2009ak)				< 5.9	
$b_1^-K^{*+}$	< 5.0		(Aubert, 2009ak)				< 5.0	
$b_1^0K^{*+}$	< 6.7		(Aubert, 2009ak)				< 6.7	
$b_1^0K^{*0}$	< 8.0		(Aubert, 2009ak)				< 8.0	
$b_1^0\rho^+$	< 3.3		(Aubert, 2009ak)				< 3.3	
$b_1^0\rho^0$	< 3.4		(Aubert, 2009ak)				< 3.4	
$b_1^+\rho^0$	< 5.2		(Aubert, 2009ak)				< 5.2	
$a_1^\pm a_1^\mp$	$47.3 \pm 10.5 \pm 6.3$		(Aubert, 2009ae)				47.3 ± 12.2	

The b_1 is the $I^G = 1^+$ member of the $J^{PC} = 1^{+-}$, $^1P_1$ nonet while the $a_1(1260)$ is the $I^G = I^-$ state in the $J^{PC} = 1^{++}$, $^3P_1$ nonet. The decays that happen via a tree diagram favor final states with a pion due to Cabibbo-favored coupling ($B^+ \to b_1^0\pi^+$, $B^0 \to b_1^-\pi^+$) while penguin loop decays favor the kaon final states ($B^+ \to b_1^0 K^+$, $B^0 \to b_1^- K^+$). The even G-parity of the b_1 means only amplitudes in which the b_1 contains the spectator quark from the B meson are allowed (apart from isospin-breaking and radiative correction effects). This is because the weak current has a G-parity even vector part and a G-parity odd axial-vector part. Neither part can produce a G-parity odd scalar meson such as the $a_1^0(1260)$. The W^+ is constrained to decay to states of even G-parity. As a result, the decay $B^0 \to b_1^+\pi^-$ is suppressed with respect to $B^0 \to b_1^-\pi^+$. The $B^0 \to b_1^- K^+$ decays can be used to measure A_{CP} while $B^0 \to b_1\pi^\pm\pi^\mp$ can also measure C and CP-conserving ΔC (Aubert, 2007aj, 2008aj). The dominant decay of the b_1 is through $\omega\pi$.

B decays involving an $a_1(1260)$ are similarly of interest to the b_1 but with the added distinction that decays to $a_1(1260)$ with a π^+ proceed via a $b \to u\overline{u}d$ transition and the angle ϕ_2 can be measured through the time-dependent decay rate asymmetry caused by interference between the direct decay and the decay after $B\overline{B}$ mixing. The branching fraction, when combined together with decays of the $a_1(1260)$ and K_1 can be used to differentiate between QCD and naïve factorization model predictions for branching fractions and branching fraction ratios, as well as $B \to a_1(1260)$ transition form factors calculations. These decays can also be an important background to other ϕ_2 measurements, such as $\rho\pi$ and $\rho\rho$. The measurements can be combined with $SU(3)$ symmetry arguments to place bounds on the deviation $\Delta\phi_2$ of the measured ϕ_2 from the true value. The $a_1(1260)$ decays predominantly to $\pi\pi\pi$ via intermediate states involving a vector P-wave ρ or scalar S-wave σ but most analyses assume a pure $\rho\pi$ intermediate decay.

The branching fractions $\mathcal{B}(B^0 \to b_1^-\pi^+)$ are expected to be much greater than $\mathcal{B}(B^0 \to b_1^+\pi^-)$ and that of $\mathcal{B}(B^0 \to a_1^+(1260)\pi^-)$ to be much greater than $\mathcal{B}(B^0 \to a_1^-(1260)\pi^+)$ and this has been confirmed (Aubert, 2006aj, 2007aj). The branching fractions for charged and neutral decays $B \to b_1 K$ and $B \to b_1\pi$ are also in line with expectations (Aubert, 2006am, 2007aj, 2008aj). A_{CP} has also been successfully measured in $B^+ \to b_1^+ K^0$, $B^0 \to b_1^- K^+$, $B^+ \to b_1^0 K^+$, $B^+ \to b_1^0\pi^+$, $B^0 \to b_1^\pm\pi^\mp$ and is compatible with zero (see Table 17.4.11).

For the $B \to a_1(1260)K$ and $B \to a_1(1260)\pi$ decays, both the neutral B^0 decays (Aubert, 2006aj, 2008ae) and the charged B^+ modes (Aubert, 2007i, 2008ae) have been measured as well as the asymmetries A_{CP} and S in $B^+ \to a_1^+(1260)\ K_S^0$ and $B^0 \to a_1^-(1260)\ K^+$ (Aubert, 2008ae). There is strong evidence for $B^+ \to a_1^\pm(1260)\pi^0$ and $B^+ \to a_1^0(1260)\pi^\pm$ (Aubert, 2007i). The neutral decay $B^0 \to a_1^\pm(1260)\pi^\mp$ has been observed (Aubert, 2006aj) and a separate paper later measured A_{CP}, the mixing induced CP asymmetry, and the direct CP asymmetry (Aubert, 2007ae); as a result the angle ϕ_2 was extracted (see Chapter 17.7). Belle have recently published their results and report the first evidence for mixing-induced CP violation in $B^0 \to a_1^\pm(1260)\pi^\mp$ (Dalseno, 2012).

The B meson decay $B \to K_1\pi$, which changes the strangeness by one unit $\Delta S = 1$, is sensitive to the presence of penguin amplitudes because its CKM couplings are larger than the corresponding $\Delta S = 0$ penguin amplitudes. Therefore, measurements of the decay rate for $\Delta S = 1$ transitions sharing the same $SU(3)$ flavor multiplet as $a_1(1260)$ can be used to put constraints on ϕ_2 (Aubert, 2010d). This is similar to the $SU(3)$-based approach to measuring ϕ_2 in $\pi^+\pi^-$, $\rho^\pm\pi^\mp$ and $\rho^+\rho^-$ channels. The decay rate to $K_{1A}\pi$ (where K_{1A} is the $SU(3)$ partner of the $a_1(1260)$ and a nearly equal admixture of $K_1(1270)$ and $K_1(1400)$ with the quantum numbers $I^{JP} = 1/2^{1+}$) can be derived from the decay rates to $K_1(1270)\pi$ and $K_1(1400)\pi$. The K_1 is reconstructed through its predominant decay to $K\pi\pi$ final states.

There are a number of results for the branching fractions of B meson decays to Axial-Vector (AV) and Axial-Axial (AA) final states. Decays to a b_1 and a vector meson (ρ or K^*) have been searched for as a possible measurement of longitudinal polarization f_L, but only upper limits on the branching fractions $\mathcal{B}(B \to b_1 K^*) \leq 8 \times 10^{-6}$ and $\mathcal{B}(B \to b_1\rho) \leq\ (3.3 - 5.2) \times 10^{-6}$ have been measured (Aubert, 2009ak). $B^0 \to a_1^\pm(1260)\rho^\mp$ has also been searched for as it is both a background to ϕ_2 measurements in $B \to \rho\rho$ and a possible place to measure ϕ_2 itself. An upper limit of $< 61 \times 10^{-6}$ has been obtained (Aubert, 2006as). However this was only performed with $100\,\text{fb}^{-1}$.

The $B^+ \to \phi K_1(1270)^+$, $B^+ \to \phi K_1(1400)^+$, and $B^+ \to a_1^+(1260)K^{*0}$ modes have been searched for (Aubert, 2008ad; del Amo Sanchez, 2010l) and f_L in $B^+ \to \phi K_1(1270)^+$ has been measured.

AA modes such as $a_1^+(1260)\ a_1^-(1260)$, $a_1^+(1260)\ a_1^0(1260)$, $a_1^+(1260)\ b_1^-$, and $a_1^+(1260)\ b_1^0$ should have branching fractions in the range $(20-40)\times 10^{-6}$. Although all the branching fractions have been measured, only $\mathcal{B}(B^0 \to a_1^+(1260)a_1^-(1260)) = (47.3 \pm 10.5 \pm 6.3) \times 10^{-6}$ has been observed (Aubert, 2009ae).

17.4.5.6 $B \to$ VT, TP

Table 17.4.8 summarizes the reported branching fractions $\mathcal{B}$ and A_{CP} asymmetries from Belle and *BABAR* and their HFAG averages for Tensor-Pseudoscalar (TP) and Vector-Tensor (VT) states. The hierarchy of branching fractions is shown in Figure 17.4.12. There are as yet very few predictions for these modes.

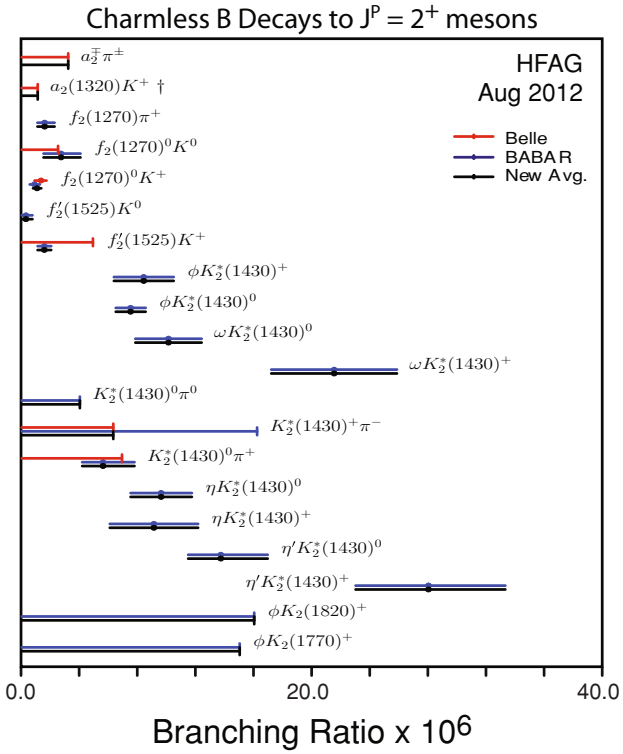

Figure 17.4.12. Summary of branching fraction measurements ($\times 10^{-6}$) and HFAG averages for $J^P = 2^+$ final states, including Tensor-Pseudoscalar (TP) and Tensor-Vector (TV) states (Amhis et al. (2012)).

Table 17.4.8. Charmless B decays branching fractions $\mathcal{B}$ and CP asymmetries A_{CP} for *BABAR* and Belle for $J^P = 2^+$ final states, including Tensor-Pseudoscalar (TP) and Tensor-Vector (TV) states. The averages come from HFAG (Amhis et al. (2012)).

	BABAR results			Belle results			Averages	
Final state	$\mathcal{B}$ ($\times 10^{-6}$)	A_{CP}	Ref.	$\mathcal{B}$ ($\times 10^{-6}$)	A_{CP}	Ref.	$\mathcal{B}$ ($\times 10^{-6}$)	A_{CP}
$K_2^*(1430)^+\pi^-$	< 16.2		(Aubert, 2008g)	< 6.3		(Garmash, 2007)	< 6.3	
$K_2^*(1430)^0\pi^+$	$5.6 \pm 1.2^{+1.8}_{-0.8}$	$0.05 \pm 0.23^{+0.18}_{-0.08}$	(Aubert, 2008j)	< 6.9		(Garmash, 2005)	$5.6^{+2.2}_{-1.4}$	$0.05^{+0.29}_{-0.24}$
$K_2^*(1430)^0\pi^0$	< 4.0		(Aubert, 2008g)				< 4.0	
$\eta K_2^*(1430)^+$	$9.1 \pm 2.7 \pm 1.4$	$-0.45 \pm 0.30 \pm 0.02$	(Aubert, 2006l)				9.1 ± 3.0	-0.45 ± 0.30
$\eta K_2^*(1430)^0$	$9.6 \pm 1.8 \pm 1.1$	$-0.07 \pm 0.19 \pm 0.02$	(Aubert, 2006l)				9.6 ± 2.1	-0.07 ± 0.19
$\eta' K_2^*(1430)^+$	$28.0^{+4.6}_{-4.3} \pm 2.6$	$0.15 \pm 0.13 \pm 0.02$	(del Amo Sanchez, 2010h)				$28.0^{+5.3}_{-5.0}$	
$\eta' K_2^*(1430)^0$	$13.7^{+3.0}_{-1.9} \pm 1.2$	$0.14 \pm 0.18 \pm 0.02$	(del Amo Sanchez, 2010h)				$13.7^{+3.2}_{-2.2}$	
$a_2(1320)K^+$				< 1.1		(Garmash, 2005)	< 1.1	
$f_2(1270)\pi^+$	$1.57 \pm 0.42^{+0.55}_{-0.25}$	$0.41 \pm 0.25^{+0.18}_{-0.15}$	(Aubert, 2009h)				$1.57^{+0.69}_{-0.49}$	$0.41^{+0.31}_{-0.29}$
$f_2(1270)^0K^+$	$0.88 \pm 0.26^{+0.26}_{-0.21}$		(Aubert, 2008j)	$1.33 \pm 0.30^{+0.23}_{-0.34}$		(Garmash, 2006)	$1.06^{+0.28}_{-0.29}$	
$f_2(1270)^0K^0$	$2.7^{+1.0}_{-0.8} \pm 0.9$		(Aubert, 2009av)	< 2.5		(Garmash, 2007)	$2.7^{+1.3}_{-1.2}$	
$f_2'(1525)K^+$	$1.56 \pm 0.36 \pm 0.30$	$0.14 \pm 0.10 \pm 0.04$	(Lees, 2012y)	< 4.9		(Garmash, 2005)	1.56 ± 0.47	0.14 ± 0.11
$f_2'(1525)K^0$	$0.29^{+0.27}_{-0.18} \pm 0.36$		(Lees, 2012y)				$0.29^{+0.45}_{-0.40}$	
$\omega K_2^*(1430)^+$	$21.5 \pm 3.6 \pm 2.4$	$0.14 \pm 0.15 \pm 0.02$	(Aubert, 2009af)				21.5 ± 4.3	0.14 ± 0.15
$\omega K_2^*(1430)^0$	$10.1 \pm 2.0 \pm 1.1$	$0.37 \pm 0.17 \pm 0.02$	(Aubert, 2009af)				10.1 ± 2.3	0.37 ± 0.17
$\phi K_2(1770)^+$	< 15		(Aubert, 2008ad)				< 15	
$\phi K_2(1820)^+$	< 16		(Aubert, 2008ad)				< 16	
$\phi K_2^*(1430)^+$	$8.4 \pm 1.8 \pm 1.0$	$-0.23 \pm 0.19 \pm 0.06$	(Aubert, 2008ad)				8.4 ± 2.1	-0.23 ± 0.20
$\phi K_2^*(1430)^0$	$7.5 \pm 0.9 \pm 0.5$	$-0.08 \pm 0.12 \pm 0.05$	(Aubert, 2008bf)				7.5 ± 1.0	-0.08 ± 0.13

The angular distributions for the VT final states is given in Eq. 12.2.14. The longitudinal polarization f_L for the VT mode $\phi K_2^*(1430)$ is close to $0.8 - 0.9$ (Aubert, 2008ad,bf) but there is a large transverse component in the VA mode $\phi K_1(1270)^+$ with $f_L \sim 0.46$ (Aubert, 2008ad). This lower value of f_L is also seen in $\omega K_2^*(1430)$ (Aubert, 2009af).

Table 17.4.9 itemizes a few measurements that have been a by-product of the analyses described above. In a number of cases, the non-resonant component of B meson decays has been measured, primarily by Belle (Chiang, 2008, 2010; Kyeong, 2009). *BABAR* has extended their analysis of $B \to \phi K^*$ to include the higher mass and higher spin resonances $K^*(1680)^0$, $K_3^*(1780)^0$, and $K_4^*(2045)^0$ (Aubert, 2007ap). Rather than look at individual modes, the partial branching fractions of the inclusive charmless decays $B \to K^+ X$, $B \to K^0 X$, and $B \to \pi^+ X$ have been measured. The inclusive branching fraction of B mesons to charmless final states is about 2%. Here X represents any accessible final state above the endpoint for B meson decays to charmed mesons and the branching fractions and A_{CP} are reported for a restricted range of K and π momentum range.

17.4.5.7 A_{CP} summary

A subset of the most precise A_{CP} measurements currently available are shown graphically in Fig. 17.4.13. Figures 17.4.14, 17.4.15, and 17.4.16 show the A_{CP} *CP* asymmetries for kaonic modes, separated into final states with a kaon or pion (both quasi-two-body and three-body), final states with an η or ϕ, and final states with an ρ, ω, f, a_1, or b_1, respectively.

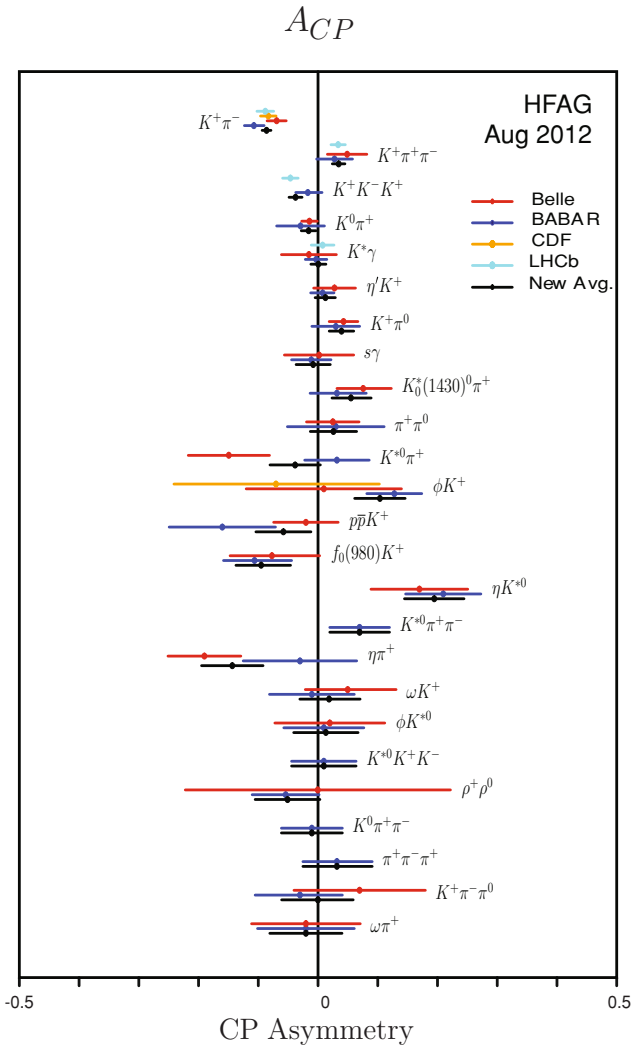

Figure 17.4.13. Summary of the most precise A_{CP} measurements (Amhis et al. (2012)).

17.4.6 Dalitz experimental techniques

A quasi-two-body approach to extracting CKM parameters is not ideal as these modes often interfere with other resonances as well as non-resonant decays to the same final state. As a result, quasi-two-body measurements have an unknown uncertainty in their reported results that requires careful consideration. In principle, these effects can be taken into account by a Dalitz Plot (also known as a Dalitz Plane) analysis. The major advantage to the Dalitz Plot is that it gives access to the phases as well as the magnitudes of the resonances. Since the weak phase changes sign under *CP* but the strong phase does not, the weak and strong phase components can be extracted by subtracting or adding together the B meson flavor-tagged Dalitz Plots. In some Dalitz Plots, the weak phase can often be directly interpreted as one of the Wolfenstein angles *e.g.* Dalseno (2009). The mathematical formalism for a Dalitz Plot analysis is given in Chapter 13. In this section we consider the experimental problems in its implementation.

The extension of quasi-two-body charmless decays to three-body charmless decays brings with it greater complexity but provides a deeper understanding of the decays and their *CP* properties. As the integrated luminosity increases, the analyses have started with inclusive measurements of branching fractions and charge asymmetries, integrated over the three-body phase space (*e.g.* $B \to \pi\pi\pi$). This has been followed by exploring intermediate states ignoring interference (*e.g.* $B \to \rho\pi$) before finally performing a full Dalitz Plot analysis taking into account interference between all intermediate resonance states. And finally, time-dependent asymmetries can be extracted from individual resonances. The choice is dictated by the luminosity, expected signal and background, and the understanding of the intermediate resonances (such as the presence or absence of poorly known states such as σ/κ, and higher mass f_0 and K^*).

The Dalitz Plots of B meson decays are usually interpreted in the scattering matrix (S-matrix) or isobar model (see Section 13.2.1). If a more detailed understand-

Table 17.4.9. Charmless B decays branching fractions $\mathcal{B}$ and CP asymmetries A_{CP} for *BABAR* and Belle for non-resonant decays and other unclassified modes. The averages come from HFAG and may include measurements from other experiments such as CLEO, CDF and DØ (Amhis et al. (2012)).

	BABAR results			Belle results			Averages	
Final state	$\mathcal{B}$ ($\times 10^{-6}$)	A_{CP}	Ref.	$\mathcal{B}$ ($\times 10^{-6}$)	A_{CP}	Ref.	$\mathcal{B}$ ($\times 10^{-6}$)	A_{CP}
K^+X	< 187	$0.57 \pm 0.24 \pm 0.05$	(del Amo Sanchez, 2011c)					
K^0X	$195^{+51}_{-45} \pm 50$		(del Amo Sanchez, 2011c)					
π^+X	$372^{+50}_{-47} \pm 59$	$0.10 \pm 0.16 \pm 0.05$	(del Amo Sanchez, 2011c)					
$K^+X(1812)$				< 0.32		(Liu, 2009)	< 0.32	
$\phi K_3^*(1780)^0$	< 2.7		(Aubert, 2007ap)				< 2.7	
$\phi K_4^*(2045)^0$	< 15.3		(Aubert, 2007ap)				< 15.3	
$K^+\pi^-K^+\pi^-$				< 6.0		(Chiang, 2010)	< 6.0	
$K^+\pi^-\pi^+K^-$				< 72		(Chiang, 2010)	< 72	
$K^+\pi^-\pi^+\pi^-$				< 2.1		(Kyeong, 2009)	< 2.1	
$\pi^+\pi^-\pi^+\pi^-$	< 23.1		(Aubert, 2008r)	< 19.3		(Chiang, 2008)	< 19.3	

ing of the amplitude properties is required, for instance the spin, the scattering amplitude can be expressed in terms of partial-wave amplitudes. The drawback of the S-matrix formalism is that it is not unitary and as a result the sum of the amplitudes of the resonances in the Dalitz Plot can be greater or less than the inclusive Dalitz Plot amplitude depending on whether the overall interference is constructive or destructive. The individual branching fractions are therefore often reported as fit fractions (FF), defined as the integral of a single amplitude squared divided by the coherent matrix element squared for the whole Dalitz Plot (Section 13.4.1). An alternative parameterization uses the K-matrix formalism which is unitary by construction but has a drawback that the masses and widths can be different to the S-matrix results. The K-matrix formalism is more commonly used in Dalitz Plot analyses of D meson decays (section 13.2.2). This is because many of the resonances in the D meson Dalitz Plot contain a large number of events and the S-matrix approximation of a Breit-Wigner or similar shape for the decay of the resonance is no longer adequate, especially when the resonances overlap in the Dalitz Plot.

The selection criteria for three-body decays are very similar to that employed for quasi-two-body analyses. An obvious exception is that the B meson decay is treated as a decay to the three final state particles and no intermediate resonance vertex is formed when reconstructing the B meson. As the number of neutral final state particles increases the importance of any constraint from the beam spot on the B meson vertex position also increases.

In quasi-two-body analyses, event shape variables and multivariate discriminants can be used to extract the signal yield because the reconstruction efficiency is flat in the small volume of phase space under consideration. In Dalitz Plot analyses, this is no longer true and variables that depend on momentum vectors are correlated with position in phase space. Even variables like $m_{\rm ES}$ and ΔE need to be treated carefully. Some analyses deal with the problem using an elliptical selection region in ($m_{\rm ES}$, ΔE). Others rotate ($m_{\rm ES}$, ΔE) about a point to eliminate the linear correlation component. If the event-by-event resolution on ΔE changes significantly, this can be compensated for by using a derived observable such as $\Delta E/\sigma(\Delta E)$. For similar reasons, multivariate discriminants need to be carefully constructed from variables that are as independent as possible from the position of the event in the Dalitz Plot.

As in quasi-two-body analyses, care must be taken with charm mesons that either decay to the same final state or are mis-reconstructed *e.g.* where a lepton is mistaken for a pion or kaon. This is particularly important in searches for highly suppressed modes such as $B^- \to K^+\pi^-\pi^-$ Aubert (2008aw). The charm background can usually be much reduced by applying mass range criteria about known resonances such as D mesons, J/ψ and $\psi(2S)$. This will result in empty bands in the Dalitz Plot that must be carefully considered when calculating efficiencies and migrations. Alternatively, some charm decays are deliberately kept in the Dalitz Plot. A motivation for this comes from resonances such as the χ_{c0} that have no weak phase and so can be used in an interference analysis to extract the weak phase from the Dalitz Plot. Unfortunately, the branching fraction for $B \to \chi_{c0}h$ is too small to be useful currently.

When the Dalitz Plot is represented as a Cartesian coordinate system, with the square of the mass of pairs of final state particles as the x and y axes, the phase space is roughly triangular in shape. Figure 17.4.17 illustrates the distribution of events extracted from data in the decay of $B^0 \to K^0_S\pi^+\pi^-$. The distribution of events on the Dalitz Plot is plotted after applying a constraint on the B meson mass ($m_{\rm ES} = m_B$). This improves the resolution and ensures that all events fall within the kinematic boundaries of the Dalitz Plot. An alternative often used is a "square" Dalitz Plot where one of the axes is transformed into a "helicity-like" variable *e.g.* (Aubert, 2007v) or see Chapter 13. Although this transforms the distribution of resonances from simple bands parallel to the axes to more complex hyperboloids, the 'square" Dalitz Plot has a number of benefits. It can expand the region near areas where large variations are occurring such as in narrow resonances like the ϕ. Bands near the Dalitz Plot edges also

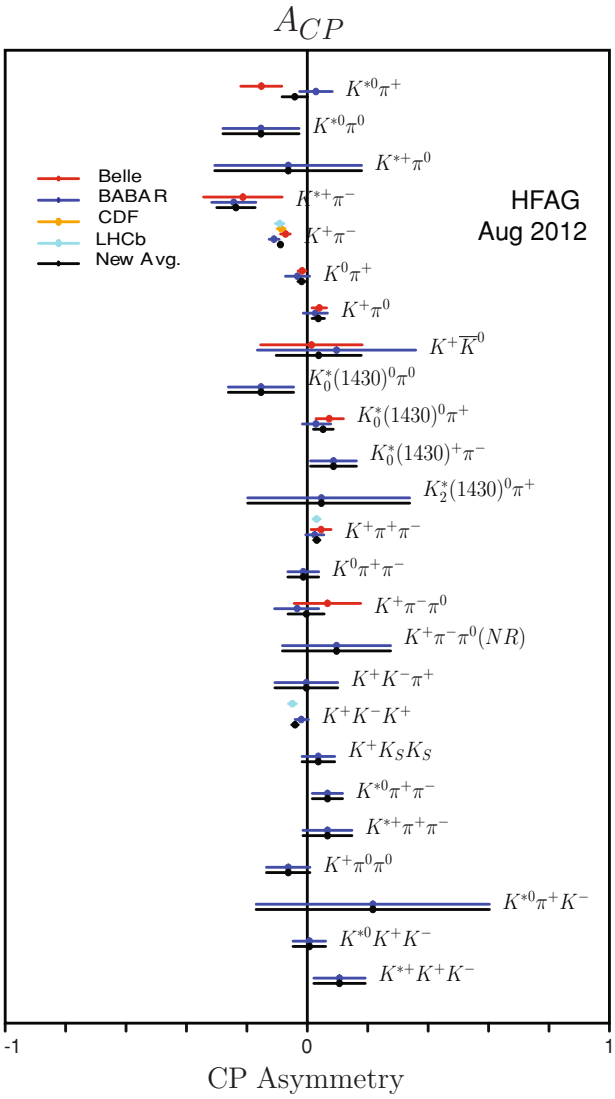

Figure 17.4.14. A_{CP} measurements for kaonic modes with kaons or pions (Amhis et al. (2012)).

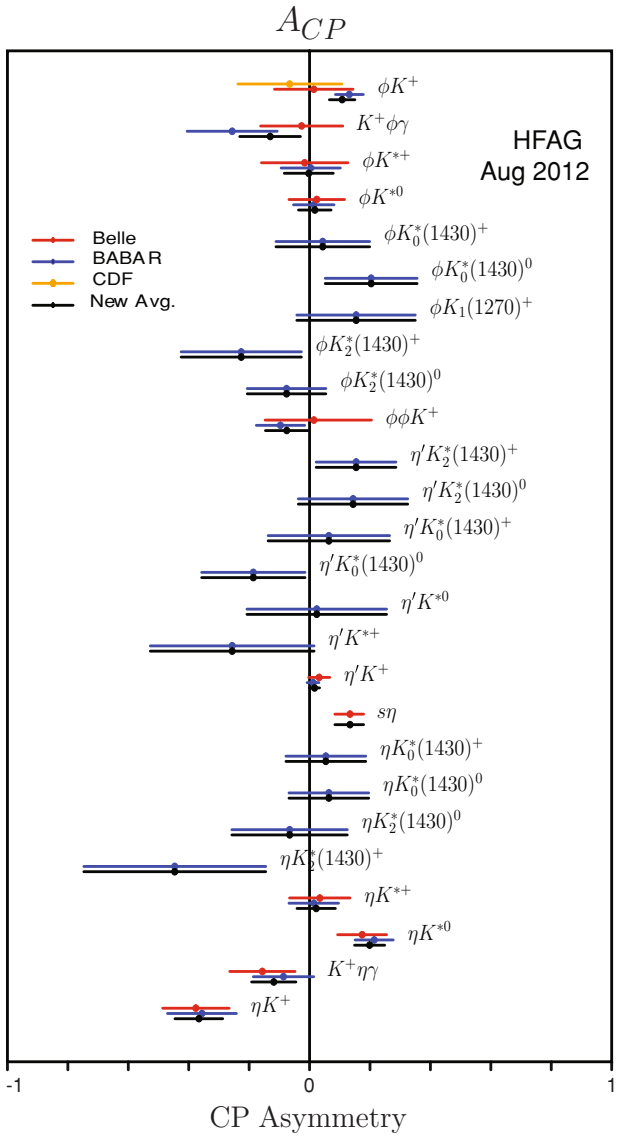

Figure 17.4.15. A_{CP} measurements for kaonic modes with η or ϕ (Amhis et al. (2012)).

get expanded, enabling finer control over regions where the efficiency is changing (such as the ρ meson in $B \to \pi\pi\pi$). However attention must be paid to the Jacobian as equal areas in the "square" Dalitz Plot no longer correspond to equal areas of phase-space.

Whatever the choice of Dalitz Plot, care must be taken in plotting the candidates, especially in three-body states which have two or more final state identical particles of the same mass and sign (*e.g.* $B^+ \to \pi^+ \pi^+ \pi^-$). Typical choices are to randomly select one of the pair, to fold the Dalitz Plot about the diagonal, or to consistently plot the higher mass pair on one of the axes. Even so, artificial ordering of the candidates must be eliminated or controlled. Such effects can be introduced by, for example, reconstruction tracking software that, through its track-finding algorithm, can result in momentum ordering.

The reconstruction efficiency over the Dalitz Plot can be modeled with a two-dimensional histogram, a technique that benefits from the "square" Dalitz Plot. All selection criteria are applied apart from any mass vetoes. A ratio is taken between the histogram of reconstructed events and a histogram of the true Dalitz Plot distribution of all generated MC simulated events. The reconstructed events are re-weighted to take into account any known differences between MC simulation and data such as particle identification and tracking efficiencies. The ratio can be used to provide event-by-event weighting, with linear interpolation between histogram bins where needed. The efficiency

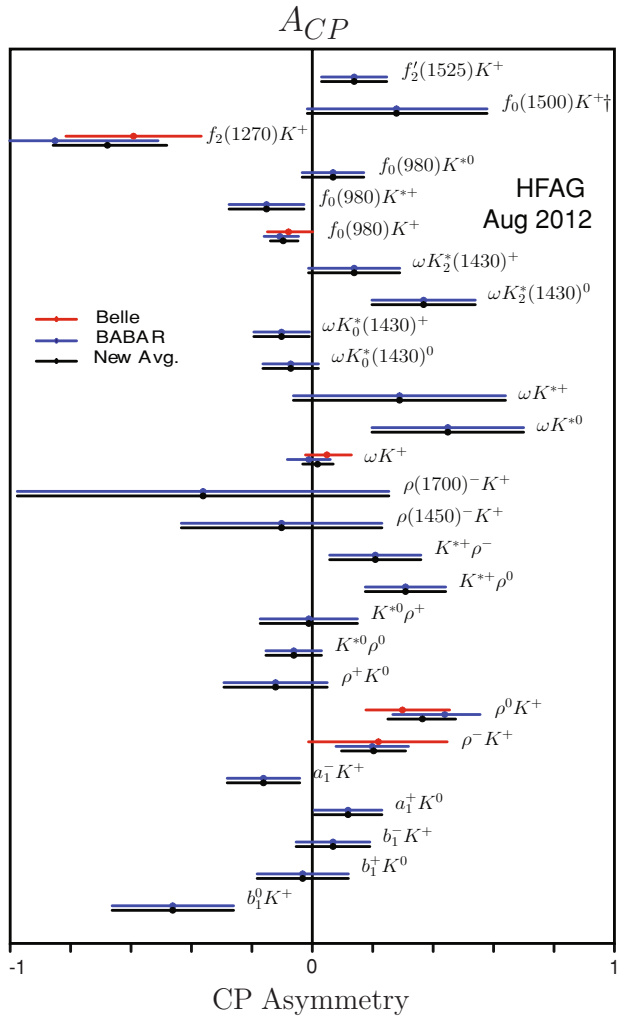

Figure 17.4.16. A_{CP} measurements for kaonic modes with ρ, ω, f, a_1, or b_1 (Amhis et al. (2012)).

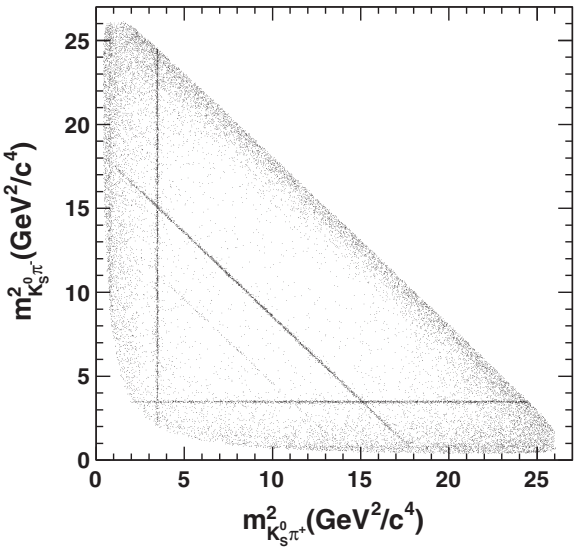

Figure 17.4.17. Dalitz Plot of data selected from $B^0 \to K^0_S\pi^+\pi^-$ decays (Aubert, 2009av). The narrow bands correspond to $D^{\pm}\pi^{\mp}$, $J/\psi K^0_S$, and $\psi(2S)K^0_S$ background events. As in many charmless B meson decay Dalitz Plots, the events of interest are often at the edges of the allowed kinematic region.

can be calculated from phase-space generated MC simulated events, but this will result in poor accuracy for narrow resonances such as the ϕ. Better accuracy can be obtained by generating the MC with a model that contains the expected resonances in the Dalitz distribution, perhaps guided by previous quasi-two-body measurements or theory. Interference is a secondary effect but full Dalitz Plot MC simulation models which include interference effects can be used to achieve a more uniform accuracy on the efficiency. Narrow resonances pose an additional problem since their reconstructed width is dominated by the detector resolution.

If the reconstruction resolution is poor compared to the size of the histogram bin then it is necessary to take into account migrations from the true Dalitz Plot position to the reconstructed position. This becomes more important as the number of neutral particles in the final state increases. Care needs to be taken near the Dalitz Plot edges where migrations can be systematically in one direction, and also near mass regions that are close to any region that is excluded by the selection criteria *e.g.* D meson mass vetoes.

The identification of the $B\overline{B}$ backgrounds is an intensive task. These backgrounds arise from combinations of unrelated tracks; three- and four-body decays involving intermediate D mesons; charmless two- and four-body decays with an extra or missing track; and three-body decays with one or more particles misidentified. The number of such decays can be large (~ 50). For fitting purposes, modes are combined that have similar behavior in the discriminating variables such as $m_{\rm ES}$ and ΔE. The relative contributions are estimated from the reconstruction efficiency and estimates of the branching fractions either from measurement or theory. In some cases, the $B\overline{B}$ backgrounds are included in the maximum likelihood (ML) fit through the use of two-dimensional histograms rather than *p.d.f.*s.

The term "non-resonant" is used quite loosely by experimentalists and is often used as a short-hand for continuum background. In Dalitz Plot analyses, it should strictly refer to decays that are uniformly distributed in phase-space. In principle, this allows phenomenological predictions of the distribution to be used in the fits. These typically involve decaying exponential distributions as a function of the invariant mass-squared of the pairs of particles (*e.g.* $Ae^{-c_1 m^2}$). These functions attempt to describe the increase in the number of background events near the borders and corners of the Dalitz Plot. This increase originates from the jet-like structure of the continuum background (Garmash, 2007). However, these distri-

butions have turned out not to be very satisfactory and other more complex functions are called upon. This can partly be explained as the influence of poorly understood resonances (such as the σ/κ or the higher mass resonances mentioned above). As a result "non-resonant" has come to mean anything that is not modeled by a resonance. In practical terms, this means the distributions often have to come from MC simulations, off-resonance data or sideband data, or a combination of all three. In the case of sideband data, MC samples must be used to remove events from B meson decays that are also present and to determine possible differences in the background shape between the sideband and signal regions. Linear interpolation between bins can be used where needed.

The backgrounds are constructed separately for both the B^0 and $\overline{B}^0$ events and a *p.d.f.* or histogram is formed taking into account any asymmetry that might be present in the background distributions (see, for example Eq. 20 in Aubert (2009h)).

The observables that are used in the ML depend on the analysis under consideration. Typically, a combination of ΔE, $m_{\rm ES}$, multivariate discriminant, position in the Dalitz Plot and charge (flavor) of the B meson candidate is used. Sometimes a cut is applied to the observable first (*e.g.* on the multivariate discriminant) and then this observable is excluded from the fit. This usually happens for observables that are correlated with position in the Dalitz Plot.

As in two-body and quasi-two-body decays, certain D meson decays to the same or similar final state can be used as a calibration channel and allow for correction to fitted parameters derived just from MC simulation.

Although many of the resonances in the Dalitz Plot can be predicted from previous quasi-two-body measurements, there is still a large uncertainty in the number and type of resonances that should be included in any particular model. Examples include the exact parameterization of the non-resonant three-body decay component, the σ/κ with masses in the region $400-600\,\mathrm{MeV}/c^2$ and widths that are large and uncertain, the $\omega(782)$, the χ_{c0} and χ_{c2}, and the higher mass partners of the ρ, $f_0(980)$, and K^*. The addition of a resonance to the model that is not present in the data can be just as problematic as any exclusion of a resonance that is present. The problem is exacerbated if a blind fit is being performed. One technique is to use the log-likelihood reported by a particular model fitted to the data or to calculate a χ^2 statistic based on the number of events predicted from a fit and the number of real events in a bin in the Dalitz Plot. The statistical significance of the presence of a component can be estimated by evaluating the difference $\Delta \ln \mathcal{L}$ between the negative log-likelihood of the nominal fit and that of a fit where the amplitude and A_{CP} is set to zero. This is then used to evaluate a p value which is the integral from $2\Delta \ln \mathcal{L}$ to infinity of the *p.d.f.* of the χ^2 distribution.

An important goal of the Dalitz Plot analysis is the extraction of *CP* asymmetries either from a time-integrated or time-dependent analysis. Consequently, the resonances are parameterized not just in terms of their widths and masses but as functions of the decay dynamics, angular distributions, and the transition form factors for the B meson and the resonances (see Chapter 13.2.1). As explained in more detail in Chapter 13.4.2, complex coefficients are used to parameterize the B and $\overline{B}$ meson decay. The same parameterization is not consistently used between papers or experiments, although they are all mathematically related. As a specific example from (Dalseno, 2009), the intermediate resonances i in B and $\overline{B}$ meson decay are parameterized respectively as:

$$\begin{aligned} a_i' &= a_i(1+c_i)e^{i(b_i+d_i)} \\ \bar{a}_i' &= a_i(1-c_i)e^{i(b_i-d_i)} \end{aligned} \tag{17.4.13}$$

where b_i and d_i represent the strong and weak phase respectively (notice the strong phase does not change sign). Consequently, the *CP* asymmetry for each resonance i can be written as:

$$A_{CP}(i) = \frac{|\bar{a}_i'|^2 - |a_i'|^2}{|\bar{a}_i'|^2 + |a_i'|^2} = \frac{-2c_i}{1+c_i^2} \tag{17.4.14}$$

In the case of time-dependent Dalitz plot analyses, the resonance parameterizations above are combined with the equation describing the time-dependent decay properties of the B and $\overline{B}$ meson as given in Equation 13.2.17. In this case, a great deal of attention has to be given to the tagging and resolution functions.

Charmless B decays, especially those without access to tree decay diagrams, may have a large non-resonant contribution. This can be as high as 90% for $B \to KKK$. The contribution is not uniform across the Dalitz diagram and so a parameterization must be adopted that depends on position in the Dalitz Plot. In some analyses, *BABAR* and Belle have adopted the same non-resonant parameterization but in most cases they differ, which can complicate comparisons.

The statistical errors on the measured fit fractions and *CP* parameters are often derived from fits to a large number of MC experiments generated with the fitted parameters obtained from the data. These MC experiments are also vital for understanding the minimization process. With a large number of floating parameters, the fit can sometimes have more than one local minimum. There can be systematic shifts in the fit caused by the starting values of the floating parameters. A number of techniques for investigating this effect have been applied, including using different minimizers, scanning through a set of starting values, randomly initializing the starting values, and the use of genetic algorithms. Each has its benefits and drawbacks but there is no one method that works better than the others in all circumstances.

The systematic uncertainties that affect the final result are very similar to those seen in other charmless B decays. However their effects can be modified since there are more opportunities for correlations between parameters and the fitted results are often reported as ratios rather than absolute numbers. Although the magnitude and phase of the complex coefficients of the amplitude are sometimes transformed to a more orthogonal set of parameters, this

does not wholly eliminate the correlations. Systematic uncertainties that are unique to the Dalitz Plot are: the asymmetries in the background; limited statistics from the sidebands used to form the continuum histograms (if histograms are used); the mass rejection regions; differences in the continuum shape between the sideband and the signal region; and charge bias introduced either by the detector response or the selection criteria. A model dependent error derived from performing fits with an alternative set of resonances is sometimes quoted either in quadrature with the systematic error or its own. As with quasi-two-body modes, an important systematic is associated with uncertainty on the parameters that are fixed in the fit. If a resonance is deemed to be significant, the mass and width may still not be well known. Rather than float the mass and width, a series of fits can be performed with the mass and width fixed at different values and the change in the likelihood used as a guide to the best values. Even so, it may be necessary to modify a model after unblinding, particularly to remove resonances that are not significant.

17.4.7 Three-body and Dalitz decays

Approximately seven B^0 and eleven $B^\pm$ Dalitz Plots have been investigated by *BABAR* and Belle. It is impossible to do justice to the wealth of information available. Decays involving three pions, particularly $B \to \rho\pi$, are important for the measurement of ϕ_2 and are considered in Chapter 17.6. Decays with an η, η', ω, $f_0(980)$, or K^* in the final three-body state are itemized in the tables and figures of this section but are not described in detail. Instead, this section concentrates on modes with one or more kaons in the final state.

B meson decays to three-body final states $B \to Khh$ proceed predominantly via $b \to u$ tree-level diagrams (T and C diagrams in Fig. 17.4.1) and $b \to s(d)$ penguin diagrams (P in Fig. 17.4.1). The other diagrams can contribute but are expected to be much smaller. Final states with an odd number of kaons (s-quarks) are expected to proceed dominantly via $b \to s$ penguin transitions as the $b \to u$ transition is color-suppressed. If there are two kaons, the decay proceeds through the color-allowed $b \to u$ tree diagram and the $b \to d$ penguin decay with no $b \to s$ penguin contribution. As a result, these Dalitz decays provide an excellent opportunity to understand the relative contribution of tree and penguin amplitudes in charmless decays. This is shown in Fig. 17.4.18 where the extracted values of $\sin 2\phi_1$ in $b \to s$ penguin transitions are compared to $b \to c\bar{c}s$ decays.

Table 17.4.10 summarizes the reported branching fractions and asymmetries. In many cases, no resonances have been found in a Dalitz Plot and so consequently it has only been possible to give a branching fraction (or upper limit) and a *CP* asymmetry for the whole Dalitz Plot. Figure 17.4.19 shows the relative values of the reported branching fractions so far measured.

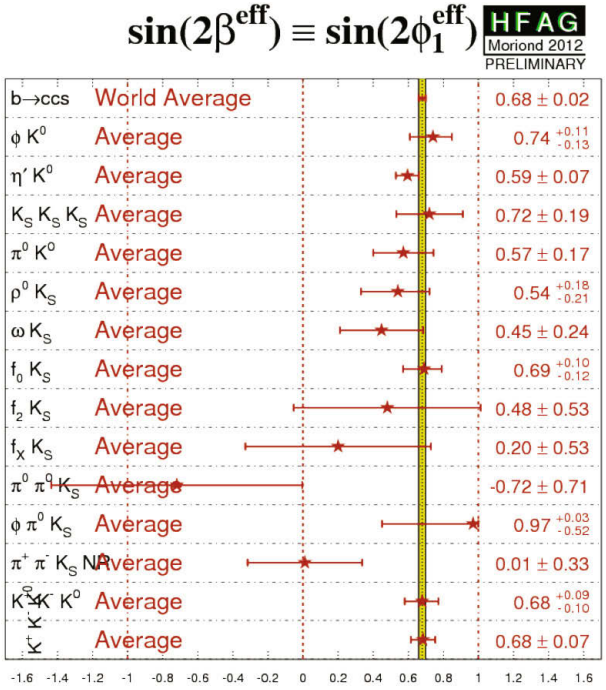

Figure 17.4.18. Comparison between the value of $\sin 2\phi_1$ from $b \to c\bar{c}s$ decays such as $B^0 \to J/\psi K^0$ (indicated by "World Average") and strange charmless $b \to u\bar{u}s$ decays (Amhis et al. (2012)).

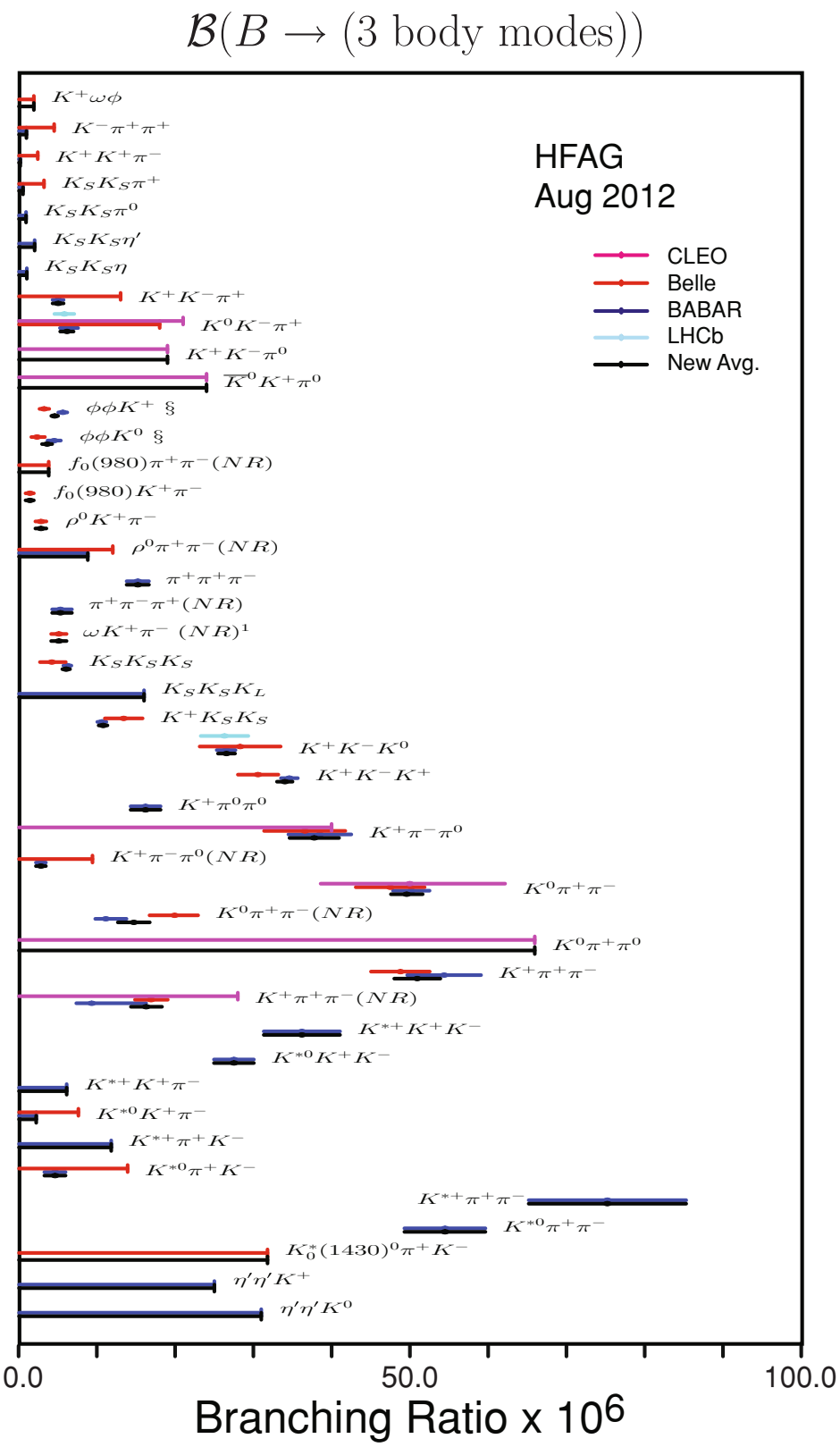

Figure 17.4.19. Summary of branching fraction measurements ($\times 10^{-6}$) and HFAG averages for decays with three mesons in the final state (Amhis et al. (2012)).

Table 17.4.10. Charmless B decays branching fractions $\mathcal{B}$ and CP asymmetries A_{CP} for *BABAR* and Belle for decays with three mesons in the final state. The averages come from HFAG and may include measurements from other experiments such as CLEO and LHCb (Amhis et al. (2012)).

	BABAR results			Belle results			Averages	
Final state	$\mathcal{B}$ ($\times 10^{-6}$)	A_{CP}	Ref.	$\mathcal{B}$ ($\times 10^{-6}$)	A_{CP}	Ref.	$\mathcal{B}$ ($\times 10^{-6}$)	A_{CP}
$K^+K^+\pi^-$	< 0.16		(Aubert, 2008aw)	< 2.4		(Garmash, 2004)	< 0.16	
$K^+K^-K^+$	$34.6 \pm 0.6 \pm 0.9$	$-0.017^{+0.019}_{-0.014} \pm 0.014$	(Lees, 2012y)	$30.6 \pm 1.2 \pm 2.3$		(Garmash, 2005)	34.0 ± 1.0	-0.017 ± 0.026
$K^+K^-K^0$	$26.5 \pm 0.9 \pm 0.8$		(Lees, 2012y)	$28.3 \pm 3.3 \pm 4.0$		(Garmash, 2004)	26.6 ± 1.1	
$K^+K^-\pi^+$	$5.0 \pm 0.5 \pm 0.5$	$0.00 \pm 0.10 \pm 0.03$	(Aubert, 2007an)	< 13		(Garmash, 2004)	5.0 ± 0.7	0.00 ± 0.10
$K^+K^-\pi^0$							< 19	
$K^+K^0_SK^0_S$	$10.6 \pm 0.5 \pm 0.3$	$0.04 \pm 0.05 \pm 0.02$	(Lees, 2012y)	$13.4 \pm 1.9 \pm 1.5$		(Garmash, 2004)	10.8 ± 0.6	0.04 ± 0.05
$K^+\pi^+\pi^-(NR)$	$9.3 \pm 1.0^{+6.9}_{-1.7}$		(Aubert, 2008j)	$16.9 \pm 1.3^{+1.7}_{-1.6}$		(Garmash, 2006)	16.3 ± 2.0	
$K^+\pi^+\pi^-$	$54.4 \pm 1.1 \pm 4.6$	$0.028 \pm 0.020 \pm 0.023$	(Aubert, 2008j)	$48.8 \pm 1.1 \pm 3.6$	$0.049 \pm 0.026 \pm 0.020$	(Garmash, 2006)	51.0 ± 3.0	0.038 ± 0.022
$K^+\pi^-\pi^0(NR)$	$2.8 \pm 0.5 \pm 0.4$	$0.10 \pm 0.16 \pm 0.08$	(Lees, 2011a)	< 9.4		(Chang, 2004)	2.8 ± 0.6	$0.23^{+0.22}_{-0.28}$
$K^+\pi^-\pi^0$	$38.5 \pm 1.0 \pm 3.9$	$-0.030^{+0.045}_{-0.051} \pm 0.055$	(Lees, 2011a)	$36.6^{+4.2}_{-4.3} \pm 3.0$	$0.07 \pm 0.11 \pm 0.01$	(Chang, 2004)	37.8 ± 3.2	0.00 ± 0.06
$K^+\pi^0\pi^0$	$16.2 \pm 1.2 \pm 1.5$	$-0.006 \pm 0.006 \pm 0.004$	(Lees, 2011g)				16.2 ± 1.9	
$K^+\omega\phi$				< 1.9		(Liu, 2009)	< 1.9	
$K^-\pi^+\pi^+$	< 0.95		(Aubert, 2008aw)	< 4.5		(Garmash, 2004)	< 0.95	
$K^0K^-\pi^+$	$6.4 \pm 1.0 \pm 0.6$		(del Amo Sanchez, 2010j)	< 18		(Garmash, 2004)	6.4 ± 1.2	
$K^0\pi^+\pi^-(NR)$	$11.1^{+2.5}_{-1.0} \pm 0.9$		(Aubert, 2009av)	$19.9 \pm 2.5^{+1.7}_{-2.0}$		(Garmash, 2007)	14.7 ± 2.0	
$K^0\pi^+\pi^-$	$50.2 \pm 1.5 \pm 1.8$	$-0.01 \pm 0.05 \pm 0.01$	(Aubert, 2009av)	$47.5 \pm 2.4 \pm 3.7$		(Garmash, 2007)	49.6 ± 2.0	-0.01 ± 0.05
$K^0\pi^+\pi^0$							< 66	
$K^{*+}K^+K^-$	$36.2 \pm 3.3 \pm 3.6$	$0.11 \pm 0.08 \pm 0.03$	(Aubert, 2006h)				36.2 ± 4.9	0.11 ± 0.09
$K^{*+}K^+\pi^-$	< 6.1		(Aubert, 2006h)				< 6.1	
$K^{*+}\pi^+K^-$	< 11.8		(Aubert, 2006h)				< 11.8	
$K^{*+}\pi^+\pi^-$	$75.3 \pm 6.0 \pm 8.1$	$0.07 \pm 0.07 \pm 0.04$	(Aubert, 2006h)				75.3 ± 10.1	0.07 ± 0.08
$K^{*0}K^+K^-$	$27.5 \pm 1.3 \pm 2.2$	$0.01 \pm 0.05 \pm 0.02$	(Aubert, 2007ah)				27.5 ± 2.6	0.01 ± 0.05
$K^{*0}K^+\pi^-$	< 2.2		(Aubert, 2007ah)	< 7.6			< 2.2	
$K^{*0}\pi^+K^-$	$4.6 \pm 1.1 \pm 0.8$	$0.22 \pm 0.33 \pm 0.20$	(Aubert, 2007ah)	< 13.9			4.6 ± 1.4	0.22 ± 0.39
$K^{*0}\pi^+\pi^-$	$54.5 \pm 2.9 \pm 4.3$	$0.07 \pm 0.04 \pm 0.03$	(Aubert, 2007ah)	$4.5^{+1.1+0.9}_{-1.0-1.6}$			54.5 ± 5.2	0.07 ± 0.05
$K^*_0(1430)^0\pi^+K^-$				< 31.8		(Chiang, 2010)	< 31.8	
$K^0_SK^0_SK_L$	< 16		(Aubert, 2006at)				< 16	
$K^0_SK^0_SK^0_S$	$6.19 \pm 0.48 \pm 0.19$		(Aubert, 2005e)	$4.2^{+1.6}_{-1.3} \pm 0.8$		(Garmash, 2004)	6.2 ± 0.9	
$K^0_SK^0_S\eta$	< 1.0		(Aubert, 2009am)				< 1.0	
$K^0_SK^0_S\eta'$	< 2.0		(Aubert, 2009am)				< 2.0	
$K^0_SK^0_S\pi^+$	< 0.51		(Aubert, 2009ar)	< 3.2		(Garmash, 2004)	< 0.51	
$K^0_SK^0_S\pi^0$	< 0.9		(Aubert, 2009am)				< 0.9	
$\eta'\eta'K^+$	< 25		(Aubert, 2006al)				< 25	
$\eta'\eta'K^0$	< 31		(Aubert, 2006al)				< 31	
$\omega K^+\pi^-$ $(NR)^1$				$5.1 \pm 0.7 \pm 0.7$		(Goldenzweig, 2008)	5.1 ± 1.0	
$\overline{K}^0K^+\pi^0$							< 24	
$\phi\phi K^+$	$5.6 \pm 0.5 \pm 0.3$	$-0.10 \pm 0.08 \pm 0.02$	(Lees, 2011e)	$3.2^{+0.6}_{-0.5} \pm 0.3$	$0.01^{+0.19}_{-0.16} \pm 0.02$	(Abe, 2008b)	4.6 ± 0.4	-0.08 ± 0.07
$\phi\phi K^0$	$4.5 \pm 0.8 \pm 0.3$		(Lees, 2011e)	$2.3^{+1.0}_{-0.7} \pm 0.2$		(Abe, 2008b)	3.6 ± 0.7	
$\pi^+\pi^+\pi^-$	$15.2 \pm 0.6 \pm 1.3$		(Aubert, 2009h)				15.2 ± 1.4	
$\pi^+\pi^-\pi^+(NR)$	$5.3 \pm 0.7^{+1.3}_{-0.8}$	$-0.14 \pm 0.14^{+0.18}_{-0.08}$	(Aubert, 2009h)				$5.3^{+1.5}_{-1.1}$	$-0.14^{+0.23}_{-0.16}$
$\rho^0K^+\pi^-$				$2.8 \pm 0.5 \pm 0.5$		(Kyeong, 2009)	2.8 ± 0.7	
$\rho^0\pi^+\pi^-(NR)$	< 8.8		(Aubert, 2008r)	< 12		(Chiang, 2008)	< 8.8	
$f_0(980)K^+\pi^-$				$1.4 \pm 0.4^{+0.3}_{-0.4}$		(Kyeong, 2009)	$1.4^{+0.5}_{-0.6}$	
$f_0(980)\pi^+\pi^-(NR)$				< 3.8		(Chiang, 2008)	< 3.8	

CP asymmetries are expected in $b \to s\bar{s}s$ decays consistent with asymmetries measured in $b \to c\bar{c}s$. The tree contributions are small and the amplitude is dominated by loop contributions, where new virtual particles can contribute. In $B^0 \to K^+K^-K^0$, both the direct *CP* asymmetry A_{CP} and ϕ_1^{eff} ($\phi_1 = arg(-V_{cd}V_{cb}^*/V_{td}V_{tb}^*)$) have been measured for the whole Dalitz Plot and the dominant individual resonances. *BABAR* find two equally likely solutions for $B^0 \to \phi K^0$ and $B^0 \to f_0(980)K^0$, the first consistent with the SM and the second with a significantly different phase ϕ_1^{eff} for $B^0 \to f_0(980)K^0$. In the high mass region, the *CP*-conserving case $\phi_1^{eff} = 0$ is excluded at the 5.1 standard deviations level. Across the whole Dalitz Plot the *CP* asymmetry is $A_{CP} = -0.015 \pm 0.077 \pm 0.053$ and $\phi_1^{eff} = 0.352 \pm 0.076 \pm 0.026$ (Aubert, 2007af). Belle, with approximately twice the data size, find four solutions for ϕ_1^{eff} but solution 1 is preferred when external constraints, such as known branching fraction ratios, are included (Nakahama, 2010). Belle see no evidence for A_{CP} in $B^0 \to \phi K_S^0$ nor in $B^0 \to f_0(980)K_S^0$ and measure ϕ_1^{eff} to be $(33.2 \pm 9.0 \pm 2.6 \pm 1.4)^\circ$ for $B^0 \to \phi K_S^0$ and $(31.3 \pm 9.0 \pm 3.4 \pm 4.0)^\circ$ for $B^0 \to f_0(980)K_S^0$ (solution 1). These are consistent with ϕ_1^{eff} measurements from other $b \to c\bar{c}s$ transitions, such as $B^0 \to J/\psi K^0$.

BABAR performed a binned fit to the $B^+ \to K^+K^+K^-$ Dalitz Plot and found no evidence for *CP* violation, neither for the whole plane ($A_{CP} = -0.017 \pm 0.026 \pm 0.015$) nor for any resonance (Aubert, 2006i). Belle in their analysis (Garmash, 2005) do not report asymmetries but their results for branching and fit fractions do not agree well with *BABAR*. This is primarily due to the fact that *BABAR* report a broad scalar resonance, which they label $X_0(1550)$, while Belle include only the $f_0(980)$ in their model.

The Dalitz Plot structure of $B^0 \to K_S^0K_S^0K_S^0$ has been investigated and the inclusive branching fractions measured. The product branching fractions of $f_0(980)K_S^0$, $f_0(1270)K_S^0$ and $f_2(2010)K_S^0$ have been measured and there are hints of $f_2'(1525)$ and $f_0(1500)$ (Lees, 2012c). The mixing-induced *CP*-violation parameters for $B^0 \to K^0K^0K^0$ are measured to be $S = -0.94^{+0.24}_{-0.21} \pm 0.06$ and $C = -0.17 \pm 0.18 \pm 0.04$. These are compatible within 2 standard deviations with those measured in tree-dominated $B^0 \to J/\psi K_S^0$ decays. As a result *CP* conservation is excluded at the 3.8 standard deviation level. Belle have looked at $B^0 \to K_S^0K_S^0K_S^0$ and intermediate resonances that decay to the final state $K^+K^-K_S^0$ (Chen, 2007a).

Belle measure $\sin 2\phi_1$ in $B^0 \to \eta' K^0$ to be $0.64 \pm 0.10 \pm 0.04$ with a significance of 5.6 standard deviations and find no evidence for direct *CP* violation. *BABAR* also measure a significant value of $\sin 2\phi_1 = 0.58 \pm 0.10 \pm 0.03$ (5.5 standard deviations significance) in $B^0 \to \eta' K^0$ (Aubert, 2007am). However, in this case, the direct *CP* result $A_f = -0.16 \pm 0.07 \pm 0.03$ is 2.1 standard deviation from zero.

For $B^+ \to K^0K^0K^+$, Belle report branching fractions (Garmash, 2004), while *BABAR* has also extracted the *CP* charge asymmetry $A_{CP} = -0.04 \pm 0.1 \pm 0.02$ (Aubert, 2004b).

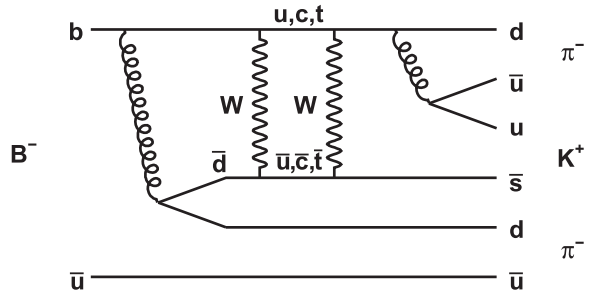

Figure 17.4.20. Example of the SM suppressed decay diagram for the decay $B^- \to K^+\pi^-\pi^-$.

Modes with just two kaons in the final state are important as they proceed through $b \to d$ penguin loops and are suppressed. Consequently, small branching fractions are expected and the opportunities for measuring asymmetries are few.

There have been no measurements of the decay $B^0 \to K^+K^-\pi^0$ by *BABAR* or Belle. The decay $B^+ \to K^+K^-\pi^+$ has been observed by *BABAR* (Aubert, 2007an) with $\mathcal{B} = (5.0 \pm 0.5 \pm 0.5) \times 10^{-6}$ and $A_{CP} = 0.00 \pm 0.10 \pm 0.03$; Belle have placed upper limits (UL) on the branching fraction $< 13 \times 10^{-6}$ (Garmash, 2004). The mode $B^+ \to K^+K^+\pi^-$ is additionally suppressed by a factor $|V_{td}V_{ts}^*| \sim 3 \times 10^{-4}$ but could be enhanced in SM extensions with extra Z' bosons. *BABAR* finds for this decay a branching fraction UL of 0.16×10^{-6} (Aubert, 2008aw). The decay $B^0 \to K_S^0K^\pm\pi^\mp$ has been observed by *BABAR* with branching fraction $(3.2 \pm 0.5 \pm 0.3) \times 10^{-6}$ at 5.2 standard deviation significance (del Amo Sanchez, 2010j).

Both Belle and *BABAR* have made significant progress in measuring $B \to K_S^0K_S^0h$ where h includes mesons such as π^+, π^0, η, and η'. The $b \to d$ transition has been measured in $B^0 \to \pi^+\pi^-\pi^0$ where the beauty flavor changes by $\Delta F = 2$ (due to mixing) but in $B^+ \to K_S^0K_S^0\pi^+$ by $\Delta F = 1$ (due to decay). Both *BABAR* and Belle have placed upper limits of $\mathcal{B}(B^+ \to K_S^0K_S^0\pi^+) < 0.51 \times 10^{-6}$ (Aubert, 2009ar) and $< 3.2 \times 10^{-6}$ (Garmash, 2004), respectively. *BABAR* find ULs on $\mathcal{B}(B^0 \to K_S^0K_S^0\pi^0)$, $\mathcal{B}(B^0 \to K_S^0K_S^0\eta)$, and $\mathcal{B}(B^0 \to K_S^0K_S^0\eta')$ of 2×10^{-6} and below (Aubert, 2009am).

Large *CP* asymmetries are expected in $B^+ \to \rho^0K^+$. *BABAR* find evidence of direct *CP* violation in $B^+ \to \rho^0K^+, \rho^0 \to \pi^+\pi^-$ with $A_{CP} = (0.44 \pm 0.10 \pm 0.04^{+0.06}_{-0.13})$ (Aubert, 2008j) at the 3.7σ level and Belle report very similar results, with $A_{CP} = (0.30 \pm 0.11 \pm 0.02^{+0.11}_{-0.04})$ with 3.9σ significance (Garmash, 2006) A Dalitz analysis is essential due to the possibility of interference of the wide ρ^0 width with neighboring resonances. *CP* asymmetries in $B^+ \to K^{*0}\pi^+$, $B^+ \to K_0^{*0}(1430)\pi^+$, and $B^+ \to K_2^{*0}(1430)\pi^+$, on the other hand, are small. The SM-suppressed mode $B^- \to K^+\pi^-\pi^-$ has also been investigated by both experiments and the decay diagram is shown in Fig. 17.4.20. *BABAR* and Belle place UL on the branching fraction of 0.95×10^{-6} (Aubert, 2008aw) and $< 4.5 \times 10^{-6}$ (Garmash, 2004), respectively.

The decay $B^+ \to K^+\pi^-\pi^+$ is important for searching for direct *CP* violation in $B \to K^*\pi$ decays. *BABAR* find four compatible solutions of the Dalitz Plot (Lees, 2011a). When combined with the time-dependent analysis of $B^0 \to K^0_S\pi^-\pi^+$ (Aubert, 2009av), *BABAR* report $A_{CP} = -0.24 \pm 0.07 \pm 0.02$ with a significance of 3.1σ for $B \to K^{*+}\pi^-$ decays. A similar Belle analysis has half the number of events and is restricted to branching fraction measurements and ranges for A_{CP} (Chang, 2004).

In $B^0 \to \pi^+\pi^-K^0_S$, the decay $B^0 \to f_0(980)K^0_S$ is expected to be dominated by $b \to s$ transitions. The $f_0(980)$ can overlap with nearby resonances, requiring a Dalitz analysis to extract a robust estimate of $\sin 2\phi_1$, taking interference into account. Belle find no evidence for direct *CP* violation in $B^0 \to \rho^0 K^0_S$, $B^0 \to f_0(980)K^0_S$, and $B^0 \to K^{*+}\pi^-$ and measure $A_{CP}(K^{*+}\pi^-) = -0.21 \pm 0.11 \pm 0.05 \pm 0.05$ (Dalseno, 2009; Garmash, 2007). The $\sin 2\phi_1$ measurements for $B^0 \to \rho^0 K^0_S$ and $B^0 \to f_0(980)K^0_S$ are consistent with $\sin 2\phi_1$ from $b \to c\bar{c}s$ decays. The phase difference between $B^0 \to K^{*+}\pi^-$ and $\overline{B}^0 \to K^{*-}\pi^+$, which could lead to a measurement of ϕ_3, is reported as $\Delta\phi(K^{*+}\pi^-) = (-0.7^{+23.5}_{-22.8} \pm 11.0 \pm 17.6)^\circ$. *BABAR* has also looked at this mode but only report ranges for ϕ_1 in $B^0 \to \rho^0 K^0_S$ and $B^0 \to f_0(980)K^0_S$ but they measure $A_{CP}(K^{*+}\pi^-)$ consistent with Belle (Aubert, 2009av).

The B Factories have started to look at Dalitz Plots involving short-lived particles such as the K^*. The branching fractions of the decays $B^0 \to K^{*0}\pi^+K^-$ and $B^+ \to K^{*+}\pi^+K^-$ are sensitive to the CKM matrix elements V_{td} and V_{ub}. Additionally, a branching fraction of the Standard Model suppressed decay $B^0 \to K^{*0}K^+\pi^-$ comparable or larger than that of $B^0 \to K^{*0}\pi^+K^-$ would be an indication of new physics (Aubert, 2006h, 2007ah). There is no evidence for this in the current data with branching fraction measurements of $\mathcal{B}(B^0 \to K^{*0}K^+\pi^-) = (4.6 \pm 1.1 \pm 0.8) \times 10^{-6}$ and $\mathcal{B}(B^0 \to K^{*0}\pi^+K^-) < 2.2 \times 10^{-6}$.

As an example of the detail of information that can be extracted from a Dalitz Plot analysis, Table 17.4.11 shows the branching fractions, charged asymmetries, fit fractions, and phases for the decay $B^+ \to K^+K^+K^-$. Similar results exist for a number of the Dalitz Plots listed in Table 17.4.10.

17.4.8 Summary

Together *BABAR* and Belle have collected well over $1\,\text{ab}^{-1}$ of B meson decays. Even with low branching fractions, the study of charmless hadronic B decays have enabled the measurement of: the CKM angles ϕ_1, ϕ_2, ϕ_3; the discovery of many new decay modes with a measured branching fraction; new branching fraction upper limits placed on many rare decays; direct and indirect *CP* asymmetries; G-parity conservation tests; longitudinal polarization; interference effects; and weak and strong phases. This has enabled a comprehensive comparison with theoretical predictions and models. These theoretical models continue to progress, with more precise calculations over a wider range of observables. Yet despite this, the study of charmless hadronic decays is still only partially complete. Work is still on-going in understanding the hierarchy of the longitudinal polarization. Some measured branching fractions do not agree with predictions. The prediction, understanding and interpretation of the phases and amplitudes in three-body Dalitz Plots are still in their infancy.

Table 17.4.11. An illustration of the results that can be extracted from a full Dalitz Plot analysis of $B^+ \to K^+K^+K^-$ for *BABAR* (Aubert, 2006i) and Belle (Garmash, 2005). The extracted parameters are: the branching fraction $\mathcal{B}$ or product branching fraction $\mathcal{B} \times \mathcal{B}_f$ ($\times 10^{-6}$); the charged *CP* asymmetry A_{CP} (%); the fit fraction FF (%); the phase δ (°) relative to the reference decay; mass M and width Γ (GeV/c^2); NR is the non-resonant component and some errors have been rounded.

Decay	Param.	*BABAR*	Belle
$K^+\ K^+\ K^-$	$\mathcal{B}$	$33.5 \pm 0.9 \pm 1.6$	$30.6 \pm 1.2 \pm 2.3$
	A_{CP}	$-0.02 \pm 0.03 \pm 0.02$	
ϕK^+	$\mathcal{B}$	$8.4 \pm 0.7 \pm 0.7$	$9.60 \pm 0.92 \pm 0.71$
	A_{CP}	$0 \pm 8 \pm 2$	
	FF	$11.8 \pm 0.9 \pm 0.8$	14.7 ± 1.3
	δ	$-7 \pm 0.11 \pm 3$	-123 ± 10
$\phi(1680)K^+$	$\mathcal{B} \times \mathcal{B}_f$		< 0.8
$f_0(980)K^+$	$\mathcal{B} \times \mathcal{B}_f$	$6.5 \pm 2.5 \pm 1.6$	< 2.9
	A_{CP}	$-31 \pm 25 \pm 8$	
	FF	$19 \pm 7 \pm 4$	
	δ	$28 \pm 9 \pm 5$	
$f_X(1500)K^+$	$\mathcal{B} \times \mathcal{B}_f$	$43 \pm 6 \pm 3$	
	A_{CP}	$-4 \pm 7 \pm 2$	
	FF	$121 \pm 19 \pm 6$	63.4 ± 6.9
	δ	$74 \pm 5 \pm 2$	0 (fixed)
	M	1.539 ± 0.020	1.524 ± 0.014
	Γ	0.257 ± 0.033	0.136 ± 0.023
$f_0(1710)K^+$	$\mathcal{B} \times \mathcal{B}_f$	$1.7 \pm 1.0 \pm 0.3$	
$f'(1525)K^+$	$\mathcal{B} \times \mathcal{B}_f$		< 4.9
$a_2(1320)K^+$	$\mathcal{B} \times \mathcal{B}_f$		< 1.1
NR	$\mathcal{B}$	$50 \pm 6 \pm 4$	$24.0 \pm 1.5 \pm 1.8$
	FF	$141 \pm 16 \pm 9$	74.8 ± 3.6
	δ	0 (fixed)	-68 ± 9

17.5 B-meson lifetimes, $B^0 - \overline{B}^0$ mixing, and symmetry violation searches

Editors:
Soeren Prell (BABAR)
Bruce Yabsley (Belle)

Additional section writers:
Thomas Mannel

The charged and neutral B meson lifetimes, τ_{B^+} and τ_{B^0}, and the $B^0 - \overline{B}^0$ oscillation frequency Δm_d, are fundamental parameters of B meson decays. They provide important input for the determination of the CKM matrix elements $|V_{cb}|$ and $|V_{td}|$ (discussed in Sections 17.1 and 17.2). In addition, precise knowledge of τ_{B^0} and Δm_d is necessary for the extraction of CP asymmetries from the neutral B decay-time distributions. Here we describe precision measurements of τ_{B^+}, τ_{B^0} (Section 17.5.1), and Δm_d (Section 17.5.2); measurements of $\Delta\Gamma_d$ are also discussed (Section 17.5.2.6). By relaxing the assumptions behind standard mixing analyses, it is also possible to test the quantum-mechanical nature of $B^0 - \overline{B}^0$ oscillations (Section 17.5.3), search for violations of CP, T, or even CPT symmetry in mixing (Section 17.5.4), and search for violations of Lorentz symmetry (Section 17.5.5).

17.5.1 B-meson lifetimes

In 1983 the MAC and MARK II Collaborations (Fernandez et al., 1983; Lockyer et al., 1983) discovered, in 29 GeV center-of-mass energy e^+e^- collisions recorded at the PEP storage ring at SLAC, that the impact parameters of high-momentum leptons in hadronic final states were largely positive. From the measured impact parameter distributions and assuming these leptons originated mostly from b hadron decays, the collaborations estimated a b hadron lifetime of the order of one picosecond. Such a long lifetime was unexpected. At the time, the phenomenological guidance on the strength of weak b hadron decays was the mixing between the first and second quark generation, characterized by the Cabibbo angle θ_C (Section 16). If quark mixing between the second and the third generation was similar, the expected b lifetime would be around 0.1 ps (Barger, Long, and Pakvasa, 1979). The long lifetime of b hadrons was the first evidence that the magnitude of the CKM matrix element V_{cb} is much smaller than $\sin\theta_C$. Along with first limits on the branching fractions of semileptonic $b \to u$ transitions, and thus $|V_{ub}/V_{cb}|$, from experiments at Cornell around the same time (Chen et al., 1984; Klopfenstein et al., 1983) and unitarity constraints, the measurement of $|V_{cb}|$ led to the first complete picture of the magnitudes of all the CKM matrix elements (Ginsparg and Wise, 1983). Soon after, it was realized that due to its long lifetime the B^0 can oscillate into a $\overline{B}^0$ before it decays, allowing for measurements of $B^0 - \overline{B}^0$ mixing and time-dependent CP asymmetries.

At the time when the B Factories started to record their first data, the Particle Data Group listed in their 2000 Review of Particle Physics (Groom et al., 2000) the averages of the B^0 and B^+ lifetimes and their ratio as: $\tau_{B^0} = (1.548 \pm 0.032)$ ps, $\tau_{B^+} = (1.653 \pm 0.028)$ ps, and $\tau_{B^+}/\tau_{B^0} = 1.062 \pm 0.029$, with relative uncertainties of 2.1%, 1.7%, and 2.7%, respectively.

While the first measurements of the magnitude of the CKM matrix element V_{cb} were provided by the initial b hadron lifetime measurements, the most precise determination of $|V_{cb}|$, based on advances in the theoretical descriptions of B-meson decays, now comes from semileptonic branching ratios (see Section 17.1).

In the following, we briefly discuss the theory of B meson lifetimes (Section 17.5.1.1), and the motivation and principles of lifetime measurements (Section 17.5.1.2), before reviewing lifetime measurements at the B Factories using fully-reconstructed (Section 17.5.1.3) and partially-reconstructed final states (Section 17.5.1.4). Averages of the B lifetimes and their ratio are presented in Section 17.5.1.5.

17.5.1.1 Theory of B meson lifetimes

From the theoretical side the lifetime (or equivalently the total decay rate Γ) of a heavy quark hadron is a fully inclusive quantity for which a systematic expansion in powers of $\Lambda_{\rm QCD}/m_Q$ can be performed (Bigi, 1996; Neubert and Sachrajda, 1997). Schematically one obtains an expression of the form

$$\Gamma = \Gamma_0 + \Gamma_1 \left(\frac{\Lambda_{\rm QCD}}{m_Q}\right) + \Gamma_2 \left(\frac{\Lambda_{\rm QCD}}{m_Q}\right)^2 + \Gamma_3 \left(\frac{\Lambda_{\rm QCD}}{m_Q}\right)^3 + \cdots \tag{17.5.1}$$

The leading term in the decay rate

It turns out that the leading term of this expansion does not depend on any hadronic matrix element and is simply the decay of a free quark. This is illustrated in Fig. 17.5.1: It depicts the square of the amplitude of a heavy quark decaying via a four quark operator into three final state fermions, *i.e.* the internal lines should not be interpreted as propagators, but rather as the corresponding phase space integration. Since only the heavy quark is involved, to this level of the expansion, the lifetime of all charm and

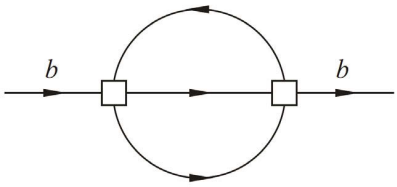

Figure 17.5.1. Illustration of the leading term of the heavy quark expansion for the total rate.

bottom hadrons, respectively, are predicted to be identical. Neglecting CKM suppressed contributions and the masses of the electron, the muon, the up and the down quark, the leading term for charm hadrons (*i.e.* without QCD corrections) can be written as,

$$\Gamma_c = |V_{cs}|^2 \left[N_c \Gamma(c \to s\overline{u}d) + 2\Gamma(c \to s\ell\overline{\nu}_\ell) \right], \quad (17.5.2)$$

where N_c is the number of colors, $\ell = e, \mu$, and

$$\Gamma(c \to s\overline{f}f') = \frac{G_F^2 m_c^5}{192\pi^3} f_{\rm PS}, \quad (17.5.3)$$

where $f_{\rm PS}$ is a phase space factor depending on the mass of the charm and the strange quarks.

For bottom hadrons this expression is slightly more complicated since more final states are involved. For the leading term, neglecting again CKM suppressed contributions, setting $|V_{cs}| = |V_{ud}| \approx 1$, and neglecting the e, μ, u, and d masses, one obtains

$$\Gamma_b = |V_{cb}|^2 \Big[N_c [\Gamma(b \to c\bar{c}s) + \Gamma(b \to c\overline{u}d)] + 2\Gamma(b \to c\ell\overline{\nu}_\ell) + \Gamma(b \to c\tau\overline{\nu}_\tau) \Big], \quad (17.5.4)$$

where now

$$\Gamma(b \to c\overline{f}f') = \frac{G_F^2 m_b^5}{192\pi^3} f_{(\overline{f}f')}, \quad (17.5.5)$$

and $f_{(\overline{f}f')}$ is a phase space function depending on the bottom and the charm mass as well as on the masses of the two additional fermions f and f'.

Although the analytic expression for the phase space functions are not complicated, we give here only a simple numerical consideration. Putting in the phase space functions, one obtains

$$\Gamma_c \approx 3.5 \times \frac{G_F^2 m_c^5}{192\pi^3} |V_{cs}|^2 = [1.1 \times 10^{-12}\,{\rm s}]^{-1}, \quad (17.5.6)$$

$$\Gamma_b \approx 2.9 \times \frac{G_F^2 m_b^5}{192\pi^3} |V_{cb}|^2 = [1.2 \times 10^{-12}\,{\rm s}]^{-1}. \quad (17.5.7)$$

Being the first term of a systematic expansion, it is reassuring that these numbers are in the right ballpark. Note that the rates have to be proportional to m_Q^5 to compensate the dimension of the Fermi coupling G_F; however the full dependence on the heavy quark mass is not as strong due to the phase space factors. The fact that the bottom and charm lifetimes are still comparable is due to the small magnitude of the CKM element $|V_{cb}|$ relative to $|V_{cs}|$.

The prediction that the heavy-hadron lifetimes are identical was considered a problem in the early days of the heavy quark expansion. In fact, we have for example $\tau(D^+)/\tau(D^0) = 2.52 \pm 0.09$, indicating large corrections from higher-order terms in the expansion. Furthermore, the leading term depends on a high power of m_Q, such that any uncertainty in m_Q would be amplified so much that it was originally believed that no precise predictions could be made. However, including QCD corrections in combination with suitable mass definitions, this could be remedied.

We note in passing that the naïve spectator model also predicts the semileptonic branching ratios. Taking into account only the Cabibbo-allowed contributions and neglecting the masses of the final state fermions we obtain

$$\mathcal{B}(D \to X\ell\overline{\nu}) = \frac{\Gamma(c \to s\ell\overline{\nu})}{N_c \Gamma(c \to s\bar{d}u) + N_{\rm lept}\Gamma(c \to s\ell\overline{\nu})}, \quad (17.5.8)$$

where $\ell = e$ or μ, $N_c = 3$ is the number of colors, and $N_{\rm lept} = 2$ is for the two leptons that can appear as a final state in a D decay. With the approximation $|V_{cs}| = |V_{ud}| \sim 1$, and final state masses neglected, the partial widths are equal,

$$\Gamma(c \to s\bar{d}u) = \Gamma(c \to s\ell\overline{\nu}) = \frac{G_F^2 m_c^5}{192\pi^3}, \quad (17.5.9)$$

so we find

$$\mathcal{B}(D \to X\ell\overline{\nu}) = \frac{1}{3+2} = 0.2. \quad (17.5.10)$$

For bottom we can perform the same calculation, however here one has to take into account phase space factors, since the phase space for *e.g.* $b \to c\bar{c}s$ is significantly different from that for $b \to c\overline{u}d$. Taking this effect into account one arrives at

$$\mathcal{B}(B \to X\ell\overline{\nu}) = 0.17\,. \quad (17.5.11)$$

Again these predictions are in the right ballpark, but depend strongly on the quark masses and the definitions used for these masses. Including the higher order terms in α_S as well as in the heavy quark expansion improves the precision of the predictions dramatically. In particular, the determination of $|V_{cb}|$ is performed on the basis of the total semileptonic rate, which is computed at the percent level of precision.

Higher-order terms

The higher order terms in the heavy quark expansion have been investigated in detail. The term of order $\Lambda_{\rm QCD}/m_Q$ vanishes due to heavy quark symmetries, so the first non-perturbative input to the lifetimes appears at the second order of the expansion. To this order, the kinetic energy parameter μ_π^2 and the chromo-magnetic moment μ_G^2 appear as non-perturbative input (for the precise definition of these parameters see Section 17.1). However, assuming light-quark flavor symmetry, one obtains $\mu_\pi^2(B^0) = \mu_\pi^2(B^\pm) = \mu_\pi^2(B_s^0)$ and hence the second order in the expansion still does not induce a lifetime difference between B^0, $B^\pm$, and B_s^0.

A lifetime difference between the bottom mesons needs to involve the spectator quark. Contributions of this kind are illustrated in Fig. 17.5.2. However, such contributions are induced only at order $(\Lambda_{\rm QCD}/m_Q)^3$, which was taken as an embarrassment at the time this was derived, since the lifetimes in the D meson system differ by a factor

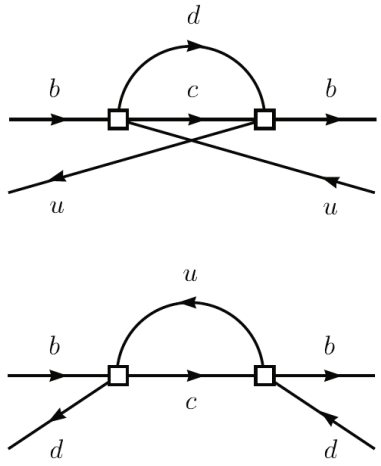

Figure 17.5.2. Spectator contributions.

as large as 2.5. However, subsequently it has been found that the coefficient Γ_3 can be enhanced by a loop factor $16\pi^2$, which at least qualitatively explains this large effect. This can actually be seen by comparing Figs 17.5.1 and 17.5.2: the leading term shown in Fig 17.5.1 is a two-loop diagram, leading to a factor $(1/(16\pi^2))^2$, whereas the spectator contributions shown in Fig 17.5.2 are one-loop diagrams with only a single power of $1/(16\pi^2)$ (Neubert and Sachrajda, 1997).

Over the past ten years lifetime calculations have been refined by adding higher order terms in the $1/m_b$ expansion as well as QCD corrections. A recent review can be found in Lenz (2008).

17.5.1.2 Motivation and principles of lifetime measurements

There were both theoretical and experimental reasons for the B Factories to measure the B-meson lifetimes more precisely:

- Predictions for lifetime ratios based on a naïve estimate of the hadronic matrix elements yielded $\tau_{B^+}/\tau_{B^0} = 1.067 \pm 0.027$ (Becirevic, 2001). While in agreement with this prediction, the pre-B Factory data were not conclusive on whether the charged or neutral B lifetime was longer, motivating a more precise measurement of τ_{B^+}/τ_{B^0} to provide a stronger test of these calculations.
- The B^0 meson lifetime provides an essential input to the measurements of the $B^0 - \overline{B}^0$ oscillation frequency (see Section 17.5.2) and time-dependent CP asymmetries including the angles ϕ_1 and ϕ_2 of the Unitarity Triangle (see Sections 17.6 and 17.7). Accurate values of τ_{B^0} and Δm_d reduce the systematic uncertainties in these analyses of time-dependent CP asymmetries.

The most precise measurements of the B-meson lifetimes before the first B Factory results became available were from experiments at the Z^0 resonance and CDF. These experiments measured the distance l the B meson travels from its production point to its decay vertex. The production point is, respectively, the e^+e^- or $p\overline{p}$ interaction point and the decay vertex is determined from the B decay products. From this decay distance l, the measured B momentum p_B, and the known B mass m_B, they determined the proper time of the B-meson decay $t = l/c(\beta\gamma)_B = m_B l/(p_B c)$. The proper-time distribution of the B-meson candidates is given by $\Gamma(t) = \frac{1}{\tau_B}\exp(-t/\tau_B)$ before accounting for detector resolution and backgrounds. The experiments extracted the B-meson lifetimes from fits to the measured proper-time spectra. While the ARGUS and CLEO experiments had collected large samples of B mesons at the $\Upsilon(4S)$ resonance, their B mesons were essentially produced at rest in the laboratory frame, rendering a proper-time method through decay-length measurements impossible.

These earlier B-lifetime measurements are characterized by high-precision measurements of the relative decay length of the B mesons ($\sigma_l/\langle l\rangle \approx 10\%$), but typically suffered from a combination of relatively small signal samples, large backgrounds, and in the case of partially-reconstructed B mesons, a poor measurement of the B momentum. In contrast, the measurements from *BABAR* and Belle have worse $\sigma_l/\langle l\rangle$ resolution, but their high-statistics B samples have little background and excellent knowledge of the B momentum.

A principal difference between the B-meson lifetime measurements at previous experiments and at the asymmetric-energy B Factories is the knowledge of the B production point. At all experiments the B mesons are produced in the luminous region of the particle beams (beam spot). The coordinates of the beam spot are well known. The beam spot size is much smaller in the plane transverse to the beam direction than along the beam direction. At the LEP and Tevatron experiments and at SLD most B mesons travel a measurable distance in the transverse plane before they decay, and the B meson proper time is derived from this distance. In fits to the proper-time distributions, events with measured $t < 0$ provide valuable information about the proper-time resolution function. Since there are no true negative proper times, all events with measured $t < 0$ are due to resolution effects. In contrast, at the B Factories the B mesons are barely moving in the center-of-mass frame. Thus their transverse momentum and transverse flight distance are close to zero and cannot be used for a precise proper-time measurement. The length of the beam spot in the z direction is about a centimeter in *BABAR* and Belle and there are no fragmentation tracks coming from the B production point (as only a $B\overline{B}$-pair is produced in the decay of the $\Upsilon(4S)$). Therefore the z coordinate of the B production vertex cannot be reconstructed with good precision. Instead, at the B Factories the distance Δz between the decay vertices of the two B mesons is measured. The proper-time difference is then given to good approximation by

$$\Delta t \approx \Delta z/(c(\beta\gamma)_B), \qquad (17.5.12)$$

where $(\beta\gamma)_B$ is the Lorentz boost factor of the B meson in the lab frame (see Section 6.5). The Δt distribution is given by

$$\Gamma(\Delta t) = \frac{1}{2\tau_B} \exp\left(-|\Delta t|/\tau_B\right). \quad (17.5.13)$$

It is symmetric around $\Delta t = 0$. Detector resolution effects will smear this distribution, but there is no region in Δt that allows a similarly clean access to the Δt resolution function as in the experiments at the Z^0 and CDF and DØ (see Fig. 17.5.3). One of the challenges of the B-lifetime measurements at the B Factories is to disentangle the underlying true Δt distribution from the resolution function.

Both *BABAR* and Belle use multiple samples of B mesons to determine the B^0 and B^+ lifetimes and their ratio. One of the B mesons, $B_{\rm rec}$, is typically reconstructed in an exclusive final state. The various samples differ in their B meson yield per inverse femtobarn and in their signal purity.[57] More exclusive samples have less background, but also a smaller yield. In the lifetime analyses, the z position of the $B_{\rm rec}$ decay vertex $z_{\rm rec}$ is determined from its decay products. The z position $z_{\rm oth}$ of the decay vertex of the other B meson, $B_{\rm oth}$, is reconstructed from the tracks not belonging to $B_{\rm rec}$. The proper-time difference Δt is then calculated from $\Delta z = z_{\rm rec} - z_{\rm oth}$ using Eq. (17.5.12). It turns out that the uncertainty in Δt is dominated by the uncertainty in $z_{\rm oth}$ and is almost the same for all lifetime analyses at the B Factories. The B lifetimes are extracted from a fit to the Δt distributions of the selected candidates after accounting for detector resolution effects and background. In the following, we will briefly describe the various measurements of the B-meson lifetimes by the B Factories. The results of these analyses are summarized in Table 17.5.1; averages are discussed in Section 17.5.1.5.

17.5.1.3 Fully-reconstructed final states

B lifetime measurements with samples in which one B decays to an exclusive hadronic final state have the lowest background. *BABAR* measures the B^0 and B^+ lifetimes with the hadronic decays $B^0 \to D^{(*)-}\pi^+$, $D^{(*)-}\rho^+$, $D^{(*)-}a_1^+$, $J/\psi K^{*0}$ and $B^+ \to \overline{D}^{(*)0}\pi^+$, $J/\psi K^+$, $\psi(2S)K^+$ in a data sample of 20.6 fb^{-1} (Aubert, 2001c). Belle performs an analysis combining the exclusive hadronic final states $B^0 \to D^{(*)-}\pi^+$, $D^{*-}\rho^+$, $J/\psi K_S^0$, $J/\psi K^{*0}$ to measure the B^0 lifetime and the modes $B^+ \to \overline{D}^0\pi^+$, $J/\psi K^+$ to measure the B^+ lifetime in a sample of 29.1 fb^{-1} (Abe, 2002m). The decay channels $K^+\pi^-$, $K^+\pi^-\pi^0$, $K^+\pi^-\pi^+\pi^-$, and $K_S^0\pi^+\pi^-$ are used to reconstruct $\overline{D}^0$ candidates, while the modes $K^+\pi^-\pi^+$ and $K_S^0\pi^-$ are used for D^- candidates (Belle does not use the D decay modes involving a K_S^0). Charged D^{*-} candidates are formed by combining a $\overline{D}^0$ with a soft π^-.

[57] The signal purity is the fraction of signal events in the selected candidates (see also Section 4.3). It is often defined for a region of about ±2 standard deviations around the signal peak (for example, in $m_{\rm ES}$ or ΔE).

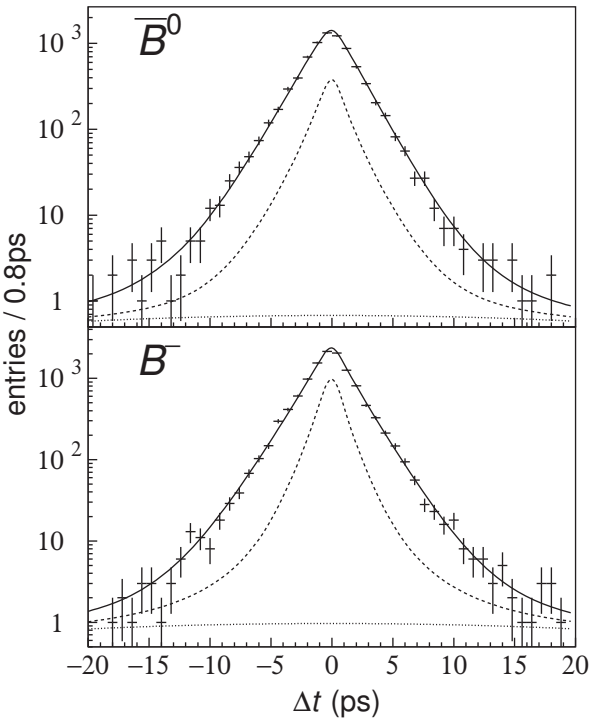

Figure 17.5.3. The Δt distributions of $\overline{B}^0$ (top) and B^- (bottom) candidates (plus *c.c.*) for fully-reconstructed B decays to hadronic final states. The dashed lines represent the sum of the background and outlier components, and the dotted lines represent the outlier component (Abe, 2002m).

The B^0 candidates are formed by combining a D^{*-} or D^- with a π^+, ρ^+ ($\rho^+ \to \pi^+\pi^0$) or a_1^+ ($a_1^+ \to \pi^+\pi^-\pi^+$). The $B^0 \to J/\psi K^{*0}$ and $B^0 \to \psi(2S)K^{*0}$ candidates are reconstructed from combinations of a J/ψ or a $\psi(2S)$ candidate, in the decay modes e^+e^- and $\mu^+\mu^-$, with a K^{*0} ($K^{*0} \to K^+\pi^-$). The $\psi(2S)$ candidates are reconstructed in their decays to $J/\psi\pi^+\pi^-$. In these measurements, the collaborations impose constraints on the B candidates requiring them to be compatible with one of the final states mentioned above. The corresponding branching fractions for the B and D decays to these final states are at most a few percent. Therefore, the selected signal samples have relatively small B^0 and B^+ yields (for example, 291 B^0 and 304 B^+ per inverse femtobarn of data for the *BABAR* analysis). Due to the tight selection criteria, a main background present in other analyses that arises from incorrect combinations of tracks is highly suppressed, leading to event samples with high signal purities of 80%–90%.

The z position of the decay vertex, $z_{\rm rec}$, of the fully-reconstructed B meson, $B_{\rm rec}$, is measured with high precision, typically of the order of $\sigma(z_{\rm rec}) \sim 50$ μm. The decay vertex position of the other B, $z_{\rm oth}$, is determined from all tracks not belonging to $B_{\rm rec}$ as described in Chapter 6. For these samples, the $z_{\rm rec}$ resolution is 100–200 μm with an RMS value of about 170 μm. Thus, the Δz resolution

Table 17.5.1. B Factory measurements of τ_{B^0}, τ_{B^+}, and τ_{B^0}/τ_{B^+} along with the journal paper, selected final state, signal purity $f_{\rm signal}$, B meson signal yield, and integrated luminosity for each measurement. The purity and yield values marked with an asterisk * are approximate.

Experiment	Method	$f_{\rm signal}$	Yield $[B/\text{fb}^{-1}]$	$\int \mathcal{L}\, dt$ $[\text{fb}^{-1}]$	
Neutral B meson lifetime τ_{B^0}:					τ_{B^0} [ps]
BABAR (Aubert, 2001c)	Excl. hadronic modes	90%	291	21	$1.546 \pm 0.032 \pm 0.022$
BABAR (Aubert, 2003e)	Incl. $D^*\pi$, $D^*\rho$	55%	603	21	$1.533 \pm 0.034 \pm 0.038$
BABAR (Aubert, 2003m)	Excl. $D^* l\nu$	76%	680	21	$1.523^{+0.024}_{-0.023} \pm 0.022$
BABAR (Aubert, 2002f)	Incl. $D^* l\nu$	53%	4430	21	$1.529 \pm 0.012 \pm 0.029$
BABAR (Aubert, 2006s)	Incl. $D^* l\nu$	64%	605	81	$1.504 \pm 0.013^{+0.018}_{-0.013}$
Belle (Abe, 2002m)	Excl. hadronic modes	82%*	220*	29	$1.554 \pm 0.030 \pm 0.019$
Belle (Abe, 2005c)	Excl. had. modes + $D^* l\nu$	81%	707	140	$1.534 \pm 0.008 \pm 0.010$
BABAR-Belle average					$1.530 \pm 0.005 \pm 0.009$
Charged B meson lifetime τ_{B^+}:					τ_{B^+} [ps]
BABAR (Aubert, 2001c)	Excl. hadronic modes	93%	304	21	$1.673 \pm 0.032 \pm 0.023$
Belle (Abe, 2002m)	Excl. hadronic modes	75%*	310*	29	$1.695 \pm 0.026 \pm 0.015$
Belle (Abe, 2005c)	Excl. hadronic modes	81%	319	140	$1.635 \pm 0.011 \pm 0.011$
BABAR-Belle average					$1.640 \pm 0.010 \pm 0.010$
τ_{B^+}/τ_{B^0}*:*					τ_{B^+}/τ_{B^0}
BABAR (Aubert, 2001c)	Excl. hadronic modes	93%, 90%	304, 291	21	$1.082 \pm 0.026 \pm 0.012$
Belle (Abe, 2002m)	Excl. hadronic modes	75%, 82%*	310, 220*	29	$1.091 \pm 0.023 \pm 0.014$
Belle (Abe, 2005c)	Excl. had. modes + $D^* l\nu$	81%, 81%	319, 707	140	$1.066 \pm 0.008 \pm 0.008$
BABAR-Belle average					$1.068 \pm 0.009 \pm 0.007$

is dominated by the resolution of $z_{\rm oth}$. It is similar for all decay modes ($\sigma(\Delta z) = 180 - 190\ \mu$m). Belle converts the measured Δz into a Δt value according to Eq. (17.5.12), whereas in fully-reconstructed decays *BABAR* uses a more precise approximation by exploiting the precise knowledge of the B flight direction to correct for the B momentum in the $\Upsilon(4S)$ frame (Eq. 6.5.5). The Δt distributions of the selected B^0 and B^+ candidates are then fit to a likelihood function that describes the true Δt distribution of the signal events (Eq. 17.5.13), convoluted with a Δt signal resolution function $\mathcal{R}_{\rm sig}$ to account for the uncertainty in the Δt measurements; and to an empirical Δt distribution describing background events. *BABAR* uses a signal Δt resolution function $\mathcal{R}_{\rm sig}$ consisting of the sum of a Gaussian distribution with zero mean and its convolution with an exponential decay that models the bias of $z_{\rm oth}$ due to tracks originating from a displaced decay vertex of a charm meson. Charged and neutral B decays are described with the same Δt resolution function. Belle's signal Δt resolution function $\mathcal{R}_{\rm sig}$ is formed by the convolution of four components: the detector resolutions for $z_{\rm rec}$ and $z_{\rm oth}$, the bias in $z_{\rm oth}$ due to tracks originating from the decay of a charm meson, and the kinematic approximation that the B mesons are at rest in the center-of-mass frame (Tajima, 2004). Both resolution functions have a term accounting for a small number of poorly reconstructed vertices, so-called Δt outliers. Both experiments describe the background Δt distribution with a prompt term (*i.e.* zero lifetime) and a term with an effective background lifetime. The background Δt resolution functions for the component with effective lifetime is of the same form as the signal resolution functions, but with separate parameters in order to minimize correlations with the signal resolution parameters. The Δt resolution function is discussed further in Chapter 10.

BABAR and Belle determine the values of τ_{B^0} and τ_{B^+} from a simultaneous fit to the samples of B^0 and B^+ candidates. *BABAR* measures $\tau_{B^0} = (1.546 \pm 0.032 \pm 0.022)$ ps and $\tau_{B^+} = (1.673 \pm 0.032 \pm 0.023)$ ps, while Belle measures $\tau_{B^0} = (1.554 \pm 0.030 \pm 0.019)$ ps and $\tau_{B^+} = (1.695 \pm 0.026 \pm 0.015)$ ps. The measurements of the B^0 and the B^+ lifetimes share the same sources of systematic uncertainty. Some of these uncertainties cancel in the ratio of the lifetimes $r_\tau \equiv \tau_{B^+}/\tau_{B^0}$. In a separate fit the parameter τ_{B^+} is replaced with $r_\tau \cdot \tau_{B^0}$ to estimate the statistical error of the lifetime ratio. *BABAR* and Belle measure, respectively, $\tau_{B^+}/\tau_{B^0} = 1.082 \pm 0.026 \pm 0.012$ and $\tau_{B^+}/\tau_{B^0} = 1.091 \pm 0.023 \pm 0.014$. The largest contribu-

tions to the systematic uncertainties in the measured lifetimes come from the modeling of the signal Δt resolution function (0.009 – 0.014 ps) and the background Δt distribution (0.005 – 0.012 ps), the alignment of the vertex detector (0.008 ps), the knowledge of the z scale of the detector (0.008 ps), and limited statistics of the MC simulation (0.007 – 0.009 ps). The dominant contributions to the systematic error in r_τ come from limited MC statistics (0.005 – 0.006), uncertainties in the background Δt distributions (0.005 – 0.011), and the signal Δt resolution function (0.006 – 0.008).

In another analysis *BABAR* uses events in which $B_{\rm rec}$ is reconstructed in the semileptonic decay $B^0 \to D^{*-} l^+ \nu$ ($l = e, \mu$) to determine the B^0 lifetime (Aubert, 2003m). The B yield is larger than for the hadronic final state analysis due to the large B semileptonic branching fraction. They reconstruct 680 $B/\,\mathrm{fb}^{-1}$. Due to the missing neutrino the background level is higher than in the sample of fully-reconstructed hadronic B decays. The combinatorial D^{*-} background is about 18% and the sum of the backgrounds from events where the D^{*-} and the lepton come from different B decays, events with a fake lepton candidate and events from continuum $c\bar{c} \to D^{*-} X$ processes add up to $5 - 8\%$ depending on the lepton flavor. In this analysis, *BABAR* simultaneously fits for τ_{B^0} and the $B^0 - \overline{B}^0$ mixing frequency Δm_d (see also Section 17.5.2). Because of the different Δt distributions for mixed ($B^0 B^0$ or $\overline{B}^0 \overline{B}^0$) and unmixed ($B^0 \overline{B}^0$) events, separately fitting the two Δt distributions enhances the sensitivity to the common signal Δt resolution function. As a result the uncertainty of τ_{B^0} is reduced by approximately 15%. *BABAR* measures the B^0 lifetime to be $\tau_{B^0} = (1.523^{+0.024}_{-0.023} \pm 0.022)$ ps. The dominant systematic error sources are the same as for the analyses of the hadronic final states and similar in size. A large additional systematic uncertainty in the τ_{B^0} measurement comes from the limited statistical precision in determining the bias due to the background modeling. By comparing the fitted τ_{B^0} in simulated events, *BABAR* observes a shift of (0.022 ± 0.009) ps between a signal-only sample and a signal-plus-background sample. The measured B^0 lifetime is corrected for the observed bias from the fit to the MC sample with background; the full statistical uncertainty in τ_{B^0} from this fit (± 0.018 ps) is assigned as systematic uncertainty.

Belle also performs a measurement of the B lifetimes and their ratio in a larger sample of $140\,\mathrm{fb}^{-1}$ (Abe, 2005c). In this analysis they reconstruct B^0 and B^+ candidates in the same hadronic decay modes as in their previous analysis. In addition they reconstruct B^0 candidates in the semileptonic decay $B^0 \to D^{*-} l^+ \nu$. Using a fit to the Δt distributions of the signal candidates, they determine the B^0 and B^+ lifetimes and the $B^0 - \overline{B}^0$ mixing frequency Δm_d simultaneously. The analysis of the neutral B decays is described in more detail in Section 17.5.2. Belle measures $\tau_{B^0} = (1.534 \pm 0.008 \pm 0.010)$ ps, $\tau_{B^+} = (1.635 \pm 0.011 \pm 0.011)$ ps and $\tau_{B^+}/\tau_{B^0} = 1.066 \pm 0.008 \pm 0.008$. The largest contributions to the systematic uncertainties in the measured lifetimes come from uncertainties in the vertex reconstruction (0.005 – 0.007 ps) and the modeling of the background (0.007 ps). The dominant contributions to the systematic error in r_τ come from uncertainties in the background Δt distributions (0.005) and the signal Δt resolution function (0.004).

17.5.1.4 Partially-reconstructed final states

BABAR also measures the B^0 meson lifetime in a sample of $21\,\mathrm{fb}^{-1}$ using the decay modes $B^0 \to D^{*-} l^+ \nu$ (Aubert, 2002f) and $B^0 \to D^{*-} \pi^+$, $B^0 \to D^{*-} \rho^+$ (Aubert, 2003e) with a partially-reconstructed D^{*-} in the final state. These measurements also serve as a proof-of-principle for the analyses of the time-dependent CP asymmetries in $B \to D^{(*)\mp} \pi^\pm$ to extract $\sin(2\phi_1 + \phi_3)$ (see Section 17.8.5).

In the measurement of τ_{B^0} with $B^0 \to D^{*-} l^+ \nu$ decays, *BABAR* requires a high-momentum lepton ($1.4 < p^*_l < 2.3\,\mathrm{GeV}/c$) and an opposite-charge soft pion (π_s) consistent with coming from the decay $D^{*-} \to \overline{D}^0 \pi^-_s$ ($p^*_{\pi_s} < 0.19\,\mathrm{GeV}/c$). The D^{*-} momentum is inferred from the π_s momentum without reconstructing the $\overline{D}^0$ (see Eq. 7.3.6). The analysis of this inclusive final state does not suffer from the small $\overline{D}^0$ branching fractions to exclusive final states and consequently has a large B yield (4430 $B/\,\mathrm{fb}^{-1}$). However, without the additional constraints from the $\overline{D}^0$ reconstruction the signal purity of the selected B candidates is only 53%. The $B_{\rm rec}$ decay vertex is calculated from the lepton and π_s tracks, and the beam spot. The decay point of the $B_{\rm oth}$ is determined from the remaining tracks in the event. In events that have another high-momentum lepton ($p^*_l > 1.1$ GeV/c), the B vertex is calculated from this lepton track constrained to the beam spot in the transverse plane. Otherwise, all tracks with a center-of-mass angle greater than 90° with respect to the π_s direction are considered. This requirement removes most of the tracks from the decay of the $\overline{D}^0$ daughter of the D^{*-}, which would otherwise bias the reconstruction of the $B_{\rm oth}$ vertex position. Tracks are also removed if they contribute more than 6 to the vertex χ^2. *BABAR* measures the B^0 lifetime with a binned maximum likelihood fit to the Δt and $\sigma_{\Delta t}$ distributions of the selected B candidates to be $\tau_{B^0} = (1.529 \pm 0.012 \pm 0.029)$ ps. For this result, the fitted B^0 lifetime is multiplied by a correction factor $\mathcal{R}_{\overline{D}^0} = 1.032 \pm 0.007 \pm 0.007$ to account for daughter tracks of the $\overline{D}^0$ included in the calculation of the $B_{\rm oth}$ decay vertex. The largest systematic uncertainties in τ_{B^0} are due to the knowledge of the fractions and parameterizations of the background types (0.015 ps), the Δt resolution model (0.017 ps) and $\mathcal{R}_{\overline{D}^0}$ (0.015 ps).

In a more recent analysis with $81\,\mathrm{fb}^{-1}$, *BABAR* uses $B^0 \to D^{*-} l^+ \nu$ decays with a partially-reconstructed D^{*-} to measure τ_{B^0} and the $B^0 - \overline{B}^0$ oscillation frequency Δm_d (Aubert, 2006s). They require the other B^0 in the event $B_{\rm oth}$ also to decay semileptonically and determine its decay vertex by constraining the high-energy lepton to the beam spot. After correcting for a small bias (-0.006 ps) observed in MC-simulated events they measure $\tau_{B^0} = (1.504 \pm 0.013^{+0.018}_{-0.013})$ ps. The dominant contributions to

the systematic error in τ_{B^0} come from uncertainties in the alignment ($^{+0.013}_{-0.004}$ ps) and z scale (0.007 ps) of the SVT, and from MC statistics (0.007 ps).

BABAR also measures the B^0 lifetime with a partially-reconstructed D^{*-} in the decays $B^0 \to D^{*-}h^+$, where h^+ is either a π^+ or a ρ^+ (Aubert, 2003e). Similarly to the partial reconstruction of the semi-leptonic final state, they reconstruct only the soft pion π_s from the decay $D^{*-} \to \overline{D}^0\pi_s^-$ and the D^{*-} momentum is inferred from the π_s momentum. The main variable to suppress background in this analysis is the missing $\overline{D}^0$ mass $m_{\rm miss}$, which peaks at the nominal D^0 mass with a spread of 3 MeV/c^2 for $B^0 \to D^{*-}\pi^+$ and 3.5 MeV/c^2 for $B^0 \to D^{*-}\rho^+$. Additional variables to suppress backgrounds include the angle between h and the B^0, the D^{*-} and ρ^+ helicity angles, and event shape variables. After all selection requirements are applied, the signal purity is approximately 55%. The dominant background comes from continuum events. The remaining background from $B\overline{B}$ events is due to random h and π_s combinations and feed-down from $B \to D^{**}\pi$, $B^0 \to D^{*-}\rho^+$ (for $B^0 \to D^{*-}\pi^+$), and $B^0 \to D^{*-}a_1^+$ (for $B^0 \to D^{*-}\rho^+$). The z position of the B^0 decay vertex is determined from the h and π_s tracks constrained to the nominal beam spot. The decay vertex of $B_{\rm oth}$ is determined in the same way as in *BABAR*'s early analysis of $B^0 \to D^{*-}l^+\nu$ (Aubert, 2002f). For the mode $B^0 \to D^{*-}\pi^+$ they calculate an event-by-event Δz correction to account for tracks from the $\overline{D}^0$ included in the vertex of $B_{\rm oth}$. In both modes a small additional correction to the fitted B^0 lifetime is applied. *BABAR* uses several data control samples to determine the different background fractions in the signal sample and their *p.d.f.* parameters. These parameters are fixed in the fit to the signal sample. The fitted lifetimes are $\tau_{B^0} = (1.510 \pm 0.040 \pm 0.041)$ ps in $B^0 \to D^{*-}\pi^+$ and $\tau_{B^0} = (1.616 \pm 0.064 \pm 0.075)$ ps in $B^0 \to D^{*-}\rho^+$. The combined result accounting for correlated errors is $\tau_{B^0} = (1.533 \pm 0.034 \pm 0.038)$ ps. The dominant uncertainties in the measurements with the modes $B^0 \to D^{*-}\pi^+$ and $B^0 \to D^{*-}\rho^+$ come from the knowledge of the composition of the background and its *p.d.f.* parameters (0.024 ps, 0.050 ps), limited MC statistics (0.021 ps, 0.042 ps), and the $\overline{D}^0$ track bias (0.017 ps, 0.026 ps).

17.5.1.5 Averages of τ_{B^0}, τ_{B^+} and τ_{B^+}/τ_{B^0}

The world averages of the B^0 and B^+ lifetimes and their ratio are calculated by HFAG from the *BABAR* measurements in Aubert (2001c, 2002f, 2003e,m, 2006s), the Belle measurements in Abe (2005c) and measurements from CDF, DØ, ALEPH, DELPHI, L3, OPAL, SLD and ATLAS (Beringer et al., 2012) to be, respectively, $\tau_{B^0} = (1.519 \pm 0.007)$ ps, $\tau_{B^+} = (1.641 \pm 0.008)$ ps and $\tau_{B^+}/\tau_{B^0} = (1.079 \pm 0.007)$ ps. The most precise measurements contributing to these averages come from the B Factories and a recent set of measurements from CDF using fully-reconstructed $B \to J/\psi K^{(*)}$ events (Aaltonen et al., 2011a). DØ provides a precise measurement of τ_{B^+}/τ_{B^0} from samples of $B \to D^{*+}\mu\overline{\nu}X$ and $B \to D^0\mu\overline{\nu}X$ (Abazov et al., 2005). By using only the B Factories measurements, one obtains the averages $\tau_{B^0} = (1.530 \pm 0.010)$ ps, $\tau_{B^+} = (1.640 \pm 0.014)$ ps and $\tau_{B^+}/\tau_{B^0} = (1.068 \pm 0.011)$ ps.

The measurements of the charged and neutral B lifetimes and their ratio now have errors of about half a percent, and the B^+ lifetime is now measured to be larger than the B^0 lifetime by many standard deviations. The precision in these measurements exceeds that of existing theoretical calculations. Thus, with the original motivations fully addressed by the current set of measurements and the multitude of relevant systematic error sources that come with sub-percent precision measurements, it is unlikely that there will be improved measurements using the full data set of the B Factories or the even larger data sets of future super flavor factories.

17.5.2 $B^0 - \overline{B}^0$ mixing

Neutral meson-antimeson oscillations were predicted by Gell-Mann and Pais (1955) and first observed in 1956 in the $K^0 - \overline{K}^0$ system (Lande, Booth, Impeduglia, Lederman, and Chinowsky, 1956). Mixing in the $B^0 - \overline{B}^0$ system was discovered in 1987 by the ARGUS collaboration (Albrecht et al., 1987b). It was clear from the first B_s^0 measurements that mixing was an important effect in the $B_s^0 - \overline{B}_s^0$ system (see for example the review of Danilov, 1993), although the mixing frequency was not resolved until much later by the CDF collaboration (Abulencia et al., 2006b) as previous results established only lower limits on $x_s = \Delta m_s/\Gamma_s$. Finally, $D^0 - \overline{D}^0$ mixing was first observed by the B Factories and is described in detail in Section 19.2.

Meson-antimeson oscillations proceed in general through both long distance effects (common decay modes) and second order weak interactions as described by box diagrams containing virtual quarks (Figure 10.1.1). $B^0 - \overline{B}^0$ mixing is predominantly a short-distance phenomenon; among the various box diagrams, those containing the top quark dominate due to the large top mass. The observation of mixing, in fact, provided the first indication that the top quark was very heavy: see the discussion in Section 16.1. The mixing frequency Δm_d is sensitive to the CKM matrix element V_{td} (see Section 17.2). In the neutral K, D (see Section 19.2), and B_s^0 meson systems, mixing also has contributions from real intermediate states accessible to both the meson and the antimeson. Real intermediate states lead to a difference in the decay rate for the two mass eigenstates of the neutral meson system. However, for the B_d^0 system, the decay rate difference $\Delta\Gamma$ is expected to be of $O(10^{-2} - 10^{-3})$ times smaller than the average decay rate and the mixing frequency (Lenz and Nierste, 2011), and is typically ignored in the measurements of Δm_d.

In the following, we briefly review the principles of Δm_d measurements (Section 17.5.2.1), and then summarize the techniques and results of the B Factory measurements using dilepton (Section 17.5.2.2), partially-reconstructed (Section 17.5.2.3), and fully-reconstructed

final states (Section 17.5.2.4). The average of these results is discussed in Section 17.5.2.5. Throughout, we set $\Delta\Gamma = 0$; the specialized analyses allowing $\Delta\Gamma \neq 0$, and setting constraints on its value, are discussed in Section 17.5.2.6 below.

17.5.2.1 Principles of Δm_d measurements

The time-evolution of the $B^0 - \overline{B}^0$ system is given by a phenomenology-based 2×2 Hamiltonian matrix (for details see Chapter 10). Solving this system of equations gives the time-dependent probabilities for $B^0 - \overline{B}^0$ oscillations. For a $\overline{B}^0$ decay to a flavor eigenstate that is not accessible from a B^0 decay (*e.g.* the semileptonic decay $\overline{B}^0 \to D^{*+} l^- \nu_l$), the parameter λ in Eqs (10.1.10–10.1.15) and (10.2.2–10.2.5) is zero. Neglecting *CP* violation in mixing, the probability that a B^0 produced at time $t = 0$ decays as $\overline{B}^0$ at time t is given by

$$P_{B^0 \to \overline{B}^0}(t) = \frac{e^{-t/\tau_{B^0}}}{2\tau_{B^0}} \times [1 - \cos(\Delta m_d t)], \qquad (17.5.14)$$

where Δm_d is the $B^0 - \overline{B}^0$ oscillation frequency and τ_{B^0} is the neutral B lifetime. Similarly, the probability that a produced B^0 decays as B^0 (for example through $B^0 \to D^{*-} l^+ \overline{\nu}_l$) is given by

$$P_{B^0 \to B^0}(t) = \frac{e^{-t/\tau_{B^0}}}{2\tau_{B^0}} \times [1 + \cos(\Delta m_d t)]. \qquad (17.5.15)$$

Likewise the probabilities for a produced $\overline{B}^0$ to decay as a B^0 or a $\overline{B}^0$ are given, respectively, by

$$P_{\overline{B}^0 \to B^0}(t) = \frac{e^{-t/\tau_{B^0}}}{2\tau_{B^0}} \times [1 - \cos(\Delta m_d t)], \qquad (17.5.16)$$

and

$$P_{\overline{B}^0 \to \overline{B}^0}(t) = \frac{e^{-t/\tau_{B^0}}}{2\tau_{B^0}} \times [1 + \cos(\Delta m_d t)]. \qquad (17.5.17)$$

The first measurements of $B^0 - \overline{B}^0$ oscillations were time-integrated measurements by ARGUS (Albrecht et al., 1987b) and CLEO (Artuso et al., 1989). They measured the time-integrated probability χ_d that a B^0 ($\overline{B}^0$) produced in $\Upsilon(4S) \to B^0\overline{B}^0$ decays as a $\overline{B}^0$ (B^0),

$$\chi_d = \frac{x_d^2}{2\,(1 + x_d^2)}, \qquad (17.5.18)$$

where $x_d = \Delta m_d / \Gamma_d = \Delta m_d \tau_{B^0}$. In 1993 the LEP experiments started to provide the first time-dependent measurements of Δm_d, made possible through their precision vertex detectors and highly-boosted B^0 mesons from Z^0 decays (Abreu et al., 1994; Acciarri et al., 1996; Akers et al., 1994b; Buskulic et al., 1993b). The CDF collaboration published their first Δm_d measurement in 1998 (Abe et al., 1998). In the 2000 Review of Particle Physics (Groom et al., 2000) the PDG calculated an average $B^0 - \overline{B}^0$ oscillation frequency from time-dependent measurements by the LEP experiments and CDF of $\Delta m_d = (0.478 \pm 0.018)$ ps^{-1}. Including the measurements of the time-integrated mixing probability $\chi_d = 0.156 \pm 0.024$ by CLEO and ARGUS, they obtained $\Delta m_d = (0.472 \pm 0.017)$ ps^{-1}.

The experimental strengths and weaknesses in Δm_d measurements, when comparing these older experiments to the B Factories, are the same as for measurements of the B lifetimes. The former benefit from high-precision proper-time measurements, whereas the latter have the advantage of low-background, high-statistics B samples, and excellent B-momentum resolution.

The experimental methods of the Δm_d analyses are very similar to those used in the measurement of time-dependent *CP* asymmetries in B decays to *CP* eigenstates (see the measurement of $\sin 2\phi_1$ in Section 17.6). In particular, fully-reconstructed B decays to flavor final states $B_{\rm flav}$, such as $\overline{B}^0 \to D^{(*)+}\pi^-$, have the same B vertex resolutions and thus Δt resolution function as B decays to $(c\overline{c})s$ *CP* eigenstates, B_{CP} (see Chapter 6 and Section 17.6). The same B flavor-tagging algorithms are used to determine the flavors of $B_{\rm flav}$ and B_{CP} at the time of their production (see Chapter 8). In both cases, maximum likelihood fits are used to extract the parameters of the time-dependent asymmetries from the measured Δt distributions. By-products of the Δm_d measurement with fully-reconstructed final states are the B flavor-tagging mistag rates, which cannot be determined with *CP* eigenstates. In addition, a confirmation of the Δm_d results of previous experiments served as a convincing proof-of-principle of this novel technique for measuring time-dependent *CP* asymmetries at the asymmetric beam-energy B Factories. So, it is no coincidence that one of the first measurements from the B Factories was the precise time-dependent measurement of Δm_d. On the other hand, improving the knowledge of Δm_d has been and still is interesting in its own right. The oscillation frequency Δm_d is proportional to $|V_{td}|^2$ (Eq. 17.2.1). Thus, a precise Δm_d measurement along with a measurement of the $B_s^0 - \overline{B}_s^0$ oscillation frequency Δm_s from hadron colliders, combined with lattice QCD calculations of the decay constants and QCD bag parameters of B^0 and B_s^0 mesons (for details see Section 17.2) provide strong constraints on the Unitarity Triangle (see Section 25.1).

The time-dependent Δm_d measurements by the B Factories all follow the same basic idea. In the $\Upsilon(4S) \to B^0\overline{B}^0$ decay the two neutral B mesons are produced in a coherent P-wave state. If one of the B mesons, referred to as $B_{\rm tag}$, can be ascertained to decay to a state of known flavor (*i.e.* B^0 or $\overline{B}^0$) at a certain time $t_{\rm tag}$, the other B, referred to as $B_{\rm rec}$, at that time must be of the opposite flavor as a consequence of Bose symmetry. Consequently, the probabilities to observe *unmixed* (+) $B^0\overline{B}^0$, or *mixed* (−) $B^0B^0/\overline{B}^0\overline{B}^0$ events, are functions of the proper-time difference $\Delta t = t_{\rm rec} - t_{\rm tag}$ and of Δm_d:

$$\begin{aligned} P_{B^0\overline{B}^0 \to B^0\overline{B}^0}(\Delta t) &\equiv P_+(\Delta t) \\ &= \frac{e^{-|\Delta t|/\tau_{B^0}}}{4\tau_{B^0}} \times [1 + \cos(\Delta m_d \Delta t)]\,, \end{aligned}$$

$$P_{B^0\overline{B}^0\to B^0B^0/\overline{B}^0\overline{B}^0}(\Delta t) \equiv P_-(\Delta t) = \frac{e^{-|\Delta t|/\tau_{B^0}}}{4\tau_{B^0}} \times [1-\cos(\Delta m_d \Delta t)]\,. \tag{17.5.19}$$

From these two equations one can define the so-called $B^0\overline{B}^0$ mixing asymmetry as

$$A_{\rm mix}(\Delta t) \equiv \frac{P_+(\Delta t) - P_-(\Delta t)}{P_+(\Delta t) + P_-(\Delta t)} = \cos(\Delta m_d \Delta t). \tag{17.5.20}$$

The functions $P_\pm(\Delta t)$ are illustrated in Fig. 17.5.4. The mixed event function (P_-) rises slowly from zero at $\Delta t = 0$ until it reaches a maximum at around $\Delta t = 2.6$ ps.

The B Factories have measured the $B^0 - \overline{B}^0$ oscillation frequency with various final states and B-reconstruction techniques. In the analyses of dilepton inclusive final states, the flavors of both B mesons are identified only through high-momentum leptons from semileptonic decays. In all other Δm_d measurements one B is reconstructed through its decay to an exclusive flavor final state, $B_{\rm rec}$, while the remaining charged particles in the event are used to identify (or "tag") the flavor of the other B (referred to as $B_{\rm tag}$), as a B^0 or $\overline{B}^0$. The proper-time difference $\Delta t = \Delta z / \langle\beta\gamma\rangle c$ is determined from the z positions of the B decay vertices $\Delta z = z_{\rm rec} - z_{\rm tag}$ and the average boost of the $\Upsilon(4S)$ frame in the lab frame $\langle\beta\gamma\rangle$. The boost is known to good precision from the e^+ and e^- beam energies, so that the Δz measurement dominates the Δt resolution (see Chapter 6). The value of Δm_d is then extracted from a simultaneous fit to the Δt distributions of the unmixed and mixed events. There are two principal experimental complications to the probability distributions in Eq. (17.5.19). First, the flavor tagging algorithm sometimes incorrectly identifies the $B_{\rm tag}$ flavor. The probability to incorrectly identify the flavor of $B_{\rm tag}$, w, reduces the observed amplitude for the oscillation by a factor $(1-2w)$. Second, the resolution of Δt is comparable to the oscillation period and must be accounted for. The *p.d.f.*s for the unmixed and mixed signal events $\mathcal{H}_{\pm,{\rm sig}}$ can be expressed as the convolution of the underlying Δt distribution,

$$h_{\pm,{\rm sig}}(\Delta t; \Delta m_d, w) = \frac{e^{-|\Delta t|/\tau_{B^0}}}{4\tau_{B^0}} [1 \pm (1-2w)\cos(\Delta m_d \Delta t)]\,, \tag{17.5.21}$$

with a signal Δt resolution function $\mathcal{R}_{\rm sig}$ containing parameters $\hat{a}_j$:

$$\mathcal{H}_{\pm,{\rm sig}}(\Delta t; \Delta m_d, w, \hat{a}_j) = h_{\pm,{\rm sig}}(\Delta t; \Delta m_d, w) \otimes \mathcal{R}_{\rm sig}(\Delta t; \hat{a}_j). \tag{17.5.22}$$

The functions $\mathcal{H}_{\pm,{\rm sig}}$ are shown in Fig. 17.5.4. The impact of typical mistag and Δt resolution effects is clearly visible in the comparison with the functions $P_\pm(\Delta t)$ that represent ideal detector performance.

A fit is then performed to simultaneously extract the mistag rates w, the resolution function parameters $\hat{a}_j$, and the mixing frequency Δm_d. In the following sections we give brief descriptions of the various Δm_d measurements by the B Factories, in dilepton (Section 17.5.2.2), partially-reconstructed (17.5.2.3), and fully-reconstructed (17.5.2.4) final states. The results are summarized in Table 17.5.2; their average is discussed in Section 17.5.2.5.

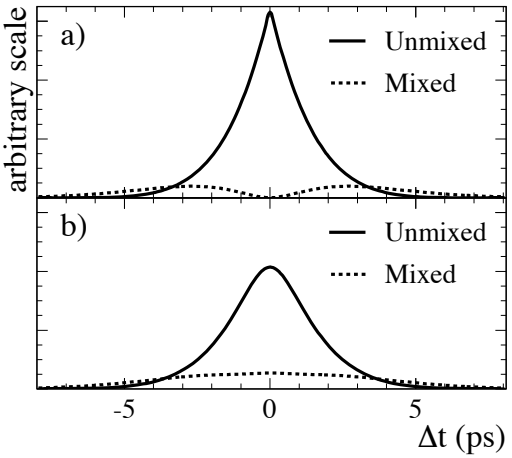

Figure 17.5.4. The Δt distributions of mixed and unmixed events (a) with perfect tagging and Δt resolution ($P_\pm(\Delta t)$) (b) with mistag rates and Δt resolution typical at the B Factories ($\mathcal{H}_{\pm,{\rm sig}}(\Delta t)$). From Aubert (2002a).

17.5.2.2 Dilepton final states

Belle published their first measurement of Δm_d using dilepton events in a sample of $5.9\,{\rm fb}^{-1}$ (Abe, 2001b). In a later analysis of the same final state, they used a sample of $29\,{\rm fb}^{-1}$ (Hastings, 2003). *BABAR* published one measurement of Δm_d with dilepton events using a sample of $21\,{\rm fb}^{-1}$ (Aubert, 2002e).

The inclusive nature of the dilepton final state provides large event samples. The measurements are based on the identification of events containing pairs of high-momentum leptons (ee, $\mu\mu$ and $e\mu$) from semileptonic decays of B mesons. The flavors of the B mesons at the time of their decay are determined by the charges of the leptons in the final state. For $\Upsilon(4S)$ resonance decays into $B^0\overline{B}^0$ pairs, opposite-sign charge (OS) and same-sign charge (SS) lepton pairs correspond to unmixed and mixed events, respectively. Both experiments apply selection requirements on the lepton momenta, overall event shape, and track quality to ensure a well-measured Δt and to suppress backgrounds from fake leptons, continuum events, J/ψ decays, and so-called B cascade decays. In the latter, one lepton originates from the semileptonic decay of a charm meson, which can come from the same or the opposite B as the other lepton. An irreducible background comes from semileptonic decays of B^+B^- pairs.

Belle determines the z coordinates of the B decay vertices from the intersections of the lepton tracks with the profile of the beam interaction point (IP) convoluted with the average B^0 flight length ($\sim 20\,\mu$m in the $\Upsilon(4S)$ rest frame). The mean position and width of the IP are determined on a run-by-run basis using hadronic events (see Chapter 6). The proper-time difference Δt is calculated from the z positions of the two lepton vertices using Eq. (17.5.12), where $\Delta z = z_1 - z_2$ is the distance along the beam axis between the two vertices. For OS events, the

Table 17.5.2. B Factory measurements of Δm_d along with the journal paper, selected final state, signal purity $f_{\rm signal}$, B meson signal yield, and integrated luminosity for each measurement. The Δm_d measurements in Hara (2002) and Tomura (2002b) have been superseded by Abe (2005c), and those in Abe (2001b) by Hastings (2003); the superseded measurements are not separately included in the B Factories average (Asner et al., 2010).

Experiment	Method	$f_{\rm signal}$	Yield $[B/\,{\rm fb}^{-1}]$	$\int \mathcal{L}\,dt$	Δm_d $[{\rm ps}^{-1}]$
BABAR (Aubert, 2002a,b)	Excl. hadronic modes	86%	214	30 fb^{-1}	$0.516 \pm 0.016 \pm 0.010$
BABAR (Aubert, 2002e)	Incl. dilepton			21 fb^{-1}	$0.493 \pm 0.012 \pm 0.009$
BABAR (Aubert, 2006s)	$D^* l\nu$ (partial)	64%	605	81 fb^{-1}	$0.511 \pm 0.007 \pm 0.007$
BABAR (Aubert, 2003m)	Excl. $D^* l\nu$	76%	680	21 fb^{-1}	$0.492 \pm 0.018 \pm 0.014$
Belle (Abe, 2001b)	Incl. dilepton			6 fb^{-1}	$0.463 \pm 0.008 \pm 0.016$
Belle (Hastings, 2003)	Incl. dilepton			29 fb^{-1}	$0.503 \pm 0.008 \pm 0.010$
Belle (Zheng, 2003)	$D^*\pi$ (partial)	70%	118	29 fb^{-1}	$0.509 \pm 0.017 \pm 0.020$
Belle (Hara, 2002)	Excl. $D^* l\nu$	80%	453	29 fb^{-1}	$0.494 \pm 0.012 \pm 0.015$
Belle (Tomura, 2002b)	Excl. hadronic modes	80%	229	29 fb^{-1}	$0.528 \pm 0.017 \pm 0.011$
Belle (Abe, 2005c)	Excl. hadronic modes, $D^* l\nu$	81%	707	140 fb^{-1}	$0.511 \pm 0.005 \pm 0.006$
BABAR-Belle average					$0.508 \pm 0.003 \pm 0.003$

positively charged lepton is taken as the first lepton (z_1). For SS events Belle uses the absolute value of Δz. *BABAR* applies a beam spot constraint to the two lepton tracks to find the primary vertex of the event in the transverse plane. The positions of closest approach of the two tracks to this vertex in the transverse plane are computed and their z coordinates are denoted z_1 and z_2, where the subscripts refer to the highest and second highest momentum leptons in the $\Upsilon(4S)$ rest frame. The vertex fit constrains the lepton tracks to originate from the same point in the transverse plane, thereby neglecting the nonzero transverse flight length for B^0 mesons. As a consequence, the Δt resolution function is Δz dependent, becoming worse at higher $|\Delta z|$. Neglecting this dependence introduces a small bias that *BABAR* accounts for in the systematic uncertainty.

BABAR and Belle use binned maximum likelihood fits to the Δt and Δz distributions, respectively, of the selected dilepton candidates to extract Δm_d. *BABAR* fits the shapes of the Δt distributions with the *p.d.f.*s for OS and SS dilepton events as given in Eq. (17.5.22). Belle fits the Δz distributions and constrains the integrated mixing probability to χ_d. Their Δz distributions are described by converting the constrained signal Δt distributions $\mathcal{P}_\pm(\Delta t)$ to Δz distributions using Eq. (17.5.12) and convolving them with the Δz resolution function. The constrained signal Δt distributions are given by

$$\mathcal{P}_\pm(\Delta t) = N_{\Upsilon(4S)} f_0 b_0^2 \epsilon_{ll}^\pm \frac{e^{-|\Delta t|/\tau_{B^0}}}{4\tau_{B^0}} \left[1 \pm \cos(\Delta m_d \Delta t)\right],$$
$$\mathcal{P}_{\rm ch}(\Delta t) = N_{\Upsilon(4S)} f_{\rm ch} b_{\rm ch}^2 \epsilon_{ll}^{\rm ch} \frac{e^{-|\Delta t|/\tau_{B^+}}}{2\tau_{B^+}}, \qquad (17.5.23)$$

where $N_{\Upsilon(4S)}$ is the total number of $\Upsilon(4S)$ events, f_0 and $f_{\rm ch}$ are the branching fractions of the $\Upsilon(4S)$ to neutral and charged B pairs (assuming $f_0 + f_{\rm ch} = 1$), b_0 and $b_{\rm ch}$ are the semileptonic branching fractions for neutral and charged B mesons, and $\epsilon_{ll}^\pm$ are the efficiencies for selecting dilepton events of unmixed and mixed origins. Belle determines the ratio $\epsilon_{ll}^+ : \epsilon_{ll}^-$ from MC simulation and fixes it in the fit to the data assuming detector effects that are not simulated correctly equally affect events with these origins. The Δz distributions are obtained for these distributions by conversion from Δt and convolution with the Δz resolution function.

BABAR describes the Δt resolution function for dilepton events as the sum of three Gaussian distributions. The resolution function parameters are free parameters in the fit. Belle determines the signal Δz resolution function from J/ψ decays in data. For these decays the true Δz is equal to zero and the measured Δz distribution, after the contributions of backgrounds are subtracted, yields the Δz resolution function. A comparison between data and MC simulation shows that after convolving the MC Δz distribution of J/ψ decays with a Gaussian of width $\sigma = (50 \pm 18)\,\mu$m, the MC distribution agrees with data.

The Δt and Δz distributions of background events are determined from MC-simulated events and data control samples. The large background from semileptonic B^+B^- events has the same resolution function as the signal events. The numbers of selected OS and SS dilepton pairs along with the corresponding mixing asymmetry as a function of Δt from the *BABAR* analysis are shown in Fig. 17.5.5. Due to the small mixing frequency, OS signal events are much more abundant than SS events. Most of the background events are also OS (for example from B^+B^- events). Therefore, even a small mistag probability will blur the characteristic features of the SS Δt distribution. This is particularly evident at $\Delta t = 0$ where the OS $\mathcal{P}_+$ distribution has its maximum and the SS Δt distribution $\mathcal{P}_-$ is zero: the measured Δt distribution of selected SS events does not have a dip at zero. However, the mixing asymmetry

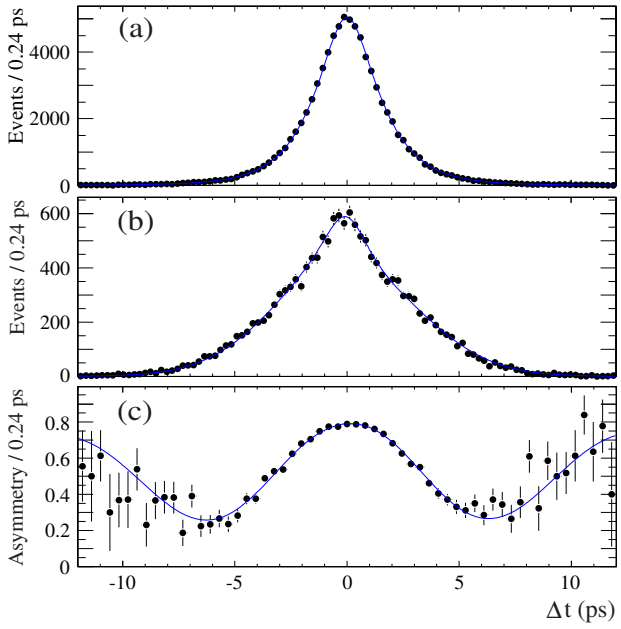

Figure 17.5.5. The Δt distributions for (a) opposite-sign and (b) same-sign charge dilepton events; (c) mixing asymmetry between opposite-sign and same-sign dilepton events. The points are the data and lines correspond to the projection of the likelihood fit (Aubert, 2002e).

still shows the expected cosine shape as mis-tagging and non-oscillating backgrounds, respectively, only reduce the amplitude and shift the baseline of the asymmetry curve.

From dilepton events *BABAR* measures $\Delta m_d = (0.493 \pm 0.012 \pm 0.009)\,\text{ps}^{-1}$ in a sample of $21\,\text{fb}^{-1}$ (Aubert, 2002e) while Belle measures $\Delta m_d = (0.503 \pm 0.008 \pm 0.010)\,\text{ps}^{-1}$ in a sample of $29\,\text{fb}^{-1}$ (Hastings, 2003), where the first errors are statistical and the second are systematic. The largest contributions to the systematic errors come from the uncertainties in the B^0 and B^+ lifetimes ($\sim 0.006\,\text{ps}^{-1}$) and in the Δz and Δt resolution functions ($\sim 0.006\,\text{ps}^{-1}$).

17.5.2.3 Partially-reconstructed final states

BABAR measures Δm_d with a sample of partially-reconstructed $\overline{B}^0 \to D^{*+} l^- \overline{\nu}_l$ events in $81\,\text{fb}^{-1}$ (Aubert, 2006s). They select $\overline{B}^0 \to D^{*+} l^- \overline{\nu}_l$ ($l = e$ or μ) events with partial reconstruction of the decay $D^{*+} \to D^0 \pi_s^+$, using only the charged lepton from the neutral B decay (l_{rec}) and the soft pion (π_s^+) from the D^{*+} decay. This decay mode has a large selection efficiency since the D^0 decay is not reconstructed and the branching fraction of $\overline{B}^0 \to D^{*+} l^- \overline{\nu}_l$ is about half of the semileptonic branching ratio of the $\overline{B}^0$. The other B in the event is identified through a second high-momentum lepton (l_{tag}).

Events are required to have at least four charged tracks. The normalized second Fox-Wolfram moment R_2 (see Chapter 9) must be less than 0.5 to reduce background from light quark production in continuum events. The lepton from the B decay must have a momentum in the range 1.3–2.4 GeV/c, and the soft pion momentum must be between 60 and 200 MeV/c. By approximating the D^{*+} momentum from the π_s^+ momentum, they calculate the square of the missing neutrino mass $(m^{\nu}_{\text{miss}})^2$. The $(m^{\nu}_{\text{miss}})^2$ distribution peaks at zero for signal events, while it is spread over a wide range of mostly negative values for background events.

BABAR determines the B_{rec} decay vertex from a vertex fit of the l_{rec} and π_s tracks, constrained to the beam spot position in the transverse plane, but accounting for the average $\overline{B}^0$ flight distance. The decay point of B_{tag} is determined from l_{tag} and the beam spot following a procedure similar to that of the B_{rec} decay vertex. The flavor of B_{rec} is determined from the l_{rec} and soft pion charges. The flavor of the other B in the event is determined from the charge of l_{tag}.

After all selection criteria *BABAR* finds 49,000 signal events over a background of 28,000 events in the region $(m^{\nu}_{\text{miss}})^2 > -2.5\,\text{GeV}^2/c^4$. Background studies are done with events in the region $(m^{\nu}_{\text{miss}})^2 < -2.5\,\text{GeV}^2/c^4$ if no signal candidate is found in the event.

BABAR simultaneously fits the distributions of $(m^{\nu}_{\text{miss}})^2$, Δt, and its uncertainty $\sigma_{\Delta t}$, for mixed and unmixed events, with a binned maximum-likelihood method. Probabilities for a given event to belong to any of the identified background sources ($e^+e^- \to q\overline{q}$ continuum, $B\overline{B}$ combinatorial, and B^+ peaking background) are calculated based on the background $(m^{\nu}_{\text{miss}})^2$ distributions. Signal is considered to be any combination of a lepton and a charged D^{*+} produced in the decay of a single $\overline{B}^0$ meson. They further divide their signal events according to the origin of the tag lepton into primary, cascade, and decay-side lepton tags. A primary lepton tag is produced in the direct decay $B^0 \to X l^+ \overline{\nu}_l$, a cascade lepton tag is produced in the process $B^0 \to \overline{D} X$, $\overline{D} \to l^- Y$, and a decay-side tag is produced by the semi-leptonic decay of the unreconstructed D^0. The relative normalization between mixed and unmixed signal events is constrained based on the time-integrated mixing rate χ_d. The Δt signal *p.d.f.* for both unmixed and mixed events consists of the sum of *p.d.f.*s for primary, cascade, and decay-side tags each convoluted with its own resolution function. They use the standard three Gaussian resolution function with event-by-event Δt uncertainties.

From the fit *BABAR* obtains $\tau_{B^0} = (1.504 \pm 0.013^{+0.018}_{-0.013})\,\text{ps}$ and $\Delta m_d = (0.511 \pm 0.007^{+0.007}_{-0.006})\,\text{ps}^{-1}$, where the first errors are statistical and the second are systematic. The statistical correlation between τ_{B^0} and Δm_d is 0.7%. The results include corrections of $-0.006\,\text{ps}$ on τ_{B^0} and $+0.007\,\text{ps}^{-1}$ on Δm_d due to biases from event selection, boost approximation, B^- peaking background, and combinatorial $B\overline{B}$ background based on MC studies. The systematic error in Δm_d is dominated by uncertainties in the SVT alignment ($^{+0.0038}_{-0.0033}\,\text{ps}^{-1}$), the selected range of Δt and $\sigma_{\Delta t}$ ($0.0033\,\text{ps}^{-1}$), and analysis bias ($0.0035\,\text{ps}^{-1}$), whereas the largest systematic error sources in the τ_{B^0} measurement are the SVT alignment

($^{+0.0132}_{-0.0038}$ ps), the z scale of the detector (0.0070 ps), and analysis bias (0.0070 ps).

Belle measures Δm_d with a sample of partially-reconstructed $\overline{B}^0 \to D^{*+}\pi^-$ events in 29.1 fb^{-1} (Zheng, 2003). They select $\overline{B}^0 \to D^{*+}\pi_h^-$ events with partial reconstruction of the decay $D^{*+} \to D^0\pi_s^+$, using only the hard pion (π_h^-) from the $\overline{B}^0$ decay and the soft pion (π_s^+) from the D^{*+} decay. Using this partial reconstruction method, Belle obtains an order of magnitude more events compared to the full reconstruction of the D^{*+}. The flavor of the other B in the event is identified through a high-momentum lepton $l_{\rm tag}$ from semileptonic decay.

Hadronic events are selected by applying requirements on track multiplicity and total energy variables. The hard pion from the B decay must have a momentum in the range 2.05–2.45 GeV/c and the soft pion momentum must be below 450 MeV/c. Belle applies impact parameter requirements on π_h^- and π_s^+ to suppress backgrounds from interactions of beam particles with residual gas in the beam pipe or the beam pipe wall. They require both tracks to have SVD information and to not be identified as leptons.

The event kinematics are fully constrained by four-momentum conservation in the decays $\overline{B}^0 \to D^{*+}\pi_h^-$ and $D^{*+} \to D^0\pi_s^+$, the masses of all particles in these decays, the $\overline{B}^0$ energy, and the π_h^- and π_s^+ momenta. Belle uses two variables, the missing D^0 mass, $M_{D_{\rm miss}}$, and the cosine of the angle between the soft pion in the D^{*+} rest frame and the momentum of the D^{*+} in the center-of-mass frame $\cos\theta^*_{\pi_s}$. The $M_{D_{\rm miss}}$ distribution for signal events peaks sharply at the nominal D^0 mass, while background events spread towards smaller values. Signal events are required to have $M_{D_{\rm miss}} > 1.85$ GeV/c and $0.3 < |\cos\theta^*_{\pi_s}| < 1.05$.

The flavor of $B_{\rm rec}$ is determined from the π_h charge. The flavor of the other B in the event is determined from the charge of $l_{\rm tag}$. The tag lepton is required to have momentum greater than 1.1 GeV/c and to pass similar requirements on SVD hits and impact parameter as the $B_{\rm rec}$ pions. Tag leptons are rejected if when combined with any other lepton in the event the pair has an invariant mass consistent with a J/ψ. Belle determines the $B_{\rm rec}$ ($B_{\rm tag}$) decay vertex from the intersection of the π_h ($l_{\rm tag}$) track with the beam spot accounting for the B meson flight distance.

After all selection criteria Belle finds 3433 signal events over a background of 1466 events which are used in the Δm_d measurement. Studies of MC-simulated events show that a significant fraction of the selected events come from $\overline{B}^0 \to D^{*+}\rho^-$ decays.

Belle simultaneously fits the Δt distributions of the mixed and unmixed events with an unbinned maximum-likelihood method. The $B^0\overline{B}^0$ mixing frequency Δm_d is the only free parameter in the fit. The B^0 lifetime is fixed to the world average. The signal Δt resolution function uses a triple-Gaussian *p.d.f.* (see Eq. 10.4.2) in the Δt residuals. The resolution function parameters are determined from decays of J/ψ to e^+e^- and $\mu^+\mu^-$. Backgrounds are divided into peaking and non-peaking categories. Non-peaking background is dominated by random combinations of π_h^- and π_s^+ with primary leptons from B^0 and $B^\pm$ decays, and combinatorial background from continuum. Peaking background is dominated by the following sources: $\overline{B}^0 \to D^{*+}\pi^-$ and $\overline{B}^0 \to D^{*+}\rho^-$ with secondary-lepton or fake lepton tags; $B^0 \to D^{**-}\pi^+$, $B^+ \to \overline{D}^{**0}\pi^+$, and $B^0 \to D^{*-}\pi^+\pi^0$ decays with primary-lepton, secondary-lepton, or fake lepton tags. Peaking and non-peaking background *p.d.f.*s are convolved with their own resolution functions.

From the fit Belle obtains $\Delta m_d = (0.509 \pm 0.017 \pm 0.020)\,{\rm ps}^{-1}$, where the first error is statistical and the second is systematic. The systematic error in Δm_d is dominated by uncertainties in the background fractions (0.014 ps^{-1}) and the signal Δt resolution function (0.012 ps^{-1}).

17.5.2.4 Fully-reconstructed final states

Hadronic decay modes

BABAR reconstructs neutral B mesons in the decay modes $B^0 \to D^{(*)-}\pi^+$, $D^{(*)-}\rho^+$, $D^{(*)-}a_1^+$, $J/\psi K^{*0}$ using a data sample of 29.7 fb^{-1} (Aubert, 2002a,b). Belle uses the B decays to the hadronic final states $D^-\pi^+$, $D^{*-}\pi^+$, and $D^{*-}\rho^+$ in a data sample of 29.1 fb^{-1} (Tomura, 2002b). The $B^0\overline{B}^0$ mixing analyses with fully-reconstructed final states reconstruct the same decay modes of the B^0 daughters as in the B^0 lifetime measurements described in Section 17.5.1.3 (Aubert, 2001c; Abe, 2002m). Both experiments reduce background from continuum events by applying requirements on the normalized second Fox-Wolfram moment R_2 and the angle between the thrust axis of the particles that form the reconstructed B candidate and the thrust axis of the remaining tracks and unmatched calorimeter clusters in the event, computed in the $\Upsilon(4S)$ frame. Neutral B candidates are identified by their ΔE and $m_{\rm ES}$ values. *BABAR* selects events with $m_{\rm ES} > 5.2$ GeV/c^2 and $|\Delta E|$ within $\pm 2.5\sigma$ of zero. They use the events in the background-dominated region $m_{\rm ES} < 5.27$ GeV/c^2 to determine the parameters of the background Δt distributions. Belle requires $m_{\rm ES}$ and ΔE to be within $\pm 3\sigma$ around their expected means. They use candidates from a sideband region in the $m_{\rm ES} - \Delta E$ plane to determine the background parameters.

Events with a reconstructed B^0 are then analyzed to determine the flavor of the other B using the B flavor tagging algorithms described in detail in Chapter 8. Belle assigns 99.5% of the events to a flavor tag category, while *BABAR* rejects the 30% of events with marginal flavor discrimination.

The decay time difference Δt between B decays is determined from the measured separation $\Delta z = z_{\rm rec} - z_{\rm tag}$ along the z axis between the vertices of the reconstructed $B_{\rm rec}$ and the flavor-tagging $B_{\rm tag}$ according to Eq. (17.5.13). *BABAR* applies an event-by-event correction for the directions of the B meson momenta with respect to the z direction in the $\Upsilon(4S)$ frame. A description of this correction and details of the calculation of $z_{\rm rec}$ and $z_{\rm tag}$ and their respective resolutions for fully-reconstructed B decays are given in Chapter 6. In its paper, *BABAR* notes

a correlation between the Δt residual $\delta\Delta t = \Delta t - \Delta t_{\rm true}$ and $\sigma_{\Delta t}$ (see Fig. 6.5.4). It is due to the fact that, in B decays, the vertex error ellipse for the D decay products is oriented with its major axis along the D flight direction, leading to a correlation between the D flight direction and the calculated uncertainty on the vertex position in z of the $B_{\rm tag}$. In addition, the flight length of the D in the z direction is correlated with its flight direction. Therefore, the bias in the measured $B_{\rm tag}$ vertex position due to including the D decay products is correlated with the D flight direction. Taking into account these two correlations, *BABAR* concludes that D mesons that have a flight direction perpendicular to the z axis in the laboratory frame will have the best z resolution and will introduce the least bias in a measurement of the z position of the $B_{\rm tag}$ vertex, while D mesons that travel forward in the laboratory will have poorer z resolution and will introduce a larger bias in the measurement of the $B_{\rm tag}$ vertex.

After all selection criteria are applied, *BABAR* (Belle) finds 6300 (5300) signal events with an average purity of 86% (80%). Both experiments use an unbinned maximum likelihood fit to extract Δm_d from the Δt distributions of the selected candidates. The *p.d.f.* describing the data accounts for the presence of backgrounds with terms added to the signal description of Eq. (17.5.22):

$$\mathcal{H}_{\pm,i} = f_{{\rm sig},i}\mathcal{H}_{\pm,{\rm sig},i} + \sum_{j={\rm bkgd}} f_{i,j}\mathcal{B}_{\pm,i,j}(\Delta t, \hat{b}_{\pm,i,j}). \tag{17.5.24}$$

The background Δt *p.d.f.*s $\mathcal{B}_{\pm,i,j}(\Delta t, \hat{b}_{\pm,i,j})$ provide an empirical description for the Δt behavior of background events in each tagging category i. The background Δt types considered are a prompt component and an exponentially decaying component with an effective lifetime. The prompt term is modeled with a delta function $\delta(\Delta t)$. Both experiments describe the background resolution *p.d.f.* with the same function as the signal resolution *p.d.f.*, but with separate parameters to minimize correlations. Both experiments determine the signal probability $f_{{\rm sig},i}$ for each B candidate i from its $m_{\rm ES}$ and ΔE values (*BABAR* only uses $m_{\rm ES}$) based on separate fits to the $m_{\rm ES}$ and ΔE distributions.

In the likelihood fit *BABAR* approximates the signal Δt resolution function by a sum of three Gaussian distributions (core, tail, and outlier) with different means and different widths (see Chapter 10). The resolution is determined separately for each signal candidate depending on the uncertainty of its Δt value. *BABAR* uses separate resolution function parameters for each tagging category, while Belle uses a common parameterization.

In the final fit Belle lets only Δm_d and the mistag rates w_i (i = 1–6) vary. *BABAR*'s likelihood fit has 44 free parameters: Δm_d, average mistag rate and difference between B^0 and $\overline{B}^0$ for each tagging category (8), signal resolution function parameters (16), and parameters for background time dependence (5), Δt resolution (6), and effective mistag rates (8).

In fully-reconstructed B decays to hadronic final states *BABAR* measures in a sample of 29.7 fb^{-1} $\Delta m_d = (0.516 \pm 0.016 \pm 0.010)\,{\rm ps}^{-1}$, where the first error is statistical and the second is systematic. The central value has been corrected by $(-0.002 \pm 0.002)\,{\rm ps}^{-1}$ to account for a small variation of the background composition as a function of $m_{\rm ES}$. An additional correction of $(-0.007 \pm 0.003)\,{\rm ps}^{-1}$ has been applied to account for a bias observed in fully-simulated MC events due to correlations between the mistag rate and the Δt resolution that are not explicitly included in the likelihood function. Belle measures $\Delta m_d = (0.528 \pm 0.017 \pm 0.011)\,{\rm ps}^{-1}$ in a sample of 29.1 fb^{-1}.

The largest contributions to the systematic uncertainty in the Belle measurement come from the uncertainties in the signal Δt resolution function parameters ($0.008\,{\rm ps}^{-1}$) and limited MC statistics ($0.005\,{\rm ps}^{-1}$). In the *BABAR* fit the parameters of the signal and background Δt resolutions functions are allowed to vary, and their contribution to the uncertainty on Δm_d is included as part of the statistical error. The largest remaining systematic uncertainties come from uncertainties in the B^0 lifetime ($0.006\,{\rm ps}^{-1}$) and in the alignment of the SVT ($0.005\,{\rm ps}^{-1}$).

Semileptonic decays $B^0 \to D^{*-}l^+\nu_l$

BABAR performs a simultaneous measurement of the B^0 lifetime and Δm_d with a sample of semileptonic $B^0 \to D^{*-}l^+\nu_l$ decays using 21 fb^{-1} of data (Aubert, 2003m). The D^{*-} candidates are selected in the decay mode $D^{*-} \to \overline{D}^0\pi^-$, and the $\overline{D}^0$ candidates are reconstructed in the modes $K^+\pi^-$, $K^+\pi^-\pi^+\pi^-$, $K^+\pi^-\pi^0$, and $K^0_S\pi^+\pi^-$. Candidate $B^0 \to D^{*-}l^+\nu_l$ events are rejected if they fail selection criteria required to suppress backgrounds and ensure a well-measured Δt. These requirements include lepton and kaon identification, momenta of the lepton and the D^{*-} and $\overline{D}^0$ daughter tracks and π^0, the $\overline{D}^0$ invariant mass, the $D^{*-} - \overline{D}^0$ mass difference, vertex probabilities, $\cos\theta^*_{\rm thrust}$, the absolute value of Δz, and the calculated error on Δt. Furthermore they use two angular variables. The first angle is $\theta_{D^*,l}$, the angle between the D^{*-} and the lepton candidate in the $\Upsilon(4S)$ frame. The second is θ_{B,D^*l}, the inferred angle between the direction of the B^0 and the vector sum of the D^{*-} and the lepton candidate momenta, calculated in the $\Upsilon(4S)$ frame.

The B yield is larger than for the hadronic final state analysis due to the large B semileptonic branching fraction. They reconstruct 680 $B/\,{\rm fb}^{-1}$. Due to the missing neutrino the background level is higher than in the sample of fully-reconstructed hadronic B decays. The combinatorial D^{*-} background is about 18%, and the sum of the backgrounds from events where the D^{*-} and the lepton come from different B decays, events with a fake lepton candidate, and events from continuum $c\bar{c} \to D^{*-}X$ processes add up to 5–8%, depending on the lepton flavor.

The measurements of the decay vertex of the $B^0 \to D^{*-}l^+\nu_l$ candidate and that of the other B in the event in this analysis is similar to *BABAR*'s Δm_d analysis of fully-reconstructed hadronic final states. The decay time difference is determined from the z positions of these vertices according to Eq. (17.5.12). The flavor of $B_{\rm tag}$ is determined from the charged tracks in the event that do not

belong to the $B^0 \to D^{*-}l^+\nu_l$ candidate using the algorithms described in Chapter 8. About 30% of the selected signal candidates have a mistag rate close to 50%. These events are not sensitive to Δm_d, but they increase the sensitivity to the B^0 lifetime. In this paper, *BABAR* describes an interesting correlation between the mistag rate and the Δt resolution for the tagging category based on identified charged kaons.[58] Both the mistag rate for kaon tags and the calculated $\sigma_{\Delta t}$ depend inversely on $\sqrt{\sum p_t^2}$, where p_t is the transverse momentum with respect to the z axis of tracks from the $B_{\rm tag}$ decay. The mistag rate dependence originates from the kinematics of the physical sources for wrong-charge kaons. The three major sources of mis-tagged events in the kaon tag category are wrong-sign D^0 mesons from B decays to double charm ($b \to c\bar{c}s$), wrong-sign kaons from D^+ decays, and kaons produced directly in B decays. All these sources produce a spectrum of tracks that have smaller $\sqrt{\sum p_t^2}$ than B decays that produce a correct tag. The $\sigma_{\Delta t}$ dependence originates from the $1/p_t^2$ dependence of σ_z for the individual contributing tracks due to multiple scattering in the SVT and the beam pipe.

After all selection requirements are applied, the $B^0 \to D^{*-}l^+\nu_l$ selected event sample contains contributions from the following types of background: events with a misreconstructed D^{*-} candidate, events from continuum $c\bar{c} \to D^{*-}X$ processes, events with a fake lepton candidate, events with a charged B, and events in which the lepton does not come from the primary B decay. They model the Δt distributions of each background with combinations of prompt, exponential, and oscillatory functions convolved with background resolution functions. The parameters of background *p.d.f.*s are obtained from fits to control samples and simulated events. *BABAR* split their data into two signal samples and ten control samples depending on whether the data was taken on or off the $\Upsilon(4S)$ resonance, whether the lepton candidate was on the same side or opposite side to the D^{*-} candidate, and whether the lepton candidate was an electron, muon, or fake lepton. Furthermore they split each of these samples into subsamples according to the reconstruction of the soft pion, the $\overline{D}^0$ decay mode, and the B flavor-tagging category for a total of 360 subsamples.

They extract the B^0 lifetime and Δm_d from a simultaneous fit to the Δt and $\sigma_{\Delta t}$ values of the events of the 360 event samples. The fit has 70 additional free parameters to describe the signal and background Δt resolution functions and mistag rates, and the background Δt shapes. From the fit they determine $\tau_{B^0} = (1.523^{+0.024}_{-0.023} \pm 0.022)\,\text{ps}$ and $\Delta m_d = (0.492 \pm 0.018 \pm 0.013)\,\text{ps}^{-1}$. The statistical correlation coefficient between τ_{B^0} and Δm_d is -0.22. Dominant systematic error sources in the Δm_d measurement are the SVT alignment and the signal and background probabilities. An additional systematic uncertainty in the Δm_d measurement comes from the limited statistical precision in determining the bias due to the background modeling. By comparing the fitted Δm_d in simulated events, *BABAR* observes a shift of $(0.020 \pm 0.005)\,\text{ps}^{-1}$ between a signal-only sample and a signal-plus-background sample. The measured Δm_d is corrected for the observed bias from the fit to the MC sample with background, and the full statistical uncertainty in Δm_d of $\pm 0.012\,\text{ps}^{-1}$ is assigned as a systematic uncertainty.

Belle also measures Δm_d with a sample of semileptonic $B^0 \to D^{*-}l^+\nu_l$ decays corresponding to $29.1\,\text{fb}^{-1}$ of data (Hara, 2002). They select D^{*-} candidates in the decay mode $D^{*-} \to \overline{D}^0\pi^-$ and the $\overline{D}^0$ candidates are reconstructed in the modes $K^+\pi^-$, $K^+\pi^-\pi^+\pi^-$, and $K^+\pi^-\pi^0$. Candidate events are rejected if they fail selection criteria required to suppress backgrounds and ensure a well-measured Δt. The applied requirements are similar to those in the *BABAR* Δm_d measurement described above.

Belle uses its standard algorithms for the Δt measurements and B flavor tagging in this analysis, which are the same as in its measurement of $\sin\phi_1$ (Abe, 2002k). The algorithms are described in more detail in Chapters 6 and 8. After all selection criteria, including flavor tagging and vertex reconstruction, are applied, Belle reconstructs 453 $B^0/\,\text{fb}^{-1}$ with a signal purity of 80.4%. The background consists of misreconstructed D^* mesons (7.8%), $B \to D^{**}l\nu$ events (7.4%), random combinations of D^* mesons with leptons with no angular correlation (2.6%), and continuum events (1.8%).

Belle measures Δm_d from a simultaneous fit to the Δt and $\sigma_{\Delta t}$ distributions of the mixed and unmixed events. The fit has a total of ten free parameters including Δm_d, six flavor mistag rates, the fraction of the D^{**} background coming from charged B decays, its effective lifetime, and the fraction of charged B decays. All other parameters are determined from MC simulation and data control samples. The likelihood fit gives $\Delta m_d = (0.494 \pm 0.012 \pm 0.015)\,\text{ps}^{-1}$. Dominant systematic error sources in the Δm_d measurement are due to uncertainties in the D^{**} branching fractions ($0.007\,\text{ps}^{-1}$), the selected $|\Delta t|$ range ($0.007\,\text{ps}^{-1}$), the background Δt *p.d.f.* parameters ($0.006\,\text{ps}^{-1}$), the signal Δt resolution function ($0.006\,\text{ps}^{-1}$), and the B^0 lifetime ($0.005\,\text{ps}^{-1}$).

Belle hadronic and semileptonic combination

Belle's most recent measurement of Δm_d comes from a simultaneous analysis of B decays to the exclusive hadronic final states $B^0 \to D^{(*)-}\pi^+$, $D^*\rho^+$, $J/\psi K^0_S$, $J/\psi K^{*0}$, and the semileptonic decay $B^0 \to D^{*-}l\nu$ in a sample of $140\,\text{fb}^{-1}$ (Abe, 2005c). In the same analysis, they also determine the B^0 lifetime and, using the decays $B^+ \to \overline{D}^0\pi^+$ and $J/\psi K^+$, the B^+ lifetime.

The signal modes and selection criteria of the hadronic final states are similar to the ones used in Tomura (2002b), while the $B^0 \to D^{*-}l^+\nu$ selection follows that described in Zheng (2003). The Δt reconstruction uses the algorithm described in Tajima (2004). The B flavor tagging algorithm is similar to the one used in Belle's previous analyses of fully-reconstructed final states, but they allow for separate mistag rates for B^0 and $\overline{B}^0$ tagged events. The

[58] This correlation is already observed and accounted for in Aubert (2002b), but is not described in that paper.

overall B^0 signal purity after all selection criteria are applied is 80.9%, and the B^0 signal yield is 707 $B/\,\mathrm{fb}^{-1}$.

Belle performs an unbinned maximum likelihood fit to the Δt distributions of the selected B^0 and B^+ candidates to simultaneously obtain values of the B^0 and B^+ lifetimes (2), Δm_d (1), the mistag fractions (12), the signal Δt resolution function parameters (14), and parameters to describe the B^+ background in B^0 decays (3). The signal resolution function has two parameters added to the ones described in Tajima (2004) to better describe the effect of charmed particle decays on the B_{tag} vertex. The same Δt resolution function is used for B^0 and B^+ signal candidates. The background for the hadronic B decay modes is described by the convolution of the sum of a prompt term and a term with an effective background lifetime with a background Δt resolution function. The background for the $B^0 \to D^{*-} l^+ \nu$ decays is the same as in the earlier study of this mode (Hara, 2002) described above. The Δt behavior of the backgrounds is modeled with prompt and lifetime terms. The backgrounds due to D^{**} and misreconstructed D^* candidates also have an oscillatory component.

Belle extracts the B^0 lifetime and Δm_d to be, respectively, $\tau_{B^0} = (1.534 \pm 0.008 \pm 0.010)\,\mathrm{ps}$ and $\Delta m_d = (0.511 \pm 0.005 \pm 0.006)\,\mathrm{ps}^{-1}$. Dominant systematic error sources in the Δm_d measurement are the B vertex reconstruction ($0.004\,\mathrm{ps}^{-1}$) and the D^{**} background parameters ($0.003\,\mathrm{ps}^{-1}$).

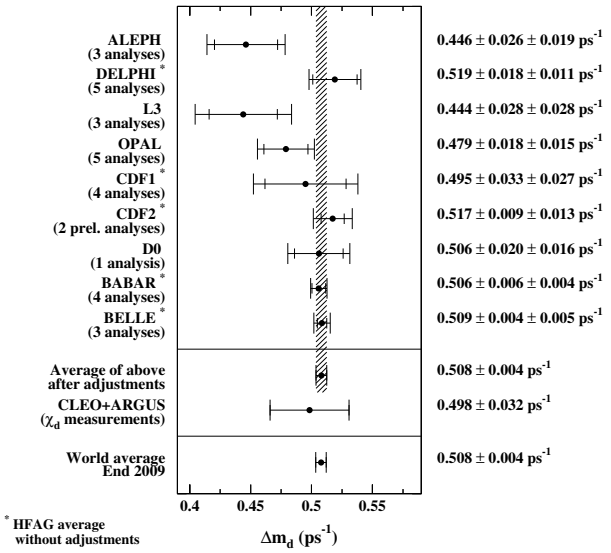

Figure 17.5.6. The $B^0\overline{B}^0$ oscillation frequency Δm_d as measured by the different experiments along with their average. Averages are also given separately for the time-dependent measurements by the B Factories and the LEP and Tevatron experiments, and the time-integrated measurements by CLEO and ARGUS (Asner et al., 2010).

17.5.2.5 Average of Δm_d

The various measurements of Δm_d by the B Factories listed in Table 17.5.2 have been averaged by the Heavy Flavor Averaging Group (HFAG; Asner et al., 2010), where results superseded by more recent ones have been omitted from the average. Before being combined, the Δm_d measurements have been adjusted to a common set of input values, including the B meson lifetimes. The total systematic uncertainty in Δm_d is of the same size as the statistical uncertainty, although only a small fraction of the total B Factories' data sets have been used in the measurements. Systematic correlations arise from common physics sources (*e.g.* B lifetimes and branching fractions) and common experimental techniques and algorithms (*e.g.* flavor tagging, Δt resolution, and background description). Combining the B Factories Δm_d measurements and accounting for all identified correlations, HFAG quotes

$$\Delta m_d = (0.508 \pm 0.003 \pm 0.003)\,\mathrm{ps}^{-1}, \qquad (17.5.25)$$

where the first error is statistical and the second is systematic (Asner et al., 2010). Combining the B Factories Δm_d average with time-dependent measurements from the LEP and Tevatron experiments, and time-integrated measurements from CLEO and ARGUS, gives the same value. The values of Δm_d as measured by different experiments along with the time-dependent and time-integrated averages are shown in Fig. 17.5.6. Two recent measurements by the LHCb Collaboration, $\Delta m_d = (0.516 \pm 0.005 \pm 0.003)\,\mathrm{ps}^{-1}$ (Aaij et al., 2013b) and $\Delta m_d = (0.499 \pm 0.032 \pm 0.003)\,\mathrm{ps}^{-1}$ (Aaij et al., 2012f), are not included in the HFAG average and the figure. The 2013 PDG world average including these results is $\Delta m_d = (0.510 \pm 0.004)\,\mathrm{ps}^{-1}$ (Beringer et al., 2012). The world average of the $B^0\overline{B}^0$ oscillation frequency Δm_d is an input to the calculation of the magnitude of the CKM matrix element V_{td}. Along with Δm_s, the $B_s^0\overline{B}_s^0$ oscillation frequency as measured by CDF and DØ, Δm_d is used to calculate the ratio of CKM matrix elements $|V_{td}/V_{ts}|$ (see Section 17.2).

17.5.2.6 Measurements of $\Delta\Gamma_d$

Transitions between a B^0 state and a $\overline{B}^0$ state can be mediated by a box diagram involving virtual top quarks (see Fig. 10.1.1) or by real intermediate states accessible to both B^0 and $\overline{B}^0$. The former process determines the magnitude of Δm_d, while the latter gives rise to a difference in decay width of the neutral B mass eigenstates. The decay width difference is defined as $\Delta\Gamma_d \equiv \Gamma_{H,d} - \Gamma_{L,d}$,[59] where H and L refer to the heavy and light B^0 states, respectively. In the B_s^0 system the corresponding relative decay width difference is large, $\Delta\Gamma_s/\Gamma_s = (15 \pm 2)\%$ (Beringer et al., 2012), due to the significant branching fractions of B_s^0 and $\overline{B}_s^0$ to $D_s^{(*)+} D_s^{(*)-}$. Since the decays of B^0 and

[59] Note, the Particle Data Group (Beringer et al., 2012) uses the definition $\Delta\Gamma_d = \Gamma_{L,d} - \Gamma_{H,d}$.

$\overline{B}^0$ to common final states are strongly suppressed, $\Delta\Gamma_d$ is expected to be much smaller than $\Delta\Gamma_s$. A recent SM calculation predicts $\Delta\Gamma_d/\Gamma_d = (-4.2 \pm 0.8) \times 10^{-3}$ (Lenz and Nierste, 2011). The best limit prior to the B Factories measured by DELPHI was $\Delta\Gamma_d/\Gamma_d < 0.18$ at 95% C.L. (Abdallah et al., 2003). The small value of $\Delta\Gamma_d$ in the SM makes it a sensitive parameter in the search for new physics (Dighe, Hurth, Kim, and Yoshikawa, 2002).

In the derivation of the time-dependent decay rates in Chapter 10 we have neglected the case of non-zero $\Delta\Gamma_d$. This is justified because of the small values of $\Delta\Gamma_d/\Gamma_d$ and $\Delta\Gamma_d/\Delta m_d$ predicted by the SM. The decay rates given in Eqs (10.2.2) and (10.2.3) are sufficient for all measurements of Δm_d (Section 17.5.2) and *mixing-induced CP* asymmetries in B decays (Sections 17.6–17.8). However, physics from processes beyond the SM can lead to a sizable $\Delta\Gamma_d$. *BABAR* (Aubert, 2004e,f) and Belle (Higuchi, 2012) have both measured $\Delta\Gamma_d$ as part of analyses that search for *CP*, T, and *CPT* violation in $B^0\overline{B}^0$ mixing. The analyses are described in detail below (see Section 17.5.4). Here we describe the sensitivity to $\Delta\Gamma_d$ and the results from the B Factories.

The time-dependence of the decay rates for B decays to *CP* eigenstates and flavor-specific final states in the absence of *CP* and *CPT* violation in $B^0\overline{B}^0$ mixing, but including additional terms due to $\Delta\Gamma_d$, are given by

$$f_{\pm}^{\Delta\Gamma_d}(\Delta t) \propto e^{-|\Delta t|/\tau_{B^0}} \left[\cosh\left(\frac{\Delta\Gamma_d \Delta t}{2}\right) \mp C\cos(\Delta m_d \Delta t) + A^{\Delta\Gamma_d} \sinh\left(\frac{\Delta\Gamma_d \Delta t}{2}\right) \pm S\sin(\Delta m_d \Delta t) \right], \tag{17.5.26}$$

with

$$C = \frac{1-|\lambda|^2}{1+|\lambda|^2},\ S = \frac{2\,\mathrm{Im}\lambda}{1+|\lambda|^2},\ A^{\Delta\Gamma_d} = \frac{2\,\mathrm{Re}\lambda}{1+|\lambda|^2}. \tag{17.5.27}$$

The parameter $\lambda = \frac{q}{p}\frac{\overline{A}_f}{A_f}$ has been introduced in Chapter 10, where A_f ($\overline{A}_f$) represents the amplitude for the decay of a B^0 ($\overline{B}^0$) to the final state f, and q/p is the weak phase in $B^0\overline{B}^0$ mixing. Note that $(S)^2 + (C)^2 + \left(A^{\Delta\Gamma_d}\right)^2 = 1$ by definition. The time-dependence for a B^0 ($\overline{B}^0$) tagged event is given by $f_+^{\Delta\Gamma_d}$ ($f_-^{\Delta\Gamma_d}$).

For B decays to *CP* eigenstates that proceed through a single weak amplitude, $|\lambda| = 1$ and thus $C = 0$, $S = \mathrm{Im}\lambda$, and $A^{\Delta\Gamma_d} = \mathrm{Re}\lambda$. For example, the time-dependence for the *golden CP* mode $B \to J/\psi K_S^0$ (see Chapter 10 and Section 17.6) simplifies to

$$f_{\pm}^{J/\psi K_S^0,\Delta\Gamma_d}(\Delta t) \propto e^{-|\Delta t|/\tau_{B^0}} \left[\cosh\left(\frac{\Delta\Gamma_d \Delta t}{2}\right) + \cos(2\phi_1)\sinh\left(\frac{\Delta\Gamma_d \Delta t}{2}\right) \pm \sin(2\phi_1)\sin(\Delta m_d \Delta t) \right], \tag{17.5.28}$$

where ϕ_1 is one of the angles of the Unitarity Triangle.

For B decays to flavor-eigenstates which are only accessible from either a B^0 or a $\overline{B}^0$, $|\lambda|$ is zero or infinite and thus $C = 1$, $S = A^{\Delta\Gamma_d} = 0$. The corresponding time-dependence is given by

$$h_{\pm}^{\Delta\Gamma_d}(\Delta t) \propto e^{-|\Delta t|/\tau_{B^0}} \left[\cosh\left(\frac{\Delta\Gamma_d \Delta t}{2}\right) \pm \cos(\Delta m_d \Delta t) \right], \tag{17.5.29}$$

where $h_+^{\Delta\Gamma_d}$ and $h_-^{\Delta\Gamma_d}$ refer to unmixed and mixed events, respectively.

BABAR and Belle both use samples of B decays to *CP* eigenstates and flavor-specific final states in their measurement of $\Delta\Gamma_d$. The *BABAR* analysis is performed with 88×10^6 $B\overline{B}$ pairs and uses the B_{flav} decays to $D^{(*)-}\pi^+(\rho^+, a_1^+)$, $J/\psi K^{*0}(\to K^+\pi^-)$ and B_{CP} decays to $J/\psi K_S^0$, $\psi(2S)K_S^0$, $\chi_{c1}K_S^0$, and $J/\psi K_L^0$. The Belle analysis is performed with 535×10^6 $B\overline{B}$ pairs and uses the B_{flav} decays to $D^{(*)-}\pi^+$, $D^{*-}\rho^+$, and $D^{*-}\ell^+\nu_l$ and B_{CP} decays to $J/\psi K_S^0$ and $J/\psi K_L^0$. The cosh and sinh terms in Eqs (17.5.28) and (17.5.29) do not change sign with the flavor of B_{tag}. This allows the experiments to also use events without a flavor-tagged B in their analyses. The time-dependence of the B_{CP} samples include a $\sinh\left(\frac{\Delta\Gamma_d \Delta t}{2}\right)$ term, which is practically linear in $\Delta\Gamma_d$. The B_{flav} sample is only sensitive to $\Delta\Gamma_d$ through a $\cosh\left(\frac{\Delta\Gamma_d \Delta t}{2}\right)$ term and thus effectively to $\mathcal{O}(\Delta\Gamma_d^2)$. Therefore, even though the B_{CP} events represent only 8% (4%) of the selected signal events in the *BABAR* (Belle) analysis, they dominate the $\Delta\Gamma_d$ measurement.

The experiments perform unbinned likelihood fits to the Δt distributions of the flavor-tagged and untagged B_{CP} and B_{flav} samples (after accounting for experimental effects such as the Δt resolution and B flavor-tagging) to extract parameters that violate *CP*, T, or *CPT* symmetries and $\Delta\Gamma_d$. In the fit the sign of $A^{\Delta\Gamma_d}$ is fixed to the value obtained from global CKM fits (see Section 25.1). *BABAR* measures $\Delta\Gamma_d/\Gamma_d = -0.008 \pm 0.037 \pm 0.018$ and Belle measures $\Delta\Gamma_d/\Gamma_d = -0.017 \pm 0.018 \pm 0.011$. The dominant systematic error contributions arise from uncertainties in the reconstruction of the B vertices and the Δt resolution function. The results are consistent with each other. The B Factories average value is $\Delta\Gamma_d/\Gamma_d = -0.015 \pm 0.019$ (Beringer et al., 2012), consistent with the small predicted value. Larger B samples at LHCb and future super flavor factories should allow the measurement of $\Delta\Gamma_d$ at the SM value or find discrepancies as evidence of new physics (Gershon, 2011), if the systematic uncertainties can be kept under control.

17.5.3 Tests of quantum entanglement

The B-lifetime and $B^0 - \overline{B}^0$ mixing results of the previous sections rely on certain assumptions about the physics of B-meson production and decay (see the discussion in Chapter 10). Some of these assumptions can be tested by performing an extended analysis including symmetry-breaking parameter(s) in the final fit. This approach is

used to test discrete symmetries, including *CPT* (Sections 17.5.4 and 17.5.5 below); if the assumption of Lorentz invariance is also relaxed, qualitatively new phenomena are expected and the $B^0 - \overline{B}^0$ mixing analysis method of Section 17.5.2 must be heavily modified (Section 17.5.5), even when a standard mixing event selection is retained.

Quantum mechanical principles governing the entangled $B^0\overline{B}^0$ state may also be tested. The careful conceptual treatment required in this case is reviewed in Section 17.5.3.1. One such analysis has been performed by Belle (Go, 2007): the event selection and background treatment are both straightforward modifications of those in the $D^*\ell\nu$ mixing analysis of Abe (2005c), as discussed in Section 17.5.3.2. The final analysis is presented in Section 17.5.3.3.

17.5.3.1 $B^0 - \overline{B}^0$ mixing and entanglement tests

As discussed in Section 10.2, $\Upsilon(4S)$ decay prepares a neutral B meson pair in the coherent state

$$\Psi = \frac{1}{\sqrt{2}}\left[\,|B^0(\boldsymbol{p})\rangle|\overline{B}^0(-\boldsymbol{p})\rangle - |\overline{B}^0(\boldsymbol{p})\rangle|B^0(-\boldsymbol{p})\rangle\,\right] \tag{17.5.30}$$

given there in a more compact notation as Eq. (10.2.1). The formulae for the time-dependent evolution of the B pair in the remainder of that section follow from this expression. Such a state is *entangled*: it cannot be represented as a product of states of the first B (with momentum $\boldsymbol{p}$) and the second B (with momentum $-\boldsymbol{p}$); it is a flavor analog of the spin-singlet state for a photon pair,

$$\Psi = \frac{1}{\sqrt{2}}\left(|\Uparrow\rangle_1|\Downarrow\rangle_2 - |\Downarrow\rangle_1|\Uparrow\rangle_2\right), \tag{17.5.31}$$

familiar from Bohm's version of the thought experiment on "EPR correlations" (Bohm, 1951; Einstein, Podolsky, and Rosen, 1935). Powerful tests of such correlations are possible (Bell, 1964), and have been carried out on photon pairs by Aspect, Grangier, and Roger (1982) and many subsequent investigators. Subject to certain experimental "loopholes", such tests exclude the hypothesis that the individual photons have definite physical states at all times (a feature of so-called "local realistic" models). Quantum entanglement thus appears to be an experimental fact, which would persist even if quantum mechanics (QM) itself were replaced by future developments.

Bell tests using photons rely on experimental choice of the orientation (polarization axis) of analyzers, in experiments of the Aspect type; or on fixed analyzers, and experimental choice of phase shifts imposed on the photons in flight (following Franson, 1989); see Fig. 17.5.7(a) and (b) for schematics of both arrangements. $B^0 - \overline{B}^0$ mixing is analogous to the latter case, as a flavor-tagging decay projects a neutral B meson onto one of two fixed axes: B^0, equivalent to spin-up for a fermion or vertical polarization for a photon; or $\overline{B}^0$, equivalent to spin-down or to horizontal polarization. For discussion of this *quasi-spin* analogy, see Lee and Wu (1966), Lipkin (1968), and

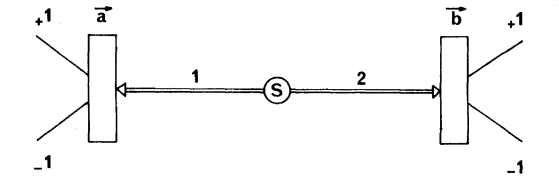

(a) Aspect: freely-chosen analyzer orientations $\boldsymbol{a}$, $\boldsymbol{b}$.

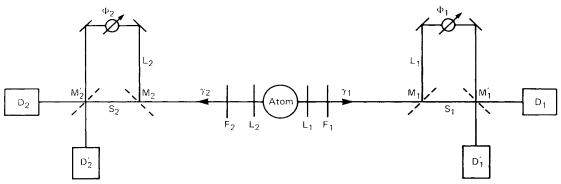

(b) Franson: freely-chosen phase shifts ϕ_1, ϕ_2.

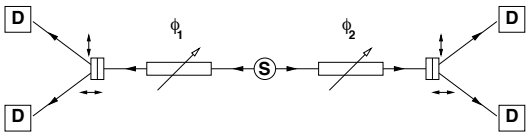

(c) Go: fixed analyzers; variable phase shifts ϕ_1, ϕ_2.

Figure 17.5.7. Schematics of the Bell inequality tests with photons by (a) Aspect, Grangier, and Roger (1982); (b) the position-time test proposed by Franson (1989); and (c) an optical analog of the Go (2007) analysis of $B^0\overline{B}^0$ pairs (from Yabsley, 2008). To perform a Bell test, projective measurements must be performed onto axes determined outside the system under study. In (a), the analyzer orientations can be freely chosen; in (b) the projections recorded by the detectors D_i are fixed, but phase shifts imposed on the photons can be chosen; in (c), neither the projection axes ($\updownarrow \equiv B^0$ or $\leftrightarrow \equiv B^0$) nor phase shifts ($\phi_i = \Delta m_d t_i$) are subject to experimental control.

Bertlmann and Hiesmayr (2001); the assignment of spin and polarization states to flavors is arbitrary. If we ignore B-meson decay, the state $|B^0\rangle$ at production evolves to the state

$$\frac{1}{2}\left[\{1+\cos(\Delta m_d t)\}|B^0\rangle + \{1-\cos(\Delta m_d t)\}|\overline{B}^0\rangle\right] \tag{17.5.32}$$

at a later time t, from Eqs (10.1.6) and (10.1.7); *cf.* Eqs (17.5.14)–(17.5.17) above. For a $B^0\overline{B}^0$ pair undergoing two flavor-tagging decays, the product $\Delta m_d \Delta t$ therefore corresponds to the difference in phase shifts $\Delta\phi$ imposed in a Franson-type experiment, or the angle between polarization analyzers chosen in an Aspect-type experiment (see Fig. 17.5.7(c)).

An early attempt to re-interpret B Factory mixing results as Bell inequality tests was presented by Go (2004). In fact, no such test is possible using B Factory measurements of the $B^0 - \overline{B}^0$ system (Bertlmann, Bramon, Garbarino, and Hiesmayr, 2004):

1. *Flavor measurements at the B Factories are passive,* relying on spontaneous decay of the B mesons rather

than (say) interactions with converters placed in the path of each B. It is therefore not possible to exclude local models where EPR-like decays of the two B mesons have been determined in advance, as $\Delta m_d \Delta t$ is not subject to experimental control. Schematic diagrams comparing this case and entangled-photon experiments are shown in Fig. 17.5.7; note that in photon experiments, control of analyzer orientations has been demonstrated for spacelike-separated measurements (for example Weihs, Jennewein, Simon, Weinfurter, and Zeilinger, 1998).

2. *The rate of B^0_d-mixing is too low,* relative to the rate of decay, to construct a Bell test even in the case of active measurements. The crucial value of $x = \Delta m/\Gamma$ is found to be 2.0; *cf.* $x_d = \Delta m_d/\Gamma_d = (0.775 \pm 0.007)$. Note that as $x_s = \Delta m_s/\Gamma_s = (26.82 \pm 0.23) \gg 2.0$, a Bell test using active measurements of the $B^0_s - \overline{B}^0_s$ system is possible in principle, although not practical with foreseeable technology. Values are taken from the 2013 update of Beringer et al., 2012.

Artificial local models which reproduce QM predictions for B Factory results have been constructed by Bertlmann, Bramon, Garbarino, and Hiesmayr (2004), following Kasday (1971); and by Santos (2007), to further demonstrate that such models cannot be excluded as a class.

It is however possible to compare B Factory results with the predictions of both quantum mechanics and various local models. The Belle analysis (Go, 2007) tested both decoherence models (following Bertlmann, Grimus, and Hiesmayr, 1999), and a broad class of models that reproduce the QM predictions for uncorrelated B decays (Pompili and Selleri, 2000). Predictions for the $B^0\overline{B}^0$ mixing asymmetry $A_{\rm mix}(\Delta t)$ of Eq. (17.5.20) are shown in Fig. 17.5.8 for QM and for spontaneous disentanglement (SD), an extreme form of decoherence corresponding to $\zeta = 1$ in the $\{B^0, \overline{B}^0\}$ basis in Bertlmann et al., or the hypothesis of Furry (1936); asymmetries for models in the Pompili and Selleri class must lie between the two curves $\mathrm{PS}_{\max}$ and $\mathrm{PS}_{\min}$. With sufficient resolution, $A_{\rm mix}(\Delta t)$ measurements can discriminate between these models; with reconstruction of individual decay times (not just Δt), much stronger discrimination would be possible at a next-generation flavor factory (see Eqs (2)–(5) of Go, 2007, and Figure 4 of Yabsley, 2008).

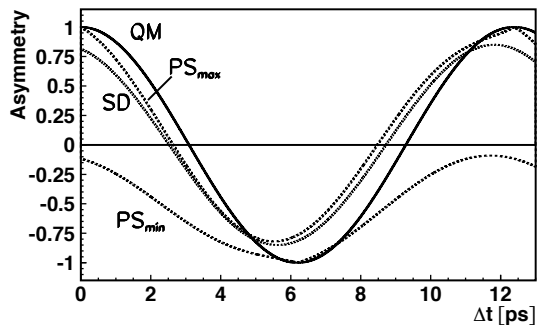

Figure 17.5.8. Time dependent asymmetry predictions for (QM) quantum mechanics, (SD) spontaneous disentanglement, and ($\mathrm{PS}_{\max}$ to $\mathrm{PS}_{\min}$) the allowed range for models in the class described by Pompili and Selleri (2000). See the discussion in the text. From Go (2007).

17.5.3.2 Event selection and background treatment

The Belle analysis (Go, 2007) uses a sample of $B^0\overline{B}^0$ events where one B is reconstructed as $B^0 \to D^{*-}\ell^+\nu$ (or charge conjugate), and the remaining tracks are subjected to the Belle flavor-tagging algorithm (Section 8.6.4). Taken from $140\,\mathrm{fb}^{-1}$ of data, the sample is a subset of the $D^*\ell\nu$ sample of Abe (2005c) discussed in Sections 17.5.1.3 and 17.5.2.4 above. To perform the entanglement analysis, the event selection and background treatment of Abe (2005c) are modified in the following ways:

1. *Only events with the highest-purity flavor tag are used* (*i.e.* $0.875 < r < 1.000$; see Section 8.6.4), with the further restriction that the tag is based on a reconstructed lepton. This reduces the sample from 84823 to 8565 events.
2. *The data are binned*, separately for opposite-flavor (OF) and same-flavor (SF) events, into 11 variable-width bins in Δt.
3. *Backgrounds are subtracted*, in both OF and SF samples, using the same background categorization as Abe (2005c): $e^+e^- \to q\overline{q}$ continuum (found to be negligible), non-D^* events, wrong D^*-lepton combinations, and $B^+ \to \overline{D}^{**0}\ell^+\nu$ events; $B^0 \to \overline{D}^{**-}\ell^+\nu$ events, which undergo mixing, are retained.
4. *Remaining reconstruction effects are unfolded* using deconvolution with single value decomposition (Höcker and Kartvelishvili, 1996) separately on the OF and SF samples, based on 11×11 response matrices built from MC $D^*\ell\nu$ events; see Go (2007) for the details.

To avoid potential bias due to the MC events underlying the response matrices, the deconvolution procedure is validated on Monte Carlo samples generated according to each of the QM, SD, and PS models. Differences between results and inputs are averaged over the three models, and subtracted from the measured asymmetry; the largest remaining deviation in each Δt bin, over all three models, is then assigned as a contribution to the systematic uncertainty.

The resulting asymmetry $A_{\rm mix} = (N_{\rm OF} - N_{\rm SF})/(N_{\rm OF} + N_{\rm SF})$ in bins of the time difference Δt, with statistical and four categories of systematic uncertainties, is given in Table 1 of Go (2007); systematics become comparable to statistical uncertainties for $\Delta t > 4.0$ ps, with the uncertainties due to background subtraction and deconvolution dominant in the final $[13.0, 20.0]$ ps bin. These results can be directly compared with theoretical models that lie outside the analysis discussed in the following section.

17.5.3.3 Analysis and interpretation

For each model, a weighted least-squares fit is performed, to the asymmetries $A_{\rm mix}$ and their total uncertainties as

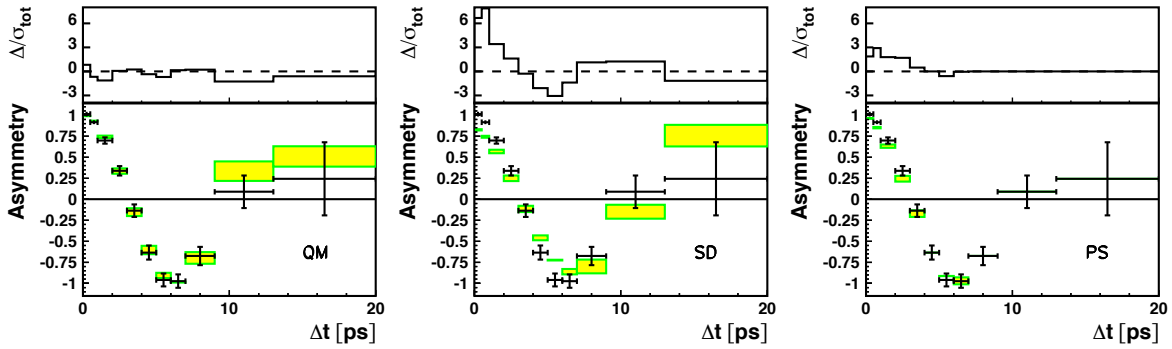

Figure 17.5.9. Asymmetry $A_{\rm mix}$ and its total uncertainty (crosses) in bins of Δt, and the results of fits to predictions from (left: QM) quantum mechanics, (middle: SD) spontaneous decomposition, and (right: PS) the Pompili and Selleri (2000) class of models. The shaded boxes show the variation in the predictions as the fitted value of Δm_d is allowed to vary by $\pm 1\sigma$; see the text, in particular for handling of the PS case. The upper panels show normalized residuals in each bin. From Go (2007).

data, and the function shown in Fig. 17.5.8 as the prediction. The mass difference Δm_d appears as a parameter in each model, however the world-average value of Δm_d is dominated by B Factory measurements, which assume time evolution according to QM in their analysis (see Section 17.5.2.1). An average of results then available (Barberio et al., 2006), excluding B Factory measurements, was therefore performed, yielding $\langle \Delta m_d \rangle = (0.496 \pm 0.014)\,\mathrm{ps}^{-1}$. The uncertainty was treated by including Δm_d as a parameter in the fit, and adding an additional term $[(\Delta m_d - \langle \Delta m_d \rangle)/\sigma_{\Delta m_d}]^2$ to the least-squares statistic; this technique is now in common use for treating systematic uncertainties *e.g.* at LHC experiments).

The results of the fits are shown in Fig. 17.5.9. The predictions of quantum mechanics are favored over spontaneous disentanglement at 13σ; more general decoherence models are treated by fitting the data with a function $(1-\zeta)A_{\rm QM} + \zeta A_{\rm SD}$, equivalent to modifying the interference term in the $\{B^0, \overline{B}^0\}$ basis, or assuming disentanglement into B^0 and $\overline{B}^0$ of a fraction of neutral B pairs (Bertlmann, Grimus, and Hiesmayr, 1999). The result, $\zeta = 0.029 \pm 0.057$, is consistent with no decoherence.

The analysis of Pompili and Selleri (2000) constrains the relevant models to have an asymmetry within a range ($\mathrm{PS_{max}}$ to $\mathrm{PS_{min}}$; see Fig. 17.5.8 and Section 17.5.3.1). If the data fall within this range, a null deviation is assigned; otherwise, the nearest boundary is treated as the PS prediction. Even with this conservative treatment, this class of models is disfavored at 5.1σ. The discrepancy with data is concentrated at $\Delta t < 4.0\,\mathrm{ps}$, where statistical uncertainty dominates. In summary the Belle results are consistent with a QM description of entangled neutral B meson pairs created via $\Upsilon(4S)$ decay.

17.5.4 Violation of *CP*, *T*, and *CPT* symmetries in $B^0 - \overline{B}^0$ mixing

The phenomenological description introduced in Section 10.1 of $B^0 - \overline{B}^0$ mixing with a 2×2 matrix effective Hamiltonian already allows for the possibility of *CP*, *T*, and *CPT* symmetry violations. Section 17.5.4.1 discusses the parameterization of the Hamiltonian including new variables that represent the magnitudes of the symmetry violations. In Section 17.5.4.2 we summarize the B Factory measurements of these variables. In the case of *CPT* violation, one would expect on general grounds that violation of Lorentz invariance would also occur; an extended formalism is required to treat this consistently. Such an approach, and the B Factory analysis taking this into account, are presented in Section 17.5.5.

The *CP* symmetry violations discussed in this section pertain to *CP violation in mixing*.[60] These differ from asymmetries due to *mixing-induced CP violation* that result from non-trivial values of the angles of the Unitarity Triangle, ϕ_1, ϕ_2, and ϕ_3, discussed in Sections 17.6–17.8. The recent observation of T violation by *BABAR* (Lees, 2012m) is discussed in Section 17.6. The large observed T asymmetry is expected in the Standard Model and can be understood as a consequence of the CKM phase. If *CPT* symmetry is conserved, there is a direct correspondence between the T asymmetry resulting from the CKM phase and the magnitude of the corresponding *CP* asymmetry (here $\sin 2\phi_1$). As such one could call this violation of T symmetry *mixing-induced T violation*. In this section we discuss searches for T *violation in mixing*.

17.5.4.1 Parameterization of mixing with *CP*, *T*, *CPT* violation

The effective Hamiltonian of $B^0 - \overline{B}^0$ mixing, $\mathcal{H}_{\rm eff} = \mathbf{M} - i\mathbf{\Gamma}/2$, defined in Eq. (10.1.1), is completely described by only eight independent real quantities. Four of them are the masses and decay rates of the eigenstates. These four quantities are sufficient to describe the $B^0 - \overline{B}^0$ oscillations expected in the Standard Model accurately enough for the sensitivity of the B Factories.

To allow for *CP*, *T* and *CPT*-violating effects in mixing, it is necessary to extend the treatment presented in

[60] For a brief overview of the types of *CP* violation relevant for B mesons see Section 16.6.

Section 10.1; there are many different conventions in the literature. For consistency with B Factory papers we follow the notation of Aubert (2004f).

The quantity q/p (Eq. 10.1.3) is given by

$$\frac{q}{p} \equiv \sqrt{\frac{M_{12}^* - \frac{i}{2}\Gamma_{12}^*}{M_{12} - \frac{i}{2}\Gamma_{12}}}. \tag{17.5.33}$$

Its magnitude is expected to be very close to unity:

$$\left|\frac{q}{p}\right|^2 \approx 1 - \mathrm{Im}\left(\frac{\Gamma_{12}}{M_{12}}\right). \tag{17.5.34}$$

If $|q/p| - 1$ differs from zero, CP and T symmetries are broken, but CPT symmetry can still hold. In the Standard Model, $|q/p| - 1$ is small because $|\Gamma_{12}| \ll |M_{12}|$ and because $\mathrm{Im}(\Gamma_{12}/M_{12})$ is suppressed with respect to $|\Gamma_{12}/M_{12}|$. The size of this suppression is $(m_c^2 - m_u^2)/m_b^2 \approx 0.1$. The suppression reflects the fact that CP violation is not possible if two of the quark masses are identical. In that case one could redefine the quark states such that one of them does not mix with the other two, and mixing between two quark generations is insufficient to allow for CP violation. The phase of q/p is convention-dependent and unobservable.[61] Therefore, the physics of $\mathcal{H}_{\rm eff}$ is determined by only seven real parameters.

To allow for CPT-violating effects in mixing, we introduce the complex parameter

$$z \equiv \frac{\delta m - \frac{i}{2}\delta\Gamma}{\Delta m - \frac{i}{2}\Delta\Gamma}, \tag{17.5.35}$$

where $\delta m \equiv M_{11} - M_{22}$ and $\delta\Gamma \equiv \Gamma_{11} - \Gamma_{22}$ are the differences of the diagonal terms of $\mathcal{H}_{\rm eff}$. If $z \neq 0$ CP and CPT symmetries are broken, but T symmetry can be conserved. In the Standard Model, z is zero.[62]

With these definitions, the mass eigenstates of Eq. (10.1.2) are replaced by

$$|B_{1,2}\rangle = p\sqrt{1 \mp z}\,\left|B^0\right\rangle \pm q\sqrt{1 \pm z}\,\left|\overline{B}^0\right\rangle, \tag{17.5.36}$$

and the time-evolved states given in Eq. (10.1.6) are replaced by

$$\begin{aligned}
|B^0(t)\rangle &= [f_+(t) + z f_-(t)]\left|B^0\right\rangle + \sqrt{1-z^2}\frac{q}{p} f_-(t)\left|\overline{B}^0\right\rangle, \\
|\overline{B}^0(t)\rangle &= [f_+(t) - z f_-(t)]\left|\overline{B}^0\right\rangle + \sqrt{1-z^2}\frac{p}{q} f_-(t)\left|B^0\right\rangle,
\end{aligned} \tag{17.5.37}$$

where the functions $f_\pm(t)$ are defined in Eq. (10.1.7). In Section 17.5.2.6, Eq. (17.5.26), we have already introduced a non-zero $\Delta\Gamma_d$ in the time-dependent decay rate of B meson pairs from $\Upsilon(4S)$ decays. We extend this expression to include the CP, T, and CPT-violating parameters defined above:

$$\begin{aligned}
N(\Delta t) \propto e^{-\Gamma|\Delta t|} \times & \\
&\left\{\frac{1}{2}c_+ \cosh(\Delta\Gamma_d \Delta t/2) + \frac{1}{2}c_- \cos(\Delta m_d \Delta t)\right. \\
&\left. -\mathrm{Re}(s)\sinh(\Delta\Gamma_d\Delta t/2) + \mathrm{Im}(s)\sin(\Delta m_d \Delta t)\right\},
\end{aligned} \tag{17.5.38}$$

where

$$c_\pm = |a_+|^2 \pm |a_-|^2, \quad s = a_+^* a_-. \tag{17.5.39}$$

The complex expressions $a_\pm$ depend on the decay amplitudes for a set of specific final states of $B_{\rm tag}$ and $B_{\rm rec}$ and on the symmetry-violating parameters q/p and z:

$$\begin{aligned}
a_+ &= -A_{\rm tag}\overline{A}_{\rm rec} + \overline{A}_{\rm tag}A_{\rm rec}, \\
a_- &= \sqrt{1-z^2}\left[\frac{p}{q}A_{\rm tag}A_{\rm rec} - \frac{q}{p}\overline{A}_{\rm tag}\overline{A}_{\rm rec}\right] \\
&\quad + z\left[A_{\rm tag}\overline{A}_{\rm rec} + \overline{A}_{\rm tag}A_{\rm rec}\right].
\end{aligned} \tag{17.5.40}$$

The amplitudes $A_{\rm tag}$ ($A_{\rm rec}$) and $\overline{A}_{\rm tag}$ ($\overline{A}_{\rm rec}$) represent the cases where $B_{\rm tag}$ ($B_{\rm rec}$) is reconstructed, respectively, as a B^0 or a $\overline{B}^0$.

We can write Eq. (17.5.38) explicitly for the cases where the flavors of the two B mesons from a $\Upsilon(4S)$ decay are reconstructed as B^0B^0, $\overline{B}^0\overline{B}^0$, or $B^0\overline{B}^0$:[63]

$$N^{BB} \propto \frac{e^{-|\Delta t|/\tau}}{2}\left|\frac{p}{q}\right|^2\left\{\cosh\left(\frac{\Delta\Gamma\Delta t}{2}\right) - \cos(\Delta m_d \Delta t)\right\}$$

$$N^{\overline{B}\overline{B}} \propto \frac{e^{-|\Delta t|/\tau}}{2}\left|\frac{q}{p}\right|^2\left\{\cosh\left(\frac{\Delta\Gamma\Delta t}{2}\right) - \cos(\Delta m_d \Delta t)\right\}$$

$$N^{B\overline{B}} \propto \frac{e^{-|\Delta t|/\tau}}{2}\left\{\cosh\left(\frac{\Delta\Gamma\Delta t}{2}\right) + 2\mathrm{Re}(z)\sinh\left(\frac{\Delta\Gamma\Delta t}{2}\right)\right.$$

[61] In addition, different conventions for the sign of the phase of q/p are used in the literature. Here we set the phase of q/p using Eqs (10.1.3) and (17.5.33). The convention in Aubert (2004f) differs by $e^{i\pi} = -1$. As a result their Eqs (9) and (10) have a negative sign in front of the $\sqrt{1-z^2}$ term relative to our Eq. (17.5.37). The same comment applies to Eq. (12.30) of the 2013 PDG review on CP violation in meson decays (Beringer et al., 2012), where the phase of q/p is not explicitly stated. Our expressions otherwise agree with those of Aubert (2004f).

[62] In Hastings (2003), Belle uses a different parameterization, following Mohapatra, Satpathy, Abe, and Sakai (1998), based on complex parameters θ and ϕ. The relationship between these and several other notations is discussed by Kostelecký (2001): in particular, $\cos\theta = -z = \xi$, and $|\exp(i\phi)| = |q/p| = w$, where ξ (complex) and w (real) are the parameters preferred by Kostelecký. While we rely heavily on this and related references in the Lorentz-violation discussion below (Section 17.5.5), we use the notation of Eq. (17.5.35) throughout. In neutral kaon mixing, CPT violation is described by $\delta_K = -z/2$.

[63] In Eqs (17.5.41)–(17.5.43) we assume that the B transition to a flavor eigenstate f has a single weak amplitude A_f and that the B decay does not violate CPT symmetry, *i.e.* $A_f = \overline{A}_{\overline{f}}$. We also assume that the amplitude for the B decay to the CP conjugate final state is zero, *i.e.* $A_{\overline{f}} = \overline{A}_f = 0$.

$$+\cos(\Delta m_d\Delta t) - 2\mathrm{Im}(z)\sin(\Delta m_d\Delta t)\Bigg\}; \quad (17.5.41)$$

here we have ignored terms quadratic in z. The first (second) B in the superscript denotes the flavor of $B_{\rm tag}$ ($B_{\rm rec}$).

If one of the B mesons decays through a $b \to (c\bar{c})s$ transition to a CP eigenstate B_{CP} such as $J/\psi K^0_S$ or $J/\psi K^0_L$, and the other B meson decays to a flavor state (B^0 or $\overline{B}^0$), the time-dependent decay rates are given by

$$\begin{aligned} N^{BB_{CP}} \propto{}& \frac{e^{-|\Delta t|/\tau}}{2} \times \\ &\Bigg\{ [1 \mp \mathrm{Re}(z)\cos 2\phi_1 \mp \mathrm{Im}(z)\sin 2\phi_1]\cosh\left(\frac{\Delta\Gamma_d\Delta t}{2}\right) \\ &+ [\pm\mathrm{Re}(z)\cos 2\phi_1 \pm \mathrm{Im}(z)\sin 2\phi_1]\cos(\Delta m_d\Delta t) \\ &+ [\mp\cos 2\phi_1 + \mathrm{Re}(z)]\sinh\left(\frac{\Delta\Gamma_d\Delta t}{2}\right) \\ &+ [\pm\sin 2\phi_1 - \mathrm{Im}(z)]\sin(\Delta m_d\Delta t)\Bigg\}, \end{aligned} \quad (17.5.42)$$

$$\begin{aligned} N^{\overline{B}B_{CP}} \propto{}& \frac{e^{-|\Delta t|/\tau}}{2} \times \\ &\Bigg\{ [1 \pm \mathrm{Re}(z)\cos 2\phi_1 \mp \mathrm{Im}(z)\sin 2\phi_1]\cosh\left(\frac{\Delta\Gamma_d\Delta t}{2}\right) \\ &+ [\mp\mathrm{Re}(z)\cos 2\phi_1 \pm \mathrm{Im}(z)\sin 2\phi_1]\cos(\Delta m_d\Delta t) \\ &+ [\mp\cos 2\phi_1 - \mathrm{Re}(z)]\sinh\left(\frac{\Delta\Gamma_d\Delta t}{2}\right) \\ &+ [\mp\sin 2\phi_1 + \mathrm{Im}(z)]\sin(\Delta m_d\Delta t)\Bigg\}, \end{aligned} \quad (17.5.43)$$

where the upper (lower) sign in front of terms with $\cos 2\phi_1$ or $\sin 2\phi_1$ represents final states with $\eta_{CP} = -1$ $(+1)$. In Eqs (17.5.42) and (17.5.43), we assume $|q/p| = 1$.

The decay rates defined in Eqs (17.5.41)–(17.5.43) can be used to construct asymmetries sensitive to T, CP, and CPT violation. The *same-flavor* asymmetry $A_{T/CP}$ between the two oscillation probabilities $P(\overline{B}^0 \to B^0)$ and $P(B^0 \to \overline{B}^0)$ depends on $|q/p|$ and probes both T and CP symmetries:

$$\begin{aligned} A_{T/CP} &= \frac{P(\overline{B}^0 \to B^0) - P(B^0 \to \overline{B}^0)}{P(\overline{B}^0 \to B^0) + P(B^0 \to \overline{B}^0)} \\ &= \frac{N^{BB} - N^{\overline{B}\overline{B}}}{N^{BB} + N^{\overline{B}\overline{B}}} \\ &= \frac{1 - |q/p|^4}{1 + |q/p|^4}. \end{aligned} \quad (17.5.44)$$

The *opposite-flavor* asymmetry, $A_{CPT/CP}$, depends on z and probes both CP and CPT symmetries. Defining the decay-time difference for such events as $\Delta t = t^+ - t^-$, where t^+ (t^-) corresponds to B^0 ($\overline{B}^0$), the asymmetry

$$\begin{aligned} &A_{CPT/CP}(\Delta t;\, \Delta t > 0) \\ &= \frac{P(B^0 \to B^0) - P(\overline{B}^0 \to \overline{B}^0)}{P(B^0 \to B^0) + P(\overline{B}^0 \to \overline{B}^0)} \\ &= \frac{N^{B\overline{B}}(\Delta t) - N^{B\overline{B}}(-\Delta t)}{N^{B\overline{B}}(\Delta t) + N^{B\overline{B}}(-\Delta t)} \\ &\simeq 2\frac{\mathrm{Im}(z)\sin(\Delta m_d\Delta t) - \mathrm{Re}(z)\sinh(\Delta\Gamma_d\Delta t/2)}{\cos(\Delta m_d\Delta t) + \cosh(\Delta\Gamma_d\Delta t/2)} \\ &\simeq \frac{2\mathrm{Im}(z)\sin(\Delta m_d\Delta t) - \mathrm{Re}(z)\Delta\Gamma_d\Delta t}{\cos(\Delta m_d\Delta t) + \cosh(\Delta\Gamma_d\Delta t/2)}, \end{aligned} \quad (17.5.45)$$

where the approximation in the third line is the neglect of terms of higher order in z; in the fourth line, as $|\Delta\Gamma_d/\Gamma| \ll 1$, we take $\sinh(\Delta\Gamma_d\Delta t/2) \simeq \Delta\Gamma_d\Delta t/2$.

By comparing the rates of a B versus a $\overline{B}$ decaying to a CP eigenstate, we can define another asymmetry that is sensitive to z using Equations (17.5.42) and (17.5.43):

$$\begin{aligned} A'_{CPT/CP}(\Delta t) &= \frac{P(\overline{B}^0 \to B_{CP}) - P(B^0 \to B_{CP})}{P(\overline{B}^0 \to B_{CP}) + P(B^0 \to B_{CP})} \\ &= \frac{N^{BB_{CP}}(\Delta t) - N^{\overline{B}B_{CP}}(\Delta t)}{N^{BB_{CP}}(\Delta t) + N^{\overline{B}B_{CP}}(\Delta t)} \\ &\simeq \{\pm\mathrm{Re}(z)\cos 2\phi_1[-1 + \cos(\Delta m_d\Delta t)] \\ &\quad + [\pm\sin 2\phi_1 - 2\mathrm{Im}(z)]\sin(\Delta m_d\Delta t)\}/ \\ &\quad \{1 \pm \mathrm{Im}(z)\sin 2\phi_1[-1 + \cos(\Delta m_d\Delta t)] \\ &\quad \mp \cos 2\phi_1\Delta\Gamma_d\Delta t/2\}. \end{aligned} \quad (17.5.46)$$

In the last step we have again neglected terms of higher than linear order in z and $\Delta\Gamma_d$, and the upper (lower) sign in front of terms with $\cos 2\phi_1$ or $\sin 2\phi_1$ refers to final states with $\eta_{CP} = -1$ $(+1)$.

In the expressions of the decay rates (Eqs 17.5.41–17.5.43) and associated asymmetries (Eqs 17.5.44–17.5.46) we have assumed that a B flavor state can unambiguously be identified by its decay products. In the quark model, this is true for semi-leptonic decays. For hadronic B decays to flavor final states, however, the presence of doubly-CKM-suppressed decays (DCS) makes it impossible to determine the original flavor of the B meson without ambiguity. Accounting for DCS decays leads to more complicated expressions for $c_\pm$, s, and the resulting decay rates and asymmetries. A complete list of general expressions of $c_\pm$ and s can be found in Aubert (2004f).

In the SM the asymmetry $A_{T/CP}$ is expected to be very small (Beneke, Buchalla, Lenz, and Nierste, 2003; Ciuchini, Franco, Lubicz, Mescia, and Tarantino, 2003). A recent calculation predicts $A_{T/CP} = (-0.40 \pm 0.06) \times 10^{-3}$ or correspondingly $|q/p| - 1 = (0.20 \pm 0.03) \times 10^{-3}$ (Nierste, 2012). A measurement significantly different from zero with the data samples of the B Factories would be evidence for new physics. In the Standard Model CPT symmetry is conserved and $\mathrm{Re}(z)$ and $\mathrm{Im}(z)$ as well as $A_{CPT/CP}$ are expected to be zero. The asymmetry $A'_{CPT/CP}$ reduces to the CP-violating, but CPT-conserving asymmetry, $-\eta_{CP}\sin 2\phi_1\sin(\Delta m_d\Delta t)$. It is a measurement of mixing-induced CP violation.

17.5.4.2 Results on CP, T and CPT violation in $B^0 - \overline{B}^0$ mixing

BABAR and Belle published several papers on searches for violation of T, CP, and CPT symmetries in $B^0 - \overline{B}^0$ mixing. The analyses are performed with inclusive dilepton final states or fully-reconstructed hadronic and semileptonic final states. Here we review the measurements of $|q/p| - 1$, Re(z), and Im(z).

Measurements of $|q/p| - 1$

Earlier measurements of the asymmetry $A_{T/CP}$ have been performed by CLEO (Behrens et al., 2000; Jaffe et al., 2001), ALEPH (Barate et al., 2001), and OPAL (Abbiendi et al., 2000b; Ackerstaff et al., 1997a) before the B Factories took their data. In the 2002 Review of Particle Physics (Hagiwara et al., 2002) the PDG calculated an average[64] of $A_{T/CP} = (0 \pm 16) \times 10^{-3}$ corresponding to a value of $|q/p| - 1 = (0 \pm 8) \times 10^{-3}$.

BABAR and Belle both measure $|q/p| - 1$ with inclusive samples of semileptonic B^0 decays. In these events only the two leptons from semileptonic decays $B \to Xl\nu$ ($l = e, \mu$) are reconstructed. The charge of the lepton l^+ (l^-) unambiguously identifies the flavor of the parent B meson to be a B^0 ($\overline{B}^0$). The asymmetry between the numbers of same-sign dilepton pairs, $N^{BB} = N(l^+l^+)$ and $N^{\overline{B}\overline{B}} = N(l^-l^-)$, is related to the two oscillation probabilities $P(\overline{B}^0 \to B^0)$ and $P(B^0 \to \overline{B}^0)$ as given in Eq. (17.5.44). Although $A_{T/CP}$ is a time-independent asymmetry, both experiments use the decay time difference Δt between the two B decays to discriminate signal events from background.

BABAR and Belle measure $|q/p|-1$ in samples of 211 fb^{-1} (Aubert, 2006aq) and 78 fb^{-1} (Nakano, 2006), respectively. The *BABAR* result supersedes an earlier measurement with 21 fb^{-1} (Aubert, 2002i). The event selections in these analyses are similar to the ones for measurements of Δm_d with dilepton events described above (see Section 17.5.2.2), but with attention to keeping charge-dependent asymmetries in reconstruction and PID efficiencies small and under control. Events with two identified leptons in a momentum range (0.8 GeV/c (*BABAR*) or 1.2 GeV/c (Belle) $< p^* <$ 2.3 GeV/c) and with topology consistent with that of semileptonic B decays are selected. Leptons that originate from photon conversions in the detector or from J/ψ and $\psi(2S)$ decays are explicitly vetoed. Both experiments carefully determine detector-induced charge asymmetries in their lepton identification (Chapter 5). *BABAR* uses a control sample of radiative Bhabha events and Belle uses two photon production of e^+e^- to study electron ID asymmetries. The charge asymmetry in muon ID is determined with $e^+e^- \to \mu^+\mu^-\gamma$ events by *BABAR* and with events in which a simulated muon track is embedded in a hadronic event by Belle. Hadron fake rates are determined with pions from $K^0_S \to \pi^+\pi^-$, kaons from $D^{*+} \to D^0\pi^+_s \to (K^-\pi^+)\pi^+_s$ (*BABAR*) and from $\phi \to K^+K^-$ (Belle), and protons from $\Lambda \to p\pi^-$. The distance between the two B decay vertices Δz is measured as described in Section 17.5.2.2. *BABAR* fits the Δt distributions of the l^+l^+ and l^-l^- events and randomly assigns the sign of Δt for each event. Belle fits the $\Delta z = z_1 - z_2$ distribution, where z_1 (z_2) is the z coordinate of the higher- (lower-) momentum lepton. The majority of the events are events where both leptons originate from a B decay. *BABAR* distinguishes background from events in which one lepton is a primary lepton from a B decay and the other lepton comes from a secondary charm decay ($b \to c \to l$), events with one direct lepton and one lepton from a tau ($b \to \tau \to l$) or charmonium ($b \to (c\overline{c}) \to l$) cascade decay, and events from the light quark $e^+e^- \to q\overline{q}$ continuum. Belle subtracts the contribution from light quark continuum candidates to their dilepton sample. The background events from $B\overline{B}$ decays are separated into correctly tagged and wrongly tagged events. The wrongly tagged sample is dominated by events where one lepton is from a primary B decay and the other one from a cascade charm decay. The correctly tagged background sample consists mainly of events in which both leptons come from secondary charm decays. *BABAR* extracts $|q/p|-1$ from a binned likelihood fit to the Δt distribution of the selected dilepton sample.[65] The likelihood function

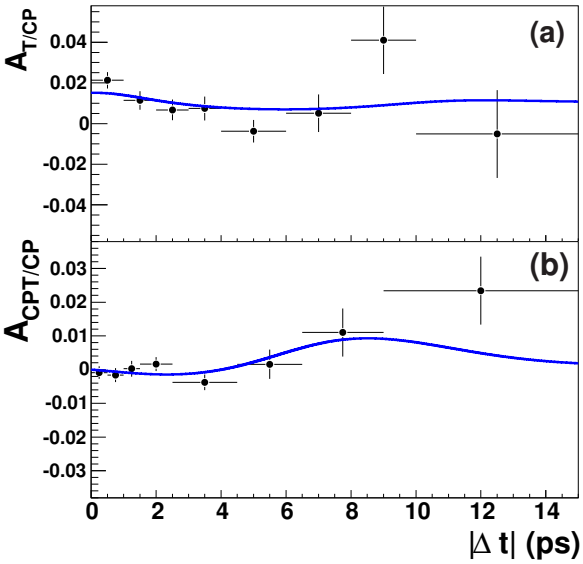

Figure 17.5.10. The measured asymmetries (a) $A_{T/CP}$ and (b) $A_{CPT/CP}$ from inclusive dilepton events, as functions of $|\Delta t|$ (Aubert, 2006aq). The deviation from zero in $A_{T/CP}$ is a result of background from cascade muons that is dominant at small $|\Delta t|$.

[64] The PDG quotes $\mathrm{Re}(\epsilon_B)/(1+|\epsilon_B|^2) = (0\pm4)\times10^{-3}$, where $\epsilon_B = (p-q)/(p+q)$ corresponds to the parameter ϵ_K describing the corresponding asymmetry in the neutral kaon system and $A_{T/CP} \approx 4\mathrm{Re}(\epsilon_B)/(1+|\epsilon_B|^2)$ for small $A_{T/CP}$.

[65] In the same analysis *BABAR* measures the CP- and CPT-violating parameter z (see below). They employ a simultaneous

combines detector-related charge asymmetries and time-dependent *p.d.f.*s for signal and background events. The measured asymmetry $A_{T/CP}$ as a function of $|\Delta t|$ is shown in Fig. 17.5.10. Belle determines a raw dilepton asymmetry from their selected events as a function of Δz, applies a bin-wise background correction, and calculates an average $A_{T/CP}$ in a range $0.15\,\text{mm} < |\Delta z| < 2\,\text{mm}$. *BABAR* measures $|q/p| - 1 = (-0.8 \pm 2.7 \pm 1.9) \times 10^{-3}$ and Belle measures $A_{T/CP} = (-1.1 \pm 7.9 \pm 8.5) \times 10^{-3}$, which corresponds to $|q/p| - 1 = (0.5 \pm 4.0 \pm 4.3) \times 10^{-3}$. The largest contributions to the systematic error in the *BABAR* measurement come from potential charge asymmetries in track reconstruction (1.0×10^{-3}) and electron identification (1.0×10^{-3}). Belle's systematic error in $|q/p| - 1$ is dominated by potential charge asymmetries in the track finding efficiency (2.6×10^{-3}) and uncertainties in the continuum background subtraction (2.4×10^{-3}).

BABAR also measures $|q/p| - 1$ in an analysis of fully-reconstructed B decays to hadronic final states in a sample of 88×10^6 $B\overline{B}$ pairs (Aubert, 2004e,f). One B is reconstructed either in a flavor state or a *CP* eigenstate. In the same analysis *BABAR* measures $\Delta\Gamma_d$ (Section 17.5.2.6) and the *CP* and *CPT*-violating parameters $\text{Re}(z)$ and $\text{Im}(z)$ (Section 17.5.4.2) from the Δt distributions of the selected events. The sensitivity to $|q/p| - 1$ comes from events in which both B mesons have the same flavor. Because the branching fractions to exclusive flavor states are much smaller than the inclusive semileptonic branching fraction, the signal sample is comparatively small compared to event samples in the dilepton analyses. From the analysis of fully-reconstructed hadronic final states *BABAR* quotes $|q/p| - 1 = (29 \pm 13 \pm 11) \times 10^{-3}$.

The average of the measurements of $|q/p| - 1$ published by the B Factories is $(0.3 \pm 2.8) \times 10^{-3}$ (see Table 17.5.3). While we were finishing the writing of this Book, *BABAR* submitted another measurement of $|q/p| - 1$ for publication (Lees, 2013g). In that analysis one B meson is reconstructed as $B^0 \to D^{*-} l^+ \nu_l$ (and the D^{*-} is partially-reconstructed using only the slow pion) and the flavor of the other is tagged with a charged kaon. The value of $|q/p| - 1 = (0.29 \pm 0.84^{+1.88}_{-1.61}) \times 10^{-3}$ measured in this analysis represents the most precise single measurement of $|q/p| - 1$ by the B Factories. However, due to the overlap of events used in this analysis with those used for the $|q/p| - 1$ measurement in Aubert (2006aq), a simple average could not be calculated for this Book. The PDG in their 2013 partial update of the Review of Particle Physics quotes a world average of $\text{Re}(\epsilon_B^0)/(1 + |\epsilon_B^0|^2 = (0.6 \pm 0.7) \times 10^{-3}$ corresponding to $|q/p| - 1 = (-1.2 \pm 1.4) \times 10^{-3}$ (Beringer et al., 2012), which includes two recent measurements from DØ corresponding to $|q/p| - 1 = (0.6 \pm 2.6) \times 10^{-3}$ (Abazov et al., 2011) and $|q/p| - 1 = (-3.4 \pm 2.2 \pm 0.8) \times 10^{-3}$ (Abazov et al., 2012).

There has been significant interest in the measurement of $|q/p|$ or the corresponding asymmetry $A_{T/CP}$ since DØ announced evidence for an anomalous like-sign dimuon charge asymmetry in $p\overline{p}$ collisions (Abazov et al., 2010a,b). The asymmetry A^b_{sl} is defined similarly to Eq. (17.5.44), but has contributions from the charge asymmetries of B^0_d mesons ($A_{T/CP}$) and B^0_s mesons ($A^s_{T/CP}$):

$$A^b_{\text{sl}} = C_d A_{T/CP} + C_s A^s_{T/CP} \tag{17.5.47}$$

with $C_d = 0.594 \pm 0.022$, $C_s = 0.406 \pm 0.022$ (Abazov et al., 2011). With their latest measurement of $A^b_{\text{sl}} = (-7.87 \pm 1.72 \pm 0.93) \times 10^{-3}$ DØ claims a 3.9σ discrepancy with the Standard Model prediction of $A^b_{\text{sl}}(\text{SM}) = (-0.28^{+0.05}_{-0.06}) \times 10^{-3}$ (Abazov et al., 2011). However, no significant measurement has yet been observed in either $A_{T/CP}$ or $A^s_{T/CP}$. The world average for $|q/p| - 1$ corresponds to $A_{T/CP} = (2.4 \pm 2.8) \times 10^{-3}$. Based on two DØ measurements HFAG calculates the corresponding average for B^0_s mesons of $A^s_{T/CP} = (-11 \pm 6) \times 10^{-3}$ (Amhis et al., 2012). It is important to improve the measurements of $A_{T/CP}$ or $A^s_{T/CP}$ to understand if there is *CP* and *T* violation in the mixing of B^0_d or B^0_s mesons or both. LHCb is expected to improve the measurement of $A^s_{T/CP}$ in the near future. The B Factories have only analyzed fractions of their full datasets for $|q/p|$. Some improvement in $A_{T/CP}$ will be possible by using more data, but systematic uncertainties are already of comparable size to the statistical errors. LHCb may be able to reduce the error in $A_{T/CP}$ using fully-reconstructed semileptonic B^0 decays similar to the DØ analysis described in (Abazov et al., 2012). The large data set of a future super flavor factory paired with analyses of fully-reconstructed semi-leptonic decays could substantially reduce the overall uncertainty in $A_{T/CP}$.

Table 17.5.3. B Factory measurements of $|q/p| - 1$ along with the journal paper and selected final state for each measurement. The measurement in Aubert (2002i) has been superseded by Aubert (2006aq) and is not included in the B Factories average.

Experiment	Method	$\lvert q/p\rvert - 1$ [10^{-3}]
BABAR (Aubert, 2006aq)	Incl. dilepton	$-0.8 \pm 2.7 \pm 1.9$
BABAR (Aubert, 2002i)	Incl. dilepton	$-2 \pm 6 \pm 7$
BABAR (Aubert, 2004e,f)	Hadr. modes	$29 \pm 13 \pm 11$
Belle (Nakano, 2006)	Incl. dilepton	$0.5 \pm 4.0 \pm 4.3$
BABAR-Belle average		0.3 ± 2.8

Measurements of $\text{Re}(z)$ *and* $\text{Im}(z)$

Prior to the B Factories a search for *CPT* violation in $B^0 - \overline{B}^0$ mixing was performed by the OPAL collaboration (Ackerstaff et al., 1997a). They quote their result in terms of the *CPT* parameter δ_B, a variable with a definition equivalent to δ_K, which is used to characterize *CPT* violation in kaon mixing (Beringer et al., 2012). OPAL's result $\text{Im}(\delta_B) = -0.020 \pm 0.016 \pm 0.006$ corresponds to

fit to both same-sign and opposite-sign dilepton pairs to determine the Δt resolution in addition to the symmetry-violating parameters.

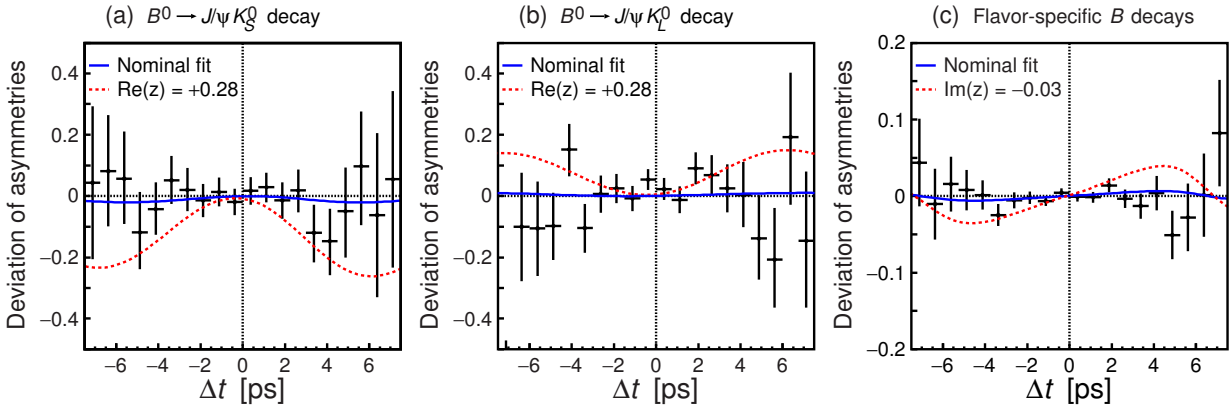

Figure 17.5.11. Deviations of the asymmetries from the reference asymmetry [$\mathrm{Re}(z) = \mathrm{Im}(z) = \Delta\Gamma_d/\Gamma_d = 0$] in fully-reconstructed hadronic and semileptonic final states (Higuchi, 2012). Shown are raw asymmetries uncorrected for backgrounds, flavor mis-tagging, and Δt resolution. The underlying asymmetries for (a) and (b) corresponding to $\eta_{CP} = -1$ and $+1$, respectively, are given by Eq. (17.5.46). The asymmetry tested in (c) is given in Eq. (17.5.45). The crosses with error bars are data. The solid curves are deviations for the nominal fits. The dashed curves are for illustration only: they represent scenarios where either $\mathrm{Re}(z) = +0.28$ or $\mathrm{Im}(z) = -0.03$. These values are equal to approximately 5× the total uncertainty of the corresponding parameter.

$\mathrm{Im}(z) = 0.040 \pm 0.032 \pm 0.012$. The world averages for the real and imaginary parts of δ_K determined from kaon experiments are $\mathrm{Re}(\delta_K) = (2.5 \pm 2.3) \times 10^{-4}$ and $\mathrm{Im}(\delta_K) = (-1.5 \pm 1.6) \times 10^{-5}$ (Beringer et al., 2012). The corresponding limit on the mass difference between K^0 and $\overline{K}^0$ normalized to the mass average is $|m_{K^0} - m_{\overline{K}^0}|/m_{\mathrm{average}} < 6 \times 10^{-19}$, assuming $\Gamma_{K^0} = \Gamma_{\overline{K}^0}$.

BABAR and Belle have studied samples of inclusive dilepton events and fully-reconstructed hadronic and semileptonic events to measure $\mathrm{Re}(z)$ and $\mathrm{Im}(z)$ in $B^0 - \overline{B}^0$ mixing. In dilepton events the Δt distribution of opposite-sign dilepton pairs has been used to search for violation of *CP* and *CPT* asymmetry. The asymmetry $A_{CP/CPT}$ between events with positive and negative *true* Δt is related to the two oscillation probabilities $P(B^0 \to B^0)$ and $P(\overline{B}^0 \to \overline{B}^0)$ as given in Eq. (17.5.45). Here the decay-time difference is defined as $\Delta t = t^+ - t^-$, where t^+ (t^-) corresponds to l^+ (l^-).

BABAR measures the *CP*- and *CPT*-violating parameters $\mathrm{Re}(z)$ and $\mathrm{Im}(z)$ with opposite-sign dilepton pairs in a sample of $211\,\mathrm{fb}^{-1}$ (Aubert, 2006aq). The selection criteria are the same as for the measurement of $|q/p| - 1$ with same-sign dilepton pairs in the same paper (see above). The parameter $\mathrm{Im}(z)$ appears as coefficient to the $\sin(\Delta m_d \Delta t)$ term in the Δt distribution of opposite-sign dilepton pairs $N^{B\overline{B}}$ given by Eq. (17.5.41) and the corresponding asymmetry $A_{CPT/CP}$ of Eq. (17.5.45). Thus a measurement of the shape of the Δt distribution is sensitive to $\mathrm{Im}(z)$. On the other hand, sensitivity to $\mathrm{Re}(z)$ only comes from the $\sinh(\Delta\Gamma_d \Delta t/2)$ term. Since $\Delta\Gamma_d$ is a small quantity and has not been measured, *BABAR* substitutes $\sinh(\Delta\Gamma_d \Delta t/2) \simeq \Delta\Gamma_d \Delta t/2$ and quotes only the product $\Delta\Gamma_d \times \mathrm{Re}(z)$ in their paper. In the $\cosh(\Delta\Gamma_d \Delta t/2)$ term they use $|\Delta\Gamma_d| = (5 \pm 3) \times 10^{-3}\,\mathrm{ps}^{-1}$. Although *BABAR* fits the Δt distributions of the same-sign and opposite-sign dilepton pairs in a single fit, they do not constrain the ratio between the numbers of events of the two types. *BABAR* quotes $\mathrm{Im}(z) = (-13.9 \pm 7.3 \pm 3.2) \times 10^{-3}$ and $\Delta\Gamma_d \times \mathrm{Re}(z) = (-7.1 \pm 3.9 \pm 2.0) \times 10^{-3}\,\mathrm{ps}^{-1}$. The statistical correlation between the measurements of $\mathrm{Im}(z)$ and $\Delta\Gamma_d \times \mathrm{Re}(z)$ is 76%. The systematic errors in $\mathrm{Im}(z)$ and $\Delta\Gamma_d \times \mathrm{Re}(z)$ are dominated by uncertainties in the *p.d.f.* modeling (2.5× and 1.2×10^{-3}), the external parameters τ_{B^0}, τ_{B^-}, Δm_d, and $\Delta\Gamma_d$ (1.9× and 1.1×10^{-3}) and SVT alignment (0.6× and 1.2×10^{-3}). Assuming $\Delta\Gamma_d = 0$, *BABAR* obtains $\mathrm{Im}(z) = (-3.7 \pm 4.6 \pm 2.9) \times 10^{-3}$. The measured asymmetry $A_{T/CP}$ as a function of $|\Delta t|$ is shown in Fig. 17.5.10.

Belle's results on $\mathrm{Re}(z)$ and $\mathrm{Im}(z)$ with $29.4\,\mathrm{fb}^{-1}$ of data are published in Hastings (2003). The analysis uses the same selection criteria as in their measurement of Δm_d with dilepton pairs (see Section 17.5.2.2) that is described in the same paper. A major difference to the *BABAR* analysis is that Belle constrains the time-integrated fractions of same-sign and opposite sign events to

$$\chi_d = \frac{|1 - z^2|x_d^2}{|1 - z^2|x_d^2 + 2 + x_d^2 + |z|^2 x_d^2}, \qquad (17.5.48)$$

where $x_d = \tau_{B^0} \Delta m_d$. $N^{B\overline{B}}$ (N^{BB}, $N^{\overline{B}\overline{B}}$) is proportional to opposite-sign (same-sign) dilepton efficiency. Belle determines the ratio of the efficiencies from MC simulation. They quote $\mathrm{Re}(z) = (0 \pm 12 \pm 1) \times 10^{-2}$ and $\mathrm{Im}(z) = (-3 \pm 1 \pm 3) \times 10^{-2}$. These measurements supersede the results from an earlier Belle paper (Abe, 2001b). The dominant systematic uncertainties in $\mathrm{Im}(z)$ come from data/MC agreement of the Δt *p.d.f.* and the requirement that the polar angle of the lepton tracks be in the fiducial volume. The largest contribution to the systematic error in $\mathrm{Re}(z)$ comes from the MC-modeling of the Δt resolution.

Table 17.5.4. Measurements of $\mathrm{Re}(z)$ and $\mathrm{Im}(z)$ and, if given in the paper, the corresponding limits (at 90% C.L.) on the mass difference and width difference between B^0 and $\overline{B}^0$. In Aubert (2006aq), *BABAR* measures $\Delta\Gamma_d \times \mathrm{Re}(z) = (-0.71 \pm 0.39 \pm 0.20) \times 10^{-2}$ ps^{-1}, but does not quote a value for $\mathrm{Re}(z)$.

Experiment	Method	$\mathrm{Re}(z)$ $[10^{-2}]$	$\mathrm{Im}(z)$ $[10^{-2}]$	$\lvert\delta m/m\rvert$ $[10^{-14}]$	$\delta\Gamma/\Gamma$
BABAR (Aubert, 2006aq)	Incl. dilepton	—	$-1.39 \pm 0.73 \pm 0.32$	—	—
Belle (Hastings, 2003)	Incl. dilepton	$0.0 \pm 12 \pm 1$	$-3 \pm 1 \pm 3$	< 1.16	$\lvert\delta\Gamma/\Gamma\rvert < 0.11$
Belle (Abe, 2001b)	Incl. dilepton	$0 \pm 15 \pm 6$	$-3.5 \pm 2.9 \pm 5.1$	< 1.6	$\lvert\delta\Gamma/\Gamma\rvert < 0.161$
BABAR (Aubert, 2004e,f)	Hadronic	$2.0 \pm 5.1 \pm 4.9$	$3.8 \pm 2.9 \pm 2.5$	< 1.0	$-0.156 < \delta\Gamma/\Gamma < 0.042$
Belle (Higuchi, 2012)	Hadr. + semilep.	$1.9 \pm 3.7 \pm 3.3$	$-0.57 \pm 0.33 \pm 0.33$	—	—

BABAR and Belle also measure $\mathrm{Im}(z)$ and $\mathrm{Re}(z)$ in samples of fully-reconstructed hadronic and semi-leptonic final states. *BABAR* reconstructs B^0 decays to the flavor final states $D^{(*)-}\pi^+/\rho^+/a_1^+$ and $J/\psi K^{*0}$ and *CP*-eigenstates $J/\psi K_S^0$, $\psi(2S)K_S^0$, $\chi_{c1}K_S^0$, and $J/\psi K_L^0$ in 88 million $B\overline{B}$ events (Aubert, 2004e,f). Belle reconstructs signal events in the decays $B^0 \to D^{(*)-}\pi^+$, $D^{*-}\rho^+$, $D^{*-}l\nu$, $J/\psi K_S^0$, and $J/\psi K_L^0$ in a sample of 535 million $B\overline{B}$ events (Higuchi, 2012). Raw asymmetries as function of Δt for $J/\psi K_S^0$, $J/\psi K_L^0$ and flavor-specific final states overlaid with curves representing the nominal fit result and scenarios with significant *CPT* violation are shown in Fig. 17.5.11. In addition to z both analyses also measure $\Delta\Gamma_d$ and $|q/p|-1$. These results are described above. The measurements use the Δt reconstruction and flavor tagging methods of the standard time-dependent analyses of the B Factories described in earlier Chapters (6, 8, 10). The time-dependent *p.d.f.*s for events to final states that contain a fully-reconstructed B_{rec} identified either as B^0, $\overline{B}^0$, or B_{CP} , and a B_{tag} with identified flavor as B^0 or $\overline{B}^0$ are given in Eqs (17.5.42) and (17.5.43). However, interference effects between the amplitudes for dominant decays of flavor-eigenstates (*e.g.* $B^0 \to D^-\pi^+$) and for doubly-CKM-suppressed decays (*e.g.* $B^0 \to D^+\pi^-$) lead to more complicated *p.d.f.*s (Aubert, 2004f). These interference effects are present when either B_{rec} or B_{tag} is reconstructed in a flavor state. In principle, the ratio of favored and DCS decay amplitudes is different for each mode. *BABAR* shows that an effective ratio can be defined for ensembles of final states as long as terms linear in $|z|$, $|q/p|-1$, and in the amplitude ratios of the contributing modes can be neglected. Belle treats the effects of DCS decays as part of the systematic error. The dominant contribution of $\mathrm{Im}(z)$ to the time-dependence is through the coefficient of $\sin(\Delta m_d \Delta t)$ for flavor final states, while $\mathrm{Re}(z)$ contributes primarily to the coefficients of the $\cosh(\Delta\Gamma_d\Delta t/2) \approx 1$ and $\cos(\Delta m_d \Delta t)$ terms for *CP* eigenstates. The main physics parameters extracted in *BABAR*'s analysis are $\mathrm{sgn}(\mathrm{Re}\lambda_{CP})$, $\Delta\Gamma_d/\Gamma_d$, $|q/p|$, $\mathrm{Im}(z)$, and $(\mathrm{Re}\lambda_{CP}/|\lambda_{CP}|) \times \mathrm{Re}(z)$. The parameters $(\mathrm{Im}\lambda_{CP}/|\lambda_{CP}|)$ and Δm_d are determined together with the main parameters as cross checks against earlier measurements. *BABAR* measures $(\mathrm{Re}\lambda_{CP}/|\lambda_{CP}|) \times \mathrm{Re}(z) = 0.014 \pm 0.035 \pm 0.034$ and $\mathrm{Im}(z) = (3.8 \pm 2.9 \pm 2.5) \times 10^{-2}$. Using *BABAR*'s measurement of $\sin 2\phi_1$ $(\mathrm{Im}\lambda_{CP})$ on the same data set (Aubert, 2005i) and assuming $|\lambda_{CP}| = 1$, we calculate a value of $\mathrm{Re}(z) = (+2.0 \pm 5.1 \pm 4.9) \times 10^{-2}$. Belle quotes the physics parameters $\mathrm{Re}(z) = (+1.9 \pm 3.7 \pm 3.3) \times 10^{-2}$ and $\mathrm{Im}(z) = (-5.7 \pm 3.3 \pm 3.3) \times 10^{-3}$. The fit has a twofold ambiguity in the sign of $\mathrm{Re}\lambda_{CP}$. The sign of $\mathrm{Re}(z)$ has been determined assuming $\mathrm{Re}\lambda_{CP} > 0$, which is a result of global fits of the Unitarity Triangle (see Section 25.1). The largest systematic uncertainty in $\mathrm{Re}(z)$ comes from the knowledge of tag-side interference (0.028). The error in $\mathrm{Im}(z)$ is dominated by uncertainties in vertex reconstruction (0.0028).

The results of all $\mathrm{Re}(z)$ and $\mathrm{Im}(z)$ measurements by the B Factories are summarized in Table 17.5.4. The measurements are still mostly statistically limited and many of the systematic uncertainties are statistical in nature. Using the full data sets will allow one to further improve the constraints on these *CP* and *CPT*-violating parameters. Future super flavor factories should be able to improve current limits even further. How much they can improve will depend on how well the systematic uncertainties can be controlled.

17.5.5 Lorentz invariance violation in $B^0 - \overline{B}^0$ mixing

If we go beyond a purely phenomenological treatment of *CPT*-violating effects, Lorentz violation should also be considered. *CPT* invariance follows from assumptions that are currently understood to hold in the low-energy (Standard Model-like) domain: point particles, the applicability of quantum field theory, and in particular, Lorentz invariance (Jost, 1957; Luders, 1954; Pauli, 1955; Streater and Wightman, 2000). If *CPT* symmetry is broken, then one or more of these conditions must be violated.

In particle physics, Lorentz violation is usually studied in the framework of the Standard Model Extension. This theory and its application to B mixing is briefly reviewed in Section 17.5.5.1. We then describe the analysis carried out within this framework by *BABAR* (Section 17.5.5.2), and discuss the implications for work at future facilities (Section 17.5.5.3).

17.5.5.1 The Standard Model Extension and mixing

Simplifying assumptions are required to make an effective search for Lorentz violation in data. If we posit a fundamental theory whose dynamics are both *CPT*- and Poincaré-invariant,[66] and a low-energy effective theory that exhibits *spontaneous CPT*- and Lorentz-symmetry breaking, we obtain the so-called Standard Model Extension (SME) of Colladay and Kostelecký (1997, 1998); see also Kostelecký (2004). In this theory *nature remains invariant under translations, and is covariant under changes in the inertial frame of the observer*: the usual kinematic expressions may consistently be used to analyse particle motion, reconstruct invariant masses, and so on. However under boosts of individual particles, *CPT* is broken and certain Lorentz-violating terms appear, due to the (constant) expectation values of one or more Lorentz tensors (*cf.* the mass terms due to particles coupling to the [scalar] Higgs field in the Standard Model). The Lorentz-violating coefficients due to these background fields vary from particle to particle in general; the resulting parameters are similar in number to the supersymmetric couplings, and have been exhaustively tabulated, together with current bounds from experimental and observational tests, by Kostelecký and Russell (2011). As neutral-meson oscillation is flavor-changing, *CPT*-violation measurements in mixing provide access to couplings that are not constrained by other experimental tests (Kostelecký, 1998).

For a neutral meson, the Lorentz-violating parameters are given by the four-vector $\Delta a_\mu \equiv r_{q_1} a_\mu^{q_1} - r_{q_2} a_\mu^{q_2}$, the difference in the couplings of the two valence quarks q_i (Kostelecký, 2001; Kostelecký and Potting, 1995).[67] These parameters are constant in any inertial frame. We then find, for the *CPT*-violating parameter defined in Eq. (17.5.35),

$$z \equiv \frac{\delta m - \frac{i}{2}\delta\Gamma}{\Delta m_d - \frac{i}{2}\Delta\Gamma} \simeq \frac{\beta^\mu \Delta a_\mu}{\Delta m_d - \frac{i}{2}\Delta\Gamma}, \tag{17.5.49}$$

where $\beta^\mu = \gamma(1, \boldsymbol{\beta})$ is the meson four-velocity. The approximation in Eq. (17.5.49) is due to the neglect of higher-order effects in the SME, and does not otherwise rely on the size of z (Kostelecký, 2001; Kostelecký and Potting, 1995).[68] Note that the relative values of the imaginary and real parts of z are fixed by the B-mixing parameters (Kostelecký and Potting, 1995),[69]

$$\frac{\mathrm{Im}\, z}{\mathrm{Re}\, z} = \frac{\Delta\Gamma}{2\Delta m_d}, \tag{17.5.50}$$

[66] That is, invariant under translations, as well as rotations and boosts.

[67] The factors r_{q_i}, which represent the effect of binding the quarks q_i within the meson, are not used consistently in the literature, disappearing (for example) in Kostelecký (1998).

[68] *BABAR* (Aubert, 2008ar) cites Kostelecký (1998), where a further approximation exists due to the use of another parameter, $\delta \approx -z/2$ in the case of small T- and *CPT*-violating effects.

[69] The *BABAR* analysis (Aubert, 2008ar) derives this condition from Eq. (17.5.49) using $\Delta\Gamma \ll \Delta m_d$, but it is derived from fundamental considerations by Kostelecký and Potting (1995), assuming only that T- and *CPT*-violating effects are small.

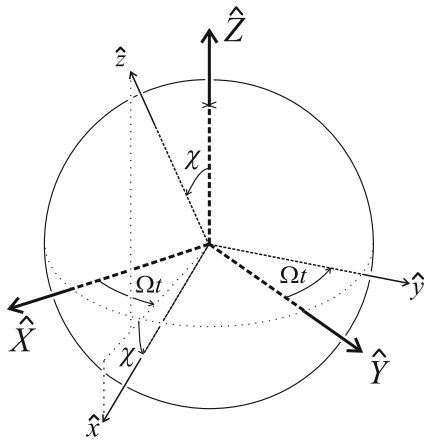

Figure 17.5.12. Transformation between non-rotating and laboratory (rotating) reference frames for the Lorentz-violation analysis: from Kostelecký and Lane (1999).

providing a distinctive signature for *CPT*-violating effects within this scheme.

The motion of the laboratory must be taken into account: the (non-relativistic) velocity may be neglected, but the earth's rotation changes the relative orientation of the detector coordinate system and the spatial components $\Delta\boldsymbol{a}$. *BABAR* (Aubert, 2008ar) chooses a non-rotating frame $(\hat{X}, \hat{Y}, \hat{Z})$ following Kostelecký and Lane (1999), with $\hat{Z}$ parallel to the earth's rotation axis, and $\hat{X}$ ($\hat{Y}$) at right ascension 0° (90°). With the further choices that the laboratory coordinate $\hat{z}$ lies along $-\boldsymbol{\beta}$, and $\hat{y}$ lies in the equatorial plane (declination 0°), it follows from Eq. (14) of Kostelecký (2001) that

$$\begin{aligned}\beta^\mu \Delta a_\mu = \gamma\,[&\Delta a_0 - \beta \Delta a_Z \cos\chi \\ &- \beta \sin\chi\,(\Delta a_Y \sin\Omega\, t_{\mathrm{sid}} \\ &+ \Delta a_X \cos\Omega\, t_{\mathrm{sid}})]\,,\end{aligned} \tag{17.5.51}$$

where $\cos\chi \equiv \hat{z}\cdot\hat{Z} = 0.628$ for *BABAR*, t_{sid} is the sidereal time, and $\Omega = 2\pi/d_{\mathrm{sid}}$ the sidereal frequency; $d_{\mathrm{sid}} \simeq 0.99727$ solar days. The transformation between laboratory and non-rotating coordinates is illustrated in Fig. 17.5.12. The sidereal time t_{sid} is given by the right ascension of $\hat{z}$; this will become important when comparing results from different experiments (Section 17.5.5.3 below).

From Eqs (17.5.49) and (17.5.51) it is clear that in the general case, the measured *CPT*-violating parameter z will vary with a period of one sidereal day (d_{sid}); a value z obtained from data without time-binning will depend on the latitude of the experiment and the distribution of meson momenta in the laboratory frame.

17.5.5.2 The *BABAR* analysis

The Lorentz violation study in Aubert (2008ar) is an extension of the *CPT*-violation search of Aubert (2006aq),

Table 17.5.5. Parameters from fits to the asymmetry A_{CPT} as a function of sidereal time, assuming constant (z_0) and sinusoidal (z_1) contributions according to the Standard Model Extension. Statistical and total systematic uncertainties are shown; a breakdown of systematic contributions is given in Table I of Aubert (2008ar). Results are shown without (center) and with (right) the SME constraint of Eq. (17.5.50) on the real and imaginary parts of z.

A_{CPT} parameter		unconstrained	SME constraint
$\mathrm{Im}\, z_0$	$[10^{-3}]$	$-14.2 \pm 7.3 \pm 2.2$	$-5.2 \pm 3.6 \pm 1.9$
$\mathrm{Re}\, z_0\, \Delta\Gamma$	$[10^{-3}/\mathrm{ps}]$	$-7.3 \pm 4.1 \pm 1.8$	
$\mathrm{Im}\, z_1$	$[10^{-3}]$	$-24 \pm 11 \pm 3.3$	$-17.0 \pm 5.8 \pm 1.9$
$\mathrm{Re}\, z_1\, \Delta\Gamma$	$[10^{-3}/\mathrm{ps}]$	$-18.5 \pm 5.6 \pm 1.7$	
ϕ	[rad]	$2.63 \pm 0.31 \pm 0.21$	$2.56 \pm 0.36 \pm 0.15$

discussed in Section 17.5.4.2 above, using the same sample of opposite-sign dilepton events to measure the *CP*- and *CPT*-violating asymmetry between $B^0 \to B^0$ and $\overline{B}^0 \to \overline{B}^0$ rates,

$$A_{CPT/CP}(\Delta t) = \frac{2\mathrm{Im}\, z \sin(\Delta m_d \Delta t) - \mathrm{Re}\, z \Delta\Gamma \Delta t}{\cos(\Delta m_d \Delta t) + \cosh(\Delta\Gamma \Delta t/2)}; \tag{17.5.52}$$

see Eq. (17.5.45) for the full expression. As in Aubert (2006aq), same-sign dilepton events are used to provide additional information on the fractions of the various signal and background components.

The analysis is extended to include the sidereal time t_{sid}, allowing for variations in z of the form

$$z = z_0 + z_1 \cos(\Omega t_{\mathrm{sid}} + \phi); \tag{17.5.53}$$

the discrete ambiguity ($z_1 \to -z_1$, $\phi \to \phi + \pi$) does not affect the physical parameters Δa_μ of Eq. (17.5.51). A two-dimensional maximum likelihood fit is performed, with opposite- and same-sign events separately binned in $(\Delta t, t_{\mathrm{sid}})$; 24 sidereal-time bins are used. The values obtained for the parameters $z_{0,1}$ and ϕ are shown in Table 17.5.5. Individual systematic uncertainties are itemized in Table I of Aubert (2008ar): the dominant terms are due to alignment of the *BABAR* SVT and the absolute z scale (especially for ϕ), and modeling of the resolution.

Deviations from zero are seen for both the constant and sidereal-time-dependent *CPT*-violating terms in Eq. (17.5.53). The constant terms $\mathrm{Re}\, z_0\, \Delta\Gamma$ and $\mathrm{Im}\, z_0$ are almost identical to those in the time-independent analysis (Aubert, 2006aq), where a χ^2 of 3.25 for 2 degrees of freedom is quoted (the results have a correlation coefficient of 0.76 in both analyses): consistent with *CPT* invariance at 19.7% confidence. The sidereal-time dependence of A_{CPT} is shown in Figure 17.5.13; events at small time differences $|\Delta t| < 3$, while included in the fit, are suppressed in the figure as their predicted asymmetry is small.

Results are consistent with the SME condition of Eq. (17.5.50), so a further fit is performed with this expression used as a constraint, to improve the precision of the measurement: these results are also shown in the table. Consistent results are found if second-order terms $|z|^2 = \rho^2 \cos^2(\Omega t_{\mathrm{sid}} + \phi)$ are added to the fit (*cf.* the derivation of Eq. (17.5.41) above).

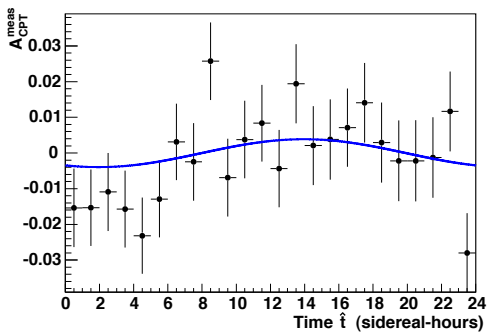

Figure 17.5.13. Measured asymmetry A_{CPT} for opposite-sign dilepton events with 3 ps $< |\Delta t| <$ 15 ps, as a function of sidereal time $\hat{t} = t_{\mathrm{sid}}$. The curve shows a projection of the full two-dimensional $|\Delta t| <$ 15 ps fit, also requiring 3 ps $< |\Delta t|$. From Aubert (2008ar).

Two kinds of significance estimates are quoted for the sidereal-time-dependent results. Based on the likelihood fit, $(\mathrm{Re}\, z_1\, \Delta\Gamma, \mathrm{Im}\, z_1)$ differ from zero at 2.8σ, with or without the SME constraint. Based on the periodogram method (Lomb, 1976; Scargle, 1982) measuring the spectral power $\mathcal{P}(\nu)$ for variations in z at test frequencies ν, a value $\mathcal{P}(1/d_{\mathrm{sid}}) = 5.28$ is found; the probability to exceed this value in the absence of an oscillatory signal is

$$\begin{aligned} P\left[\mathcal{P}(\nu) > S\right] &= e^{-S} \\ &= 5.1 \times 10^{-3} \ \text{ for } S = 5.28, \end{aligned} \tag{17.5.54}$$

also corresponding to 2.8σ. This is significantly stronger than the result at the solar-day frequency, where effects due to diurnal variations in detector response would occur: $\mathcal{P}(1/d_{\mathrm{solar}}) = 1.47$. The largest spectral power among the $M = 9500$ independent frequencies tested is $\mathcal{P}(0.46312/d_{\mathrm{sid}}) = 8.78$; the probability of finding a larger spectral power than this is

$$\begin{aligned} P\left[\mathcal{P}(\nu)|_{\max} > S;\, M\right] &= 1 - \left(1 - e^{-S}\right)^M \\ &= 76\% \ \text{ for } S = 8.78. \end{aligned} \tag{17.5.55}$$

However we note that the frequency expected within the SME is unambiguous: $\nu = 1/d_{\mathrm{sid}}$.

Final results are quoted for the SME quantities:

$$\begin{aligned} \Delta a_0 - 0.30\Delta a_Z &= (-3.0 \pm 2.4)(\Delta m_d/\Delta\Gamma) \times 10^{-15}\ \mathrm{GeV}, \\ \Delta a_X &= (-22 \pm 7)(\Delta m_d/\Delta\Gamma) \times 10^{-15}\ \mathrm{GeV}, \\ \Delta a_Y &= (-14^{+10}_{-13})(\Delta m_d/\Delta\Gamma) \times 10^{-15}\ \mathrm{GeV}. \end{aligned} \tag{17.5.56}$$

17.5.5.3 Implications for future measurements

A study of Lorentz covariance violation has not been performed by Belle, nor has the full available *BABAR* dataset

been used to update the Aubert (2008ar) analysis. The results of that analysis thus remain untested. If confirmed, a non-zero measurement would be a result of the utmost importance; the burden of proof for such a measurement is correspondingly high.

At face value, the Aubert (2008ar) analysis provides weak evidence for *CPT* violation together with departures from Lorentz covariance, consistent with the Standard Model Extension. Combining the confidence levels of the time-independent ($\alpha_1 = 0.197$) and sidereal-time-dependent results ($\alpha_2 = 5.1\times10^{-3}$) discussed above, using Eq. (11.35) of James (2006), we find an overall result compatible with zero at $\alpha = \alpha_1\alpha_2[1-\ln(\alpha_1\alpha_2)] = 7.9\times10^{-3}$: a 2.66σ effect. While there is greater spectral power at some frequencies $\nu \neq 1/d_{\rm sid}$, and even the largest such signal is within expectations in the absence of oscillation, this adds little new information beyond the relative weakness of the sidereal-time dependence; within the SME, the predicted signal is not at some undetermined frequency but at $\nu = 1/d_{\rm sid}$ — there is no "look-elsewhere effect".

The current results are statistically limited. While much larger datasets are foreseen at super flavor factories, even the final *BABAR* and Belle samples exceed those used by Aubert (2008ar) by factors of 2.0 and 3.3 respectively, allowing for both a repetition of the analysis on independent data, and a test on different equipment with statistical errors reduced by a factor $\sqrt{3.3} = 1.82$. Assuming no change in central value, systematics, or intrinsic power, a hypothetical Belle result with statistical uncertainty of 3.2×10^{-3} and systematic uncertainty of 1.9×10^{-3} (*cf.* Table 17.5.5) would have 4.6σ significance for the sidereal-time-dependent measurement alone; the probability to exceed the corresponding spectral power, at *any* frequency, would be 5% (from Eqs (17.5.54) and (17.5.55), assuming the same number of frequencies tested by Aubert, 2008ar).

The latitude of Belle is similar to that of *BABAR*, and by chance the compass orientations of the $\Upsilon(4S)$ boost are also similar for the two experiments. The longitudes are substantially different at the two sites: this leads to a difference in the right ascension of $\hat{z}$, and thus an offset in $t_{\rm sid}$ in Eq. (17.5.51) at a given clock time. The phase ϕ of sidereal-time dependence in Eq. (17.5.53) predicted in the SME for Belle therefore differs from that at *BABAR* by a fixed amount, whereas for results due to statistical fluctuation, the phase would be arbitrary.

The dominant systematic uncertainties — alignment, the z-scale, and the modeling of resolution — are amenable to improvement at a redesigned experiment, although the underlying time-dependent analysis techniques (Chapter 10) would need to be mature. Even without a significant reduction in systematics, a super flavor factory could perform a measurement of overwhelming statistical power.

17.6 ϕ_1, or β

Editors:
Chih-hsiang Cheng (BABAR)
Yoshihide Sakai (Belle)
Ikaros Bigi (theory)

Additional section writers:
Tagir Aushev, Eli Ben-Haim, Adrian Bevan, Bob Cahn, Chunhui Chen, Ryosuke Itoh, Alfio Lazzaro, Owen Long, Fernando Martinez-Vidal, Vincent Poireau, Klaus Schubert

Precision measurement of the *CP* asymmetries in $B \to J/\psi K_S^0$ decays was the principal motivation for building the B Factories. With the accumulation of data samples larger than anticipated, the *BABAR* and Belle experiments at the B Factories are able to study *CP* asymmetries in a wide range of related channels. This section describes measurements of the Unitarity Triangle angle ϕ_1, also known as β in the literature. An overview of ϕ_1 measurements and their motivation is presented in Section 17.6.1, followed by a review of the quark transitions and the formalism of ϕ_1 measurements in Section 17.6.2. The various channels for ϕ_1 measurement, and the B Factories results, are then described in Sections 17.6.3–17.6.7. Resolution of discrete ambiguities is discussed in Section 17.6.8, and a summary of ϕ_1 results is presented in Section 17.6.10.

In the Standard Model, non-zero asymmetries measured in these analyses reflect violation of both the *CP* and T symmetries. Performing the measurement in a way that directly demonstrates T violation, without assuming (for example) *CPT* symmetry, requires special care. Such an analysis has been performed at *BABAR*, and is presented in Section 17.6.9. Tests of *CPT* symmetry are presented in Section 17.5.

17.6.1 Overview of ϕ_1 measurement at the B Factories

Initially, *CP* violation seemed isolated from the mainstream of particle physics. Since it was seen only in the K_S^0-K_L^0 system, it was possible to imagine that it was due entirely to a $\Delta S = 2$ operator as postulated in the superweak theory (Wolfenstein, 1964). Two developments put *CP* violation at center stage. The first was A. D. Sakharov's demonstration (Sakharov, 1967) that *CP* violation was one of the three requirements for the existence of the baryon anti-baryon asymmetry of the universe (see Section 16.2). The second was Kobayashi's and Maskawa's demonstration that *CP* violation was natural if there were three generations of quarks (see Chapter 16). With the subsequent discovery of the last three quarks, testing the CKM model became urgent.

The K_S^0-K_L^0 system was not sufficient by itself to test the CKM picture. The measured parameters, Δm_K, ϵ_K and ϵ'_K, depended not just on the fundamentals of the weak interactions, but on non-perturbative hadronic matrix elements. Moreover, *CP* violation in the kaon system was feeble. Since ϵ_K was measured in 1964, it took until 1973 before Kobayashi and Maskawa provided a real theory for *CP* violation. It needed many years to demonstrate that the parameter ϵ' was non-zero. Even *before* the unexpected 'long' lifetime of B mesons was discovered, the B meson system was recognized as the ideal testing ground for *CP* violation (Bigi and Sanda, 1981) and the decay $B \to J/\psi K_S^0$ as ideal for the purpose. Detection of the final state is especially clean because the J/ψ decays to lepton pairs and the K_S^0 is sufficiently long-lived to decay into pairs of oppositely charged pions at a secondary vertex displaced from the interaction region.

Unlike neutral kaons, the neutral B mesons start oscillating just after their production, since their mixing rate Δm_d is comparable to their natural widths Γ (see Section 17.5). If we begin with a B^0, at a later time the state will be a superposition of B^0 and $\overline{B}^0$. The decay to $J/\psi K_S^0$ will occur through both components and the interference pattern will depend on the relative phases between the B^0 and $\overline{B}^0$ components, which is directly calculable in the CKM model. The interference pattern depends on the two decay amplitudes to the final state. Because the final state is a *CP* eigenstate and because there is only one significant pathway to it from B^0 or $\overline{B}^0$, the two decay amplitudes are identical, up to another calculable phase. As a result, the oscillation pattern can be predicted simply in terms of the phases due to the CKM matrix without any dependence on hadronic physics. The time-dependent formalism required for the measurement of $\sin 2\phi_1$ can be found in Chapter 10.

In order to test the CKM paradigm we need to know if we are starting with a B^0 or with a $\overline{B}^0$. The $\Upsilon(4S)$ is very near the threshold for $B\overline{B}$ so if one B is observed, the remaining particles must come from another B. Moreover, by Bose symmetry, if a $\overline{B}^0$ is observed the other particle must be a B^0 at that instant, since the two mesons must be in an antisymmetric state to produce the unit of angular momentum carried by the $\Upsilon(4S)$. Thus "tagging" one B meson tells us both, when to start the clock and the type of B at that time (see Chapter 8).

The decay $B^0 \to J/\psi K_S^0$ is just one of a large family of related decays due to a $b \to c\bar{c}s$ transition. Of particular interest is the decay to $J/\psi K_L^0$ because the final state has the opposite *CP* eigenvalue, and we expect exactly the opposite oscillation. Other charmonia can take the place of J/ψ, including $\psi(2S), \eta_c$, and χ_{c1}. The decay $B^0 \to J/\psi K^{*0}$ is more complex because the spins of the final state particles can be combined to produce an overall spin equal to 0, 1, or 2, and correspondingly the orbital angular momentum will be 0, 1, or 2. This complexity has the advantage that it can help resolve the ambiguity inherent in determining the angle ϕ_1 when only $\sin 2\phi_1$ is known.

At first, the B Factories concentrated on measuring time-dependent asymmetries in the so-called charmonium "golden modes" concentrating on $B^0 \to J/\psi K_S^0$, $\psi(2S)K_S^0$, $\chi_{c1}K_S^0$, $J/\psi K_L^0$, and $J/\psi \pi^0$. However, it was understood that there were other ways to measure ϕ_1. Once an understanding of how to do these measurements started to develop, the experiments branched out to study similar

final states that were more difficult to isolate from the data. These states either had smaller branching fractions, or were experimentally more challenging to isolate. Studies performed in the *BABAR* physics book (Harrison and Quinn, 1998), prior to the commencement of data taking, assumed that a data sample of $30\,\text{fb}^{-1}$ would be available to use for testing the SM. In reality this data sample was quickly attained on both sides of the Pacific Ocean and the B Factories program of measuring ϕ_1 expanded, both in terms of the number of measurements and in terms of the complexity of analysis used, to accommodate the rich harvest of B meson pairs. The first results on the measurement of $\sin 2\phi_1$ were shown at the International Conference on High Energy Physics in 2000, which became known colloquially within *BABAR* and Belle as 'the Osaka conference'. The B Factories presented values of $\sin 2\phi_1$ of $0.12 \pm 0.37 \pm 0.09$ (Aubert, 2000) and $0.45^{+0.43}_{-0.44}{}^{+0.07}_{-0.09}$ (Aihara, 2000a) at this conference. A year later Belle and *BABAR* established large *CP* asymmetry in this final state. Since then both B Factories have accumulated much larger data samples, and the final results obtained by *BABAR* and Belle are significantly more precise than these first measurements (see Section 17.6.3).

While the charmonium decays were the primary focus of the ϕ_1 program, final states mediated by other transitions were also studied in subsequent waves of measurements that quickly followed the first results. In particular the modes $B \to \phi K^0_S$, $B \to \eta' K^0_S$, and $D^{(*)+}D^{(*)-}$ were highlighted. The expectation was that these would provide alternative ways of constraining ϕ_1, and would complement the constraint on the Unitarity Triangle given by the golden mode measurements. Any measurement of ϕ_1 that differed significantly from expectations, or any two measurements that disagreed with each other, could reveal physics beyond the Standard Model.

The first few measurements of $S \simeq \sin(2\phi_1)$ in a quasi-two-body analysis of $B \to \phi K^0_S$ decays in 2003 were far from the SM expectation. While these were low statistics studies, with only a handful of high purity events (well tagged events with a low mistag probability, see Chapter 8), the community was tantalized by the possibility that this could herald a new age in modern physics. As a result, the interest in alternative measurements of ϕ_1 blossomed, and this remains a vibrant area a decade later. Alas, the early deviations from the SM turned out to be statistical fluctuations, and the most recent measured values of ϕ_1 obtained from the B Factories are compatible with SM expectations within experimental and theoretical uncertainties.

The early fluctuation had several consequences. First, a large number of neutral B meson decays to *CP* eigenstate or admixture final states have been studied in the hope that one or more of them might yield a result incompatible with the SM. Second, both the theoretical and experimental communities started to take possible hadronic uncertainties more seriously in both golden and alternative measurements of ϕ_1. Today the constraints on hadronic uncertainties in these modes are a mixture of theoretical calculations and data-driven constraints obtained via a more phenomenological approach. The golden channels are theoretically clean, up to the extent that analysis at the B Factories would be concerned about. This has been determined via theoretical calculation, and via a data-driven interpretation of results. However other final states, in particular those dominated by penguin loop amplitudes, have non-negligible uncertainties. The cleanest modes are $B \to \eta' K^0_S$, which is the most precisely measured charmless final state, and $B \to \phi K^0_S$. These have hadronic uncertainties of a few percent on the measured value of S. In the case of $B \to f_0 K^0_S$ there are only partial calculations where, for example, long distance effects are ignored, and the estimated hadronic uncertainties for this mode provide a lower bound. More details on this part of the B Factory program can be found in Section 17.6.6.

Early time-dependent studies of B decays to charmless final states relied on a simplified analysis paradigm by imposing the quasi-two-body assumption that resonances are particles of definite mass, so that interference between amplitudes could be neglected. As the recorded data samples of the two experiments increased, more sophisticated techniques were incorporated. Just as the measurements of ϕ_2 ultimately required that the B Factories pioneer the use of time-dependent Dalitz plot techniques, so eventually one had to perform similar analyses in order to constrain ϕ_1. The ability to study amplitudes in a Dalitz plot leads to the possibility of resolving the four-fold ambiguity in the value of ϕ_1 obtained from the golden mode measurement, and complements other approaches such as the full angular analysis of the $B^0 \to J/\psi K^*$ final state. Results from three-body charmless decays on ϕ_1 are discussed in Section 17.6.7, and resolution of discrete ambiguities on the value of this angle using other modes is considered in Section 17.6.8.

The large amounts of data accumulated by the B Factories also required an improvement in understanding the systematic uncertainties involved in the measurements themselves. In particular the concept of flavor tagging as originally conceived, while good enough to describe semileptonic tagged events, turned out to be an approximation for hadronically tagged final states. It is possible to have a small level of *CP* violation manifest on the tag side of the event that would need to be considered as a systematic uncertainty in order to ensure that one reports the correct level of *CP* violation obtained for a given result. In some cases with small expected *CP* violating asymmetries, such as the measurement of $\sin(2\phi_1 + \phi_3)$, this so-called tag-side interference needs to be incorporated into the measurement technique. The main systematic uncertainties for time-dependent measurements at the B Factories, including tag-side interference, are discussed in Chapter 15.

The final measurement of $\sin 2\phi_1 \equiv \sin 2\beta$ obtained by the B Factories has a combined precision of 3%. This can be compared with the estimated relative statistical precision for this measurement estimated in the *BABAR* physics book, 12%, using a foreseen data sample of $30\,\text{fb}^{-1}$ (Harrison and Quinn, 1998). The achieved precision is a nice example of exceeding the initial expectations put forward before the startup of the B Factories. The final result of

the B Factories is not systematically limited and may be improved upon by the next generation of experiments.

17.6.2 Transitions and formalism

The Unitarity Triangle angle $\phi_1 = \beta$ is defined as

$$\phi_1 \equiv \beta \equiv \arg[-(V_{cd}V_{cb}^*)/(V_{td}V_{tb}^*)]. \quad (17.6.1)$$

It describes *CP* violation in the interference between decays with and without B^0-$\overline{B}^0$ mixing and is best measured in $B^0 \to J/\psi(\psi(2S))K_S^0$ transitions, which have *CP*-odd final states (ignoring the small *CP* violation in K^0-$\overline{K}^0$ mixing). As discussed in Section 10.1, $\Delta B = 2$ transitions in the SM are produced by quark box diagrams $O_{\rm box}$ including QCD radiative corrections for Δm_d.

The most precise technique for measuring ϕ_1 uses B^0 decays to *CP* eigenstates with quark transitions of the type $b \to c\bar{c}s$ (Fig. 17.6.1). Since the final state f is accessible to both B^0 and $\overline{B}^0$, the amplitudes for $B^0 \to f$ (direct decay) and $B^0 \to \overline{B}^0 \to f$ (decay preceded by neutral meson oscillation) will interfere. As described in Section 10.2,[70] the resulting time-dependent *CP* asymmetry is given as

$$\mathcal{A}(\Delta t) = S\sin(\Delta m_d \Delta t) - C\cos(\Delta m_d \Delta t), \quad (17.6.2)$$

where $S = 2{\rm Im}\lambda/(1+|\lambda|^2)$, $C = (1-|\lambda|^2)/(1+|\lambda|^2)$, and $\lambda = (q/p)(\overline{A}_f/A_f)$. In the SM, $q/p = V_{td}V_{tb}^*/V_{td}^*V_{tb}$ to a good approximation. For the final state $f = J/\psi K_S^0$, the B decay is dominated by a tree $b \to c\bar{c}s$ (or its *CP* conjugate) amplitude[71] followed by K^0-$\overline{K}^0$ mixing.[72] The result is $\lambda = \eta_f \frac{V_{td}V_{tb}^*}{V_{tb}V_{td}^*}\frac{V_{cb}V_{cd}^*}{V_{cd}V_{cb}^*}$, which leads to $C = 0$ and $S = -\eta_f \sin 2\phi_1$, where $\eta_f = \eta_{J/\psi K_S^0} = -1$ is the *CP* eigenvalue. $B^0 \to J/\psi K_L^0$ has $\eta_f = \eta_{J/\psi K_L^0} = +1$ and has the opposite sign for S. The same magnitude is expected for the *CP*-even and -odd modes up to a small correction for *CP* violation in K^0-$\overline{K}^0$ oscillations.

To understand the penguin amplitude contributions, one can group tree (T) and penguin (P^q) amplitudes according to their CKM factors, remove the $V_{tb}V_{ts}^*$ term using the unitarity condition

$$\sum_{q=u,c,t} V_{qb}V_{qs}^* = 0, \quad (17.6.3)$$

and express the $b \to c\bar{c}s$ decay amplitude as

$$A_{c\bar{c}s} = V_{cb}V_{cs}^*(T + P^c - P^t) + V_{ub}V_{us}^*(P^u - P^t), \quad (17.6.4)$$

where the superscripts indicate the quark in the loop. The second term has a different phase but the magnitude is suppressed by $|V_{ub}V_{us}^*/V_{cb}V_{cs}^*| \sim \mathcal{O}(\lambda^2_{\rm Cabibbo})$. Therefore, the effect of the penguin amplitude on ϕ_1 is expected to be very small.

[70] See in particular Eqs (10.2.2, 10.2.4, 10.2.4, and 10.1.10).

[71] B decay amplitude ratio provides a factor $\eta_f \frac{V_{cb}V_{cs}^*}{V_{cb}^*V_{cs}}$.

[72] K^0-$\overline{K}^0$ mixing provides a factor $V_{cd}^*V_{cs}/V_{cd}V_{cs}^*$.

Within the SM the level of *CP* violation in decay ($|A_f/\bar{A}_{\bar{f}}| \neq 1$) is expected to be inaccessible to existing experiments, and new physics (NP) beyond the SM is unlikely to generate large effects due to the dominance of the tree amplitude in decay. However, NP could modify the time-dependent *CP* asymmetry across different modes by affecting the phase in q/p and lead to inconsistencies between ϕ_1 and other observables that determine the Unitarity Triangle.

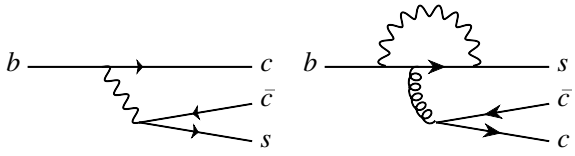

Figure 17.6.1. Tree and penguin diagrams of $b \to c\bar{c}s$.

In $b \to c\bar{c}d$ (Fig. 17.6.2) decays, the difference between the CKM phase of the tree diagram and that of $b \to c\bar{c}s$ is negligible. This allows the measurements of $\sin 2\phi_1$ through decays to *CP* eigenstates of $b \to c\bar{c}d$ (such as $B^0 \to J/\psi\pi^0$ and D^+D^-) in the same way as $b \to c\bar{c}s$. Unlike $b \to c\bar{c}s$, however, the CKM factors of the penguin diagrams here are of the same order ($\mathcal{O}(\lambda^3_{\rm Cabibbo})$) as the tree diagram. The possible contribution of the $b \to c\bar{c}d$ penguin diagrams, which have a different CKM phase, can alter the measured value of $\sin 2\phi_1$. Any such deviation would be due to the effect of penguin contributions or due to NP.

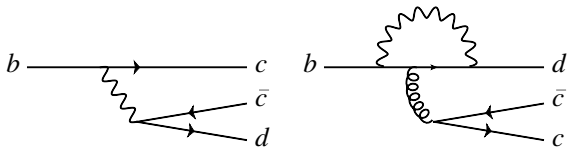

Figure 17.6.2. Tree and penguin diagrams of $b \to c\bar{c}d$.

The $b \to c\bar{u}d$ transition (Fig. 17.6.3) proceeds through a tree diagram, and has no penguin contribution. It can again be used to probe $\sin 2\phi_1$ if the final state is accessible to both B^0 and $\overline{B}^0$ (*e.g.*, in the case of intermediate D^0 and $\overline{D}^0$ decays to the same final state). However, in this case, the process $b \to u\bar{c}d$ also contributes. The relative CKM factor of these two tree diagrams, $V_{ub}V_{cd}^*/V_{cb}V_{ud}^*$, has a large phase and the magnitude is approximately 0.02. Therefore, the deviation from the $b \to c\bar{c}s$ value for $\sin 2\phi_1$ obtained in these decays is expected to be small.

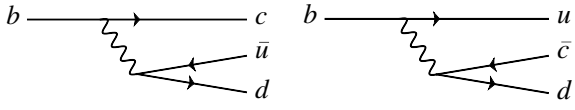

Figure 17.6.3. Tree diagrams of $b \to c\bar{u}d$ and $b \to u\bar{c}d$.

The decays to *CP* eigenstates dominated by $b \to s\bar{q}q$ penguin transitions (Fig. 17.6.4) also can be used for $\sin 2\phi_1$ measurements in the SM. Similar to Eq. (17.6.4), the dominant penguin contribution has the same phase as that in the $b \to c\bar{c}s$ tree diagram, and the sub-dominant term is suppressed. Any deviation of S from the $b \to c\bar{c}s$ decay (beyond theoretical uncertainty) is a clear indication of the effect of NP. The decays proceeding via $b \to s\bar{s}s$ penguin diagrams, such as $B^0 \to \phi K^0$, $K^0_S K^0_S K^0_S$, and $\eta' K^0$, have a small theoretical uncertainty on S due to the lack of a tree amplitude contribution. These decays are particularly promising for future new physics searches.

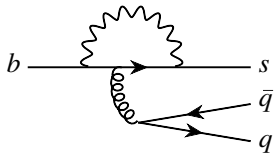

Figure 17.6.4. Penguin diagram of $b \to q\bar{q}s$.

Measurements of $\sin 2\phi_1$ have a four-fold ambiguity in ϕ_1: $\phi_1 \leftrightarrow \pi/2 - \phi_1$, $\phi_1 + \pi$ and $3\pi/2 - \phi_1$ (all these four values result in the same $\sin 2\phi_1$). The $\phi_1 \leftrightarrow \pi/2 - \phi_1$ and $3\pi/2 - \phi_1$ ambiguity can be resolved in one of several ways: the full time-dependent angular analysis of vector-vector final states such as $B^0 \to J/\psi K^{*0}[K^0_S\pi^0]$; time-dependent Dalitz analysis of three-body decays; time-dependent Dalitz analysis of $D^0 \to K^0_S\pi^+\pi^-$ in $B^0 \to D^{(*)0}h^0$; and time-dependent measurements in two separate Dalitz regions in $B^0 \to D^{*+}D^{*-}K^0$. Using these measurements the ambiguity is partially resolved and only the two fold ambiguity $\phi_1 \to \phi_1 + \pi$ remains, which cannot be resolved by a single measurement. When combining with other CKM measurements, one can clearly see which of the two remaining solutions is ruled out. See Chapter 25 for details.

The following sections describe the different measurements of ϕ_1 made at the B Factories.

17.6.3 ϕ_1 from $b \to c\bar{c}s$ decays

The decays to *CP* eigenstates via a $b \to c\bar{c}s$ transition include B^0 decays to charmonium ($c\bar{c}$) and a K^0_S or K^0_L. These modes have experimentally clean signals, and large signal yields are expected due to relatively large branching fractions (they are CKM favored, though color suppressed[73]). These decays are also theoretically very clean for ϕ_1 determination, *i.e.*, the deviation due to the contribution of penguin diagrams with a different CKM phase is expected to be at the $\leq 1\%$ level (H. Boos and Reuter, 2004, 2007). As a result the $B^0 \to J/\psi K^0_S$ decay is called a "Golden mode".

Since the observation of *CP* violation in B decays and the precise measurements of $\sin 2\phi_1$ are the primary goals of the asymmetric B Factories, the measurements made using $b \to c\bar{c}s$ modes were performed shortly after data taking commenced, and have been updated several times during the course of data taking. Both B Factories have updated their measurements using the whole data sample collected by each experiment. *BABAR* (Aubert, 2009z) uses 465×10^6 $B\overline{B}$, while Belle (Adachi, 2012c) uses 772×10^6 $B\overline{B}$ pairs. For ϕ_1 measurements with $b \to c\bar{c}s$ decays, the B^0 decays to the final states $J/\psi K^0_S$, $J/\psi K^0_L$, $\psi(2S)K^0_S$, $\chi_{c1}K^0_S$, $\eta_c K^0_S$, and $J/\psi K^*(890)^0[K^0_S\pi^0]$ are used. The $J/\psi K^0_L$ state is *CP*-even, and $J/\psi K^*(890)^0$ is an admixture of two *CP* states. All the others are *CP*-odd states.

The J/ψ and $\psi(2S)$ mesons are reconstructed via their decays to $\ell^+\ell^-$ ($\ell = e, \mu$). For decays to an e^+e^- final state, photons near the direction of the $e^\pm$ are added to recover the energy lost by radiated bremsstrahlung. The $\psi(2S)$ mesons are also reconstructed in the $J/\psi\pi^+\pi^-$ final state. The χ_{c1} mesons are reconstructed in the $J/\psi\gamma$ final state, and these photons must not be consistent with photons from π^0 decays. The η_c mesons are reconstructed in the $K^0_S K^+\pi^-$ final states, and the regions that contain the dominant intermediate resonant states in $K^+\pi^-$ and $K^0_S K^+$ are selected. Candidate K^0_S mesons are reconstructed via decays to the $\pi^+\pi^-$ final state. For the $B^0 \to J/\psi K^0_S$ decay mode, K^0_S mesons are also reconstructed in the $\pi^0\pi^0$ final state. Inclusion of the $K^0_S \to \pi^0\pi^0$ channel increases a signal yield by about 20% of the $K^0_S \to \pi^+\pi^-$ channel. The masses of J/ψ, $\psi(2S)$, χ_{c1}, and K^0_S candidates are constrained to their respective nominal values to improve their momentum resolutions. Candidate K^0_L mesons are identified using information from the electromagnetic calorimeter and IFR/KLM detectors (see Chapter 2), requiring that the signals in these detectors are not associated with any charged tracks. Since the energy of a K^0_L cannot be measured precisely, only the flight direction is used when reconstructing $B^0 \to J/\psi K^0_L$ decay candidates. The K^{*0} candidates are selected by combining K^0_S and π^0 mesons. *BABAR* uses all of the aforementioned final states for their analysis. While Belle (Abe, 2001g) used the same set of modes for earlier iterations of their analysis, more recent updates do not include the $J/\psi K^0_S(\to \pi^0\pi^0)$, $\eta_c K^0_S$, and $J/\psi K^{*0}$ final states.

Candidate B^0 mesons are reconstructed by combining charmonium and K^0_S, K^0_L, or K^{*0} candidates. Two kinematic variables ΔE and $m_{\rm ES}$ (see Section 7.1.1) are used to select signal candidates, with the exception of the $B^0 \to J/\psi K^0_L$ channel. For the latter case a kinematic constraint is applied assuming a two-body decay of the B^0, and both *BABAR* and Belle use ΔE and the momentum of the reconstructed B^0 in the center-of-mass (CM) system (p^*_B) to isolate signal candidates. Figure 17.6.5 shows the $m_{\rm ES}$ and ΔE distributions for candidates satisfying the flavor tagging and vertex reconstructions in the *BABAR*

[73] Each of the two quarks ($\bar{c}s$) from the virtual W is paired with the quark originating from the initial state ($b\bar{d}$) to form a hadron. Since hadrons have to stay color-neutral, the color of $\bar{c}$ and s must match that of b and $\bar{d}$. Therefore the overall amplitude is 1/number-of-colors smaller than the decays in which $W^* \to \bar{q}q'$ hadronize by themselves.

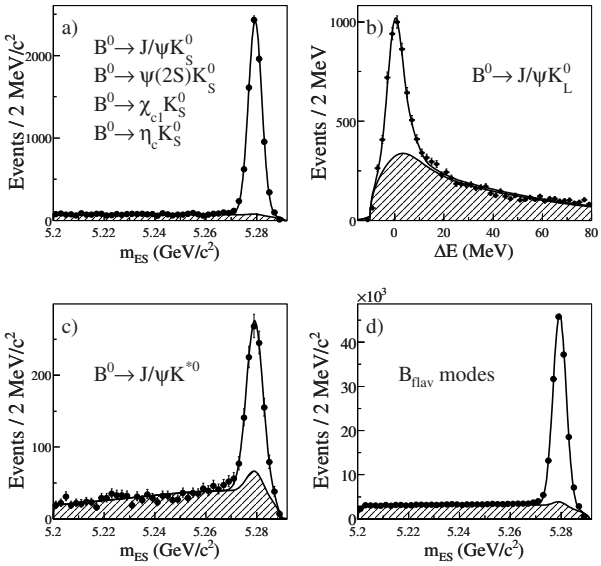

Figure 17.6.5. Distributions of $m_{\rm ES}$ or ΔE for (a) $B^0 \to (c\bar{c})K^0_S$, (b) $B^0 \to J/\psi K^0_L$, (c) $B^0 \to J/\psi K^{*0}$, and (d) B^0 decays to flavor-specific final states for the samples used in the *BABAR* measurement (Aubert, 2009z) of ϕ_1. The shaded regions represent the estimated background, and the solid lines are the projections of the fits to the data.

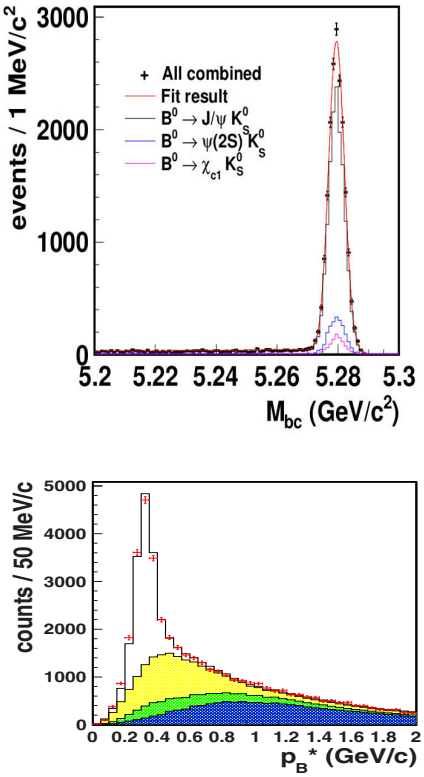

Figure 17.6.6. Distributions of $m_{\rm ES}$ $(= M_{\rm bc})$ for $B^0 \to (c\bar{c})K^0_S$ (top) and p^*_B for $B^0 \to J/\psi K^0_L$ (bottom) obtained with the samples used for the Belle measurement (Adachi, 2012c) of ϕ_1. The shaded regions in the bottom plot represent the estimated background components: (from top to bottom) real J/ψ and real K^0_L (yellow), real J/ψ and fake K^0_L (green), and fake J/ψ (blue).

analysis. Figure 17.6.6 shows the $m_{\rm ES}$ and p^*_B distributions for the Belle analysis.

Vertex reconstruction and B meson flavor tagging algorithms (described in Chapters 6 and 8) are applied to the selected signal candidates. Time-dependent *CP* asymmetry parameters are extracted from fits to the distributions of proper decay time difference between signal and tagged B mesons as described in Chapter 10. *BABAR* extracts the time-dependent asymmetry parameters (S and C) from a simultaneous fit to both the B_{CP} and $B_{\rm flav}$ (see Section 10.2) samples with 69 additional free parameters, where tagging and resolution parameters are transparently propagated into the *CP* analysis as part of the final statistical error. Belle takes a multi-step approach: the final fit includes only S and C as free parameters, and all the fit model parameters, which include signal fractions, flavor tagging performance parameters, and proper time difference resolution function parameters are fixed to the values determined from separate fits to the $B_{\rm flav}$ and B_{CP} samples. Effects arising from the uncertainties of these parameters are included in the final result as systematic errors.

The results of the time-dependent *CP* asymmetry measurements are summarized in Table 17.6.1 for each decay mode, and for the combined set of modes. As described in Section 17.6.8, the time-dependent full angular analysis of the $B^0 \to J/\psi K^{*0}$ decay can provide a value for $\cos 2\phi_1$ in addition to $\sin 2\phi_1$. The angular information presented in the table has been averaged over, resulting in a dilution of the measured *CP* asymmetry by a factor of $1 - 2R_\perp$, where $R_\perp$ is the fraction of the *CP*-odd component. *BABAR* uses the previously measured value $0.233 \pm 0.010 \pm 0.005$ (Aubert, 2007x). Systematic errors on the time-dependent asymmetry parameters are summarized in Table 17.6.2. The dominant sources for S are due to the uncertainties in vertex reconstruction and Δt resolutions, flavor tagging, and background in the $J/\psi K^0_L$ mode. The systematic error on C is dominated by tag-side interference. For this source, Belle takes into account a cancellation between *CP*-even and *CP*-odd states, while *BABAR* does not. Chapter 15 discusses the main sources of systematic uncertainty on time-dependent *CP* asymmetry parameter measurements in detail.

The Δt distributions and asymmetries obtained from the data for all modes combined are shown in Fig. 17.6.7. The values of C obtained are consistent with zero in accordance with SM expectations, and hence $-\eta_f S$ gives essentially $\sin 2\phi_1$. The average of the two experiments

Table 17.6.1. Summary of the time-dependent *CP*-asymmetry measurements using B^0 decays to charmonium + K^0 final states, for each decay mode and for all modes combined. $N_{\rm tag}$ and P are the number of candidates and signal purity (in %), respectively, in the signal region after flavor tagging and vertex reconstruction requirements have been applied. S and C are the *CP* asymmetry parameters for the final state with the *CP* eigenvalue η_f.

	BABAR (Aubert, 2009z)				Belle (Adachi, 2012c)			
Mode	$N_{\rm tag}$	P	$-\eta_f S$	C	$N_{\rm tag}$	P	$-\eta_f S$	C
$J/\psi K^0_S$	6750	95	$0.657 \pm 0.036 \pm 0.012$	$0.026 \pm 0.025 \pm 0.016$	13040	97	$0.670 \pm 0.029 \pm 0.013$	$0.015 \pm 0.021\ ^{+0.023}_{-0.045}$
$J/\psi K^0_L$	5813	56	$0.694 \pm 0.061 \pm 0.031$	$-0.033 \pm 0.050 \pm 0.027$	15937	63	$0.642 \pm 0.047 \pm 0.021$	$-0.019 \pm 0.026\ ^{+0.041}_{-0.017}$
$\psi(2S)K^0_S$	861	87	$0.897 \pm 0.100 \pm 0.036$	$0.089 \pm 0.076 \pm 0.020$	2169	91	$0.738 \pm 0.079 \pm 0.036$	$-0.104 \pm 0.055\ ^{+0.027}_{-0.047}$
$\chi_{c1}K^0_S$	385	88	$0.614 \pm 0.160 \pm 0.040$	$0.129 \pm 0.109 \pm 0.025$	1093	86	$0.640 \pm 0.117 \pm 0.040$	$0.017 \pm 0.083\ ^{+0.026}_{-0.046}$
$\eta_c K^0_S$	381	79	$0.925 \pm 0.160 \pm 0.057$	$0.080 \pm 0.124 \pm 0.029$				
$J/\psi K^{*0}$	1291	67	$0.601 \pm 0.239 \pm 0.087$	$0.025 \pm 0.083 \pm 0.054$				
All	15481	76	$0.687 \pm 0.028 \pm 0.012$	$0.024 \pm 0.020 \pm 0.016$	32239	79	$0.667 \pm 0.023 \pm 0.012$	$-0.006 \pm 0.016 \pm 0.012$

Table 17.6.2. Summary of systematic errors on the time-dependent *CP* asymmetry parameters measured in B^0 decays to charmonium + K^0 for all modes combined.

	BABAR		Belle	
Source	S	C	S	C
Vertex and Δt	0.007	0.003	0.010	0.007
Flavor tagging	0.006	0.002	0.004	0.003
$J/\psi K^0_L$ background	0.006	0.001	0.004	0.002
Other signal/background	0.005	0.003	0.002	0.001
Physics parameters	0.003	0.001	0.001	0.000
Tag-side interference	0.001	0.014	0.001	0.008
Possible fit bias	0.002	0.003	0.004	0.005
Total	0.012	0.016	0.012	0.012

(Amhis et al., 2012) gives

$$\sin 2\phi_1 = 0.677 \pm 0.020 \quad \text{and} \quad C = 0.006 \pm 0.017. \quad (17.6.5)$$

This corresponds to $\phi_1 = (21.30 \pm 0.78)^\circ$ (up to the four-fold ambiguity mentioned above). An accuracy of 3% on $\sin 2\phi_1$ (0.8° on ϕ_1) is achieved.

The evolution of the measured value of $\sin 2\phi_1$ can be seen in Fig. 17.6.8. Central values for the initial measurements from both experiments were slightly lower than the current world average. A significant milestone in the measurement of $\sin 2\phi_1$ was achieved in the summer of 2001 when both *BABAR* and Belle observed *CP* violation in B^0 meson decay.[74] The data samples used for these measurements each consists of about 30×10^6 $B\overline{B}$ pairs. Since that time, improved measurements have proved to be stable, and the results reported by *BABAR* and Belle have remained consistent with each other.

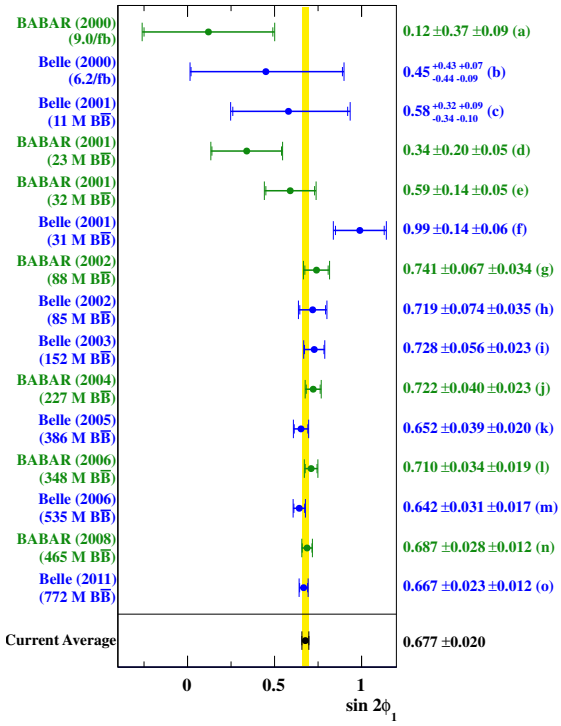

Figure 17.6.8. History of the $\sin 2\phi_1$ measurements with $b \to c\bar{c}s$ decays, ordered by the dates they appeared in public. References: (a) (Aubert, 2000), (b) (Aihara, 2000a), (c) (Abashian, 2001), (d) (Aubert, 2001a), (e) (Aubert, 2001e), (f) (Abe, 2001g), (g) (Aubert, 2002g), (h) (Abe, 2002b), (i) (Abe, 2005c), (j) (Aubert, 2005i), (k) (Abe, 2005j), (l) (Aubert, 2006j), (m) (Chen, 2007a), (n) (Aubert, 2009z), (o) (Adachi, 2012c).

17.6.4 ϕ_1 from $b \to c\bar{c}d$ decays

17.6.4.1 $B^0 \to J/\psi\pi^0$

The decay $B^0 \to J/\psi\pi^0$ is a $b \to c\bar{c}d$ transition into a *CP*-even final state. The final state has contributions from both a color- and Cabibbo-suppressed tree amplitude, and penguin amplitudes with different weak phases. In the absence of penguin contributions one can measure the Unitarity Triangle angle ϕ_1 using this decay. If there are significant penguin contributions, the measured value of ϕ_1, called the "effective phase" ϕ_1^{eff}, may differ from that obtained from the tree-dominated $B \to J/\psi K^0$ decays. There are two motivations for such a measurement; firstly it is possible to constrain theoretical uncertainties in $B \to J/\psi K^0$ decays using $B^0 \to J/\psi\pi^0$ (Ciuchini, Pierini, and Silvestrini, 2005), and secondly one may be able to probe, or constrain, possible new physics contributions to $b \to c\bar{c}d$ transitions manifesting via loop diagrams.

[74] A commonly accepted definition of "observation" is a result with a statistical significance of at least five standard deviations if the uncertainties are treated as Gaussian.

Unlike $b \to c\bar{c}s$ decays, which are experimentally clean, one has to consider significant background contributions when trying to extract information from $B^0 \to J/\psi\pi^0$ signal events. These background contributions include events from B decays to $J/\psi\rho^0$, $J/\psi K^0_S$, $J/\psi K^{*0}$, $J/\psi K^{*\pm}$, and $J/\psi\rho^\pm$ final states as well as smaller contributions from other B decays to final states including a J/ψ. The aforementioned backgrounds populate the negative ΔE region (peak ~ -0.2 GeV) and have a tail in the signal region around $\Delta E \sim 0$ (see Fig. 17.6.9). Since these modes are well measured, the B Factories have relied on existing branching fraction measurements from the Particle Data Group (Yao et al., 2006) in order to fix the normalization of background contributions while extracting signal yields and *CP* asymmetry parameters. The normalization of the combinatorial background is allowed to vary in the fit.

Both experiments perform an unbinned maximum likelihood fit to data using discriminating variables: m_{ES}, ΔE, and Δt. In order to suppress background from light-quark continuum events, *BABAR* also includes a Fisher discriminant as one of the discriminating variables in their fit to data. This is computed using three variables: L_0, L_2

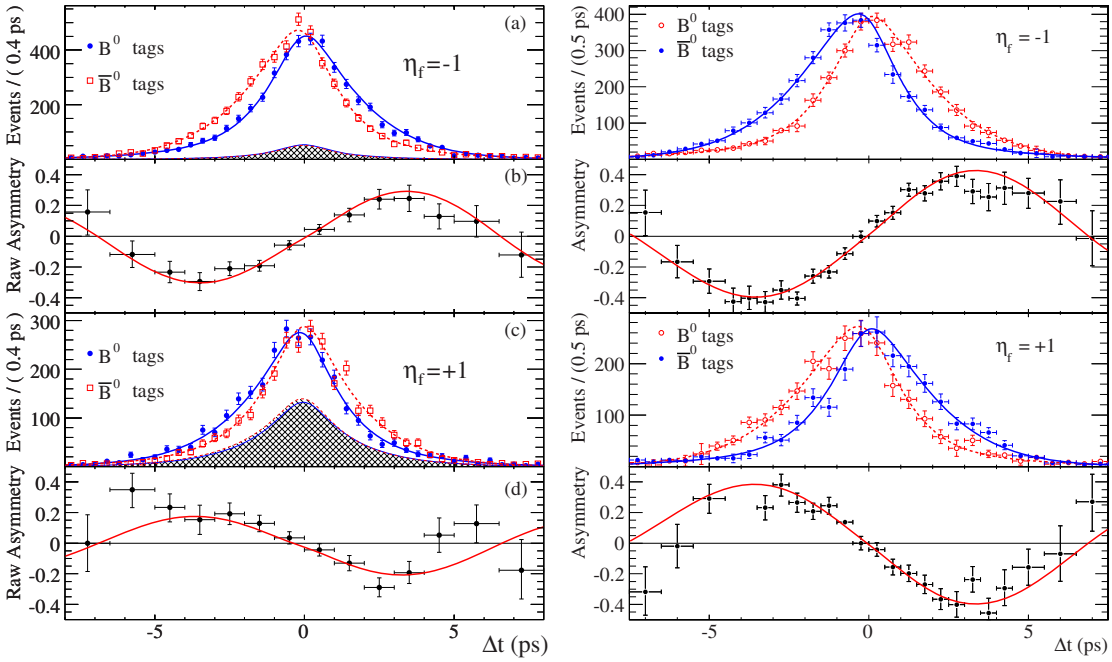

Figure 17.6.7. Flavor-tagged Δt distributions (a,c) and raw *CP* asymmetries (b,d) for the *BABAR* (left, (Aubert, 2009z)) and Belle (right, (Adachi, 2012c)) measurements of $\sin 2\phi_1$. The top two plots show the $B \to (c\bar{c})K^0_S$ ($\eta_f = -1$) samples, and the bottom two show the $B \to J/\psi K^0_L$ ($\eta_f = +1$) sample. The shaded regions for *BABAR* represent the fitted background, while the Belle distributions are background subtracted. The two experiments adopt the opposite color code in Δt distribution plots.

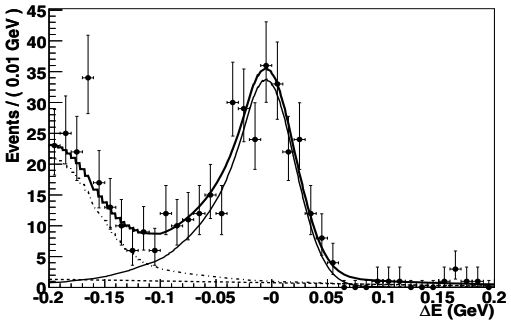

Figure 17.6.9. Distributions of ΔE for $B^0 \to J/\psi\pi^0$ samples used in the Belle measurement (Lee, 2008) of ϕ_1. The superimposed curves show the signal (solid line), $B \to J/\psi X$ background (dot-dashed line), combinatorial background (dashed line) and the sum of all the contributions (thick solid line).

(Eq. (9.4.1)), and $\cos\theta_H$, where θ_H is the angle between the positively charged lepton and the B candidate momenta in the J/ψ rest frame. In contrast, Belle achieves continuum background rejection by applying a cut on the ratio of zeroth to second Fox-Wolfram moments, $R_2 < 0.4$. Details on these background suppression techniques can be found in Chapter 9.

The most recent results obtained by *BABAR* (Aubert, 2008i) and Belle (Lee, 2008) use 465 $\times 10^6$ and 535 $\times 10^6$ $B\overline{B}$ pairs, respectively, and are summarized in Table 17.6.3. *BABAR* finds *CP* violation with 4.0σ significance, and Belle finds 2.4σ significance. Both results, and their average, are consistent with the value of S measured in $b \to c\bar{c}s$ decays. The obtained value of C is consistent with zero.

Table 17.6.3. The time-dependent *CP* asymmetry parameters $-\eta_f S$ and C for the decay $B^0 \to J/\psi\pi^0$. The first quoted uncertainty is statistical, and the second is systematic. The averages are obtained by HFAG (Amhis et al., 2012).

Experiment	$-\eta_f S$	C
BABAR	$1.23 \pm 0.21 \pm 0.04$	$-0.20 \pm 0.19 \pm 0.03$
Belle	$0.65 \pm 0.21 \pm 0.05$	$-0.08 \pm 0.16 \pm 0.05$
Average	0.93 ± 0.15	-0.10 ± 0.13

17.6.4.2 $B^0 \to D^{(*)\pm}D^{(*)\mp}$

The decay $B^0 \to D^{(*)\pm}D^{(*)\mp}$ is dominated by a color-favored tree-diagram in the SM. When neglecting the penguin (loop) diagram, the mixing induced *CP* asymmetry of $B^0 \to D^{(*)\pm}D^{(*)\mp}$ is also determined by $\sin 2\phi_1$. The

effect of neglecting the penguin amplitude has been estimated in models based on factorization and heavy quark symmetry, and the corrections are expected to be a few percent (Xing, 1998, 2000). Significant deviation of S in $B^0 \to D^{(*)\pm}D^{(*)\mp}$ decays with respect to $\sin 2\phi_1$ determined from $b \to c\bar{c}s$ transitions, or a large non-zero value of C, could indicate physics beyond the SM (Grossman and Worah, 1997; M. Gronau and Pirjol, 2008; Zwicky, 2007).

The $B^0 \to D^{(*)\pm}D^{(*)\mp}$ candidates are formed from oppositely charged $D^{(*)}$ mesons reconstructed in the following channels: $D^{*+} \to D^0\pi^+$, $D^{*+} \to D^+\pi^0$, $D^0 \to K^-\pi^+$, $D^0 \to K^-\pi^+\pi^0$, $D^0 \to K^-\pi^+\pi^-\pi^+$, $D^0 \to K^0_S\pi^+\pi^-$, and $D^+ \to K^-\pi^+\pi^+$. Belle also uses the $D^0 \to K^+K^-$, $D^+ \to K^0_S\pi^+$ and $K^0_S\pi^+\pi^0$ channels. In the $B^0 \to D^{*+}D^{*-}$ mode, B^0 candidates where both D^* mesons decay to $D\pi^0$ are excluded because of its smaller branching fraction and larger backgrounds. At least one D meson is required to decay via $D^+ \to K^-\pi^+\pi^+$ for the $B^0 \to D^+D^-$ decay.

Both *BABAR* and Belle also analyze these decays using partially reconstructed events. However, while Belle includes these events in their analysis of fully reconstructed events, *BABAR* performs a separate $B^0 \to D^{*+}D^{*-}$ analysis of partially reconstructed events. For the partial reconstruction method one D^{*-} (or a $D^- \to K^+\pi^-\pi^-$) is fully reconstructed as described in the previous paragraph. For the other D^{*+}, only a slow pion $\pi^+_{\rm slow}$ from the decay $D^{*+} \to D^0\pi^+_{\rm slow}$, is reconstructed. The details of the partial reconstruction technique are described in Section 7.3. Due to low B meson CM momentum and small energy release in the D^{*+} decay, the momenta of $\pi^+_{\rm slow}$ and $D^{(*)-}$ are almost back-to-back. This signature is used as a discriminator in Belle's analysis. *BABAR* on the other hand exploits the kinematics of the event and calculates the B four-momentum up to an unknown azimuthal angle around the direction of the fully reconstructed D^*. *BABAR* uses the median value for this angle based on simulation to calculate the recoil mass of the unreconstructed D^0 and uses this recoil mass as a fit variable to separate signal and background. Belle requires the CM momenta of the reconstructed mesons in the $D^{*+}D^-$ mode to satisfy $1.63\ \text{GeV}/c < p^*_{D^{(*)-}} < 1.97\ \text{GeV}/c$ and $p^*_{\pi^+_{\rm slow}} < 0.18\ \text{GeV}/c$. *BABAR* selects events with $1.3\ \text{GeV}/c < p^*_{D^{*-}} < 2.1\ \text{GeV}/c$ and $p^*_{\pi^+_{\rm slow}} < 0.6\ \text{GeV}/c$.

In the partial reconstruction technique used by both experiments, a lepton $\ell_{\rm tag}$ is used to provide flavor tagging, suppress continuum background to a negligible level, and reduce combinatorial $B\overline{B}$ background. In addition to leptons *BABAR* also uses kaons for flavor tagging. The vertex of the reconstructed B ($B_{\rm rec}$) is determined by a fit with the fully reconstructed $\overline{D}^0$ or D^- mesons to the interaction region. On the tagging side, the $\ell_{\rm tag}$ is fitted to the interaction region to provide the $B_{\rm tag}$ vertex information. For the kaon-tagged events (*BABAR*), all tracks that do not belong to $B_{\rm rec}$ and are outside of a cone of $\cos\theta = 0.5$ around the missing D^0 direction are used for $B_{\rm tag}$ vertexing. A kinematic cut is applied to remove a large fraction of the background events from $B \to D^{(*)-}\ell^+X$ decays or other sources where the tagging track originates from the same B as the fully reconstructed D^* or D^-. In Belle's analysis, the calculated angle between the B and $D^{(*)}\ell_{\rm tag}$ combination is required to be outside the physical region of $B \to D^{(*)-}\ell^+X$, *i.e.*,

$$\cos\theta_{B,D\ell} = \frac{(E_{\rm beam} - E^*_{D\ell})^2 - p^{*2}_B - p^{*2}_{D\ell}}{2p^*_B p^*_{D\ell}} < -1.1. \tag{17.6.6}$$

In *BABAR*'s analysis, the angle between the tagging lepton (kaon) and the missing D^0 is required to be larger than arccos 0.75 (arccos 0.5). This kind of background (tagging and reconstructed particles originating from the same B) cannot be completely eliminated, and care is taken to evaluate the mistag effects.

For each $B^0 \to D^{(*)\pm}D^{(*)\mp}$ candidate, *BABAR* constructs a likelihood function $\mathcal{L}_{\rm mass}$ from the masses and mass uncertainties of the D and D^* candidates. The values of $\mathcal{L}_{\rm mass}$ and ΔE are used to reduce the combinatorial background. From the simulated events, the minimum allowed values of $-\ln\mathcal{L}_{\rm mass}$ and $|\Delta E|$ for each individual final state are optimized to obtain the highest expected signal significance.

The technique used to fit the Δt distribution is analogous to the one used in $b \to c\bar{c}s$ decays. Since the $B^0 \to D^{*+}D^{*-}$ final state contains two vector mesons, it is an admixture of *CP*-even and *CP*-odd states depending on the orbital angular momentum of the decay products (Chapter 12). In the partial reconstruction approach, the helicity angles are calculated ignoring the B meson momentum. In the fit to data, two scenarios are considered. In the first scenario, the *CP*-even amplitude is allowed to have different *CP*-violating parameters (C_+ and S_+) from those of the *CP*-odd amplitude ($C_\perp$ and $S_\perp$). In the second scenario, we assume that $C_+ = C_\perp = C_{D^{*+}D^{*-}}$ and $S_+ = -S_\perp = S_{D^{*+}D^{*-}}$.[75] In the absence of penguin contributions, $S_{D^+D^-} = S_+ = -S_\perp = -\sin 2\phi_1$ and $C_{D^+D^-} = C_+ = C_\perp = 0$.

As $B^0 \to D^{*\pm}D^{\mp}$ is not a *CP* eigenstate, the expressions for the different S and C parameters are related, $S_{D^{*\pm}D^{\mp}} = -\sqrt{1 - C^2_{D^{*\pm}D^{\mp}}}\sin(2\phi_1^{\rm eff} \pm \delta)$ (see Eq. 10.2.6) , where δ is the strong phase difference between the $D^{*+}D^-$ and $D^{*-}D^+$ amplitudes. Neglecting the penguin contributions, $\phi_1^{\rm eff} = \phi_1$ and $C_{D^{*+}D^-} = -C_{D^{*-}D^+}$. It is convenient to express the *CP* asymmetry parameters as

$$\begin{aligned} S_{D^*D} &= \frac{1}{2}(S_{D^{*+}D^-} + S_{D^+D^{*-}}), \\ C_{D^*D} &= \frac{1}{2}(C_{D^{*+}D^-} + C_{D^+D^{*-}}), \\ \Delta S_{D^*D} &= \frac{1}{2}(S_{D^{*+}D^-} - S_{D^+D^{*-}}), \\ \Delta C_{D^*D} &= \frac{1}{2}(C_{D^{*+}D^-} - C_{D^+D^{*-}}). \end{aligned} \tag{17.6.7}$$

[75] In some literature, the opposite sign convention of $S_\perp$ is used, *i.e.*, $S_+ = +S_\perp = S_{D^{*+}D^{*-}}$.

Table 17.6.4. Summary of *CP* asymmetry parameter measurements for $B^0 \to D^{(*)\pm}D^{(*)\mp}$ decays. Signal yields quoted here include tagged and untagged events. Reference: (a) (Aubert, 2009ad); (b) Lees (2012k); (c) (Kronenbitter, 2012); (d) (Rohrken, 2012).

	BABAR	Belle
$B^0 \to D^{*+}D^{*-}$	934 ± 40 (a)	1225 ± 59 (c)
S_+	$-0.76 \pm 0.16 \pm 0.04$	$-0.81 \pm 0.13 \pm 0.03$
C_+	$+0.00 \pm 0.12 \pm 0.02$	$-0.18 \pm 0.10 \pm 0.05$
$-S_\perp$	$-1.80 \pm 0.70 \pm 0.16$	$-1.52 \pm 0.62 \pm 0.12$
$C_\perp$	$+0.41 \pm 0.49 \pm 0.08$	$+0.05 \pm 0.39 \pm 0.08$
$S_{D^{*+}D^{*-}}$	$-0.70 \pm 0.16 \pm 0.03$	$-0.79 \pm 0.13 \pm 0.03$
$C_{D^{*+}D^{*-}}$	$+0.05 \pm 0.09 \pm 0.02$	$-0.15 \pm 0.08 \pm 0.04$
$B^0 \to D^{*+}D^{*-}$ (partial rec.)	4972 ± 453 (b)	-
$S_{D^{*+}D^{*-}}$	$-0.49 \pm 0.18 \pm 0.08$	-
$C_{D^{*+}D^{*-}}$	$+0.15 \pm 0.09 \pm 0.04$	-
$B^0 \to D^*D$	724 ± 37 (a)	887 ± 39 (d)
S_{D^*D}	$-0.68 \pm 0.15 \pm 0.04$	$-0.78 \pm 0.15 \pm 0.05$
C_{D^*D}	$+0.04 \pm 0.12 \pm 0.03$	$-0.01 \pm 0.11 \pm 0.04$
ΔS_{D^*D}	$+0.05 \pm 0.15 \pm 0.02$	$-0.13 \pm 0.15 \pm 0.04$
ΔC_{D^*D}	$+0.04 \pm 0.12 \pm 0.03$	$-0.12 \pm 0.11 \pm 0.03$
$B^0 \to D^+D^-$	152 ± 17 (a)	269 ± 21 (d)
$S_{D^+D^-}$	$-0.63 \pm 0.36 \pm 0.05$	$-1.06\ ^{+0.21}_{-0.14} \pm 0.08$
$C_{D^+D^-}$	$-0.07 \pm 0.23 \pm 0.03$	$-0.43 \pm 0.16 \pm 0.05$

The parameters S_{D^*D} and C_{D^*D} characterize mixing induced *CP* violation and flavor-dependent direct *CP* violation, respectively. ΔS_{D^*D} and ΔC_{D^*D} are insensitive to *CP* violation. In the case of *BABAR*'s $B^0 \to D^{*+}D^{*-}$ partial reconstruction method, the fit parameter S is $(1 - 2R_\perp)S_{D^{*+}D^{*-}}$, where $R_\perp$ is the *CP*-odd fraction measured from fully reconstructed $D^{*+}D^{*-}$ events.

The most recent measurements of the *CP* violation in $B^0 \to D^{(*)\pm}D^{(*)\mp}$ decays by *BABAR* are based on the full data sample, 467×10^6 $B\overline{B}$ pairs (Aubert, 2009ad), while Belle measurements are based on 772×10^6 $B\overline{B}$ pairs (Kronenbitter, 2012; Rohrken, 2012). The results are summarized in Table 17.6.4. These supersede the previous *BABAR* (Aubert, 2003g, 2005u, 2007n,u) and Belle (Aushev, 2004; Fratina, 2007; Miyake, 2005; Vervink, 2009) measurements, except for the Belle result based on the $B^0 \to D^*D$ partial reconstruction (Aushev, 2004).

The averages of *BABAR* and Belle results (Amhis et al., 2012) are $S_{D^{*+}D^{*-}} = -0.77 \pm 0.10$, $S_{D^*D} = -0.73 \pm 0.11$, and $S_{D^+D^-} = -0.98 \pm 0.17$, and other parameters are consistent with zero within uncertainties. All three modes have significant *CP* violation asymmetries ($> 5\sigma$), which are consistent with the SM expectation with small penguin amplitude contributions (S parameters are consistent with the $\sin 2\phi_1$ value from $b \to c\bar{c}s$ decays).

17.6.5 ϕ_1 from $b \to c\bar{u}d$ decays

17.6.5.1 $B^0 \to D^{(*)}h^0$

The decay $B^0 \to D^{(*)}h^0$, where h^0 is a light, unflavored neutral meson, is dominated by a $b \to c\bar{u}d$ color-suppressed tree diagram in the SM. The final state $D^{(*)}h^0$ is a *CP* eigenstate if the neutral D meson decays to a *CP* eigenstate as well. In this case, the time-dependent asymmetry in B^0 decays is similar to that of $b \to c\bar{c}s$ decays but with a small correction from the $b \to u\bar{c}d$ amplitude. This amplitude is suppressed by $V_{ub}V_{cd}^*/V_{cb}V_{ud}^* \simeq 0.02$, and therefore the deviation is expected to be small in the SM (Fleischer, 2003a,b; Grossman and Worah, 1997). R-parity violating ($\not{R}_p$) supersymmetric processes (Grossman and Worah, 1997) could enter at the tree level in these decays, leading to a deviation from the SM prediction.

In *BABAR*'s analysis (Aubert, 2007ad) with 383×10^6 $B\overline{B}$ pairs, the B^0 meson is fully reconstructed in the following channels: $D^{(*)}\pi^0$ ($D \to K^+K^-$, $K_S^0\omega$) and $D^{(*)}\eta$ ($D \to K^+K^-$), where $D^{*0} \to D^0\pi^0$, and $D\omega$ ($D \to K^+K^-$, $K_S^0\omega$, $K_S^0\pi^0$). The η mesons are reconstructed via $\gamma\gamma$ and $\pi^+\pi^-\pi^0$ final states, and the ω candidates are reconstructed from the $\pi^+\pi^-\pi^0$ decay mode. The event selection criteria are determined by maximizing the expected signal significance using Monte Carlo simulated signal events and simulated samples of generic $B\overline{B}$ and $e^+e^- \to q\bar{q}$ ($q = u, d, s, c$) continuum events.

Angular distributions of the $D \to K_S^0\omega$ decay mode are exploited to take advantage of the polarization in the decay. The background from continuum $q\bar{q}$ production is suppressed by a Fisher discriminant constructed using several event shape variables and angular distributions (see Chapter 9).

The signal and combinatorial background yields are determined by a fit to the $m_{\rm ES}$ distribution using a Gaussian and a threshold function (ARGUS, see Eq. (7.1.11)) for the signal and combinatorial background components, respectively. The contribution from each mode is shown in Table 17.6.5. Peaking background contributions are studied using both simulation and D^0 sideband data. The contributions to *CP*-even and *CP*-odd modes are $(0.8 \pm 2.6)\%$ and $(11 \pm 6)\%$, respectively.

The fit technique adopted to extract the *CP* violating parameters S and C is similar to that used in $b \to c\bar{c}s$ decays. The mistag parameters and the resolution function are determined from a large data control sample of $B^0 \to D^{(*)-}h^+$ decays, where h^+ is a π^+, ρ^+, or a_1^+ meson. An exponential decay is used to model the Δt p.d.f. of the peaking background and accounts for possible *CP* asymmetries in the systematic uncertainty. In addition to the fit to the entire sample, fits to *CP*-even and *CP*-odd subsamples are performed to check consistency. As the SM corrections due to the sub-leading-order $b \to u\bar{c}d$ diagram are different for D_{CP+} and D_{CP-} (Fleischer, 2003a,b), a fit is also performed allowing different *CP* asymmetries for D_{CP+} and D_{CP-}. The results are summarized in Table 17.6.5, and the Δt distribution projections and the asymmetry of the events in the signal region are shown in Fig. 17.6.10. The result is consistent with the world

Table 17.6.5. Summary of the $B^0 \to D^{(*)0}_{CP} h^0$ analysis from *BABAR* (Aubert, 2007ad). The *CP* eigenvalue of the D^0 final state is indicated in the column 'D_{CP}'.

$\eta_f = +1$ (*CP* even)			$\eta_f = -1$ (*CP* odd)		
Mode	D_{CP}	$N_{\rm signal}$	Mode	D_{CP}	$N_{\rm signal}$
$D^0_{K^0_S\omega}\pi^0$	$-$	26.2 ± 6.3	$D^0_{KK}\pi^0$	$+$	104 ± 17
$D^0_{K^0_S\pi^0\omega}$	$-$	40.0 ± 8.0	$D^0_{KK}\eta_{\gamma\gamma}$	$+$	28.9 ± 6.5
$D^0_{K^0_S\omega}\omega$	$-$	23.2 ± 6.8	$D^0_{KK}\eta_{3\pi}$	$+$	14.2 ± 4.7
$D^{*0}_{KK}\pi^0$	$+$	23.2 ± 6.3	$D^0_{KK}\omega$	$+$	51.2 ± 8.5
$D^{*0}_{KK}\eta_{\gamma\gamma}$	$+$	9.8 ± 3.5	$D^{*0}_{K^0_S\omega}\pi^0$	$-$	5.5 ± 3.3
$D^{*0}_{KK}\eta_{3\pi}$	$+$	6.8 ± 2.9			
Combined		131 ± 16			209 ± 23
$\eta_f S$		-0.17 ± 0.37			-0.82 ± 0.28
C		-0.21 ± 0.25			-0.21 ± 0.21
$\eta_f S$ (combined)		$-0.56 \pm 0.23 \pm 0.05$			
C (combined)		$-0.23 \pm 0.16 \pm 0.04$			
		D_{CP+}			D_{CP-}
$\eta_f S$		$-0.65 \pm 0.26 \pm 0.06$			$-0.46 \pm 0.45 \pm 0.13$
C		$-0.33 \pm 0.19 \pm 0.04$			$-0.03 \pm 0.28 \pm 0.07$

average of $-\sin 2\phi_1$, and is 2.3σ from the *CP*-conserving hypothesis $S = C = 0$.

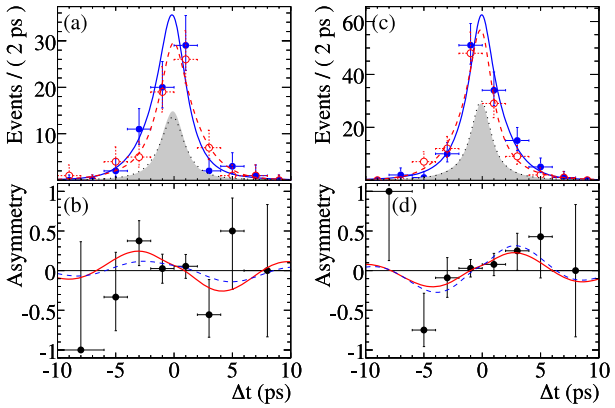

Figure 17.6.10. Δt distributions and asymmetries of $B^0 \to D^{(*)0}_{CP} h^0$ candidates from *BABAR* (Aubert, 2007ad) for (a, b) *CP*-even and (c, d) *CP*-odd candidates in the signal region ($m_{\rm ES} > 5.27\,{\rm GeV}/c^2$). In (a) and (c), the solid points and curve (open circles and dashed curve) are B^0-tagged ($\overline{B}^0$-tagged) candidates and Δt projection curves. Shaded areas (dotted lines) are background distributions for the B^0-tagged ($\overline{B}^0$-tagged) candidates. In (b) and (d), the solid curve represents the combined fit result, and the dashed curve represents the result of the fits to *CP*-even and *CP*-odd modes separately.

17.6.6 ϕ_1 from charmless quasi-two-body B decays

The time-dependent *CP* asymmetry parameter S measured in charmless decays to *CP* eigenstates via $b \to s\bar{q}q$ penguin transitions is also equal to $S = -\eta_f \sin 2\phi_1$ in the SM. These decays are particularly sensitive to new physics because any unobserved heavy particle could contribute an additional penguin loop and alter the value of the measured weak phase. If the measured S in one or a group of charmless decays deviates significantly from that in tree-dominated processes, it could be a signature of new physics effects. The comparison between loop and tree-dominated decays, however, must to be made with careful estimates of the SM corrections from higher order topologies. The key issue in the theoretical understanding of these *CP* asymmetries is the tree-to-penguin ratio, both in short- and long-distance interactions. The typical deviations in theoretical calculations are below a few percent, and the corresponding uncertainty can be as small as one or two percent. The modes that benefit from the least theoretical uncertainties are $\eta' K^0_S$, ϕK^0_S, and $K^0_S K^0_S K^0_S$ (Beneke, 2005; Cheng, Chua, and Soni, 2005a,b).

Of the charmless decays of interest, two-body and quasi-two-body final states are the simplest states to study experimentally. The term "quasi-two-body" refers to a final state that includes a resonance whose interference with any other amplitude is ignored (details in Section 17.4.5). The experiments at the B Factories have studied the *CP*-odd states $B^0 \to \eta' K^0_S$, ωK^0_S, $\pi^0 K^0_S$ and the *CP*-even states $B^0 \to \eta' K^0_L$ and $\pi^0 K^0_L$. Measurements of time-dependent asymmetries in three-body decays are discussed in Section 17.6.7.

Due to the similarity between the experimental techniques used to reconstruct the $B^0 \to \pi^0 K^0_S$ and $B^0 \to K^0_S K^0_S$ decays, the latter measurement is included in this section. The $2K^0_S$ mode is dominated by a $b \to d\bar{s}s$ penguin transition. Assuming top-quark dominance in the virtual loop, the time-dependent *CP* asymmetry parameters in this decay are expected to vanish, *i.e.* $S_{K^0_S K^0_S} = C_{K^0_S K^0_S} = 0$ (Fleischer, 1994). If a significant discrepancy is observed, this would be a clear signature of new physics (Giri and Mohanta, 2004).

Measurements of time-dependent asymmetry parameters of B mesons decaying into $\eta' K^0$, ωK^0_S, $\pi^0 K^0$, and $K^0_S K^0_S$ are described in the following.

17.6.6.1 $B^0 \to \eta' K^0$

The branching fraction of the $B^0 \to \eta' K^0$ decay was first measured by CLEO (Behrens et al., 1998) and was surprisingly large compared to naïve expectations. This result is confirmed by both Belle (Abe, 2001d) and *BABAR* (Aubert, 2001d). Because of the large branching fraction, this mode provides the most precise time-dependent *CP* asymmetry parameter measurement of any $b \to s\bar{q}q$ decay mode. The first measurements were made in 2002 by Belle (Chen, 2002) and in 2003 by *BABAR* (Aubert, 2003i). For these measurements, the η' candidates were reconstructed via $\eta' \to \eta\pi^+\pi^-$ and $\eta' \to \rho^0\gamma$ decays, with $\eta \to \gamma\gamma$ and $\rho^0 \to$

$\pi^+\pi^-$. Only the $B^0 \to \eta' K^0_S$ mode was considered, using $K^0_S \to \pi^+\pi^-$. The measured values of S were consistent between the two experiments but the uncertainties were large. Over the years both experiments have improved the measurements method and increased the available data sample. The decays $\eta \to \pi^+\pi^-\pi^0$ and $K^0_S \to \pi^0\pi^0$ are added to the reconstructed sub-decays listed above. All the combinations of the sub-decays are used except for the $\eta' \to \pi^+\pi^-\pi^0$, $K^0_S \to \pi^0\pi^0$ combination. Belle also excludes the $\eta' \to \rho^0\gamma$, $K^0_S \to \pi^0\pi^0$ combination. A tension between these results and the SM expectation at a level of 3σ was reported by *BABAR* in 2005 (Aubert, 2005w), but was not confirmed by Belle (Chen, 2005b). In the 2007 update of the measurements (Aubert (2007am); Chen (2007a)), the decay $B^0 \to \eta' K^0_L$ with $\eta' \to \eta\pi^+\pi^-$ (both sub-decays of the η considered) is also added. With these measurements, both experiments are able to establish the existence of *CP* violation in the $B^0 \to \eta' K^0$ mode, obtained from the combination of the $B^0 \to \eta' K^0_S$ and $B^0 \to \eta' K^0_L$ decays. This is the first observation of *CP* violation (with a significance greater than 5σ) in $b \to s\bar{q}q$ transitions. These measurements are consistent with the SM expectation.

In the most recent measurements, *BABAR* and Belle use data samples of 467×10^6 and 535×10^6 $B\overline{B}$ pairs (Aubert (2009aa); Chen (2007a)), respectively. The kinematic variables used to identify B^0 candidates are $m_{\rm ES}$ and ΔE for $\eta' K^0_S$; ΔE (*BABAR*) or p^*_B (Belle) for $\eta' K^0_L$. As with other charmless B decays, the dominant background comes from $e^+e^- \to q\bar{q}$ ($q = u, d, s, c$) continuum events. Loose cuts are applied to continuum suppression variables. These variables are also used together with the aforementioned kinematic variables in the fit to extract signals. *BABAR* uses a Fisher discriminant formed from shape variables, while Belle uses a likelihood ratio formed from a Fisher discriminant with modified Fox-Wolfram moments (see Chapter 9). The flavor tagging, vertex reconstruction, and fit procedures used to extract the *CP* asymmetry parameters are essentially the same as for $b \to c\bar{c}s$ decays. The results obtained are shown in Table 17.6.6. The time-dependent event yields and asymmetry from Belle are shown in Fig. 17.6.11. Both experiments measure asymmetry parameters consistent with results from $b \to c\bar{c}s$ decays. These measurements are limited by statistical uncertainties. Most of the systematic uncertainties are in common with the $b \to c\bar{c}s$ modes, and summarized in Section 15.3. The main contributions to the systematic uncertainty arise from the *CP* content of the $B\overline{B}$ background and the likelihood fit model used.

In the course of the book preparation the final Belle result in this mode became available, using the integrated luminosity of 711 fb^{-1} (Santelj, 2013). The measurement mainly profits from the increased statistical power of the sample due to both, the increase in the luminosity as well as the reprocessing of data (see Section 3.3). The result including K^0_S and K^0_L final states is in agreement with the SM prediction,

$$S = 0.68 \pm 0.07 \pm 0.03$$
$$C = 0.03 \pm 0.05 \pm 0.03\ . \qquad (17.6.8)$$

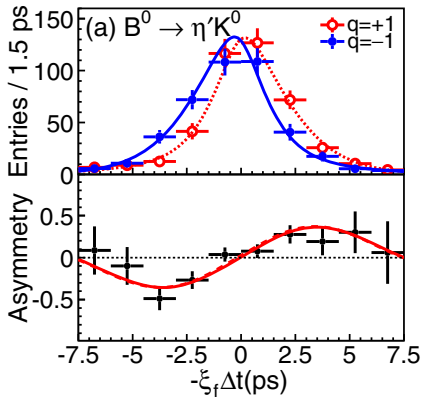

Figure 17.6.11. Background subtracted Δt distributions and time-dependent asymmetry for $B^0 \to \eta' K^0$ events with a good flavor tag from Belle (Chen, 2007a).

17.6.6.2 $B^0 \to \omega K^0_S$

$B^0 \to \omega K^0_S$ candidates are reconstructed via $\omega \to \pi^+\pi^-\pi^0$ and $K^0_S \to \pi^+\pi^-$ sub-decay channels. The ω candidates are selected by requiring the $\pi^+\pi^-\pi^0$ invariant mass to be within a window around the nominal mass. As for $B^0 \to \eta' K^0_S$, $m_{\rm ES}$, ΔE, and continuum suppression variables are used to extract signals from background. *BABAR* also includes the invariant mass of $\pi^+\pi^-\pi^0$ and $\mathcal{H}$ in the fit to data to improve signal to background discrimination. The variable $\mathcal{H}$ is the cosine of the angle between the opposite direction of the B meson and the normal to the decay plane in the ω rest frame. *BABAR* (Aubert, 2009aa) and Belle (Abe, 2007e) analyze data samples of 467×10^6 and 535×10^6 $B\overline{B}$ pairs, respectively. Results are shown in Table 17.6.6, where the number of signal events obtained is small ($\sim$ 100) and the uncertainties on S and C are large.

17.6.6.3 $B^0 \to \pi^0 K^0$

Since the $B^0 \to \pi^0 K^0_S$ decay does not produce charged tracks at the B^0 decay vertex, it is experimentally challenging to perform a time-dependent analysis. The decay position is determined from the intersection of the K^0_S trajectory, which is determined from the π^+ and π^- tracks and the profile of the interaction point. *BABAR* imposes the constraint that the sum of the two B decay times ($t_{CP} + t_{\rm tag}$) is equal to $2\tau_{B^0}$ with an uncertainty $\sqrt{2}\tau_{B^0}$ in order to further improve the accuracy of the reconstructed value of Δt. The π^+ and π^- tracks are required to be well measured in the silicon vertex detector. Since $c\tau$ of a K^0_S is 2.84 cm, about 60% and 30% of K^0_S candidates satisfy this condition at *BABAR* and Belle, respectively. Flavor tagged signal events can contribute to the precision obtained on C. Events that fail to satisfy the requirement are also used in the fit with a p.d.f which is obtained by

Table 17.6.6. Summary of time-dependent asymmetry parameter measurements for charmless two-body and quasi-two-body decays. Signal yields quoted here are for tagged and untagged events for *BABAR* and only tagged events for Belle. The $B^0 \to K_S^0 K_S^0$ mode is expected to have $S = C = 0$ in the SM, and $S = -\eta_f \sin 2\phi_1$ and $C = 0$ for the other modes.

	BABAR	Belle	Average (Amhis et al., 2012)
		$\eta' K^0$	
Ref.	Aubert (2009aa)	(Chen, 2007a)	
Yield	2515 ± 69	1875 ± 60	
$-\eta_f S$	$0.57 \pm 0.08 \pm 0.02$	$0.64 \pm 0.10 \pm 0.04$	0.59 ± 0.07
C	$-0.08 \pm 0.06 \pm 0.02$	$0.01 \pm 0.07 \pm 0.05$	-0.05 ± 0.05
		ωK_S^0	
Ref.	(Aubert, 2009aa)	(Abe, 2007e)	
Yield	163 ± 18	118 ± 18	
$-\eta_f S$	$0.55^{+0.26}_{-0.29} \pm 0.02$	$0.11 \pm 0.46 \pm 0.07$	0.45 ± 0.24
C	$-0.52^{+0.22}_{-0.20} \pm 0.03$	$0.09 \pm 0.29 \pm 0.06$	-0.32 ± 0.17
	$\pi^0 K_S^0$	$\pi^0 K^0$	
Ref.	(Aubert, 2009aa)	(Fujikawa, 2010)	
Yield	556 ± 32	919 ± 62	
$-\eta_f S$	$0.55 \pm 0.20 \pm 0.03$	$0.67 \pm 0.31 \pm 0.08$	0.57 ± 0.17
C	$0.13 \pm 0.13 \pm 0.03$	$-0.14 \pm 0.13 \pm 0.06$	0.01 ± 0.10
		$K_S^0 K_S^0$	
Ref.	(Aubert, 2006ai)	(Nakahama, 2008)	
Yield	32 ± 9	58 ± 11	
S	$-1.28^{+0.80+0.11}_{-0.73-0.16}$	$-0.38^{+0.69}_{-0.77} \pm 0.09$	-1.08 ± 0.49
C	$-0.40 \pm 0.41 \pm 0.06$	$0.38 \pm 0.38 \pm 0.05$	-0.06 ± 0.26

integrating the time-dependent p.d.f. with respect to Δt. *BABAR* (Aubert, 2009aa) and Belle (Fujikawa, 2010) analyze 467×10^6 and 657×10^6 $B\overline{B}$ pairs, respectively. The continuum background suppression method adopted by the two experiments is discussed in more detail in Chapter 9.

Belle also includes $B^0 \to \pi^0 K_L^0$ decays. Here $m_{\rm ES}$ is calculated using the direction of the K_L^0 meson assuming that the parent B^0 is at rest in the CM system. The signal is extracted using $m_{\rm ES}$ and a likelihood ratio variable for continuum suppression. Since the vertex position cannot be calculated, $B^0 \to \pi^0 K_L^0$ only contributes to the determination of C. The signal yield obtained for the K_L^0 mode is 285 ± 52 events compared to 634 ± 34 for the K_S^0 mode.

The *CP* asymmetry parameters S and C are obtained by fitting the events with and without the vertex position information. The results are shown in Table 17.6.6. While the C values measured by *BABAR* and Belle have opposite signs, they are consistent at the level of $\sim 1.5\sigma$.

17.6.6.4 $B^0 \to K_S^0 K_S^0$

As with the $B^0 \to \pi^0 K_S^0$ case, prompt charged tracks from the B vertex are absent in $B^0 \to K_S^0 K_S^0$ decays. Therefore, the study of time-dependent *CP* asymmetry parameters uses the same technique developed for $B^0 \to \pi^0 K_S^0$. In this case both charged pions from at least one of the K_S^0 mesons are required to have been well reconstructed using hits in the silicon vertex detector. The efficiency is approximately 82% and 61% for *BABAR* and Belle, respectively. Events in which both K_S^0 mesons decay outside the silicon vertex detector do not have a well reconstructed B vertex; they are only used to determine C.

Data samples of 348×10^6 and 657×10^6 $B\overline{B}$ pairs are used for the *BABAR* (Aubert, 2006ai) and Belle (Nakahama, 2008) measurements, respectively. The suppression of the continuum background is achieved in the same way as for the $B^0 \to \pi^0 K_S^0$ measurement. The results obtained for the time-dependent asymmetry parameters are shown in Table 17.6.6. The dominant sources of systematic uncertainty are due to the fit model parameterization. These results are consistent with the SM prediction of no *CP* asymmetry in $b \to d\bar{s}s$ penguin modes.

17.6.7 ϕ_1 from charmless three-body decays

Charmless three-body decays through $b \to s\bar{q}q$ penguin transitions also provide measurements of ϕ_1. In general, three-body decays are not *CP* eigenstates and also often include intermediate resonances. These resonances complicate the extraction of useful *CP* violation parameters. However, for $B^0 \to P^0 P^0 X^0$ decays, where P^0 and X^0 are any spin-0 neutral particles, the final state has a definite *CP* eigenvalue, that of the X^0 (Gershon and Hazumi, 2004), regardless of intermediate states. The decay $B^0 \to K_S^0 K_S^0 K_S^0$ is of particular interest since it proceeds only

through a $b \to s$ penguin transition and is free from any $b \to u$ contribution. The $\pi^0\pi^0 K^0_S$ final state also has a definite *CP* (even) eigenvalue but has a $b \to u$ tree contribution, similar to $B^0 \to K^0_S\pi^0$, discussed in Section 17.6.6. As with similar loop-dominated transitions, the deviations of measured *CP* asymmetry parameters from those found in $b \to c\bar{c}s$ decays are expected to be quite small in the SM. If a large deviation were to be measured, then this could indicate the presence of new physics.

In general, analysis of the Dalitz plane for three-body decays can be used to extract the amplitude of each contribution. Time-dependent Dalitz plot analysis, therefore, can be used to extract *CP* asymmetry parameters of each intermediate two-body *CP* eigenstate and also those of any non-resonant *CP* eigenstate components (see Chapter 13). This method is applied to $B^0 \to K^+K^-K^0$ and $B^0 \to \pi^+\pi^-K^0$ decays.

17.6.7.1 $B^0 \to K^0_S K^0_S K^0_S$

The first measurement of *CP* asymmetry parameters for $B^0 \to K^0_S K^0_S K^0_S$ decays is made by Belle (Sumisawa, 2005) with 275×10^6 $B\overline{B}$ pairs. The latest measurements reported by *BABAR* (Lees, 2012c) and Belle (Chen, 2007a) use 468×10^6 and 535×10^6 $B\overline{B}$ pairs, respectively.

The K^0_S candidates are reconstructed in the $K^0_S \to \pi^+\pi^-$ and $K^0_S \to \pi^0\pi^0$ modes. $B^0 \to K^0_S K^0_S K^0_S$ decays are reconstructed with all K^0_S mesons decaying into a $\pi^+\pi^-$ final state ($B_{3K^0_S(+-)}$) and also with one of the K^0_S mesons decaying into a $\pi^0\pi^0$ final state ($B_{3K^0_S(00)}$). Signal is extracted by fitting the distributions of kinematic variables ($m_{\rm ES}$ and ΔE) and a continuum suppression variable.

Since $B^0 \to \chi_{c0,2}K^0_S$ ($\chi_{c0,2} \to K^0_S K^0_S$) decays give the same final states but proceed through a $b \to c\bar{c}s$ transition, vetoes are applied for candidates with a $K^0_S K^0_S$ mass combination within a window around the nominal χ_{c0} mass. The contribution from χ_{c2} is found to be negligible. Belle also applies a veto based on the measured D^0 mass to remove the decays $B^0 \to D^0 K^0_S$ ($D^0 \to K^0_S K^0_S$). In case of multiple candidates in an event, a single candidate is selected based on the reconstructed K^0_S mass or the quality of a fit with a constraint on the D^0 mass.

The decay vertex position of the reconstructed B is obtained using the trajectories of the K^0_S mesons in the $\pi^+\pi^-$ channels constraining the reconstructed K^0_S mesons to come from the beam spot. As is the case for $\pi^0 K^0_S$ and $K^0_S K^0_S$ decays, these measurements use $K^0_S \to \pi^+\pi^-$ candidates reconstructed from tracks that are well measured in the silicon vertex detectors.

The usual flavor tagging and fitting procedure are applied to extract the *CP* asymmetry parameters. The results obtained are summarized in Table 17.6.7. The Δt distribution and the time-dependent asymmetry from *BABAR* is shown in Fig. 17.6.12.

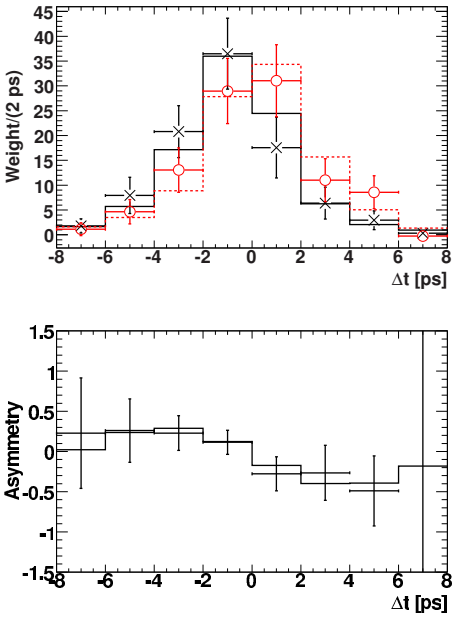

Figure 17.6.12. (Top) Δt distribution and (bottom) *CP* asymmetry as a function of Δt, for the $B^0 \to K^0_S K^0_S K^0_S$ signal (points) obtained by *BABAR* (Lees, 2012c) using the *${}_s\mathcal{P}lot$* technique (see Section 11.2.3), superimposed on the fit results (histograms). The data points marked with crosses (circles) and solid (dashed) histograms correspond to B^0 ($\overline{B}^0$) tagged events.

Table 17.6.7. Summary of *CP* asymmetry measurements for charmless $B^0 \to K^0_S K^0_S K^0_S$ decays, (Lees, 2012c) and (Chen, 2007a). The signal yield includes both tagged and untagged events.

	BABAR	Belle	Average
Signal	$263\ ^{+21}_{-19}$	185 ± 17	
S	$0.94\ ^{+0.24}_{-0.21} \pm 0.06$	$0.30 \pm 0.32 \pm 0.08$	0.74 ± 0.17
C	$-0.17 \pm 0.18 \pm 0.04$	$-0.31 \pm 0.20 \pm 0.07$	-0.23 ± 0.13

17.6.7.2 $B^0 \to \pi^0\pi^0 K^0_S$

The event reconstruction of $B^0 \to \pi^0\pi^0 K^0_S$ is similar to that of $B^0 \to K^0_S\pi^0$ (Section 17.6.6) with an additional π^0. Even though no charged tracks come directly from the interaction point, the intersection of the K^0_S trajectory and the beamspot provide adequate measurement of the B^0 decay vertex. Approximately 70% of the candidates at *BABAR* have well measured $K^0_S \to \pi^+\pi^-$ tracks in the silicon vertex detector. This is higher than that in $B^0 \to K^0_S\pi^0$ because the K^0_S momentum spectrum is softer in $B^0 \to \pi^0\pi^0 K^0_S$ decays. *BABAR* uses a neural network (Section 4.4.4) with event shape variables to discriminate against continuum background. Events consistent with $B^0 \to K^0_S\pi^0$, $D^0\pi^0$, $\eta^{(\prime)}K^0_S$, and $\chi_{c0,2}K^0_S$ decays are vetoed. In case of multiple candidates in an event, the candidate with the smallest value of $\sum_{i=1}^{2}(m^{(i)}_{\gamma\gamma} - m_{\pi^0})^2$

is selected, where $m_{\gamma\gamma}^{(1)}$ and $m_{\gamma\gamma}^{(2)}$ are the invariant masses of the two $\pi^0 \to \gamma\gamma$ candidates.

The fit uses $m_{\rm ES}$, $\Delta E/\sigma(\Delta E)$, the neural-network output, Δt, $\sigma(\Delta t)$, and flavor tagging as variables. Using a sample of 227×10^6 $B\overline{B}$ pairs, *BABAR* (Aubert, 2007t) finds 117 ± 27 signal events, and $S = 0.72 \pm 0.71 \pm 0.08$ and $C = 0.23 \pm 0.52 \pm 0.13$. Belle has not measured this channel.

17.6.7.3 $B^0 \to K^+K^-K^0$ time-dependent Dalitz plot analysis

$B^0 \to \phi K^0$ decays proceed almost purely through a $b \to s\bar{s}s$ penguin transition. This is one of the most promising modes to search for new physics. In general, the decays $B^0 \to K^+K^-K^0$ have a contribution from the $b \to u\bar{u}s$ tree transition. Therefore, its theoretical uncertainty must be taken into account when comparing asymmetry parameter results with those obtained from charmonium decays.

The measurements were originally made treating this decay in terms of the quasi-two-body process $B^0 \to \phi K^0$, where $\phi \to K^+K^-$ (Abe (2003e,f); Chen (2007a); Aubert (2004o, 2005m)). Other analyses measuring *CP* asymmetry parameters in $B^0 \to K^+K^-K_S^0$ decays excluded the ϕ mass region in the K^+K^- invariant mass spectrum (Abe, 2003e,f, 2007e) (Aubert, 2005m), where they found the phase space was dominantly *CP*-even.

There can be nonresonant $B^0 \to K^+K^-K^0$ contributions and also $B^0 \to f_0(980)K^0$ that may interfere with the $B^0 \to \phi K^0$ decay. Therefore, the measurement of $B^0 \to \phi K^0$ as a quasi-two-body decay would ultimately have limited precision. This problem can be resolved via the use of a time-dependent amplitude analysis of the three-body final state. The amplitudes and time-dependent asymmetry parameters can be extracted for each intermediate state (including any nonresonant component) while simultaneously accounting for interference between amplitudes as discussed in Chapter 13. With increasingly large data samples this became feasible, and such a measurement was first made by *BABAR* (Aubert, 2007af) using 383×10^6 $B\overline{B}$ pairs. The latest measurements are made using 470×10^6 $B\overline{B}$ pairs by *BABAR* (Lees, 2012y) and 657×10^6 $B\overline{B}$ pairs by Belle (Nakahama, 2010).

The $B^0 \to K^+K^-K^0$ decays are reconstructed in $K_S^0 \to \pi^+\pi^-$ and $K_S^0 \to \pi^0\pi^0$ channels (in the first *BABAR* measurement, the $K^+K^-K_L^0$ channel was also used). Belle uses only $K_S^0 \to \pi^+\pi^-$ decay. Signal components are extracted using kinematic variables ($m_{\rm ES}$, ΔE) and an $e^+e^- \to q\bar{q}$ continuum suppression variable (a Fisher discriminant, a neural network, or a flavor-tagging quality, see Chapter 9).

In the Dalitz plot analysis, each amplitude of an intermediate resonant or nonresonant state r (called "isobar") is parameterized as

$$a_r = c_r(1 + b_r)e^{i(\phi_r+\delta_r)}, \quad \bar{a}_r = c_r(1 - b_r)e^{i(\phi_r-\delta_r)}, \tag{17.6.9}$$

for B^0 and $\overline{B}^0$ decays respectively, where c_r is the magnitude of the amplitude. Only weak phase of the two amplitudes is written in the above equation, and the *CP* violating weak phase difference is $2\delta_r$. The magnitudes of B^0 and $\overline{B}^0$ decay amplitudes are also allowed to be different, parameterized by b_r. With this parameterization and following Eqs (10.2.4 and 10.2.5), the direct *CP* asymmetry, effective phase $\phi_1^{\rm eff}$, and time-dependent *CP* coefficient are given, respectively, as

$$C_r \approx -A_{CP}^r = -\frac{|\bar{a}_r|^2 - |a_r|^2}{|\bar{a}_r|^2 + |a_r|^2} = \frac{2b_r}{1 + b_r^2}, \tag{17.6.10}$$

$$\phi_1^{{\rm eff},r} = \phi_1 + \delta_r, \tag{17.6.11}$$

$$-\eta_r S_r \approx \frac{1 - b_r^2}{1 + b_r^2} \sin[2\phi_1^{{\rm eff},r}]. \tag{17.6.12}$$

The measured phase is referred to as "effective" because one measures ϕ_1 up to theoretical uncertainties related to higher order contributions, which can be significant.

Belle vetoes events consistent with a B^0 decaying into the following final states using appropriate mass windows: $\overline{D}^0K_S^0$, $D_{(s)}^-K^+$, and $J/\psi K_S^0$, where $\overline{D}^0 \to K^+K^-$, $K^+\pi^-$, $D^- \to K_S^0K^-$, $K_S^0\pi^-$, $D_s^- \to K_S^0K^-$, and $J/\psi \to K^+K^-$. The $B^0 \to \chi_{c0}K_S^0$ amplitude is included in the fit. On the other hand, *BABAR* includes $B^0 \to J/\psi K_S^0$, D^-K^+, $D_s^-K^+$, and $\overline{D}^0K_S^0$ as background components in the fit. The latest *BABAR* analysis finds 1419 ± 43 $K^+K^-K_S^0[\pi^+\pi^-]$ signal events and 160 ± 17 $K^+K^-K_S^0[\pi^0\pi^0]$ signal events. Belle obtains 1176 ± 51 signal events.

Both experiments perform a time-dependent fit to the whole Dalitz plane, using three sets of $\phi_1^{\rm eff}$ and A_{CP} parameters; the first two are for $\phi(1020)K_S^0$ and $f_0(980)K_S^0$, and the third is shared by all the other charmless isobars.

Due to the possible presence of multiple solutions, the same fit is performed many times with different starting parameter values to ensure the global minimum of the likelihood is reached. Scans of log-likelihood values are done to study the behavior of the p.d.f. near the minimum and the statistical uncertainties. The latest *BABAR* analysis finds five local minima within 9 units in $-2\ln\mathcal{L}$; the second solution is 3.9 larger than the global minimum. Belle finds four solutions, separated by approximately 10 units in $-2\ln\mathcal{L}$; Solution 1 is taken as the preferred one based on external information though it has the second lowest $-2\ln\mathcal{L}$ value, which is 3.1 units larger than the lowest one (Solution 2). The results are summarized in Table 17.6.8.

It should be noted that the discrete ambiguities on the value of ϕ_1 can be resolved using the time-dependent Dalitz plot fit method because the log-likelihood values can be compared for multiple solutions. In both $B^0 \to \phi K_S^0$ and $f_0(980)K_S^0$ decays the $\phi_1^{\rm eff} < \pi/2$ solution is clearly preferred. *BABAR* excludes the $\pi/2 - \phi_1^{\rm eff}$ value at 4.8 standard deviations.

17.6.7.4 $B^0 \to \pi^+\pi^-K_S^0$ time-dependent Dalitz plot analysis

The decay $B^0 \to \pi^+\pi^-K_S^0$ includes transitions via $B^0 \to \rho^0K_S^0$, $B^0 \to f_0(980)K_S^0$, and $B^0 \to K^{*+}\pi^-$. The measurements of time-dependent asymmetry parameters for

Table 17.6.8. Results for time-dependent asymmetry parameters for $B^0 \to K^+K^-K^0$ decays. The three uncertainties are statistical, systematic and Dalitz plot model uncertainty (for *BABAR* the latter is included in the systematic uncertainty). The solutions with the (three) smallest $-2\ln\mathcal{L}$ value(s) are shown for *BABAR* (Belle).

	BABAR (Lees, 2012y)	Belle (Nakahama, 2010)		
	Solution 1	Solution 1	Solution 2	Solution 3
$A_{CP}(\phi K^0_S)$	$-0.05 \pm 0.18 \pm 0.05$	$+0.04 \pm 0.20 \pm 0.10 \pm 0.02$	$+0.08 \pm 0.18 \pm 0.10 \pm 0.03$	$-0.01 \pm 0.20 \pm 0.11 \pm 0.02$
$\phi_1^{\rm eff}(\phi K^0_S)$	$(21 \pm 6 \pm 2)^\circ$	$(32.2 \pm 9.0 \pm 2.6 \pm 1.4)^\circ$	$(26.2 \pm 8.8 \pm 2.7 \pm 1.2)^\circ$	$(27.3 \pm 8.6 \pm 2.8 \pm 1.3)^\circ$
$A_{CP}(f_0(980)K^0_S)$	$-0.28 \pm 0.24 \pm 0.9$	$-0.30 \pm 0.29 \pm 0.11 \pm 0.09$	$-0.20 \pm 0.15 \pm 0.08 \pm 0.05$	$+0.02 \pm 0.21 \pm 0.09 \pm 0.09$
$\phi_1^{\rm eff}(f_0(980)K^0_S)$	$(18 \pm 6 \pm 4)^\circ$	$(31.3 \pm 9.0 \pm 3.4 \pm 4.0)^\circ$	$(26.1 \pm 7.0 \pm 2.4 \pm 2.5)^\circ$	$(25.6 \pm 7.6 \pm 2.9 \pm 0.8)^\circ$
A_{CP}(others)	$-0.02 \pm 0.09 \pm 0.03$	$-0.14 \pm 0.11 \pm 0.08 \pm 0.03$	$-0.06 \pm 0.15 \pm 0.08 \pm 0.04$	$-0.03 \pm 0.09 \pm 0.08 \pm 0.03$
$\phi_1^{\rm eff}$(others)	$(20.3 \pm 4.3 \pm 1.2)^\circ$	$(24.9 \pm 6.4 \pm 2.1 \pm 2.5)^\circ$	$(29.8 \pm 6.6 \pm 2.1 \pm 1.1)^\circ$	$(26.2 \pm 5.9 \pm 2.3 \pm 1.5)^\circ$

the first two of these decays were initially made using a quasi-two-body approach (Aubert (2007aa); Abe (2007e)), similar to the $B^0 \to K^+K^-K^0_S$ (ϕK^0) case above. Observation of direct *CP* asymmetry in $B^0 \to K^+\pi^-$ and evidence of *CP* asymmetry in resonances in other similar three-body decays such as $B^+ \to K^+\pi^+\pi^-$ (see Chapter 17.4) suggest possible large *CP* asymmetry in resonances in $B^0 \to K^0_S\pi^+\pi^-$ decays. Time-dependent *CP* asymmetry measurements of $B^0 \to \pi^+\pi^-K^0_S$ may shed light on the $A_{CP}(K\pi)$ puzzle together with the *CP* asymmetry of other $B \to K^*\pi$ decays (see for example (Li and Mishima, 2011)). In addition, the phase difference between $B^0 \to K^{*+}\pi^-$ and $\overline{B}^0 \to K^{*-}\pi^+$ decays can be used to determine ϕ_3 (Ciuchini, Pierini, and Silvestrini, 2006; Deshpande, Sinha, and Sinha, 2003; Gronau, Pirjol, Soni, and Zupan, 2007). Time-dependent Dalitz plot analysis of $B^0 \to \pi^+\pi^-K^0_S$ decays can provide all these measurements simultaneously.

BABAR (Aubert, 2009av) analyzes a sample of 383×10^6 $B\overline{B}$ pairs and Belle (Dalseno, 2009) analyzes 657×10^6 $B\overline{B}$ pairs. The $B^0 \to \pi^+\pi^-K^0_S$ candidates are identified using the kinematic variables $m_{\rm ES}$ and ΔE. The $e^+e^- \to q\bar{q}$ continuum background is suppressed by a loose requirement on the continuum suppression variable. This requirement retains about 90% of the signal. *BABAR* uses the neural-network output from various shape parameters while Belle uses a likelihood ratio. Belle applies vetoes for $B^0 \to D^-\pi^+$ decays and $B^0 \to (c\bar{c})K^0_S$ decays, while *BABAR* includes them as a background in the fit. Belle finds that 20–30% of events have multiple candidates in quasi-two-body modes. By selecting the B candidate with $m_{\rm ES}$ closest to the nominal B mass, the fraction of misreconstructed events is reduced to the level of a few percent. The signal yield is found to be 1944 ± 98 events using the ΔE distribution. *BABAR* finds that 1–8% of the events have multiple candidates and selects single events randomly The fraction of misreconstructed candidates is 4–8% depending on the intermediate states. The signal yield is extracted using $m_{\rm ES}$, ΔE, and neural-network output information; 2182 ± 64 signal events are obtained.

Both groups use square Dalitz plot variables (Section 13.4.1) in the fit. The phase difference for flavor specific decays is given as

$$\Delta\phi_r = 2\delta_r. \tag{17.6.13}$$

As in $B^0 \to K^+K^-K^0_S$ decays, the fits lead to multiple solutions: two for *BABAR* and four for Belle. Table 17.6.9 shows the two most likely solutions in each experiment. *CP* violation parameters for the $B^0 \to f_0(980)K^0_S$ and $\rho^0(770)K^0_S$ decays are similar for two solutions in the Belle result, while they differ in the *BABAR* measurement (note that the statistical uncertainties between different solutions are correlated). In both cases, the $\phi_1^{\rm eff}$ values are consistent with the value of ϕ_1 measured in $b \to c\bar{c}s$ decays.

17.6.7.5 Summary of ϕ_1 from charmless decays

Figure 17.6.13 (17.6.14) shows a summary of measurements of $\sin 2\phi_1^{\rm eff}$ (vs. C) from charmless decays including both quasi-two-body and three-body decays. The favored solutions are shown for $B^0 \to K^+K^-K^0$ and $B^0 \to \pi^+\pi^-K^0$ decays.

The measured $\sin 2\phi_1^{\rm eff}$ values for all of the individual modes are consistent with the $\sin 2\phi_1$ value measured in $b \to c\bar{c}s$ decays within statistical and theoretical uncertainties. However, the current statistical precision is not enough to draw definite conclusions about the presence of new physics; a much larger data sample is necessary.

17.6.8 Resolving discrete ambiguities in ϕ_1

Since the time-dependent *CP* asymmetry parameter measurements described so far usually provide a value for $\sin 2\phi_1$, there is a four-fold ambiguity on the angle, $\phi_1 \to \pi/2 - \phi_1$, $\phi_1 + \pi$ and $3\pi/2 - \phi_1$. As mentioned in Section 17.6.7, time-dependent Dalitz plot analyses of charmless three-body decays measure (effective) values of $2\phi_1$, rather than $\sin 2\phi_1$, and can resolve the $\phi_1 \to \pi/2 - \phi_1$ ambiguity. However, charmless decays are dominated by penguin transitions, which can be affected by NP entering in loops. Resolving the ambiguity using decays dominated by a $b \to c$ tree transition can avoid such complication Several tree level $b \to c$ measurements are possible, and those performed at the B Factories are described in the following.

Table 17.6.9. Results of *CP* asymmetry parameters for $B^0 \to \pi^+\pi^- K^0$ decays. The first uncertainty is statistical, the second is systematic, and the third represents the Dalitz plot signal model dependence.

	BABAR (Aubert, 2009av)		Belle (Dalseno, 2009)	
	Solution 1	Solution 2	Solution 1	Solution 2
$A_{CP}(f_0(980)K^0_S)$	$-0.08 \pm 0.19 \pm 0.03 \pm 0.04$	$-0.23 \pm 0.19 \pm 0.03 \pm 0.04$	$-0.06 \pm 0.17 \pm 0.07 \pm 0.09$	$+0.00 \pm 0.17 \pm 0.06 \pm 0.09$
$\phi_1^{\rm eff}(f_0(980)K^0_S)[^\circ]$	$36.0 \pm 9.8 \pm 2.1 \pm 2.1$	$56.2 \pm 10.4 \pm 2.1 \pm 2.1$	$12.7\ ^{+6.9}_{-6.5} \pm 2.8 \pm 3.3$	$14.8\ ^{+7.3}_{-6.7} \pm 2.7 \pm 3.3$
Fraction [%]	$13.8\ ^{+1.5}_{-1.4} \pm 0.8 \pm 0.6$	$13.5\ ^{-1.4}_{-1.3} \pm 0.8 \pm 0.6$	14.3 ± 2.7	14.9 ± 3.3
$A_{CP}(\rho^0(770)K^0_S)$	$0.05 \pm 0.26 \pm 0.10 \pm 0.03$	$0.14 \pm 0.26 \pm 0.10 \pm 0 : 03$	$+0.03\ ^{+0.23}_{-0.24} \pm 0.11 \pm 0.10$	$-0.16 \pm 0.24 \pm 0.12 \pm 0.10$
$\phi_1^{\rm eff}(\rho^0(770)K^0_S)[^\circ]$	$10.2 \pm 8.9 \pm 3.0 \pm 1.9$	$33.4 \pm 10.4 \pm 3.0 \pm 1.9$	$+20.0\ ^{+8.6}_{-8.5} \pm 3.2 \pm 3.5$	$+22.8 \pm 7.5 \pm 3.3 \pm 3.5$
Fraction [%]	$8.6\ ^{+1.4}_{-1.3} \pm 0.5 \pm 0.2$	$8.5\ ^{+1.3}_{-1.2} \pm 0.5 \pm 0.2$	6.1 ± 1.5	8.5 ± 2.6
$A_{CP}(K^{*-}\pi^+)$	$-0.21 \pm 0.10 \pm 0.01 \pm 0.02$	$-0.19\ ^{+0.10}_{-0.11} \pm 0.01 \pm 0.02$	$-0.21 \pm 0.11 \pm 0.05 \pm 0.05$	$-0.20 \pm 0.11 \pm 0.05 \pm 0.05$
$\Delta\phi(K^{*-}\pi^+)[^\circ]$	$72.2 \pm 24.6 \pm 4.1 \pm 4.4$	$-175.1 \pm 22.6 \pm 4.1 \pm 4.4$	$-0.7\ ^{+23.5}_{-22.8} \pm 11.0 \pm 17.6$	$+14.6\ ^{+19.4}_{-20.3} \pm 11.0 \pm 17.6$
Fraction [%]	$45.2 \pm 2.3 \pm 1.9 \pm 0.9$	$46.1 \pm 2.4 \pm 1.9 \pm 0.9$	9.3 ± 0.8	9.0 ± 1.3

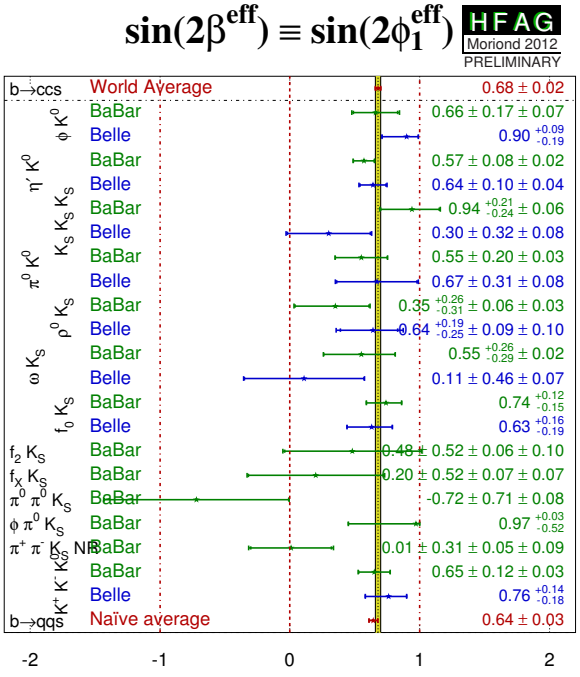

Figure 17.6.13. Summary of $\sin 2\phi_1^{\rm eff}$ measurements from charmless B^0 decays (Amhis et al., 2012).

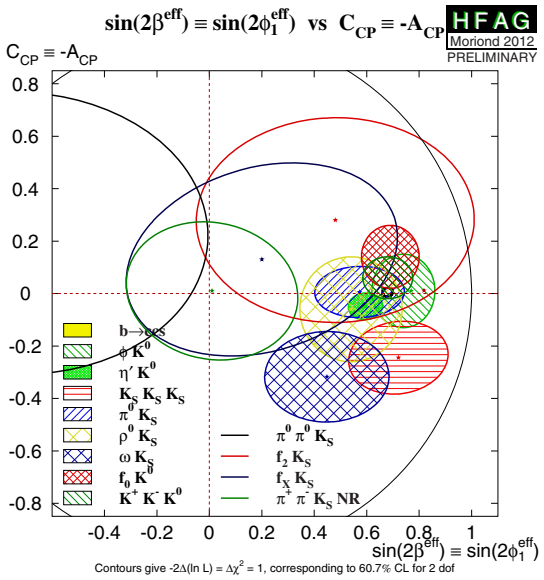

Figure 17.6.14. Summary of C vs. $\sin 2\phi_1^{\rm eff}$ measurements from charmless B^0 decays (Amhis et al., 2012).

17.6.8.1 Time-dependent angular analysis in $B^0 \to J/\psi K^{*0}$

There are two classes of parameters obtained through the angular analysis of the B meson decay to the two vector mesons J/ψ and K^{*0}. The first is the measurement of the decay amplitudes of the three angular states. These can be obtained using a time-integrated angular analysis to flavor-specific decays (see Chapter 12). The second class comprises the *CP* parameters ($\sin 2\phi_1$ and $\cos 2\phi_1$) that are measured through a time-dependent angular analysis. In particular, the measurement of $\cos 2\phi_1$, which appears in the time-dependent interference terms (Eq. (12.1.9)), is important both to solve the two-fold ambiguity in $2\phi_1$ and to test the consistency of this determination with the more precise value from other $b \to c\bar{c}s$ decays.

The decay of a pseudo-scalar to vector-vector final state can be described with three angles defined in the transversity basis (Dunietz, Quinn, Snyder, Toki, and Lipkin, 1991), where the three amplitudes, A_0, $A_\parallel$, and $A_\perp$ have well-defined *CP* eigenvalues. The amplitudes are determined by a time-integrated angular analysis of $B^0 \to$

Table 17.6.10. Measured decay amplitudes for $B^0 \to J/\psi K^{*0}$. The first uncertainty is statistical, and the second is systematic.

	BABAR (Aubert, 2007x)	Belle (Itoh, 2005b)
$\lvert A_0\rvert^2$	$0.556 \pm 0.009 \pm 0.010$	$0.574 \pm 0.012 \pm 0.009$
$\lvert A_\parallel\rvert^2$	$0.211 \pm 0.010 \pm 0.006$	$0.231 \pm 0.012 \pm 0.008$
$\lvert A_\perp\rvert^2$	$0.233 \pm 0.010 \pm 0.005$	$0.195 \pm 0.012 \pm 0.008$
$\arg(A_\parallel)$	$-2.93 \pm 0.08 \pm 0.04$	$-2.89 \pm 0.09 \pm 0.01$
$\arg(A_\perp)$	$2.91 \pm 0.05 \pm 0.03$	$2.94 \pm 0.06 \pm 0.01$

$J/\psi K^{*0}[K^+\pi^-]$ and $B^+ \to J/\psi K^{*+}[K^0_S\pi^+, K^+\pi^0]$ decays. Belle (Itoh, 2005b) and *BABAR* (Aubert, 2007x) analyze the data samples of 275 and 232×10^6 $B\overline{B}$ pairs, respectively.

Figure 17.6.15 shows the projected angular distributions for $B^0 \to J/\psi K^{*0}$ decays, where $K^{*0} \to K^+\pi^-$, from Belle. The decay amplitudes determined from the fit are summarized in Table 17.6.10.

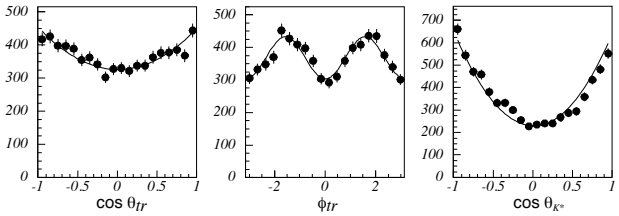

Figure 17.6.15. Angular distributions of $B^0 \to J/\psi K^{*0}(K^+\pi^-)$, as obtained by Belle (Itoh, 2005b). The angles are defined in Eq. (12.2.6), where $\theta_1 = \theta_{K^*}$. The curves show the fit results.

There is a two-fold ambiguity in the choice of the phases. *BABAR* resolves this ambiguity by extending the formalism to include a $K\pi$ S-wave amplitude and then measuring the $K\pi$ invariant mass dependence of its phase difference with respect to the dominant $K^*(892)$ P-wave around its mass peak (Aubert, 2005c). The result agrees with the prediction where the s-quark helicity is conserved as predicted by Suzuki (Suzuki, 2001). Belle adopts this choice in their analysis as well. The phases shown in Table 17.6.10 are given for this choice.

The values of $\sin 2\phi_1$ and $\cos 2\phi_1$ are determined by the time-dependent angular analysis of the decays to the CP eigenstate $B^0 \to J/\psi K^{*0}$, where $K^{*0} \to K^0_S\pi^0$, from the same data set of 275×10^6 $B\overline{B}$ pairs by Belle (Itoh, 2005b), and a sample of 88×10^6 $B\overline{B}$ pairs by *BABAR* (Aubert, 2005c). The P-wave amplitudes are fixed to the results obtained from the time-independent analysis of the flavor-definite final states described above. Figure 17.6.16 shows the Δt distributions for B^0 and $\overline{B}^0$ tags and the raw asymmetry between them by *BABAR*. Since $\sin 2\phi_1$ and $\cos 2\phi_1$ are independent parameters in the analysis, they can be obtained simultaneously using a fit. However, since the precision of the $\sin 2\phi_1$ measurement using only $B^0 \to J/\psi K^{*0}$ decays is limited by statistics, the value of $\cos 2\phi_1$ is also obtained by fixing $\sin 2\phi_1$ to the world average at that time, 0.726 (Belle) or 0.731 (*BABAR*). The results are summarized in Table 17.6.11.

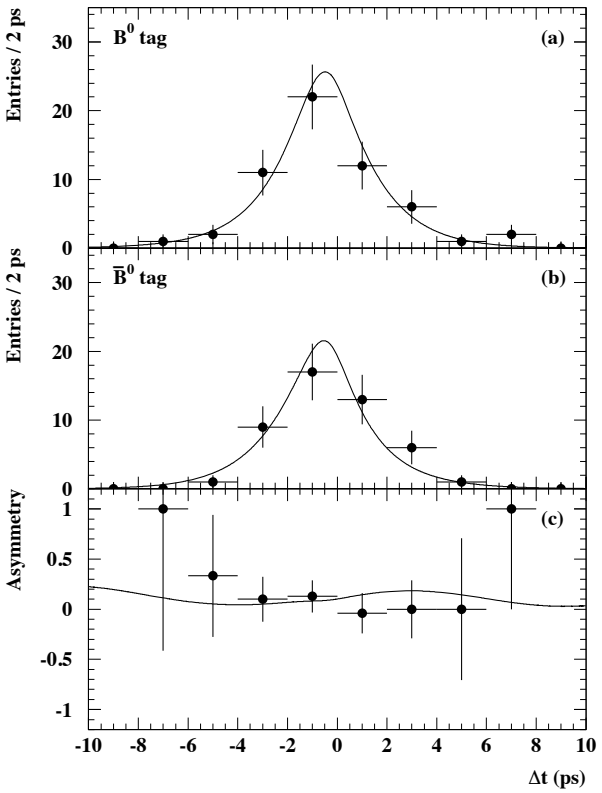

Figure 17.6.16. Δt distributions for (a) B^0 and (b) $\overline{B}^0$ tagged $B^0 \to J/\psi K^{*0}$ events, and (c) raw asymmetry between them by *BABAR* (Aubert, 2005c).

The sign of $\cos 2\phi_1$ is positive in both measurements, which is consistent with the value of ϕ_1 predicted by global CKM fits obtained using other measurements (see Section 25.1).

17.6.8.2 Time-dependent Dalitz analysis in $B^0 \to D^{(*)0}[K^0_S\pi^+\pi^-]h^0$

Another method to resolve discrete ambiguities uses a time-dependent Dalitz plot analysis with $B^0 \to D^{(*)0}h^0$, $D^0 \to K^0_S\pi^+\pi^-$ decays, where h^0 is a light neutral meson, such as π^0, η, η', and ω (Bondar, Gershon, and Krokovny, 2005). As described in Section 17.6.5, the $B^0 \to D^{(*)0}h^0$ decay is dominated by a color-suppressed $b \to c\overline{u}d$ tree amplitude. Neglecting a small contribution from $b \to u\overline{c}d$, the decay amplitude for $B^0 \to \overline{D}^0[K^0_S\pi^+\pi^-]h^0$ can be factorized as $A_f = A_B A_{\overline{D}^0}$ and for $\overline{B}^0$ as $\overline{A}_f = A_{\overline{B}} A_{D^0}$,

Table 17.6.11. $\sin 2\phi_1$ and $\cos 2\phi_1$ determined for $B^0 \to J/\psi K^{*0}, K^{*0} \to K^0_S\pi^0$. The first two numbers show the result of the simultaneous fit with both $\sin 2\phi_1$ and $\cos 2\phi_1$ treated as free parameters. The final set of values for $\cos 2\phi_1$ are obtained with $\sin 2\phi_1$ fixed at the world average at the time of the analysis.

	BABAR (Aubert, 2005c)	Belle (Itoh, 2005b)
$\sin 2\phi_1$	$-0.10 \pm 0.57 \pm 0.14$	$+0.24 \pm 0.31 \pm 0.05$
$\cos 2\phi_1$	$+3.32^{+0.76}_{-0.96} \pm 0.27$	$+0.56 \pm 0.79 \pm 0.11$
$\cos 2\phi_1$ (fixed value of $\sin 2\phi_1$)	$+2.72^{+0.50}_{-0.79} \pm 0.27$ (0.731)	$+0.87 \pm 0.74 \pm 0.12$ (0.726)

where $A_{D^0} = f(m^2_+, m^2_-)$ and $A_{\overline{D}^0} = f(m^2_-, m^2_+)$ with $m^2_\pm = M^2_{K^0_S\pi^\pm}$. The Δt distribution is given as

$$f_\pm(\Delta t) \propto \frac{e^{-|\Delta t|/\tau_{B^0}}}{2}|A_B|^2[(|A_{\overline{D}^0}|^2 + |\lambda|^2|A_{D^0}|^2) \mp (|A_{\overline{D}^0}|^2 - |\lambda|^2|A_{D^0}|^2)\cos(\Delta m_d \Delta t) \pm 2|\lambda|\xi_{h^0}(-1)^L \mathrm{Im}(e^{-2\phi_1}A_{D^0}A^*_{\overline{D}^0})\sin(\Delta m_d \Delta t)], \quad (17.6.14)$$

where ξ_{h^0} is the *CP* eigenvalue of h^0 and L is the orbital angular momentum of the Dh^0 system. One notices that if $A_{D^0} = A_{\overline{D}^0}$ (*e.g.*, if the final state is a *CP* eigenstate), this equation reduces to Eq. (10.2.2). An additional factor of -1 is required in the $\sin(\Delta m_d \Delta t)$ term for the $D^{*0}[D^0\pi^0]$ mode to take into account the *CP* eigenvalue of the π^0. The $\sin(\Delta m_d \Delta t)$ term can be written as

$$\mathrm{Im}(e^{-2\phi_1}A_{D^0}A^*_{\overline{D}^0}) = \mathrm{Im}(A_{D^0}A^*_{\overline{D}^0})\cos 2\phi_1 - \mathrm{Re}(A_{D^0}A^*_{\overline{D}^0})\sin 2\phi_1. \quad (17.6.15)$$

Therefore, $\cos 2\phi_1$ and $\sin 2\phi_1$ can be independently determined by fitting the time-dependent Dalitz plot distribution.

Belle (Krokovny, 2006) and *BABAR* (Aubert, 2007s) perform the measurements using 386×10^6 and 383×10^6 $B\overline{B}$ pairs, respectively. They use $D\pi^0$, $D\eta$, $D\omega$, $D^*\pi^0$, and $D^*\eta$ decay modes. *BABAR* also uses $D\eta'$. The reconstruction includes the decay chains $D^{*0} \to D^0\pi^0$, $D^0 \to K^0_S\pi^+\pi^-$, $K^0_S \to \pi^+\pi^-$, $\eta \to \gamma\gamma$ and $\pi^+\pi^-\pi^0$, $\eta' \to \eta\pi^+\pi^-$, and $\omega \to \pi^+\pi^-\pi^0$. The B^0 signal candidates are identified by m_{ES} and ΔE. The reconstruction of the tag-side B meson and flavor tagging are performed in the same way as other time-dependent *CP* asymmetry measurements.

The parameters $\sin 2\phi_1$ and $\cos 2\phi_1$ are obtained by fitting the Dalitz plot (m^2_+, m^2_-) and Δt distributions for the events in the signal region in m_{ES} and ΔE. The isobar model described in Chapter 13 is used for the $D^0 \to K^0_S\pi^+\pi^-$ decay amplitude. The results are summarized in Table 17.6.12. Belle fixes $|\lambda|$ to unity as expected in the SM, while *BABAR* measures $|\lambda| = 1.01 \pm 0.08(\mathrm{stat.}) \pm 0.02(\mathrm{syst.})$. Belle and *BABAR* determine the sign of $\cos 2\phi_1$ to be positive at 98.3% and 86% C.L., respectively.

17.6.8.3 Time-dependent *CP* asymmetry in $B^0 \to D^{*+}D^{*-}K^0_S$

Another way to resolve the $\phi_1 \to \pi/2 - \phi_1$ ambiguity is to study the decay channel $B^0 \to D^{*+}D^{*-}K^0_S$. No direct *CP* violation is expected in this mode since the penguin contributions are negligible. It is shown (Browder, Datta, O'Donnell, and Pakvasa, 2000) that a time-dependent analysis can be performed in this channel, where in principle the values of $\sin 2\phi_1$ and $\cos 2\phi_1$ can be extracted. The time-dependent Δt distribution, considering the mistag probability w and the difference $\Delta w = w(B^0) - w(\overline{B}^0)$, is given by

$$f_\pm(\Delta t) \equiv \frac{\mathrm{e}^{-|\Delta t|/\tau_{B^0}}}{4\tau_{B^0}}\Big\{(1 \mp \Delta w) \pm (1 - 2w). \times \Big[\eta_y \frac{J_c}{J_0}\cos(\Delta m_d \Delta t) - \Big(\frac{2J_{s1}}{J_0}\sin 2\phi_1 + \eta_y \frac{2J_{s2}}{J_0}\cos 2\phi_1\Big)\sin(\Delta m_d \Delta t)\Big]\Big\}, \quad (17.6.16)$$

where f_+ and f_- correspond respectively to a B^0 and $\overline{B}^0$ tag. This equation is defined in the half Dalitz plane $s^+ < s^-$ or $s^+ > s^-$, where $s^+ \equiv m^2(D^{*+}K^0_S)$ and $s^- \equiv m^2(D^{*-}K^0_S)$. The parameter η_y is equal to $+1$ or -1 for $s^- < s^+$ or $s^- > s^+$, respectively. The parameters J_0, J_c, J_{s1}, and J_{s2} are the integrals over the half Dalitz phase space with $s^+ < s^-$ of the functions $|A|^2 + |\overline{A}|^2$, $|A|^2 - |\overline{A}|^2$, $\mathrm{Re}(\overline{A}A^*)$, and $\mathrm{Im}(\overline{A}A^*)$, where A and $\overline{A}$ are the amplitudes of $B^0 \to D^{*+}D^{*-}K^0_S$ and $\overline{B}^0 \to D^{*+}D^{*-}K^0_S$ decays, respectively. The values of these parameters depend strongly on the intermediate resonances present in this final state. The presence of the $D_{s1}(2536)$ resonance is well established (Section 19.3) in this decay mode, but this meson is narrow and does not contribute much to J_{s2}. Although it had not been studied specifically in $B^0 \to D^{*+}D^{*-}K^0_S$ decays, the $D^*_{s1}(2700)$ meson (Section 19.3) is expected to have a large contribution due to its large width. $D^*_{s1}(2700)$ decays to D^*K and has a large width, 125 ± 30 MeV. This implies that J_{s2} is nonzero and that J_c may be large.

BABAR (Aubert, 2006u) and Belle (Dalseno, 2007) study this decay mode using 230×10^6 and 449×10^6 $B\overline{B}$ pairs, respectively. The mode $B^0 \to D^{*+}D^{*-}K^0_S$ is reconstructed from $D^{*+} \to D^0\pi^+$ and $D^{*+} \to D^+\pi^0$, requiring at least one $D^0\pi^+$ decay. Candidate D mesons are reconstructed in the modes $D^0 \to K^-\pi^+$, $K^-\pi^+\pi^0$, $K^-\pi^+\pi^-\pi^+$, and $D^+ \to K^-\pi^+\pi^+$. Belle also includes the modes $D^0 \to K^0_S\pi^+\pi^-, K^-K^+$, and $D^+ \to K^-K^+\pi^+$, rejecting cases with two $D^0 \to K^0_S\pi^+\pi^-$ decays. When multiple B mesons are reconstructed in an event, *BABAR*

Table 17.6.12. Results of the time-dependent Dalitz plot analysis for $B^0 \to D^{(*)0}[K^0_S\pi^+\pi^-]h^0$ decays. $N_{\rm sig}$ is a signal yield obtained from the fit to data. The uncertainties are statistical, systematic, and those due to the Dalitz model, respectively. The uncertainties in the averages include all sources.

	BABAR (Aubert, 2007s)	Belle (Krokovny, 2006)	Average
$N_{\rm sig}$	335 ± 32	325 ± 31	
$\sin 2\phi_1$	$0.29 \pm 0.34 \pm 0.03 \pm 0.05$	$0.78 \pm 0.44 \pm 0.20 \pm 0.1$	0.45 ± 0.28
$\cos 2\phi_1$	$0.42 \pm 0.49 \pm 0.09 \pm 0.13$	$1.87\ ^{+0.40}_{-0.53}\ ^{+0.20}_{-0.30} \pm 0.1$	1.01 ± 0.40

selects the one with the smallest $|\Delta E|$ value; Belle chooses the best candidate by using a χ^2 test based on the mass differences from the world averages of the particles present in the final state.

In *BABAR*, the signal yield is extracted from a fit to the $m_{\rm ES}$ distribution with an additional peaking component to account for misreconstructed events from $B^+ \to \overline{D}^{*0}D^{*+}K^0_S$ decays ($\sim 1.4\%$ of the signal yield). The unbinned maximum likelihood fit yields 201 ± 17 signal events. In Belle, the signal yield is extracted from a simultaneous fit to the $m_{\rm ES}$ and ΔE distributions. The fit result from Belle, shown in Fig. 17.6.17, has a signal yield of 131 ± 15 events.

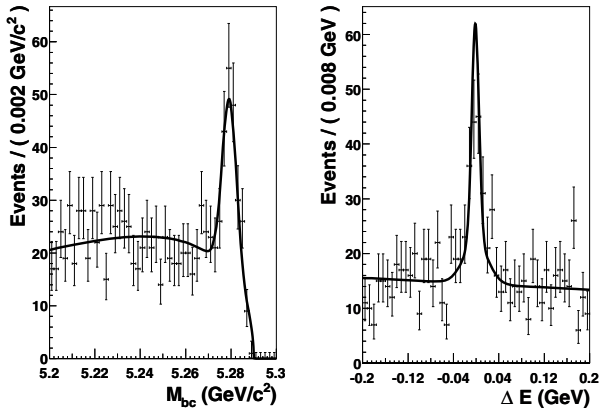

Figure 17.6.17. The (left) $m_{\rm ES}$ and (right) ΔE distributions of $B^0 \to D^{*+}D^{*-}K^0_S$ candidates in Belle (Dalseno, 2007). The curves show the fit projections.

A time-dependent analysis is performed using the event samples described previously. *BABAR* rejects events in which the invariant mass of the $D^{*\pm}K^0_S$ pair is less than $2.55\,{\rm GeV}/c^2$ in order to exclude the $D_{s1}(2536)$ meson, while Belle accounts for this resonance in the systematic uncertainties. Table 17.6.13 shows the results of both experiments and their averages using the half Dalitz plane to fit the coefficients as described in Eq. (17.6.16). Figure 17.6.18 shows the projections in Δt of the fits in *BABAR*'s analysis. Belle also uses the whole Dalitz plane to determine the *CP* asymmetry parameters to be:

$$C = +0.01^{+0.28}_{-0.28}\ ({\rm stat}) \pm 0.09\ ({\rm syst}) \quad (17.6.17)$$

$$D \sin 2\phi_1 = +0.06^{+0.45}_{-0.44}\ ({\rm stat}) \pm 0.06\ ({\rm syst}), \quad (17.6.18)$$

where D is the dilution factor defined by $D = 1 - 2w$. No evidence for either mixing-induced or direct *CP* violation is found.

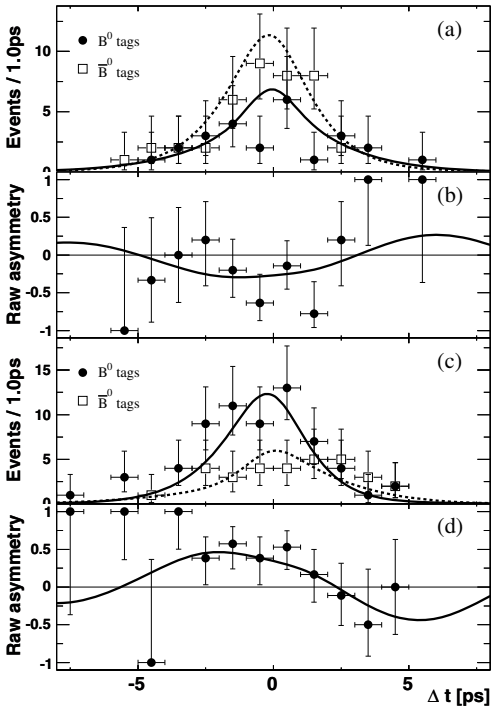

Figure 17.6.18. Fit results from *BABAR* for $B^0 \to D^{*+}D^{*-}K^0_S$ (Aubert, 2006u). (a) Distribution of Δt in the region $m_{\rm ES} > 5.27\ {\rm GeV}/c^2$ for B^0 ($\overline{B}^0$) tag candidates in the half Dalitz space $s^+ < s^-$ ($\eta_y = -1$). The solid (dashed) curve represents the fit projections in Δt for B^0 ($\overline{B}^0$) tags. (b) Raw asymmetry $(N_{B^0} - N_{\overline{B}^0})/(N_{B^0} + N_{\overline{B}^0})$, as a function of Δt, where N_{B^0} ($N_{\overline{B}^0}$) is the number of candidates with a B^0 ($\overline{B}^0$) tag. (c) and (d) contain the corresponding information for the B^0 candidates in the other half Dalitz space $s^+ > s^-$ ($\eta_y = +1$).

The main sources of systematic uncertainties, listed here in decreasing order of magnitude, consist of non-uniform acceptance over the Dalitz plane, vertex resolution, mistag fraction, Δt resolution function, fit bias, misreconstructed signal events, limited MC statistics, knowledge of the background, and tag-side interference.

The ratio J_c/J_0 is found to be significantly different from zero, which confirms a sizable contribution of a broad resonance in the decay $B^0 \to D^{*+}D^{*-}K^0_S$. Since $(2J_{s2})/J_0$ is predicted to be positive when a wide resonance is present (Browder, Datta, O'Donnell, and Pakvasa, 2000), the sign of $\cos 2\phi_1$ can be deduced, in principle, from the measurements presented here. These results are not precise enough to allow one to conclusively determine the sign of $\cos 2\phi_1$. However, the *BABAR* data do prefer a value of $\cos 2\phi_1$ that is positive at the 94% confidence level.

As described above, all of the three independent measurement methods, which use different decay modes and rather different techniques, indicate that confidence levels for $\cos 2\phi_1 > 0$ are around 90% or higher. Therefore, $\cos 2\phi_1$ is experimentally proved to be positive with relatively high confidence. Furthermore, the global fit results discussed in Section 25.1 prove that $\cos 2\phi_1 > 0$ with a large confidence.

17.6.9 Time-reversal violation in $b \to c\bar{c}s$ decays

Entangled pairs of neutral B mesons from $\Upsilon(4S)$ decays have been used for establishing *CP* violation in the interference between amplitudes with and without $B^0 - \overline{B}^0$ mixing in decays into $c\bar{c}s$ states (as discussed above, see Sections 17.6.1-17.6.3), and also for demonstrating time-reversal violation in this interference. Just as one B meson in a pair is prepared in the $\overline{B}^0$ state at the time when the other B is identified as a B^0 by a decay into a flavor-specific decay such as $e^+\nu_e X$, the decay of one B into $c\bar{c}K^0_S$ prepares the other B in the well defined state B_+, which does not decay into $c\bar{c}K^0_S$. Similarly, when the first B decays into $c\bar{c}K^0_L$, the second B is prepared in the state B_-, which does not decay into $c\bar{c}K^0_L$.

Violation of *CP* symmetry has been established by observing the difference between the transition rates of $B^0 \to c\bar{c}K^0_S$ and $\overline{B}^0 \to c\bar{c}K^0_S$. In the same way, as proposed by Bañuls and Bernabeu (1999), the difference between the rates of the transitions $B^0 \to B_-$ and $B_- \to B^0$ probes time-reversal symmetry. Such an analysis has been performed by *BABAR* (Lees, 2012m). In the following we define the states B_+ and B_- as linear combinations of B^0 and $\overline{B}^0$ and show their relevance for time reversal. We then describe the analysis and its results, which are independent of Standard Model or other model assumptions and are only based on quantum mechanics and entanglement.

The time-reversal transformation, usually called T, consists of changing the sign of the time coordinate t in the equations of motion. In quantum mechanics, this transformation involves changing the sign of all odd variables under $t \to -t$ in the Hamiltonian $\mathcal{H}$, such as velocities, momenta and spins (called $\widehat{T}$ in the following), and the exchange of final and initial states (Branco, Lavoura, and Silva, 1999; Sachs, 1987). Since it is difficult to prepare the time-reversed process, methods based on $\widehat{T}$-odd observables for non-degenerate stationary states (*e.g.* electric dipole moments for particles), or for final states after weak decay, have been used. The latter, however, require detailed understanding of final-state interactions (FSI), since they may lead to $\widehat{T}$ symmetry violation without the occurrence of T violation (Wolfenstein, 1999).

For T-symmetric processes, the probability of an initial state i being transformed into a final state f is the same as the probability that an initial state identical to f, but with all momenta and spins reversed, transforms into the state i with all momenta and spins reversed,

$$|\langle f|\mathcal{S}|i\rangle|^2 = |\langle i_T|\mathcal{S}\,|f_T\rangle|^2, \qquad (17.6.19)$$

where $\mathcal{S}$ is the transition matrix given by the Hamiltonian $\mathcal{H}$. This is referred to as detailed balance (Sachs, 1987). In Eq. (17.6.19), $|i\rangle \equiv |\mathbf{p}_i, \mathbf{s}_i\rangle$ and $\langle f| \equiv \langle \mathbf{p}_f, \mathbf{s}_f|$ are the initial and final states, $\langle i_T|$ and $|f_T\rangle$ are the T-transformed states of $|i\rangle$ and $\langle f|$, respectively, $\langle i_T| \equiv T|i\rangle = \langle -\mathbf{p}_i, -\mathbf{s}_i|$ and $|f_T\rangle \equiv T\langle f| = |-\mathbf{p}_f, -\mathbf{s}_f\rangle$.
It should be noted that T invariance is a sufficient, but not necessary, condition for detailed balance. Therefore, detailed-balance breaking is an unambiguous signal for T violation. If $\mathcal{S}$ is Hermitian, $|\langle f|\mathcal{S}|i\rangle| = |\langle i_T|\mathcal{S}|f_T\rangle| = |\langle f_T|\mathcal{S}|i_T\rangle|$; in this case, T invariance implies $\widehat{T}$ invariance, and vice versa. This occurs, for instance, to first order in the weak interactions when FSI may be neglected (Branco, Lavoura, and Silva, 1999; Sachs, 1987).

Within the framework of the Wigner-Weisskopf approximation (Weisskopf and Wigner, 1930a,b), the two contributions to *CP* violation in $K^0 \leftrightarrow \overline{K}^0$ transitions are described by the parameters $\mathrm{Re}\epsilon$ (violation of *CP* and T symmetry) and $\mathrm{Re}\delta + i\mathrm{Im}\delta$ (violation of *CP* and *CPT* symmetry). Here, *CP* and T symmetry is known to be violated since 1970, when a Bell-Steinberger unitarity analysis determined $\mathrm{Re}\epsilon \neq 0$ ($|q_K/p_K| \neq 1$) with a significance of about 5σ (Schubert et al., 1970). Direct evidence for the violation of *CP* and T, however, has been found only 28 years later (Angelopoulos et al., 1998), through the measurement of detailed-balance breaking in $K^0 \leftrightarrow \overline{K}^0$ transitions with a significance of about 4σ, leading to a value of $\mathrm{Re}\epsilon$ consistent with that obtained using Bell-Steinberger unitarity.

CP violation in $B \to c\bar{c}K^0$ decays is described by the parameter $\lambda = q\overline{A}/pA$, where $A = \langle c\bar{c}K^0|\mathcal{D}|B^0\rangle$, $\overline{A} = \langle c\bar{c}\overline{K}^0|\mathcal{D}|\overline{B}^0\rangle$, and the operator $\mathcal{D}$ is the B decay contribution to $\mathcal{S}$ (Section 10.2). Assuming that the amplitude A can be described by a single weak phase with only one FSI phase shift, the two parts of λ (*CP* with T violation, and *CP* with *CPT* violation) are easily identified by separating it into its modulus and phase: $\lambda = |\lambda| \exp(i\phi)$. *CPT* invariance in the decay requires $|\overline{A}/A| = 1$ (Lee, Oehme, and Yang, 1957). With $|q/p| = 1$, which is observed to be well fulfilled (see Section 17.5.4), it follows that $|\lambda| = 1$. T invariance of $\mathcal{S}$ requires $\phi = 0$ or π, *i.e.* $\mathrm{Im}\lambda = 0$ (Enz and Lewis, 1965). Conversely, if A is the

Table 17.6.13. Time-dependent *CP* parameters obtained from *BABAR* (Aubert, 2006u) and Belle (Dalseno, 2007) for the decay $B^0 \to D^{*+}D^{*-}K^0_S$. The first uncertainty is statistical and the second is systematic. The averages of the two experiments and their total uncertainty are also shown.

	BABAR	Belle	Average
$\frac{J_c}{J_0}$	$0.76 \pm 0.18 \pm 0.07$	$0.60^{+0.25}_{-0.28} \pm 0.08$	0.71 ± 0.16
$\frac{2J_{s1}}{J_0}\sin 2\phi_1$	$0.10 \pm 0.24 \pm 0.06$	$-0.17 \pm 0.42 \pm 0.09$	0.03 ± 0.21
$\frac{2J_{s2}}{J_0}\cos 2\phi_1$	$0.38 \pm 0.24 \pm 0.05$	$-0.23^{+0.43}_{-0.41} \pm 0.13$	0.24 ± 0.22

sum of two (or more) amplitudes, $|\overline{A}/A| \neq 1$ when both the strong and weak phase differences between the two decay amplitudes do not vanish, even if $\mathcal{D}$ is *CPT* symmetric (direct *CP* violation, see Section 16.6). Therefore, if $|\overline{A}/A| = 1$ then we either have both *CPT* symmetry in decay and a single amplitude, or an unlikely "accidental" cancellation of T and *CPT* violation in the decay.

The first significant observations of large *CP* violation in $B \to c\bar{c}K^0$ decays (Aubert, 2001e; Abe, 2001g) (see Sections 17.6.2 and 17.6.3) found $C = (1-|\lambda|^2)/(1+|\lambda|^2)$ to be consistent with zero ($|\lambda| = 1$) and $S = 2\mathrm{Im}\lambda/(1+|\lambda|^2) \neq 0$. These results are obtained from the $\Delta t = t_\beta - t_\alpha$ distributions of events $\Upsilon(4S) \to B^0\overline{B}^0 \to (c\bar{c}K^0_S$ or $c\bar{c}K^0_L)$ and $(e^+\nu_e X$ or $e^-\overline{\nu}_e X)$ at times t_β and t_α, respectively, parameterized according to Eq. (10.2.2) in Section 10.2. This expression assumes a negligible difference between the decay rates of the mass eigenstates (*i.e.* $\Delta\Gamma_d = 0$), $|q/p| = 1$ and $\mathrm{Re}z + i\mathrm{Im}z = 0$ (see Section 17.5.4); *i.e. CP* symmetry in $B^0 - \overline{B}^0$ mixing. However, it is valid for both signs of Δt and neither requires T nor *CPT* symmetry in decay. Within the framework of the Wigner-Weisskopf approximation, the results are compatible with *CP* and *CPT* symmetry in decay, and violate *CP* and T symmetry in the interference between decay and mixing (Fidecaro, Gerber, and Ruf, 2013). 11 years later, time-reversal violation has been directly observed in the measurement of detailed-balance breaking (Lees, 2012m), as described in the following.

Experimentally we know to a sufficiently good approximation that K^0_S and K^0_L are orthogonal states. Adopting an arbitrary sign convention, we have

$$K^0_S = \left(K^0 - \overline{K}^0\right)/\sqrt{2},$$
$$K^0_L = \left(K^0 + \overline{K}^0\right)/\sqrt{2}, \qquad (17.6.20)$$

within $\mathcal{O}(10^{-3})$ due to *CP* violation in $K^0 - \overline{K}^0$ mixing.[76] Furthermore, assuming the absence of wrong strangeness B decays, *i.e.* the $\overline{B}^0$ does not decay into $c\bar{c}K^0$ and the B^0 does not decay into $c\bar{c}\overline{K}^0$, $\langle c\bar{c}K^0|\mathcal{D}|\overline{B}^0\rangle = \langle c\bar{c}\overline{K}^0|\mathcal{D}|B^0\rangle = 0$, we have

$$\lambda_S = q\overline{A}_S/pA_S = -\lambda,$$
$$\lambda_L = q\overline{A}_L/pA_L = \lambda, \qquad (17.6.21)$$

where

$$A_{S,L} = \langle c\bar{c}K^0_S, c\bar{c}K^0_L|\mathcal{D}|B^0\rangle,$$
$$\overline{A}_{S,L} = \langle c\bar{c}K^0_S, c\bar{c}K^0_L|\mathcal{D}|\overline{B}^0\rangle. \qquad (17.6.22)$$

With the aforementioned approximations, the normalized states

$$B_+ = \mathcal{N}\left(B^0 + \frac{A}{\overline{A}}\overline{B}^0\right),$$
$$B_- = \mathcal{N}\left(B^0 - \frac{A}{\overline{A}}\overline{B}^0\right), \qquad (17.6.23)$$

with $\mathcal{N} = |\overline{A}|/\sqrt{|A|^2 + |\overline{A}|^2}$, have the property that the former decays into $c\bar{c}K^0_L$, but not into $c\bar{c}K^0_S$, and the latter into $c\bar{c}K^0_S$, but not into $c\bar{c}K^0_L$ (Alvarez and Szynkman, 2008; Bernabeu, Martinez-Vidal, and Villanueva-Perez, 2012). Like the two mixing eigenstates B_H and B_L, the two states B_+ and B_- are well defined and phase-convention-free physical states, but all four are not *CP* eigenstates. In contrast to the K^0, D^0 and B^0_s systems, where the mass eigenstates are approximate *CP* eigenstates, none of the linear combinations of B^0 and $\overline{B}^0$ has this approximate property because of large *CP* violation in the system. The states B_+ and B_- are orthogonal, *i.e.* $\langle B_+|B_-\rangle = 0$, if $|\overline{A}/A| = 1$. An extended discussion, including wrong strangeness and wrong sign (*i.e.* $\langle e^+\nu_e X\mathcal{D}|\overline{B}^0\rangle \neq 0$, $\langle e^-\bar{\nu}_e X\mathcal{D}|B^0\rangle \neq 0$) B decays has been very recently presented by Applebaum, Efrati, Grossman, Nir, and Soreq (2013).

Preparing the four initial states B^0, $\overline{B}^0$, B_+ and B_- by entanglement, the *BABAR* analysis (Lees, 2012m) determines the four differences

$$|\langle c\bar{c}K^0_S|\mathcal{S}|B^0\rangle|^2 - |\langle e^+\nu_e X|\mathcal{S}|B_-\rangle|^2,$$
$$|\langle c\bar{c}K^0_L|\mathcal{S}|B^0\rangle|^2 - |\langle e^+\nu_e X|\mathcal{S}|B_+\rangle|^2,$$
$$|\langle c\bar{c}K^0_S|\mathcal{S}|\overline{B}^0\rangle|^2 - |\langle e^-\overline{\nu}_e X\mathcal{S}|B_-\rangle|^2,$$

[76] In general $K^0_{S(L)} \propto K^0(1+\epsilon) - (+)\overline{K}^0(1-\epsilon)$, where $|\epsilon| = (2.228 \pm 0.011) \times 10^{-3}$(Beringer et al., 2012).

$$|\langle c\bar{c}K^0_L|\mathcal{S}|\overline{B}^0\rangle|^2 - |\langle e^-\overline{\nu}_e X|\mathcal{S}|B_+\rangle|^2, \quad (17.6.24)$$

where $\mathcal{S} = \mathcal{D}U(t)$ and $U(t)$ describes the time evolution of $B^0 \leftrightarrow \overline{B}^0$ transitions, given by $\mathbf{M}$ and $\mathbf{\Gamma}$, the two-by-two mass and decay Hermitian matrices of the effective Hamiltonian, as introduced in Section 10.1, and $t > 0$ is the elapsed time between the first and second B decay of the entangled pair. If $|\overline{A}/A| = 1$ (Schubert, Gioi, Bevan, and Di Domenico, 2014), the four differences in Eq. (17.6.24) are equal to the differences

$$\begin{aligned}
&|\langle B_-|U(t)|B^0\rangle|^2 - |\langle B^0|U(t)|B_-\rangle|^2,\\
&|\langle B_+|U(t)|B^0\rangle|^2 - |\langle B^0|U(t)|B_+\rangle|^2,\\
&|\langle B_-|U(t)|\overline{B}^0\rangle|^2 - |\langle \overline{B}^0|U(t)|B_-\rangle|^2,\\
&|\langle B_+|U(t)|\overline{B}^0\rangle|^2 - |\langle \overline{B}^0|U(t)|B_+\rangle|^2, \quad (17.6.25)
\end{aligned}$$

respectively. The observation that these differences are non-zero, with a $\sin\Delta m_d t$ time dependence, is a clear demonstration of detailed-balance breaking.

Within the same approximation, differences like

$$|\langle c\bar{c}K^0_S|\mathcal{S}|B^0\rangle|^2 - |\langle e^-\overline{\nu}_e X|\mathcal{S}|B_-\rangle|^2, \quad (17.6.26)$$

demonstrate *CPT* symmetry.

The experimental analysis (Lees, 2012m) uses the same data sample as the most recent *CP*-violation study in $B \to c\bar{c}K^0$, consisting of 426 fb^{-1} of integrated luminosity (Aubert, 2009z) (see Section 17.6.3). The analysis relies on identical reconstruction algorithms, selection criteria and calibration techniques. Events are selected in which one B candidate is reconstructed in a $c\bar{c}K^0_S$ or $c\bar{c}K^0_L$ state, and the other B in a flavor eigenstate. We denote generally as ℓ^-X (ℓ^+X) final states that identify the flavor of the B as $\overline{B}^0$ (B^0), which can be either semileptonic decays such as $B^0 \to e^+\nu_e X$ or flavor-specific hadronic decays. The selection leads to event classes (f_1, f_2) where the final state f_1 is reconstructed at time t_1, and the final state f_2 is reconstructed at time $t_2 > t_1$. Thus, only the eight event classes given in Table 17.6.14 are used for further analysis. Within the same approximations and if $|\overline{A}/A| = 1$ can experimentally be proven, these eight classes correspond to the transitions reported on the right column of the table. For example, the event class $(\ell^+X, c\bar{c}K^0_L)$ involves the decay of one B meson at time t_1 into a ℓ^+X final state, thus at this time the B is in a B^0 state. It then follows that the still living (second) B meson is, at that time, in a $\overline{B}^0$ state. If this same B meson decays and is reconstructed at time $t_2 > t_1$ as $c\bar{c}K^0_L$, it is a B_+ state at t_2. Hence, it undergoes a transition $\overline{B}^0 \to B_+$ in the elapsed time $t = t_2 - t_1$. Each of the four time-reversal symmetry differences in Eq. (17.6.24) uses a pair of event classes involving four different final states, ℓ^+X and ℓ^-X at times t_1 (or t_2) and t_2 (or t_1), and $c\bar{c}K^0_S$ and $c\bar{c}K^0_L$ at times t_2 (or t_1) and t_1 (or t_2), respectively.

Assuming $\Delta\Gamma_d = 0$, each of the eight transitions has a time-dependent rate $g^{\pm}_{\alpha,\beta}(t)$ given by

$$e^{-\Gamma t}[1 + S^{\pm}_{\alpha,\beta}\sin(\Delta m_d t) + C^{\pm}_{\alpha,\beta}\cos(\Delta m_d t)], \quad (17.6.27)$$

Table 17.6.14. Event classes (f_1, f_2) and their corresponding transitions between B meson states, assuming that K^0_S and K^0_L are orthogonal states, the $\overline{B}^0$ (B^0) does not decay into $c\bar{c}K^0$ ($c\bar{c}\overline{K}^0$), and $|\overline{A}/A| = 1$. The effect of the first two assumptions is well below the statistical sensitivity, whereas the third is directly demonstrated in the same analysis (see text).

Event class	Transition
$(\ell^+X, c\bar{c}K^0_L)$	$\overline{B}^0 \to B_+$
$(\ell^+X, c\bar{c}K^0_S)$	$\overline{B}^0 \to B_-$
$(\ell^-X, c\bar{c}K^0_L)$	$B^0 \to B_+$
$(\ell^-X, c\bar{c}K^0_S)$	$B^0 \to B_-$
$(c\bar{c}K^0_L, \ell^+X)$	$B_- \to B^0$
$(c\bar{c}K^0_S, \ell^+X)$	$B_+ \to B^0$
$(c\bar{c}K^0_L, \ell^-X)$	$B_- \to \overline{B}^0$
$(c\bar{c}K^0_S, \ell^-X)$	$B_+ \to \overline{B}^0$

where the lower indices $\alpha = \ell^+, \ell^-$ and $\beta = K^0_S, K^0_L$ stand for the final reconstructed states ℓ^+X, ℓ^-X and $c\bar{c}K^0_S$, $c\bar{c}K^0_L$, respectively, and the upper indices indicate if the flavor eigenstate (+) or the *CP* eigenstate (−) is reconstructed first. The coefficients $S^{\pm}_{\alpha,\beta}$ and $C^{\pm}_{\alpha,\beta}$ are model-independent; the eight pairs of S and C coefficients can be written in terms of eight complex λ parameters, as $2\mathrm{Im}\lambda/(1+|\lambda|^2)$ and $(1-|\lambda|^2)/(1+|\lambda|^2)$, respectively. The state $c\bar{c}K^0_S$ is identified by the final states with $c\bar{c} = J/\psi$, $\psi(2S)$ or χ_{c1}, while $c\bar{c}K^0_L$ only by $J/\psi K^0_L$. As in Aubert (2009z), the flavor eigenstates labeled ℓ^+X and ℓ^-X are identified by prompt leptons, kaons, pions from D^* mesons, and high-momentum charged particles, combined in a neural network. The final sample contains 7796 $c\bar{c}K^0_S$ events, with purities ranging between 87% and 96%, and 5813 $J/\psi K^0_L$ events with a purity of 56%.

The coefficients $S^{\pm}_{\alpha,\beta}$ and $C^{\pm}_{\alpha,\beta}$ are determined by a simultaneous, unbinned maximum likelihood fit to the four measured $\Delta t = t_\beta - t_\alpha$ distributions. The time difference Δt is determined as described in Section 6.5 and used in the *CP*-violation studies based on the same decay modes (see Section 17.6.3). Neglecting time resolution, the elapsed time between the first and second decay is $t = \Delta t$ if the first B decays into a flavor eigenstate, and $t = -\Delta t$ if it decays into a *CP* eigenstate. Time resolution mixes events with positive and negative true Δt, *i.e.*, a true event class $(\ell^+X, c\bar{c}K^0_L)$, corresponding to a $\overline{B}^0 \to B_+$ transition, could appear reconstructed as $(c\bar{c}K^0_L, \ell^+X)$, corresponding to a $B_- \to B^0$ transition, and vice versa. Therefore, the fit cannot be performed with eight event classes but only with four. The separate determination of the coefficients for the event classes with flavor before *CP* eigenstates and those with *CP* before flavor eigenstates, *i.e.*, the unfolding of time ordering and Δt resolution, is accomplished by using a signal *p.d.f.* for the four distributions of the form

$$\mathcal{H}_{\alpha,\beta}(\Delta t) = g^{+}_{\alpha,\beta}(\Delta t_{\mathrm{true}})H(\Delta t_{\mathrm{true}}) \otimes \mathcal{R}(\delta t; \sigma_{\Delta t}) +$$

$$g^{-}_{\alpha,\beta}(-\Delta t_{\rm true})H(-\Delta t_{\rm true}) \otimes \mathcal{R}(\delta t;\sigma_{\Delta t}), \tag{17.6.28}$$

where $\Delta t_{\rm true} \equiv \pm t$ is the signed difference of proper time between the two B decays in the limit of perfect Δt resolution, H is the Heaviside step function, $\mathcal{R}(\delta t;\sigma_{\Delta t})$ is the resolution function with $\delta t = \Delta t - \Delta t_{\rm true}$, and $\sigma_{\Delta t}$ is the estimate of the Δt uncertainty obtained by the reconstruction algorithms (Bernabeu, Martinez-Vidal, and Villanueva-Perez, 2012). A total of 27 parameters are varied in the likelihood fit: eight pairs $(S^{\pm}_{\alpha,\beta}, C^{\pm}_{\alpha,\beta})$ of signal coefficients and 11 for describing possible CP and T violation in the background. All remaining signal and background parameters are treated in an identical manner as done in the CP violation analysis (see Section 17.6.3). From the 16 signal coefficients, reported in Table 17.6.15, we construct six pairs of independent asymmetry parameters $(\Delta S^{\pm}_{T}, \Delta C^{\pm}_{T})$, $(\Delta S^{\pm}_{CP}, \Delta C^{\pm}_{CP})$, and $(\Delta S^{\pm}_{CPT}, \Delta C^{\pm}_{CPT})$, as shown in Table 17.6.16. The asymmetry parameters have the advantage that the breaking of time-reversal symmetry would directly manifest itself through any nonzero value of $\Delta S^{\pm}_{T}$ or $\Delta C^{\pm}_{T}$, or any difference between $\Delta S^{\pm}_{CP}$ and $\Delta S^{\pm}_{CPT}$, or between $\Delta C^{\pm}_{CP}$ and $\Delta C^{\pm}_{CPT}$.

Table 17.6.15. Measured values of the $S^{\pm}_{\alpha,\beta}$ and $C^{\pm}_{\alpha,\beta}$ coefficients (Lees, 2012m). The first uncertainty is statistical and the second systematic. The indices ℓ^-, ℓ^+, K^0_S, and K^0_L stand for reconstructed final states that identify the B meson state as $\overline{B}^0$, B^0 and B_-, B_+, respectively.

Transition	Parameter	Result
$\overline{B}^0 \to B_+$	$S^{+}_{\ell^+,K^0_L}$	$-0.69 \pm 0.11 \pm 0.04$
	$C^{+}_{\ell^+,K^0_L}$	$-0.02 \pm 0.11 \pm 0.08$
$\overline{B}^0 \to B_-$	$S^{+}_{\ell^+,K^0_S}$	$0.55 \pm 0.09 \pm 0.06$
	$C^{+}_{\ell^+,K^0_S}$	$0.01 \pm 0.07 \pm 0.05$
$B^0 \to B_+$	$S^{+}_{\ell^-,K^0_L}$	$0.51 \pm 0.17 \pm 0.11$
	$C^{+}_{\ell^-,K^0_L}$	$-0.01 \pm 0.13 \pm 0.08$
$B^0 \to B_-$	$S^{+}_{\ell^-,K^0_S}$	$-0.76 \pm 0.06 \pm 0.04$
	$C^{+}_{\ell^-,K^0_S}$	$0.08 \pm 0.06 \pm 0.06$
$B_- \to B^0$	$S^{-}_{\ell^+,K^0_L}$	$0.70 \pm 0.19 \pm 0.12$
	$C^{-}_{\ell^+,K^0_L}$	$0.16 \pm 0.13 \pm 0.06$
$B_+ \to B^0$	$S^{-}_{\ell^+,K^0_S}$	$-0.66 \pm 0.06 \pm 0.04$
	$C^{-}_{\ell^+,K^0_S}$	$-0.05 \pm 0.06 \pm 0.03$
$B_- \to \overline{B}^0$	$S^{-}_{\ell^-,K^0_L}$	$-0.83 \pm 0.11 \pm 0.06$
	$C^{-}_{\ell^-,K^0_L}$	$0.11 \pm 0.12 \pm 0.08$
$B_+ \to \overline{B}^0$	$S^{-}_{\ell^-,K^0_S}$	$0.67 \pm 0.10 \pm 0.08$
	$C^{-}_{\ell^-,K^0_S}$	$0.03 \pm 0.07 \pm 0.04$

Table 17.6.16. Measured values of the asymmetry parameters, defined as the differences in $S^{\pm}_{\alpha,\beta}$ and $C^{\pm}_{\alpha,\beta}$ between symmetry-transformed transitions (Lees, 2012m). The parameters $\Delta S^{\pm}_{T}$, $\Delta C^{\pm}_{T}$ and the differences $\Delta S^{\pm}_{CP} - \Delta S^{\pm}_{CPT}$, $\Delta C^{\pm}_{CP} - \Delta C^{\pm}_{CPT}$ are all T violating. The first uncertainty is statistical and the second systematic.

Parameter	Result
$\Delta S^{+}_{T} = S^{-}_{\ell^-,K^0_L} - S^{+}_{\ell^+,K^0_S}$	$-1.37 \pm 0.14 \pm 0.06$
$\Delta S^{-}_{T} = S^{+}_{\ell^-,K^0_L} - S^{-}_{\ell^+,K^0_S}$	$1.17 \pm 0.18 \pm 0.11$
$\Delta C^{+}_{T} = C^{-}_{\ell^-,K^0_L} - C^{+}_{\ell^+,K^0_S}$	$0.10 \pm 0.14 \pm 0.08$
$\Delta C^{-}_{T} = C^{+}_{\ell^-,K^0_L} - C^{-}_{\ell^+,K^0_S}$	$0.04 \pm 0.14 \pm 0.08$
$\Delta S^{+}_{CP} = S^{+}_{\ell^-,K^0_S} - S^{+}_{\ell^+,K^0_S}$	$-1.30 \pm 0.11 \pm 0.07$
$\Delta S^{-}_{CP} = S^{-}_{\ell^-,K^0_S} - S^{-}_{\ell^+,K^0_S}$	$1.33 \pm 0.12 \pm 0.06$
$\Delta C^{+}_{CP} = C^{+}_{\ell^-,K^0_S} - C^{+}_{\ell^+,K^0_S}$	$0.07 \pm 0.09 \pm 0.03$
$\Delta C^{-}_{CP} = C^{-}_{\ell^-,K^0_S} - C^{-}_{\ell^+,K^0_S}$	$0.08 \pm 0.10 \pm 0.04$
$\Delta S^{+}_{CPT} = S^{-}_{\ell^+,K^0_L} - S^{+}_{\ell^+,K^0_S}$	$0.16 \pm 0.21 \pm 0.09$
$\Delta S^{-}_{CPT} = S^{+}_{\ell^+,K^0_L} - S^{-}_{\ell^+,K^0_S}$	$-0.03 \pm 0.13 \pm 0.06$
$\Delta C^{+}_{CPT} = C^{-}_{\ell^+,K^0_L} - C^{+}_{\ell^+,K^0_S}$	$0.14 \pm 0.15 \pm 0.07$
$\Delta C^{-}_{CPT} = C^{+}_{\ell^+,K^0_L} - C^{-}_{\ell^+,K^0_S}$	$0.03 \pm 0.12 \pm 0.08$

All eight $C^{\pm}_{\alpha,\beta}$ coefficients are compatible with zero. Since $C = (1-|\lambda|^2)/(1+|\lambda|^2)$, $\lambda = q\overline{A}/pA$ and $|q/p| \approx 1$, $C = 0$ implies $|\overline{A}/A| = 1$. Therefore, the time dependence with only a $\sin\Delta m_d t$ function proves experimentally the approximation $|\overline{A}/A| = 1$ required for the demonstration of time-reversal violation. With this observation (*i.e.* the absence of all eight $\cos\Delta m_d t$ terms) the two states B_+ and B_- are orthogonal; we have the association between event classes and B meson transitions given in Table 17.6.14, and the differences in Eqs (17.6.24) and (17.6.25) become identical.

For visualizing the T-violating differences of the transition rates, the fit results are shown in Fig. 17.6.19 in the form of asymmetries such as (for the transition $\overline{B}^0 \to B_-$)

$$A_T(\Delta t) = \frac{\mathcal{H}^{-}_{\ell^-,K^0_L}(\Delta t) - \mathcal{H}^{+}_{\ell^+,K^0_S}(\Delta t)}{\mathcal{H}^{-}_{\ell^-,K^0_L}(\Delta t) + \mathcal{H}^{+}_{\ell^+,K^0_S}(\Delta t)}, \tag{17.6.29}$$

where $\mathcal{H}^{\pm}_{\alpha,\beta}(\Delta t) = \mathcal{H}_{\alpha,\beta}(\pm\Delta t)H(\Delta t)$. With this construction, $A_T(\Delta t)$ is defined only for positive Δt values. Neglecting reconstruction effects,

$$A_T(t) \approx \frac{\Delta S^{+}_{T}}{2}\sin(\Delta m_d t) + \frac{\Delta C^{+}_{T}}{2}\cos(\Delta m_d t). \tag{17.6.30}$$

The three other asymmetries in Fig. 17.6.19 are constructed in an analogous way and have the same time dependence, with ΔS^{+}_{T} replaced by ΔS^{-}_{T}, ΔS^{-}_{CP} $-\Delta S^{-}_{CPT}$, and ΔS^{+}_{CP} $-\Delta S^{+}_{CPT}$, respectively, and equally for ΔC^{+}_{T}.

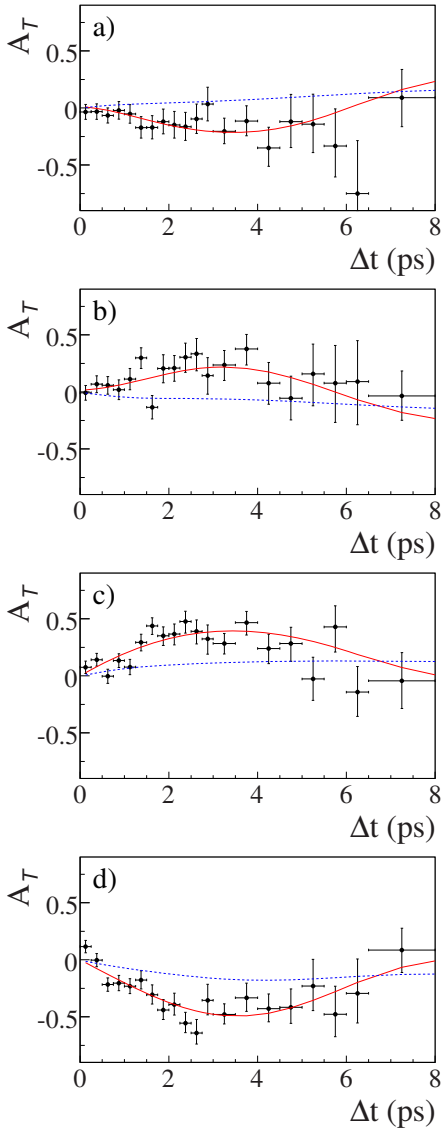

Figure 17.6.19. The four independent time-reversal violating asymmetries (Lees, 2012m) for transition a) $\overline{B}^0 \to B_-$ $(\ell^+X, c\bar{c}K_S^0)$, b) $B_+ \to B^0$ $(c\bar{c}K_S^0, \ell^+X)$, c) $\overline{B}^0 \to B_+$ $(\ell^+X, J/\psi K_L^0)$, d) $B_- \to B^0$ $(J/\psi K_L^0, \ell^+X)$, for combined flavor categories with low misidentification (leptons and kaons), in the signal region $(5.27 < m_{\rm ES} < 5.29\ {\rm GeV}/c^2$ for $c\bar{c}K_S^0$ modes and $|\Delta E| < 10$ MeV for $J/\psi K_L^0)$. The points with error bars represent the data, the red solid and dashed blue curves represent the projections of the best fit results with and without time-reversal violation, respectively.

The evaluation of systematic uncertainties, reported in Table 17.6.16, follows closely that of the *CP* analysis based on the same final states, discussed in Section 17.6.3. A possible *CP* violation in right- and wrong-sign flavor-specific B decays (denoted $\ell^\pm X$) is found to have an impact on the measurement well below the statistical uncertainty.

As seen in Fig. 17.6.19, time-reversal symmetry is clearly violated in all four transition comparisons. The significance of the observed T violation is obtained from the log-likelihood value $\ln\mathcal{L}$. The difference $2\Delta\ln\mathcal{L}$ between the best fit and the fit without T violation, including systematic errors, is 226 with 8 d.o.f., which corresponds, assuming Gaussian errors, to 14σ. Using the same procedure for the *CPT*-symmetry differences such as in Eq. (17.6.26), no *CPT* violation is observed. The difference $2\Delta\ln\mathcal{L}$ between the values for the best fit and the fit with *CPT* symmetry is 5, equivalent to 0.3σ. The analysis also determines four *CP* asymmetries; the results are compatible with those obtained from the standard *CP* violation analysis based on the same *CP* final states (Aubert, 2009z); the observed significance of *CP* violation is equivalent to 17σ. This is larger than 14σ for T violation since the comparison between two $(\ell^\pm, c\bar{c}K_S)$ rates has a higher statistical and systematic significance than the comparison of the rates $(\ell^\pm, c\bar{c}K_S)$ and $(\ell^\pm, c\bar{c}K_L)$.

In the Standard Model, the eight coefficients $S^\pm_{\alpha,\beta}$ are measurements of $\sin 2\phi_1$. Hence the four measured T-violating asymmetries, $\Delta S_T^\pm$ and $\Delta S_{CP}^\pm - \Delta S_{CPT}^\pm$, can be seen as four measurements of $2\sin 2\phi_1$. The results in Table 17.6.16 lead to a mean value $\phi_1 = (21.8 \pm 2.0)^\circ$, which is of course completely correlated with the ϕ_1 value obtained from the *CP*-asymmetry measurements discussed in Sections 17.6.3 and 17.6.10.

In conclusion, the *BABAR* experiment (Lees, 2012m) has demonstrated with a large significance of 14σ that detailed balance and therefore time-reversal symmetry are violated. In $b \to c\bar{c}s$ decays, T and *CP* symmetry breakings are seen in two different observations, are time dependent with only a $\sin\Delta mt$ term, are of order $\mathcal{O}(10^{-1})$, and are induced by the interference between $q\overline{A}$ and pA, *i.e.* the interference between decay and mixing. All these properties are different from those of the earlier observed flavor mixing asymmetry in $K^0 - \overline{K}^0$ transitions, where *CP* and T transformations lead to the same observation, the asymmetry is time independent, is of order $\mathcal{O}(10^{-3})$, and is produced by the interference of absorptive (Γ_{12}) and dispersive (M_{12}) contributions to mixing.

17.6.10 ϕ_1 summary

Establishing *CP* violation in B^0 meson decays by measuring $\sin 2\phi_1$ was the most important initial goal of the B Factories. Both experiments achieved this goal after two years of operation through time-dependent analyses of $b \to c\bar{c}s$ transitions. This represents the first observation of *CP* violation outside of the neutral kaon system (Christenson, Cronin, Fitch, and Turlay, 1964). With a combined final data set of 1.2 billion $B\overline{B}$ pairs, the achieved precision on $\sin 2\phi_1$ is 0.020. *BABAR* have also demonstrated T violation in $b \to c\bar{c}s$ transitions which provides an additional test of the CKM matrix (this is statistically completely correlated with the *CP* violation result). The ambiguity between ϕ_1 and $\pi/2 - \phi_1$ is resolved by several measurements. They all use interference with known or measured strong phases (transversity states

and $K^* \to K\pi$ phases for $B^0 \to J/\psi K^*$, and Dalitz plot phases for $B^0 \to D^{(*)0}[K^0_S\pi^+\pi^-]h^0$ and $D^*D^*K^0_S$ and other three-body decays). The result in terms of angle is $\phi_1 \equiv \beta = (21.30 \pm 0.78)^\circ$. The direct *CP* asymmetry parameter C is found to be consistent with zero in these channels, as expected in the SM. The consistency between ϕ_1 and other CKM angles and sides of the Unitarity Triangle demonstrates that the KM mechanism is the dominant source of *CP* violation in the SM. Kobayashi and Maskawa shared the 2008 Nobel Prize in physics for their work on the KM mechanism presented in (Kobayashi and Maskawa, 1973). The test of the CKM matrix by examining the agreement between different measurements is discussed in Section 25.1.

A number of other channels have been studied by the experiments at the B Factories. These are suppressed to various degrees in the SM compared to $b \to c\bar{c}s$ transitions. They are either tree dominated modes with a penguin (or another tree) contribution that has a different weak phase ($J/\psi\pi^0$, $D^{(*)}D^{(*)}$ or $D^{(*)}h^0$), or charmless modes ($b \to sq\bar{q}$). The penguin-dominated modes are particularly sensitive to the presence of any postulated new heavy particles that could contribute to such a loop transition.

The most precisely determined time-dependent asymmetry parameters from a loop dominated $b \to sq\bar{q}$ channel come from $B^0 \to \eta' K^0$ and $K^+K^-K^0$ with a precision of 0.07 on $\sin 2\phi_1$. The uncertainties of other modes range from around 0.2 to 0.7. The $\sin 2\phi_1$ results obtained from these measurements are consistent with the value measured in the $b \to c\bar{c}s$ golden channels. The naïve average of charmless decays is within one sigma of $b \to c\bar{c}s$ results. However, it should be noted that the naïve average is not a good observable to use when searching for NP, as the hadronic uncertainties vary from mode to mode. The most recent measurements of these decays are consistent with the SM.

No significant direct *CP* asymmetry is found in the channels discussed in this section. However some of these channels exhibit central values that are more than 2σ from $C = 0$ (*e.g.*, D^+D^- for Belle and ωK^0_S for *BABAR*). The global χ^2 among the different channels studied is consistent with the interpretation that these measurements are the result of a statistical fluctuation.

17.7 ϕ_2, or α

Editors:
Yury Kolomensky (BABAR)
Tagir Aushev (Belle)
Ikaros Bigi (theory)

Additional section writers:
Adrian Bevan, Cheng-Chin Chiang, Jeremy Dalseno, J. William Gary, Mathew Graham, Akito Kusaka, Fernando Palombo, Kolja Prothmann, Aaron Roodman, Abner Soffer, Alexander Somov, Alexandre Telnov, Karim Trabelsi, Pit Vanhoefer, Georges Vasseur, Fergus Wilson

In the Standard Model of particle physics the CKM matrix results in a set of nine unitary relationships, six of which are triangles in a complex plane (Chapter 16). The imaginary components of these triangles are manifestations of a single complex phase that dictates the amount of *CP* violation in the theory. The measurement of ϕ_1 described in Chapter 17.6 establishes one of the angles of the Unitarity Triangle associated with B_d decays, introduced in Section 16.5. To check the self-consistency of the triangle one has to measure its other two angles and the sides. The second angle of the Unitarity Triangle to be measured is ϕ_2, which is the subject of this chapter. Together the measurements of ϕ_1 and ϕ_2 are sufficient to test the predictions of the SM. Constraints on the third angle, ϕ_3 , are discussed in Chapter 17.8 and how one typically interprets these results in the context of the SM is reviewed in Chapter 25.1.

A probe that can be used to determine ϕ_2 is the measurement of the time-dependent *CP* asymmetry in $B^0 \to \pi^+\pi^-$ transitions. This *CP* violation is produced by the interference of the dominant box diagram for $B^0-\overline{B}^0$ mixing with the tree diagram $b\overline{d} \to u\overline{u}d\overline{d}$. If these were the only contributing diagrams, the resulting *CP* asymmetry parameters would be $S = \sin 2\phi_2$ and $C = 0$. However the situation is not so simple: this final state is also produced by higher order weak transitions, and of particular relevance is the one-loop diagram usually called the 'penguin' diagram (Shifman, Vainshtein, and Zakharov, 1977). The presence of penguin contributions with weak phases that differ from the leading order tree results in theoretical uncertainties on ϕ_2 that are sometimes referred to as 'penguin pollution' in the literature. The penguin contribution affects $\mathcal{B}(B^0 \to \pi^+\pi^-)$ and its *CP* asymmetry (Bigi, Khoze, Uraltsev, and Sanda, 1989). Gronau and London (1990) suggested using isospin symmetry to correct for the effect of penguin contributions when extracting ϕ_2. At first it was thought that penguin contributions are very small in the SM for $B^0 \to \pi\pi$, since the amplitude $b \to dq\overline{q}$ is suppressed by a factor of $|\lambda| = |V_{us}|$ relative to $b \to sq\overline{q}$. However, data showed that the $B^0 \to \pi^0\pi^0$ rate is larger than had been initially expected, and this is explained by the presence of a sizable penguin contribution; therefore penguin amplitudes can significantly affect the extraction of ϕ_2. Thus the measurement of ϕ_2 with $B \to \pi\pi$ requires a more complicated approach than the measurement of ϕ_1 with $B \to J/\psi K^0_S$. The theoretical issues associated with this approach are described in Section 17.7.1.1, and the corresponding experimental treatment is summarized in Section 17.7.3.1. It is worth noting that new physics (NP) could enhance penguin contributions significantly. Experimentally one could identify such contributions by observing a significant difference between values of ϕ_2 obtained using different decay modes.

The impact of penguin amplitudes in general is different for different final states, and as $b\overline{d} \to u\overline{u}d\overline{d}$ decays can be used to measure ϕ_2, it became necessary to explore experimentally and theoretically more difficult scenarios in the hope that nature was kind enough to permit measurement of this angle in one or another way. Having determined that the measurement of ϕ_2 via $B^0 \to \pi\pi$ would be less sensitive than anticipated, the B Factories approached the problem using a rather different technique: a time-dependent analysis of the Dalitz plot of $B^0 \to \pi^+\pi^-\pi^0$. The theoretical issues related to this measurement are introduced in Section 17.7.1.2, while the corresponding experimental discussion can be found in Section 17.7.4. The resulting constraints obtained from *BABAR* and Belle data do not add a significant amount of information to improve the accuracy of the SM solution for ϕ_2, however they suppress the discrete ambiguities arising from the interpretation of other measurements. For the future higher statistics experiments, the decay $B^0 \to \pi^+\pi^-\pi^0$ is expected to dominate the experimental determination of ϕ_2 and to provide a sensitive probe for the impact of NP and its features as a non-leading source of *CP* violation.

After several years of data taking it became apparent that extraction of ϕ_2 from the B Factories is a difficult enterprise. Thus it was realized that one has to think about other final states and *BABAR* started to investigate other related options such as $B \to \rho\rho$ decays. They were previously dismissed by the community as experimentally and theoretically too challenging to be a viable alternative compared with the already ambitious attempts to study $B \to \pi\pi$ and $B \to \rho\pi$. When the experimental work commenced, the outcome of this endeavor was not entirely clear; however, there were hints that indicated these modes could be more promising than originally thought. The presence of two vector particles in the final state meant that one would have to perform a full angular analysis of the final state (see Chapter 12) in addition to constraining penguin contributions. However, it was possible to piece together sufficient information from various sources in order to motivate attempting the measurement of ϕ_2 with $B \to \rho\rho$ decays. Ultimately a full angular analysis was not required to constrain ϕ_2 as the fraction of longitudinal polarization in $B \to \rho\rho$ decays was found to almost completely dominate (Section 17.7.3.2). The result of this approach turned out to provide the most stringent constraint on ϕ_2, where the efforts of *BABAR* and Belle are summarized in Section 17.7.3.2. The time-dependent analysis of $B^0 \to \rho^0\rho^0$ promises to help resolve some of the discrete ambiguities inherent in the isospin analysis and is discussed in Section 17.7.3.3. An additional cross-check

using $SU(3)$ for $B \to \rho\rho$ and $K^*\rho$ decays is discussed in Section 17.7.6.

As a further development one constrains ϕ_2 using final states including vector and axial-vectors particles, in particular using $B \to a_1(1260)\pi$ decays, where one can determine the impact of penguin contributions with the aid of $SU(3)$ flavor symmetry. This theoretical approach is discussed in Section 17.7.1.3. Time-dependent measurements of $B \to a_1(1260)\pi$ and the complementary studies of $B \to K_1\pi$ decays are used to control penguin pollution as discussed in Section 17.7.5.

In contrast to the initial expectations of the B Factories where it was anticipated that $\pi\pi$ final states would provide a measurement of ϕ_2 and $\rho\pi$ would be used to resolve ambiguities, 'reality' told a different story. Measurements of $B \to \rho\rho$ decays dominate the determination of the angle ϕ_2 and $B \to a_1(1260)\pi$ decays provide additional precision on the overall measurement of this angle. The study of $\rho\pi$ final states provides additional discrimination: the power to resolve some of the discrete ambiguities, as originally expected. The B Factories have been able to make an accurate measurement of ϕ_2, using B decays to $\pi\pi$, $\rho\pi$, $\rho\rho$, and $a_1\pi$ final states, as discussed in Section 17.7.7.

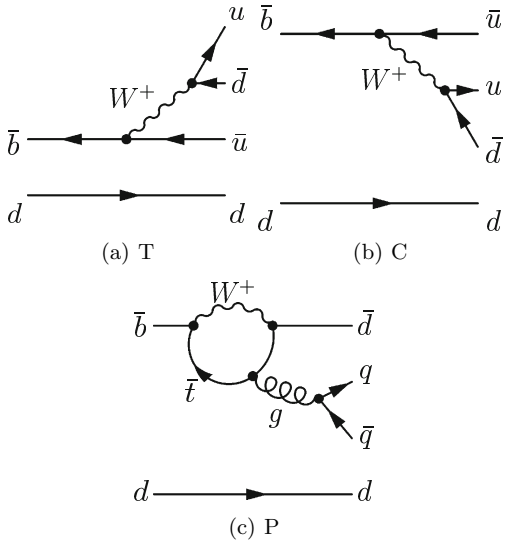

Figure 17.7.1. Feynman diagrams contributing to the charmless B decays $B^0 \to \pi\pi$ or $B^0 \to \rho\rho$: (a) external tree (T), (b) internal (or color suppressed) tree (C), and (c) gluonic penguin (P). Nearby quarks are implied to be grouped into mesons.

17.7.1 Introduction

The angle ϕ_2 can be inferred from time-dependent CP asymmetries in charmless $b \to u$ transitions. Feynman diagrams describing these decays, such as $B^0 \to \pi\pi$ and $B^0 \to \rho\rho$, are shown in Fig. 17.7.1. Interference between the leading tree amplitude and the amplitude of $B^0 - \overline{B}^0$ mixing (Fig. 10.1.1) provides access to the observable ϕ_2. As explained above, if the tree amplitude was the only decay amplitude (as is the case for $B^0 \to J/\psi K^0_S$), the S parameter in $B^0 \to \pi^+\pi^-$ would be equal to $\sin 2\phi_2$ and C zero (see Eq. 16.6.8). However, the penguin contributions to charmless B decays cannot be ignored. In general S measures $\sin 2\phi_2^{\rm eff}$ instead $\sin 2\phi_2$, where $\phi_2^{\rm eff}$ is related to ϕ_2 up to a shift $\Delta\phi_2$ resulting from penguin amplitudes with a different weak phase to that of the leading order tree contribution, *i.e.* $\Delta\phi_2 = \phi_2^{\rm eff} - \phi_2$. We have to understand how to control the penguin contributions and determine the difference between $\phi_2^{\rm eff}$ and ϕ_2.

In the following, we discuss four complementary techniques to extract the angle ϕ_2 from time-dependent CP asymmetry measurements in $B \to 2\pi$, 3π and 4π decays.

- Isospin analysis in $B \to \pi\pi$ and $B \to \rho\rho$;
- Dalitz analysis in $B \to \rho\pi$;
- $SU(3)$ analysis of $B \to a_1(1260)\pi(K)$;
- $SU(3)$ constraints in charmless B decays to two vector meson final states.

The analysis methodology outlined in the remainder of this chapter in terms of the study of four body final states relies on the quasi-two-body approximation (see Section 17.4.3), which is sufficient for work at the B Factories. However, it should be borne in mind that in the future one will want to probe the impact of NP in 4π and $2\pi K\overline{K}$ final states to search for possible non-leading sources of CP violation. Amplitude analyses, introduced in Section 13, will be required for such searches and future super flavor factory will have to adopt a more general approach for such analyses.

The combined accuracy on ϕ_2 obtained by the B Factories is discussed in Section 17.7.7. Some time-integrated measurements are required to constrain penguin contributions in various decays; those are discussed in Section 17.4.

17.7.1.1 Isospin analysis of $B \to \pi\pi$ and $B \to \rho\rho$

The CP asymmetry in $B^0 \to \pi^+\pi^-$ depends on ϕ_2. However (unlike $B^0 \to J/\psi K^0_S$), because of the two contributing amplitudes (tree and penguin, see Section 16.6) in the SM one expects direct CP violation to be manifest in $B^0 \to \pi^+\pi^-$, hence:

$$\frac{\Gamma(\overline{B} \to \pi^+\pi^-) - \Gamma(B \to \pi^+\pi^-)}{\Gamma(\overline{B} \to \pi^+\pi^-) + \Gamma(B \to \pi^+\pi^-)} = C\cos\Delta m_d\Delta t - S\sin\Delta m_d\Delta t \tag{17.7.1}$$

with

$$C = \frac{1-|\lambda|^2}{1+|\lambda|^2}, \qquad S = \frac{2\,{\rm Im}\lambda}{1+|\lambda|^2}\,, \tag{17.7.2}$$

where $\lambda = (q/p)\overline{A}/A$ as noted in Chapter 10, and from Chapter 16 we recall that

$$0 \le C^2 + S^2 \le 1. \tag{17.7.3}$$

CP violation is manifest if $0 < C^2 + S^2$, *i.e.* if either of the asymmetry parameters are non-zero. Here $\lambda = (q/p)\overline{R}(\pi^+\pi^-)$ where $\overline{R}(\pi^+\pi^-)$ refers to the amplitude of the $\overline{B}^0$ decay to the final state normalized by the B^0 decay to the same one (Eq. 17.7.4):

$$\overline{R}(\pi^+\pi^-) \equiv \frac{A(\overline{B}^0 \to \pi^+\pi^-)}{A(B^0 \to \pi^+\pi^-)} \,. \tag{17.7.4}$$

Without penguin contributions one predicts in the SM (Bigi, Khoze, Uraltsev, and Sanda, 1989)

$$\left|\frac{q}{p}\overline{R}(\pi^+\pi^-)\right| \simeq 1,$$
$$\mathrm{Im}\left[\frac{q}{p}\overline{R}(\pi^+\pi^-)\right] \simeq \sin 2\phi_2. \tag{17.7.5}$$

However, penguin amplitudes do contribute. In this case one finds $|\frac{q}{p}\overline{R}(\pi^+\pi^-)| \neq 1$ and therefore $C^2 \neq 0$. Our knowledge of the quantitative impact of penguin amplitudes and in general non-perturbative QCD is rather limited.

One technique for measuring ϕ_2 is to study time-dependent *CP* asymmetries in $B^0 \to \pi^+\pi^-$ decays (Aubert (2002h); Abe (2003b)). The data show (see Section 17.7.3.1) that:

$$S = -0.66 \pm 0.07,$$
$$C = -0.30 \pm 0.05, \tag{17.7.6}$$

which are consistent with expectation from the SM. The non-zero value of C, indicating direct *CP* violation in this mode, arises from the interference of tree and penguin amplitudes with different weak and strong phases. It is not possible to determine if the penguin amplitudes are consistent with the SM expectation, or include contributions from physics beyond the SM. The SM level of contribution to these decays can be determined using the isospin analysis described below, the results of which can be found in Section 17.7.7. Therefore one cannot directly obtain ϕ_2 from the time-dependent analysis and use this with the value of ϕ_1 from $B^0 \to J/\psi K^0_s$, discussed in Section 17.6, to construct the SM Unitarity Triangle. A complementary study in $B^0 \to \rho^+\rho^-$ was pioneered by *BABAR* (Aubert, 2004ag) with the hope of being able to contribute to the measurement of ϕ_2. However once again the extraction of this angle is complicated by the presence of both tree and penguin amplitudes, with different weak phases. An isospin analysis of the $\pi\pi$ or $\rho\rho$ system is necessary (Gronau and London, 1990) to disentangle the tree contribution, and hence determine ϕ_2 as explained in the following.

The all-charged modes ($B^0 \to \pi^+\pi^-$ and $B^0 \to \rho^+\rho^-$) are dominated by the external tree (T) and gluonic penguin (P) amplitudes, while the all-neutral modes ($B^0 \to \pi^0\pi^0$ and $B^0 \to \rho^0\rho^0$) are very sensitive to the P contribution, since the internal tree diagram (C) is color-suppressed. The amplitudes $A^{00} \equiv A(B^0 \to h^0h^0)$, $A^{+-} \equiv A(B^0 \to h^+h^-)$, and $A^{+0} \equiv A(B^+ \to h^+h^0)$, where $h = \pi, \rho$, and their complex conjugates, obey the Gronau-London isospin relation (Gronau and London, 1990). Here we note that $I = 1/2$ for u and d quarks only and as a result the isospin decomposition of $B \to \pi\pi$ decays follows the corresponding $K \to \pi\pi$ case. Bose statistics forbids $I = 1$ $\pi\pi$ final states, which simplifies the isospin construction of these decays. The tree topologies shown in Fig 17.7.1 come from operators that describe $\Delta I = 1/2$ or $\Delta I = 3/2$ transitions, and so as a B meson has $I = 1/2$, the corresponding final states can either be $I = 0$ or 2. In contrast the gluonic penguin contributions come from a $\Delta I = 1/2$ operator, hence these can only be $I = 0$. Both h^+h^- and h^0h^0 final states can be $I = 0$ or 2, and so in general these decays may proceed via both tree and penguin transitions. In contrast, the h^+h^0 final state is $I = 2$ and therefore can only have tree contributions. The resulting isospin relations obtained by Gronau and London are:

$$A^{+-}/\sqrt{2} + A^{00} = A^{+0},$$
$$\overline{A}^{+-}/\sqrt{2} + \overline{A}^{00} = \overline{A}^{-0}, \tag{17.7.7}$$

each of which can be represented by a triangle in a complex plane (Fig. 17.7.2). The *CP* conjugate relation is usually shown with a tilde replacing the bar to denote that the bases of the two isospin triangles have been aligned such that $A^{+0} = \widetilde{A}^{+0}$, which explicitly neglects any effect coming from electroweak (EW) penguins.[77] The relative sizes and phases of each amplitude can be extracted from the complete isospin analysis of the three decay rates and corresponding *CP* asymmetries (Gronau and London, 1990). The angle between the sides of lengths $A^{+-}/\sqrt{2}$ and $\widetilde{A}^{+-}/\sqrt{2}$ is $2\Delta\phi_2$.

Experimentally, the complete isospin analysis of the $B \to \pi\pi$ system is complicated by the need to measure time-dependent *CP* asymmetry of the all-neutral final state decay of B^0 mesons to $\pi^0\pi^0$. This is not possible at the present level of statistics, although high luminosity super flavor factory may be able to constrain the decay vertex of the $B^0 \to \pi^0\pi^0$ candidate using Dalitz decays of one or both π^0 mesons, or events where one or more photons convert in the detector material. The situation is further exacerbated by the relatively large observed branching fraction of $B^0 \to \pi^0\pi^0$ decays (Aubert (2003k); Abe (2003a)); this implies a large penguin contribution, which results in a significant uncertainty in the extraction of ϕ_2. The branching fraction measurements of the decays $B^0 \to \pi^0\pi^0$ and $B^+ \to \pi^+\pi^0$ are described in Section 17.4.

The isospin analysis of the vector-vector modes $B \to \rho\rho$ is more complicated than that for $B \to \pi\pi$. The $\rho\rho$ final states include three contributions: one longitudinal and two transverse amplitudes following the discussion

[77] Electroweak penguins have the same topology as the gluonic penguin shown in Fig 17.7.1, but are mediated by a photon or Z^0 boson. It is expected that EW penguins are small and can be neglected. This assumption can be tested by constraining the level of direct *CP* violation found in $B^+ \to h^+h^0$ decays, which is predicted to be zero in the absence of any EW penguin contribution.

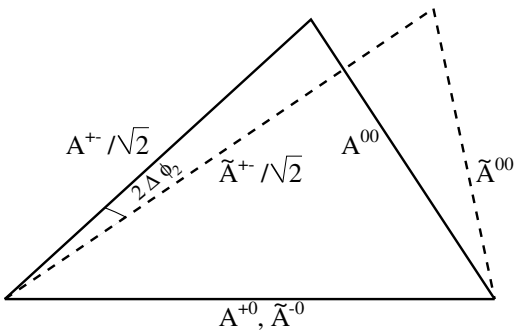

Figure 17.7.2. Gronau-London isospin triangles for $B^0 \to hh$ (solid lines) and $\overline{B}^0 \to hh$ (dashed lines), drawn for illustration purposes (not to scale). The $\overline{B}^0$ amplitudes are denoted with a tilde to highlight that the two triangles have been rotated relative to each other so that the h^+h^0 and h^-h^0 amplitudes are aligned.

in Chapter 12. As a result there are three isospin analyses that can be performed, one for each of the transversity amplitudes. Naïve factorization expectations (Suzuki, 2002) indicated that one would expect the longitudinal polarization (*CP*-even) to dominate over the transverse one (a *CP* admixture), which had the implication that analysis of these decays could be simplified from a full angular treatment to a partial angular one where only the fraction of longitudinally polarized events needed to be extracted from data (see Chapter 12). However, the polarization measurements of charmless B decays available at the time were not straightforward and did not all support the expectation of nearly a 100% longitudinal polarization contribution (see Section 17.4). It had also been noted in (Aleksan et al., 1995) that using naïve factorization calculations one obtains a definite hierarchy of penguin contributions in $B \to \pi\pi$, $\rho\pi$ and $\rho\rho$ final states. The results of these calculations implied that the penguin contributions would be largest for $B \to \pi\pi$ decays and smallest for $B \to \rho\rho$. However at the time the B Factories started taking data this message had not been widely appreciated by the community. Given that one expects the ratio of amplitudes of $\rho\rho$ to $\pi\pi$ decays to be $\mathcal{O}(f_\rho^2/f_\pi^2) \sim 2.5$, one could piece together a credible theoretically motivated scenario that indicated the $\rho\rho$ final states might be an attractive alternative way to measure ϕ_2, if one could overcome the experimental challenges. Fortunately, the longitudinal polarization in $B^0 \to \rho^+\rho^-$ final state has been found to be consistent with unity (Aubert (2004w); Somov (2006)). Moreover, the neutral branching fraction $B^0 \to \rho^0\rho^0$ was found to be relatively small (Aubert (2007h, 2008r); Chiang (2008)), which constrains the penguin uncertainty in the $B \to \rho\rho$ system significantly (see Section 17.4 for the details of the branching fraction measurements of the decays $B^0 \to \rho^+\rho^-$, $B^0 \to \rho^0\rho^0$ and $B^+ \to \rho^+\rho^0$). Shortly after the observation of $B^0 \to \rho^+\rho^-$, *BABAR* performed a time-dependent *CP* asymmetry measurement as a proof of principle that one could indeed constrain ϕ_2 (Aubert, 2004ag) using larger data samples. It has been noted by Falk et al. (2004) that there could be a small $I = 1$ component to $B \to \rho\rho$, which could be tested by measuring S as a function of the difference between the mass of the two ρ's. Any departure from uniformity would indicate that there is an $I = 1$ component, in which case the isospin construct required to correct for penguins would require some modification.

17.7.1.2 Dalitz analysis of $B \to \rho\pi$

The B Factories have performed analyses of the quasi-two-body final states $B \to \rho\pi$ to check our theoretical control over extracting ϕ_2.

A proposed analysis of quasi-two-body final states (Lipkin, Nir, Quinn, and Snyder, 1991; Snyder and Quinn, 1993) relies on the isospin symmetry of the rates of all $B \to \rho\pi$ modes. The decay channels $B^+ \to \rho^0\pi^+$ and $B^0 \to \rho^\pm\pi^\mp$ have been observed first by Belle (Gordon, 2002) and then by *BABAR* (Aubert, 2003h). Evidence for the $B^0 \to \rho^0\pi^0$ mode, which was expected to be small, has been reported by Belle (Dragic, 2004) with a rate higher than an upper bound obtained by *BABAR* (Aubert, 2004g). However, these two results are in agreement at the level of 1.5σ. The remaining mode $B^+ \to \rho^+\pi^0$ has two neutral pions in the final state that makes it a challenging measurement. *BABAR* has reported the observation of this mode (Aubert, 2004g). These analyses are described in detail in Section 17.4.

A better approach uses a Dalitz-plot analysis of $B \to 3\pi$ final states, which relaxes the quasi-two-body approximation and uses information from the interference between resonances in the corners of the Dalitz plot. Snyder and Quinn (1993) pointed out that a time-dependent Dalitz-plot analysis (TDPA) of $B^0 \to \rho\pi \to \pi^+\pi^-\pi^0$ offers a unique way to determine the angle ϕ_2 without discrete ambiguities. The TDPA uses isospin symmetry and takes into account contamination from $b \to d$ penguin transitions. Additional information to constrain ϕ_2 can be provided by the measurements of $B^+ \to \rho^+\pi^0$ and $\rho^0\pi^+$ (Gronau, 1991; Lipkin, Nir, Quinn, and Snyder, 1991). Technicalities required to perform a TDPA can be found in Chapter 13.

A preliminary TDPA was reported by *BABAR* at ICHEP in 2004 using a data sample of 213 million $B\overline{B}$ pairs. Subsequent analyses have been published by both Belle (Kusaka, 2007) and *BABAR* (Aubert, 2007v; Lees, 2013c) using larger data samples.

Future Flavor Factories should study the Dalitz plots for $B \to 3\pi$ states beyond intermediate $\rho\pi$ contributions and also explore $B \to K\overline{K}\pi$ to search for possible signs of NP as a non-leading source of *CP* violation.

17.7.1.3 $B \to a_1(1260)\pi$, $B^0 \to a_1(1260)K$ constraints

The last set of decay modes considered at the B Factory experiments for the extraction of ϕ_2 is $B^0 \to a_1^\pm(1260)\pi^\mp$,

with $a_1^{\pm}(1260) \to \pi^{\mp}\pi^{\pm}\pi^{\pm}$. As with the previous examples these decays proceed mainly via $b \to u\bar{u}d$ tree amplitudes which can be used to measure time-dependent *CP* asymmetries and allow one to extract the angle ϕ_2. As with the other modes discussed in this section the existence of non-trivial penguin amplitudes complicates the extraction of ϕ_2.

Similar to $B \to \rho\pi$ decays, B meson decays to $a_1^{\pm}(1260)\pi^{\mp}$ final states are not *CP* eigenstate decays, so to extract ϕ_2 from these channels one needs to simultaneously consider $B^0(\overline{B}^0) \to a_1^+(1260)\pi^-$ and $B^0(\overline{B}^0) \to a_1^-(1260)\pi^+$ transitions (Aleksan, Dunietz, Kayser, and Le Diberder, 1991). One might cope with the difficulty due to the contribution of penguin amplitudes by using isospin symmetry (Gardner, 1999; Gronau, 1991; Gronau and London, 1990; Gronau and Zupan, 2004; Lipkin, Nir, Quinn, and Snyder, 1991) or a TDPA (Quinn and Silva, 2000; Snyder and Quinn, 1993) or approximate $SU(3)$ flavor symmetry (Charles, 1999; Gronau, London, Sinha, and Sinha, 2001; Grossman and Quinn, 1998).

A full isospin analysis requires the precise measurement of the branching fractions and time-dependent asymmetries in the five modes (and their *CP* conjugates) $B^0 \to a_1^+(1260)\pi^-$, $a_1^-(1260)\pi^+$, $a_1^0(1260)\pi^0$, $B^+ \to a_1^+(1260)\pi^0$, $a_1^0(1260)\pi^+$. Currently the poor precision of most of these measurements (Aubert, 2007i,ae) does not permit the application of this method.

As pointed out in the references (Quinn and Silva, 2000; Snyder and Quinn, 1993) the angle ϕ_2 may be extracted without ambiguities from a TDPA. This method has been successfully applied to the decay $B^0 \to \pi^+\pi^-\pi^0$ by both experiments. This approach could also be applied to the decay $B^0 \to \pi^+\pi^-\pi^0\pi^0$ with contributions from $a_1^+(1260)\pi^-$, $a_1^-(1260)\pi^-$, $a_1^0(1260)\pi^0$, and $\rho^+\rho^-$ amplitudes or to the decay $B^0 \to \pi^+\pi^-\pi^+\pi^-$ with contributions from $a_1^+(1260)\pi^-$, $a_1^-(1260)\pi^+$, and $\rho^0\rho^0$ amplitudes. Such analyses would be difficult because of the four particles in the final state, the small overlapping region of the phase space of the pions from the $a_1^{\pm}(1260)$ and $a_1^0(1260)$ mesons, uncertainties in the $a_1(1260)$ meson parameters and line shape, the small number of signal events and the large expected background.

Gronau and Zupan (2006) proposed an $SU(3)$-based procedure for extracting ϕ_2 in the presence of penguin contributions that the B Factories have followed. This procedure requires measurements of B meson decays into the axial-vector plus pseudoscalar final states $a_1\pi$, a_1K, and $K_1\pi$.

BABAR (Aubert, 2006aj) and Belle (Dalseno, 2012) measure the branching fraction of the B^0 meson decay to $a_1^{\pm}(1260)\ \pi^{\mp}$ to be relatively large ($\sim 3 \times 10^{-5}$, see Section 17.4). Following on from the observation of this decay mode *BABAR* performed a set of measurements of $a_1\pi$ and a_1K decays to extract the angle ϕ_2. This includes the time-dependent asymmetry measurement of B decays to $a_1^{\pm}(1260)\pi^{\mp}$ (Aubert, 2007ae), and observation of both $B^+ \to a_1^+(1260)K^0$ and $B^0 \to a_1^-(1260)K^+$ decays (Aubert, 2008ae). The final piece of information required to constrain ϕ_2 using this approach is the branching fraction of B decays to $K_1\pi$, which was also measured by *BABAR* (Aubert, 2010d), where K_1 denotes the axial vector excited K meson states.

The method chosen by *BABAR* for the study of $B^0 \to a_1^{\pm}(1260)\pi^{\mp}$ decays follows the quasi-two-body approximation. The decays $B^0(\overline{B}^0) \to a_1^{\pm}(1260)\pi^{\mp}$ have been reconstructed with $a_1^{\pm}(1260) \to \pi^{\mp}\pi^{\pm}\pi^{\pm}$. The other subdecay modes with $a_1^{\pm}(1260) \to \pi^{\pm}\pi^0\pi^0$ could be used to enhance statistics, however these are ignored as they have low reconstruction efficiency and large background. From a time-dependent *CP* analysis one extracts an effective angle $\phi_2^{\rm eff}$ which, in analogy with the approaches described above, is an approximate measure of the angle ϕ_2. Details on this approach for the decays $B^0 \to a_1^{\pm}(1260)\pi^{\mp}$ are discussed by Gronau and Zupan (2006). Applying flavor $SU(3)$ symmetry one can determine an upper bound on $\Delta\phi_2 = |\phi_2 - \phi_2^{\rm eff}|$ by relating the $B^0 \to a_1^{\pm}(1260)\pi^{\mp}$ decay rates with those of the $\Delta S = 1$ transitions involving the same $SU(3)$ multiplet of $a_1(1260)$, $B \to a_1(1260)K$ and $B \to K_{1A}\pi$. The K_{1A} meson is a nearly equal admixture of the $K_1(1270)$ and $K_1(1400)$ resonances (Amsler et al., 2008). The rates of $B \to K_{1A}\pi$ decays can be derived from the decay rates of $B \to K_1(1270)\pi$ and $B \to K_1(1400)\pi$.

Motivated by the $B \to a_1\pi$ study *BABAR* performed a search for the related decay $B \to a_1^{\pm}\rho^{\mp}$ using a data sample of $100\,{\rm fb}^{-1}$, but were unable to establish the presence of a significant signal (Aubert, 2006as). Future experiments may have sufficient data to isolate a clean sample of $a_1^{\pm}\rho^{\mp}$ and augment the list of channels used in the determination of ϕ_2.

17.7.1.4 $SU(3)$ constraints on ϕ_2 using $B^0 \to \rho^+\rho^-$ and $B^+ \to K^{*0}\rho^+$ decays

A way to constrain penguin contributions to $B^0 \to \rho^+\rho^-$ decays using $SU(3)$ flavor symmetry was proposed by Beneke, Gronau, Rohrer, and Spranger (2006), and is referred to here as the BGRS method. The amplitude of this decay has SM contributions from both tree and penguin topologies, so may be written as

$$A(B^0 \to \rho^+\rho^-) = Te^{i\phi_3} + Pe^{i\delta_{PT}}, \qquad (17.7.8)$$

where T and P are the magnitudes of the tree and penguin contributions to the decay, ϕ_3 is the Unitarity Triangle angle introduced in Chapter 16, and δ_{PT} is the strong phase difference between the tree and penguin contributions. Interference between the amplitudes in Eq. (17.7.8) and those responsible for $B^0 - \overline{B}^0$ mixing results in the time-dependent asymmetry of this decay being sensitive to ϕ_2 as discussed above. The $SU(3)$ related decay $B^+ \to K^{*0}\rho^+$ only proceeds via a penguin transition, so one can use knowledge of the branching fraction and longitudinal polarization fraction of this decay to constrain the corresponding penguin contribution in $\rho^+\rho^-$ up to $SU(3)$ breaking corrections.[78]

[78] As the fraction of longitudinally polarized events is near one it is possible to neglect information contained in the *CP*